

Hong Jiang *Editor*

Proceedings of The 20th Pacific Basin Nuclear Conference

Volume 3



 Springer

The Springer logo, which consists of a stylized chess knight icon followed by the word 'Springer' in a serif font.

Proceedings of The 20th Pacific Basin Nuclear Conference

Hong Jiang
Editor

Proceedings of The 20th Pacific Basin Nuclear Conference

Volume 3



 Springer

Editor
Hong Jiang
China Nuclear Power Engineering Co., Ltd
Beijing
China

ISBN 978-981-10-2313-2 ISBN 978-981-10-2314-9 (eBook)
DOI 10.1007/978-981-10-2314-9

Library of Congress Control Number: 2016954597

© Springer Science+Business Media Singapore 2017

This work is subject to copyright. All rights are reserved by the Publisher, whether the whole or part of the material is concerned, specifically the rights of translation, reprinting, reuse of illustrations, recitation, broadcasting, reproduction on microfilms or in any other physical way, and transmission or information storage and retrieval, electronic adaptation, computer software, or by similar or dissimilar methodology now known or hereafter developed.

The use of general descriptive names, registered names, trademarks, service marks, etc. in this publication does not imply, even in the absence of a specific statement, that such names are exempt from the relevant protective laws and regulations and therefore free for general use.

The publisher, the authors and the editors are safe to assume that the advice and information in this book are believed to be true and accurate at the date of publication. Neither the publisher nor the authors or the editors give a warranty, express or implied, with respect to the material contained herein or for any errors or omissions that may have been made.

Printed on acid-free paper

This Springer imprint is published by Springer Nature
The registered company is Springer Nature Singapore Pte Ltd.
The registered company address is: 152 Beach Road, #22-06/08 Gateway East, Singapore 189721, Singapore

Organising Committee

TPC:

Track	Chair	Co-Chair	Secretariat
1	Tianmin Xin	Jiejuan Tong, Guowei He, Guohan Chai, Zhegang Ma, Jean Marie Mattei, Hussein S. Khalil, Jordi Roglans-Ribas	Denghua Chen, Yuchen Jiang
2	Tao Zhang	Yamin Miu, Tunfeng Qi, Tan Hong, Chuming Zhang, Xi Zhao, Chris Dawes, Pierre Tremblay, Chunkuan Shih	He Zhang
3	Chunning Jing	Zhiwei Zhou, Shenjie Gu, Donghui Zhang, Patrick Mariteau, Cecilia Martin-del-Campo, Takashi Takata	Wanjue Wang
4	Guoqing Deng	Yawei Mao, Shengdong Zhang, Anxi Cui, Xinhua Liu, Ju Wang, Stephane Bargues, Pascal Chollet, Chilton Huang, Gerd-Michael Burow	Chuan Zhang
5	Ming Li	Jianshe Chai, Zhaohua Chi, Liming Fan, Xingqiang Zhou, Hottelart Herve, Jenq-Hong Liang, King Lee	Chan Zhou
6	Guoan Ye	Jing Chen, Qingnuan Li, Shuming Peng, Jean Pierre Gros, Christophe Poinssot, Temitope Taiwo, Kazuhiro Suzuki	Jiali Xiong
7	Danrong Song	Xuru Duan, Dongsheng Li, Hadid Subki, Dan Ingersoll, Joel Guidez, Alain Becoulet, Marco E. Ricotti	Jing Lei, Tuo Shao
8	Changhong Yuan	Bo Yang, Tao Li, Yun Lou, Sichao Tan, Laura Hermann, Mimi Limbach, Pascal Chollet	Xiaoqing Liu, Jia Yang
9	Xiaozhe Ling	Jiang Hu, Chunhua Lu, Daguang Zhu, Jianfeng Wang	Xiangting Chen
10	Zuoxiang He	Sijin Li, Yongxue Zhang, Zhifu Luo, Yaming Li, Yuejin Hua, Henry Bom	Qingxin Xia
11	Suyuan Yu	Liangming Pan, Tomio Okawa, Igor Pioro, Sama Bilbao y Leon, Hyoung Kyu Cho	Cheng Chen

Contents

Part I Power Reactor and New Buildings

Analysis and Design of the Common Raft for a Chinese Third-Generation Nuclear Power Plant	3
Sun Xiaoying, Sui Ran, Meng Jian and Liu Yulin	
A Fatigue-Crack Propagation Analysis Program and Its Application	17
Yongjun Gao	
A Study on the Tensile Properties of Materials at Elevated Temperature in RCC-M	29
Lifeng Guo, Yuxin Wang and Zhe Li	
Analysis Method of the Temperature for the Heavy Reflector	43
Shi Lin, Fang Jian and Ran Xiaobing	
Analysis on Super-Long Frame Structure of Main Building of Conventional Island	55
Shi Lichao, Wang Zhicong, Jia Weichao and Huang Yankun	
Application of an Adaptive COMET Method to a PWR Benchmark Problem with Gadolinium	69
Kyle Remley, Farzad Rahnema, Dingkang Zhang and Andrew Johnson	
Calculation and Analysis of Cavitation for Low-Head Safety Injection Pump	85
Changliang Liu, Sheng Meiling, Jingmeng Qiu and Wenhong He	
Coupled Neutronics and Thermal-Hydraulics Analysis of Annular Fuel Assembly for SCWR	93
Chuanqi Zhao, Kunpeng Wang, Liangzhi Cao, Hongchun Wu and Youqi Zheng	

Dynamic Sliding Mode Control of Nuclear Steam Generator Water Level Using LPV Schemes	105
Li Jie, Huang Rongyi and Wang Junling	
Experimental Flow Instability Study of a Natural Circulation Loop with Supercritical CO₂	121
Lei Zhang, Vijay Chatoorgoon and Robert Derksen	
Experimental Study on Secondary Passive Residual Heat Removal System	143
Haiyan Xu, Xiaohang Wu, Qinglong Wen, Donghua Lu and Liangguo Li	
I²S-LWR Concept Update	153
Bojan Petrovic, Farzad Rahnema, Chaitanya Deo, Srinivas Garimella, Preet Singh, KkochNim Oh, Ce Yi, Dingkang Zhang, Annalisa Manera, John Lee, Thomas Downar, Andrew Ward, Paolo Ferroni, Fausto Franceschini, David Salazar, Belle Upadhyaya, Matt Lish, Indrajit Charit, Alireza Haghighat, Matthew Memmott, Guy Boy, Abderrafi Ougouag, Geoffrey Parks, Dan Kotlyar, Marco Ricotti, Nikola Čavlina, Davor Grgić, Dubravko Pevec, Mario Matijević and Nick Irvin	
Main Building of Conventional Island Performance Assessment Based on Different Methods of Elasto-Plastic Analysis	169
Lichao Shi, Zhicong Wang, Weichao Jia and Yankun Huang	
Monte Carlo Study on Radial Burnup and Isotope Distribution	179
Cenxi Yuan, Shengli Chen and Xuming Wang	
Numerical Instability Study of Supercritical Water Flowing Upward in Two Heated Parallel Channels	187
Sujuan Li, Vijay Chatoorgoon and Scott Ormiston	
Numerical Investigations of the Helium Flow in Mini-Scale Gaps	201
Haoran Peng and Jun Sun	
Numerical Simulation on Water Hammer Phenomenon for Single Feedwater Line	219
Meiling Sheng, Ting Hou and Jiaming Zhao	
Power Transients of the HTR-10 During Reactivity Insertion ATWS Tests	231
Feng Gou, Fubing Chen and Yujie Dong	
Research on Controlling Conditions of Cooling Water from Small Modular Reactors at Coastal Site	239
Ben-jing Tang, Shu-qiang Hou and Wei Bai	

**Steam Hammer Calculation and Study of Nuclear Island
Main Steam Pipe Network** 257
 Jiaming Zhao, Yemin Dong, Meiling Sheng and Yao Pi

**Study on Improvement of Capacity Expansion of Spent Fuel
Pit Cooling System in PWR Nuclear Power Plants** 267
 Yupei Piyue

**Study on Standards Applicable for Primary and Secondary
Water Chemical Analysis in the Third-Generation PWR** 275
 Qinghua Li, Guangfei Wang, Yao Pi, Bo Li and Xiaoli Yang

**Study on the Localization of Instrumentation Installation
Materials for AP1000** 283
 Shuen Lu, Chengli Qin and Haibo Wu

**The Affection Analysis of Cross Talk on Power Range
Measured Signal** 291
 Chu-hua Tang, Jie Chen and Wei Chen

**The CFD Simulation on Grid-Spacer and Wire
for Lead-Cooled Fast Reactor** 299
 Gao Xinxin and Qiu Ruoxiang

Development of a 3D Core Calculation Code: COCO 313
 Li Cai, Chen Jun, Gao Shengnan, Lu Haoliang and Li Jinggang

The Gen-III Nuclear Power Technology in the World 321
 Yanrui Li, Chao Chen, Pingping Xin, Yajun Chen and Huiqun Hou

**The Methodology to Compensate Ex-core Nuclear
Instrument Signal by In-core Nuclear Instrument Signal** 329
 Chu-hua Tang, Jie Chen and Wei Chen

**The Numerical Simulation Research of Gas-Liquid Two-Phase
Flow in Small-Break Loss-of-Coolant Accidents** 339
 Yilin Zhang, Shanfang Huang, Xiaoyu Guo and Renjie Xiao

**The Resistance Characteristics Study of Emergency
Feedwater System** 349
 Qiu Jimmeng, Sheng Meiling, Liu Changliang and Liu Jiang

**The Setting of RPN Power Range Calculation Parameters
in Fuqing Nuclear Power Plant** 357
 Fanfeng Meng

**Transient Analyses of Main Steam Line Break Accident
for High-Power Passive Reactor** 365
 Zhuang Shaoxin, Sun Wei, Jing Jianping, An Jieru
 and Zhang Chunming

Transmutation Analysis of Nuclear Waste in a Gas Fast Reactor.	375
Cecilia Martin-del-Campo, Ricardo Reyes-Ramirez, Guillermo Bastida-Ortiz and Juan-Luis Francois	
“Practical Elimination on Large Release of Radioactive Materials” and Safety Performance Research on HPR1000.	385
Xing Ji and Wang Hui	
Part II Waste Management	
Research on Treatment of Simulated Nuclear Power Plant Waste Liquid.	401
Wenjun Zheng and Zhentao Zhang	
An Introduction to Sanmen Nuclear Power Plant’s Radwaste Management Information System	413
Liu Huichun	
Analysis of Liquid Effluents Discharge Method Under Normal Condition of One Inland NPP in the Northern Areas of China.	425
Lei Xing, Yongchun Yang, Hang Lv and Guanghui Ma	
Application Method Study of Erica Model and R&D128 Model in Radiological Impact Assessment of Terrestrial Organisms	431
Hongyan Du, Xiaoping Bai, Qiming Wei and Yawei Mao	
Derivation of Activity Limits of Spent Radioactive Source for Near-Surface Disposal.	441
Liu Jianqin, Xiong Xiaowei, Sun Qinghong and An Hongxiang	
Development and Application of Gamma-Radioactivity Nondestructive Measurement System for Complex Radiation Field	453
Yongjun Gao	
Development of the Concrete Cask Storage System for PWR Spent Nuclear Fuel in Korea	469
Baeg Chang-Yeal and Cho Chun-Hyung	
Evaluation of Algorithms of Dispersion Coefficients with a Field Tracer Experiment over Complex Terrain	473
Hao Zhu and Fengju Li	
Influences of Additives on the Performances of the Cementation of Simulated Radioactive Fluoride Liquid Wastes	487
Zhenghua Qian, Xueyang Liu, Yanbo Qiao, Shuai Wang, Hongjun Ma and Yaping Sun	
Minor Actinides Incineration in a Small Molten Salt Fast Reactor.	497
Chenggang Yu, Chunyan Zou, Yuwen Ma and Jingen Chen	

Overview of Radioactive Waste Treatment in Domestic Nuclear Power Plants of Pressurized Water Reactor	507
Meng Hongshe	
Solidification of Simulated α-HLLW in Iron Phosphate Glass-Ceramics	515
Pan Sheqi, Wan Xiaogang, Xi Chengcheng, Su Wei, Zhang Hailing and Wang Yongpeng	
Study on Effect of Density Heterogeneity for Nuclear Waste Drum Samples in Segmented Gamma Scanning Analysis	525
Honglong Zheng, Xianguo Tuo, Shuming Peng, Rui Shi and Chao Deng	
Study on In-Drum Drying Technology of Waste Concentrates	535
Liang Dong	
Study on Radioactive Contaminated Soil Remediation Technologies and Selection Principles	547
Wang Shaowei, Shang Zhaorong, Wang Ping, Wei Guoliang and Dany Yuqin	
The Importance of Influence Factors of the Fly Ash Cement Solidification	555
Xue-yang Liu, Zheng-hua Qian, Yan-bo Qiao, Shuai Wang, Hong-jun Ma and Ya-ping Sun	
The Influence of Thermal Irradiation Synchronously Aging on the Structure of Modified Sodium Bentonite	563
Wei Liu, Shuaiwei Zhao, Liang Dong, Zhontian Yang, Honghui Li, Jianqin Liu and Lei Wan	
The Introduction of the Safety Assessment of HLW Disposal in 2014–2017 in China	577
Hong-hui Li	
The Melting Treatment of Radioactive Steel Scrap from Decommissioning Nuclear Facility	589
Junxian Deng, Xin Li and Feng Deng	
The Radioactive Waste Minimization of Tianwan NPP Units 3&4	597
Tiejun Liu, Zhiyin Zhang and Xiaorui Qu	
The Management Status and Advices of Radioactive Solid Waste from Development and Utilization of Mineral Resources	607
Caixia Lv, Shujun Xie, Keyan Teng, Qing Sheng and Ailing Zhang	
The Study of Microwave Ashing for Spent Radioactive Resin	617
Chao Gao, Meilan Jia and Yadong Wang	

Preliminary Study on the Vitrification of Molten Salt Reactor Radwastes Containing Fluorides by Phosphate Glass.	623
Yan-bo Qiao, Ya-ping Sun, Xue-yang Liu, Zheng-hua Qian, Shuai Wang and Hong-jun Ma	
Part III Acquiring Medical and Biological Benefits	
An Organic Adsorbent Resin for Ga-68 Generator	637
Ming-Hsin Li	
Assessment of Production Channels of Isotopes for Combined PET/SPECT Imaging	641
Chary Rangacharyulu, Ramy Tannous and Christine K. Roh	
Part IV Student Program	
2D Multi-group Transport Calculation on Hexagonal Geometry with the Method of Characteristics	649
Haodong Shan, Hong Yu and Li Xu	
A Detection of ²²⁶Ra Concentration in Water Around a Decommissioned Uranium Mine in Hunan Province.	661
Hui Jin and Tianyuan Xin	
A Study of Spray Application by a Fire Truck for the Mitigation of Severe Accident Outside the Nuclear Power Plant.	671
JongWook Go, Irfan Younus and ManSung Yim	
Application of Planar Laser-Induced Fluorescence to Measurement of Concentration Field in the Downcomer.	681
Tingjie Zhao, Sichao Tan, Xiaoyu Wang, Yunjia Yang and Ruiqi Wang	
Assessing the Conservatism in EPZ Determined on Plume Centerline Dose: A CALPUFF-Based Method Used in Level 3 PSA.	691
Weipeng Shu, Yawei Mao and Wei Liu	
Preparation and Properties of Multifunctional Pt/Ce_{0.7}Zr_{0.3}O₂ Honeycomb Catalyst for Detritiation.	705
Quanwen Wu, Wenhua Luo, Jingwen Ba, Xiayan Yan and Daqiao Meng	
Classification Methodologies for Nuclear Spent Fuel Forensic.	711
Sanghwa Lee, Seungmin Lee and Gyunyoung Heo	
Developing a Conceptual Design of Suction-Based Ex-containment Radioactive Release Barrier System and Defining its Design Limits.	723
Seong-Woo Kang and Man-Sung Yim	

Development and Validation of Subchannel Code SUBSC 743
 Jun Chen, Liangzhi Cao, Chuanqi Zhao, Hongchun Wu
 and Zhouyu Liu

**Wall Temperature Fluctuation Under Flow Pulsation
 in a Vertical Tube** 757
 Xin Liu, Sichao Tan, Hongsheng Yuan and Li Feng

**Experimental Study on Natural Circulation Flow
 in Rectangular Channel Under Rolling** 771
 Jiangwen Wang, Puzhen Gao and Chong Chen

High-Heat-Flux Heat Removal Using a Porous-Micro-Channel. 781
 Junki Ohashi, Akihiro Tsukamoto, Koji Enoki and Tomio Okawa

**Neutronics Characteristics Study of Conceptual Space
 Heat-Pipe-Cooled Fast Reactor Core** 791
 Hui Zhao, Hongli Chen, Chong Chen, Qin Zeng
 and Haoran Zhang

**Numerical Simulation on Thermal Stratification
 in the Containment after LOCA** 799
 Ke Zhao, Tianmin Xin, Yong Yu and Hui Wang

Optimal Control Rod for Boron-Free Small Modular PWR 809
 Jiwon Choe, Ho Cheol Shin and Deokjung Lee

Power Optimization of Steam Generators Under Fault Conditions. 817
 Huasong Cao, Peiwei Sun and Jianmin Zhang

**Propagation of Nuclear Data Uncertainties for PWR Burnup
 Calculation** 835
 Chenghui Wan, Liangzhi Cao, Hongchun Wu, Tiejun Zu
 and Wei Shen

**Research on Multi-objective Optimization Method
 for Maintenance Decision of Nuclear Power Plant** 845
 Lv Yan, Liu Jingquan and Zeng Yuyun

**Simulation Analysis of Condensation Heat Transfer Inside
 C-type Tubes Based on RELAP5/MOD3.2** 865
 Wangsheng Tian, Xiabin Cao, Zhongning Sun, Yongyong Yang
 and Wenjing Lei

**Sodium-Cooled Fast Breed Reactor Fuel Failure Detection
 Based on Cover Gas Monitoring** 881
 Han Rui and Chen Shu-ming

Study on Two-Phase Flow Instabilities in Straight and Helical Tubes 893
Ruiting Dong, Fenglei Niu and Yuan Zhou

Validation of the Cross-Calibration Multispectral Infrared Thermography in Surface Temperature Measurements. 905
Auve Benjamin, Huber Alexander, Sergienko Gennady, Joffrin Emmanuel, Sun Jun, Huber Valentina, Price Marcus and Silburn Scott

Validation of Wall Friction Model in Multidimensional Component of Mars with Two-Phase Flow Experiments Describing ECC Behavior in Downcomer 929
Chi-Jin Choi, Jin-Hwa Yang, Hyoung-Kyu Cho, Dong-Jin Euh and Goon-Cherl Park

Part I
Power Reactor and New Buildings

Analysis and Design of the Common Raft for a Chinese Third-Generation Nuclear Power Plant

Sun Xiaoying, Sui Ran, Meng Jian and Liu Yulin

Abstract This paper describes the analysis and design of the common raft for a Chinese third-generation nuclear power plant. The configuration of the common raft and the key methodologies involving in its analysis and design were studied. The general finite element software ANSYS was used to build the finite element model of nuclear island buildings, apply the loads on the model, and finally obtain the stress distribution and therefore the reinforcement requirement. During the process, transient temperature analysis method was adopted to get the temperature distribution in the common raft when accident condition happened. Instead of quasistatic method, the time history analysis method was employed in the stability analysis of the common raft. The common raft design was optimized by using the advanced techniques mentioned above.

Keywords Nuclear island building · Common raft · Finite element method · Time history analysis · Stability analysis

1 Introduction

The target nuclear power plant in this paper adopts china's advanced third-generation nuclear power technology. Provision of one common raft for nuclear island building is the characteristic of this third-generation technology. Because the reactor building, the safeguard building, the fuel building, and the electrical building (R-building, S-building, F-building, and E-building) shared one raft foundation, which is called common raft, the plane size of the common raft is very large (approximately 100×100 m). Furthermore, the thickness of common raft is not uniform and it varies in some local regions. The common raft has a complex geometry configuration, which leads into a complicated stress distribution in the transition zone between two buildings. The seismic responses of the buildings

S. Xiaoying (✉) · S. Ran · M. Jian · L. Yulin
China Nuclear Power Engineering Co., Ltd, Beijing, China
e-mail: Sunxy@cnpe.cc

supported by the common raft are different and are not simultaneous. Thus, a more accurate method is required to evaluate the sliding forces and the overturning moments caused by loads from these buildings. In addition, the temperature distribution in the common raft is not linear under the accident condition. A transient temperature analysis method should be used to obtain an accurate temperature distribution to avoid an overconservative design. All these key aspects and methodologies were studied in this paper. The general finite element software ANSYS was used to analyze the stress distribution in the common raft to make sure that the design of the common raft is safe and economical.

2 Analysis and Design Process

2.1 Finite Element Model

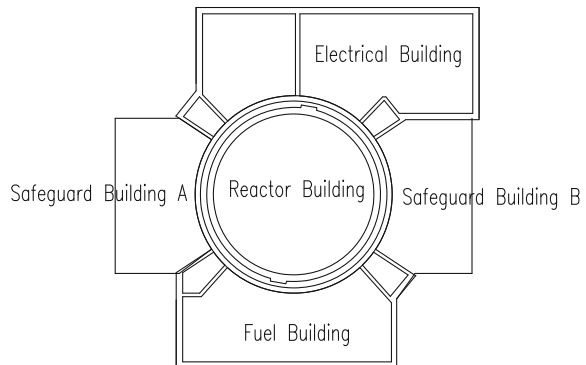
2.1.1 Finite Element Model of Common Raft

The reactor building, the safeguard building, the fuel building, and the electrical building of the nuclear island share one common raft whose plane size is about 100×100 m. Figure 1 shows the plan view of the common raft:

The average thickness of the common raft under the F-building, the E-building, and the S-building is 2.2 m, while the thickness under the R-building is 4.2 m. Additionally, the thickness above the gallery is 6.7 m. When modeling the common raft in ANSYS, different element types were chosen according to the different thickness requirements. The common raft portion having the thickness of 2.2 m was modeled by shell element using SHELL181, while the common raft portion thicker than 2.2 m was modeled by solid element using SOLSH190. Figure 2 shows the finite element model of the common raft:

The shell element and solid element were connected using a special shell element. The special shell elements shared the common nodes with solid elements,

Fig. 1 Plan view of the common raft



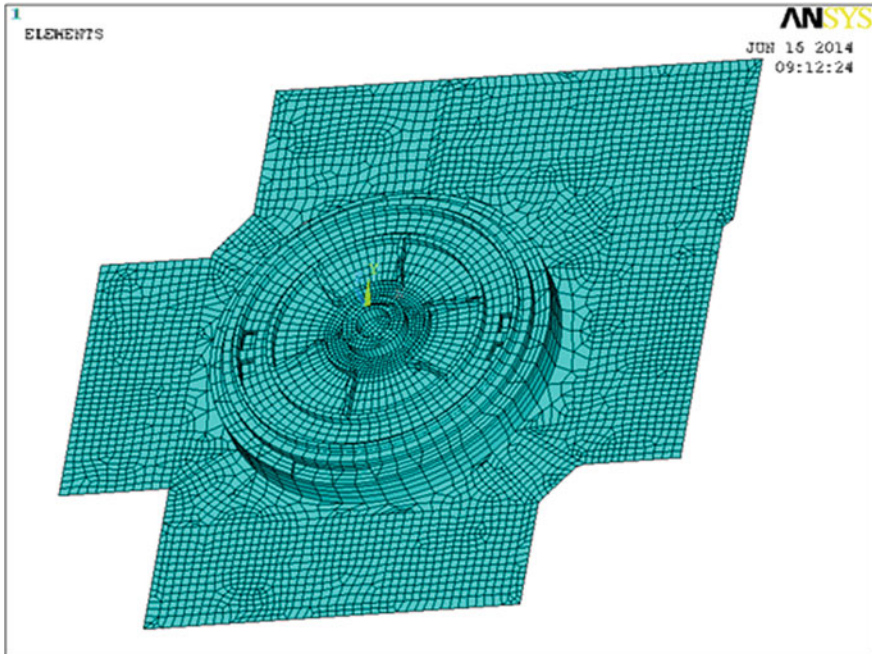


Fig. 2 Model of the common raft

having the same thickness with the elements of the adjacent walls but a very small density. The special shell elements also have the common nodes with the shell elements of the common raft. As shown in Fig. 3, the shell elements and the solid elements are connected well and the moment from the superstructures can be transferred to the common raft appropriately.

2.1.2 Models of Superstructures

The superstructures (R-building, S-building, F-building, and E-building) were modeled by shell elements according to its actual geometries and dimensions. It should be noted that only main structural members such as walls, slabs, and columns were modeled. The masses of equipment were considered as an equivalent density being added to the elements of local position. Figures 4 and 5 show the finite element models of the superstructures above the common raft.

2.1.3 Finite Element Model of Foundation

The soil elements were modeled by the group of spring elements under the common raft. The total stiffness of the foundation is calculated according to *Code for Seismic*

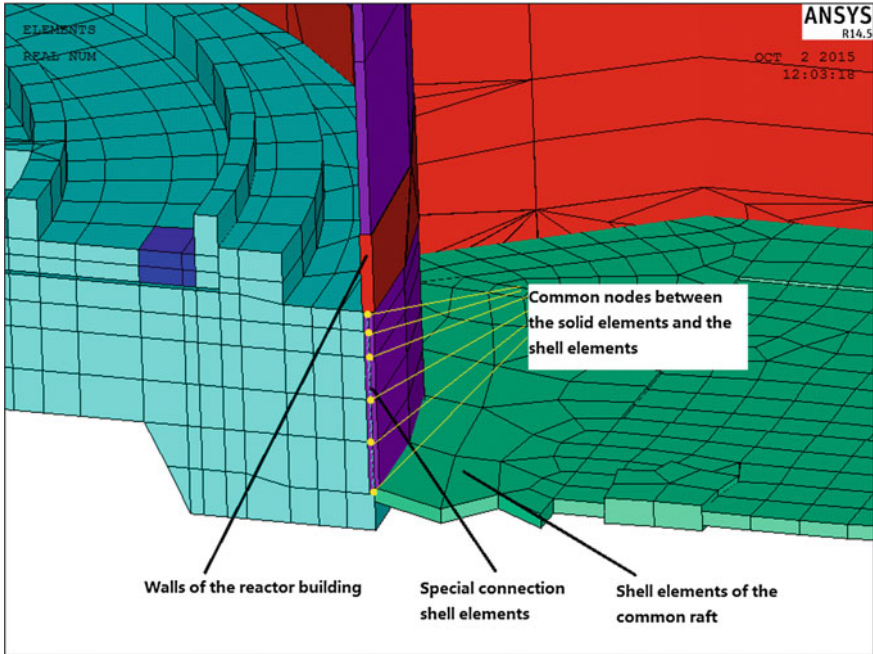


Fig. 3 Model of the common raft

Design of Nuclear Power Plants [1] and then distributed to each nodes of the common raft based on the specific principles. Each node has five spring elements (horizontal X-axis, horizontal Y-axis, vertical, rocking around X-axis, rocking around Y-axis). The collection of those springs can simulate the supporting of the soil foundation to the nuclear island buildings.

2.2 Stress Analysis and Reinforcement Calculation

2.2.1 Load and Member Forces

According to *Design Requirements for Prestressed Concrete Containment for Pressure Water Reactor Nuclear Power Plant* [2], the elementary loads considered in the common raft design are as follows:

- (1) D: permanent loads, including dead weight of structures, lateral earth pressure, hydrostatic pressure, equipment dead loads, effects of concrete creep, and shrinkage;
- (2) L: live loads, including live loads of movable equipment and other live loads (such as personnel weight, construction loads, polar crane loads);

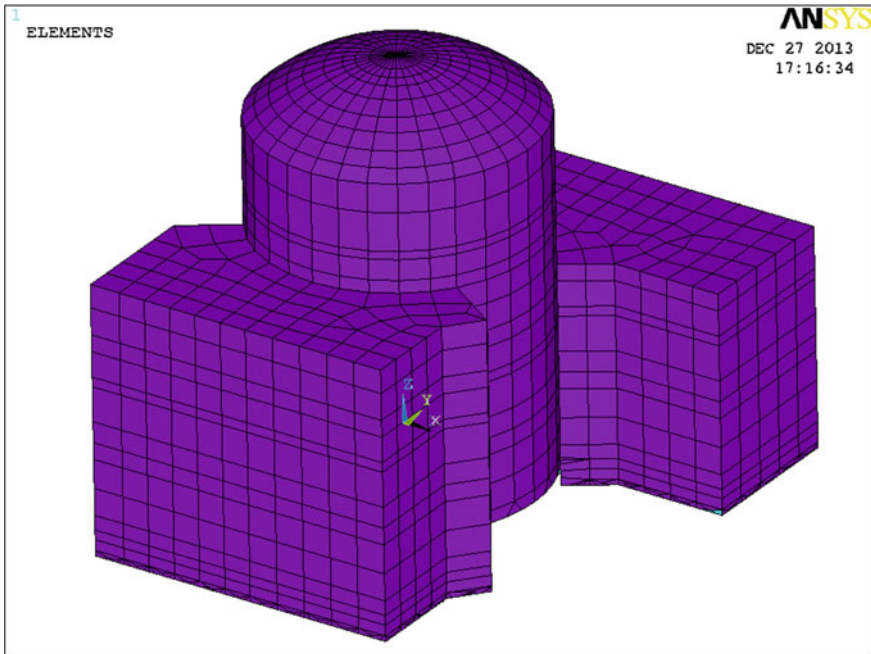


Fig. 4 Model of the reactor building

- (3) T_0 : thermal effects during normal operating or shutdown conditions;
- (4) F : loads resulting from application of prestressing;
- (5) P_a : pressure load generated by design basis accident;
- (6) T_a : thermal effects generated by design basis accident;
- (7) SL-1: operating basis earthquake; and
- (8) SL-2: safe shutdown earthquake.

It should be noted that (1) transient temperature analysis method was used in present analysis to obtain accurate temperature distribution in the common raft to model rapid temperature increase and decrease when loss of coolant accident (LOCA) occurs; (2) the peak ground acceleration for E_2 is 0.3 g.

Totally eighteen load combinations were considered according to the code *Design Requirements for Prestressed Concrete Containment for Pressure Water Reactor Nuclear Power Plant* [2]. The member forces of the common raft (such as axial force, moment, shear force) for each load combination were calculated in ANSYS. Figure 6 shows only the member forces of the solid element of the common raft. The transverse axis in the Fig. 2.6a represents the radial distance between reactor core and the section under consideration. The longitudinal axis represents the value of the member forces. The curves with different colors represent the variation of the member forces. The indexes on the curves represent the load combination number.

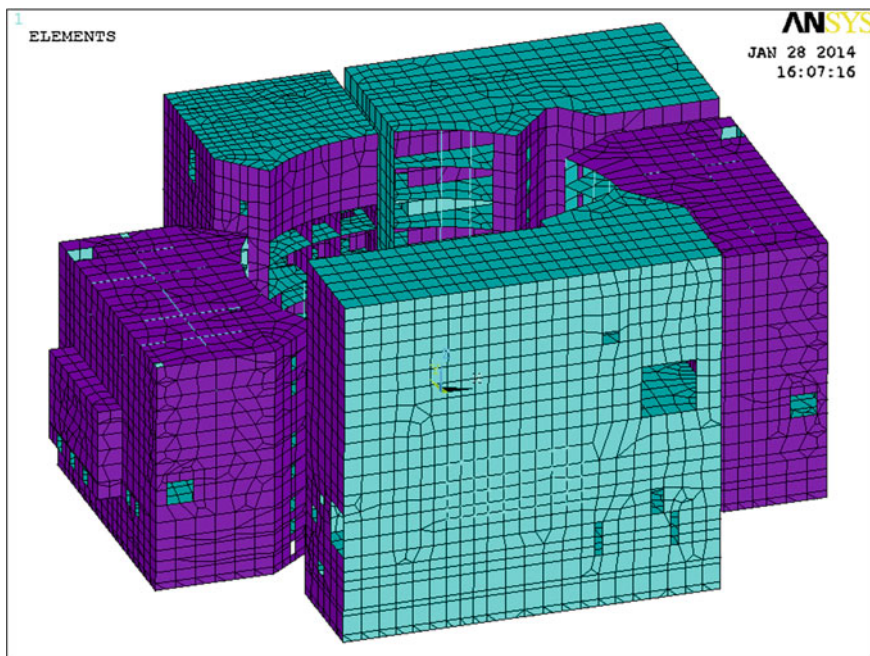


Fig. 5 Models of the S-building, E-building, and F-building

The member forces of the shell element of the common raft were not presented in this section because of the limited space.

2.2.2 Reinforcement Calculation and Layout

The required reinforcement including longitudinal reinforcement and shear reinforcement for each load combination is calculated according to *Design Requirements for Nuclear Safety Related Concrete Structure for Pressure Water Reactor Nuclear Power Plant* [3]. Figure 7 shows the reinforcement requirement of the common raft (solid element). As mentioned in Sect. 2.2.1, the transverse axis represents the radial distance between the reactor core and the section under consideration. The longitudinal axis represents the reinforcement amount. The curves with different colors represent the required reinforcement of the cross sections at different radii. The reinforcement amounts of the 18 load combinations were enveloped for the design of reinforcement.

Figure 8 shows the contour plan of the required reinforcement of the common raft (shell element). It should be noted that the required reinforcement was obtained by enveloping the required reinforcement of 18 load combinations. Different colors represent different reinforcement amounts that can be approximately estimated from the legend.

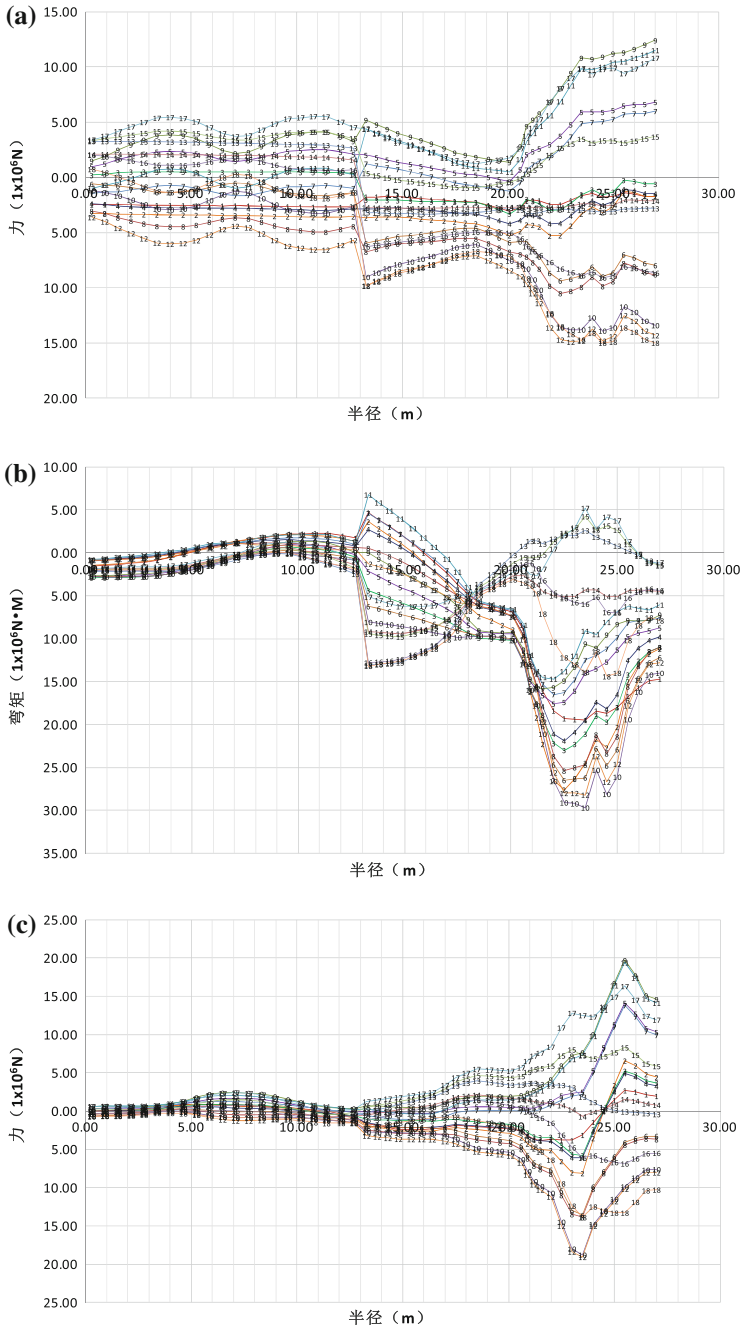


Fig. 6 Member forces of the common raft (*solid elements*) for different load combinations: **a** axial forces; **b** moment; **c** shear forces

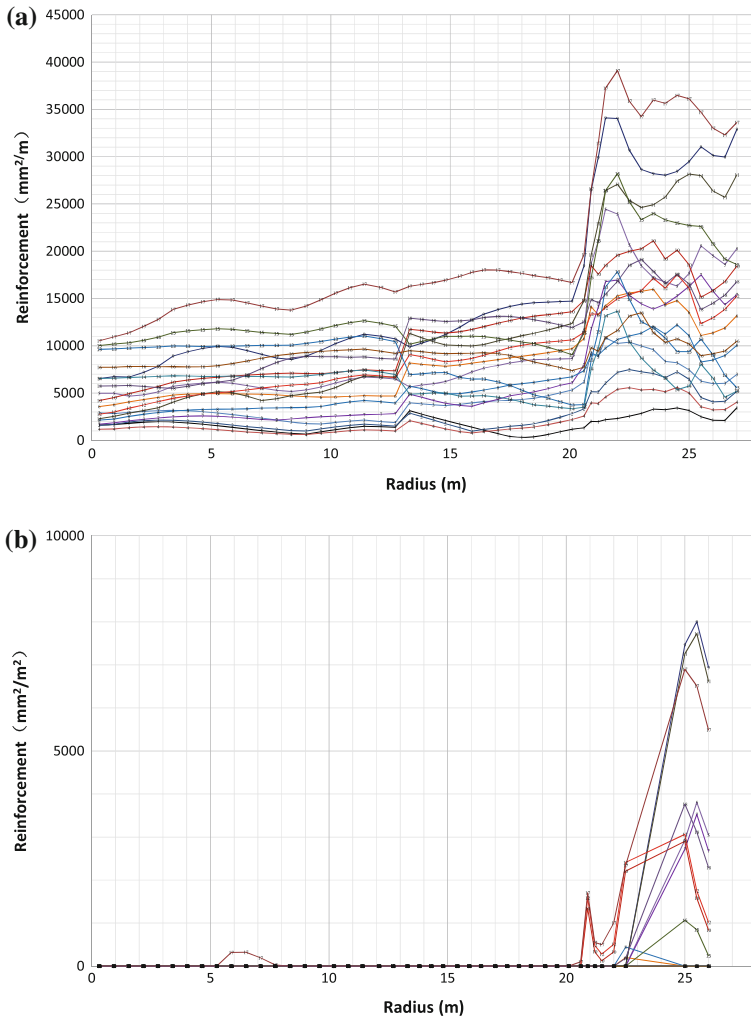


Fig. 7 Reinforcement requirement of the common raft (*solid elements*) for different load combinations: **a** longitudinal reinforcement; **b** shear reinforcement

Based on the enveloped reinforcement requirement and the configuration of the common raft, the reinforcement layout has been determined. Figure 9 shows only the reinforcement layout sketch in one location where the layout of the reinforcement is the most complicated. Reinforcement layout of other locations was not presented in this section because of limited space.

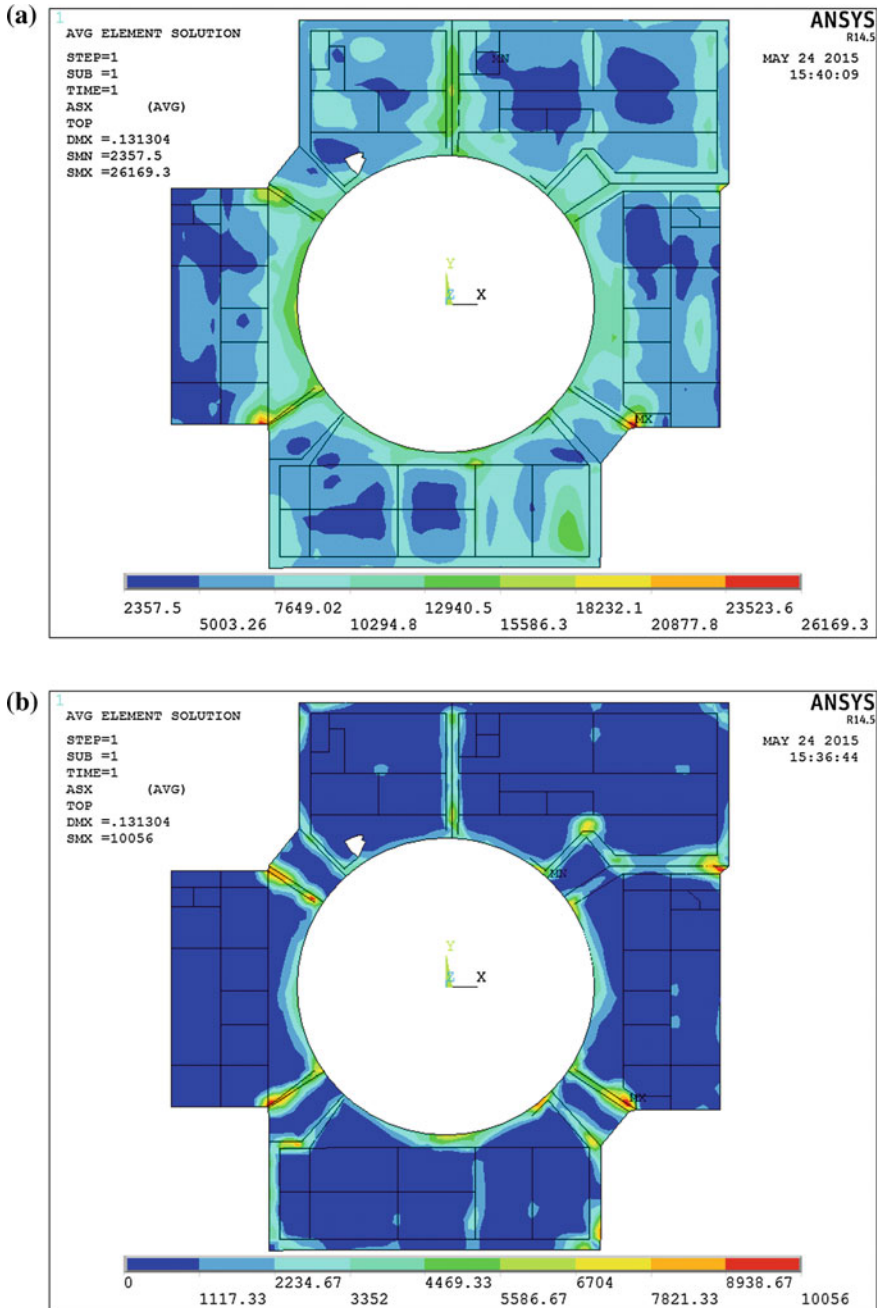


Fig. 8 Reinforcement requirement of the common raft (*shell elements*) for different load combinations: **a** longitudinal reinforcement; **b** shear reinforcement

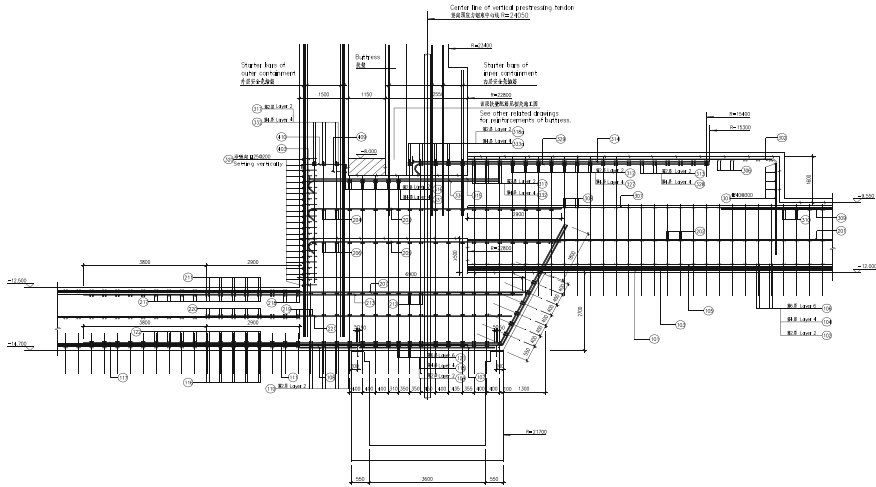


Fig. 9 Reinforcement layout sketch of the common raft

3 Stability Evaluation

The stability of the common raft was analyzed according to *Code for Seismic Design of Nuclear Power Plants* [1] and *Design code for nuclear safety related plants foundation for pressure water reactor nuclear power plants*. It should be noted that the partial factors of loads in load combination are 1.0 when evaluating the stability of the common raft.

3.1 Safety Against Sliding

According to *Code for Seismic Design of Nuclear Power Plants* [1] and *Design code for nuclear safety related plants foundation for pressure water reactor nuclear power plants* [4], the safety against sliding is calculated using the following formula:

$$\frac{E_r}{E_h} \geq K_h \quad (1)$$

where

E_r horizontal resistance acting on foundation (kN);

E_h sliding force acting on the common raft (kN);

K_h factor of safety against sliding, see *Code for Seismic Design of Nuclear Power Plants* [1].

Table 1 Factor of safety against sliding

SL-1	X-direction	E_r (10^5 kN)	20.08	
		E_h (10^5 kN)	5.26	
		E_r/E_h	3.81	
	Y-direction	E_r (10^5 kN)	21.79	
		E_h (10^5 kN)	6.93	
		E_r/E_h	3.144	
	Safety factor limit	K_h	1.5	
	SL-2	X-direction	E_r (10^5 kN)	16.27
			E_h (10^5 kN)	13.61
E_r/E_h			1.2	
Y-direction		E_r (10^5 kN)	20.98	
		E_h (10^5 kN)	18.21	
		E_r/E_h	1.15	
Safety factor limit		K_h	1.1	

Time history analysis method was used to obtain accurate total sliding forces caused by loads of all superstructures above the common raft. The traditional quasistatic method assumes that the seismic response at different floor elevations occurs at the same time, and the response of different superstructures is simultaneous. By using time history method, the time histories of the sliding force for each building can be obtained and added to get the trend of total sliding force varied with time. It can also be found that when the maximum sliding force happens. By substituting the maximum sliding force and the horizontal resistance into formula (1), the minimum factor of safety against sliding can be calculated. Table 1 shows the evaluation results for the safety factor of common raft against sliding under SL-1 and SL-2 earthquakes.

3.2 Safety Against Overturning

According to *Code for Seismic Design of Nuclear Power Plants* [1] and *Design code for nuclear safety related plants foundation for pressure water reactor nuclear power plants* [4], the safety against overturning is calculated using following formula:

$$\frac{\sum M_r}{\sum M_q} > K_q \quad (2)$$

where

M_r , moments resisting overturning (kN m) around X-axis or Y-axis, including resistance moment caused by gravity. The negative effect from upward vertical earthquake and buoyancy shall be considered;

Table 2 Factor of safety against overturning

SL-1	Around X-axis	$M_r(10^6 \text{ kN-m})$	224.96
		$M_q(10^6 \text{ kN-m})$	51.11
		M_r/M_q	4.4
	Around Y-axis	$M_r(10^6 \text{ kN-m})$	230.29
		$M_q(10^6 \text{ kN-m})$	43.6
		M_r/M_q	5.28
Safety factor limit	K_q	1.5	
SL-2	Around X-axis	$M_r(10^6 \text{ kN-m})$	224.96
		$M_q(10^6 \text{ kN-m})$	144.88
		M_r/M_q	1.56
	Around Y-axis	$M_r(10^6 \text{ kN-m})$	230.29
		$M_q(10^6 \text{ kN-m})$	118.17
		M_r/M_q	1.95
	Safety factor limit	K_q	1.1

M_q overturning moments (kN m) around X-axis or Y-axis due to horizontal earthquake and upward vertical earthquake;

K_q factor of safety against overturning, see *Code for Seismic Design of Nuclear Power Plants* [1].

Because of the same reason mentioned in Sect. 3.1, time history analysis method was also used here to obtain the time history of the total overturning moments caused by all the superstructures. By substituting the maximum total overturning moment and resisting moment into formula (2), the minimum factor of safety against overturning can be calculated. Table 2 shows the evaluation results of safety factors for the common raft against overturning under SL-1 and SL-2 earthquakes.

The results in Tables 1 and 2 shows that the factor of safety against overturning and sliding meets the design requirements. There is no underground water in the target nuclear power plant site; therefore, the floatation evaluation is not required to perform.

4 Conclusions

This paper mainly focused on the common raft analysis and design of a Chinese third-generation nuclear power plants. Using the general finite element software ANSYS, the stress distribution in the common raft and the required reinforcement were computed according to the Chinese national codes. The stability of the common raft was also evaluated.

The advance techniques were applied in the design of the common raft, which are as follows: (1) multitype finite element modeling method to make sure that the finite element model of the common raft is close to the actual structure; (2) transient

temperature analysis method to obtain accurate temperature distribution in the common raft under LOCA accident; and (3) time history analysis method to capture the variation of the total sliding force and overturning moment under earthquake to avoid an overconservative evaluation. All these techniques made the common raft design more safe and economical. The whole design methodology can be a reference to other third-generation nuclear power plants, which also adopt the common raft for the nuclear island buildings.

References

1. Code for Seismic Design of Nuclear Power Plants GB50267-97.
2. Design Requirements for Prestressed Concrete Containment for Pressure Water Reactor Nuclear Power Plant NB/T 20303-2014.
3. Design Requirements for Nuclear Safety Related Concrete Structure for Pressure Water Reactor Nuclear Power Plant (NB/T20012-2010);
4. Design code for nuclear safety related plants foundation for pressure water reactor nuclear power plants(NB/T 20308-2014).

Author Biography

Sun Xiaoying is working as senior engineer at Building Design Department of China Nuclear Power Engineering CO., Ltd. and mainly involves in the following: (1) application of advance techniques for the analysis and design of complex nuclear island structures; (2) fluid structure interaction analysis; and (3) seismic soil–structure interaction analysis.

A Fatigue-Crack Propagation Analysis Program and Its Application

Yongjun Gao

Abstract The theoretical models, calculation algorithms, and an application example of LBB-FATIGUE program are described. Based on the crack propagation analysis method of linear elastic fracture mechanics (LEFM), LBB-FATIGUE program is developed to calculate the propagation length versus the design-transient loads and operational time as well as the lifetime of a fatigue crack in austenite stainless steel pipes within the primary coolant environment of PWR or BWR plants or in the air ($t > 100$ °C). The main calculation models are as follows: (1) The influence of the primary coolant environment to the fatigue-crack growth rate(FCGR) is considered; (2) according to the superposition principle, the variation range of the total stress intensity factor K_I is expressed as the sum of tension subpart K_I^t and bending subpart K_I^b ; (3) F functions given by Sander's analysis for pure-tension load and pure-bending load are adopted; (4) the design-transient loads are a series of variable amplitude loads which are considered as an equal amplitude load alone, and expressed as variation range of tension force and bending moment; (5) Newton method or the chasing method is used to calculate the variation of the crack propagation length versus design-transient cyclic numbers. In the leak-before-break (LBB) analysis for the primary circuit of CPR1000 nuclear power plant (NPP), the propagation length and the lifetime of a postulated circumferential through-wall crack (TWC) in the sensitive fractural position under design-transient loads are calculated by LBB-FATIGUE program.

Keywords LBB-Fatigue Program • Fatigue-Crack Propagation Analysis • LBB Analysis

Y. Gao (✉)

Nuclear Safety Center, Suzhou Nuclear Power Institute,
Xihuan Road, No. 1788, Suzhou, Jiangsu Province, China
e-mail: gaoyongjun@cgnpc.com.cn

1 Introduction

In the LBB analysis for the primary circuit of NPP, it is necessary to demonstrate that the operators have adequate time to take protective measures before the fast catastrophic fracture (the instable propagation) takes place in the primary pipes. In order to meet these needs, LBB-FATIGUE program has been developed to estimate the crack subcritical propagation lifetime and the crack length versus the design-transient loads and operational time.

The crack propagation can be divided into the instable propagation and the subcritical propagation [1]. The instable propagation implies that the structure damage will occur if the crack propagates a step further. The subcritical growth rate is relevant to the propagation mechanisms, the load magnitudes, etc. According to the load types and the environmental media, the subcritical propagation mechanisms include the creep, the fatigue, the stress corrosion, and corrosion fatigue [2, 3].

Because the maximum design temperature of the primary circuit of NPP is lower than the creep temperature of the austenite stainless steel (about 450 °C), there is no need to consider the creep failure mechanism in the LBB analysis of the primary circuit. In the meanwhile, the operational limits (such as the limits for the pH value, Cl^- and SO_4^{2-} concentration) of the primary circuit can ensure that the probability of pipe failure caused by the stress corrosion and the corrosion fatigue is extremely low [2–4]. So, the fatigue is considered as the sole mechanism of the crack subcritical propagation in the LBB analysis of the primary circuit.

The methods for estimating the crack fatigue lifetime include the crack propagation analysis method of LEFM, S–N nominal stress method, and ϵ –N local strain method [6, 7]. The crack propagation analysis method of LEFM is based on the classic Paris law to estimate the propagation lifetime of the fatigue crack. At present, the curves of the crack growth rate of a great deal of engineering materials and the solutions of the stress intensity factor of each type of structures with cracks can be obtained, so the crack propagation analysis method of LEFM has been widely applied in the engineering projects.

However, there are four key issues shall be solved in the application of the crack propagation analysis method of LEFM for analyzing the propagation of the fatigue crack in the primary circuit of NPP: (1) How to consider the influences of the coolant environment conditions within the primary circuit to the FCGR? (2) How to calculate the stress intensity factor under the complex tension and bending loads? (3) How to consider the decomposition of the complicated design-transient loads? (4) How to design an effective algorithm for solving the differential equation? In this chapter and Chapter “[A Study on the Tensile Properties of Materials at Elevated Temperature in RCC-M](#)”, the theoretical models and calculation algorithms of LBB-FATIGUE program are described. In Chapter “[Analysis Method of the Temperature for the HeavyReflector](#)”, a calculation example of LBB-FATIGUE program for LBB analysis of primary circuit of CPR1000 NPP is given.

2 Theoretical Models

LBB-FATIGUE program adopts the crack propagation analysis method of LEFM to calculate the propagation length versus the design-transient loads and operational time as well as the lifetime of a fatigue crack in austenite stainless steel pipes within the primary coolant environment of PWR or BWR plant or in the air ($t > 100$ °C). The calculation models of LBB-FATIGUE program are described in this chapter.

2.1 Symbol Table

1. K_I : the total type I stress intensity factor, $\text{MPa}\sqrt{\text{m}}$
2. K_I^t and K_I^b : the type I tension stress intensity factor and the type I bending stress intensity factor, $\text{MPa}\sqrt{\text{m}}$
3. K_I^{max} and K_I^{min} : the maximum and minimum values of the type I stress intensity factor in a load cycle, $\text{MPa}\sqrt{\text{m}}$
4. ΔK_I : the variation range of the total type I stress intensity factor in a load cycle, $\text{MPa}\sqrt{\text{m}}$
5. ΔK_I^t and ΔK_I^b : the variation range of the type I tension stress intensity factor and the type I bending stress intensity factor in a load cycle, $\text{MPa}\sqrt{\text{m}}$
6. ΔK_{th} : the threshold value of the variation range of the stress intensity factor, $\text{MPa}\sqrt{\text{m}}$
7. r ratio: $K_I^{\text{min}}/K_I^{\text{max}}$
8. F and M : tension force and bending moment, N and $N\text{ m}$
9. ΔF and ΔM : the variation range of the tension force and the bending moment in a load cycle, N and $N\text{ m}$
10. σ_t and σ_b : the tension stress and the bending stress, N/m^2
11. $\Delta\sigma_t$ and $\Delta\sigma_b$: the variation range of the tension stress and the bending stress in a load cycle, N/m^2
12. F_t and F_b : F function for the pure-tension loads and the pure-bending loads
13. a , a_0 and a_c : the half length, the initial half length, and the critical half length of a crack, m
14. a_0^i and a_f^i : the crack half length at the beginning and the end of the i th design transient, m
15. R , R_o and R_i : the average radius, the outer radius, and the inner radius of the pipe, m
16. θ : the half angle of the crack opening
17. N : the number of the load cycles
18. N_c : the fatigue-crack propagation lifetime
19. N_d^i : the cycle number of the i th design transient
20. da/dN : FCGR, m/cycle
21. C and m : the parameters in Paris law

22. C_0 : the parameter used to consider the temperature influence
23. S : the parameter used to consider the influence of r ratio
24. T : the temperature, °F
25. T_r : ascending time of the load in a load cycle, s
26. I : the inertia moment, kg m²

2.2 Law of the Fatigue-Crack Propagation

The FCGR is related to the variation range of the stress intensity factor around the crack tip (ΔK_I) [1, 10]. When $\Delta K_I \leq \Delta K_{th}$, the crack does not propagate. When $a \geq a_c$, the fast instable propagation occurs. When $\Delta K_I > \Delta K_{th}$ and $a < a_c$, the slow stable propagation takes place.

Under the condition of slow stable propagation, the FCGR and ΔK_I show linearity relationship in the dual-logarithm coordinates system (i.e., coincide with Paris law [10, 11]):

$$\frac{da}{dN} = C(\Delta K_I)^m \quad (1)$$

here, C and m are up to material type and the environment media.

2.3 FCGR of the Austenite Stainless Steel Within Primary Coolant Environment of PWR Plant

The fatigue-crack propagation behavior of the austenite stainless steel is influenced by the temperature, r ratio, and the environment media.

Under the condition of air media, the FCGR of the austenite stainless steel is [11]:

$$\left[\frac{da}{dN} \right]_{\text{AIR}} = C_{\text{AIR}}(\Delta K_I)^m \quad (2)$$

here, the units of da/dN and ΔK_I are inch/cycle and ksi $\sqrt{\text{in}}$, respectively. The parameter C_{AIR} and m can be calculated by the following correlations, respectively:

$$C_{\text{AIR}} = C_0 \times S \quad (3)$$

$$m = 3.3 \quad (4)$$

Here, C_0 is used to consider the temperature influence and can be expressed as the function of the temperature. S is used to consider the influence of r ratio and can be expressed as the function of r ratio.

Equation (2) can be rewritten as [12]:

$$\left[\frac{da}{dt}\right]_{\text{AIR}} = C_{\text{AIR}}(\Delta K_I)^m / T_r \quad (5)$$

The following correlation is used to calculate the FCGR of the austenite stainless steel within the primary coolant environment of PWR plants:

$$\left[\frac{da}{dt}\right]_{\text{PWR}} = \left[\frac{da}{dt}\right]_{\text{AIR}} + 1.5 \times 10^{-4} \left[\frac{da}{dt}\right]_{\text{AIR}}^{0.5} \quad (6)$$

Here, the unit of da/dt is m/s.

2.4 FCGR of the Austenite Stainless Steel Within Primary Coolant Environment of BWR Plant

The FCGR of the austenite stainless steel within the BWR coolant environment is [14]:

$$\frac{da}{dN} = 8.17 \times 10^{-12} T_r^{0.5} (\Delta K_I)^{3.0} / (1 - r)^{2.12} \quad (7)$$

here, $1 \text{ MPa}\sqrt{\text{m}} \leq \Delta K \leq 50 \text{ MPa}\sqrt{\text{m}}$. If $T_r < 1 \text{ s}$, then $T_r = 1 \text{ s}$. If it is difficult to give T_r value, then $T_r = 1000 \text{ s}$. If $r \geq 0$, then $\Delta K_I = K_I^{\text{max}} - K_I^{\text{min}}$. If $r < 0$, then $\Delta K_I = K_I^{\text{max}}$.

The ratio of the FCGR of the austenite stainless steel in the air, PWR, and BWR coolant environment is 1:2:3.5 for the same crack dimension [12, 13]. So, it is conservative to calculate the FCGR in the PWR coolant environment by using the correlation (7).

2.5 FCGR of the Steel in the Air ($t > 100 \text{ }^\circ\text{C}$)

The FCGR of the steel (include the stainless steel) in the air ($t > 100 \text{ }^\circ\text{C}$) or in the non-caustic environment can be calculated by the following correlation:

$$\frac{da}{dN} = 5.21 \times 10^{-13} (\Delta K_I)^{3.0} \tag{8}$$

here, the units of da/dN and ΔK_I are mm/cycle and $N/mm^{3/2}$, respectively.

The influences of load ratio r , the ascending time of the load T_r , and the environment are not considered in the above correlation. So, if this correlation is used to calculate the growth length of the postulated crack in the PWR primary circuit, the result is not conservative (smaller).

2.6 Calculation of the Crack-Opening Half Length

The fatigue-crack propagation lifetime N_c is the cyclic number propagated from the initial crack half length a_0 to the critical half length a_c . Under the equal amplitude alternate load, N_c can be calculated by the following equation:

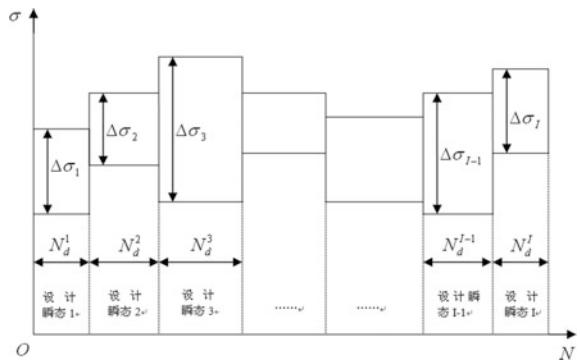
$$N_c = \int_{a_0}^{a_c} \frac{da}{C(\Delta K)^m} \tag{9}$$

The design-transient loads of the pipe are a sequence of the variable amplitude loads, but each type of the design-transient load can be considered as the equal amplitude load shown in Fig. 1).

For the i th design transient, it assumes that the initial half length of the crack is a_0^i , and the final half length is a_f^i after the crack experiences N_d^i cycles. a_f^i can be calculated by using the following equation:

$$N_d^i = \int_{a_0^i}^{a_f^i} \frac{da_i}{C(\Delta K_i)^m} \tag{10}$$

Fig. 1 The stress variation of the design transients



2.7 Calculation of the Variation Range of the Stress Intensity Factor

In the elastic range, according to the superposition principle, the variation range of the total stress intensity factor ΔK_I can be expressed as the sum of tension subpart and bending subpart:

$$\begin{aligned}\Delta K_I &= \Delta K_I^t + \Delta K_I^b \\ &= \sqrt{\pi R\theta}[\Delta\sigma_t F_t(\theta) + \Delta\sigma_b F_b(\theta)]\end{aligned}\quad (11)$$

2.8 Calculation of the Variation Range of the Stress

The variation range of the tension stress and the bending stress can be calculated by the following equations, respectively:

$$\Delta\sigma_t = \frac{\Delta F}{2\pi R t} \quad (12)$$

$$\Delta\sigma_b = \frac{\Delta M R}{I} \quad (13)$$

2.9 Calculation of F Function

F functions of the circumferential TWC under the pure-tension load and the pure-bending load given by Sander's analysis [9] are adopted:

$$F_t(\theta) = 1 + A_t \left(\frac{\theta}{\pi}\right)^{1.5} + B_t \left(\frac{\theta}{\pi}\right)^{2.5} + C_t \left(\frac{\theta}{\pi}\right)^{3.5} \quad (14)$$

$$F_b(\theta) = 1 + A_b \left(\frac{\theta}{\pi}\right)^{1.5} + B_b \left(\frac{\theta}{\pi}\right)^{2.5} + C_b \left(\frac{\theta}{\pi}\right)^{3.5} \quad (15)$$

here, the coefficients (i.e., $A_t, B_t, C_t, A_b, B_b,$ and C_b) in F functions are the functions of R/t .

3 Calculation Algorithms

The main algorithms and procedures are as follows:

1. Input data such as the pipe and crack dimensions and the loads.
2. Calculate $\Delta\sigma_t$ and $\Delta\sigma_b$ by using Eqs. (12) and (13).
3. Calculate F function by using correlation (14) and (15).
4. Calculate C and m , and calculate ΔK_I by using Eq. (11).
5. Solve the root a_f^i of equation $N_d^i - \int_{a_0}^{a_f^i} \frac{da_i}{C(\Delta K_I)^m} = 0$ by using Newton method or the chasing method.
6. Calculate Δa^i and $\left(\frac{da}{dt}\right)^i$.
7. Goes to [2] until $i > I$ (I is the number of the design transients).

Newton method is a standard method for solving the root of the equation and will not be described in detail.

The procedures of the chasing method are as follows:

1. Initialize the relevant data.
2. $a = a + \Delta a$, and calculate C , m and ΔK_I .
3. $NX = NX + \frac{\Delta a}{C(\Delta K_I)^m}$.
4. $\varepsilon_{ABS} = ABS(NX - N_d^i)$ and $\varepsilon_{REL} = \varepsilon_{ABS}/N_d^i$.
5. If $\varepsilon_{ABS} \leq \varepsilon_{ABS}^0$ and $\varepsilon_{REL} \leq \varepsilon_{REL}^0$, then the iteration stops, otherwise goes to [2].

Δa should be small enough to ensure the convergence criteria ($\varepsilon_{ABS} \leq \varepsilon_{ABS}^0$ or $\varepsilon_{REL} \leq \varepsilon_{REL}^0$) are satisfied. Δa can be automatically regulated by LBB-FATIGUE program according to the convergence status.

4 Application Example

In Ref. [16], it has been demonstrated that the leakage of the primary circuit of CPR1000 NPP can be detected by the leakage detective system before the fast catastrophic fracture takes place. According to the LBB criteria, the allowable time for the operators to take relevant measures shall be smaller than the time for propagating to the critical length after the leakage is detected and before the critical length reaches.

The following assumptions are made in the fatigue-crack propagation analysis:

- (a) The initial length of the TWC is the length corresponding to the minimum detectable leakage rate of the leakage detective system (4 gpm, safety factor 10 is considered). When the length of the TWC is smaller than the initial length, the leakage of the TWC is not detected by non-destructive examination (NDE), the leakage detective system or other checking ways (such as the daily round check).

- (b) The variation (transient) of the temperature and the pressure of the primary coolant leads to the stress variation and fatigue propagation of the TWC. The influences of other failure mechanisms (such as stress corrosion crack) are not considered.

4.1 Initial Dimension of the TWC

The initial length of the TWC is the length corresponding to the minimum detectable leakage rate of the leakage detective system (0.3169 m).

The allowable maximum length of the TWC is the critical length of the leaked TWC (0.343 m, safety margin 2 is considered).

4.2 Stress Amplitudes and Cyclic Number

In Ref. [17], the stress amplitudes and cyclic number of each design transient in susceptible fractural locations are given. By using these parameters, the propagation length of the leaked TWC can be conservatively estimated for the sake of comparing with the critical length of the leaked TWC.

It is not convenient to calculate the stress amplitudes of the design transients because there is a great deal of the relevant data, so it is necessary to make some simplifications. Because the FCGR of the TWC is related to the stress amplitudes, stress cyclic number and the ascending time, the following assumptions and considerations are made in the simplifications:

- (a) The similar design transients are merged, and the stress amplitudes of the post-merged design transients adopt the maximum stress amplitude of the pre-merged design transients.
- (b) It is assumed that the allowable time for the operators to take measures (such as the shutdown and repair) is 7 days after the leakage is detected, and the number of the design transients is conservatively estimated according to this assumption (less than once is regarded as once).
- (c) The ascending time of each design transient adopts the conservative value.
- (d) The design transients causing the crack closure are deleted.

4.3 Calculation Results and Analyses

The FCGR and the crack length of the TWC in 7 days are calculated by using LBB-FATIGUE program. The main results are as in Table 1.

Table 1 Results of fatigue propagation analysis

Transient no	Crack half length (m)	Increment of crack half length (m)	Average FCGR (m/s)	ΔK_I (MPa \sqrt{m})	C	m
Initial	0.1585	0.00E+00	0.00E+00	90.10	2.49E-10	3.30
1	0.1586	1.09E-04	2.76E-09	90.20	2.49E-10	3.30
3	0.1588	2.70E-04	3.21E-08	84.70	3.55E-10	3.30
8	0.1652	6.40E-03	2.07E-08	46.30	4.12E-10	3.30
12	0.1652	4.30E-06	4.30E-06	56.30	3.97E-10	3.30
15.2	0.1653	4.83E-05	1.34E-08	96.10	2.58E-10	3.30
25	0.1653	5.51E-05	3.67E-06	130.00	3.24E-10	3.30
59	0.1654	1.69E-05	9.39E-10	41.00	2.01E-10	3.30

It can be seen that the final propagation length of the TWC is 0.3308 m (the half length is 0.1654 m) which is smaller than the critical length of the leaked TWC. So, the operators have adequate time to take relevant measures to deal with the primary circuit leakage accident after the leakage is detected and before the critical length reaches.

5 Conclusion and Prospction

The theoretical models and calculation methods of LBB-FATIGUE program are described in this paper. LBB-FATIGUE program adopts the crack propagation analysis method of LEFM to calculate the crack propagation length versus the design-transient loads and operational time as well as the lifetime of a fatigue crack in austenite stainless steel pipes within the primary coolant environment of PWR or BWR plants or in the air ($t > 100$ °C).

An application example of crack propagation analysis for the primary circuit of CPR1000 NPP shows that there is adequate time for the operators to take protective measures to cope with the primary circuit leakage accident after the leakage is detected and before the critical length reaches (so one of the LBB criteria is met).

LBB-FATIGUE program is a useful tool for crack propagation analysis, especially for time-dependent fatigue-crack analysis problems such as the LBB demonstration.

LBB-FATIGUE program should be verified in detail in the future by comparing the calculation results with those of other similar-function credible programs.

References

1. Zhuang Zhuo, Jiang Chiping, “Engineering Fracture and Damage” (in Chinese), ISBN 7-111-14278-0, Machinery Industry Press, April 2004.
2. U.S. NRC, “Leak-Before-Break Evaluation Procedures”, Standard Review Plan (SRP), Section 3.6.3, NUREG-0800.
3. European Commission of Nuclear Safety and the Environment, “European Safety Practices on the Application of Leak-Before-Break (LBB) Concept”, EUR 18549 EN, January 2000.
4. Westinghouse Electric Company, “Technical Justification for Eliminating Pressurizer Surge Line Rupture as the Structure Design Basis for Point Beach Units 1 and 2 Nuclear Plants”, WCAP-15066, August 1998.
5. IAEA, “Reactor Water Chemistry Relevant to Coolant-Cladding Interaction”, IAEA-TECDOC- 429, Vienna, 1987.
6. Lin Xiaobin, “Virtual Fatigue Lifetime and Engineering Design” (in Chinese), Virtual Engineering and Science, P. 100–110, May 2001.
7. Yao Weixing, “Analysis of Structure fatigue Lifetime” (in Chinese), ISBN7-118-02946-7, National Defence Industry Press, October 2004.
8. Klecker R., Brust F, etc, “NRC Leak-Before- Break (LBB.NRC) Analysis Method for Circumferential Through-Wall-Cracked Pipes under Axial plus Bending Loads”, NUREG/CR- 4572, May 1986.
9. Sanders J. L, Jr, “Circumferential Through-Cracks in Cylindrical Shell under Combined Bending and Tension”, Journal of Applied Mechanics, March 1983, Vol.50, P.221.
10. Paris P, Erdogan F, “A Critical Analysis of Crack Propagation Laws”, ASME Journal of Basic Engineering, Vol.85, No.2, 1963, P.528.
11. ASME BPVC, “Rules for In-Service Inspection of Nuclear Power Plant Components”, ASME Code, Section XI, Appendix C, New York, 1998.
12. Chopra O. K, “Mechanism and Estimation of Fatigue Crack Initiation in Austenitic Stainless Steels in LWR Environments”, NUREG/CR- 6787, ANL-01/25, August 2002.
13. Shack W. J, etc, “Review of Environment Effects on Fatigue Crack Growth of Austenitic Stainless Steels”, NUREG/CR-6176, ANL-94/1, May 1994.
14. Itatani M, etc, “Fatigue Crack Growth Curve for Austenitic Stainless Steels in BWR Environment”, Journal of Pressure Vessel Technology, Vol.123, P.166–172, May 2001.
15. British Standards Institution, “Guide on Methods for Assessing the Acceptability of Flaws in Metallic Structures”, BS 7910:1999.
16. Gao Yongjun, “LBB Analysis for the Primary Circuit of CPR1000 NPP” (in Chinese), internal report of Suzhou Nuclear Power Institute, June 2009.
17. Gao Yongjun, “Reduction of Limiters and Dampers and the Stress Analysis for the Primary Circuit of CPR1000 NPP” (in Chinese), internal report of Suzhou Nuclear Power Institute, June 2009.

Author Biography

Gao Yongjun Gao Yongjun (1969–) is a senior engineer of researcher’s grade, graduated from the nuclear reactor engineering specialty of Shanghai Jiaotong University in 1991, engaged in incore fuel management calculation in Research Institute of Nuclear Power Operation (RINPO) in 1991–2005, goes in for the independent verification and review of the reactor core reloading design for the NPPs of CGNPC, nuclear safety research, and safety review of domestic NPPs, etc., in Suzhou Nuclear Power Institute (SNPI) from 2005 till now.

A Study on the Tensile Properties of Materials at Elevated Temperature in RCC-M

Lifeng Guo, Yuxin Wang and Zhe Li

Abstract The tensile properties of materials at elevated temperature shall be ensured for PWR (pressurized water reactor) nuclear components as the components normally are used in elevated temperature applications. ASME BPVC and RCC-M provide tensile properties at elevated temperature which are used to derive the allowable design stress for high-temperature service. However, it always confuses the code user to notice verification of elevated temperature tensile properties is required in RCC-M, while such requirement never appears in ASME BPVC. In this article, technical basis of the temperature-dependant tensile properties in ASME (Table U and Table Y-1 in Section II Part D) and RCC-M (Annex I Table ZI 2.0 and Table ZI 3.0 in Section I Subsection Z) is investigated, followed by an analysis on the effectiveness of verification tests in RCC-M. It is found that basically, the temperature-dependent tensile properties in RCC-M come from ASME BPVC, which is based on a so-called ratio-trend-curve method. The values given by this method are derived from the trend curve of the material and are different from the specified minimum properties at high temperature in EN standard, which are mandatory requirements for the material. Verification of tensile properties at certain temperature in RCC-M will improve the confidence to ensure the actual tensile results at high temperature will not be less than those listed in Table ZI 2.0 and Table ZI 3.0 (a 10% decrease for S_u need to be accounted); nevertheless, it does not mean the tensile properties in the whole range of elevated temperature can be guaranteed in RCC-M as those in EN standards, which provide a high confidence level and normally result in a decreased specified tensile properties at high temperature. Finally, suggestion for localization of nuclear code on requirements of temperature-dependent tensile properties is given.

Keywords Tensile properties · Elevated temperature · RCC-M

L. Guo (✉) · Y. Wang · Z. Li
China Nuclear Power Engineering Co. Ltd, Beijing, China
e-mail: guolf@cnpe.cc

© Springer Science+Business Media Singapore 2017
H. Jiang (ed.), *Proceedings of The 20th Pacific Basin Nuclear Conference*,
DOI 10.1007/978-981-10-2314-9_3

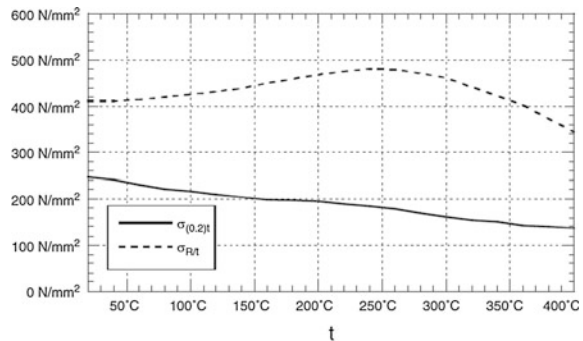
1 Introduction

The tensile properties, including ultimate tensile strength and yield strength, are critical material characteristics for design of pressure-retaining components. These properties are not only determined by the materials itself, but also are influenced by temperature, and time in some circumstances [1], which further results in creep and rupture strength. As the nuclear components for PWR are designed under the material “creep” range, only the effect of temperature needs to be taken into account.

Figure 1 demonstrates typical behavior of temperature-dependent tensile properties for carbon steel. It is noticeable that yield strength decreases with the increase in temperature, while ultimate tensile strength increases initially within a moderate range of temperatures and then decreases. The shape and the size of the tensile properties vs. temperature curve may be different for various steel grades. For austenitic stainless steel and nickel alloy, the behavior may be significantly different from that of carbon steel. To assure a reasonable design, the temperature-dependent strength properties of various materials shall be thoroughly investigated, and provide for the establishment of allowable design stress. In ASME BPVC (Boiler and Pressure Vessel Code), the tensile strength S_u and yield strength S_y at elevated temperature are tabulated in Table U and Table Y-1 of Section II Part D, and in RCC-M, the values are provided in Annex I Table ZI 2.0 and Table ZI 3.0 in Section I Subsection Z, respectively.

It is interesting to note there are specified minimum tensile properties at high temperature in RCC-M, whereas such requirements never appear in ASME BPVC. This fact always confuses the code user. This article will review the technical basis of the S_u and S_y values in ASME and RCC-M and analyse the verification tests at high temperature in RCC-M, with the aim to promote deeper understanding on this topic and give suggestion on the nuclear codes and standards in China.

Fig. 1 Typical behavior of temperature-dependent tensile strength and yield strength for carbon steel [1]



2 Technical Basis of S_u and S_y in ASME BPVC

In the USA, the evaluation of tensile properties at elevated temperature can be traced back to the work by ASTM-ASME Joint Committee on Effect of Temperature on the Properties of Metals in some decades ago [2, 3]. The committee sought to offer best possible assessments of various properties of materials as the basis to establish allowable stresses in design. The testing data were collected from different industries, government, institute, and university laboratories in the USA and generally did not represent systematic or coordinated test programs; i.e., the testing were conducted independently. The data were processed by a “ratio-trend-curve” method to evaluate the behavior of the temperature-dependent properties. To illustrate the basic principle of the method, an example is given below to evaluate yield strength of type 304L stainless steel.

The original data included testing data of type 304L from different lot and different product form (bar, plate, pipe, etc.). As the data were not generated by systematic test programs, it is not usually feasible to develop the trend curve for yield strength with temperature by simply passing a curve through the averages of the data at different temperatures. Such a curve would be subject to local distortion by limited data representing lots differing from the average. Therefore, the original data were normalized in terms of ratio of strength at temperature to the strength at room temperature, on the premise that a lot of material which exhibits relatively high strength at room temperature may reasonably be expected to exhibit high strength at elevated temperatures. By this treatment, it becomes possible to utilize all of the available data at high temperature if corresponding test data at room temperature are available [2].

Figure 2 shows the strength ratio vs. temperature for type 304L. Some data (identified with “x” mark) appeared to lie outside the general scatter band and were excluded from analysis by the committee. The excluded data were invariably on the high side for conservative purpose. Trend curve was derived for the remaining data by polynomial regression analysis. The regression process terminated at the polynomial degree for which there was no further reduction in the sum of the squares of the residuals. The best fit curve developed by the regression analysis is given in Fig. 2.

The derived strength ratios trend curve is believed to be the best estimation of the behavior of the temperature-dependent yield strength of type 304L. Therefore, specified minimum yield strength at room temperature may be computed directly with the ratio-trend-curve method to obtain the most probable value of the yield strength at temperature for a product whose yield strength at room temperature is equal to the specified minimum yield strength at room temperature. Figure 3 provides the curve of yield strength versus temperature when the specified minimum yield strength is 25 ksi at room temperature. The curve of tensile strength versus temperature is determined with the same approach.

In ASME BPVC, yield strength S_y in Table Y-1 of Section II Part D at ambient temperatures is based on the published values in the applicable material

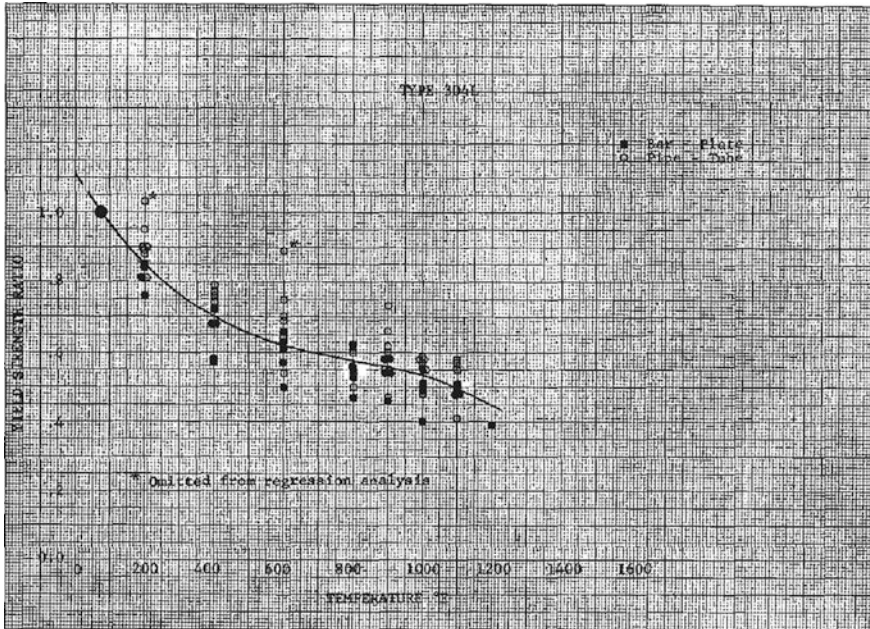


Fig. 2 Ratio versus temperature and derived trend curve for type 304L stainless steel [2]

specification, i.e., specified minimum yield strength; those at elevated temperatures are determined by the “ratio-trend-curve” method mentioned above. Tensile strength S_u in Table U is obtained with the same manner except at temperatures above the ambient temperature, the value are increased up to 10% as long as they do not exceed the specified minimum tensile strength at ambient temperature [4]. In the general note of Table Y-1, the ASME Committee states S_y do not corresponds exactly to “minimum” or “average” value of the material. Neither the ASME Section II nor Section III requires yield strength testing at high temperature for production material used in component fabrication. It is not intended that results of such tests, if performed, be compared with S_y for acceptance/rejection purpose. There is a similar description in the general notes of Table U.

The ASME process avoids the need for material organization to collect or guarantee elevated temperature strength of material. The process was developed at a time when there was substantial participation by material producers in the ASME code process, and they objected to having collected such data. Since the ASME process is a consensus process (rather than one determined by a government agency), a method was developed to avoid the necessity of collecting such data except when a new material is proposed to enter into the Code [5].

Supporting material cannot be found in the literature to justify why component designed with ASME BPVC is still safe even the actual material strength at elevated temperature, in some cases, may be lower than $S_u/1.1$ or S_y from which the

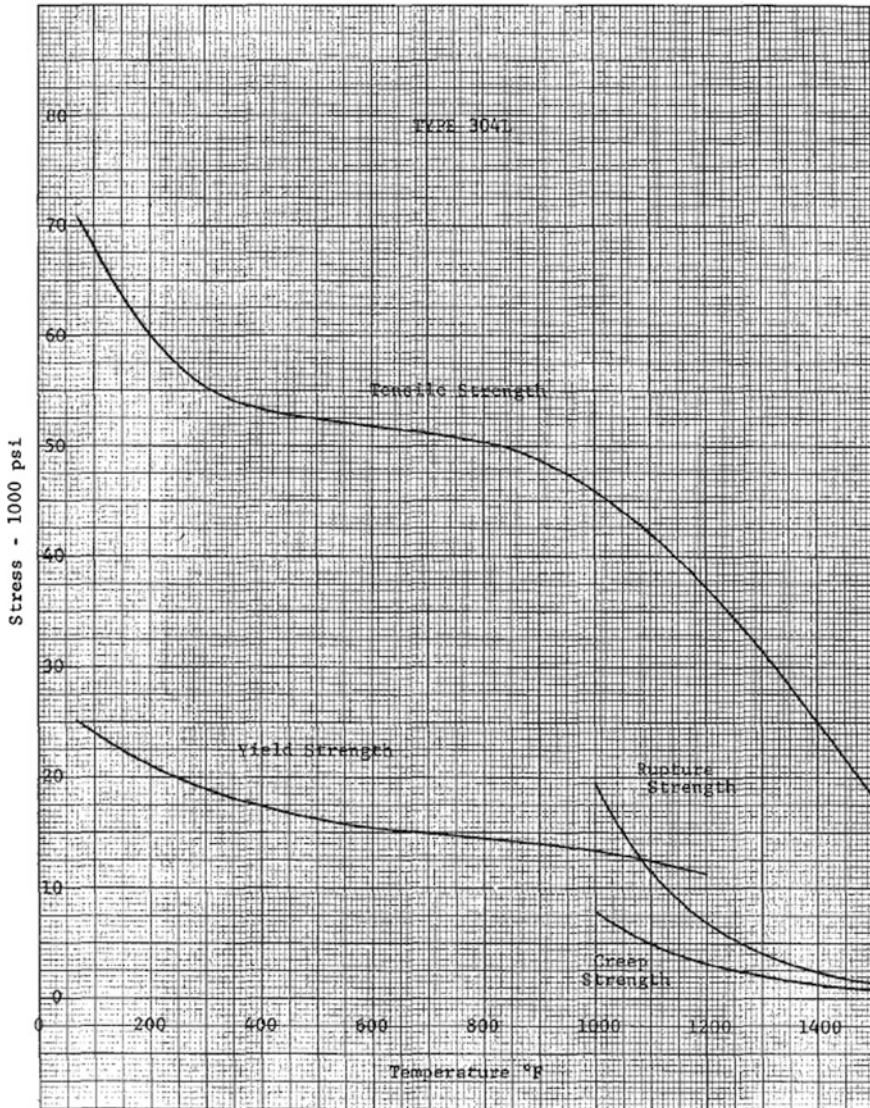


Fig. 3 Yield strength versus temperature for type 304L when the yield strength at room temperature is equal to 25 ksi. Other curves are also given in this plot [2]

allowable stress is derived for design calculation. It is assumed that enough margins have been provided by the ASME Committee by other mechanisms such as design factor, and as the approach has its historical reason, ASME Committee does not allow question previous practices which have good experience feedback.

3 Source of S_u and S_y in RCC-M

It is well known that RCC-M is established on the basis of ASME BPVC, with the combination of French industrial practice, feedback, and regulatory requirements. The S_u and S_y in RCC-M Annex I Table ZI 2.0 and Table ZI 3.0 of Section I Subsection Z are also strongly dependent on the ASME BPVC Section II Part D. The mechanical properties and allowable stresses of the materials were taken from the ASME Code whenever the requirements of RCC-M met the requirements of the ASME Code for a given grade (chemical composition and specified mechanical properties) [6]. A typical example is 16MND5 in RCC-M, an equivalent grade for SA-508 Gr.3 Cl.1. Table 1 shows their specified properties at room temperature and S_y values at elevated temperature. For S_u , the two materials are all equal to 552 Mpa at elevated temperature below creep range.

Table 1 shows although 16MND5 has raised the specified minimum yield strength at room temperature (R_e) from 345 MPa of its ASME counterpart to 400 Mpa, the S_y at high temperature is still anchored to S_y at 20 °C, which is equal to R_e of SA-508 Gr.3 Cl.1. There are minor differences for S_y at elevated temperature between the two materials, which may be caused by following reasons:

- Various editions of ASME Code may have minor differences on S_y in Table Y-1, which reflects continuous efforts of the ASME Committee on assessment of material behavior in the later edition with increasing testing data. The ASME edition referred by RCC-M 2007 is not the 2010 edition used in Table 1.
- Difference occurs during rounding when conversion from U.S. Customary Units to SI Units, as only customary data were available in earlier edition of ASME Code. Furthermore, in earlier edition, the S_y value is only given at integer interval in Fahrenheit temperature like 200 °F, 300 °F, 400 °F. To obtain the values at integer Celsius degree like 100 °C, 150 °C, 200 °C, interpolation will be needed and may bring additional conversion error.

Table 1 Specified tensile properties at room temperature and S_y value for some ASME BPVC and RCC-M materials [7, 8] (MPa)

Grade	R_e	R_m	S_y at 20 °C	S_u at 20 °C	50 °C	100 °C	150 °C	200 °C	250 °C	300 °C	350 °C
M2111 16MND5	400	550	345	552	340	326	318	311	308	303	299
SA-508 Gr.3 Cl.1	345	550	345	550	^a .	323	314	305	299	292	285
M3304 Z2CN18.10	175	490	173	483	165	145	131	121	113	108	104
SA-213 TP304L	170	485	172	483	^b	146	132	121	114	108	104

^aNo data available at 50 °C. S_y at 65 °C is 332 MPa

^bNo data available at 50 °C. S_y at 65 °C is 157 MPa

Nevertheless, the design stress intensity value S_m is same (184 MPa) for the two materials, thanks to S_m actually depends on the S_u for these two materials.

Table 1 also provides an example for stainless steel seamless pipe RCC-M M 3304 Z2CN18.10 and its ASME equivalent grade SA-213 TP304L. The data are highly consistent with each other and conform to yield strength curve in Fig. 3, which was derived by Dr. G. V. Smith some decades ago.

When the RCC-M grade has no equivalent in the ASME BPVC, the values of specified minimum yield strength at elevated temperature given in the NFA or EN standards were chosen as values of S_y . The value of S_u was taken equal to the specified R_m value at room temperature, until this value reaches 110% of the tensile strength value given in the standard [6]. An example is RCC-M M1131 P265GH carbon plate, which is widely used for fabrication of classes 2 and 3 components. Table 2 shows S_y values of M1131 P265GH with $t \leq 30$ mm is basically the same as that specified yield strength $R_{p0.2}$ at temperature in EN standard for $40 < t \leq 60$ mm. AFCEN does not take the value for $16 < t \leq 40$ mm in the standard. It demonstrates the Code Committee (here AFCEN) has arbitrary judgment during determination of S_y based on the published material property data, and the decision is carried out in a conservative way.

SA/EN10028-2 P265GH has been approved by ASME BPVC 2013 Edition in Part D. It is interesting to compare S_y between ASME and RCC-M for this material. Table 2 shows a marked increase in S_y in ASME BPVC, for instance, around 18% greater than that of RCC-M at 300 °C. The difference is because the S_y value given in ASME is still based on the “ratio-trend-curve” method, other than the specified minimum yield strength value in the standard. The example clearly shows that S_y obtained by “ratio-trend-curve” method has significant difference from the specified minimum yield strength value of the material.

In RCC-M Section II, the material specification stipulates tensile properties at certain elevated temperature, i.e., at 300 °C for carbon steel, and at 350 °C (in certain circumstances 360 °C) for stainless steel and nickel alloys. The required tensile strength and yield strength are based on the value in Annex I Table ZI 2.0 and Table ZI 3.0, and a 10% decrease of S_u is taken into account. Unlike ASME, this verification test is used for material acceptance/rejection. Obviously, this additional requirement will increase the confidence level that the actual tensile properties of the lot to be tested will be no less than the value used to derive the data for design calculation in Annex I.

4 Analysis of the Verification Test at Elevated Temperature in RCC-M

Before RCC-M 2000 Edition, only yield strength is required to be verified at high temperature, and tensile strength at high temperature is only for information purpose. For welding material, verification of tensile strength at high temperature is not a mandatory requirement till today. As the allowable stress is derived from yield

Table 2 Specified tensile properties and S_y value for P265GH in different codes and standard (MPa)

Grade	Thickness (mm)	R_e	R_m	S_y at 20 °C	S_u at 20 °C	50 °C	100 °C	150 °C	200 °C	250 °C	300 °C	350 °C
EN10028-2:2003 P265GH	16 < t ≤ 40	255	410			247	232	215	197	181	166	154
EN10028-2:2003 P265GH	40 < t ≤ 60	245	410			237	223	206	190	174	160	148
M1131 P265GH	t ≤ 30	245	410	245	410	234	223	206	191	176	157	142
SA/EN10028-2 P265GH	t ≤ 60	245	410	245	410	^a	223	217	210	202	191	180

^aNo data available at 50 °C. S_y at 65 °C is 230 MPa

strength and tensile strength at room and elevated temperature, and tests at room temperature are always required, the code user may doubt about the effectiveness of verifying yield strength at high temperature only. To evaluate the verification test at elevated temperature in RCC-M, the parameter dominating the allowable stress is analyzed among R_m , R_e , S_u , and S_y . If the allowable stress is not determined by S_y , the verification test of S_y is not critical as even S_y is not satisfied; the allowable stress may not be influenced.

For RCC-M Class 1 components (and Class 2 components using the design method in RCC-M C3200) other than bolts, the allowable basic stress intensity S_m is determined by:

$$S_m = \min(1/3R_m, 1/3S_u, 2/3R_e, 2/3S_y) \text{ for ferritic steels,}$$

$$S_m = \min(1/3R_m, 1/3S_u, 2/3R_e, 0.9S_y) \text{ for stainless steels and nickel alloys.}$$

The value of $\min(1/3R_m, 1/3S_u)$ minus $\min(2/3R_e, 2/3S_y)$ for ferritic steel and $\min(1/3R_m, 1/3S_u)$ minus $\min(2/3R_e, 0.9S_y)$ for austenitic steel and nickel alloys is calculated at room and high temperature for 4 typical material grades, M1131 P265GH ($t \leq 30$ mm), M2111 16MND5, M3304 Z2CN18.10, and M4103 NC15Fe, which are representative of carbon steel, low alloys steel, stainless steel, and nickel alloy. The plot is given in Fig. 4. The value below zero corresponds to the region where S_m is controlled by S_u , as S_u cannot be greater than R_m , and they have the same reduction factor. On the other hand, when the value is above zero, R_e or S_y will dominate the S_m . For ferritic steel, the controlled parameter will be S_y as R_e and S_y have the same reduction factor and S_y is not greater than R_e . For stainless steel and nickel alloys, the temperature-dependent value of $2/3R_e - 0.9S_y$ is plotted in Fig. 5 to determine which one plays a critical role on S_m .

Figures 4 and 5 clearly demonstrate S_m is governed by different parameters for different types of materials:

- For M2111 16MND5, S_m is invariably governed by S_u . Actually, S_u is equal to R_m within the temperature range in RCC-M for carbon steel and low-alloy steel, which conforms the characteristic of increased tensile strength at elevated temperature shown in Fig. 1. Verification of S_y and S_u has little contribution to guarantee S_m value for M2111 16MND5; this is particularly true as R_e has increased to 400 MPa, instead of 345 MPa used for S_u at room temperature in RCC-M,
- For P265GH, S_m is initially governed by S_u . With the increase in temperature, the effect of S_y becomes more dominant and the controlled parameter is changed to S_y at around 150 °C. Verification test of S_y is normally conducted at 300 °C. At this point, $1/3S_u - 2/3S_y$ is more than 30 MPa, i.e. S_u has more than 90 MPa margin before it can influence S_m . Verification of S_y is normally enough for material properties at 300 °C.
- For Z2CN 18.10, S_m is initially governed by R_e , and the controlled parameter is changed to S_y at around 150 °C. Verification of S_y is normally carried out at 350 °C. At this point, $1/3S_u - 0.9S_y$ is more than 35 MPa which corresponds to

Fig. 4 The temperature-dependent difference between tensile strength and yield strength at room and high temperature with reduction factor for S_m

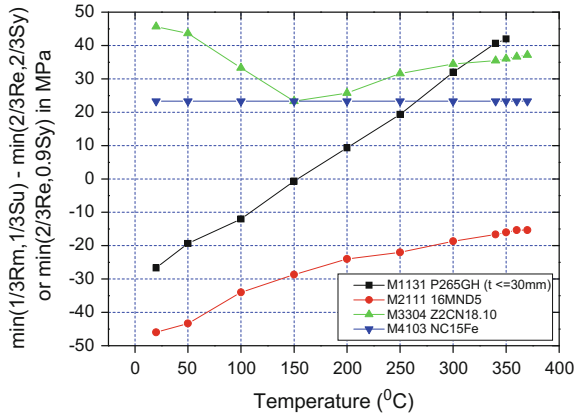
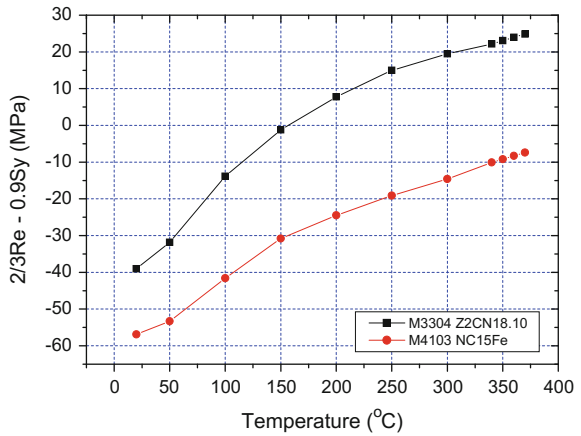


Fig. 5 The temperature-dependent difference between yield strength at room and high temperature with reduction factor for S_m



nearly 100 MPa margin for S_u before it can influence S_m . Verification of S_y is normally enough for material properties at 350 °C.

- For NC 15 Fe, S_m is always governed by R_e . Verification test at high temperature has no contribution.

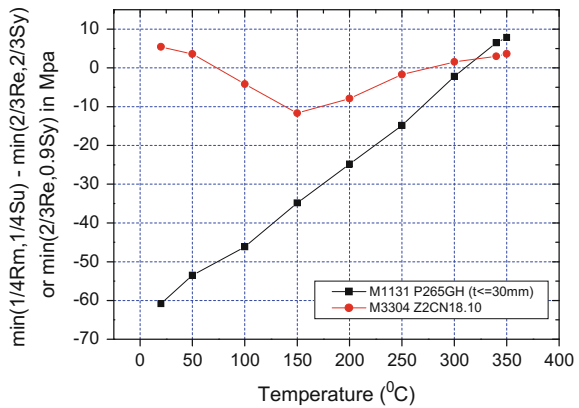
For RCC-M Class 2 (except those designed by RCC-M C3200) and Class 3 components other than bolts, similar analysis can be conducted for allowable basic stress S , which is governed by:

$$S = \min(1/4R_m, 1/4S_u, 2/3R_e, 2/3S_y) \text{ for ferritic steels,}$$

$$S = \min(1/4R_m, 1/4S_u, 2/3R_e, 0.9S_y) \text{ for stainless steels and nickel alloys}$$

As 16MND5 and NC 15Fe are rarely used for classes 2 and 3 components, only P265GH and Z2CND18.10 are analyzed, and the results are given in Fig. 6. For

Fig. 6 The temperature-dependent difference between tensile strength and yield strength at room and high temperature with reduction factor for S



allowable basic stress S, P265GH and Z2CN 18.10 are all dominated by S_u within the majority of temperature range in RCC-M until at around 300 °C. The result is not surprising as a quite big reduction factor of 4 is adopted by RCC-M 2007 Edition (the value is reduced to 3.5 in 2012 Edition). However, the differences between $1/4S_u$ and $2/3S_y$ (for carbon steel) or $0.9S_y$ (for stainless steel) are quite small at the typical verification temperature 300 °C and 350 °C, respectively, which means only verification of S_y may not be enough to guarantee S. The revision about verification of both S_u and S_y from 2000 Edition becomes reasonable for the two materials. Besides, there is actually no work added as tensile test at high temperature can measure both tensile strength and yield strength.

The analysis shows that although verification of tensile tests at high temperature will, in general, improve the confidence level that the actual tensile properties of the lot to be tested will be no less than the value used to derive the data for design calculation in RCC-M Annex I, its effectiveness cannot be overemphasized. For 16MND5 and NC15Fe, the verification has little contribution. Moreover, the verification is only conducted at a single high temperature. There is no evidence to support an acceptable verification test at a single high temperature can assure same conclusion can be obtained for the whole temperature range. If a specific design needs measured tensile properties of the materials to be guaranteed at the service temperature, it is suggested to conduct verification test at that specific service temperature, instead of the temperature stipulated in the material specifications in RCC-M Section II.

Meanwhile, if the actual tensile properties within the whole temperature range need to be assured, a method similar to that adopted in EN standard is suggested. For instance, EN 10314 can derive elevated tensile properties data with a confidence level of 98% [9]. Nevertheless, this method will bring a reduced value for tensile properties at elevated temperature, and when adopted by design code, the wall thickness calculated will be greater than that based on “ratio-trend-curve” approach, which means cost will increase.

5 Conclusions

- (1) S_u and S_y in ASME BPVC are based on “ratio-trend-curve” method. The ASME Committee does not require verification tests at high temperature and does not consider the result of such tests can be used to reject the material, probably due to good feedback of previous practice.
- (2) S_u and S_y in RCC-M are essentially the same as that in ASME BPVC when material has the equivalent in ASME. In addition, some materials use the value specified in EN or NFA standard to establish S_u and S_y . Verification of tensile tests can improve the confidence level that the actual tensile properties of the lot to be tested will be no less than the value used to derive the data for design calculation in Annex I.
- (3) However, the effectiveness of verification tests cannot be overemphasized. If a specific design needs measured tensile properties of the materials to be guaranteed at the service temperature, it is suggested to conduct verification test at that specific service temperature. Moreover, if the actual tensile properties within the whole temperature range need to be assured, a method similar to that adopted in EN standard is suggested.

The data of material properties are the foundation of the design code. For localization of nuclear code, it is suggested to establish specific organization which is responsible for collection, processing, and publication of property data (including tensile properties at high temperature). The data from ASME BPVC can be used, but it does not mean further analysis is not necessary. The material properties data shall be continuously obtained, analyzed, and reflected by the update in the later edition of the code, to improve the accuracy and reliability of the data used for design.

References

1. Donatello Annaratone, *Pressure Vessel Design*, Springer, 2007.
2. G. V. Smith, *An Evaluation of the Yield, Tensile, Creep, and Rupture Strengths of Wrought 304, 316, 321, and 347 Stainless Steels at Elevated Temperatures*, ASTM Data Series DS 5S2, American Society for Testing and Materials, New Jersey, 1969.
3. G. V. Smith, *An Evaluation of the Elevated Temperature Tensile and Creep-rupture Properties of Wrought Carbon Steel*, ASTM Data Series DS11S1, American Society for Testing and Materials, New Jersey, 1970.
4. K. R. Rao, *Companion Guide to the ASME Boiler & Pressure Vessel Code: Criteria and Commentary on Select Aspects of the Boiler & Pressure Vessel and Piping Codes*, 4th Ed., American Society of Mechanical Engineers, 2012.
5. Elmar Uptis, Michael Gold, *Comparison of ASME Specifications and European Standards for Mechanical Testing of Steels for Pressure Equipment*, ASME Standard Technology, LLC., 2005.
6. *RCC-M Criteria: Prevention of Damages in Mechanical Components*, 2014 Ed., AFCEN.

7. Design and Construction Rules for Mechanical Components of PWR Nuclear Islands (RCC-M), 2007 Ed., AFCEN.
8. ASME Boiler and Pressure Vessel Code, 2010 Ed., American Society of Mechanical Engineers, 2010.
9. EN 10028-3, Flat Products Made of Steels for Pressure Purposes – Part 3: Weldable Fine Grain Steels, Normalized, 2003.

Author Biography

Guo Lifeng is the Head of Welding Section of Nuclear Equipment Division, CNPE. He is a member of AFCEN CSUG (China Specialized User Group) for RCC-M (Construction) and a member of ASME BPVC CIWG (China International Working Group) for Section III. He got his PhD degree from the Hong Kong Polytechnic University in 2005. He has more than 10 years of experience in the field of welding and NDE for nuclear industry and is a major contributor for Chinese standard on welding procedure qualification of nuclear components, NB/T 20002 part 3. He can be reached at +86 10 8802 2537 (office phone), +86 10 8802 2883 (fax) and guolf@cnpe.cc (email).

Analysis Method of the Temperature for the Heavy Reflector

Shi Lin, Fang Jian and Ran Xiaobing

Abstract The metal is much more than the water for the heavy reflector. More heat will generate due to gamma irradiation, and creep failure may occur. Temperature should be calculated. ANSYS can be used for two-dimensional analysis to calculate the temperature distribution of the heavy reflector. The sensitivity of the mesh can be analyzed, and the factors affecting the temperature can be evaluated. The maximum temperature of the heavy reflector is less than 350 °C from analysis results, which can satisfy the material requirements.

Keywords Heavy reflector · ANSYS · Temperature · Reactor

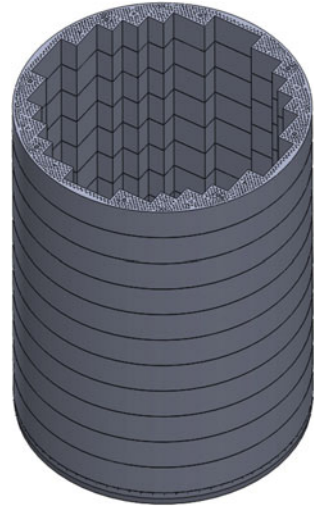
1 Introduction

The heavy reflector is located inside the core barrel, surrounding the core. It rests on the lower plate and extends nearly all the way up to the core cavity, but is not in contact with the upper core plate.

The heavy reflector consists of a stack of twelve austenitic stainless steel-forged slabs without any welds and bolts on core side. The inner contour of the heavy reflector is the same as the outer contour of the core, and the outer contour of the heavy reflector is cylindrical. The upper eleven slabs with vertical hole are similar. The bottom plate is a chamber structure with many holes, arranging lateral hole, drainage slots, and distribution chamber (see Fig. 1).

The heavy reflector has radiation shielding ability, good neutron reflectivity, and strong structural integrity as compared to the widely used baffle and former structure, but the metal is much more than the water for the heavy reflector, and more heat will generate due to gamma irradiation. Creep failure may occur in metal

S. Lin (✉) · F. Jian · R. Xiaobing
China Nuclear Power Design Company, Ltd, Shenzhen 518172, Guangdong, China
e-mail: shilin@cgnpc.com.cn

Fig. 1 Heavy reflector

with high temperature, but the creep failure has a very low probability with temperature controlled under 350 °C. Therefore, it is necessary to analysis the thermal filed and to calculate the maximum temperature of the heavy reflector [1].

There is no method for the analysis method of the heavy reflector in domestic. First, temperature field is calculated with ANSYS, and then, the results are evaluated; thereby, the thermal analysis of the heavy reflector is completed.

2 Analysis Method and Calculation Modal

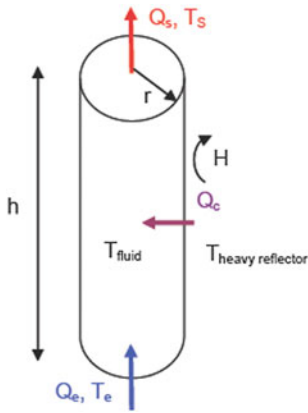
2.1 Analysis Method

Considering the small diameter water holes and the high heavy reflector, 3D model size has large different dimension, and the number of mesh model will be tens of millions. Therefore, 2D model is used for the analysis. Method is described in below.

- (1) Because the heavy reflector is composed of 12 slabs which are connected together with tie rods. Therefore the 12 slabs are considered as a whole when calculating. Therefore, we will not consider each of the connecting members, and forging as a whole, not to consider local gap created between the slabs and heat insulation problems caused.
- (2) Since the bottom plate of the heavy reflector is located in an area outside the active section, heat generation rate is very small. The structure is so more complex that not easy to simulate. Therefore, the bottom plate is not to be considered in analysis.

The twelfth slab is cooled sufficiently, and the temperature is low by calculation. So the twelfth slab is also not to be considered in analysis. Thereby, the model can be simplified as calculating from the second slab up to the eleventh slab.

- (3) The middle cross section is to be selected in 2D analysis.
- (4) The second slab inlet temperature is the same as the lower plenum temperature. The heavy reflector temperature will rise due to gamma radiation heat. The coolant temperature will rise through convective heat transfer. Therefore, the heavy reflector and coolant in the heavy reflector outlet temperature distribution will be gained.
- (5) The $n + 1$ slab inlet coolant temperature is the same as the n slab outlet coolant temperature.



Fluid temperature in a slab is described as follows.

For every slab, the quantity of heat evacuated by the fluid (Q_s) is equal to the quantity of heat conveyed by the fluid which enters the slab (Q_e) plus the quantity of heat received from the structure by forced convection (H) with the steel structure (Q_c):

$$Q_c = Q_s - Q_e \tag{1}$$

The quantity of heat evacuated by the fluid can be used to calculate the temperature increase (ΔT) in the water which goes through a slab.

Knowing the temperature of the water at the inlet of the slab (T_e), the quantity of heat received during the crossing (Q_c) is used to determine the temperature in canals at the outlet of the slab (T_s). The ΔT is then calculated as follows:

$$Q_c = Q_s - Q_e = mC_p\Delta T \tag{2}$$

where

m Mass flow
 C_p Specific heat

$$Q_c = HS(T_{\text{heavy reflector}} - T_{\text{fluid}}) \quad (3)$$

where

H The heat transfer coefficient between the heavy reflector and the fluid
 S The area of contact between the heavy reflector and the fluid
 $T_{\text{heavy reflector}}$ The heavy reflector temperature
 T_{fluid} The fluid temperature

$$S = 2\pi rh$$

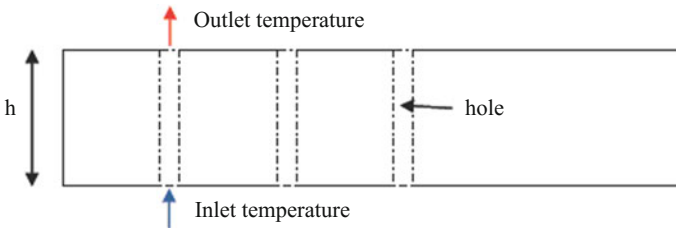
r Radius of the cylinder
 h The length of contact

$$\Delta T = \frac{Q_c}{mC_p} = \frac{Q_c}{\rho S'VC_p} = \frac{HS(T_{\text{heavy reflector}} - T_{\text{fluid}})}{\rho S'VC_p} \quad (4)$$

where

ρ Fluid density
 V The fluid velocity
 S' The cylinder section [2]

$$S' = \pi r^2$$



2.2 Calculation Modal

2.2.1 Mesh Modal

- (1) Considering the structure symmetry of the fuel assembly and the heavy reflector, a quarter of the model will be selected to calculate.
- (2) There are 40,412 nodes and 36,287 elements in mesh modal with global size 8 mm, local water hole 3 mm, and 2-layer mesh boundary expansion. PLANE55 thermal analysis elements will be used [3]. Mesh modal is shown in Fig. 2.

2.2.2 Mesh Sensitivity Analysis

Evaluating the influence of different mesh schemes depends on calculating results with considering the quality of mesh. Mesh schemes, calculation results, and the quality of mesh are shown in Table 1.

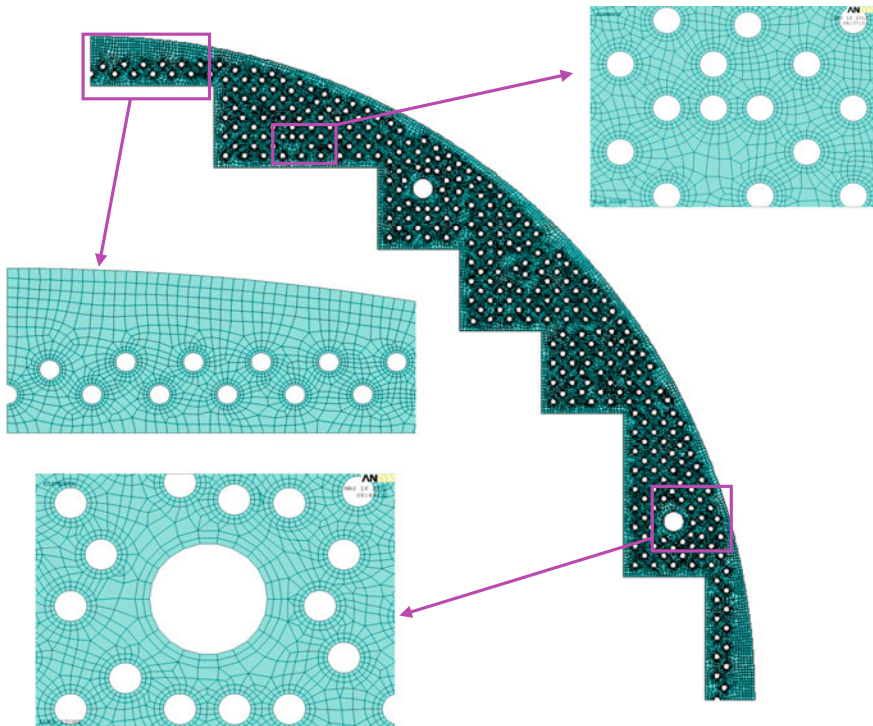


Fig. 2 Mesh model of heavy reflector

Table 1 Mesh schemes

Scheme	Description	Nodes	Elements	Calculating temperature	Deviation (%)	Quality
1	Global size 16 mm	9079	6664	644.587		0.46
2	Global size 10 mm	14,710	11,365	647.918	0.514108267	0.564
3	Global size 8 mm	20,963	16,898	649.377	0.224676883	0.61
4	Global size 8 mm; local water hole 3 mm, 1-layer mesh boundary expansion	34,189	30,071	650.604	0.188593983	0.81
5	Global size 8 mm; local water hole 3 mm, 2-layer mesh boundary expansion	40,412	36,287	651.175	0.087687642	0.82
6	Global size 8 mm; local water hole 3 mm, 3-layer mesh boundary expansion.	48,467	44,354	651.286	0.017043204	0.74

The calculation results change so small when global size reaches to 8 mm from schema 1, 2, 3. Therefore, global mesh size sets to 8 mm. In order to verify mesh sensitivity, some examples are calculated. The suitable mesh modal is gained through comparing calculation results. Moreover, the quality of mesh becomes worse when 3-layer mesh boundary expansion is used. Therefore, 2-layer mesh boundary expansion is used. In summary, scheme 5 with global mesh size 8 mm, local water hole 3 mm, and 2-layer mesh boundary expansion is used.

Accordinging mesh sensitivity analysis, the mesh quality is guaranteed when the number of mesh is more than 30,000. Scheme 5 satisfies this requirement. Mesh sensitivity analysis is shown in Fig. 3.

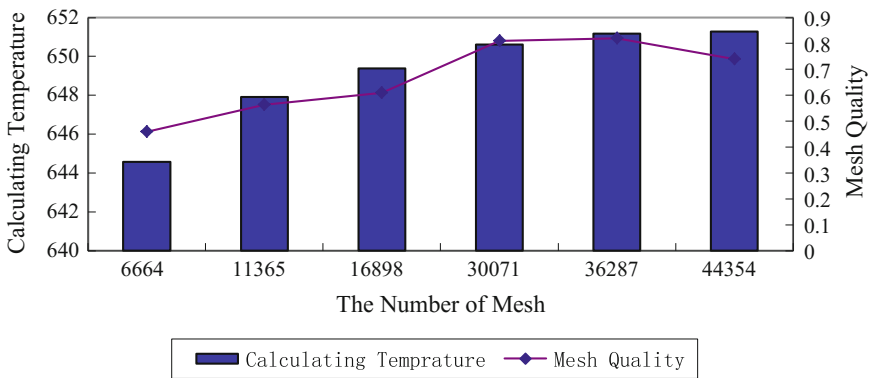


Fig. 3 Sensitivity analysis of mesh model

2.3 Boundary and Load Conditions

2.3.1 Boundary Conditions

According to Dittus-Boelter formula, heat transfer coefficient is calculated under the corresponding temperature.

$$Pr = \frac{\mu C_p}{\lambda} \tag{5}$$

$$Re = \frac{\rho D_h V}{\mu} \tag{6}$$

$$H = 0.023 \frac{\lambda}{D_h} Re^{0.8} Pr^{0.4} \tag{7}$$

where

- Pr Prandtl number
- μ Viscosity;
- C_p Specific heat;
- λ Thermal conductivity;
- Re Reynolds number;
- ρ Fluid density;
- D_h Hydraulic diameter;
- V Fluid velocity;
- H Heat transfer coefficient [4]

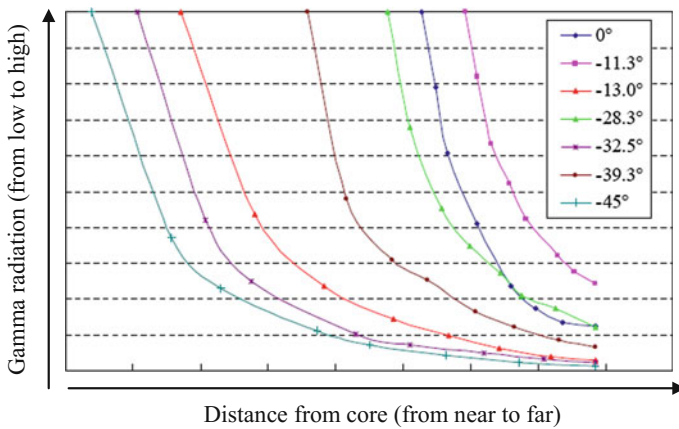


Fig. 4 Radial distribution curve of heavy reflector

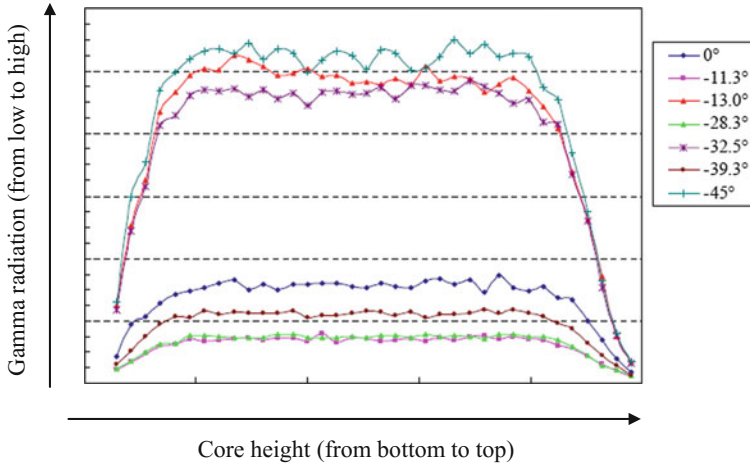


Fig. 5 Axial distribution curve of heavy reflector

2.3.2 Load

Heat generation due to gamma radiation is obtained by combining the radial distribution as shown in Fig. 4 and axial distribution as shown in Fig. 5.

3 Results Analysis and Evaluation

3.1 Calculation Results

The temperature in each slab is shown in Table 2. The temperature distribution is similar from second to eleventh slab. The maximum temperature is 341.5 °C in the tenth slab, and it satisfies material requirements below 350 °C. The temperature contours in tenth slab is shown in Fig. 6.

Table 2 Temperatures of slabs

Slab	Maximum temperature (°C)	Minimal temperature (°C)	Average temperature (°C)
2	313.9	288.8	293.7
3	329.1	289.6	297.0
4	333.4	290.7	299.3
5	333.0	291.9	300.8
6	334.6	293.1	302.8
7	335.4	294.3	304.6
8	339.0	295.6	306.6
9	340.2	296.9	308.5
10	341.5	298.2	310.1
11	337.3	299.1	310.9

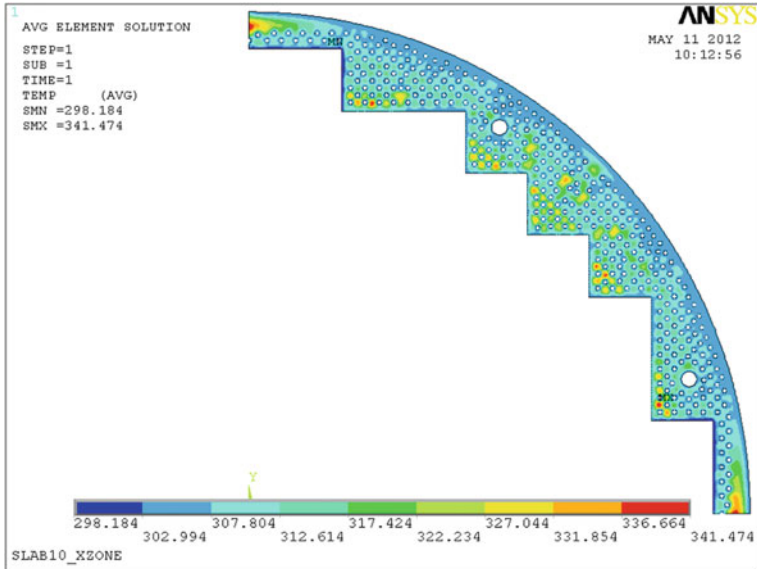


Fig. 6 Temperature contours of tenth slab

3.2 Factors Affecting Temperature Field

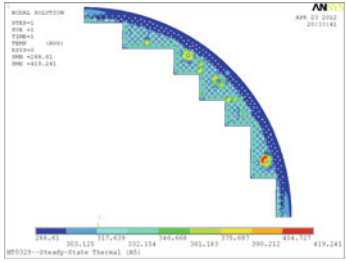
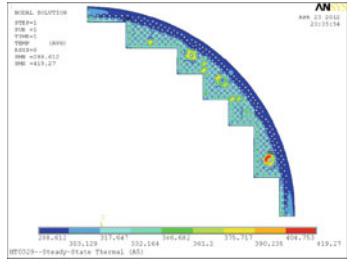
3.2.1 Influence of Loading Method

The influence of the results is verified by two examples when heat generation due to gamma radiation is applied in elements or nodes.

	Example 1	Example 2
Loading method	Heat generation rate is applied in nodes	Heat generation rate is applied in elements
Calculation results	<p>Maximum temperature 419.164 °C</p>	<p>Maximum temperature 419.241 °C</p>
Conclusion	There is a similar result: Either heat generation rate is applied in nodes or applied in elements	

3.2.2 Influence of Loading Conditions

The influence of the results is verified by two examples when different load conditions are applied.

	Example 3	Example 4
Loading conditions	Temperature, heat transfer coefficient, heat generation due to gamma radiation	Heat transfer coefficient, heat generation due to gamma radiation
Calculation results	 <p>Maximum temperature 419.241 °C</p>	 <p>Maximum temperature 419.27 °C</p>
Conclusion	There is a similar result: Either temperature is applied or not. Because the temperature is included in the heat transfer coefficient	

3.2.3 Influence of Material Properties

The influence of the results is verified by several examples when two variables are fixed, but the third variable is changed. The thermal conductivity increases with increasing temperature; therefore, the thermal conductivity variable with increasing temperature is used in analysis. Density and specific heat have almost no impact on the results.

3.2.4 Influence of Initial Temperature

Changing the initial slab temperature has almost no impact on the results, because the heat transfer coefficient depends on the coolant temperature but not on the initial temperature of the slab.

4 Conclusions

2D thermal analysis is used for the heavy reflector in this paper. The mesh sensitivity is analyzed, and calculation results are evaluated. Conclusions are described as follows:

- (1) The workload is effectively reduced on meshing, and calculation depends on 2D analysis. The number of meshes is small in this calculation method, so the calculation speed is fast. It is suit for repeating calculation when the structure is changed a litte.
- (2) The mesh sensitivity and calculation results' sensitivity are analyzed, so accuracy is improved.
- (3) The maximum temperature is no more than 350 °C, and the material requirements are fulfilled.

References

1. ZHAO Feiyun, HUANG Qing, ZHU Kun et. Temperature Analysis Study on Core Shroud Based on Thermal-Fluid-Structure Coupling Effect [J]. Nuclear Power Engineering, 2011, 32 (1):134–136.
2. YANG Shiming, TAO Wenshuan. Heat Transfer [M]. Beijing: Higher Education Press, 2006.
3. XU Jiangrong, QIU Zheyong. Mathematical modeling and numerical simulation of heat process [M]. Beijing: National Defense Industry Press, 2010.
4. I.E. Idelchik. Handbook of Hydraulic Resistance [M]. Greta R. Malyavskaya. USA: Hemisphere Publishing Corporation, 1986.

Author Biographies

Shi Lin (1986–) is an engineer, graduated from nuclear subject in Tsinghua University in 2011, obtained his master's degree, and engaged in reactor design. E-mail: shilin@cgnpc.com.cn.

Fang Jian (1981–) is an senior engineer, graduated from mechanical subject in Huazhong University of Science and Technology in 2011, obtained his master's degree, and engaged in reactor design.

Ran Xiaobing (1969–) is a research senior engineer, graduated from mechanical subject in Harbin Engineering University in 1993, obtained his bachelor's degree, and engaged in reactor design.

Analysis on Super-Long Frame Structure of Main Building of Conventional Island

Shi Lichao, Wang Zhicong, Jia Weichao and Huang Yankun

Abstract Longitudinal length of main building of conventional island of nuclear power plant is far beyond the stipulation of relevant specifications about the maximum interval of the expansion joint. In this article, the influence of structure internal force and material utilization amount is analyzed from considering anti-seismic and thermal action. And the conclusion is given in the end.

Keywords Main building of conventional island of nuclear power plant · Super-Long frame structure · Thermal action

1 Introduction

The longitudinal length of main building of conventional island of nuclear power plant is general between 110 and 120 m. When using of reinforced concrete structure, the longitudinal length is far beyond the requirement of 75 m which is the maximum distance of the temperature expansion joint in the norms. If the expansion joint is not considered, the temperature function is calculated and the effective measures are taken to meet the design requirements. How much impact on the internal forces and the amount of material the temperature effect has? There are two options about the main building with joint or not to compare the effect. In this article, the influence of structure internal force and material utilization amount is analyzed from considering anti-seismic and thermal action.

S. Lichao (✉) · W. Zhicong · J. Weichao · H. Yankun
China Nuclear Power Engineering Co., Ltd, Hebei Branch,
Shijiazhuang, Hebei, China
e-mail: jianghong@cnpe.cc

© Springer Science+Business Media Singapore 2017
H. Jiang (ed.), *Proceedings of The 20th Pacific Basin Nuclear Conference*,
DOI 10.1007/978-981-10-2314-9_5

2 A Brief Introduction of Main Building of Conventional Island

2.1 Main Building of Conventional Island Layout Scheme

A main building of conventional island of nuclear power plant uses aboveground layout scheme and reinforced concrete frame structure.

The longitudinal axis length of turbine generator building and deaerator bay is 115.5 m, and column spacing has three kinds as 12.5, 12, and 9.5 m. The span of turbine generator building is 42.5 m, and deaerator bay is 13 m. The bottom elevation of roof truss of turbine house is about 40.0 m. Chemical workshop is along the lateral of deaerator bay, and single-layer reinforced concrete frame structure, with the height of 10.0 m. Two bridge cranes with lifting capacity 300/60 t and 90/20 t are placed in turbine generator building, and the elevation of rail-top is 35.7 m.

The main structure floors of turbine generator building are turbine generator building zero meter floor (± 0.0 m), middle floor (8.0 m), operation floor (18.0 m), and roof; the main structure floors of deaerator bay are zero meter floor (0.0 m), middle floor (8.0 m), electrical mezzanine (13.0 m), operation floor (18.0 m), deaerator floor (27.0 m), and roof.

The plan and section of operation floor without expansion joint are shown in Figs. 1 and 2.

Project with expansion joint has an expansion joint on the right of axis T.6, and the distance of double column axis is 1.5 m. The distance of T.6'-T.7 is 11 m. The length of the plant remains unchanged and is still 115.5 m. Plane layout is shown in Fig. 3. The rest is not changed.

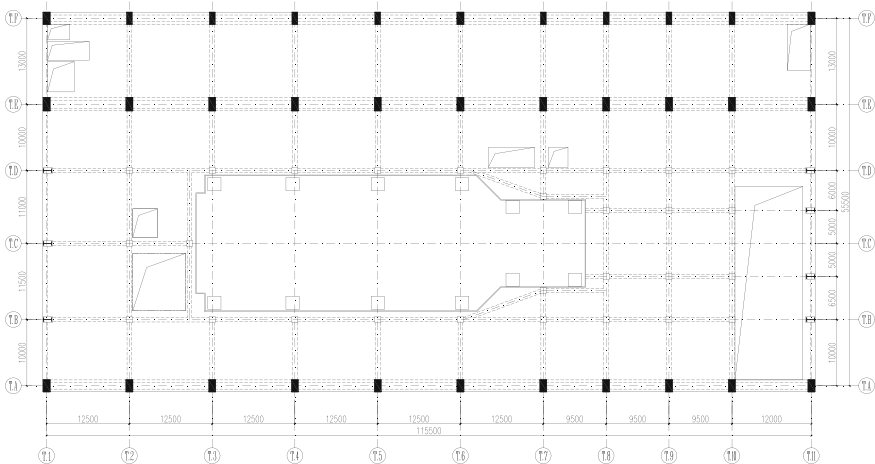


Fig. 1 Plan of operation floor

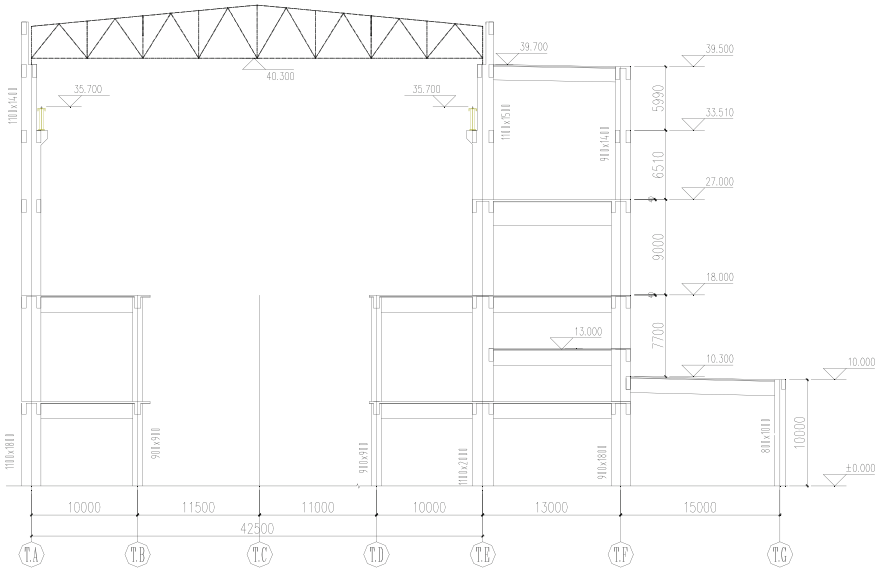


Fig. 2 Section

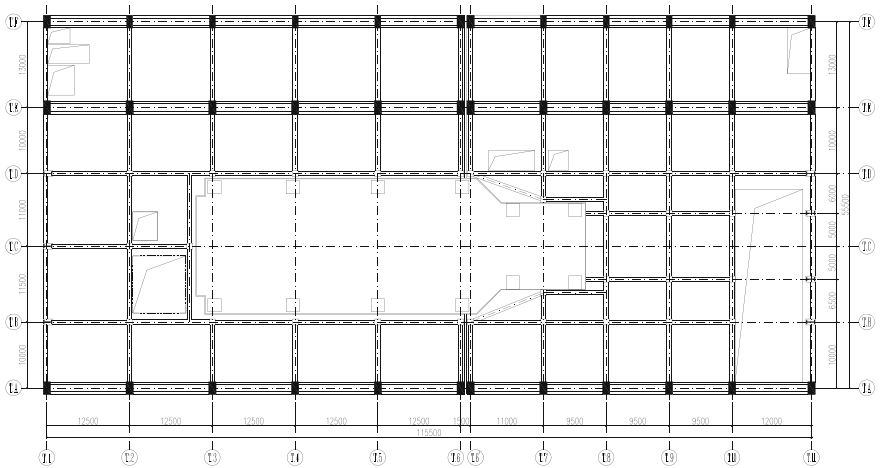


Fig. 3 Plan of operation floor

2.2 Material and Main Section

Concrete strength grade of frame beams, columns, and slabs is all C40.

Column section of grid A is 1100×1800 , column section of grid B is 1100×2000 , column section of grid C is 900×1800 , and column section of platform is 900×900 .

The section of transverse main frame beam is 700×1400 , 700×1600 , 700×2400 , and the section of longitudinal main frame beam is $2-400 \times 1200$.

Slab thickness of middle floor, operation floor, and deaerator floor is 150 mm; slab thickness of electrical mezzanine is 100 mm or 120 mm, and slab thickness of roof is 100 mm.

2.3 Seismic Design Requirements and Natural Conditions

Seismic precautionary intensity used for seismic measures of main building of conventional island is considered as intensity 7. Grade of seismic design details of main building of conventional island is considered as intensity 8.

Reference wind pressure: $W_0 = 0.45 \text{ kN/m}^2$. Surface roughness category: A. Reference snow pressure 0.35 kN/m^2 .

2.4 Thermal Action

Maximum temperature rise: $26 \text{ }^\circ\text{C}$, maximum temperature drop: $-43 \text{ }^\circ\text{C}$, concrete shrinkage effect are translated into $12.5 \text{ }^\circ\text{C}$ temperature drop.

2.5 Live Load

The live load value of floor and roof follows “Technical code for design load of main building in fossil-fired power plant and the conventional island of nuclear power plant” (DL/T5095-2013) and “Load code for the design of building structures” (GB 50009-2012).

3 Contrast Analysis of Structure Internal Force and Deformation of Frame Structure with Joint or not Under Earthquake

Seismic performance analysis and comparison of the amount of material will be done from structural vibration period, floor displacement (or displacement ratio), scrambling.

3.1 *Structural Vibration Period*

Column spacing of main building is large between axis T.1 and T.6, and there is turbine generator foundation which is completely disengaged from main building between axis T.3 and T.6. Middle floor and operation floor are partial discontinuous. Structural rigidity is small, and period is long. Structural misalignment is large. The component of torsional vibration is large in the first two translational modes. Periodic ratio of the structure: $T_3/T_1 = 0.76 < 0.9$. The overall torsional rigidity meets the requirements.

Column spacing of main building is not very large between axis T.6' and T.11, and there is turbine generator foundation which is completely disengaged from main building between axis T.6' and T.8. There is also the lifting hole between axis T.10 and T.11. Middle floor and operation floor are partial discontinuous, but the overall layout is better than the T.1–T.6. Structural rigidity is relatively larger, and period is short. Structural misalignment is small. The component of torsional vibration is small in the first two translational modes. Periodic ratio of the structure: $T_3/T_1 = 0.85 < 0.9$. The overall torsional rigidity meets the requirements.

For the overall structure with no temperature joint, structure between T.1 and T.6 which is flexible and structure between T.6' and T.11 which is rigid become to a unitary structure. The circs that middle floor and operation floor are partial discontinuous is improved, and structural misalignment is also reduced. Natural period of the overall structure is between the periods of the first two structures. The component of torsional vibration in the first two translational modes is also between the first two structures. Periodic ratio of the structure: $T_3/T_1 = 0.80 < 0.9$. The overall torsional rigidity is also between the first two structures.

To sum up, the overall structure is more reasonable than the structure with joint. Structural misalignment is small. The structure can be better coordinated to work together.

3.2 *Floor Displacement*

With temperature expansion joint, floor horizontal displacement and story drift of the two-part structure are shown in Tables 1 and 2.

Floor horizontal displacement and story drift of the overall structure with no joint is shown in Table 3.

LX is (0.0°) specified horizontal force

PX is (0.0°) positive misalignment specified horizontal force

MX is (0.0°) negative misalignment specified horizontal force

LY is (90.0°) specified horizontal force

PY is (90.0°) positive misalignment specified horizontal force

Table 1 Floor horizontal displacement and story drift of the structure between T.1 and T.6

	Floor maximum horizontal displacement (mm)	Range of maximum horizontal displacement of each floor and floor average displacement ratio	Maximum story drift angle
LX	27.09	1.09–1.12	1/1156
PX	28.69	1.16–1.19	1/1072
MX	25.48	1.02–1.06	1/1253
LY	25.93	1.03–1.12	1/1195
PY	28.63	1.14–1.25	1/1123
MY	26.71	1.05–1.12	1/1199
EX	28.25	1.20–1.22	1/1020
EY	25.16	1.09–1.16	1/1224

Table 2 Floor horizontal displacement and story drift of the structure between T.6' and T.11

	Floor maximum horizontal displacement (mm)	Range of maximum horizontal displacement of each floor and floor average displacement ratio	Maximum story drift angle
LX	21.54	1.01–1.11	1/1365
PX	23.20	1.11–1.21	1/1236
MX	23.27	1.03–1.08	1/1387
LY	25.74	1.01–1.06	1/1077
PY	26.87	1.06–1.12	1/1034
MY	27.56	1.08–1.17	1/1048
EX	21.18	1.07–1.17	1/1315
EY	22.42	1.05–1.08	1/1123

Table 3 Floor horizontal displacement and story drift of the structure between T.1 and T.11

	Floor maximum horizontal displacement (mm)	Range of maximum horizontal displacement of each floor and floor average displacement ratio	Maximum story drift angle
LX	24.22	1.03–1.05	1/1269
PX	25.00	1.06–1.09	1/1223
MX	24.01	1.00–1.04	1/1268
LY	26.34	1.05–1.17	1/1217
PY	27.65	1.05–1.12	1/1062
MY	30.61	1.22–1.36	1/1064
EX	23.85	1.06–1.09	1/1214
EY	27.56	1.20–1.29	1/1052

MY is (90.0°) negative misalignment specified horizontal force

EX is (0.0°) earthquake action

EY is (90.0°) earthquake action

Horizontal displacement ratio of the structure between T.1 and T.6 under earthquake action in the X direction is more than 1.2 but less than 1.4 and belongs to torsional irregular. Maximum story drift angle all can meet requirement.

Under earthquake action in the X direction, the displacement of the structure between T.6' and T.11 is both smaller than the displacement of the structure between T.1 and T.6 in two directions. Horizontal displacement ratio is also more than 1.2 but less than 1.4 and belongs to torsional irregular. Maximum story drift angle all can meet requirement.

For the overall structure with no temperature joint, the displacement in the X direction is between the first two structures, and the displacement in the Y direction is larger than both. Horizontal displacement ratio is also more than 1.2 but less than 1.4, belongs to torsional irregular. Maximum story drift angle all can meet requirement.

By comparison analysis, the overall structure can meet the requirement of relevant floor displacement (displacement ratio) and flat, vertical irregular for seismic design. The circs that middle floor and operation floor are partial discontinuous is improved, and structural misalignment is also reduced. The structure can be better coordinated to work together.

3.3 The Amount of Material Analysis

Without considering thermal action, contrast analysis of the amount of material between the overall structure without considering thermal action and the structure with joint. The result is shown in Table 4.

From the table, we can see that without considering thermal action, the amount of material of the overall structure is less than the structure with joint. This is mainly because the structure with joint has one more frame structure of reinforced concrete and steel roof truss.

Table 4 Contrast of the amount of material

The amount of structural material	With joint (A)	Without joint (B)	Difference (B-A)
	Total (two part)	T.1-T.11	
Reinforcement in beam (t)	255.1	251.8	-3.3
Reinforcement in column (t)	378.5	349.3	-29.2
Steel of steel seam (t)	3063	2961	-102
Concrete of beam (m ³)	4335.2	4236.4	-98.8
Concrete of column (m ³)	3820	3515.6	-304.4

Fig. 4 Structural deformation under the thermal action

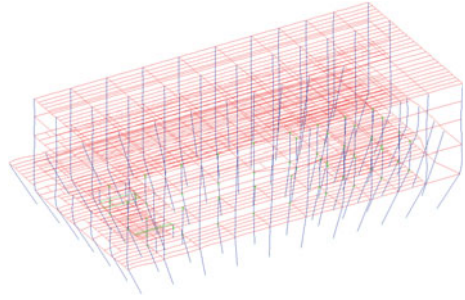
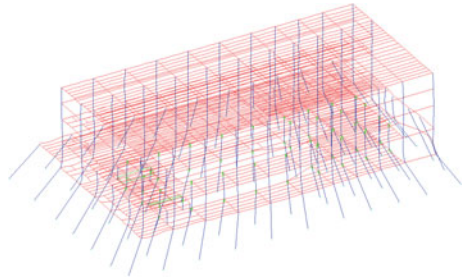


Fig. 5 Structure deformation with elevated temperatures and cooling



4 Calculation and Analysis of the Super-Long Frame Structure Under the Thermal Action

4.1 Structural Deformation Under the Thermal Action

Structure deformation with elevated temperatures and cooling is shown in Figs. 4 and 5.

According to the deformation diagram, the relative deformation of the structure is almost all concentrated in the bottom layer. The internal force of the bottom column and the beam of one floor under the temperature load is the maximum. Under working condition of elevated temperatures, the deformation of the structure is expanding; cooling condition, the deformation of the structure is shrinkage.

4.2 Analysis of the Internal Force Under the Thermal Action

By calculation, the internal force analysis is as follows:

- (1) The ratio relationship of internal force of beam and column with cooling 43° and heating 26° is 1.654 times, that is, internal force of beam and column with

cooling 43° = internal force of beam and column with heating $26^\circ \times (43/26)$, but the direction is opposite.

- (2) The internal force of 12.5° of concrete shrinkage and cooling 43° is proportional (error within 5%).
- (3) The maximum tensile force in the frame beam is 1671.3 kN, and when using HRB400 reinforcement, the reinforcement area is $1671.3 \times 1000/360 = 4642.5 \text{ mm}^2$.

The cross section of longitudinal beam is $2-400 \times 1200$. If the diameter of lumbar reinforcement is 18 mm, and the number of each side is 5, the pulling force of lumbar reinforcement is $20 \times 254.5 \times 360 = 20 \times 91.62 = 1832.4 \text{ kN}$, fully able to meet the requirements of the maximum tension.

Reference to the relevant nuclear power conventional island project, the diameter of lumbar reinforcement in longitudinal frame beam takes 16 mm, and the number of each side is 5.

The tension of the single bar received $201.1 \times 360 = 72.4 \text{ kN}$.

The tension of normal reinforcement is able to provide $4 \times 5 \times 72.4 \text{ kN} = 1448 \text{ kN}$ and can completely meet the tension of the vast majority beam.

- (4) Under the thermal action, the maximum axial pressure of the frame column is -353.8 kN , and the maximum axial tension is 585.1 kN , both in grid A. In grid A, the maximum axial force is -8645 kN under the action of dead load, and the minimum is -3981 kN . So, the effect of the axial force of the column under the thermal action is very small.
- (5) Under the thermal action, the maximum shear force of the frame column in the X direction is 924 kN and in the Y direction is 1114 kN . Under the action of earthquake, the maximum shear force of the frame column in the X direction is 350 kN and in the Y direction is 605 kN . So, the effect of the shear force of the column under the thermal action is big. But the shear capacity of the concrete section of the bottom column is

$$V_c = 1/\gamma R_E * 0.15\beta_c * f_c * b * h_0 = 6674 \text{ kN}$$

Shear force under the thermal action has no effect on the calculation of stirrups.

- (6) Under the thermal action, the maximum bending moment of the frame column in the X direction is 6279.4 kNm and in the Y direction is 7699.6 kNm . Under the action of earthquake (without considering seismic adjustment), the maximum bending moment of the frame column in the X direction is 2317 kNm and in the Y direction is 4626 kNm . So, the effect of the bending moment of the column under the thermal action is big. Longitudinal reinforcement in the column increases slightly.

4.3 *Analysis of the Material Consumption Under the Earthquake Action and Thermal Action*

After a variety of working conditions, the amount and increment of the reinforcement in the frame beam and column are shown in Table 5.

From the table,

- (1) When do not consider the earthquake action and only consider the effect of the thermal action, the increase of reinforcement in beam is relatively large, and the change of the reinforcement in column is very small. The maximum increment of the reinforcement in beam is 21 tons. The increment is $21/191 = 11\%$ of beam reinforcement and 5.16% of the overall framework.
- (2) When considering the earthquake action, the amount of the reinforcement in beam and column under various thermal actions is increased. The maximum increment of the reinforcement in beam is 13.4 tons. The increment is $13.4/252 = 5.3\%$ of beam reinforcement. The maximum increment of the reinforcement in column is 7 tons. The increment is $7/349 = 2\%$ of column reinforcement. But they are not in the same condition. The whole reinforced maximum increment is 16.5 tons, and the increment is 2.74% of the overall framework.
- (3) When do not considering thermal action, and the anti-seismic grade of the structures is 2, the amount of the reinforcement in beam is 60 tons more than without considering the earthquake action, and the increment is 32% of beam reinforcement. The amount of the reinforcement in column is 138 tons more, and the increment is 66% of column reinforcement. The increment is 50% of the overall framework.
- (4) When considering of the thermal action, the anti-seismic grade of the structures is 2, and the increment of reinforcement is less than 3% of the framework.

Further analysis of the distribution of longitudinal reinforcement in the up and bottom of the beam, stirrups, and torsional longitudinal reinforcement, by do not considering temperature as a benchmark, the amount of the reinforcement in beam is all increased when considering temperature. The maximum increment is 13 tons. However, the amount of the longitudinal reinforcement in the bottom of the beam with considering temperature is all less than the amount without considering temperature. The amount of the longitudinal reinforcement in the up of the beam is increased at part load conditions, especially the beam of the first floor which force is bigger. The upper floors and part load conditions are decreased. Under different temperature conditions, stirrups is increased, and the maximum increment is $63 - 53 = 10$ tons; torsional longitudinal reinforcement is also increased, and the maximum increment is $3.821 - 2.48 = 1.34$ tons.

Further analysis of changes of the longitudinal reinforcement and stirrup in the frame column is not considering the earthquake action, and the amount of the reinforcement in column is basically unchanged under various conditions of

Table 5 Amount and increment of the reinforcement in the frame beam and column

Calculation combination	Reinforcement in beam (t)	Reinforcement in column (t)	Total	With thermal action as the benchmark, the reinforcement increment	Increment percentage (%)
Seismic action is not considered	No thermal action	190.896	401.68	0	0.00
	Heating up 26 °C	207.271	418.20	16.527	4.11
	Cooling 43 °C	208.642	419.37	17.696	4.41
	Cooling 43 °C	211.682	422.41	20.736	5.16
	12.5 °C of shrinkage				
	Cooling 55.5 °C	210.12	210.752	420.87	19.191
Anti-seismic grade of the structures is 2.	No thermal action	251.792	601.09	0	0.00
	Heating up 26 °C	254.753	606.32	5.236	0.87
	Cooling 43 °C	257.787	610.22	9.129	1.52
	Cooling 43 °C	265.159	617.58	16.491	2.74
	12.5 °C of shrinkage				
	Heating up 26 °C	259.805	353.894	613.69	12.607
Cooling 43 °C					
Heating up 26 °C	261.261	356.252	617.51	16.421	2.73
Cooling 55.5 °C					
No thermal action	252.741	348.485	601.22	0.134	0.02
Elastic plate					

thermal action. In the normal design of considering seismic action, the column reinforcement has a slight increase, and the maximum increment is 7 tons. The incremental percentage is $7/349.3 = 2\%$. The reinforcement is almost all concentrated in the change of the first layer of column longitudinal reinforcement. On the whole structure, considering the temperature effect, in addition to one layer, the column reinforcement basically has no change.

4.4 The Comparison of the Frame Materials with the Super-Long Frame Structure and the Joint Structure

The comparison of the materials with the overall structure with the most unfavorable temperature effect and the joint structure is shown in Table 6.

For the overall structure with considering temperature, the reinforcement in beam and column saves 8 tons. Steel saves 102 tons. The volume of concrete frame beam and column saves 400 m³.

4.5 Analysis and Comparison of the Material Quantity of Floor Slab Considering Temperature Effect

Temperature rises under working conditions, and the maximum tensile strength in the floor is 81 kN/m. The tensile strength in each floor is less than the tension that the floor can withstand. Reinforcement of floor slab is unchanged.

Table 6 Material quantity comparison

Structural style	The structure with joint	The overall structure without considering temperature	B-A	The overall structure with considering temperature	C-A
Component name	Total: A	T.1–T.11: B		T.1–T.11: C	
Reinforcement in beam (t)	255.1	251.8	−3.3	268.547	13.447
Reinforcement in column (t)	378.5	349.3	−29.2	356.25	−22.25
Steel (t)	3063	2961	−102	2961	−102
Concrete of beam (m ³)	4335.2	4236.4	−98.8	4236.4	−98.8
Concrete of column (m ³)	3820	3515.6	−304.4	3515.6	−304.4

Under cooling conditions, because large tensile force is produced in the floor with contractile structure, the maximum tension in the floor is 792 kN/m. The tensile strength in each floor is larger than the tension that the floor can withstand, so each layer of the slab reinforcement has a growth. Considering the double two-way reinforcement type, the amount of the reinforcement in floor will increase 220 tons than without considering temperature.

5 Conclusions

- (1) The overall structure is more reasonable than the structure with joint. Structural misalignment is small. The structure can be better coordinated to work together.
- (2) The internal force of beam and column is proportional completely, but the direction is opposite. The internal force under the condition of concrete shrinkage and cooling is proportional (error within 5%).
- (3) Considering the thermal action, the amount of the reinforcement in beam is increased. But the amount of the longitudinal reinforcement in the bottom of the beam with considering temperature is all less than the amount without considering temperature. The amount of the longitudinal reinforcement in the up of the beam is increased at part load conditions, especially the beam of the first floor which force is bigger. The upper floors and part load conditions are decreased. Stirrups and torsional longitudinal reinforcement is also increased.
- (4) Considering the thermal action, the column reinforcement has a slight increase. The reinforcement is almost all concentrated in the change of the first layer of column longitudinal reinforcement.
- (5) Considering the thermal action, and considering the double two-way reinforcement type, the amount of the reinforcement in floor will increase 220 tons than without considering temperature.
- (6) When the anti-seismic grade of the structures is 2 and considered thermal action, comparing the two structures with joints with not considering thermal action, the reinforcement in beam and column saves 8 tons. The reinforcement in the floor increases 220 tons. Steel saves 102 tons. The volume of concrete frame beam and column saves 400 m³.

References

1. GB 50009-2012 Load code for the design of building structures [S]. Beijing: China Architecture & Building Press, 2012.
2. GB 50010-2010 Code for design of concrete structures [S]. Beijing: China Architecture & Building Press, 2010.

3. GB 50011-2010 Code for seismic design of building [S]. Beijing: China Architecture & Building Press, 2010.
4. DL/T 5095-2013 Technical code for design load of main building in fossil-fired power plant and the conventional island of nuclear power plant [S]. Beijing: China Planning Press, 2014.

Application of an Adaptive COMET Method to a PWR Benchmark Problem with Gadolinium

Kyle Remley, Farzad Rahnema, Ding kang Zhang
and Andrew Johnson

Abstract Coarse Mesh Radiation Transport (COMET) is a reactor physics method and code that has been used to solve reactor core problems. The method has been shown to be accurate in both its calculation of core eigenvalue as well as its calculation of fission density for every pin in the core. COMET solutions also enjoy excellent computational efficiency, as calculations are performed in a runtime that is several orders of magnitude less than Monte Carlo techniques. The method is a response-based, decomposing the problem domain into subvolumes, called coarse meshes, which allows for the global eigenvalue problem to be converted into a system of fixed-source problems. This produces no approximation if fluxes on coarse mesh interfaces are known. However, these are not known a priori, so an approximation is made in the form of a flux expansion. Responses to an assumed incoming boundary flux using an assumed expansion function are computed for each unique coarse mesh in a precalculation and stored in a response library. A deterministic iterative algorithm uses these precomputed responses to solve the coupled system of fixed-source problems, resulting in a full-core solution. In an effort to improve the computational efficiency of the code, a method has been developed that allows for automated adaptive selection of flux expansion orders in a COMET solution. An ideal flux expansion should be low in order to ensure computational efficiency but still ensure satisfactory accuracy in a calculation. In previous implementations of the COMET method, this flux expansion has been held constant throughout a problem and has been dependent upon user input and numerical experimentation. The method described in this paper allows the flux expansion to vary based upon both mesh-dependent (e.g., mean free path) and problem-dependent (e.g., imposition of boundary conditions and loading patterns in a reactor core) factors. Previous work with the method has shown that it has selected flux expansions that maintain accuracy in COMET calculations while increasing computational efficiency as compared to a COMET calculation employing maximum expansions in the response library for both small problems as well as a full-core PWR benchmark problem. This work extends the method to

K. Remley · F. Rahnema (✉) · D. Zhang · A. Johnson
Georgia Institute of Technology, Atlanta, GA, USA
e-mail: farzad@gatech.edu

another benchmark problem that is larger in size with different material composition. The benchmark problem selected in this paper is a 4-loop PWR core with gadolinium. The adaptive method will select expansion orders to obtain an accurate solution for this problem relative to the benchmark COMET solution, and its performance in terms of both accuracy and computational efficiency will be assessed. Results will be provided in the full paper.

1 Introduction

The COMET (coarse mesh radiation transport) method has been developed and used to solve whole reactor core eigenvalue and flux distribution problems. COMET enables exact modeling of problem geometry without spatial homogenization while calculating global and local solutions with accuracy comparable to stochastic computations. A strength of the method is its formidable computational efficiency. COMET calculations are carried out in a computational runtime that is several orders of magnitude faster than Monte Carlo computations. The method has been found to be highly accurate and efficient in various reactor configurations typical of light and heavy water reactors (e.g., PWR, BWR, CANDU) [1], prismatic configurations such as a sodium-cooled fast reactor [2], and gas-cooled reactors [3].

COMET is a response-based method. A whole-core eigenvalue problem can be transformed into a system of fixed-source problems by decomposing a reactor core problem into non-overlapping coarse meshes. If the global flux on coarse mesh surfaces and the core eigenvalue are known, this decomposition produces no approximation. However, these are not known a priori, so a way to proceed is via a flux expansion. Responses (e.g., resulting outgoing fluxes and pin fission density) to incoming boundary fluxes using an assumed expansion function are calculated for every unique coarse mesh in a precalculation. These computed responses are stored in a database and are used in a deterministic iterative algorithm to solve the decomposed system of fixed-source problems, allowing for a global solution to be found.

The flux expansion, which allows for the solution of the system of fixed-source problems to be found, is an important element in the COMET calculation. In this paper, the adaptive method previously developed by Remley and Rahnema [4–6] that allows the flux expansion to vary in a problem is described and applied to a new PWR benchmark problem.

For the benefit of the reader, a brief review of the COMET method is provided in Sect. 1. Section 2 details the adaptive method. The benchmark problem solved in this study is described in Sect. 3. The results are presented and discussed in Sect. 4. Concluding thoughts are given in Sect. 5.

2 COMET Method Review

In this section, we briefly review the COMET method. While a more thorough description of the method is given in the references [7, 8], the method is detailed here for completeness and the sake of the reader. Emphasis in this section will be placed on the domain decomposition and flux expansion on mesh surfaces since these expansions motivate the adaptive method.

2.1 Domain Decomposition

The COMET method begins with the transport equation for a steady-state distribution of neutrons in a large heterogeneous volume V given as

$$\begin{aligned}
 & \widehat{\Omega} \cdot \nabla \psi(\vec{r}, \widehat{\Omega}, E) + \sigma(\vec{r}, kE) \psi(\vec{r}, \widehat{\Omega}, E) \\
 &= \int_0^\infty dE' \int_{4\pi} d\widehat{\Omega}' \sigma_s(\widehat{\Omega}', E' \rightarrow \widehat{\Omega}', E) \psi(\vec{r}, \widehat{\Omega}', E') \\
 &+ \frac{\chi(\vec{r}, E)}{4\pi k} \int_0^\infty dE' \nu \sigma_f(\vec{r}, E') \int_{4\pi} d\widehat{\Omega}' \psi(\vec{r}, \widehat{\Omega}', E') \quad (1)
 \end{aligned}$$

with the boundary condition

$$\psi(\vec{r}_b, \widehat{\Omega}, E) = B\psi(\vec{r}_b, \widehat{\Omega}', E'), \hat{n} \cdot \widehat{\Omega} < 0, \hat{n} \cdot \widehat{\Omega}' > 0, \vec{r}_b \in \partial V. \quad (2)$$

In the boundary value problem (1–2), ψ is the angular flux distribution about phase space $(\vec{r}, \widehat{\Omega}, E)$ covering position \vec{r} , angle $\widehat{\Omega}$, and energy E . The problem has global eigenvalue k , boundary denoted by ∂V , unit outward normal \hat{n} , and boundary condition operator B . For notational convenience, it is common to rewrite Eq. (1) in operator form, where transport and fission operators are given in their typical forms:

$$\begin{cases}
 H\psi(\vec{r}, \widehat{\Omega}, E) = \frac{1}{k} F\psi(\vec{r}, \widehat{\Omega}, E) \\
 H = \widehat{\Omega} \cdot \nabla + \sigma(\vec{r}, E) - \int_0^\infty dE' \int_{4\pi} d\widehat{\Omega}' \sigma_s(\widehat{\Omega}', E' \rightarrow \widehat{\Omega}, E) \\
 F = \frac{\chi(\vec{r}, E)}{4\pi} \int_0^\infty dE' \nu \sigma_f(\vec{r}, E') \int_{4\pi} d\widehat{\Omega}'
 \end{cases} \quad (3)$$

The COMET method then decomposes this heterogeneous volume V into non-overlapping subvolumes V_i , called coarse meshes. Within each coarse mesh, the angular flux φ_i is determined by the boundary value problem

$$\begin{cases} H\varphi_i(\vec{r}, \widehat{\Omega}, E) = \frac{1}{k}F\varphi_i(\vec{r}, \widehat{\Omega}, E) \\ \varphi_i^-(\vec{r}_{is}, \widehat{\Omega}, E) = \psi(\vec{r}_{is}, \widehat{\Omega}, E), \vec{r}_{is} \in V_{is} \end{cases} \quad (4)$$

In boundary value problem (4), the “-” superscript indicates incoming flux, and V_{is} represents surface s of the i th coarse mesh. It should be noted that the problem given by (4) is equivalent to the problem given by (1–2) when the k in (4) is held to the global eigenvalue. This restriction, along with the boundary condition in (4), makes this a fixed-source rather than an eigenvalue problem. If a solution to problem (4) is found, the angular flux within coarse mesh V_i is equivalent to the global angular flux ψ . Therefore, if local angular fluxes can be calculated for the coupled (through the mesh interfaces) system of equations given by (4), then the global problem (1–2) can be solved with this domain decomposition without approximation.

2.2 Flux Expansion

In practice, however, the boundary condition in (4) requires the global angular flux and eigenvalue, which are not known a priori in reactor calculations. A way to proceed, then, is via a flux expansion. The COMET method expands the incoming and outgoing angular fluxes on mesh surfaces in a known set of orthogonal polynomials

$$\psi^{+/-}(\vec{r}_{is}, \widehat{\Omega}, E) = \sum_m J_{s,m}^{i,+/-} \Gamma_m(\vec{r}, \widehat{\Omega}, E), \quad (5)$$

where the “+/-” superscripts indicate incoming and outgoing directions, $J_{s,m}^{i,+/-}$ are expansion coefficients for surface s , and m is moment for the i th coarse mesh. Γ_m is a known orthogonal polynomial of moment m . Using this flux expansion and the linearity of the transport equation, the angular flux within an mesh can be constructed as a superposition of response functions $R_{s,m}^i$:

$$\varphi_i = \sum_s \sum_m J_{s,m}^{i,-} R_{s,m}^i. \quad (6)$$

The response function satisfies the transport equation in coarse mesh V_i

$$HR_{s,m}^i(\vec{r}, \widehat{\Omega}, E) = \frac{1}{k} FR_{s,m}^i(\vec{r}, \widehat{\Omega}, E) \quad (7)$$

with fixed global eigenvalue k and the boundary condition

$$R_{s,m}^i(\vec{r}_{is}, \widehat{\Omega}^-, E) = \begin{cases} \Gamma^m(\vec{r}_{is}, \widehat{\Omega}^-, E) & \text{for } \vec{r} \in \partial V_{is} \\ 0, & \text{otherwise} \end{cases} \quad (8)$$

The expansion coefficients are defined the half-space (incoming or outgoing) as

$$J_{s,m}^{i,+/-} = \int dE \int_{\partial V_{is}} d\vec{r} \int_{n^{+/-} \cdot \widehat{\Omega} > 0} d\widehat{\Omega} (\hat{n}_{is}^{+/-} \cdot \widehat{\Omega}) \varphi_i^{+/-}(\vec{r}, \widehat{\Omega}, E) \Gamma^m \quad (9)$$

The expansion set Γ_m can vary depending upon the implementation of the method [3, 7, 8]. However, the implementation used in this study is orthogonal polynomials in space (Legendre polynomials in x and y directions on the mesh face) and angle (Chebyshev polynomials of the second kind in polar angle cosine μ and Legendre polynomial in azimuthal angle φ) and a delta function in energy in accordance with multigroup formulation:

$$\Gamma^{ijklg} = \delta(E - E_g) P_i(x) P_j(y) U_k(\mu) P_l(\varphi). \quad (10)$$

We see that the zeroth-order expansion function is unity regardless of expansion set $\{x, y, \mu, \varphi\}$, which means that the 0th-order expansion coefficients are simply the incoming and outgoing partial currents on each mesh, thus guaranteeing currents to be continuous across mesh interfaces for converged solutions. Furthermore, if the expansion set is complete, an infinite flux expansion solves the problem without approximation. However, in practice, truncation of the expansion (and therefore an approximation) must be made. Clearly, an ideal choice for expansion order is one that is low enough to maintain computational efficiency while simultaneously preserving desired accuracy in reactor calculations.

2.3 Solution Method

COMET calculations are carried out in two stages. The first stage is response generation. Each unique coarse mesh is modeled individually, a fixed-source problem described by Eqs. (7)–(8) is solved. These calculations are done with a stochastic method to allow for explicit modeling of problem geometry. Outgoing fluxes are tallied in response to the assumed boundary condition as well as other quantities of interest (e.g., pin fission densities). Calculations are carried out for each surface of each unique mesh, and the responses are stored in a library.

It should be noted that in this precomputation phase, only unique subvolumes in a reactor problem need to be modeled. Regardless of a particular coarse mesh appearing in a reactor multiple times, it need only be modeled once in this calculation stage. As such, after responses for unique meshes are computed, reactor problems using any loading this unique coarse meshes can be solved. Therefore, a significant advantage of the method lies in its ability to quickly handle repeated calculations (e.g., for optimization studies in reactor design).

The second stage of COMET calculations is the deterministic sweep. In this stage, the coupled system of fixed-source problems given by Eq. (4) is solved. Starting from an initial guess for both flux and global eigenvalue, two layers of iterations converge the solution. Inner iterations update flux, and outer iterations update eigenvalue. Both sets of iterations continue a converged solution is found. This deterministic algorithm is often aided by two forms of acceleration: low-order acceleration (LOA) and Chebyshev polynomial filtering. LOA increases efficiency by using a low-order solution as an improved initial guess on flux and eigenvalue, and Chebyshev polynomial filtering increases the convergence rate of the inner iterations through the use of the Chebyshev polynomials. For more information on both calculation stages of the method as well as a more thorough explanation of the acceleration methods, the reader is encouraged to review the references [8].

3 Adaptive Method Theory

In the previous section, it was mentioned that a feature of the method was a careful selection of expansion order that allowed for both sufficient accuracy and computational efficiency to be achieved in reactor calculations. The optimal flux expansion may vary in a problem depending upon physics within meshes (e.g., neutron mean free path or angular flux gradient), interaction with other meshes, and imposition of boundary conditions. In an effort to find this optimal flux expansion, Remley and Rahnema [4–6] have developed a method that adaptively selects flux expansions for each mesh based upon problem- and mesh-dependent phenomena. The method is briefly described here, but the reader is encouraged to review the references [6] for a more thorough description of the method.

The adaptive criterion focuses on information retained in truncation flux expansions. If high-ordered terms offer small contributions to the overall expansion, they can be discarded. If a flux expansion is truncated after n terms, then e bounds the error, given by

$$\left| \varphi(\vec{r}, \hat{\Omega}, E) - \sum_{m=1}^n J_m^- R_m(\vec{r}, \hat{\Omega}, E) J \right| \leq e \quad (11)$$

In Eq. (10), summation over surface and coarse mesh index has been suppressed for notational convenience. The inequality (10) may not be useful *prima facie* since

it compares to an unknown true solution φ , but if one assumed that a flux expansion of maximum order is sufficiently close to φ (a fair assumption given COMET demonstrated accuracy using previously selection flux expansions), then the error bound can be written as

$$\sum_{m=1}^N J_m^- R_m(\vec{r}, \widehat{\Omega}, E) - \sum_{m=1}^N J_m^- R_m(\vec{r}, \widehat{\Omega}, E) \leq e. \quad (12)$$

Dividing both sides by the maximum (N th)-ordered expansion, then the following inequality is yielded:

$$\left| \frac{\sum_{m=1}^n J_m^- R_m(\vec{r}, \widehat{\Omega}, E)}{\sum_{m=1}^N J_m^- R_m(\vec{r}, \widehat{\Omega}, E)} - 1 \right| \leq \varepsilon. \quad (13)$$

From inequality (12), the adaptive criterion arises: if a truncation expansion of order n differs a sufficiently small amount ε from the maximum expansion of order N , then truncation to order n is appropriate.

It should be noted that this criterion requires a comparison with the maximum-ordered expansion. Therefore, some knowledge of the maximum expansion is needed, and some iterations with the maximum expansion must be carried out. An addition to the deterministic solution algorithm described in the previous section must be made. Typical COMET calculations involve an initial guess for flux and eigenvalue followed by sets of inner iterations of a fixed number followed by an outer iteration. Typically, the number of inner iterations used is 150, as this has been seen to satisfactorily converge flux in between updates in eigenvalue. However, these many iterations with the maximum expansion are unnecessary for successful application of the adaptive method and can slow a calculation with too many full-ordered calculations. With the use of the acceleration techniques described in the previous section, the first set of inner iterations employing the maximum expansion is limited to 10 iterations before the adaptive selection of expansion orders. This limitation has worked well in previous studies [6] and works well with the benchmark used in this paper.

In inequality (12), the effects of problem-dependent phenomena are contained in the expansion coefficients J_m^- , which vary for each coarse mesh used in a problem, while the responses R_m only vary for each unique mesh. With this knowledge, the inequality (12) could be applied to each surface of each mesh, and a unique expansion could be used for each mesh, including repeated meshes of the same response type. However, for an arbitrarily large problem, the memory requirement of tracking and applying mesh-dependent information to so many meshes could limit the method's applicability. Instead, the expansion used for each unique mesh is allowed to vary, and problem-dependent effects are accounted through averaging methods.

We proceed by applying the inequality (12) to every mesh in the problem, including repeated meshes of same response type. The relative differences ε are combined in a weighted average for each unique mesh type. These averaged ε values are used to decide the ideal point of truncation for each unique mesh type. The type of averaging used is partial current-weighted averaging:

$$\varepsilon_l = \frac{\sum_s \sum_i J_{s,0,l}^{-i} \varepsilon_{s,i,l}}{\sum_s \sum_i J_{s,0,l}^{-i}}. \quad (14)$$

In Eq. (13), $\varepsilon_{s,i,l}$ is the relative difference on surface s of mesh i of unique mesh type l . $J_{s,0,l}^{-i}$ is the incoming partial current on surface s of mesh i of unique coarse mesh l .

We have mentioned that a relative difference of ε between expansions is sufficient for an expansion to be truncated below the maximum. However, the decision for an appropriate value of ε depends on problem- and mesh-dependent factors and could vary between different unique mesh types. To determine what value of ε to use for differing mesh types, we use a parameter p to help give insight in deciding the appropriate relative difference between a full and truncated expansion on mesh-dependent basis. The parameter is given as

$$\left\{ \begin{array}{l} p_l = \frac{\text{prod}_l}{\text{abs}_l} - k_{\text{guess}}, \\ \text{prod}_l = \frac{\sum_{s,d} J_{s,0}^{-i} \sum_{s,m} J_{s,m}^{-i} R_{NF}^{l,s,m}}{\sum_{s,i} J_{s,0}^{-i}}, \\ \text{abs}_l = \frac{\sum_{s,d} J_{s,0}^{-i} \sum_{s,m} J_{s,m}^{-i} R_{AB}^{l,s,m}}{\sum_{s,i} J_{s,0}^{-i}}. \end{array} \right. \quad (15)$$

In Eq. (14), prod_l and abs_l are the neutron production and absorption values in unique mesh l , k_{guess} is the initial guess for eigenvalue in a calculation, and $R_{NF}^{l,s,m}$ and $R_{AB}^{l,s,m}$ are neutron production and absorption responses, respectively. We use the values for ε at different values of p from the reference [6]. These values are provided in Table 1. As in [6], the value α is chosen to be 0.1.

Table 1 Values of ε for associated values of p

Mesh type	ε
$ p < \alpha$	1.0E-3
$ p \geq \alpha$	5.0E-4
$ p = k_{\text{mesh}}$	5.0E-4

4 Benchmark Specification

We demonstrate the adaptive COMET method on a full-core PWR benchmark problem. This section describes the benchmark problem and the computational model used in calculating a core eigenvalue and pin fission density profile for each configuration of the benchmark. The problem selected is a stylized full-core PWR with gadolinium derived from Douglass et al. [9], and the standard COMET method solved this problem previously [1, 10]. While a full description of the benchmark is given in the references, the problem is briefly described here.

The problem is comprised of 193 square fuel assemblies 21.505 cm on a side. Standard fuel assemblies in the reactor core contain uranium oxide fuel pins, enriched to 4.1% weight enrichment of U-235. In addition, there are assemblies that contain fuel rods doped with gadolinium as a burnable reactivity control feature. In such fuel rods, the fuel is enriched to 2.6% by weight U-235, and contains 6% gadolinium by weight. In addition, the core features assemblies at different burn levels: fresh fuel, 15 GWd/T (once burned), 33 GWd/T (twice burned), and 50 GWd/T (thrice burned). A radial cross section of the core is illustrated in Fig. 1, where the different colors designate different fuel assemblies. Figure 2 shows the axial meshing of the core used in modeling the problem, which features 17 zones along the active core length.

There are three configurations of this problem depending upon control rod insertion: all-rods-in (ARI), all-rods-out (ARO), and some-rods-in (SRI). Control rods are inserted into assemblies as indicated by Fig. 1. In the ARI configuration, all control rods are inserted into the core. In the SRI configuration, only control rods in the assemblies marked “P” will have control rods inserted. In the ARO configuration, no control rods are inserted.

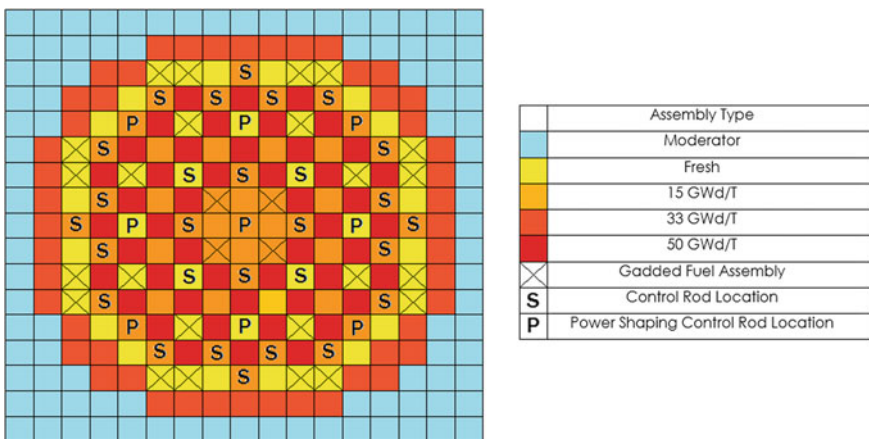
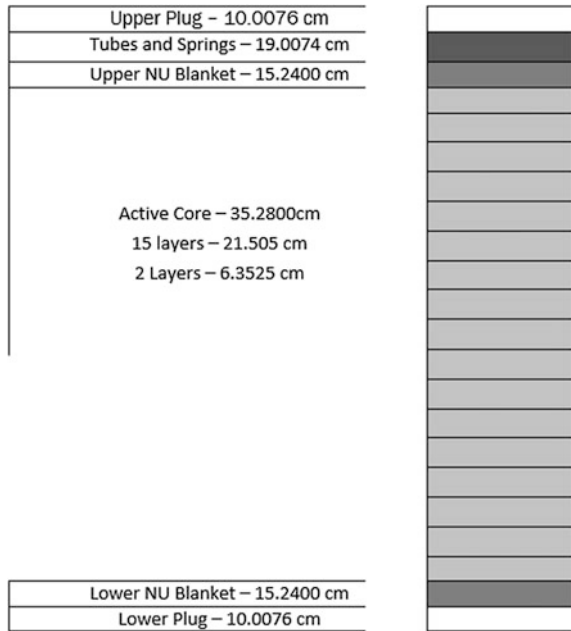


Fig. 1 Radial view of the PWR

Fig. 2 Axial meshing of PWR



4.1 Computational Model

Using a two-energy group cross-sectional library as indicated by Ref. [9], a response library was computed using the stochastic code MCNP5 [11]. 50 million particles were run for each case. Surface flux, pin fission density, neutron production, and neutron absorption responses were calculated. The maximum expansion computed in the library was sixth order in space and second order in angle. In previous COMET solutions to this problem as well as other PWR problems [1], it was seen that an expansion of fourth order in space and second order in angle is sufficient to attain desired accuracy; however, we view a good test of the adaptive method is its ability to select appropriate expansions when a higher expansion is available, thus improving computational efficiency in this case.

The computational model used to solve the benchmark problem consists of 39 unique coarse meshes. These unique meshes are numbered and specified in Table 5 in the next section.

5 Results

In evaluating the results, the standard COMET solutions employing the maximum {6,6,2,2} expansion to this problem are taken as the benchmark. This is because we seek to demonstrate the adaptive COMET method’s ability to maintain accuracy while demonstrating increased efficiency over the standard solution. In all cases (both standard and adaptive), both LOA and Chebyshev polynomial filtering are used to accelerate the COMET solutions. In all cases, the standard and adaptive COMET solutions for both eigenvalue and pin fission density distributions are compared. Eigenvalue results are given in Table 2.

In Table 2, both the statistical uncertainty (one standard deviation) and differences in eigenvalue are reported in pcm. From this table, it can be seen that the adaptive COMET solution is in excellent agreement in eigenvalue with the standard {6,6,2,2} COMET solution for all core configurations, with differences under 1 pcm and within the combined uncertainty of the results. The eigenvalue results can be considered virtually identical.

To measure pin fission density agreement, several statistical measures were used. The error (E), average error (AE), mean relative error (MRE), root-mean-square error (RMSE), and maximum error (ME) are defined as

$$E = \left| \frac{FD_s - FD_a}{FD_s} \right| \tag{16}$$

$$AE = \frac{1}{n} \sum_i E_i \tag{17}$$

$$MRE = \frac{\sum_i E_i FD_s^i}{\sum_i FD_i} \tag{18}$$

$$RMSE = \sqrt{\frac{1}{n} \sum_i E_i^2} \tag{19}$$

$$ME = \text{MAX}_i(E_i) \tag{20}$$

Using these measures, the pin fission density agrees with the standard {6,6,2,2} COMET solution for the adaptive COMET solution. The results are tabulated in Table 3. All values are reported in percent.

Table 2 Eigenvalue results

	ARO	SRI	ARI
Standard {6,6,2,2}	1.053225 ± 0.6	1.051636 ± 0.6	0.973930 ± 0.5
Adaptive	1.053220 ± 0.6	1.051634 ± 0.6	0.973926 ± 0.5
Difference in mk—Adaptive	0.5 ± 0.8	0.2 ± 0.8	0.6 ± 0.7

Table 3 Pin fission density agreement

	ARO	SRI	ARI
AE	0.09	0.08	0.08
MRE	0.07	0.07	0.08
RMSE	0.2	0.2	0.1
ME	1.6	1.6	1.5

Table 4 Speedups for difference core configurations

	ARO	SRI	ARI
Standard {6,6,2,2}	1.0 (4.2 h)	1.0 (4.0 h)	1.0 (4.7 h)
Adaptive	5.8 (0.72 h)	4.5 (0.89 h)	5.2 (0.90 h)

In addition, the average and maximum uncertainties in pin fission density values were 0.1 and 0.3%, respectively. From Table 3, it is seen that the adaptive COMET solution preserves the pin fission density accuracy of the standard {6,6,2,2} COMET solution very well—with the exception of the maximum error, the pin fission density solutions are nearly identical.

The relative runtimes of the solution methods are compared as well. The speedups of the adaptive COMET solutions are calculated as the ratio of the {6,6,2,2} runtime to the adaptive runtime. The speedups are tabulated in Table 4. In addition, runtimes for each case are indicated in parentheses in each cell of the table.

From Table 4, it is seen the adaptive COMET solutions are much faster computations than the standard {6,6,2,2} solutions. From the differences in accuracy between the solution methods, it can be concluded that the standard {6,6,2,2} solution is not necessary, and the adaptive method leads to a much more efficient problem solution.

The flux expansion results from the use of the adaptive COMET solution method are presented in Table 5.

From Table 5, it is seen that our assertion that a full {6,6,2,2} COMET solution is not necessary to obtain accurate results for this benchmark problem is supported by the selected expansions. With the exception of some controlled assemblies and the peripheral active core assemblies in the SRI and ARI configurations, the automatically selected flux expansions chosen by the adaptive method are lower than the maximum {6,6,2,2} expansion order allowed. Indeed, an expansion set of {4,4,2,2} or lower works well for the active core region and primarily an expansion set of {2,2,2,2} works well for core periphery regions. From the literature [1, 10], it is seen that {4,4,2,2} expansions sets in standard COMET solutions have been used to reach satisfactory accuracy in solving problems of PWR type. Because of this, the {4,4,2,2} standard COMET solution is the “state-of-the-art” solution method, and a comparison between this solution and the adaptive COMET solution is appropriate.

Table 5 Unique coarse mesh types and flux expansions selected x, y, μ, φ

	Coarse mesh type	ARO	SRI	ARI
1	UO ₂ uncontrolled, fresh, full size	3,3,2,2	3,3,2,2	4,4,2,2
2	UO ₂ controlled, fresh, full size	N/A	6,6,2,2	6,6,2,2
3	UO ₂ gadded, fresh, full size	4,4,2,2	4,4,2,2	4,4,2,2
4	UO ₂ uncontrolled, once burned, full size	2,2,2,2	3,3,2,2	3,3,2,2
5	UO ₂ controlled, once burned, full size	N/A	6,6,2,2	6,6,2,2
6	UO ₂ gadded, once burned, full size	2,2,2,2	3,3,2,2	3,3,2,2
7	UO ₂ uncontrolled, twice burned, full size	4,4,2,2	4,4,2,2	5,5,2,2
8	UO ₂ uncontrolled, thrice burned, full size	3,3,2,2	3,3,2,2	4,4,2,2
9	UO ₂ uncontrolled, fresh, small size	4,4,2,2	4,4,2,2	5,5,2,2
10	UO ₂ controlled, fresh, small size	N/A	6,6,2,2	6,6,2,2
11	UO ₂ gadded, fresh, small size	4,4,2,2	6,6,2,2	6,6,2,2
12	UO ₂ uncontrolled, once burned, small size	6,6,2,2	6,6,2,2	6,6,2,2
13	UO ₂ controlled, once burned, small size	N/A	6,6,2,2	6,6,2,2
14	UO ₂ gadded, once burned, small size	4,4,2,2	6,6,2,2	6,6,2,2
15	UO ₂ uncontrolled, twice burned, small size	6,6,2,2	6,6,2,2	6,6,2,2
16	UO ₂ uncontrolled, thrice burned, small size	6,6,2,2	6,6,2,2	6,6,2,2
17	UO ₂ uncontrolled blanket, fresh	4,4,2,2	4,4,2,2	4,4,2,2
18	UO ₂ controlled blanket, fresh	N/A	6,6,2,2	6,6,2,2
19	UO ₂ uncontrolled plug, fresh	2,2,2,2	2,2,2,2	2,2,2,2
20	UO ₂ controlled plug, fresh	N/A	6,6,2,2	4,4,2,2
21	UO ₂ gadded plug, fresh	2,2,2,2	2,2,2,2	2,2,2,2
22	UO ₂ uncontrolled plug, once burned	2,2,2,2	2,2,2,2	2,2,2,2
23	UO ₂ controlled plug, once burned	N/A	6,6,2,2	4,4,2,2
24	UO ₂ gadded plug, once burned	2,2,2,2	2,2,2,2	2,2,2,2
25	UO ₂ uncontrolled plug, twice burned	2,2,2,2	2,2,2,2	2,2,2,2
26	UO ₂ uncontrolled plug, thrice burned	2,2,2,2	2,2,2,2	2,2,2,2
27	UO ₂ uncontrolled tube spring, fresh	2,2,2,2	2,2,2,2	2,2,2,2
28	UO ₂ controlled tube spring, fresh	N/A	4,4,2,2	4,4,2,2
29	UO ₂ gadded tube spring, fresh	2,2,2,2	2,2,2,2	2,2,2,2
30	UO ₂ uncontrolled tube spring, once burned	2,2,2,2	2,2,2,2	2,2,2,2
31	UO ₂ controlled tube spring, once burned	N/A	4,4,2,2	4,4,2,2
32	UO ₂ gadded tube spring, once burned	2,2,2,2	2,2,2,2	2,2,2,2
33	UO ₂ uncontrolled tube spring, twice burned	2,2,2,2	2,2,2,2	2,2,2,2
34	UO ₂ uncontrolled tube spring, thrice burned	2,2,2,2	2,2,2,2	2,2,2,2
35	Moderator 1	4,4,2,2	4,4,2,2	4,4,2,2
36	Moderator 2	4,4,2,2	4,4,2,2	4,4,2,2
37	Moderator 3	4,4,2,2	4,4,2,2	4,4,2,2
38	Moderator 4	2,2,2,2	4,4,2,2	2,2,2,2
39	Moderator 5	2,2,2,2	2,2,2,2	2,2,2,2

5.1 Comparison with {4,4,2,2}

As with the adaptive COMET solution, the standard {4,4,2,2} COMET solution nearly exactly recovers the eigenvalue of the full-ordered solution. The results are given in Table 6.

Similarly, the fission density agreement between {6,6,2,2} and {4,4,2,2} is nearly identical to the agreement between {6,6,2,2} and the adaptive COMET solution. These results are given in Table 7.

In addition, the relative speedups of the standard {4,4,2,2} over the standard {6,6,2,2} were calculated and are presented in Table 8.

From Tables 6, 7 and 8, we see that the adaptive COMET method recovers the same level of accuracy as the standard {4,4,2,2} COMET solution method with a similar speedup over the standard {6,6,2,2} COMET solution. While the standard {4,4,2,2} COMET solution is faster than the adaptive COMET solution for the SRI and ARI cases, the differences in runtimes between the adaptive COMET method and this standard COMET solution method are small compared to the large speedup relative to the {6,6,2,2} solution. In addition, the flux expansions used in the adaptive COMET solution are automatically selected, while the {4,4,2,2} expansion set was selected through numerical experimentation—multiple standard COMET solutions at various expansions were used to determine if a satisfactory level of accuracy had been reached, but a single adaptive COMET calculation reached the desired accuracy in the solution.

Table 6 Comparison of eigenvalues between {6,6,2,2} and {4,4,2,2}

	ARO	SRI	ARI
Standard {6,6,2,2}	1.053225 ± 0.6	1.051636 ± 0.6	0.973930 ± 0.5
Standard {4,4,2,2}	1.053222 ± 0.6	1.051633 ± 0.6	0.973924 ± 0.5
Difference	0.2 ± 0.8	0.1 ± 0.8	0.4 ± 0.7

Table 7 Pin fission density agreement for {4,4,2,2}

	ARO	SRI	ARI
AE	0.07	0.07	0.1
MRE	0.04	0.04	0.09
RMSE	0.1	0.1	0.2
ME	1.6	1.6	1.6

Table 8 Speedups for {4,4,2,2}

	ARO	SRI	ARI
Standard {6,6,2,2}	1.0 (4.2 h)	1.0 (4.0 h)	1.0 (4.7 h)
Standard {4,4,2,2}	5.5 (0.76 h)	5.2 (0.76 h)	6.2 (0.76 h)

6 Conclusion

The work done in this study extends the use of the adaptive COMET method from the references [4–6] to a new PWR benchmark. As in the previous work with the method, accuracy is preserved from standard COMET solutions while appreciably increasing computational efficiency. As in [6], this computational efficiency is comparable to that of previous COMET solutions but with the benefit of automatically selected flux expansions. This will limit the need for numerical parameter studies in the future when COMET is applied to new designs and configurations, as appropriate flux expansions to retain desired accuracy can be automatically selected, provided the response library is sufficiently high-ordered.

Future work includes applying this adaptive COMET method to other reactor cores (e.g., fast reactors) as an important area of study. In addition, new weighted averaging techniques in the adaptive method such as adjoint weighted averaging are of interest.

Acknowledgments The first author's work was supported under a Department of Energy Nuclear Energy University Program (NEUP) Graduate Fellowship. The second author's work was supported under the Nuclear Regulatory Commission (NRC) Graduate Fellowship. The 2nd author owns equity in a company that has licensed the COMET technologies from Georgia Tech. This study which is a demonstration of COMET could affect his personal financial status. The terms of this arrangement have been reviewed and approved by Georgia Tech in accordance with its conflict of interest policies.

References

1. Rahnema, F., Zhang, D., Connolly, K., "The COMET method for reactor physics calculations," PBNC2014-099, Presented at the Pacific Basin Nuclear Conference, Vancouver, British Columbia, Canada, August 24–28 2014.
2. Ulmer, R., Rahnema, F., Connolly, K.J., "A neutronic benchmark specification and COMET Solution for the advanced burner test reactor," *Ann. Nucl. Energy*, accepted, July (2015).
3. Connolly, K.J., Rahnema, F., "Heterogeneous coarse mesh radiation transport method for neutronic analysis of prismatic reactors," *Ann. Nucl. Energy*, **56**, 87–101 (2013).
4. Remley, K., Rahnema, F., "Fuel pin problem solution via an accelerated COMET method," Transactions of the American Nuclear Society, Presented at the American Nuclear Society Winter Meeting, Anaheim, CA, November 9–13 2014.
5. Remley, K., Rahnema, F., "An adaptive COMET solution to a configuration of the C5G7 benchmark problem," ANS MC2015 - Joint International Conference on Mathematics and Computation (M&C), Supercomputing in Nuclear Applications (SNA) and the Monte Carlo (MC) Method, Presented at ANS MC2015, Nashville, Tennessee, April 19–23 2015.
6. K. Remley and F. Rahnema, "A method for the adaptive selection of angular flux expansion orders in the coarse mesh radiation transport (COMET) method," *Nuclear Science and Engineering*, accepted November (2015).
7. S. W. Mosher and F. Rahnema, "The incident flux response expansion method for heterogeneous coarse mesh transport problems," *Transport Theory and Statistical Physics*, Vol. 35, 2006, pp. 55–86.

8. D. Zhang and F. Rahnema, "An efficient hybrid stochastic/deterministic coarse mesh neutron transport method," *Annals of Nuclear Energy*, Vol. 41, 2012, pp. 1–11.
9. S. Douglass, F. Rahnema, and J. Margulies, "A stylized three dimensional PWR whole-core benchmark problem with gadolinium," *Annals of Nuclear Energy*, Vol. 27, 2010, pp. 1384–1403.
10. D. Zhang and F. Rahnema, "COMET whole-core solutions to a 3-dimensional PWR benchmark problem with gadolinium," PHYSOR 2012 – Advances in Reactor Physics, Knoxville, Tennessee, 2012 April 15–20.
11. X-5 Monte Carlo Team, "MCNP—A general Monte Carlo n-particle transport code, version 5," Los Alamos National Laboratory, 2005.

Calculation and Analysis of Cavitation for Low-Head Safety Injection Pump

Changliang Liu, Sheng Meiling, Jingmeng Qiu and Wenhong He

Abstract Net positive suction head available (NPSHa) under different temperatures is calculated for the low-head safety injection pump in a pressurized water reactor power plant, and the temperature impact on NPSHa is analyzed. The analysis results show that, when the water reaches saturation, NPSHa of the low-head safety injection pump is minimum, but still larger than net positive suction head required (NPSHr) of low-head safety injection pump, so the pump cavitation will not occur.

Keywords Nuclear energy science and engineering · Low-head safety injection pump · Net positive suction head available (NPSHa) · Net positive suction head required (NPSHr) · Safety injection system

1 Introduction

Low-head safety injection pump (LHSI) is an important equipment for the safety injection system of pressurized water reactor nuclear power plant. In the event of loss of coolant accident (LOCA) or main steam line break (MSLB) and other accidents, the low-head safety injection pump was put in service rapidly by a safety injection signal and a great amount of boric water is injected into the core for cooling the core, so as to prevent the core returning to the critical. As an engineered safety system, the safety injection system is mainly used to mitigate the design basis

C. Liu (✉) · S. Meiling · J. Qiu
Process and Layout Design Division, China Nuclear Power
Engineering Co.Ltd., Beijing, China
e-mail: 18610087233@163.com

S. Meiling
e-mail: shengml@cnpe.cc

W. He
Purchase Department, China Nuclear Power Engineering Co.Ltd., Beijing, China

accident and prevent this kind of accident becoming serious accident. So the low-head safety injection pump plays an important role in nuclear power plant.

Cavitation is a common pump failure. When the pump is in operation, if the absolute pressure of the liquid is reduced to the evaporation pressure at that time in the partial liquid flow area, the liquid begins evaporation and the steam is formed. The steam bubbles with the liquid flow into the high-pressure region of the impeller, and under the action of high pressure and in a very short period of time, the bubble ruptures and recondenses into liquid. The liquid around the bubble is centralized to the center of the bubble, which produces a large impact. The impact acts on the wall of the pump and forms the destruction to the pump. The production and development of cavitation will change the velocity distribution in the flow channel, so that the efficiency and total head of the pump are reduced, which will cause the pump vibration and noise, and damage of the inner wall of the impeller and pump case [1, 2].

At present, the vertical centrifugal pump has been used as the low-head safety injection pump of pressurized water nuclear power plant, which has the possibility of cavitation. If the low-head safety injection pump cavitation occurs, it will cause an immeasurable impact on the safety of nuclear power plant. In this work, the cavitation margin of a nuclear power plant's low-head safety pump was calculated and analyzed which can be used to judge whether the cavitation will occur and provide reference not only for the operation of pressurized water nuclear power plant, but also for other nuclear power plants.

2 The Theory of NPSH

NPSHa is the surplus energy of unit weight liquid which is more than the vaporization pressure at the pump inlet, also known as the effective net positive suction head. NPSHa is determined by the system parameters of liquid suction pipe and medium flow in the pipeline, which is independent of the structure of centrifugal pump.

NPSHr is the pressure drop of the pump's own inlet, and its significance is to ensure that the pump cavitation does not occur and the unit weight liquid at the pump inlet has surplus energy more than the vaporization pressure, also known as the required net positive suction head. NPSHr is determined by the centrifugal pump manufacturers based on the correlative test which usually uses 20 °C water under the rated flow, and the unit is generally used the meter water column on project. NPSHr is determined by the pump structure and has a direct relationship with the structure of centrifugal pump.

$NPSHa > NPSHr$ is the condition to avoid cavitation. NPSHa and NPSHr should use the same datum.

3 Calculation of NPSHa

3.1 Whole Calculation

The configuration in upstream of low-head safety injection pump for the safety injection system of the nuclear power plant is shown in Fig. 1. The low-head safety injection pump absorbs water from the containment sump via the filter, valve, elbow, and piping, and then, the water is pressurized by the pump and injected into the reactor coolant system. Figure 1 shows only the part related to the calculation of cavitation for the low-head safety injection pump, and the safety injection system in the actual nuclear power plant is far more complex than that. It is needed to explain that there is only one bend in Fig. 1; however, in fact, this section of the pipeline has a total of four bends.

If the pressure unit is meter water column uniformly, then the NPSHa of the low-head safety injection pump can be calculated using formula (1).

$$\begin{aligned}
 \text{NPSHa} = & \text{Qualitative pressure} + \text{Lifting height} - \text{Pipeline total pressure drop} \\
 & - \text{Saturation pressure}
 \end{aligned}
 \tag{1}$$

“Qualitative pressure” in the formula (1) refers to the containment pressure above the surface of the sump; “Lifting height” refers to potential energy between the containment sump level and low-head safety injection pump suction port; “Pipeline total pressure drop” includes the pressure drop of the pipe, elbow, valve, and sump filter; “Saturation pressure” refers to the water saturation pressure of sump.

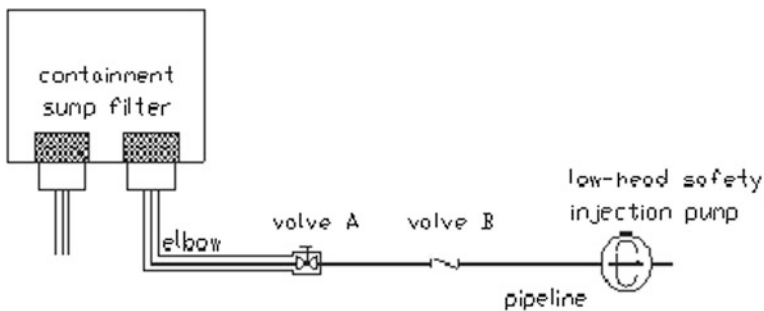


Fig. 1 Configuration in upstream of low-head safety injection pump

3.2 Calculation of Qualitative Pressure

In order to calculate different NPSHa of low-head safety injection pump under different temperatures, the water temperature of sump is selected as 30, 80, 90, 100, and 120 °C. Containment sump water is low-concentration borated water which can be as purity water on project, and the thermodynamic properties of the sump water can be looked up on diagram of water and steam thermodynamic properties [3]. The containment is designed to withstand the maximum negative pressure value of 0.025 MPa, while the pressure is 0.101325 MPa and the minimum pressure inside the containment is 0.076325 MPa.

According to Formula (1), the smaller the qualitative pressure is, the more conservative the calculation is. When the sump water is not saturated, the minimum pressure inside the containment is chosen as qualitative pressure, which is 0.076325 MPa. When the sump water is saturated, the sump water saturation pressure is chosen as qualitative pressure. The value of qualitative pressure is shown in Table 1. There are two qualitative pressures “MPa” and “meter water column” in Table 1, and they are not equal because the density of water is different at different temperatures.

3.3 Calculation of Lifting Height

The centerline height of low-head safety injection pump suction port is -6.255 m, and the containment sump level is conservatively assumed as the lowest water level of -2.2 m, so the lifting height is 4.055 m.

3.4 Calculation of Pipeline Total Pressure Drop

The pipeline total pressure drop is related to the flow rate of safety injection system and the water temperature of containment sump. The maximum value 950 m³/h that

Table 1 Values of the qualitative pressure

Temperature (°C)	Containment minimum design pressure (MPa)	Saturation pressure (MPa)	Qualitative pressure (MPa)	Qualitative pressure (meter water column)
30	0.076325	0.00425	0.076325	7.814
80	0.076325	0.0474	0.076325	8.006
90	0.076325	0.0702	0.076325	8.06
100	0.076325	0.101	0.101	10.743
120	0.076325	0.199	0.199	21.509

may occur during the system recirculation operation is elected as the flow rate. The water temperatures of sump such as 30, 80, 90, 100, and 120 °C are selected.

According to the actual situation, in the calculation of the pipeline total pressure drop, there are some assumptions as follows:

- (a) The pipeline is insulation; that is, the physical parameters of the fluid do not change;
- (b) The flow is in square resistance region; that is, the resistance coefficient of local pressure drop is independent of the flow velocity.

3.4.1 Pressure Drop of Pipeline

Pressure drop of pipeline is calculated by formula (2)–(6) [4]:

$$dp = k \frac{\rho v^2}{2} \quad (2)$$

$$k = f \frac{L}{d} \quad (3)$$

$$v = \frac{Q}{\pi \left(\frac{d}{2}\right)^2} \quad (4)$$

$$f = \left[1.14 - 2 \log \left(\frac{\varepsilon}{d} + \frac{9.35}{\text{Re} \sqrt{f}} \right) \right]^{-2} \quad (5)$$

$$\text{Re} = \frac{\rho v d}{\mu} \quad (6)$$

In the formula, dp refers to pressure drop, k refers to the resistance coefficient, ρ refers to the density, Q refers to the flow rate, v refers to the fluid flow velocity, d refers to the inner diameter, f refers to the friction coefficient, ε refers to the roughness (desirable 0.0125), and Re refers to the Reynolds number.

Firstly, the Formula (5) is solved by the iterative method, and then, the final result will be obtained by the combination of the Formula (2)–(6).

3.4.2 Pressure Drop of Elbow

Pressure drop of elbow is calculated by Formula (2) and Formula (7).

$$k = ABC \quad (7)$$

In the formula, A refers to the influence coefficient of the elbow angle δ ; B refers to the influence coefficient of relative bending radius r/D ; and C refers to the influence coefficient of relative height-width ratio a_0/b_0 . The calculation method of coefficients (A, B, C) can be found in reference [4].

3.4.3 Pressure Drop of Valve

Pressure drop of valve is calculated by Formula (2) and Formula (8).

$$k = \left[\frac{29.9d^{27}}{C_v} \right]^2 \tag{8}$$

In the formula, C_v refers to the C_v value of valve; k refers to the resistance coefficient; d refers to the inner diameter and the unit is inch.

3.4.4 Pressure Drop of Sump Filter

According to the data provided by the sump filter supplier, the pressure drop of sump filter under different temperatures is shown in Table 2.

3.4.5 Pipeline Total Pressure Drop

Pipeline total pressure drop is the summation of pressure drop of pipeline, pressure drop of elbow, pressure drop of valves, and pressure drop of sump filter. Calculation results are shown in Table 2.

Table 2 Pipeline total pressure drop

Temperature (°C)	Pressure drop of pipeline (m)	Pressure drop of elbow (m)	Pressure drop of two valves (m)	Pressure drop of sump filter (m)	Pipeline total pressure drop (m)
30	0.22635	0.27516	0.26088	3.4	4.162
80	0.22590	0.27516	0.26068	1.47	2.232
90	0.22586	0.27516	0.26078	1.3	2.062
100	0.22583	0.27516	0.26068	1.15	1.912
120	0.22578	0.27549	0.26068	1	1.762

3.5 Calculation of Saturation Pressure

The sump water saturation pressure can be found in the thermodynamic property chart of water and steam. The saturation pressure values of sump water under different temperatures are shown in Table 3, with the conversion of unit into meter water column.

3.6 Calculation Results of NPSHa

The calculation results of NPSHa for low-head safety injection pump are shown in Table 3.

4 Analysis and Conclusion

When the sump water is saturated, the qualitative pressure is equal to the saturation pressure, and the formula (1) can be simplified as follows:

$$NPSHa = \text{Lifting height} - \text{pipeline total pressure drop} \tag{9}$$

The lifting height is a certain value, and the NPSHa is only related to the pipeline total pressure drop. As can be seen from Table 3, with the increase in temperature, the pipeline total pressure drop decreases and the NPSHa increases.

When the sump water is not saturated, the qualitative pressure is greater than the saturation pressure, so the NPSHa at unsaturation water is more than the NPSHa at saturation water.

So the sump water has just reached saturation, and the NPSHa of low-head safety injection pump is the minimum.

Under the assumptions of this paper, when the sump water temperature is 100 °C, the NPSHa of low-head safety injection pump is the minimum value of 2.143 m. According to the pump manufacturer’s test data, when the flow rate is 950 m³/h, the

Table 3 Calculation results of NPSHa for low-head safety injection pump

Temperature (°C)	Qualitative pressure (m)	Pipeline total pressure drop (m)	Lifting height (m)	Saturation pressure (m)	NPSHa (m)
30	7.814	4.162	4.055	0.434	7.273
80	8.006	2.232	4.055	4.792	4.857
90	8.06	2.062	4.055	7.413	2.64
100	10.743	1.912	4.055	10.743	2.143
120	21.509	1.762	4.055	21.509	2.293

NPSHr of low-head safety injection pump is 0.8 m. NPSHa is greater than NPSHr under various temperatures, so the NPSHa of low-head safety injection pump meets the requirements, and the possibility of cavitation is less which can meet the requirements of nuclear power plant operation.

References

1. Guan Xingfan, Technical Manual of Modern Pumps [S], China Astronautic publishing house, 1995.
2. Liang Chao, Investigation of Fault Diagnosis of Cavitation in Centrifugal Pump Using Pressure Fluctuation Method [D], Database of China's Outstanding Masters' Degree Thesis, 2010.
3. Yan Jialu, Yu Xiaofu, The Table and Diagram for Water and Steam [S], Higher Education Press, 2004.
4. CRANE. Flow of Fluids Through valves, fittings and pipe [S]. U.S.A. 2010.

Coupled Neutronics and Thermal–Hydraulics Analysis of Annular Fuel Assembly for SCWR

Chuanqi Zhao, Kunpeng Wang, Liangzhi Cao, Hongchun Wu and Youqi Zheng

Abstract During pre-conceptual design of supercritical water-cooled reactor (SCWR), assembly design is very important and affects core performance. Coupled neutronics and thermal–hydraulics analysis is required for dramatic changes of water density in SCWR. Annular fuel assembly is optimized from the point of view of neutronics and thermal–hydraulics performance using three-dimensional coupling code. Three-dimensional diffusion calculation for annular fuel assembly is carried out using FENNEL-N. Pin power distribution is obtained. With these power, SUBSC is used to perform sub-channel analysis. The effects of fuel rod distance and gap between fuel rods and assembly box on assembly performance are researched in the coupled analysis. Results have shown that increasing fuel rod distance and rod-to-box gap will increase k_{inf} and assembly power peaking factor. It is also shown in the results that heating heterogeneity of sub-channels plays a big role in assembly thermal performance and adding grid will flatten coolant outlet temperature as well as decrease maximum cladding surface temperature. Safety analysis of annular fuel assembly shows that the assembly is safe from the point of view of neutronics.

Keywords SCWR · Annular fuel assembly · Coupling calculation

1 Introduction

Supercritical light water reactor (SCWR) is a thermal reactor cooled and moderated by supercritical water [1]. Water does not exhibit a phase change from liquid to gas above 22.1 MPa. Therefore, the plant system is simpler and more compact than PWRs and BWRs without a dryer, water-steam separators, and recirculation pumps.

C. Zhao (✉) · K. Wang
Nuclear and Radiation Safety Center, Beijing, China
e-mail: zhaochuanqi@chinansc.cn

L. Cao · H. Wu · Y. Zheng
School of Nuclear Science and Technology, Xi'an Jiaotong University, Xi'an, Shaanxi, China

The coolant outlet temperature is high because there is no limitation of saturation temperature at supercritical pressure. This results in high thermal efficiency, which is good not only for producing electricity but also for reducing the amount of spent fuel per generated watt of electricity.

In 2001, annular fuel is proposed by MIT to improve the power density of PWR [2, 3]. Annular fuel has many advantages over traditional solid fuel: Firstly, annular fuel has larger heat transfer area; thus, lower fuel temperature can be achieved which means more safety margin. Secondly, fission gas release at high burn-ups decreases as the fuel temperature decreases. Thirdly, the gap at both sides of fuel pellet provides more space for fuel swelling, and the probability of cladding damage decreases. Fourthly, annular fuel has larger rod diameter and it is helpful to avoid flow-induced vibration (FIV). Lastly, density of coolant in the center is large enough to provide sufficient moderation. In 2014, a pre-conceptual design of SCWR with annular fuel is proposed by Xi'an JiaoTong University [4]. In that design, the optimization is focused on core design. More optimization of fuel assembly should be carried out.

In this study, the annular fuel assembly is analyzed using three-dimensional neutronics and thermal-hydraulics coupling method. At first, the coupling code is developed. Traditional two-step method is used for neutronics calculation, and sub-channel method is introduced in thermal-hydraulics calculation. Then, optimization is performed using this code to improve the fuel assembly performance. At last, the safety of the fuel assembly is estimated from the viewpoint of neutronics.

2 Neutronics/Thermal-Hydraulics Coupling Code

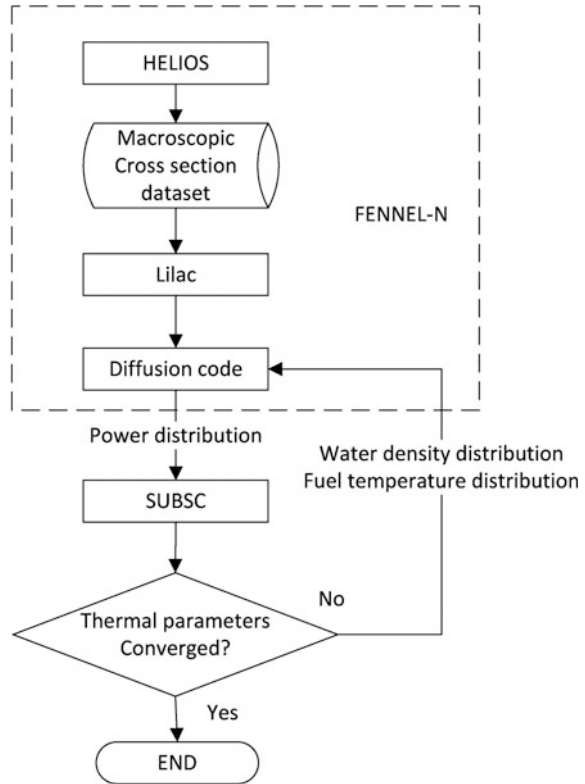
2.1 Calculation Code

A three-dimensional coupling code for fuel assembly analysis is developed in this study. There are three modules in this code, including neutronics module FENNEL-N, sub-channel analysis module SUBCS, and the coupling module. The coupling flow chart is shown in Fig. 1.

FENNEL-N is based on two-step method which is widely used in PWRs calculations. HELIOS is suitable to calculate complex geometry, and it is chosen to carry out fuel assembly calculation [5]. Macroscopic cross sections obtained in assembly calculation are fitting using Lilac code [6]. The diffusion code uses these fitting coefficients to get macroscopic cross sections for diffusion calculation. A three-dimensional code for hexagonal geometry, SIXTUS, is used as diffusion solver [7].

SUBSC is a sub-channel code for steady state single-phase flow calculation. Three-dimensional conduction model is introduced in fuel rod conduction calculation to get accurate fuel temperature distribution. SUBSC uses IAPWS-IF97 formulation to calculate water properties over supercritical pressure. Heat transfer

Fig. 1 Flow chart of coupling calculation



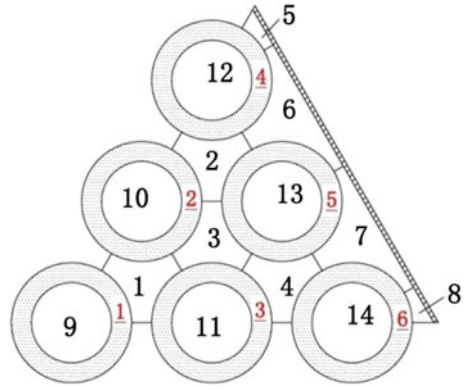
correlations will affect results, and the commonly used Bishop correlation [8] is chosen for supercritical water.

In the coupling calculation, FENNEL-N carries out the diffusion calculation based on initial water density and fuel temperature distribution. The three-dimensional power distribution can be obtained in diffusion calculation. This power is transferred to SUBSC for sub-channel calculation. SUBSC will provide new water density and fuel temperature distribution. If these thermal parameters are converged with the previous ones, the coupling calculation is finished. Otherwise new thermal parameters are used to update the macroscopic cross sections for next diffusion calculation. The data transmission between FENNEL-N and SUBSC is processed by coupling module.

2.2 Calculation Model

In neutronics calculation, a single fuel assembly with axial reflector at both top and bottom is calculated. Reflection and vacuum conditions are taken as radial and axial

Fig. 2 Sub-channel Division of 1/6th assembly



boundary condition, respectively. Average linear power density of the j th layer $P_{j\text{home}}$ is obtained after three-dimensional diffusion calculation. With the results of HELIOS assembly calculation and fitting coefficient, the power form factor of the i th fuel rod at j th layer f_{ij}^{hete} is calculated. The power distribution for each fuel rod in the fuel assembly can be calculated by Eq. (1).

$$P_{ij} = f_{ij}^{\text{hete}} \cdot P_j^{\text{homo}} \tag{1}$$

The sub-channel calculation is performed with the fuel rod power distribution. In annular fuel rod, the channel at the center is closed and it is called internal channel; channels among fuel rods are connected, and these are called external channel. Because of symmetrical geometry, one-sixth of the fuel assembly is calculated in sub-channel calculation as shown in Fig. 2. In Fig. 2, division and serial number of sub-channel are given. Besides, the serial number of fuel rod is given in red underlined number. The coolant flows into internal channels from the top and flows upwards through the assembly in external channels. External sub-channels can be categorized into three groups. The first group is called center channel, including channels 1 and 4. The second group is called side channel, including channels 6 and 7. The last group is called corner channel, including channels 5 and 8. Water density distribution in each channel and each fuel rod temperature distribution can be obtained after sub-channel calculation. These parameters are used in FENNEL-N for next neutronics calculation.

3 Fuel Assembly Optimization

The hexagonal fuel assembly is shown in Fig. 3. The fuel assembly is consist of 19 fuel rods which are optimized in reference 4. In order to adjust coolant flow rate, closed fuel assembly is chosen in SCWR. The gap between adjacent fuel rods D_g and the gap between fuel rod and assembly boxes D_{box} will affect the neutronics

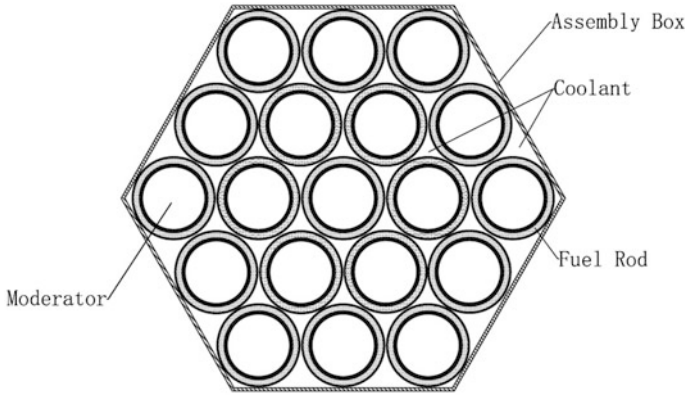


Fig. 3 Sketch of annular fuel assembly

and thermal–hydraulics performance. The coupled code is used to analyze the fuel assembly performance, and optimizations are done based on the analysis.

3.1 Neutronics Performance

In order to analyze neutronics performance of the fuel assembly, moderator density is set 600.0 kg m^{-3} and the coolant density is set 150.0 kg m^{-3} . HELIOS is used to calculate the change of k_{inf} with D_g and D_{box} . The results are shown in Fig. 4. It can be seen that k_{inf} increases with the increase in D_g and D_{box} . This is because there is more water in the fuel assembly with the increase in D_g and D_{box} , and more moderation is provided.

Fig. 4 Change curve of assembly k_{inf} with D_g and D_{box}

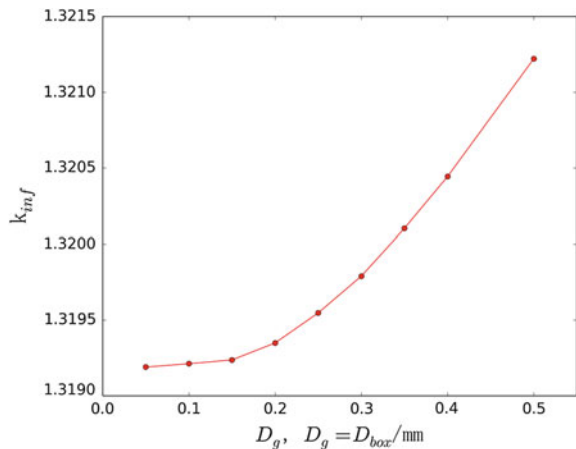
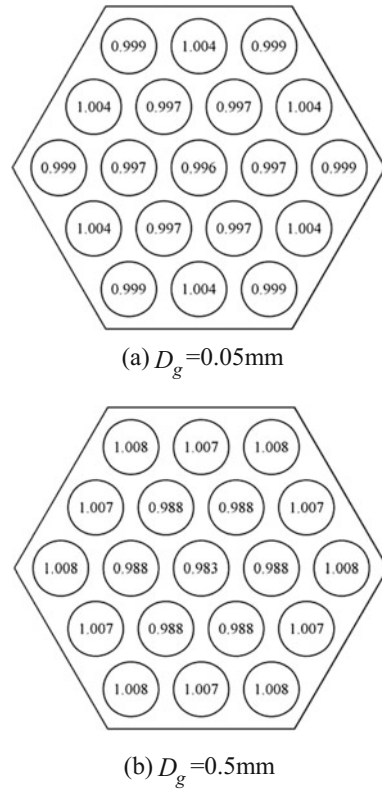


Fig. 5 Assembly relative power distribution.
a $D_g = 0.05$ mm.
b $D_g = 0.5$ mm



The power distribution inside the fuel assembly will also change with D_g and D_{box} (assuming $D_g = D_{\text{box}}$). The results show that the relative power peaking factor changes from 1.004 to 1.008 while D_g changes from 0.05 to 0.5 mm. Power distributions of $D_g = 0.05$ mm and $D_g = 0.5$ mm are shown in Fig. 5. In Fig. 5, the circle represents annular fuel rod and the number in it means relative power factor. The hexagon represents assembly box. It can be seen that the power of 6 fuel rods at the corner increases with increase in D_g . This is because there is more water in the corner with the increase of D_g and more moderation is provided. Figure 5 also shows that the relative power peaking factor is low for annular fuel assembly which is beneficial to decreasing the MCST.

3.2 Thermal–Hydraulics Performance

There are many aspects in thermal–hydraulics performance, such as axial water density distribution, fuel temperature distribution, cladding temperature distribution, flow distribution, and coolant outlet temperature distribution. Coolant outlet

temperature distribution is important among them. Flat coolant outlet temperature is helpful to increase safety margin.

Coupled code is used to analyze the thermal–hydraulics performance. In the calculation, the coolant inlet temperature is 280 °C, and outlet temperature is 500 °C. The system pressure is 25 MPa.

The coupling calculation is carried out with different D_g and D_{box} . In order to analyze the results, a variable named peaking factor is defined as the ratio of maximum value to average value of one thermal parameter in external sub-channels. The peaking factor of coolant outlet temperature and coolant outlet flow rate is shown in Fig. 6. As shown in Fig. 6, the peaking factors of coolant outlet temperature and flow rate decrease with the increase in D_g and D_{box} . The Maximum cladding surface temperature (MCST) is also shown in Fig. 6. The MCST decreases with the increase in D_g and D_{box} .

In order to explain the result in Fig. 6, a variable named HA is declared to represent the heterogeneous of different sub-channel group. The HA can be calculated by Eq. (2).

$$HA = \frac{P_h}{A} \tag{2}$$

where, P_h —sub-channel heat perimeter/cm; A —sub-channel flow area/cm².

The change of sub-channel HAs and its ratios with D_g and D_{box} are shown in Fig. 7. When D_g and D_{box} increase, the HAs of three sub-channel groups decrease, which means different sub-channels are heated more evenly. With the mixture between sub-channels, the flow rate distribution and coolant outlet temperature are

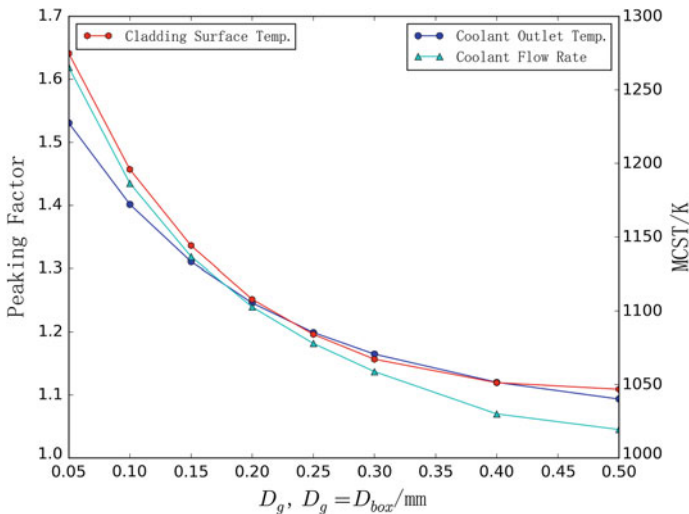


Fig. 6 Changing curve of peaking factor and MCST with D_g

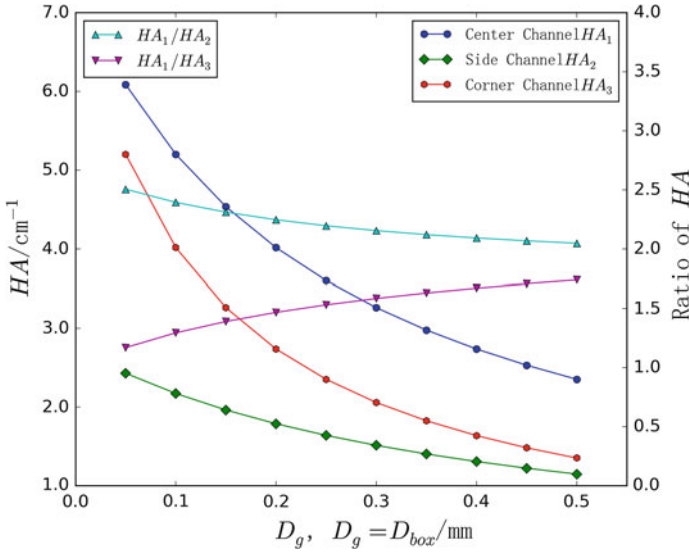


Fig. 7 Changing curve of sub-channel HA and ratios with D_g

more flat. It will cause the decrease in MCST, which is consistent with the result in Fig. 6.

As shown in Fig. 7, the HA ratio of different sub-channel group is high, which is not good for flat flow rate distribution. When $D_{box} = 0.5D_g$, the HA of corner channel and center channel is equal. The HA of side channel is always less than that of other two groups with increase in D_g . Therefore, increasing the HA of side channel will decrease the HA ratio and flatten flow rate distribution and outlet temperature distribution.

The HA of side channel can be increased by decreasing its flow area. There are two ways to decrease its flow area: structure inside the assembly box and spacer grid. Structure inside the assembly box will introduce more stainless steel which will absorb neutron. With spacer grid, the flow area can be changed by changing of mixing vane size. Using spacer grid makes less effect on neutronics performance because of less stainless steel.

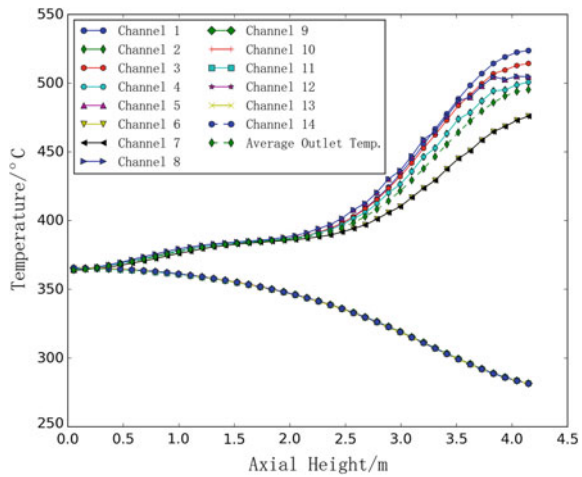
When $D_{box} = 0.5D_g$, the HAs of center channel and side channel are made to be equal by adjusting mixing vane. There are 13 grids in axial direction. The first grid is 21.0 cm above the bottom, and grid space is 31.5 cm. The coupling calculation is carried out with 3 different D_g . The peaking factors of coolant outlet temperature and flow rate and MCST are shown in Table 1.

As shown in the table, the peaking factor of outlet temperature and flow rate and MCST decreases after adding spacer grid and mixing vane. When $D_g = 0.3$ cm, the MCST is lowest. MCST is higher when D_g is smaller. It is because sub-channel heterogeneity is larger and peaking factor is larger. MCST is higher when D_g is larger. It is because the coolant flow rate is low and the heat transfer coefficient is

Table 1 Assembly thermal performance with grid

D_g/cm	Center channel HA/cm^{-1}	Peaking factor		MCST/K
		Outlet temperature	Flow rate	
0.1	5.201	1.170	1.341	997.6
0.3	3.261	1.073	1.241	975.8
0.5	2.352	1.040	1.181	995.1

Fig. 8 Axial water temperature distribution of each sub-channel



low. The fuel assembly has better thermal–hydraulics performance when $D_g = 0.3$ cm.

It has been found that when HA ratio of center channel to side channel is equal to 1.2, peaking factor of outlet temperature and flow rate decreases to 1.037 and 1.193, respectively, and MCST decreases to 971.5 K. The axial distribution of coolant and moderator temperature is shown in Fig. 8. The coolant outlet temperature of channels 6 and 7 who have smaller HA is lower than the average value.

The MCST appears at fuel rod No. 4 and 6, the MCST is almost the same because of geometry symmetry. Taking fuel rod No. 4 as an example, the surface temperature of inner and outer cladding is shown in Fig. 9. The cladding temperature is different at different part of fuel rod facing different sub-channel. In Fig. 9, different fuel rod parts are distinguished by the sub-channel number which they are facing. The inner cladding surface temperature is low because of low moderator temperature. The change in external cladding surface temperature is mild because the coolant temperature is near pseudo-critical temperature and the heat transfer coefficient is high. The disturbance of cladding surface temperature is caused by spacer grid. The MCST appears at the top because of axial power distribution. The MCST will decrease after optimization of axial power distribution.

Fig. 9 Axial distribution of inside and outside cladding surface temperature

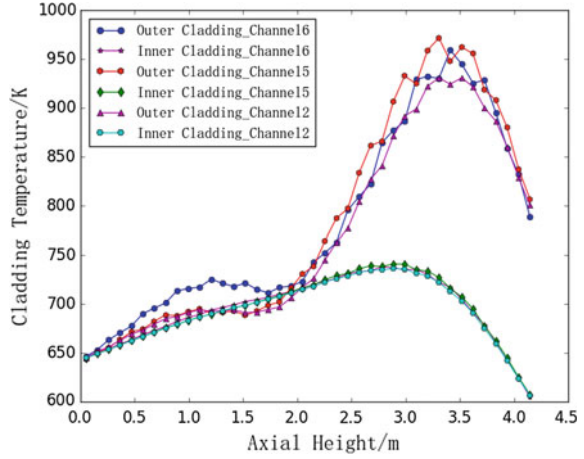


Table 2 Assembly design parameters

Parameters	Values
Distance between fuel rods D_g/cm	0.30
Distance between fuel rod and assembly box D_{box}/cm	0.15
Number of spacer grid	13
Grid spacing/cm	31.5
Assembly box thickness/mm	1.0

The design of assembly box is referred to HPLWR [9]. The material is stainless steel SS316L, and the thickness is 1.0 mm. Design parameters of the annular fuel assembly is shown in Table 2.

4 Assembly Safety

In order to ensure the assembly and core safety, negative void reactivity effect and negative Doppler reactivity coefficient is required.

By increasing void fraction, void reactivity effects for a fuel assembly change as shown in Fig. 10. It decreases as void fraction and burn-up increase and keeps negative.

The Doppler reactivity coefficient is calculated for a typical fuel assembly at the reference fuel temperature of 1000 K. The change in Doppler reactivity coefficient with burn-ups is shown in Fig. 11. The Doppler reactivity coefficient decreases with increase of burn-up and keeps negative.

Fig. 10 Changing curves of void effect with void fraction at different burn-ups

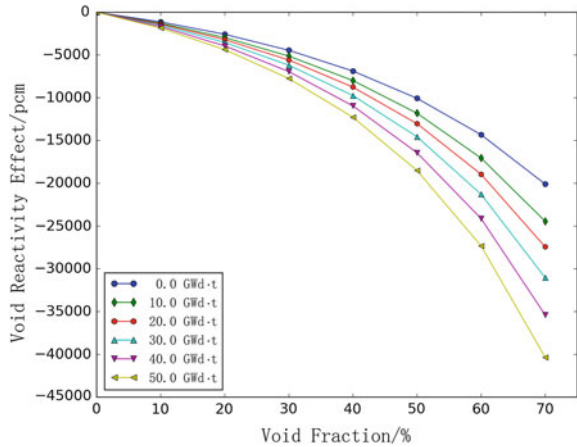
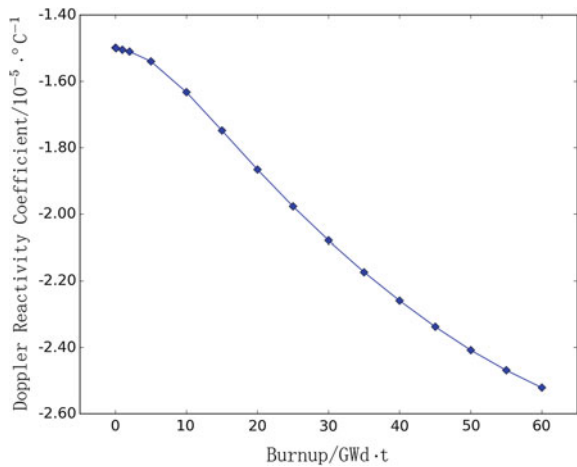


Fig. 11 Changing curve of fuel temperature coefficient with burn-ups



5 Conclusions

Neutronics and thermal–hydraulics performance of annular fuel is analyzed and optimized using three-dimensional coupling code in this study. The results show that increasing of fuel rod gap and gap between fuel rod and assembly box increases k_{inf} but it almost does not affect fine power distribution. The heterogeneity of sub-channels causes ununiformed coolant outlet temperature and flow rate, and it makes the MCST higher. The MCST decreases by adding spacer grid. The safety analysis shows that the assembly has negative void reactivity effect and negative Doppler reactivity coefficient; thus, it is safe from the viewpoint of neutronics.

References

1. DOE U.S., “A Technology Roadmap for Generation IV Nuclear Energy Systems[C],” Washington, DC, USA (2002).
2. Hejzlar P, Driscoll MJ, Kazimi MS, “High Performance Annular Fuel for Pressurized Water Reactors,” *Transactions of the American Nuclear Society*, **84**, 192–204 (2001).
3. Feng D, Hejzlar P, Kazimi MS. “Thermal-Hydraulic Design of High-Power-Density Annular Fuel in PWRs,” *Nuclear Technology*, **160**, 16–44 (2007).
4. Chuanqi Zhao, Liangzhi Cao, Hongchun Wu, *et al.*, “Pre-conceptual core design of SCWR with annular fuel rods,” *Nuclear Engineering and Design*, **267**, 23–33 (2014).
5. Stamml’er R., *User’s Manual for Helios*, Studsvik Scandpower, USA(1994).
6. Gao Shengnan, Wu Hongchun, Li Yunzhao, *et. al.*, “Study on group parameters handling method of PWR[C],” *Conference of Reactor Physics and Particle Transport*, ChengDu, China (2014).
7. Arkuszewski JJ. “Sixtus2 - A Two Dimensional Diffusion Theory Nodal Code in Hexagonal Geometry[J],” *Progress in Nuclear Energy*, **18**, 123–136 (1986).
8. Bishop A.A. SRO, Tong L.S. “Forced Convection Heat Transfer to Water at near-Critical Temperatures and Supercritical Pressures,” Report Wcap-2056 Part IV[R]. Pittsburgh, USA (1964).
9. Hofmeister J, Waata C, Starflinger J, *et al.* “Fuel Assembly Design Study for a Reactor with Supercritical Water,” *Nuclear Engineering and Design*, **237**, 14, 1513–1521 (2007).

Dynamic Sliding Mode Control of Nuclear Steam Generator Water Level Using LPV Schemes

Li Jie, Huang Rongyi and Wang Junling

Abstract Poor control of U-Tube steam generator water level in nuclear power station can lead to frequent reactor shutdowns or damage of turbine blades. The control problem is difficult due to its “swell and shrink” effect and the dynamic characteristics. Therefore, designing a suitable controller for all power levels is extremely necessary to increase the plant safety and availability. This paper is concerned with the design of a linear parameter-varying (LPV)-based sliding mode controller for the water level control of a nuclear steam generator which has parameter-varying dynamics. The proposed controller guarantees both stability and dynamic properties in the entire operating region. The systematical design method for the controller which is automatically adjusted along the reactor power, in terms of LPV theory, is shown. Simulation results illustrate that the controller realizes the quick and accurate control in full operating range, and its performance is superior to conventional PID controllers.

Keywords Nuclear Power Station · Steam generator · Water level control · Dynamic sliding mode controller · Linear parameter-varying theory

1 Introduction

The U-Tube steam generator (UTSG) is one of the main devices in PWR nuclear power station, in order to ensure the safety of nuclear reactor and to prevent the damage of turbine blades during operation, the steam generator’s water level must be controlled in a certain range [1, 2]. However, the control problem is challenging owing to the steam generator is a highly complex, nonlinear, and time-varying system; also, the nonminimum phase effects are significantly greater at low power

L. Jie (✉) · H. Rongyi
China Nuclear Power Engineering Co., Ltd, Beijing, China
e-mail: lee0734@sina.com

W. Junling
Harbin Engineering University, Harbin, Heilongjiang, China

due to the so-called swell and shrink effect. It is well known that traditional PID controller cannot work satisfactorily over all power levels. Therefore, many advanced control methods that include adaptive controllers [3], optimal controllers [4], and predictive controllers [5, 6] have been suggested to solve the water level control problem of nuclear steam generators. However, most of these controllers only handle the problem around a local operating point, with no clear understanding of how to address the global level control problem over the entire operating power range. Furthermore, these controllers are complex both in the design procedures and implementation.

A successful strategy to control uncertain nonlinear systems is sliding mode control (SMC). The sliding mode controller is an attractive robust control algorithm because of its inherent insensitivity and robustness to plant uncertainties and external disturbances. Besides, compared with the traditional sliding mode control method, dynamic SMC method in the sliding surface is selected not only depending on the state of the system, but also the system input or input-order or higher-order derivatives, which greatly weakened the chattering of the sliding mode system [7]. On the other hand, LPV theory can describe the nonlinear system effectively with dependency parameters. Although a sliding mode controller for SG has been proposed by G. R. Ansarifard [8], it does not solve the control problem when the working conditions vary within a wide range. In this context, this paper investigates the potential of employing a LPV-based sliding mode controller for controlling the water level in the entire operating region.

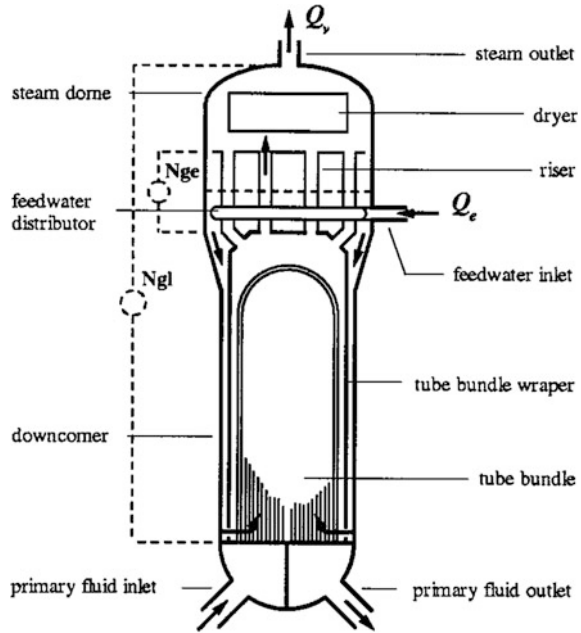
2 Plant Description

2.1 U-Tube Steam Generator (UTSG)

As the most important components of PWR nuclear power station, UTSG transfers thermal energy from the reactor coolant system in the primary side to the secondary side, thus creating steam that will drive the turbines to generate electricity. Figure 1 shows the schematic of a UTSG used in the PWR.

Due to the complex two-phase nature of the steam/water mixture in the steam generator, the water level in the down-comer is not a well-defined quantity. As shown in Fig. 1, there are two kinds of water level measurements: wide range level (N_{gl}) and narrow range level (N_{ge}). The main control objective is to maintain the narrow range water level N_{ge} in the UTSG down-comer within its upper and lower limits. Too high, a level leads to improper functioning of the moisture separators, increasing the moisture in the exiting steam, thereby increasing the erosion of the turbine blades and reducing turbine efficiency. Too low, a level of water leads to insufficient cooling of the primary circuit [6].

Fig. 1 The schematic of a UTSG



2.2 Mathematical Model of Steam Generator

In order to be useful from the point of a model-based control, the UTSG models that we adopted have to be as simple as possible, but still keep a meaningful physical relationship among its main variables. Some theoretical models for UTSG based thermodynamic principles and fundamental conservation equations have been developed. However, the model is too complex for use in controller design.

This paper considers the UTSG model derived by Irving [9, 10]. The model is simple and captures the essential SG dynamics at the same time, which has been widely used for control purpose. The model is described as the following fourth-order Laplace transfer function

$$\begin{aligned}
 Y(s) = & \frac{G_1}{s} (Q_e(s) - Q_v(s)) - \frac{G_2}{1 + \tau_2 s} (Q_e(s) - Q_v(s)) \\
 & + \frac{G_3 s}{\tau_1^{-2} + 4\pi^2 T^{-2} + 2\tau_1^{-1} s + s^2} Q_e(s)
 \end{aligned} \tag{1}$$

where s is the Laplace variable, all constants are positive. The dynamics of a UTSG described in terms of the control input (feed water flow rate Q_e), measurable disturbance (steam flow rate Q_v), and output (water level Y). In (1), G_1/s is the mass capacity term that describes the UTSG level due to the water mass in the UTSG, $-G_2/(1 + \tau_2 s)$ corresponds to the reverse dynamic effect due to swell and shrink

phenomena, and the last term is a mechanical oscillation term caused by the manometer effect.

Considering Eq. (1) and taking the inverse Laplace transform, we can rewrite the transfer function in the following equivalent state-space form:

$$\begin{aligned} \dot{x}(t) &= A(p)x(t) + B(p)u(t) + W(p)q_v(t) \\ y(t) &= Cx(t) \end{aligned} \quad (2)$$

where $x(t) = [x_1^T(t) \ x_2^T(t) \ x_3^T(t) \ x_4^T(t)]^T$, p is the operating power, u denotes the control input, and

$$A(p) = \begin{bmatrix} 0 & 0 & 0 & 0 \\ 0 & a_{22} & 0 & 0 \\ 0 & 0 & a_{33} & 1 \\ 0 & 0 & a_{43} & 0 \end{bmatrix}, B(p) = \begin{bmatrix} b_1 \\ b_2 \\ b_3 \\ 0 \end{bmatrix}, W(p) = \begin{bmatrix} w_1 \\ w_2 \\ 0 \\ 0 \end{bmatrix}, C = [1 \ 1 \ 1 \ 0].$$

with $a_{22} = -\tau_2^{-1}(p)$, $b_1 = G_1(p)$, $b_2 = -G_2(p)/\tau_2(p)$, $a_{33} = -2\tau_1^{-1}(p)$, $b_3 = G_3(p)$, $w_1 = -G_1(p)$, $w_2 = -G_1(p)/\tau_2(p)$, $a_{43} = -\tau_1^{-2}(p) - 4\pi^2 T^{-2}(p)$.

The model parameters of (2) at several power levels, are given in Table 1, for a generic plant. And the parameters are very different according to the power levels. Thus, the control problem was viewed a single input/single output (SISO) control problem with the feed water u as the manipulated variable, the water level as the controlled variable, and the turbine steam demand as an unknown disturbance.

We consider Irving's model as four piecewise LPV systems in accordance with operating power: Region 1 for $5\% \leq p \leq 15\%$, Region 2 for $15\% < p \leq 30\%$, Region 3 for $30\% < p \leq 50\%$, and Region 4 for $50\% < p \leq 100\%$, and then, the system model in each region is supposed to be affine LPV as follows:

$$\begin{aligned} \dot{x}(t) &= A^{(i)}(p)x(t) + B^{(i)}(p)u(t) + W^{(i)}(p)q_v(t) \\ y(t) &= Cx(t) \end{aligned} \quad (3)$$

$i = 1, 2, 3, 4$

Here, the system matrices $A^{(i)}(p)$, $B^{(i)}(p)$ and $W^{(i)}(p)$ are affine functions of p , i represents region.

Table 1 Typical power point parameters of a SG model

$p(\%)$	5	15	30	50	100
$q_v(\text{kg/s})$	57.4	180.8	381.7	660	1435
G_1	0.058	0.058	0.058	0.058	0.058
G_2	9.63	4.46	1.83	1.05	0.47
$\tau_2(\text{s})$	48.4	21.5	4.5	3.6	3.4
$\tau_1(\text{s})$	41.9	26.3	43.4	34.8	28.6
$T(\text{s})$	119.6	60.5	17.7	14.2	11.7
G_3	0.181	0.226	0.310	0.215	0.105

3 Sliding Mode Control

Sliding mode control is a good robust control method. In a more detail, the SMC system could drive the trajectories onto the so-called sliding surface in a finite time and maintain on it thereafter, and on the sliding surface, the system is insensitive to internal parameter perturbations and external disturbances. The control schemes proposed in this section are based on a combination of LPV theory and SMC to achieve a high performance and stability range.

An LPV system is a system where the state-space representation is in the form:

$$\begin{aligned} \dot{x}(t) &= A(\theta(t))x(t) + B(\theta(t))u(t) + D(\theta(t))\zeta(t) \\ y(t) &= C(\theta(t))x(t) \end{aligned} \quad (4)$$

where $y(t)$ denotes the measured output vector and $\zeta(t)$ the disturbance input vector, and $u(t)$ the control inputs, respectively. Here, θ is a vector of time-varying plant parameters, and all plant matrices are functions of the θ .

Following the approach developed by Shtessel [11] is applicable to specify a sliding mode controller:

$$u = \begin{cases} u^+, S(x, e, t) > 0 \\ u^-, S(x, e, t) < 0 \end{cases} \quad (5)$$

where $S(x, e, t)$ is the equation of the dynamic sliding surface. It is defined as a dynamic operator, operating upon some states and upon the output tracking error of the system; u^+, u^- are smooth functions of x and t to make the system output $y(t)$ tracking the given reference output trajectory $y^*(t)$ on sliding surface with the given eigen structure and providing the existence of sliding surface, that is, $\lim_{t \rightarrow \infty} |y^*(t) - y(t)| = \lim_{t \rightarrow \infty} |e(t)| = 0$.

For designing a dynamic sliding surface, system (4) is transformed to a “regular form” [12] which is a system representation usually used for SMC controller design. In regular form, the LPV system in (3) can be written as:

$$\underbrace{\begin{bmatrix} \dot{x}_1(t) \\ \dot{x}_2(t) \end{bmatrix}}_{\dot{x}(t)} = \underbrace{\begin{bmatrix} A_{11}(\theta) & A_{12}(\theta) \\ A_{21}(\theta) & A_{22}(\theta) \end{bmatrix}}_{A(\theta)} \underbrace{\begin{bmatrix} x_1(t) \\ x_2(t) \end{bmatrix}}_{x(t)} + \underbrace{\begin{bmatrix} 0 \\ b_2(\theta) \end{bmatrix}}_{B(\theta)} u(t) + \underbrace{\begin{bmatrix} D_1(\theta) \\ 0 \end{bmatrix}}_{D(\theta)} \zeta(t) \quad (6)$$

where $x_1 \in \mathfrak{R}^{n-1}$, $x_2 \in \mathfrak{R}^1$, $\zeta(t), u(t) \in \mathfrak{R}^1$, and $b_2 \neq 0$.

Considering the state variable x_2 as a virtual control input, we can offer a dynamic sliding surface for this control system as follows:

$$S = \sigma + x_2 = 0 \quad (7)$$

Here, the function σ is a dynamic operator of x_1 . In next section, a state-feedback algorithm is proposed for designing σ . Once (7) is defined, a control law can be synthesized in order to guarantee that the sliding surface is reached in finite time, and subsequently maintained.

Supposing that the sliding mode exists in the system defined by (6) occurs on the dynamic sliding surface $S = 0$, the sliding motion of the system can be described as follows:

$$\begin{cases} \dot{x}_1 = A_{11}(\theta)x_1 - A_{12}(\theta)\sigma + D(\theta)\zeta \\ y = c_1(\theta)x_1 \end{cases} \quad (8)$$

The control law u^+, u^- must be identified guarantees that the existence of the sliding motion in the LPV system (6) with the desired features. A stronger condition, guaranteeing an ideal sliding motion, is the ρ -reachability condition [13] given by

$$S\dot{S} \leq -\rho|S|, \rho > 0 \quad (9)$$

In this case, the condition will be met in a finite time $t_r = |\tau(0)|/\rho$, and thereafter, the system's trajectory will stay on the surface; thus, a sliding motion will take place, here $\tau(0)$ is an original value of a sliding surface (7). The condition in (9) is deduced for the system given by (6) and is transformed into inequalities as follows:

$$\begin{cases} u^+ < -\frac{1}{b_2}[\dot{\sigma} + \rho + A_{21}x_1 + A_{22}x_2] \\ u^- < -\frac{1}{b_2}[\dot{\sigma} - \rho + A_{21}x_1 + A_{22}x_2] \end{cases} \quad (10)$$

where b_2 is supposed to be positive, ρ is a strictly positive constant which determines the desired reaching time to the sliding surface.

4 Sliding Mode Controller Design for Water Level Control

The block diagram of a steam generator water level control system is shown in Fig. 2.

The open loop feed water valve dynamics is modeled as a first-order system whose time constant is 1. The state-space equation is described as follows:

$$\dot{u} = -u + u_c \quad (11)$$

Hence, the dynamics of the whole system can be represented by the following state-space equations

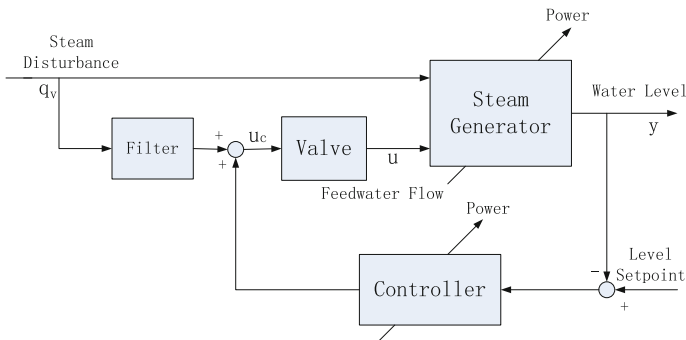


Fig. 2 Diagram of the SG water level control system

$$\begin{cases} \dot{\hat{x}}(t) = \hat{A}(p)\hat{x}(t) + \hat{B}(p)u_c(t) + \hat{W}(p)q_v(t) \\ \hat{y}(t) = \hat{C}\hat{x}(t) \end{cases} \quad (12)$$

with $\hat{A}(p) = \begin{bmatrix} A(p) & B(p) \\ 0 & -1 \end{bmatrix}$, $\hat{B}(p) = \begin{bmatrix} 0 \\ 1 \end{bmatrix}$, $\hat{W}(p) = \begin{bmatrix} W(p) \\ 0 \end{bmatrix}$, $\hat{C} = [C \ 0]$.
 Where $\hat{x}(t) = [x^T(t) \ u(t)]^T$ and $u_c(t)$ is the control function. Considering (6), for this problem: $x_1(t) = x(t), x_2(t) = u(t)$.

4.1 Dynamic Sliding Surface Design

Taking into account (7), the sliding surface is chosen to be the form

$$S = u + \sigma \quad (13)$$

For the purposes of the dynamic operator σ design which facilitates the design of dynamic sliding surface, a state-feedback model-based algorithm based on the pole-placement approach was proposed by Ansarifar [8]:

$$\sigma = Kx + \alpha q \quad (14)$$

where

$$K = [k_1 \ k_2 \ k_3 \ k_4], \dot{q} = e = y^* - y \quad (15)$$

The design of the dynamic operator part can improve the dynamic performance and eliminate the static error of the controlled system simultaneously. Here, an integrator is used in the feed forward path between the plant and the error for rejecting the effect of the unknown disturbance $q_v(t)$ for the output tracking error

e in a steady state. The system dynamics can be governed by the combination of (2) and (15):

$$\begin{bmatrix} \dot{x} \\ \dot{q} \end{bmatrix} = \begin{bmatrix} A(p) & 0 \\ -C & 0 \end{bmatrix} \begin{bmatrix} x \\ q \end{bmatrix} - \begin{bmatrix} B(p) \\ 0 \end{bmatrix} \sigma + \begin{bmatrix} 0 \\ 1 \end{bmatrix} y^* + \begin{bmatrix} W(p) \\ 0 \end{bmatrix} q_v \quad (16)$$

where $\bar{A}(p) = \begin{bmatrix} A(p) & 0 \\ -C & 0 \end{bmatrix}$, $\bar{B}(p) = \begin{bmatrix} B(p) \\ 0 \end{bmatrix}$. It is known that if $\{A(p), B(p)\}$ is a controllable pair, then the pair $\{\bar{A}(p), \bar{B}(p)\}$ in (16) is controllable as well. Therefore, the matrix $L = [K \ \alpha]$ can be used to provide the given eigenvalues placement to the matrix $(\bar{A}(p) - \bar{B}(p)L)$. The required state-feedback gain matrix L can be determined using the transformation matrix T that transforms the system state equation into the controllable canonical form as follows [14]:

$$L = [\beta_5 \ \beta_4 \ \beta_3 - \alpha_3(p) \ \beta_2 - \alpha_2(p) \ \beta_1 - \alpha_1(p)] \bullet T^{-1} \quad (17)$$

where $\alpha_i(p)$, $i = 1, 2, 3$ are coefficients of the characteristic polynomial of (15) as follows:

$$|sI - \bar{A}(p)| = s^5 + a_1(p)s^4 + a_2(p)s^3 + a_3(p)s^2 = 0 \quad (18)$$

And, β_i , $i = 1 \sim 5$ are coefficients of desired polynomial; in this study, the Integration of Time with the Absolute magnitude of the Error (I.T.A.E) criteria [15] are utilized to determine the desired eigenvalues for eigen structure assignment.

$$P(s) = s^5 + \beta_1 s^4 + \beta_2 s^3 + \beta_3 s^2 + \beta_4 s + \beta_5 = 0 \quad (19)$$

The transformation matrix T in (17) is given by $T = MF$, and M is the controllability matrix of (16) which is defined as

$$M = \begin{bmatrix} \bar{B}(p) & \bar{A}(p)\bar{B}(p) & \bar{A}^2(p)\bar{B}(p) & \bar{A}^3(p)\bar{B}(p) & \bar{A}^4(p)\bar{B}(p) \end{bmatrix}$$

$$F = \begin{bmatrix} 0 & \alpha_3(p) & \alpha_2(p) & \alpha_1(p) & 1 \\ \alpha_3(p) & \alpha_2(p) & \alpha_1(p) & 1 & 0 \\ \alpha_2(p) & \alpha_1(p) & 1 & 0 & 0 \\ \alpha_1(p) & 1 & 0 & 0 & 0 \\ 1 & 0 & 0 & 0 & 0 \end{bmatrix}$$

4.2 Sliding Mode Control Laws

To complete the design of the dynamic SMC controller (5) and (7), the realizable control functions u^+, u^- have to be identified. They have to meet the existing conditions (10) in some sliding domain of the dynamic sliding surface (13). This control law will guarantee the system's motion to the dynamic sliding surface in finite time and the motion in this surface thereafter. The existing conditions (10) become

$$u_c = -[\rho \text{sign}(S) + \dot{\sigma} - u] \quad (20)$$

where $\rho > 0$. In particular, this paper proposed the use of gain scheduling based on LPV theory for schedule the gains of the dynamic compensators between diverse operating points so as to obtain a LPV SMC controller which is applicable in the entire operating regime of the UTSG.

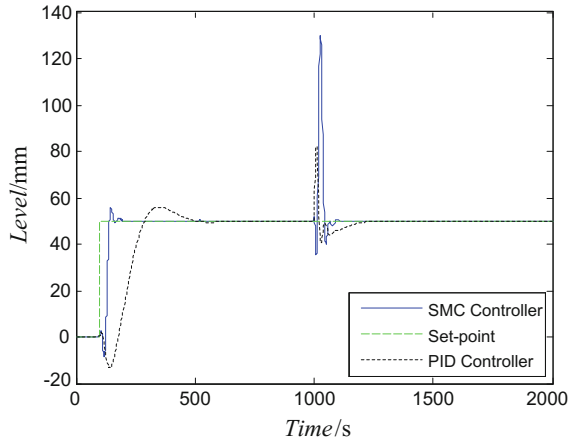
5 Simulation Results

In view of the flow sensors are known to be unreliable at low powers (<15–20%) and during start-up, the UTSG water level usually adopt manual control in practice. Therefore, we focus on the performance of the proposed controller at relatively high power levels in the simulation. It is assumed that initially, the controlled plant water level is in the steady-state condition. All results represent the difference from the corresponding steady-state values. The set point of the water level is suddenly increased from 0 to 50 mm at $t = 100$ s, and a step increase (30 kg/s) in the steam flow rate occurs at $t = 1000$ s.

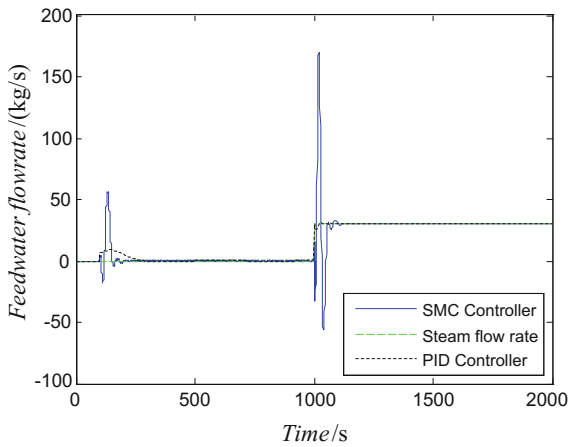
Figures 3, 4 and 5 show the performance of the LPV SMC controller when the water level set point and the steam flow rate change at 15, 30, and 50% reactor power levels. The positive constant from (9) has been chosen as $\rho = 30$.

It is observed that the LPV model-based SMC method is satisfactory in the presence of the steam flow disturbance and water level set point variation at low power levels. The proposed LPV SMC controller gives better performance than a well-tuned conventional PID controller. Its advantage is faster settling time with smaller or at least similar overshoot.

Fig. 3 Performance of the proposed controller and convention PID Controller (15% power)



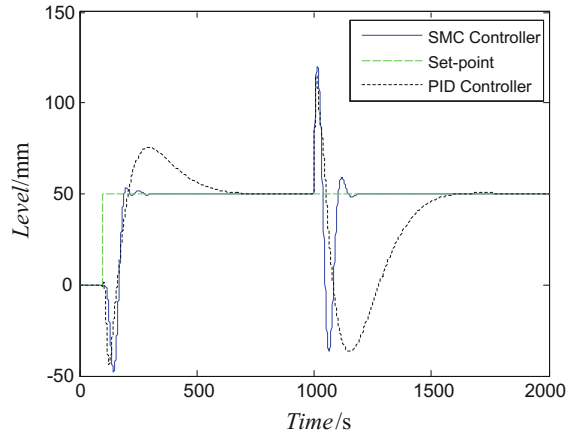
(a) Water level



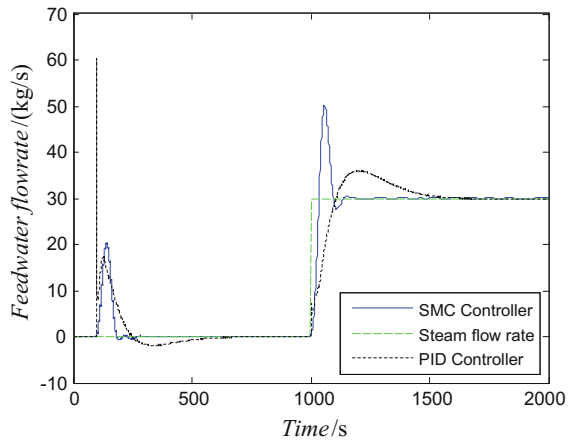
(b) Feedwater flow rate

To observe the dynamic responses of the SG water level control system under small extent of disturbance, a step change of the steam flowrate is introduced above. Actually, the operation power of a reactor is not under the step change. In the next simulation, suppose the plant is operating in the steady working condition initially,

Fig. 4 Performance of the proposed controller and convention PID Controller (30% power)



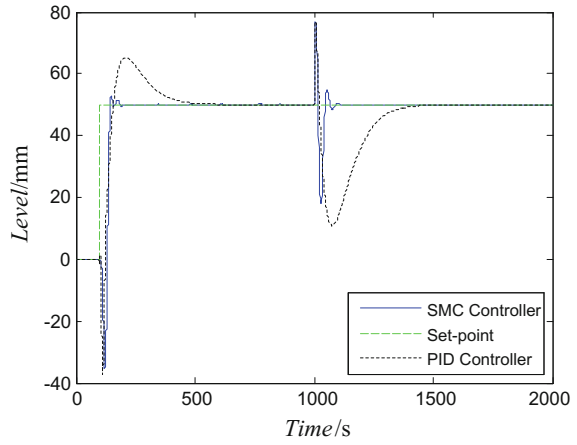
(a) Water level



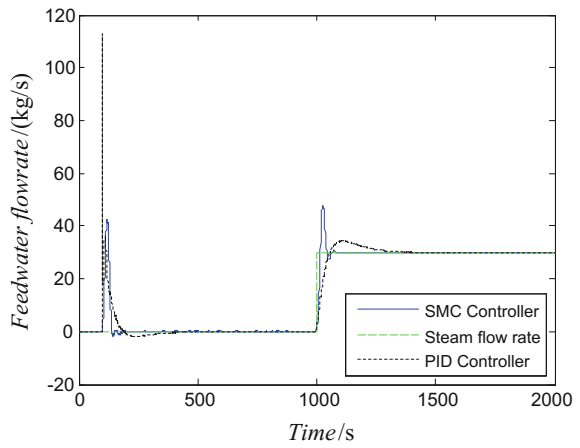
(b) Feedwater flow rate

we focus on the performance of the proposed controller where power varies from 10 through 20 to 10%. Then, the operating power varies from 100 through 50 to 100%. The corresponding simulation is depicted in Figs. 6 and 7.

Fig. 5 Performance of the proposed controller and convention PID Controller (50% power)



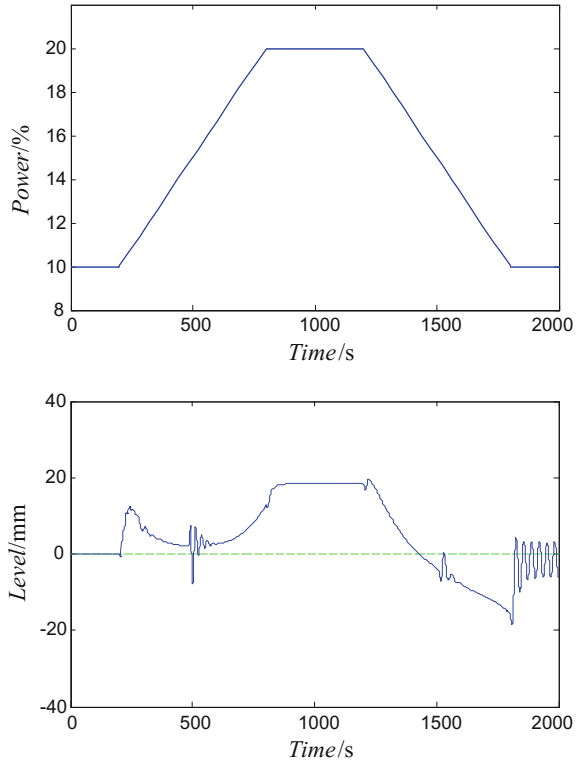
(a) Water level



(b) Feedwater flow rate

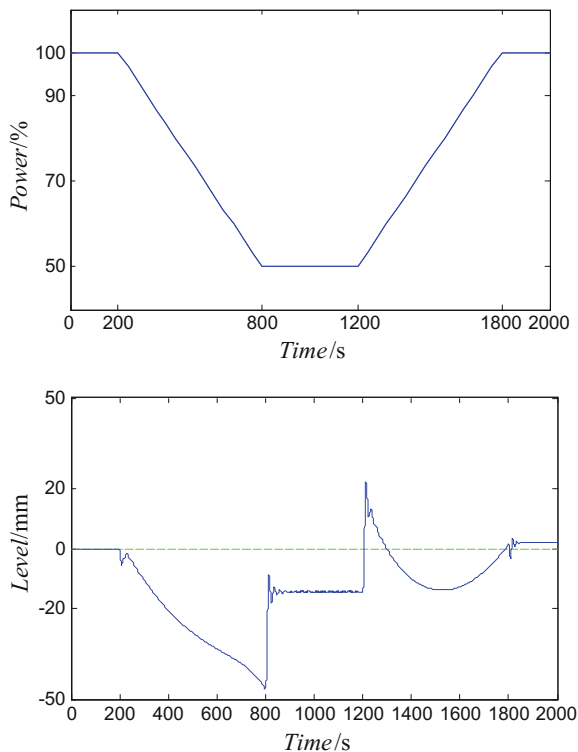
The efficacy of the LPV SMC controller is also supported from the results shown in Figs. 6 and 7, whether it is in the process of rising or falling power, the controller can effectively reduce the water level fluctuations caused by changes in operating

Fig. 6 Steam generator water level where power varies from 10 through 20–10%



condition, so that the water level is smooth transition from a condition to the other. Therefore, the proposed control strategy exhibits a good robustness behavior and thereby increasing the plant safety and availability.

Fig. 7 Steam generator water level where power varies from 100 through 50–100%



6 Conclusions

The design of a dynamic sliding mode controller using Linear Parameter-Varying ideas for controlling a nuclear steam generator water level has been presented. The control aim is to maintain the water level in a certain range. The steam generator model is presented in a form suitable for the design of the LPV SMC controller. The LPV SMC controller comprises a dynamic compensator for stabilization of internal dynamics. Simulations are carried out in diverse operating conditions, and the results illustrate the efficacy of the proposed scheme over the entire operating region. In performance viewpoint, the comparison between the LPV SMC controller and the conventional PID controller showed a great improvement in water set point tracking and an increased ability in disturbance (in the form of steam flow rate changes) rejection, which makes the proposed approach attractive to be utilized and explored further in the area of controlling a nuclear steam generator water level.

References

1. A.G. Parlos, O.T. Rais, "Nonlinear control of U-tube steam generators via H^∞ control," *Control Eng Practice*, vol 8, pp 921–936, 2000.
2. Z. Daoxi, W. Jie and M. Xiaoqian, "Water level control study of steam generator in nuclear power station based on LMIS," *Atom Energy Science and Technology*, vol. 48, no. 11, pp. 2038–2044, 2014.
3. S.R. Munasinghe, M.S. Kim, and J.J. Lee, "Adaptive neurofuzzy controller to regulate UTSG water level in nuclear plants," *IEEE Transactions on Nuclear Science*, vol. 52, no. 1, pp. 421–429, Feb. 2005.
4. W. Wei, W. Junling, and H. Weishi, "Piecewise H^∞ control for water level of steam generator," *Nuclear Power Engineering*, vol. 30, no. 5, pp. 105–109, 2009.
5. H. Eliasia, H. Davilua, and M. B. Menhaj, "Adaptive fuzzy model based predictive control of nuclear steam generators," *Nuclear Engineering and Design*, vol. 237, pp. 668–676, 2007.
6. M.G. Na, "Auto-tuned PID controller using a model predictive control method for the steam generator water level," *IEEE Transactions on Nuclear Science*, vol. 48, no. 5, pp. 1664–1671, Oct. 2001.
7. Young, V.I. Utkin, Ozguner U. "A control engineer's guide to sliding mode control,". *IEEE Transactions on Control Systems Technology*, vol. 7, pp. 328–342, 1999.
8. G.R. Ansarifar, H. Davilu, H.A. Talebi. "Gain scheduled dynamic sliding mode control for nuclear steam generators,". *Progress in Nuclear Energy*, vol 53, pp. 651–653, 2011.
9. E. Irving, C. Miossec, J. Tassart. *Towards Efficient Full Automatic Operation of the PWR Steam Generator with Water Level Adaptive Control [A]*. *Proceedings of Conference on Boiler Dynamics and Control in Nuclear Power Stations[C]*. London: [s.n], 1980, pp. 309–329.
10. K. Myung-Ki, H.S. Myoung. "A gain-scheduled L2 control to nuclear steam generator water level," *Annals of Nuclear Energy*, vol.26, pp 905–916, 1999.
11. Y. Shtessel. "Nonlinear Nonminimum phase output tracking via dynamic sliding manifolds," *Franklin Inst*, vol 335, pp. 841–850, 1998.
12. C. Edwards and S.K. Spurgeon. *Sliding Mode Control: Theory and Applications*. Taylor & Francis, 1998.
13. R. DeCarlo, S.H. Zak, G.P. Matthews. "Variable structure control of nonlinear multivariable systems: a tutorial," *IEEE Proc*. 76, pp. 212–232, 1988.
14. K. Ogata, *Modern Control Engineering*. Prentice Hall, 2002.
15. C.D. Richard, H.B. Robert. *Modern Control Systems*. Wesley Longman Inc, 1998.

Author Biographies

Li Jie is an Assistant Engineer at the Department of Commissioning, China Nuclear Power Engineering Co., Ltd. He works at the commissioning test of nuclear power plant.

Huang Rongyi is an Engineer at the Department of Commissioning, China Nuclear Power Engineering Co., Ltd. He is specializing in the commissioning test of nuclear power plant.

Wang Junling is a professor at College of Nuclear Science and Technology, Harbin Engineering University. Her research interests include the control of nuclear power plants, fault detection, and control for complex nonlinear system.

Experimental Flow Instability Study of a Natural Circulation Loop with Supercritical CO₂

Lei Zhang, Vijay Chatoorgoon and Robert Derksen

Abstract Flow instabilities of a natural circulation loop were experimentally studied with supercritical CO₂ as the working fluid. The experimental loop is a rectangular loop with single horizontal heated channel locating on the bottom of a rectangular loop. Parameters such as system pressure, inlet temperature, and outlet throttling effects' on both steady state and flow instabilities were studied. Results show that the increase in system pressure would shift the peak mass flow rate to the right side of flow-power map and stabilize the system. The increase in outlet throttling caused the opposite effect. The instability boundary did not change much within the given test range of inlet temperature. Instabilities were found when the outlet temperature of the heating section went far beyond the pseudo-critical temperature. All the instability points were located on the negative slope of flow-power curve. One of the interesting findings was that the instability will disappear when the accumulator is isolated from the main loop. Numerical studies were also conducted with both the SPORTS and CATHENA codes to model the experimental results. Results show that the CATHENA code is capable of predicting flow instabilities in natural circulation loop at supercritical pressures. A new method of converting the CO₂ results to H₂O results is proposed by making use of the dimensionless $Fr-N_{tpc}$ map, and the method is verified numerically.

Keywords Flow instability · Natural circulation loop · Supercritical CO₂ · CATHENA code

Nomenclature

M	Mass flow rate (kg/s)
P	System pressure (MPa)
T	Temperature (°C)
K	Local loss coefficient
C_p	Specific heat at constant pressure (J/(kg °C))
Q	Heating power (kW)

L. Zhang · V. Chatoorgoon (✉) · R. Derksen
University of Manitoba, Winnipeg, MB, Canada
e-mail: vijay.chatoorgoon@umanitoba.ca

H	Loop height (m)
N_{spc}	Sub-pseudocritical number
N_{tpc}	Trans-pseudocritical number
Fr	Froude number
h	Fluid specific enthalpy (J/kg)
w	Velocity (m/s)
g	Gravitational acceleration (m^2/s)

Greek letters

β Isobaric thermal expansion coefficient (K^{-1})

Subscripts

c	Critical
pc	Pseudo-critical
p	Constant pressure
in	Inlet of heated channel
out	Outlet of heated channel
channel	Heated channel

1 Introduction

Supercritical water reactor (SCWR) is proposed as one of the promising GEN-IV reactor design due to its potential in high thermal efficiency and compact design. The performance and safe operation of a SCWR relies on the coolant system. Both forced circulation and natural circulation cooling are considered in the new GEN-IV reactor designs [1–3]. For either cooling reactor core at fully power or removing core decay after reactor shut down, using natural circulation system has an obvious advantage in the elimination of pumps and the need for emergency power supplies to operate circulation pumps which would improve the reliability of the core-cooling system. However, there are still some challenges that have to be addressed before the commercial reliance on natural circulation cooling can be realized. One of the main concerns is flow instabilities. Because of the sharp variations of the fluid properties such as density near to the pseudo-critical point, the fluid behavior is very complex due to combined effects of buoyancy and flow acceleration. Flow instabilities similar to two-phase flow instabilities under sub-critical conditions can occur. Hence, it is essential to study the flow characteristics in natural circulation at supercritical pressures with both steady state flow conditions and unstable flow conditions.

During natural circulation, the steady state flow rate initially increases with power, attains a maximum, and then decreases with power. Chatoorgoon [4, 5] conducted both analytical and numerical studies on supercritical flow in a single natural circulation loop by postulating that instability would occur when mass flow rate attains its maximum. Lomperski et al. [6] reported experiments of supercritical CO₂ in a natural circulation loop but no instability data were found in their range tested. Jain and Corradini [7] developed a linear code to analyze the experimental results of Lomperski [6]. Their results showed that instability can occur with the same experimental conditions which contradicted the experimental findings. They further showed that the stability threshold power of a natural circulation loop with supercritical fluids is not restricted to the peak region of the steady state flow-power curve.

Sharma [8] conducted steady state and linear stability analysis of a supercritical water natural circulation loop using an in-house linear code SUCLIN. Parametric effects of loop diameter, loop height, local loss coefficient on the hot leg or cold leg on stability map were studied. It was finally concluded that the instability boundary is not confined to the peak of the steady state mass flow rate versus power curve. Sharma [9] conducted experiments of a closed supercritical pressure natural circulation loop with carbon dioxide as the working fluid. Flow instability was observed when the fluid inlet temperature was about 27–31 °C and the outlet temperature oscillated about 29–45 °C. No instability was found with the configuration of vertical heater and vertical cooler. T'Joen and Rohde [10] experimentally studied the instability of a natural circulation loop using Freon R23. No pure thermo-hydraulic instability was found for their power range.

Compared with two-phase flow instability data, experimental instability data of supercritical natural circulation flow are sparse. The experimental and numerical results only match qualitatively to date. Quantitative discrepancies between the predicted instability boundary and experiment still exist. A lack of reliable experimental data (both steady state and instability data) is a major concern. Good and plenteous experiment data are required to validate licensing numerical codes.

2 Objective and Work Scope

To provide good and plenteous experimental data, a supercritical natural circulation loop with three horizontal channels and one vertical loop with two vertical channels were built at the University of Manitoba. The main objectives of this present experimental study are as follows:

- (1) To collect both steady state and instability data as well as determine the locations of the instability boundary on the flow-power curve.
- (2) To study the effects of different parameters such as pressure, inlet temperature, outlet valve throttling on the steady state, and flow instability of natural circulation flow.
- (3) To determine what effect can extinguish the flow instability altogether.

Numerical simulations were also conducted by employing an in-house nonlinear SPORTS code [11] and a licensed nonlinear code CATHENA (version 3.5.4.4) [12] to model the experiments presented in this paper.

3 Experiment Setup and Apparatus

3.1 Loop Design and Parameters Measurement

The experimental setup is a rectangular loop with a horizontal single test channel located at the bottom tier. The heated channel is a 2.6 m long Inconel 625 polished circular pipe (ID: 12.95 mm, OD: 19.05 mm). The rest of the loop is made of XXH stainless steel 316L pipe (ID: 22.75 mm, OD: 42.16 mm) which is connected by various socket welded joints, flanges, and valves. Electro-pneumatic valves were installed at inlet and outlet of test sections for adding resistance of system. As shown in Fig. 1, the experimental loop mainly consists of a pressure control system ①, purging system ②, power supply system ③, evacuation and vacuum system ④, cooling system ⑤, and data acquisition system. DC power is generated by an EMHP 20-1500 rectifier (EMHP Power Supply) and supplied on both ends of test section as a heating source. Though the ideal output of rectifier is 30 kW, the actual heating load generated by the test section is about 15 kW due to resistance of test channel itself. Heat is removed by a shell and tube heat exchanger connected with a 30 kW capable chiller on secondary side. The pressure control system mainly includes a Nitrogen gas cylinder (Praxair® industrial Nitrogen with 2200 psi), check valve, single stage pressure regulator (PR-50 series, GO regulator®), bladder type accumulator (Hydac®), and a high pressure back pressure regulator (BP-60 series, Go regulator®). The bladder inside the accumulator acts as a gas-proof screen and separates the liquid CO₂ from the Nitrogen gas.

The parameters measured during the experimental tests include system pressure, pressure drops, CO₂ flow rate, secondary-side coolant flow rate, channel inlet and outlet fluid temperature, heat exchanger inlet and outlet coolant temperature, test section wall temperatures, voltage drop across test section, voltage drop across shunt resistor located at the back part of rectifier. Two absolute pressure transducers were mounted on the loop; one is located just below the accumulator to measure the absolute pressure near the accumulator, and the other is located on loop side in front of the turbine flow meter which measures the system pressure when the accumulator is isolated. A total of nine differential pressure transducers (Validyne) were installed to measure pressure drops at different parts of loop. It includes total pressure drop and segment pressure drops along the test section, pressure drop across inlet and outlet electro-pneumatic valves, and pressure drop across the heat exchanger. A FTB-1421 turbine flow meter (OMEGA) was installed upstream of the heated channel for accurate measurement of the CO₂ flow rate. Secondary-side coolant flow rate was measured by a turbine flow meter (Seametrics SPX series)

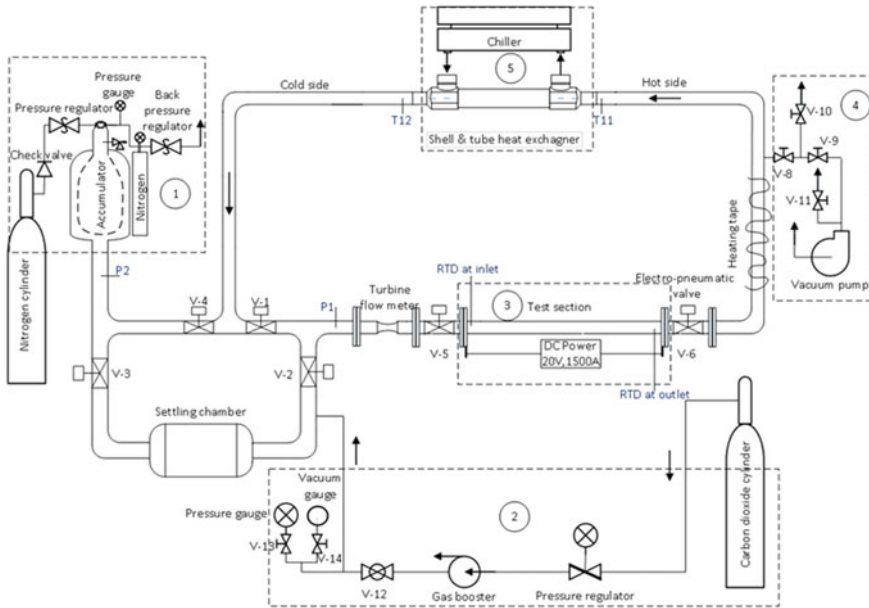


Fig. 1 Schematic of natural circulation loop with horizontal channels

combined with a FT400 series rate/total indicator (Seametrics). Fluid temperatures at the inlet and outlet of test sections were measured by two ultraprecise RTD sensors (OMEGA). Flow temperatures of CO₂ and secondary coolant at the heat exchanger inlet and outlet were measured with K-type thermocouples (1/8" sheath diameter) from OMEGA Company. Twelve K-type thermocouples with 1/16" sheath diameter were spot welded with equal intervals on the top and bottom of the heated test section surface to measure wall temperatures. Heating power was calculated by multiplying the voltage drop across the heated channels and current passing through it. A 9% heat loss was already taken into consideration for the power in this paper. The uncertainties on measured or calculated parameters are summarized in Table 1.

Table 1 Uncertainties in measured and calculated parameters

Parameters	Uncertainty
Pressure (MPa)	±0.02
Mass flow rate (kg/s)	±10% of measured values
RTD at channel inlet (°C)	±0.4
RTD at channel outlet (°C)	±0.6
Thermocouple (°C)	±1.0
Power supply (kW)	±0.1

3.2 *Operation Procedures and Experimental Method*

Before starting the tests, the experimental loop is prepared by calibrating the instruments such as differential pressure transducers, leakage test, evacuation, and pressurization. If no leakage is found, the loop is flushed several times with CO₂ (99.995% purity) and then evacuated by a vacuum pump (R5-PB0003 A, Busch) for 24 h to eliminate air and moisture. To pressurize the loop, the accumulator is pre-charged to a pressure of 900 psi (6.2 MPa). Valves V-1, V-2, V-8, V-9, V-10, and V-14 would be closed. Valves V-3, V-4, and V-13 would be partially opened for protecting the turbine flow meter. The pressure regulator of the purging system would be adjusted to slowly release some CO₂ (99.995% purity) into the loop. Once a balance of pressure is achieved between the loop and CO₂ cylinder, the booster pump is turned on to further pressurize the loop to operating pressure of about 7.50 MPa. The loop is left unchanged for several hours to settle down. The settling chamber is isolated from the loop by closing valve V-2 and V-3 in all test cases. The right vertical leg is wrapped with a heating tape. The heating tape is turned on for about 20 min to bias the flow in the anticlockwise direction before the channel power is turned on. Simultaneously, the chiller is activated and the secondary coolant passes through the shell and tube heat exchanger to cool down the CO₂ inside loop.

The experimental loop is run first in steady state conditions. For each test case, the inlet temperature and system pressure are kept constant while the heating power is adjusted for each new steady state condition. The chiller, for cooling the secondary-side flow, is adjusted to ensure the heat exchanger removes all the heat added to the system so the inlet CO₂ temperature is constant. The supercritical CO₂ expands with added heat and the loop pressure rises. There are two ways to keep the loop pressure constant. One way is to adjust the back pressure regulator of the pressure control system, which would release some nitrogen into atmosphere so more CO₂ could come into the bladder and press the bladder until a new balance is reached. Another way is to open valve V-8 and V-10 and release CO₂ into the atmosphere. This will cause the nitrogen in the bladder accumulator to expand and push more CO₂ into loop until a new balance is reached. The electro-pneumatic valves are actuated and adjusted at the beginning of the test case to study the inlet and outlet local loss effect on flow behavior. They are not touched after the initial adjustment and until one case is finished. LabVIEW interface is used to monitor all the parameters being measured. The turbine flow meter results indicate whether or not the flow is stable or oscillatory. The loop would be left untouched for about 15–30 min to settle down and become steady after any changes made to parameters like heating power, inlet temperature, or system pressure. Steady state results were recorded for about 2–3 min. The heating power increment was about 1 kW in a stepwise way for each steady state. The increment was reduced to 0.5 kW while searching for the flow instability boundary, which occurred at higher powers. This methodology was followed for every case.

Table 2 Experimental cases and instability boundary

Cases No.	P (MPa)	T_{in} ($^{\circ}$ C)	K_{out}	Boundary heating power (kW)	Boundary mass flow rate (kg/s)
1	8	20	12.1	None found	None found
2	7.6	20	11.5	12.203	0.0560
3	8	20	14.4	12.210	0.0537
4	8	20	18.3	11.207	0.0492
5	7.6	20	19.7	9.880	0.0426
6	8.6	20	12.9	14.309	0.0557
7	8	20	30.4	9.014	0.0393
8	8	18	18.8	11.306	0.0509
9	8	23	18.1	11.006	0.0451
10	8	23	20.7	10.504	0.0419

4 Experimental Results

The flow characteristic of natural circulation loop rely on the loop geometry, input power, system pressure, and inlet fluid temperature. To study the effects of these parameters on both steady state characteristic and flow oscillation, the power was gradually increased while keeping system pressure, inlet fluid temperature, and outlet valve position constant during the test. The operating pressure for all the experimental cases was 7.6–8.6 MPa. The inlet temperature range was 18–26 $^{\circ}$ C. The outlet valve local loss coefficient range was 0–30. A total of ten experimental cases were done; these are summarized in Table 2.

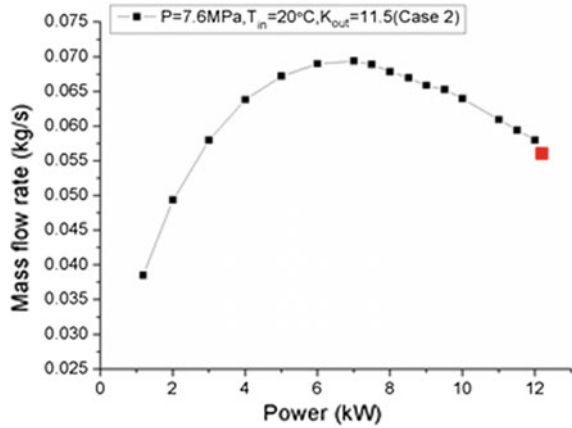
4.1 Steady State Results

4.1.1 Flow-Power Map with Instability Boundary

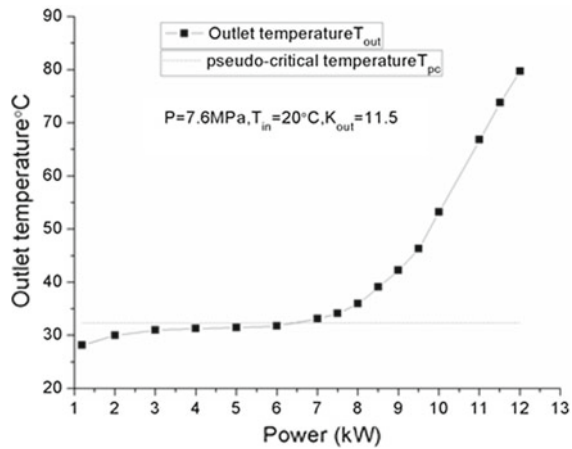
Steady state flow-power maps of obtained experimental cases are illustrated in Figs. 2, 3, 4, 5 and 6. As explained by previous investigators [6, 8], dominant buoyancy force induced by density difference drives the mass flow rate up until a peak value is reached. After that, frictional forces take over and cause a lowering of the mass flow rate. In addition, the maximum mass flow rate occurs when the channel outlet temperature is around the pseudo-critical temperature, shown in Fig. 2a and b.

The instability boundary points, presented by solid red dots, are included in flow-power plots. Different from a previous study [9] which reported that the flow oscillation mainly occurs near the peak region, and all instability cases found in present studies are on the negative slope of the flow-power curve with outlet

Fig. 2 **a** Flow-power map (Case 2). **b** Outlet temperature (Case 2)



(a) Flow-power map (Case 2)



(b) Outlet temperature (Case 2)

temperatures exceeding the pseudo-critical temperature. This finding is very similar to the type II instability under two-phase flow conditions proposed by Fukuda [13].

4.1.2 Parameter Effects

Parameter effects on steady state characteristics have already been extensively studied. However, corresponding experimental studies with instability boundary points are rare. Figures 3, 4 and 5 represent pressure, inlet temperature, and outlet K factor effects on steady state characteristics and instability boundary of the loop, respectively. Due to the sensitivity of electro-pneumatic valves, K factors cannot be kept exactly the same for different cases. Nevertheless, the general conclusions

Fig. 3 Effect of system pressure

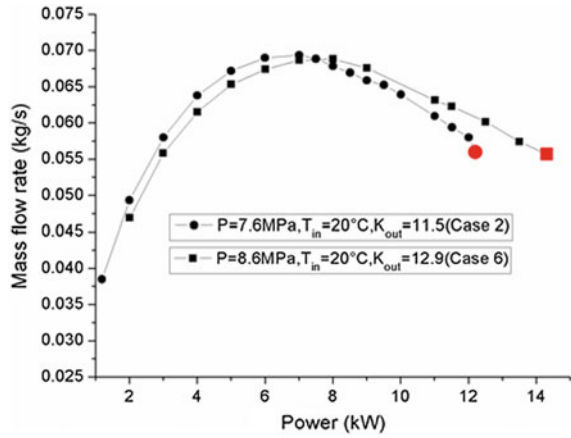


Fig. 4 Effect of inlet temperature

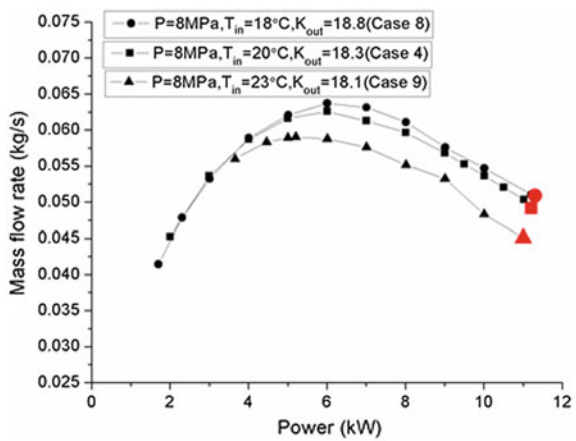


Fig. 5 Effect of outlet local loss coefficients

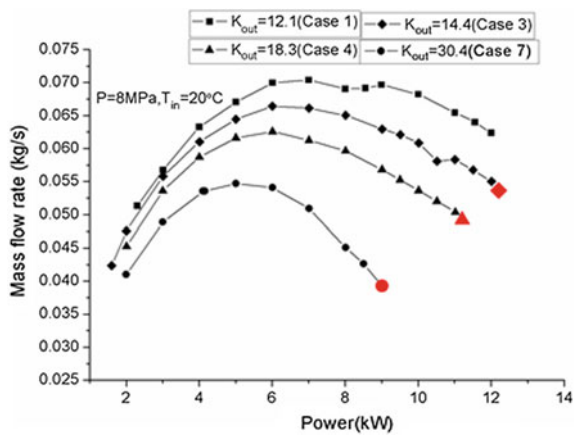
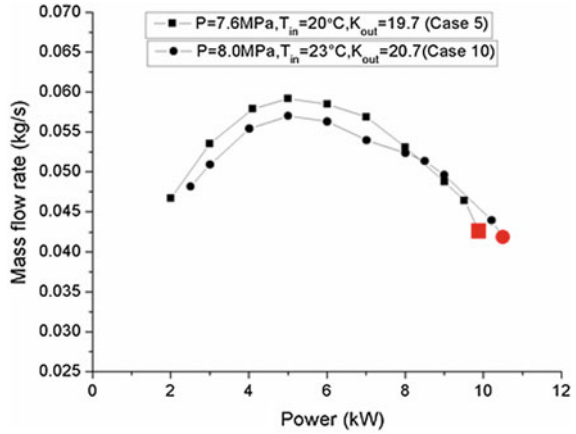


Fig. 6 Flow-power map for Cases 5 and 10



drawn still hold true to some extent and are consistent with previous numerical and analytical findings [8, 14]:

- (1) Increase in system pressure raises pseudo-critical point temperature resulting in a shift of peak mass flow rate to the right and stabilizes the system.
- (2) Lower inlet temperature causes a larger density difference between the hot and cold legs also leading to a shift of peak mass flow rate to the right. In present test range, instability boundary is not dramatically influenced by inlet temperature change.
- (3) The increase in outlet K factors decreases mass flow rate significantly and moves the peak point to the left. The stability boundaries indicate a more unstable system.

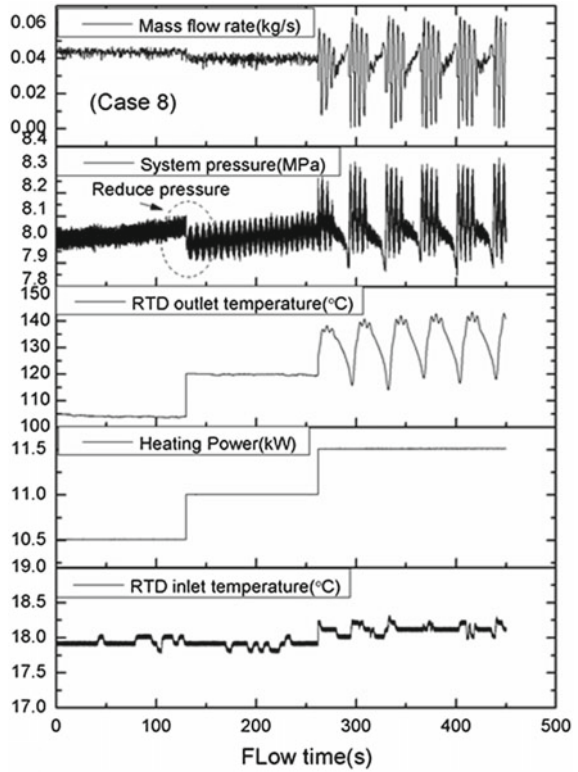
Steady state flow-power curves of Cases 5 and 10 are also shown in Fig. 6 for future numerical validation.

4.2 Flow Instability Results

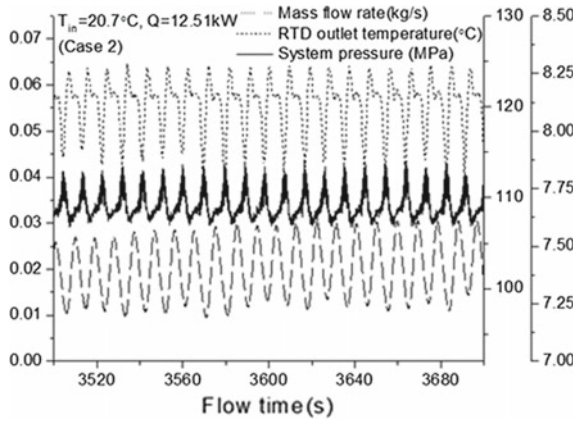
4.2.1 Determination of Instability Boundary

An increment of 0.5 kW was applied first to observe mass flow rate transient responses and estimate the instability threshold power. When oscillation occurred, the heating power was reduced in decrements of 0.1 kW to search for a more accurate boundary power. During this process, other parameters were kept constant. When the system pressure was higher than the desired value, some supercritical CO_2 was released to the environment. The working fluid inlet temperature was controlled by adjusting coolant temperature on secondary side.

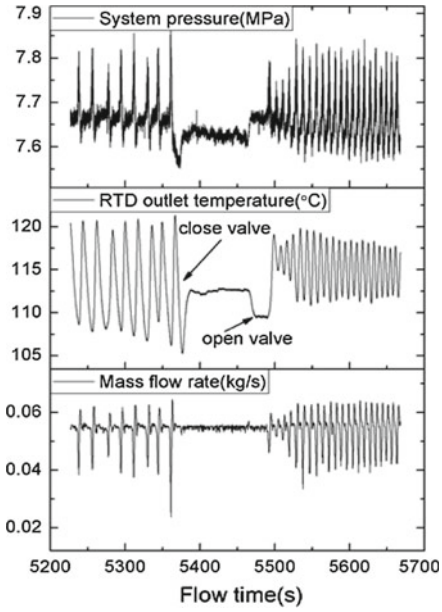
Fig. 7 a Instability phenomenon (Case 8).
b Limit cycle phenomenon (Case 2)



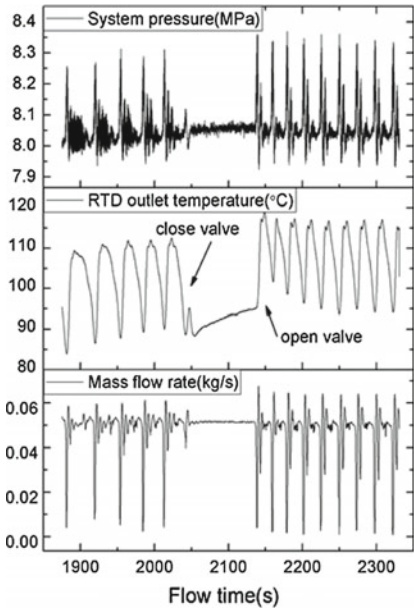
(a) Instability phenomenon (Case 8)



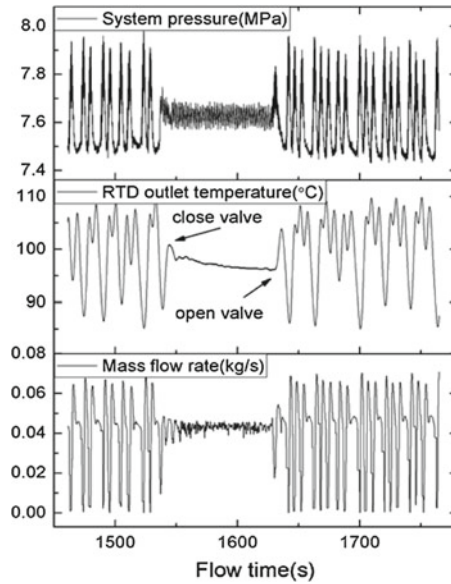
(b) Limit cycle phenomenon (Case 2)



(a) Accumulator effect (Case 2)



(b) Accumulator effect (Case 4)



(c) Accumulator effect (Case 5)

Fig. 8 **a** Accumulator effect (Case 2). **b** Accumulator effect (Case 4) **c** Accumulator effect (Case 5)

4.2.2 Flow Instability Behavior

For Case 8, instability occurred when the heating power was increased from 11.0 to 11.5 kW, see Fig. 7a. The mass flow rate oscillated periodically with large amplitude accompanied by short-period fluctuations. The system pressure also oscillated (0.3 MPa) but out of phase with the mass flow rate. The RTD placed at the end of test section indicates periodic temperature oscillations (15 °C) almost in phase with the inlet mass flow rate. The phase relationship can be seen more clearly from Fig. 7b, Case 2.

4.2.3 Accumulator Effect on Flow Instability

The accumulator effect on flow instability was also tested by closing valve V1-4 to isolate the accumulator when instability occurred. As shown in Fig. 8a, with the elimination of the accumulator, the periodic oscillation of several parameters including system pressure, mass flow rate, and RTD outlet temperature immediately disappeared and the whole system became stable. When the valve was reopened to activate the accumulator, the system became unstable again. This indicates that the accumulator plays an important role in flow instability of a natural circulation loop. It works as a compressible volume and interacts with the hot leg of the loop which is also compressible when the fluid temperature is beyond the pseudo-critical temperature. The accumulator effect has been tested in all instability cases to make sure the phenomenon was not accidental. Another two examples are given in Figs. 8b and c. The results are the same in all cases.

5 Numerical Results

Numerical simulations were also conducted by employing an in-house nonlinear SPORTS code [11] and a licensed nonlinear code CATHENA (version 3.5.4.4) [12] to model the experimental results present in this paper. The CATHENA code can simulate H₂O at supercritical pressures, but the current version used does not model CO₂. The SPORTS code is capable of modeling supercritical flow instability with both H₂O and CO₂. Three cases were chosen for numerical modeling, Cases 2, 5, and 9.

5.1 Physical Model and Boundary Conditions

The geometry used for numerical study was a simplified physical model of the experimental loop. A sketch with dimensions and local loss K factors was shown in Appendix. The physical model for CATHENA code was the whole loop system

including the accumulator and pipeline connecting the rectangular loop and accumulator. The boundary condition was a reservoir with constant pressure and temperature to represent the accumulator. As for SPORTS code, the physical model was only the rectangular loop with constant inlet pressure, temperature, and constant outlet pressure boundary conditions. A maximum time step used for CATHENA code was 0.01 s for searching instability boundary. The time step used for SPORTS code was 0.02 s throughout the transient. Number of nodes adopted in CATHENA and SPORTS codes are the same, listed in Appendix Tables 4 and 5. Wall effects were not included in these numerical models. Hence, no heat transfer package was used.

5.2 Verification of Numerical Code

The SPORTS code was firstly performed with supercritical CO₂ to directly model the experimental Case 2. Figure 9 illustrates the plot of steady state result obtained with SPORTS code predictions and experimental measurement. Considering the uncertainty of measured mass flow rate, the SPORTS code calculations show an acceptable agreement with the experimental steady state results which means the pressure drop (wall friction and local loss) is well distributed over the loop.

The SPORTS code was further employed to simulate the same physical model but using supercritical H₂O as the working fluid. The CATHENA code was also conducted to simulate the same supercritical H₂O case. Figure 10 shows good agreement (within 3%) of steady state results between two numerical codes. Except the working fluid was changed from CO₂ to H₂O, there is no physical and numerical option change about the SPORTS code.

Fig. 9 Comparison of SPORTS code calculation and experimental result (Case 2)

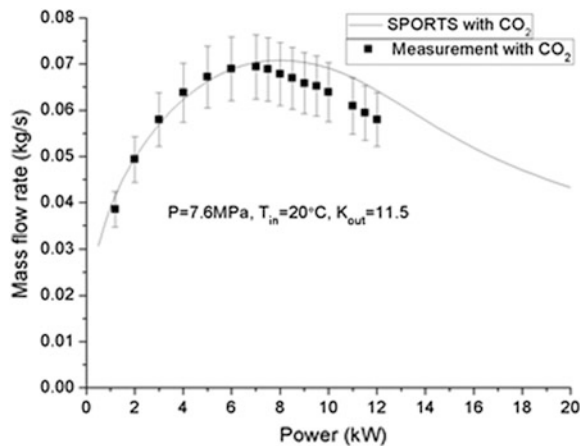


Fig. 10 Comparison of SPORTS code results and CATHENA code results (Corresponding H₂O results for Case 2)

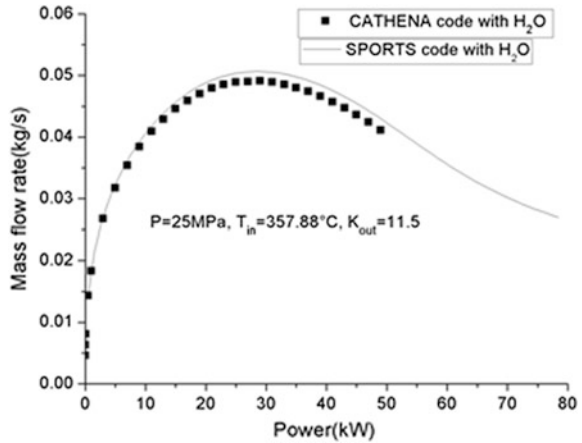


Figure 11 shows the supercritical H₂O flow instability captured by the CATHENA code. The mass flow rate at the inlet of the heated section and outlet of the heated section oscillates with a phase lag.

5.3 *Scaling the Supercritical CO₂ Results to Supercritical H₂O*

As the current version of CATHENA code cannot model CO₂, but can model H₂O, a way was sought to convert the CO₂ data to H₂O so CATHENA can be used to model the CO₂ experiments. The experimental results were converted from

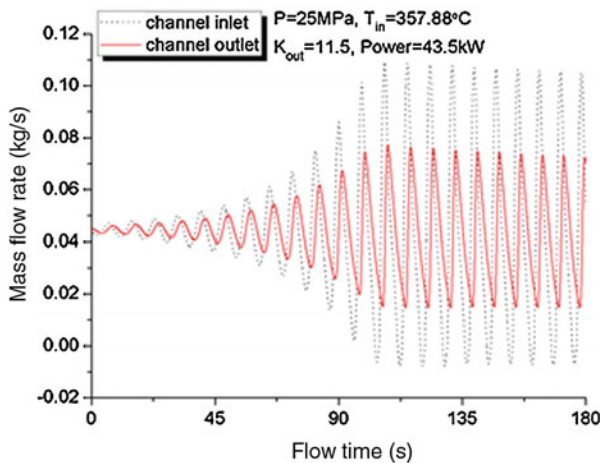


Fig. 11 CATHENA simulation of supercritical flow instability (Corresponding H₂O results for Case 2)

supercritical CO₂ to supercritical H₂O by utilizing Ambrosini's [15] nondimensional parameters N_{spc} , N_{tpc} , and Fr.

$$N_{\text{spc}} = \frac{\beta_{\text{pc}}}{C_{p,\text{pc}}} (h_{\text{pc}} - h_{\text{in}}) \quad (1)$$

$$N_{\text{tpc}} = \frac{Q_{\text{channel}}}{M_{\text{channel}}} \frac{\beta_{\text{pc}}}{C_{p,\text{pc}}} \quad (2)$$

$$\text{Fr} = \frac{w_{\text{in}}}{\sqrt{g \cdot H}} \quad (3)$$

These three nondimensional parameters have been used in heated channel systems with fluids at supercritical pressures as well as natural circulation loops, but they have not been reported tested for converting from one fluid to another fluid in a given natural circulation loop, and in particular, the flow-power curve of natural circulation loops.

The method used is straightforward. The experimental CO₂ results are firstly organized into N_{spc} , N_{tpc} , and Fr parameters. The same was used to determine the corresponding H₂O case. With a given system pressure, the inlet temperature of supercritical H₂O case can be obtained by doing a reverse calculation of Eq. (1). For example, the H₂O temperature at heated section inlet was calculated to be 357.88 °C at 25 MPa based on the experimental Case 2.

Figure 12 plots the results of the SPORTS code for CO₂ and H₂O, the CATHENA code for H₂O, and the experimental CO₂ results all together in the Fr- N_{tpc} plane. Inspection of the plot shows that the results generated from the numerical codes with different fluids match very well. This lends credibility to scaling the CO₂ data to H₂O data.

Fig. 12 Froude number versus trans-pseudo-critical number (Case 2)

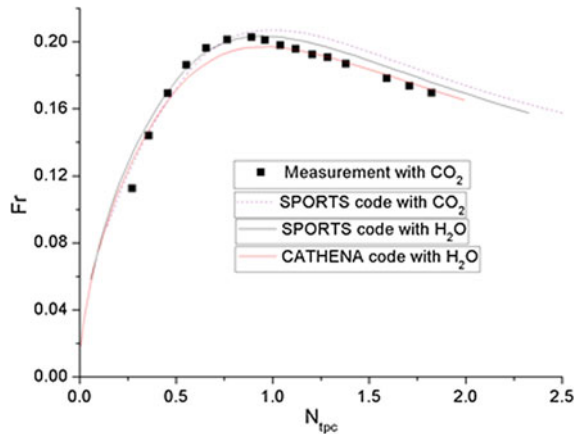


Fig. 13 Dimensionless CATHENA code results versus experimental results (Case 5)

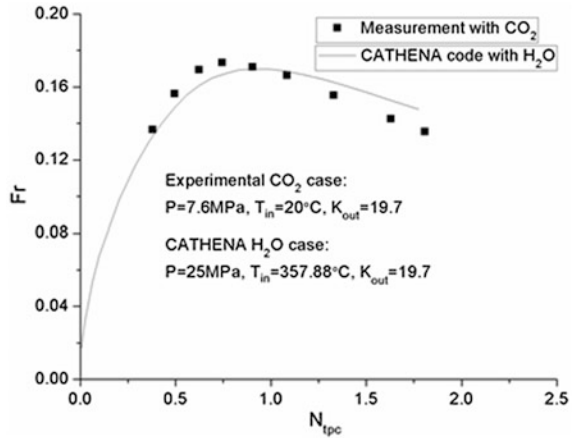


Fig. 14 Dimensionless CATHENA code results versus experimental results (Case 9)

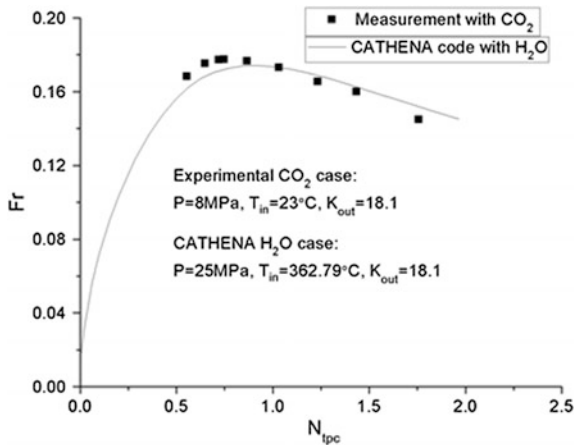


Table 3 Experimental cases with CO₂ and corresponding numerical cases with H₂O

Parameters	Case 2		Case 5		Case 9	
	CO ₂	H ₂ O	CO ₂	H ₂ O	CO ₂	H ₂ O
<i>P</i> (MPa)	7.6	25	7.6	25	8.0	25
<i>T</i> _{in} (°C)	20	357.88	20	357.88	23	362.79
<i>K</i> _{out}	11.5	11.5	19.7	19.7	18.1	18.1

Another two experimental cases (Cases 5 and 9) were converted to supercritical H₂O cases and simulated with the CATHENA code. Results of steady state points were also presented in the nondimensional $Fr-N_{tpc}$ plane in Figs. 13 and 14. Both

cases indicate a general agreement between experiment and numerical simulation which verified the correctness of the nondimensional parameters in scaling supercritical CO₂ results to supercritical H₂O results within the current natural circulation loop. More simulation of experimental cases including both steady state and instability are ongoing. Relevant parameters of the three cases modeled are summarized in Table 3.

6 Conclusion

Natural circulation loop with supercritical fluids was studied experimentally and numerically. The following conclusions can be drawn from the present study:

- (1) It was experimentally verified that the mass flow rate increases with increase in system pressure and the peak flow rate will shift to the right on flow-power map. Decrease in inlet temperature or outlet K factor will have the same effect.
- (2) All the flow instability boundary points were found on the negative slope of power-flow map. As was expected, the location of the instability boundary indicates that increase in system pressure makes the system more stable. Increase in outlet K factors will always destabilizes the system. The boundary heating power does not change much with the inlet temperature range tested.
- (3) During the flow oscillations, the mass flow rate oscillated periodically with large amplitude. The system pressure was also oscillating (0.3 MPa) but out of phase with the mass flow rate. The RTD placed at the end of test section indicates periodic temperature oscillating (15 °C) almost in phase with inlet mass flow rate.
- (4) By isolating the accumulator, flow oscillations disappeared. The flow oscillation returned when the accumulator was reconnected.
- (5) The CATHENA code was proved to be capable of modeling supercritical flow instabilities with natural circulation loop. The steady state results matched well with the experimental results.
- (6) By employing the nondimensional parameters N_{spc} , N_{tpc} , and Fr , the traditional flow-power map can be converted to the nondimensional Fr - N_{tpc} map, which is very useful for scaling supercritical CO₂ results to supercritical H₂O results, or any other fluids, at different supercritical pressures.

Acknowledgments This work is financially supported by Atomic Energy of Canada Limited (AECL). The first author is also grateful to Sviatoslaw Karnaukh for technical support of the experiment as well as Dr. Aleksandar Vasic, Dr. Thomas Beuthe, and Dr. Tong Liu at Canadian Nuclear Laboratories who provided invaluable guidance and support about the CATHENA code.

Appendix A.1

The shell and tube heat exchanger consists of 127 horizontal parallel small tubes ($\Phi 3.175 \times 0.3175$ mm) with a length of 0.414 m. The supercritical CO_2 flows inside the small tubes and outside the small tubes are coolant water. An equally distributed of $K = 8.1$ for heat exchanger part was adopted for all numerical cases. The inlet K factor K_{in} was kept to be 0 for both experiments and numerical study. The outlet K factor K_{out} was changed based on the throttling of outlet valve in experimental cases. Other K factors are left unchanged during numerical simulation and listed in Table 5 (Fig. 15 and Table 4).

Table 4 Dimensions of simplified experimental loop

Label	Length (m)	I.D. (mm)	Wall thickness (mm)	Nodes number (in modeling)
L1	1.57	22.75	9.7	31
L2	0.34	15.21	9.09	7
L3	0.406	15.21	9.09	8
L4	2.94	12.95	3.048	59
L5	0.28	15.21	9.09	7
L6	0.889	15.21	9.09	16
L7	0.95	22.75	9.7	19
L8	1.02	22.75	9.7	20
L9	3.4814	22.75	9.7	70
L10	0.414			8
L11	3.4814	22.75	9.7	70
L12	1.02	22.75	9.7	20
L13	0.08	22.75	9.7	2
L14	1.7	22.75	9.7	32
L15	0.39	22.75	9.7	7

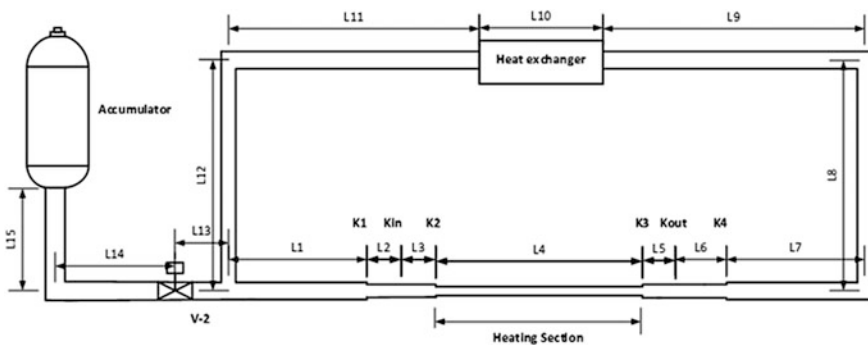


Fig. 15 Simplification of experimental loop

Table 5 Local K factors used for numerical simulation of simplified experimental loop

Name	$K1$	$K2$	$K3$	$K4$	Elbow
Value	0.07	0.18	0.1	0.3	0.45

References

- Schulenberg, T., J. Starflinger, and J. Heinecke, Three pass core design proposal for a high performance light water reactor. *Progress in Nuclear Energy*, 2008. 50(2–6): p. 526–531.
- Dimmick, G.R., et al., Natural-convection studies for advanced CANDU reactor concepts. *Nuclear Engineering and Design*, 2002. 215(1–2): p. 27–38.
- Yetisir, M., et al., The Supersafe© Reactor: A Small Modular Pressure Tube SCWR. *CNL Nuclear Review*, 2012. 1(2): p. 13–18.
- Chatoorgoon, V., Stability of supercritical fluid flow in a single-channel natural-convection loop. *International Journal of Heat and Mass Transfer*, 2001. 44(10): p. 1963–1972.
- Chatoorgoon, V., A. Voodi, and D. Fraser, The stability boundary for supercritical flow in natural convection loops: Part I: H₂O studies. *Nuclear Engineering and Design*, 2005. 235(24): p. 2570–2580.
- Lomperski, S., et al., Stability of a Natural Circulation Loop with a Fluid Heated Through the Thermodynamic Pseudo-critical Point. 2004. Medium: X; Size: page(s) 1736–1741.
- R. Jain, M.L.C., A Linear Stability Analysis For Natural Circulation Loops Under Supercritical Conditions. 2006.
- Sharma, M., et al., Steady state and linear stability analysis of a supercritical water natural circulation loop. *Nuclear Engineering and Design*, 2010. 240(3): p. 588–597.
- Sharma, M., et al., Steady state and stability characteristics of natural circulation loops operating with carbon dioxide at supercritical pressures for open and closed loop boundary conditions. *Nuclear Engineering and Design*, 2013. 265: p. 737–754.
- T'Joen, C. and M. Rohde, Experimental study of the coupled thermo-hydraulic–neutronic stability of a natural circulation HPLWR. *Nuclear Engineering and Design*, 2012. 242: p. 221–232.
- Chatoorgoon, V., SPORTS - A simple non-linear thermalhydraulic stability code. *Nuclear Engineering and Design*, 1986. 93(1): p. 51–67.
- Hanna, B.N., CATHENA: A thermalhydraulic code for CANDU analysis. *Nuclear Engineering and Design*, 1998. 180(2): p. 113–131.
- Fukuda, K. and T. Kobori, Classification of Two-Phase Flow Instability by Density Wave Oscillation Model. *Journal of Nuclear Science and Technology*, 1979. 16(2): p. 95–108.
- Jain, P.K. and u. Rizwan, Numerical analysis of supercritical flow instabilities in a natural circulation loop. *Nuclear Engineering and Design*, 2008. 238(8): p. 1947–1957.
- Ambrosini, W. and M. Sharabi, Dimensionless parameters in stability analysis of heated channels with fluids at supercritical pressures. *Nuclear Engineering and Design*, 2008. 238(8): p. 1917–1929.

Author Biographies

Lei Zhang is currently a Ph.D student at University of Manitoba whose research area is about supercritical flow instabilities in channels and natural circulation systems.

Vijay Chatoorgoon is a professor at University of Manitoba whose research area is in aerospace engineering, acoustic wave propagation, and supercritical flow stability.

Robert Derksen is a professor at University of Manitoba whose research area is in fluid machinery and aerodynamic optimization.

Experimental Study on Secondary Passive Residual Heat Removal System

Haiyan Xu, Xiaohang Wu, Qinglong Wen, Donghua Lu
and Liangguo Li

Abstract The secondary passive residual heat removal system, which is one of several passive safety systems, is designed to enhance the safety of the reactor core. Experiments on transient and steady state natural circulation performance of the secondary passive residual heat removal system had been performed by using the high temperature, high pressure, and thermal–hydraulic test facility (natural circulation test loop of FITY, CGN). The experiment results showed that the residual heat can be removed successfully from the steam generator to atmosphere by steady state and transient natural circulation in test facility, and the heat transfer capability gets stronger with the increase of loop pressure. The result also shows natural circulation can be set up with good stability.

Keywords Passive · Residual heat removal · Experimental study

1 Introduction

As we know, nuclear safety is the most important issue in the nuclear industries, especially after the Fukushima nuclear accident. In most of the existing second-generation and second-generation plus nuclear power plants, residual heat is usually removed by active system to ensure the safety of the reactor core. However, in case of a station blackout accident, active system based on electrical supply is off, the core will be melt down. The advanced secondary passive residual heat removal system (ASP) is designed to solve this problem and then improve the integrated safety. ASP system, which has a simple structure, can set up natural circulation in the loop and remove the residual heat to the atmosphere in 72 h without human operation and power supply.

H. Xu (✉) · X. Wu · Q. Wen · D. Lu · L. Li
China Nuclear Power Technology Research Institute Co. Ltd, Shenzhen,
Guangdong, China
e-mail: xuhaiyan@cgnpc.com.cn

To ensure the reactor core safety, the ASP system needs to remove the residual heat from the system in a stable and continuous way. Xiong [1] and Zhou [2] studied the start-up characteristic and influence factor of secondary passive residual heat removal system with RELAP5/MOD3.3. Yan [3] calculated the transient characteristics of the secondary passive residual heat removal system under station blackout accident condition with RELAP5/MOD3.2 and investigated the factor influence the capability of natural circulation. Zhang [4] and Chen [5] studied the characteristic of flow in the secondary passive residual heat removal system of CPR1000. Chen [6] conducted experimental study on secondary passive residual heat removal system of AC600, Hyun-sik Park [7] investigated influence of open time and water capability on SMART test facility, Xi [8] designed test facility based on secondary passive residual heat removal system of HPR1000 and conducted experimental study on 72 h natural circulation test.

An experimental facility was built to study the advanced secondary passive residual heat removal system and characteristics of start-up and heat transfer were obtained.

2 Test Facility

The tests were carried out in the high-pressure and high-temperature steam water two-phase flow test loop, named Secondary Passive Residual Heat Removal system Test facility, SPRHRTY). The SPRHRTY was designed according to H2TS scaling method. Scaling ratio of the test facility is shown in Table 1.

The schematic diagram of the test facility is shown in Fig. 1.

The test facility represents the primary and secondary side of reactor. The major components of the test facility are as follows: the steam generator, C-type condenser, core simulator, high-pressure canned motor pump, pressurizer, water storage tank, valve, and associated piping. Test part includes the following: the C-type condenser, steam generator, riser, and down-comer of the secondary passive residual heat removal system. Deionized water was used as the flowing media.

Primary side of test facility was designed with a maximum pressure of 17.2 MPa and a maximum temperature of 360 °C, while secondary side was designed with a maximum pressure of 9.0 MPa and a maximum temperature of 310 °C.

The 1.0 MW capability heater was mounted in the core simulator to simulate the variation of decay heat. High-precision N-type and T-type thermocouples were used

Table 1 Simulation scaling of test facility

Parameter	Scaling ratio
Height	1:4
Pressure, temperature	1:1
Time	1:2
Volume	1:207
Power	1:104

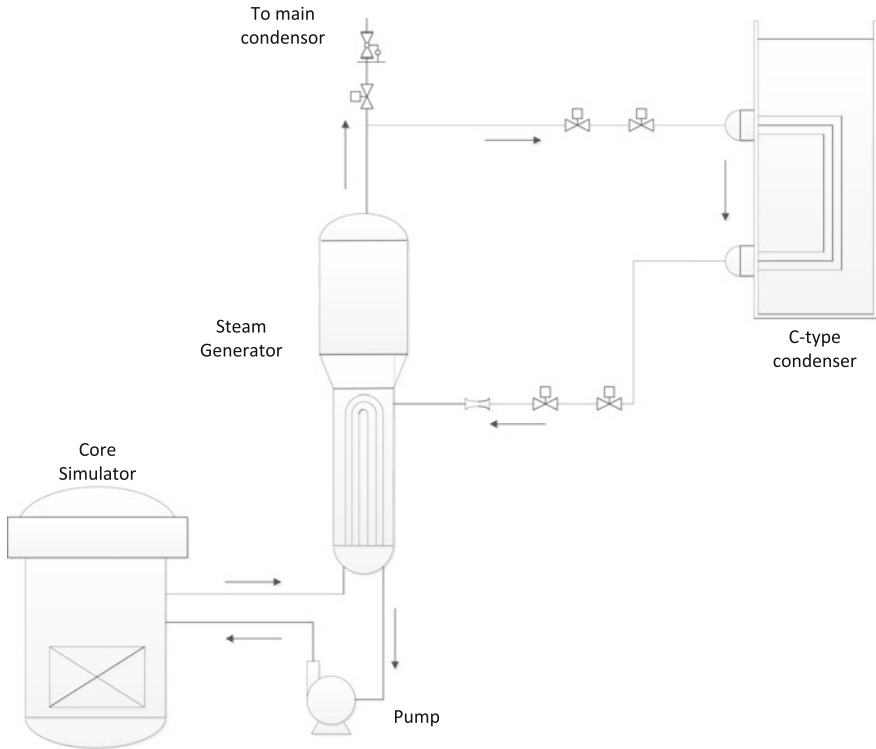


Fig. 1 Schematic of test facility

to measure the temperature of flow and tank, and the measurement accuracy was ± 0.25 °C. Differential pressure sensors and pressure sensors with an accuracy of 0.065% at full scale were used to measure the pressure. The flow rate was measured using a venture flowmeter with an accuracy of 0.5% at full scale. A comprehensive measurement and control system was built to record all the measurement data and control instrument using an industrial computer.

The instruments and pipeline were wrapped by the polythene insulating material to reduce the heat loss of the experiment system.

3 Test Matrix and Test Procedure

3.1 Test Matrix

In this paper, steady state heat transfer test and transient natural circulation test were conducted. The test matrix is shown in Tables 2 and 3.

Table 2 Transient natural circulation test conditions

Pressure of SG (MPa)	8.6
Temperature of C-type cooling water pool (°C)	Room temperature
Water level of SG (%)	20%
Open time of inlet valve(s)	10
Interval (s)	5
Open time of outlet valve(s)	10

Table 3 Steady heat transfer test matrix

Case	Pressure of SG (MPa)	Temperature of C-type cooling water pool (°C)
C1-1	1.5	Room temperature
C1-2	1.5	60
C1-3	1.5	100
C1-4	3	Room temperature
C1-5	3	60
C1-6	3	100
C1-7	6	Room temperature
C1-8	6	60
C1-9	6	100
C1-10	8	Room temperature
C1-11	8	60
C1-12	8	100

3.2 Test Procedure

The non-condensable gases were excluded from the whole loop and instruments before the start-up. Then the power of electrical heater was increased and the pump keeps on working to transfer the heat from primary side to secondary side. Then the test loop was adjusted to the test temperature and pressure.

During the transient test process, the valves open following the order reset by measurement data and control system, the ASP start operation. The steam was discharged into the C-type condenser, which was flooded in the pool, and then the condensed water flowed back to the steam generator. Natural circulation was built automatically, and the data was collected and saved.

During the steady test process, the heater in primary loop was maintained at steady state. The test section kept the same water capability and the same valve position. The water level in the C-type heater cooling water pool kept higher than tubes, while water temperature kept steady. The power of electrical heater was changed until the pressure and temperature met requirement, and data was collected and saved.

4 Results and Discussion

4.1 Transient Natural Circulation

Figures 2 and 3 show that mass flow rate of natural circulation and pressure varies with time. It is obviously that as the riser valve is open, pressure of C-type heat exchanger region increases rapidly and keep the same as that in steam generator. After 5 s, the down-comer valve opens, mass flow increase rapidly and became reduce shortly, while pressure started reduces. At the initial state, the down-comer pipe was full of water, when valve is open, water flows into the steam generator, so water level of down-comer drops while water level in steam generator rises (Fig. 4), respectively, the force that drives water flow became smaller and smaller. Meanwhile, steam in the steam generator was injected into heat transfer pipes, intensive condensation happens. Large quality of condensed water fall into the down-comer, and then wave crest happened, making continuous natural circulation. The flow rate and pressure of steady state natural circulation depends on electrical power, so finally flow became stable.

4.2 Steady State Natural Circulation

The variations at the heat transfer capability of C-type heat exchanger vs the pressure under four different C-type water pool temperatures are shown in Fig. 5. Similarly mass flowrate vs the pressure under four different C-type water pool

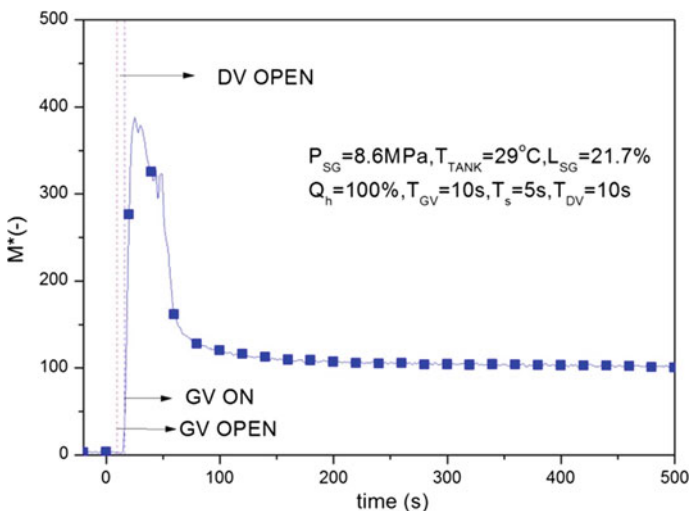


Fig. 2 Mass flow of natural circulation in system start-up experiment

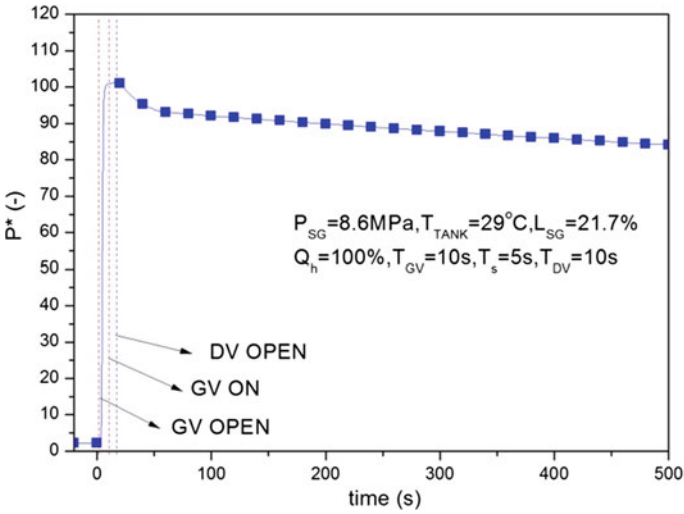


Fig. 3 Variation of pressure in start-up experiment

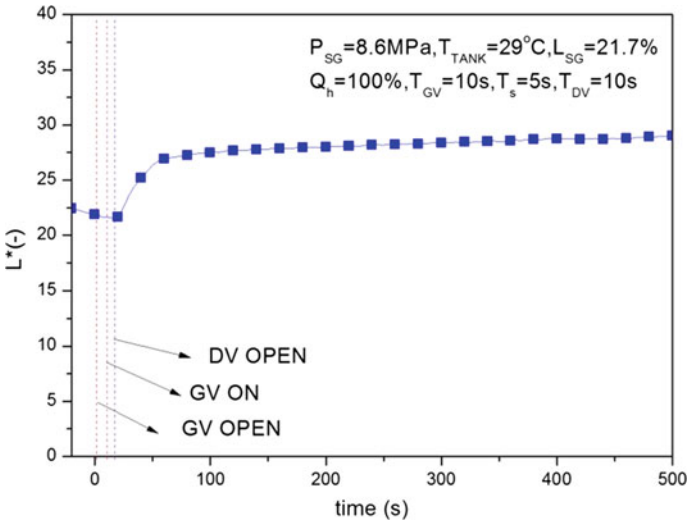


Fig. 4 Variation of SG water level in start-up experiment

temperatures are shown in Fig. 6. Under the same water pool temperature, the heat transfer capability and mass flow rate increased as the pressure increased, indicating that the pressure affects the heat transfer capability and mass flow rate significantly. In addition, at the same pressure, the heat transfer capability increased as the water pool temperature increased, while the mass flow rate increased as the temperature increased to 1.5 MPa, but similar with that at higher temperature. Compare to

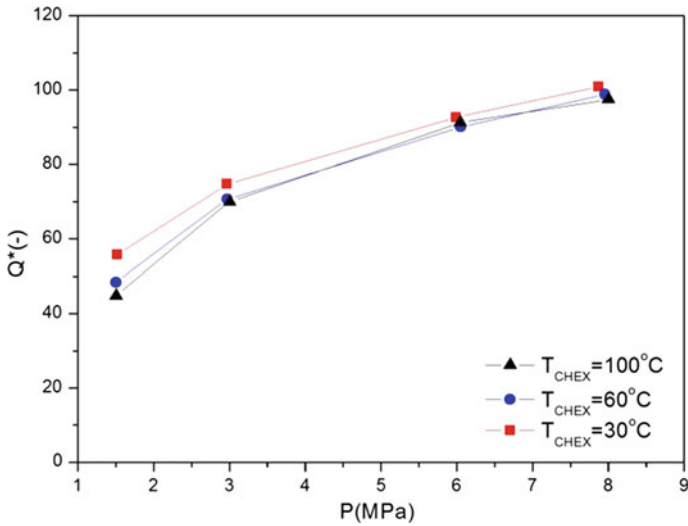


Fig. 5 Heat transfer capability in steady state experiment

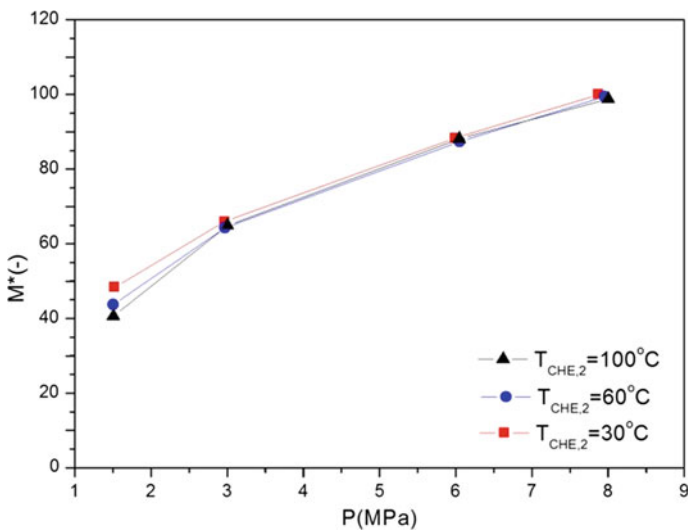


Fig. 6 Mass flow rate of natural circulation in steady state experiment

temperature of water pool, pressure has large impact on the natural circulation more significantly.

Figure 7 shows that the variation at the heat transfer coefficient vs the increasing pressure under four different C-type water pool temperatures. The heat transfer coefficient increased with pressure, when pressure is higher than 3 MPa, the heat

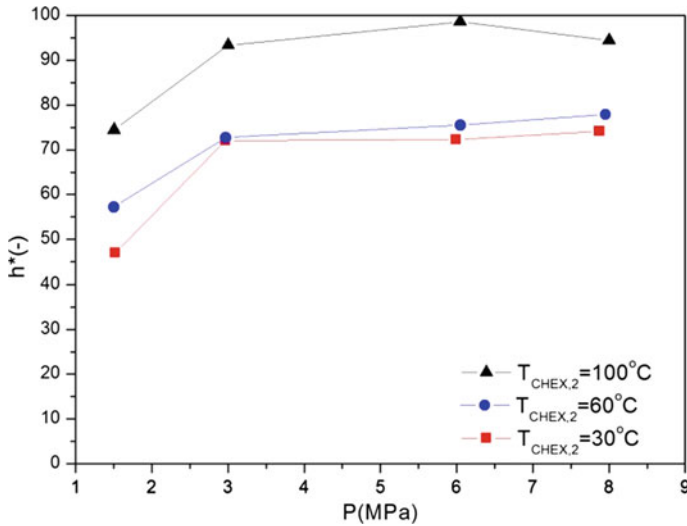


Fig. 7 Heat transfer efficiency in steady state experiment

transfer increased much slower. This is because when the pressure was low, heat transfer capability was low, and water around the C-type heat exchanger was heated but far from boiling. While the higher pressure means higher heat transfer capability, the water around the heat exchanger tubes start boiling and create more and more bubble. As a result, heat transfer coefficient keeps low increase rate in this stage.

5 Conclusions

A set of tests were performed to investigate the steady state and transient of ASP test facility according to the scaling laws. The experiments lead to the following conclusions:

- (1) The residual heat is successfully removed from the steam generator to atmosphere by natural circulation in the test facility.
- (2) The system shows good stability in the start-up process of transient natural circulation.
- (3) The characteristics of steady state natural circulation and heat removal capability at varying pressure and C-type cooling water pool were obtained. Heat transfer capability keeps positive increases with pressure, while decreases with temperature of cooling water.

References

1. Xiong Wanyu, Gong Houjun, Xi Zhao, Zhuo Wenbin, Huang Yanping. Preliminary evaluation of RELAP5 for design of secondary side passive residual heat removal system. *Nuclear Power Engineering*. Vol. 36, No. 2 (2015):143–146
2. Zhou Lei, Xi Zhao, Xiong Wanyu, Yan Xiao, Xiao Zejun. Analysis of influencer for secondary-side passive residual heat removal system based on RELAP5 code. *Nuclear Power Engineering*. Vol. 33, No. 6 (2012):72–75
3. Yan Chun, Wang Jianjun, Yan Changqi. Transient analysis of secondary-side passive residual heat removal system. *Nuclear Power Engineering*. Vol. 31, No. 4 (2010): 25-30
4. Zhang Yapei, Tian Wenxi, Qiu Suizheng, Su Guanghui. Analysis on flow instability of passive residual heat removal system for CPR1000. *Nuclear Power Engineering*. Vol. 32, No. 2 (2011): 38–41
5. Chen Wei, Zhang Yanan, Cao Xiixin, Yan Changqi, Zhang Wangsuo. Design and demonstration analysis on secondary side passive residual heat removal system. *Nuclear Power R & D*. Vol. 5, No. 2 (2011): 118–125
6. Chen Bingde, Xiao Zejun, Zhuo Wenbin. The heat removal study of AC600 passive system. *Journal of Engineering Thermophysics*. Vol. 20, No. 1(1999):17–21
7. Hyun-sik Park, Ki-yong Choi, Seok Cho, Sung-Jae Yi, Choon-kyung Park, Moon-ki Chung. Experiments on the performance sensitivity of the passive residual heat removal system of an advanced integral type reactor. *Nuclear engineering and Technology*. Vol 41, No. 1 (2009):53–62
8. Xi Zhao, Xiong Wanyu, Xie Feng, Gong Houjun, Zhuo Wenbin, Li Peng zhou. Experimental study on natural circulation characteristics of passive residual heat removal system. *Nuclear Power Engineering*. Vol. 36, No. 4 (2015): 1–3

Author Biography

Haiyan Xu Reactor thermal and hydraulic test engineer. China Nuclear Power Technology Research Institute Co. Ltd. Graduated from Shandong University in 2011.

I²S-LWR Concept Update

Bojan Petrovic, Farzad Rahnema, Chaitanya Deo, Srinivas Garimella, Preet Singh, KkochNim Oh, Ce Yi, Dingkang Zhang, Annalisa Manera, John Lee, Thomas Downar, Andrew Ward, Paolo Ferroni, Fausto Franceschini, David Salazar, Belle Upadhyaya, Matt Lish, Indrajit Charit, Alireza Haghghat, Matthew Memmott, Guy Boy, Abderrafi Ougouag, Geoffrey Parks, Dan Kotlyar, Marco Ricotti, Nikola Čavlina, Davor Grgić, Dubravko Pevec, Mario Matijević and Nick Irvin

Abstract Pressurized water reactor of integral configuration (iPWR) offers inherent safety features, such as the possibility to completely eliminate large-break LOCA and control rod ejection. However, integral configuration implemented using the current PWR technology leads to a larger reactor vessel, which in turn, due to the vessel manufacturability and transportability restrictions, limits the reactor power. It is reflected in the fact that there are many proposed iPWR SMR concepts, with power levels up to approximately 300 MWe, but not many iPWR

B. Petrovic (✉) · F. Rahnema · C. Deo · S. Garimella · P. Singh · K. Oh · C. Yi · D. Zhang
Georgia Institute of Technology, Atlanta, GA, USA
e-mail: bojan.petrovic@gatech.edu

A. Manera · J. Lee · T. Downar · A. Ward
University of Michigan, Ann Arbor, MI, USA

P. Ferroni · F. Franceschini · D. Salazar
Westinghouse Electric Company, Cranberry Township, PA, USA

B. Upadhyaya · M. Lish
University of Tennessee, Knoxville, TN, USA

I. Charit
University of Idaho, Moscow, ID, USA

A. Haghghat
Virginia Tech, Blacksburg, VA, USA

M. Memmott
Brigham Young University, Provo, UT, USA

G. Boy
Florida Institute of Technology, Melbourne, FL, USA

A. Ougouag
Idaho National Laboratory, Idaho Falls, ID, USA

G. Parks · D. Kotlyar
University of Cambridge, Cambridge, UK

concepts with power level corresponding to that of large traditional PWR NPPs (900 MWe or higher). While SMRs offer certain advantages, they also have specific challenges. Moreover, large energy markets tend to prefer NPPs with larger power. The Integral Inherently Safe Light Water Reactor (I²S-LWR) concept is an integral PWR, of larger power level (1000 MWe), that at the same time features integral configurations, and inherent safety features typically found only in iPWR SMRs. This is achieved by employing novel, more compact, technologies that simultaneously enable integral configuration, large power, and acceptable size reactor vessel. This concept is being developed since 2013 through a DOE-supported Integrated Research Project (IRP) in Nuclear Engineering University Programs (NEUP). The project led by Georgia Tech includes thirteen other national and international organizations from academia (University of Michigan, University of Tennessee, University of Idaho, Virginia Tech, Florida Institute of Technology, Brigham Young University, Morehouse College, University of Cambridge, Politecnico di Milano, and University of Zagreb), industry (Westinghouse Electric Company and Southern Nuclear), and Idaho National Laboratory. This concept introduces and integrates several novel technologies, including high power density core, silicide fuel, fuel/cladding system with enhanced accident tolerance, and primary micro-channel heat exchangers integrated with flashing drums into innovative power conversion system. Many inherent safety features are implemented as well, based on all passive safety systems, enhancing its safety performance parameters. The concept aims to provide both the enhanced safety and economics and offers the next evolutionary step beyond the Generation III + systems. This paper presents some details on the concept design and its safety systems and features, together with an update of the project progress.

Keywords I²S-LWR · Advanced reactors · Integral PWR · Inherent safety features · Accident tolerant fuel

1 Introduction

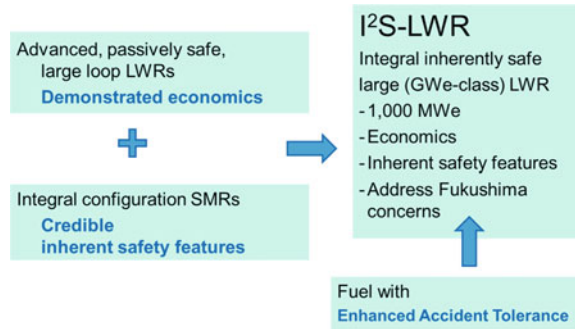
Small modular reactors (SMRs), with power output up to about 300 MWe, are attracting significant attention recently. In particular, light water SMRs are frequently of iPWR type. The integral configuration simplifies design and promotes

M. Ricotti
Politecnico di Milano, Milan, Italy

N. Čavlina · D. Grgić · D. Pevec · M. Matijević
University of Zagreb, Zagreb, Croatia

N. Irvin
Southern Company, Birmingham, AL, USA

Fig. 1 I²S-LWR approach to safety and economics



enhanced safety. However, for larger energy markets, higher power output units are frequently desirable. Thus, ideal design (for these markets) would extend SMR safety features to higher power units, e.g., around 1000 MWe (Fig. 1). Additionally, it is necessary to address post-Fukushima concerns.

While the goal is clear, it is not feasible to achieve it with the current PWR technology. Therefore, the I²S-LWR Team is developing several enabling innovative technologies.

2 Project and Team

The I²S-LWR concept is being developed since 2013 through a DOE-supported Integrated Research Project (IRP) in Nuclear Engineering University Programs (NEUP). The project [1, 2] is led by Georgia Tech and includes thirteen other national and international organizations from academia, industry, and national laboratory.

The team partners, with their main areas of responsibilities, are shown in Table 1.

3 I²S-LWR Performance Requirements

The I²S-LWR top-level requirements are summarized in Table 2. The first column lists the requirement, the second is the mandatory requirement, while the third column gives the ‘stretch target’ that the project is aiming to achieve, but it is acceptable to fall back to the mandatory requirement.

Table 1 The team partners, with their main areas of responsibilities

	Team members	Main area(s) of involvement	Faculty/researcher
Lead	Georgia Tech	Project management, integration, and overall design; materials; MCHX; shielding; economics	B. Petrovic, F. Rahnema, C. Deo, S. Garimella, P. Singh
Academia	Brigham Young University	Systems/components; safety	M. Memmott
	Florida Institute of Technology	Human-centered design	G. Boy
	University of Idaho	Cladding materials	I. Charit
	University of Michigan	Safety; systems/components	A. Manera, T. Downar, J. Lee
	Morehouse College	Outreach	L. Muldrow
	University of Tennessee	Instrumentation and control	B. Upadhyaya, W. Hines
	Virginia Tech	SFP monitoring	A. Haghighat
Industry	Westinghouse Electric Company	Core design, materials, plant system design, expert support in several areas	P. Ferroni, F. Franceschini, D. Salazar
	Southern Nuclear	Utility perspective	N. Irvin, N. Smith
National laboratory	Idaho National Laboratory	Fuel materials	A. Ougouag
International academia	Politecnico di Milano, Italy	Economics	M. Ricotti
	University of Cambridge, UK	Thorium cycle option	G. Parks, D. Kotlyar
	University of Zagreb, Croatia	Shielding, economics	D. Pevec, N. Čavlina, D. Grgić

4 I²S-LWR Main Features

The main features of I²S-LWR are as follows:

- pressurized water reactor, grounded on proven and well-understood technology;
- 1000 MWe unit power, to respond to markets requiring larger units and to facilitate economic competitiveness;
- integral primary circuit configuration to promote inherent safety features. As the most obvious examples, it avoids large-break loss-of-coolant accident (LOCA) and control rod ejection;

Table 2 I²S-LWR top-level requirements

	Requirement	Stretch target	Rationale
Application-driven requirements			
Power	>910 MWe	1000 MWe	For markets preferring large plants, economy of scale
Electricity production efficiency	>32%	35%	Competitiveness, reduced reject heat
Design lifetime	60 years	100 years	Competitiveness, economics, sustainability
Reactor pressure vessel	Radius smaller than or equal to current large PWRs		Manufacturability, transportability
Fuel-related requirements			
Fuel/cladding system	Enhanced accident tolerance ^a		Post-Fukushima considerations
Fuel enrichment	Baseline reloading with <5% enriched fuel	Option to use fuel cycle with 5–8% enriched fuel	Baseline uses existing infrastructure for <5% enrichment
Refueling	Multi-batch, refueling interval 12 months or longer	Options for 12–18–24-month refueling	12-month cycle is acceptable. Offer longer cycles when required by utilities
Safety and security			
Safety philosophy	Inherent safety features Full passive safety		Eliminate accident initiators Eliminate need for offsite power in accidents
Safety indicators	CDF < 3 × 10 ⁻⁷ LERF < 3 × 10 ⁻⁸	CDF < 1 × 10 ⁻⁷ LERF < 1 × 10 ⁻⁸	Improve safety indicators relative to current Gen-III + passive plants
Grace period	At least 1 week	Indefinite for high percent of scenarios with no or minimum operator action	Resistance to LOOP and Fukushima-type scenarios
Seismic design	Single compact building	Seismic isolators	Allow siting at many locations
Deployment requirements			
Economics	Competitive with current LWRs		
Operational flexibility	2-batch and 3-batch At least 12-month cycle	Load follow with MSHIM	Reduced effluents (environmental)
Decommissioning and dismantling (D&D)	Easily returned to green site		Sustainability and public acceptance

^a–ability to tolerate loss of cooling for extended time without, or with limited, interaction with coolant

- compact, high power density core to allow integral configuration at GW-e power level;
- innovative compact in-vessel primary heat exchanger (for the same reason);
- fuel/clad system with enhanced accident tolerance to address Fukushima-prompted concerns;
- enhanced safety-by-design and security-by-design;
- fully passive safety systems with as high as practical level of passivity;
- enhanced resilience to seismic and other external events; and
- passive decay heat removal system, capable of either indefinitely (in most scenarios) removing heat or (in remaining cases) extending the grace period without need for any operator actions.

5 I²S-LWR Enabling Technologies

Novel technologies are required to enable the I²S-LWR approach, and specifically high power output within the constraints of an integral configuration, which implies limited reactor vessel volume. Main enablers include the following:

- (i) high power density core (15–40% higher than current LWRs);
- (ii) high volumetric heat transfer rate heat exchangers; and
- (iii) novel steam generation system (SGS).

5.1 High Power Density Core [3]

The current LWR oxide fuel with Zr-based cladding performs well. However, (i) there is not much margin in its thermal performance for power uprate; (ii) its heavy metal (HM) loading may not provide optimum refueling interval for the uprated power; and (iii) Zr-based cladding may generate hydrogen in accident situations. Therefore, a novel fuel/cladding system is proposed, consisting of U₃Si₂ silicide fuel [2, 4] and advanced cladding. Initially, FeCrAl-type steel cladding is considered; it is recently receiving attention with experimental/testing activities ongoing or planned. Longer term SiC cladding will be used, when its performance is demonstrated. This system offers higher conductivity (thus potentially increased thermal margin) and increased HM loading. However, the use of traditional oxide fuel is examined as well, at least for the first units, to enable near-term deployment, while the silicide fuel and advanced cladding are test-irradiated and its performance is validated. Even with the standard oxide fuel and Zr-based cladding, I²S-LWR provides enhanced accident tolerance due to its other inherent safety features. In summary, I²S-LWR works with today's fuel, with a range of ATFs, and provides a

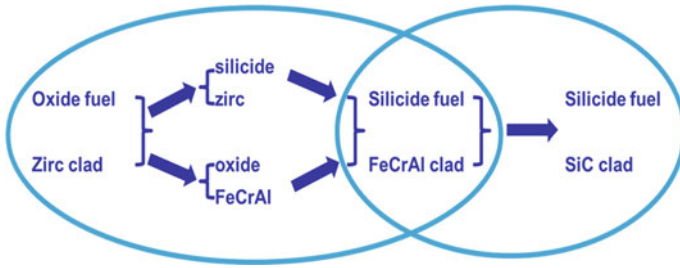


Fig. 2 I²S-LWR approach to deployment of advanced fuel/cladding system

viable route to incremental deployment of advanced fuel and/or cladding, as indicated in Fig. 2.

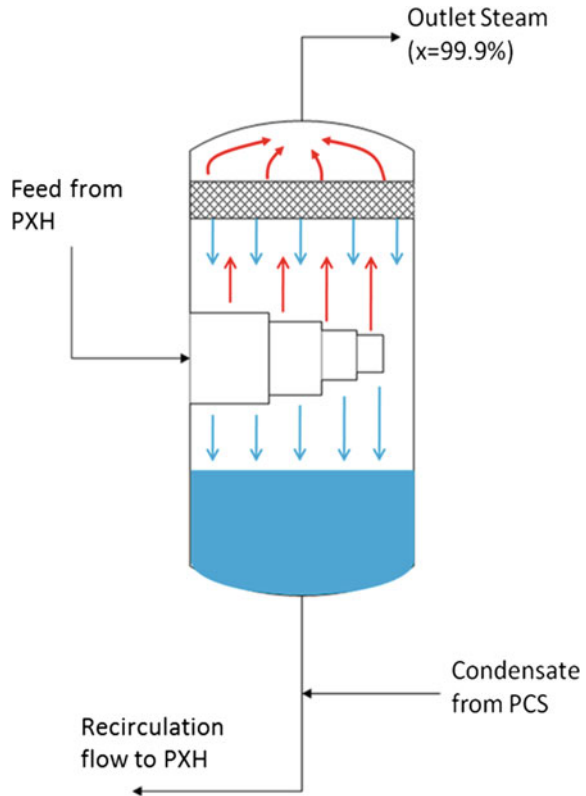
5.2 High Power Density Primary Heat Exchangers (PHXs)

Primary heat exchangers (PHXs) transferring heat from the primary to the secondary coolant are located within the RPV and therefore also require compact design. Several alternatives were considered, with the primary selection incorporating micro-channel-type heat exchangers (mC-HX). Small channels provide large heat transfer area per volume, making it possible to remove close to 3000 MWt with PHX that could fit within the RPV without causing an unacceptable increase in the RPV size. The mC-HX type of heat exchangers is successfully used in other industries, but not in nuclear (at least not in primary circuit). However, it has been assessed that they may be a viable and licensable option. A commercially available mC-HX module has been selected as the basic building block. In I²S-LWR, each PCX unit is axially composed of 11 such modules. Eight units are grouped in pairs forming four subsystems, enhancing maintenance and replacement capability.

5.3 Novel Steam Generation System (SGS) [5]

The use of mC-HX for steam generators was previously proposed; however, the two-phase flow results in significant challenges and may not be viable under practical conditions and requirements. Instead, I²S-LWR uses mC-HX as single-phase primary heat exchangers, which are then combined with flashing steam drums (four, one per each PCX subsystem) into a steam generation system (SGS). The use of a flashing drum for steam generation is sketched in Fig. 3. The power conversion system (PCS) is optimized for performance to match the characteristics of the steam generated by SGS, but is otherwise similar to the current PWR PCS.

Fig. 3 Illustration of secondary system flashing drum



6 I²S-LWR Layout

6.1 Integral Primary Circuit

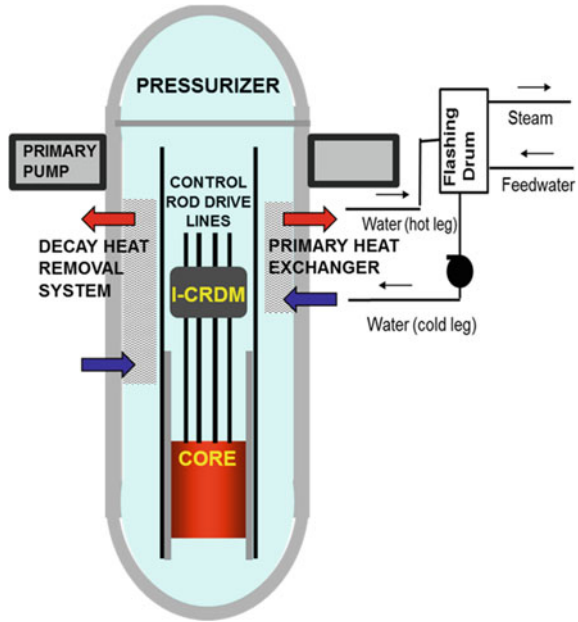
An integral primary circuit configuration (Fig. 4) is deployed [6] with primary coolant and all primary circuit components contained within the RPV. These include the following:

- core,
- core barrel and internals,
- 8 primary heat exchangers (PHXs),
- 4 decay heat exchangers (DHXs),
- control rod drive mechanisms (CRDMs), and
- pressurizer located in the upper vessel head.

Eight canned-motor reactor coolant pumps are attached to the vessel.

The primary coolant operating parameters (temperature and pressure) are essentially identical to those of current PWRs. The coolant flows (Fig. 5) upward through the core (where it is heated), continues through the riser, turns around in the

Fig. 4 Schematic of the I²S-LWR integral configuration with flashing drum indicated



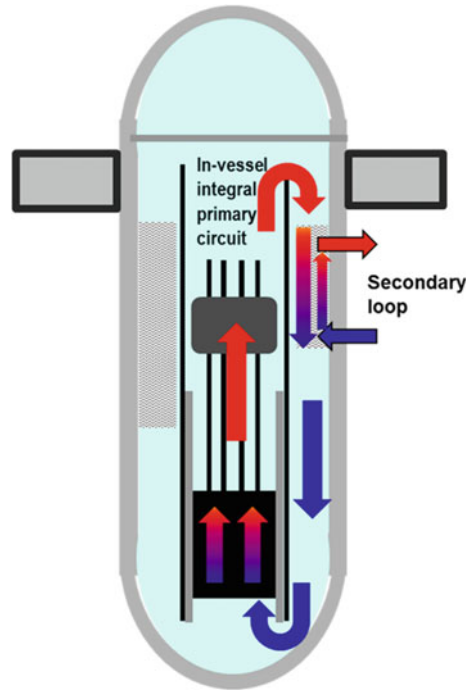
plenum/pumps area, and flows downward through the PXHs, upon exiting continues downward through the downcomer, to the lower vessel head, where it again turns upward, enters the core, and repeats the cycle. Preliminary scoping and trade-off studies were used to develop the initial sizing and arrangement. A fairly detailed preliminary layout has been developed and a 3D reactor vessel model printed (Fig. 6, left and right, respectively).

6.2 Core and Radial Arrangement Within the Vessel

The proposed core configuration is similar to a Westinghouse 2-loop PWR with 121 fuel assemblies (Fig. 7). I²S-LWR allows flexible reloading and fuel management. Several options have been developed based on oxide or silicide fuel, with standard or advanced cladding, with cycle lengths of 12, 18, and 24 months, and using a 2-batch or 3-batch refueling strategy. Due to the high power density, economically viable fuel cycles with oxide fuel are limited to 12 and 18 months, while silicide fuel (with higher heavy metal loading) allows a 24-month cycle as well [7].

A number of primary and secondary heat exchangers (PHXs and DHXs), providing an adequate redundancy, is located in the annulus between the core barrel and RPV. PHXs are part of SGS under power operation, as well as used for decay heat removal. DHXs are part of a fully passive, redundant, and diverse DHRS, providing decay heat removal capability in accident conditions [8]. A schematic illustrating their placement is also shown in Fig. 7.

Fig. 5 Schematic of the primary and secondary coolant flow directions



7 Safety

7.1 Safety Goals

The overarching goal of the I²S-LWR safety is to implement long-term self-sustained decay heat removal capability with no or very minimal operator intervention in case of an accident, including the loss of external power. This is achieved through multiple lines of defense and dedicated novel safety systems.

7.2 Defense in Depth

The first line of defense—inherent safety features—is the most effective since it eliminates or limits event initiators and precursors. Examples include the following:

- Integral primary circuit eliminates occurrence of large-size and intermediate-size break LOCA and control rod ejection.
- Seismic isolators eliminate or limit the impact of seismic events.
- Partial burying of the containment and underground placement of spent fuel pool eliminates the possibility or limits the impact of external malevolent threats.

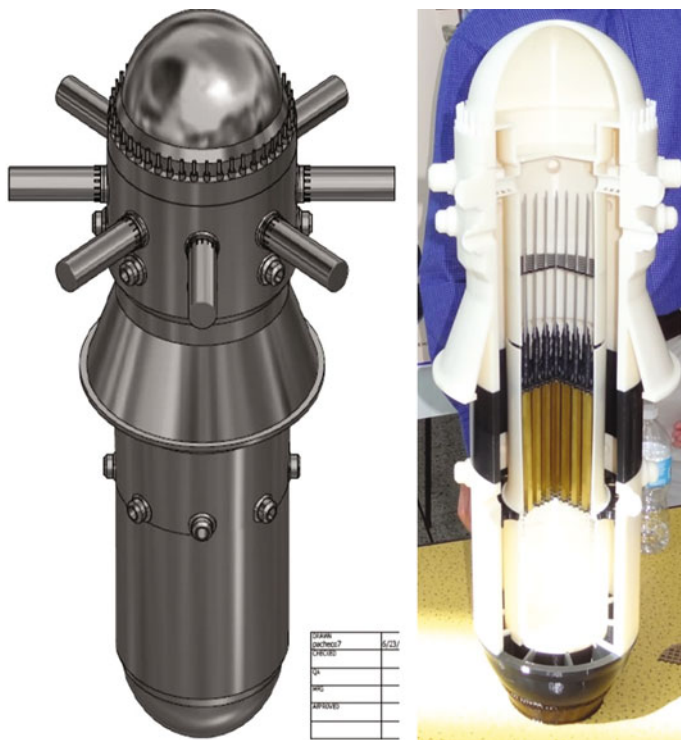
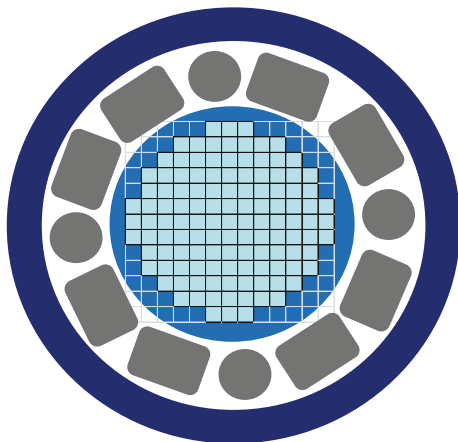


Fig. 6 Reactor vessel model (*left*) and 3D printed (*right*)

Fig. 7 Schematic of the radial view of the RPV arrangement with PHX and DHX shown (not to scale)



The second line of defense is prevention. All safety systems are passive with a high degree of passivity and deterministically prevent core damage for Design Basis Accidents (DBAs).

The third line of defense is mitigation:

- Integral configuration with small penetrations limits the loss of RPV inventory.
- Fuel with enhanced accident tolerance extends grace period.
- Passive DHRS extends grace period (potentially indefinitely).
- DPRA-guided design utilizes passive and active systems to improve response to Beyond Design Basis Events (BDBEs).

The fourth line of defense is protection:

- Containment vessel cooling by air or other medium in natural circulation regime protects public by avoiding or postponing release of radioactivity.

7.3 *Safety Philosophy*

The I²S-LWR safety philosophy is summarized as follows:

- Eliminate—by design choices—accident initiators as much as achievable.
- Implement as high level of passivity as possible.
- Limit the loss of inventory during LOCAs.

7.4 *Safety Systems*

To ensure high reliability and operation under assumed LOOP conditions, all safety systems in I²S-LWR are passive:

- Passive decay heat removal system (P-DHRS).
- PHX is also used as a passive heat removal system.
- Containment pressure suppression system (PSS).
- Four accumulators (ACC) drive borated water using pressurized nitrogen gas and provide emergency borated water into the reactor at medium pressure levels during the reactor depressurization phase in case of LOCAs.
- Core makeup tank (CMT) provides a diverse means of reactor shutdown by delivering borated water into the reactor. It injects coolant into the RPV downcomer and provides a limited gravity feed makeup water to the primary system.
- Automatic depressurization system (ADS).
- Passive reactor cavity cooling system (PRCCS).
- Passive containment cooling system (PCCS).

7.5 Safety Analyses

Safety analyses were performed to evaluate the performance for relevant scenarios including:

Undercooling events:

- loss of forced circulation (LOFC),
- main feedwater line break (MFLB),
- micro-channel heat exchanger (MCHX) blockage, and
- station blackout (SBO).

Loss-of-coolant-inventory events:

- SBLOCA (PZR valve stuck open) and
- spurious ADS actuation (SPADS).

Reactivity insertion accidents:

- inadvertent rod withdrawn, and
- boron dilution (unlikely due to configuration).

Overcooling events:

- main steam line break and
- inadvertent actuation of DHRS.

Analyses have been completed for most transients, demonstrating satisfactory safety performance [9]. Successful completion of the remaining analyses is expected soon.

Moreover, PRA analyses are performed not only to evaluate the relevant probabilistic indicators, but also to inform the design and to identify the design modifications and improvements with positive impact on safety. Level-1 PRA analyses performed so far estimate very low core damage frequency (CDF) and plant damage frequency (PDF).

8 Conclusions

I²S-LWR project is making progress toward developing a novel concept of an integral PWR with approximately 1000 MWe power output, with inherent safety features and competitive economics. Its integral configuration and novel enabling technologies allow extending the safety features typically reserved for SMRs (with power levels limited to 300 MWe or lower), to a GWe power level PWRs.

The project was started in February 2013 and has made significant progress since then. The initial scoping and trade-off analyses have established a consistent baseline. Early development of a realistic and fairly detailed 3D reactor vessel model facilitated addressing fabricability, constructability, maintainability, and repairs from early project stages. Studies performed so far suggest that the proposed concept is technically feasible and attractive in terms of safety and economics. Flexible refueling options have been established both with the standard oxide/Zr fuel/clad system and for silicide fuel with advanced cladding (FeCrAl or SiC). Moreover, I²S-LWR provides a viable pathway to deployment of new silicide fuel and advanced cladding options. Safety philosophy emphasizes simple design, prevention of accidents, and the use of passive safety systems. Conceptual design and sizing of safety systems are being completed. Safety analyses completed so far confirm exceptional safety performance. Economic analysis is in progress aiming to evaluate the economic competitiveness.

Acknowledgments This paper is based on the studies and results obtained by the whole project team, including—in addition to the co-authors listed—many other dedicated individuals (post-doctoral researchers, graduate students, and undergraduate students).

This research is being performed using funding received from the DOE Office of Nuclear Energy's Nuclear Energy University Programs (NEUP).

References

1. B. PETROVIC et al. "Integral Inherently Safe Light Water Reactor (I²S-LWR) Concept", *Proposal to DOE NEUP*, Georgia Tech (2012).
2. B. PETROVIC, "The Integral Inherently Safe Light Water Reactor," *Nuclear Engineering International*, pp. 26–29 (March 2014).
3. P. FERRONI, B. PETROVIC, G. SJODEN, M. CHIN, "Preliminary thermal-hydraulic feasibility evaluation of the Integral Inherently Safe LWR (I²S-LWR) high power density core," *Proceedings of ICAPP 2014* (Paper 14316), Charlotte, USA, April 6–9, 2014, ANS (2014).
4. S. RAY, E. LAHODA, F. FRANCESCHINI, "Assessment of Different Materials for Meeting the Requirement of the Future Fuel Designs," *2012 Reactor Fuel Performance/TopFuel*, Manchester, UK, Sep. 2–6, 2012 (2012).
5. M. MEMMOTT, A. MANERA, "The Use of a Flashing Drum to Generate Steam in the Integral Inherently Safe (I²S) Light Water Reactor," *Proc. 2014 Intl. Congress on Advances in Nuclear Power Plants (ICAPP 2014)*, Charlotte, NC, April 6–9, 2014, Paper 14193, pp. 60–70 (2014).
6. M. MEMMOTT, M. MARCHESE, B. PETROVIC, "Integral Inherently Safe Light Water Reactor (I²S-LWR) Concept: Integral Vessel Layout," *Proc. 2014 Intl. Congress on Advances in Nuclear Power Plants (ICAPP 2014)*, Charlotte, NC, April 6–9, 2014, Paper 14313, pp. 86–94 (2014).
7. B. PETROVIC, F. FRANCESCHINI, P. FERONI, "Fuel Cycle Cost Trade-off Studies for I²S-LWR (Integral Inherently Safe LWR) Fuel Design Selection," *2013 LWR Fuel Performance/TopFuel*, Charlotte, NC, USA, Sep. 15–19, 2013, ANS (2013).

8. A. MANERA, M. MEMMOTT, “Design and Trade-off Studies of the Passive Decay Heat Removal System (DHRS) of the Integral Inherently Safe LWR (I²S-LWR),” *Proc. 10th Intl. Conf. on Nuclear Option in Countries with Small and Medium Electricity Grids*, Zadar, Croatia, June 1–4, 2014 (2014).
9. E. WELCH, A. MANERA, M. MEMMOTT, P. FERRONI, M. WANG, J.C. LEE, “Preliminary Safety Considerations for the Integral Inherently Safe Light Water Reactor (I²S-LWR),” *Trans. Am. Nucl. Soc.* **111**, 961–964 (2014).

Author Biography

Dr. Bojan Petrovic is a professor in Nuclear and Radiological Engineering at Georgia Tech, Atlanta, USA. His research focuses on advanced reactors, nuclear fuel cycle, and numerical simulations of nuclear systems. Prior to joining Georgia Tech, he was fellow scientist at Westinghouse R&D working on novel SMR design and advanced fuels. Prof. Petrovic is a fellow of the American Nuclear Society and has authored or co-authored over 300 publications (parts of books and monographs, articles in journals and conference proceedings, and technical reports).

Main Building of Conventional Island Performance Assessment Based on Different Methods of Elasto-Plastic Analysis

Lichao Shi, Zhicong Wang, Weichao Jia and Yankun Huang

Abstract After introduction of three different methods about elasto-plastic analysis, the analysis on main building of conventional island of nuclear power plant has been done, and the performance is evaluated under SL-2 earthquake action. The applicability of different methods on this kind of structural system is reviewed, so that it can be used accurately in the relevant engineering designs.

Keywords Main building of conventional island of nuclear power plant · Elasto-plastic analysis methods · Performance assessment

1 Introduction

Structural system of main building of conventional island is very complex. There are lots of equipment and piping layout. The distribution of story stiffness is uneven. The load is very big, and distribution is seriously uneven. Under the action of earthquake, the structure is extremely damaged seriously. In order to ensure the safety of nuclear island plant, main building of conventional island needs to maintain structural integrity under the ultimate safety ground of SL-2.

Based on performance of seismic design theory and difference of analytical methods, the performance of main building of conventional island of nuclear power plant is evaluated, and the applicability of different methods on this kind of structural system is reviewed.

L. Shi (✉) · Z. Wang · W. Jia · Y. Huang
China Nuclear Power Engineering Co., Ltd, Hebei Branch, Shijiazhuang, Hebei, China
e-mail: jianghong@cnpe.cc

2 Analysis Methods

2.1 Simplified Analysis Method

For framed structures that do not exceed 12 stories in height and with no abrupt change of story stiffness as well as single-story factory buildings with reinforced concrete column, the simplified method in criterion may be used to check the performance characteristics of the structure under the rarely earthquake.

2.1.1 Basic Principle

This method is based on elasticity under rarely earthquake. Elasto-plastic response of the structure is obtained by proper modification. Simplified calculation formula is as follows:

$$\Delta u_p = \eta_p \Delta u_e = \mu \Delta u_y = \frac{\eta_p}{\xi_y} \Delta u_y \quad (1)$$

In the formula:

- $\Delta \mu_p$ elasto-plastic story drift
- $\Delta \mu_y$ yield story drift
- $\Delta \mu_e$ elastic story drift under the rarely earthquake
- μ story ductility factor
- ξ_y yield strength coefficient story
- η_p amplifying factor for elasto-plastic story drift

2.1.2 Applicability of the Method

The performance of the structure under the rarely earthquake can be obtained by elastic calculation and appropriate correction. The method is simple and convenient, but it has certain applicability. For multi-story structures with a uniform distribution of story yield strength coefficient ξ_y or yield strength coefficient story ξ_y is not uniform distribution, but elastic stiffness along the height is relatively smooth, the simplified method is applicability.

2.2 Static Elasto-Plastic Analysis Method

Some form of horizontal load or lateral displacement along the height of the structure is applied, and the structure to displacement limits or formation collapse mechanism is pushed over, so as to understand elasto-plastic performance of the structure, and the weak part of the structure is evaluated.

2.2.1 Basic Principle

Some form of equivalent lateral force along the structural height to simulate earthquake is applied, and lateral force is gradually increased from small to large, gradually making the structure state elasto-plastic state from elastic state, eventually reach and exceed the prescribed elasto-plastic displacement.

The load–displacement curve is established under lateral load, and the structure performance point is obtained, and then, the structural performance evaluation is carried out.

2.2.2 Main Steps

(1) Transformation of capacity spectrum

With the increase in the lateral load, the relationship between the base shear and the peak displacement is obtained, which is the capacity curve (*Pushover curve*). The ability curve is converted to capacity spectrum curve, and each point needs to be converted. From any point of V_i , Δ_{roof} in the capacity curve converted to the corresponding capacity spectrum of S_{ai} and S_{di} ; the conversion formula is as follows.

$$S_{ai} = \frac{V_i/G}{\alpha_1} \quad S_{di} = \Delta_{\text{roof}}/\gamma_1 X_{1,\text{roof}} \quad (2)$$

In the formula α_1 is mass participation factor of the first mode, γ_1 is participation factor of the first mode, $X_{1,\text{roof}}$ is the peak amplitude of the first mode, S_{ai} is spectral acceleration and S_{di} is spectrum displacement.

Modal participation factor is defined as follows:

$$\alpha_1 = \frac{[\sum_{i=1}^N (m_i \phi_{i1})]^2}{[\sum_{i=1}^N m_i][\sum_{i=1}^N (m_i \phi_{i1}^2)]} \quad (3)$$

$$\gamma_m = \frac{\sum_{i=1}^N (m_i \phi_{im})}{\sum_{i=1}^N (m_i \phi_{im}^2)}$$

In the formula γ_m is participation factor of the m mode, m_i is the quality of i -layer, ϕ_{im} is the amplitude of m mode in i -layer and N is the number of layers.

(2) Demand spectrum conversion

According to the *ADRS* (acceleration–displacement response spectrum) format, the structure capacity curve and the demand spectrum are drawn using the coordinates of the acceleration response spectrum. By the standard acceleration response spectrum (S_a - T spectrum) converted to S_a and S_d spectrum (spectral acceleration for the vertical coordinates, spectral displacement for the horizontal coordinates), is the

ADRS spectrum. The first point on the response spectrum curve has certainly a relationship with spectral acceleration S_a , velocity spectrum S_v , spectrum displacement S_d and period T . By the standard acceleration response spectrum (S_a - T spectrum) mode converted to *ADRS* mode, it is must to determine every point value of S_{di} corresponding to the value of S_{ai} and T_i on curve. The relationship can be derived from the following formula:

$$S_{di} = \frac{T_i^2}{4\pi^2} S_{ai} g \quad (4)$$

The standard demand response spectrum contains a constant acceleration spectrum and a constant velocity spectrum, which have the following relations at the period T_i :

$$S_{ai} g = \frac{2\pi}{T_i} S_v \quad S_{di} = \frac{T_i}{2\pi} S_v \quad (5)$$

(3) Determine performance points

Use double lines to represent the capacity spectrum. The area under the capacity spectrum and the double line representation area are equal. If the reduced demand spectrum and capacity spectrum intersect at point (S_{api}, S_{dpi}) or intersect at the range of 5% of S_{dpi} , then the intersection point is the performance point; if the intersection is not in the allowed range, the calculation process should be repeated until it is satisfied.

(4) Seismic performance evaluation

Through the following two aspects, the structural seismic performance is evaluated: (1) story drift: whether the limit value of elastic story drift in seismic code can be satisfied; (2) structure deformation: using to plastic hinge distribution, the weak position of the structure is determined. According to the state of plastic hinge, whether the structural member can satisfy the seismic performance level under the specified earthquake action is determined.

2.2.3 Applicability of the Method

The basic assumption of the method of static elasto-plastic analysis:

- (1) The response of the structure is related to the freedom system of equivalent single degree, that is, the structural response is controlled by the first mode of the structure;
- (2) The deformation along the height of the structure is expressed by the mode of the vibration type, that is, in the whole seismic response, the inertia force remains the same as the structure mass distribution or the mode of vibration.

From above basic assumptions, we can see that the static elasto-plastic analysis has applicability and limitations. Related research results show that the structure which 1 and 2 cycles is given priority to translation and the height is not more than 150 m; this method can accurately analyze the seismic reaction of the structure.

2.3 Dynamic Elasto-Plastic Analysis Method

Because of nonlinear properties of the structure, the building is considered an elasto-plastic vibration system. Earthquake ground motion displacement, velocity and acceleration brought by natural or artificial earthquake wave act on the structure. In order to obtain instantaneous displacement, velocity and acceleration, research dynamic response, damage mode and weak links etc. in the earthquake, finally evaluate seismic performance of the structure, dynamic equation is calculated by step-by-step integration method.

2.3.1 Basic Principle

Numerical method is used to solve nonlinear motion equation of $M\ddot{u}_t + C\dot{u}_t + Ku_t = F_t$. Calculating the response of displacement, velocity and acceleration of the structure under earthquake at any moment obtains the process of elastic and elasto-plastic stage internal force change and the bearing force change of the structure under earthquake action.

The dynamic response of the structure is analyzed, which can be divided into several small time periods, and the numerical solution is obtained by the numerical integration of the dynamic equation. As the structural stiffness recovery degree will constantly change according to the size of the structural response, each step of the analysis must be based on structure response status, to determine the stiffness of the structure, and then, the next step of calculation can be done.

2.3.2 Main Considerations

(1) Choosing of earthquake wave

The correct choice of seismic acceleration time history curve needs to consider three factors: frequency spectrum characteristic, effective peak value segment and duration. Frequency spectrum characteristic can be characterized with the seismic influence coefficient curve, which is based on the category of the site and the design earthquake grouping. The effective duration of time history curve of the earthquake wave is general from the first time to reach the point which is the 10% of the maximum peak, until reaching the last point which is the 10% of the maximum peak. Generally speaking, the effective duration is 5–10 times of the structure

period, that is, the displacement of the structure vertex can be repeated 5–10 times according to the basic cycle.

(2) Material model

The restoring force model of the material is mainly composed of two parts, the first is the skeleton curve and the second is the hysteresis curve with different characteristics. The skeleton curve refers to the connection of the peak points of the hysteresis curve. Experiments show that the connection of the peak points is very close to the force–deformation curve when the load is monotonic. Hysteresis curve shows the plastic properties of the component. The area enclosed by hysteresis loop represents the energy dissipation capacity of component.

(3) Unit model

The applicable unit model is selected according to different computing software. One-dimensional elasto-plastic units (beams and columns) mainly include fiber bundle model and plastic hinge model; two-dimensional elasto-plastic element (shear wall, floor) mainly include fiber beam model, the shell element injury model, elasto-plastic of wall element model and the multilayer shell model, etc.

(4) Result output and judgment

After elasto-plastic analysis, the results in several aspects are needed to see: the consistency of the elasto-plastic model and the elastic model, the total shear force, displacement and deformation, and the evaluation of the performance of the components.

2.3.3 Applicability of the Method

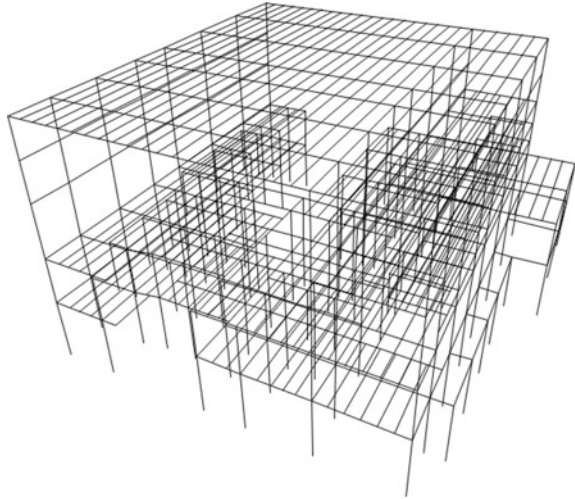
The premise and the assumption of the method are relatively few, and the applicability is strong. It is the most direct and accurate method to evaluate the seismic performance of structures.

3 Engineering Example

Taking a project as an example, the performance of the main power house under earthquake action of SL-2 is assessed and compared.

The span of turbine generator building is 42.5 m. Column spacing is of four kinds as 8, 10, 12 and 13 m. The roof of turbine generator building is composed of pitched steel roof trusses. Steel beam is layout on steel roof truss, and in situ reinforced concrete slabs formed on profiled steel sheets are placed on steel secondary beam. The main structure floors of turbine generator building are: bottom layer (−12.00 m), middle layer (± 0.00 m), operation floor (9.25 m) and roof; Seismic fortification intensity is 7°.

Fig. 1 3D finite element model



Structural system of main building is complex, and the vertical stiffness variation is large. The performance reaction of the structure under earthquake action of SL-2 is needed to be obtained. So the simplified method in criterion does not apply. Static elasto-plastic and dynamic elasto-plastic analysis methods are used to analyze, and the results are compared.

3.1 Model Building

The 3D finite element analysis model is established according to the design drawing, the load distribution map and the simplified principle. At the same time, the plastic behavior of the structural unit is specified. The beam and column element adopt the plastic hinge element, and the wall adopts the layered shell element as shown in Fig. 1.

3.2 Seismic Performance Evaluation of Structure

3.2.1 Story Drift

(1) Static elasto-plastic analysis method

By calculating two loading mode of the uniform load and modal load, in X direction the maximum story drift that occurred on the second floor is $1/84$; in Y direction the maximum story drift that occurred on the fifth floor is $1/81$.

(2) Dynamic elasto-plastic analysis method

Acceleration history data which are obtained from Seismological Bureau are used to obtain dynamic elasto-plastic time history analysis. In X direction, the maximum story drift that occurred on the fourth floor is 1/185; in Y direction, the maximum story drift that occurred on the fifth floor is 1/191.

- (3) It can be seen from the story drift that the results of the two methods are basically consistent. The story drift of static elasto-plastic analysis method is bigger than the story drift of dynamic elasto-plastic analysis method, because static elasto-plastic analysis method uses spectrum, and dynamic elasto-plastic analysis method only uses a specific time history curve.

3.2.2 Hinge Case

Under the earthquake of SL-2, the results of hinge case by using the two analysis methods are basically consistent. The end of beams appears as plastic hinge basically, and many ends of column appear as plastic hinge. Part of the plastic hinge enters into the stage of life safety (LS), but do not enter into the stage of collapse prevention (CP) as shown in Figs. 2 and 3.

Fig. 2 Hinges under earthquake in X direction

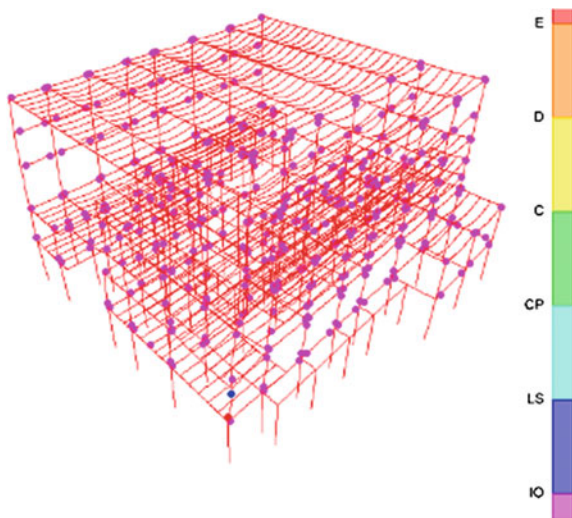
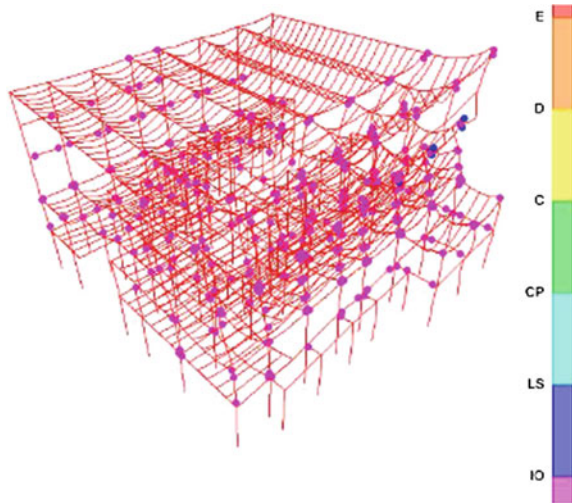


Fig. 3 Hinges under earthquake in *Y* direction



4 Conclusions

- (1) The simplified method is not suitable for performance evaluation of main building of conventional island under the earthquake of SL-2.
- (2) Static elasto-plastic analysis method and dynamic elasto-plastic analysis method are both suitable for performance evaluation of main building of conventional island under the earthquake of SL-2. The trend of the results of the two methods is basically consistent.
- (3) The static elasto-plastic analysis method is based on the spectrum, and the dynamic elasto-plastic analysis method is based on the specific time history curve, so the static elasto-plastic analysis method is more conservative than the dynamic elasto-plastic analysis method.

References

1. GB 50011-2010 Code for seismic design of building [S]. Beijing: China Architecture & Building Press, 2010
2. Guide for use in Chinese of SAP2000 [M]. Beijing: China Communications Press, 2012

Monte Carlo Study on Radial Burnup and Isotope Distribution

Cenxi Yuan, Shengli Chen and Xuming Wang

Abstract The radial distribution of the power, the isotope distributions, and other properties of the UO₂ and MOX fuel in the PWR are investigated with the increasing average burnup through the continuous-energy Monte Carlo code TRIPOLI-4. The local burnup phenomena mainly come from the high (n, γ) reaction rates of ²³⁸U and ²⁴⁰Pu near the surface of the fuel rod because of the self-shielding mechanism. The present Monte Carlo study shows that the local burnup and cumulative ²³⁹Pu near the surface are much larger compared with those at the center of the fuel rod. The local burnup and the isotope distributions are investigated up to 45 MWd/kgU in UO₂ fuel and 84 MWd/kgU in MOX fuel.

Keywords Monte Carlo simulation · Burnup · Isotope distribution · UO₂ fuel · MOX fuel

1 Introduction

In a thermal reactor, the local burnup near the surface of the fuel rod is much higher than that at the center. The mechanical structure of the high burnup region near the surface of the fuel rod can be very different from that at the center. Many investigations are performed to understand the structure of the high burnup region [1–3]. The bubbles in the high burnup region, which are highly overpressurized [4], are formed by the fission fragments depending on the reaction rate [5]. It is important to study the radial burnup and the isotope distribution when the increment of average burnup is considered.

The theoretical calculations and simulations are very important in nuclear science. In the fundamental research, the binding energies, levels, electromagnetic moments and transitions, Gamow–Teller transitions, and other properties of the

C. Yuan (✉) · S. Chen · X. Wang
Sino-French Institute of Nuclear Engineering and Technology, Sun Yat-Sen University,
Zhuhai 519082, Guangdong, China
e-mail: yuancx@mail.sysu.edu.cn

stable, extreme neutron- and proton-rich nuclei can be well described through the nuclear shell model, as shown in our previous works [6–8]. Because of the safety reason, the calculations and simulations are even more important in the nuclear reactor. Several of the models can be used to solve the present problem on the local burnup and the isotope distribution.

The most important origin of the high burnup near the surface is the (n, γ) reaction of the ^{238}U and ^{240}Pu . At the resonance region, the (n, γ) reaction rates of the ^{238}U and ^{240}Pu have certain large peaks [9], resulting in strong absorption of neutrons at certain energies. The moderator in the thermal reactor slows down the neutrons. If the slowed neutrons enter the fuel rods with those energies, they are almost all absorbed by the fuel near the surface, resulting in large production rate of ^{239}Pu and ^{241}Pu . The cumulated ^{239}Pu and ^{241}Pu near the surface correspond to the large local fission reaction rates and the burnup. In general, the other reactions induced by the slowed neutron have larger reaction rates near the surface, such as those of the (n, f) reactions of ^{235}U and ^{239}Pu , but not as obvious as the (n, γ) reaction of ^{238}U and ^{240}Pu .

Based on the origin of the local burnup, various models are suggested to obtain the numerical results on the local burnup and the isotope distributions, such as the TRANSURANUS [10–12], RAPID [13], and DIONISIO [14–16]. Our recent work suggested a simple formula based on approximately constant of the relative reaction rate [17].

In the present work, the single fuel rod with UO_2 and MOX fuel is simulated through the Monte Carlo (MC) code, TRIPOLI-4 [18]. After obtaining the reaction rates, the Bateman equation is solved by assuming the reaction rates do not change during a burnup step. The concentrations of next burnup level are thus got to be used as the next round simulation. Through such procedures, the local burnup and the isotope distributions are simulated up to certain burnup levels.

2 Description of Model

The present used MC code, TRIPOLI-4 developed by CEA, is a three-dimensional, continuous-energy code solving the Boltzmann equation based on the MC methods. The continuous-energy cross sections of the code are in ENDF format, from several evaluations, such as JEFF-3.1.1, ENDF/B-VII.0, JENDL4, and FENDL2.1.

The MC code simulates the reaction rates when the geometry sizes and the concentration of each isotope are given. The Bateman equation for each isotope can be solved by assuming the reaction rates do not change during time T :

$$\Delta N_i(r) = [-R_{a,i}(r) + R_{c,i+1}(r)]\Delta T,$$

where i is one kind of the nuclide and $i + 1$ is the nuclide which finally transforms to i in the reactor. If the nuclide i does not transform from other nuclei in the

reactor, there is no the term $R_{c,i+1}(r)$. $R_a(r)$ and $R_c(r)$ are the absorption and the captured reaction rates per unit volume at the radius r , respectively. $\Delta N(r)$ is the change in the concentration at the radius r during the time ΔT . The link between change in the average burnup ΔBU and the time duration ΔT is:

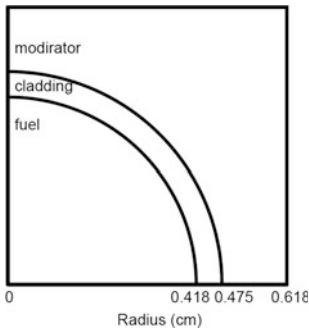
$$\Delta BU = Q\Delta T \Sigma R_{f,i}(r) / \rho,$$

where Q is the energy released per fission, $R_f(r)$ is the fission reaction rate per unit volume at the radius r , and ρ is the density of the fuel.

Through the MC simulations and the above equations, the local burnup and the isotope distributions can be obtained.

3 Calculation and Discussion

In the following discussion, one fuel rod model is used for the MC simulation. The size of the fuel rod is shown in the following figure.

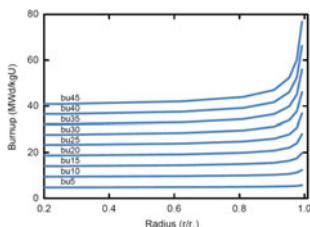


The simulations are based on three types of the fuel, UO_2 , MOX with low and high Pu concentration. The enrichment of each isotope in the fuel is listed in the following table.

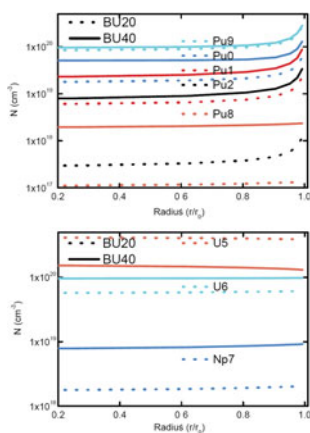
	UO_2	MOX_Low	MOX_High
^{235}U	3.3	0.24	0.226
^{238}U	96.7	95.562	89.975
^{238}Pu	0	0.063	0.147
^{239}Pu	0	2.528	5.9
^{240}Pu	0	1.029	2.401
^{241}Pu	0	0.37	0.862
^{242}Pu	0	0.21	0.49

The MC simulations are based on the above geometry sizes and enrichment.

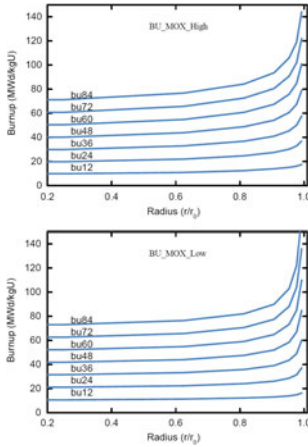
The local burnup of the UO₂ fuel is shown in the following figure. It is seen that the local burnup near the surface is around two times of that at the center, when the average burnup is 45 MWd/kgU. The phenomenon of the local burnup becomes obvious when the average burnup reaches 15 MWd/kgU.



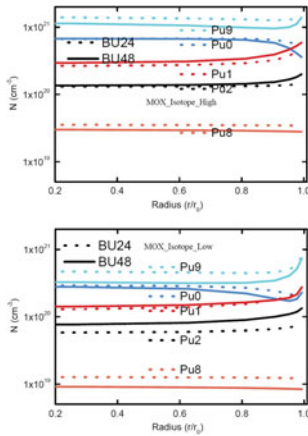
The following figure presents the isotope distribution of ^{235,236}U, ²³⁷Np, and ^{238,239,240,241,242}Pu at the average burnup 20 and 40 MWd/kgU. It is found that the concentration of ²³⁹Pu is almost the same from 20 to 40 MWd/kgU burnup, which means that the production and cost of ²³⁹Pu obtain a balance.



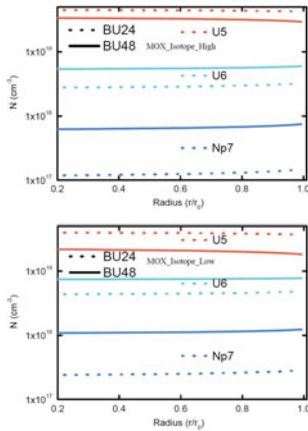
The local burnup of high and low concentration of MOX fuel is shown in the following figure. Generally speaking, the shape of the local burnup is more flat in the MOX fuel than that in the UO₂ fuel. The local burnup of the high-concentration MOX fuel has similar local burnup to that of the UO₂ fuel near the surface, two times of that at the center. The low-concentration MOX fuel has the larger local burnup near the surface, more than two times of that at the center.



The Pu isotope distributions of the MOX fuel at the average burnup 24 and 48 MWd/kgU are presented in the following figure. The shapes of the isotope distributions of the MOX fuel are similar to those of the UO₂ fuel, except that of the ²⁴⁰Pu. In the UO₂ fuel, all ²⁴⁰Pu comes from ²³⁹Pu. The shapes of their distributions are also similar to each other. But in the MOX fuel, the ²⁴⁰Pu originally exists in the fuel rod, and the cost is larger than the production near the surface.



The U and Np isotope distributions of the MOX fuel at the average burnup 24 and 48 MWd/kgU are presented in the following figure. The shapes of the distribution of these isotopes are more or less the same between the UO₂ fuel and high- and low-concentration MOX fuel, but much smaller in the latter.



4 Conclusions

In summary, the local burnup and the isotope distribution of three types of the fuel are investigated through the MC simulation using TRIPOLI-4. The different results between the UO_2 and MOX fuel are shown, originated from the existence of Pu isotopes at the beginning in the latter.

Acknowledgments The authors acknowledge our collaborator CEA for the authorization of the TRIPOLI-4. This work has been supported by the National Natural Science Foundation of China under Grant No. 11305272, the Specialized Research Fund for the Doctoral Program of Higher Education under Grant No. 20130171120014, the Guangdong Natural Science Foundation under Grant No. 2014A030313217, the Pearl River S&T Nova Program of Guangzhou under Grant No. 201506010060, and the Fundamental Research Funds for the Central Universities under Grant No. 14lgy29.

References

1. K. Nogita, K. Une, J. Nucl. Mater. 226, 302 (1995).
2. J. Noirot, L. Desgranges, and J. Lamontagne, J. Nucl. Mater. 372, 318 (2008).
3. M. Amaya, J. Nakamura, and T. Fuketa, J. Nucl. Mater. 392, 439 (2009).
4. Y.H. Koo, *et al.*, J. Nucl. Mater. 295, 207 (2001).
5. C.B. Lee, Y. H. Jung, J. Nucl. Mater. 279, 207 (2000).
6. C.X. Yuan, *et al.*, Nucl. Phys. A 883, 25 (2012).
7. C.X. Yuan, *et al.*, Phys Rev. C 85, 064324 (2012).
8. C.X. Yuan, *et al.*, Phys Rev. C 89, 044327 (2014).
9. <http://www.nndc.bnl.gov/exfor/endf00.jsp>.
10. K. Lassmann, *et al.*, J. Nucl. Mater. 208, 223 (1994).
11. K. Lassmann, C.T. Walker, J. van de Laar, J. Nucl. Mater. 255, 222 (1998).
12. A. Schubert, *et al.*, J. Nucl. Mater. 376, 1 (2008).

13. C.B. Lee, *et al.*, J. Nucl. Mater. 282, 196 (2000).
14. A. Soba, *et al.*, J. Nucl. Mater. 433, 160 (2013).
15. A. Soba, *et al.*, Ann. Nucl. Energy 70, 147 (2014).
16. M. Lemes, A. Soba, A. Denis, J. Nucl. Mater. 456, 174 (2015).
17. C.X. Yuan, X.M. Wang, S.L. Chen, Sci. Technol. Nucl. Ins. In press.
18. O. Petit, F.X. Hugot, Y.K. Lee, C. Jouanne, "TRIPOLI-4 version 4 user guide," CEA-R-6169, CEA (2008). <http://www.nea.fr/abs/html/nea-1716.html> (2008).

Author Biography

Cenxi Yuan is now working at the Sino-French Institute of Nuclear Engineering and Technology, Sun Yat-Sen University. He obtained his bachelor degree in physics and doctor degree in nuclear physics both at the Peking University. During doctoral program, he visited the University of Tokyo as a research student for more than one year. His research area includes nuclear physics, reactor physics, and neutronics.

Numerical Instability Study of Supercritical Water Flowing Upward in Two Heated Parallel Channels

Sujuan Li, Vijay Chatoorgoon and Scott Ormiston

Abstract A three-dimensional (3D) numerical simulation has been carried out using a RANS model in CFD ANSYS CFX v15.0 to investigate the out of phase oscillation instability between two heated parallel channels with supercritical water flowing upward. Spatial and temporal grid sizes effects on flow instability are studied first. High sensitivity of the CFD code on time step size is investigated, while spatial grid size refinement influence is not noteworthy. Oscillatory instability boundaries of three experimental cases are predicated by CFD code with the standard $k-\varepsilon$ turbulence model. Chatoorgoon's 1D nonlinear SPORTS code is also used to determine the instability boundary for comparison purposes. These new numerical results are compared with experimental data and previous numerical results. In general, there is a good agreement between numerical instability results of this paper and the experiments. Certain instability thresholds difference is observed among different numerical simulations, and possible reasons are pointed out. A previous finding that CFD results clearly yield better predictions of the instability boundary than a 1D solution is disputed in this paper.

Keywords Supercritical water · Instability · Parallel channels · Numerical simulation · CFD

1 Introduction

In order to improve the economics and efficiency of the light water reactor (LWR) and make full use of the technologies of supercritical water-cooled fossil-fired power plants, a new concept reactor named supercritical water-cooled reactor (SCWR) was proposed as one of the most promising GEN-IV nuclear reactors. In Europe, a joint research project called high-performance light water reactor (HPLWR) has been formed for investigations of SCWR concept. In SCWR

S. Li · V. Chatoorgoon (✉) · S. Ormiston
University of Manitoba, Winnipeg, MB, Canada
e-mail: vijay.chatoorgoon@umanitoba.ca

© Springer Science+Business Media Singapore 2017
H. Jiang (ed.), *Proceedings of The 20th Pacific Basin Nuclear Conference*,
DOI 10.1007/978-981-10-2314-9_15

loop design, water at 25 MPa and 500 °C leaves the reactor core, providing a high thermal efficiency of approximately 45% much higher than other LWRs (33%) [1]. Additionally, the direct cycle design of SCWR with coolant flowing from core to turbine directly at supercritical operating conditions makes installation of pressurizers, steam generators, recirculation pumps, and dryers unnecessary. This design simplification distinguishes a SCWR from other LWRs.

However, water properties will experience sharp changes as its temperature transitions through the pseudo-critical point, which can trigger thermal hydraulic instabilities. Flow instability in a nuclear reactor must be avoided as it is a mandatory safety requirement. As a result, the study of flow instability at supercritical pressure conditions has become popular, and large numbers of theoretical and numerical studies are emerging from around the world.

Zuber [2] theoretically investigated supercritical flow instability in a once through straight pipe flow system, and similar behaviors between supercritical flow instability and two-phase flow instability were found out. Chatoorgoon [3] performed an investigation about supercritical flow instability within natural circulation loop. Later he reported flow instability in heated parallel channels and derived a group of non-dimensional parameters which were validated by 94 numerical simulation cases [4]. Ambrosini and Sharabi [5] proposed two new dimensionless parameters for stability analysis of supercritical fluids. The newly derived non-dimensional parameters were a direct counterpart of the sub-cooling and phase change numbers introduced under two-phase flow conditions. Flow instability in single heated channel was simulated using the RELAP5 code and a 3D computational fluid dynamics (CFD) code by Ambrosini in 2007 [6], and the effects of inlet/outlet pressure loss coefficient and axial power distribution on stability boundary were reported. Xiong et al. [7, 8] performed both experimental and numerical studies on supercritical water flow instability in two heated parallel channels. Flow instability boundaries were obtained at different system pressures and inlet temperatures, and the experimental data were compared with their own 1D in-house code results, which proved that 1D numerical model can predict the onset of flow instability well. Subsequently, Xi et al. [9] also simulated Xiong's experiment with a 3D CFD code (an older version of CFX) and compared their results with experimental data. They concluded that their 3D model can predict the onset of instability better than Xiong's 1D model [8]. For the given geometry, a rather coarse mesh was used. Thus, their results and conclusion are revisited in this study. Xi et al. [10] also carried out another experimental investigation about flow instability between two heated parallel channels with supercritical water in 2014. The experimental loop was same as Xiong's [7], but Xi et al. used a much thicker wall channel in heated section and divided each heated channels into two sections to separately control the heating power. In this way, the influence of axial power shape on the flow instability was studied.

In this paper, both commercial CFD code ANSYS CFX v15.0 and Chatoorgoon's 1D nonlinear SPORTS code [11] were used to simulate Xiong's experiment [7]. For the CFD simulation, the standard $k-\varepsilon$ turbulence model with

scalable wall function was used. Obtained results were then compared with experiment and other previous numerical instability results.

2 Experimental Setup

A supercritical water loop had been constructed in Nuclear Power Institute of China, and more detailed information can refer to Xiong’s experiment paper [7]. Test section of this experimental loop is a two-parallel-channel system, and its schematic diagram is shown in Fig. 1. The two heated sections are INCONEL Alloy pipes with inner diameters 6 mm and heated length 3000 mm.

With these experimental facilities, a subsequent flow instability experiment had been carried out at different system pressures and inlet temperatures in 2012. Nine typical instability cases were obtained, summarized in Table 1. In this paper, cases: #1, 3, and 7 are simulated.

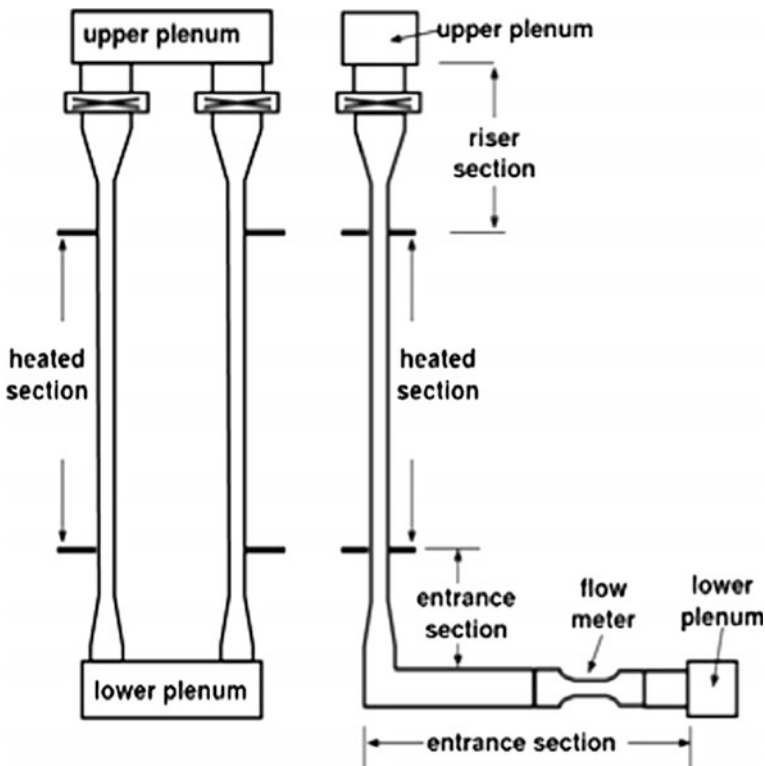


Fig. 1 Schematic of the experimental test section

Table 1 Experimental cases under different conditions

Cases	System pressure (MPa)	Inlet temperature (K)	Inlet mass flow rate (kg/s)	Threshold power (KW)
Case 1	23	453	0.0342	67.9
Case 2	23	473	0.0333	66.0
Case 3	23	493	0.0333	65.6
Case 4	24	473	0.0333	67.0
Case 5	24	493	0.0333	66.0
Case 6	24	513	0.0331	64.6
Case 7	25	473	0.0328	69.3
Case 8	25	493	0.0333	68.9
Case 9	25	513	0.0339	67.9

3 Numerical Modeling

3.1 Geometrical Model

The test section with two heated parallel channels is numerically modeled. Referring to Xiong's experiment [7] and 1D simulation paper [8], a simplified equivalent geometry was presented and that geometry was modeled here. The inner diameter of each heated channels was 6 mm. Plenum sizes were chosen large enough (length 430 mm, height 23 mm and width 10 mm) so that plenum effects on instability analysis are expectedly negligible.

Considering that the whole physical geometry is symmetrical, to save computational time only one half of the simplified model is simulated by applying a symmetry boundary condition. Figure 2a, b, respectively, illustrates the 3D view and specific dimensions of the geometrical model used in this study.

Due to manufacture and installation differences of the channels, asymmetry inlet and outlet pressure drop coefficients between the two parallel channels were previously reported by Xiong et al. [7]:

$$K_{in,1} = 5.40, K_{in,2} = 5.50, K_{out,1} = 4.93, K_{out,2} = 6.46$$

These K factors were also used in this study.

3.2 Governing Equations

The governing equations used in CFX are the standard mass, momentum, energy, and turbulence equations. Details of those equations can be found in [12].

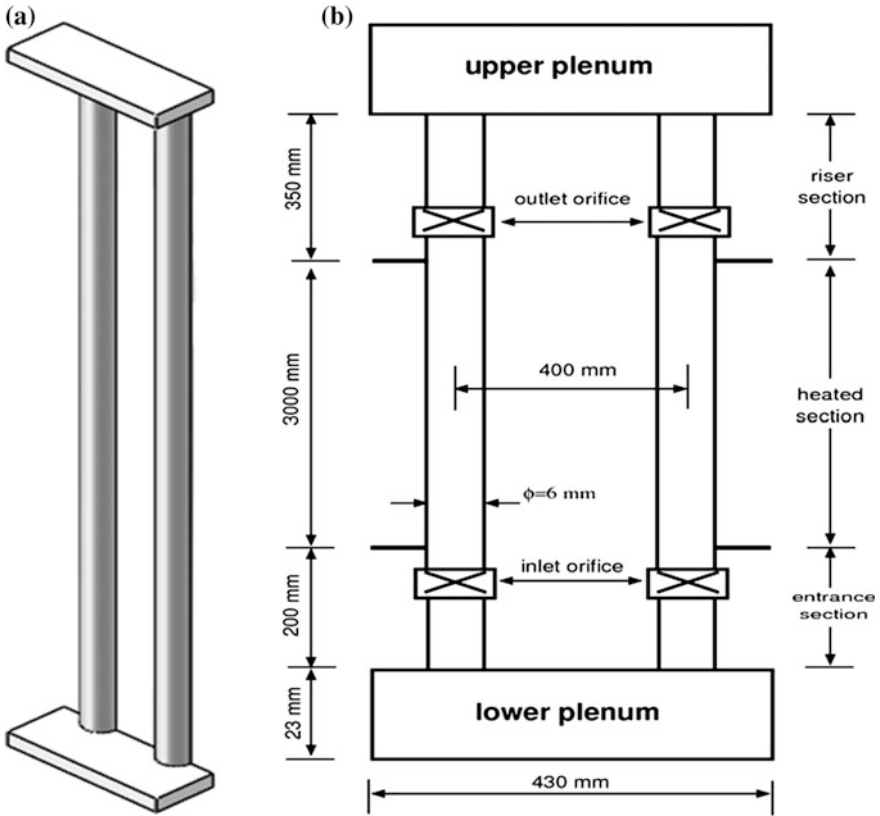


Fig. 2 a 3D view of simplified model. b Specific dimensions of simplified model

3.3 Domain Definitions and Boundary Conditions

To simulate local pressure drop with experimental K factors, subdomains are introduced. Domain separations are represented in Fig. 3, and Table 2 gives domain definitions as well as boundary conditions for each domain in Fig. 3.

3.4 Supercritical Water Properties

In CFX, thermodynamic properties of water stem from the IAPWS-IF97 database, formulated by Wagner et al. [13]. This database provides an accurate equation of state for water and steam properties. The range of validity for this property package in CFX is as follows:

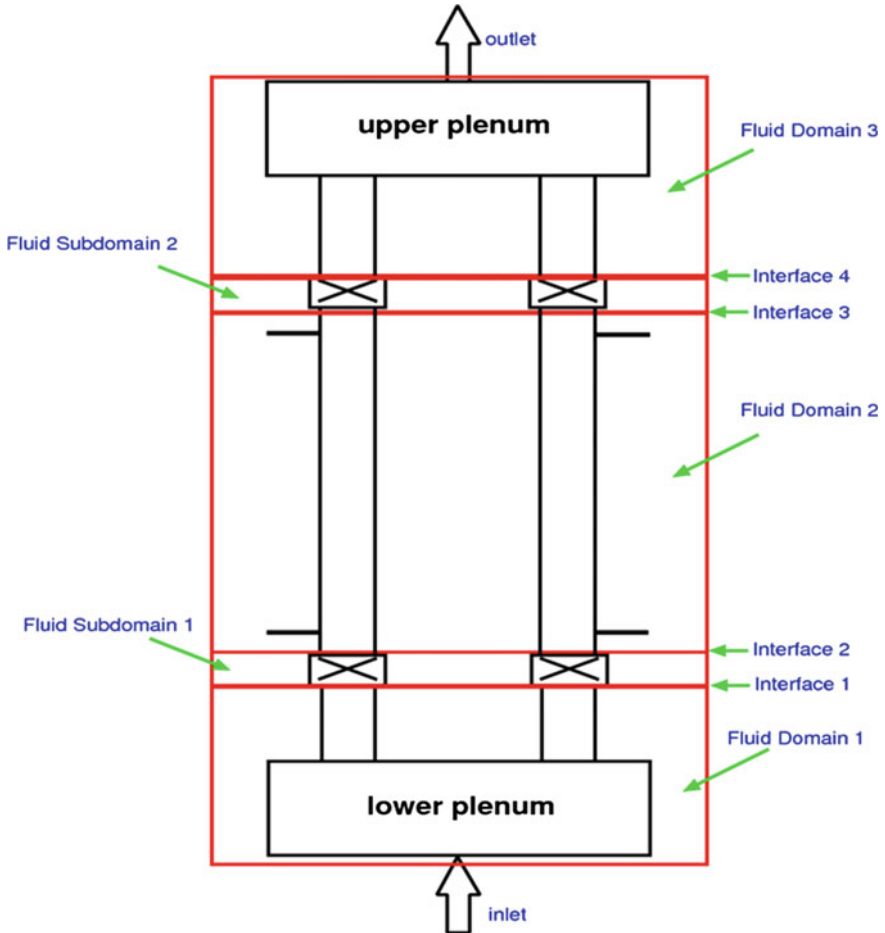


Fig. 3 Domain separations of simplified model

$$\begin{aligned}
 0(^{\circ}\text{C}) < T \leq 800(^{\circ}\text{C}) & \text{ for } 10(\text{MPa}) \leq P \leq 100(\text{MPa}) \\
 800(^{\circ}\text{C}) < T < 2000(^{\circ}\text{C}) & \text{ for } P < 10(\text{MPa})
 \end{aligned}$$

3.5 Numerical Solution Method

ANSYS CFX v.15.0 is used to generate meshes and solve the governing equations. The spatial domain is discretized into finite control volumes by CFX, and the governing equations are integrated over each control volume to ensure conservation of mass, momentum, energy, etc. Based on Rhie and Chow's work [14], a fully

Table 2 Domain definitions and boundary conditions

Fluid Domain 1, 2, & 3	<ul style="list-style-type: none"> • Buoyancy model: $g_x = 0, g_y = -9.81 \text{ m/s}^2, g_z = 0, \rho_{\text{ref}} = 500 \text{ kg/m}^3$ • Turbulence model: standard $k-\epsilon$ with scalable wall function • Turbulent Prandtl Number: 0.95 • Buoyancy turbulence: production and dissipation
Fluid Subdomain 1& 2	<ul style="list-style-type: none"> • General Momentum Source: $S_{M,x} = 0, S_{M,y} = -\frac{1}{2} \frac{K}{0.01} \frac{\dot{m}}{A} v, S_{M,z} = 0$ • Momentum source coefficient: $\frac{1}{2} \frac{K}{0.01} \frac{\dot{m}}{A}$
Inlet	<ul style="list-style-type: none"> • Specified mass flow rate • Specified inlet temperature • Turbulence: medium intensity ($I = 5\%$) • Flow direction: normal to boundary condition
Outlet	<ul style="list-style-type: none"> • Relative pressure: 0 (Pa)
Wall	<ul style="list-style-type: none"> • No-slip wall with uniform heat flux for fluid domain 2 • No-slip adiabatic wall conditions for other domains
Symmetry	<ul style="list-style-type: none"> • Applied on the x-y plane that split geometry into half
Domain Interface	<ul style="list-style-type: none"> • Conservation of mass, momentum, turbulence, and heat transfer between two domains

coupled solver that solves velocity and pressure equations as a single system is realized in CFX-5.

Double precision was used for the computations throughout. If the maximum normalized residual of each discretized equations was less than 1×10^{-6} , the steady state calculation was considered to be converged. For transient analyses, first-order transient scheme was used and the solver relaxation parameter was set to be 1.0 rather than the default value of 0.9. Furthermore, 30 iterations were performed during each time step. The high-resolution advection scheme was used for both steady state and transient analyses.

3.6 Numerical Procedure

3.6.1 Determining the Instability Threshold

Starting from a relatively high mass flow rate, a steady state analysis was done first to provide initial conditions for the corresponding transient runs. During the transient analyses, inlet and outlet channel mass flow rate responses with time were monitored to judge flow stability or instability.

For oscillatory instability, the flow would oscillate with diverging amplitudes in time. Converging flow oscillation amplitudes with time represented a stable system, while diverging amplitudes represented an unstable system. Theoretically,

instability threshold was defined as the mass flow rate that led to sustained mass flow rate oscillation without amplification or decay. When simulating particular experimental cases, a decrement of 0.0002 kg/s was applied to find the threshold mass flow rate. Within this change range, if the higher mass flow rate leads to stable flow while the lower mass flow rate triggers unstable flow, then the in-between mass flow rate was chosen as the threshold mass flow rate or instability boundary.

3.6.2 Spatial Grid Refinement Effects on Instability Boundary

Three meshes (see Table 3) with different spatial grid sizes were chosen to study grid refinement effects on instability boundary. For this study, 0.02 s was adopted as the time step size.

Oscillatory instability boundaries of case 1 and case 3 were predicted by CFD code with these three meshes, summarized in Table 4. If we choose the fine mesh (mesh 3) result as ‘best,’ the maximum difference in the threshold mass flow rate between mesh 1 and mesh 3 in case 3 is only 0.83%. Furthermore, considering the mass flow rate change used was 0.0002 kg/s (small enough), the instability boundaries predicted by these three different meshes are very close. Hence, spatial grid refinement does not make significant effects on the stability boundary. However, as a balance between reasonable results and convergence rate, mesh 2 with 450,000 nodes is considered adequate to be the final mesh for following analyses.

3.6.3 Time Step Size Effects on Instability Boundary

For case 1 in Table 1, the transient behavior of inlet mass flow rate in channel 1 at the four different time steps: 0.01, 0.02, 0.05, and 0.1 s were plotted and compared in Fig. 4.

Table 3 Meshes used for numerical simulation

Meshes	Number of nodes
Mesh 1	150,000
Mesh 2	450,000
Mesh 3	1,000,000

Table 4 Instability boundaries predicted by CFD code with different meshes

	Mesh 1	Mesh 2	Mesh 3
Case 1	0.0341	0.0341	0.0343
Case 3	0.0365	0.0360	0.0362

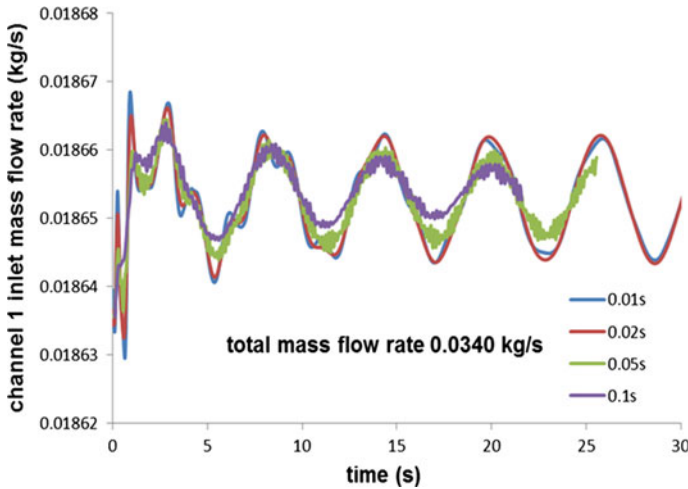


Fig. 4 Channel 1 inlet mass flow rate time response at different time steps

From Fig. 4, the effect of time step size on the transient mass flow rate can be discerned. With increasing the time step size from 0.01 s, the sine-wave oscillation shape becomes more rugged and less smooth, and its amplitude also decreases. Responses at 0.01 and 0.02 s collapse onto each other and agree reasonably well. The 0.05 and 0.1 s responses show that temporal convergence has not been achieved, and it would be wrong to use these time steps to determine the stability boundary. Furthermore, if we compare the threshold mass flow rates obtained with these four time steps (illustrated in Fig. 5), it can be noticed that 0.01 and 0.02 s predict essentially the same instability boundary. In addition, when the time step is increased from 0.02 to 0.1 s, the threshold mass flow rate drops strikingly from 0.0341 to 0.0321 kg/s, meaning the flow system becomes more stable with the larger time step. This is in agreement with the point of view proposed by Xiong et al. [8], obtained with their 1D code results.

To sum up the findings, 0.05 and 0.1 s are too large a time step for accurate stability analyses, and 0.02 s can be said to be the ‘optimum’ time step for it does not only require less computing efforts but also guarantee accuracy.

4 Results and Discussion

4.1 Prediction of Threshold Mass Flow Rate by CFD and 1D Codes

Three experimental cases (#1, 3, and 7) in Table 1 are numerically studied with a time step of 0.02 s and mesh 2.

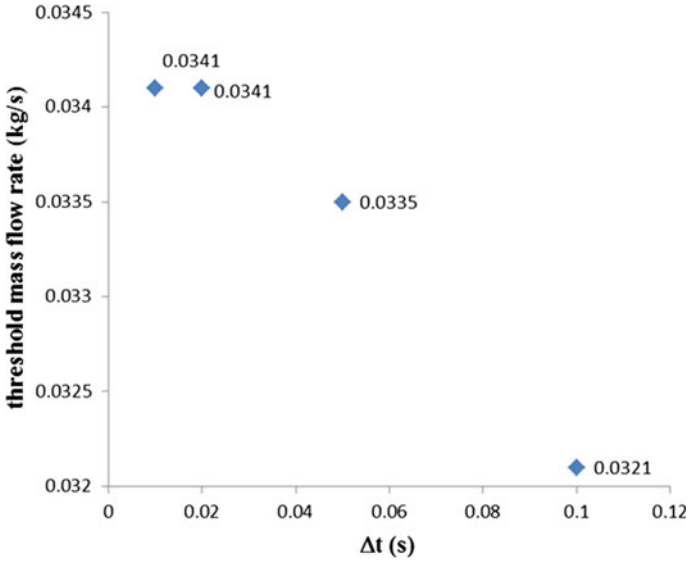


Fig. 5 Effect of time step on the threshold mass flow rate

Figure 6 indicates under case 1 flow conditions, the monitored inlet mass flow rate transient responses in channel 1 with total mass flow rate 0.0340 and 0.0342 kg/s. As shown in Fig. 6, for a total mass flow rate 0.0340 kg/s, the oscillation amplitude grows; contrarily, it decays for total mass flow rate 0.0342 kg/s. Therefore, the flow is unstable with a total mass flow rate of 0.0340 kg/s and is stable with a total mass flow rate of 0.0342 kg/s. Hence, 0.0341 kg/s is taken as the threshold mass flow rate of case 1.

The inlet boundary condition for this parallel channel system is constant total mass flow rate, so channel 1 and channel 2 will behave out of phase oscillation to conserve total mass flow rate, demonstrated in Fig. 7. Considering channel 2 has a larger outlet K factor, the mass flow rate in channel 2 is relatively smaller than that of channel 1.

Table 5 summarizes threshold mass flow rates predicted by 3D numerical CFD code for case 1, case 3, and case 7 in Table 1.

Oscillatory instability boundaries were also obtained by a 1D nonlinear SPORTS code [11] with the same flow conditions. Different from CFD code, calculating the wall shear friction automatically via the wall functions, a 1D code has to rely on an empirical friction-factor correlation to determine the friction pressure drop. Same as the 1D in-house code of Xiong et al. [8], Haaland approximate explicit relation [15] has been used for 1D SPORTS code.

Instability boundaries predicted by 1D nonlinear SPORTS code are listed in Table 6 below.

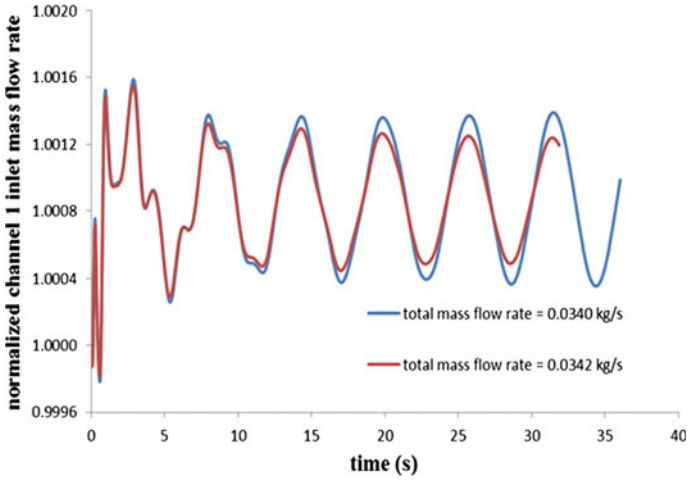


Fig. 6 Mass flow rate time responses with different mass flow rates for case 1

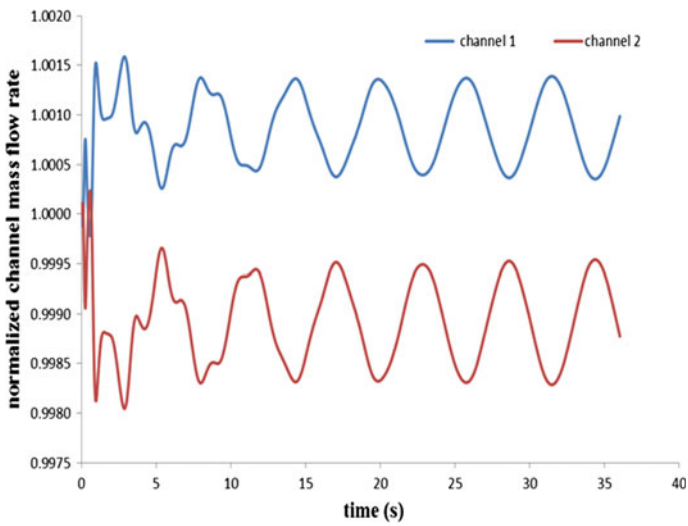


Fig. 7 Inlet mass flow rate responses with time in two parallel channels

Table 5 Threshold mass flow rates for different cases predicted by CFD code

Cases	Threshold mass flow rate predicted by CFD (kg/s)
Case 1	0.0341
Case 3	0.0360
Case 7	0.0349

Table 6 Threshold mass flow rates for different cases predicted by 1D non-linear code

Cases	Threshold mass flow rate predicted by 1D nonlinear code (kg/s)
Case 1	0.0338
Case 3	0.0354
Case 7	0.0346

4.2 Comparison Between Numerical Simulations and Experiment

For this flow instability experiment, about two heated parallel channels with supercritical water flowing upward, several numerical simulations (1D and 3D) have already been done and reported [8, 9]. In those studies, they held the flow rate constant and varied the total channel power until the threshold power was found. In this study, we held the power constant and varied the total mass flow rate until the stability boundary was found. We found that if the results are normalized to Ambrosini’s dimensionless parameter [5], N_{TPC} , both approaches give exactly the same answer.

Figure 8 and Table 7 give the comparison of N_{TPC} between the calculated result and experimental result. Only three experimental cases (#1, 3, and 7) are presented in this paper due to time constraints. We plan to do additional simulations of other cases and will report on those cases later.

Considering the experimental uncertainty, which is expected to be at least $\pm 10\%$, the new numerical results presented here are considered to be within the experimental uncertainty.

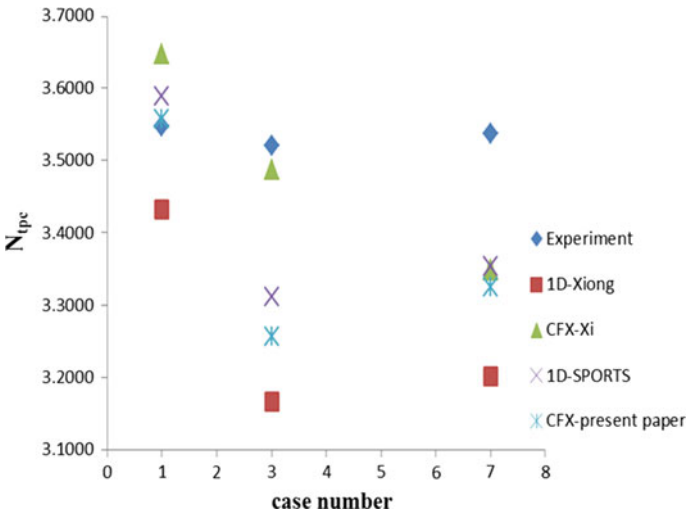


Fig. 8 Comparison between the numerical simulation and experiment results

Table 7 N_{TPC} comparison between numerical simulation and experiment results

Cases	Experiment [7]	1D-Xiong [8]		1D-SPORTS [11]		CFX-Xi [9]		CFX-present paper	
		N_{TPC}	Relative Error	N_{TPC}	Relative Error	N_{TPC}	Relative Error	N_{TPC}	Relative Error
Case 1	3.5476	3.4326	-3.24%	3.5895	1.18%	3.6468	2.80%	3.5580	0.29%
Case 3	3.5200	3.1659	-10.06%	3.3112	-5.93%	3.4878	-0.91%	3.2560	-7.50%
Case 7	3.5379	3.2010	-9.52%	3.3539	-5.20%	3.3490	-5.34%	3.3250	-6.02%

In general, there is no one group that predicts the best instability boundary compared with experiment. For example, CFX-present paper predicts best for case 1 with smallest relative error 0.29%; while for case 3, CFX-Xi gives the smallest relative error -0.91%. In spite of this, 1D code results carried out by Xiong et al. [8] deviate most from the experiment. We believe that was due to the pressure boundary condition they imposed at the inlet and outlet of the channels. They imposed equal static pressure at the channel inlet and outlet, whereas SPORTS imposes equal stagnation pressure at the channel inlet and outlet.

Firstly, if we compare the two 1D code results, 1D SPORTS code results are better in all cases. Reasons have already been mentioned above.

Secondly, if we compare the two 3D CFD code results, due to different CFX versions with different solver methods used, instability boundaries obtained are somewhat different. 3D numerical results obtained by Xi et al. [9] appear to be closer to the experiment, but our view is that their numerical results are not properly converged results due to the large time step used. Because of the 0.1-s time step, they will have a more stable flow system, leading to a higher N_{TPC} . Possibly, this is also one of the reasons why their N_{TPC} values of all three cases in Table 7 are higher than those of this paper.

Thirdly, if we compare 1D-SPORTS with 3D CFX-Xi results, except for case 3, 1D results of SPORTS code predict better than Xi’s 3D results. Therefore, the viewpoint proposed by Xi et al. [9] that 3D code would predict the onset of flow instability better than 1D code is not supported by these results.

Lastly, 1D-Xiong instability boundaries were also obtained with a time step of 0.02 s. If we only observe N_{TPC} distribution trend of 1D-Xiong, 1D-SPORTS and present CFX results in Fig. 8, we will notice that their trends are consistent, different from CFX-Xi’s trend with a 0.1-s time step. Hence, this interesting finding further proves the importance of time step size.

5 Conclusions

Both 3D and 1D numerical study are conducted to simulate flow instability between two parallel channels with supercritical water flowing upward. Present study results somewhat deviate from those reported by previous investigators. For 3D simulation differences, they may be related to dissipative and dispersive effects of large temporal and spatial grid size adopted in previous investigations. Different numerical

model and commercial code version used can also generate differences. 1D solution deviations of Xiong et al. are believed to be caused by imposing equal static pressure boundary condition at the channel inlet and outlet, whereas we believe it should be equal stagnation pressure.

Earlier finding that 3D code would predict the onset of flow instability better than 1D code is not supported by the results of this study. More experimental cases will be simulated to further compare 3D and 1D's capability to predict the instability boundary.

Spatial grid size refinement does not have a dramatic influence on the instability boundary, whereas there is a high sensitivity to the time step size.

References

1. Schulenberg, T., et al., Design and analysis of a thermal core for a high performance light water reactor. *Nuclear Engineering and Design*, 2011. 241(11): p. 4420–4426.
2. Zuber, N., An analysis of thermally induced flow oscillations in the near-critical and super-critical thermodynamic region: final report. 1966: Huntsville, AL: George C. Marshall Space Flight Center, 1966.
3. Chatoorgoon, V., Stability of supercritical fluid flow in a single-channel natural-convection loop. *International Journal of Heat and Mass Transfer*, 2001. 44(10): p. 1963–1972.
4. Chatoorgoon, V., A. Voodi, and D. Fraser, The stability boundary for supercritical flow in natural convection loops. *Nuclear Engineering and Design*, 2005. 235(24): p. 2570–2580.
5. Ambrosini, W. and M. Sharabi, Dimensionless parameters in stability analysis of heated channels with fluids at supercritical pressures. *Nuclear Engineering and Design*, 2008. 238(8): p. 1917–1929.
6. Ambrosini, W. and M.B. Sharabi, Assessment of stability maps for heated channels with supercritical fluids versus the predictions of a system code. *Nuclear Engineering and Technology*, 2007. 39(5): p. 627–636.
7. Xiong, T., et al., Experimental study on flow instability in parallel channels with supercritical water. *Annals of Nuclear Energy*, 2012. 48: p. 60–67.
8. Xiong, T., et al., Modeling and analysis of supercritical flow instability in parallel channels. *International Journal of Heat and Mass Transfer*, 2013. 57(2): p. 549–557.
9. Xi, X., et al., Numerical simulation of the flow instability between two heated parallel channels with supercritical water. *Annals of Nuclear Energy*, 2014. 64: p. 57–66.
10. Xi, X., et al., An experimental investigation of flow instability between two heated parallel channels with supercritical water. *Nuclear Engineering and Design*, 2014. 278(0): p. 171–181.
11. Chatoorgoon, V., SPORTS - A simple non-linear thermalhydraulic stability code. *Nuclear Engineering and Design*, 1986. 93(1): p. 51–67.
12. SAS IP, I. ANSYS CFX-Solver Theory Guide, Release 15.0. 2013.
13. Wagner, W., et al., The IAPWS Industrial Formulation 1997 for the Thermodynamic Properties of Water and Steam. *Journal of Engineering for Gas Turbines and Power*, 2000. 122(1): p. 150–184.
14. Rhie, C.M. and W.L. Chow, Numerical study of the turbulent flow past an airfoil with trailing edge separation. *AIAA Journal*, 1983. 21(11): p. 1525–1532.
15. Haaland, S.E., Simple and Explicit Formulas for the Friction Factor in Turbulent Pipe Flow. *Journal of Fluids Engineering*, 1983. 105(1): p. 89–90.

Numerical Investigations of the Helium Flow in Mini-Scale Gaps

Haoran Peng and Jun Sun

Abstract According to the loose body structure design of the high temperature gas-cooled reactor (HTGR), narrow gaps between the graphite and carbon blocks are widely distributed in the reactor core and become possible bypass flow paths. Related to the effective cooling flow rate in the primary loop, the bypass flow distribution is important to the thermal hydraulic design and safety analyses of the HTGR. Typical gaps of bypass flow paths are mini-scale rectangular gaps with small height/width ratio of the cross section, and their sizes are about 1.0 mm. Due to non-circular cross section, small height/width ratio and mini-scale sizes, helium flow in those gaps may be laminar, transient, or turbulent so that the resistance performance of each gap is difficult to predict and is crucial to analyze the bypass flow distribution in the reactor core. In this paper, commercial Computational Fluid Dynamic (CFD) software ANSYS Fluent was utilized to simulate helium flow in mini-scale gaps to investigate the reasonable models for predicting the resistance performances. Two-dimensional simulation results were compared with experimental data conducted in South Africa. The RNG k - ϵ model with enhanced wall treatments was more appropriate to simulate flows with Reynolds number up to 2×10^4 in mini-scale gaps. Based on the CFD models validated by the pressurized helium flow experiments, they can be further used to study more complex bypass flows in the HTGR.

Keywords HTR-PM · Bypass flow · Mini-scale · Resistance · CFD

H. Peng · J. Sun (✉)

Institute of Nuclear and New Energy Technology, Collaborative Innovation Center of Advanced Nuclear Energy Technology, Key Laboratory of Advanced Reactor Engineering and Safety of Ministry of Education, Tsinghua University, Beijing, China
e-mail: sunjun@tsinghua.edu.cn

1 Introduction

Due to the excellent inherent safety features, HTR-PM (High-temperature Reactor Pebble-bed Module), designed by Institute of Nuclear and New Energy Technology, Tsinghua University [1], has received worldwide attention in the field of nuclear energy and is considered as one of the candidates for the next-generation reactors. The helium serves as the coolant while large amount of graphite blocks are the neutron reflector, the structural material as well as the helium flow channels. Due to the loose body structure design of the reactor as well as the result of manufacturing and temperature constraints of reactor core internals, narrow gaps between the graphite and carbon blocks are widely distributed in the reactor core (as seen in Fig. 1).

As the coolant flow directions of HTR-PM demonstrated in Fig. 2, the helium at low temperature from main helium blower flows upward in coolant rising channels and mixes in the cold plenum. Then, most of the cold helium gas flows downward through the pebble bed in the reactor core to the hot plenum and becomes effective coolant flow. Meanwhile, due to the pressure gradient over the pebble bed (approximately 90 kPa), a small part of coolant will flow in the interconnected gaps and become bypass flow. All the coolant will converge into the hot plenum before heat exchange in the steam generator.

Ensuring effective and sufficient cooling flow of the reactor core is one of the key issues of thermal hydraulic analysis of HTR-PM. However, bypass flows will reduce the amount of effective coolant flow of pebble bed, which will influence fuel

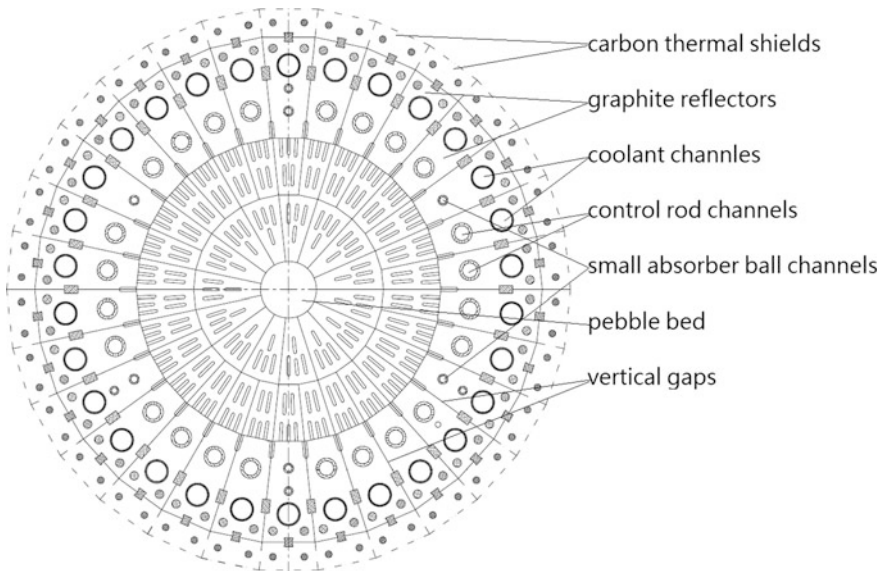


Fig. 1 Cross section of the HTR-PM structure

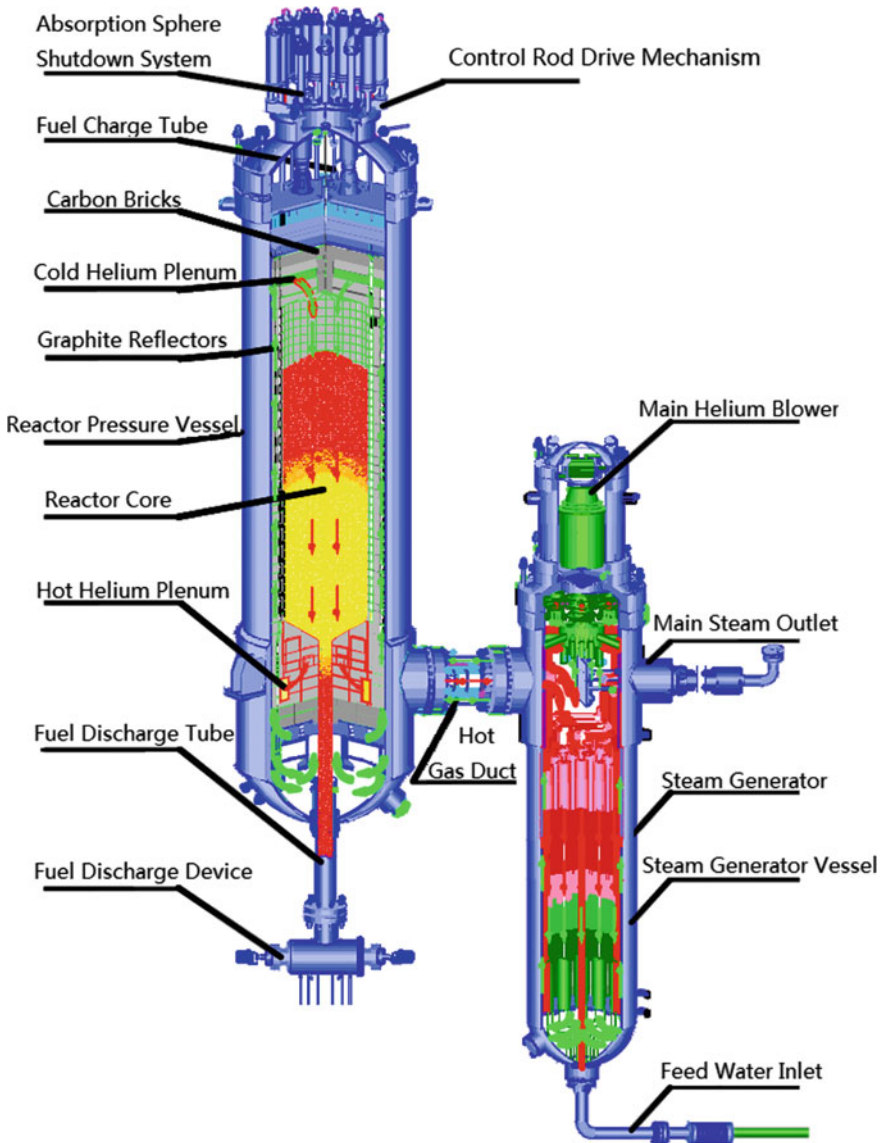


Fig. 2 Longitudinal section of the HTR-PM structure [3]

element temperature to a certain extent. In turn, a higher fuel temperature will lead to sooner fission product diffusion out of fuel pebbles and decrease the safety margin of HTR-PM. Therefore, the analysis and evaluation of the bypass flow effect are a key part of safety analysis and have important significance to HTR-PM.

Typical gaps have rectangular cross sections with small height/width ratios, and the heights are around 1.0 mm in the range of mini-scale. According to preliminary safety analysis of HTR-PM, the bypass flow ratio was about 6% [2], and the Reynolds numbers of bypass flows in gaps ranged from E4 to E5. Due to non-circular cross sections, small height/width ratios, and mini-scale sizes, it is difficult to determine the flow pattern of helium flow in those gaps. Meanwhile, in the mini-scale gaps, the condition of wall surfaces also affects the flows in gaps a lot. In order to analyze the distribution and the influence of bypass flow of HTR-PM, it is indeed necessary to study the resistance performance of helium flows in mini-scale gaps.

In this paper, Computational Fluid Dynamic (CFD) method was utilized to simulate helium flow in mini-scale gaps. A detailed comparison was made between the two-dimensional CFD simulations and the experimental data conducted in South Africa [4]. In order to investigate the reasonable turbulence CFD models for predicting the resistance performances of mini-scale gaps, different models and near-wall treatments were used in ANSYS Fluent. Finally, the appropriate turbulence model and near-wall treatment was recommended for CFD simulations of helium flow in mini-scale gaps.

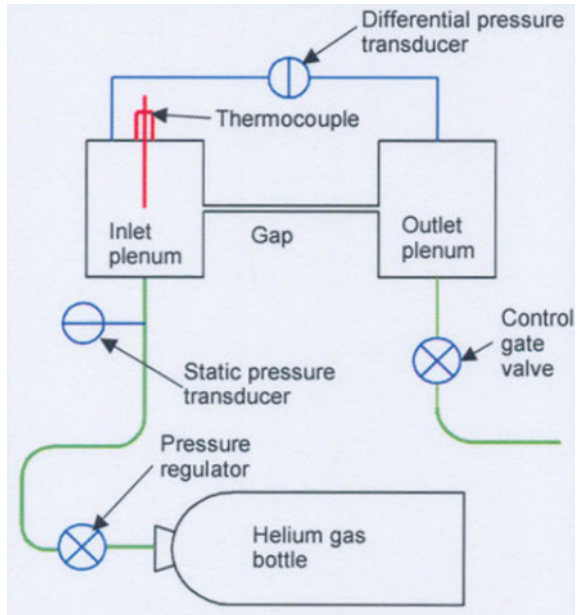
2 Reference Experimental Facility and Data

2.1 *Experimental Facility*

The experimental facility was constructed at North-West University, South Africa, to determine helium flow pattern in mini-scale gaps. Figure 3 presents the schematic diagram of the experimental test rig. The helium source was a 20 MPa pressurized gas cylinder connected to a pressure regulator in order to maintain the constant predefined pressure in approximately 3 MPa. In this experiment, the sizes of the gaps were 0.175/0.280/0.380 mm in height, 60 mm in width, and 80 mm in length.

The static pressure was measured by a pressure transducer at the end of the inlet line and at the entry to the test piece inlet plenum. From the inlet plenum, the helium flowed through the thin gap, into the outlet plenum and out to the atmosphere via the outlet line. The control gate valve on the outlet line was used to manually set the predefined static pressure drop through the gap by altering the mass flow rate. A differential pressure transducer was utilized to measure the difference in static pressure across the gap between the inlet and outlet plenums. Temperature readings were measured with a thermocouple. The tip of the sensor was positioned approximately in the center of the inlet plenum. Output from the transducers was conditioned as needed and then passed to a digital oscilloscope. To get the accurate mass flow rate in the experiment, the entire test rig together with the helium gas bottle was placed on a counterbalanced scale so that the change in mass due to venting of the gas through the test piece was measured directly with a load cell.

Fig. 3 Experiment rig of North-West University



2.2 Experimental Results

Although three different sizes of gaps were studied in the experiment, only the 0.380 mm one is close to the typical size of gaps in HTR-PM, which is about 1.0 mm, much wider than the other two sizes. Meanwhile, according to the experimental results shown in Table 1, the Reynolds number of the 0.380 mm height size gap with 73,500 Pa pressure drop case was close to the bypass flow in HTR-PM, which is about $2E4$. And the height size in this case is also closer to the typical gap size in HTR-PM, so that only the 0.380 mm height size gap with 73,500 Pa pressure drop case was simulated in this paper. Other experimental cases will be studied in the future.

3 CFD Methodology

3.1 Gap Geometry and Numerical Mesh

Due to the small height/width ratio of the gap, the CFD model of the test facility could be simplified as two-dimensional as shown in Fig. 4 with structure parameters.

According to the simplified two-dimension geometry, the mesh was prepared by Gambit 2.4.6 as shown in Fig. 5. The CFD model contained five calculation zones: inlet pipe, inlet plenum, gap, outlet plenum, and outlet pipe, in which, the details of

Table 1 Experimental results of South Africa

Gap height (mm)	Mass flow rate (g/s)	Pressure drop (Pa)	Reynolds number
0.175	1.014	5000	1745
0.175	4.974	76,333	8584
0.175	6.852	150,000	11,758
0.175	8.620	250,000	14,715
0.280	2.183	5250	3707
0.280	8.127	75,166	13,827
0.280	11.621	150,000	19,794
0.280	13.942	250,000	23,886
0.380	2.718	5100	4629
0.380	9.556	73,500	16,316

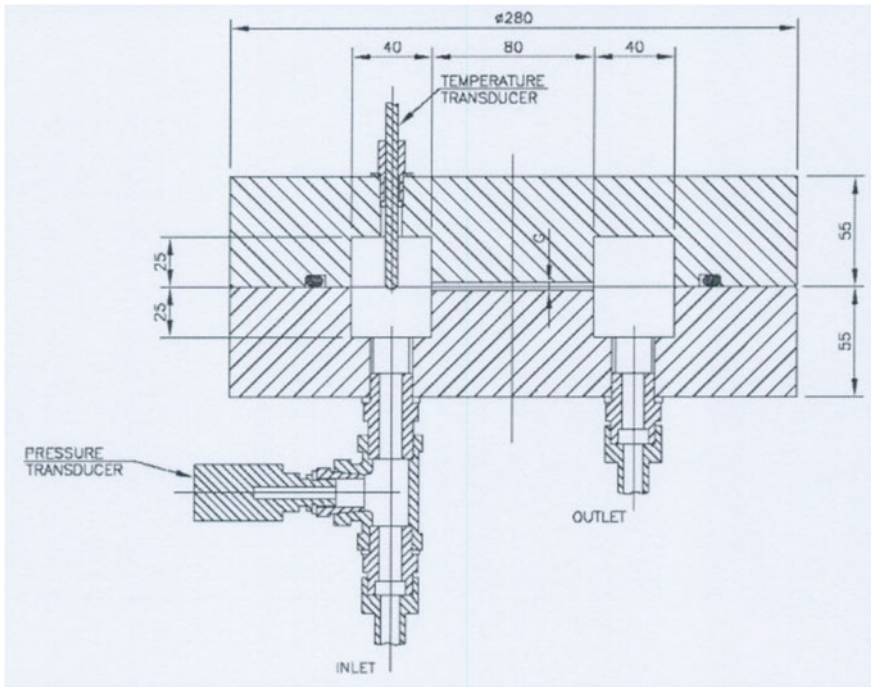


Fig. 4 Cross section of test piece geometry

gap inlet zone are shown in Fig. 6. After the geometrical preparation and mesh generation, mesh independence analysis was conducted with various refined mesh structures and cell densities. The meshes for the inlet, the middle part, and also the outlet of gap were analyzed, respectively.

Fig. 5 2D mesh of helium flow path

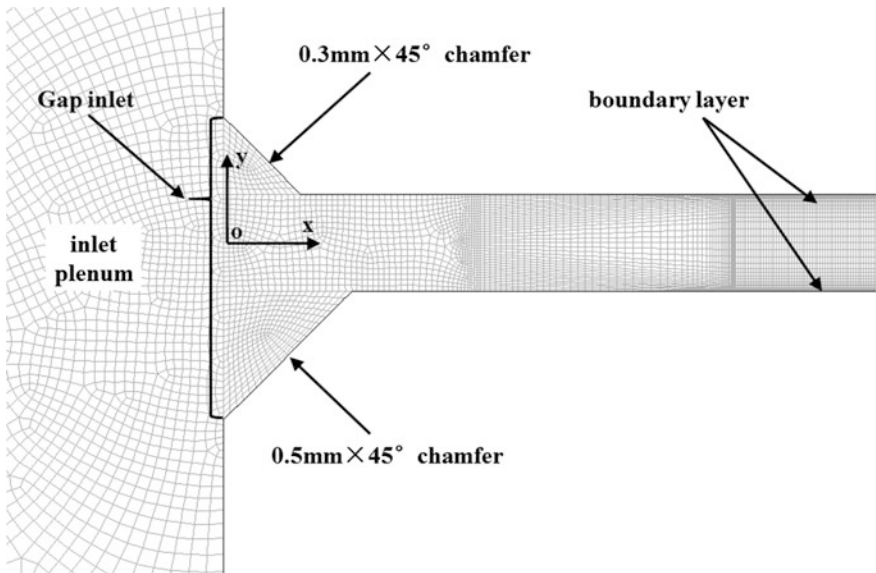
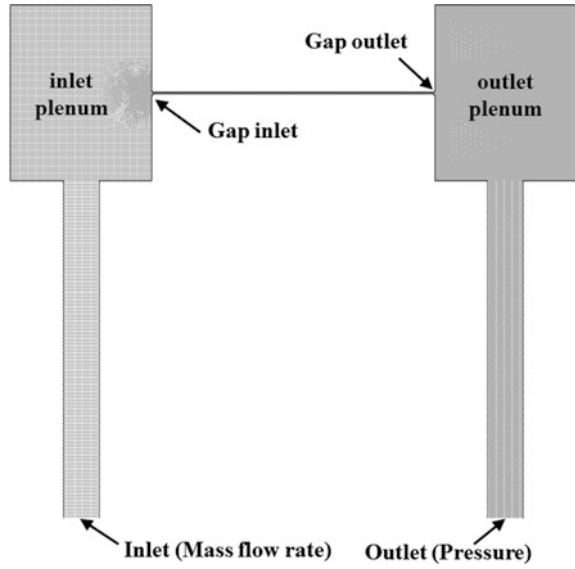


Fig. 6 Mesh structure of gap inlet

3.2 Boundary Conditions and Differencing Schemes

The boundary conditions in the CFD simulations boundaries were given as follows:

1. There is no significant heat transfer in the experiment, and the wall boundary was therefore defined as adiabatic.
2. Since experiments were conducted at room temperature, the helium inlet temperature was 20 °C.
3. The operating pressure in CFD simulations was 3 MPa, same as the experiments.
4. Helium inlet was set as mass flow rate inlet boundary, and the outlet was pressure outlet boundary.
5. The helium thermal properties of helium obeyed the ideal gas law.

As for the differencing schemes, the second-order upwind differencing and SIMPLC scheme were utilized.

3.3 Turbulence Models

Among the several turbulence models, two-equation turbulence models are employed since the models are expected to calculate with reasonable computational time and accuracy. In order to determine which turbulence model is more appropriate to simulate helium flows in mini-scale gap, three different turbulence model were used in this paper: standard k- ε model, RNG k- ε model, and Shear-Stress Transport (SST) k- ω model.

The standard k- ε model proposed by Launder and Spalding [5, 10] is based on the following transport equations:

$$\frac{\partial}{\partial t}(\rho k) + \frac{\partial}{\partial x_i}(\rho k u_i) = \frac{\partial}{\partial x_j} \left[\left(\mu + \frac{\mu_t}{\sigma_k} \right) \frac{\partial k}{\partial x_j} \right] + G_k + G_b - \rho \varepsilon \quad (1)$$

$$\frac{\partial}{\partial t}(\rho \varepsilon) + \frac{\partial}{\partial x_i}(\rho \varepsilon u_i) = \frac{\partial}{\partial x_j} \left[\left(\mu + \frac{\mu_t}{\sigma_\varepsilon} \right) \frac{\partial \varepsilon}{\partial x_j} \right] + C_{1\varepsilon} \frac{\varepsilon}{k} G_k - C_{2\varepsilon} \rho \frac{\varepsilon^2}{k} \quad (2)$$

Here, ρ is density, k is turbulence kinetic energy, ε is dissipation rate, u is velocity magnitude, μ is viscosity, σ_k and σ_ε are turbulent Prandtl numbers for turbulence kinetic energy and dissipation rate, G_k and G_b represent the generation of turbulence kinetic energy due to the mean velocity gradients and buoyancy. The model constants $C_{1\varepsilon}$ and $C_{2\varepsilon}$ have the values of 1.44 and 1.92, respectively.

The RNG k- ε model [6] is derived from the instantaneous Navier–Stokes equations, using a mathematical technique called “renormalization group” (RNG) methods [7]. The analytical derivation results in a model with constants different from those in the standard k- ε model, and additional terms and functions in

the transport equations for k and ε . The RNG k - ε model has a similar form transport equations to the standard k - ε model:

$$\frac{\partial}{\partial t}(\rho k) + \frac{\partial}{\partial x_i}(\rho k u_i) = \frac{\partial}{\partial x_j} \left(\alpha_k \mu_{\text{eff}} \frac{\partial k}{\partial x_j} \right) + G_k + G_b - \rho \varepsilon \quad (3)$$

$$\frac{\partial}{\partial t}(\rho \varepsilon) + \frac{\partial}{\partial x_i}(\rho \varepsilon u_i) = \frac{\partial}{\partial x_j} \left(\alpha_\varepsilon \mu_{\text{eff}} \frac{\partial \varepsilon}{\partial x_j} \right) + C_{1\varepsilon} \frac{\varepsilon}{k} G_k - C_{2\varepsilon} \rho \frac{\varepsilon^2}{k} \quad (4)$$

The SST k - ω model [8] used in ANSYS Fluent is based on Wilcox k - ω model [9]. It includes all the refinements of the BSL k - ω model [8] and in addition accounts for the transport of the turbulence shear stress in the definition of the turbulent viscosity. These features make the SST k - ω model more accurate and reliable for a wider class of flows than the standard and BSL k - ω model. The transport equations of SST k - ω model are as follows:

$$\frac{\partial}{\partial t}(\rho k) + \frac{\partial}{\partial x_i}(\rho k u_i) \frac{\partial}{\partial x_j} \left(\Gamma_k \frac{\partial k}{\partial x_j} \right) + G_k - Y_k \quad (5)$$

$$\frac{\partial}{\partial t}(\rho \omega) + \frac{\partial}{\partial x_i}(\rho \omega u_i) = \frac{\partial}{\partial x_j} \left(\Gamma_\omega \frac{\partial \omega}{\partial x_j} \right) + G_\omega - Y_\omega \quad (6)$$

Here, ω is specific dissipation rate, Γ_k and Γ_ω is effective diffusivity of turbulence kinetic energy and specific dissipation rate, G_ω represents the generation of specific dissipation rate, and Y_k and Y_ω represent the dissipation of turbulence kinetic energy and specific dissipation rate.

Turbulent flows are significantly affected by the presence of walls. Considering the mini-size, the near-wall modeling significantly impacts the fidelity of numerical solutions of helium flows in mini-scale gaps. The standard wall functions are based on the work of Launder and Spalding [10] and have been most widely used in industrial flows. As for the enhanced wall treatment for ε -equation, it is a near-wall modeling method that combines two layers with enhanced wall functions. If the near-wall mesh is fine enough to be able to resolve the viscous sub-layer (typically with the first near-wall node placed at $y^+ \approx 1$), then the enhanced wall treatment will be identical to the traditional two-layer zonal model. In this paper, both the standard wall functions and enhanced wall treatment were utilized to identify which one is more appropriate.

4 Results and Discussions

4.1 Mesh Sensitivity Analysis

Before the CFD results analyses, mesh independence analysis should be finished. According to the enhanced wall treatment requirement, the first near-wall node

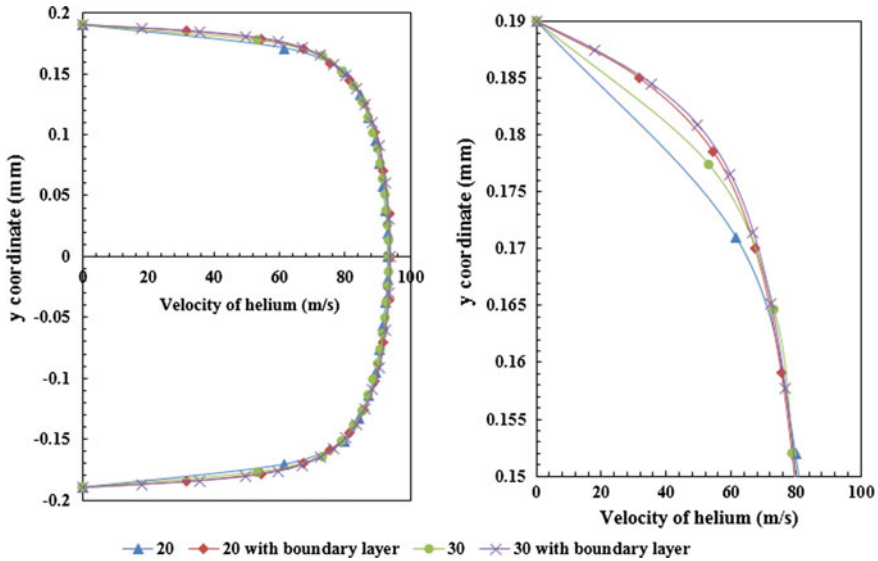


Fig. 7 Velocity profiles in the gap with various mesh schemes ($x = 40$ mm)

should be placed at $y^+ \approx 1$, which meant boundary layer should be used when generating mesh. To analyze the influence of boundary layer, four different mesh structures were prepared and simulated, in which, the number of nodes along the gap height was 20 or 30, with or without boundary layer, respectively.

As velocity profiles shown in the left of Fig. 7, the velocities at the gap center were almost the same, no matter how many nodes of gap in height and with or without boundary layer. The major differences were the velocities near walls in the right of Fig. 7, which revealed the necessity of adopting boundary layer in this case.

To further get the mesh independent results, the influences of node numbers for the inlet, outlet, and middle sections of the gap were analyzed, respectively. Figure 8 shows the total static pressure losses with different mesh number of the gap inlet and outlet, while the middle section of gap had 40 meshes in height. When the mesh number was above 20, the pressure loss along the gap was not sensitive with the inlet and outlet mesh numbers; thus, 20 nodes at gap inlet and outlet satisfied the mesh independence requirements. The influence of mesh number in the gap middle section was also simulated with 20/30/36/40 meshes, respectively, while the mesh number of gap inlet and outlet 20. From the static pressure losses in Fig. 9, mesh number above 36 in height for the gap middle section meets the mesh-independence requirement. Therefore, the following CFD simulations were based on the mesh, in which, the mesh numbers in gap height were 20 for the inlet and outlet, and 36 for the middle section.

Fig. 8 Mesh independence analysis of gap inlet and outlet (mesh number of gap middle section is 40)

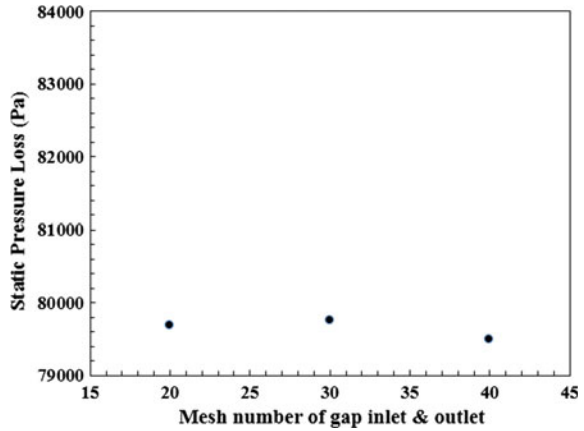
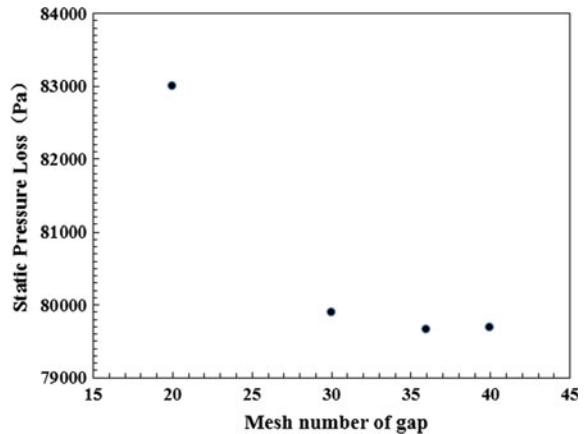


Fig. 9 Mesh sensitivity analysis of gap center (mesh number of gap inlet and outlet: 20)



4.2 Results Analysis

4.2.1 Flow Loss in Gap Inlet and Outlet

Figure 10 shows the gauge pressure distribution in gap center ($y = 0$ mm). Since there is an abrupt compression at the gap inlet, the gauge pressure has a big decline at the gap inlet. After that the helium flow in gap became a fully developed fluid, which characterized with a linear gauge pressure drop with flow distance. As for the abrupt expansion at the gap outlet, it may not affect the upstream helium flows in the gap, but it will influence the flow status at the outlet plenum. The velocity vector at gap outlet and outlet plenum is shown in Figs. 11 and 12. Due to the high speed of helium at the gap center, the helium flow from gap to outlet plenum was somehow just like an injection flow. The high-speed helium from gap led to the two

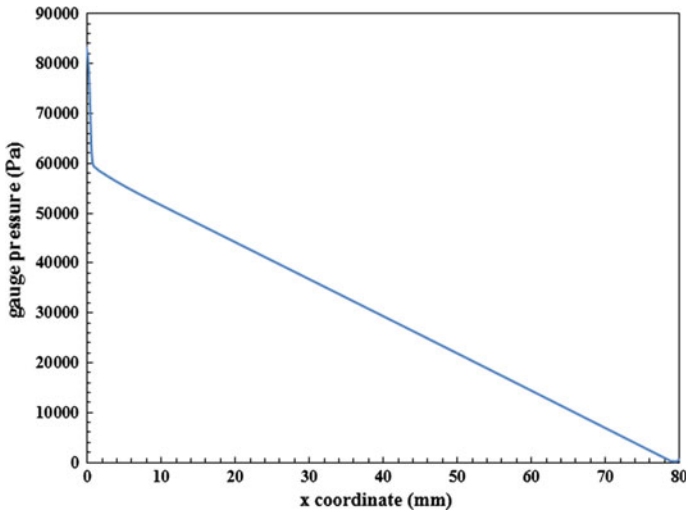


Fig. 10 Gauge pressure distribution along the gap *center line* ($y = 0$ mm, operating pressure = 3 MPa)

big eddies at the outlet plenum, and there were some small eddies at the corner and the chambers of gap outlet.

Due to the abrupt compression and expansion of geometry at the gap inlet and outlet, the flow condition there will be complex and may influence the flow status in gap. The gauge pressure and velocity distributions at the gap inlet and outlet are shown in Figs. 13 and 14. The abrupt compression of the gap inlet causes a big pressure loss which is shown in Fig. 13a. Since there was an asymmetric chamfer at the gap inlet, the velocity distribution was also asymmetric at the inlet zone. However, the helium flow in gap was then gradually developed and fully developed at the place whose x coordinate is 10 mm. As for the abrupt expansion at gap outlet, this asymmetric chamfer geometry also makes the gauge pressure change. But it did not influence the helium flow in gap so much as the gap inlet geometry. According to the velocity distributions shown in Fig. 14b, the velocity is almost the same at the places whose x coordinate is 70/75/78 mm. According to the analysis above, the influence distance of gap inlet is approximately 10 mm while the outlet is 2 mm.

4.3 Turbulence Models and Wall Functions

In order to find out the most appropriate CFD turbulence models to simulate the helium flows in mini-scale gaps, different turbulence models and near-wall treatments were utilized. The results are shown in Table 2 and Fig. 15. From the static pressure losses of gap center with different turbulence models and near-wall

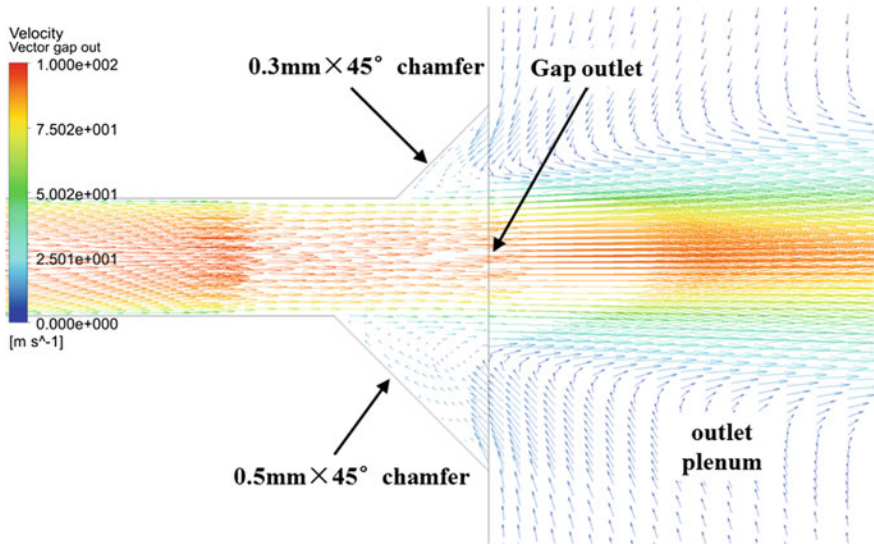


Fig. 11 Helium vector in gap inlet and outlet plenum

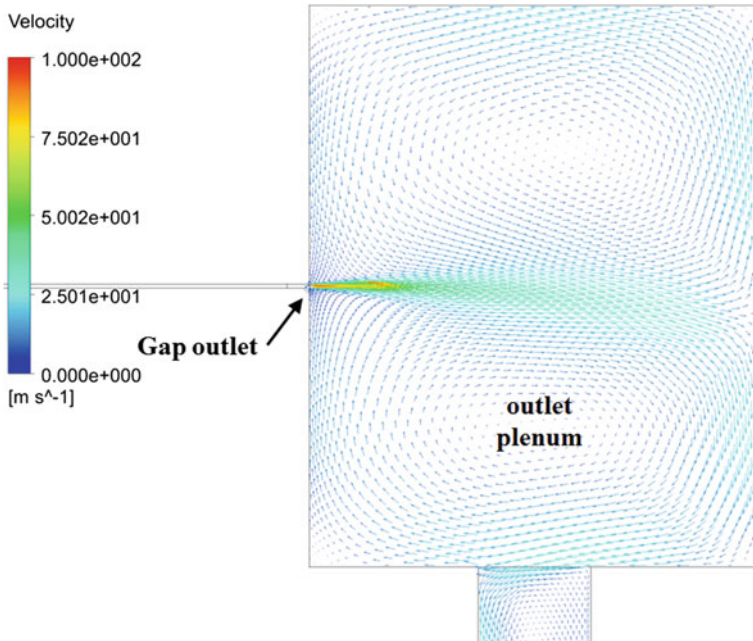


Fig. 12 Helium vector in outlet plenum

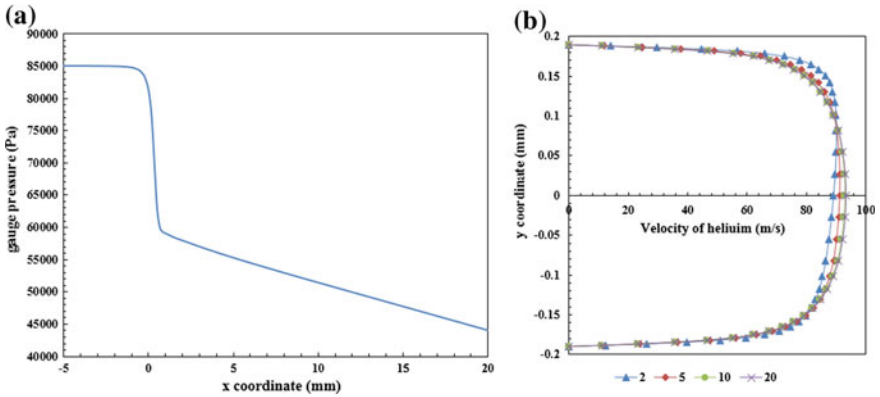


Fig. 13 Gauge pressure (a) and velocity (b) distributions of gap inlet

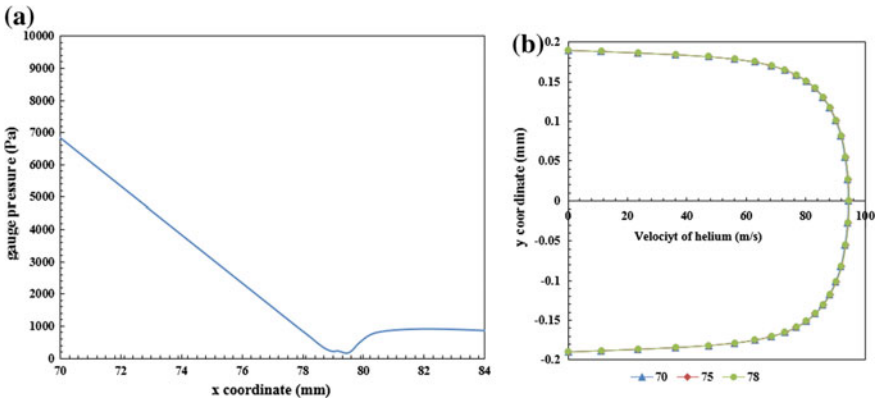


Fig. 14 Gauge pressure (a) and velocity (b) distributions of gap outlet

treatments, it was obvious that the near-wall treatments affected the results of the gap center the most. That is because the effect of the wall surface will affect the flow conditions more in a mini-scale gap than other regular situations. As for the calculative pressure loss at gap inlet and outlet, the results show turbulence models determine the results rather than the near-wall treatments. Comparing the calculative results of RNG $k-\epsilon$ turbulence model with enhanced wall treatment and SST $k-\omega$ model (shown in Table 2 and Fig. 15), the results were very close. However, the relative tolerance of RNG $k-\epsilon$ turbulence model with enhanced wall treatment is closer to the experimental result, which means that the previous one is more appropriate to simulate the helium flow in mini-scale gap.

Table 2 Pressure losses (Pa) of Helium flow with different turbulence models (total pressure loss from experiment: 73,500 Pa)

Turbulence models near-wall treatment	Pressure loss at gap inlet (Pa)	Pressure loss at gap middle (Pa)	Pressure loss at gap outlet (Pa)	Total static pressure loss (Pa)	Relative tolerance (%)
RNG k-ε enhanced wall function	28041.0	50568.9	1050.1	79660.0	8.38
RNG k-ε standard wall function	33140.4	93656.6	1030.4	127827.4	73.91
Standard k-ε enhanced wall function	33616.2	50646.3	709.0	84971.5	15.61
Standard k-ε standard wall function	41851.2	97122.6	762.6	139736.5	90.12
SST k-ω	27662.1	50792.6	2063.9	80518.6	9.55

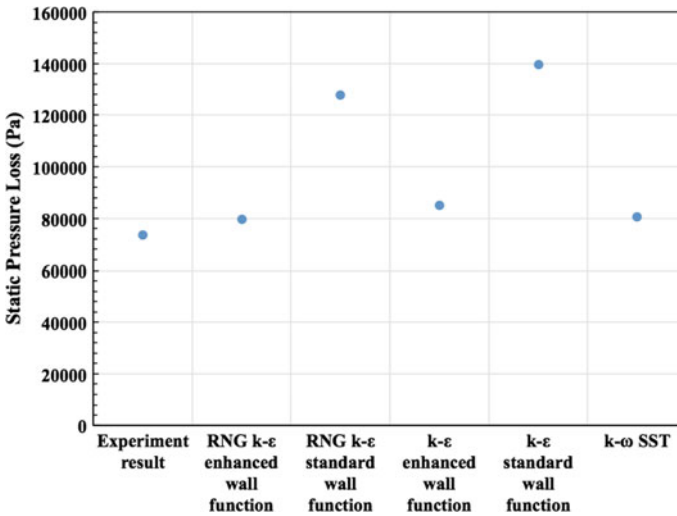


Fig. 15 Comparison of experimental and calculative total static pressure loss

5 Conclusions

By commercial CFD software ANSYS Fluent, two-dimensional helium flows in gap with 0.380 mm height size were simulated. Based on the mesh independence analysis result, the mesh generation method of mini-scale gap was set. According to

the comparison results of experimental and calculative results, the main conclusions are as follows:

1. Mesh is extremely important to the simulation of helium flow in mini-scale gaps. One of the most essential issues for optimal performance of turbulence models is the proper resolution of the boundary layer;
2. According to the CFD simulation and experiment results of gap with 0.38 mm height and 73.5 kPa pressure drop, the two-layer RNG k- ϵ turbulence model with enhanced wall treatment is more appropriate to simulate helium flows with Reynolds number about $2E4$ in mini-scale gap;

Since the CFD models were validated by the pressurized helium flow experiments, they can be further used to study more complex bypass flows in the HTR-PM.

Acknowledgments This work has been supported by the National S&T Major Project (Grant No. ZX069) and the National Natural Science Foundation of China (Grant No. 51406102).

References

1. Zhang, Z, et al. Current status and technical description of Chinese 2×250 MWth HTR-PM demonstration plant. *Nuclear Engineering and Design*, 2009. 239(7): p. 1212–1219.
2. Sun, J, Zheng, Y and Li, F, Researches of Bypass Flows from Cold Plenum to Hot Plenum in HTR-PM by the Flow Network Method, in 20th International Conference on Nuclear Engineering, 2012: Anaheim, California, USA.
3. Zheng, Y, Shi, L and Dong, Y.J, Thermohydraulic transient studies of the Chinese 200MWe HTR-PM for loss of forced cooling accidents. *Annals of Nuclear Energy*, 2009. 36(6): p. 742–751.
4. Van WYK, M, Verification of leakage through the side reflector graphite of the PBMR reactor. 2004, North-West University: Potchefstroom. p. 82.
5. D B Spalding, B.E.L, Lectures in Mathematical Models of Turbulence. 1972, London, England: Academic Press.
6. Yakhot, V. and S.A. Orszag, Renormalization Group Analysis of Turbulence I Basic Theory. *Journal of Scientific Computing*, 1986. 1(1): p. 1–51.
7. Orszag, S.A. et al. Renormalization Group Modeling and Turbulence Simulations, in International Conference on Near-Wall Turbulent Flows. 1993: Tempe Arizona.
8. Menter, F.R. Two-Equation Eddy-Viscosity Turbulence Models for Engineering Applications. *AIAA Journal*, 1994. 8(32): p. 1598–1605.
9. Wilcox, D.C. Turbulence Modeling for CFD. 1998, DCW Industries, Inc: La Canada California.
10. Launder, B.E. and D.B. Spalding, The Numerical Computation of Turbulent Flows. *Computer Methods in Applied Mechanics and Engineering*, 1974: p. 269–289.

Author Biographies

Peng Haoran Institute of Nuclear and New Energy Technology, Collaborative Innovation Center of Advanced Nuclear Energy Technology, Key Laboratory of Advanced Reactor Engineering and Safety of Ministry of Education, Tsinghua University. Beijing 100084, China.

Sun Jun Institute of Nuclear and New Energy Technology, Collaborative Innovation Center of Advanced Nuclear Energy Technology, Key Laboratory of Advanced Reactor Engineering and Safety of Ministry of Education, Tsinghua University, Beijing 100084, China.

Numerical Simulation on Water Hammer Phenomenon for Single Feedwater Line

Meiling Sheng, Ting Hou and Jiaming Zhao

Abstract Since the feedwater line is susceptible to water hammer phenomenon, the effect of water hammer on single feedwater line was numerically analysed using the PIPENET software package. The main devices of the single feedwater line include a feedwater pump, a feedwater isolation valve, a feedwater control valve, and a feedwater check valve. Calculation and analysis of the water hammer were carried out based on the feedwater isolation valve which was instantaneously closed with various diameters and lengths and also different Poisson ratio and elastic modulus of the feedwater line. The results showed that the water hammer pressure and load in the lines reached the maximum at the moment of the feedwater isolation valve closing. After a long period of time, the final pressure of the lines was maintained at the initial pressure value and the final water hammer load tended to zero. The larger diameter and the shorter length of the feedwater lines would obtain the less water hammer pressure and load. The smaller the length–diameter ratio was, the lesser the water hammer pressure and load will be. When the length–diameter ratio reached a certain value, the water hammer load showed a fluctuation trend. The larger Poisson ratio and elastic modulus would obtain the higher peak values of water hammer pressure and load, but different Poisson ratios and elastic modulus of common materials had little effect on water hammer pressure and load. These calculation results in this work can provide some technical support for the diameter and material selection and length arrangement of the feedwater lines and also offer certain design basis for the stress analysis of the feedwater system.

Keywords Water hammer · Single feedwater line · PIPENET · Numerical simulation · Water hammer pressure · Water hammer load

M. Sheng (✉) · T. Hou · J. Zhao
Process and Layout Design Division, China Nuclear Power Engineering Co., Ltd,
Beijing, China
e-mail: meiling.jiaotong@163.com; shengml@cnpe.cc

© Springer Science+Business Media Singapore 2017
H. Jiang (ed.), *Proceedings of The 20th Pacific Basin Nuclear Conference*,
DOI 10.1007/978-981-10-2314-9_17

1 Introduction

Water hammer is a kind of pressure wave in pipe transient flow case, which is the result of the flow rate changes of one cross section. This change may be normal flow regulation or flow cutoff caused by some accident so that the pressure generates at a sudden jump or fall. This pressure wave transient is called water hammer phenomenon [1, 2].

The PIPENET software is advanced and reliable network flow calculation and analysis software, which is available for pipe network calculation and optimization, equipment selection, and water hammer analysis in accident condition. Particularly, PIPENET can calculate and generate the dynamic load versus time and then pass the load to pipe stress analysis software, when the dynamic load such as water hammer load and steam hammer load occurs in nuclear power plant or thermal power pipes [3, 4].

As the main pressure pipe, the feedwater line is susceptible to water hammer event. To better understand the impact of water hammer for the pipeline, the water hammer characteristic for single feedwater line was simulated and calculated in this paper using the PIPENET transient module.

2 Simulation and Calculation

The water hammer phenomenon is a very complex instantaneous process, and the water hammer pressure and load are selected to symbolize the energy of water hammer. There are a great many factors affecting the water hammer, such as the closure time of feedwater isolation valve, the diameters and lengths, and also Poisson ratio and elastic modulus of the feedwater line. In this work, the effect of water hammer on single feedwater line was analysed using the PIPENET software package, when the feedwater isolation valve was instantaneously closed with various diameters and lengths and also different Poisson ratio and elastic modulus of the feedwater line.

2.1 Model

The feedwater system in nuclear power plant is used to ensure cooling the steam generator and is a complex system. The main devices of the feedwater line include feedwater pump, feedwater isolation valve, feedwater control valve, feedwater check valve, and some related measuring instruments. The flowchart of single feedwater line is shown in Fig. 1.

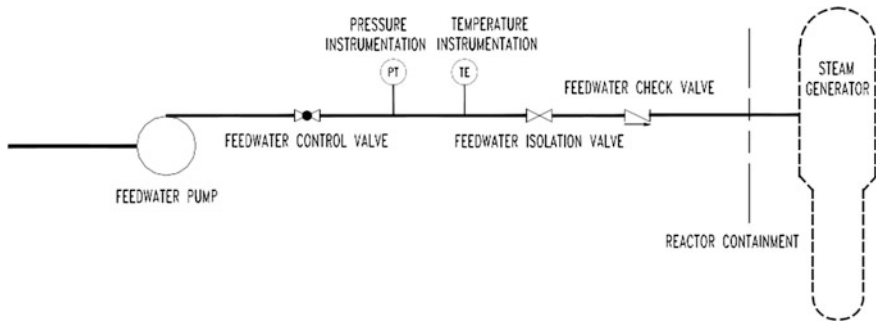


Fig. 1 Flowchart of single feedwater line



Fig. 2 Calculation model of single feedwater line: 1 feedwater pump; 2 feedwater control valve; 3 feedwater isolation valve; 4 feedwater check valve

In the calculation of this study, the feedwater line model was simplified as single line and shown in Fig. 2. On the single feedwater line, there are a feedwater pump, a feedwater control valve, a feedwater isolation valve, and a feedwater check valve. In the model, the inlet of feedwater pump is the input and the downstream of feedwater check valve (upstream of the steam generator) is the output. The input and output of both constant pressure are, respectively, 1.025 MPa.a and 5.9 MPa.a.

2.2 Closing of the Feedwater Isolation Valve

The feedwater isolation valve performs feedwater isolation, steam generator isolation and containment isolation function. To prevent water flow from either side of the break of the isolation valve in severe conditions, the feedwater isolation valve is asked to close in a certain time. This work analyzed the water hammer pressure and load changes in the feedwater line when the closure time of feedwater isolation valve is 4 s. The isolation valve closing curve is shown in Fig. 3, and the maximum water hammer pressure and load change curves are shown in Figs. 4 and 5.

The results showed that the water hammer pressure and load in the lines reached the maximum at the moment of the feedwater isolation valve closing. After a long period of time, the final pressure of the lines is maintained at the initial pressure value and the final water hammer load tends to zero.

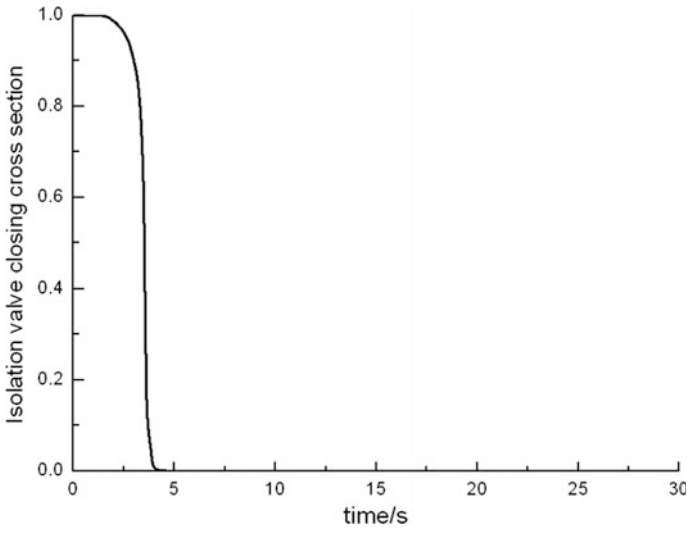


Fig. 3 The isolation valve closing curve

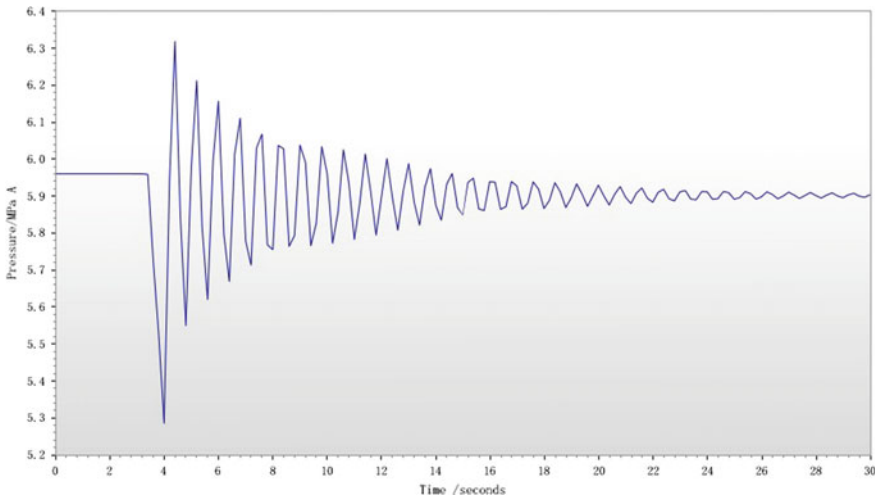


Fig. 4 Maximum water hammer pressure versus time

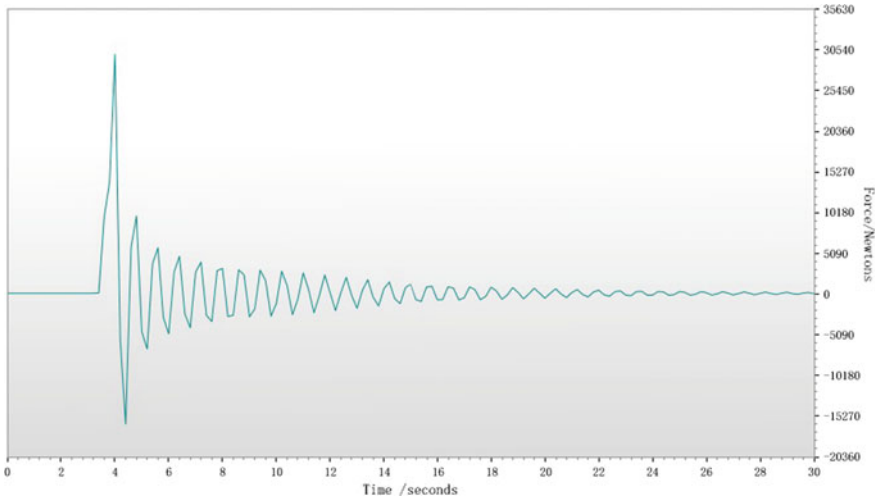


Fig. 5 Maximum water hammer load versus time

2.3 Relationship Between Water Hammer and Diameters of Feedwater Line

Since various diameters of feedwater lines have an impact on water hammer, this section analyzes the impact on water hammer by different pipe diameters. When the diameter varies from 300 to 650 mm, the relationship curve between water hammer and diameters was obtained and shown in Fig. 6.

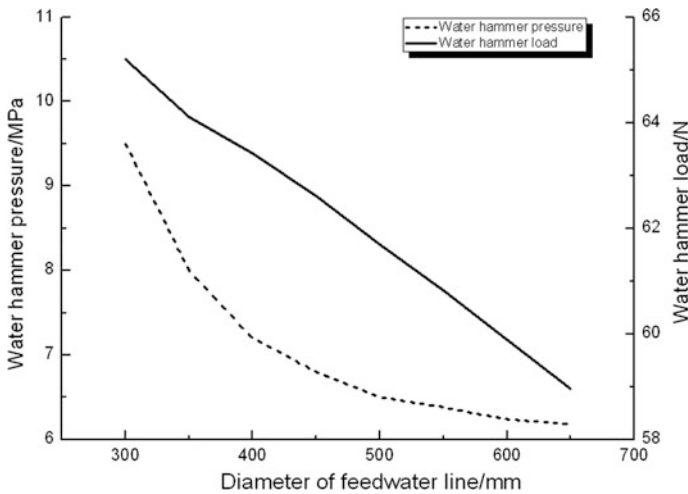


Fig. 6 Relationship between water hammer and diameters of feedwater line

According to the Fig. 6, it was clear that the larger the diameter was, the smaller the water hammer energy will be. When the diameter was 300 mm, the water hammer load reached 65 kN and the water hammer pressure reached 9.5 MPa.a so that the water hammer impact on the stress and design pressure of the feedwater line should be considered.

2.4 Relationship Between Water Hammer and Lengths of Feedwater Line

Since various lengths of feedwater lines also have an impact on water hammer, this section analyzes the impact on water hammer by different pipe lengths. When the length varies from 50 to 90 m, the relationship curve between water hammer and lengths was obtained and shown in Fig. 7.

According to the Fig. 7, it was clear that the shorter the length was, the smaller the water hammer energy will be. When the length was about 85 m, the water hammer load reached 103 kN and the water hammer pressure reached 8.6 MPa.a.

2.5 Relationship Between Water Hammer and Length–Diameter Ratio of Feedwater Line

After independently analyzing the impact of diameters and lengths of feedwater lines on water hammer, the synthesis influence was taken into account namely

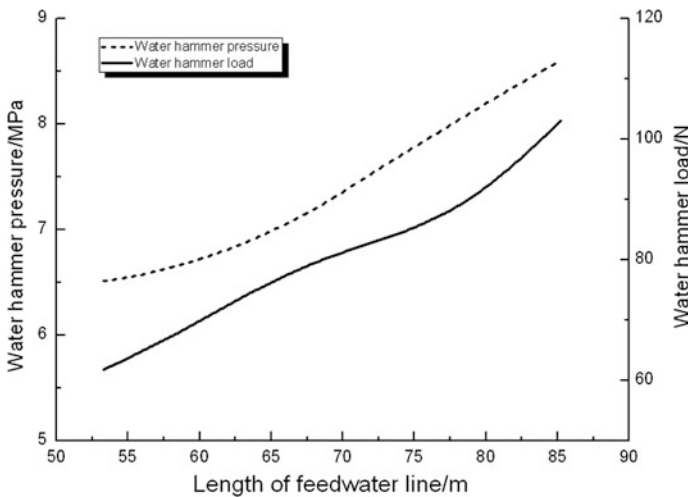


Fig. 7 Relationship between water hammer and lengths of feedwater line

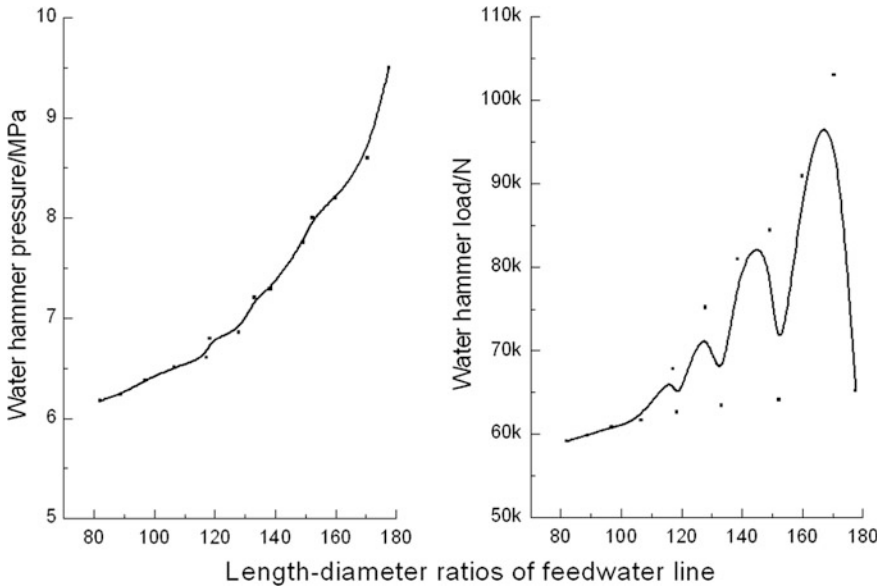


Fig. 8 Relationship between water hammer and length–diameter ratios of feedwater line

various length–diameter ratios. The relationship curve between water hammer and length–diameter ratios was obtained and shown in Fig. 8.

According to the left cure between water hammer pressure and length–diameter ratios of Fig. 8, it was clear that the smaller the length–diameter ratio was, the less the water hammer pressure will be. According to the right cure between water hammer load and length–diameter ratios of Fig. 8, it was clear that the smaller the length–diameter ratio was, the less the water hammer load will be, and when the length–diameter ratio reached a certain value, the water hammer load showed a fluctuation trend. Therefore, when the diameter selection and length arrangement of the feedwater lines is carried out, the water hammer should be calculated particularly.

2.6 Relationship Between Water Hammer and Poisson Ratio of Feedwater Line

The Poisson ratio is an inherent elasticity parameter of material, and the Poisson ratios of some common materials vary from 0.23 to 0.42. The water hammer pressure and load were calculated with the Poisson ratio, respectively, being 0.23, 0.33, and 0.42. The maximum water hammer pressure and load curves with different Poisson ratios of feedwater line were, respectively, shown in Figs. 9 and 10.

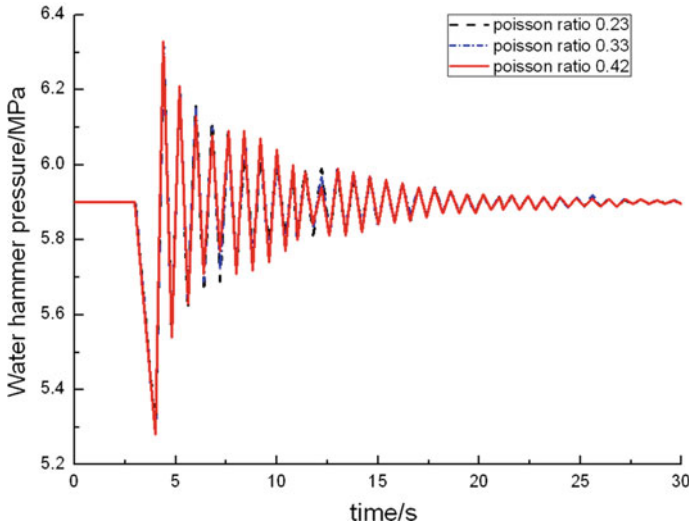


Fig. 9 Maximum water hammer pressure curves with different Poisson ratios of feedwater line

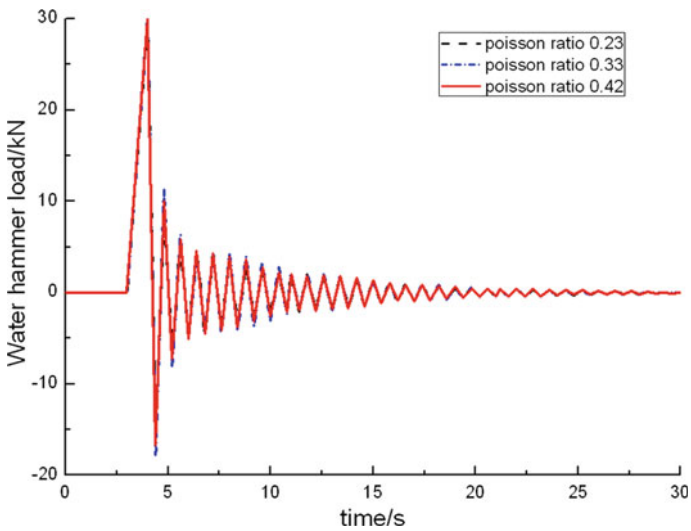


Fig. 10 Maximum water hammer load curves with different Poisson ratios of feedwater line

According to Figs. 9 and 10, the change trend of the maximum water hammer pressure and load was almost same. However, the larger the Poisson ratio was, the higher the peak values of water hammer pressure and load will be.

Since the Poisson ratio was elected from some common materials, the change range of Poisson ratio was small and the difference of water hammer pressure and load was little.

2.7 Relationship Between Water Hammer and Elastic Modulus of Feedwater Line

The elastic modulus is also an inherent elasticity parameter of material, and the elastic modulus of some common materials may vary from 70 to 216 GPa. The water hammer pressure and load were calculated with the elastic modulus, respectively, being 70, 143, and 216 GPa. The maximum water hammer pressure and load curves with different elastic modulus of feedwater line are, respectively, shown in Figs. 11 and 12.

According to Figs. 11 and 12, the change trend of the maximum water hammer pressure and load was almost same. However, the larger the elastic modulus was, the higher the peak values of water hammer pressure and load will be. Besides, the larger the elastic modulus was, the greater the attenuation speed of water hammer pressure and load will be.

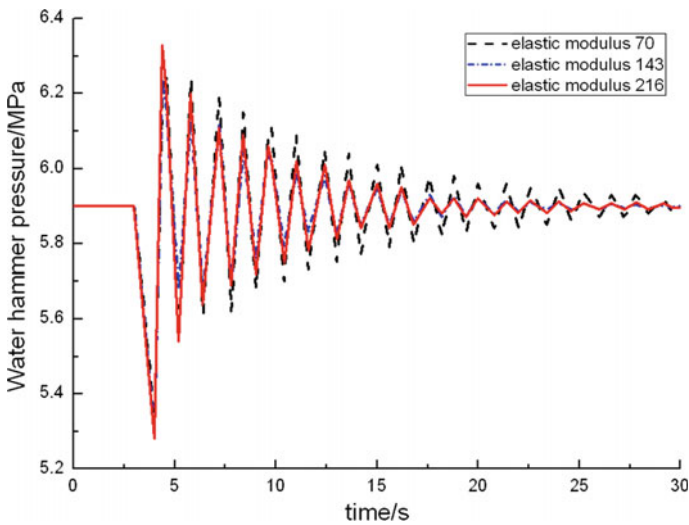


Fig. 11 Maximum water hammer pressure curves with different elastic modulus of feedwater line

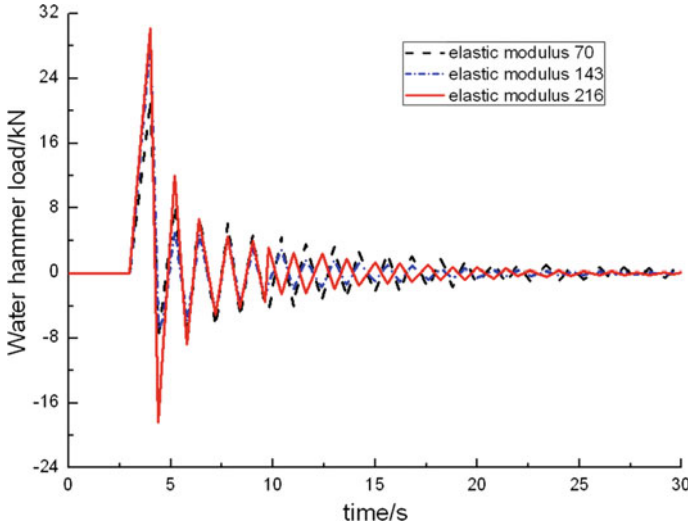


Fig. 12 Maximum water hammer load curves with different elastic modulus of feedwater line

Since the elastic modulus was elected from some common materials, the change range of elastic modulus was small and the difference of water hammer pressure and load was little.

3 Conclusions

The effect of water hammer on single feedwater line was numerically analysed using the PIPENET software package. The water hammer pressure and load in the lines reached the maximum at the moment of the feedwater isolation valve closing. After a long period of time, the final pressure was maintained at the initial pressure value and the final water hammer load tended to zero. The larger diameter and the shorter length of the feedwater lines would obtain the less water hammer pressure and load. The smaller the length–diameter ratio was, the less the water hammer pressure and load will be. When the length–diameter ratio reached a certain value, the water hammer load showed a fluctuation trend. The larger Poisson ratio and elastic modulus would obtain the higher peak values of water hammer pressure and load, but different Poisson ratios and elastic modulus of common materials had little effect on water hammer pressure and load.

Through the brief calculation in this work, the water hammer effect should be considered when carrying out the diameter selection and length arrangement of the feedwater lines and also the stress analysis of the feedwater system.

References

1. Wenxi Tian, G.H. Su, Gaopeng Wang, Suizheng Qiu, Zejun Xiao. Numerical simulation and optimization on valve-induced water hammer characteristics for parallel pump feedwater system [J]. *Annals of Nuclear Energy* 35(2008) 2280–2287.
2. HU Zhimin, WANG Wei, MENG Haibo. A dynamic analysis of second loop water hammers in the water supply of a nuclear power plant [J]. *Ship & Ocean Engineering*, 2007, 36(3): 90–93 (in Chinese).
3. ZHANG Kexiong, MAO Weizhi, CHEN Hao, et al. Application of pipenet hydraulic analysis in CFD platform [J]. *Technology & Development of Chemical Industry*, 2011, 40(5): 50–52 (in Chinese).
4. SHENG Meiling, TIAN Weiwei, QIU Jinneng, LI Jun, YU Pei. Simulation and calculation of Water Hammer to main feedwater line in passive advanced nuclear power plant [J]. *Atomic Energy Science and Technology*, 2015, 49 (Suppl.): 200–204 (in Chinese).

Author Biography

Meiling Sheng (1989–). Process and Layout Design Division, China Nuclear Power Engineering Co., Ltd. Beijing, China. Study on process design of nuclear reactor.

Power Transients of the HTR-10 During Reactivity Insertion ATWS Tests

Feng Gou, Fubing Chen and Yujie Dong

Abstract After the full power operation of the 10 MW High Temperature Gas-cooled Reactor-Test Module (HTR-10), two reactivity insertion tests were successfully conducted on this reactor by withdrawing a single control rod under 30% rated power. The reactor shutdown system was intentionally bypassed during such kind of tests, thus reflecting the anticipated transient without scram (ATWS) scenario. In the two tests, 1 and 5‰ $\Delta k/k$ positive reactivity were, respectively, introduced into the core by the control rod movement. In this study, post-test analyses are performed for the HTR-10 reactivity insertion ATWS tests using the THERMIX code. Both the analysis and the test results indicate that in the case of inadvertent control rod withdrawal the HTR-10 can be automatically shut down merely due to the negative reactivity feedback. The investigation of the reactor recriticality and the power oscillations in long term leads to a better understanding of the HTR-10 transients. For each test, the code reproduces the reactor power reasonably and accurately. Good agreement between the calculations and the tests proves the THERMIX simulation capability for the HTR-10 reactivity insertion ATWS tests.

Keywords HTR-10 · Reactivity insertion · ATWS · THERMIX · Validation

1 Introduction

The 10 MW High Temperature Gas-cooled Reactor-Test Module (HTR-10) is a graphite-moderated and helium-cooled pebble-bed reactor located in the Institute of Nuclear and New Energy Technology (INET) of Tsinghua University. Figure 1 shows the primary system of the HTR-10 [1]. The reactor and the steam generator

F. Gou · F. Chen (✉) · Y. Dong

Collaborative Innovation Center of Advanced Nuclear Energy Technology, Key Laboratory of Advanced Reactor Engineering and Safety, Ministry of Education, Institute of Nuclear and New Energy Technology, Tsinghua University, Beijing 100084, China
e-mail: chenfubing@tsinghua.edu.cn

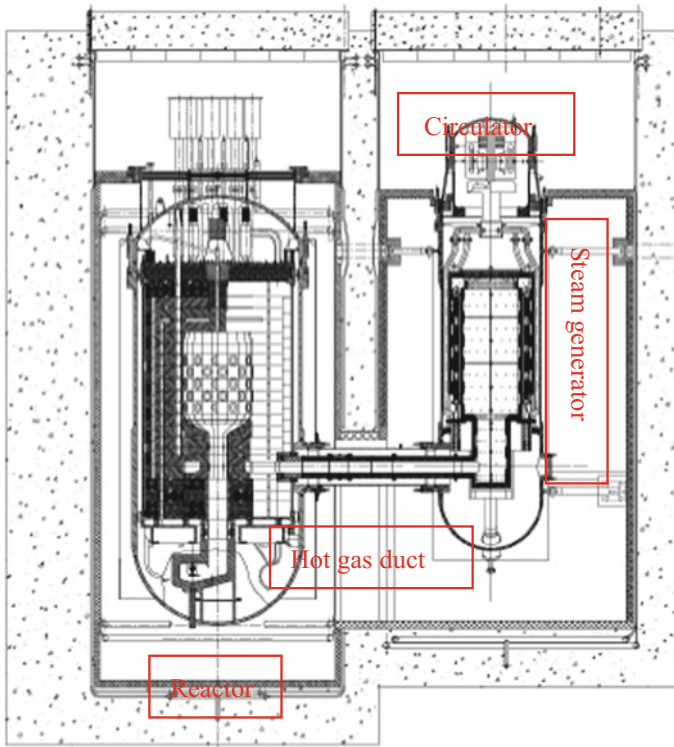


Fig. 1 Primary system of the HTR-10

are installed in two separate steel pressure vessels and connected to each other by a horizontal hot gas duct pressure vessel. Under normal operation, all these steel pressure vessels are in touch with the cold helium coming from the helium circulator.

After the HTR-10 full power operation in 2003, two reactivity insertion tests were successfully conducted by withdrawing a single control rod under 3 MW power level. With the purpose of representing the anticipated transient without scram (ATWS) scenario, the reactor shutdown system was intentionally bypassed during such kind of tests. In the first test 1‰ $\Delta k/k$ positive reactivity was generated, while in the second one 5‰ $\Delta k/k$ positive reactivity was introduced [2].

In INET, the THERMIX code is one of the main tools for thermal hydraulics calculation and accident analysis of pebble-bed high-temperature reactors (HTRs). In this study, the two reactivity insertion ATWS tests are reanalysed using this code. Both the simulation and the test results reveal the built-in passive safety features of the HTR-10, i.e. during reactivity insertion ATWS condition, the reactor power at first increases because of the control rod withdrawal, but soon decreases rapidly to the decay heat level merely due to the negative reactivity feedback. In long term, the reactor meets recriticality and experiences several power oscillations

before the final stabilization. Satisfactory agreement between the analysis results and the test data indicate the applicability and reasonability of the THERMIX code.

2 Test Conditions

Before the initiation of a reactivity insertion ATWS test, it was confirmed that the HTR-10 was under normal operation of 3 MW (30% rated power). From the test procedure illustrated in Fig. 2, it can be seen that the reactor shutdown system was bypassed to represent the ATWS conditions, and each test was initiated by withdrawing a single control rod. The rod position during the two tests is presented in Fig. 3. The initial conditions of the two tests were very close. The helium inlet temperature was about 207 °C, and the outlet temperature was about 650 °C.

The HTR-10 shutdown system contains 10 control rods, which are symmetrically arranged in the side reflector. Through the reactivity worth measurement test [3], the worth curve of a single control rod was obtained, as shown in Fig. 4. The integral worth is about $14 \times 10^{-3} \Delta k/k$, and the linear segment of the curve is from 600 to 1500 mm of the rod position. The control rod movement can change the reactor power directly via the reactivity insertion into the core.

3 Analysis Code

The THERMIX code is used for the reanalysis of the two reactivity insertion ATWS tests. It is a modular software package for steady-state thermal-hydraulic calculation as well as transient analysis of pebble-bed HTRs. The code mainly

Fig. 2 Procedure of a reactivity insertion ATWS test

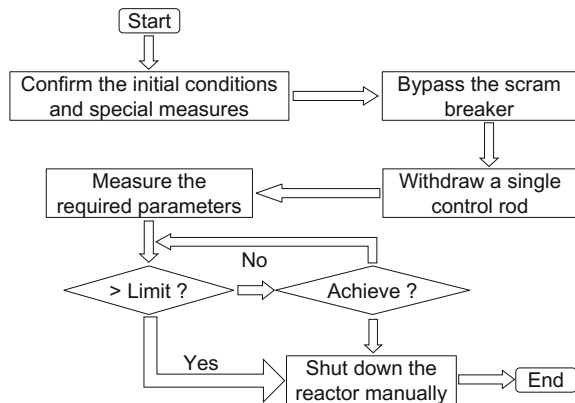


Fig. 3 Control rod position during the two tests

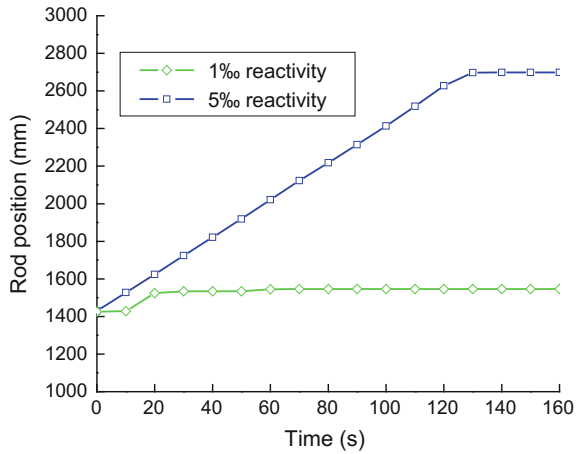
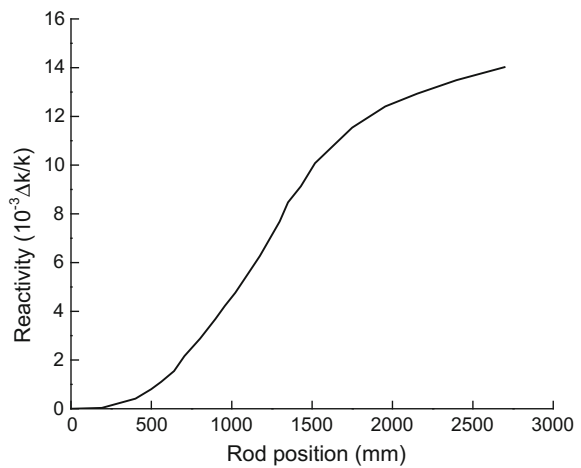


Fig. 4 Worth curve of a single control rod



comprises modules for neutron kinetics calculation, solid heat conduction calculation in reactor, gas convection calculation in reactor and fluid flow calculation in primary circuit. Detailed description of these modules is given by Gao and Shi [4, 5]. For the HTR-10, main components (the pebble-bed core, the graphite reflectors, the carbon bricks and the reactor pressure vessel, etc.), flow passages (e.g. the reactor core, the cold helium channels, the cold and the hot helium plena) and different components in the primary circuit (including the hot gas duct, the steam generator, the helium circulator) can be modelled by the THERMIX code.

4 Analysis Results

According to the actual test conditions, the dynamic simulations of the two reactivity insertion ATWS tests are performed for 3 h using the THERMIX code.

The reactor power transients during the two tests are, respectively, shown in Figs. 5 and 6, from which similar phenomena can be observed. After the initiation of such tests, the reactor power increases very fast due to the positive reactivity insertion caused by the control rod withdrawal. At 20 s in the first test and at 12 s in the second test, the signal of “power growth rate is too high” comes to trigger the reactor protection system. Although the control rods cannot be inserted into their guide channels, the helium circulator is stopped and the blower baffle is closed, and therefore, the reactor core loses forced cooling. The power ascension and the core

Fig. 5 Power during the 1‰ reactivity insertion ATWS test

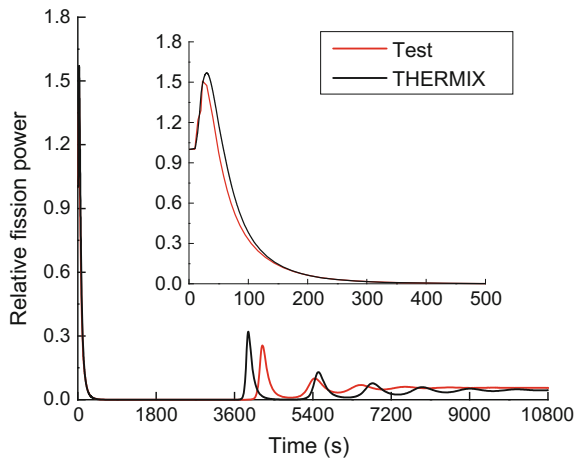
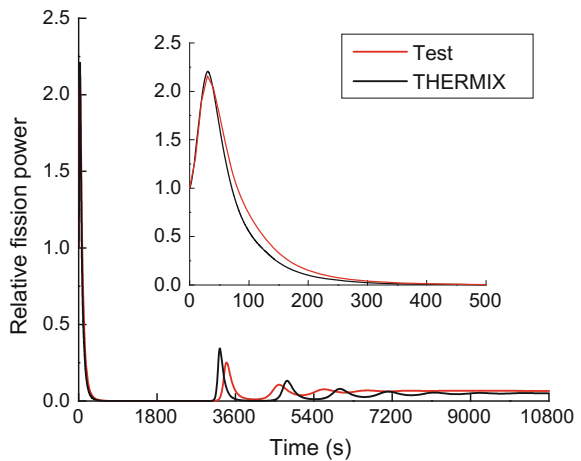


Fig. 6 Power during the 5‰ reactivity insertion ATWS test



heat-up make the fuel temperature rise rapidly. Due to a considerable negative reactivity feedback, the reactor is shut down. Accordingly, the reactor power decreases sharply to residual heat level after a peak value. In the first test, the calculated peak power is 5146 kW occurring at 30 s, while the test result reaches 5037 kW at 23 s. In the second test, the peak power is about 7240 kW at 30 s, and the calculation result agrees well with the test result.

As shown in Fig. 7, the average fuel temperature after the reactor shutdown still increases because the instantaneous reactor power is still larger than the heat dissipated from the core. This makes the total reactivity in the core continuously drop, as presented in Fig. 8. Along with the core cooldown, the fuel temperature begins to decrease, and thus, the total reactivity begins to increase from its minimum. According to the code results, the reactor becomes recritical at 2815 s in the first

Fig. 7 Calculated average fuel temperature

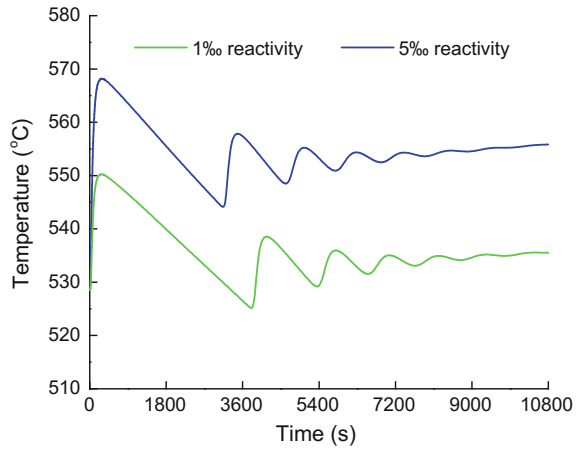


Fig. 8 Calculated total reactivity of the core

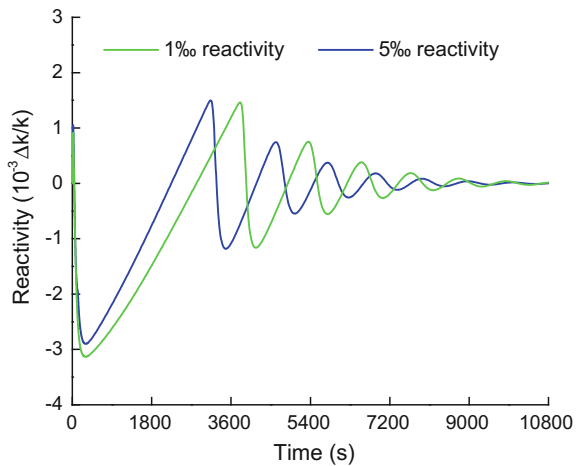
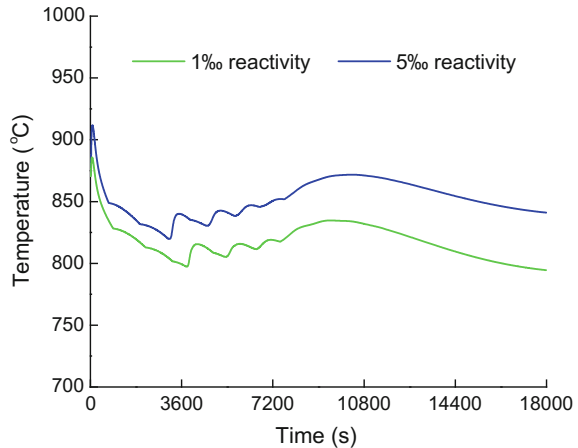


Fig. 9 Calculated maximum fuel temperature



test and at 2250 s in the second test since the total reactivity reaches zero at these time points. Because of the recriticality, the fuel temperature rises once again after its downtrend is stopped. Hence, the total reactivity declines again after experiencing a maximum. Soon, the reactor becomes subcritical once more after the total reactivity descends to zero.

In long term, the reactor power, the fuel temperature and the total reactivity oscillate several times due to the interaction of these three parameters. In the two tests, the measured reactor power stabilizes at about 180 kW. As regards the long-term behaviour, the phenomena of reactor recriticality, power fluctuations and final stabilization are well reproduced by the THERMIX code. In the first test, the calculated first peak power after the recriticality approaches 1070 kW at 3920 s, while the measured value is 853 kW that occurs at 4240 s. In the second test, the calculation result approaches 1152 kW at 3245 s, while the test one is 845 kW that occurs at 3400 s.

The safety limit for the maximum fuel temperature is 1620 °C. During the two tests, this value is never exceeded, as illustrated in Fig. 9.

5 Conclusions

In this study, two reactivity insertion ATWS tests are reanalysed using the THERMIX code. The investigation results lead to the following conclusions.

- (1) Following the initiation of such tests, the reactor power rises rapidly due to the positive reactivity insertion and then decreases because of the negative reactivity feedback. The short-term peak power is sensitive to the amount and the rate of the external reactivity.

- (2) As a result of bypassing the shutdown system, the reactor meets criticality again because of the positive reactivity produced by the core cooling.
- (3) In the two tests, the reactor power finally maintains a stable level after some oscillations. The heat generated by the core can be rejected by the passive cavity cooling without any problems.
- (4) The maximum fuel temperature, which is the most important safety-related parameter, is always far below the safety limit of 1620 °C.
- (5) For each test, THERMIX can reproduce good results for the power transient. It is concluded that this code is a useful tool for reanalysing these two tests.

Acknowledgments This work has been supported by the Chinese National S&T Major Project (Grant No. ZX069).

References

1. Z. Wu, D. Lin and D. Zhong, “The design features of the HTR-10”, *Nuclear Engineering and Design*, Vol. 218, No. 1–3, pp. 25–32, 2002.
2. S. Hu, R. WANG, and Z. Gao, “Safety Demonstration Tests on HTR-10”, 2nd International Topical Meeting on High Temperature Reactor Technology, Beijing, China, 2004.
3. Q. Su, R. Wang, S. Hu, et al. Commissioning procedures of the 10 MW high temperature gas-cooled reactor-test module. *Nuclear Engineering and Design*, 2002, 218(1–3): 241–247.
4. Z. Gao and L. Shi, “Thermal hydraulic calculation of the HTR-10 for the initial and equilibrium core”, *Nuclear Engineering and Design*, Vol. 218, No. 1–3, pp. 51–64, 2002.
5. Z. Gao, L. Shi. Thermal hydraulic transient analysis of the HTR-10. *Nuclear Engineering and Design*, 2002, 218(1–3): 65–80.

Author Biography

Fubing Chen got his doctor degree in nuclear science and engineering from the institute of nuclear and new energy technology (INET), Tsinghua University in 2009. His research interests include the validation of system analysis codes and thermal hydraulics of pebble-bed HTRs.

Research on Controlling Conditions of Cooling Water from Small Modular Reactors at Coastal Site

Ben-jing Tang, Shu-qiang Hou and Wei Bai

Abstract Based on the summarizing of previous research results, a two-dimensional mathematical model of average distribution along water depth is developed for the research on controlling conditions of cooling water from Small Modular Reactors at coastal site. This paper proposed two kinds of boundary conditions: straight shoreline and concave type bay. The result shows that for straight shoreline, the average depth of 5 m can be used as a control condition of cooling water for flat seabed and the slope of 0.4 m/km can be used as a control condition of cooling water for sloping seabed. The result also shows that for concave type bay, the average depth of 6 m can be used as a control condition of cooling water for flat seabed and the slope of 0.53 m/km can be used as a control condition of cooling water for sloping seabed. Besides, is that the near-zone water really participates in the mixed dilution and diffusion of warm water rather than the tidal prism plays a decisive role on the corresponding water area as the bay is large enough. The research results may serve as reference for the determination of fitness standards about Small Modular Reactors at coastal site.

Keywords Small modular reactors · Cooling water · Straight shoreline · Concave type bay · Control conditions

1 Introduction

The Small Modular Reactors is a new type of reactor developed on the basis of mature technology in the nuclear power and nuclear submarines. It can replace the traditional coal-fired boilers in the aspects of thermoelectric cogeneration, industrial gas supply, desalination, and special regional power supply. In particular, after the Fukushima nuclear accident, the excellent advanced technology and inherent safety of Small Modular Reactors become the current international hot spot of new nuclear

B. Tang (✉) · S. Hou · W. Bai
China Nuclear Power Engineering Co., Ltd., Beijing, Haidian, China
e-mail: bjtang89@126.com

development [1]. Developing Small Modular Reactors not only consistent with the national energy saving and green energy policies, but also have very broad market prospects.

The current international and domestic all lack entirely suitable technical standards for siting, which restricted the promotion and development of Small Modular Reactors to some extent. It is used as one of the main site selection technical conditions. Carrying out coastal site drainage control conditions of cooling water can provide scientific support to establishment technical standards for the coastal site comply with the technical and security of Small Modular Reactors.

The thermal discharge simulation technology is maturing as many scholars have done a lot of research on the power plant thermal discharge. Strictly speaking, the thermal discharge flow tend to have a three-dimensional characteristics and the engineering examples in recent years continue to emerge, but the near buoyant jet simulation area is still not very consistent with the actual. The coastal estuaries receiving water body in China are mostly wide and shallow-type region and the horizontal scale is much larger than the vertical dimension. The change of hydraulic parameters in the horizontal direction is much greater than the vertical and its flowing can represented by the average momentum along the depth available. The two-dimensional mathematical model for the thermal discharge is sufficient to meet most of the engineering precision.

In view of the thermal discharge in coastal area, this paper amended the relevant mathematical model calculation parameters and explored the principles of typical hydrological conditions selecting, and depending on the type of site characteristics typical of sites has been generalized [2]. Based on this, to carry out numerical simulation of thermal discharge, ultimately proposed site for small heap of thermal discharge control conditions provides reference and basis for subsequent small heap site selection. This paper carried out numerical simulation of thermal discharge, ultimately put forward thermal discharge control conditions for Small Modular Reactors sites and provide reference and basis for the subsequent site selection.

2 Establishment of Model and Selection of Calculation Conditions

2.1 Construction of Mathematical Models of Thermal Discharge

The depth of the near-shore coastal NPP sites' sea area is generally shallow, and the three-dimensional bodies of the water are not strong. According to the terrain, boundaries, and flow characteristics of the coastal NPP sites, a two-dimensional plane mathematical model of along the depth-averaged is developed to calculate and analyze the water temperature field [3].

2.1.1 The Basic Equations

The continuity equation

$$\frac{\partial Z}{\partial t} + \frac{\partial uH}{\partial x} + \frac{\partial vH}{\partial y} = q \tag{1}$$

The momentum equation

$$\begin{aligned} \frac{\partial uH}{\partial t} + \frac{\partial uuH}{\partial x} + \frac{\partial uvH}{\partial y} = & -gH \frac{\partial Z}{\partial x} + \frac{\partial}{\partial x} \left(v_t H \frac{\partial u}{\partial x} \right) \\ & + \frac{\partial}{\partial y} \left(v_t H \frac{\partial u}{\partial y} \right) + \frac{\tau_{sx}}{\rho} - g \frac{u\sqrt{u^2 + v^2}}{c^2} \\ & + fvH + qu^* \end{aligned} \tag{2}$$

$$\begin{aligned} \frac{\partial vH}{\partial t} + \frac{\partial uvH}{\partial x} + \frac{\partial vvH}{\partial y} = & -gH \frac{\partial Z}{\partial y} + \frac{\partial}{\partial x} \left(v_t H \frac{\partial v}{\partial x} \right) \\ & + \frac{\partial}{\partial y} \left(v_t H \frac{\partial v}{\partial y} \right) + \frac{\tau_{sy}}{\rho} - g \frac{v\sqrt{u^2 + v^2}}{c^2} \\ & - fuH + qv^* \end{aligned} \tag{3}$$

The temperature field equation

$$\begin{aligned} \frac{\partial H\Delta T}{\partial t} + \frac{\partial uH\Delta T}{\partial x} + \frac{\partial vH\Delta T}{\partial y} = & \frac{\partial}{\partial x} \left(E_x H \frac{\partial \Delta T}{\partial x} \right) + \frac{\partial}{\partial y} \left(E_y H \frac{\partial \Delta T}{\partial y} \right) \\ & - \frac{K_S \Delta T}{\rho C_p} + q\Delta T^* \end{aligned} \tag{4}$$

In the above formula, where H and Z represent water depth and level; u, v represent velocity; q is the flow rate per unit area; ρ is the density of water; v_t represents the turbulent viscosity coefficient; c is Chezy coefficient; f is the Coriolis force coefficient; τ_{sx} and τ_{sy} represent free surface wind shear stress; ΔT represents water temperature rise; E presents the diffusion coefficient; K_S represents comprehensive heat transfer coefficient of water; C_p represents specific heat; ΔT^* represents the over-temperature value of water along the way.

2.1.2 Definite Conditions

The initial conditions

$$\begin{cases} Z(x, y, 0) = Z_0(x, y) \\ u(x, y, 0) = u_0(x, y) \\ v(x, y, 0) = v_0(x, y) \\ \Delta T(x, y, 0) = \Delta T_0(x, y) \end{cases} \quad (5)$$

The boundary condition of the flow is the tide line process. The fixed boundary used sliding conditions. The temperature boundary can be expressed as $\Delta T = \Delta T(t)$ and $\partial \Delta T / \partial n = 0$.

2.1.3 Solution Method

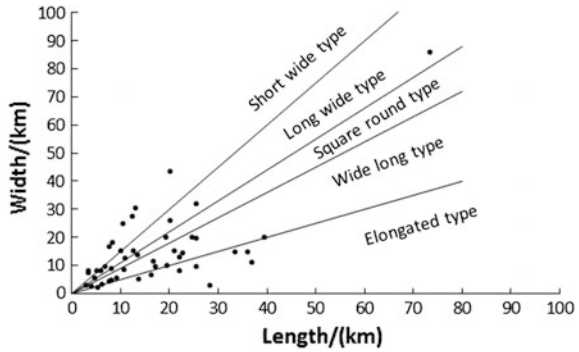
The above equations with nonlinear mixing operator can cut algorithm for solving discrete. According to the equation contained operators' different characteristics, the equation split into several different suboperator equations and each suboperator equations numerical method for solving its adapting. This numerical method has good computational stability and high accuracy for effectively solving the nonlinear equations' free surface and identifying problems [4].

2.2 Construction of Mathematical Models of Thermal Discharge

The mainland coastline of China is about 18,400 km. According to the near-shore coastal zone boundary survey analysis, shoreline basically consists of several main types of straight shoreline, slightly curved coastline, bays and estuaries, and other components. The statistical analysis result of 46 typical coastal bays shape coefficient shows that generalized narrow type (including narrow and wide long type) bays accounting for about 54%, generalized short wide type (including length and width and short width type) bays accounts ratio of about 35%, and Radius type bay only about 11%, as shown in Fig. 1.

For straight and slightly curved shoreline morphology, set the drain in the middle of the shoreline. For small-scale bays, the boundaries can generally follow straight shoreline situation as the thermal discharge is out of bay by the tides. As the scale of the bay is large enough to accommodate the power plant thermal discharge, its hydraulic dispersion feature has the characteristic of the bays.

Fig. 1 The shape statistics and classification of main typical bays in China



2.3 Select Calculation Conditions

The drainage impact temperature range is correspondingly small as the displacement of the Small Modular Reactors nuclear power units is smaller. Taking into account that the results of the partial conservative, select the warm drainage generalized model ranges for straight shoreline waters of 30 km × 15 km and for narrow bay type the range is 15 km × 10 km, and the shape coefficient is 0.67.

The calculation region can split by triangular element mesh. In straight shore, for example, a total of 6436 nodes arranged 12,528 units, of which offshore grid spacing of 200 m, from the open sea to gradually drain grid encryption, the minimum grid spacing in the vicinity of the drain of about 5 m.

Most of tidal type in China’s coastal areas belongs to semidiurnal tide type, only in some South China Sea belongs to all-day type. This paper focuses on the semidiurnal tide type, the calculation conditions, and case combinations as shown in Table 1.

Table 1 Calculation and combinations of conditions

Design parameters	Installed capacity 2 × 100 MW	Discharge water 10.0 m ³ /s	Temperature rising 8.0 °C
Hydrological condition	regulation semidiurnal tide with spring range	regular semidiurnal tide with microrange	Irregular semidiurnal tide with microrange
	Tidal range of 4.0 m	Tidal range of 2.0 m	
Combination conditions	H	i	A
	3, 4, 5, 6, 7, 8, 9, 10 m	0.20, 0.40, 0.53, 0.67, 0.87 m/km	15 km × 10 km, 12 km × 10 km, 15 km × 8 km, 12 km × 8 km, 15 km × 6 km
Calculation parameters ^[5]	$E_x = E_y = 0.5 \text{ m}^3/\text{s}$	$T = 20 \text{ }^\circ\text{C}$	$K_s = 30.0 \text{ W}/(\text{m}^2 \text{ }^\circ\text{C})$
	v_t	n	
	$v_t = \alpha u_* H$	$n = \begin{cases} 0.018 & \text{Based roughness coefficient} \\ 0.016 + \frac{0.002}{H} & H \geq 1.0 \text{ m} \end{cases}$	

3 Parameter Sensitivity Analysis

This paper used single factor analysis method, respectively, for roughness, turbulent diffusion coefficient, and overall heat transfer coefficient were parameters sensitivity analysis of the temperature distribution impacts. When calculating, the boundary is generally taken as straight shoreline and flat seabed, depth of 5 m. Regular semidiurnal tide with microrange was selected as the hydrological conditions.

3.1 Roughness Sensitivity Analysis

The temperature distribution was calculated and analyzed by straight shoreline sea area of the different seabed roughness values to obtain a full tide area with the maximum temperature rise envelope roughness change results, as shown in Fig. 2. Thus, other conditions remain unchanged, with the increase in roughness and temperature, and flow rate of the drain tide is gradually reduced.

3.2 Sensitivity Analysis of Turbulent Diffusion Coefficient

The temperature distribution was calculated and analyzed by straight shoreline sea area of different turbulent diffusion coefficient values to obtain a full tide area with the maximum temperature rise envelope turbulent diffusion coefficient change results, as shown in Fig. 3. Thus, in the other conditions remain unchanged, the flow turbulence diffusion capacity decreases, turbulent diffusion coefficient

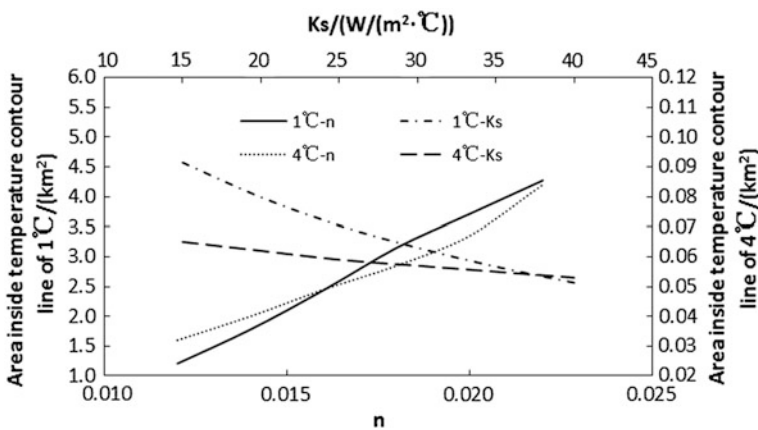


Fig. 2 Curve of temperature rising envelope area with roughness and comprehensive heat transfer coefficient changing

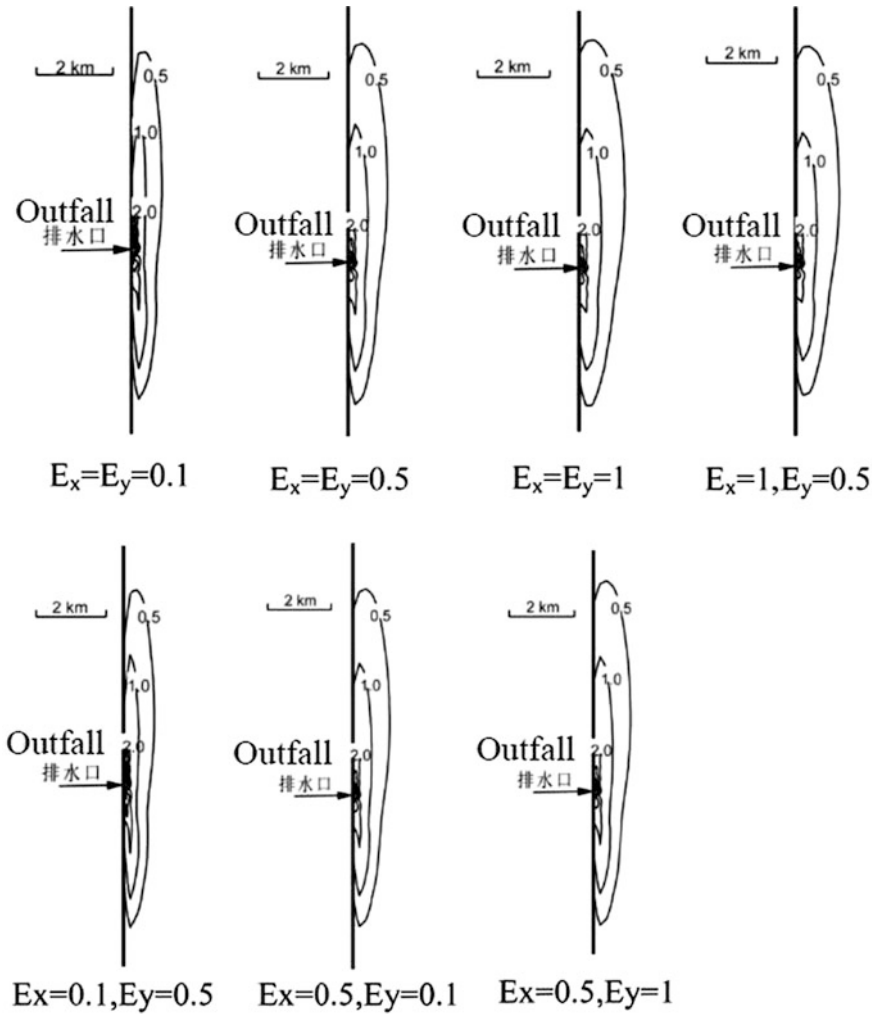


Fig. 3 The temperature rising envelope area of different turbulent diffusion coefficient values

weakened, and the temperature rise range was smaller as in the case $E_x = E_y$. The temperature rising area mainly affected by E_x , as the temperature rise near the outfall mixing zone with a fluidized complicated reflux zone exists $E_x \neq E_y$. The tide direction is substantially parallel to the shoreline (y -direction) away from the waters of the mixing zone, so the temperature distribution shape is more flat $E_x < E_y$ and some more fatter as the case $E_x > E_y$.

3.3 Sensitivity Analysis of Comprehensive Heat Transfer Coefficient

The temperature distribution was calculated and analyzed by straight shoreline sea area of the different comprehensive heat transfer coefficient values. The full tide area with the maximum temperature rise envelope turbulent diffusion coefficient change results, shown in Fig. 2.

Thus, in the other conditions remain unchanged, with the increase in comprehensive heat transfer coefficient, the capability of heat exchange between the water and air increased and the temperature rising area is gradually reduced. The high temperature rising mixed zone of 4.0 °C is less influenced by comprehensive heat transfer coefficient because of its smaller area. The temperature rising mixed zone of 1.0 °C decreases with the increase in comprehensive heat transfer coefficient very obviously as its area is relatively large.

The calculation above is in view of the straight sea coast and flat seabed conditions. But in practical engineering, the impact of above parameters to tidal power and thermal discharge temperature range and distribution patterns will be weakened because of the combined effects of seabed topography, islands, headlands, storms, seasonal changes, and other factors. The value of the parameters should be reasonably determined by trend verified based on the measured hydrological data during thermal discharge calculations.

4 Research on Controlling Conditions of Cooling Water for Straight Shoreline Region

This paper used a two-dimensional mathematical model for the calculation and analysis on the distribution of temperature field of straight shoreline region under the conditions of different water depths, different seabed slope, and different hydrological conditions. Then, control conditions of cooling water should be provided for straight shoreline region.

4.1 Depth Control Conditions

The regular semidiurnal tidal with microrange was selected as hydrological conditions, and the temperature field distribution under different water depth is analyzed and calculated for the straight shoreline region. The results of the full tide maximum temperature rise envelope are shown in Figs. 4 and 5.

From these results, it can be drawn:

- a. The other conditions remain unchanged, only changing the depth of the straight shoreline region; it is obvious that the trend of temperature field affected area with water depth increases to reduce.
- b. The temperature and drainage impact on both sides of the north and south more or less when the water depth is about 4 m. Thereafter, with the increase in water depth, the degree of influence of thermal discharge north of outfall gradually increases and the temperature envelope more shape. For low-temperature rise region, the trends become more pronounced.

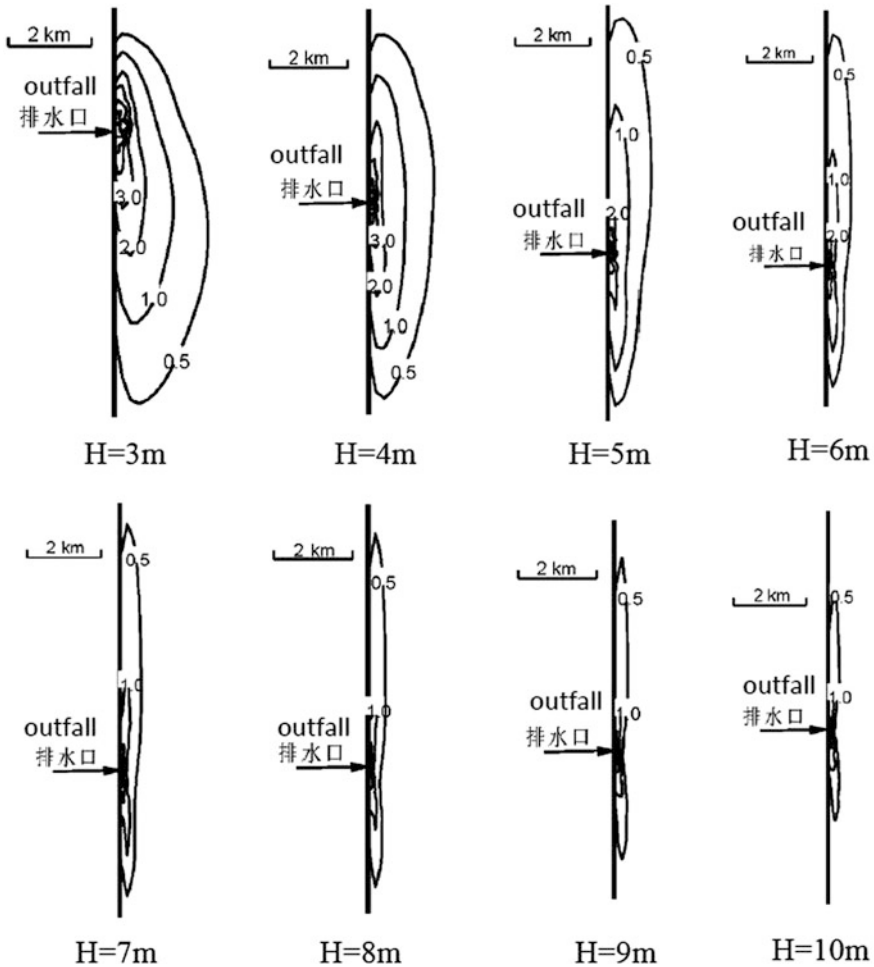


Fig. 4 The temperature rising envelope area of different seawater depth

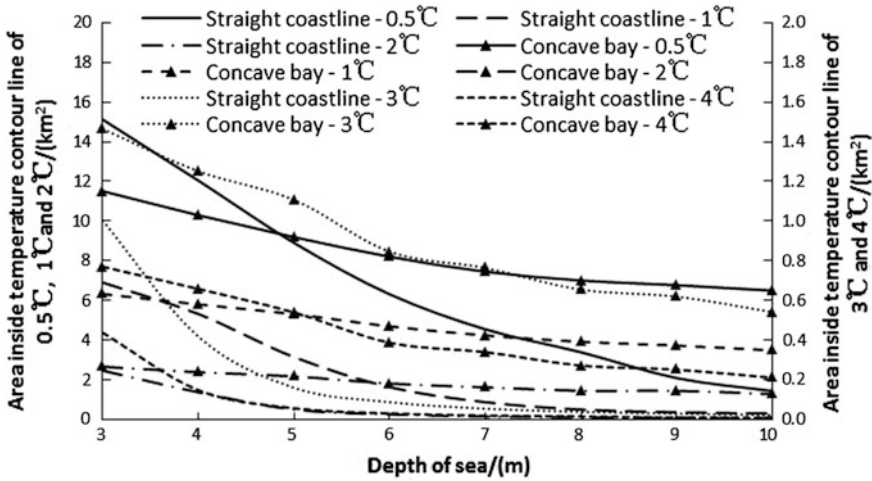


Fig. 5 Temperature rise area change with seawater depth

- c. Considering the water depth condition only, the temperature influence area is larger under the shallow water condition. The change of temperature envelope characteristic parameters trends to slow down under the water depth of 4.0–5.0 m condition. The envelope characteristic parameters of the temperature rising region have no significant change after the water depth exceeds 5.0 m. Therefore, the average depth of 5.0 m can be the hydraulic depth control condition for straight shoreline thermal discharge meet emission dispersion characteristic.

4.2 Seabed Slope Control Conditions

On the basis of generally assumed flat seabed in shoreline region, further considering the case from the land to the seabed off the coast of terrain gradually decreasing. In calculating the gradient changes uniformly assumed waters, for fixed land seabed depth of 2.0 m, changing water depth off the coast at the border open, get a different slope condition, as shown in Table 1.

Select the regular semidiurnal tidal with microrange hydrological conditions and the temperature field distribution under different seabed slope is analyzed and calculated for the straight shoreline region. The results of the full tide maximum temperature rise envelope are shown in Figs. 6 and 7.

From these results, it can be drawn:

- a. The other conditions remain unchanged, only changed the seabed slope of the straight shoreline region, the temperature gradient field on range was decreased with the seabed slope increased.
- b. When the seabed slope of 0.20 m/km and the near-shore water depth shallow, the thermal discharge diffusion width wider of seaward and the temperature envelope distributions of partial more “fat.” The temperature and drainage diffusion slope varies with the width of the open sea change has not sensitive after the slope increases and reached 0.53 m/km.

Considering the seabed slope condition only, the temperature influence area is larger under the 0.20 m/km condition. When the seabed slope increased to 0.40 m/km, the change in temperature envelope characteristic parameters trends to a lesser extent with the seabed slope continues to increase. Therefore, the average slope of 0.40 m/km can be the seabed slope control condition for straight shoreline thermal discharge, which meets emission dispersion characteristic.

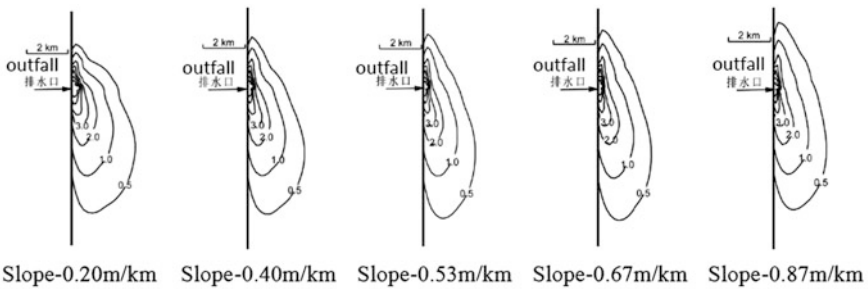


Fig. 6 The temperature rising envelope area of different seabed slope

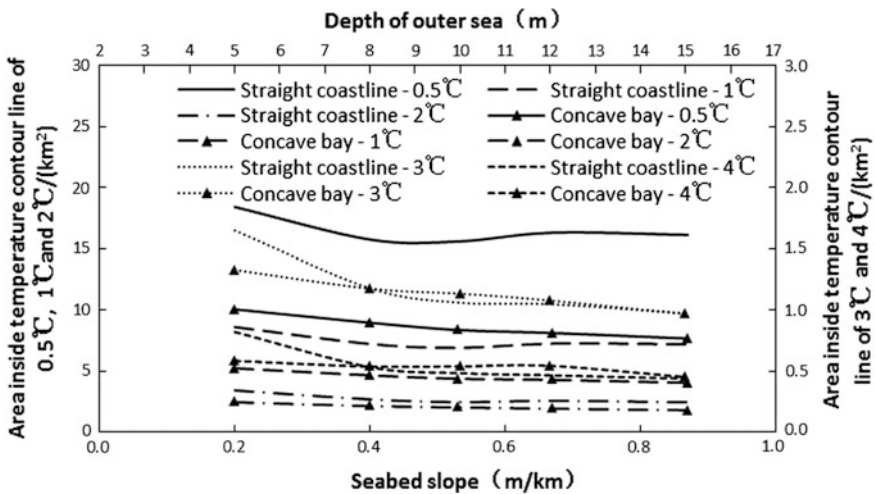


Fig. 7 Temperature rise area change with seabed slope

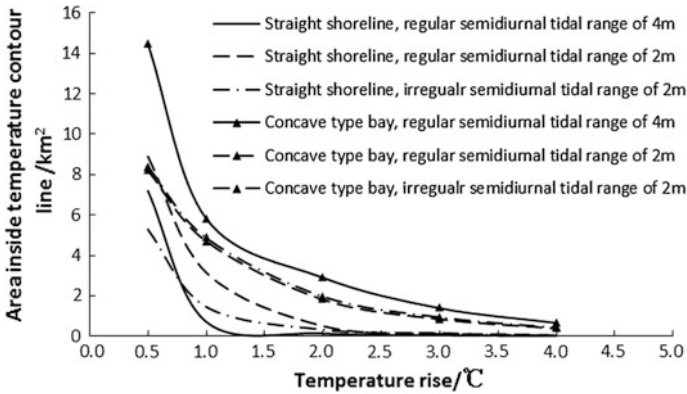


Fig. 8 Temperature rise area change with hydrological conditions

4.3 Hydrological Control Conditions

The selected three kinds of hydrological conditions including regulation semidiurnal tide with spring range, regular semidiurnal tide with microrange, and irregular semidiurnal tide with micro range. The temperature field distribution under different hydrological conditions is analyzed and calculated for the straight shoreline region. The results of the full tide maximum temperature rise curve of envelope area change with the hydrological conditions as shown in Fig. 8.

From these results, it can be drawn:

- a. The type of tide and tidal range is two important parameters of hydrological conditions. For straight shoreline waters warm drainage distribution, the influence of tidal range is greater than the type of tide. The drainage impact temperature range has a smaller scale as the tide with microrange hydrological condition, and the higher the temperature, the difference between the temperature-rising regions is more obvious.
- b. The temperature rising affects a wide range of fields under the regular semidiurnal tide with microrange hydrological condition, it can be used as the hydrological control conditions for straight shoreline thermal discharge studies.

5 Research on Controlling Conditions of Cooling Water for Concave Type Bay

This paper used a two-dimensional mathematical model for the calculation and analysis on the distribution of temperature field of concave type bay under the conditions of different water depths, different seabed slope, and different

hydrological conditions. Control conditions of cooling water should be provided for concave type bay.

5.1 Depth Control Conditions

The regular semidiurnal tidal with microrange was selected as hydrological conditions, and the temperature field distribution under different water depth is analyzed and calculated for the concave type bay. The results of the full tide maximum temperature rise envelope are shown in Figs. 9 and 5.

From these results, it can be drawn:

- a. The other conditions remain unchanged, only changing the depth of the concave-type bay region; it is obvious that the trend of temperature field-affected area with water depth increases to reduce.
- b. When the water depth is shallow, the thermal discharge outward diffusion long distance and the temperature envelope distributions present oblong shape.

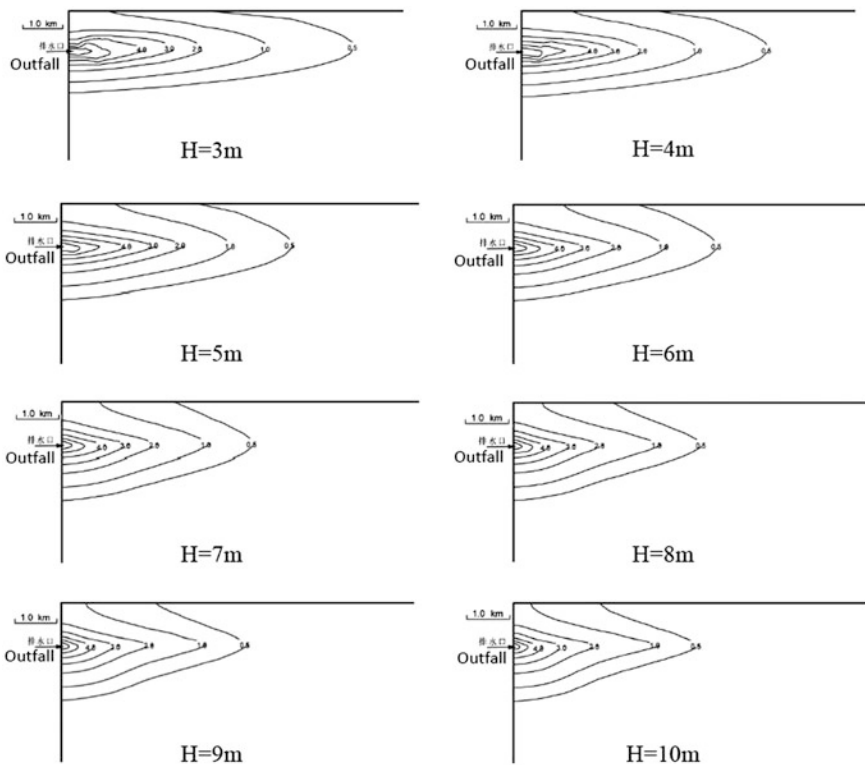


Fig. 9 The temperature rising envelope area of different seawater depth

Thereafter, the temperature and drain diffusion distance out of the sea is gradually reduced with the increase in water depth; the temperature rise envelope shape began partial “fat.” For low-temperature rise region, the trends become more pronounced.

- c. Considering the water depth condition only, the temperature influence area is larger under the shallow water condition. The change in temperature envelope characteristic parameters trends to slow down under the water depth of 6.0 m condition. The envelope characteristic parameters of the temperature rising region have no significant change after the water depth exceeds 7.0 m. Therefore, the average depth of 6.0 m can be the hydraulic depth control condition for concave-type bay thermal discharge, which meets emission dispersion characteristic.

5.2 Seabed Slope Control Conditions

The regular semidiurnal tidal with microrange was selected as hydrological conditions and the temperature field distribution under different seabed slope is analyzed and calculated for the concave-type bay region. The results of the full tide maximum temperature rise envelope are shown in Figs. 10 and 7.

From these results, it can be drawn:

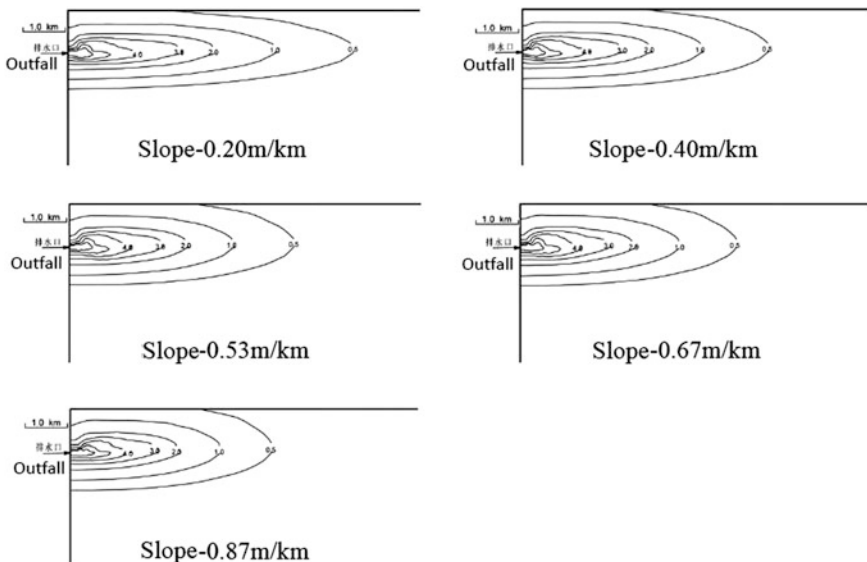


Fig. 10 The temperature rising envelope area of different seabed slope

- a. The other conditions remain unchanged, only changing the seabed slope of the concave-type bay region; the temperature gradient field on range was decreased with increase in the seabed slope.
- b. When the seabed slope is slightly curved and the near-shore water depth is shallow, the thermal discharge diffusion long distance of seaward and the temperature envelope distributions present oblong shape. The temperature and drainage diffusion slope varies with the width of the open sea change has not sensitive after the slope increases and reached 0.53 m/km.
- c. Concerned the seabed slope condition only, the temperature influence area is larger under the slightly slower condition. When the seabed slope increased to 0.53 m/km, the change in temperature envelope characteristic parameters trends to a lesser extent with the seabed slope continues to increase. Therefore, the average slope of 0.53 m/km can be the seabed slope control condition of concave-type bay region thermal discharge, which meets emission dispersion characteristic.

5.3 *Hydrological Control Conditions*

The selected three kinds of hydrological conditions include regulation semidiurnal tide with spring range, regular semidiurnal tide with microrange, and irregular semidiurnal tide with micro range. The temperature field distribution under different hydrological conditions is analyzed and calculated for the concave-type bay region. The results of the full tide maximum temperature rise curve of envelope area change with the hydrological conditions are shown in Fig. 8.

From these results, it can be drawn:

- a. For the regulation semidiurnal tide with spring range tide hydrological conditions, the tidal range and bay tidal volume are very large and also there is a large thermal discharge affect area as the diffusion length is longer during ebb tide time. The thermal discharge affect area is less under the influence of microtidal range hydrological conditions, and the difference between the two hydrological conditions is not very obvious, indicating that the tidal range is the main factors impact the thermal discharge mixing and diffusion of the bay.
- b. The temperature rise affects a wide range of fields under the regular semidiurnal tide with spring range hydrological condition, it can be used as the hydrological control conditions for concave-type bay thermal discharge studies.

6 Conclusions

The characteristic of thermal discharge is an important factor in the evaluation of Small Modular Reactors site adaptability. Based on the summary of the previous studies, this paper utilizes the mathematical model of a two-dimensional plane along the depth-averaged current temperature field, analyzes the thermal discharge characteristic of coastal Small Modular Reactors nuclear power plant site, proposes the two site boundary types of straight coastline, and concave bay, respectively, and researches the thermal discharge control condition from the sea-water depth, seabed slope, and hydrological factors; the following results are concluded and could be referred for future research and practical application of Small Modular Reactors site.

- a. According to the analysis of parameter sensitivity, the sphere of influence thermal discharge increases along with the growing roughness, the growing turbulent diffusion coefficient, and decreasing integrated heat transfer coefficient. However, the impact of the above parameters will be reduced because of the complex sea conditions in real project; therefore, the reasonable values of the parameters should be determined by the validation of the trend, based on the hydrological data.
- b. According to the calculation of straight shoreline waters concentration field, the hydrological conditions of the average seawater depth of 5.0 m, seabed slope 0.40 m/km, and regular semidiurnal tide with microrange meet the control conditions of thermal discharge characteristics on straight shoreline waters.
- c. According to the calculation of concave bay concentration field, the hydrological conditions of the average seawater depth of 6.0 m, seabed slope 0.53 m/km, and regulation semidiurnal tide with spring range meet the control conditions of thermal discharge characteristics on concave bay.

References

1. HAO Rui-xia, HAN Xin-sheng. Quasi 3-D numerical model for flow and heat transport of power plant cooling water discharged into coastal area [J]. *Journal of Hydraulic Engineering*, 2004, 8:66–70.
2. MA Jin-rong, ZHANG Xiao-yan, ZHANG Xing-nan. Thermal buoyancy effect in two-dimensional cooling water mathematical models[J]. *Hydro-Science and Engineering*, 2005 (03), 37–40.
3. Chieh S H. Two-Dimensional Numerical Model of Thermal Discharges in Coastal Regions[J]. *Journal of Hydraulic Engineering*, 1987, 113(8):1032–1040.
4. CHEN Yong-ping, LIU Jia-ju, YU Guo-hua. A study on eddy viscosity coefficient in numerical tidal simulation [J]. *Journal of Hohai University (Natural Sciences)*, 2002, 30(1):39–43.
5. GB/T 50102-2014, Code for design of cooling for industrial recirculating water.

Author Biography

Ben-jing Tang working at China Nuclear Power Engineering Co., Ltd., now researches on circulating water intake and drainage project of NPPs.

Steam Hammer Calculation and Study of Nuclear Island Main Steam Pipe Network

Jiaming Zhao, Yemin Dong, Meiling Sheng and Yao Pi

Abstract The aim of this study was to study the steam hammer by fast closing of the main steam isolation valve of the nuclear island main steam pipe network in some nuclear power plant, establish the model using “PIPENET” software and calculate the most steam hammer load and the occurrence time in different pipes. The results show that the most steam hammer loads appear when closing the valve and the steam hammer load after the main steam isolation valve is larger than the one before the valve, because of the relief device set before the valve. Meanwhile, the flowrate of the relief device that has lower opening set point and nearer the main steam isolation valve is bigger. Further, only setting one train steam dump piping and only reducing the capacity of steam dump valves have complex steam hammer influence, and the steam hammer influence of the former is about ten times of the latter. All above can be used for system piping design, stress calculation of pipe, and optimizing piping layout, which has great significance for improving the safety of main steam system and nuclear power plants.

Keywords Main steam pipe network · Main steam isolation valve closing · Steam hammer pressure · Steam hammer load · PIPENET

1 Introduction

The closing of the main steam isolation valve will cause the steam hammer phenomenon in the main steam pipe network. That is, if the fluid flow state in the pipe changes suddenly before or after the isolation valve, pressure wave is formed and transferred along the pipe axis in the speed of sound in the fluids. In the process of pressure wave propagation, pressure isn't balanced in the piping system, the impulse load will be generated. The transients load will be great and might cause serious

J. Zhao (✉) · Y. Dong · M. Sheng · Y. Pi
China Nuclear Power Engineering Co. Ltd, Beijing, China
e-mail: zhaojm@cnpe.cc

damage to pipe and equipment. Therefore, during the design and layout of the main steam piping, the impact of steam hammer should be considered [1-3].

The study of steam hammer calculation analysis is based on the main steam system from the outlet of the steam generator to the main steam pipe which is located inside the nuclear island of a nuclear power plant and takes the advantage of modeling by PIPENET. The study could be the input of system design and piping stress calculation analysis, which is used for optimizing the layout of the main steam pipe and has important significance for improving the reliability and safety of the main steam system and nuclear power plant.

2 Modeling in PIPENET

PIPENET is an advanced and reliable network fluid calculation and analysis software which has been applied widely for pipeline water and hammer calculation in nuclear power or thermal power plants. This paper models the main steam system by PIPENET in which the prototype is based on the system layout and equipment parameters of the main steam system in a nuclear power plant and the model is shown in Fig. 1.

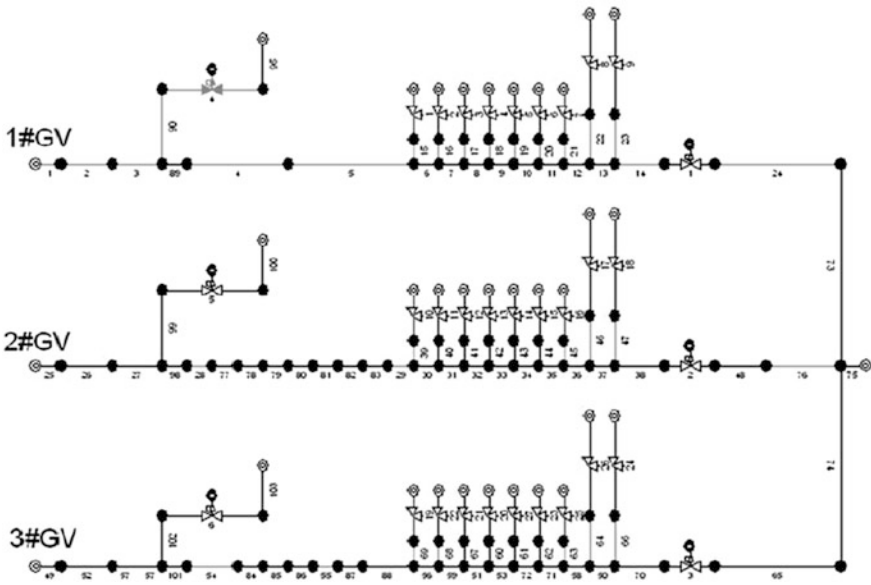


Fig. 1 PIPENET model of nuclear island main steam pipe network in a nuclear power plant

3 Calculation Input

The main steam system includes the following major equipment: two sets of safety valve (1# safety valve and 2# safety valve), two sets of steam dump valve (1# steam dump valve and 2# steam dump valve) and MSIV (main steam isolation valve). The main calculation inputs are as follows: 1# safety valve opening set point is 8.5 MPa, and 2# safety valve opening set point is 8.7 MPa. Both opening set points of the steam dump valve are 7.85 MPa. The main steam isolation valve closing time is 5 s.

The calculation is based on the main steam system full power operation condition. The main steam flow rate is 568 kg/s, the end of the model is main steam header pipe, the operation pressure is 6.78 MPa, and the calculation time step is 0.01 s in the PIPENET model.

4 Calculation Results

The steam hammer load of each pipe is calculated. The partial pipe maximum steam hammer load and corresponding time of 1#GV are presented in Table 1, with relatively large steam hammer load.

It is shown that in the above table the maximum load appears on the 24# pipe which locates after the MSIV, while the steam hammer load of 14# pipe before the main steam isolation valve is only 10.8% of the 24# pipe. The steam hammer load of 6# pipe, which is near the safety valve before the main steam isolation valve, is only 4.5% of the 24# pipe, because of setting the relief device which causes the smaller steam hammer load by the opening of the steam dump valves and main steam safety valves. In addition, the steam hammer load is also bigger on the 2/3/4/5# pipes because they have more elbows, and elevation variation locates at the outlet of steam generator. During the mechanical calculation and analysis for pipe section with relatively large steam hammer load, the impact of the hammer load should be paid more attention particularly. Design and layout of the piping could be modified if necessary.

Table 1 The partial pipe maximum force and occurrence time of steam hammer of 1#GV

Pipe no.	Maximum force (N)	Time (s)	Pipe no.	Maximum force (N)	Time (s)
2	-6295	5.34	6	-737	5.6
3	-12597	5.35	13	1591	5.5
4	-7122	5.36	14	1787	5.5
5	-12362	5.36	24	16473	5.5

Besides, we calculate and analyze the steam hammer pressure and steam hammer load characteristics of the 3# pipe downstream the 1#GV, the 14# pipe before main steam isolation valve, the 24# pipe after main steam isolation valve, and the flow characteristics of the relief devices. Meanwhile, we calculate and analyze the impact of steam hammer because of the changing of the relief devices.

4.1 Steam Hammer Pressure and Load of the 3# Pipe in the Outlet of 1#GV

The following figures present the steam hammer pressure and load curve of 3# pipe which locates downstream the 1#GV.

Figure 2 shows that the 3# pipe pressure gradually increases to about 8.7 MPa. In the early stage of valve closing, the pressure variation is relatively slow, and in the late stage the pressure variation of the valve is relatively fast. Figure 3 shows that the steam hammer load of the 3# pipe changes with the time, and the maximum load appears around 5.5 s and then gradually become smaller and more stable. Because the elevation variation of the 3# pipe is bigger, the influence of the steam hammer load should be paid more attention in the calculation and analysis of piping stress, if necessary, piping designation and layout should be adjusted.

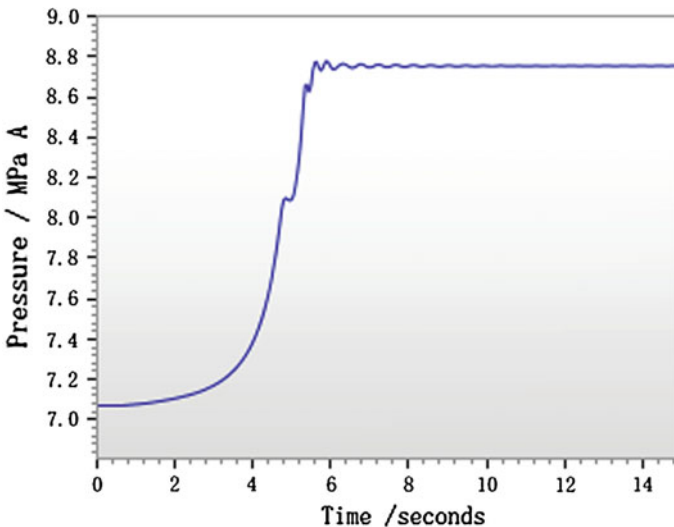


Fig. 2 Steam hammer pressure before MSIV

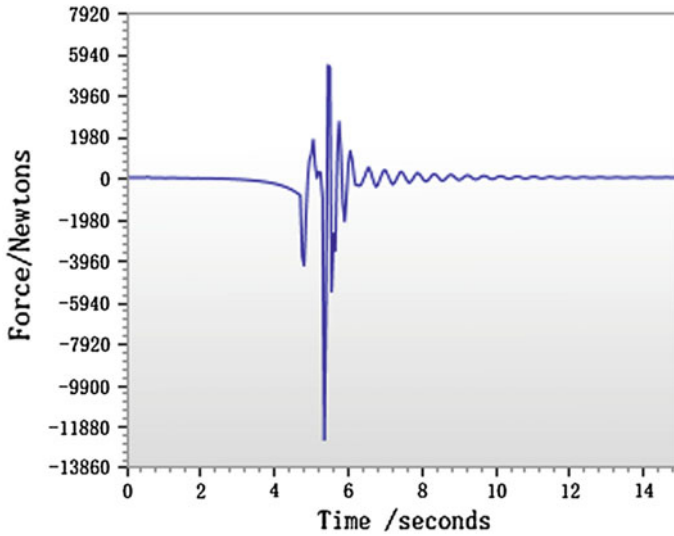


Fig. 3 Steam hammer load before MSIV

4.2 Steam Hammer Pressure and Load of the 14# and 24# Before and After MSIV

The following figures present variation curve of the steam hammer pressure and load on the 14# and 24# pipes which locate before and after MSIV on 1#GV.

Figure 4 shows that the steam hammer pressure of the 14# pipe before main steam isolation valve tends to about 8.7 MPa, which is denoted as 1. The steam hammer pressure of the 24# pipe after main steam isolation valve fluctuates from 6.2 MPa to 7.3 MPa, which is denoted as 2. With the extension of time, the pressure fluctuation range gradually becomes smaller, and the pressure fluctuation decreases gradually and tends to stable with time. The steam hammer pressure before main steam isolation valve is larger than the one after main steam isolation valve.

Figure 4 shows that the fluctuation range and fluctuation frequency of steam hammer load of the 24# pipe after main steam isolation valve are relatively larger, which is noted as 2, and the most steam hammer load is larger than the one of the 14# pipe, which is denoted as 1.

By contrast, the fluctuation frequency of steam hammer pressure and load of the 24# pipe after main steam isolation valve is relatively larger, and the steam hammer pressure changing is not proportional to the steam hammer load. So when system is designed and piping layout is carried out, the feature above should be considered.

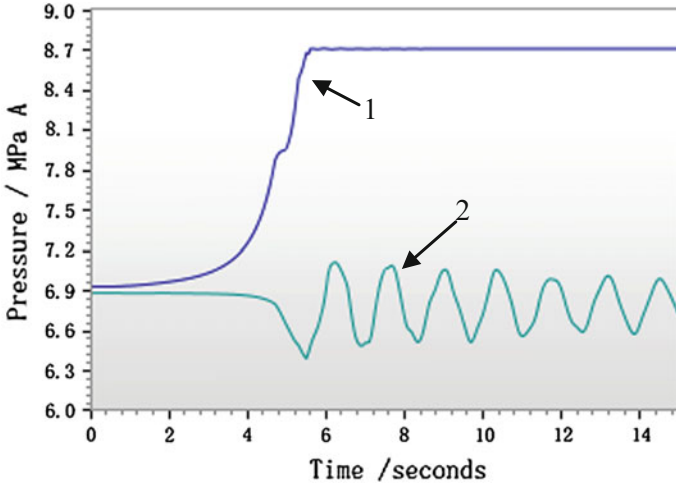


Fig. 4 Steam hammer pressure before and after MISV (0–15 s)

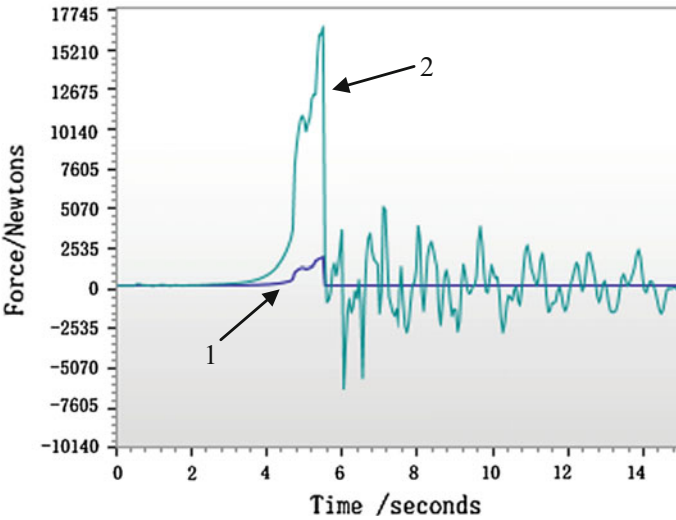


Fig. 5 Steam hammer load before and after MISV (0–15 s)

Besides, steam hammer pressure and load of the 24# pipe after main steam isolation valve in Figs. 4 and 5 have poor convergent within 15 s, and it is necessary to calculate using longtime focusing the direction of the change. Figures 6 and 7 show the changing within 100 s. The maximum load appears around 5.5 s, and then, the load gradually decreases and tends to stable.

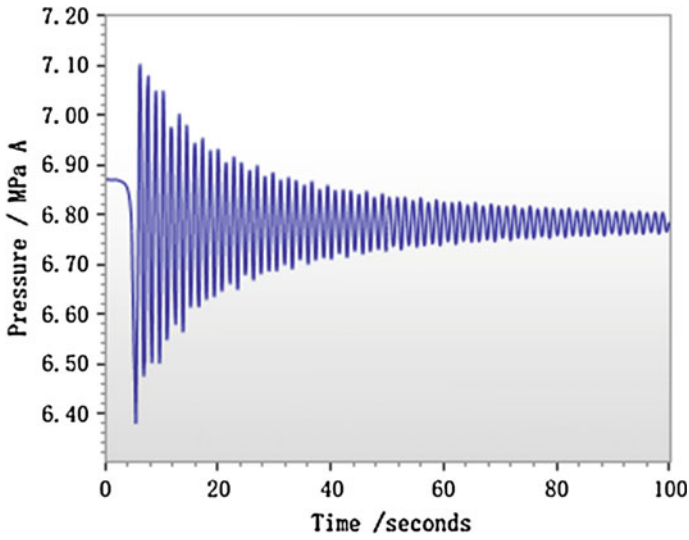


Fig. 6 Steam hammer pressure after MISV (0–100 s)

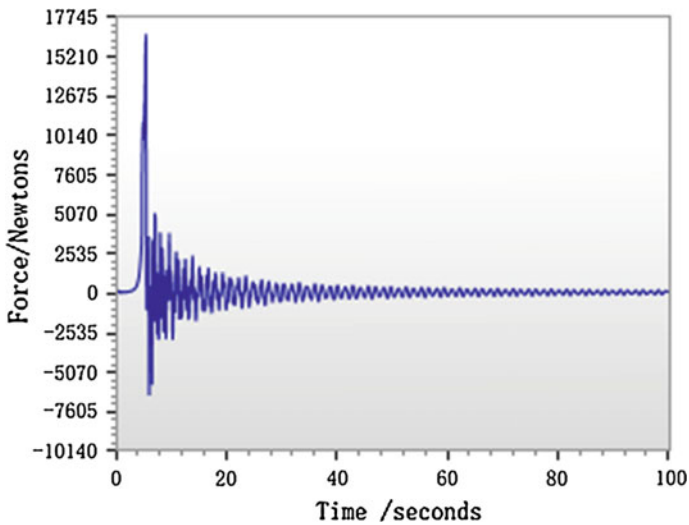


Fig. 7 Steam hammer load after MISV (0–100 s)

4.3 Flow Characteristics of Pressure Relief Device

According to the production principle of the steam hammer, the maximum steam hammer pressure and load appear at the inlet and outlet of the pipe on the valve closing moment. But the steam hammer load on the inlet pipe of MSIV in a nuclear

power plant is not that big, because the design takes the advantage of pressure relief device which are on the inlet of the pipe including 7 safety valves and 2 steam dump valves. On the closing moment of MSIV, steam dump valves and the safety valves will be opened with related steam pressures set point which is 7.85 MPa, 8.5 MPa and 8.7 MPa. The steam will be released to atmosphere so that the pressure in the pipe will decrease. The displacement of the above 9 sets of valves is shown in Figs. 8 and 9.

In Fig. 8, the flowrate of the 2 steam dump valves is same, because the layout position is closed and the opening set point is same that is 7.85 MPa. In Fig. 9, the

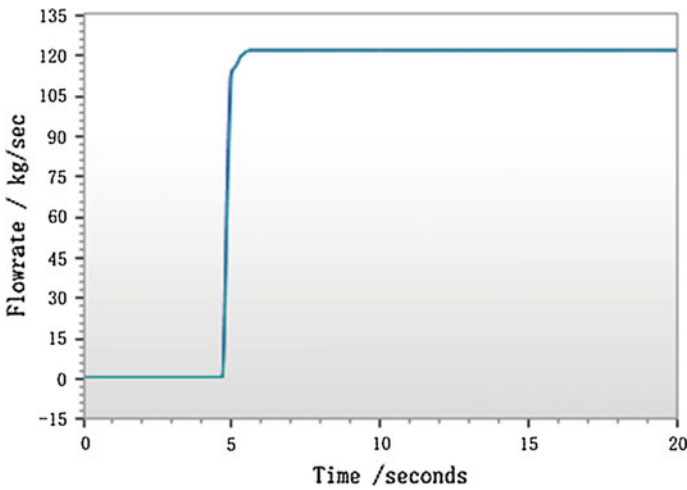


Fig. 8 Flowrate of steam dump valves

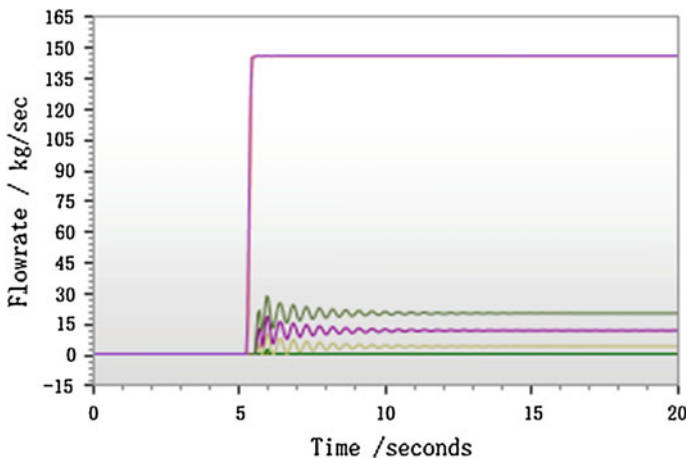


Fig. 9 Flowrate of safety valves

maximum flowrate curve is actually two curves which are for the two safety valves which have the same opening set point 8.5 MPa, the other five curves for the other five safety valves have the same opening set point 8.7 MPa, and these curves from top to bottom represent that the safety valves are farther from the main steam isolation valve gradually. These safety valves have slightly different opening scales. The safety valve which is farthest from the main steam isolation valve has minimum open and flowrate.

4.4 Influence from Relief Device

There is a lot of factor affecting the steam hammer of main steam system, for example elevation variation, the setting of relief device, the setting of piping, and the closing time of main steam isolation valve. This paper just considers the sensitive influence of steam dump changing, the flowrate which belongs to the reasonable range of accident analysis.

This paper considers two assumptive conditions:

Firstly, only the flowrate of the steam dump valve changed from 154 kg/s to 124 kg/s, the other parameters do not change.

Secondly, only setting one train steam dump piping, the other parameters do not change.

If only the flowrate of the steam dump valve changed from 154 kg/s to 124 kg/s, the other parameters do not change, the steam hammer load of the 3# pipe which locates downstream the 1#GV is 12809 N, which increases 1.7% comparing with the before value, while the steam hammer load of the 24# pipe after main steam isolation valve is 16295 N, which falls 1.1% comparing with the before value.

If only setting one train steam dump piping, the other parameters do not change, the steam hammer load of the 3# pipe which locates downstream the 1#GV is 11018 N, which falls 12.5% comparing with the before value, while the steam hammer load of the 24# pipe after main steam isolation valve is 18329 N, which increases 11.3% comparing with the before value.

From the two assumptive conditions, the changing tendency of the steam hammer load of the 3# pipe before the main steam isolation valve is opposite to the 24# pipe after the main steam isolation valve, and the change of the steam hammer load of the second assumptive condition is larger.

The configuration of main steam system affecting the steam hammer is complex, so the reasonable configuration should balance the accident analysis and steam hammer influence.

5 Conclusions

This sample is illustrated to help your understanding on the paper format. We are looking forward to seeing you at the PBNC-2016.

The steam hammer will be induced during fast closing of the MSIV, and the hammer force is continuous pressure fluctuation and impact load in short period; such kind of fluctuations and shocks may cause serious damage to the pipeline and equipment and influence the safety operation of power plant.

The paper combined the layout and device parameters of the main steam system in a nuclear power plant, modeled and calculated the main steam piping which was based on the PIPENET. The paper presents the maximum steam hammer load of partial pipe of 1#GV and related appearing time. It is shown that the maximum steam hammer load is on the 3# pipe before the MSIV and 24# pipe after the MSIV, and the load appearing moment is almost near the totally closing moment of the MSIV. The steam hammer load before the MSIV is smaller than the load after the MSIV due to the relief device which is located before the MSIV.

Besides, the setting of relief device has bigger influence on main steam hammer. The flowrate of the steam dump valve which is closest to the main steam isolation valve is biggest. The flowrate of the safety valve which is farthest to the main steam isolation valve is smallest with slightly open. If only the flowrate of the steam dump valve drops (condition 1) or only setting one train steam dump piping (condition 2), the steam hammer load caused by condition 2 is ten times of the condition 1. Since there is much influence factor for steam hammer which is complex, the configuration of main steam system should consider various factor and accident safety analysis synthetically.

So the steam hammer calculation should be the input for system design and piping stress computational analysis, which is necessary for optimizing the nuclear island main steam piping and has significant meaning for improving safety operation of the main steam system and nuclear power plant.

References

1. ZHAO Jiaming, HAN Shichao, PI Yao, YU Pei, Research on Steam Hammer of Main Steam System in a Nuclear Reactor Type [J], NanFang NengYuan JianShe, 2015, 2(4): 62–66
2. HE Wenjie, PEI Yufeng, GUO Xiaoke, et al. Evaluating and Analysis of Steam Hammer Loads in Steam Piping Systems [J], Jilin Electric Power, 2014, 42(3): 5–8
3. LI Lin, QU Shunli, Application of precise time-history analysis in piped water (steam) hammer calculations [J], Chemical Engineering Design, 2010, 20(6): 18–23

Study on Improvement of Capacity Expansion of Spent Fuel Pit Cooling System in PWR Nuclear Power Plants

Yupei Piyue

Abstract Based on the analysis of domestic second-generation modified million-kilowatt-class nuclear power-generating mature technology, by means of Flowmaster software calculation and design optimization, cooling capacity of spent fuel pit cooling system is evaluated, improved scheme is put forward to increase cooling capacity of spent fuel pit cooling system, and the design scheme that meets the third-generation nuclear power technology is put forward.

Keywords Cooling capacity · Spent fuel pit cooling system · Spent fuel pit cooling pump · Heat calculation

1 Introduction

It is necessary for nuclear power plants to keep replacing the new nuclear fuel and removing the spent fuel throughout the life cycle. The spent fuel is radioactive and continues to emit decay heat; in particular cases, it is possible to return to critical. Therefore, for the spent fuel, the storage, cooling and other issues need to be resolved. In recent twenty years, with the rapid development of Chinese nuclear energy industry [1], the continuous improvement of nuclear power installed capacity, and the increasing of production and accumulation of spent fuel, the pressure on spent fuel in plant storage occurs directly. On the one hand, many nuclear power plants have taken the spent fuel intensive storage. On the other hand, the time limit for the storage of spent fuel in the plant has been raised from 7–10 to 20 years, which means that the maximum number storage of spent fuel elements in a power plant can reach thousand. Also with the improvement of fuel handling machine, at present nuclear power plant refueling method and refueling period have great changes relative to the original design basis. It changes from original design basis that is one-third of the refueling method to full core refueling method;

Y. Piyue (✉)

China Nuclear Power Engineering CO. LTD, Shenzhen 100840, China
e-mail: yupei@cnpe.cc

moreover, refueling time shortens from 14 days to 6–8 days, this may cause the cooling capacity of the spent fuel pool cooling system insufficient. At the Fukushima nuclear accident, due to lack of pool cooling water, a plurality of component faces meltdown risk [2]. Fukushima nuclear accident highlights the importance of fuel storage safety and cooling, Chinese nuclear safety agency is also pay attention to this issue during the dialogue. Based on the analysis of the mature technology of the second-generation nuclear power plant, the cooling capacity of the spent fuel cooling system is calculated in operated and building power plant, and the improvement scheme of the cooling capacity of the spent fuel cooling system is put forward in this paper by calculation and analysis. It satisfied the third-generation NPP technology.

2 Calculation of Heat Load of Spent Fuel

For the operated and constructing nuclear power plant, fuel management scheme is usually in accordance with the 12 months period. The heat load of the spent fuel includes the whole reactor core and the heat load of the spent fuel discharged into the pool more than one cycle.

The decay heat of the whole reactor core discharged into the pool after shutdown is shown in Fig. 1.

Assuming that the spent fuel pool is full at 20 years, a year refueling period is 305 days. The 19 batches spent fuel assemblies discharged into the spent fuel pool over a cycle. Considering about the envelope of the calculation results, the spent fuel assemblies in transition cycle are overlooked. The heat load of 19 batches of spent fuel assemblies removed into the spent fuel pool is 1.115 MW. Due to the

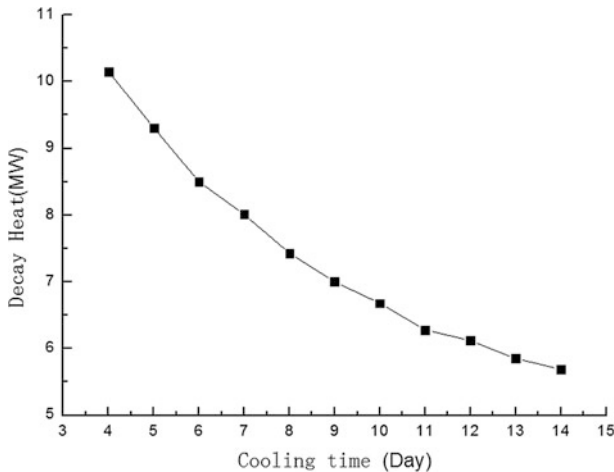


Fig. 1 Core decay heat curve

Fig. 2 The proportion of decay heat with different refueling time

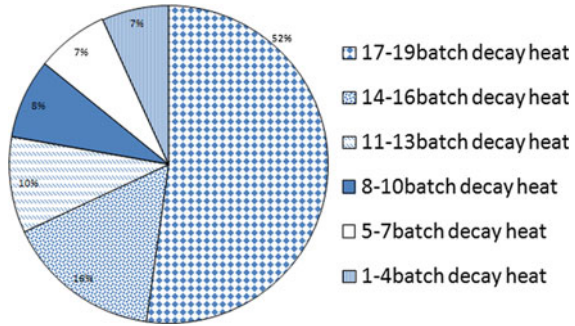


Table 1 The decay heat of spent fuel assemblies with different refueling completion time

Time (day)	Heat (MW)	Time (day)	Heat (MW)	Time (day)	Heat (MW)
4	11.265	8	8.545	12	7.235
5	10.4245	9	8.1157	13	6.9685
6	9.615	10	7.795	14	6.805
7	9.1249	11	7.3969		

different batches assemblies suffered different cooling time, the proportion of decay heat with different refueling time is shown in Fig. 2.

From Fig. 2, we can see that the earlier the fuel assemblies are discharged into the pool, the effect of the fuel assemblies on the heat load is lower. Therefore, for the simplified calculation, the thermal load of the spent fuel assemblies has been discharged into the pool is 1.115 MW.

Because the refueling time shortens from 14 days to 6–8 days, it is necessary to analyze heat load with different refueling time, the load including the decay heat of the total core and the spent fuel stored in the pool; the calculation results are shown in Table 1.

3 Cooling Capacity Evaluation of Generation Two Cooling System

The second-generation improved pressurized water reactor spent fuel pool cooling system design condition is that: using 1/3 core reloading method, when the temperature of the component cooling water system is 35 °C, spent fuel pool cooling system with one train operation, component cooling water side with series operation ensure spent fuel pool temperature below 50 °C. The flow diagram is shown in Fig. 3.

However, with refueling technology improvement, the heat load is enhanced caused by the whole core reloading and it is necessary to reevaluate the cooling capacity of the system. The calculation method of heat efficiency of heat exchanger

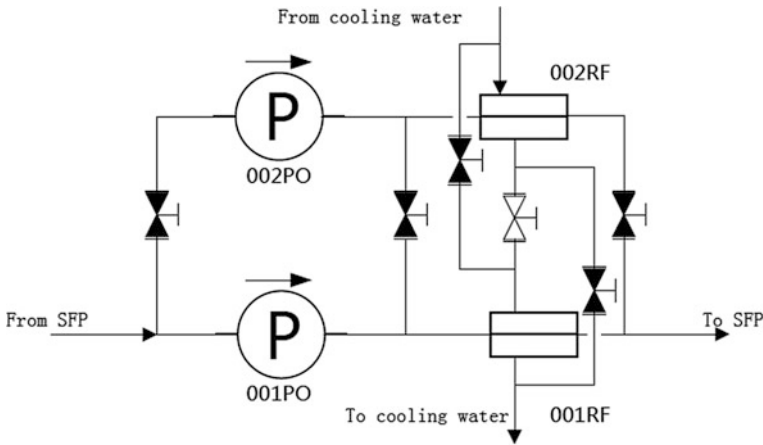


Fig. 3 Concept flow diagram of generation two reactor spent fuel pit cooling system

has 4 kinds; commonly, ϵ -NTU method and logarithmic mean temperature difference (LMTD) method are used. The heat exchanger of Flowmaster software calculation unit is used ϵ -NTU method, and specific methods are as follows

$$q = \epsilon C_{\min}(t_{hi} - t_{ci})^* \tag{1}$$

*h-hotside; c-coolside; i-inlet; o-outlet;

C_{\min} Min capacity between two sides;

ϵ Efficiency of heat transfer;

When the heat loss of the heat exchanger to environment is overlooked, the heat generated by the hot fluid is equal to the heat absorbed by the cold fluid [3]. That is:

$$q = C_c(t_{co} - t_{ci}) \tag{2}$$

$$q = C_h(t_{hi} - t_{ho}) \tag{3}$$

In this paper, the Flowmaster software is used to build the system model, as shown in Fig. 4.

Per heat exchanger spent pool side flow is 542.25 m³/h, equipment cooling water side flow is 361.5 m³/h. Ensuring the spent fuel pool temperature is lower than 50 °C, different refueling time corresponds to the equipment cooling water temperature is calculated as shown in Table 2.

According to the above table analysis, in the case of considering the dirt coefficient, if refuel is completed in the seventh days after shutdown, according to the spent fuel pool cooling system operation, the temperature of the water in the equipment cooling water system must be lower than 20 °C, for the requirement that the temperature of spent fuel pool is lower than 50 °C. According to the site of the

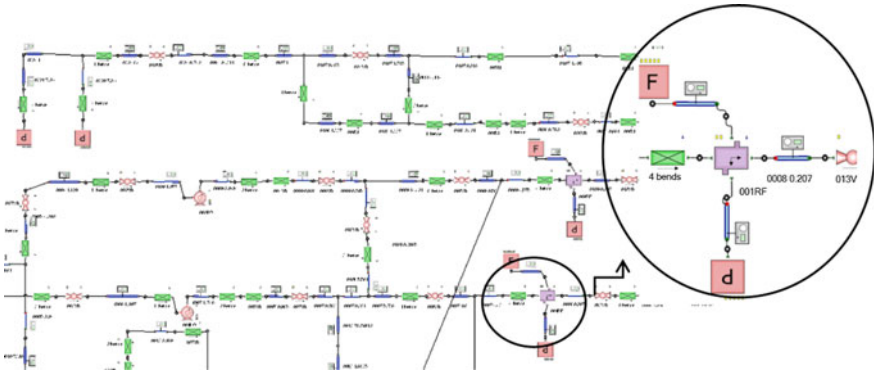


Fig. 4 Spent fuel pit cooling system mode

Table 2 The temperature requirement of component cooling system with different refueling completion time

Day	14	13	12	11	10	9	8	7
Tci (°C)	27	27	26	25	24	23	22	20

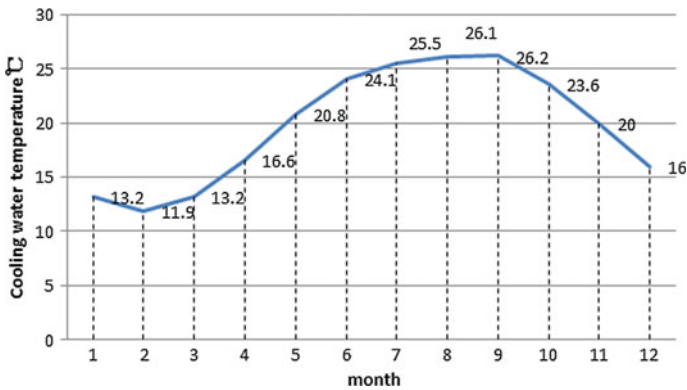


Fig. 5 Sea temperature with different months

nuclear power plant distribution, this requirement in the summer is difficult to meet, as shown in Fig. 5, cooling water temperature for a domestic nuclear power plant.

Therefore, to meet the character that the layout conditions and the progress are fixed in the operated plant and plant in construction, the improved method is supplied to fulfill the requirements of the project schedule and cooling capacity requirements.

4 Analysis of Improved Method in Operation Plant and the Plant Under Construction

4.1 Changing Operation Mode of System in Operated Plant

For operated plant, the main equipment of the spent fuel cooling system includes the spent fuel cooling water pump and the tube shell type heat exchanger: they are arranged in the fuel building, the plant layout is very compact, and increasing the number of equipment and modifying the pipeline will have a great impact on the operation of power plant. Therefore, we propose to modify the operating mode of the spent fuel pool cooling system and the cooling water side to enhance the cooling capacity of the system without modifying the existing lines.

As shown in Fig. 6, as active part of the system such as the pump need to meet the principle of a single failure, only one pump can be put into operation; therefore, only the mode where a pump and two heat exchanger operation are put into operation to improve cooling capacity can be used. Opening the column isolation valve and adjusting the equipment cooling water system pipeline valve from series to parallel both increase the heat exchanger area and reducing the cooling water inlet temperature of each heat exchanger. The per heat exchanger spent pool side flow is $180 \text{ m}^3/\text{h}$, equipment cooling water flow is $542.25 \text{ m}^3/\text{h}$, and to ensure the spent fuel pool temperature is lower than $50 \text{ }^\circ\text{C}$, different refueling time corresponds to the equipment cooling water temperature is calculated, as shown in Table 3.

According to the above analysis: in the case of considering the dirt coefficient, if refuel is completed in the seventh day after shutdown, according to the spent fuel pool cooling system operation, the temperature of the water in the equipment cooling water system must be lower than $20 \text{ }^\circ\text{C}$, for the requirement that the temperature of spent fuel pool is lower than $50 \text{ }^\circ\text{C}$. According to seawater

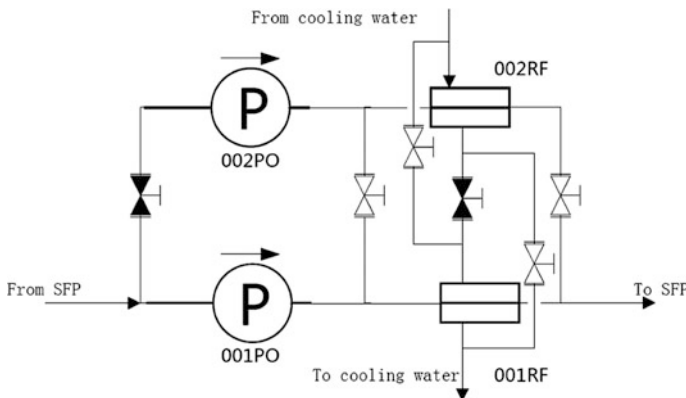


Fig. 6 Concept flow diagram of the amended operation mode

Table 3 The temperature requirement of component cooling system with different refueling completion time after changing the operation mode

Day	14	13	12	11	10	9	8	7
Tci (°C)	29	28	27	26	25	24	23	22

temperature in Fig. 5, when refueling in the summer, it needs to shutdown after 11 days of complete refueling can meet spent pool temperature requirements. The improved scheme can provide a great help to ease the difficulties in the field operation.

4.2 Add a Cooling Pump in Plant Under Construction [4]

As shown in Fig. 7 on the basis of the spent fuel cooling system, a pump (006PO) and the corresponding connecting pipes, instrumentation and valves are added. The new pump type and performance parameters is same as the existing pump (horizontal axial flow pump, the flow is 421.5 m³/h). During the refueling operation, 006PO-001RF 002PO-002RF are in serve, 001PO is as backup of the two series, cooling water side operated in parallel, same as Sect. 4.1. Per heat exchanger spent pool side flow is 361.5 m³/h, and equipment cooling water side flow is 542.25 m³/h. To ensure the spent fuel pool temperature is lower than 50 °C, different refueling time corresponds to the equipment cooling water temperature is calculated and is shown in Table 4.

According to the analysis on the table, spent fuel cooling system through the method adding a pump that three pumps in the two pumps operating in parallel manner, if the refueling is completed in 7 days, equipment cooling water temperature 35 °C will be able to meet the requirement that the spent fuel pool temperature

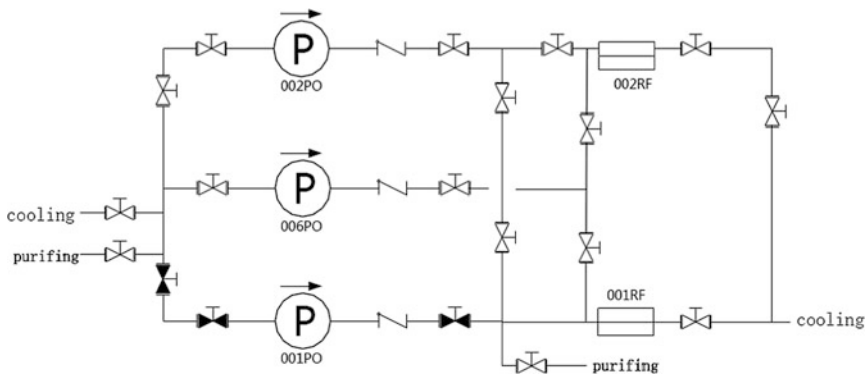


Fig. 7 Concept flow diagram of increasing one pump

Table 4 The temperature requirement of component cooling system with different refueling completion time after increasing one pump

Day	12	11	10	9	8	7	6	5	4
Tci (°C)	35	35	35	35	35	35	34	32	31

is lower than 50 °C. Even the refueling is completed in 4 days, cooling water temperature is lower than 31 °C to meet refueling requirements.

5 Conclusions

- (1) In this paper, the heat load of the spent fuel pool is calculated by using Flowmaster, and the cooling water temperature can be used to guide the operation of nuclear power station.
- (2) Through evaluation cooling capacity for second-generation improved pressurized water reactor spent fuel pool cooling system, when temperature of cooling water system is below 20 °C, the requirement that refueling after shutdown 7 days can be satisfied.
- (3) The mode for operational plant to improve the cooling capacity of the system is by changing the operation mode, and the mode for construction plant is by adding a new cooling pump to improve the cooling capacity of the system and is feasible.

References

1. Safety Analysis Report of Spent Fuel Cooling Systems for PWR Nuclear Power Plant, A 2014.12.
2. Hanxu, Changmeng, Wengfangjian, Study on Design of Spent Fuel Cooling Systems for PWR Nuclear Power Plant [J]. Nuclear Safety, 2012. 1. P 42–44.
3. T. Kuppan 《Heat exchanger design manual》 [D], Beijing. China petrochemical press.
4. Changmeng, Wengfangjian, Hanxu. Analysis of the Design Improvement of Spent Fuel Pool Cooling System [J], Nuclear Safety, 2012. 2. P 72–75.

Author Biography

Yupei (1985–), FM, Engineer, mainly engaged in nuclear power plant system design.

Study on Standards Applicable for Primary and Secondary Water Chemical Analysis in the Third-Generation PWR

Qinghua Li, Guangfei Wang, Yao Pi, Bo Li and Xiaoli Yang

Abstract With starting construction of the third-generation PWR, study on standards applicable for primary and secondary water chemical analyses in the third-generation PWR, which are the bases to establish the water chemical analysis procedures, becomes the subject required to be developed and concluded urgently. The aim of the study was to compare the primary and secondary water chemical parameters and limits in the third generation with that of the second generation plus pressure water reactor, then determine the Chinese national and guild standards applicable for primary and secondary water chemical analysis in the third-generation PWR, and put forward analysis methodologies for chemical parameters no applicable standards.

Keywords The third generation · The second-generation plus PWR · Primary and secondary water chemical analysis · Chinese national and guild standards · Analysis methodologies

Q. Li (✉) · G. Wang · Y. Pi · B. Li · X. Yang
CNPE, Beijing, China
e-mail: liqh@cnpe.cc

G. Wang
e-mail: wanggf@cnpe.cc

Y. Pi
e-mail: piyao@cnpe.cc

B. Li
e-mail: libo@cnpe.cc

X. Yang
e-mail: yangxl@cnpe.cc

1 Foreword

With starting construction of the third-generation PWR, study on the Chinese national and guild standards applicable for primary and secondary water chemical analyses, which are the bases to establish water chemical analysis procedures, becomes the subject required to be developed and concluded urgently.

By collection and study the primary and secondary water chemical parameters and limits in the third-generation PWR and the second-generation plus PWR, besides Chinese national and guild standards applicable for the primary and secondary water chemical analysis in the second-generation plus PWR. Then, comparison of the primary and secondary water chemical parameters and limits between the two types PWR is made to determine the Chinese national and guild standards applicable for primary and secondary water chemical analysis in the third-generation PWR and put forward analysis methodologies for chemical parameters no applicable standards.

2 Comparison of Primary and Secondary Water Chemical Parameters and Limits Between the Two Types of PWRS

A domestic 1000 MW second-generation plus PWR in service is selected as representation, and the differences in primary and secondary water chemical parameters and limits between the two types of PWRs are compared.

2.1 *Comparison of the Primary Water Chemical Parameters and Limits Between the Two Types of PWRs*

The principal function of the primary system coolant in the third-generation PWR is to provide for safe, reliable, and efficient transfer of heat from the reactor core to the secondary system. Consistent with the design of the reactor core, the reactor coolant is also required to support, along with the use of control rods, reactivity control of the core. A suitable coolant additive (boric acid) is maintained for this purpose in the primary system at an appropriate concentration during the course of the fuel cycle, i.e., the water chemistry of the primary system is a boron water system.

As such, the water quality and how it is controlled must support these requirements through a program as follows:

- (1) The presence of halogens (e.g., chloride) and other impurities (e.g., calcium, magnesium, aluminum) in the system is controlled in order to prevent impurity ingress as low as possible.

- (2) Additives for the control of pH and oxidation potential (lithium hydroxide to offset acidity from boric acid, hydrazine during startup, then sufficient dissolved hydrogen, minimizing ongoing corrosion through the addition of zinc, etc.) are used to minimize corrosion of the key material boundaries, minimize corrosion product transport, and minimize the radioactivity in the system.
- (3) Continuously purify and filter impurities, as well as solid and dissolved radioactive materials.

Comparing the primary water chemistry control mode with that in the second-generation plus PWR, the primary water chemistry control modes and objectives are consistent with each other, except that minimizing ongoing corrosion through the addition of zinc. For comparison of the primary water chemical characteristics for the two types of PWRs, refer to Table 1.

Compared with the second-generation plus PWR, conclusion of the primary water chemical characteristics for the third-generation PWR is as follow:

Table 1 Comparison of the primary water chemical characteristics

		The third generation	The second generation plus
Parameters	Units	Limits [1]	Limits [2]
pH		4.2–10.5(25 °C)	6–10.5(25 °C)
Conductivity	μS/cm	1–40	–
Boric acid	ppm	<4000	<2500
Hydrogen	cc H ₂ (STP)/kg H ₂ O	25–50	25–50
Oxygen	ppm	<0.1	<0.10
Chloride	ppm	<0.15	<0.15
Fluoride	ppm	<0.15	<0.15
Lithium	ppm	<6	<5
Silica	ppm	<1.0	<1.0
Aluminum	ppm	<0.05	<0.08
Calcium + magnesium	ppm	<0.05	–
Calcium	ppm	–	<0.08
Magnesium	ppm	<0.025	<0.05
Zinc	ppm	<0.04	–
Suspended solids	ppm	<0.2	<0.3
Sulfate	ppm	<0.15	<0.15
Hydrazine	ppm	<10	–
Hydrogen Peroxide	ppm	<15	–
Iron, nickel	ppm	<10	–

- (1) The limits for hydrogen, oxygen, chloride, fluoride, silica, and sulfate are consistent in the two types of PWRs.
- (2) The limits for boric acid and lithium and pH are higher than in the second-generation plus PWR, which is consistent with the boron–lithium coordinate curve in the third-generation PWR.
- (3) The limits for calcium, magnesium, aluminum, and suspended solids are little higher than that in the second-generation plus PWR, minimizing the deposition on the surface of the fuel rod shells.
- (4) Zinc injection is used in the third-generation PWR.
- (5) There are limits requirements for conductivity, hydrazine, hydrogen peroxide and iron, and nickel in the third-generation PWR. Although there are no specific limits for above parameters in the second generation PWR, in order to judge the system operation states and corrosion of devices and pipes, these parameters have also been analyzed as requirements.

2.2 Comparison of the Secondary Water Chemical Parameters and Limits Between the Two Types of PWRs

The secondary water chemistry control mode in the third-generation PWR adopts the all-volatile treatment (AVT) to regulate the oxidation–reduction conditions in the secondary water loop. The chemical additives include hydrazine and ammonia (or amine, or compounds of ammonia and amine). Hydrazine is used to reduce the dissolved oxygen, and ammonia or amine is used to regulate pH.

The AVT serves to:

- (1) Ensure complete integrity of devices in the secondary loop, including the steam generators, turbines, and auxiliary devices.
- (2) Reduce or minimize the deposits on the vanes of turbine and the heat transfer surfaces.
- (3) Reduce the dissolved oxygen in feedwater prior to entry into the steam generator.
- (4) Reduce the possibility for the formation of free acids or bases.

Compared with the secondary water chemistry control mode in the second-generation plus PWR, the AVT is adopted for both of them. For comparisons of the secondary water chemical characteristics for the steam generator blowdown water, feedwater and condensate water between the two types of PWRs, refer to Tables 2, 3 and 4 separately.

The secondary water chemical characteristics are similar because their secondary water chemistry control modes are consistent for both the two types of PWRs.

Table 2 Comparison of the steam generator blowdown water chemical characteristics

		The third generation	The second generation plus
Parameters	Units	Limits [1]	Limits [2]
Cation conductivity	$\mu\text{S/cm}$	<1–7	<7
Sodium	ppb	0–1000	500
Chloride	ppb	0–1000	<500
Sulfate	ppb	0–1000	<1000
pH (25 °C)	–	9.00–10.50	8.8–10.5
Specific conductivity (25 °C)	$\mu\text{S/cm}$	0–100	–
Silica	ppb	0–300	<1000
Hydrazine	ppm	0–400	75–200
Ammonia	ppm	–	<10
Oxygen	ppb	≤ 100	<100
Suspended solids	ppb	<1000	<1000

Table 3 Comparison of the main feedwater chemical characteristics

		The third generation	The second generation plus
Parameters	Units	Limits [1]	Limits [2]
pH 25 °C		8.5–10.5	8.8–10
Ammonia	ppm	–	As pH requirement
Hydrazine	ppb	20–1000	$>3[\text{O}_2]$ and ≥ 100
Oxygen	ppb	≤ 100	<100
Total iron	ppb	≤ 20	<100
Total copper	ppb	≤ 1	–
Specific conductivity (25 °C)	$\mu\text{S/cm}$	0–100	–
Cation conductivity (25 °C)	$\mu\text{S/cm}$	≤ 1.0	<1
Suspended solids	ppb	≤ 100	<100
Sodium, chloride and sulfate	ppb	≤ 1.0	<5
Silica	ppb	≤ 20	–

The specific differences for the same parameters in the same kind of water are possibly due to the differences in their devices design and operation modes in the secondary loop. The main specific differences in their water chemical characteristics are as follow:

- (1) The limits in the steam generator blowdown water are almost same.
- (2) The limits of total iron, sodium, chloride, and sulfate in the feedwater are more restricted than in the second-generation plus PWR, benefiting to reduce the corrosion in the secondary loop and maintain the thermodynamics performance of system devices.

Table 4 Comparison of the condensate water chemical characteristics

		The third generation	The second generation plus
Parameters	Units	Limits [1]	Limits [2]
pH 25 °C		9.0–10.5	8.8–10.0
Hydrazine	ppb	20–1000	>3[O ₂]和 ≥100
Oxygen	ppb	≤10	<12
Cation conductivity (25 °C)	μS/cm	≤0.3	<0.5
Specific conductivity (25 °C)	μS/cm	3–30	–
Suspended solids	ppb	–	<100
Total iron	ppb	–	<100
Sodium	ppb	≪1.0	<5
Chloride		–	–
Sulfate		–	–
Silica	ppb	≤20	–
TOC	ppb	<100	–
TDS	ppb	<1	–

- (3) There are definite limits requirements for TOC, TDS, and total copper in the condensate water. The inquiry finds that the above parameters are analyzed periodically too in the domestic second-generation plus PWR; the chemical monitor indicates that the content of above parameters is too low to be ignored, and there are no big changes, so the above limits are not definite in the practical chemical surveillance.

3 The Determination on the Standards and Methodologies Applicable for the Primary and Secondary Water Chemical Analysis in Third-Generation PWR

The above research result indicates that the primary and secondary water chemical characteristics are almost same because their water chemistry control modes are consistent for the two types of PWR. So the Chinese national and guild standards adopted in the second-generation plus PWR are basically applicable for that in the third-generation PWR.

The applicable standards and methodologies can be determined based on the above research as follows:

- (1) For the parameters and limits consistent with the second-generation plus PWR, the Chinese national and guild standards for water chemical analysis of these parameters can be determined by searching the related Chinese national and guild standards (update revision) base on the second-generation plus PWR.

- (2) For the parameters and limits special or big different from the second-generation plus PWR, firstly select related Chinese national and guild standards, then analyze, and research the applicability of these standards for monitoring of the parameters.
- (3) For the parameters including the dissolved hydrogen, lithium hydroxide, and hydrogen peroxide, no applicable Chinese national and guild standards can be searched. The analysis methodologies can be adopted based on the established second-generation plus PWR because these parameters and limits are almost same.

4 Conclusions

By the above study, the Chinese national and guild standards applicable for the primary and secondary water chemical analysis in the third-generation PWR can be determined. For the parameters no applicable analysis standards, applicable analysis methodologies can also be put forward. The lists of the Chinese national and guild standards and analysis methodologies are the bases to establish the water chemical analysis procedures in the third generation of China.

References

1. EPRI Pressurized Water Reactor Primary and Secondary Water Chemistry Guidelines-revision 6.
2. Chemical Characteristic of Primary and Secondary Coolant of Lingao Units 3,4-revision B.

Authors Biography

Qinghua Li from China Nuclear Power Engineering Co., LTD (CNPE), engages in site laboratory design and water chemistry research on NPPs.

Guangfei Wang from China Nuclear Power Engineering Co., LTD (CNPE), engages in nuclear auxiliary system design on NPPs.

Yao Pi from China Nuclear Power Engineering Co., LTD (CNPE), engages in nuclear auxiliary system design on NPPs.

Bo Li from China Nuclear Power Engineering Co., LTD (CNPE), engages in nuclear auxiliary system design on NPPs.

Xiaoli Yang from China Nuclear Power Engineering Co., LTD (CNPE), engages in general design and research management on NPPs.

Study on the Localization of Instrumentation Installation Materials for AP1000

Shuen Lu, Chengli Qin and Haibo Wu

Abstract This paper analyzed the standards of instrumentation installation components for the nuclear island of AP1000 NPP, made a comparison with Chinese standards, studied the localization of the instrumentation tube and fittings, and proposed the material substitution principles during construction. To decrease the quantity of changes, materials of original design will be used for priority. If original materials cannot be bought in China, they can be substituted by materials of national standards. If the substitution is needed the American standards, national standards should be compared carefully. The chemical composition of two materials should be similar. The composition that is beneficial to the performance of the material should not be lower than the original material, while composition that is harmful should not be higher than the original. And the mechanical performance of the material should not be lower than the original material.

Keywords Localization · Material · Standards · Instrumentation installation

1 Introduction

AP1000 reactor was designed by Westinghouse, and the materials for instrumentation tubes, fittings, and supports are mainly of American standards. According to the experiences of referenced power plants, during the construction, some of the American standard materials cannot be bought in China and the construction had to be delayed. To avoid such problems in the construction of subsequent AP1000 power plants, this paper studied the localization of materials for instrumentation tubes, fittings, and supports.

S. Lu (✉) · C. Qin · H. Wu
China Nuclear Power Engineering Co., Ltd., Zhengzhou Branch,
Zhengzhou, Henan, China

© Springer Science+Business Media Singapore 2017
H. Jiang (ed.), *Proceedings of The 20th Pacific Basin Nuclear Conference*,
DOI 10.1007/978-981-10-2314-9_23

283

2 Requirements of Instrumentation Installation Materials for AP1000

2.1 Requirements of Installation Materials

There are four classifications of instrumentation tubes and fittings of AP1000: YBB, YBC, YBD, and YBE the materials of which are all austenitic stainless steel. The design standards for them are given in Table 1.

Design standard for safety class tubes and fittings (YBB/YBC) is ASME BPVC (BOILER & PRESSURE VESSEL CODE) Sect. III, Rules for Construction of Nuclear Facility Components, in which part NC is for class B components and part ND is for class C components.

The design standard for non-safety class (YBD/YBE) tubes and fittings is ASME B31.1 Power Piping.

The material standards for instrumentation tubes and fittings are shown in Table 2. Material of safety class components is of ASME standard and that of non-safety class is of ASTM standard. When materials from ASTM are adopted by ASME to use for pressure equipment, this material will become ASME material. Most of the ASME materials are from ASTM. In each ASME material code, there is an introduction to the relation between ASTM materials. Usually there are more testing items in ASME code than in ASTM.

The comparison between ASME SA-213 and ASTM A 213: In ASME code (2004, the subsequent quotations are all 2004 version) SA-213 there is a special notification: Identical with ASTM Specification A 213/A 213M-99a except for the additional H grade heat treatment requirements in 6.4 and the deleted part 11.5 and the added T92 class in 6.13. The material for instrumentation tube is 316 SS which has no relation with modification of parts 6.4 and 6.13. The deleted 11.5 part of ASTM A 213 is for hydrostatic test. In part 4.1 of SA-213, it points out materials of this code should follow A 450/A 450M of current version if there is no additional regulation in this specification. In A450, there are requirements for hydrostatic test. So despite the deleted part 11.5, the requirement of ASME code is not lower than that of ASTM. Above all, for 316 SS instrumentation tubes in AP1000, there is no difference between ASME SA-213 and ASTM A 213.

ASME SA-479 is Specification for Stainless Steel Bars and Shapes for Use in Boilers and Other Pressure Vessels, which is identical with ASTM A479/A479M-99a.

Table 1 Design standards for instrumentation tubes and fittings

Materials	Classification	Codes/standards
Tubes and fittings	YBB	ASME BPVC III-NC
Tubes and fittings	YBC	ASME BPVC III-ND
Tubes and fittings	YBD/YBE	ASME B31.1

Table 2 Material standards for instrumentation tubes and fittings

Components	Classification	Standard	Classification	Standard
Tubes	YBB/YBC	ASME SA-213 TP 316 SEAMLESS	YBD/YBE	ASTM A-213 TP 316 SEAMLESS
Ball valves (tube) and check valves	YBB/YBC	ASME SA-479 GR 316	YBD/YBE	ASTM A-479 GR 316
Nozzle seats	YBB/YBC	ASME SA-479 GR 316	YBD/YBE	ASTM A-479 GR 316
Flanges	YBB/YBC	ASME SA-182 GR 304L, B16.5	YBD/YBE	ASTM A-182 GR F316L, B16.5
Bends	YBB/YBC	ASME SA-479 GR 316	YBD/YBE	ASTM A-479 GR 316
Tees	YBB/YBC	ASME SA-479 GR 316	YBD/YBE	ASTM A-479 GR 316
Socket weld joint	YBB/YBC	ASME SA-479 GR 316	YBD/YBE	ASTM A-479 GR 316
Plugs	YBB/YBC	ASME SA-479 GR 316	YBD/YBE	ASTM A-479 GR 316
Tube caps	YBB/YBC	ASME SA-479 GR 316	YBD/YBE	ASTM A-479 GR 316
Gasket seal	YBB/YBC	FLEXITALLIC STYLE CG (CL150/300)CGI (> CL600)	YBD/YBE	FLEXITALLIC STYLE CG (CL150/300)CGI (>CL600)
Bolts/nuts	YBB/YBC	ASME SA-193 GR B7 STUDS, W/SA-194 GR 2H HEX NUTS FOR CL150 THRU CL1500 B16.5 FLANGES.	YBD/YBE	ASTM A-193 GR B7 STUDS, W/A-194 GR 2H HEX NUTS FOR CL 1500 B16.5 FLANGES.

ASME SA-182/SA-182M is Specification for Forged or Rolled Alloy-Steel Pipe Flanges, Forged Fittings, and Valves and Parts. This specification is identical with ASTM A182/A182M-99 except for the added S3328 and S30815, direct heat treatment is not allowed in 5.3.1, and editorial modification in 1.2, 2.1 and Table 2.

There is only pressure class for gasket seal, CG(CL150/300)CGI(>CL600), and no material standard is required.

ASME SA-193 is Specification for Alloy-Steel and Stainless Steel Bolting Materials for High temperature. And it is identical with ASTM Specification A 193/A 193M-98a except for differences in paras. 3.1.1 and 19.4, Note 6 of Table 1, and editorial differences in Table 2.

ASME SA-194 is Specification for Carbon and Alloy Steel Nuts for Bolts for High Pressure or High Temperature Service or Both. It is identical with ASTM

A194/A 194M-01a except for the added part 6.7. Part 6.7 is about the chemical composition of nuts.

For the above material specifications, ASME specifications are stricter than ASTM specifications. This paper will compare ASME specifications with Chinese national material standards.

2.2 The Materials Used for Reactors in Construction

At present, non-safety tubes and fittings in referenced reactors are supplied by domestic suppliers and safety class tubes and fittings are supplied by foreign suppliers (Swagelok). But the standards for the materials are all standards of original design except for the standard of tees. According to the 管道等级表, material for safety class tubes and fittings is ASME SA-479 GR 316. This material in Sanmen NPP is changed to SA-479 GR 316 or SA-182 GR F316. Compared with SA-182, SA-479 adds the requirement of nitrogen content. Reduction in area for SA-182 is 50% and for SA-479 is 40%. SA-182 has better plastic performance and is used for the body of tees which is hard to be made in bars. Other components like fittings still use SA-479. The supplier Swagelok has no production base in China. All the safety class tubes and fittings are purchased from America.

3 Comparison of Material Standards

3.1 Differences in Standard Content

In China, there is no standard system like ASME. And there is no corresponding relation between national standards of China and ASME code. For example, SA-213 has a corresponding national standard GB 13296. But for SA-479, such national standard has not been found. There is only a similar standard GB/T 1220. This paper takes GB 13296-2007 as an example to analyze the differences between national standard and ASME code.

In GB 13296-2007, there is a notification, ‘this standard corresponds to ASME SA-213/SA-213M-2001 but it is not equivalent to it’

- (1) Scope of application: not so detailed as SA-213.
- (2) Standards quoted: 37 standards are quoted as part of this standard. This is quite different from SA-213 which quotes fewer standards.
- (3) Ordering information: Ordering information part for the two standards is similar.
- (4) Size, shape and weight: The outer diameter is 6–159 mm and wall thickness is 1.0–14 mm. In SA-213, outer diameter is 3.2–127 mm and wall thickness is 0.4–12.7 mm

- (5) Technical requirements: This part includes chemical composition, mechanical performance, and corrosion test.

In national standard, the steel grade is expressed like this: 0Cr17Ni12Mo2N. In ASME code, UNS is used, for example, S31651. S31651 and 0Cr17Ni12Mo2N have similar chemical composition.

- (6) Test method: There are 11 tests totally. Standards for sampling are given.
 (7) Checking rules: Checking department, grouping rules, and quantity of sampling are cleared.
 (8) Package, mark, and quality certification: Standards for package are pointed out.

3.2 Comparison of the Specific Material

The material for instrument tubes and fittings in AP1000 is ASME SA-213/SA-213M TP316. The grade is S31600. According to the chemical composition, it is similar to 0Cr17Ni12Mo2 in GB 13296-2007. This paper will compare the two materials in detail.

3.2.1 Chemical Composition and Mechanical Performance

The comparison of chemical composition and mechanical performance of two materials is shown in Table 3.

The only difference for the two materials is the content of Si and S. Si content in 0Cr17Ni12Mo2 is higher, and content of S is lower. Tensile strength of 0Cr17Ni12Mo2 is higher. In ASME code, there is no density. According to the

Table 3 Comparison of chemical composition and mechanical performance

Items		ASME	GB
		ASME SA-213	GB 13296
Material		S31600	0Cr17Ni12Mo2
Chemical composition	C	≤ 0.08	≤ 0.08
	Si	≤ 0.75	≤ 1.00
	Mn	≤ 2.00	≤ 2.00
	P	≤ 0.040	≤ 0.035
	S	≤ 0.030	≤ 0.030
	Ni	11.0–14.0	11.00–14.00
	Cr	16.0–18.0	16.00–18.00

(continued)

Table 3 (continued)

Items		ASME	GB	
		ASME SA-213	GB 13296	
	Mo	2.0–3.0	2.00–3.00	
Mechanical performance	Tensile strength/Mpa	≥ 515	≥ 520	
	Yield strength/Mpa	≥ 205	≥ 205	
	Min elongation rate %	35	35	
	Hardness	HBW	≤ 192	≤ 187
		HRB	≤ 90	≤ 90
		HV	≤ 200	≤ 200
Density (g/cm ³)		–	7.98	

chemical composition and mechanical performance, 0Cr17Ni12Mo2 of GB 13296 has a better performance.

3.2.2 Requirements of Manufacturing

Smelting method in GB 13296 is quite simple. But in ASME code SA-213, ASTM A450 is quoted to introduce the smelting method which is more specific.

There is no clear requirement for heat treatment in GB 13296-2007. In SA-213, heat treatment method is given.

3.2.3 Dimension Error

Error of outer diameter: For hot-rolled steel, percentage error is used in national standard, while absolute error is used in ASME code. In GB 13296-2007 for hot-rolled tubes ($D < 140$ mm), the permitted error is $\pm 1.25\%D$. In SA-213 for hot-rolled tubes ($D < 101.6$ mm), the error is -0.8 mm to $+0.4$ mm. For cold-rolled tubes, absolute error is used in both national standard and SA-213. In SA-213 for cold-rolled tubes ($D < 25.4$ mm), permitted error is -0.1 mm to $+0.1$ mm. In GB 13296-2007 for cold-rolled tubes ($6 \text{ mm} < D < 30$ mm), the permitted outer diameter error is -0.2 mm to $+0.15$ mm.

Wall thickness errors for the two standards are the same. For hot-rolled tubes, it is 0–40%. For cold-rolled tubes, it is 0–20%.

3.2.4 Experiment Requirements

The tests of two standards are listed in Table 4. The test items for the two standards are similar, but the standards the test items depend on are quite different. For

Table 4 Test items of two standards

ASME SA-213(2004)			GB 13296-2007			
No.	Test items	Standards	No.	Test items	Test method	Sampling method
1	Chemical composition	A751	1	Chemical composition	GB/T 223 GB/T 11170	GB/T 20066
2	Mechanical test	A370	2	Tensile test	GB/T 228	GB/T 2975
3	Flattening test	A450	3	Flattening test	GB/T 246	GB/T 246
4	Reverse flattening test	A450	4	Hardness test	GB/T 230.1 GB/T 231.1 GB/T 4340.1	GB/T 2975
5	Flare test	A450	5	Flare test	GB/T 242	GB/T 242
6	Flanging test	A450	6	Intergranular corrosion	GB/T 4334.5	GB/T 4334.5
7	Hardness test	A450	7	Grain size	GB/T 5394	GB/T 6394
8	Hydrostatic test	A450	8	Hydraulic test	GB/T 241	
9	Underwater pressure test	A450	9	Ultrasonic test	GB/T 5777	
10	Nondestructive electronic test	A450	10	Eddy current test	GB/T 7735	
			11	Hot tensile test	GB/T 4338	GB/T 2975

example, for the flare test and flattening test, requirement for GB 13296 is the wall thickness must be less than 10 mm. But in ASME SA-213, there is no such requirement.

According to the above comparison, for the chosen standard and material, on the chemical composition and mechanical performance, there are few differences between the material of national standards and that of American standards. But on manufacture requirements, dimension error, and test requirements, there exist evident differences. The requirements of American standards are higher than that of national standards.

4 Conclusion

Material standards of a country are part of its industry system. They have close relation with the country's industry level and material technology. It is not wise to judge the performance of two materials only by their chemical composition and

mechanical performance. For safety-grade instrumentation tubes and fittings, it is not advised to design according to national standards. There are no such experiences.

References

1. 王森 纪纲 仪表常用数据手册 化学工业出版社 2006.6.
2. 刘天模 徐庆梓 工程材料 机械工业出版社 2001.9.
3. ASME锅炉及压力容器规范 II 材料 A篇 铁基材料 2004.7.
4. GB 13296-2007锅炉、热交换器用不锈钢无缝钢管.

The Affection Analysis of Cross Talk on Power Range Measured Signal

Chu-hua Tang, Jie Chen and Wei Chen

Abstract Due to the cross talk, the power detected by the upper power range detector includes not only the top part of the core, but also the partial bottom of the core and vice versa. On the basis of detection principle and general mode, it is analyzed how the cross talk effect on power range (PR) measured signal using a simplified neutron scattering model. And then power range measured signal is analyzed based on current AP1000 calculation model. According to the analysis result, the current AP1000 model for PR measured signal is established only under the condition that axial offset is zero or there is a special axial offset.

Keywords Cross talk · Core · Neutron scattering mode · Axial offset · Power range

1 Introduction

As the input to generating the reactor thermal power and the axial flux difference (AFD) in the reactor protection and monitoring system (PMS), the excore power range (PR) channel signals is much important to the reactor over-power protection, the over-temperature ΔT Trip (OTDT) and the over-power ΔT Trip (OTDT) for the PMS, and to the reactor coolant average temperature adjustment and the axial power offset controlling for the plant control system (PLS).

C. Tang
Jinzhou, Hubei, China

J. Chen (✉)
Enshi, Hubei, China
e-mail: ezreal.cccc@outlook.com

W. Chen
Hubei, China

Regretfully, the PR signals cannot be used directly to get the reactor average power, because the power range detector just responds to the neutron escaped from the core periphery fuel assembly. The PR signals cannot be used directly to get AFD as well, because the cross talk between the upper detector and the bottom detector confuses the respective neutron from each other. The methodology has been proposed to solve the first problem in several other papers, and this paper majors to analyze and solve cross talk problem.

2 Conception

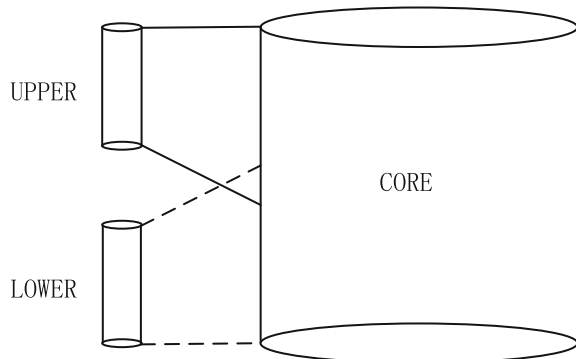
The following conceptions are defined to allow an understanding of their use within this paper.

Weighting factors: The power range nuclear instrumentation detectors see fast neutrons generated by the peripheral assemblies which escape from the vessel. Neutrons generated centrally in the core never reach the excore detectors since they are shielded by peripheral fuel assemblies. Detector technically sees power at each location in core multiplied by a weighting factor for that location. Weighting factors can be determined by neutron transport calculation and are separated into axial and radial values. The weighting factors will be denoted by WPP, WPAO, AO_{WP} , etc.

Mechanical SHIM: Control rods are used to regulate core power and Xenon changes. The control rods will be inserted into the core during power operation with the MSHIM control strategy, which results in significant errors on the excore detector measurements.

Cross talk: Figure 1 illustrates the concept of cross talk. The upper detector sees mostly the top part of the core and the bottom detector sees mostly the bottom of the core.

Fig. 1 Detector point of view



3 The Affection of Cross Talk

Figure 1 illustrates the concept of cross talk. The upper detector sees mostly the top part of the core, and the bottom detector sees mostly the bottom of the core. However, when power goes down, the component of the signal from the bottom of the core that the upper detector sees goes up, so the net signal that the upper detector sees reduces less than the fractional reduction in the peripheral power in the assemblies it sees.

Here we assume that about: show detectors very close and far from the core.

Far from the core, both the detectors just see the core, and the slope of an AO_{ex} versus AO_{wpa} curve would be zero.

Very close and the upper detector would only see the power change in the top and vice versa, so slope would be 1.0.

To evaluate the extent of the cross talk, this paper calculates the shares of the cross talk versus itself, by a simplified model. To simplify the model, the ideal conditions below are assumed:

- (1) The neutrons is isotropy for fuel cell in assemblies;
- (2) The scatter influence by vessel material and coolant is ignored;
- (3) The influence of the neutron traveling is ignored;
- (4) The assembly nearest to detector is considered.

The simplified conditions above reduce the influence of the cross talk, but it can be easily seen the great influence is introduced from the simplified model.

For the neutrons escaped from a fuel cell, only the shares in a fan cone can be seen by the power range detector. The radial angle of the fan cone will changes with the positions of the fuel cell, but the radial angle change is limited to a ignorance value by the geometry structure of the fuel cell and detector. So, the fan cone is replaced by a fan to simplify the calculation, which is given in Fig. 2. By this way, the sum of the angle for every fuel cell on the upper detector and the bottom detector can be used to analysis the influence of the cross talk. Figures 3 and 4 are the result of the simplified model by the parameter of the AP1000 geometry structure.

The assembly is divided equally into 420 cells in radial, and contributions to the upper detector and bottom detector are calculated for each cell. Figures 3 and 4 show the contributions of bottom half assembly, and Fig. 3 presents the ratio of weighting factors that the upper detector and the bottom detector sees each cell at different positions. Nonlinearity is obviously observed, and the cross talk influence is more serious at middle position than at terminal position. Figure 4 shows cross talk power distribution on the condition that the core axial power distribution conforms to cosine pattern.

Summarizing the contributions of the upper detector and so as to the bottom one, it can be concluded that the upper detector sees mostly the top part of the core and that the bottom detector sees mostly the bottom of the core. On the further, the ratio of power that the upper detector sees the bottom of the core versus the upper

Fig. 2 Simplified model of cross talk

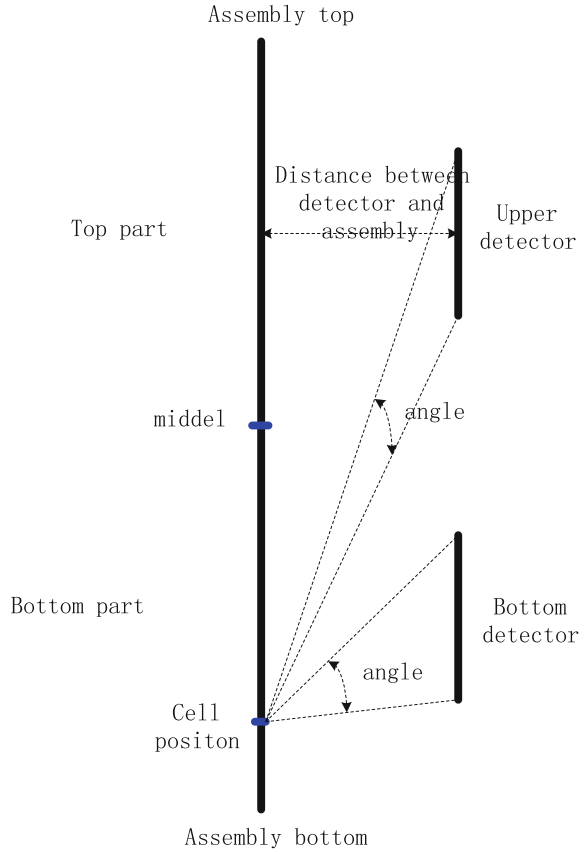


Fig. 3 Cross talk weighting distribution

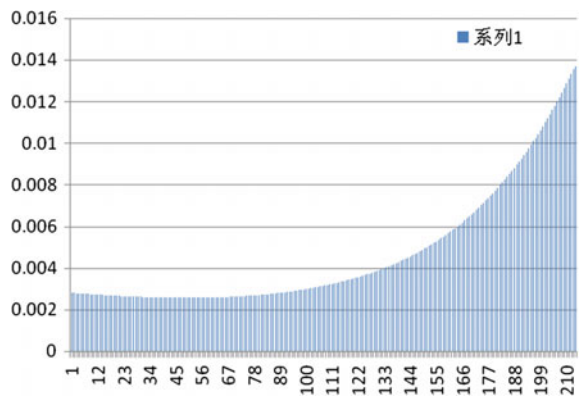
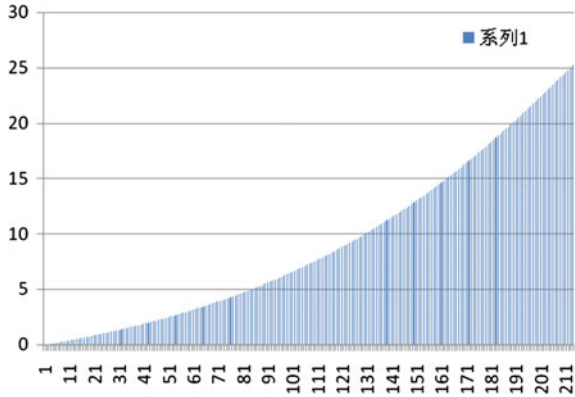


Fig. 4 Cross talk power distribution



detector sees the top part of the core is about 37.9%, and the error is about 27.5% influent by the cross talk if there is no compensation is introduced. In fact, the real condition may be more serious for simplified model is applied in calculation.

4 Model Analysis

The analysis for the incore–excore calibration method is made to illustrate that bias is introduced in nuclear power station due to the cross talk above mentioned [1, 2].

Figure 5 is what the software does with the measured currents in the nuclear power station [1]. P_U and P_L here are the indicated upper and lower powers as calculated by the software. KISC which is E/%RP in Fig. 5 is a coarse scaling constant to convert current into something that looks like power. It is the same for upper and lower detectors, and we do not care what it is since it gets multiplied by another gain in the next blocks, and the composite of the two gains is what matters. The offset is intended to allow for a fitting correlation which we do not need, and we set it to zero. The coolant temperature is introduced to compensate the density change. Then the P_U and P_L is obtained as formula (1) and (2) below:

$$P_U = G_U * KISC * [m_u * WPAO + b_U] * WPP \tag{1}$$

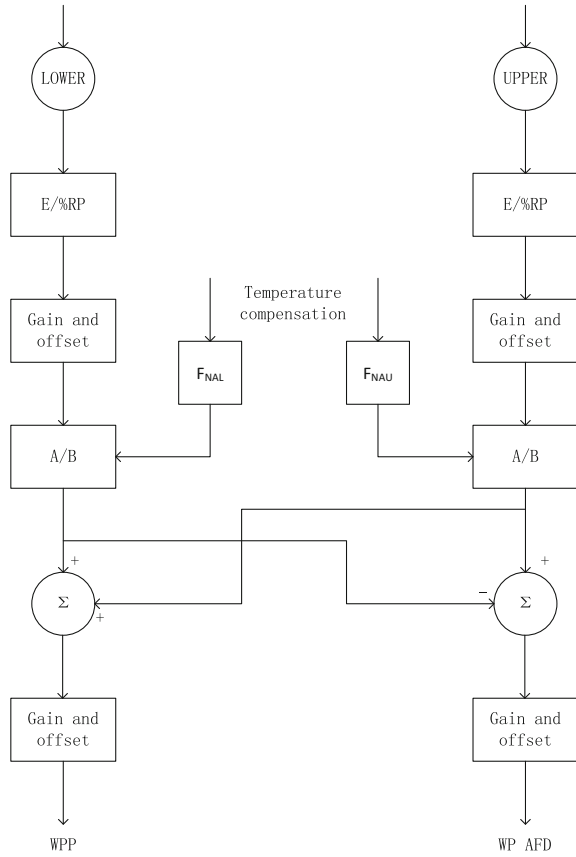
$$P_L = G_L * KISC * [m_L * WPAO + b_L] * WPP \tag{2}$$

When $WPAO = 0$, then:

$$P_U = P_T^{WP} = \frac{WPP}{2} = P_L = P_B^{WP}$$

The gain can be easily obtained by substituting P_U and P_L with $WPP/2$ in formula (1) and (2), then:

Fig. 5 Coarse scaling constant



$$P_U = \frac{m_U}{2 * b_U} * WP\ AFD + \frac{WPP}{2} \tag{3}$$

$$P_L = \frac{m_L}{2 * b_L} * WP\ AFD + \frac{WPP}{2} \tag{4}$$

$$P_U + P_L = WPP + \frac{1}{2} \left[\frac{M_U}{B_U} + \frac{M_L}{B_L} \right] * WPAO \tag{5}$$

$$WP\ AFD = P_T^{WP} - P_B^{WP} = \frac{2}{\left[\frac{m_U}{b_U} - \frac{m_L}{b_L} \right]} * (P_U - P_L) \tag{6}$$

To illustrate that bias is introduced in nuclear power station due to the cross talk above mentioned, the following conception is introduced, and $G_U = G_L = G_1$ is assumed to simplify the calculation.

i'_U the current that the upper detector sees the top part of the core;
 $\Delta i'_U$ the current that the upper detector sees the bottom of the core;
 i'_L the current that the bottom detector sees the bottom of the core;
 $\Delta i'_L$ the current that the bottom detector sees the top part of the core;

Then:

$$WPP = P_U + P_L = G_2 * (i'_U + \Delta i'_L + i'_L + \Delta i'_U) \quad (7)$$

$$WP AFD = (P_U - P_L) * G = G_1 * (i'_U + \Delta i'_L - i'_L - \Delta i'_U) * G \quad (8)$$

The real AFD in core is:

$$WP AFD' = G_1 * (i'_U + \Delta i'_U - (\Delta i'_L + i'_L)) \quad (9)$$

The formula (8) should be equal to formula (9), then:

$$\begin{aligned}
 G_1 * (i'_U + \Delta i'_U - (\Delta i'_L + i'_L)) \\
 = G_1 * (i'_U + \Delta i'_L - i'_L - \Delta i'_U) * k
 \end{aligned} \quad (10)$$

And then:

$$\begin{aligned}
 (1 - k)i'_U + (1 + k)\Delta i'_U \\
 = (1 - k)i'_L + (1 + k)\Delta i'_L
 \end{aligned} \quad (11)$$

When WPAO = 0, the formula (11) is always equal, this can be easily derived from the analysis in section three.

On the condition that $\Delta i'_U$ is linear to i'_U , and $\Delta i'_L$ is linear to i'_L , then:

$$\begin{aligned}
 (1 - k)i'_U + m_1 * (1 + k)i'_U \\
 = (1 - k)i'_L + m_2 * (1 + k)i'_L
 \end{aligned} \quad (12)$$

Then:

$$\frac{i'_U}{i'_L} = \frac{1 - k + m_2 * (1 + k)}{1 - k + m_1 * (1 + k)} \quad (13)$$

During power operation, the axial power change in accordance with a same pattern as the total power changes on the condition that the value of WPAO maintain constant. So, the formula (13) is always equal since the weighting factor is constant for each cell and the axial power is linear to each other, which is given in Figs. 3 and 4.

The formula (10) is not equal except that $WPAO = 0$ and axial power pattern changes in accordance with the same pattern when calibrating maneuver happens. That is to say, the incore–excore calibration method is a constant bias estimation.

5 Conclusion

The paper analyzes the influence of the cross talk and illustrates that the incore–excore calibration method is a constant bias estimation due to the influence of cross talk on the power range detectors. Though the result is derived from the AP1000, it is applicable to the M310.

References

1. In-core Instrumentation System-System Specification Document.
2. Nuclear Instrumentation System-System Specification Document.

The CFD Simulation on Grid-Spacer and Wire for Lead-Cooled Fast Reactor

Gao Xinxin and Qiu Ruoxiang

Abstract In order to separate the fuel rods along radial in one fuel assembly, there are two ways, one is using the grid-spacer, the other is using the wire-wrapped. In this paper, choose three situation (with grid-spacer, with wire-wrapped, without any of them) to show the effects of grid-spacer or wire-wrapped on average temperature, average pressure, coolant velocity, rod temperature. On the other hand, two planes (cross section at the mid-plane through the spacer and cross section 2 cm downstream of the spacer) were carried to analyze effect on temperature and velocity. The results show that the grid-spacer or wire-wrapped has little effect on the average temperature in the sub-channel. But it is clearly shown that the effect on the maximum temperature, average pressure, and coolant velocity. Moreover, local heat transfer was enhanced at the grid-spacer and wire.

Keywords Lead-cooled fast reactor · Grid-spacer · Wire-wrapped · CFD

1 Introduction

Generation IV reactor can solve the issues of nuclear safety, spent fuel, and waste. On the 'GIF' forum in 2012, gas-cooled fast reactor, lead-cooled fast reactor (LFR), molten salt reactor, sodium-cooled fast reactor (SFR), supercritical water-cooled reactor, and ultra-high-temperature reactor were chosen as Generation IV reactor. In those reactors, four was fast neutron reactor; SFR has the highest level of maturity, the most abundant of construction, and operation experience. But the fatal disadvantage is sodium-water reaction, which does not exist in LFR. LFR has the following advantages: (1) high boiling point of lead: it can improve the core thermal parameter and ensure enough thermal margin; (2) low reaction: it would not react with water. Thanks all these advantages, LFR has advanced and strong competitiveness. And the thermal performance of the reactor has great influence on safety,

G. Xinxin (✉) · Q. Ruoxiang
China Nuclear Power Technology Research Institute, Shenzhen, Guangdong, China
e-mail: gao.xinxin@cgnpc.com.cn

reliability, and economy of the reactor. In this paper, CFD computational tool ANSYS FLUENT is used to calculate the thermal hydraulic phenomena in the bare rod channel, with spacer channel, with wire channel. And a good grid, which should have lower pressure drop to enable long-term cooling of core. When maintaining the peak clad temperature below the critical one [1], the maximum velocity should be lower than 2 m/s [2]. It is concluded that the spacer and wire have little influence on the average temperature distribution of the coolant in the channel. But the spacer has a great influence on the maximum temperature of the cladding, and significant influence on the pressure drop and velocity field.

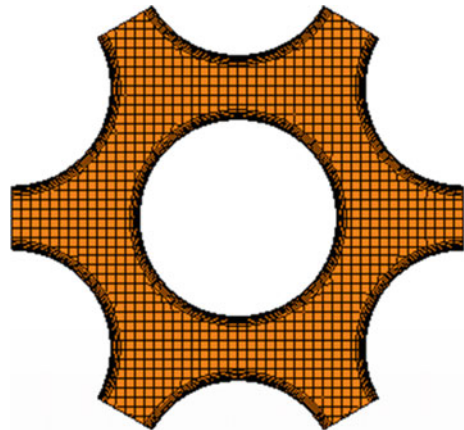
2 Geometry Model

The shape of the core fuel assembly is hexagonal, and the arrangement form of the fuel rod is triangular, $P/D = 1.32$, active length of the fuel pin is 60 cm. In general, there are two forms of fixed mode, wire and spacer. Wire is used for the thin rod and the rod bundle with smaller spacing. In order to investigate the influence of wire and spacer on the flow in the rod bundle channel, it is considered that it is reasonable to use both the spacer and the wire in this channel. In the paper, we choose one rod and its adjacent sub-channel with ICFM-CFD to meshing.

2.1 Bare Rod Model

The computational fluid domain around a single fuel rod is discretized into a mesh of approximately 2 million as shown in Fig. 1, and there are 5 boundary layers.

Fig. 1 Bare rod model



2.2 Rod with Spacer Model

The spacer length is 20 mm, each unit consists of a short board and two long panels (Fig. 2). The spacer is located in the positive center of the active segment. Due to the point contact between the spacer and the fuel rod, the difficulty of the geometric modeling has been increased, and the quality of the grid in the point contact position has deteriorated rapidly, and the point contact is modeled as a small surface contact [3]. Total mesh is 9.22 million.

2.3 Rod with Wire Model

The diameter of wire is 2 mm, and pitch is 100 mm (Fig. 3). The point contact is also modeled as a small surface contact like spacer. Total mesh is 4 million.

3 Boundary Condition

Inlet velocity is 1.5 m/s, inlet temperature is 673 K, and heat flux per fuel pin is $700,000 \text{ W/m}^2$. The following assumptions are set up: (1) spacer and wire do not produce heat; (2) the vertical planes are symmetry plane; and (3) the material of spacer and wire is T91.

In the comparative assessment, SST $k-\omega$ turbulence model is used, which is mentioned by Menter. By mixing function of the standard $k-\omega$ turbulence model and the standard $k-\epsilon$ model together, the core idea is to capture the viscous sub-layer of the flow near the wall by robustness of $k-\omega$ model. But in the mainstream, $k-\epsilon$ model is used, which can avoid the inlet turbulent dynamic

Fig. 2 Spacer model

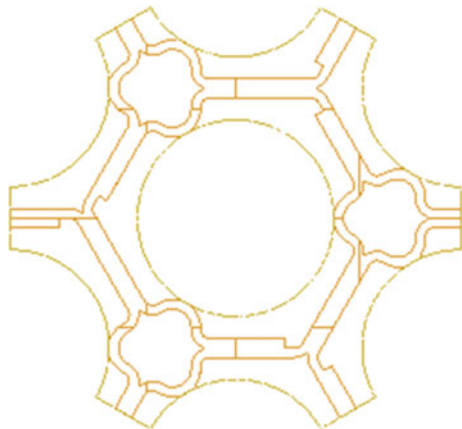


Fig. 3 Wire model

parameters too sensitive to the disadvantage when use $k-\omega$ model. It is found that there is a certain degree of distortion when use k -epsilon model to deal with the geometric model of the spiral wall, but the shear stress transport (SST) model combined with k -epsilon and k - model can be simulated well [4].

The properties of lead are referred to Lead-Bismuth Handbook (2015) [5].

4 Results and Analysis

4.1 Influence of Spacer

To analyze two surfaces near the position of spacer: We can use Plane A (cross section through the spacer) and Plane B (cross section 20 mm downstream the spacer).

4.1.1 The Influence on Fluids

By comparing the average velocity of the radial cross section from the inlet to the outlet (Fig. 4). The average velocity of the cross section of the spacer rod is higher than that of the bare rod.

When it is a bare rod, the velocity distribution of the cross section is more uniform (Fig. 5) and highest velocity is 1.51 m/s; when it has spacer, the velocity distribution of the whole cross section is obviously disturbed, and the fluid velocity increases with the gap between the spacer and rod; the non-uniformity of cross-sectional flow is obviously increased, and in the hole of spacer, it arrives in the highest velocity of 2.066 m/s.

Fig. 4 Average velocity of the cross section through the spacer

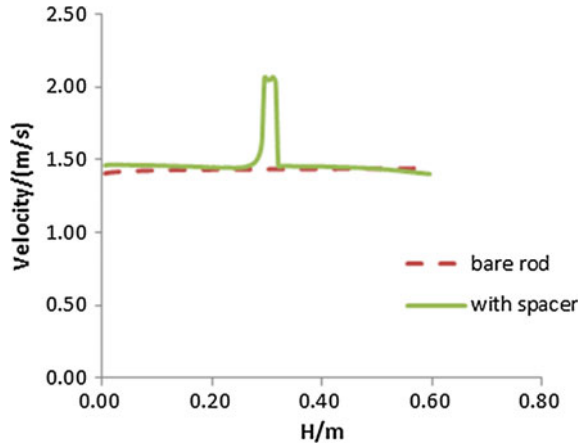


Figure 6 shows the velocity contours, the spacer still made a disturbance in the velocity of the downstream, which is the same with on plane A. But compare velocity and temperature of outlet with each other, we can see that the flow pattern at outlet is basically the same. With the passage of the fluid flow, the spacer has little effect on the flow at the outlet, and the flow at the outlet is fully recovered.

4.1.2 The Influence on Temperature

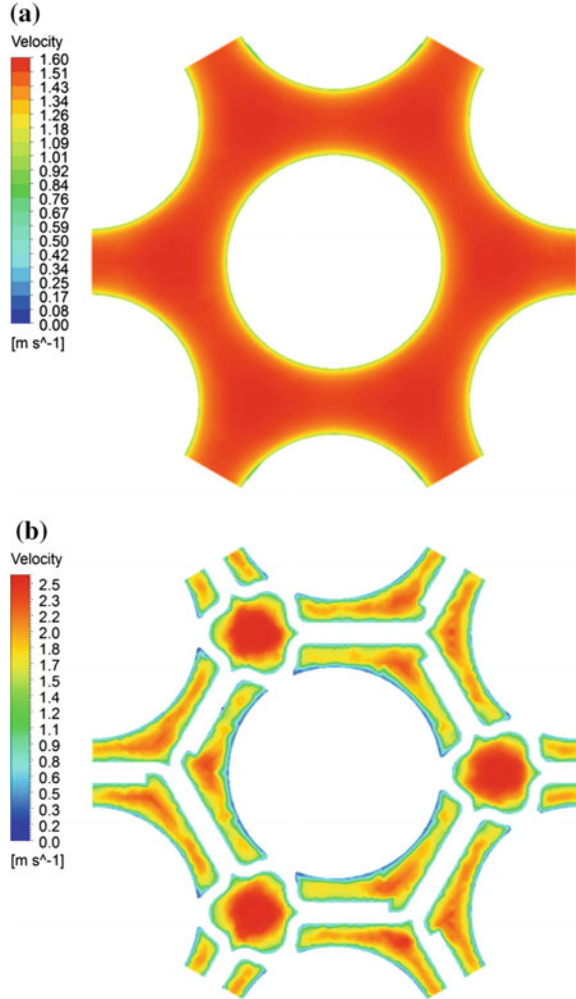
In the vicinity of spacer, due to the presence of flow stagnation point, the spacer grids and fuel rods gap have a high temperature (Fig. 7). Within the boundary layer detachment in downstream of spacer, it forms recirculation zone fluid and has slow mass exchange which causes heat to be taken away hard, so that local fluid temperature is very high (Fig. 8).

Average temperature distribution along the length of the sub-channel is shown in Fig. 9. Obviously, the influence of spacer on the average temperature of the sub-channel can be neglected; their relation curves are very nearly. And when considered the conduction of spacer, its contour of spacer is shown in Fig. 10. By comparing the location of hot spots, the highest temperature appeared in the contact area of grid and fuel rods, and at the same time, the local temperature of the fuel rods will be high. When it is a bare rod, the highest temperature of cladding is 771 K, and when is with spacer, it is 780 K.

4.1.3 The Influence on Pressure Drop

When lead flows spacer, sudden change is occurred in the flow surface, and it will lead a pressure loss of the vortex; this pressure loss is known as the shape drag drop [6]. Figure 11 shows the pressure along the length of the sub-channel. It is clear that

Fig. 5 Contours of axial velocity at plane A: **a** bare rod, **b** with spacer



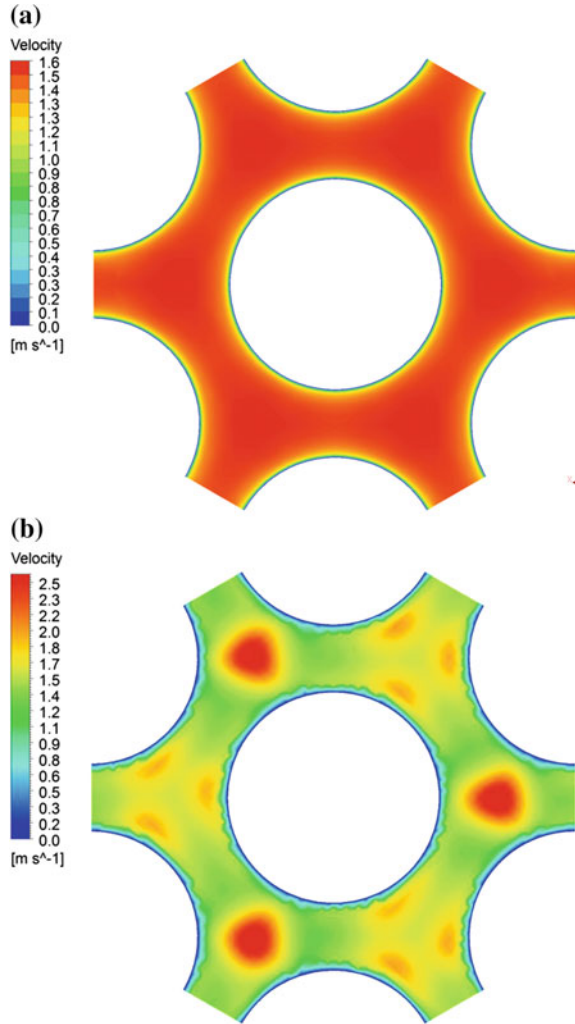
the effect of the spacer on pressure. And the pressure drop due to the presence of the spacer is estimated to be about 6480 Pa.

4.2 Influence of Wire

4.2.1 Influence on Fluid

The existence of wire brings a strong inhomogeneity to the axial flow rate of the sub-channel. The average velocity of the radial cross section of bare rod and rod

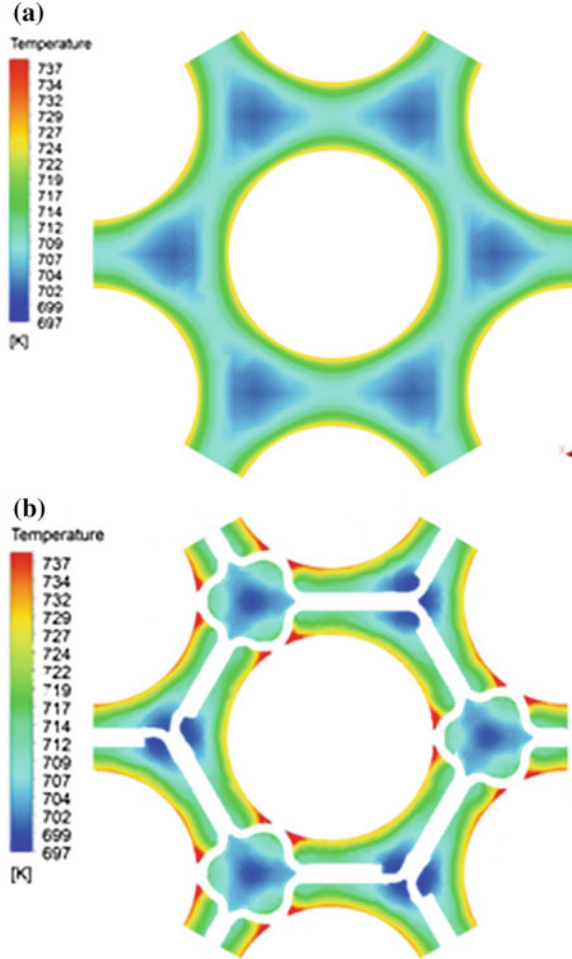
Fig. 6 Contours of axial velocity at plane B: **a** bare rod, **b** with spacer



with wire are shown in Fig. 12. The velocity fluctuation of the whole flow process is periodic. This is due to the fuel rods of spiral wire, which generates periodic effects of flow at each node on passage. And the axial flow rate of the wire is higher than that of the bare rod, which also because the wire has caused strong effect on fluid mixing, and the highest velocity (1.51 m/s) is in the connection of wire and rod.

In addition, wire is spirally coiled on the fuel rods, which makes the coolant in sub-channel of lateral flow occurrence. The lateral flow is favorable to the heat transfer of fuel rods, strengthen the strength of convection heat transfer, lower the highest temperature of the coolant, and promote the uniform distribution of coolant in rod bundle channel.

Fig. 7 Contours of temperature at plane A: **a** bare rod, **b** with spacer

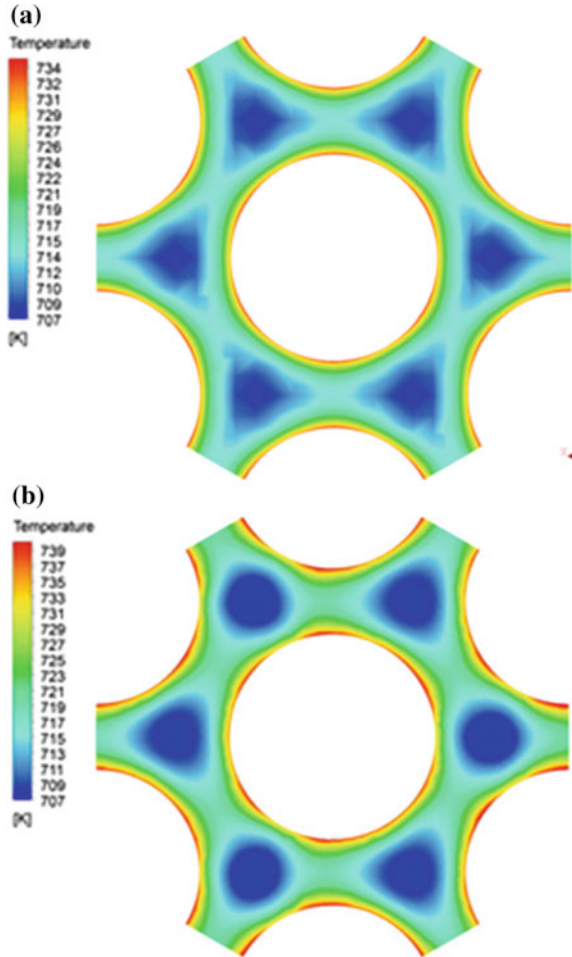


4.2.2 The Influence on Temperature

The average temperature of the radial cross section of bare rod and rod with wire is shown in Fig. 13. The wire has little influence on the average temperature of the whole cross section, but it has an impact on the maximum temperature of the cross section along the sub-channel (Fig. 14). The axial temperature rise in sub-channels is different from the average temperature, it is not straight up with a linear function, which is due to the wire has strengthened the transverse mixing flow intensity, and mixing the fluid in the cross section, reducing the temperature of the coolant.

From Fig. 15, we can see the contour of temperature along the cladding. The whole law is the same as the rod with spacer. In the vicinity of the fuel rod and the

Fig. 8 Contours of temperature at plane B: **a** bare rod, **b** with spacer



wire around the wire, the temperature of the area is generally high due to the stagnation point of the fluid encountered in the area. And the high temperature zone is generated along the direction of wire twinning the rod; the maximum temperature on cladding is 781 K.

4.2.3 The Influence on Pressure Drop

Figure 16 shows the pressure along the length of the sub-channel. It can be seen that the channel pressure drop is more regular and bigger, which is close to linear. This is because the flow surface in the whole channel is basically the same.

Fig. 9 Average temperature along the length of sub-channel

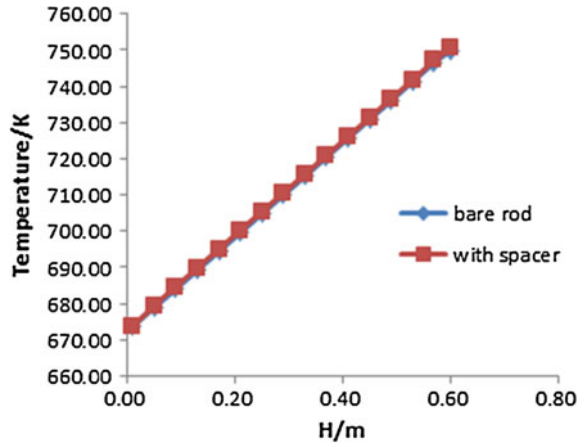


Fig. 10 Contours of spacer

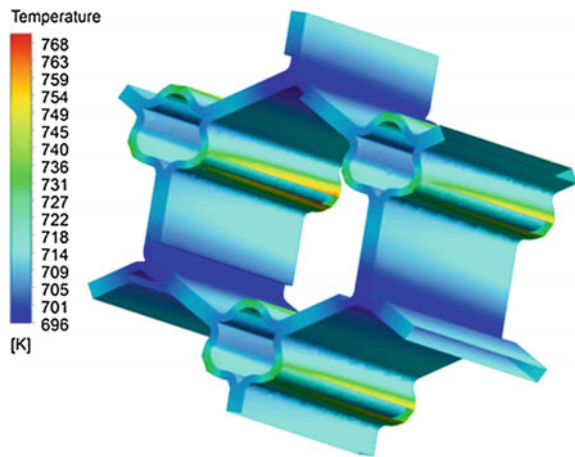


Fig. 11 Average pressure drop along the length of sub-channel

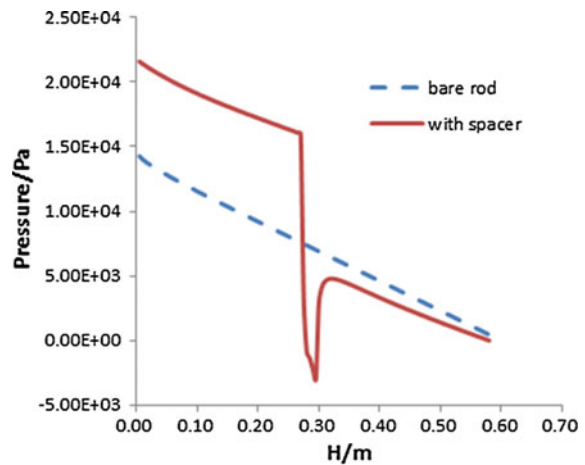


Fig. 12 Average velocity along the length of sub-channel

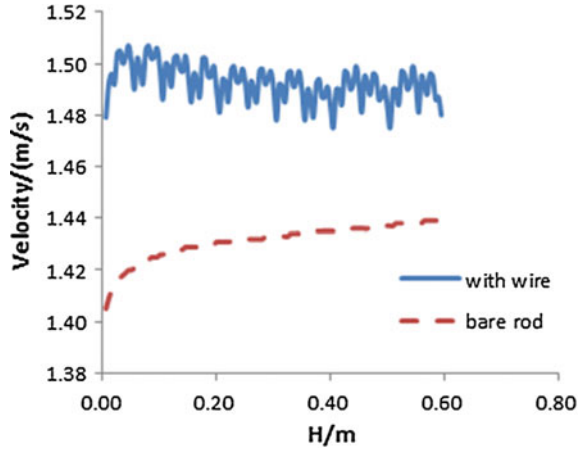


Fig. 13 Average temperature along the length of sub-channel

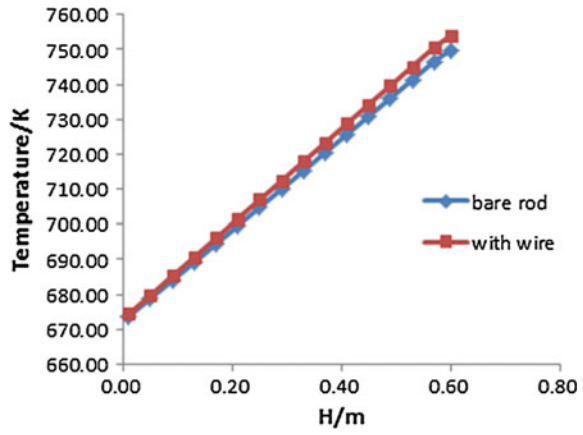


Fig. 14 Maximum temperature of the cross section along the sub-channel

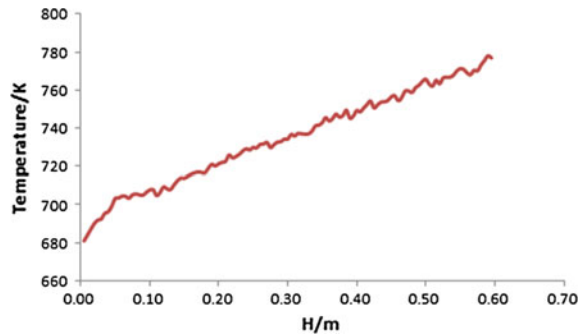


Fig. 15 Contours of cladding in wire rod

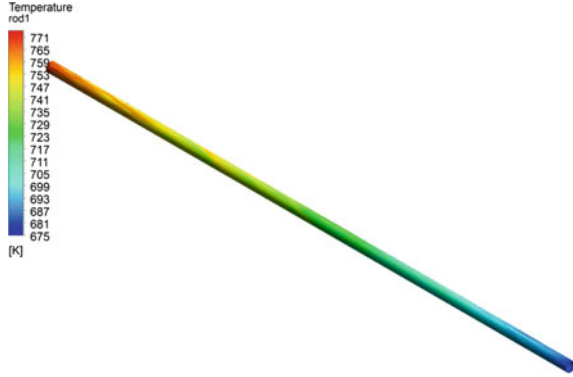
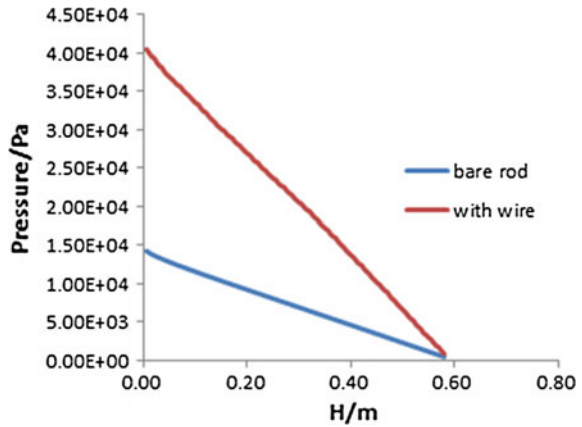


Fig. 16 Average pressure drop along the length of sub-channel



5 Conclusions

From CFD results of three kinds of channel, we can see the following:

- (1) The effect of spacer to velocity is near the spacer, the velocity distribution in other regions is basically the same as the bare rod. But the influence of the wire on the flow rate of the channel exists in the whole channel, which because wire is arranged from inlet to outlet. In addition, the influence of the grid-spacer on fluid flow rate is more severe than of wire; its maximum average velocity is higher than 2 m/s, but the wire makes good lateral mixing on fluid, and its average velocity is in 1.48–1.52 m/s.
- (2) Spacer and wire have little influence to axial average temperature, and they have influence on cladding maximum temperature. It is due to the stagnation point of coolant when fluid faces obstacles such as wire and spacer and cannot take away the cladding heat. So the hot spots are always located near the fuel rods.

- (3) When it is a bare rod, channel pressure drop is close to the linear, but when with spacer or wire, it will generate the shape drag drop. The pressure drop of spacer rod is happened suddenly; the pressure drop of wire rod is more linear, but higher.

References

1. A. Alemberti, J. Carlsson, E. Malambu, A. Orden, D. Struwe, P. Agostini and S. Monti. European lead fast reactor – ELSY. Nucl. Eng. and Design 241 (2011):3470–3480.
2. D. De Bruyn, G. Grasso, D. Mattioli, C. Petrovich and L. Mansani. 2011. Design options for the ETR. LEADER Del 02. Mol. Belgium.
3. GAJAPATHYR, VELUSAMY K, SELVARJP, et al. CFD investigation of helical wire-wrapped 7-pin fuel bundle and the challenges in modeling full scale 217 pin bundle [J]. Nuclear Engineering and Design, 2007, 237:2332–2342.
4. CHEN Bingde, XIONG Wanyu, WANG Xiaojun, et al. Application of calculation grid fluid dynamic in thermal hydraulic analysis of the fuel assemblies and design of the spacer grid [J]. Nuclear Power Engineering, 2004, 25(5):403–407(in Chinese).
5. Handbook on Lead-bismuth Eutectic Alloy and Lead Properties. Materials Compatibility, Thermal-Hydraulics and Technologies. OECD 2015. NEA No. 7268. 2015.
6. STEWART C W. COBRA-IV: The models and the methods, BNWL-2214[R]. Richland, USA: Battelle Pacific Northwest Laboratories, 1977.

Author Biography

Gao Xinxin is an advanced energy technology engineer in Reactor Design and Safety Research Center, China Nuclear Power Technology Research Institute.

Development of a 3D Core Calculation Code: COCO

Li Cai, Chen Jun, Gao Shengnan, Lu Haoliang and Li Jinggang

Abstract In the framework of Hualong Pressurized Reactor (HPR1000) developed by Chinese General Nuclear (CGN) Company, various industrial reactor design codes have been developed since 2010. In order to carry out efficient and reliable nuclear reactor designs, robust core calculation code is a cornerstone. COCO, a three-dimensional (3D) diffusion code based on nodal solver, is capable to perform the following calculations: the core loading pattern search calculation, the critical boron concentration calculation, the burnup and power distribution calculations, the control rod worth calculations, different types of reactivity coefficient and the shutdown margin calculations. The validation work of COCO code is complete, including the use of several international benchmark results as well as the realistic nuclear reactors' experimental results. The final comparison showed that the COCO code can give out reliable results with high precision which meets the industrial nuclear core design requirements.

Keywords Core design · Nodal solver · Burnup calculation

1 Introduction

The core calculation code takes a highly important place in the whole nuclear reactor design, fuel management and unit operation work. It serves mainly in the following detailed items: the layout of fuel assemblies, the layout of control rods, the design of burnable poison, the core reloading pattern search and providing necessary neutronics data for safety analyses.

In order to answer the demand of exportation of our home-designed reactors, CGN company has decided to develop associated nuclear reactor calculation code

L. Cai (✉) · C. Jun · G. Shengnan · L. Haoliang · L. Jinggang
China Nuclear Power Technology Research Institute, Shenzhen, Guangdong, China
e-mail: caili2015@cgnpc.com.cn

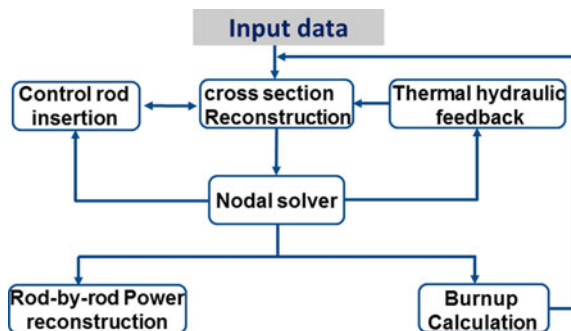
COCO which should include the associated functionalities for core design work. Firstly, the COCO code can handle three-dimensional geometry problems. As for symmetrical core, COCO is able to simulate one-quarter of the core with rotation reflective boundary conditions. Then, COCO can give out steady-state calculation results, such as the effective multiplicative factor K_{eff} , the flux map and the power distribution map. Furthermore, COCO can perform related fuel management calculations, re-establish the rod-by-rod power distribution and figure out the associated safety parameters. As the whole operation process is maintained by moderating boron concentration or modifying control rod positions, the code COCO can also predict precisely the related physical parameters ($F_{\Delta H}$, F_Q ...).

This paper describes a part of the theoretical models employed in COCO including the nodal solver, the thermal-hydraulic feedback module, the burnup calculation module and the rod-by-rod power reconstruction module. Then, some industrial applications are illustrated while comparing our results to experimental measurements.

2 Theoretical Models

The main calculation scheme in COCO code is illustrated Fig. 1. The core simulation starts from taking the input data produced by the previous assembly calculation. The cross-sectional reconstruction module will build up its usable cross-sectional tables on the basis of the previous input data via interpolation processing. These cross sections will then be used in the nodal solver module to calculate K_{eff} values, flux map, power distribution map, etc. The output information from the nodal solver will be exploited in other modules, such as the thermal-hydraulic module, the control rod insertion module, the burnup calculation module and the rod-by-rod power distribution module. In the following paragraphs, several of them are picked up to be demonstrated individually.

Fig. 1 Principal calculation algorithm in the COCO code



2.1 Nodal Solver Module

The nodal solver used in COCO is based on a non-linear semi-analytical nodal expansion method. The intra-node flux is projected on the polynomial Legendre basis for the 0 to second order as well as hyperbolic sine and hyperbolic cosine functions for higher orders. Thus, the main purpose is to figure out the development coefficients associated with these functions. Here, we solve a two-node coupled system. It means that for a 2-group problem, 20 unknowns have to be solved. Therefore, 20 equations need to be established using node-averaged flux, interface flux, current continuity condition and residual weight technics. In addition, the whole process is accelerated using a coarse-mesh finite-difference (CMFD) method [1, 2]. This solver allows calculating the effective multiplication factor, the flux distribution and the power map in three-dimensional core.

2.2 Thermal–Hydraulic Feedback Module

The thermal–hydraulic model coupled to the COCO code is a closed channel model which does not consider the heat transfer between two neighbour channels. Radially, each channel takes a node surface. Axially, every single channel measures the entire core height including both the up-reflector and the down-reflector. According to different calculation precision requirements, one channel can be axially divided into different number of layers. Each layer is noted as one node. Various physical and thermal–hydraulic parameters such as the power density, the coolant temperature and the void fraction are calculated for each node. In return, the coolant temperature is used for calculating the effective fuel temperature, and the coolant density serves as the input data for updating the cross sectional tables in order to continue the neutronic and thermal–hydraulic iteration.

2.3 Burnup Calculation Module

Being able to perform burnup calculation is quite important for any nuclear core design code. The burnup calculation in COCO aims to simulate the whole cycle life precisely in order to predict some physical parameters such as the essential isotope density, the node-based burnup distribution and the node surface burnup. In practice, the entire cycle is divided into time step, which could affect the simulation time and the calculation precision. The approximation used here is that under each time step, the core is considered under a steady-state situation. So with the knowledge of information from the moment t_i , one can calculate the core's physical parameter at the next moment t_{i+1} . Generally, there are two kinds of burnup calculation: microscopic and macroscopic aspects.

The first one focuses on the isotopes of fission products, minor actinides, etc. In fact, the isotope density respects a balance relationship, cf Eq. (1).

$$\frac{dN_k(t)}{dt} = G_k - L_k N_k(t) \quad (1)$$

where $N_k(t)$ represents the atomic density of the isotope k at the moment t , G_k is the generation from absorption or fission for isotope k , L_k is the disappearing rate of isotope k .

The second one serves reconstructing the intra-node burnup distribution. As one node occupies actually a certain volume, the burnup within each node is there for spatially dependent. The formula used to calculate one surface burnup is illustrated in Eq. (2).

$$\text{Bu}_{s,i+1} = \text{Bu}_{s,i} + 10^{-3} \frac{t_{i+1} - t_i}{\rho} \sum_{g=1}^2 \kappa^g \sum_{s,f} \varphi_{s,i}^g \quad (2)$$

where $\text{Bu}_{s,i}$ represents the surface average burnup for any node at time step i ; t_i and t_{i+1} are, respectively, the time moment i and $i + 1$; ρ is the mass density of heavy metal in the current node; κ^g is the energy released by fission reaction on surface s at step i for group g .

$$\kappa^g \sum_{s,f} \varphi_{s,i}^g$$

With surficial burnup, one can deduce the surficial macroscopic cross sections. Then, the flux and cross sections can be reconstructed within each node. Finally, the node-averaged cross sections are corrected, which enable more accurate core simulation.

3 Industrial Applications

COCO has already been applied to numerous industrial reactors. In this chapter, one example will be chosen to demonstrate the industrial calculation results as well as the comparison results with experimental measurement results.

The demonstration is done for the unit 1 of Ningde NPP in Fig. 1. It is the first reactor in China of which the control rods in the first cycle used Gd_2O_3 as burnable poison. Meanwhile, it is the first reactor which began the 18-month reloading mode since its second cycle (Fig. 2).

The first cycle takes use of a high leakage loading pattern, while the second cycle uses a low leakage one. The calculation results to be shown are namely the critical boron concentration under hot zero power (HZP) state, the values of control

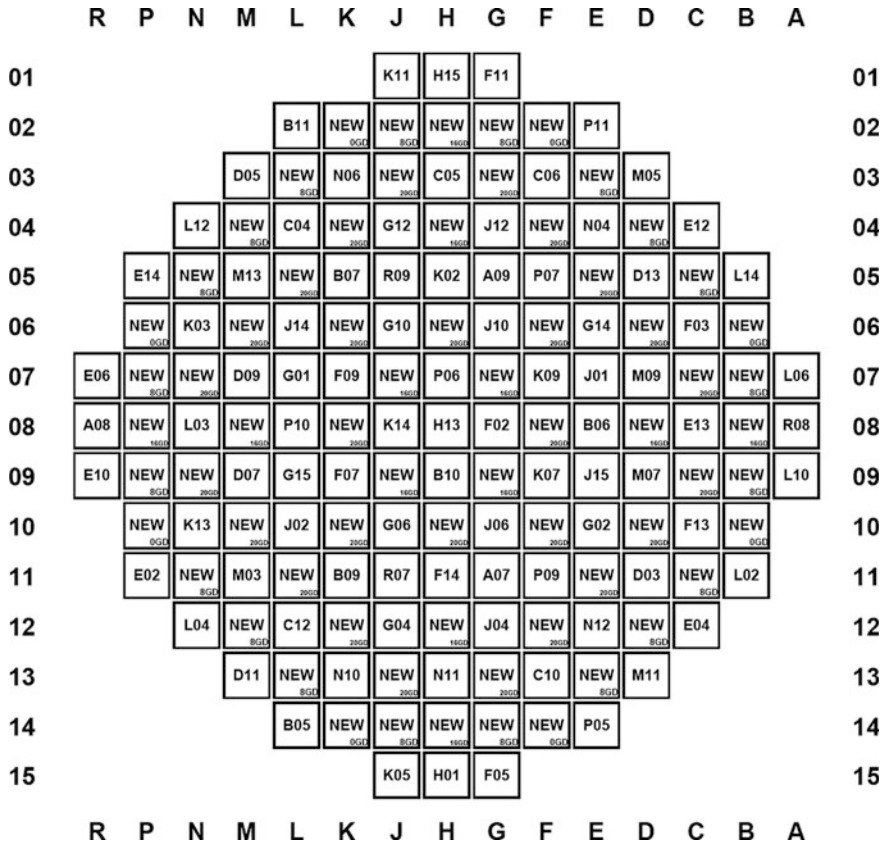


Fig. 2 Schema of the loading pattern of Ningde Unit 1

rods under HZP at beginning of length (BOL), the critical boron concentration curve versus the burnup. The results of both cycle 1 and cycle 2 will be given.

Table 1 presents the critical boron concentration difference between measurement and calculation results for Ningde NPP Unit 1 under HZP at the beginning of cycle 1. Three different states of control rods are tested, which are namely all rods out (ARO), only the rod R in (R-in) and rods R and G1 in (R + G1-in). The comparisons from Table 1 demonstrate that COCO is able to give consistent results according to experiment measurements. Moreover, the differences of the critical boron concentration are limited to 9 ppm.

In Table 2, the relative differences of values of each bundle of control rods between experimental measurements and calculation results are, respectively, listed. The tests are done under HZP situation at beginning of cycle 1 of Ningde NPP Unit 1. It can be seen from the below table that the relative differences are all inferior to 3%. The comparison results declare that COCO is capable of giving consistent control rod values with respect to experimental measurements.

Table 1 The critical boron concentration difference between measurement and calculation of Ningde Unit 1 at HZP and BOL of cycle 1

Control rod states	Critical boron concentration difference (ppm)
	M—COCO
ARO	-9
R-in	-7.1
R + G1-in	-6.8

Table 2 Relative differences of control rod values between measurements and calculations for Ningde NPP Unit 1 under HZP at BOL of cycle 1

Control rods	Difference of control rod value (%)
	M—COCO
G1	0
G2	2.11
N1	1.15
N2	-0.50
R	2.08
SA	0.17
SB	1.57
SC	1.76
SD	2.88

The curves of critical boron concentrations versus the burnup of the first cycle of the unit 1 of Ningde NPP are plotted in Fig. 3. The left ordinate axis represents the critical boron concentration, while the right one represents the difference between measurement value and calculation result. Firstly, we can observe that the calculation results from COCO follow the same tendency with the experimental measurements. A steep decrease in the critical boron concentration is found around 150 MWd/tU, which is induced by the fact that amount of Xe has been accumulated since the start-up and the equilibrium of Xe is established from this point. After 150 MWd/tU, the critical boron concentration continues going down because of the decrease in fissile materials in the core. Furthermore, the discrepancies between measurement and simulations are, respectively, illustrated by dash lines. It is obvious to tell that COCO can well predict the boron concentrations and the discrepancies are limited to 50 ppm which comes from the safety criterion.

The same comparison of control rod values is performed for the second cycle of the unit 1 of Ningde NPP. The associated results are listed in Table 3. The relative differences between experimental measurements and calculation results are limited to 10%, which meets the industrial requirement. It is proven again that COCO can give consistent control rod value compared with experiment results.

The following Table 4 resumed the critical boron concentration results under two different operation conditions. The first one is performed at the beginning of cycle 2 under hot zero power condition with all of the control rods out of the core which is noted as HZP-BOL-ARO state. The second one is operated under hot full

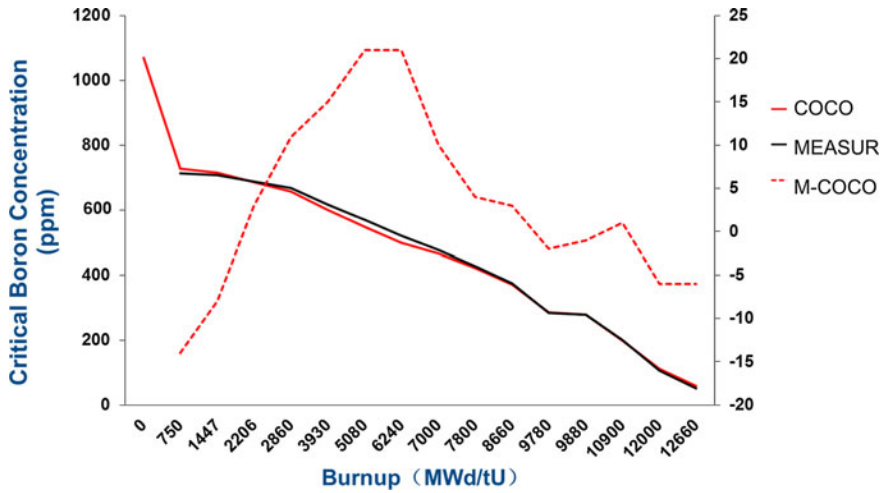


Fig. 3 The variation of the critical boron concentration versus burnup of the first cycle of Ningde NPP Unit 1

Table 3 Relative differences of control rod values between measurements and calculations for Ningde NPP Unit 1 under HZP at BOL of cycle 2

Control rods	Difference of control rod value (%)
	M-COCO
G1	-4.5
G2	-0.7
N1	-2.1
N2	-1.5
R	-3.5
SA	-0.8
SB	-2.4
SC	0.7
SD	-3.3

Table 4 The critical boron concentration difference between measurement and calculation of the second cycle of the Ningde NPP Unit 1 under two different operation conditions

Control rod states	Differences of critical boron concentration (ppm)
	M-COCO
HZP-BOL-ARO	-1
HFP-BLX	-30

power condition while the concentration of Xe reaching equilibrium. The latter one is marked as HFP-BLX state. Table 4 tells that COCO calculations have overestimated the critical boron concentration. However, COCO simulation gave rather consistent results regarding the measured values.

4 Conclusions

COCO, our home-made three-dimensional core design code, is able to give out reliable results with high precision which meets the industrial nuclear core design requirements. In conclusion, COCO is applicable to core design of nuclear engineering. It will also be used to Hualong Pressurized Reactor.

References

1. V. G. ZIMIN, H. NINKOKATA, Nodal neutron kinetics Model Based On Nonlinear Iteration Procedure For LWR Analysis, *Annals of Nuclear Energy*, Vol.25, No.8, pp. 507–528, 1998.
2. V. G. Zimin, Ninokata, Acceleration of the outer iterations of the space-dependent neutron kinetics equations solution et al. *Ann. Nucl. En.* 23:17 Nov 1996.

Author Biography

Li CAI doctor of nuclear reactor engineering, is interested in nuclear reactor physics, nuclear simulation code development, cycle and fuel management.

The Gen-III Nuclear Power Technology in the World

Yanrui Li, Chao Chen, Pingping Xin, Yajun Chen and Huiqun Hou

Abstract There are about seven types of the Gen-III pressurized nuclear power technology in the world. They are AP1000, EPR, CAP1400, APR1400, HPR1000, ABWR and VVER-1200. The paper describes the design features of the seven technologies, introduces the present construction situation of them and calculates the capacity under construction. There are eight reactors being constructed in China and America using AP1000 technology. Four reactors are being constructed using EPR technology in China, France and the Netherlands. The United Arab Emirates is constructing four reactors using APR1400 technology. One reactor adopting HPR1000 technology is being constructed in China, and one is not yet started. VVER technology gets a lot of orders in the world and is being constructed in many countries. The author hopes that the scholars will know the current development situation of Gen-III nuclear power technology better through this paper.

Keywords Gen-III nuclear power technology · Pressurized water reactor · Design features · Construction situation · Net electrical capacity

1 Introduction

The world's first nuclear power plant, Obninsk Nuclear Power Plant, is located in Kaluzhskaya Oblast of Russia and was built in 1954. Since then, the world reactor technology has developed four generations [1].

The differences between the four reactor generations are obvious. Gen-I reactors were developed in 1950–60s and are run in no country other than Britain. Gen-II reactors are most in operation elsewhere. Gen-III reactors are the advanced reactors discussed in this paper. Gen-IV reactors are in the research and development stage.

Y. Li (✉) · C. Chen · P. Xin · Y. Chen · H. Hou

CNNC General Institute of Technology & Economic, Haidian District, Beijing, China
e-mail: liyanrui2006_511@126.com

C. Chen

China National Nuclear Corporation, Beijing, China

© Springer Science+Business Media Singapore 2017

H. Jiang (ed.), *Proceedings of The 20th Pacific Basin Nuclear Conference*,

DOI 10.1007/978-981-10-2314-9_27

The first Gen-III reactors are in operation in Japan, which are advanced boiling water reactors (ABWR). Other Gen-III reactors are under construction or are being planned.

The paper only focuses on large Gen-III pressurized water reactors (PWR) whose generation power is more than 700 MWe, since PWR is the main-stream commercial reactor type. Smaller advanced reactors or advanced boiling water reactors will not be described here.

2 Design Features

America, China, Europe, Russia, South Korea and some other countries are constructing or planning to build Gen-III PWRs. Gen-III PWRs are AP1000, APR1400, CAP1400, EPR and HPR1000, and they have some following features.

- Standardized design: each type expediting licensing and reducing capital cost and construction time.
- Simpler and more rugged design: making them easier to operate and less vulnerable to operational upsets.
- 60-year life: higher availability and longer operating life.
- Core damage frequency: less than 1×10^{-4} .
- Requirements: meeting user requirements document (URD) and European Utility Requirements (EUR).
- Higher burn-up: using fuel more fully and efficiently and reducing the amount of waste.
- Substantial grace period: following shutdown the plant requiring no active intervention typically for 72 h.
- Resistance to serious damage: allowing no large radiological release from an aircraft impact.
- Load-following: being capable of load-following between 50 and 100% of capacity.
- Modular construction: many small components being assembled in a factory environment (offsite or onsite) into large structural modules weighing up to 1000 tons.

3 Gen-III Reactors

The passive or inherent safety features in Gen-III reactors require no active controls or operational intervention to avoid accidents in the event of malfunction. They may rely on gravity, natural convection and resistance to high temperatures, not on functioning of engineered components.

3.1 AP1000

The Westinghouse AP1000 is a two-loop PWR. US Nuclear Regulatory Commission (NRC) certified one of the first new reactor designs in 2005. AP1000 adopts simplification design [2]. All safety systems, normal operating systems, the control room, construction techniques, and instrumentation and control systems provide cost savings with improved safety margins. AP1000 has a core cooling system including passive residual heat removal by convection, improved containment isolation, passive containment cooling system to the atmosphere and in-vessel retention of core damage with water cooling around it [3]. It does not need safety-related pumps or ventilation system. There are totally eight AP1000 reactors being built in China and USA, four at the Sanmen and Haiyang sites and four at Vogtle and summer sites. The gross capacity is 1250 MWe, the design net capacity is 1110–1117 MWe and the thermal capacity is 3415 MWt. Westinghouse earlier claimed a 36-month construction time to fuel loading. The first ones being built in China were on a 51-month timeline to fuel loading, or 57-month schedule to grid connection.

The main design features of AP1000 include primary loop system and equipment using sophisticated plant design, simplified enhancing passive safety and severe accident prevention and mitigation measures [4]. AP1000 adopts modular construction techniques. At Sanmen in China, where the first AP1000 units are under construction, the first module lifted into place weighed 840 tonnes. More than 50 other modules used in the reactors' construction weigh more than 100 tonnes, while 18 weigh in excess of 500 tonnes. Many are larger than predecessors. Increasingly they involve international collaboration. However, certification of designs is on national and safety bases [5].

AP1000 is strongly economical. The modular construction of the building shortens the construction period to three to four years [6]. AP1000 large-scale stand-alone capacity and up to 60-year design life may be able to compete with natural gas combined cycle power plant. In addition, compared to the power plant equipment in operation, the valves, pumps, safety stage pipeline and cable are reduced by about 50, 35, 80 and 70% [7, 8].

3.2 EPR

EPR is the abbreviation for European pressurized water reactor. Areva NP has developed EPR. EPR was confirmed in mid 1995 as the new standard design for France and received French design approval in 2004. Its thermal capacity is 4590 MWt, with typically 1750 MWe gross power and 1630 MWe design net capacity. EPR is a four-loop design derived from the German Konvoi types with features from the French N4. It is expected to provide power about 10% cheaper than the N4. It operates flexibly to follow loads. EPR is designed to have fuel

burn-up of 65 GWd/tU, a high thermal efficiency of 37% and net efficiency of 36%. It is capable of using full core load of MOX. The availability of EPR is expected to be 92%, and the service life is over 60 years.

EPR has double containment and four separate and redundant active safety systems. It boasts a core catcher under the pressure vessel. The safety systems are physically separated through four ancillary buildings on the same concrete raft, and two of them are aircraft crash protected. EPR equips diesel generators and tertiary battery. The primary diesel generators have fuel for 72 h, the secondary back-up ones for 24 h and tertiary battery back-up lasts 12 h.

There are totally four EPR reactors under construction. The first unit is being built at Olkiluoto in Finland, the second at Flamanville in France, and the other two at Taishan in China. The EPR has undergone the UK Generic Design Assessment, with some significant changes to the instrumentation and control systems. The Electricite De France and the Chinese nuclear enterprises will adopt EPR technology and invest 24.5 billion pounds to built Hinkley Point C power plant in the UK.

3.3 *HPR1000*

There are two indigenous reactor designs with modern features in China [9]. The China National Nuclear Corporation developed the ACP1000 nuclear power technology. ACP1000 has load-following capability and 177 fuel assemblies. Its nominal power is 1100 MWe [10]. The China General Nuclear Power Group led the development of ACPR1000. ACPR1000 has 157 fuel assemblies, and its nominal power is also 1100 MWe.

In order to meet the going-out nuclear strategy, China's National Energy Administration presided the Gen-III nuclear technology innovation and cooperation meeting. China National Nuclear Corporation and China General Nuclear Power Group agreed to incorporate each other's Gen-III technology, ACP1000 and ACPR1000+, as a whole. It is Hualong One technology and that is HPR1000.

The Hualong One has 177 fuel assemblies in the core. The fuel assembly is 3.66 m long. The refueling cycle is 18–24 months, and the average burn-up is 45000 MWd/tU. The design life is 60 years. It has three coolant loops, double containment and active safety systems with some passive elements. The design net capacity, gross capacity and thermal capacity, respectively, are 1092 MWt, 1150 and 3150 MWe. Seismic shutdown is at 300 gal. Instrumentation and control systems will be from Areva–Siemens. The target cost is \$2500/kWe. The three of the first four units has started to be constructed in China. The three are Fuqing 5&6 units and Fangchenggang 3 unit. The other one is under construction in Karachi in Pakistan. The units of Fangchenggang 4 and Karachi coastal 2 both using HPR1000 may pour the first major tank of concrete in 2016.

3.4 *CAP1400*

Westinghouse has been jointly working with the State Nuclear Power Technology Corporation and the Shanghai Nuclear Engineering Research and Design Institute in China to develop a passively safe reactor, the CAP1400. The design net capacity is 1500 MWe, and the thermal capacity is 4040 MWt. It is a two-loop design adopted from the AP1000. CAP1400 has 193 fuel assemblies in the core and two improved steam generators. Its design life is 60 years. The coolant outlet temperature is 323 °C. It is designed for 72-hour nonintervention period when there is a postulated accident. The average discharge burn-up is about 50 GWd/TU, and the maximum burn-up is up to 59.5 GWd/tU. Operation flexibility includes MOX capacity, 18–24-month cycle and load-following. The design seismic rating is 300 gal. The CAP1400 project may extend to a larger, three-loop CAP1700 or CAP 2100 design if the passive cooling system can be scaled to that level. The State Nuclear Power Technology Corporation owns the intellectual property rights of CAP1400 as the Westinghouse declared that if any AP1000 derivatives over 1350 MWe, State Nuclear Power Technology Corporation would own the rights. In China, the CAP1400 demonstration project has entered the last part of the review and is expected to be approved in early 2016. The first demonstration project will be constructed in Shandong Shidao Bay.

3.5 *APR1400*

The APR1400 of South Korea is an evolution version from the System 80+ [11, 12]. APR1400 has two-loop primary circuit and absorbed the enhanced safety and seismic robustness. APR1400 was earlier known as the Korean Next Generation Reactor [13]. The Korean Institute of Nuclear Safety awarded design certification to APR1400 in May 2003. Its gross power is 1455 MWe, the design net capacity is 1350–1400 MWe and the thermal capacity is 4000 MWt. Shin-Kori 3&4 and Shin Hanul 1&2 are the first four units of APR1400 technology. These are under construction in Korea [14, 15]. The first criticality date of Shin-Kori 3 unit was on December 29, 2015, and its first grid connection date was on January 15, 2016. It is expected to be operated in 2016. The first four APR1400 reactors were chosen as the basis of the United Arab Emirates nuclear program. In mid-2009, the South Korean won the bid for the United Arab Emirates' nuclear power program and would constructed four APR1400 reactors for the later. The first reactor started to build on 19 July, 2012, and now four units are under construction there.

The nuclear fuel of APR1400 has burnable poison, and the burn-up will have up to 55 GWd/tU. The refueling cycle is about 18 months, and the coolant outlet temperature is 324 °C. The projected cost is planned about \$ 2300 per kW. The construction time is 48 months, plant life is 60 years and seismic design basis is 300 Gal. An 1800-rpm low-speed turbine may match an APR1400 reactor.

3.6 AES-92 and V-392

Russia has some reactor models conforming to Gen-III technology features. The models derive their origin from VVER, the Russian pressurized water reactor. AES-91 and AES-92 are the Gidropress late model of VVER technology. The two models with enhanced safety are being built in Tianwan Nuclear Power Plant of China and Kudankulam Nuclear Power Plant of India. Two variant reactors, model V466B, are under construction in Belene of Bulgaria. The AES-92 is certified as meeting European Utilities Requirements. Its V-392 reactor is considered state of the art. The thermal capacity is rated 3000 MWt. AES-92 and V-392 both have four coolant loops and 163 fuel assemblies.

3.7 AES-2006

AES-2006 is a standardized Gen-III reactor model and conforms to both Russian standards and European Utilities Requirements. It has two variant models, V-392M and V-491. They have enhanced safety features including related to earthquakes and aircraft impact with some passive safety, double containment and core catcher. The thermal capacity and gross power of AES-2006 are typically 1170–1200 MWe and 3200 MWt, respectively. It has a 60-year life with non-replaceable equipment, and the capacity factor may be up to 90%. Its conversion efficiency is 34.8%, and the burn-up is up to 70 GWd/tU. It is an evolutionary development in the AES-92 and AES-91 plants. AES-2006 retains four coolant loops, and the reactor core has 163 FA-2 fuel assemblies [16].

Seven AES-2006 reactors are now being built in Russia. Two V-392M reactors are under construction in Novovoronezh II. Two V-491 reactors are being built in Leningrad II, one in Baltic and two in Belarus. The four lead units are expected to be operation in 2016. The design net capacity of V-392M is 1114 MWe, gross capacity 1199 MWe and thermal capacity 3200 MWt. According to Novovoronezh II and Leningrad II, it is speculated that an AES-2006 plant may consist of two of these reactor units.

Although the first contract was about \$2100/kW, the overnight capital cost may be US\$ 1200/kW. The serial construction time is designed by 54 months, but according to the current progress, the lead units have been postponed.

V-392M and V-491 have different ways on the cooling systems. Passive safety systems prevail in V-392M design, while V-491 design focuses on active safety systems.

4 Conclusions

Gen-III reactor technology meets the safety requirements of user requirements document and European Utility Requirements. It has excellent passive or inherent safety features. The standardized design, longer operating life, higher burn-up,

modular construction and other features make the technology expediting licensing and reducing capital cost and construction time.

AP1000, EPR, APR1400, HPR1000 and VVER-1200 are the Gen-III reactor models under construction. China, South Korea, Russia, France, Finland, UAE and USA are constructing Gen-III reactor units. By the end of January 31, 2016, there are sixty-six units under construction in fifteen countries, and the total net electrical capacity is 65028 MWe. Among the under construction reactor units, eight AP1000 reactors, totally 8000 MWe net electrical capacity, are being built, four in China and four in USA; four EPR reactors, totally 6550 MWe net electrical capacity, are being built one in Finland, one in France and two in China; seven APR1400 reactors, totally 9400 MWe net electrical capacity, are being built, three in South Korea and four in UAE; four HPR1000 reactors, totally 4500 MWe net electrical capacity, are being built, three in China and one in Pakistan; nine VVER Gen-III reactors, totally 9705 MWe net electrical capacity, are being built, five in Russia, two in China and two in Belarus. So, there are thirty-two Gen-III nuclear reactors being built in eight countries, and the total net electrical capacity is 38155 MWe.

Some other countries are planning to build nuclear power plants with Gen-III reactor technology. Gen-III pressurized reactor technology will be the main trend in the future nuclear industry.

Acknowledgments The authors wish to thank the research funding supported by National Key Basic Research Program from China's Ministry of Science & Technology and China Institute of Nuclear Information & Economics, the most comprehensive nuclear industry information center in China, for providing the excellent work environment and favorable information.

Funding Support: Supported by 973 Program under Grant No. 2015CB453000

Disclaimer This work was prepared under an agreement with and funded by the P.R. China. Neither the PRC or its employees, nor any of its contractors, subcontractors or their employees, makes any express or implied as followed:

1. Warranty or assumes any legal liability for the accuracy, completeness, or the use or results of any information in the text. 2. Representation that such use or results of such use would not infringe privately owned rights. 3. Endorsement or recommendation of any specifically identified commercial product, process or service. Any views and opinions of authors expressed in this work do not necessarily state or reflect those of the PRC, or its contractors, or subcontractors.

References

1. IAEA. Advaced Nuclear Power Reactors. <http://world-nuclear.org/info/Nuclear-Fuel-Cycle/Power-Reactors/Advanced-Nuclear-Power-Reactors/>.
2. C. Queral, J. Montero-Mayorga, J. Gonzalez-Cadelo, G. Jimenez. AP1000 Large-Break LOCA BEPU analysis with TRACE code, *Annals of Nuclear Energy*, v85, p 576–589, 2015.
3. Di Maio F, et al. Invariant methods for an ensemble-based sensitivity analysis of a passive containment cooling system of an AP1000, *Reliability Engineering and System Safety* (2015), <http://dx.doi.org/10.1016/j.ress.2015.10.006>.

4. Qiang Xu, Jianyun Chen, Chaobi Zhang, Jing Li, Chunfeng Zhao. Dynamic Analysis of AP 1000 Shield Building Considering Fluid and Structure Interaction Effects, *Science Direct*, p 1–13, 2015.
5. C. Qeral, J. Montero-Mayorga. Risk reduction due to modification of normal residual heat removal system of AP1000 reactor to meet European Utility Requirements, *Annals of Nuclear Energy*, v91, p 65–78, 2016.
6. Wu Hao, Gan Quan, Luo Qi, Xiao Sanping, Liu Yan, Chen Shushan. Decay Heat Removal Performance Analysis of AP1000 Startup Feed Water during Non-LOCA Accident, *Nuclear Power Engineering*, v36, p 92–96, 2015.
7. XIAO San-ping, QIAN Hui, WU Hao, CHEN Shu-shan. Performance Study of Low Pressure Safety Injection for AP1000 Nuclear Power Plant IRWST, *Atomic Energy Science and Technology*, v48, 437–440, 2014.
8. YANG Jiang, WANG Ting, TAO Jun, GAO Ling-yuan, LU Xiang-hui. Study on Early Phase of AP1000 Accident Under Fukushima Condition, *Atomic Energy Science and Technology*, v7, p 1206–1210, 2014.
9. Ming Zeng, Shicheng Wang, Jinhui Duan, Jinghui Sun, Pengyuan Zhong, Yingjie Zhang. Review of nuclear power development in China: Environment analysis, historical stages, development status, problems and countermeasures, *Renewable and Sustainable Energy Reviews*, v59, p 1369–1383, 2016.
10. Wang Dan, Bai Jia. The third Generation Nuclear Power Technology “Wisdom Creation” in China of “Hualong One”, *China Nuclear Power*, v8, p 290–292, 2015.
11. Sang W. Noh, Kune Y. Suh. Critical heat flux for APR1400 lower head vessel during a severe accident, *Nuclear Engineering and Design*, v258, p 116–129, 2013.
12. Rae-Joon Park, Kwang-Soon Ha, Bo-Wook Rhee, Hwan Yeol Kim. Detailed evaluation of two phase natural circulation flow in the cooling channel of the ex-vessel core catcher for EU-APR1400, *Nuclear Engineering and Design*, v298, p 33–40, 2016.
13. J.H. Song, J.H. Baik, S.K. Zee, S.Y. Park, S. Choi, B.D. Chung, W.P. Baek. Development of a high power three-loop nuclear power plant, *Nuclear Engineering and Design*, v240, p 3621–3631, 2010.
14. Xin-Guo Yua, Hyun-Sik Park, Yeon-Sik Kim, Kyoung-Ho Kang, Seok Cho, Ki-Yong Choi. Systematic analysis of a station blackout scenario for APR1400 with test facility ATLAS and MARS code from scaling viewpoint, *Nuclear Engineering and Design*, v259, p 205–220, 2013.
15. Jongtae Kim, Seong-Wan Hong, Sang-Baik Kim, Hee-Dong Kim. Three-dimensional behaviors of the hydrogen and steam in the APR1400 containment during a hypothetical loss of feed water accident, *Annals of Nuclear Energy*, v34, p 992–1001, 2007.
16. World Nuclear Association. Nuclear Power in Pakistan. <http://www.world-nuclear.org/information-library/country-profiles/countries-o-s/pakistan.aspx>.
17. Zhen-Yu Hung, Yuh-Ming Ferng, Wen-Sheng Hsu, Bau-Shei Pei, Yen-Shu Chen. Analysis of AP1000 containment passive cooling system during a loss-of-coolant accident, *Annals of Nuclear Energy*, v85, p 717–724, 2015.

Author Biography

Yanrui Li is a worker at China Institute of Nuclear Information & Economics, and his research area is the nuclear science and technology intelligence research.

The Methodology to Compensate Ex-core Nuclear Instrument Signal by In-core Nuclear Instrument Signal

Chu-hua Tang, Jie Chen and Wei Chen

Abstract The use of Mechanical Shim to control core reactivity changes causes rod position-dependent changes in calibration relationships used to determine the values of Reactor Power and Axial Flux Difference (AFD) determined from Power Range detectors. To support the real-time plant control system, it is required to compensate this Power Range signal. This paper introduces a new method of Ex-core nuclear instrument signal compensated by continuous measured In-core nuclear instrument signal, and the compensated signal is used for Tavg and AFD control.

Keywords AFD · Self power detector · Rod shadowing · Ex-core nuclear instrument signal · In-core nuclear instrument signal

1 Introduction

The use of Mechanical SHIM (MSHIM, control rods used to regulate core power and Xenon changes) to control core reactivity changes at steady state and during reactor power maneuvers causes rod position-dependent changes in the calibration relationships used to determine the values of Reactor Power and Axial Flux Difference (AFD) determined from the PR detector signals. These changes in the calibration relationships result in the erroneous inputs. This type of effect is present in existing operating plants during reactor power maneuvers where control rods are deeply inserted. This phenomenon is known as rod shadowing [1]. Simulations of PR detector response during reactor power maneuvers using MSHIM indicate the rod shadowing errors can be much larger than typical allowances of reactor trip setpoint.

C. Tang · W. Chen
Jinzhou, Hubei, China

J. Chen (✉)
Enshi, Hubei, China
e-mail: ezreal.cccc@outlook.com

This paper describes how the signals from the Self Powered Detectors (SPD) in the AP1000 In-core Instrument Thimble Assemblies (IITA) can be used to provide adjustments to the AFD and Reactor Power level determined by the excore Power Range detector channels that are used by the AP1000 Plant Control System (PLS) to compensate for the PR calibration changes that occur during MSHIM operations to avoid the likelihood of the AO control rods moving in a way that produces undesirable AO control behaviors.

2 Overview

As the input to the $f(\Delta I)$ penalty function generator that provides input to the over-temperature ΔT Trip (OTDT) Setpoints in PMS, the Axial Flux Difference errors between the Power Range detector and actual incore average amounts should be limited within 3% [2]. The motion of the control rods changes the relationship between the core average $\Delta\Phi$ and the $\Delta\Phi$ that exist in the fuel assemblies on the core periphery that produce the neutrons seen by PR detectors. This results in the core average $\Delta\Phi$ input to the $f(\Delta I)$ penalty calculation being in error, which can significantly exceed the current 3% error allowance. Consequently, the Weighted Peripheral Assembly (WPA) $\Delta\Phi$ is introduced in PMS, and it is possible to identify a very stable and accurate calibration between the PR detector signals and the Weighted Peripheral Assembly (WPA) $\Delta\Phi$.

These modified AFD inputs are also provided to the PLS. The PLS Rod Control System uses input AFD values to direct motions of axial offset control bank [3]. The direct use of the PMS AFD inputs by the PLS can cause the PLS to move the AO control rods during MSHIM operations in a fashion leading to improperly controlled changes in the core axial power distribution.

The paper proposes a methodology to calibrate the reactor power signals and make the AFD error within 3% error allowance.

3 AFD Adjustment Methodology

The values of AFD determined by each of the four PR channels represent the difference between the average amounts of thermal power produced in the top and bottom halves of the reactor core [4]. During the Zero Boron Change rapid reactor power level maneuvers performed using only control bank motions, the calibration relationships established for PR detector AFD measurements may see significant effective changes in the calibration relationship with $\Delta\phi$ established during quasi-steady-state conditions. These calibration changes may cause the error in the PR AFD signals used in the PLS to increase beyond the AFD error allowance assumptions. This behavior may cause the PLS to move the AO control rods used to control the AFD to an established target value in a fashion that causes non-optimum

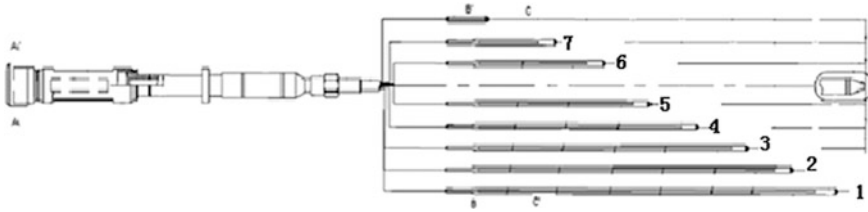


Fig. 1 The axial configuration of the Vanadium SPD elements inside the AP1000 in-core instrument thimble assemblies

axial power distribution control and results in undesirable axial power distribution oscillations or power level maneuver restrictions. The signals from the SPD inside the IITA can be used to provide an alternative indication of the reactor axial power distribution that can be used to adjust the PR AFD measurements used in the PLS.

Figure 1 presents the axial configuration of the Vanadium SPD elements inside the AP1000 IITA [2].

It can be seen that the thermal power in the top half of the core (P_T) in core location j will be proportional to:

$$P_{Tj} = K_j^T \left[I_{5j} + \left(\frac{I_{4j} - I_{5j}}{2} \right) \right] = K_j^T \left[\frac{I_{5j} + I_{4j}}{2} \right] \tag{1}$$

The power in bottom half of the core (P_B) is proportional to:

$$P_{Bj} = K_j^B \left[I_{1j} - \left(\frac{I_{4j} + I_{5j}}{2} \right) \right] \tag{2}$$

The value of core average $\Delta\phi = (P_T - P_B)$ for the IITA incore location j is then given by the expression:

$$\Delta\Phi = K_j(I_{5j} + I_{4j} - I_{1j}) \tag{3}$$

I_{ij} values refer that the subscript i is the SPD element number and the subscript j is the number of SPD. K is the coefficient of current. P is reactor power, where the subscript T is the top half of the power and B is the bottom half of the power.

In order to determine AFD adjustments for each of the 4 PR channels that provide input to the PLS, we need to determine an average SPD AFD adjustment for each core quadrant associated with each PR channel. In general, we can say that the true value of $\Delta\phi$ is related to the SPD element currents in core quadrant i by the expression:

$$\Delta\Phi = m_i \left[\frac{1}{N_i} \sum_{j=1}^{N_i} I_{5j} + \frac{1}{M_i} \sum_{k=1}^{M_i} I_{4k} - \frac{1}{P_i} \sum_{l=1}^{P_i} I_{1l} \right] + b_i \tag{4}$$

where N_i is the number of operable SPD element number 5s in quadrant i ; M_i is the number of operable SPD element number 4s in quadrant i ; P_i is the number of operable SPD element number 1s in quadrant i . The relationship for SPD and quadrant can be seen in Fig. 2, where M, AO and S are the locations of control rods, and X is the location of SPD. It is convenient to assign the SPD signals from 9 IITA in each core quadrant to be used to calculate the value of AFDs for the quadrant. The calibration coefficients m_i and b_i are determined manually from a linear fit of the average SPD signal calculated axial power shape in core quadrant i versus the corresponding measured $\Delta\phi$ value determined by the BEACON System at enough different axial power shape conditions to allow the resultant standard error of regression of relationship identified in Eq. 4 to be less than or equal to the uncertainty allowance corresponding to the AFD input to the PMS. The calibration coefficients will be manually determined during the initial power ascension in each operating cycle. The calibrated value of $\Delta\phi$ derived from the SPD signals in core quadrant i is called In-core Axial Power in quadrant i (IAP $_i$). The IAP value derived from the SPD signals can be used to adjust the PR AFD in the associated core quadrant.

		R	P	N	M	L	K	J	H	G	F	E	D	C	B	A	
									180°								
1																	
2						1X	SD4	2X	MC	3X	SD4	4X					
3						M2		SD2		SD2		M2					
4				5X	MB	6X	AO	7X	M1	8X	AO	9X	MB	10X			
5				M2		SD1		SD3		SD3		SD1		M2			
6			SD4	11X	AO	12X	MA	13X	MD	14X	MA	15X	AO	16X	SD4		
7			17X	SD2		SD3		SD1		SD1		SD3		SD2	18X		
8	90°		MC	19X	M1	20X	MD	21X	AO	22X	MD	23X	M1	24X	MC		270°
9			25X	SD2		SD3		SD1		SD1		SD3		SD2	26X		
10			SD4	27X	AO	28X	MA	29X	MD	30X	MA	31X	AO	32X	SD4		
11				M2		SD1		SD3		SD3		SD1		M2			
12				33X	MB	34X	AO	35X	M1	36X	AO	37X	MB	38X			
13						M2		SD2		SD2		M2					
14						39X	SD4	40X	MC	41X	SD4	42X					
15																	
									0°								

Fig. 2 IITA assigned to each PR channel

The PLS needs to control the core average axial power distributions to maintain control of the core average axial xenon distribution to avoid debilitating axial power oscillations and power level restriction. The PLS receives the AFDWP values from PMS on an essentially continuous basis. In order to allow the PLS to control the core to the desired target value of $\Delta\phi$ needed to avoid axial xenon distribution oscillations, the input values of AFDWP from the PMS need to be adjusted to represent $\Delta\phi$, or the IAP values should completely replace the PMS AFDWP values. The optimum usage of the IAP measurements is strongly determined by the operating characteristics of the Vanadium SPD elements contained in the AP1000 IITA.

The signal response of a Vanadium-51 atom to the absorption of a neutron is governed by an n, β reaction that has a half-life of approximately 225.6 s. Consequently, the signals output directly from the Vanadium SPD elements following a step change in reactor power will represent the local power distribution that existed up to 15 min in the past. Direct usage of the Vanadium detector signals in the PLS would cause the axial power distribution control piece of the PLS to attempt to control an axial power shape that may no longer exist. Fortunately, the AP1000 IIS contains a methodology that uses the simple response characteristics of the Vanadium SPD elements to accelerate the effective SPD element response time. The signal response acceleration methodology has been shown to decrease effective response time from approximately 15 min to less than 1 min. If the accelerated SPD signals were used to produce IAP for the PLS, the effective response time of the PLS to actual changes in $\Delta\phi$ would be of order of 2 min. The AP1000 IIS currently provides updated accelerated SPD signal values at one-second intervals.

The response of the PR channels to a change in reactor power is instantaneous. However, the PR channels are to be calibrated to produce $\Delta\phi_{wp}$ instead of $\Delta\phi$. It is possible to use both the prompt responding PR AFDWP and the IAP values simultaneously to produce an AFD for the PLS that maintains a prompt component and has the accuracy provided by the value of IAP. The approach requires that a correction term be derived from the difference between IAP and AFDWP. The AFD value used by the PLS can account for the inherent lag of IAP relative to AFDWP and the SPD signal variability associated with the response time acceleration process by lagging the AFDWP to be consistent with the accelerated SPD signal response and averaging the difference between AFDWP and IAP over some reasonably small time interval. The resulting SFD from core quadrant i to be used by the PLS would have the algebraic time-domain form:

$$AFD_i(t) = AFD_{wp_i}(t) + \frac{1}{N} \sum_{j=0}^{N-1} (IAP_i(t-j) - AFD_{wp_i}(t-j-\tau)) \quad (5)$$

where N is the number of one-second time intervals needed to achieve optimum accelerated SPD signal stability and τ is the effective lag time between the PR detector response and the SPD signal response. This approach preserves some of

the prompt element of PR response and applies a correction base on the more accurate IAP values that is only of the order of a couple of minutes old.

4 Reactor Power Level Indication Adjustment Description

Figure 3 presents the Vanadium SPD current versus reactor thermal power relationship derived from a single full assembly length Vanadium SPD element installed in a peripheral fuel assembly [4]. The data indicate a strong linear relationship with reactor thermal power. This information supports the use of the full-length SPD elements in each SP1000 IITA to provide an adjustment to the reactor power level indication input to the PLS from the PMS. The time lag associated with even the accelerated SPD signals makes use of the SPD information for power level correction somewhat more problematic, but since we are correcting the reactor power indication for rod shadowing effects, the size of the correction term will not vary more quickly than the rods will move during a load maneuver. This fact means that an approach like that used to correct the PMS AFDWP should also provide sufficient power level correction response. Since the SPD signal appears to produce a signal linearly related to reactor power, we can assume a time-domain relationship between reactor power $P(t)$, PMS indicated reactor power $PPMS(t)$, and power derived from the longest operable SPD element in each IITA ($PSPD(t)$) in core quadrant i of the form:

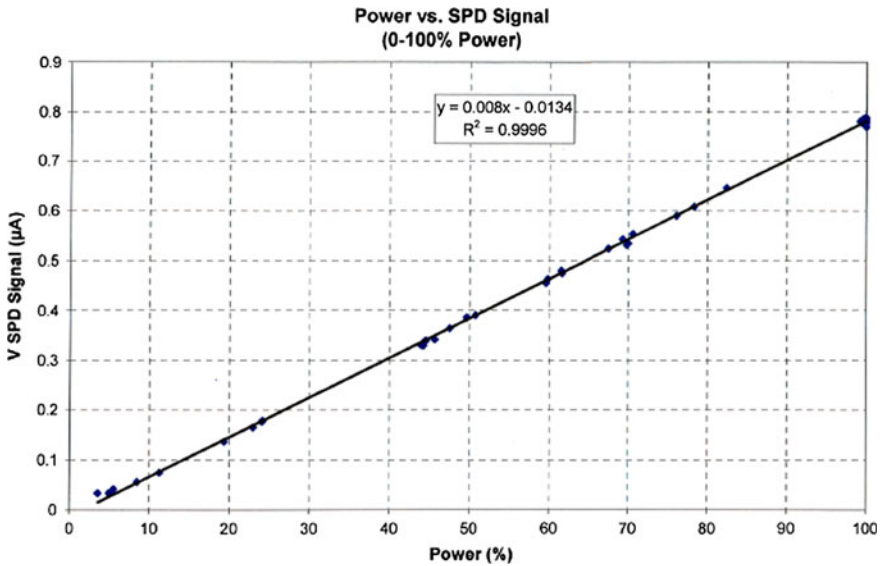


Fig. 3 SPD current versus reactor thermal power

$$P_i(t) = P_{P_i}(t) + \frac{1}{N} \sum_{j=0}^{N-1} (P_{SPD_i}(t-j) - P_{P_i}(t-j-\tau)) \quad (6)$$

The value of PSPD for each core quadrant i is determined from the calibration relationship with respect to calorimetric power (Q_{TH}):

$$Q_{TH_i} = m_i \frac{1}{N_i} \sum_{j=1}^{N_i} I_{1ij} + b_i = P_{SPD_i} \quad (7)$$

The values of I_{1ij} represent the signal from the SPD element 1 in each IITA in core quadrant i as illustrated in Fig. 2. The value of N_i represents the number of operable SPD element 1 in quadrant i that are contributing SPD signals to the SPD signal measurement summation. The time interval between the SPD signal measurements is one second. The calibration coefficients m_i and b_i can be determined from a manual linear fitting of data acquired during the initial power ascension in each operating cycle performed external to the Application Server. The value of b_i can be manually updated and entered into the Application Server processing software while the reactor is operating at constant power as often as required to maintain the desired accuracy of P_{SPD_i} (e.g., daily). As with the AFD adjustment function, this approach preserves some of the prompt element of PR response and applies a correction based on the more accurate P_{SPD} values that is only of the order of a couple of minutes old.

The weighted peripheral AFD adjustment term as a function of time for core quadrant i , $\Delta A_i(t)$, to be used by the PLS to create the needed core average AFD value from the value provided to the PLS by the PMS is given by the expression:

$$\Delta A_i(t) = \frac{1}{N} \sum_{j=0}^{N-1} (IAP_i(t-j) - AFD_{WP_i}(t-j-\tau)) \quad (8)$$

The terms in Eq. 8 are as defined in Eq. 5.

The reactor power adjustment term as a function of time for core quadrant i , $\Delta P_i(t)$, to be used by the PLS to minimize the impact of change in rod shadowing on the Power Range detector reactor power is given by the expression:

$$\Delta P_i(t) = \frac{1}{N} \sum_{j=0}^{N-1} (P_{SPD_i}(t-j) - P_{P_i}(t-j-\tau)) \quad (9)$$

The terms in Eq. 8 are as defined in Eq. 6.

The Application Servers that receive the IIS SPD data will host the function required to generate the values of $\Delta A_i(t)$ and $\Delta P_i(t)$ defined in Eqs. 8 and 9. These adjustment terms will be transmitted once per second over a redundant dedicated data link to the PLS computational hardware that receive the $P(t)$ and

AFD_{WP}(*t*) values from the PMS. The PLS will adjust the PMS input values of AFD_{WP_{*i*}}(*t*) and PPM_{S_{*i*}}(*t*) using the relationships:

$$\text{AFD}_i(t) = \text{AFD}_{\text{WP}_i}(t) + \Delta A_i(t) \quad (10)$$

$$P_i(t) = P_{P_i}(t) + \Delta P_i(t) \quad (11)$$

The values of AFD_{WP_{*i*}}(*t*) and PPM_{S_{*i*}}(*t*) needed to determine the adjustment terms will be provided to the Application Servers BEACON that process Eqs. 8 and 9 at one-second intervals from the PLS computational hardware receiving these data from the PMS. Since there are four core quadrants, a total of 8 terms will be moving across the data link each way at one-second intervals. Ideally, this transfer will occur over the same data link. The calculations of AFD(*t*) and *P*(*t*) for each core quadrant as shown in Eqs. 10 and 11 will be performed in the PLS computational hardware. If the adjustment terms should become unavailable, it is assumed that the last valid reactor power and AFD adjustments will continue to be used until the transmission of valid data resumes.

The Application Servers labeled “Application Server BEACON A” and “Application Server BEACON B” are suitable for use to perform the adjustment calculations and communicate with the PLS application hardware. Dedicated redundant data link hardware will need to be designed and implemented to support the exchange of information between IIS and PLS.

Even though the methodology described in this paper has no Safety Analysis or Tech Spec impacts, the PLS AFD adjustment calibration constants shown in Eq. 4 should be determined or updated at the same intervals, and use the same recalibration trigger allowances, as used to determine the need to recalibrate the PR AFD values input to the PMS. The bias term of the SPD power relationship identified in Eq. 7 used to determine the PLS Power adjustment term should be adjusted to maintain the adjusted PLS Power within 0.5% of calorimetric power. The agreement between the PLS Power and the calorimetric power should be checked and updated as necessary concurrent with the corresponding surveillance of the PMS PR channel.

5 Conclusions

The methodology proposed in this paper can be applied to calibrate AFD and indicated power level for reactor units in which IITA is used like AP1000. The problem of the axial power distribution oscillations introduced by rod shadowing will be resolved by this methodology, and the precision of indicated power level will be improved as well.

References

1. zhongsheng Xie, Nuclear Reactor Physical Analysis, Atomic Energy Press, 2003
2. In-core Instrumentation System-System Specification Document
3. Nuclear Instrumentation System-System Specification Document
4. Plant Control System-System Specification Document

The Numerical Simulation Research of Gas–Liquid Two-Phase Flow in Small-Break Loss-of-Coolant Accidents

Yilin Zhang, Shanfang Huang, Xiaoyu Guo and Renjie Xiao

Abstract During small-break loss-of-coolant accidents (LOCA), gas entrainment, which occurs with the lower coolant level, the relief of the loss of coolant, can reduce risk in reactor. Therefore, the gas–liquid two-phase flow through a small hole has become a focal point these years. Considering that the existing researches are mostly about experimental study, and it is difficult to set a limit working condition, this paper simulates and analyzes the flow processes in primary circuit pressure boundary when the small-break LOCA happens by the FLUENT software, on the premise of verifying the computational fluid dynamics model. By means of changing the shape, size, length of break, the gas volume fraction, and the pressure drop, the author discovers that the sharp, long channel break increases the resistance of fluid blowdown and decreases the blowdown velocity, and the loss of coolant is more likely to be reduced in such condition. By simulating the flow processes after flash distillation condition, the author found that in cross section of break, the average blowdown velocity increases with the initial gas volume fraction, while the mass flow rate decreases contrarily considering that the gas volume fraction can meanwhile influence the fluid density. Besides, the larger the initial gas volume is, the earlier the gas entrainment will occur and the loss of coolant will be reduced. According to the results of numerical simulation, the author finds that gas entrainment will decrease the mass flow rate of break, reduce the loss of coolant, and save time for emergency core cooling.

Keywords Two-phase flow · Gas entrainment · Small break · Gas volume fraction · Mass flow rate

Y. Zhang (✉) · S. Huang (✉) · X. Guo
Department of Engineering Physics, Tsinghua University, Beijing, China
e-mail: yyhistory@163.com

S. Huang
e-mail: sfhuang@mail.tsinghua.edu.cn

R. Xiao
Nuclear Power Institute of China, Chengdu, Sichuan, China

1 Background Introduction

In small-break LOCA, gas entrainment can relieve the loss of coolant and reduce risk in reactor.

In order to investigate the two-phase flow through a small hole, American Scientist Craya (1949) [1] began to study on OLE (the onset of liquid entrainment) model. Whereafter, by transient experiment, Lubin and Hurwitz (1966) [2] proposed the concept of critical height HOGC when OGC (the onset of gas entrainment) occurs, and obtained its relationship with the Froude number (Fr). In recent years, with the development of engineering technology and monitoring equipment, a large number of experimental studies have been conducted, in which similar conclusions have been shown [3]. Liang, another scholar in this field, summarized the relationship between gas entrainment and liquid level, pressure difference according to the separated flow distribution model [4].

However, the existing studies are mostly related to experiment. Since the difficulties on setting an extreme condition in experiment, numerical simulation is a good choice. Numerical simulation can not only save manpower and material resources, but also shorten the time of research work, let alone its good repeatability. Considering the lack of numerical simulation, this paper uses the CFD software FLUENT to simulate and analyze the gas–liquid two-phase flow when the small-break LOCA happens. The author will use the method of numerical simulation to simulate flow processes in different pressures, break types, and gas volume fractions [5].

As shown in Fig. 1, in the phase distribution of FLUENT, if somewhere is all gas phase (phase volume fraction is 1), the color there is dark red; if somewhere is all liquid phase (phase volume fraction is 0), the color there is dark blue; if somewhere is two-phase gas–liquid mixture, the color there is between red and blue (i.e., the interface of these two phases). If there are no other special explain in following article, the gas–liquid two-phase distribution is described in this way.

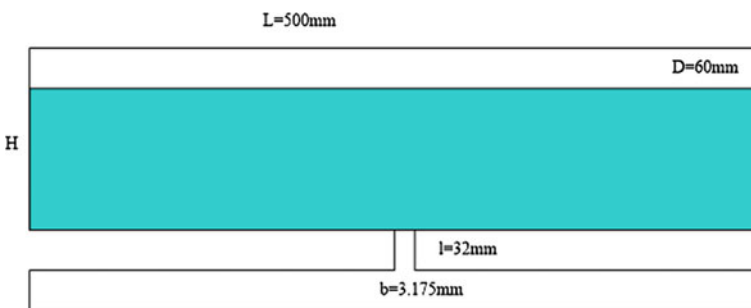


Fig. 1 Gas entrainment critical height model

2 Analysis of Results

There are many causes of small-break LOCA in the primary loop pressure boundary, which would make the break type complex. The shape, size, and length of break are hard to predict. In addition, when loop coolant ejection occurs, high-temperature high-pressure liquid water encountered low-temperature low-pressure external environment suddenly, and then, flash distillation occurs under great pressure difference and form gas-water mixture. After the flash distillation, the process of gas-liquid two-phase flow through the break also deserves attention.

2.1 Effect of Break on Fluid Blowdown

2.1.1 Effect of Break Shape on Fluid Blowdown

Sharp Break

Sharp breaks may be due to random mechanical impact in pipe wall or abnormal open of T-branch pipe. Calculation model is shown as Fig. 1.

The initial water level is set to be 50 mm, the internal and external pressure difference is 1000 kPa, and the impact of gravity is considered here. 0.01 s after entrainment phenomenon occurs, compare the velocity distribution on the cross section with the stable condition, the result is shown in Fig. 2. Obviously, at 0.01 s

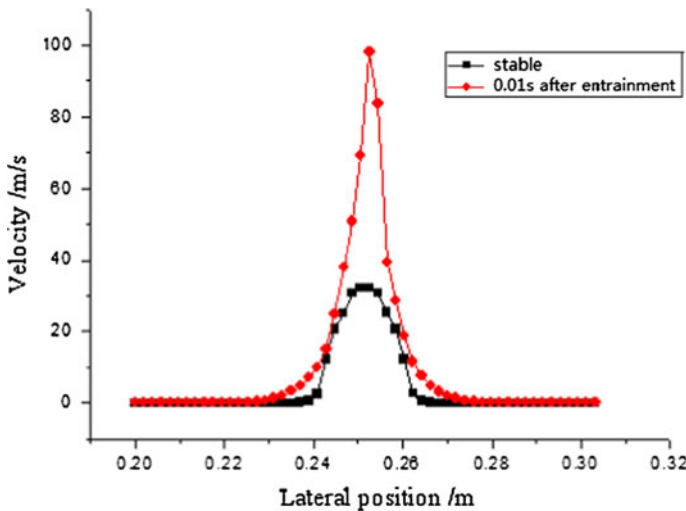


Fig. 2 Velocity distribution before and after entrainment

after entrainment, the lateral velocity gradient distribution is much steeper than the stable condition.

In general, with the gas entrained into the break, the flow pattern changes from bubbly flow to annular flow. Meanwhile, the entrained gas directly affects the pressure and velocity distribution. Gas entrainment has important impact on blowdown, and it is worth further study.

Round Break

Another typical shape is the round break, as shown in Fig. 3.

Using exactly the same CFD model and parameter settings with the sharp break, making pressure difference from 100 to 10000 kPa, the author monitored the comparison with sharp break in each condition.

Figure 4 shows the mass flow rate under pressure 100 kPa in sharp and round break. It can be easily found that in the stable period, mass flow rate in round break is always greater than that in sharp break; while in entrainment period, although both of them are in unstable fluctuations occur, but the curve of round break is generally above the sharp break. Therefore, in the entire period, liquid is discharged more in round break.

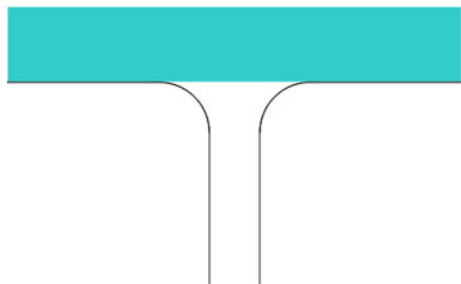
As shown in Fig. 5, comparing the mass flow rates under different pressure in sharp and round break, we can found that the mass flow rates are always larger in round break than sharp break no matter the pressure.

At the same time, the velocity distribution on the cross section is shown in Fig. 6. It can be observed that in the central portion the velocity of round break is greater, while near the pipe wall, the difference is not very obvious due to the value is small.

Although the analysis above is under the pressure difference of 100 kPa, in the case of other internal and external pressure difference, the results have the same trend with that in Fig. 6 with just a little difference in absolute number. Therefore, the author believes that there is no need to set out all those numbers.

Through the analysis above, when small-break LOCA occurs, sharp break can prevent the loss of coolant more effectively than round break. It is reasonable to believe that, if the inlet pipe connections was rectangular shaped rather than arc

Fig. 3 Round break schematic



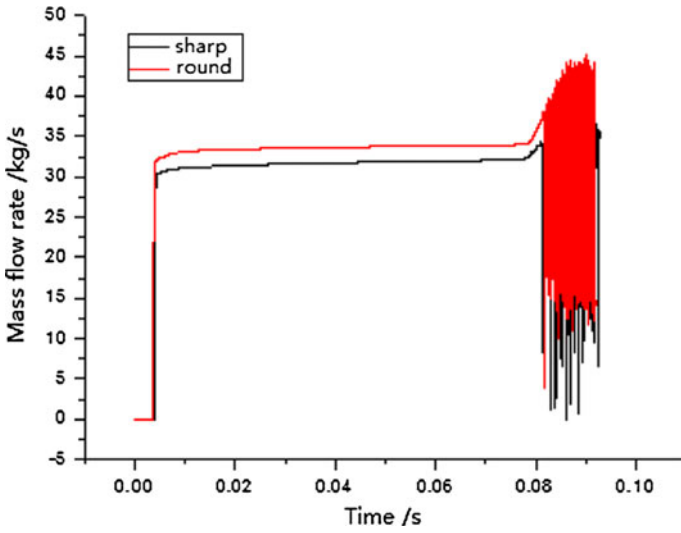


Fig. 4 Mass flow rate in *sharp* and *round* break

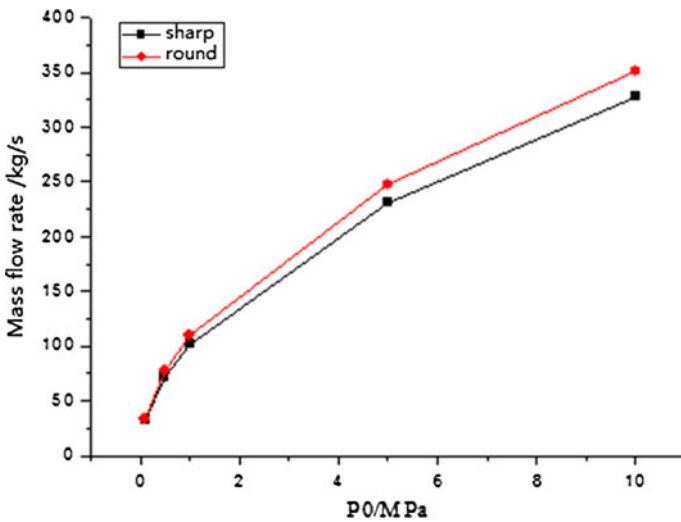


Fig. 5 Mass flow rates under different pressure in *sharp* and *round* break

shaped, the nuclear reactor may be safer. Nonetheless, in normal operation of nuclear power plants, rectangular T-tubes consume more energy, which increases the power of the drive motor and reduces the profits. In nuclear power plants, the economy and safety are usually contradictory, and the final choice should be according to the actual situation.

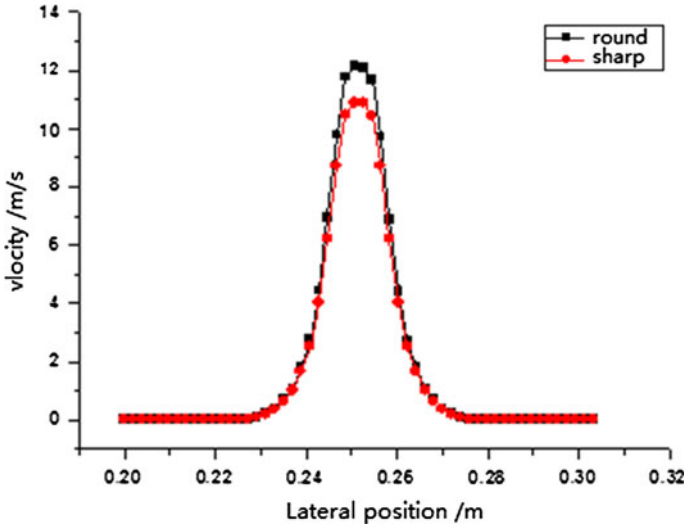


Fig. 6 Velocity distribution in *round* and *sharp* break under 100 kPa

2.1.2 Effect of Break Size on Fluid Blowdown

In the previous paper, the break equivalent diameter is 3.175 mm. Now we still use that model but only change the break size to 6.35 mm, the pressure difference to 1000 kPa.

For sharp break, 0.01 s after entrainment occurs, the distribution in large and small break is shown as Fig. 7:

In the larger sharp break, annular flow is formed completely. While in the smaller one, although there are some annular flow structure in the upper part of the channel, its development is not sufficient and will become plug flow in the lower part.

2.1.3 Effect of Break Length on Fluid Blowdown

Increasing the length of the break channel could directly increase the frictional pressure drop, the corresponding effect is slowing down the blowdown velocity and decreasing the mass flow rate. Look at large sharp break, for example, we increase its break channel length to 120 mm while the other parameters remain unchanged, monitor the break mass flow rate and compare it to that in large short break. As shown in Fig. 8, mass flow rate in short channel break is significantly greater than the value of the long channel break.

If we compute the integral of these mass flow rate curves, we can get the liquid loss in both conditions, as shown in Table 1:

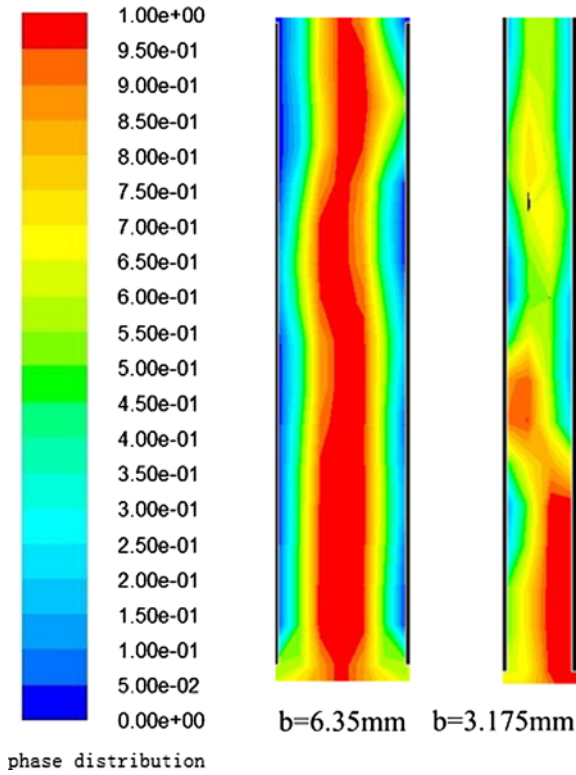


Fig. 7 Phase distribution under 1000 kPa, 0.01 s after entrainment

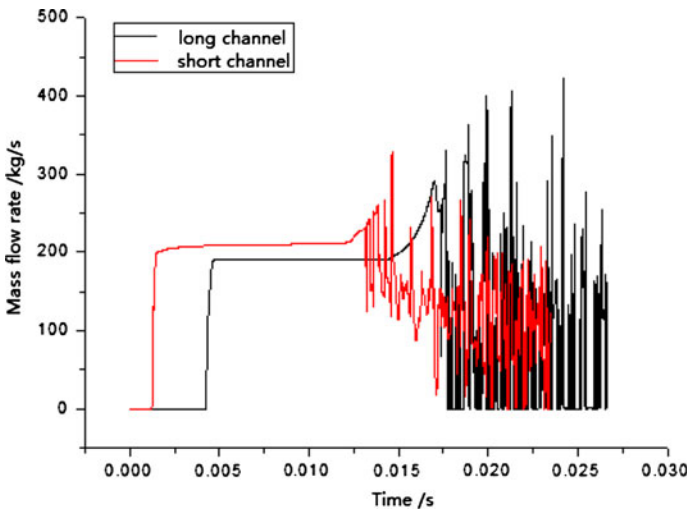


Fig. 8 Mass flow rate under 1000 kPa

Table 1 Liquid loss in sharp break of different channel lengths

Channel length	Liquid loss in stable period/kg	Liquid loss, 0.01 s after entrainment/kg	Liquid loss gross/kg
Short	2.55238	1.22748	3.77986
Long	2.39877	1.07217	3.47094

Although gas entrainment occurs earlier in short channel break, but its liquid loss is still larger than that in long channel break. This indicates that in nuclear power plant LOCA, the longer the break channel is, the greater the resistance is, which is helpful to save precious coolant and benefits nuclear safety. But it also increases resistance and reduces profits.

In summary, sharp break results in greater local resistance than round break, long channel break results in greater on-way resistance than short channel break. Since the resistance directly impact the blowdown volume, in LOCA the long channel sharp break could result in greatest total resistance, in such conditions the loss of coolant can be relived to the greatest extent.

2.2 Blowdown of Uniform Mixed Phases

When loop coolant ejection occurs, high-temperature high-pressure liquid water encountered low-temperature low-pressure external environment suddenly, then flash distillation occurs under great pressure difference and form gas–water mixture. Next part is about the processes after flash distillation, including the distribution of velocity and gas volume fraction. During blowdown process, because that the gas phase is mixed in system, the density of fluid and pressure drop are changed, which will affect the blowdown velocity. Velocities of different gas volume fraction are shown in Fig. 9. It indicates that the larger the initial gas volume fraction is, the greater the average velocity in cross-section is average velocity of the fluid is. Since the near wall movement of the bubbles decreases the shear stress and reduces energy loss; at the same time, the existence of the gas phase reduces the equivalent mass and increases the equivalent acceleration. Therefore, the velocity distribution in Fig. 9 is explicable. That is to say, the larger the initial gas volume fraction is, the greater its average blowdown velocity is.

Considering the average mass flow rate within 0.01 s after gas entrainment in each phase volume fractions, the results are shown in Fig. 10. With the increase in initial gas volume fraction, the velocity becomes larger, but gas volume fraction decreases the density more effectively; therefore, the mass flow rate is reduced.

In this condition, the time gas entrainment occurs is shown in Table 2:

Thus, it can be seen that, the greater the gas volume fraction is, the earlier entrainment can occur, the more loss of coolant can be saved.

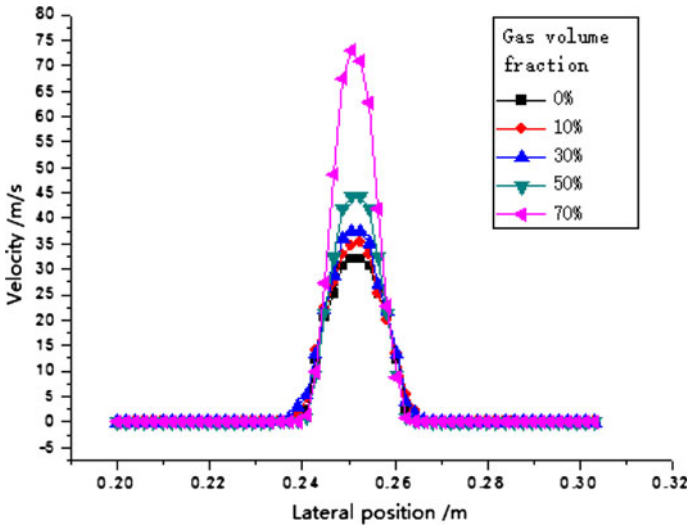


Fig. 9 Velocity of different gas volume fraction under 1000 kPa

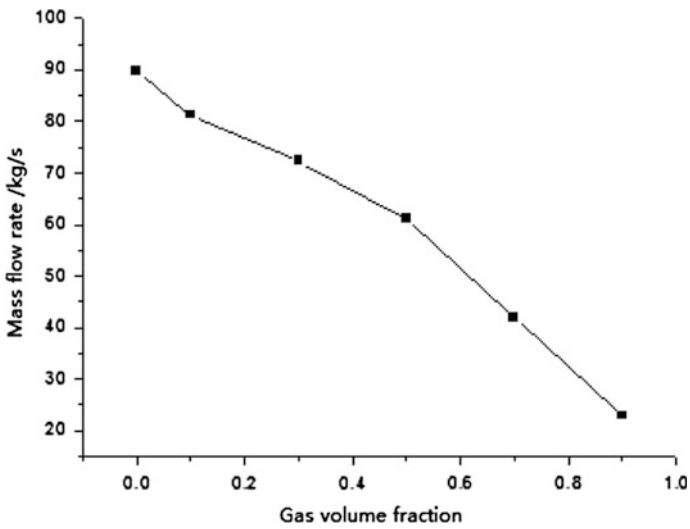


Fig. 10 Mass flow rate of different gas volume fraction under 1000 kPa

Table 2 Time entrainment occurs of different gas volume fraction

Initial gas volume fraction	0	0.1	0.3	0.5	0.7	0.9
Time entrainment occurs/s	0.02955	0.02878	0.02105	0.02021	0.01890	0.01879

3 Conclusions

This paper uses a CFD model to simulate the flow processes in primary circuit pressure boundary when the small-break LOCA occurs. The final result is that the sharp, long channel break can increase the resistance and reduce the mass flow rate.

As for flash distillation phenomenon caused by the break, the average density, the velocity distribution, and the mass flow rate are all changed a lot due to the influence of gas phase. The velocity increases with the initial gas volume fraction, while the mass flow rate decreases contrarily considering that the gas volume fraction can meanwhile influence the fluid density. Besides, the larger the initial gas volume is, the earlier the gas entrainment will occur and the loss of coolant will be reduced. Thus, the author believes that gas entrainment will reduce the loss of coolant and save time for emergency core cooling.

References

1. Craya A. Theoretical research on the flow of nonhomogeneous fluids [J]. *La Houille Blanche*, 1949, 4: 44–55.
2. Lubin B T, Hurwitz M. Vapor Pull-Through at a Tank Drain—With and Without Dielectrophoretic Baffling[C]//Conference on Long Term Cryo-Propellant Storage in Space. 1966: 173.
3. Bowden R C, Hassan I G. The onset of gas entrainment from a flowing stratified gas–liquid regime in dual discharging branches: Part I: Flow visualization and related phenomena [J]. *International Journal of Multiphase Flow*, 2011, 37(10): 1358–1370.
4. Fachun Liang. The application of gas-liquid two-phase flow sampling distributor in flow metering [D]. Xi'an: Xi'an Jiao Tong University, 2006.
5. Liejin Guo. Two-phase and multiphase flow dynamics [M]. Xi'an: Xi'an Jiao Tong University press, 2002:594–596.

The Resistance Characteristics Study of Emergency Feedwater System

Qiu Jimeng, Sheng Meiling, Liu Changliang and Liu Jiang

Abstract As an important engineered safety system, in the event of failure of the normal feedwater systems, the Emergency Feedwater System operates to supply feedwater to steam generator and remove residual core heat. In this work, the resistance characteristics of the Emergency Feedwater System of the third-generation reactor are studied by FLOWMASTER. The effects of the aperture of the orifice and the opening rate of the control valves on feedwater flow rate were analyzed, and the reasonable aperture of the orifice and the opening rate of the control valves were determined to ensure that the system meets the requirements of the third-generation nuclear power plant.

Keywords Emergency feedwater system · Resistance characteristics · Aperture of the orifice · Opening rate of the control valves · FLOWMASTER · Thermal-hydraulic

1 Introduction

The Emergency Feedwater System (EFWS) serves as a backup system for supplying feedwater to the secondary side of the steam generators upon loss of the main feedwater supply and removes the residual heat of the core until the Reactor Coolant System could be cooled by the Residual Heat Removal System.

Q. Jimeng (✉) · S. Meiling · L. Changliang · L. Jiang
China Nuclear Power Engineering Co., Ltd, Beijing, China
e-mail: qiujm@cnpe.cc

S. Meiling
e-mail: shengml@cnpe.cc

L. Changliang
e-mail: 18610087233@163.com

L. Jiang
e-mail: liujiang@cnpe.cc

With the rapid development of the nuclear technology, lots of studies on the reliability of the EFWS have been done [1–4]. The resistance characteristics of the EFWS are mainly studied by the commissioning tests of the nuclear power plant, but these commissioning tests are just suitable for some particular conditions [5]. This method could not be applied to the new-generation reactor system design.

According to the higher safety requirements, the EFWS of the third-generation reactor should provide enough feedwater to the generations and prevent the generation from overflow during the first 30 min of the accident without the manual operation. The thermal-hydraulic model of the EFWS was established from the FLOWMASTER, and the system resistance characteristic was assessed in this work: the influence of the orifice's aperture and the opening rate of the control valves on the flowrate of the feedwater. The appropriate aperture of the orifice and opening rate of control valves were recommended in this work, to ensure the EFWS can be able to meet the safety requirements of the third-generation reactor.

2 Resistance Characteristic Study

2.1 Simulation Modeling

The key equipment of the EFWS consists of two storage pools, a pump subsystem and a set of injection lines equipped with flow control valves, orifices and feedwater isolation valves connected to the steam generators. And the main equipment of the pump subsystem includes two 50% flow rate turbine-driven pumps, which are steam-supplied from main steam lines upstream of the SG steam isolation valves and exhausting to the atmosphere via mufflers, and two 50% flow rate motor-driven pumps, which are powered by emergency power (diesel generators). The thermal-hydraulic model of the EFWS was established through the FLOWMASTER software, and the sketch of the model is shown in Fig. 1.



Fig. 1 Sketch of the EFWS thermal-hydraulic model

The aperture of the orifice, the opening rate of the control valves, the steam generator's pressure and the performance of the pumps influenced the feedwater flow rate. After the selection of the pump, it was difficult to meet all of the system's transient analyses by optimizing the performance of the pumps, and the different SG's pressure were the inputs of the system's transient analyses. Therefore, the influences of the orifice's aperture and the control valves' opening rates on the system's resistance were studied in this work, in order to obtain the reasonable system parameters to meet all the requirements of the operation conditions.

The requirements of the feedwater flow rate of the third-generation EFWS mainly include:

- (1) Minimum flow rate: the minimum flow rate scenario would occur when either of the two feedwater series was failure and one of the three steam generators was failure too, that is, only one motor-driven pump and one turbine-driven pump could be useful. In this case, the minimum flow rate to the intact SGs should be more than 45 m³/h.
- (2) Maximum flow rate: the maximum flow rate scenario would occur when all the pumps (two motor-driven pumps and two turbine-driven pumps) operate and one series of control valves are fully open and other series of control valves are at the minimum opening rate. In this case, the maximum flow rate to the broken SG should be less than 250 m³/h.

2.2 The Influence of the Orifice's Aperture on the System Resistance

In this section, the feedwater flow characteristics of different orifice's apertures in the above two scenarios are simulated by FLOWMASTER, in order to determine the optional orifices' aperture for the system operation.

2.2.1 The Influence of the Minimum Flow Rate

The effect of the different orifice's apertures on the minimums feedwater flow rate was analyzed in the case of only one of feedwater branches available. As shown in Fig. 2, if the EFWS meets the minimums feedwater requirement, the orifice's aperture shall be more than 17.2 mm. It also shows that the larger the aperture, the greater the feedwater flow rate is, so the effect of the increase in the aperture on the feedwater flow rate should be considered: the increase in the flow rate to the faulted steam generator. So, the both of aspects should be considered to determine the range of the orifice's aperture.

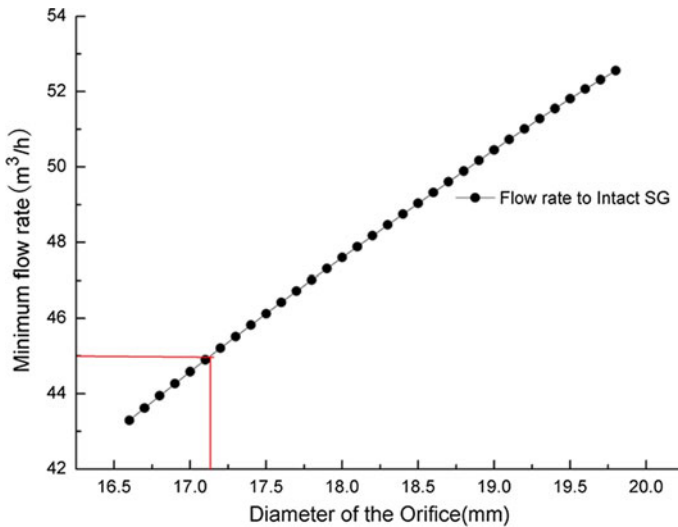


Fig. 2 Minimum flow rate in different apertures

2.2.2 The Influence of the Maximum Flow Rate

The effect of the different orifice's apertures on the maximum feedwater flow rate was analyzed in the case of all the EFWS pumps operating at the same time one train of the control valves was fully open and the other train of the control valves at the minimum opening rate. As shown in Fig. 3, if the EFWS system meets the maximum feedwater requirement, the orifice's aperture shall be less than 20 mm. It also shows that the smaller the aperture of the orifice, the smaller the maximum water flow rate, but also must be considered at the same time, and it may cause the minimum flow rate cannot meet the requirements.

2.2.3 Result of Orifice Study

According to the above analysis results, in order to meet the requirement of the maximum and minimum feedwater flow rate of the EFWS, the aperture of the orifice must be in the range of 17.2–20.0 mm.

2.3 Effect of the Control Valve's Opening Rate on the Feedwater Flow Rate

Because the common feedwater pipe is disposed downstream of the EFWS pumps, the change in the control valve's opening rate in any branch can cause the change

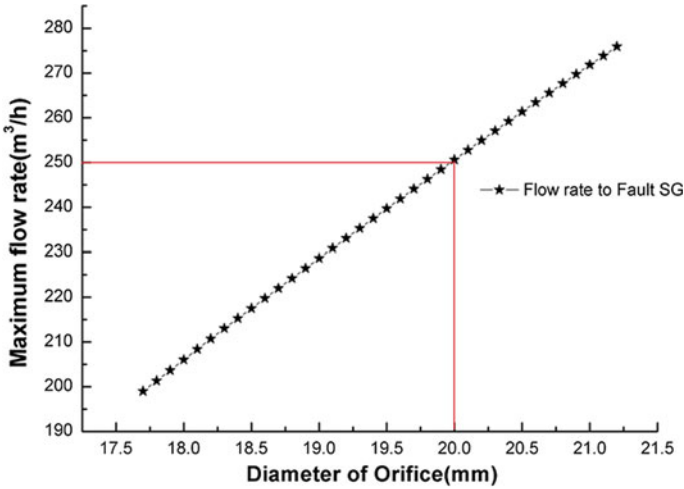


Fig. 3 Maximum flow rate in different apertures

flow rate of all the feedwater branch pipes. In this section, the condition that would lead to the steam generator overflow is analyzed, in order to determine the reasonable opening rate, to ensure the feedwater flow rate to the intact steam generators well enough, at the same time to the steam generator which occurred SGTR accident without overflow.

2.3.1 The Change in the One Train of Control Valves

Assuming that one train of control valves is fully open, another train of control valves is in different opening rate, the calculation results of the feedwater flow rate to the intact SGs before and after isolation from the fault SG are shown in Fig. 4. As shown in Fig. 4, the range of the opening rate from 20 to 60% has a significant influence on the feedwater flow rate. According to the requirement of the accidental analysis, the feedwater flow rate to the any one of the intact steam generator at any time shall not be more than 100 m³/h; therefore, as shown in Fig. 4, the small opening setting value of the control valves in the closed-loop adjustment condition should not be greater than 45%.

2.3.2 Synchronous Adjustment of the Both Trains of Control Valves' Opening Rate

Assuming that the both trains of the control valves are in a state of synchronous adjustment, the calculation results of the feedwater flow rate to the intact SGs before and after isolation from the fault SG are shown in Fig. 5. As shown in Fig. 5,

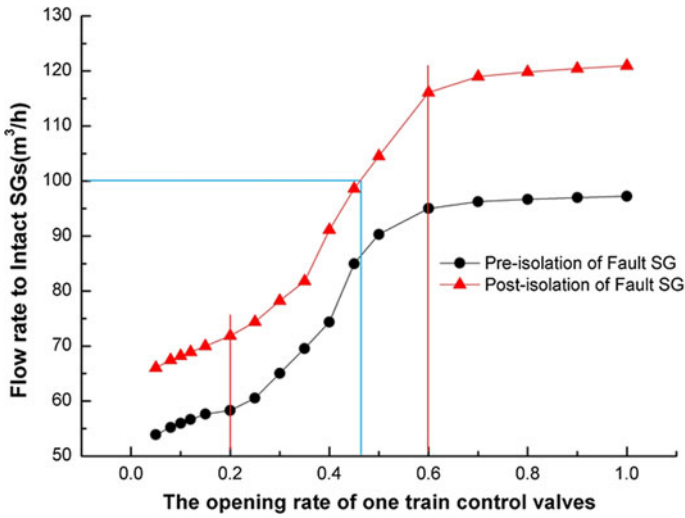


Fig. 4 Feedwater flow rate to the intact SG with one train valves in different opening rates

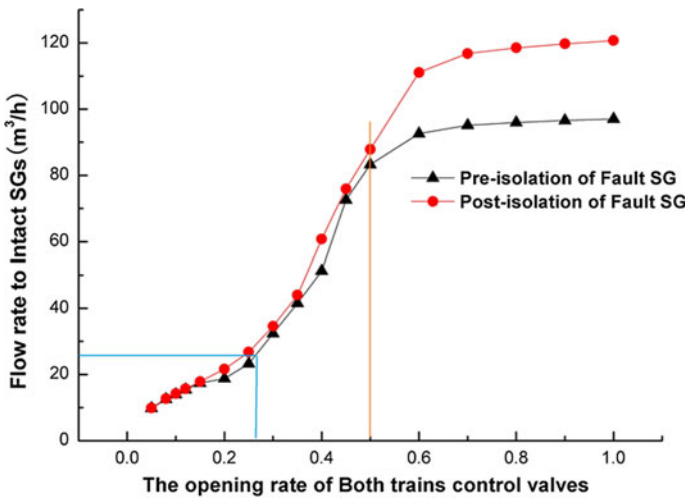


Fig. 5 Feedwater flow rate to the intact SGs with both trains of control valves synchronous adjustment

when the opening rate of the both trains of control valves in the 0–50% range, the feedwater flow rates to the intact SGs before and after isolation from the fault SG are almost the same; however, when the opening rate of the both trains of control valves in the 50–100% range, there is a significantly difference between before isolation and after isolation from the fault SG. According to the requirement of the accidental analysis, the feedwater flow rate to the any one of the intact steam

generator at any time shall be more than $25 \text{ m}^3/\text{h}$; therefore, the small opening rate setting value of the control valves in the closed-loop adjustment condition should not be less than 28%.

2.3.3 Result of Control Valves Study

According to the above analysis, the small opening rate setting value of the control valves in the closed-loop adjustment condition should be in the 28–45% range, so as to be in line with the requirement of maximum and minimum feedwater flow rate.

3 Conclusions

Through the FLOWMASTER software to simulate and calculate the EFWS, the resistance characteristics of the system were evaluated, analysis of the influence of the apertures of the orifice and the opening rate of the control valves on the feedwater flow rate.

On the basis of meeting the requirements of the EFWS, the aperture of the orifice should be in the range 17.2–20.0 mm and the small opening rate setting value of the control valves in the closed-loop adjustment condition should be in the 30–45% range.

Finally, the reliability and availability of the proposal of the EFWS was verified by the thermal-hydraulic simulation results.

References

1. Han Pinling, Feng Bingliang, Bao Zhonglin, et al. Auxiliary Feedwater System Reliability Analysis for Qinshan Nuclear Power Plant [J]. Nuclear Power Engineering, 1986, 7(2): 29–34 (in Chinese).
2. Han Xiaofeng, Xue Dazhi. On the Reliability of the Auxiliary Feed-Water System Design [J]. Nuclear Power Engineering, 1988, 9(5): 29–35(in Chinese).
3. Kan Qiangsheng, Huang Canhua. Design of Auxiliary Feedwater System for Nuclear Power Plant [J]. Nuclear Power Engineering, 1998,19(3):208–213(in Chinese).
4. Chu Yongyue, Yi Yan, Li Huwei. Reliability Analysis of Auxiliary Feed Water System (AFWS) at Nuclear Power Plant by Using GO-FLOW Methodology [J]. Radiation Protection Bulletin, 2012, 23(5): 19–23(in Chinese).
5. Tian Weiwei, Li Jun, Wang Zhigang. System Retrofits of Emergency Feedwater System Flowrates Deviation [J]. Atomic Energy Science and Technology, 2012, 46(Suppl.): 277–282 (in Chinese).

Author Biographies

Jinqing Qiu (1981–) Senior Engineer, Process and Layout Design Division, China Nuclear Power Engineering Co., Ltd. Beijing, China. As a system engineer to be responsible for the design work of nuclear power plant auxiliary systems and engineered safety systems during conceptual design, preliminary design and final construction design.

Meiling Sheng (1989–) Process and Layout Design Division, China Nuclear Power Engineering Co., Ltd. Beijing, China. Study on process design of nuclear reactor.

Changliang Liu (1981–) Male, System and Layout Department of China Nuclear Power Engineering Co, Ltd., system and equipment design and research.

Liu jiang (1972–) Process and Layout Design Division, China Nuclear Power Engineering Co., Ltd. Beijing, China. Study on process design of nuclear reactor.

The Setting of RPN Power Range Calculation Parameters in Fuqing Nuclear Power Plant

Fanfeng Meng

Abstract The function of RPN in Fuqing Nuclear Power Plant is to continuously monitor the reactor power, the power level and its distribution changes. The nuclear power signal measured by the four power range in RPN is sent to DCS to monitor the nuclear power, the power distribution, rod control, reactor protection and so on. It is thus of great significance for the security of Fuqing Nuclear Power Plant to ensure the accuracy of measuring results of the RPN power range. In Fuqing's RPN power range, the nuclear power (P_r) and the setting parameters of the axial power deviation (ΔI) are experimented and calculated by using the software of ETALONG. However, the calculation processes, methods, as well as the parameters in the software ETALONG are inconsistent with the implementation logic of P_r and ΔI in the present RPN. Besides, the software ETALONG does not explain the P_r and ΔI calculation processes, methods and parameters, either. In this paper, through analyzing both the implementation logic of P_r and ΔI in the present RPN and that of in the software ETALONG, I get the definite methods of power range calculation parameters and the explicit setting formulas of parameters of RPN power range in Fuqing Nuclear Power Plant so as to ensure its accuracy of measuring results.

Keywords Nuclear power · Axial power deviation · Calculation processes · ETALONG

1 Introduction

Fuqing Nuclear Power Plant Instrumentation System (RPN) function is continuous monitoring of reactor power, change the power level and power distribution. Nuclear power signal RPN 4 \uparrow power range measurement is sent to a distributed control system (DCS), and for power supervision, supervision of power distribution, control rod program, reactor protection. Thus, ensuring RPN power range

F. Meng (✉)

Fujian Fuqing Nuclear Power Co. Ltd., Fuqing 350318, China
e-mail: mengff@fqnp.com

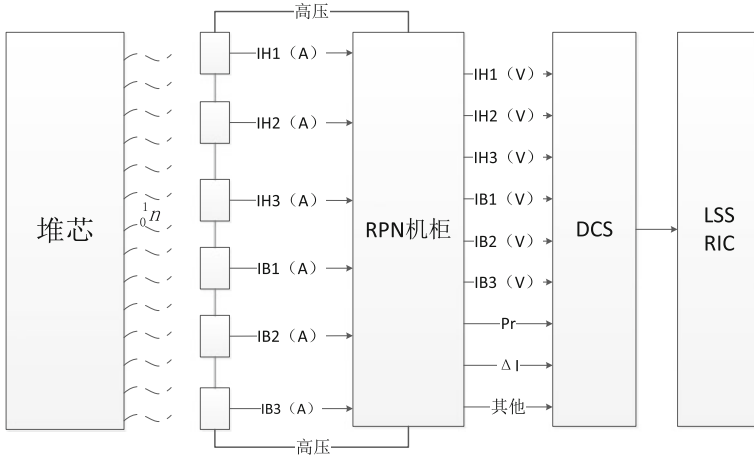


Fig. 1 Power range measurement schematic

measurement accuracy for the safe operation of the Fuqing Nuclear Power Plant is very important. Fujian Fuqing Nuclear Power Plant RPN kernel power range (Pr) and an axial power deviation (ΔI) by the test setup parameters and using software to calculate ETALONG determined. But the RPN power range of Pr and ΔI in the realization of the logic and software Pr and ΔI calculation process, methods, parameters are inconsistent, and software manuals and no explanation thereof Pr and ΔI calculation processes, methods and parameters. In this paper, RPN power range and ETALONG software to achieve logic Pr and ΔI were analyzed to determine the method of Fujian Fuqing Nuclear Power Plant RPN calculation parameters derived power range, defined the parameters set formula to ensure that the power range of power measurements accuracy.

RPN 4 power range channel evenly distributed in the outer core, each of the power range channel is formed by six separate boron neutron sensitive lining base uncompensated ionization chambers, each chamber away from the power-saving current value during power operation measured current value of the input to the RPN cabinet, the current signal is processed to RPN calculation software, complete with ΔI and Pr calculation and each power range measurement is schematically shown in Fig. 1.

2 RPN Power Range of Pr and ΔI Implement Logic

According to “Fujian Fuqing Nuclear Power Plant Unit 1 and 2 Software Requirement Specification Power Range Channel,” RPN in Fuqing Nuclear Power Plant, nuclear power and axial power deviation calculation process and functions is shown in Fig. 2.

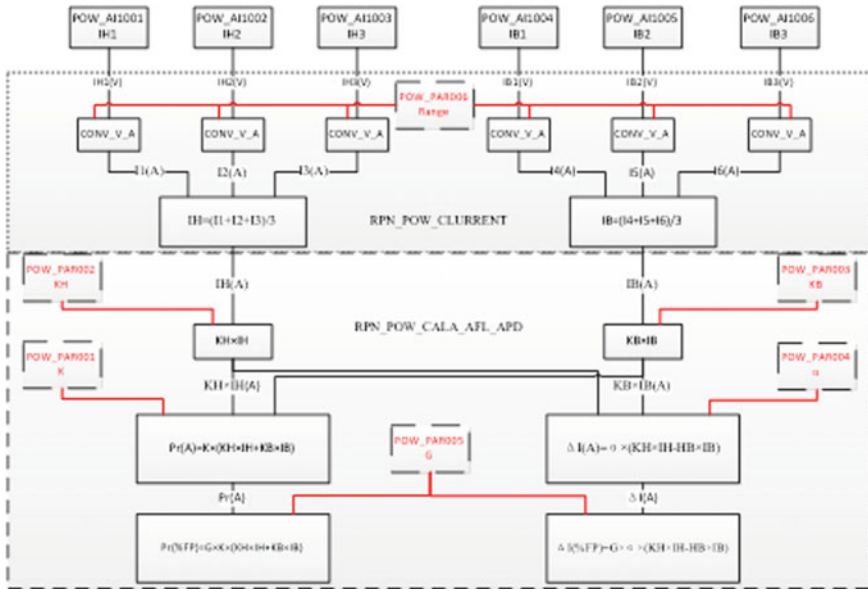


Fig. 2 Power range nuclear power to achieve the axial power deviation function

The figure shows, RPN six power-saving current ionization chamber measurements obtained through POW_AIj001-POW_AIj006 ($j = 1, 2, 3, 4$, on behalf of four power ranges) and other six modules of conversion, the output voltage signal IHi, IBi ($i = 1, 2, 3$, unit V); IHi and IBi are converted to a current signal Ii ($i = 1, 2, 3, 4, 5, 6$, unit A) by the conversion of module CONV_V_A:

$$Ii = K1 \times IHi \quad (i = 1, 2, 3) \tag{1}$$

$$Ii = K1 \times IBi \quad (i = 4, 5, 6) \tag{2}$$

$$K1 = \frac{I_{max}}{10} \tag{3}$$

where:

$K1$ Voltage–current conversion factor, A/V;

I_{max} The maximum output current module CONV_V_A

$I1, I2, I3$ signal through the upper portion of the calculated average current IH , $I4, I5, I6$ calculated average signal through the lower portion of the current IB :

$$IH = \frac{\sum_{i=1}^3 Ii}{3} \tag{4}$$

$$IB = \frac{\sum_{i=4}^6 I_i}{3} \quad (5)$$

IH, AB through RPN_POW_CALA_AFL_APD module calculated reactor power and axial power deviation:

$$Pr = K_{RPN} \times G \times (KH \times IH + KB \times IB) \quad (6)$$

$$\Delta I = \alpha_{RPN} \times G \times (KH \times IH - KB \times IB) \quad (7)$$

According to Eqs. (1)–(7), calculated Pr and ΔI of each power range as follows:

$$Pr = \frac{I_{\max} \times K_{RPN} \times G}{30} \times [KH \times (IH1 + IH2 + IH3) + KB \times (IB1 + IB2 + IB3)] \quad (8)$$

$$\Delta I = \frac{I_{\max} \times G \times \alpha_{RPN}}{30} \times [KH \times (IH1 + IH2 + IH3) - KB \times (IB1 + IB2 + IB3)] \quad (9)$$

where:

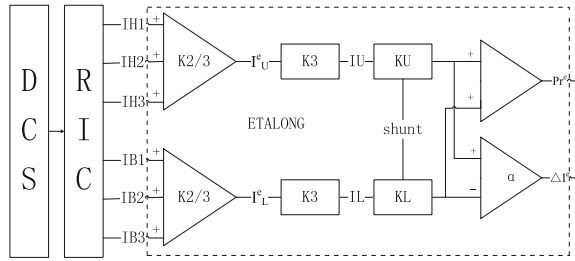
I_{\max}	the maximum output current module CONV_V_A, A, depending POW_PAR006 range;
K_{RPN}	power adjustment factor, dimensionless, depending POW_PAR001 K;
G	current–power conversion factor, % FP/A, depending POW_PAR005 G;
α_{RPN} , KH, KB	amplification factor, dimensionless, depending on whether POW_PAR004, POW_PAR002 KH, POW_PAR003 KB.

In summary, according to the formula (8) and (9), to ensure the accuracy of RPN power range Pr and ΔI calculations required to accurately set within RPN POW_PAR001 K, POW_PAR002 KH, POW_PAR003 KB, POW_PAR004, POW_PAR005 G, POW_PAR006 range these six parameters.

3 Pr and ΔI Within ETALONG Software Implementation Logic

The determination of KH, KB in Fujian Fuqing Nuclear Power Plant is made by test calculated using ETALONG software to achieve, but there is no documentation of software calculation process, and the formula will be described within the software Pr and ΔI , by ETALONG outcome document reverse analysis of data obtained within the software Pr and ΔI formula and process.

Fig. 3 Power distribution and data processing software process



ETALONG software “RPN power scale factor scale test” is calculated based on the measurement data obtained for the software kernel power and axial power deviation calculation parameters α (dimensionless), KU (% FP/ μ A), KL (% FP/ μ A), shunt (μ A/V), ETALONG software Pr and ΔI calculation process shown in Fig. 3.

IHi, IBi through K 2/3 module to give the core, the lower the current and the equivalent value I_U^e, I_L^e , their relationship are as follows:

$$I_U^e = K2 \frac{IH1 + IH2 + IH3}{3} \tag{10}$$

$$I_L^e = K2 \frac{IB1 + IB2 + IB3}{3} \tag{11}$$

Where:

K2 amplification factor, dimensionless;

I_U^e the equivalent current value of the upper portion of the core, V;

I_L^e the equivalent current value of the lower portion of the core, V

I_U^e, I_L^e After K3 module to give the core, the lower current and IU, IL, follows the relationship:

$$IU = K3I_U^e \tag{12}$$

$$IL = K3I_L^e \tag{13}$$

where:

K3 amplification factor, dimensionless;

IU the upper part of the core current, V;

IL the lowerpart of the core current, V

IU, IL binding parameters $\alpha, KU, KL, shunt$, calculated Pr and ΔI :

$$Pr^E = shunt \times (KU \times IU + KL \times IL) \tag{14}$$

$$\Delta I^E = \alpha \times \text{shunt} \times (K_U \times I_U - K_L \times I_L) \quad (15)$$

Formulas (14) and (15) are the formulas of Pr and ΔI within ETALONG.

4 The Computing Settings and Test Parameters of Power Range

4.1 The Setting of KH, KB, α_{RPN}

Power range and core power distribution measuring data processing software to calculate the nuclear power and axial power deviation should be consistent, that is, $\text{Pr}^E = \text{Pr}$, $\Delta I^E = \Delta I$. According to Eq. (8)–(15) can be obtained:

$$\text{KH} = 10 \times \frac{K_2 K_3 \text{shunt}}{I_{\text{max}} K_{\text{RPN}} G} K_U \quad (16)$$

$$\text{KB} = 10 \times \frac{K_2 K_3 \text{shunt}}{I_{\text{max}} K_{\text{RPN}} G} K_L \quad (17)$$

$$\alpha_{\text{RPN}} = K_{\text{RPN}} \alpha \quad (18)$$

After analyzing the data core power distribution, data processing software process and result file obtained: $K_2 = 3/5$, $K_3 = 3/5$, shunt = 100, can be seen, formulas (16) and (17) can be simplified for:

$$\text{KH} = \frac{360}{I_{\text{max}} K_{\text{RPN}} G} K_U \quad (19)$$

$$\text{KB} = \frac{360}{I_{\text{max}} K_{\text{RPN}} G} K_L \quad (20)$$

The formula (18)–(20) is the setting of KH, KB in Fujian Fuqing Nuclear Power Plant.

4.2 K_{RPN} 的设定

By the formula (8) shows that, in the case of other power ranges calculated parameters remain unchanged, Pr proportional K_{RPN} :

$$\frac{Pr^1}{Pr^2} = \frac{K_{RPN}^1}{K_{RPN}^2} \tag{21}$$

where

- Pr^1 before K_{RPN} adjustment power range measurement obtained nuclear power;
- Pr^2 After K_{RPN} adjusting the power range measured nuclear power;
- K_{RPN}^1 setpoint before adjustment K_{RPN} ;
- K_{RPN}^2 setpoint after adjustment K_{RPN}

Consistent with the adjusted power range measurement of nuclear power should be measured with a thermal power KME, namely:

$$Pr^2 = P_{KME} \tag{22}$$

By the formulas (21) and (22) seen:

$$K_{RPN}^2 = \frac{P_{KME}}{Pr^1} K_{RPN}^1 \tag{23}$$

Equation (23) is the setting of K_{RPN} in Fuqing Nuclear Power Plant.

4.3 G and Imax Setting

POW_PAR006 range value Fujian Fuqing Nuclear Power Plant will be at the factory by the factory staff in RPN setting, set value 4, value Imax POW_PAR006 range varies with changes as given in Table 1.

POW_PAR005 G values Fujian Fuqing Nuclear Power Plant will be set at the factory by the factory staff in RPN setting is 1E + 6.

Value and G Imax using factory set value during operation of the plant, usually without modification.

Table 1 Imax value change table with POW_PAR006 range

Range	Imax (A)
1	4E-5
2	1E-4
3	1.2E-4
4	2E-4
5	5E-4

5 Conclusion

In this paper, RPN power range and ETALONG software Pr and ΔI to achieve logic analysis, Fuqing nuclear power plant in Fujian RPN power range calculation coefficient set formula to ensure that the RPN power range measurement Pr and ΔI accuracy. In the actual operation of the power plant, Pr and ΔI obtained by RPN power measurement are accurate and effective, and the correctness of the formula is proved.

Transient Analyses of Main Steam Line Break Accident for High-Power Passive Reactor

Zhuang Shaoxin, Sun Wei, Jing Jianping, An Jieru
and Zhang Chunming

Abstract Passive reactor is quite different from traditional “two generation” nuclear power plants in the world at present. The primary system of passive nuclear power plant is modeled using RELAP5/MOD 3.3 code, and the transient thermal hydraulic characteristics are analyzed under the accident sequence of main steam line break (MSLB). DNBR of core is calculated by VIPRE code. Break spectrum is summarized as: When the break size is less than 0.058 m^2 , the reactor will not shut down; when the break size is between 0.059 and 0.105 m^2 , the reactor will shut down by overpower ΔT reactor trip; and when the break size is between 0.106 and 0.15 m^2 , the reactor will shut down by the steam pipe low-pressure injection signal. And the limited condition is 0.105 m^2 . The results of the limited condition show that the core heat flux, reactor coolant system (RCS) pressure and temperature fluctuate by time. The minimum value of the DNBR is 1.914, greater than limited value 1.45. The DNB design basis is met for the steam system piping failure event. DNB of a MSLB is not precluded by the criteria. The preceding result shows that no DNB exists for the main steam line rupture.

Keywords RELAP5/MOD 3.3 code · High-power passive · MSLB

1 Introduction

Passive reactor is quite different from traditional “two generation” nuclear power plants in the world at present. Using passive safety simplifies plant system a lot, according to which, safety and reliability have also been improved [1]. As the passive safety system is introduced, lots of differences have been found in thermal hydraulic phenomena and accident scenarios between passive reactor plants and traditional PWRs. Researches on passive reactor plant accident analyzing with system analysis codes have been developed widely [2–5]. But most of the research-

Z. Shaoxin (✉) · S. Wei · J. Jianping · A. Jieru · Z. Chunming
Nuclear and Radiation Safety Center, MEP, Beijing, China
e-mail: 13716931366@163.com

ches were focused on LOCAs, while there were few analyses on other design basis accidents.

The main steam line break (MSLB) accident belongs to the increase in heat removal from the primary system accidents, which is classified as a Condition IV or III event. This paper built a complete model of high-power passive reactor with RELAP5/MOD 3.3, to analyze the key parameters of thermal hydraulic characteristics and passive system characteristics, which were observed from the primary and secondary loops.

2 Code Introduction and Node Model

2.1 Code Introduction

SNAP is used to build the graphical model and for post-processing of calculation results during the transient analyses of MSLB accident in this paper. RELAP5/MOD 3.3 is used to perform transient calculation.

2.1.1 Introduction of SNAP

The Symbolic Nuclear Analysis Package (SNAP) consists of a set of integrated applications to simplify the process of performing engineering analysis. SNAP is established in engineering analysis of common application framework, to create and edit engineering analysis code input and a wide range of functions, for submission and monitoring, and it provides a highly flexible framework and specification of the interactions.

SNAP is coupled to many codes, such as RELAP5, PARCS, TRACE, MELCOR, COBRA, CONTAIN and FRAPCON-3.

2.1.2 Introduction of RELAP5

The RELAP5/MOD 3.3 code was published in 1979. Thereafter, the code has been widely accepted around the world commercial and experimental analysis of light water reactor (LWR) systems and their associated scale system. By evolution and use, the code becomes more complex, while the user base is significantly increased. The number of types of problems that can be handled by the code is also increased [8, 9].

2.1.3 Introduction of VIPRE

To Westinghouse VIPRE-01 version, a three-dimensional channel coding, have been development to hydraulic and nuclear effect of core channels and enthalpy

liters for Safety Analysis Report. VIPRE-01 core modeling is based on one-channel modeling method. Mass, axial and transverse momentum conservation equations, and energy solutions of fluid enthalpy, axial flow, transverse flow, and pressure drop. The VIPRE-01 core model is approved by the NRC (reference 83) using the applicable DNB correlation to determine the DNBR along the core of the thermal channel under all expected operating conditions. VIPRE-01 can be used for instantaneous DNB analysis.

2.2 Node Model

The high-power passive reactor coolant system (RCS) consists of two reactor coolant circuits, which are connected in parallel with a reactor vessel, from a pressure vessel containing a nuclear fuel. Each reactor coolant circuit consists of a steam generator, two pumps, one pressurizer, pipes and related instrumentation. In addition, the primary system includes components such as core make-up tank (CMT), accumulator, IRWST, PRHRHX and control system. The node graph in Fig. 1 is based on the RELAP5/MOD 3.3 model of high-power passive reactor system.

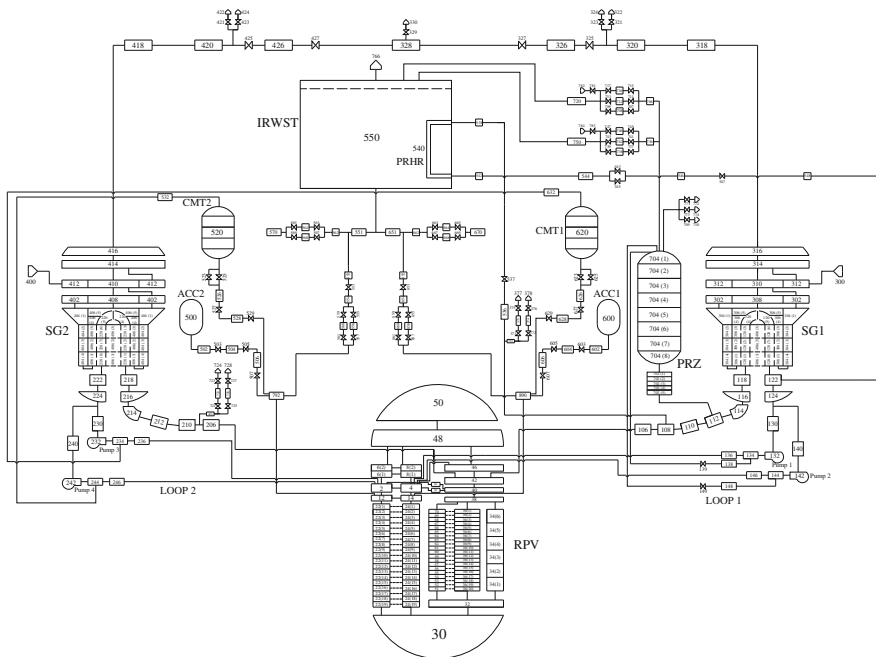


Fig. 1 Node model for high-power passive reactor

3 Accident Description and Analysis Assumptions

3.1 Accident Description

The process of AP1000 plant major feedwater line rupture can be divided into 3 phases as follows.

In a MSLB event, the steam release flow increases firstly, then decreases because of the falling of steam pressure. Coolant temperature reduces because of the energy removal from the RPV, so as pressure.

If most of the active RCCA is assumed to remain in its fully drawn-out position after the reactor's travel, there is an increase in the likelihood that it becomes critical to return to the power core. Returning to the electricity steam pipeline rupture is a potential problem, mainly because of the existing high power peaking factors, assuming the most lively RCCA into a fully retracted position. The core is the ultimate closure of boric acid solution that provides the core a cooling system passively.

3.2 Analysis Assumptions

Considering the MSLB is a DNB limited condition, initial conditions would be assumed as same as rated conditions (Table 1).

The case analyzed assumes a double-ended rupture of the main steam line at full power. Major assumptions used in the analysis are as follows.

3.2.1 Operational Parameters Assumptions

The plant is initially operating at 100 percent of the design plant rating.

A MSLB is classified as a Condition IV event.

3.2.2 Reactor Core Assumptions

- 1) A maximum moderator temperature coefficient is assumed.
- 2) A minimum Doppler reactive coefficient is assumed.

Table 1 Sequence of MSLB accident for high-power passive reactor

Events	Time (s)
Main steam line break	0.0
Overpower reactor ΔT setpoint reached	14.7
Rods begin to drop	17.0
Minimum DNBR occurs	17.4
Maximum core heat flux occurs	17.4

The most reactive RCCA is assumed stuck in its fully withdrawn position. In analysis here, with RCCA insertion, several seconds is used as insertion time to dashpot entry.

3.2.3 Control System Assumptions

Press trip and heap occurred received the “S” signal.

3.2.4 Accident Causes and Function Assumptions

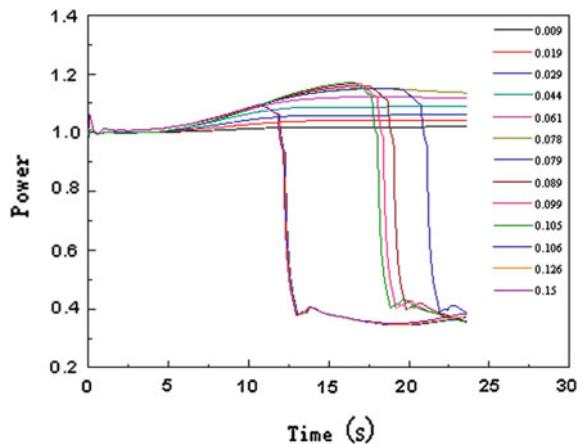
A fast-acting main steam isolation valve is provided in each steam line. These valves are assumed to fully close within some seconds of actuation following a large break in the steam line. For breaks downstream of the main steam line isolation valves, closure of at least one valve in each line terminates the blowdown.

4 Results Analysis

Break spectrum is summarized as:When the break size is less than 0.058 m², the reactor will not shut down; when the break size is between 0.059 and 0.105 m², the reactor will shut down by overpower ΔT reactor trip; and when the break size is between 0.106 and 0.15 m², the reactor will shut down by the steam pipe low-pressure injection signal. And the limited condition is 0.105 m² (Fig. 2).

With assumptions and initial conditions mentioned above, this paper used the RELAP5 high-power passive reactor plant model to compute the MSLB transient. According to the computation, the faulted steam line break resulted in the loss of

Fig. 2 Break spectrum



steam of both steam generators at the time of 0 s. It would cause the heat removal capability of secondary loop to increase, primary loop pressure to decrease and steam generator water level to decrease. At the time of 14.7 s, overpower reactor ΔT setpoint was reached, and after a 2-second delay, reactor tripped.

Figure 3 shows core nuclear power during MSLB transient. Initial operation power was set as rated power. Nuclear power increased because of moderator temperature coefficient and Doppler reactive coefficient. The overpower reactor ΔT setpoint was reached at 14.7 s. Reactor trip signal was sent out after that with a 2-second delay. Nuclear power reduced quickly and reactor tripped successfully. As in Fig. 4, the heat flux is basically consistent with the power.

Figure 5 is the curve of pressurizer pressure versus time. As the figure shows, from 0 to 100 s, the secondary loop heat removal capability increased. Also, pressure of RCS decreased. After reactor tripped, the primary loop temperature and pressure reduced quickly, and the transient ended when the pressurizer level was less than 28.3 m³ (Fig. 6).

Fig. 3 Nuclear power versus time

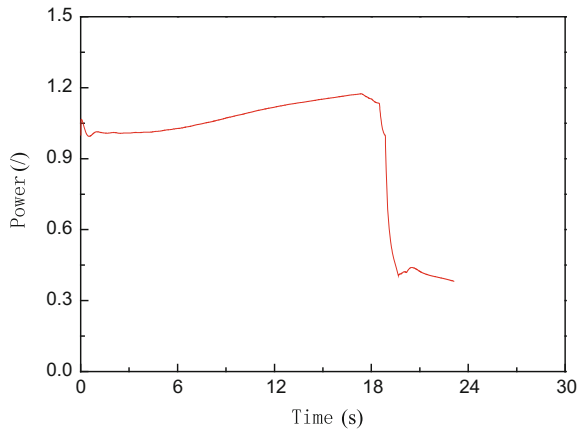


Fig. 4 Heat flux versus time

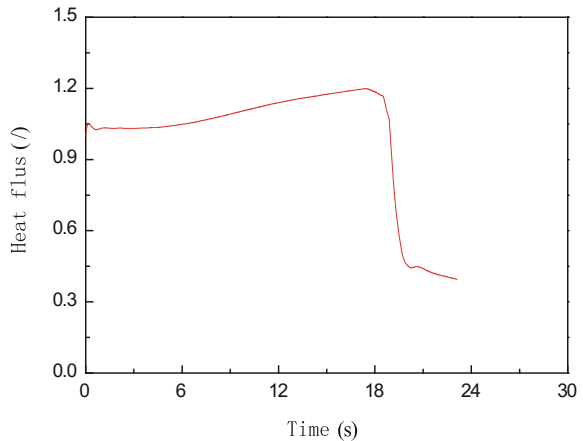


Fig. 5 RCS pressure versus time

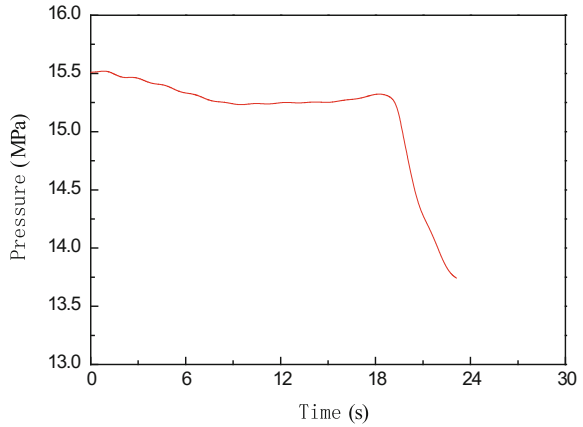


Fig. 6 RCS pressure level versus time

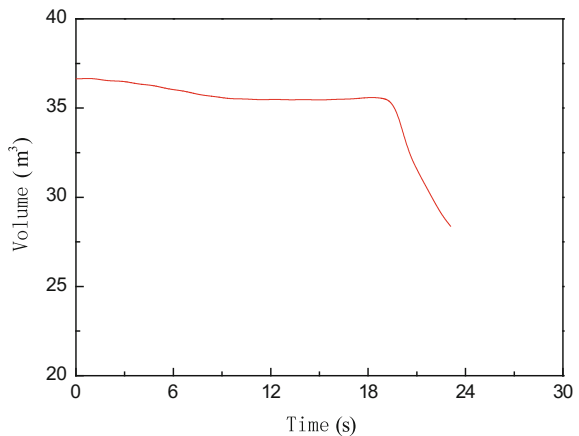


Figure 7 shows the curve of vessel inlet temperature versus time. The curves tell that the temperature transients are almost corresponding with the pressurizer pressure transient, decreasing, a little increasing and decreasing again. It was mainly because that heat power was changing over time after the transient began.

Figure 8 is the curve of steam generator pressure, both the faulted one and the intact one. As is shown, the steam generator pressure is also corresponding with the pressurizer pressure transient, decreasing, a little increasing and decreasing again. It was mainly because that break flow was changing over time after the transient began.

Figure 9 shows steam mass flow transient. In a MSLB event, the steam release flow increases firstly, then decreases because of the falling of steam pressure.

At last, we should focus on DNB. As a result, the minimum DNBR is conservatively calculated using VIPRE and is above the 95/95 limit.

Fig. 7 RCS temperature versus time

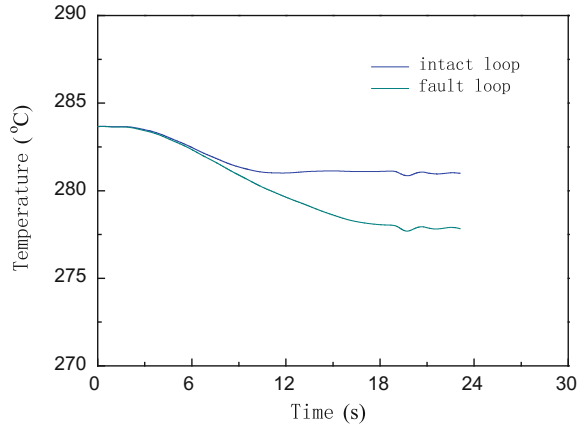


Fig. 8 Steam generator pressure versus time

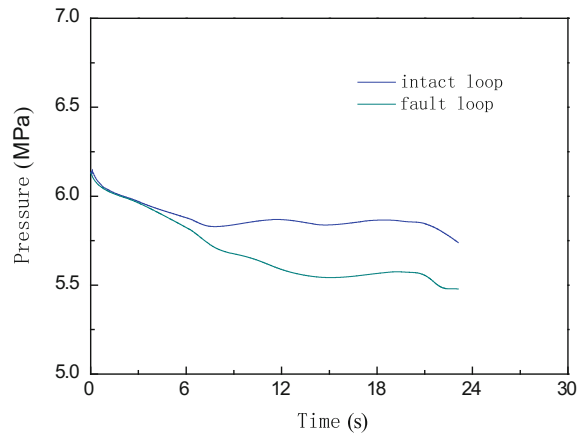
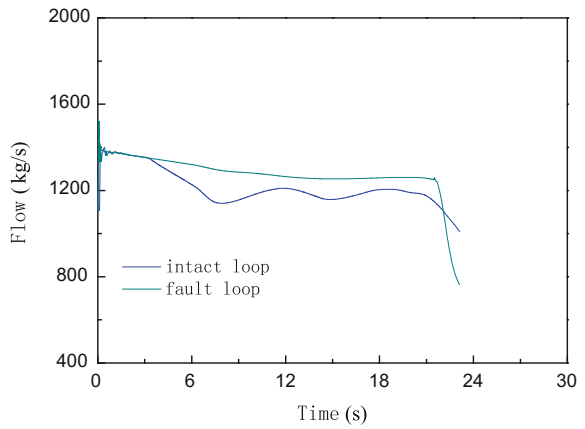


Fig. 9 Steam mass flow versus time



5 Conclusions

The high-power passive reactor plant was modeled with code RELAP5/MOD 3.3, and the characteristics of MSLB transient were analyzed. Results show that:

The design basis of DNB is to meet the pipeline failure event of the steam system. DNB and possible perforation of the cladding layer after the rupture of the steam pipe do not rule out the standard. The analysis showed that no DNB occurred in main steam pipeline rupture assuming the most active RCCA card in its fully retracted position.

Acknowledgments This work was supported by the large advanced pressurized water reactor and high-temperature gas-cooled reactor nuclear power plant national science and technology major projects “CAP1400 safety review technology and independent verification test” (Contract No. 2011ZX06002-010) and “CAP1400 safety review key technology research” (Contract No. 2013ZX06002001).

References

1. Chengge Lin, Zusheng Yu. Nuclear Power Technology of Passive Safety Advanced Pressurized Water Reactor. Beijing: Atomic Energy Press, 2010:60–61.
2. Feng Luo and so on. Analysis of Pump Shaft Accident of Supercritical Water Cooled Reactor. Huadian Technology, 2012, 34 (11):22–25.
3. Jinguo Yao, Zaipeng Li, Xiaoqiang Yang. Analysis of Main Pump Shaft Accident for the Tianwan Nuclear Power Plant. The Safety of Nuclear Power, 2011:174–179.
4. Lixia Ren. Analysis of Primary Pump Shaft Seizure Accident for CEFR. China Institute of Atomic Energy, 2005:13–14.
5. B. Chatterjee, S. K. Gupta, H. S. Kushwaha, V. Venkat Raj. Analysis of the Thermal Hydraulic Consequences Following Common Mode Pump Seizure in a Nuclear Power Plant. Journal of Pressure Vessel Technology, 2002, 124(4).
6. Jianping JING and so on, Discussion on the Thermal-Hydraulic Analysis Codes in the Field of Nuclear Power, The Nuclear Safety, 2012, 33 (3):70–74.
7. Wei Sun and so on. The Application of SNAP to NPP Safety Analysis. [J]. Chinese Technology Information, 2010 (5) 86–87.
8. Shanghai Nuclear Engineering Research and Design Institute. The Analysis of 1&2 Unit SANMEN Nuclear Power Project Final Safety Report. Shanghai: National Nuclear Power Shanghai Nuclear Engineering Research and Design Institute, 2012.
9. Weiwei Wang, Guanghui Su, Wenxi Tian, et al. Development of Thermal- Hydraulic Transient Analysis Code Retac for AP1000 Primary Loop. Atomic Energy Science and Technology, 2011, 45 (10):1185–1190.
10. Yapei Zhang, Wenxi Tian, Zheng Qiu Shi, et al. Transient Analyses of Station Black out Accident for CPR1000. Atomic Energy Science and Technology, 2011, 45 (9):1056–1059.

Transmutation Analysis of Nuclear Waste in a Gas Fast Reactor

Cecilia Martin-del-Campo, Ricardo Reyes-Ramirez,
Guillermo Bastida-Ortiz and Juan-Luis Francois

Abstract It is a given that fast reactors are sustainable nuclear energy sources, for both utilization of fissile material and minimization of nuclear waste, due to the hard neutron spectrum and the strategies for recycling the nuclear fuel materials. The goal of the gas-cooled fast reactor (GFR) is to convert it into an economic electricity generator, with good sustainability and safety characteristics, but also capable of minimizing nuclear waste via transmutation of minor actinides. This work presents a contribution to the neutronic analysis of the GFR as a transmutation facility of minor actinides. In this study, the fuel assembly is a hexagonal lattice of fuel pins. The materials used are mixes of uranium and plutonium carbide or oxide as fuel in pins, silicon carbide as cladding, and helium gas as coolant. The Monte Carlo code SERPENT was used to perform the criticality calculations during the fuel depletion. Two different fuel mixes of uranium, plutonium and minor actinides in the pins of the assembly were compared during a burnup of 1200 days of irradiation (equivalent to 50 GWd/t). The evolution of the atomic densities and the mass inventory, that of consumption versus production, and that of different fissile, minor actinides, fission products and transuranic nuclides in the fuel, as well as the k-effective multiplication factor during the irradiation time, were tracked. The results confirmed that the radiotoxicity of the nuclear waste of LWRs can be reduced using GFRs. One of the fuel mixes studied came from nuclear fuel discharged of a typical PWR with a burnup of 48 GWd/t and five years of cooling post-discharge. This mix was compared with another resulting from a second recycling. Results for several nuclides are presented and an assessment in terms of advantages for breeding and/or transmutation capabilities of each mix is discussed in the paper.

Keywords Transmutation · Breeding · Recycling · Gas fast reactor

C. Martin-del-Campo (✉) · G. Bastida-Ortiz · J.-L. Francois
National Autonomous University of Mexico, Mexico City,
Distrito Federal, Mexico
e-mail: cecilia.martin.del.campo@gmail.com

R. Reyes-Ramirez
Chapingo Autonomous University, Mexico City, Distrito Federal, Mexico

© Springer Science+Business Media Singapore 2017
H. Jiang (ed.), *Proceedings of The 20th Pacific Basin Nuclear Conference*,
DOI 10.1007/978-981-10-2314-9_33

1 Introduction

The International Project on Innovative Nuclear Reactors and Fuel Cycles (INPRO) was launched in the year 2000, based on resolutions of the IAEA General Conference (GC(44)/RES/21) [1]. It is important to remember that the INPRO methodology covers two aspects of environment, and these are the impact of stressors on environment and the depletion of resources in the environment.

Concerning the availability of resources for nuclear reactors, there are:

- (a) Primary resources: natural uranium (U_{nat}) and natural thorium (Th);
- (b) Secondary resources: depleted uranium (DU), highly enriched uranium (HEU), spent nuclear fuel (SNF) as reprocessed uranium (REPU) and recycled plutonium (Pu); and
- (c) Other non-renewable resources: zirconium (Zr).

Primary resources for fueling current nuclear power reactors in the world are abundant. With current consumption rates and prices, conventional uranium resources identified to date will last for about 80 years. This situation is acceptable when compared with reserves of 30–50 years of other commodities, e.g., copper, zinc, petroleum, and natural gas. However, reprocessing and recycling nuclear secondary resources, as well as the use of the technology of fast breeder reactors, would multiply by 60 the longevity of U_{nat} resources currently identified.

It is well known that the main drawbacks of light water reactors (LWRs) technology are probably the limited exploitation of U_{nat} resources coupled with the high-level long-term radiotoxicity of the final waste produced [2]. Furthermore, fuel and metallurgical burnup limits do not allow to achieve high fuel burnup levels in current LWRs operating with open cycles. With such aim GEN-IV reactors are needed in nuclear resources exploiting and waste radiotoxicity reduction. GFR (gas-cooled fast reactor) was proposed by GIF as one of six advanced reactor concepts. GFR is a fast system which uses He as coolant, so that high temperature (until 850 °C) can be reached [3] and high efficiency obtained. Thanks to its fast spectrum, GFR presents a better neutron economy and a great freedom in choosing structural and fuel materials [4]. GFR has also a potential for the reduction in the volume and radiotoxicity of both its own spent fuel and depleted fuel discharged from other reactors, as well as for extending the uranium resources by various orders of magnitude beyond the capability of what the current open fuel cycle can realize. Minor actinide isotopes from existing light water reactor stockpiles can be included in the recycling of a GFR. On the other hand, self-generation of plutonium in the core is also a goal of this fast reactor.

As a result of fuel depletion in any reactor, all kinds of nuclear reactions are happening in the core and the isotopic composition inventory of fuel is in a state of continuous change during the operating lifetime [5]. Changes in power density distribution, variation in the neutron flux, the local power peaking factors, and total reactivity strongly influence the reactor operating life, control, and stability.

Among the phenomena that negatively influence total reactivity, we can cite the poisoning by Xe-135 and Sm-149, the temperature, and obviously fuel depletion [6]. However, the conversion factor from fertile to fissile is a positive effect which, in fast reactors, as is the case of the GFR, compensates for the negative effects. These phenomena must be studied by means of core simulations, and this work presents a contribution to this topic.

2 Study

2.1 Gas-Cooled Fast Reactor Core Characteristics

The GFR is one of the six selected systems by the Generation IV International. GFR operates in the fast neutrons energy spectrum, at high temperature, and in high irradiation environments. Ceramic compounds of carbides and nitrates are proposed for the fuel as they exhibit good performance under the anticipated operating conditions. Given that the neutron reactions are occurring mainly in a high-energy spectrum, it is not necessary to use a moderator material. GFR uses helium as coolant and has a thermodynamic efficiency close to 50%. Helium is an inert gas; it does not suffer phase changes and it does not generate explosive mixtures. However, it should be remembered that helium has poor thermal inertia.

The closed fuel cycle of the GFR permits the use of depleted fuel, duly reprocessed from the own GFR, or from another nuclear reactor. This characteristic makes it possible for the GFR to become an incinerator of actinides.

Research of different fuel design options and materials has resulted in an innovative fuel/cladding layout of U + Pu carbide for the fuel, while refractory materials (SiC and fiber-reinforced SiC) constitute the fuel-containing structure. Carbide (UC–PuC) has high thermal conductivity and a high density of fissile atoms, but high swelling and poor compatibility with air and water. On the other hand, oxide (UO₂–PuO₂) has low thermal conductivity and a low density of fissile atoms, but it does not react with lead or sodium, and it is well known in all the main countries.

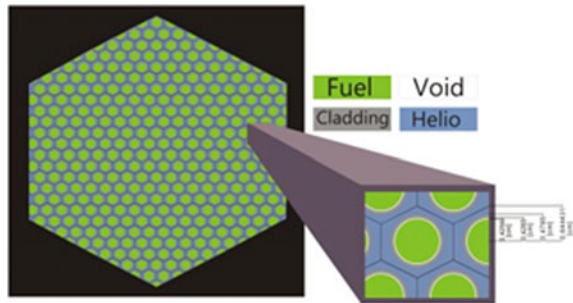
The Allegro reactor is the second line of French-led Fast Neutron Reactor development—and European Union Euratom project under Sustainable Nuclear Industrial Initiative (ESNII). Allegro is a 50–100 MWt experimental GFR version [7] which is envisaged by 2025. This will have either a ceramic core with 850 °C outlet temperature, or a MOX core at 560 °C.

2.2 Methodology

In this paper, neutronics calculations of three different fuel compositions in a GFR lattice are presented. Two of them are oxides and the third is carbide. Oxide composition 1 corresponds to the isotopes from the first recycling of a boiling water reactor

Table 1 Fuel pin compositions in the hexagonal lattice

Nuclide	at/b-cm		
	Oxide composition 1	Oxide composition 2	Carbide composition
U ²³⁵	5.42E-05	4.97E-05	5.67E-05
U ²³⁸	2.14E-02	1.96E-02	7.94E-03
Np ²³⁷	1.70E-04	2.05E-04	0.00E+00
Pu ²³⁹	1.51E-03	1.88E-03	1.75E-03
Pu ²⁴⁰	7.85E-04	1.33E-03	7.93E-04
Pu ²⁴¹	3.10E-04	4.20E-04	3.34E-04
Pu ²⁴²	2.38E-04	4.67E-04	1.51E-04
Am ²⁴¹	1.43E-04	3.16E-04	0.00E+00
Am ²⁴³	5.93E-05	1.23E-04	0.00E+00
Cm ²⁴⁴	1.96E-05	6.50E-05	0.00E+00
Oxigene	4.95E-02	4.94E-02	0.00E+00
Graphite	0.00E+00	0.00E+00	8.531E-02

Fig. 1 Fuel lattice geometry in the core

spent fuel with a discharge burnup of 48 GWd/t; oxide composition 2 corresponds to those from a second recycle. The fuel pin compositions are given in Table 1. Figure 1 shows the fuel lattice geometry. The outside pin radius is 0.4256 cm, the cladding has 0.4285 and 0.4785 as inner and outside radii, respectively, and the pitch between pins is 0.6444 in hexagonal geometry. Total reflection conditions were applied on the six lateral faces and the two axial faces of the assembly.

2.3 Fuel Burnup Calculations

The materials used in the fuel assembly are: oxide or carbide of uranium and plutonium as fuel in pins, silicon carbide as cladding, and helium gas as coolant. The change in the isotopic composition during the burnup should be evaluated by a neutronics simulator in each burnup step. In our study, the code used to perform the calculations of criticality and fuel depletion was SERPENT [8] with JEFF3.1

libraries of effective cross sections at hot operating conditions (fuel temperature = 1200 K).

To obtain a successful depletion calculation involves accounting for the reactivity effects of as many fission products as possible. The creation of the fission product isotopes is probabilistic in nature and follows a distribution. For a given fission event from a specific nuclide, hundreds of fission product nuclide yield combinations are possible. Each fissionable nuclide also contains different yield

Fig. 2 Exposure steps during burnup

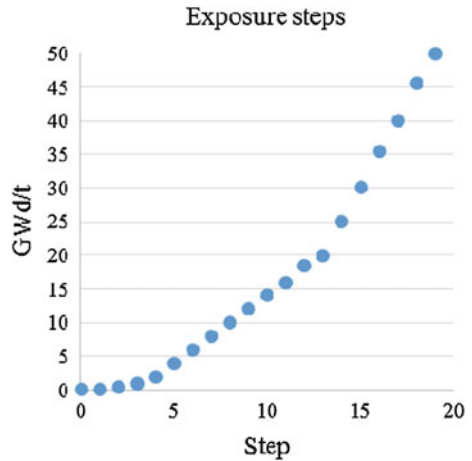
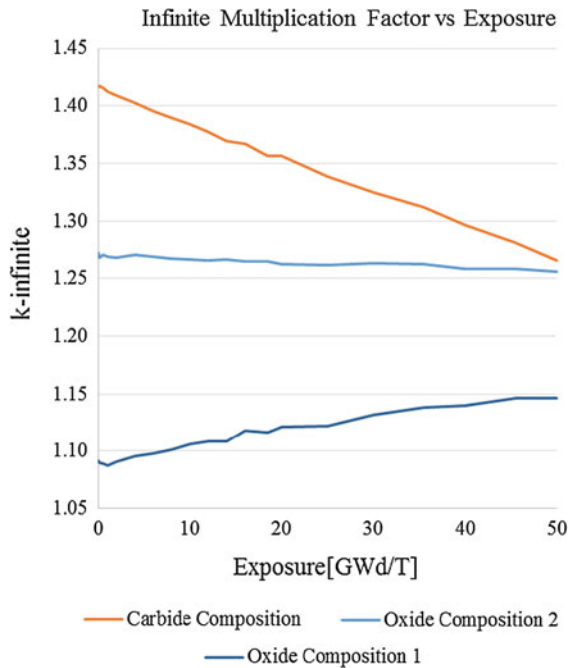


Fig. 3 Infinite multiplication factor evolution



distributions. Taking into account that, the lattices were simulated, using SERPENT, during a period exposure of 1200 days which is equivalent to a burnup of 50 GWd/t using 20 steps (see Fig. 2).

Figure 3 shows the evolution of the k-infinite multiplication factor as function of exposure for the three lattices.

It is important to note that carbide composition has a high decrement of k-infinite with exposure, and the oxide composition 2 has a k-infinite multiplication factor very stable. For the oxide composition 1, this parameter increases with burnup and, however, has a lower value.

The atomic densities of fissile nuclides at the beginning of exposure are shown in Fig. 4. In order to see the main changes in fuel compositions, Table 2 shows the differences of the atomic densities during the exposure period from 0 to 50 GWd/t.

Changes in atomic densities with burnup of uranium, plutonium, americium, neptunium, and curium are plotted in Fig. 5. The main changes are in U^{238} , Pu^{239} , and Pu^{241} .

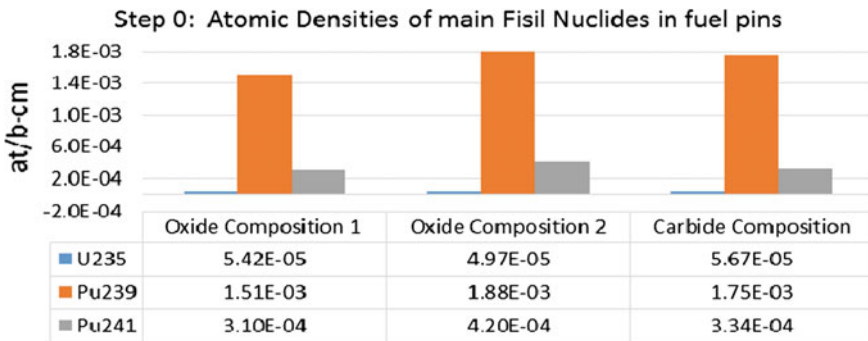


Fig. 4 Step 0 atomic densities of fissile nuclides

Table 2 Changes in atomic densities with fuel burnup

Final (At 50 GWd/t)–initial (at 0 GWd/t)			
	Oxide composition 1 delta (at/b/cm)	Oxide composition 2 delta (at/b/cm)	Carbide composition delta (at/b/cm)
U^{235}	-2.42E-05	-1.81E-05	-1.71E-05
U^{238}	-1.64E-03	-1.21E-03	-3.76E-04
Np^{237}	-5.58E-05	-5.47E-05	1.61E-06
Pu^{239}	4.55E-04	1.88E-04	-2.11E-04
Pu^{240}	6.36E-05	-2.05E-05	6.66E-05
Pu^{241}	-1.17E-04	-1.33E-04	-9.09E-05
Pu^{242}	-5.84E-06	-2.15E-05	6.43E-06
Am^{241}	-2.84E-05	-6.09E-05	3.79E-05
Am^{243}	2.06E-06	-3.60E-08	1.13E-05
Cm^{244}	1.28E-05	1.14E-05	1.53E-09

Fig. 5 Total changes in atomic densities

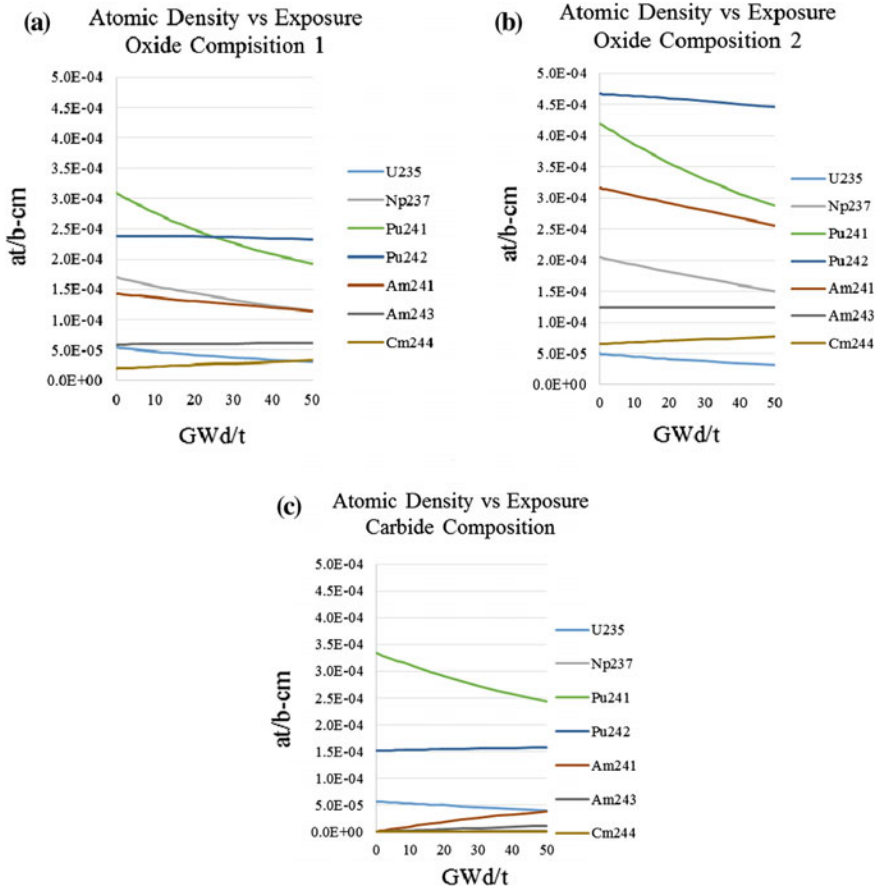
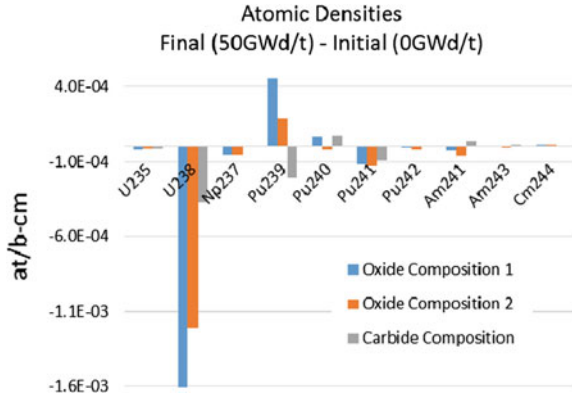


Fig. 6 a Atomic density evolution, oxide 1, b atomic density evolution, oxide 2, c atomic density evolution, carbide

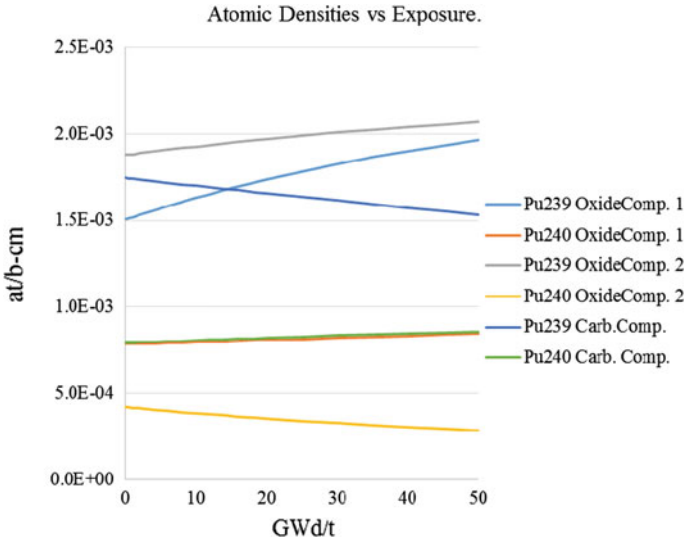


Fig. 7 Atomic density evolution of Pu²³⁹ and Pu²⁴⁰ all the compositions

Figure 6 shows the evolution of the following isotopes: U²³⁵, Np²³⁷, Pu²⁴¹, Pu²⁴², Am²⁴¹, Am²⁴³, and Cm²⁴⁴, during burnup: 6a for oxide composition 1; 6b for oxide composition 2; and 6c for carbide composition. The three graphs use the same Y-axis scale (0–5E–04) to show the differences under the same relative values. Another graph was used for isotopes: Pu²³⁹ and Pu²⁴⁰, shown in Fig. 7, because the values were out the scale on the graphs of Fig. 6.

3 Conclusions and Comments

Based on the results, we can conclude the following:

- Oxide compositions are better options than carbide composition for breeding fissile materials as Pu²³⁹ and Pu²⁴¹. This is a good point for the objective of extend the nuclear fuel availability, which is a goal for the global sustainability of nuclear energy.
- Oxide compositions burn better than carbide minor actinides such as Am²⁴¹, Np²³⁷, and Pu²⁴², which is a good result for the reduction in radiotoxic minor actinides by transmutation inside the reactor core.
- Finally, oxide compositions 1 and 2, obtained from a first and second recycling of the spent fuel of LWRs, can be used in GFRs as a very good strategy for improving fuel utilization and transmutation of minor actinides.

References

1. IAEA, Department of Nuclear Energy, “Methodology for the assessment of innovative nuclear reactors and fuel cycles Report of Phase 1B (first part) of the International Project on Innovative Nuclear Reactors and Fuel Cycles (INPRO) IAEA-TECDOC-1434”, Vienna. 2004.
2. Cerullo et al., 13 – Generation IV reactor designs, operation and fuel cycle. Nuclear Fuel Cycle Science and Engineering. Pages 333–395. 2012.
3. Gen IV International Forum, <http://www.gen-4.org/>.
4. Van Rooijen, W.F.G. et al., Actinide Transmutation in GFR. Deliverable 31 GCFR STREP. <https://www.gcfr.org> 2008.
5. Martín-del-Campo, Cecilia, Ricardo Reyes-Ramírez, and Juan-Luis François. “Validation of simplified methods for fuel depletion calculations in gas-cooled fast reactors”, Annals of Nuclear Energy, 2013.
6. Duderstadt, J James, Hamilton, Louis J., “Nuclear Reactor Analysis”, 1976.
7. WNN. Countries move to host Allegro reactor. http://www.world-nuclear-news.org/NN_Countries_move_to_host_Allegro_reactor_2805101.html. May 2010.
8. Jaakko Leppänen. “Serpent Progress Report 2012”, Research Report VTT-R-00300-1428. 2012.

Author Biography

Cecilia Martin-del-Campo is professor at the Faculty of Engineering of the National University of Mexico. She is Energy Engineer from the Metropolitan University of Mexico, Nuclear Engineer from INSTN of the CEA, France, and PhD in Nuclear Engineering from the University of Paris XI, France.

“Practical Elimination on Large Release of Radioactive Materials” and Safety Performance Research on HPR1000

Xing Ji and Wang Hui

Abstract Evolution of concept on “practical elimination on possibility elimination on large release of radioactive materials” is summarized systemically in this paper, and then some insights, including the definition of “practical elimination,” the meaning of “large release,” the radioactive materials source and the severe accident condition, should be practically eliminated, and the demonstration method of “practical elimination” is presented. After that, analysis and research on domestic third nuclear power plant HPR1000 are conducted from the perspective of “practical elimination on large release of radioactive materials”; the results indicate that: with completed measures of severe accident prevention and mitigation, HPR1000 has achieved the safety goal of “practical elimination on large release of radioactive materials.”

Keywords Practical elimination · Large release · HPR1000 · Severe accident · Safety performance

1 Introduction

On March 11, 2013, the Fukushima Nuclear accident induced by beyond design earthquake and tsunami resulted in large radioactive material releasing into surrounding environment and enormously threatened the public safety. China central government launched the comprehensive safety inspection on the nuclear installations after Fukushima accident immediately and issued “Nuclear Safety and Radioactive Pollution Protection for 12th Five Year Plan and Prospect for 2020” (shortened for PLAN in the following paragraphs). The PLAN addressed that the new nuclear power plants (NPPs) built during 13th Five Year and after should practically eliminated the possibility of large release of radioactive materials as far as possible.

X. Ji · W. Hui (✉)

China Nuclear Power Engineering Co., Ltd., Beijing, People’s Republic of China
e-mail: wanghuia@cnpe.cc

According to the requirements of the PLAN, it is necessary to analyze the type of new NPPs built during 13th Five Year and after and verify whether they meet the safety goal of practical elimination of large release of radioactive materials. The introduction and evolution of the concept of practical elimination of large release of radioactive materials are summarized in this paper, and some related technical insights are proposed. And then, the review of safety performance of China domestic third reactor HPR1000 is conducted.

2 Evolution of “Practical Elimination”

The concept of “practical elimination” was firstly introduced by Europe and then adopted by IAEA. American nuclear industry has not adopted this concept until now. The documents related to “practical elimination” from Europe and IAEA are summarized and compared below.

2.1 Europe

The concept of “practical elimination” comes from the document with the name of “GPR/RSK Proposals for a Common Safety Approach for Future Pressurized Water Reactors,” which aims at setting safety design goals for the next-generation PWR NPPs. Since the fraction of containment early releases is large in the total large release, the document requires that accident situations that would lead to large early releases have to be practically eliminated. Here “practically eliminated” means that when these accident situations cannot be considered as physically impossible, design provisions have to be taken to design them out.

The concept of “practical elimination” was reserved in “Technical guidelines for the design and construction of the next generation of nuclear power plants with pressurized water reactors” that was issued by GPR in 2000. In this document, detail requirements on “practical elimination of large early releases” were addressed, including prevention of high-pressure melt injection and direct containment heating, prevention of fast reactivity insertions, prevention of steam explosion, prevention of hydrogen explosion, prevention of containment bypass and prevention of melt of spent fuel in spent fuel pool.

“TSO Study Project on Development of a Common Safety Approach in the EU for Large Evolution Pressurized Water Reactors” that was issued by EU in 2011 followed the proposals from GPR/RSK, which was that for next generation of plants, severe accident sequences that could lead to large early releases should be practically eliminated and the containment function should be improved substantially during other severe accident sequences. In this document, “practical elimination” of hypothetical severe accident sequences that could lead to large early releases means that concerning such sequences, when they cannot be considered as

physically impossible, sufficient design and operation provisions have been taken so that these sequences can be considered as extremely unlikely with a high degree of confidence. It is stated that the demonstration of “practical elimination” should be provided through deterministic and/or probabilistic means. In this document, severe accidents should be practically eliminated including core melt in shutdown states with open containment, high-pressure core melt situation, core melt with containment bypass, hydrogen explosion, in-vessel and ex-vessel steam explosions.

RHWG of WENRA issued a document with the name of “Safety Objectives for New Power Reactors” in 2009. In this document, it is stated that accidents with core melt that could lead to early or large releases have to be practically eliminated. It is also stated that the practical elimination of a condition cannot be claimed solely based on compliance with a general cutoff probabilistic value. Even if the probability of a condition is very low, any additional reasonable design features to lower the risk should be implemented.

“Safety of new NPP designs” issued by RHWG in 2013 addressed the demonstration methodology of “practical elimination.” It is highly emphasized that the demonstration of “practical elimination” should show sufficient knowledge of the accident condition analyzed and of the phenomena involved, substantiated by relevant evidence. In this document, accidents conditions that could cause a large or early release are summarized systematically, which can be classified as three categories that are unacceptable initiating faults, unacceptable consequential faults and fuel melt sequences challenging the confinement.

2.2 IAEA

The concept of “practical elimination” in IAEA comes from Europe. The introduction and meaning of “practical elimination” in INSAG-12 “Basic Safety Principles for Nuclear Power Plants” in 1999 and NS-G-1.10 “Design of Reactor Containment Systems for Nuclear Power Plants” are the same with Europe at the same period. Accident sequences that have to be practically eliminated listed in NS-G-1.10 are adopted by RHWG and listed in “Safety Objectives for New Power Reactors” report.

According to the understanding of “practical elimination,” in SSR-2/1 “Safety of Nuclear Power Plants: Design,” IAEA modified the states in NS-R-1 “Safety of Nuclear Power Plants: Design,” which were “The design for safety of a nuclear power plant applies the principle that plant states that could result in high radiation doses or radioactive releases are of very low probability (likelihood) of occurrence, and plant states with significant probability (likelihood) of occurrence have only minor or no potential radiological consequences. An essential objective is that the need for external intervention measures may be limited or even eliminated in technical terms, although such measures may still be required by national

authorities” to the states which were “The design for safety of a nuclear power plant applies the safety principle that practical measures must be taken to mitigate the consequences for human life and health and the environment of nuclear or radiation incidents: plant event sequence that could result in high radiation does or radioactive releases must be practically eliminated and plant event sequences with a significant frequency of occurrence must have no or only minor potential radiological consequences. An essential objective is that the necessity for off-site intervention measures to mitigate radiological consequences be limited or even eliminated in technical terms, although such measures might still be required by the responsible authorities.”

Compared with NS-R-1, SSR-2/1 has some important improvements related to nuclear safety. In order to avoid misinterpreted of these improvements, IAEA issued a TECDOC with the name of “Considerations on the Application of the IAEA Safety Requirements for Design of Nuclear Power Plants (Draft)” in 2014. In this TECDOC, the definition of “practical elimination” is “the possibility of certain conditions occurring is considered to have been practically eliminated if it is physically impossible for the conditions to occur or if the conditions can be considered with a high degree of confidence to be extremely unlikely to arise.” For conditions which are extremely unlikely to arise, the cutoff probability is expected as $10^{-7}/y$ in this TECDOC.

3 Technical Insights on “Practical Elimination of Large Releases of Radioactive Materials”

3.1 Definition of “Practical Elimination”

Based on the summarization in Sect. 2, it is seen that nuclear industry has a common view on the definition of “practical elimination,” which is that “the possibility of certain conditions occurring is considered to have been practically eliminated if it is physically impossible for the conditions to occur or if the conditions can be considered with a high degree of confidence to be extremely unlikely to arise.”

3.2 Radioactive Materials

After Fukushima accident, the safety of spent fuel in spent fuel pool has drawn more attentions. In the TECDOC, which are addressed above, it is required that significant fuel failure in storage pool should be practically eliminated. As a consequence, radioactive materials that are considered in “practical elimination” should include core and spent fuel.

3.3 Meaning of “Large Release”

At present, nuclear industry does not have a common view on the quantification of “large release.” According to the off-site impact of severe accidents, IAEA and Europe develop acceptable criteria, respectively.

In IAEA Safety Reports Series No. 30 “Accident Analysis for Nuclear Power Plants with Pressurized Water Reactors,” acceptable criteria for severe accidents are addressed as below:

- (1) There should be no failure of the containment because of pressure and temperature loads.
- (2) There should be no immediate health effects on the population.
- (3) For long-term effects, the ^{137}Cs release limit needs to be below the prescribed value (e.g., 100 TBq), and all the other nuclides together are not to cause a large danger after the time period specified (e.g., three months).

EUR set up safety goals for DEC (Design Extension Conditions, DEC), which is named CLI (Criteria for Limited Impact, CLI). To some extent, CLI describes the requirements that the impact of severe accidents (included in DEC) on the society should meet, in which the dose target or release target for off-site impact of severe accidents is addressed as below:

- (1) No emergency protection action beyond 800 m from the reactors (CLI-1);
- (2) No delayed actions at any time beyond about 3 km from the reactors (CLI-2);
- (3) No long-term actions at any distance beyond 800 m from the reactor (CLI-3);
- (4) Limited economic impact out of the plant (CLI-4).

In the above criteria, CLI-1 is addressed for the radioactive release during the first 24 h of accident progression; CLI-2 is for the radioactive release after 4 days; and CLI-3 is for the long-term radioactive impact which results from the radioactive depositions.

As stated above, American nuclear industry does not have detailed requirements for the quantification of large release. URD requires that the containment integrity should be assured during severe accidents.

At present, the quantification of large release is not clear in China. In this paper, CLI is used as the criteria for large release. If the impact of severe accident conditions can meet the CLI with kinds of measures, then the radioactive release is not large release, and these conditions are practically eliminated.

3.4 Severe Accidents Phenomena, Condition and Sequence

Based on the evolution of “practical elimination” concept, it is clear that the concept is introduced for specific severe accidents phenomena, condition or sequence. In the documents related to “practical elimination,” RHWG 2013 report gives the

comprehensive summarization of severe accidents that can lead to large release and should be practically eliminated; however, it is very difficult and impossible to make rigorous deterministic and (or) probabilistic analysis for all the severe accidents, which are listed in RHWG 2013 report based on our understanding and knowledge on severe accidents.

“Practical elimination” should be thought as the general technical requirements to achieve safety goal, so, in order to use the concept to guide the design and improvement of important safety features of NPP in engineering, at present, we suggest that the following severe accidents caused by internal events should be practically eliminated:

- (1) Early containment failure resulted from DCH, steam explosion and hydrogen explosion;
- (2) Late containment failure resulted from containment base melt-through and containment overpressure;
- (3) Severe accidents with open containment;
- (4) Severe accidents with containment bypass;
- (5) Significant fuel failure in storage pool.

3.5 Demonstration Methodology

According to the definition of “practical elimination,” there two kinds of demonstration methodology for “practical elimination,” which are physical impossibility and extremely unlikely with a high degree of confidence.

In engineering practice, it is very difficult to demonstrate that general severe accident phenomena and conditions are physically impossible, so the methodology of “extremely unlikely with a high degree of confidence” is more useful. In IAEA 2014 TECDOC, the cutoff probability for “extremely unlikely” is $10^{-7}/y$. In our safety demonstration for HPR1000, this value is adopted.

Though “practical elimination” is addressed for specific accidents, the final safety goal of “practical elimination” is to prevent human beings and environment from radioactive harm, and we suggest apply the cutoff probability of “extreme unlikely” of “practical elimination” into release categories of source term in Level 2 PSA. If the frequency of certain release category is lower than the cutoff probability, it can be thought that the accidents resulting in the release category have been practically eliminated, otherwise it is a necessity to evaluate the release quantification and radioactive consequence of the release category.

It should have been paid high attention that even if the frequency of certain release category is lower than the cutoff probability, safety features that can prevent or mitigate the accidents resulting in the release category should been adopted in engineering project.

4 Safety Performance of HPR1000

China domestic third NPP HPR1000 sufficiently draws the lessons of TMI, Chernobyl and Fukushima nuclear accidents and the design concepts of advanced NPP abroad, innovatively adopts the concept of “combination of active and passive features,” designs multi-prevention and mitigations for severe accidents and takes the concept of “practical elimination” into practice.

4.1 Technical Measures of “Practical Elimination”

4.1.1 Defense in Depth

The concept of “Defense in depth” is the basic principle of nuclear safety for preventing accidents and mitigating their consequences. Based on the concept, it is required that in the design of NPP, the equipment and procedures of multi-levels should be provided to prevent accidents, or provide adequate protection in case of fail of preventing such accidents.

There are 5 levels of defense in depth in “Safety Rules for Nuclear Power Plant Design” (HAF 102). HPR1000 follows the rules of HAF 102 at the beginning of design and also considers the lessons learned from Fukushima nuclear accident. HPR1000 considers multiplicity, single failure, diversity, independence, fault safety design, inherent safety features, mature and conservative design to prevent common cause failure, based on these considerations. HPR1000 satisfies the independence requirement between the different levels as far as possible, follows the principle of defense in depth completely and balanced and builds an intact and balanced defense in depth system. Table 1 shows conformance analysis of defense in depth in HPR1000 with HAF 102.

The concept of DEC is included in SSR-2/1 published by IAEA in 2012, to improve the nuclear power plant ability of enduring accidents more severe than design basis and to further improve the safety of nuclear power plant after

Table 1 Defense in depth system of HPR1000

Level	Objective	Example
1	Prevent deviations from normal operation and the failure of items important to safety	Plant is soundly and conservatively sited, designed, constructed, maintained and operated
2	Detect and control deviations from normal operational states	Control systems and protect systems
3	Control design basis accidents	Safety engineered systems
4	Control severe accidents	Combustible gas control systems
5	Mitigate potential radioactive consequences	Emergency plan

Fukushima nuclear accident. According to SSR-2/1, design extension conditions are postulated accident conditions that are initiated by multiple failures of safety systems. DECs could include severe accidents in events with or without core melting. Level 4 of defense in depth is divided into two sublevels as 4a and 4b, according to reference [10], published by IAEA. Level 4a is mainly aimed at preventing design extension condition without core melting developing into core melting condition, while level 4b is aimed at mitigating the consequences of design extension condition with core melting.

HPR1000 follows all the acting plans by IAEA or other international organizations after Fukushima nuclear accident and follows all the improvement and technique requirement after Fukushima nuclear accident published by China nuclear safety office, which improvement and technique requirement are consistent with IAEA safety rules. Thus, HPR1000 totally satisfies the new requirement of defense in depth in the technique document published by IAEA, as follows,

- Level 4a: HPR1000 includes secondary passive residual heat removal system to remove core decay heat by a passive way, to prevent core melting induced by multiple failures of safety systems. Meanwhile, HPR100 includes emergency water supply system and SBO electric power, to prevent multiple failures induced by extreme external events.
- Level 4b: HPR1000 design includes active and passive cavity injection system to ensure the integrity of pressure vessel, to mitigate the consequence of extension conditions with core melting, and also includes passive containment heat removal system and combustible gases control system to maintain the integrity of the containment.

4.1.2 Prevention and Mitigation for Severe Accidents

The systematic and specific prevention measures designed in HPR1000 as stated above have extremely reduced the possibility of severe accidents. Meanwhile, mature design and management measures are included against all the severe accident phenomena, conditions or sequences mentioned in Sect. 3.4, and overall mitigation measures for severe accident are designed to maintain the integrity of pressure vessel and containment, to practically eliminate large radioactive release.

Table 2 (provided in the end of the paper) shows the comparison of prevention and mitigation measures among several third-generation NPPs. HPR1000 has multiple and complete measures against containment over pressure and is advanced compared to other third-generation nuclear power plants, while the measures against the phenomena of high-pressure core melt, hydrogen detonation, containment bypass and other aspects are almost the same level with the other third-generation NPPs.

To verify the validity of these prevention and mitigation measures, HPR1000 verified and analyzed the validation of all these measures by experiments and numerical calculations. For example, the designers has built experiment platforms

Table 2 Prevention and mitigation measures to eliminate main phenomena during severe accidents

Phenomena	Prevention and mitigation measures		
	EPR	AP1000	HPR1000
Core melt	<ul style="list-style-type: none"> – Active medium and low-pressure safety injection – Accumulator – Emergency boron injection 	<ul style="list-style-type: none"> – Core water supply tank – Accumulator – Passive residual heat removal system 	<ul style="list-style-type: none"> – Active medium and low-pressure safety injection – Accumulator – Secondary passive residual heat removal – Emergency boron injection
Core melt under high pressure	Primary depressurization system	ADS	Primary fast depressurization system
Pressure vessel fail	None	In-vessel retention	Cavity injection system
External steam explosion	Dry cavity	In-vessel retention	Cavity injection system
Basemat melt-through	Core catcher	In-vessel retention	Cavity injection system
Hydrogen detonation	Hydrogen recombiner	Igniter	Hydrogen recombiner
Containment overpressure	Containment spray	<ul style="list-style-type: none"> – Containment spray – Passive containment cooling system 	<ul style="list-style-type: none"> – Containment spray – Passive heat removal system – Containment filtrated venting system – Larger containment free volume
Containment bypass	Accident management and improvement in design	Accident management and improvement in design	<ul style="list-style-type: none"> – Abolish high-pressure water injection – Residual heat removal system full pressure design – Accident management
Accident in spent fuel pool	<ul style="list-style-type: none"> – Water level and temperature monitor – Water supply system after accidents 	<ul style="list-style-type: none"> – Water level and temperature monitor – Water supply system after accidents 	<ul style="list-style-type: none"> – Water level and temperature monitor – Water supply system after accidents

to verify and analyze three passive safety system designed in HPR1000 during research and developing stage, which are secondary residual heat removal system, cavity water injection system and passive containment heat removal system, which also provide database for developing calculation codes. For combustible gases control, numerical calculating method is used to guide the layout plan of hydrogen recombiners and to verify and analyze the validation.

According to rigorous deterministic calculation, all the prevention and mitigation measures, which are designed and built highly reliably, can work effectively and can practically eliminate the severe accident phenomena or conditions identified by nuclear industry, to maintain the integrity of pressure vessel and containment and to prevent large radioactive materials releasing.

Besides, since the importance of containment in preventing release of large radioactive materials, HPR1000 is designed with double containment except for practically eliminating those severe accident phenomena or conditions, which may threaten the integrity of containment. The reactor building is protected by APC shell, to ensure the integrity of inner shell in case of big commercial plane strike.

4.2 Demonstration of “Practical Elimination”

4.2.1 Preliminary Results of Level 2 PSA

As stated above, in the demonstration of “practical elimination” using probabilistic methodology, we suggest apply the cutoff probability of “extremely unlikely” into release categories of source term in Level 2 PSA.

Preliminary results of Level 2 PSA of HPR1000 are listed in Table 3, the core melt accident sequences considered in these categories include typical severe accidents such as LOCA, MSLB and SBO, in these calculations, the mitigation measures are considered as effective and disabled, respectively.

It can be seen that frequency of release category 1 with intact containment is about 10^{-7} /year while frequencies of other categories are far lower than 10^{-7} /year, so we can make a conclusion that severe accidents resulting other categories have been practically eliminated and off-site radioactive consequence for category 1 should be evaluated. The evaluation results will be shown in Sect. 4.2.2, and we will see that the off-site consequence of category 1 can meet CLI, so, there is no large release under the conditions with intact containment for HPR1000.

Though the analysis shows that severe accidents that can lead to large release have been practically eliminated, emergency plan is still be established according to

Table 3 Preliminary results of Level 2 PSA of HPR1000

No.	Description	Frequency (/y)	Fraction (%)
1	Intact containment	$\sim 1.17\text{E}-07$	90.2
2	Failure of containment isolation	$\sim 5.62\text{E}-10$	0.43
3	Containment bypass	$\sim 3.70\text{E}-09$	5.63
4	Containment early failure	$\sim 2.07\text{E}-09$	2.51
5	Containment late failure	$\sim 3.28\text{E}-13$	$2.57\text{E}-04$
6	Containment filtrated vent	$\sim 3.70\text{E}-10$	0.29
7	Containment basemat melt-through	$\sim 1.28\text{E}-09$	0.99

the relative nuclear safety laws and rules. Besides, research on EDMG for HPR1000 is ongoing, which aims at mitigating the potential radioactive consequence.

4.2.2 Evaluation Methodology of CLI

EUR gives the detailed evaluation methodology for CLI. In this methodology, the radioactive nuclides that are released into environment during severe accidents are divided into 9 reference nuclide categories, which are ¹³³Xe, ¹³¹I, ¹³⁷Cs, ^{131m}Te, ⁹⁰Sr, ¹⁰³Ru, ¹⁴⁰La, ¹⁴¹Ce and ¹⁴⁰Ba, respectively.

The following equation is used to evaluate the release dose for these 9 categories:

$$\sum R_{ig} \cdot C_{ig} + \sum R_{ie} \cdot C_{ie} < \text{criterion}$$

in which: R_{ig} and R_{ie} are the ground and stack release amount of release dose nuclide i , respectively, TBq; C_{ig} and C_{ie} are conversion factors, respectively.

As for CLI-1, CLI-2 and CLI-3, the corresponding criteria are 0.05 Sv, 0.03 Sv and 0.1 Sv; as for CLI-4, the corresponding acceptable criteria are: during radioactive release, release amount of main nuclides into environment should not larger than the corresponding limits listed in Table 4. For CLI-4, the main nuclides are ¹³¹I, ¹³⁷Cs and ⁹⁰Sr.

4.2.3 Evaluation Results

The off-site radioactive consequence of release category 1 of HPR1000 is evaluated using the above methodology. The results indicate that:

- (1) After 24 h, dose consequence for public at 800 m from the reactor is 7.2 mSv, which is lower than 500 mSv, so emergency protection action is not necessary;
- (2) After 72 h, dose consequence for public at 3000 m from reactor is 0.11 mSv, which is lower than 30 mSv, so temporary relocation is not necessary;
- (3) Long-term dose consequence of radioactive depositions for public at 800 m from reactor is about 1.3 mSv, which is lower than 100 mSv, so long-term actions are not necessary.

Table 4 Acceptable criteria of CLI-4

Nuclide	Target (unit: TBq)
I-131	4000
Cs-137	30
Sr-90	400

CLI-4 evaluation results of release category 1 for HPR1000 are given in Table 5; we can see that the release amount meets the requirements of CLI-4, so category 1 does not result in “large release,” which prove the importance of containment in preventing large release.

5 Conclusions

Evolution of concept on “practical elimination on possibility elimination on large release of radioactive materials” is summarized systemically, and evaluation of safety performance of China domestic third-generation NPP is conducted from the perspective of “practical elimination” in this paper; the conclusions are listed as below:

- (1) Nuclear industry has common view on the definition of “practical elimination” and the radioactive materials considered in “practical elimination”;
- (2) Quantification of “large release” is not clear at present, and in this paper, we use the CLI addressed by EUR as the criteria for “large release”;
- (3) In order to use the concept to guide the design and improvement of important safety features of NPP in engineering, at present, and we suggest several severe accidents caused by internal events should be practically eliminated;
- (4) As for the cutoff probability for “extreme unlikely,” we suggest take the value as $10^{-7}/y$ with rigorous deterministic analysis and we also suggest apply the cutoff probability into the release category of Level 2 PSA;
- (5) Even if the frequency of certain release category is lower than the cutoff probability, safety features that can prevent or mitigate the accidents resulting in the release category should have been adopted in engineering project;
- (6) Based on the current knowledge on severe accidents, HPR has sufficient prevention and mitigation measures against severe accidents, and the deterministic and probabilistic analysis indicates that HPR1000 has achieved the safety goal of “practical elimination”;
- (7) With the improvement of understanding on severe accidents and technologies against severe accidents, the meaning and requirements of “practical elimination” may change. HPR1000 will continually improve the safety performance with the guide of “practical elimination.”

References

1. GPR/RSK. GPR/RSK proposals for a common safety approach for future Pressurized Water Reactors[R]. 1993
2. GPR. Technical guidelines for the design and construction of the next generation of nuclear power plants with pressurized water reactors[R]. 2000
3. EU. TSO Study Project on Development of a Common Safety Approach in the EU for Large Evolutionary Pressurized Water Reactors[R]. 2001

4. WENRA/RHWG. Safety Objectives for New Power Reactors[R]. 2009
5. WENRA/RHWG. Safety of new NPP designs[R]. 2013
6. IAEA. INSAG-12 Basic Safety Principles for Nuclear Power Plants[R]. 1999
7. IAEA. NS-G1.10 Design of Reactor Containment Systems for Nuclear Power Plants[R]. 2004
8. IAEA. NS-R-1 Safety of Nuclear Power Plants: Design[R]. 2001
9. IAEA. SSR-2/1 Safety of Nuclear Power Plants: Design[R]. 2012
10. IAEA. Considerations on the Application of the IAEA Safety Requirements for Design of Nuclear Power Plants (Draft)[R]. 2014

Part II
Waste Management

Research on Treatment of Simulated Nuclear Power Plant Waste Liquid

Wenjun Zheng and Zhentao Zhang

Abstract Treatment of simulated nuclear plant waste liquid by flocculation was studied. The available flocculant and active carbon (AC) were selected through the static experiments. Polymeric flocculants of different kinds and different molecular weights were used in this research. Proper polymeric flocculant and its addition were confirmed by the removal efficiencies; active carbon used in the experiment was also selected. The integrated experimental technological process was established, and the pilot-scale test of the simulated nuclear plant waste liquid was done. The results show that this process has a preferable effect on the simulated nuclear plant waste liquid after the condition of 20- to 60-mesh coconut activated carbon, 6–10 million mol.wt polymeric flocculant, and the removal rate not less than 90%.

Keywords Flocculation · Simulated nuclear plant waste liquid · Active carbon · ^{110m}Ag · ^{60}Co

1 Introduction

According to the operating experience of China's nuclear power plants in service, ^{110m}Ag has been one of the most important radionuclides in nuclear power plant. In the primary circuit of nuclear power plant, $^{109}\text{Ag} (n, \gamma) \rightarrow ^{110m}\text{Ag}$, half-life of 249.78 days. In normal conditions, ^{110m}Ag mainly exists in colloidal form, and when our nuclear power plant in service treats the wastewater using ion exchange process, the colloidal ^{110m}Ag physically adsorbed onto the resin; it is very unstable and prone to fall off from the desalination bed, which leads to a widespread pollution on the system and equipment. On the other hand, when the colloidal ^{110m}Ag passes through the desalination bed, it can easily cause the resin saturated, more frequent replacement of resin produces more solid waste and increases operating costs [1].

W. Zheng (✉) · Z. Zhang

Department of Radiochemistry, China Institute of Atomic Energy, Beijing 102413, China
e-mail: 13811719852@163.com

Flocculant injection process means injecting polymer flocculant into the wastewater to be treated through a pipe; the electrical property of the colloidal particles in the wastewater will be changed by polymer flocculant, making the colloidal particles “agglomerate”; subsequently, wastewater was passed through the activated carbon bed, and the “agglomerated” colloidal particles can easily be adsorbed by the activated carbon bed; finally, other ions dissolved in the treated wastewater were then removed by ion exchange process. Colloidal particles often contain most of the radionuclides such as ^{110m}Ag , ^{60}Co , ^{58}Co ; the colloidal particles in the wastewater can effectively be removed by polymer flocculant injection and activated carbon adsorption, so that the entire waste processing system has a high decontamination factor.

2 Experimental Section

2.1 Primary Reagent

The following reagents were used: silver nitrate, cobalt nitrate hexahydrate, boric acid, ammonium nitrate, lithium hydroxide, ferrous sulfate, ferric nitrate (all analytical reagents). The water used in the laboratory was deionized water.

2.2 Primary Instrument

The following instruments were used: BT100-1L peristaltic pump, Baoding Longer Pump Co., Ltd; 88-1 high-power digital magnetic stirrer, Changzhou Guohua Electric Appliance Co., Ltd; PL203 electronic scales, accuracy 0.1 mg, Switzerland Mettler-Toledo Co., Ltd.

2.3 Experimental Method

2.3.1 Preparation of the Simulated Nuclear Wastewater

In Daya Bay Nuclear Power Plant, the pollution of ^{110m}Ag was more severe at part of the system, mainly in control rod absorber, pressure vessel “O” rings, and other accessories; the radiation dose of the operator contributes about 40–50% of the total pollution [2]. In Qinshan Phase II Nuclear Power Plant, ^{110m}Ag has gradually become the main radionuclide other than tritium addition, which has the share ratio of up to about 75% of radioactivity in the environment liquid effluent discharge, illustrated as follows: (Fig. 1).

Fig. 1 The proportion of each nuclide in the liquid effluent

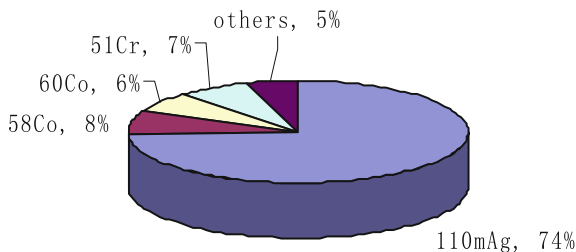


Table 1 Chemistry component range of reactor water

Composition	Unit	Number range
pH/25 °C		4.2–10.9
Chloride	ppm	0.01–0.2
Fluoride	ppm	0.05–0.15
LiOH/Li+	ppm	0.2–2.2
Silica	ppm	0.5–4
Iron	ppm	0.02–0.05
Copper	ppm	0.035–0.05
Boron	ppm	0–4000
Crud	ppm	1.00
Suspended solids	ppm	0.01–0.5
Total suspended solids	ppm	0.1–1.0
Dissolved iron max	ppm	0.50

According to the IAEA report in 1992 <Coolant Technology of Water Cooled Reactors> [3], the source term is as follows: (Table 1).

Comprehensive analysis of the source term inferred that colloid in the nuclear radioactive wastewater mainly was Fe colloid, which adsorbs ^{110m}Ag, ⁵⁸Co, ⁶⁰Co, and other radionuclides; in addition, the wastewater also contains H₃BO₃, Li⁺, NH₄⁺, etc. Thus, we should consider these ion factors in the preparation of non-simulated nuclear wastewater discharge. Therefore, concentration of each component in the simulated nuclear wastewater of this experiment is as follows: (Table 2).

Table 2 Preparation of colloidal liquid waste

Components	Unit	Value
Fe colloid	ppm	0.5
H ₃ BO ₃	ppm	2200
NH ₄ ⁺	ppm	1
Li ⁺	ppm	2.2
Ag ⁺	ppm	2.88
Co ²⁺	ppm	8.86

2.3.2 Preparation of the Polymer Flocculants

After a detailed research and analysis, the choices of high-molecular flocculants which are applicable to these experimental studies are as follows: cationic polyacrylamide(CPAM), anionic polyacrylamide(APAM), amphoteric polyacrylamide (CAPAM), sodium polyacrylate(PANa), pectin, PEG10000, sodium carboxymethyl cellulose 300-800 (CMC300-800), and sodium carboxymethyl cellulose 800-1200 (CMC800-1200). These chosen high-molecular flocculants were prepared into a certain concentration solution [4–7].

2.3.3 Pretreatment of the Activated Carbon

According to the analysis of this experimental study, two different batches of activated carbon in different models and specifications were chosen, coconut and shell. It should also consider the loading of the column experiments in hot and cold test for choosing the activated carbon; the large particles of shell activated carbon, the columnar activated carbon, and the powdered activated carbon were not suitable for loading. After the loading of large particles of shell activated carbon and the columnar activated carbon, the interstice in the activated carbon was very large; therefore, when the wastewater flows into the activated carbon column, they cannot contact sufficiently, and a large part of the wastewater flow from the gap of the activated carbon. For the powdered activated carbon, after loading the column, the wastewater is difficult to flow through the activated carbon column. The two batches of the selected activated carbon were soaked in the wastewater, which contains colloidal particles, for 24 h, then dried, and packed with number.

2.3.4 The Unit of Column Experiment

In Fig. 2, there are flocculant tank, simulated wastewater tank, blending tank, effluent liquid tank, activated carbon column, metering pumps, and the sampling points. Certain amount of activated carbon was loaded in the column; the injection amount of the flocculants and simulated wastewater was set to a certain parameter, and then, they were allowed to flow into the blending tank and stirred sufficiently; then, they flowed into the activated carbon column through the metering pump and finally into the effluent liquid tank.

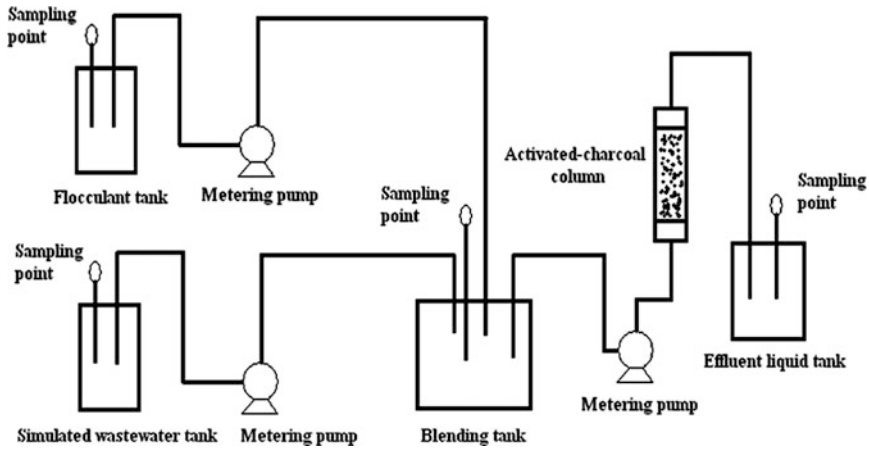


Fig. 2 Flocculation injection device

3 Results and Discussions

3.1 Screening of the Polymer Flocculant

3.1.1 Removal Rate of Ag in Different Concentrations and Different Flocculants

There were different concentrations, 0.5, 1, 2, 5, 10 ppm, and different kinds, PAM, PANa, pectin, PEG, CMC300-800, and CMC800-1200. The results are as follows:

From Fig. 3 above, we can see that the greater the concentration of polymer flocculants, the better the flocculation effect; PAM polymer flocculants are significantly better than other flocculants. For non-PAM polymer flocculants, the flocculation (removal rate of Ag) is less than 30%; the result of 10-million-molecular weight polyacrylamide is unstable; analysis of this polymer flocculant is likely to agglomerate into the beam-forming group such as “fish eye” in the preparation, and it is not completely dissolved in the aqueous, and therefore, the flocculation effect is reduced. The polymer flocculant addition should not be too large, otherwise it will cause secondary waste volume increases. Besides, when the addition concentration of polymer flocculants increases, the dissolution of polymer flocculants would be more difficult; they should be heated, stirred and other auxiliary conditions; when the polymer flocculants do not dissolve sufficiently, the activated carbon column will result in clogging, so that the activated carbon column will be replaced frequently.

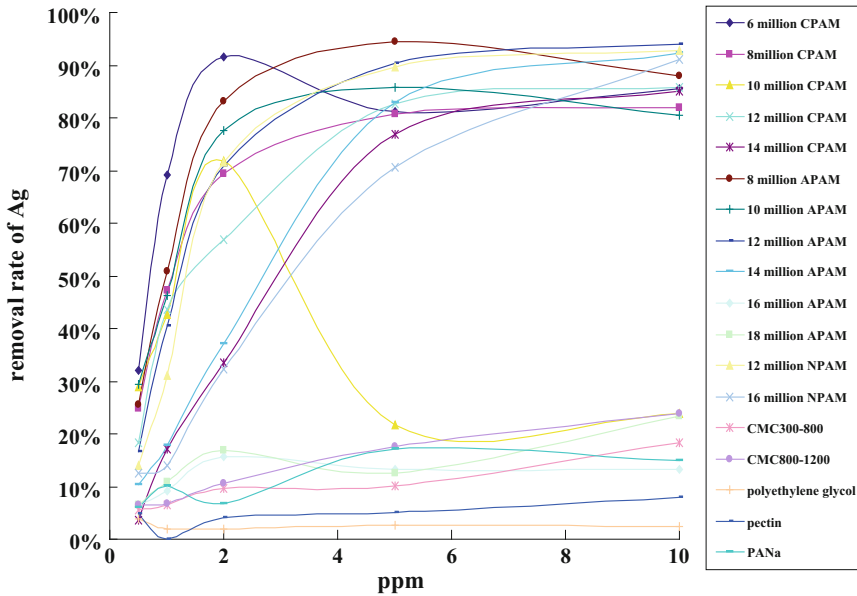


Fig. 3 Removal rate of Ag in different concentrations (ppm) and different flocculants

3.1.2 Removal Rate of Ag in Different Solid-to-Liquid Ratios and Different Flocculants

Solid-to-liquid ratio means the addition of the activated carbon and the simulated wastewater; 12 million CPAM, 12 million APAM, 12 million CAPAM, CMC300-800, CMC800-1200, polyethylene glycol, pectin, and PANa were chosen in this experiment. The concentrations of polymer flocculants were 1 ppm. The results are as follows: (Fig. 4).

As can be seen from the chart, the solid-to-liquid ratio of the activated carbon has a greater impact on flocculation treatment effect. Generally speaking, the larger the ratio, the greater the removal of Ag, and 1/20 is the best parameter. We can also see that PAM polymer flocculant treatments are better than non-PAM polymer flocculants, and CPAM has a good result than APAM and CAPAM.

3.1.3 Removal Rate of Ag and Co in Determined Solid-to-Liquid Ratio and Determined Concentrations

In addition, the flocculation effects of different types of polymer flocculants were studied, and the results are summarized as follows: (Fig. 5).

As can be seen from the chart, the removal of Ag can reach more than 70% in general; besides, a molecular weight of 8 million, 10 million, and 12 million CPAM has a better removal of Ag which has been able to achieve more than 99%; the

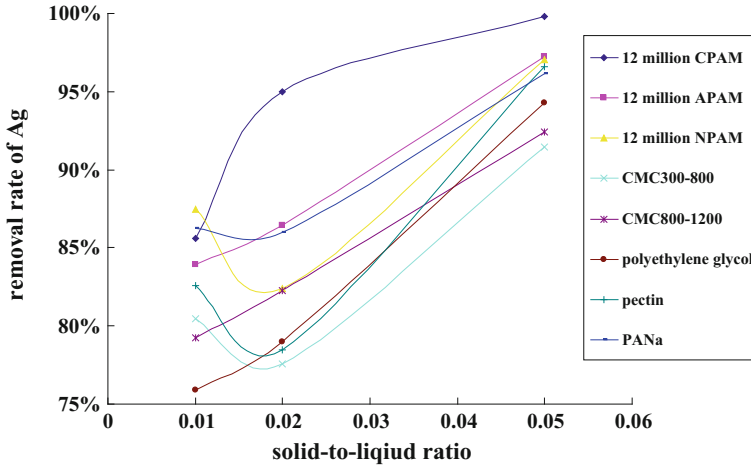


Fig. 4 Removal rate of Ag in different solid-to-liquid ratios and different flocculants

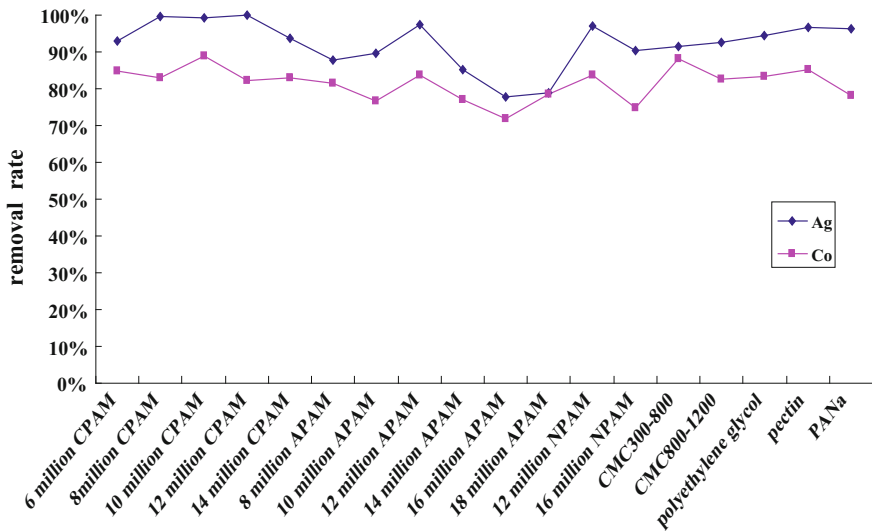


Fig. 5 Removal rate of Ag and Co in determined solid-to-liquid ratio and determined concentrations

highest removal of Co can also reach about 89%. This is because the CPAM has the charge neutralization and adsorption bridging effects with the negative charge particles in the colloidal wastewater, making the particles in the system destabilize and flocculate, thus contributing to the settlement; after the polymer flocculants adsorbed Ag and Co, the polymer adsorption micelles were adsorbed by the activated carbon, so the removal rate was increased.

3.2 Screening of Activated Carbon

In the previous experiments, we have known that the solid-to-liquid ratio of activated carbon is proportional to the flocculation effect; this is because higher solid-to-liquid ratio of activated carbon can adsorb the sediment to a greater degree. Then, we took a series of experiments to screen the activated carbon. The results are as follows: (Tables 3 and 4).

As can be seen from the two tables above, the coconut shell activated carbon's treatment is better than other types of activated carbons; this is mainly because the coconut shell activated carbon has a larger surface area, the porosity is also large, and it has a well-developed pore structure; it can more easily adsorb the micelle which is the polymer flocculant adsorbing the colloid; besides, the coconut shell activated carbon also has high fiber, high density, good chemical stability, high mechanical strength, and excellent resistance to acid, alkali, and heat, so the coconut shell activated carbon was chosen in the column experiments. The large particles of shell activated carbon and the columnar activated carbon were not suitable for the column, and the interstice in the activated carbon was very large;

Table 3 Experimental result of a group

Activated carbon	Removal rate of Ag (%)	Removal rate of Co (%)
Shell 1–2 mm	62.67	63.26
Shell 2–4 mm	99.06	50.17
Coconut 1–2 mm	98.44	25.96
Coconut 2–4 mm	99.15	60.21
Columnar 1.5 mm	81.56	52.64
Columnar 3.0 mm	96.53	52.26
Powdery 80–120 μ	98.24	34.57

Table 4 Experimental result of b group

Sample		Removal rate of Ag (%)	Removal rate of Co (%)
Coconut 100	8–20 mesh	88.89	62.45
Coconut 101	8–20 mesh	93.49	57.61
Coconut 202	8–20 mesh	84.18	46.07
Shell 101	8–20 mesh	90.80	49.61
Shell 102	16–40 mesh	85.63	41.35
Shell 103	8–20 mesh	86.30	43.27
Shell 202	8–20 mesh	86.78	48.01
Coal 216	8–30 mesh	73.85	28.39
Coal 208	1.5 mm	93.83	32.09
Coal 215	3 mm	92.18	28.45
Coal 215	4 mm	88.63	21.49

therefore, when the wastewater flows into the activated carbon column, they cannot contact sufficiently, and a large part of the wastewater flow from the gap of the activated carbon. For the powdered activated carbon, after loading the column, the wastewater is difficult to flow through the activated carbon column. Therefore, the columnar activated carbon and powdered activated carbon are not suitable for this experimental study. Similarly, when chosen the coconut shell activated carbon as the packed column, we should also consider the particle mesh factors; ultimately determined in the experimental study was about 20–60 mesh size of coconut shell activated carbon.

3.3 Column Experiments

3.3.1 Cold Sub-experiments

After the screening of the polymer flocculants and activated carbon, they will be applied to the column experiments; the process of column experiments was shown in Fig. 6.

In the cold sub-experiments, the polymer flocculant and simulated nuclear wastewater were set to a certain ratio and they flowed into the blending tank; then, the mixture flowed through the activated carbon column by an injection pump; the outlet of activated carbon column was connected to the final tank, and the effluent was sampled regularly and inspected by ICP-MS analysis. Based on the removal of Ag in the effluent and the bed volume, we could figure out the decontamination efficiency. The results are shown below:

As can be seen from the figure above, when the flow rate was 4 Bv/h, the removal rate of Ag was not less than 90%, and the treatment of simulated nuclear wastewater was greater than 1020 Bv.

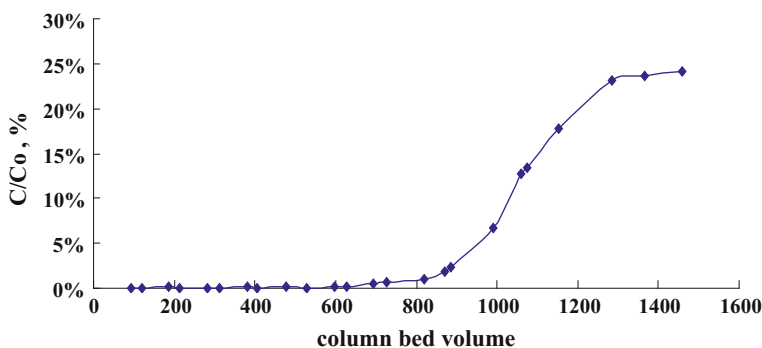


Fig. 6 Elution curve of cold test experiment

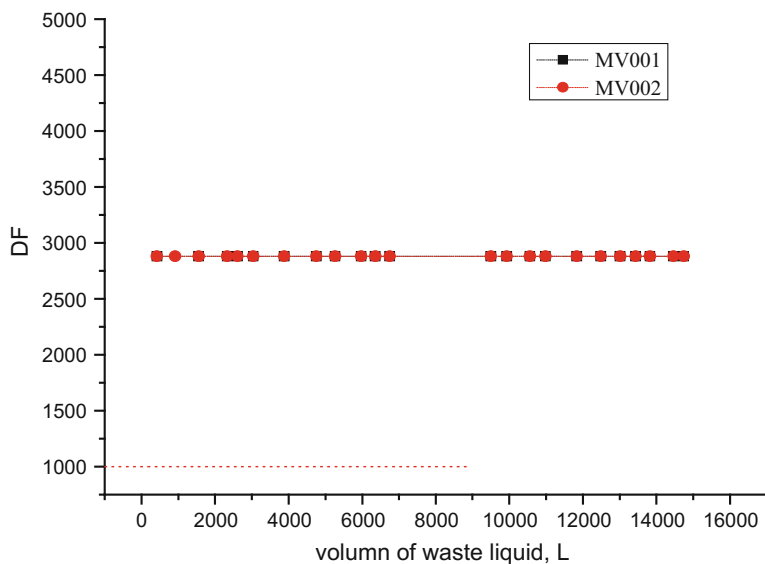


Fig. 7 Elution curve of pilot-scale cold experiment

3.3.2 Pilot-Scale Cold Experiment

After the cold sub-experiments, the pilot-scale cold experiments were carried out. The results are shown below: (Fig. 7).

As can be seen from the figure above, when the flow rate was 12 Bv/h, the treatment of simulated nuclear wastewater was greater than 15000 L(849 Bv), the concentration of Ag was still below the lower limit of detection, and the DF value was still greater than 2800.

4 Conclusions and Recommendations

- (1) The screened polymer flocculant was a 6–10-million-molecular weight PAM, and the screened activated carbon was a coconut shell activated carbon of 20–60 mesh size.
- (2) In the pilot-scale cold verification experiment, the treatment of simulated nuclear wastewater was greater than 15000 L(849 Bv), the concentration of Ag was still below the lower limit of detection, and the DF value was still greater than 2800, which means when the removal rate of Ag was not less than 90%, the treatment of simulated nuclear plant waste liquid was greater than 900 Bv.

References

1. B.C. Li, Y.D. Hou, D. Wang, ^{110m}Ag problems and countermeasures of Qinshan Phase II nuclear power plant[J], Nuclear power engineering and technology, p. 31–35, 2009(4).
2. J.D. Chen, System and operation of Daya Bay nuclear power plant[M], Atomic Energy Press, Beijing, p. 166–167, p. 424–430, p. 2123–2125, 1998.
3. IAEA, Coolant Technology of Water Cooled Reactors[R], 1992.
4. YANG Ai-li, ZHANG Hao, YANG Peng, Treatment of low-level radioactive wastewater containing plutonium using PAM[J], Journal of Nuclear and Radiochemistry, p 180–183, 2011 (33).
5. ZHAO Jun, WANG Tao, ZHANG Dong, Treatment of low-level wastewater of Pu using coagulation and microfiltration technological process[J], Journal of Nuclear and Radiochemistry, p 113–117, 2007(29).
6. REN Jun-shu, Mu Tao, YANG Sheng-ya, Treatment of high salinity low level radioactive wastewater containing Uranium and Plutonium by Flocculation[J], Journal of Nuclear and Radiochemistry, p 201–205, 2008(11).
7. Rothberg M.R, Locus S, Englewood S. Process for removal of radioactive materials from aqueous solutions, US, 4377508[P], 1983.

Author Biography

Wenjun Zheng is an assistant research fellow, China Institute of Atomic Energy, research area: radioactive waste treatment and disposal.

An Introduction to Sanmen Nuclear Power Plant's Radwaste Management Information System

Liu Huichun

Abstract This paper has introduced the Radwaste Management Information System (RMIS) of Sanmen Nuclear Power Co., Ltd and made some proposes for the authorities to construct a nationwide IT system for managing radwaste information produced by all kinds of corporations. Sanmen's RMIS consists of two types of software; one is connected to radwaste treatment systems and is used to record the status and measuring data of drums containing waste, and the other software is independent from radwaste treatment system and is used to record all the generation and treatment information of waste. Sanmen's RMIS is highly customized according to the company's radwaste management strategy and waste treatment systems. Data structure, transfer interface, and information sharing should be taken into consideration if the authorities want to construct a nationwide IT system for radwaste management.

Keywords Radwaste management • Information system • Software

1 Introduction

Sanmen Nuclear Power Plant Co., Ltd (SMNPC) has developed a set of (Solid) Radwaste Management Information System (RMIS) in support of tracking waste management and waste minimization. RMIS is highly customized in accordance with SMNPC's solid radwaste treatment systems and management strategy. It can record most of the important information produced during solid radwaste management and provides a meaningful ways of searching and displaying data. If new strategy or technology is implemented, it can be upgraded accordingly. The introduction of RMIS may provide some information for the authorities to build a nationwide IT system for radwaste management.

L. Huichun (✉)
China Nuclear Power Engineering Co., Ltd, Beijing, China
e-mail: jianghong@cnpe.cc

2 Introduction of RMIS

2.1 Processing of SMNPC's Solid Radwaste

AP1000, the NPP that SMNPC is constructing, has a set of solid radwaste treatment system (WSS) to collect and store spent resin, filters, and other dry active waste (DAW). After temporal storage in WSS, all the solid waste will be delivered to Site Radwaste Treatment Facility (SRTF) for further treatment and storage.

SRTF is an independent facility with waste treatment systems and other auxiliary systems, including pre-compaction, evaporation, drying, super-compaction, and cement-grouting. Some liquid waste which cannot be treated in the NPP's Liquid Radwaste System (WLS) because of its chemical characters will also be delivered to SRTF and become a solid waste package eventually; this part of liquid waste is called chemical waste and will be deemed as part of solid waste. The solid waste treatment flow is shown in Fig. 1. The 160-l drum (made in carbon steel) is an inner container which is used to contain compactable DAW (CDAW), chemical waste, spent resin, and HVAC filter. It will be super-compacted to a pellet by the super-compactor, placed in a 200-l drum (also made in carbon steel), and grouted with cement. The 200-l drum is the final package for storage inside SRTF. Besides super-compacted pellets, 200-l drum may also contain other radwaste, including un-compactable DAW (NCDAW), cemented high-level chemical waste, and water filter. DAW sorting, pre-compacting, 12-drum drying, and HVAC filter compacting are in-place treatments. After the drums are loaded onto conveyor, other waste treatments will be conducted remotely.

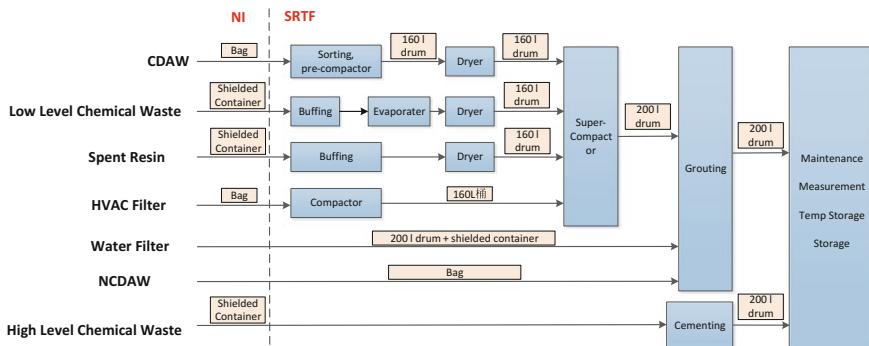


Fig. 1 SMNPC's solid radwaste treatment flow

2.2 Constitution of RMIS

RMIS is constituted by SRTF Transfer System (TFS) and Solid Waste Management Software (SWMS). TFS is one of the auxiliary systems of SRTF, which is designed with data transformation with other treatment systems in SRTF. It is used to keep real-time status and measured data of drums (both of 160-l drum and 200-l drum). The constitution of TFS is shown in Fig. 2.

SWMS is not an original software of any facility, but proposed by the radwaste management department to implement information of waste generation and treatment parameters. All the data from TFS will be imported to SWMS. SWMS is integrated with SMNPC Project Management System (SPMS), which is an integrated system of office assistance, workflow control, and many other modules. One of the modules that SWMS has the most connection with is Radiation Work Permit System (RWPS). RWPS can provide RWP information, which may contain important information for DAW generation analysis. The constitution of SWMS is shown in Fig. 3.

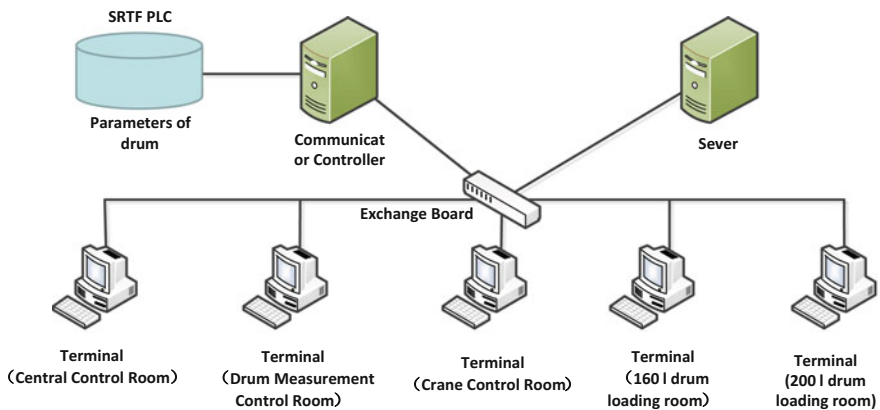


Fig. 2 Constitution of TFS

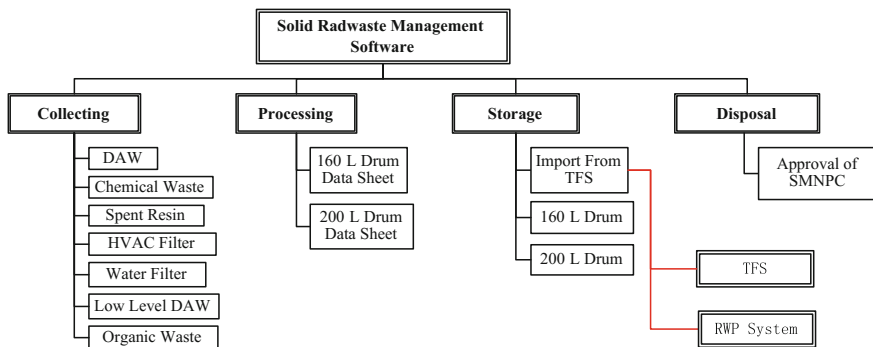


Fig. 3 Constitution of SWMS

Right now, there is no direct communication between TFS and SWMS; data can only be transferred from TFS to SWMS manually.

2.3 Operation of RMIS

2.3.1 Operation of TFS

The operation of TFS includes status updating and drum data retrieving and combining. When a pellet (used to be a 160-l drum) is placed in a 200-l drum, the information of these two drums will be bonded together, and the data of pellet will be displayed in the data sheet of 200-l drum.

- (1) Drum Initiation. When a drum is put onto conveyor, operator will input the drum's ID into the terminal of TFS and choose the type of waste it contained. As shown in Fig. 4, there are different options for 160-l drum and 200-l drum. As for the 160-l drum initiation, an empty 160-l drum is initiated when ready for the treatment of chemical waste or spent resin, so there would be a typical INITIATION status for these two types of waste. After the chemical waste or spent resin is loaded in the 160-l drum, the status will be updated as the drum is going to be super-compacted and measured. But for the CDAW, the 160-l drum is put onto the conveyor fully loaded and goes straight to super-compaction, so there is no status before UN-MEASURED. As for the 200-l drum initiation, all types of waste but NCDWA have a typical INITIATION status. Initiation is the access into TFS; all the drums' IDs should be imported into TFS before initiation. Once drum initiation is done, the sequential statuses of the drum are decided and the remaining operations are also fixed.
- (2) Status Update. As shown in Fig. 4, there are three statuses for 160-l drum (two for 160-l drum with CDAW) before put into 200-l drum, and seven statuses for 200-l drum (six for 200-l drum with NCDWA). After the 160-l drum is put into 200-l drum, the status of 160-l drum (now a pellet) will be synchronized with 200-l drum. The statuses are updated manually.
- (3) Retrieving Data. TFS has data communication with Drum Radiation Measuring Devices and Crane Control System. Once a drum is measured, the measurement results will be recorded and transferred to TFS automatically. When a drum is ready for craning, the operator in the central control room of SRTF will choose the storage coordinate and trigger a signal to the crane control room, and the operator in the crane control room will start craning following the coordinate received. After the drum is positioned, the latter operator will send back a confirm signal, and the drum's storage position will be recorded in TFS with its status updated.
- (4) Data Association. The measured data of drum are transferred to TFS without ID, and the operator has to manually choose data from measuring data lists and

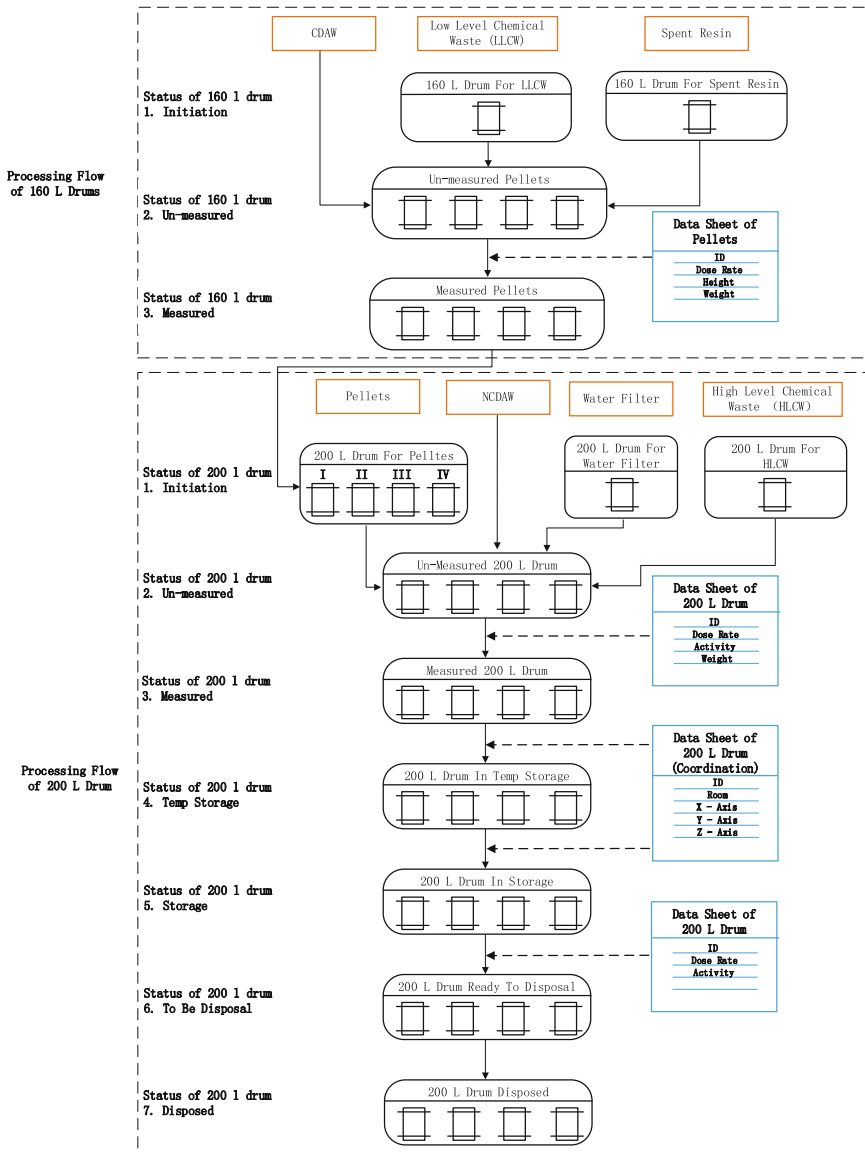


Fig. 4 Status update flow

a drum ID from corresponding drum ID lists and then combine them together. After data association, one can search a drum's ID to get its measuring data.

- (5) Other operations. TFS can display current storage information in a simulation picture. In the simulation picture, empty position is marked blank,

semi-stacked position is marked with color icon, and fully stacked position is marked with gray icon. TFS also supports data printing and exporting to Excel file.

2.3.2 Operation of Solid Waste Management Software

- (1) User Level. All the users who can log in to SPMS can access waste management information; only waste management staff can enter or import new data; only waste management supervisor and above can modify data; different managers have their corresponding right to approval application.
- (2) Data Input. As shown in Fig. 5, all the data of drum recorded in TFS will be imported to SWMS, and other collecting, processing, and disposal information will be entered into SWMS manually. Collecting information records where, when, and how much is the waste generated. If a RWP is recorded, then the waste management staff will know which specific work generates the waste. Dose rate and nuclide activity information of waste will also be measured before delivered to SRTF.
- (3) Data Association. Besides in-module data association, which will be introduced in the 3rd section, SWMS also retrieves RWP information from RWP module. RWP information covers detail information of a radiation work, including time, location, staff information, equipment, and work detail.
- (4) Data Sheet. As 200-l drum is the final storage form of waste inside SRTF, data sheet is the archives of 200-l drum, which covers all the information of waste that the 200-l drum contained and the 200-l drum itself, from waste generation to processing and 200-l drum initiation and storage. Depending on the type of waste that the 200-l drum contained, the detail content of data sheet is not the same. The data sheet can be printed and handed over to the disposal

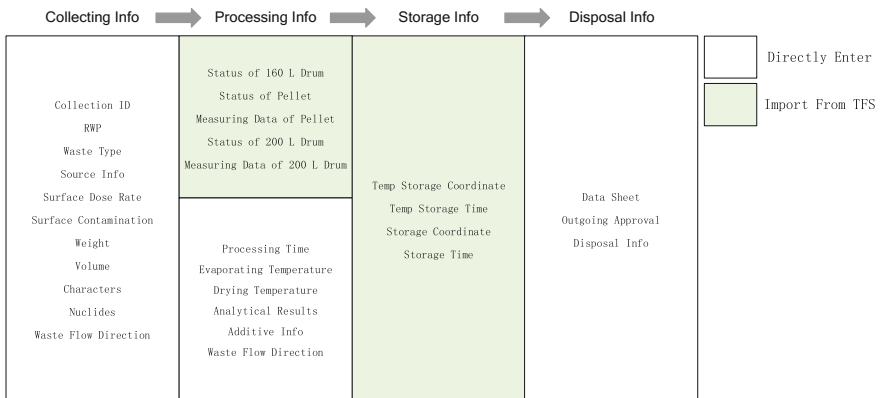


Fig. 5 Data recorded in solid waste management system

department, though it is not necessary to print all the information of a drum when delivered to disposal.

- (5) **Outgoing Approval.** Before the 200-l drum is ready for disposal, the waste management staff have to apply for approval of disposal. It should first be approved by the managers of SMNPC, and this approval is done inside SWMS.

3 Application of RMIS—Waste Tracking

Waste tracking is proposed for 200-l drum. A 200-l drum is deemed trackable when given the drum’s ID, all the detail generation and processing information of the waste it contained is specific. The operation of collecting mentioned in Sects. 3.1–3.5 means delivering waste to SRTF from other facilities. Collecting information includes waste generation information and measuring information before delivery. In order to distinguish a specific process operation, an operation ID is given to that process if no drum is involved directly; otherwise, the drum’s ID is used in place of operation ID.

3.1 Tracking of 200-L Drum Containing Chemical Waste

- (1) **Tracking of 200-L Drum containing Low-Level Chemical Waste Tracking**

Low-level chemical waste will be vaporized, dried, super-compacted, and grouted. The relations of each operation ID or drum ID are shown in Fig. 6. It is

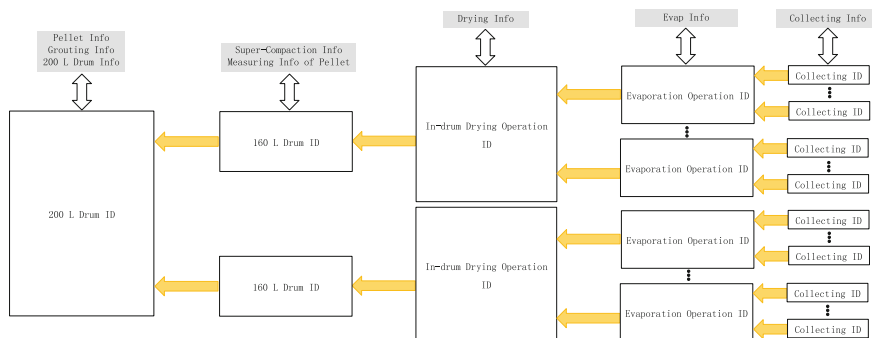


Fig. 6 Relationship between IDs involved in LLCW treatment

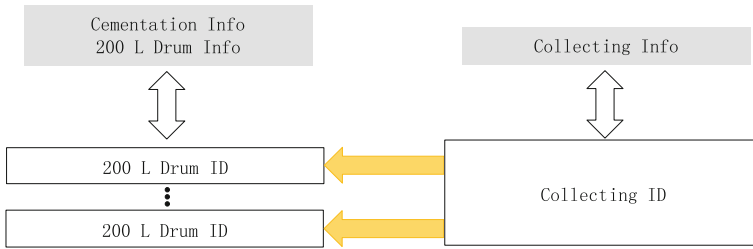


Fig. 7 Relationship between IDs involved in HLCW treatment

clear that given a 200-l drum ID, the ID of 160-l drum it contained, the in-drum drying operation ID, the evaporation operation ID, and collecting ID are all specific. Though there is more than one 160-l drum ID and corresponding operation ID, the relationship is clear and unique. Given the above, the 200-l drum containing low-level chemical waste is trackable.

(2) Tracking of 200-L Drum containing High-Level Chemical Waste

High-level chemical waste is directly cemented. The relationship between IDs is very simple, as shown in Fig. 7. Even though high-level chemical waste collected in one batch may be cemented in many 200-l drums, the collecting information is unique, which means given 200-l drum ID the chemical waste it contained is specific, because there is no difference between chemical wastes in the same collecting batch in the waste management perspective. So the 200-l drum containing high-level chemical waste is trackable.

3.2 Tracking of 200-L Drum Containing Spent Resin

Spent Resin will be dried, super-compacted, and grouted. The relationship between IDs involved in spent resin treatment is shown Fig. 8. As analyzed in Sect. 3.1, 200-l drum containing spent resin is trackable.

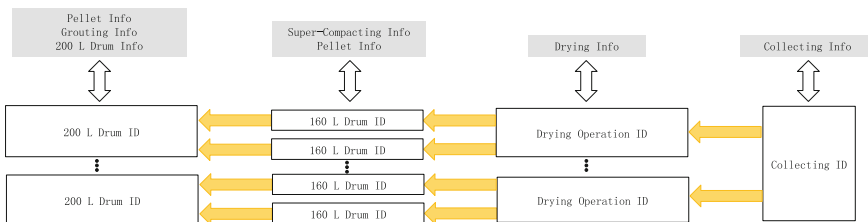


Fig. 8 Relationship between IDs involved in spent resin treatment

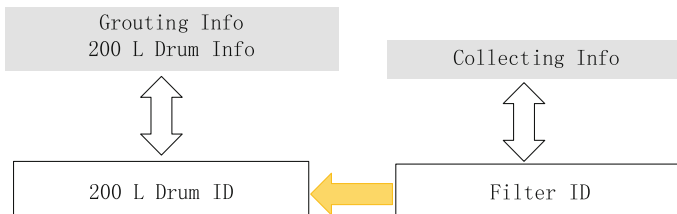


Fig. 9 Relationship between IDs involved in water filter treatment

3.3 Tracking of 200-L Drum Containing Water Filter

Water filter has unique equipment ID and name, so the equipment ID will be in place of collecting ID. Only one water filter is placed in a 200-l drum and grouted. The relationship between IDs involved in water filter treatment is shown in Fig. 9. As analyzed in Sect. 3.1, 200-l drum containing water filter is trackable.

3.4 Tracking of 200-L Drum Containing HVAC Filter

HVAC filter may not have unique equipment ID; to the convenience of recording processing data, waste management staff will label each HVAC filter with a unique ID; and this unique ID will be in place of collecting ID. The relationship between IDs is shown in Fig. 10, and as analyzed in Sect. 3.1, 200-l drum containing HVAC filter is trackable.

3.5 Tracking of 200-L Drum Containing DAW

CDAW will be pre-sorted, shredded, sorted, pre-compacted, dried, super-compacted, and grouted; NCDAW will be pre-sorted and grouted. Relationship between IDs involved in DAW treatment is shown in Fig. 11. DAW is collected in plastic bags and pre-sorted in nuclear island (NI). Depending on the

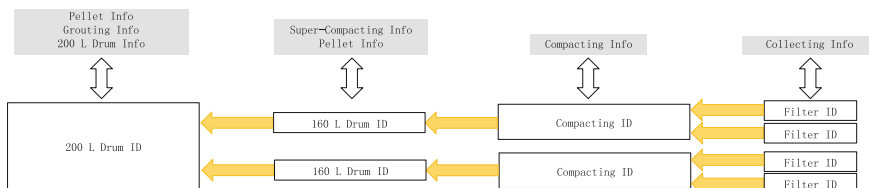


Fig. 10 Relationship between IDs involved in HVAC filter treatment

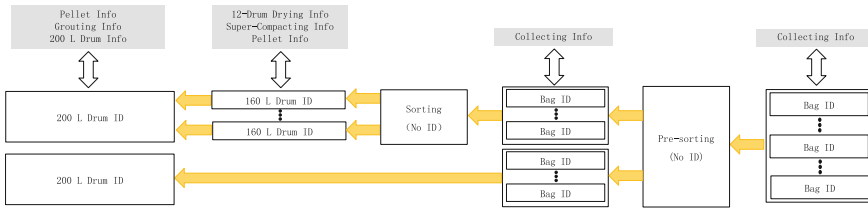


Fig. 11 Relationship between IDs involved in DAW treatment

compatibility, surface dose rate, surface contamination, and possibility of decontamination, each DAW will be treated as CDAW or NCDAW. DAWs generated in the same work and collected in the same bag may be placed in several different bags during pre-sorting and the latter bags will be loaded into shredder, and the pieces of DAWs after shredding will be put into different 160-l drums or 200-l drums. There would be no way of keeping record of which piece of waste in a 160-l drum comes from which work. The connections between IDs have been cut out during two sorting phases. Given the 200-l drum ID, the original information of the waste it contained is not clear, which means the 200-l drum containing DAW is not trackable.

4 Application of RMIS—Waste Minimization

With the data recorded in RMIS, there are two potential ways of supporting waste minimization: One is waste generation control, and the other is SRTF operation improvement. The former is more feasible for technical waste (including DAW and mixed waste); the latter is more feasible for operation waste (including filter, spent resin, and chemical waste).

Given the hypotheses that W represents quantity of collected waste during fuel cycle T , D represents quantity of 200-l drums when all the collected waste is treated, and P represents the evaluation of SRTF operation, then D would be the function of W and P in the form of:

$$D_T = f(W, P)$$

D_T represents the final evaluation of a NPP’s waste management. When the waste treatment technologies are fixed, there will be subtle variance in P .

Furthermore, given the hypotheses that R represents the malfunction rate of SRTF’s equipment, H represents human error rate, S represents operation parameters of waste processing systems, and O represents other factors, P would be the function of R , H , S , and O in the form of:

$$P = g(R, H, S, O)$$

4.1 Waste Minimization of Operation Waste

During NPP operation, the production of spent resin, water filter, and chemical waste is inevitable. W of these operation waste (W_o) is more dependent on NPP design, equipment material, and operation status, but less dependent on maintenance works. It is not difficult to find out the reasons for change in W_o . The data recorded in RMIS may help waste management staff focus on analyzing factors of P , which are R , H , and S . RMIS has detail information of D , W , and S , the equipment manage module in SPMS has detail information of R , and the operation procedures have detail information of H . Given D , W , S , R , and H and the relations between them, the operator of SRTF may control the outcome of D by adjusting S and figure out optimal parameters to run SRTF systems.

4.2 Waste Minimization of Technical Waste

Technical waste comes from human works, including radiation protection clothes and scrapped tools. The W value of technical waste (W_t) is very sensitive to human performance and waste management strategy, and it is not easy to find out the relation between specific work and the total W . Normally, the value of W_t is much bigger than W_o , and it is more efficient to spent time controlling the generation of technical waste than optimizing SRTF operation.

Even though, as discussed in Sect. 3.5, 200-l drum containing DAW is not trackable, if the waste management staff focus on generation control, the information of bag collected will be enough. Each bag collected contains the RWP that points to the work that generates the waste inside. Waste management staff can get detail RWP information by retrieving data from RWP module, including detail information of work and workers. The trend of W_t can be monitored both time-wise and work-wise. In the time-wise monitoring, waste generated by the same work at different time can be compared; in the work-wise monitoring, waste generated by different works at the same period can be compared. Details can be analyzed. Is the work simpler? Are the workers well trained about waste generation control? So the waste management staff may have a direction to figure out waste minimization.

5 Deficiencies of RMIS of SMNPC

There are mainly three important deficiencies of RMIS of SMNPC:

- (1) The waste management staff did not involve in during the design of TFS. It is not necessary to construct two parts of RMIS. The functions of TFS and SWMS can be combined, which will save a lot of time messing with data transfer.
- (2) More human work in getting data. Much of the raw data of SWMS are recorded manually and may be copied two to three times to get a better format. This may take a lot of additional time for the waste management staff. Right now, it is not sure whether all these data are useful for analyzing. More automatic ways for recording data are under consideration.
- (3) More human work in data analyzing. With so many details recorded, such as processing parameters, it is not easy to fetch all the data out of database in the desire format. Finding logics between the data is also not an easy job.

6 Suggestions for Constructing a Nationwide Waste Information System

A well-customized IT system may save a lot of time recording, updating, and saving data (for the same quantity). A nationwide waste management IT system may help the authorities make decisions and help the waste management corporations share information. If possible, the open system may be a good platform for the citizens to know what is going on about the radwaste produced, and keep the rumors out. There are several suggestions for constructing a nationwide waste management IT systems:

1. The information of waste should be focused on the final disposal container, not the waste generation or treatment.
2. Data structure should be established. RMIS of SMNPC can get raw data easily, but for the nationwide waste management IT system, it should cover all the possible waste produced, and may retrieve data from waste-generating corporations, waste treatment corporations, and waste-disposing corporations. Uniform data structure is necessary for data communicating.
3. Opening the IT system to citizens for the unclassified data should be considered. The easier the citizens can get the authoritative information, the less the rumors will be. As for this consideration, a good human-machine interface is also necessary.
4. Approval system may also be integrated in the waste management IT system. Because all the data are needed for application to treatment, disposal is already in the database.

Analysis of Liquid Effluents Discharge Method Under Normal Condition of One Inland NPP in the Northern Areas of China

Lei Xing, Yongchun Yang, Hang Lv and Guanghui Ma

Abstract Building nuclear power plant (NPP) in the inland areas of northern China complies with the requirements, including the energy planning, electricity demand, environment protection and realizing sustainable development. Taking a typical inland NPP in the northern China as an example, this paper analyzes the necessary flow rate of liquid effluents discharge and points out that the typical characteristic of northern nuclear power site is no receiving water or dilution capability insufficiency of the receiving water. Aimed at it, the discharge method of transforming liquid effluents into gaseous effluents (TLE-GE) under normal condition is produced. In order to use the existing facilities and reduce cost, two feasible engineering schemes are given, including air cooling tower TLE-GE, which makes liquid effluents naturally evaporate into gaseous effluents in the air cooling tower and discharges gaseous effluents contained in the elevating airflow to high-altitude atmosphere, and nuclear island stack TLE-GE, which makes liquid effluents forced evaporate into gaseous effluents by evaporators and discharges gaseous effluents contained in the nuclear island exhaust airflow to atmosphere through nuclear island stack. The feasibility analysis is done from operation management, total annual release and dose constraints. The relevant proposals can be used for reference on the discharge method of liquid effluents of the inland NPP located in the northern China with water resource shortage.

Keywords Water resource shortage · Northern inland areas · Nuclear power plant · Liquid effluents release · Transforming liquid effluents to gaseous effluents · Air cooling tower · Nuclear island stack

Site selection of nuclear power plant (NPP) should be subordinated to the national energy development plan. The consumption structure of energy relies mainly on coal at present in the inland provinces of northern China. Due to the influence of the haze weather, the northern provinces will face a great challenge in the total amount control of coal consumption. The demand for raising the proportion of clean energy

L. Xing (✉) · Y. Yang · H. Lv · G. Ma
China Nuclear Power Engineering Co., Ltd., Shijiazhuang, Hebei, China
e-mail: jianghong@cnpe.cc

is urgently. Therefore, building NPP is an important strategy for meeting increasing energy demand, economic and social development and realizing the coordinated development of the energy, economic and ecological environment in the northern inland areas.

The Chinese and foreign NPPs all adopt the same technical route that dilutes liquid effluents by water of river or sea and discharges to the environment at present. However, because of water resource shortage in the inland area of northern China, how to discharge liquid effluents has become the key factor of restricting the NPP construction in this area.

Taking a typical inland NPP in the northern China as an example, discharge method of liquid effluents is discussed and analyzed. The typical NPP aims at building up 4 million kilowatts level energy power generating units of HPR1000. The secondary-circuit cooling method adopts large natural draft cooling tower (called air cooling tower in the following). Eight air cooling towers are arranged for each unit with two towers.

Radioactive liquid waste generated from NPP of HPR1000 under normal condition is purified and treated into liquid effluents and then released into the environment. Radioactive gaseous waste is purified or decayed and then released into the atmosphere through the nuclear island stack. The typical NPP improves the boron recycle system and liquid radwaste treatment system of HPR1000, so the activity concentration of other nuclides except ^3H and C14 has been at a very low level. The conservative discharge of liquid effluents from four units is about $40000 \text{ m}^3/\text{a}$.

1 Analysis of Dilution Discharge by Water of NPP Liquid Effluents

The possible receiving water around the typical NPP is Reservoir A, River B and River C at the lower reaches of Reservoir A.

1.1 Analysis of the Necessary Flowrate of Liquid Effluents Discharge

Design source term of liquid effluents from four units is as follows: liquid ^3H 41.3 TBq/a, liquid C14 28.2 GBq/a and other nuclides (except ^3H and C14) 2.34 GBq/a. "Total β radioactive concentration cannot exceed 100 Bq/L, ^3H cannot exceed 1 Bq/L at 1 km downstream of the main discharge outlet in the inland site," as regulated in the Chinese standard GB6249-2011 "Regulations for environmental radiation protection of nuclear power plant." Based on the assumption that is mixed completely, to conform to the requirement of total β and ^3H radioactive concentration, liquid effluents discharge from four units demands that average flowrate of

the receiving water should be not less than 45.2 and 0.3 m³/s, respectively. Thus, it can be seen that the necessary flowrate of ³H is far more than that of other nuclides.

1.2 Analysis of the Receiving Water of the Typical NPP

The distance between the typical NPP and Reservoir A is shortest and about 3 km. But considering that Reservoir A is the important protected area of water resource, which provides industrial water, urban domestic water and irrigation agriculture water for nearby areas, so liquid effluents cannot be discharged into Reservoir A and can only be discharged into River B or C.

The distance between the typical NPP and discharge outlet of River B is about 8 km. However, River B is mountainous stream river with rise and drop suddenly. The water flow is big and the rapid during the rainstorm season. And it is very small, even drying up, during the dry season. According to the field investigation, the minimum monthly average flowrate with guarantee rate 90% of the chosen outlet section is close to zero. Therefore, River B is not suitable for receiving water due to no dilution ability.

The distance between the typical NPP and discharge outlet of River C is about 60 km. According to the measuring data of hydrometric station, water flow change is big. The average flow of wet season is 3–5 times than that of dry season. The annual average flow is 19.65 m³/s, of which wet year is 1.5 times than that of dry year. Calculated by control requirements of ³H concentration, River C can only accept about 43.5% of liquid effluents, so the dilution ability is insufficient. And it is necessary to adopt engineering measures to convey liquid effluents about 60 km from the typical NPP to River C, which belongs to long-distance discharge. Not only engineering economic cost is high, but also Chinese regulatory agencies remain objecting the long-distance discharge.

To sum up, dilution capability of the receiving water of the typical NPP is insufficient, that is the typical characteristic of inland NPP sites in the northern China.

2 Engineering Scheme of TLE-GE

The dilution capability of receiving water is insufficient around the typical NPP, so transforming liquid effluents into gaseous effluents (TLE-GE) discharge method under normal condition can be adopted. In order to use the existing facilities and reduce cost, two engineering schemes are given, including air cooling tower TLE-GE and nuclear island stack TLE-GE.

2.1 Air Cooling Tower TLE-GE

The engineering scheme is proposed to use two cooling towers for TLE-GE, one work one standby. Liquid effluents are transported from storage tanks to atomization nozzles installed above the radiator of air cooling tower by discharge pump and atomized into tiny droplets by nozzles. The tiny droplets naturally evaporate into gaseous effluents by using conditions conducive to evaporation in the tower, including relative high temperature (about 10 °C is higher than ambient temperature during operation), relative high wind speed (average wind speed is 4–8 m/s) and huge gas–liquid-contact area. Then, the elevating airflow carries gaseous effluents to release into the high-altitude atmosphere (the height of cooling tower is 200 m).

2.2 Nuclear Island Stack TLE-GE

The engineering scheme is proposed to use evaporators of liquid radwaste treatment system or boron recycle system to transform liquid effluents into gaseous effluents with forced evaporation. The gaseous effluents are transported to nuclear island stack. Then, the exhaust airflow carries gaseous effluents to releases into atmosphere through the nuclear island stack (average airflow velocity is about 10 m/s). The condensate collection facility is settled on the bottom of the stack.

3 Feasibility Analysis of TLE-GE Release Methods

Only liquid effluents discharged to environment from NPP meeting the requirements of dose constraints and total annual release, and being granted by Chinese regulatory agencies, it can be discharged under clearance. The feasibility analysis of air cooling tower TLE-GE and nuclear island stack TLE-GE are done.

3.1 Operation Management

Because of the influence of meteorological conditions on TLE-GE, two discharge methods can only be implemented with control in stages. The airflow relative humidity in the rainfall weather is high. Extreme weather will influence the airflow. So it is not discharge during the rainfall and extreme weather. According to the site meteorological conditions, total discharge time is about 250 days throughout the year. Correspondingly, average discharge from four units is about 2 L/s.

The atomizing facilities are arranged above heat exchanger in the air cooling tower, including atomization nozzles, valves and pipeline. When atomizing

facilities of a cooling tower are in trouble, the spare air cooling tower can be used for discharge.

Nuclear island stack TLE-GE adopts the evaporation facilities of two units, one work one standby. When evaporation facilities of one unit are in trouble, the spare unit can be used.

3.2 Dose Constraints

Table 1 gives the public individual doses of TLE-GE release and airborne effluents, that is the radioactive gaseous waste released through the nuclear stack. The major contributor to public exposure doses is the ^3H which is more than 90% of total dose. Table 2 shows that the maximum individual effective dose for public members around the typical NPP of these two engineering schemes is both below 10 $\mu\text{Sv/a}$ of clearance dose constraint.

3.3 Total Annual Release

Total annual release of other nuclides except ^3H and C14 from the typical NPP meets the control values of GB6249-2011. However, due to the special chemical properties, the existing treatment process cannot remove ^3H of radioactive liquid waste. And removal effect for C14 is very limited. Therefore, it is conservatively considered that ^3H and C14 all release to environment through TLE-GE. Table 1 shows that 1648.8 GBq/a of gaseous C14 is far below 2800 GBq/a of airborne effluents control value; and total annual release of gaseous ^3H is 183.56 TBq/a, that is more than 60 TBq/a of airborne effluents control value in the GB6249-2011 and

Table 1 Public radiological impact of two TLE-GE discharge methods of the typical NPP (four units)

Discharge method	Public radiological impact of gaseous effluents from the original nuclear island stack ($\mu\text{Sv/a}$)	Public radiological impact of gaseous effluents by TLE-GE ($\mu\text{Sv/a}$)	Public radiological impact of total gaseous effluents ($\mu\text{Sv/a}$)
Air cooling tower TLE-GE	3.22	0.0364	3.26
Nuclear island stack TLE-GE		3.66	6.88

Table 2 Comparison annual release of ^3H and ^{14}C from the typical NPP with control value of GB6249-2011 (four units)

Radionuclide	Annual release of gaseous effluents transformed by liquid effluents	Annual release of airborne effluents (see note)	Total annual release	GB6249-2011 multi-reactor control value of airborne effluents
^3H (TBq/a)	165.2	18.36	183.56	60
C14 (GBq/a)	112.8	1536	1648.8	2800

Note It is the radioactive gas waste released through the nuclear stack

less than 360 TBq/a of control value sum of liquid and airborne ^3H . In view of the existing regulation aimed at discharging liquid effluents into the environment water, although it does not exclude the TLE-GE discharge method, but the lack of specific requirements. So it is suggested that gaseous ^3H control value for TLE-GE discharge method should be regulated clearly.

4 Conclusion

- (1) There is no receiving water or dilution capability insufficiency of the receiving water of inland sites in the northern China. Aimed at it, TLE-GE discharge method under normal condition can be adopted. Furthermore, two engineering schemes of air cooling tower TLE-GE and nuclear island stack TLE-GE are feasible. However, building inland NPP should improve the radioactive liquid waste treatment system to treat the radioactivity of other nuclides except ^3H and C14 at the lowest possible level.
- (2) The maximum individual effective dose for public members around the typical NPP by TLE-GE discharge method is below $10 \mu\text{Sv/a}$. The radiant value for the public is less than that of clearance dose constraint, which demonstrates the feasibility of TLE-GT.
- (3) The existing regulations of China are all aiming at discharging liquid effluents into the environment water, and lack of specific requirements for TLE-GE discharge method. So it is suggested that gaseous ^3H control value for TLE-GE discharge method should be regulated clearly.

References

1. GB3097-1997. Sea water quality standard.
2. GB14587-2011. Technical requirements for discharge of radioactive liquid effluents from nuclear power plant.
3. GB8978-1996. Integrated wastewater discharge standard.
4. Liu Xinhua, Zhang Ailing. Concept and Measures of Radioactive Liquid Effluents "Near-zero Release" in Inland Nuclear Power Plants [J]. Radiation Protection, 2012, 32(3).

Application Method Study of Erica Model and R&D128 Model in Radiological Impact Assessment of Terrestrial Organisms

Hongyan Du, Xiaoping Bai, Qiming Wei and Yawei Mao

Abstract ERICA model and R&D128 model are programs widely used to assess non-human species radiation effect. Two models were briefly introduced in this paper, and taking a coastal NPP in China as example, the radiation dose rate of terrestrial organisms near the NPP was calculated and the parameters were compared. It was concluded that the calculation result of ERICA model was more conservative than R&D128 model for ^3H and ^{14}C , but the calculation result of R&D128 model was more conservative than ERICA model for most of other nuclides except for ^3H and ^{14}C . The nuclides and reference organisms of ERICA model were more comprehensive, but the radiation dose rate caused by noble gases could be calculated by R&D128 model, the radiological impact on terrestrial organisms of noble gases can be illuminated to a certain extent. It was suggested that the radiation impact of noble gases and other nuclides on terrestrial organisms should be calculated with R&D128 model and ERICA model separately. The application method of two models in radiological impact assessment of terrestrial organisms was established.

Keywords ERICA model · R&D128 model · Terrestrial organism · Radiological impact assessment · Application method

1 Introduction

Radiological impact assessment must be carried out in the licence application and each phase of environmental impact assessment such as sitting, constructing and operating of a nuclear facility. There are explicit requirements in the 7th principle of IAEA SF-1 “Fundamental Safety Principles” [1], Chinese GB6249-2011 “Regulations for environmental radiation protection of nuclear power plant” [2], and the latest draft of NEPA-RG1 “Technical Guideline for Environmental Impact

H. Du (✉) · X. Bai · Q. Wei · Y. Mao
China Nuclear Power Engineering Co., Ltd., Beijing, China
e-mail: hyduhydu@163.com

Assessment Format and Content of Environmental Impact Reports for Nuclear Power Plant” [3] published by Nuclear and Radiation Safety Center of Ministry of Environment Protection of the PRC. The research of radioecology and the biological dosimetry are at the initial phase in China, and the NPP sites are all coastal sites nowadays, so the radiological impact study recently mostly focuses on aquatic biota [4–6]. There are not much study about terrestrial organisms. In order to follow the international study progress on non-human species, assess the all-sided radiological impact of the organisms, and keep the radiological impact of NPP on local environment during normal operation within the safety limit, meet the basic requirements of radiation protection and nuclear safety and the involved requirements in the licence application and each phase of environmental impact assessment, it is necessary to study the assessment method of the radiation dose rate of terrestrial organisms around the site caused by the gaseous effluents of the NPP.

2 Brief Introduction of the Erica Model and R&D128 Model

The ERICA method is based on the FASSET programme [7] developed in 2004 and ERICA programme [8] developed in 2007 by European Union (EU), consists of ERICA code and FREDERICA radiological effect database, provides the methodology of ecological effect and radiation impact of the non-human species and the ecosystem. The screen method of radiation dose rate assessment of the representative organisms of the terrestrial, freshwater and marine ecosystem is provided in ERICA model, consisting of tier 1 simple assessment, tier 2 general assessment, and tier 3 detailed assessment. The reference organisms and calculated nuclides considered in the ERICA model are given in Tables 1 and 2.

The R&D128 method [9] is a method to assess the radiological impact of ionizing radiation on wild animals developed by UK environment agency, consists of Microsoft Excel tables of terrestrial, freshwater and marine ecosystem. We can use default or site-specific data to calculate the radiation results in the model, and the basic calculation principle is similar to ERICA model, for example the dimension, dietetic ingestion and environment external exposure of the organisms should be considered. But the categories of the organisms and nuclides are less than ERICA model. R&D128 model also considers the noble gases that are not included in ERICA model, and the important species in UK ecosystems. The reference organisms and calculated nuclides considered in R&D128 model are given in Tables 2 and 3.

Though there are differences in the origin, parameter value, terrestrial reference organisms between two models, the principle of biological dosimetry, the definition of reference organism, the transfer of nuclides in the organism, the calculation method of dose rate of two models are basically the same.

Table 1 Reference organisms of terrestrial ecosystem in ERICA model (screen 2 and 3)

Name of reference organisms	Mass (kg)	Ratio of length and width	Ratio of height and width	Data source
Amphibian	0.0314	0.375	0.313	ICRP Frog
Bird	1.26	0.333	0.267	ICRP Duck
Arthropod-detritivorous	0.000174	0.353	0.176	FASSET Turtle
Flying insects	0.000589	0.375	0.375	ICRP Bee
Mollusc-gastropod	0.0014	0.817	0.493	Snail
Grasses &Herbs	0.00262	0.2	0.2	ICRPGrass
Lichen & Bryophytes	0.00011	0.057	0.057	Lichen
Mammal-large	245	0.462	0.462	ICRPDeer
Mammal-small-burrowing	0.314	0.3	0.25	ICRP RAT
Reptile	0.744	0.03	0.03	Snake
Shrub	0.00262	0.2	0.2	ERICA
Annelid	0.00524	0.1	0.1	ICRP Earthworm
Tree	471.0	0.03	0.03	ICRPPine tree

Table 2 Nuclides of terrestrial ecosystem assessment in ERICA and R&D128 model

ERICA	ERICA	R&D128
³ H	⁵⁴ Mn	³ H
¹⁴ C	⁹⁴ Nb, ⁹⁵ Nb	¹⁴ C
³² P, ³³ P	⁵⁹ Ni, ⁶³ Ni	³² P
³⁵ S	²³⁷ Np	³⁵ S
⁵⁷ Co, ⁵⁸ Co, ⁶⁰ Co	¹⁵² Eu, ¹⁵⁴ Eu	⁴¹ Ar
⁸⁹ Sr, ⁹⁰ Sr	¹²⁴ Sb, ¹²⁵ Sb	⁸⁵ Kr
¹⁰³ Ru, ¹⁰⁶ Ru	⁷⁵ Se, ⁷⁹ Se	⁶⁰ Co
¹²⁵ I, ¹²⁹ I, ¹³¹ I, ¹³² I, ¹³³ I	⁹⁵ Zr	⁹⁰ Sr
¹³⁴ Cs, ¹³⁵ Cs, ¹³⁶ Cs, ¹³⁷ Cs	^{129m} Te, ¹³² Te	¹⁰⁶ Ru
²²⁶ Ra, ²²⁸ Ra	²¹⁰ Pb	¹²⁹ I, ¹³¹ I
²²⁷ Th, ²²⁸ Th, ²³⁰ Th, ²³¹ Th, ²³² Th, ²³⁴ Th	²¹⁰ Po	¹³⁷ Cs
²³⁴ U, ²³⁵ U, ²³⁸ U	¹⁴⁰ Ba	²²⁶ Ra
²³⁸ Pu, ²³⁹ Pu, ²⁴⁰ Pu, ²⁴¹ Pu	²⁵² Cf	²³⁴ Th
²⁴¹ Am	⁵¹ Cr	²³⁸ U
²⁴² Cm, ²⁴³ Cm, ²⁴⁴ Cm	¹⁹² Ir	²³⁹ Pu
^{110m} Ag	²³¹ Pa	²⁴¹ Am
⁹⁹ Tc	⁶⁵ Zn	
¹⁰⁹ Cd	⁴⁵ Ca	
¹⁴¹ Ce, ¹⁴⁴ Ce	¹⁴⁰ La	
³⁶ Cl		

Table 3 Reference organisms of terrestrial ecosystem in R&D128 model

Reference organisms	Mass (kg)	Dimension (mm)
Lichen	0.00131	100 × 5 × 5
Moss	0.00262	100 × 10 × 5
Tree (root)	0.00021	100 × 2 × 2
Shrub (root)	0.00021	100 × 2 × 2
Herb (root)	0.00021	100 × 2 × 2
Germinating Seed	0.0000018	6 × 1 × 1
Fungal fruiting body	0.00263	30 × 15 × 10
Caterpillar	0.00077	30 × 7 × 7
Social Insect-ants	0.00002	5 × 3 × 3
Social Insect-bee	0.002	20 × 15 × 10
Wood Louse	0.001	15 × 6 × 3
Earthworm	0.0035	100 × 5 × 5
Herbivorous Mammal (rabbit)	0.8	300 × 150 × 100
Carnivorous Mammal (fox)	5.5	670 × 350 × 180
Small Burrowing Rodent (mouse)	0.02	100 × 20 × 20
Woodland Bird (Grouse)	1.5	350 × 150 × 150
Bird egg	0.0013	40 × 25 × 25
Reptile (Grass snake)	2.26	1200 × 60 × 60

3 Radiological Dose Rate Calculation of the Terrestrial Organisms Around a Chinese NPP Site

Taking a coastal NPP of China as example, according to the field survey result of the terrestrial ecological environment around the site, birds such as egrets and night heron are the representative organisms around the site. So the radiation dose rate of the representative organisms around the site (birds) was calculated by ERICA model and R&D128 model according to the annual gaseous effluents of two units of the NPP.

3.1 Calculation of Nuclide Concentration in the Environmental Medium

Under the equilibrium condition, when we calculate the nuclide concentration in the environment medium through the SRS-19 model [10], the default values of part of the parameters were provided in the model such as the fraction of the time during the year the wind blows towards the receptor of interest, the dry and wet deposition coefficient etc. We chose the value according to the actual situation of the NPP for those parameters that there were no default values in the model.

Table 4 The concentration of nuclides calculated by SRS-19 model in the environmental medium

Nuclides	Concentration of nuclides (³ H and ¹⁴ C: Bq m ⁻³ ; Other nuclides: Bq kg ⁻¹)	Nuclides	Concentration of nuclides (³ H and ¹⁴ C: Bq m ⁻³ ; Other nuclides: Bq kg ⁻¹)
¹³¹ I	1.26×10^{-3}	⁹⁵ Zr	9.09×10^{-6}
¹³² I	1.47×10^{-6}	⁹⁵ Nb	2.12×10^{-5}
¹³³ I	4.75×10^{-5}	¹⁰³ Ru	9.36×10^{-6}
¹³⁴ I	1.40×10^{-7}	¹⁰⁶ Ru	2.05×10^{-6}
¹³⁵ I	4.66×10^{-6}	¹²⁵ Sb	1.95×10^{-6}
⁵¹ Cr	3.86×10^{-5}	¹³⁴ Cs	1.44×10^{-4}
⁵⁴ Mn	1.41×10^{-4}	¹³⁶ Cs	6.15×10^{-6}
⁵⁷ Co	1.94×10^{-5}	¹³⁷ Cs	3.14×10^{-4}
⁵⁸ Co	4.74×10^{-4}	¹⁴⁰ Ba	7.75×10^{-7}
⁶⁰ Co	3.85×10^{-4}	¹⁴¹ Ce	6.19×10^{-6}
⁵⁹ Fe	1.75×10^{-5}	³ H	2.14×10^{-1}
⁸⁹ Sr	1.13×10^{-4}	¹⁴ C	1.79×10^{-2}
⁹⁰ Sr	2.21×10^{-4}		

The concentration of ³H and ¹⁴C in the air and the concentration of other nuclides in the soil are shown in Table 4.

3.2 The Radiological Dose Rate Calculation Comparison of Two Models

Through the comparison calculation and analysis between ERICA and R&D128 model, the suitable assessment model of the radiological impact assessment of the terrestrial organisms around the site can be determined.

Because only seven nuclides of the NPP effluents can be calculated in R&D128 model, we chose seven nuclides and seven organisms in R&D128 model that can be compared with the calculation results of other nuclides except for noble nuclides of the ERICA model. The radiation dose results are shown in Table 5.

Take birds as example, the calculation results comparison of the radiation dose rate between two models are shown in Figs. 1 and 2, respectively. The figures show that the calculation results of ERICA model are more conservative than R&D128 model for ³H and ¹⁴C. The calculation results of R&D128 model are mostly more conservative than ERICA model for other nuclides except for ³H and ¹⁴C.

The comparison of concentration factors and the internal and external dose conversion coefficients of the birds of two models are shown in Figs. 3, 4, 5, 6, 7 and 8 respectively.

Table 5 Comparison of the results calculated by ERICA model and R&D128 model I ($\mu\text{Gy/h}$)

Biota nuclides		^{131}I	^{60}Co	^{90}Sr	^{106}Ru	^{137}Cs	^3H	^{14}C
Bird	ERICA	1.67E-07	1.90E-07	1.71E-07	2.78E-10	6.82E-08	2.65E-04	7.11E-04
	R&D128	2.30E-07	1.70E-07	7.00E-07	2.50E-09	1.10E-07	9.40E-05	3.60E-04
Annelid	ERICA	2.61E-07	5.01E-07	7.61E-09	2.32E-10	9.78E-08	2.65E-04	2.20E-04
	R&D128	3.30E-07	4.10E-07	5.00E-07	1.90E-09	7.50E-08	1.10E-04	1.80E-04
Reptile	ERICA	2.79E-07	4.73E-07	5.38E-08	3.77E-10	1.15E-07	2.65E-04	7.11E-04
	R&D128	2.90E-07	3.10E-07	6.80E-07	2.40E-09	5.30E-07	9.40E-05	3.60E-04
Grasses & Herbs	ERICA	1.16E-07	1.85E-07	8.81E-08	1.05E-10	8.36E-08	2.65E-04	4.56E-04
	R&D128	3.10E-07	3.30E-07	7.00E-07	2.60E-09	1.80E-07	9.40E-05	3.80E-04
Shrub	ERICA	9.07E-08	1.73E-07	2.03E-08	5.04E-10	1.21E-07	2.65E-04	4.56E-04
	R&D128	3.40E-07	4.10E-07	7.50E-08	1.60E-09	9.20E-08	1.10E-04	2.40E-04
Tree	ERICA	1.21E-07	1.52E-07	6.84E-08	8.00E-10	4.19E-08	2.65E-04	6.89E-04
	R&D128	3.40E-07	4.30E-07	1.20E-07	1.60E-09	8.80E-08	7.50E-05	6.50E-04
Lichen & Bryophytes	ERICA	1.15E-07	1.93E-07	3.25E-07	3.19E-09	1.77E-07	2.64E-04	4.61E-04
	R&D128	2.30E-07	2.10E-07	4.10E-07	1.30E-09	6.80E-08	1.10E-04	2.50E-05

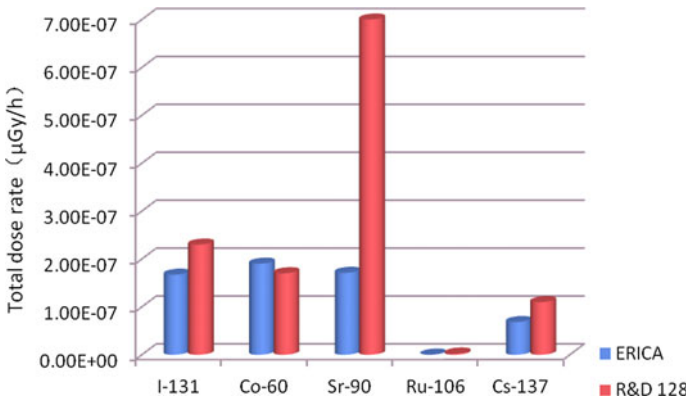


Fig. 1 Comparison between the results of bird calculated by ERICA model and R&D128 model (Other nuclides except ^3H and ^{14}C)

As Figs. 3 and 4 show, the bird’s concentration factors of ERICA model are more conservative than R&D128 model for ^3H and ^{14}C . The bird’s concentration factors of R&D128 model are more conservative than ERICA model for other nuclides except for ^3H and ^{14}C .

As Figs. 5 and 6 show, the bird’s internal dose conversion coefficients of ERICA model are close to R&D128 model for the seven kind of nuclide, almost in the same order of magnitude.

As Figs. 7 and 8 show, the bird’s external dose conversion coefficients of R&D128 model are more conservative than ERICA model for other nuclides except for ^3H and ^{14}C . For ^3H and ^{14}C , the external exposure is not considered in ERICA model, but there are considerations in R&D128 model.

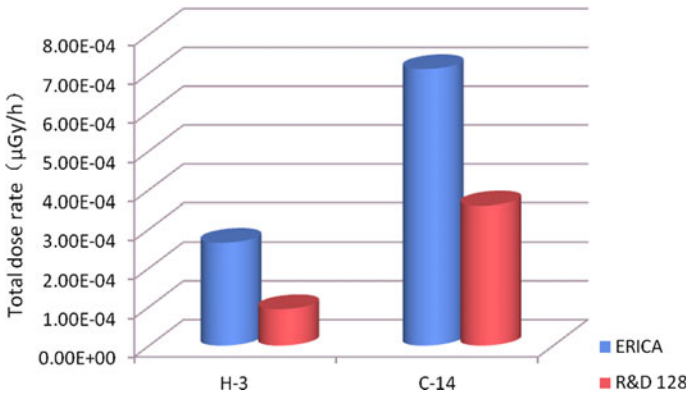


Fig. 2 Comparison between the results of bird calculated by ERICA model and R&D128 model (^3H and ^{14}C)

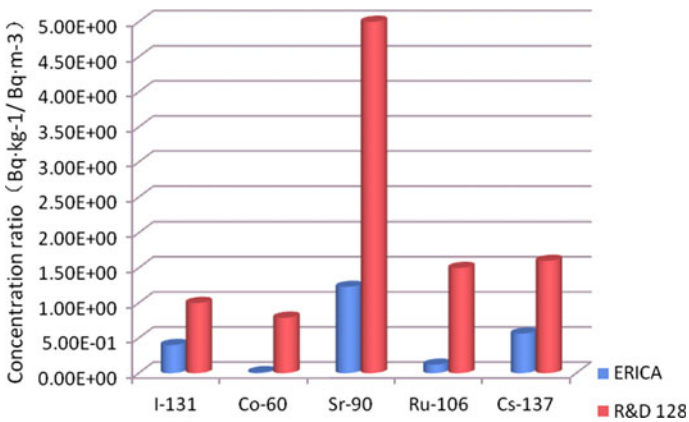


Fig. 3 Comparison of the concentration ratios of bird between two models (other nuclides except ^3H and ^{14}C)

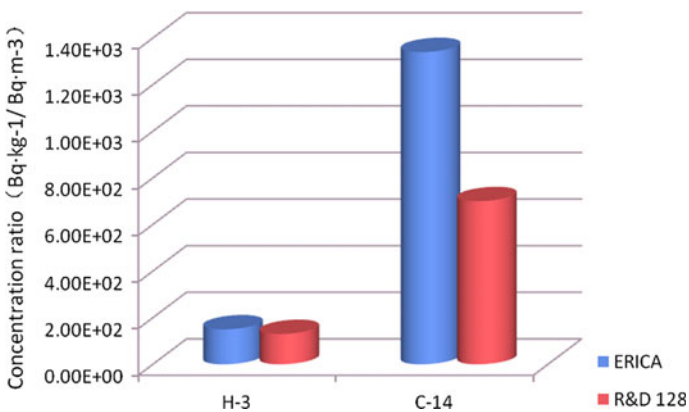


Fig. 4 Comparison of the concentration ratios of bird between two models (^3H and ^{14}C)

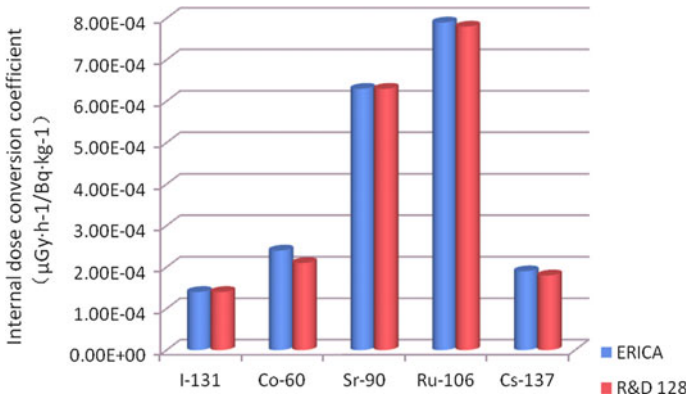


Fig. 5 Comparison of the internal dose conversion coefficients of bird between two models (other nuclides except ^3H and ^{14}C)

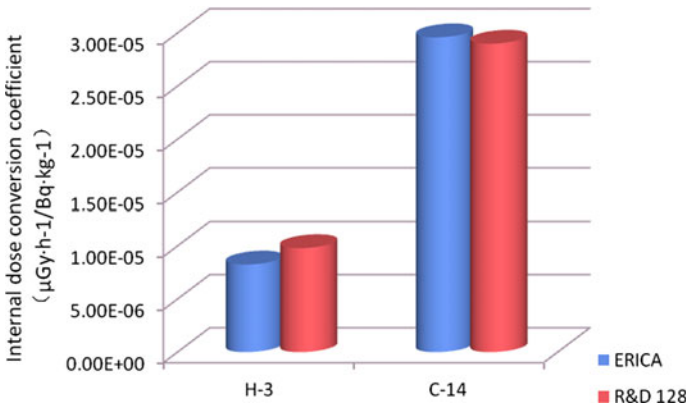


Fig. 6 Comparison of the internal dose conversion coefficients of bird between two models (^3H and ^{14}C)

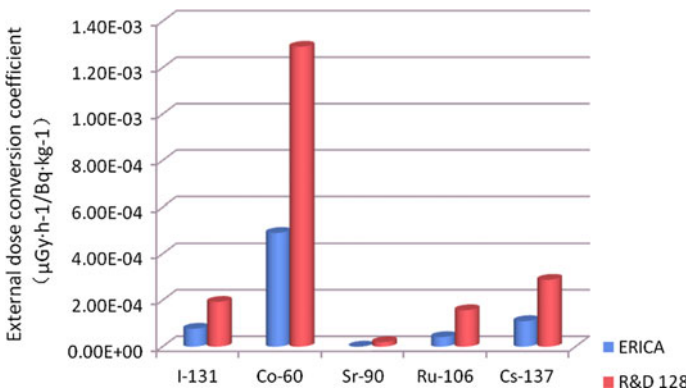


Fig. 7 Comparison of the external dose conversion coefficients of bird between two models (other nuclides except ^3H and ^{14}C)

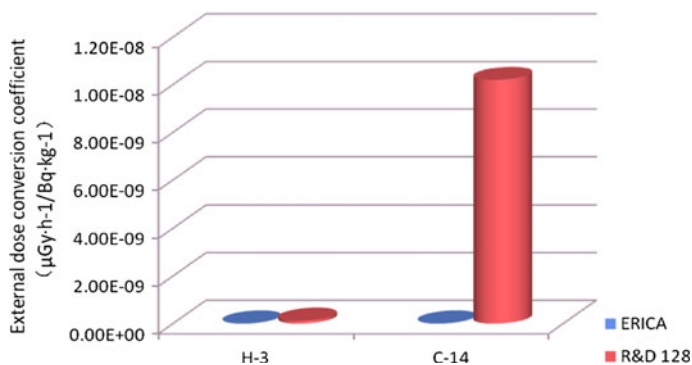


Fig. 8 Comparison of the external dose conversion coefficients of bird between two models (^3H and ^{14}C)

Through the comparison of the calculation results and parameters of two models, we know that the calculation results of ERICA model are more conservative than R&D128 model for ^3H and ^{14}C , the calculation results of R&D128 model are mostly more conservative than ERICA model for other nuclides except for ^3H and ^{14}C .

The main reason is that the concentration factors and the external dose conversion coefficients of R&D128 model are more conservative than ERICA model for other nuclides except for ^3H and ^{14}C ; the internal dose conversion coefficients of two model are close.

The concentration factors of ERICA model are more conservative than R&D128 model for ^3H and ^{14}C , the internal dose conversion coefficients of two model are close, and the external exposure are not considered in ERICA model, but there are considerations in R&D128 model.

4 Conclusions

For the nuclides released from the NPP, because there are differences between concentrations, internal and external dose conversion coefficients etc., the conservativeness of the calculation results of two models is not the same. The nuclides and reference organisms of R&D128 model are less than ERICA model, and the nuclides and reference organisms in the source term cannot be covered completely in R&D128 model, but the noble gas such as ^{85}Kr and ^{41}Ar can be calculated by R&D128 model. We can assess the radiological impact of noble gas and other nuclides through R&D128 model and ERICA model separately for the NPP.

The external exposure of ^3H and ^{14}C and the dose contribution of noble gases to terrestrial organisms were neglected in ERICA model, but the radiological impact of ^{85}Kr and ^{41}Ar and the external exposure of ^3H and ^{14}C were considered in R&D128 model. The assessment system can be more complete and suitable if we

use ERICA model associate with R&D128 model. It is necessary to integrate the advantages of two models and develop the assessment models according to the character of the ecosystems.

References

1. IAEA. Fundamental safety principles [R]. IAEA Safety Standards Series No. SF-1, Vienna: IAEA, 2006.
2. PRC National standard. GB6249-2011. Regulations of environmental radiation protection of nuclear power plant [S]. Beijing: Standards Press of China, 2011.
3. Technical Guideline for Environmental Impact Assessment Format and Content of Environmental Impact Reports for Nuclear Power Plants. NEPA-RG1.
4. Li J J, Liu S L, Chen C F, et al. Comparison between calculation of dose to Chinese sturgeon by RESRAD-BIOTA program and ERICA program. [J]. Radiation Protection Bulletin. 2009.29(6):6–13(in Chinese).
5. Zheng W, Bai X P. Preliminary study on radiological impact assessment of radioactive liquid effluent to aquatic biota. [J]. Uranium Mining and Metallurgy, 2008. 27(3):134–137 (in Chinese).
6. Du H Y, Bai X P, Zheng W, Mao Y W. Study on application of SRS-19 model and R&D 128 model in radiological impact assessment of terrestrial organisms with ERICA code.[J]. Journal of Radiological protection. 2011.31(2):65–71 (in Chinese).
7. Larsson C M. The Fasset framework for assessment of the impact of ionising radiation on non-human species [J]. Journal of Radiological protection, 2004(24):A1–A12.
8. ERICA. Environmental risk from ionising contaminants: assessment and management (EC 6th Frame-work Programme)[EB/OL]. <http://www.facilia.se/projects/erica.asp>.
9. Copplestone D., Bielby S., Jones S.R., et al. Impact assessment of ionizing radiation on wildlife [R]. Environment Agency R&D Publication 128, 2003.
10. Generic models for use in assessing the impact of discharges of radioactive substances to the environment [R]. Safety Reports Series No. 19. IAEA, Vienna. 2001.

Author Biography

Hongyan Du senior engineer, China Nuclear Power Engineering Co., Ltd. Research area: environment impact assessment.

Derivation of Activity Limits of Spent Radioactive Source for Near-Surface Disposal

Liu Jianqin, Xiong Xiaowei, Sun Qinghong and An Hongxiang

Abstract Taken Beilong Disposal Site and Northwestern Disposal Site as the reference sites, based on the drilling scenario and after drilling scenario, and considering some significant radionuclides, the activity limits for disposal of spent radioactive source in both sites were derived. The limiting scenario for ^{137}Cs is drilling scenario, and after drilling scenario is the limiting scenario for other radionuclides. The activity limits of spent radioactive source in a single waste package are not restricted by the disposal site. The acceptance limits of spent radioactive source in a single waste package are recommended, and the values for ^{90}Sr , ^{137}Cs , ^{238}Pu , ^{63}Ni , ^{241}Am , ^{226}Ra , and ^{239}Pu are 2.0×10^{10} , 6.0×10^9 , 1.0×10^6 , 1.0×10^{11} , 1.0×10^7 , 1.0×10^6 , and 8.0×10^6 Bq, respectively.

Keywords Spent radioactive source · Activity limit · Derivation · Repository · Near surface

Because of the radioactive decay, if a source is no longer unfit for the intended application, or it is disused due to other reasons, it is defined as spent radioactive source (SRS) [1]. However, the residual level of radioactivity in some sources can remain high, representing a significant radiological hazard, so we should take effective measure and manage it safely. By the end of 2010, storage facilities for nuclear technology application radioactive waste collected 86,137 disused sealed radioactive sources, among which 14,035 are in the 31 provincial storage facilities, and the remaining 72,102 are in the national centralized storage facility [2]. The disposal of spent radioactive source is a final management option that can guarantee the safety. There are currently two solid LILW disposal sites, Beilong Disposal Site and Northwestern Disposal Site, and they do not accept the spent radioactive

L. Jianqin (✉) · S. Qinghong · A. Hongxiang
China Institute for Radiation Protection, Taiyuan 030006, China

X. Xiaowei
Nuclear and Radiation Safety Centre of Ministry of Environmental
Protection, Beijing 100082, China

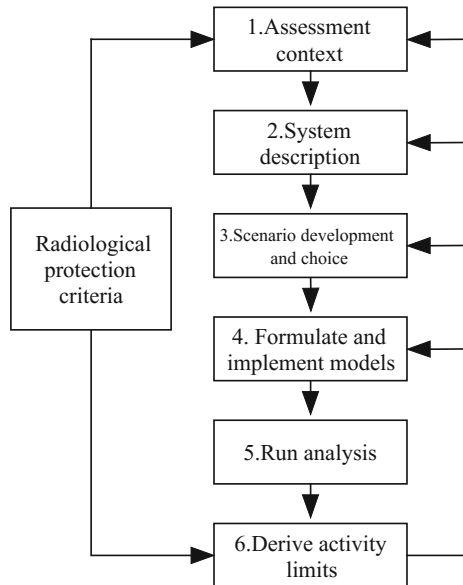
source. Spent radioactive source is different from the generic radioactive waste as a result of the small volume, large quantity, and centralized radioactivity; the special consideration of disposal of SRS is required. The safety of SRS can be assured, the storage risk and the financial burden can be reduced, if we can make use of the current near-surface disposal facility and implement the disposal of a large amount of spent radioactive sources. So the derivation of activity limits for near-surface disposal of spent radioactive source has very practical significance.

1 Approach to Deriving Activity Limits

The basics of derivation of activity limits for near-surface disposal of spent radioactive source are disposal engineering mode, scenario development and choice, and the radiological protection criteria. When determining the inventory and/or concentration limits for specific radionuclides in SRS for near-surface repository, safety assessment will be needed; the results of safety assessment for both operational and post-closure periods should satisfy the appropriate safety criterion. The approach used for deriving activity limits is shown in Fig. 1 [3].

In most safety assessments, some measure of impact on human and/or the environment is the calculation endpoint by applying the safety assessment methodology in an iterative manner. The waste activity concentrations and total activity levels are usually the starting points of the assessment. In contrast, in this study, the calculation end points are the spent radioactive source activity limits, and

Fig. 1 Approach used for deriving activity limits



the measures of impact, as specified by the radiological protection criteria, can be seen as the starting point of this calculation. However, in practice, the calculation of activity limits first requires a unit inventory to be assumed for which the appropriate measure of impact is calculated, considering all the potential scenarios. The resulting peak doses for each scenario for a unit activity of each radionuclide have to be compared to derive the limiting scenario for each radionuclide, i.e., the scenario potentially leading to the highest dose. To derive the activity limits, the highest dose for each radionuclide has to be compared with the dose limit, i.e., the selected radiological protection criteria. Assuming a linear relationship between the inventory and the impact, an activity limit is then derived for each radionuclide that meets the appropriate radiological protection criteria. For any given scenario, the activity limit of each radionuclide in the waste package can be calculated using the following formula:

$$Ap_i = \frac{\text{Dose}_{\text{lim}} \cdot A_i}{\text{MaxDose}_{iu}} \quad (1)$$

where Ap_i is the activity limit of radionuclide i for the scenario (Bq), Dose_{lim} is the relevant dose limit for the scenario ($\text{Sv} \cdot \text{a}^{-1}$), MaxDose_{iu} is the dose resulting from the initial activity of radionuclide i in the waste package ($\text{Sv} \cdot \text{a}^{-1}$), and A_i is the initial activity of radionuclide i in the waste package (Bq).

2 Process to Deriving Activity Limits

2.1 Assessment Context

The assessment purpose is to derive activity limits for disposal of spent radioactive source in the two near-surface repositories of our country, to provide the reference for establishment of acceptance requirement for near-surface disposal of spent radioactive source, sequentially the radiation impact of near surface of SRS can be retained the acceptable level.

The calculation endpoints are radionuclide activity limits that correspond to the corresponding dose limits.

Suppose the duration of institutional control period after closure of near-surface repository is 300 years. So inadvertent human intrusion into the facility can be occurred 300 years after closure of the facility.

2.2 Radiological Protection Criteria

The effective dose equivalent limits for members of the public of the normal radionuclide release by various transport pathways after closure of repositories are

0.1 mSv/a [4] and 0.01 mSv/a [5] for Beilong Disposal Site and Northwestern Disposal Site.

Any time after the institutional control period is finished, the effective dose equivalent limits for members of the public are 1 mSv for durative exposure and 5 mSv for single acute exposure [6].

2.3 Disposal System and Nature Condition Description

Spent radioactive source is a special kind of radioactive waste; conditioning of spent radioactive source will be required before it will be disposed. First, the source in its shielding is placed in stainless steel capsule and sealed, then immobilized in the package container (200-L drum) with cement, and formed the waste package, as shown in Fig. 2.

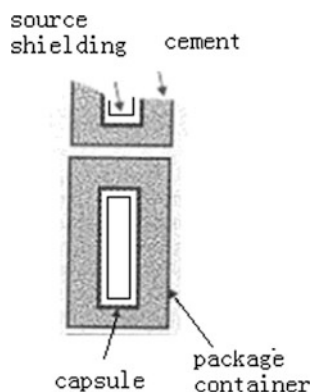
According to the component of spent radioactive sources in our country, the radionuclides that considered in derivation of activity limits will be ^{90}Sr , ^{137}Cs , ^{238}Pu , ^{63}Ni , ^{241}Am , ^{226}Ra , ^{239}Pu , and the decay chain of ^{238}Pu , ^{241}Am , ^{226}Ra and ^{239}Pu .

Beilong Disposal Site and Northwestern Disposal Site use the cement and sand as the backfills between the waste packages separately, so as to limiting the radionuclide transport. Disposal cell is concrete structure uniformly; the function is also limiting the radionuclide transport and supporting the cover layer.

Beilong Disposal Site is located in the seaside foothill zone; the climate is south semitropical zone, and the population is large. The nearest groundwater appearance point is Beilong north slope fountain that locates in the northwest 100 m.

Northwestern Disposal Site is located in the arid gobi zone, the climate is continental temperate zone, and the population is small. The nearest groundwater appearance point is Jianquanzi fountain that locates in the northwest 5000 m.

Fig. 2 Composition of waste package



2.4 Scenario Development and Choice

Scenario development is to determine the phenomenon that can facilitate radionuclide release from the near-surface repository or influence the release rate. The scenarios need to be considered in the derivation of activity limits for near-surface disposal of spent radioactive source are selected using the IAEA scenario development approach, and referencing the scenarios that be considered in Beilong Disposal Site and Northwestern Disposal Site environmental impact assessment. They can be classified into two categories:

- Operational scenarios: direct exposure scenario and drop scenario and
- Post-closure scenarios: leaching scenario, residence scenario, drilling scenario, and after drilling scenario.

The exposure during the operational period can be controlled using a routine radioactive protection technique-time, distance, and shielding, so the operational scenarios are not as the limiting condition in deriving the activity limit.

The whole disposal cell is the study object in leaching scenario and residence scenario, the activity limit that derived by the two scenarios is the activity limit in whole disposal cell. A single waste package is the study object in drilling scenario and after drilling scenario, the activity limit that derived by the two scenarios is the activity limit in a single waste package.

So drilling scenario and after drilling scenario are selected to establish the model, and to derive the activity limit in a single waste package for near-surface disposal of spent radioactive source.

2.5 Model Formulation and Implementation

2.5.1 Conceptual Model

(1) Drilling scenario

Drilling scenario is taken place after the institutional control period is ended, intruder carries through drilling task on the top of disposal site, and spent radioactive source in a single waste package will be taken out. At the time the capsule and source shielding are failed, some radionuclides are released, and pervading in ambient atmosphere. The exposure pathway to the drilling worker includes external irradiation from spent radioactive source and inhalation of radioactive dust that suspended in the atmosphere. Radionuclide transfer process and exposure pathway of drilling scenario are shown in Fig. 3. It is assumed that once institutional control period is ended (300a), the drilling task will be taken place, just considering radioactive decay loss of radionuclides in spent radioactive source.

Fig. 3 Radionuclide transfer process and exposure pathway of drilling scenario

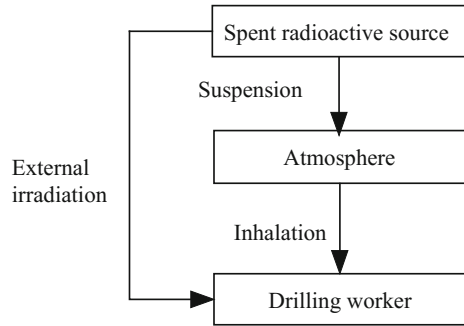
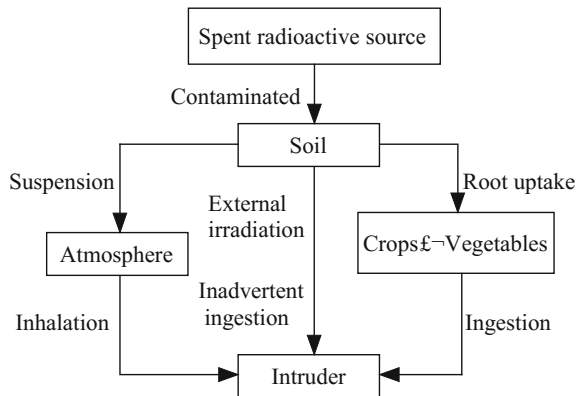


Fig. 4 Radionuclide transfer process and exposure pathway of after drilling scenario



(2) After drilling scenario

It is assumed that the time after drilling scenario taken place and the radionuclide activity in spent radioactive source will be same as the drilling scenario. A failed capsule containing spent radioactive source will be taken out and thrown away optionally by the intruder, and radionuclides will be leaked out and spread around a certain soil area equably. Then, the intruder will be engaged in farming on the contaminated soil and will be exposed by various pathways, including external irradiation from contaminated soil, inhalation of radioactive dust that suspended in the atmosphere above the soil, ingestion of crops growing on the contaminated soil, and ingestion of the contaminated soil inadvertently. Radionuclide transfer process and exposure pathway of after drilling scenario are shown in Fig. 4.

2.5.2 Mathematical Model

(1) Drilling scenario

- ① Source term modeling

The residual activity of spent radioactive source taken out by drilling is given by the following formula:

$$A_{\text{Res}} = A_{\text{Int}} e^{-\lambda t_{\text{Exp}}} \quad (2)$$

where A_{Int} is the initial activity of spent radioactive source disposed (Bq); t_{Exp} is the time that drilling taken place (a).

The concentration of a radionuclide in the atmosphere after capsule failed is given by the following formula:

$$C_{\text{Air}} = A_S C_{\text{Dust}} \quad (3)$$

where A_S is the concentration of a radionuclide, (Bq g^{-1}); C_{Dust} is the dust level in the air (g m^{-3}).

$$A_S = \min\left(A_W, \frac{A_{\text{Res}}}{\rho_W \times V_C}\right) \quad (4)$$

where A_W is mass specific activity of a radionuclide, (Bq g^{-1}); A_{Res} is residual activity of spent radioactive source taken out by drilling (Bq); ρ_W is the dry bulk density of the waste package (kg m^{-3}); and V_C is the volume of the capsule (m^3).

② Dose assessment

For γ radiation, the exposed spent radioactive source is assumed to be a point source. The γ exposure rate is given by the following formula:

$$\dot{X} = \frac{A\Gamma}{r^2} \quad (5)$$

where A is the activity of a radionuclide (Bq); Γ is exposure rate constant ($\text{R m}^2 \text{Ci}^{-1} \text{h}^{-1}$); and r is the exposure distance (m).

The annual individual effective dose to a human from external irradiation is given by the following formula:

$$D_{\text{Ext}} = f \dot{X} QNt \quad (6)$$

where f is the conversion coefficient between irradiation capacity to tissue and effective dose ($\text{Sv} \cdot \text{R}^{-1}$), for flesh tissue, $f = 9.5 \times 10^{-3} \text{Sv R}^{-1}$; Q and N are character factor and other correct factor, respectively; here, $Q = N = 1$; t is the exposure time, i.e., the handling time (h).

The annual individual effective dose from inhalation of dust in the air is given by the following formula:

$$D_{Inh,Dust} = C_{Air} O_{Out} Inh_R DC_{Inh} \quad (7)$$

where O_{Out} is the individual occupancy outdoors on the contaminated soil ($h a^{-1}$).

(2) After drilling scenario

① Source term modeling

The concentration of a radionuclide in the soil is given by the following formula:

$$C_{Soil} = \frac{A_{Res}}{V_{Soil}} \quad (8)$$

where V_{Soil} is the volume of the contaminated soil (m^3).

② Dose assessment

The annual individual effective dose to a human from the consumption of crops is given by the following formula:

$$D_{Ing,Crop} = \sum \chi_{Crop} Ing_{Crop} DC_{Ing} \quad (9)$$

The annual individual effective dose from the ingestion of soil is given by the following formula:

$$D_{Ing,Soil} = \chi_{Wet} Ing_{Soil} DC_{Ing} \quad (10)$$

where χ_{Crop} is the radionuclide concentration in crops ($Bq kg^{-1}$); Ing_{Crop} is the individual ingestion rate of the crop ($kg(\text{fresh} - \text{weight}) a^{-1}$); χ_{Wet} is the radionuclide concentration in the soil ($Bq kg^{-1} \text{wet} - \text{weight}$); Ing_{Soil} is the individual inadvertent ingestion rate of soil ($kg(\text{wet} - \text{weight}) a^{-1}$); and DC_{Ing} is the dose coefficient for ingestion ($Sv Bq^{-1}$).

The annual individual effective dose from inhalation of dust in the air is calculated by Eq. (7).

The annual individual effective dose to a human from external irradiation from soil is given by the following formula:

$$D_{Ext,Soil} = C_{Soil} O_{Out} DC_{Ext} \quad (11)$$

where DC_{Ext} is the dose coefficient for external irradiation from soil ($(Sv h^{-1})/(Bq m^{-3})$).

2.6 Derivation of Activity Limits

The activity limits in a single waste package for disposal of spent radioactive source in Beilong near-surface Disposal Site and Northwestern near-surface Disposal Site based on drilling scenario and after drilling scenario are presented in Tables 1 and 2. In addition, when determining the activity limits in a single waste package of SRS, the national standards on radioactive waste near-surface disposal, for example, «Classification of radioactive waste» (GB9133) and «Regulations for near-surface disposal of low- and intermediate-level radioactive waste» (GB9132), should be considered.

3 Results and Discussion

- (1) According to the results in Tables 1 and 2, the limiting scenario for ¹³⁷Cs is drilling scenario, and after drilling scenario is the limiting scenario for other radionuclides. The activity limits are almost same for Beilong Disposal Site and Northwestern Disposal Site, the activity limits of spent radioactive source in a single waste package are not restricted by the disposal site. So the acceptance limits of spent radioactive source in a single waste package are recommended, which are presented in Table 3.

Table 1 Activity limits of spent radioactive source in a single waste package of Beilong Disposal Site (Bq)

Radionuclide	Activity limit based on different scenarios				Deriving value according to GB9132	Activity limit in a single waste package
	Drilling scenario		After drilling scenario			
	300a	500a	300a	500a ⁽¹⁾		
⁹⁰ Sr	2.58E+11	3.65E+12	2.79E+10	3.45E+12	5.20E+13	2.79E+10
¹³⁷ Cs	6.15E+09	5.92E+11	1.29E+11	1.30E+13	3.40E+13	6.15E+09
²³⁸ Pu	2.94E+09	2.98E+09	1.61E+06	1.78E+06	(2)	1.61E+06
⁶³ Ni	7.32E+13	7.32E+13	1.12E+11	4.46E+11	5.2E+12 ⁽³⁾	1.12E+11
²⁴¹ Am	2.22E+08	3.05E+08	1.79E+07	2.47E+07	(2)	1.79E+07
²²⁶ Ra	2.60E+06	2.84E+06	1.63E+06	1.78E+06	(2)	1.63E+06
²³⁹ Pu	1.95E+10	1.95E+10	8.93E+06	9.01E+06	(2)	8.93E+06

Table 2 Activity limits of spent radioactive source in a single waste package of Northwestern Disposal Site (Bq)

Radionuclide	Activity limit based on different scenarios				Deriving value according to GB9132	Activity limit in a single waste package
	Drilling scenario		After drilling scenario			
	300a	500a	300a	500a ⁽¹⁾		
⁹⁰ Sr	2.58E+11	3.65E+12	2.80E+10	3.45E+12	5.20E+13	2.80E+10
¹³⁷ Cs	6.15E+09	5.92E+11	1.29E+11	1.30E+13	3.40E+13	6.15E+09
²³⁸ Pu	2.94E+09	2.98E+09	1.61E+06	1.78E+06	(²)	1.61E+06
⁶³ Ni	7.32E+13	7.32E+13	1.12E+11	4.46E+11	5.2E+12 ⁽³⁾	1.12E+11
²⁴¹ Am	2.22E+08	3.05E+08	1.79E+07	2.47E+07	(²)	1.79E+07
²²⁶ Ra	2.60E+06	2.84E+06	1.63E+06	1.78E+06	(²)	1.63E+06
²³⁹ Pu	1.95E+10	1.95E+10	8.93E+06	9.01E+06	(²)	8.93E+06

Notes: (1) 500a after repository closure, drilling will be taken place; (2) according to α waste category in GB9133 and GB9132, α emitting radionuclide $\leq 4.0E+5$ Bq/kg in total, the average activity limits of all α emitting radionuclide in SRS in a single waste package are $1.6E+08$ Bq in total; and (3) activity limit of ⁶³Ni in activated metal is $5.2E+13$ Bq according to GB9132

Table 3 Acceptance limits of spent radioactive source in one waste package

Radionuclide	Activity limits for Beilong Disposal Site (Bq)	Activity limits for Northwestern Disposal Site (Bq)	Acceptance limits recommended (Bq)
⁹⁰ Sr	2.79E+10	2.80E+10	2.0E+10
¹³⁷ Cs	6.15E+09	6.15E+09	6.0E+09
²³⁸ Pu	1.61E+06	1.61E+06	1.0E+06
⁶³ Ni	1.12E+11	1.12E+11	1.0E+11
²⁴¹ Am	1.79E+07	1.79E+07	1.0E+07
²²⁶ Ra	1.63E+06	1.63E+06	1.0E+06
²³⁹ Pu	8.93E+06	8.93E+06	8.0E+06

- (2) Besides ¹³⁷Cs, the amount of ⁶⁰Co source is very large (in the proportion of 26.9%) [7], among the spent radioactive sources have been stored in our country. It is not considered in derivation of activity limits, its half-live is very short, just $\sim 5.2a$, it can be decayed to clearance level regulated in GB18871 in the institutional control period of near-surface repository, so a majority of ⁶⁰Co sources are adapted to near-surface disposal. But for ⁶⁰Co source that activity greater than $1E+12$ Bq, the surface dose rate of waste package will

be about 50 mSv h^{-1} as shielding cement thickness is 0.5 m, it is not fit for disposal handling. It is advised that it should be stored for 50–100 years. If it will be disposed directly, other radioactive protect measures should be taken.

- (3) For spent radioactive sources that cannot be disposed in near-surface repository, relevant research about spent radioactive source intermediate depth disposal should be developed [8].

References

1. GB/T 4960.8-2008, Glossary of term: nuclear science and technology-Part 8: Radioactive waste management [S] (in Chinese).
2. The People's Republic of China, The 2nd national report for joint convention on the safety of spent fuel management and on the safety of radioactive waste management [R], 2011(in Chinese).
3. INTERNATIONAL ATOMIC ENERGY AGENCY. Derivation of activity limits for the disposal of radioactive waste in near surface disposal facilities [R]. Vienna: IAEA-TECDOC-1380, 2003.
4. Environmental impact assessment report for Guangdong LILW disposal site (construction applying phase) [R]. Everclean Environmental Engineering Corp, CNNC, 1997 (in Chinese).
5. Environmental impact assessment report for Northwestern China LILW disposal site (construction applying phase) [R]. Everclean Environmental Engineering Corp, CNNC, 1996 (in Chinese).
6. GB18871-2002 Basic standards for protection against ionizing radiation and for the safety of radiation sources [S] (in Chinese).
7. Research on standard of classification of disused sealed radioactive sources [R]. Beijing: Everclean Environmental Engineering Corp, CNNC, 2010 (in Chinese).
8. LIU Jianqin, XIONG Xiaowei, FAN Zhiwen. Preliminary discussion about radioactive waste intermediate depth disposal [C]. 2011 (in Chinese).

Author Biography

Liu Jianqin (1982–), resides in Shanxi, Taiyuan, is an assistant researcher. She is engaged in radioactive waste disposal.

Development and Application of Gamma-Radioactivity Nondestructive Measurement System for Complex Radiation Field

Yongjun Gao

Abstract The instrument, equipment, and computer software of the gamma-radioactivity nondestructive measurement system for complex radiation field are introduced. The high-purity germanium (HPGe) detector calibration methods for the gamma energy, full width at half maximum (FWHM), and absolute efficiency are mainly illustrated, as well as the calculation methods for gamma-flux transfer function and nuclide radioactivity. The system is used to measure the gamma spectra of the four-type radiation waste drums in the QT building of Daya Bay Nuclear Power Plant. The nuclide radioactivity inside the drums is calculated by using the absolute efficiency calibration method (adopted by this system) and “the efficiency calibration method dispensing with standard sources,” respectively. The results indicate that the calculation precision of the above-mentioned two methods is equivalent. The suitable optimized measurement condition is obtained by analyzing the influences of various measurement conditions (such as the distance, height, and orientation) on the radioactivity measurement results.

Keywords HPGe gamma spectrometer • Efficiency calibration • Flux transfer function calculation • Radioactivity measurement • Waste drums

1 Introduction

The radioactivity of the gamma source is usually measured by the gamma spectrometer. The crystal types of the gamma detectors include sodium iodide (NaI), cadmium zinc telluride (CZT), and high-purity germanium (HPGe). Among which, the HPGe detector is of excellent energy resolution and widely used in the field of radioactive environment monitoring, nuclear installation effluent monitoring, and radioactive waste measurement.

Y. Gao (✉)

Nuclear Safety Center, Suzhou Nuclear Power Institute, No. 1788, Xihuan Road, Suzhou City, Jiangsu Province, People’s Republic of China
e-mail: gaoyongjun@cgnpc.com.cn

The principle of the HPGe gamma spectrometer for measuring the gamma radioactivity is through analyzing the measured gamma spectrum of the radioactive source, and the radioactive nuclides are identified by matching the full-energy peaks with the characteristic peaks in the library. The net counts and the peak radioactivity under the full-energy peak are calculated, as well as the nuclide radioactivity. Before the gamma spectrum is analyzed, the calibrations for the energy response, full width at half maximum (FWHM), and detective efficiency must be performed. Among those, the efficiency calibration is the most difficult part.

The main characteristics of the complex gamma radiation field are many radioactive nuclides inside, high background level, complex geometrical structure, sampling difficulty, narrow space nearby, etc. Here are the reasons why the HPGe gamma spectrometer system used in the conventional radiation laboratory is usually unsuitable for measuring the radioactivity of the complex gamma radiation field: (1) The majority of influence imposed by the around background level and other uninterested radioactive sources cannot be shielded because the conventional system is not equipped with the collimator and other specific measurement equipment. (2) It is difficult to acquire the detector efficiency by means of relative efficiency calibration method because it is very difficult to prepare the calibration-purpose standard source which shape is similar to that of the measured object. (3) It is difficult to obtain the specimen because the measured gamma source is usually the tightly sealed solid source.

Nowadays, the improved systems (such as ISOCART and ISOCS) have been developed for measuring the gamma radioactivity in complex radiation field. The collimator, cart, and “efficiency calibration software dispensing with standard sources” (such as GammaCalib software) have been equipped for those systems. The above configuration overcomes parts of the shortcomings of the conventional system, but it is still necessary to make several improvements: (1) The applicable range of the recommended HPGe detector is dissatisfactory because it is unsuitable either for the higher counting rate or for the higher gamma energy ($E > 2$ MeV). (2) The system is difficult to move to the measurement location because the cart has a bigger volume and the collimator is very heavy. (3) The customization procedure of “the efficiency calibration software dispensing with standard sources” is complicated: (A) It is necessary not only to perform the detector efficiency calibration by using the standard sources in the characterization experiment, but also to calculate the detector efficiency by using MCNP program. (B) It is necessary to perform the theoretical characterization calculation of the detector efficiency for a great deal of photons with different incident angles on a large-scale parallel computation system. (4) The detector performance degeneration with time is not considered, so there has the risk that the error of measured radioactivity is bigger.

Compared with the above-mentioned system, the system described in this paper has the following advantages: (1) The HPGe detector is suitable for the bigger radiation range and gamma energy rang because the detector has been customized and optimized. (2) It is more convenient to move the system to the measurement location because of the smaller weight and volume of the collimator and the cart trestle. (3) The configuration of the cart trestle permits to more conveniently adjust

the measurement height and orientation. (4) The calibration method is more convenient. The measurement precision and the modeling and computation time of the system described in this paper is equivalent to that of the above-mentioned system.

2 Radioactivity Measurement System

The main components of the gamma-radiation measurement system include: the hardware and software of ISOCART system, GammaCalib software, MERCURE program, MICROSIELD software, and a set of standard sources used for detector calibration.

2.1 Main Instrumentation and Equipment

The hardware of ISOCART system include the HPGe detector (GEM10P4), the portable digital spectrometer (digiDART [1]), the positive high bias voltage/intelligent detector connection device (SMART-1-P), the collimator, 3-liter dewar (CFG-PG4-3), and the cart (ISOCART).

Choosing what kind of HPGe detector is mainly depended on the magnitude of the measured nuclide radioactivity and the gamma-ray energy range. For the high count rate measurements, the LEGe detector had better be chosen. For low radioactivity measurements, the high-efficiency coaxial germanium detector is more suitable. GEM10P4 is a p-type coaxial HPGe detector with wide energy response range (from 40 to 10 meV), 10% detector efficiency, high energy resolution (1.75 keV at 1.33 meV; 0.80 keV at 122 keV), and 41:1 Compton-peak ratio. Those characteristics permit that it is suitable for in situ measurement in the complex gamma-radiation environment.

DigiDART integrates the functions of the digital spectrometer, keyboard, screen display, processing software and storage, can independently accomplish the calibration, parameter setting, measurement, and analysis, and can transfer data with a computer via USB port.

SMART-1-P adopts the integrated front amplifier, high bias voltage, and high voltage protection signal interface, greatly simplifies the cable arrangement, and is especially suitable for in situ measurement and mobile measurement.

2.2 Computer Software

2.2.1 GammaVision Software

GammaVision software [2] is the main support software of ISOCART system. This software integrates the functions of the gamma-spectrum acquirement, intelligent

multi-channel analyzer (MCA), radioactivity quantitative analysis, and microcomputer workstation. By using this software, it is easy to process the gamma-spectrum file, obtain the gamma spectrum, perform the energy and efficiency calibration, mark out the regions of interest (ROI), compute the nuclide radioactivity, edit the database, and print the measurement reports, etc.

2.2.2 GammaCalib Software

GammaCalib software [3, 4] which was developed by Beijing Institute of Applied Physics and Computational Mathematics and obtained state-level appraisal is a type of “gamma-detector efficiency calibration software dispensing with standard sources.” This software adopts the numerical integration method to calculate the detector efficiency, in-builds the nuclide (H to Pu) macroscopic cross sections interacted with the different-energy photons. Before delivered to the user, this software needs to be customized. The detector characterization is the most important step in the customization procedure. The main purpose of the characterization is to obtain the detailed geometrical parameters and accurate efficiency of the detector for all photons with the different incidence angles and energy. With the aid of the powerful functions of UNIGRAPH software, three-dimensional (3D) visualization modeling for the source and shields with arbitrary shapes can be realized by using GammaCalib software.

2.2.3 MERCURE Program

MERCURE program [5] developed by France CEA is a 3D photon/neutron transport calculation software using the Monte Carlo method. This software solves the integral-form particle transport equation: under the multi-group approximation, the Monte Carlo method is adopted to perform the integration calculations for the attenuation of the point kernels in straight lines.

2.2.4 MICROSIELD Software

MICROSIELD software is a simple and easy-to-use photon/neutron shielding calculation software using point-kernel integration method.

3 Radioactivity Measurement Method

3.1 Absolute Efficiency Calibration Method

In absolute efficiency calibration method [6], it is assumed that the detector efficiency is up to the following two independent coefficients:

- Absolute efficiency $K(E)$ which is only related to the characteristics of the detector such as the geometrical structure, dimension, and material composition.
- Gamma-flux transfer function $\phi(E)$ which is only related to the characteristics of the shields and the gamma source.

$K(E)$ is determined by the detector efficiency calibration experiment:

$$K(E) \equiv \frac{\text{detected photons per second}}{\text{photon flux at crystal centre}} = \frac{S(E)}{T_a \times \phi(E)} \quad (1)$$

Here, $S(E)$ is the net count under the full-energy peak; T_a is the alive time (second); $\phi(E)$ is the gamma flux at crystal center imposed by standard sources (Bq/cm^2).

3.2 Radioactivity Calculation Method

After the in situ gamma spectrum has been measured, the radioactivity or specific radioactivity A is calculated through the equation below:

$$A = \frac{\phi^*(E)}{\phi(E)} = \frac{S(E)}{T_a \times K(E) \times \Gamma(E) \times \phi(E)} \quad (2)$$

Here, the dimension of A is Bq , Bq/cm^2 , or Bq/cm^3 ; $\phi^*(E)$ is the gamma flux at the crystal center (Bq/cm^2); $\phi(E)$ is the gamma-flux transfer function ($1/\text{cm}^2$ or cm); $\Gamma(E)$ is the gamma-ray branching ratio.

MERCURE program is used to calculate $\phi(E)$. In the calculation, the interested gamma energy range (0–2500 keV) is divided into 10 groups; the gamma flux at the crystal center imposed by linear gamma ray is calculated for one unit radioactivity of the source with specific shape (point, surface, or volume). The calculated gamma flux is equal to the gamma-flux transfer function in numerical value. As other Monte Carlo calculations, the necessary data such as the geometrical structure and material composition of the gamma source and the shields (including the detector and collimator) should be collected.

The most interested part is to calculate the radioactivity or specific radioactivity A_D of the deposits on the inner surface of the pipe:

$$A_D = \frac{\phi_T(E) - \phi_W(E) \times A_W \times \Gamma(E)}{\phi_D(E) \times \Gamma(E)} \quad (3)$$

Here, A_D and A_W (measured by sampling method) are the radioactivity or specific radioactivity of the deposits and the water, respectively; $\phi_T(E)$ is the gamma flux at the crystal center (Bq/cm^2); $\phi_D(E)$ and $\phi_W(E)$ are the gamma-flux transfer function of the gamma sources in the deposits and water, respectively.

In order to facilitate the calculation of the flux transfer function, CALTF program has been developed by using the spline interpolation method. The database of the flux transfer function necessary for CALTF program is prepared for various pipe diameters, thickness, and length (the calculation matrix).

3.3 Radioactivity Modification Method

The calculated radioactivity value unavoidably has some errors, because the input data and the calculation models have some errors. In order to reduce the errors, considering that the dose rate can be easily and precisely measured, through modifying the calculated radioactivity value by multiplying the ratio (radioactivity modification factor) of the measured dose rate to the calculated dose rate, we obtain the more precise measured radioactivity value.

The relationship between the dose rate and the radioactivity is as follows:

$$DR = \sum_{i=1}^I [A(E_i) \times \psi_{DR}(E_i)] \quad (4)$$

Here, DR is the dose rate; A is the radioactivity; ψ_{DR} is the flux transfer function; E_i is the energy under the full-energy peak i ; I is the number of the full-energy peaks.

Under the same measurement configuration (geometrical structure, dimension and material constituent, etc.), the dose rate transfer function keeps constant. Assume that the proportional relation among the radioactivity under the full-energy peaks remains constant, so the following correlation can be used to estimate the measured radioactivity value:

$$A_{\text{meas.}} \approx A_{\text{calc.}} \left(\frac{DR_{\text{meas.}}}{DR_{\text{calc.}}} \right) \quad (5)$$

Here, $A_{\text{calc.}}$ is the calculated nuclide radioactivity; $DR_{\text{meas.}}$ is the measured dose rate; $DR_{\text{calc.}}$ is the calculated dose rate; $DR_{\text{meas.}}/DR_{\text{calc.}}$ is the radioactivity modification factor.

It could be expected that the measured radioactivity basically matches with the measured dose rate because of the above-mentioned modification.

4 Radioactivity Measurement of Waste Drums

4.1 Introduction of the Basic Conditions

At present, a large number of radioactive waste drums are stored in the QS and QT buildings of Daya Bay Nuclear Power Plant. It is necessary to transport these drums

Table 1 Waste drum parameters

Drum type	Identifier	D_{in} (mm)	D_{out} (mm)	H (mm)	d_{wall} (mm)	M (kg)		Waste	
						Void	Full	Type	V/M
C1	1060142	1100	1400	1300	150	1950	4487	Waste Resin	305 L
C1	1020063	1100	1400	1300	150	1950	4691	Concentrated Salt	342 L
C4	4960019	800	1100	1300	150	1500	3467 ^a	Filter Cartridge	4 kg
200L	G960309	572	597	873	1.5	22.2	173.4	Sundries	84.6 kg

^aThis value exceeds 3000 kg (maximum mass). According to the average density of 2.35 g/cm³, this value is estimated to be 2820 kg

in batches to Beilong low and medium radiation waste repository for long-term storage. According to the requirements of relevant state regulations and policies, before these drums are shipped out, the plant shall provide the relevant data such as the species, composition, content, radioactivity of the radioactive substances inside the drums, and the dose rate around the drums.

In order to verify the applicability and validity of the technology described in this paper, and to prepare for measuring the radioactivity of a large number of drums in the future, after consulting with the relevant departments of Daya Bay Nuclear Power Plant, we measured four representative drums in the QT building. The following table gives the parameters of these drums (Table 1).

4.2 Detector Calibration Experiment

The detector calibration experiment is performed in the radiation laboratory (a class-2 metering station) in Daya Bay Nuclear Power Plant. Because it is estimated that the corrosion-product nuclides (such as Co-60, Ag-110 m and Mn-54, with long half-life) in the waste drums occupy the main contribution to the surrounding dose rate, Ba-133, Cs-137, Co-60, Y-88 standard sources are selected in the experiment in order that the gamma energy of the standard sources can cover the range of 0–2000 keV.

Before the experiment, the standard sources are bandaged together, and the collimator is removed from the cart to let the detector bare. In the Experiment, the standard source package directly faces the detector and is placed in the position of 30 cm away from the detector. The gamma-spectrum measurement and storage are performed by using digiDART. In order to evaluate the influence of the distance on the measurement results [such as K(E)], the gamma spectrum of 50 cm distance is also measured. For the sake of obtaining sufficient counts and reducing the influence of background level, 5-h measuring time is necessary.

After the experiment, the GammaVision software is adopted to perform the gamma-spectrum processing, mark out the interested regions (ROI), perform the

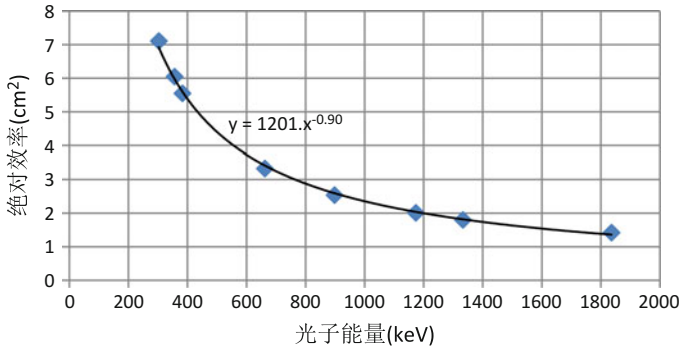


Fig. 1 The calibration curve of the detector absolute efficiency

energy and FWHM calibration, and calculate the net counts $S(E)$ under the full-energy peak. The detector absolute efficiency $K(E)$ is then calculated by using Eq. (1). The calculation results are shown in the Fig. 1.

4.3 In Situ Gamma-Spectrum Measurement

Eleven measurement schemes are performed. The detector direction should be adjusted to directly face the axis of the waste barrel. In order to evaluate the influence of the relevant parameters on the measurement results, the detector is allocated in different direction, distance, and height. The main measured parameters

Table 2 Summary of the measured parameters

Scheme no	Identifier	Direction ^a	Distance ^b (m)	Height ^c (m)	Dose rate (μSv/h)	
					Collimator	Drum surface
1	1060142	Parallel	8.63	0.74	8.8	1550.0
2	1060142	Parallel	10.6	0.74	5.7	1550.0
3	1020063	Parallel	2.38	0.74	1.1	11.0
4	1020063	Parallel	2.38	0.57	1.1	11.0
5	1020063	Vertical	1.97	0.57	1.25	11.5
6	4960019	Vertical	2.27	0.57	22.0	350.0
7	4960019	Parallel	6.62	0.57	5.2	550.0
8	4960019	Parallel	4.97	0.57	8.0	550.0
9	G960309	Parallel	0.33	0.57	2.3	5.0
10	Background level	Parallel	/	0.74	0.5	/
11	Background level	Vertical	/	0.57	0.5	/

^aThe direction of the lead wall

^bThe minimum distance between the collimator front and the drum surface

^cThe height from the collimator center to the floor

include the collimator height, the distance between the collimator and the barrel, gamma spectrum, dose rate around the barrel surface, and dose rate at the detector center. The measured parameters are summarized in the Table 2.

4.4 Efficiency Calibration Dispensing with Standard Sources

The measurement configuration analysis model includes the information related to the materials of the detector, collimator, drum and waste (the gamma source), the distance among the above objects, as well as the geometrical dimension of the above objects. Before this model is established by using GammaCalib, MERCURE, and MICROSIELD, it is necessary to estimate the average density of each mixture material (such as the concrete and the waste) and the uniformed density of each constituent.

The estimation procedures for the uniformed density of each constituent in various mixture materials are as follows: (1) to estimate the mass percentage (mixture ratio); (2) to estimate the mass; (3) to estimate the volume and the volume ratio; (4) to estimate the uniformed density. The calculation results are shown in Table 3. The measurement configuration analysis model is shown in Fig. 2. The detector efficiency curve of the measurement scheme 1 is shown in Fig. 3.

Table 3 The uniformed density of each constituent in various mixture materials

Mixture material	Average density (g/cm ³)	Constituent density (g/cm ³)						
		Waste resin	Concentrated salt	CaCO ₃	SiO ₂	Fe ₂ O ₃	Fe	C ₆ H ₁₀ O ₅
Filter cartridge of the waste resin	2.309	1.01		0.128	0.754	0.428		
Filter cartridge of concentrated salt	2.533		0.815	0.421	0.523	0.775		
Drum cover	2.35			0.06	2.014	0.276		
C1 drum wall	2.106			0.591	1.515			
Material around the waste filter	2.35			0.06	2.014	0.276		
C4 drum wall	2.282			0.64	1.642			
Sundries in 200 L drum	0.385						0.003	0.382

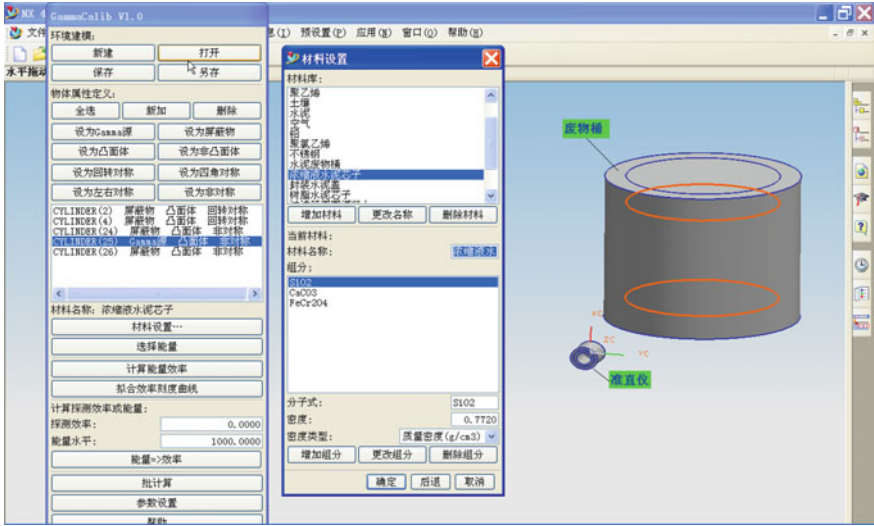


Fig. 2 Measurement configuration analysis model

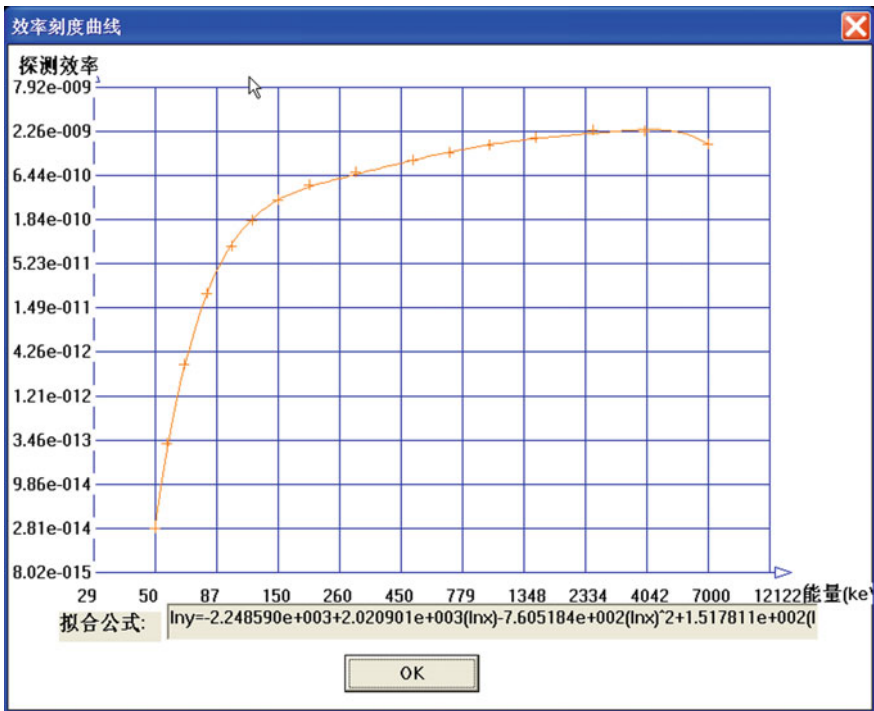


Fig. 3 Detector efficiency curve of the measurement scheme 1(1060142 A)

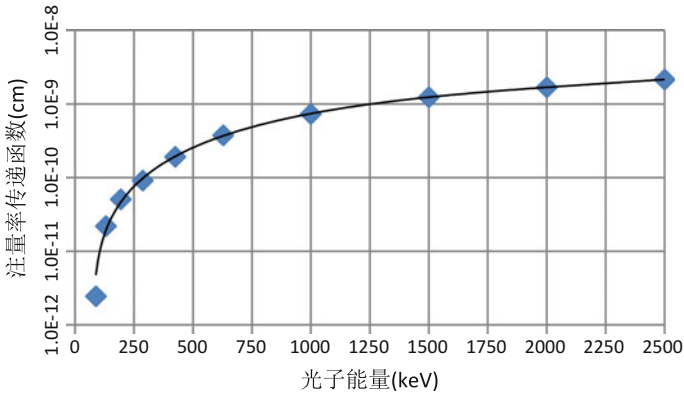


Fig. 4 Gamma-flux transfer function of the measurement scheme 1(1060142-A)

4.5 Calculation of the Gamma-Flux Transfer Function

The gamma-flux transfer function and the dose rate transfer function are calculated for specific measurement configuration by using MERCURE program and MICROSSHIELD software, respectively. The calculation methods are described in Sect. 3.1. The data used in the calculations are similar to those of GammaCalib software. The gamma-flux transfer function of the measurement scheme 1 is shown in the following figure (Fig. 4 and Table 4).

4.6 Analysis of the Measurement Results

4.6.1 Measurement Results

The radioactivity measurement results of the waste drums calculated by “the efficiency calibration method dispensing with standard sources” are listed in the following table. In this table, the ratios of the radioactivity calculated by the absolute efficient calibration method to those calculated by “the efficiency calibration method dispensing with standard sources” are given as well.

As we can see, there exist several nuclides with longer half-life and bigger radioactivity in four types of waste drums. Among which, Co-60 ($T_{1/2} = 5.27$ years), Ag-110 m ($T_{1/2} = 250$ days), and Mn-54 ($T_{1/2} = 313$ days) still exist in the concrete wastes drums, and Co-60, Ag-108 m ($T_{1/2} = 127$ years), and Cs-137 ($T_{1/2} = 30$ years) still exist in the metal waste drum. In addition, no other nuclides are measured because their half-life is relatively shorter; thus, the radioactivity have been attenuated to the negligible degree.

Table 4 Radioactivity measurement results

Scheme no	Identifier	Co-60 (Bq)/ratio	Ag-110 m (Bq)/ratio	Ag-108 m (Bq)/ratio	Mn-54 (Bq)/ratio	Cs-137 (Bq)/ratio
1	1060142-A	3.61E10/1.012	7.31E9/1.008	/ ^a	1.82E9/0.998	/
2	1060142-D	3.48E10/1.029	7.11E9/1.016	/	1.86E9/1.024	/
3	1020063-B	2.35E8/1.002	1.25E8/0.993	/	/	/
4	1020063-BH	2.35E8/0.997	1.26E8/0.984	/	/	/
5	1020063-A	2.31E8/1.011	1.23E8/1.003	/	/	/
6	4960019-A	4.01E10/1.023	/	/	/	/
7	4960019-B	4.16E10/1.021	5.30E8/1.015	/	/	/
8	4960019-C	4.03E10/0.979	3.15E8/0.982	/	/	/
9	960309-A	3.03E6/0.981	/	6.10E4/0.988	/	3.09E4/0.98

^aThe radioactivity is too small to be measured

We can also see that the deviations between the radioactivities calculated by the two methods are in the range of $\pm 3\%$. This result indicates that the calculation precision of the two methods is equivalent.

4.6.2 Optimized Measurement Conditions

By analyzing the influence of the measured parameters (such as the distance, height, direction, and time) on the radioactivity measurement results, we can obtain the suitable optimized measurement conditions which will be used in lots of measurement activities in the future.

The measured radioactivity in scheme 1, 2, 7, and 8 has a little difference. However, the measurement distance of those schemes is greatly various. That factor indicates that the influence of the measurement distance on the measurement results can be ignored. It is also worth noting that the measurement distance should be appropriate: shorter distance will induce higher count rate and more dead time. In serious conditions, the count rate is too high to perform the measurement (the signals are saturated). Longer distance will cause smaller count rate and longer measuring time. Measurement experience suggests that the dose rate in the detector center be within 2–5 mSv/h.

The measured radioactivity in schemes 3 and 4 has a little difference. However, the detector height of those schemes is greatly various. The above factor indicates that the influence of the detector height on the measurement results can be ignored. In addition, the detector height had better remain in the half-height of the waste drum, and it is necessary to ensure that the detector can “watch” the whole drum.

The measurement results show that: (1) the dose rate around the surface of C1 concrete barrel is much more uniformed; (2) however, the dose rate around the surface of C4 metal barrel is very uneven. The main reason is that: (1) before consolidation, the waste resin and the concentrated salt have been fully mixed in C1 barrel; (2) the skew position of the filter cartridge placed in C4 barrel causes the shielding-layer thickness in each orientation is different. In order to accurately measure the radioactivity inside C1 and C4 barrels, the dose rate at four azimuths should be measured, and the shielding-layer thickness around the barrel wall should be modified in the transfer function calculation.

In theory, the longer the measurement time, the better the measurement results. However, the radioactivity measurement is constrained by the funds, job schedule, onsite radiation conditions, etc. The gamma-radiation level around the measured waste barrel is high. Measurement experience suggests that when the measurement time is longer than 20 min, the shape of the full-energy peaks of the main interested nuclides in the gamma spectrum is satisfactory, and the effective counts in each channel are much higher than the background counts.

5 Conclusion and Prospection

Through the customization of HPGe detector, the structure optimization of the collimator and the cart trestle, the design of the calibration device, as well as the establishment of a whole set of the calculation and analysis method and related software, the Gamma-Radioactivity Nondestructive Measurement System for Complex Radiation Field has been developed. The nuclide radioactivity measurement results of four types of waste barrels show that the measurement precision of the absolute calibration method adopted by this paper is equivalent to that of “the efficiency calibration method dispensing with standard sources.”

Along with the development of China’s nuclear industry and nuclear technology application, and the demands for safer, friendlier environment, this system will have a wider range of purposes. In order to facilitate the practical application, the system needs some further improvements in the experiment verification, measurement precision, miniaturization, portability, automation, etc. This can be achieved by the corporation with the gamma spectrometer manufacturers at home and abroad and the related research institutes and colleges.

Acknowledgments Thanks for the helps given by Yang Junwu, Yang Jian and Ye Yongdong who are the engineers of Daya Bay Nuclear Power Plant in the detector calibration and the preparation of measurement conditions. Thanks for the helps given by Zhou Xi and Weng Fangjian (my colleagues) in the in situ gamma-spectrum measurement of waste barrels.

References

1. ORTEC, “digiDart™: Digital Portable MCA with SMART-1™ HPGe Detector Technology, Operator Manual”
2. ORTEC, “GammaVision®-32: Gamma-Ray Spectrum Analysis and MCA Emulator for Microsoft® Windows® 2000 Professional and XP® Professional, Software User’s Manual”
3. ORTEC, Help Document for the Efficiency Calibration Software GammaCalib V3.0
4. Xiao Gang, “Summary of the Efficiency Calibration Method Dispensing with Standard Sources, Relevant Software and Applications”, Beijing Institute of Applied Physics and Computational Mathematics, internal report (in Chinese)
5. C. Dupont, Mercure 5.2: “Programme de Monté Carlo à Trois Dimensions pour l’Intégration de Noyaux Ponctuels d’Atténuation en Ligne Droite”
6. R. Eimecke, S. Anthoni, “Ensemble de Mesure de la Contamination des Circuits”, 7th International Conference of Reduction Shielding, 12–16 September, 1988
7. Gao Yongjun, etc, “Evaluation for the Effectiveness of Measures to Reduce the Radioactivity of the Corrosion Products inside the Primary Circuits of CPR1000 Nuclear Power Plants”, Suzhou Nuclear Power Institute, internal report (in Chinese), No.: 2006JT13-2
8. Gao Yongjun, etc, “Radioactivity Measurement for the Radioactive Waste Drums in the QT Building of Daya Bay Nuclear Power Plant”, Suzhou Nuclear Power Institute, internal report (in Chinese), No.: 2006JT13-4

Author Biography

Yongjun Gao is a senior engineer of researcher's grade, graduated from the nuclear reactor engineering specialty of Shanghai Jiaotong University in 1991, engaged in incore fuel management calculation in Research Institute of Nuclear Power Operation (RINPO) in 1991–2005, goes in for the independent verification and review of the reactor core reloading design for the NPPs of CGNPC, nuclear safety research and safety review of domestic NPPs, etc. in Suzhou Nuclear Power Institute(SNPI) from 2005 to nowadays.

Development of the Concrete Cask Storage System for PWR Spent Nuclear Fuel in Korea

Baeg Chang-Yeal and Cho Chun-Hyung

Abstract The concrete cask storage system is under development containing canister loaded with PWR spent nuclear fuel. This storage system consists of dual-purpose canister (DPC), concrete cask, transfer cask and auxiliary equipment. The DPC as a confinement boundary consists of 21 fuel assembly-loaded baskets, canister shell, lid and closure ring. After fuel assemblies are loaded, the canister lid and closure ring are sealed by remote welding. The concrete cask is composed of reinforced concrete with steel-lined shells as a radiation shielding and structural barrier. Sufficient space is provided inside the cask to load canister, and 16 T-shaped channels are attached in radial direction to the surface of inner shell. These channels keep the proper gap between cask body and canister and also reduce the impact load exerted to canister under accident condition. Each 4 of air inlet and outlet ducts is installed at the bottom and top of the cask body, respectively, to cool down passively by natural convection. Inside the air duct, shield grids are provided for shielding purpose, and mesh screens to prevent intrusion of foreign material are installed at the entrance. The thicknesses of cask body and lid are designed to be sufficient to meet the regulatory requirements of radiation shielding. The dimensions of air inlet and outlet ducts are defined to facilitate full natural convection. And shield grids and mesh screen are installed at the entrance of ducts. The DPC and its related components are to abide by the storage requirements of the US NRC 10CFR72 and the standard review plan NUREG-1536 and the domestic transportation requirements.

Keywords Concrete cask storage system · Dual-purpose canister · Spent nuclear fuel · Natural convection · Safety test

B. Chang-Yeal (✉) · C. Chun-Hyung
Korea Radioactive Waste Agency, 168 Gajeongro, Yuseong-Gu, Daejeon, Korea
e-mail: baegcy@korad.or.kr

© Springer Science+Business Media Singapore 2017
H. Jiang (ed.), *Proceedings of The 20th Pacific Basin Nuclear Conference*,
DOI 10.1007/978-981-10-2314-9_41

469

1 Introduction

The capacity of spent nuclear fuel storage at the NPP is approaching saturation status as the years of operation increases. In order to solve the shortage of storage capacity, we are now developing the concrete cask storage system. This storage system consists of dual-purpose canister (DPC), concrete cask, transfer cask and auxiliary equipment. The DPC as a confinement boundary consists of fuel basket, canister shell, lid and closure ring. After fuel assemblies are loaded, the canister lid and closure ring are sealed by remote welding and checked for the confinement integrity by the non-destructive test and helium leak test. This storage system design is to abide by the storage-related requirements of the US NRC 10CFR72 and the transportation requirements of Korea NSSC Notice No. 2014-50 [1, 2].

2 Development of the Concrete Cask Storage System

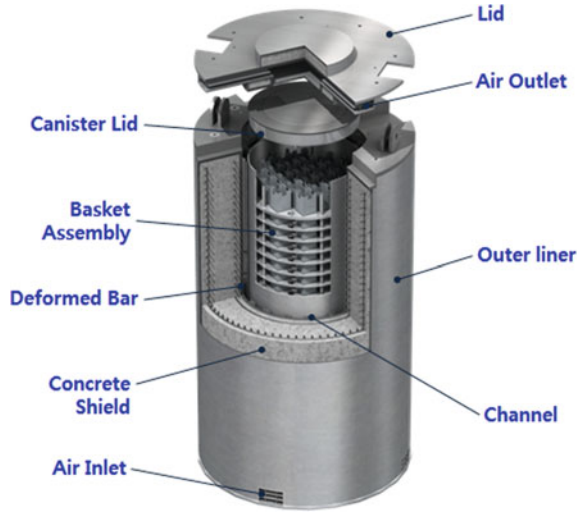
The concrete cask storage system is a cylindrical concrete cask containing canister loaded with 21 PWR spent nuclear fuel and vertically placed on the storage pad as freestanding type and consists of the following components (Figs. 1 and 2 show the design concept and configuration of concrete storage cask).

- The cask body is filled with reinforced concrete between inner and outer shells, and the cask lid is bolted into cask body to maintain structural integrity. At the top and bottom of cask body, each 4 of air inlet and outlet duct is provided to remove the decay heat generated from spent fuel by natural convection.
- The canister consists of basket assembly, disc, support rod, canister shell and baseplate, canister lid and closure ring.



Fig. 1 Design concept of concrete cask storage system

Fig. 2 Configuration of concrete storage cask



Design life	50 yrs
Capacity	21 PWR F/A (WH & CE)
Weight	145 ton
Material	Concrete, Carbon steel (Stainless steel Canister)

- To facilitate handling of the cask in vertical position, lifting lug is attached on the top surface of the cask body.
- Transfer cask is used at the interim storage facility for the safe transfer of the canister from the transportation cask to the storage cask.

The concrete cask storage system containing canister loaded with spent nuclear fuel is provided to remove passively decay heat by the natural convection. Inside the air ducts, shield grids are provided for shielding purpose, and mesh screens to prevent intrusion of foreign material are installed at the entrance. Sufficient space is provided inside the cask to load canister, and 16 T-shaped channels are attached in radial direction to the surface of inner shell of the cask body. These channels keep the proper gap between cask body and canister and also reduce the impact load exerted to canister under accident condition.

The canister consists of basket assembly, disc, support rod, canister shell and bottom plate, canister lid and closure ring.

The canister is a cylindrical vessel made of stainless steel shell. After spent nuclear fuel assemblies are loaded, canister lid, vent/drain port covers and closure ring are sealed by welding.

The number of discs supporting basket assembly is made of stainless steel circular plate and welded to stainless steel rods. The canister internal components

are designed to support spent nuclear fuel and maintain sub-criticality and heat removal function. The basket assembly consists of square tube-type cell, neutron absorber and neutron absorber cover. The basket assembly is designed to have square tube-type cell of stainless steel plate surrounded by neutron absorber.

The concrete cask storage system shall maintain the sub-criticality, shielding, structural integrity, thermal capability and confinement. The specific safety analysis and demonstrations have been confirmed to meet the requirements of the US NRC 10CFR72 and the related standard review plan NUREG-1536 and Korea NSSC Notice No. 2014-50 [3].

The confinement boundary and its internal components are sufficiently verified through the welding performance corresponding to the ASME Code Sec.III, Div.1 Sub. NB in conjunction with redundant closures, non-destructive examination and a helium leak test [4].

For the safe operation of this storage system, operating procedures are developed for loading the spent nuclear fuel into a canister at the nuclear power plant, transporting the loaded canister to the storage facility using transportation cask, and then reloading the canister from the transportation cask into a concrete cask in the interim storage facility.

3 Conclusions

The capacity of spent nuclear fuel storage at the NPP is approaching saturation status as the years of operation increases. In order to solve the shortage of storage capacity, we are now developing the concrete cask storage system.

This storage system is to abide by the storage-related requirements of the US NRC 10CFR72 and the domestic transportation requirements. Also, we have developed the operating procedures for the safe operation of this storage system.

On the basis of safety analysis and demonstrations above, we have produced a topical report and licensing data for the future implementation.

References

1. U.S. NRC 10CFR72, Licensing Requirements for the Independent Storage of Spent Nuclear Fuel, High-Level Radioactive Waste and Reactor Related Greater than Class C Waste, 2012.
2. Korea NSSC Notice No. 2014-50, Regulations for the Packaging and Transportation of Radioactive Materials, 2014.
3. U.S. NRC NUREG-1536, Standard Review Plan for Dry Cask Storage Systems, Revision 1, 2010.
4. American Society of Mechanical Engineers, ASME Code, Section III, Division 1, Subsection NB, 2010.

Evaluation of Algorithms of Dispersion Coefficients with a Field Tracer Experiment over Complex Terrain

Hao Zhu and Fengju Li

Abstract The CALMET/CALPUFF modeling system is employed to simulate the dispersion and transport of tracer gas at a nuclear power plant site located in a complex valley and upland terrain where weak wind prevails. Using the surface and upper air meteorological observations obtained from a field experiment, the three-dimensional diagnostic wind fields are generated by CALMET module. Three different algorithms of dispersion coefficients are used to model the ground concentration distributions of tracer under different wind conditions, which are using measured turbulence velocity variances, similarity theory, and PG stability-dependent dispersion curves with coefficients modified according to the in situ turbulence measurement to calculate dispersion coefficients, respectively. The results show that turbulence and modified PG methods can better predict high observed concentrations than the similarity method, while all the three methods overpredict the low observed concentrations mainly due to underestimations on wind speed and overestimations on mixing layer heights in modeling. The turbulence and modified PG methods overestimate the observed peak concentrations by less than 30%, while the similarity method underestimates by about 20%. Overall, the turbulence and modified PG methods perform better than the similarity method, with less dependence of simulated concentration residues on wind speed and mixing height. From the viewpoint of engineering application, CALPUFF model with modified PG method to calculate dispersion coefficients is recommended at the site with hilly-valley complex terrain to simulate the transport and dispersion of gaseous effluent.

Keywords CALPUFF · Complex terrain · Tracer experiment · Dispersion coefficients · Turbulence · Similarity

H. Zhu (✉) · F. Li
China Nuclear Power Engineering Co., Ltd., Beijing, China
e-mail: zuhao8586@163.com

© Springer Science+Business Media Singapore 2017
H. Jiang (ed.), *Proceedings of The 20th Pacific Basin Nuclear Conference*,
DOI 10.1007/978-981-10-2314-9_42

473

1 Introduction

Atmospheric dispersion models are necessary tools for the estimation of atmospheric dispersion from nuclear facilities in the assessment of the radiological impacts from normal and accidental releases. The most widely used models are Gaussian plume models because of their simplicity and rapidity of calculation. However, the limitations inherent in the steady-state Gaussian plume models usually make them fail over complex terrain and under calm and light wind speed conditions, which are frequently encountered at inland nuclear power plant (NPP) sites in China. In these cases, the temporal and spatial variation of meteorology and the causality effects for the plume to travel from one point to another should be taken into account.

To better understand the atmospheric dispersion characteristics at the sites of complex flow pattern, field experiments should be carried out and more suitable models should be employed. Puff models are regarded as advanced models which can overcome the limitations of Gaussian plume models and are suitable for the simulation under the above complex conditions. In addition, puff models are far less computationally expensive than particle models, thus they are often more than adequate, and are used for regulatory purposes [1]. CALPUFF is a comprehensive three-dimensional Gaussian puff model recommended by the US Environmental Protection Agency (EPA) for regulatory applications [2]. Both long-range transport and near-field impacts on complex flow or dispersion situations which may involve complex terrain, stagnation, inversion, recirculation, light, and calm wind conditions can be adequately modeled by CALPUFF. In addition to the transport wind fields, dispersion coefficients are other crucial parameters that influence the dispersion of airborne effluents and the following dose estimates. Several calculational approaches of dispersion coefficients have been developed in CALPUFF based on available data. Compared with the commonly used Pasquill–Gifford dispersion curves and other similar stability-related dispersion relationships, CALPUFF also has more sophisticated methods to calculate dispersion coefficients, which are similarity theory-based and real turbulence measurement-based dispersion schemes, and the complex schemes involve more details of input parameters.

In the present study, CALPUFF modeling system is used to study the atmospheric dispersion characteristics at an inland nuclear power plant site over complex terrain. Performances of various dispersion schemes are evaluated by comparing the modeling results with the measured tracer concentrations from the field experiments.

2 Field Experiments

The field experiments were conducted from December 20, 2008, to January 3, 2009 at a typical inland NPP site surrounded by low-level hills with a river valley traversing across the site area. Figure 1 shows the location and topography of the

site area. The site surroundings are characterized by irrigated agricultural land. The annual mean wind speed is 1.5 m s^{-1} , and the occurrence frequency of low wind speed (wind speed at 10 m height is lower than 2 m s^{-1}) is about 50% [3]. The field experiments include meteorological measurements and tracer releases and sampling under different weather conditions.

In situ wind velocity, wind direction, and temperature were measured at 5 levels (i.e., 10, 30, 50, 70, and 100 m) on the release tower every 10 min. Four CSAT3 ultrasonic anemometers of 10 Hz sampling frequency were installed at 10, 30, 50, and 100 m heights on the tower, measuring the fluctuating components of wind velocity and temperature. Eight surface meteorological stations instrumented with anemometers were set up within the radius of 10 km from the release tower. Data were recorded at 10-min intervals, and hourly averages were used for dispersion modeling. Two radiosondes were released every 2–3 h, providing wind and temperature profiles from ground to 1000 m height during the tracer experiment period. The locations of the surface and upper air stations are shown in Fig. 1b.

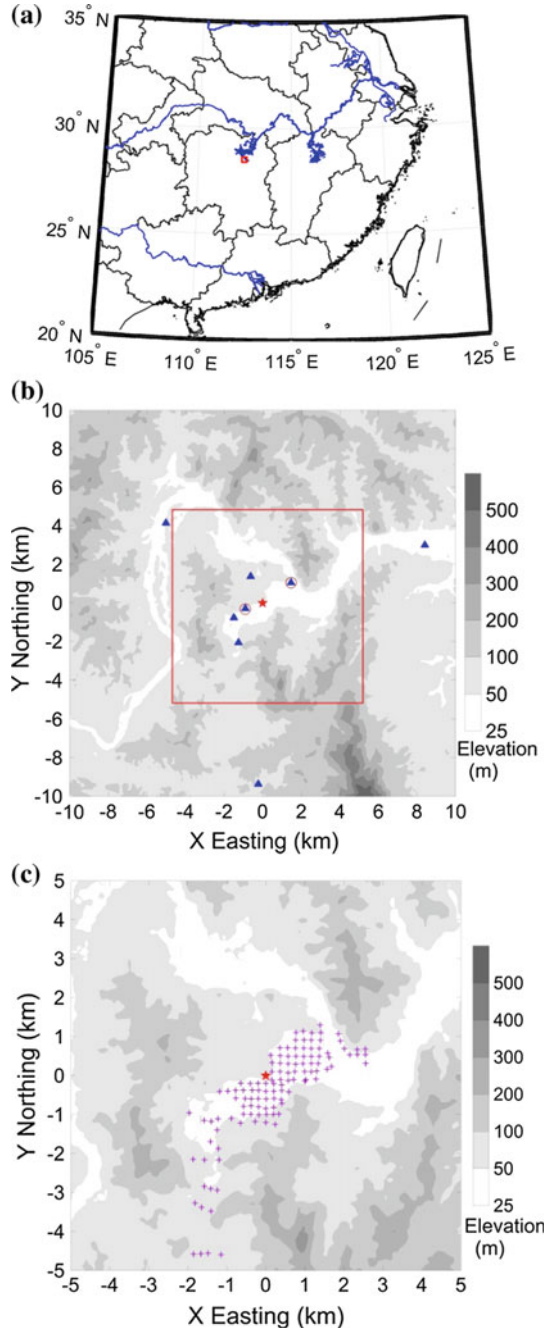
There were a total of 23 releases of sulfur hexafluoride (SF_6) with release heights 10, 30, and 70 m above the ground, respectively, mostly under unstable and neutral conditions. Except three releases lasting for about 100 min, the duration of each of the other releases is 1 h. Depending on the prevailing wind direction at the site, the sampling array consisting of 116 air samplers was set up in the river valley in the south and northeast of the release tower. Four samplings, each of which lasted for 10 min, were taken for each release trial at each sampler. The interval between adjacent two samplings was 5 min.

Constrained by the topography and logistics, the samplers were gridded distributed. The most distant sampler was about 5 km from the release tower, and the closest one was about 0.2 km. The average spacing between adjacent samplers was about 200 m. The layout of the samplers is shown in Fig. 1c. To facilitate the evaluation of modeling results, we approximate the samplers into 5 arcs according to their distances to the release source following Hanna's methods [4]. The five arcs are 500 m (450–550 m), 700 m (650–750 m), 900 m (850–950 m), 1100 m (1050–1150 m), and 1300 m (1200–1400 m) from the release point, respectively. Samplers beyond the ranges are sparsely distributed and cannot capture the overall distribution of ground concentration and thus are not used in current study. Before conducting model evaluation, the tracer concentration data went through rigorous quality assurance (QA) procedures.

3 Atmospheric Dispersion Model

The CALPUFF modeling system is used to simulate the dispersion of tracer gas over complex terrain in the present study. The model's formulations and theoretical background can be found in the related technical documents [2, 5]. The focus of this study which is the schemes to calculate dispersion coefficients is briefly highlighted below.

Fig. 1 Location, topography, and layout of the experimental site. The *red rectangles* in (a) and (b) mark the location of the modeling domain. The *triangles* and *circles* in (b) represent the surface meteorological stations and upper air stations, respectively. *Plus signs* in (c) represent the tracer samplers. The center of the domain marked by the *pentagram* is the release tower



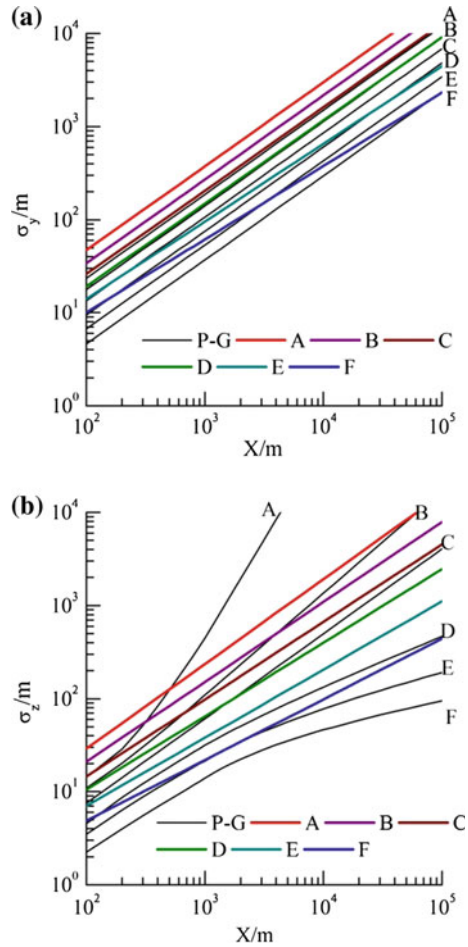
Five dispersion options, involving three levels of input data listed below, are provided in CALPUFF:

- (1) dispersion coefficients computed from direct measurements of turbulence, σ_v and σ_w ;
- (2) dispersion coefficients from internally calculated σ_v and σ_w using micrometeorological variables u^* , w^* , L , h , etc., from CALMET based on similarity theory;
- (3) dispersion coefficients from PG stability-dependent dispersion curves and user choice of various relationships.

The most desirable approach is to relate the dispersion coefficients directly to the measured turbulence velocity variances (σ_v and σ_w). However, these data are not always available and the quality of the data is very important to lead to accurate modeling results. The default dispersion option in CALPUFF is the second one, which uses similarity theory and micrometeorological variables derived from routinely available meteorological observations and surface characteristics. The third option is the commonly used dispersion methodology in Gaussian plume models, which are empirically derived and can become invalid under low wind speed conditions over complex terrain. In the present study, we use a modified form of PG stability-dependent dispersion curves with coefficients derived from the in situ turbulence measurement. Figure 2 shows the modified curves with original PG curves for comparison. It can be seen that the modified horizontal and vertical dispersion curves in the near-field with downwind distance less than 5 km at all stabilities (except for the vertical dispersion coefficient under A stability class and beyond 500 m) are above the original PG curves, which reflects the influences of local complex terrain and flow pattern on the near-field dispersion.

In the following study, the above three dispersion schemes referred as turbulence, similarity, and modified PG methods for simplification are evaluated by comparing the modeling results with the observational tracer concentrations. To carry out the evaluation on the same basis, the same hourly gridded wind fields are used for the three dispersion schemes, which are generated from the diagnostic wind field model CALMET by using the surface and upper air data listed in Sect. 2. In case of upper air data missing during high wind speed episodes, the NCEP FNL reanalysis data of $1^\circ \times 1^\circ$ resolution are used instead. The modeling domain is set to be $10 \text{ km} \times 10 \text{ km}$, with the release tower at the center (Fig. 1c). The horizontal grid spacing of the meteorological grid is 100 m, and the sampling grid size is 50 m to better predict the near-field peak concentrations. In the vertical direction, ten grid cells are used with the cell face heights 0, 20, 40, 80, 160, 300, 600, 1000, 1500, 2200, and 3000 m, respectively. The modeling time step of CALPUFF is set to be 1 min, and 40-min averages are calculated for each release trial to compare with the measured concentrations.

Fig. 2 Modified PG stability-dependent atmospheric dispersion coefficients of the site



4 Evaluation Methodology

Because typical variations in wind direction are about 20 to 40 degrees (or more in light winds), predicted plumes often completely fail to overlap observed plumes, even though the magnitude and patterns may be similar [6]. From the viewpoint of engineering application, high concentrations (or doses) are of great concern. Thus, model evaluation in the current paper is mainly based on the peak concentration anywhere along a sampling line.

The performance of the three dispersion schemes is evaluated using two basic methodologies. The first method is using scatter plots, quantile–quantile plots, and residual box plots to quantitatively compare the observed and predicted concentrations. The second method involves the application of statistical procedures that quantify several relevant performance measures.

In a scatter plot, the paired observations and predictions are plotted against each other, from which the magnitude of the model’s over- or underpredictions can be visually inspected. Quantile–quantile (Q–Q) plot is used to find out whether a model can generate a concentration distribution that is similar to the observed one. Biases at low or high concentrations are quickly revealed in this plot. In a residual box plot, model residuals defined as the ratio of predicted (C_p) to observed (C_o) concentrations are plotted, in the form of a box diagram, versus independent variables such as ambient wind speed, mixing height, and atmospheric stability. The significant points for each box diagram represent the 1st, 10th, 25th, 50th, 75th, 90th, and 99th percentiles of the cumulative distribution of the n points considered in the box. A good performing model should not show any trend of the residuals when they are plotted versus independent variables [7].

Predictions of the three dispersion schemes are compared with the experimental tracer data using the statistical performance measures recommended by Hanna et al. [8], which include the fractional bias (FB), the geometric mean bias (MG), the normalized mean square error (NMSE), the geometric variance (VG), the correlation coefficient (R), and the fraction of predictions within a factor of two of observations (FAC2). They are defined as

$$FB = (\overline{C_o} - \overline{C_p}) / (0.5(\overline{C_o} + \overline{C_p})) \tag{1}$$

$$MG = \exp(\overline{\ln C_o} - \overline{\ln C_p}) \tag{2}$$

$$NMSE = \overline{(C_o - C_p)^2} / \overline{C_o C_p} \tag{3}$$

$$VG = \exp\left[\overline{(\ln C_o - \ln C_p)^2}\right] \tag{4}$$

$$R = \overline{(C_o - \overline{C_o})(C_p - \overline{C_p})} / \sigma_o \sigma_p \tag{5}$$

$$FAC2 = \text{fraction of data for which } 0.5 \leq (C_p/C_o) \leq 2 \tag{6}$$

where C_o and C_p refer to the observed and predicted concentrations, respectively, and an overbar indicates an average. σ_o and σ_p represent the standard deviations of the observed and predicted values, respectively.

The statistical indexes FB and MG provide a value for the total error and indicate whether the predicted concentrations underestimate or overestimate the observed values. NMSE and VG both deal with variances and reflect systematic and random errors. Correlation coefficient R describes the degree of agreement between the variables. FAC2 is the most robust measure, because it is not overly influenced by outliers. A perfect model would have MG, VG, and FAC2 = 1 and FB and NMSE = 0. Chang and Hanna [7] have given suggestions regarding the magnitudes of the performance measures expected of “good” models based on unpaired in space comparisons, which are listed as below:

FAC2 is about 50%.

The mean bias is within $\pm 30\%$ of the mean.

The random scatter is about a factor of two to three of the mean.

5 Evaluation Results

Figure 3a shows the scatter plot of observed versus predicted arc maximum concentrations for turbulence, similarity and modified PG dispersion schemes. It can be seen that predictions of the turbulence and modified PG methods match well with the observed values for high and medium concentration ranges, with most of the points falling within a factor of 4 lines, while the similarity method underestimates high observed concentrations. All the three schemes tend to overpredict the low observed concentrations. From the distributions in the Q–Q plot (Fig. 3b), the underestimation at high concentration part by the similarity method and overprediction at low concentration part by all the schemes can be clearly discerned. Over most of the range, the distributions of the turbulence and modified PG method show less bias than that of the similarity method.

Figure 4 shows the percentage of predicted cases within a factor of 2, 4, 6, and more than 6 by the three schemes. The turbulence and modified PG schemes behave

Fig. 3 a Scatter plots and b Q–Q plots of observed versus predicted arc peak concentrations. The *thin solid lines* indicate a factor of two scatter, and *dashed lines* represent a factor of four scatter

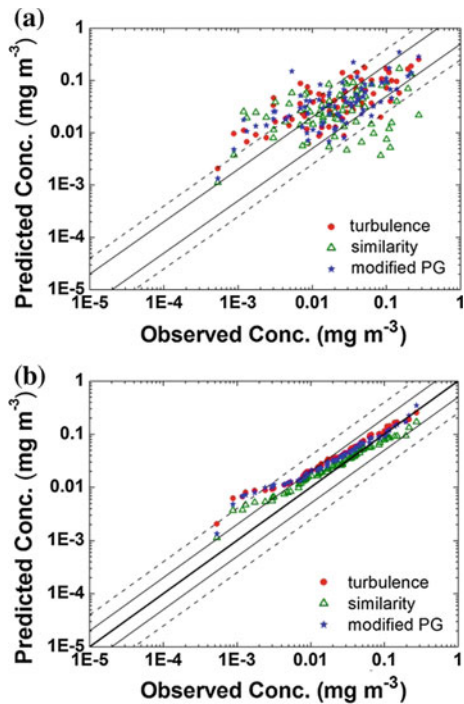
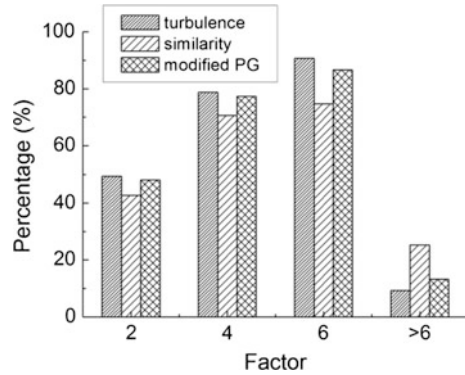


Fig. 4 Bar graph showing the percentage of predicted cases within a factor of 2, 4, 6, and more than 6 by the three schemes



quite similar, with FAC2 49.3 and 48.0%, and FAC4 78.7 and 77.3%, respectively. The magnitudes of FAC2 and FAC4 are lower for the similarity scheme, which are 42.7 and 70.7%, respectively.

Figures 5 and 6 show residual box plots of C_p/C_o as a function of wind speed and mixing height, respectively. The trend is not obvious under low and medium wind speed conditions (wind speed less than 4 m/s), with larger scatters for the similarity method. For higher wind bin with wind speed between 4 and 6 m/s, all the three methods show overpredictions. Comparison between the measured wind speeds at the surface stations with the modeled values shows that CALMET underestimates the observed wind speeds under high wind speed conditions, which results in the overestimated concentrations at high winds. Moreover, discrete tracer samplers may miss the actual plume centerlines under high wind speed conditions, when the dispersive plume is thin.

Figure 6 suggests little overall trend with mixing height for the turbulence and modified PG method. However, distinct underestimation with mixing height below 500 m and pronounced overestimation with mixing height above 1500 m is found for the similarity method. By analyzing the measured temperature profiles, cases of mixing heights below 500 m correspond to the conditions of low-level inversions with the measured mixing heights less than 300 m, while the modeling results are larger than 400 m. Overprediction of mixing heights leads to overestimation of dispersion coefficients for the similarity method and hence the underestimation of plume concentrations. Trials with mixing heights higher than 1500 m correspond to high wind conditions. Besides the reasons analyzed previously, two radiosondes were not released during high wind speed periods, thus the mixing heights were calculated using the NCEP FNL reanalysis data with a spatial resolution $1^\circ \times 1^\circ$ during these periods. The resolution is too coarse to accurately reflect the evolution of mixing layer over the complex terrain, which subsequently influences the simulation of ground concentration. Compared with the similarity method, predictions by the turbulence and modified PG methods have a less dependence on the meteorological variables.

Fig. 5 Residual box plots of **a** turbulence method, **b** similarity method, and **c** modified PG method as a function of wind speed (m/s). *Dashed lines* indicate a factor of two scatter

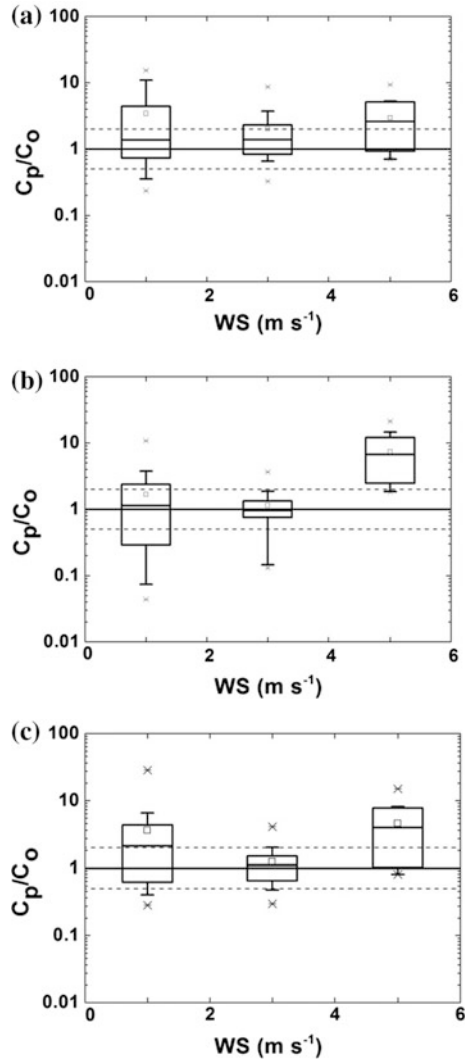


Table 1 summarizes the results of statistical performance evaluation for the three dispersion methods. Overall, the performances for the turbulence method and the modified PG method are comparable. The similarity method has a larger scatter. To better interpret the statistical measures, Eq. (1) is rewritten as following:

$$\frac{\overline{C_p}}{\overline{C_o}} = \frac{1 - 0.5FB}{1 + 0.5FB} \tag{7}$$

Ignore the random scatter between C_p and C_o , then Eq. (4) becomes [9]

Fig. 6 Residual box plots of **a** turbulence method, **b** similarity method, and **c** modified PG method as a function of modeled mixing height (m). *Dashed lines* indicate a factor of two scatter

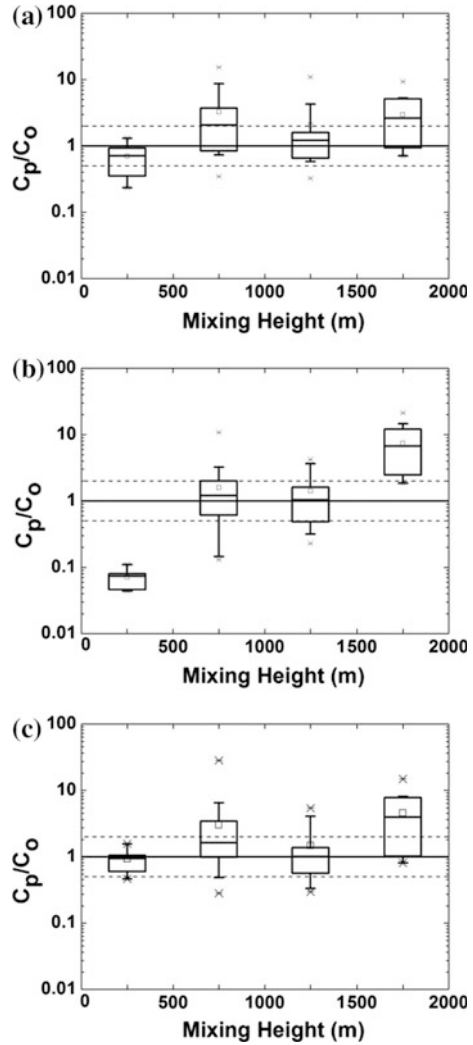


Table 1 Statistical performance measures for the three dispersion schemes

Dispersion scheme	FB	MG	NMSE	VG	R	FAC2
Turbulence	-0.234	0.566	0.807	3.364	0.687	0.493
Similarity	0.194	0.837	1.920	6.465	0.329	0.427
Modified PG	-0.211	0.604	1.089	3.471	0.638	0.480

$$VG = \exp \left\{ \left[\ln \left(\frac{C_p}{C_o} \right) \right]^2 \right\}, \text{ or } \frac{\overline{C_p}}{C_o} = \exp(\sqrt{\ln VG}) \quad (8)$$

Thus, the turbulence, similarity, and modified PG dispersion methods yield values of FB corresponding to 26.5% overprediction, 17.7% underprediction, and 23.6% overprediction, respectively, and values of VG corresponding to the random scatter of a factor of 3, 4, and 3 of the mean, respectively. FAC2 values for turbulence and modified PG methods are close to 50% and slightly lower, about 43%, for the similarity method. According to the good models' criteria in Sect. 4, CALPUFF model with the turbulence or the modified PG dispersion scheme is suitable for the inland NPP site over the complex hilly and valley terrain.

6 Conclusions and Discussion

Comprehensive field experiments including both meteorological measurements and tracer releases and samplings were conducted at a typical inland NPP site located over a complex hilly and valley terrain to investigate the site-specific atmospheric dispersion characteristics and to validate the atmospheric dispersion models. Because of the powerful abilities of CALPUFF to simulate the near-field impacts on complex flow situations, it is chosen as the preferred model. Three dispersion schemes in CALPUFF involving different levels of sophistication of input data are used to model the ground concentration distributions of the tracer gas, which are using direct measurements of turbulence, the micrometeorological variables in conjunction with the similarity theory, and the PG stability-dependent dispersion curves with coefficients modified according to the turbulence measurements, respectively, to calculate the dispersion coefficients. The modeled arc maximum concentrations are compared to the observed values by various methodologies, such as the scatter plot, quantile–quantile plot, residue box plot, and a set of statistical performance measures.

In general, the turbulence scheme and the modified PG scheme are found to have similar performance, with overall overestimation between 20 and 30% and a random scatter of a factor of 3. The two schemes predict well for the high and medium concentration ranges. An underestimation of about 20% is found for the similarity scheme, with a random scatter of a factor of 4. For the similarity scheme, the calculated dispersion coefficients strongly depend on the meteorological variables derived from CALMET. The errors of wind field and other micrometeorological variables can be transferred to the dispersion module and then influence the predicted concentrations. Thus, the model residuals show remarkable trends with wind speed and mixing height, which is not obvious for the other two schemes. The similarity scheme underestimates the high concentration part by about a factor of 2. All the three schemes overpredict the low concentration ranges mainly due to underestimations on wind speed and overestimations on mixing layer heights in

modeling, and the probable miss of plume centerline during sampling at high wind speed conditions.

Overall, CALPUFF model with the turbulence dispersion scheme or the modified PG dispersion curves shows good performance at the inland site. However, long-term measurement of turbulence is usually unavailable at most sites. In this way, the parameterization formulas of dispersion coefficients can be derived from the short-term in situ turbulence measurement, which is usually taken at Chinese NPP sites for two typical seasons (e.g., winter and summer). The modified PG stability-dependent dispersion formulas or curves can be used instead of the original PG option to better reflect the site-specific dispersion characteristics. The open access of the source codes of CALPUFF facilitates this modification. From the viewpoint of engineering application, CALPUFF model with modified PG dispersion curves is recommended at sites over such hilly and valley complex terrain.

References

1. Bluett J, Gimson N, Fisher G, et al. Good Practice Guide for Atmospheric Dispersion Modeling [R]. Ministry for the Environment, Wellington, New Zealand, 2004.
2. Scire J S, Strimaitis D G, Yamartino R J. A User's Guide for the CALPUFF Dispersion Model (version 5) [R]. Earth Tech, Inc., Concord, 2000.
3. Zhu H, Zhang H S, Cai X H, et al. Using CALPUFF for near-field atmospheric dispersion simulation over complex terrain[J]. Acta Scientiarum Naturalium Universitatis Pekinensis, 2013, 49(3): 452–462 (in Chinese)
4. Hanna S R, Britter R, Franzese P. A baseline urban dispersion model evaluated with Salt Lake City and Los Angeles tracer data [J]. Atmospheric Environment. 2003, 37(36): 5069–5082.
5. Scire J S, Robe F R, Fernau M E et al. A User's Guide for the CALMET Meteorological Model (Version 5.0) [R], Earth Tech, Inc., Concord, 2000.
6. Weil J C, Sykes R I, Venkatram A. Evaluating air quality models: review and outlook [J]. Journal of Applied Meteorology, 1992, 31: 1121–1145.
7. Chang J C, Hanna S R. Air quality model performance evaluation [J]. Meteorology and Atmospheric Physics, 2004, 87: 167–196.
8. Hanna S R, Chang J C, Strimaitis D G. Hazardous gas model evaluation with field observations [J]. Atmospheric Environment, 1993, 27A: 2265–2285.
9. Chang J C, Franzese P, Chayantrakom K., et al. Evaluations of CALPUFF, HPAC, and VLSTRACK with two mesoscale field datasets [J]. Journal of Applied Meteorology, 2003, 42: 453–466.

Author Biography

Hao Zhu Senior engineer, China Nuclear Power Engineering Co., Ltd. Research area: environment protection.

Influences of Additives on the Performances of the Cementation of Simulated Radioactive Fluoride Liquid Wastes

Zhenghua Qian, Xueyang Liu, Yanbo Qiao, Shuai Wang,
Hongjun Ma and Yaping Sun

Abstract This paper studied the influences of additives with zeolite, vermiculite, silica fume and quartz sand on the performances of the cementation of simulated radioactive fluoride liquid wastes, which mainly contains Cs^+ , Sr^{2+} , F^- , etc. Different additives were added into the cement formulation with water/cement ratio of 0.45, and then cemented waste forms were made in the $\Phi 50 \text{ mm} \times 50 \text{ mm}$ plastic molds. Our work investigated the setting time and fluidity of the cement paste, the 28 days compressive strength of the cemented waste form, and strength losses after water/freezing resistance tests. The shock resistance and leaching tests were also carried out. Through series of comparison, the study obtained the cement formulation with zeolite, silica fume and quartz sand which could satisfy the demands of cementation of simulated radioactive fluoride liquid wastes. The cement paste could set in 22 h, and its fluidity was 18.4 cm, so its performance could meet the requirements of cement solidification in the barrel. And the mechanical behavior of the cemented waste form could meet the demands of GB 14569.1-2011. Also the cemented waste form had a good anti-leaching capacity of fluorine ion, whose cumulative leaching rate was under 4.59×10^{-3} cm during 42-day leaching test.

Keywords Additive · Cementation · Performance test · Fluorine ion

1 Introduction

With the development of nuclear science, nuclear power plants and other nuclear facilities would produce a large amount of radioactive liquid wastes when they were in service. Cementation was a kind of frequently used method for the treatment of radioactive liquid wastes, and it made the radioactive liquid wastes stored in solid

Z. Qian · X. Liu · Y. Qiao (✉) · S. Wang · H. Ma · Y. Sun
Center for Thorium Molten-Salt Reactor Research (TMSR), Shanghai Institute of Applied
Physics (SINAP), Chinese Academy of Sciences (CAS), Shanghai, China
e-mail: qiaoyanbo@sinap.ac.cn

state safely and steadily [1–7]. Cementation had many advantages such as simple equipment, technology maturation, easy operation, safety, less energy intensive, low cost, and high mechanical strength of solidified waste form.

So far, most cement formulations were aimed at radioactive borated wastes of PWR [8, 9]. Molten salt reactor was different from PWR. Its coolant was molten fluorides and its fuel was mixed with the coolant. Molten salt reactor would inevitably produce radioactive fluoride liquid wastes when it was in service. In order to protect the safety of public and environment around nuclear facilities, the radioactive fluoride liquid wastes had to be solidified for storage. Research of cementation of radioactive fluoride liquid wastes had not been reported. In consideration of toxicity and leaching performance of fluoride, we needed to carry out the research of cementation of radioactive fluoride liquid wastes.

In this experiment, we used $\text{CsNO}_3/\text{Sr}(\text{NO}_3)_2/\text{NaF}$ as constituents of the simulated radioactive fluoride liquid wastes. Cement formulations with additives like zeolite/vermiculite/silica fume/quartz sand were used to solidify the simulated liquid wastes. Then we measured the performance parameters of the cement paste and the cemented waste form, and chose the suitable additives through comparing these parameters [10–13]. Make sure that the cemented waste forms made by the cement formulation could meet the request of GB 14569.1-2011. If so, our research would provide technical support to the cementation of radioactive fluoride liquid wastes in the future.

2 Reagents and Equipment of the Experiment

2.1 Reagents and Material

$\text{Sr}(\text{NO}_3)_2$ and CsNO_3 were purchased from Xiya Reagent Co., Ltd.; NaF was obtained from Sinopharm Chemical Reagent Co., Ltd.; and clinoptilolite (mesh number is 200), vermiculite (2–3 mm, without any pretreatment), silica fume ($\sim 0.3 \mu\text{m}$), quartz sand (mesh number is 1200), and 325 # ordinary Portland cement were obtained from Conch Cement in Shanghai.

2.2 Equipment and Instrument

NJ-160 cement paste mixer, NRJ-411A cement mortar mixer, ISO cement paste normal consistency and setting time testing apparatus, NLD-3 motorized cement mortar table, and cement mortar mold were purchased from Wuxi Jianyi Instrument & Machinery Co., Ltd.; YAW-300 electro-hydraulic cement compression testing machine was purchased from Ji'nan Zhong Lu Chang Testing Machine Manufacturing Co., Ltd.; YH-40B cement concrete standard curing box was obtained

Hebei Rong Chang Test Instrument Factory; and DX219-F fluorine ion electrode was bought from Mettler-Toledo International Inc.

3 Sample Preparation of the Cemented Waste Form

Constituents of the simulated radioactive fluoride liquid wastes are shown in Table 1.

A total of 0.5 L simulated radioactive fluoride liquid wastes was added into the cement mortar mixer (cement paste mixer) and mixed with cement and additives. Then after 3 min, the cement mortar (cement paste) was poured into the plastics cement mortar mold with size of $\Phi 50 \times 50 \text{ mm}^3$, and the cemented waste forms were finished.

Additives mentioned in the experiment were zeolite, vermiculite, silica fume, and quartz sand. The weight of each cemented waste form was about 200 g. Contents of the additives in each cemented waste form are shown in Table 2.

4 Measurements and Analysis

4.1 Performance Test of the Cement Paste

Cement paste should meet the requests of cement solidification process. Fluidity of the cement paste should be greater than 13 cm. Initial setting time of the cement paste should be greater than 1.5 h, and final setting time should be less than 24 h.

Table 1 Components of the simulated radioactive fluoride liquid wastes

Constituent	Sr(NO ₃) ₂	CsNO ₃	NaF
Content (g/L)	10.628	6.746	11.520

Table 2 Ratios of the additives in each cemented waste form

Number	Cement type	Cement/kg	Water-cement ratio	Additives/g			
				Zeolite	Vermiculite	Silica fume	Quartz sand
1	325 # ordinary Portland cement	1	0.45				
2		1	0.45	100			
3		1	0.45		100		
4		1	0.45			100	
5		1	0.45				300
6		1	0.45	100		100	300
7		1	0.45		100	100	300

Table 3 Influences of additives on the setting time and fluidity of the cement paste

Number	Additives	Fluidity/cm	Initial setting time/h	Final setting time/h
1	Cement paste	>30	13.5	22.5
2	Zeolite	26	9	22
3	Vermiculite	24.2	7	20
4	Silica fume	20.6	15	25.5
5	Quartz sand	26.6	10	23
6	Zeolite, silica fume and quartz sand	18.5	7.5	24
7	Vermiculite, silica fume and quartz sand	14.4	8	21

When the water–cement ratio of the cement formulation was 0.45, we studied the influence of additives on fluidity and setting time of the cement paste. We measured fluidity of the cement paste according to the regulations GB/T 2419-2005 and setting time of the cement paste according to the regulations GB/T 1346-2001 [14, 15]. Results of the test are shown in Table 3.

Table 3 showed that silica fume could obviously reduce the fluidity of the cement paste, the cement pastes with silica fume could reach the scope of 160–220 mm. Silica fume could increase the setting time of the cement paste, and other additives had little effect on this parameter.

4.2 Mechanical Property Test of the Cemented Waste Form

When curing time was over, we measured the compressive strength of the cemented waste forms according to the regulations GB 14569.1-2011 [16]. One group was tested for compressive strength directly, another group was tested after freezing resistance test, and the third group was tested after water test.

We used electrohydraulic cement compression testing machine to measure the compressive strength of the cemented waste forms. The results are recorded in Table 4.

The cemented waste forms were made to fall from height of 9 m to the concrete ground, and then each cemented waste form was broken (small pieces of edges and flaw were not treated as broken). The results are recorded in Table 5. All of specimens with quartz sand after the shock resistance test showed integrity which is given in Fig. 1.

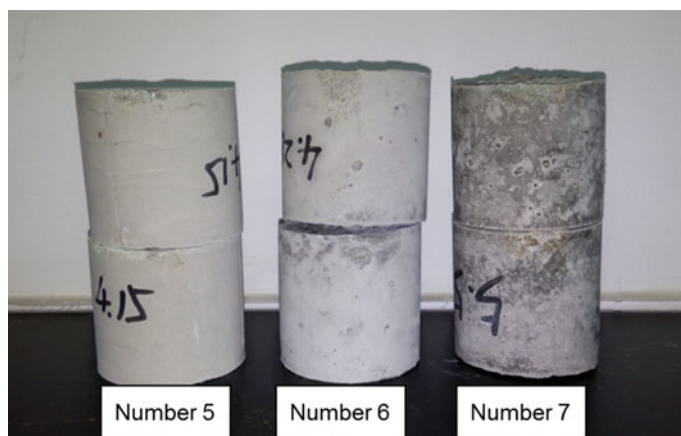
Date in Table 4 showed that compressive strength of each cemented waste form was greater than 7 MPa. Compressive strength after freezing resistance test and water test could meet the request of national standard.

Table 4 Data of the compressive strength of the cemented waste forms

Number	Additives	28-day compressive strength/MPa	Compressive strength after freezing resistance test/MPa	Compressive strength after water test/MPa
1	Cement paste	11.2	12.7	14.6
2	Zeolite	16.1	15.5	16.2
3	Vermiculite	13.9	13.9	15.4
4	Silica fume	8.1	11.1	7.4
5	Quartz sand	21.7	19.2	21.6
6	Zeolite, silica fume and quartz sand	23.8	21	24.6
7	Vermiculite, silica fume and quartz sand	19.1	19.8	21.65

Table 5 Result of the shock resistance test of the cemented waste form

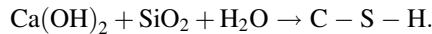
Number	Additives	Experimental result
1	Cement paste	Broken
2	Zeolite	Broken
3	Vermiculite	Broken
4	Silica fume	Broken
5	Quartz sand	Integrity
6	Zeolite, silica fume, and quartz sand	Integrity
7	Vermiculite, silica fume, and quartz sand	Integrity

**Fig. 1** Picture of the specimens with quartz sand after the shock resistance test

Zeolite slightly increased the compressive strength of the cemented waste form, vermiculite almost had no influence, and silica fume reduced the compressive strength of the cemented waste form.

The surface of the cemented waste forms which contained zeolite or vermiculite had some pores, big or small. In particular, the vermiculite without any pretreatment would create more pores for its hygroscopicity, leading to the decrease in water/cement ratio. Silica fume could well fill the gap between different particles. The compactness of cemented waste form was increased. Silica fume was advantageous to the early strength of cemented waste form, but it was disadvantageous to the long-term strength of cemented waste form because it replaced the main components of the cement.

Data in Tables 4 and 5 showed that quartz sand substantially increased the compressive strength and shock resistance of the cemented waste form. The main constitute of quartz sand was SiO_2 , it took place secondary hydration with Ca(OH)_2 which was produced by hydration of cement. The secondary hydration promoted the formation of C–S–H gel. It was conducive to increase the strength of cemented waste form. The equation is:



4.3 Leaching Performance Test of the Cemented Waste Form

We measured the leaching performance of $\text{Cs}^+/\text{Sr}^{2+}$ of all the cemented waste form according to the regulations GB/T 7023-2011 [17]. The 42-day leaching rate and cumulative leaching rate of $\text{Cs}^+/\text{Sr}^{2+}$ of all the cement formulations mentioned above are shown in Figs. 2 and 3.

As shown in Figs. 2 and 3, zeolite, silica fume, and quartz sand could reduce the leaching of Sr^{2+} , and vermiculite was just the opposite. Silica fume could reduce the leaching of Cs^+ too. The 42-day leaching rate and cumulative leaching rate of $\text{Cs}^+/\text{Sr}^{2+}$ of all the cement formulations mentioned above were under 2.04×10^{-3} cm/d and $0.205 \text{ cm}/1.17 \times 10^{-4}$ cm/d and 4.96×10^{-3} cm. It could meet the request of GB 14569.1-2011.

4.4 Fluorine Ion Leaching Test

The mass percent of the fluorine ion in the simulated radioactive fluoride liquid waste was 0.5%. In this experiment, we used fluorine ion electrode to measure the leachate of each cemented waste form, whose 42-day cumulative leaching rate was

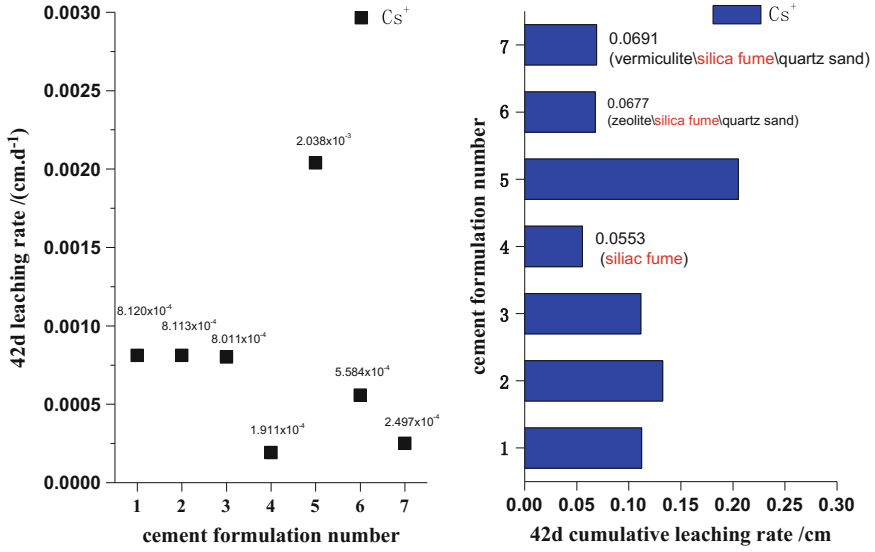


Fig. 2 42-day leaching rate and cumulative leaching rate of Cs⁺

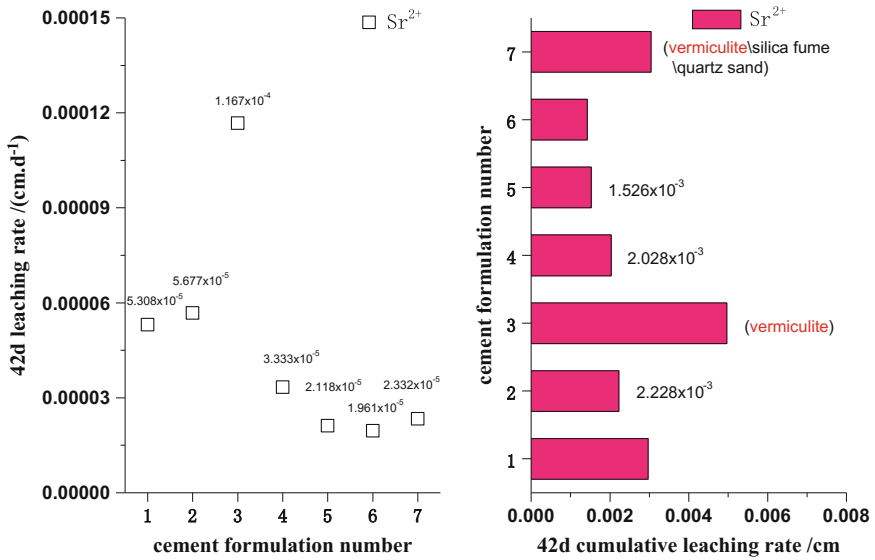
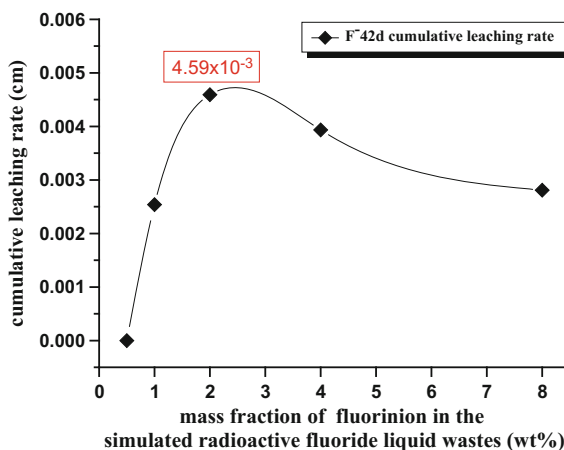


Fig. 3 42-day leaching rate and cumulative leaching rate of Sr²⁺

Fig. 4 Curve of cumulative leaching rate to mass fraction of the fluorine ion



all almost zero. It showed that additives had little effect on the leaching performance of fluorine ion.

Then we used the cement formulation whose additives were zeolite, silica fume, and quartz sand to make the cemented waste forms, in which mass percent of the fluorine ion in the simulated radioactive fluoride liquid wastes were increased twofold from 0.5 to 8 %. The cemented waste forms were maintained/soaked/taken samples as the leaching test. After 42-day leaching test, we measured the leachate of the fluorine ion in each cemented waste form. Curve of cumulative leaching rate to mass percent of the fluorine ion in each cemented waste form is shown in Fig. 4.

When the mass percent of the fluorine ion in the simulated radioactive fluoride liquid wastes was under 8%, the 42-day cumulative leaching rate of the fluorine ion rose at first and then decreased. The 42-day cumulative leaching rate was reached maximum 4.59×10^{-3} cm when the mass percent of the fluorine ion was 2%, and it was still very low. It showed that the cemented waste form made by the cement formulation mentioned above had a good anti-leaching capacity of fluorine ion.

5 Conclusions

- (1) Silica fume reduced the fluidity of the cement paste and increased its setting time; it also reduced the compressive strength of the cemented waste form. Quartz sand substantially increased the compressive strength and shock resistance of the cemented waste form.
- (2) Zeolite, silica fume, and quartz sand reduced the leaching of Sr^{2+} , vermiculite was just the opposite. Silica fume also reduced the leaching of Cs^+ . Additives had little effect on the leaching performance of fluorine ion. All the cemented waste forms had a good anti-leaching capacity of the simulated radionuclide $\text{Sr}^{2+}/\text{Cs}^+$, also the fluorine ion.

- (3) Cement paste was made by the cement formulation whose additives were zeolite, silica fume, and quartz sand, and its final setting time was 22 h and fluidity was 18.4 cm. Mechanical properties and leaching performance of the cemented waste form made by the cement formulation could meet the request of GB 14569.1-2011, and the 42-day cumulative leaching rate of the fluorine ion was under 4.59×10^{-3} cm when the mass percent of the fluorine ion was under 8%. So the cement formulation could be applied to the cementation of simulated radioactive fluoride liquid wastes.

References

1. Che Chunxia, Teng Yuancheng, Gui Qiang. Research and application status of radioactive waste solidification [J]. *Materials Review*, 2006.2, 20(2): 94–97.
2. Sun Qi'na, Li Junfeng, Wang Jianlong. Research progress in cementation of radioactive wastes [J]. *Atomic Energy Science and Technology*, 2010.12, 44(12): 1427–1435.
3. Wang Ren, Yang Jingtian. Studies on cement solidification of radioactive waste solutions produced from PWR nuclear power plant [J]. *Radiation Protection*, 1982, 2(5): 352–360.
4. Shi C, Spence R. Designing of cement-based formula for solidification/stabilization of hazardous, radioactive, and mixed wastes [J]. *Critical Reviews in Environmental Science and Technology*, 2004, 34(4): 391–417.
5. Atabek R, Bouniol P, Vitorge P, et al. Cement use for radioactive-waste embedding and disposal purposes [J]. *Cement and Concrete Research*, 1992, 22(2–3): 419–429.
6. Glasser F P. Progress in the immobilization of radioactive wastes in cement [J]. *Journal of Hazardous Materials*, 1992, 22(2–3): 201–216.
7. Sinha P K, Shanmugamani A G, Renganathan K, et al. Fixation of radioactive chemical sludge in a matrix containing cement and additives [J]. *Annals of Nuclear Energy*, 2009, 36: 620–625.
8. Sun Qi'na, Li Junfeng, Wang Jianlong. Study on cementation of simulated radioactive borated liquid wastes [J]. *Atomic Energy Science and Technology*, 2010.9, 44(s): 153–158.
9. Huang Weilan, Xie Weihong, Song Yongjie, Wang Shujuan, Xu Sikun, Su Yuemei, Li Shulian. Cementation of radioactive liquid waste containing ^{60}Co and ^{152}Eu [J]. *Atomic Energy Science and Technology*, 2001.9, 35(5): 451–455.
10. Feng Shengtao, Gong Li, Cheng Li. The study of performance improvement on cemented ash waste form [J]. *Radiation Protection*, 1997.3, 17(2): 122–129.
11. Tian Yanjie, Chen Jianhua, Li Chunguang. Effect of additives on mechanical performances of cemented waste forms [J]. *Environmental Science & Technology*, 2012.6, 35(6): 53–56.
12. Hou Xiaoqiang, Zheng Xutao, Guo Congsheng, Tan Hongbin. Effect of additives on properties of cement solidified body [J]. *Shanghai Nonferrous Metals*, 2014.9, 35(3): 123–127.
13. Li Yuxiang, Quan Ming, Yi Facheng, Xiao Zhengxue, Chen Yalan. Leaching behavior of Cs+ in cement-solidified waste forms [J]. *Atomic Energy Science and Technology*, 2011.3, 45(3): 282–287.
14. General Administration of Quality Supervision, Inspection and Quarantine of P.R.C. GB/T 2419-2005 Test method for fluidity of cement mortar [S]. Beijing: Standards Press of China, 2005.
15. General Administration of Quality Supervision, Inspection and Quarantine of P.R.C. GB/T 1346-2001 Test methods for water requirement of normal consistency, setting time and soundness of the Portland cements [S]. Beijing: Standards Press of China, 2001.

16. General Administration of Quality Supervision, Inspection and Quarantine of P.R.C. GB 14569.1-2011 Performance requirements for low and intermediate level radioactive waste form-Cemented waste form [S]. Beijing: Standards Press of China, 2011.
17. General Administration of Quality Supervision, Inspection and Quarantine of P.R.C. GB/T 7023-2011 Standard test method for leachability of low and intermediate level solidified radioactive waste forms [S]. Beijing: Standards Press of China, 2011.

Author Biography

Qian Zhenghua Shanghai Institute of Applied Physics, Chinese Academy of Sciences. Research area: electrochemistry, decommission and decontamination, radioactive waste treatment.

Minor Actinides Incineration in a Small Molten Salt Fast Reactor

Chenggang Yu, Chunyan Zou, Yuwen Ma and Jingen Chen

Abstract Minor actinides (MA) accumulated in spent fuel are the primary contributors to the long-term radiological hazards of high-level nuclear waste. Due to its outstanding features such as the function of reprocessing and refueling, large negative temperature feedback coefficient and no fuel assembly fabrication, Molten Salt Fast Reactor (MSFR) is regarded as one of the candidate reactors for MA incineration. In the present work, we evaluate the MA incineration capability for a 500 MWth MSFR by considering FLiBe fuel carrier salts with different initial MA loadings. The simulated results show that the MA transmutation capability has a positive correlation to the MA loading. When MA = 18.17 mol%, the transmutation fraction during 50-year operation can achieve about 95%. The MA feeding into the fuel salt is also analyzed to obtain its influences on the MA transmutation performance. The simulated result shows that both the amount of MA transmutation and the depletion ratio of MA to heavy nuclei also have a positive correlation to the MA feeding.

Keywords Molten salt fast reactor · Minor actinides transmutation

1 Introduction

The open fuel cycle mode is used in the commercial pressurized water reactor (PWR). In this once-through fuel cycle mode, a lot of spent nuclear wastes (SNF) are produced during the PWR operating. Most of the SNF needs geological

C. Yu · C. Zou · Y. Ma · J. Chen (✉)
Shanghai Institute of Applied Physics, Chinese Academy of Sciences,
Shanghai 201800, China
e-mail: chenjc@sinap.ac.cn

C. Yu · C. Zou · Y. Ma · J. Chen
CAS Center for Excellence in TMSR Energy System,
Chinese Academy of Sciences, Shanghai 201800, China

Y. Ma
University of Chinese Academy of Sciences, Beijing 100049, China

disposal or temporary storage up to now. However, the above processing modes are unfavorable to reduce the radioactive dose or to improve the nuclear fuel utilization. Transuranic (TRU) is the primary contributor to the long-lived high-level radioactive hazards in SNF. Transmutation of TRU is one of the most effective ways to solve the SNF safety issues [1–3]. Pu can be made as mixed oxide fuel (MOX) and reused in PWR. However, the transmutation of TRU composing only minor actinides (MA) should be paid more attention, since MA cannot be well burnt in a thermal reactor.

Accelerator-Driven Subcritical System (ADS) [4] and fast reactors including Gas-cooled Fast Reactors (GFR) [3], Sodium-cooled Fast reactor (SFR) [5] and liquid fueled fast reactors [6–8] are recognized as alternative systems to transmute MA for their larger fission-to-capture ratio, deeper burnup compared with a thermal reactor. As one of the six candidate reactors in the Generation IV International Forum (GIF), liquid fueled fast reactor has outstanding features for MA transmutation such as the functions of reprocessing and refueling, large negative temperature feedback coefficient and no fuel assembly fabrication. The MOlten Salt Actinide Recycler & Transmuter (MOSART) proposed by the Kurchatov Institute of Russia within the International Science and Technology Center project 1606 (ISTC#1606) is one of the liquid fueled fast reactors [6]. The original design objective of the MOSART is to effectively transmute TRU. The Molten Salt Fast Reactor (MSFR) proposed by the Centre National de la Recherche Scientifique (CNRS) is another liquid fueled fast reactor concept [7, 8]. The fuel breeding of Th-²³³U is the main objective for the MSFR.

The MA transmutation capability is evaluated for a small power 500 MWth MSFR (named SMSFR hereinafter) in this work. In what follows, the SMSFR geometry description, molten salt parameters and the burnup calculation tool introduction are presented in Sect. 2; the results are discussed in Sect. 3; and the conclusions are given in Sect. 4.

2 SMSFR and Neutron Physic Parameters

2.1 SMSFR Core Description

Figure 1 shows the quarter vertical section of the SMSFR core [9]. The fuel salt (3.0 m³) contains the internal fuel salt (1.5 m³) and the external fuel salt (1.5 m³). A radial Th fertile salt around the fuel salt is adopted for improving Th-U conversion. Both the compositions of the fuel salt and the fertile salt are listed in Table 1. The heavy nuclides (HN) comprise ²³²Th, ²³³U and MA in the fuel salt, while only ²³²Th is loaded in the fertile salt. It is assumed that the MA has been partitioned from the SNF of a PWR with burnup of 33 GWd/t after 3 years of cooling. The actinide weight ratio is 56.2% for ²³⁷Np, 26.4% for ²⁴¹Am, 12.0% for ²⁴³Am, 0.03% for ²⁴³Cm, 5.11% for ²⁴⁴Cm and 0.26% for ²⁴⁵Cm [10].

Fig. 1 Quarter vertical section of the SMSFR geometry (units: cm)

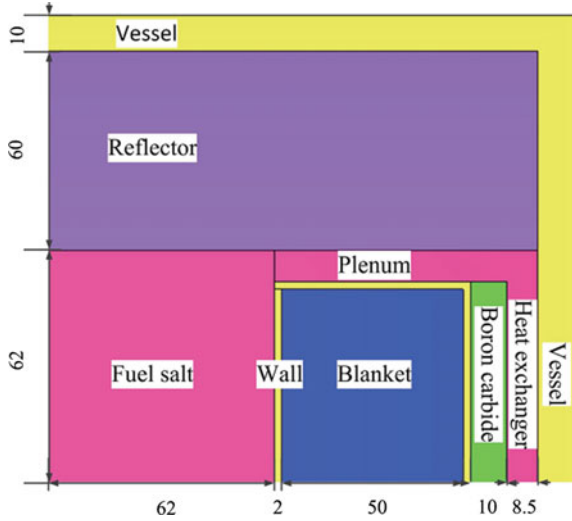


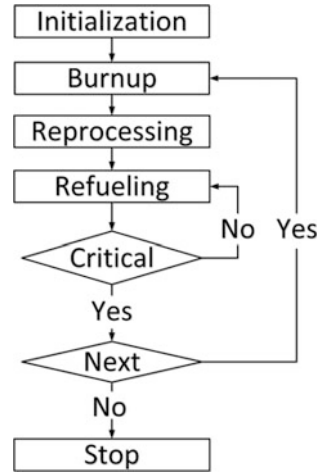
Table 1 Molten salt parameters

Parameter	Value
Compositions (mol%)	77.5 LiF-22.5 HNF ₄
⁷ Li enrichment (mol%)	99.995
Melting point (°C)	565
Dilatation coefficient (g/cc/°C)	8.82E-4
Fuel salt density at 750 °C (g/cc)	4.1
Fuel salt mean temperature (°C)	750
Fuel salt volume (m ³)	3.0
Fertile salt mean temperature (°C)	700
Fertile salt volume (m ³)	2.9

2.2 Neutron Simulation Tool

All the results in this work are obtained from the calculations with SCALE6 which was developed at ORNL for reactor criticality and safety analyses [11]. To perform the burnup calculation for a two-flow MSR with online fuel reprocessing, a special MSR reprocessing sequence (MSR-RS) was developed by coupling with the CSAS6, TRITON and ORIGEN-S modules in the SCALE6 program [9, 12]. The CSAS6 module is responsible for criticality analysis. The TRITON module performs the problem-dependent cross-sectional processing followed by a multi-group neutron transport calculation. The ORIGEN-S module is used for depletion and decay calculations. The nuclear cross-sectional data used in the MSR-RS is from the ENDF/B-VII library. The flowchart of MSR-RS is shown in Fig. 2.

Fig. 2 MSR-RS flowchart



3 Results and Discussion

The main content in this paragraph is divided into two parts. First, the effective multiplicity factor (k_{eff}) varying with MA loadings is studied to analyze the MA transmutation performance. Second, the MA transmutation capability with online Th-U and MA refeeding into the fuel salt is studied.

3.1 k_{eff}

The mole fraction of HN in both the molten salt is set as 22.5 mol% as shown in Table 1. To keep an enough excess reactivity, 5.2 mol% ^{233}U is adopted for different MA loadings. Therefore, the 17.3 mol% of the rest fraction is composed by MA and Th.

k_{eff} is defined as the ratio of neutron production to neutron disappearance in a reactor [9]:

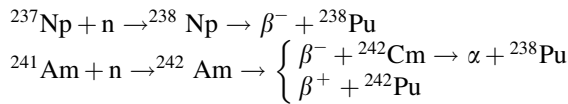
$$k_{\text{eff}} = \frac{R_p}{R_d} = \frac{\sum_i R_f(i) \cdot \bar{\nu}(i)}{\sum_j R_a(j) + L} \quad (1)$$

where R_p denotes the productive rate of neutron; R_d denotes the disappear rate of neutron; $R_f(i)$ denotes the fission rate of neutron for nuclide i ; $\bar{\nu}(i)$ denotes the fission neutron number for nuclide i ; $R_a(j)$ denotes the absorption rate of neutron for nuclide j ; and L denotes the leakage rate. So, the single nuclear fission contribution to total k_{eff} can be written as

$$k_{\text{eff}}(i) = \frac{R_f(i) \cdot \bar{\nu}(i)}{\sum_i R_a(i) + L} \tag{2}$$

One can see from Eqs. (1) and (2) that the k_{eff} relates to neutron spectrum and the inventory of HN. The single HN contribution (includes ^{233}U , MA and ^{232}Th) and the total k_{eff} with different MA loading are shown in Fig. 3. And the neutron spectrum with different MA loading is shown in Fig. 4. The spectrum hardens with the increasing MA loading. The hardening spectrum leads to the reduction of the ^{233}U one-group fission cross section. And this causes the k_{eff} (^{233}U) declining with the increasing MA loading as shown in Fig. 3. Due to the increasing of MA loading, its reactivity contribution rises with the increasing MA loading. Since the fission cross section is small, the reactivity contribution of Th is slight with the increasing MA loading.

Considering the relatively large fractions of ^{237}Np and ^{241}Am in the MA, a considerable amount of Pu can be produced from the following approaches:



The burnup for different MA loading is shown in Fig. 5. Since there are not enough fissile nuclides in the core, the k_{eff} decreases with operating time in all cases. One can also see that as MA loading increases, the k_{eff} loss decreases with operating time. The main reason of this phenomenon is the prompt reactivity provided by MA itself and the delayed reactivity by the produced Pu isotopes.

Fig. 3 k_{eff} and primary HN separate contributions

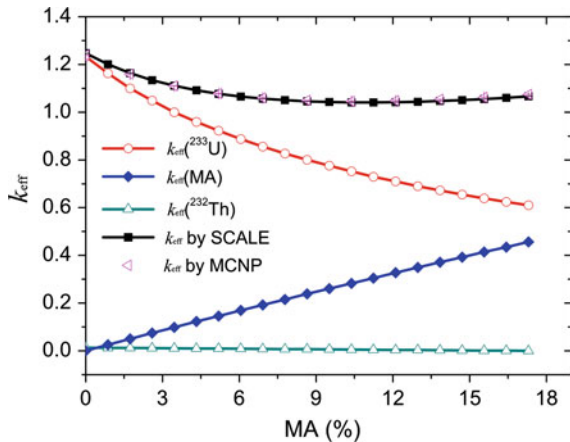


Fig. 4 Neutron spectra for different MA loadings

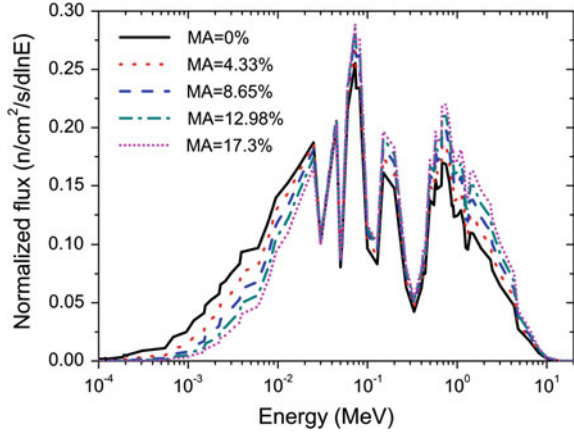
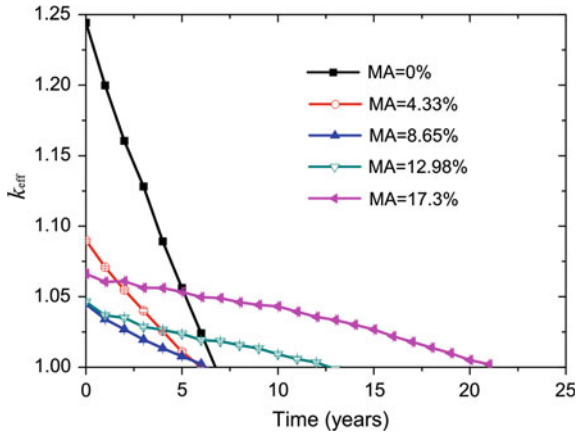


Fig. 5 Burnup performance without HN refueling for different MA loadings



When MA <10 mol%, the initial k_{eff} declines with the increasing MA loading as shown in Figs. 3 and 5. However, the effective full power year (EFPY) keeps almost constant during the operation since the k_{eff} compensation from MA and Pu. The burnup deepens significantly for MA >10 mol% since the delayed reactivity compensation from the Pu isotopes is larger than the depletion of k_{eff} .

A small reactivity at the beginning of burnup (BOB) is helpful to the SMSFR safety controlling. And a slow loss of k_{eff} during the time operating is favorable to improve the neutron economy and the MA transmutation performance. Both the above cases are desirable to transmute MA for the SMSFR. Therefore, a larger MA loading can meet the above two requirements as shown in Fig. 5.

3.2 MA Transmutation Capability

As discussed above, the k_{eff} decreases during the operating time due to the fissile fuel depletion in the fuel salt. Therefore, a HN feeding into the fuel salt case will be investigated to further deepen the burnup and improve the MA transmutation capability. As displayed in our previous work, a stable condition with $k_{\text{eff}} \approx 1$ is set by feeding HN into fuel salt. Under the small excess reactivity situation, the maximum loading of MA = 18.17 mol% is determined (slightly larger than 17.3 mol% shown in Figs. 3 and 5), corresponding to the 4.33 mol% ^{233}U loading.

A 50-year operating time of the SMSFR is analyzed considering the lifetime of the Hastelloy N alloy. In this simulation, the gaseous and non-soluble metal fission products (Xe, Kr, etc.) are online removed through the helium bubbling system with an extraction time constant of 30 s [13]. The other soluble fission products are reprocessed by the chemical reprocessing system with an extraction time constant of 180 days. To improve the utilization of ^{233}U , Pa in the fuel salt and the fertile salt is also extracted.

To evaluate the MA transmutation capability, a parameter of fractional transmutation (FT) is defined as the MA depletion to the initial MA loading [14]:

$$\text{FT}(t) = 1 - \frac{M(t)}{M_{\text{BOB}}} \quad (3)$$

where M denotes the MA inventory.

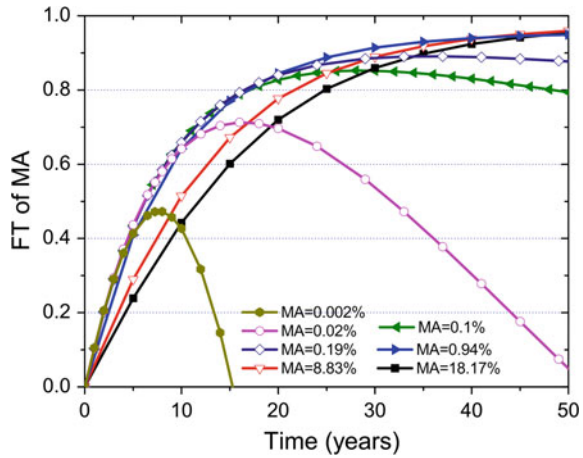
The FT with different MA loading is calculated and shown in Fig. 6. One can see from Fig. 6 that the FT increases at first and then decreases when MA < 0.19 mol%. The main reason of this phenomenon is that the MA transmutation inventory is larger at first and smaller than its production inventory afterward. The MA transmutation capability increases during the first 30 years and then becomes stable for MA = 0.19 mol%. When MA loading is greater than 0.94 mol%, about 95% of the MA transmutation efficiency can be achieved during 50-year operating.

Although the FT is about 95% at the condition of MA > 0.94 mol%, their respective net transmutation mass is different significantly. The net transmutation mass is 292 kg for MA = 0.94 mol%, while it is 5620 kg for MA = 18.17 mol%. The MA transmutation mass of the latter is 19 times greater than that of the former. Therefore, FT is insufficient to draw a definite conclusion for MA transmutation capability evaluation.

The incinerated MA relative to the total depleted HN is also an important factor for evaluating MA transmutation capability, which is defined as:

$$\text{DR} = \frac{\text{MA(depletion)}}{\text{HN(depletion)}} \quad (4)$$

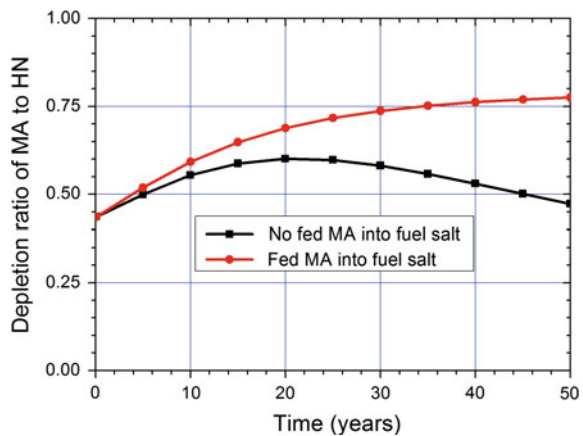
Fig. 6 MA transmutation fraction during 50 years operating



where MA(depletion) and HN(depletion) represent the incinerated MA and the depleted HN, respectively.

The time evolution of DR for MA = 18.17 mol% is shown in Fig. 7. The DR increases gradually during the first 20 years due to the considerable production of the Pu isotopes from MA and then tends to decline. It indicates that after 20 years of operation, the MA left in the fuel salt is not sufficient to be burned, which results in the decreases of both the inventory of Pu and the DR. One can also find that the DR is smaller than 0.5 after about 45 years, which implies more ^{233}U and ^{232}Th are consumed than MA. Therefore, MA is continually injected into the fuel salt to maintain the constant amount of total TRU inventory during the whole operation. In this case, the transmutation amount of MA at 50 years is about 8030 kg, improving by 42.9% than the no MA feeding condition. Moreover, the DR for the MA feeding condition increases from 0.435 at BOB to 0.775 at 50-year without any decline phenomenon.

Fig. 7 Time evolutions of depletion ratio of MA to HN for different MA transmutation scenarios at MA = 18.17%



4 Conclusions

A 500 MWth MSFR is used for evaluating the MA transmutation performance. When maintaining the amount of ^{233}U at 5.2 mol%, the decreasing of k_{eff} (^{233}U) slows down, while the k_{eff} (MA) increases linearly with the increasing MA loading. The combination of the above two contributions makes the k_{eff} firstly reduce and then increase with the increasing MA loading. As the MA loading increases, the k_{eff} loss decreases with operating time due to the delayed reactivity compensation of Pu isotopes. And the low initial k_{eff} and deepen burnup are favorable to the reactor safety controlling and MA transmutation.

The online refueling of Th, ^{233}U and MA into the fuel salt are also investigated to evaluate the MA transmutation performance. A larger MA loading is helpful to improve the MA transmutation capability. When MA = 18.17 mol%, the fractional transmutation is 95% corresponding to the 5620 kg MA transmutation mass for no MA online feeding. The MA transmutation amount and the DR are 8030 kg and 77.5%, respectively, when MA is fed into fuel salt to maintain the total TRU inventory constant during the whole operation for MA = 18.17 mol%.

The initial fuel temperature coefficient of SMSFR is -3.8 pcm/K for MA = 18.17%, and it does not change notably during the whole operation.

References

1. V. Ignatiev, O. Feynberg, I. Gnidoi, et al., Progress in development of Li, Be, Na/F molten salt actinide recycler & transmutation concept, Proceedings of ICAPP (2007) 7548.
2. C. Fiorina, M. Aufiero, A. Cammi, et al., Investigation of the MSFR core physics and fuel cycle characteristics, Progress in Nuclear Energy 68 (2013) 153.
3. Z. Perko, J. Leen Kloosterman, S. Feher, Minor actinide transmutation in GFR600, Nuclear Technology 177 (2012) 83.
4. T.M. Vu, T. Kitada, Seed and blanket ADS using thorium reprocessed fuel: Parametric survey on TRU transmutation performance and safety characteristics. Annals of Nuclear Energy 78 (2015) 176.
5. M. Zheng, W. Tian, D. Zhang, et al., Minor actinide transmutation in a board type sodium cooled breed and burn reactor core. Annals of Nuclear Energy 81 (2015) 41.
6. V. Ignatiev, O. Feynberg, I. Gnidoi, et al., Molten salt actinide recycler and transforming system without and with Th-U support: fuel cycle flexibility and key material properties, Annals of Nuclear Energy 64 (2014) 408.
7. E. Merle-Lucotte, D. Heuer, M. Allibert, et al., The thorium molten salt reactor: launching the thorium fuel cycle with the molten salt fast reactor, Proceedings of ICAPP (2011) 842.
8. D. Heuer, E. Merle-Lucotte, M. Allibert, et al., Towards the thorium fuel cycle with molten salt fast reactors, Annals of Nuclear Energy 64 (2014) 421.
9. C. Yu, X. Li, X. Cai, et al., Analysis of minor actinides transmutation for a molten salt fast reactor. Annals of Nuclear Energy 85 (2015) 597.
10. T. Mukaiyama, H. Yoshida, T. Ogawa, Minor actinide transmutation in fission reactors and fuel cycle considerations, IAEA-TECDOC-693, Vienna, Austria: IAEA (1993) 86.
11. ORNL, SCALE: A modular code system for performing standardized computer analyses for licensing evaluations, ORNL/TM-2005/39, Version6.1 (2009).

12. C. Zou, X. Cai, D. Jiang, et al., Optimization of temperature coefficient and breeding ratio for a graphite-moderated molten salt reactor. *Nuclear Engineering and Design* 281 (2015) 114.
13. A. Nuttin, D. Heuer, A. Billebaud, et al., Potential of thorium molten salt reactors detailed calculations and concept evolution with a view to large scale energy production, *Progress in Nuclear Energy* 46 (2005) 77.
14. B. Becker, M. Fratoni, E. Greenspan, Feasibility of a critical molten salt reactor for waste transmutation, *Progress in Nuclear Energy* 50 (2008) 236.

Author Biographies

Chenggang Yu Shanghai Institute of Applied Physics, Chinese Academy of Sciences, TRU transmutation in Thorium Molten Salt Fast Reactor.

Chunyan Zou Shanghai Institute of Applied Physics, Chinese Academy of Sciences, Th-U fuel cycle breeding in Thorium Molten Salt Reactor.

Yuwen Ma Shanghai Institute of Applied Physics, Chinese Academy of Sciences, Th-U fuel cycle breeding in Thorium Molten Salt Reactor.

Jingen Chen Shanghai Institute of Applied Physics, Chinese Academy of Sciences, Th-U fuel cycle and Thorium Molten Salt Reactor design.

Overview of Radioactive Waste Treatment in Domestic Nuclear Power Plants of Pressurized Water Reactor

Meng Hongshe

Abstract In accordance with the *Twelfth Five-Year Plan and 2020 Prospective Target*, China will see a coexistence of multiple reactors, different nuclear technologies, and standards in the development of nuclear power, and it is foreseeable that similar situation will also occur in radwaste treatment. This paper reviews the different radwaste treatment technologies in line with corresponding types of pressurized water reactor and proposes radwaste treatment options for newly built nuclear power plants of pressurized water reactors by drawing experience from foreign peers.

Keywords Radioactive waste · Waste disposal

1 Introduction

All industrial facilities inevitably produce wastes in its production activities, in the form of dust, heat, chemical by-product, or others. As for a nuclear power plant (NPP), it will produce some gas, liquid, and solid wastes with radioactivity due to the existence of fission materials, corrosion product, and activated coolant. Radioactive wastes (radwastes) are materials that shall not be reused due to operation on site or contaminated by radionuclides, whose concentration or activity exceeds the clearance level that defined by government regulator. Radwastes from NPP are featured with radioactive inertia gas, iodine and aerosol gas, or active product, and low–intermediate radioactive liquid and solid wastes in fission products. To protect the environment from being contaminated and to prevent the work staff and residents around NPP from overdose exposure, these radwastes have to be treated before discharge or storage.

In accordance with the *Twelfth Five-Year Plan and 2020 Prospective Target*, China will see a coexistence of multiple reactors, different nuclear technologies, and

M. Hongshe (✉)

China Nuclear Power Engineering Co., Ltd, 518124 Shenzhen, Guangdong Province, China
e-mail: menghongshe@cgnpc.com.cn

standards in the development of nuclear power, and it is foreseeable that similar situation will also occur in radwaste treatment. This paper focuses on the treatment of low–intermediate radioactive gas, liquid, and solid wastes that contain active product and fission material in nuclear power plant of pressurized water reactor (PWR NPP) and propose options for radwaste treatment in domestic PWR NPP.

2 Description of Radwaste Treatment in Domestic PWR NPP

2.1 Radwaste Treatment for AP1000

Radwastes produced from AP1000 reactors are mainly radioactive liquid, liquid, gas, spent resin, and spent filter cartridge produced from primary loop in abnormal conditions, compressible and incompressible solid dry waste, etc. The outstanding character in its radwaste treatment is the application of SRTF (site radioactivity waste treatment facility), which is a center for disposing radwaste that is shared by four or more reactors in a NPP. SRTF sees its first application in China by the method of reducing volume, which includes dewatering and supercompaction, to dispose those radwastes produced by four or more reactors that cannot be processed by nuclear island waste liquid system, which are mainly solid radwastes and wastes produced from abnormal conditions.

2.1.1 Radioactive Liquid

Liquid radwaste system processes radioactive liquid produced from normal operation or anticipated operation occurrence by filtering and ion exchanging. By filtering, suspended solids shall be purged from liquid radwaste, along with the interception of spent resin to prevent them sliding into other equipment. The filter is a fine mesh mechanical filter, whose cartridge can be changed by remote operation. There are intermittent or continuous ion exchange method adopted for disposing liquid radwaste. As for continuous method, those to-be-treated liquid radwaste shall be purified by continuously flowing around columns that made from ion exchange resin. This method is usually accepted in NPP for its high efficiency.

Advance treatment of coolant liquid radwastes that produced from normal operation and anticipated operation occurrence is adopted by canceling conventional evaporation device and simplifying process and building arrangements. These coolant liquid radwastes together with other liquids that produced from special conditions are collected and temporarily stored in nuclear island and will be further treated by a set of mobile equipments that are shared by reactors or by SRTF after shifting by shielding transferring containers. In the latter case, devices such as filter, active carbon absorption bed, ion exchange bed, R/O filter, and R/O skid are

deployed. The treated liquid radwaste then shall be sent back to nuclear island liquid radwaste system for further treatment or discharge after satisfying relevant standards, while R/O concentration solutions are sent to SRTF for drying. Mobile equipment shall be innovated along with the development of technology. At present, evaporation technology is functioning in SRTF of Sanmen NPP, but not in Haiyang NPP yet.

Liquid radwaste system consists of tanks, pumps, ion exchange bed, filter, etc.

2.1.2 Radioactive Gas

Active carbon delay beds absorb hydrogen-containing gas and fission gas produced from nuclear island. Fission gas is sent to ventilation tube after the absorption of active carbon and delayed decay. Main equipments involve gas cooler, steam separator, one active carbon protection bed, two active carbon delay bed, etc.

2.1.3 Radioactive Solid

Radioactive solid waste system only functions as collecting and interim storage without processing inside nuclear island. Solid wastes have to be sent to SRTF for volume reducing by transferring in shielded container and special vehicle. And SRTF is the first time being adopted in China, where various wastes that cannot be processed by nuclear island waste treatment system are volume-reduced by desiccating or supercompaction. SRTF is an independent facility that stays away from other buildings. Nuclear island wastes are verified and transferred in shielded container to appointed area in SRTF. SRTF is divided into waste processing area (including control access), laundry, and interim repository, and it processes wastes that are produced by itself including equipment exhaust gas, condensed solution, equipment cleaning water, and HEPA. These secondary liquid wastes shall either be sent back to chemical liquid waste treatment system or slot-discharged by evaluating their radioactivity, and the wastes thus occurred do not have to send back to nuclear island or other facilities. With its high density of processing, SRTF avoids overlapping equipment inside each single unit; therefore, costs concerning operation, management, and maintenance are greatly reduced.

2.2 Disposal of CPR1000 and EPR Radwaste

Radwastes from CPR1000 and EPR are mainly reusable radioactive liquid, disposed radioactive liquid, service liquid, gas that containing hydrogen and oxygen, spent resin, condensate solution, spent filter cartridge, and compressible and incompressible solid wastes.

2.2.1 Radioactive Liquid

Reusable liquid wastes refer to reactor coolants discharged from primary loop that are not contaminated by air and containing hydrogen and fission products. These coolants are reusable after systematic collecting and treatment. Disposed liquid wastes mean process drain, floor drain, and chemical liquid, which shall be collected, sorted, stored, filtered, demineralized or evaporated, and discharged with monitoring. Condensate solutions produced from evaporation shall be barreled after cementation.

Evaporation and condensation process refers to boiling radioactive liquid that contains volatile solvent (water) and nonvolatile material (fission product and inorganic salt) in evaporator. Part of the liquid shall be evaporated and exacted and be discharged, reused, or further treated according to its quality index after condensation and monitoring. Condensed residuals that are rich in radionuclide shall be stored or solidified.

Centrifuge technology witnesses its first application in Taishan EPR NPP, which has the benefit of without producing secondary waste.

2.2.2 Radioactive Gas

CPR1000 radioactive gas that contains hydrogen shall be discharged after a series of treatments, including condensation, storage (explosive-proof), decay, monitoring, and iodine removal by filtering and dilution. Gas that contains oxygen shall be discharged after heating and dehumidifying, iodine absorption, decay, and iodine removal by filtering.

EPR adopts active carbon delay bed and relied on active carbon's feature of transferring elements to reduce the decay activity of radioactive inertia gas.

2.2.3 Radioactive Solids

Radioactive solids can be divided into different categories by its characters, such as spent resin, concentrated solution, spent filter cartridge and other solids of strong radioactivity, compressible wastes (i.e., paper, plastics, clothes, gloves, working suit, and ventilation filter cartridge), and incompressible wastes (for instance, metal blocks used after repairing or changing, fittings, and metal tubes).

Spent resins and concentrated solutions have to be solidified, which can be divided into inside and outside categories (for detail, see Fig. 1 below).

Spent filter cartridge (dose rate higher than 2 msv/h) and other incompressible strong radioactive waste (such as metal blocks used after repairing or changing, fittings, and metal tubes) have to be treated by cementation.

Spent resin and spent filter cartridge can be directly stored in high-integrity container (HIC), which is a specially designed container with high strength, leak tightness, and chemical and thermal stability and can be loaded with radwastes that

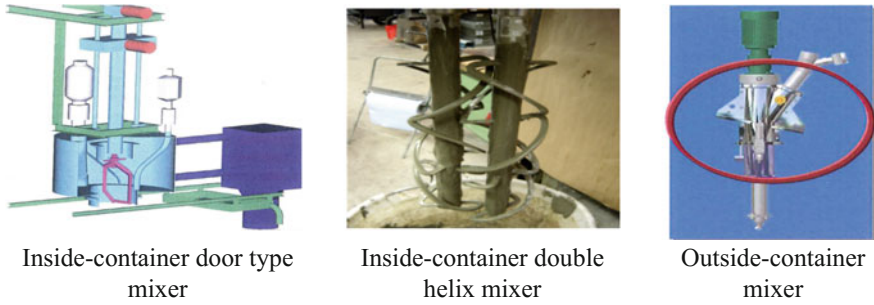


Fig. 1 Solidification inside and outside of the container [1]

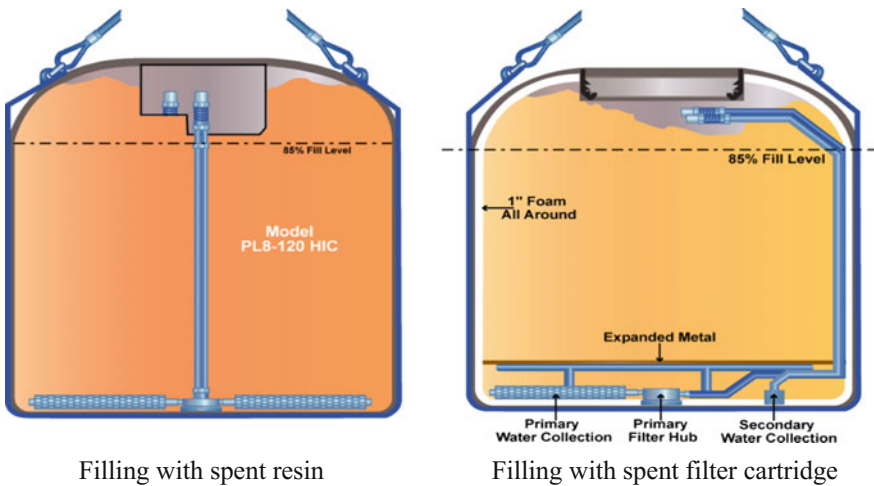


Fig. 2 High integrated container [2]

are not solidified. HIC is used to dispose radwastes such as spent resin and spent filter cartridge with dimension ranging from 0.23 to 8.5 m³ and is equipped with many internal structures and lifting devices. It is made from interlinked polyethylene and can prevent corrosion in shallow ground to improve its safety, and what's more, its storage life is longer than that of steel containers. HIC vault is fixed by threaded bolts. HIC is suitable for storing radioactive dry waste, cement cladded radioactive parts, dewatered spent rein, active carbon, etc. Details are shown in Fig. 2.

Compressible wastes (paper, plastics, clothes, gloves, working suit, ventilation filter cartridge, etc.) have to be sorted out in sorting station and then precompacted and supercompacted in a 200-L metal container. During supercompaction, the container has to be perforated to release the air contained. After supercompaction,

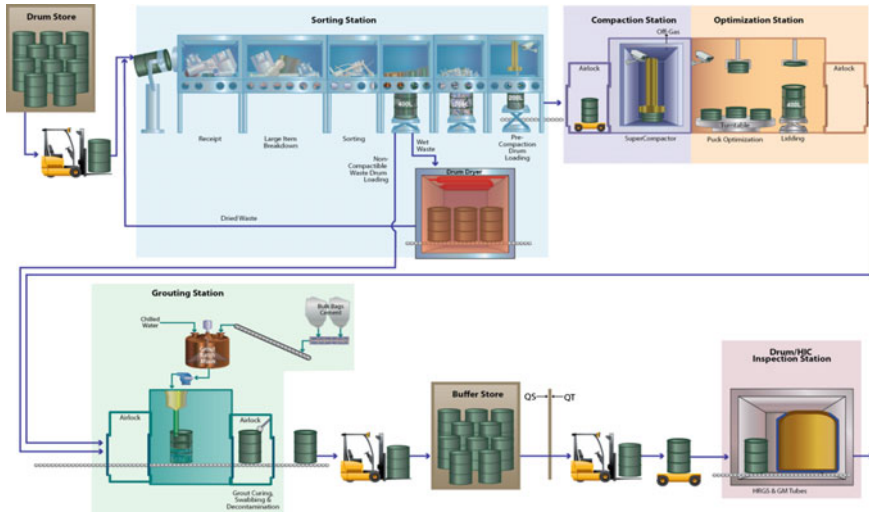


Fig. 3 Treatment of compressible waste [2]

pellets have to be measured by height, weight, and dose rate, which shall determine the allocation of pellets in 400-L metal containers for cementation (see Fig. 3).

3 Current Situation of Disposing Radwaste in Foreign NPPs

In the study, the treatment methods of liquid waste in foreign PWR NPPs used are ion exchange, membrane separation, evaporation, filtering, desiccation inside container, etc. In France, methods such as evaporation, ion exchange, filtering, and centrifuge are adopted; in Germany, evaporation, ion exchange, centrifuge, and desiccation inside container are adopted; in Japan, evaporation, ion exchange, filtering, and centrifuge are adopted.

Methods for treating gas in foreign PWR NPPs are compaction, storage (explosive-proof), decay, iodine absorption, iodine removal by filtering, dilution, active carbon delay bed absorption, heating and dehumidification etc.

There are many ways of disposing solid wastes in foreign PWR NPPs, which are cementation, HIC sealing, hot compaction and wet oxidation for spent resin, molten salt oxidation, microwaving, biodegradation, cementation, and burning. Plasma molten volume reducing technology uses thermal plasma fast pyrolyzes wastes and produces glassy inorganic. The gas it produced breaks down into atoms and simplest molecules, and most important of all, those toxic organics shall be reduced into nontoxic small molecules. In the case of NPP, radionuclides in low and intermediate solid wastes are fully clad in glassy slags and its product is in a

stable inorganic state. Plasma molten volume reducing technology has a high ratio of volume reduction with merits of stable product and free of secondary contamination, and it is widely accepted as one of the advanced technologies in the world.

4 Conclusion

To sum up, it is concluded that:

4.1 Disposal of Liquid Waste

Evaporation is mainly used in and out of China to treat liquid radwaste in PWR NPP; although filtering membrane is adopted, it is not matured yet for it brings the change of filter membrane and treatment of secondary waste.

4.2 Disposal of Gas

Active carbon absorption and decay shall be the mainstream technology. It adopts hydrogen oxygen recombiner, where nitrogen can be recycled and inertia gas shall be selectively absorbed by delay bed before discharge.

4.3 Disposal of Solids

Cementation is mainly used to dispose spent resin and concentrate, and it is divided into inside and outside mixing. Cementation of spent resin has problems such as uneven distribution and bulging.

Spent filter cartridge and waste pellets with high dose rates have to be cementated and sealed.

Metal containers shall gradually replace concrete containers.

HIC is loaded with solid waste and has long ensurence and good leakage tightness, which is suitable for dewatered resin and other wastes. However, material, manufacturing process, and product checking for HIC have to satisfy the relevant standards. For HIC package with high activity and surface dose rate, its lifting, transportation, storage, and ultimate disposal have to meet the national standards and regulations.

Thermal compaction and wet oxidation are also an option for treating spent rein. But the latter method risks explosion with the use of hydrogen peroxide, and the

oxidants are hard to control, what's more large quantities of secondary liquid waste have to be treated.

Compressible wastes (paper, plastics, clothes, gloves, working suit, low-dose filter cartridge, etc.) can be treated by compaction, cementation, and burying. However, burning is only in research phase. Plasma molten volume reducing has been put into actual use, while it does not embark on China yet.

In conclusion, radwastes are of complicate composition, and each corresponding treatment method is accompanied with defects. While in selecting the treatment method, we shall not only consider waste volume reduction, but also the safety and stability of ultimate product. By comprehensive consideration can we adopt the optimized solution, in order to produce truly clean energy from NPP.

References

1. The pictures from IRH Engineering, Westinghouse Electric Germany GmbH, AREVA GmbH.
2. The pictures from Energy Solutions, LLC.

Solidification of Simulated α -HLLW in Iron Phosphate Glass-Ceramics

Pan Sheqi, Wan Xiaogang, Xi Chengcheng, Su Wei, Zhang Hailing and Wang Yongpeng

Abstract Using iron boron phosphate glass to immobilize simulated α -HLLW has been studied. The results showed that sintering at a temperature of 930 °C, heating for 2 h, monazite-type crystal was detected only by XRD apparatus in the solidification. The samples containing different contents of simulated α -HLLW were measured by product consistency test (PCT) and showed the maximum pack capacity of up to 25% with a good chemical durability, and the normalized elemental mass release of Fe, P, and Ce is $28.10 \times 10^{-4} \text{g}\cdot\text{m}^{-2}\cdot\text{d}^{-1}$, $56.61 \times 10^{-4} \text{g}\cdot\text{m}^{-2}\cdot\text{d}^{-1}$, and $0.95 \times 10^{-4} \text{g}\cdot\text{m}^{-2}\cdot\text{d}^{-1}$, respectively.

Keywords α -HLLW · Iron phosphate glass · Solidification

1 Introduction

The spent fuel reprocessing will generate large quantities of high-level nuclear wastes, which need to be vitrified before deep geological disposal. Deep geological disposal is an appropriate method for the high-level radioactive waste disposal, whose purpose is to further isolate the waste from the biosphere system. In order to minimize the environmental impact of spent fuel discharged from nuclear power

P. Sheqi · W. Xiaogang · X. Chengcheng · S. Wei · Z. Hailing · W. Yongpeng (✉)
Institute of Materials, China Academy of Engineering Physics, Mianyang, China
e-mail: wangyongpeng@caep.cn

P. Sheqi
e-mail: pansheqi@caep.cn

W. Xiaogang
e-mail: wanxiaogan@caep.cn

X. Chengcheng
e-mail: xichengcheng@caep.cn

S. Wei
e-mail: suwei@caep.cn

reactors and the final volume of solidification matrix in the repository, TRPO (trialkyl phosphine oxide) extraction process was developed. With TRPO method, minor actinides and long-lived fission products containing little Sr and Cs can be separated from wastes and then be vitrified, making the radioactivity of original wastewater greatly decreased. Former high-level liquid wastes turn to be of low-intermediate level and short-lived wastes, which can be solidified by cement for future surface disposal. Borosilicate glass is widely used for vitrification of high-level nuclear wastes. However, borosilicate glasses are not a good option for vitrification of sulfate- or phosphate-bearing wastes as the problem of “yellow phase” often appeared in the vitrification melter, when sulfate or phosphate was present. Hence, waste loading of such glasses had to be lowered sharply, resulting in poor economy [1–4]. Meanwhile, iron phosphate glass is considered as a practical alternative for vitrifying such nuclear wastes not well suited for borosilicate glass due to its excellent resistance to water erosion, low viscosity under high-temperature melting conditions, and relatively low handling temperature. Iron phosphate glass has caught extensive attention since it was reported by Sales et al. in 1984. The chemical and thermal durability of iron phosphate glass would be both enhanced to some extent when appropriate amount of B_2O_3 was doped. In addition, the thermal neutron absorption coefficient for B_2O_3 was about two orders of magnitude higher than P_2O_5 . All these factors make iron phosphate glass more suitable to immobilize such high-level radioactive waste.

In this study, the iron phosphate glass vitrification technology for the main components of α -waste derived from TRPO extraction procedure was investigated, which would provide necessary fundamental data and technical support for the widespread application of such vitrification technology in practice.

1.1 Materials and Methods

1.1.1 Formula Design of Simulated High-Level Radioactive Waste

The main components of TRPO extracts can be seen in Table 1, which contains almost all actinide elements. Considering material source and safety during test, simulated high-level radioactive waste used did not contain neodymium, uranium, and transuranium elements, which were replaced by equal stoichiometric amount of cerium. According to the data listed in Table 1, the oxide contents of each element were also calculated stoichiometrically, and their respective mass fractions in our simulated high-level radioactive waste are listed in Table 2. The carefully weighed oxides were first stirred and powdered using ball mill and then dried before use.

Table 1 Main components of TRPO extracts

Components	Fe	La	Ce	Nd	Mo	Zr	TRU+U
Content (g/l)	0.34	0.5865	0.7755	2.038	0.5	0.01	1.83

Table 2 Oxide contents of each element in simulated high-level radioactive waste

Oxidation	Fe ₂ O ₃	La ₂ O ₃	CeO ₂	MoO ₃	ZrO ₂
Content/wt%	7.40	33.94	47.02	11.43	0.21

1.1.2 Specimen Preparation and Sintering

Simulated high-level radioactive waste and basic glass were firstly adequately blended at a proper ratio in mortars, then were pressed to form briquettes at 20 MPa with 5% polyvinyl alcohol (PVA) added as binders. The rough briquettes were powdered and sifted through 140-mesh sieve after drying for 24 h at 110 °C. Mixed with a certain amount of binders, the powdered briquettes were again pressed at 30 MPa to form specimen. Program temperature rise is used for specimen sintering. First temperature was raised at the rate of 1 °C/min until 500 °C, then kept at 500 °C for 5 h to remove the binders, then raised again at 3 °C/min until the required temperature and kept warm for certain time. Finally, the specimen was naturally cooled to room temperature.

1.1.3 Analytical Measurements and Calculations

The crystalline phase of samples was examined with X-ray diffraction (XRD) (Rigaku D/max IIIA Co., Japan) with Cu K α 1 radiation. Sample density (ρ , g/cm³) was measured using Archimedes method at 25 °C with distilled water as liquid medium. The chemical durability of samples were determined by the product consistency test (PCT, ASTM C-1285-02), procedures of which were as follows: Particles screened through mesh size of 100–200 (diameter, 75–150 μ m) were firstly washed several times with ethanol and deionized water under ultrasonic conditions and then dried according to the standard. About 3.0 g precisely weighted particles and 30 mL deionized water were placed in polythene bottles and dried in ovens with temperature controlled at 90 \pm 2 °C. Each element's mass concentration in the liquid after 7 days of erosion was measured using ultraviolet-visible spectrophotometry, and the normalized element mass release (LR_{*j*}, g m⁻² d⁻¹) was calculated according to the equation below:

$$LR_j = c_j/w_j \cdot (A_s/V) \cdot t$$

In the equation, c_j stands for the mass concentration of element j (mg L⁻¹ or g m⁻³); w_j , which was calculated based on the composition of the glass, stands for elemental mass fraction in the sample; A_s/V stands for the ratio between total surface of solid particles (A_s) and volume of erosion liquid (V), which was taken as 2000 m⁻¹ in consistence with PCT standard, while t stands for erosion time (d).

1.2 Results and Discussion

1.2.1 Sintering Temperature

XRD spectrograms of simulated radioactive waste with 20% waste loading obtained at different sintering temperatures were shown in Fig. 1. As shown, principal crystalline phase of monazite was detected in all solidification matrixes sintered over a relatively wide temperature range, indicating that the elements in simulated waste, like Ce, La, could exist steadily in the glass in the form of monazite, making such glass own a much better waste-holding stability than normal borosilicate glass [5].

When sintering temperature was raised from 800 to 950 °C, the XRD patterns of monazite in the solidification became clearer, with sharper peaks and fewer diffuse peaks. However, when sintering temperature was raised again over 1000 °C, part peaks for monazite appeared diffuse, revealing a decrease in specimen's crystallinity. With the further rise in sintering temperature, the growth and movement of crystals became faster. The initial crystals grew up quickly and blocked their adjacent crystals' growth, and the crystal–glass interface number was reduced, which would be unbeneficial for the formation of crystallite structure and cause structural defects in crystallite. Specimen's crystallinity under different sintering temperatures was calculated using MDI Jade 5.0 (Table 3). Hence, iron boron phosphate–monazite-type glass-ceramic solidified body should be sintered at 900–950 °C, according to XRD analysis and crystallinity calculation results.

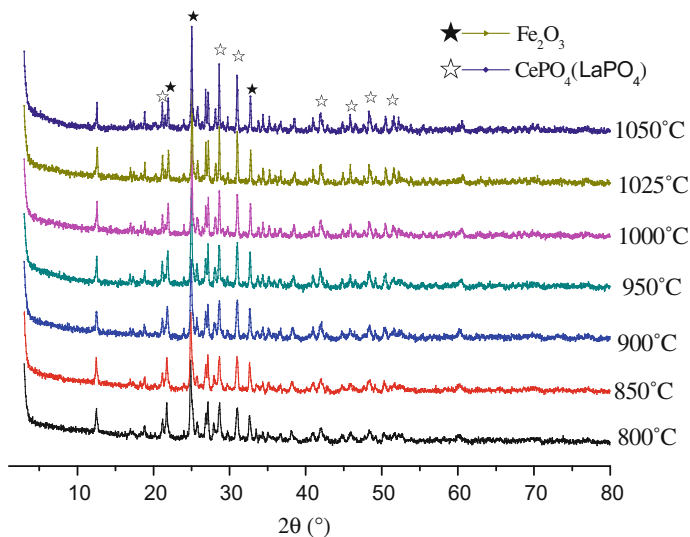


Fig. 1 XRD spectrograms of simulated radioactive waste with 20% waste loading obtained at different sintering temperatures

Table 3 Specimen's crystallinity under different sintering temperatures

Sintering temperature (°C)	800	850	900	950	1000	1025	1050
Crystallinity (%)	80.66	78.87	85.47	86.72	82.37	82.36	79.39

1.2.2 Holding Time

Holding time is another important parameter for sintering process. Prolonging holding time at certain sintering temperature would promote the growth of crystalline grains in component-fixed glass-ceramic. The crystalline grains would be more uniform in size, and overall structure and performance would be improved of the glass-ceramic. Figure 2 shows the XRD patterns of specimens produced at equal sintering temperature (950 °C) but different holding time, while the corresponding crystallinity results were listed in Table 4. The XRD patterns for monazite in each specimen in Fig. 2 were nearly the same, which was consistent with the crystallinity results. Hence, the holding time for specimen should be 1–2 h under such sintering condition since prolonging holding time would not bring better performance to glass-ceramic. In addition, prolonging holding time increased the occurrence of abnormal grain growth, which was also not economically feasible.

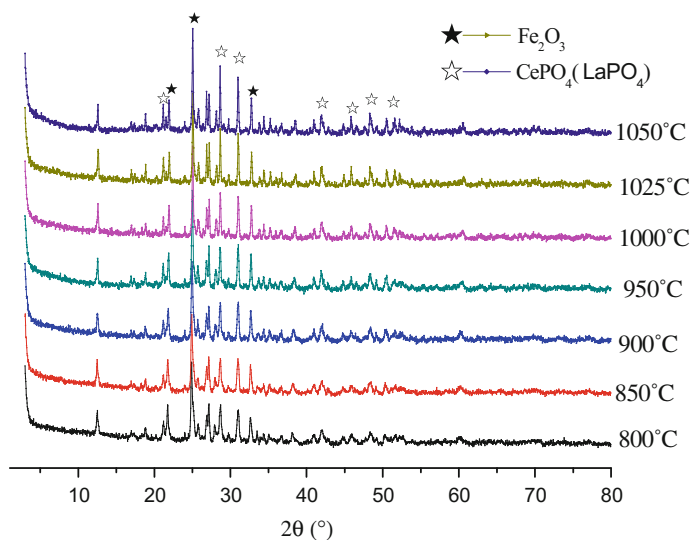


Fig. 2 XRD patterns of specimens produced at equal sintering temperature (950 °C) but different holding time

Table 4 Crystallinity results at different holding time

Holding time (h)	1	2	3	4	5
Crystallinity (%)	84.69	86.17	86.64	85.18	84.10

1.2.3 Parameter Optimization for Densification Process

Glass-ceramic solidification of high-level radioactive waste slurry was to make the vast majority of actinide elements enter into the lattice of ceramics, forming solid solution, while part of remaining actinide elements were enclosed by glass network. To achieve this aim, compact microstructure was obligatory and important for generated glass-ceramics, which required uniform grain size and uniform distribution of crystalline phase in glass phase. Three stages were experienced for specimen with set material components and sintering temperature along the sintering process, which were, respectively, shrinkage accelerating stage, shrinkage retarding stage, and shrinkage stagnating stage.

The bulk density variations of specimens obtained at different sintering temperatures and holding time were, respectively, illustrated in Figs. 3 and 4. As shown in Fig. 3, the bulk density of specimen firstly increased quickly with the rising of sintering temperature until 930 °C, then gradually decreased with further rising of sintering temperature (≥ 940 °C), indicating that crystallization temperature of specimen was lower than 940 °C. The formation of crystal hindered the movement of particles inside specimen and thus hindered further sintering and densification for specimen. As to the relationship between the bulk density and holding time, as shown in Fig. 4, the bulk density in general raised with holding time. The bulk density increased quickly when holding time was raised from 0.5 h to 1.5 h, while the rise in bulk density was largely mitigated as holding time was further increased (2–3 h) and was fairly smooth over time (3.5–4 h).

Fig. 3 Bulk density of specimen changes with sintering temperature

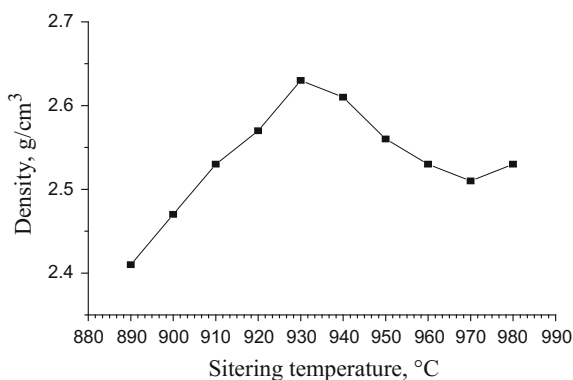


Fig. 4 Bulk density of specimen changes with holding time

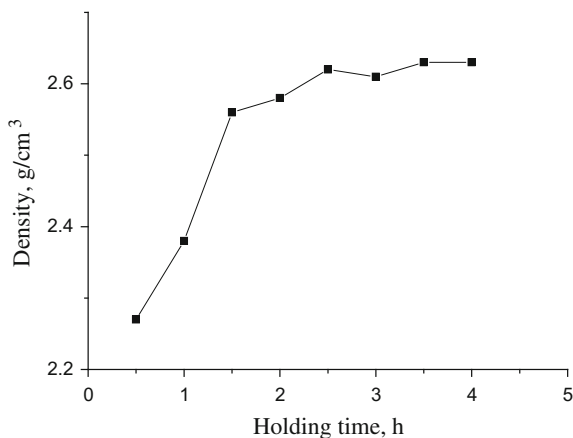


Table 5 PCT results after 7 days of soaking

Sample	Leaching rate ($\times 10^{-4}$)/g m ⁻² d ⁻¹		
	Fe	P	Ce
A	11.04	44.43	1.13
B	28.10	56.61	0.95
C	77.75	85.56	0.69
D	110.80	151.36	0.62

1.2.4 Pack Capacity for Simulated Wastes and Chemical Durability

The crystal phase change in the glass-ceramic solidified body together with the leaching rate of key elements was investigated when pack capacity for simulated wastes in solidified body was, respectively, 20, 25, 30, and 35 %. All the glass-ceramic solidified bodies were prepared with optimized process parameters, and relative results were summarized in Fig. 3 and Table 5.

Figure 5 shows the XRD patterns of part specimens. As shown, when pack capacity for simulated wastes in solidified body was 20%, the crystal phase in specimen was basically the single monazite phase; when pack capacity increased to 25%, ferric phosphate patterns began to appear, which was quite distinct as pack capacity further increased to 30%. The mole ratio of Fe to P in solidification matrix increased with the pack capacity for simulated wastes, which changed the structure of iron boron phosphate basic glass. The chemical durability of basic glass was weakened, and the main crystal phase in solidification matrix changes from single monazite phase to co-existent phase, including monazite and ferric phosphate. The results of normalized leaching rate of key elements (Table 5) also demonstrated that chemical durability of basic glass would be weakened with its rising pack capacity for simulated wastes since elemental mass release of Fe and P gradually increased. However, the content of element Ce in simulated wastes was still within the largest

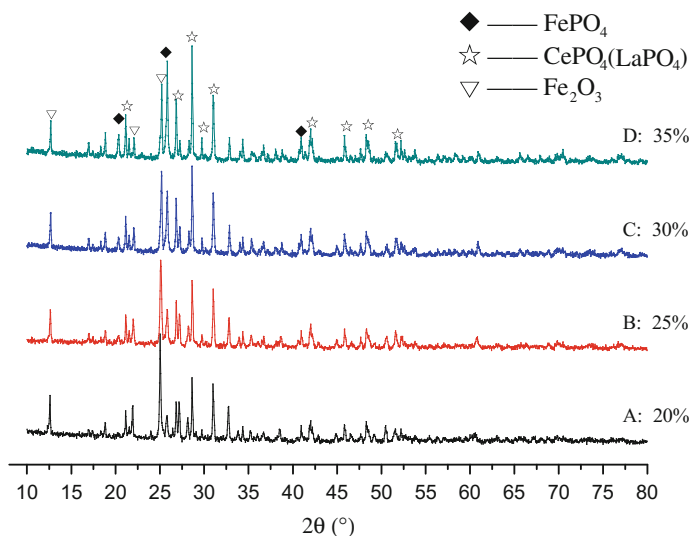


Fig. 5 XRD patterns of part specimens

pack capacity of such glass system [6], which could firmly “imprison” Ce and keep its leaching rate almost stable at 10^{-5} . Hence, the pack capacity for simulated wastes should be no more than 25% in order to obtain glass-ceramic solidification matrix of good performance.

2 Website

2.1 Website of PBNC2016

The website of PBNC2016 is <http://www.pbnc2016.org/>. For more information, please visit the website.

3 Conclusions

In this study, the simulated high-level radioactive wastewater generated from TRPO extraction process was solidified using iron boron phosphate glass, and its solidification parameters including sintering temperature, holding time, and waste pack capacity were investigated. Glass-ceramic solidification matrix with monazite as main crystal phase could be obtained at sintering temperature of 930 °C holding for 2 h. Elements La and Ce in simulated wastes were steadily enclosed in monazite

phase by solidification matrix. The recommended maximum pack capacity for simulated wastes was 25%. The solidification matrix showed good performance in chemical durability under proposed conditions and normalized leaching rate for simulated actinide element Ce could be kept at 10^{-5} .

Acknowledgments This work was supported by “Radiochemistry 909 Program” in China Academy of Engineering Physics (CAEP) and the NSFC (21407133).

References

1. W. Lutze, R.C. Ewing (Eds). Radioactive waste forms for the future [J]. North-Holland (Amsterdam), 1988:31.
2. Toshinori Okura, Tomoko Miyachi, Hideki Monma. Properties and vibrational spectra of magnesium phosphate glasses for nuclear waste immobilization [J]. Journal of the European Ceramic Society, 2006(26): 831–836.
3. C.P. Kaushik, R.K. Mishra, P. Sengupta, et al. Barium borosilicate glass—a potential matrix for immobilization of sulfate bearing high-level radioactive liquid waste [J]. Journal of Nuclear Materials, 2006, (358): 129–138.
4. Raman K. Mishra, Kumaran V. Sudarsan, Pranesh Sengupta, et al. Role of sulfate in structural modifications of sodium barium borosilicate glasses developed for nuclear waste immobilization [J]. Journal of the American Ceramic Society, 2008, 91(12): 3903–3907.
5. Bingham P A, Yang G, Hand R J, etc. Boron environments and irradiation stability of iron borophosphate glasses analysed by EELS [J]. Solid State Sciences, 2008, 10(9):1194–1199.
6. Liao Qi-long, Wang Fu, Pan She-qi, Liao Hua. Structure and chemical durability of Ce-doped iron borophosphate glasses [J]. Journal of Nuclear and Radiochemistry, 2010, 32(6): 336–341. (in chinese).
7. Song Chong-li. The concept flowsheet of partitioning process for the Chinese high level liquid waste [J]. Atomic Energy Science and Technology, 1995, 29(3): 201–209. (in chinese).
8. M.G. Mesko, D.E. Day, B.C. Bunker. Immobilization of CsCl and SrF₂ in iron phosphate glass [J]. Nuclear and chemical Waste Management, 2000, Volume 20(4):271–278.
9. Cheol-Woon Kim, Delbert E Day, Immobilization of Hanford LAW in iron phosphate glasses, Journal of Non-Crystalline Solids, Volume 331, Issues 1–3, 1 December 2003, Pages 20–31.
10. B.C. SALES, L.A. BOATNER. Lead-Iron Phosphate Glass: A Stable Storage Medium for High-Level Nuclear Waste [J]. Science, 1984, 226(4670):45–48.
11. Pan She-qi, Su Wei. Immobilization of HLLW in iron phosphate glasses [J], Engineering Materials, 2011, 10(4): 76–79. (in chinese).
12. Wang Fu, Liao Qi-long, Pan She-qi, Liao Hua. Effect of Na₂O on structure and properties of iron borophosphate glasses [J]. Radiation Protection, 2010, 30(4): 208–213. (in chinese).
13. Liao Qi-long, Wang Fu, Pan She-qi, Liao Hua. Structure and chemical durability of Ce-doped iron borophosphate glasses [J]. Journal of Nuclear and Radiochemistry, 2010, 32(6):336–341. (in chinese).
14. Yong He, Y.J. Lü, Q. Zhang, Characterization of monazite glass-ceramics as wasteform for simulated α -HLLW [J]. J. Nuclear Materials. 376 (2008) 201–206.

Study on Effect of Density Heterogeneity for Nuclear Waste Drum Samples in Segmented Gamma Scanning Analysis

Honglong Zheng, Xianguo Tuo, Shuming Peng, Rui Shi
and Chao Deng

Abstract With a segmented gamma scanning (SGS) equipment, the non-destructive transmission and emission measurement are experimented for eight radioactive waste samples with heterogeneous activity and matrix distribution. Radioactivity of both ^{137}Cs and ^{60}Co sources in those samples is calculated through a self-absorption correction method. The results show that the relative deviations between corrected and actual radioactivity of eight samples are all less than 5%. Then the effect of density heterogeneity for nuclear waste drum samples was studied, indicating that the SGS analyzed radioactivity will be deviated from its actual radioactivity along with different density of samples. With filling material density heterogeneity and average density of samples increasing, the relative deviations between corrected and actual radioactivity trend to increase gradually. The heterogeneity immediately determines the scale of relative deviations in SGS analysis. The density of samples, the energy and transmission ability of gamma ray are main factors of the deviation in SGS analysis.

Keywords Segmented gamma scanning · Radioactive waste · Density heterogeneity · Linear attenuation coefficient · Self-Absorption correction

1 Introduction

The segmented gamma scanning (SGS) technique is being widely employed to perform non-destructive assay of the radioactive waste drum. The SGS technique can quickly identify the kind of radioactive nuclide and the radioactivity of the drum. In SGS, a radioactive waste drum is rotated in front of a collimated detector. At each segment, the detector takes a spectrum. After all segments of the drum are

H. Zheng · S. Peng
China Academy of Engineering Physics, Mianyang 621900, Sichuan, China
e-mail: 965998755@qq.com

H. Zheng · X. Tuo (✉) · R. Shi · C. Deng
Sichuan University of Science and Engineering, Zigong 643000, Sichuan, China

detected, the radioactivity of the drum is calculated. In the early 1970s, Parker et al. [1] of Los Alamos National Laboratory (LANL) had begun to research the SGS technique and Espartero [2] applied it into the field of the low radioactive waste measurement. In the 1990s, Lu [3], Zhu [4], Cao [5] and some other Chinese researchers began to research the SGS technique. With the self-correction factors obtained by SGS experimental measurement, the contents of the uranium and the plutonium were analyzed in radioactive residues and wastes based on the SGS technique. Xu [6] has designed a basic model of standard source for the radioactive waste drum formed with rotating the waste drum in which several linear sources were put. Combined the Monte Carlo simulation with the experimental measurement, the effect of radial heterogeneity in SGS analysis was studied by Wang [7].

The deviation of SGS analysis consists of deviation about radial or axial heterogeneity of samples and axial deviation caused by the stratified strategy. It could reduce the deviation of analysis and improve the accuracy for a particular SGS system that adopted the suitable stratified strategy particularly [8]. This work discusses the problems for different density heterogeneity on a specific sample segment.

Based on the basic assumption that the matrix and the activity are uniformly distributed in each segment, the classic model of SGS is built. Although the heterogeneity of the matrix and the activity could be reduced through rotating measurement of samples, it still does not satisfy with the basic assumption of model completely. The purpose of this work is to explore the effect of different density heterogeneity and position migration of emission source in SGS analysis for nuclear waste drum.

2 Principle

2.1 Transmission Measurement

According to the Beer-Lambert law [9], a parallel photon beam with energy E and intensity $I_0(E)$ penetrates through a material of thickness x in Eq. (1) as follows:

$$I(E) = I_0(E) \cdot \exp[-\mu(E) \cdot x] \quad (1)$$

where $I(E)$ is the intensity of transmitted photon and $\mu(E)$ is the linear attenuation coefficient. Because the count of every channel can be recorded in experimental gamma-ray spectrum, Eq. (1) transforms to Eq. (2):

$$N(E) = N_0(E) \cdot \exp[(-\mu(E) \cdot x)] \quad (2)$$

where $N(E)$ and $N_0(E)$ are the peak net count corresponding to energy E in the spectrum obtained with the empty and filled sample, respectively. The linear

attenuation coefficient $\mu(E)$ corresponded to each energy E is derived from $N(E)$ and $N_0(E)$ in Eq. (3) as follows:

$$\mu(E) = -\frac{1}{x} \cdot \ln \left[\frac{N(E)}{N_0(E)} \right] \quad (3)$$

Because $\mu(E)$ is related to energy of gamma ray, it is recommended to produce a fitted curve between the energy and the linear attenuation coefficient. Using this curve, the linear attenuation coefficient of gamma ray could be easily obtained for most of samples to be tested.

2.2 Emission Measurement

The emission measurement problems of SGS could be described with Eqs. (4)–(6) as follows:

$$D(E) = F(E) \cdot S(E) \quad (4)$$

$$F(E) = \varepsilon(E) \cdot A(E) \quad (5)$$

$$A(E) = \exp[-\mu(E) \cdot R] \quad (6)$$

where $D(E)$ is the detector's counting rate of sample, $F(E)$ is attenuation correction efficiency, $S(E)$ is the radioactivity of sample, $\varepsilon(E)$ is the detection efficiency, $A(E)$ is the self-absorption correction factor, R is the radius of sample. According to the fitted curve between the energy and the linear attenuation coefficient from transmission measurement, $\mu(E)$ of emission gamma ray could be obtained. Radioactivity of sample could be calculated as Eq. (7):

$$S(E) = \frac{D(E)}{\varepsilon(E) \cdot \exp[-\mu(E) \cdot R]} \quad (7)$$

3 SGS System

3.1 The Description of System

The fitted curve between the energy and the linear attenuation coefficient could be obtained through carrying out with rotating transmission scanning using SGS system. The self-absorption effect of sample could be corrected by the linear attenuation coefficient of emission gamma ray determined with this fitted curve. Radioactivity of sample could be determined through the experimental

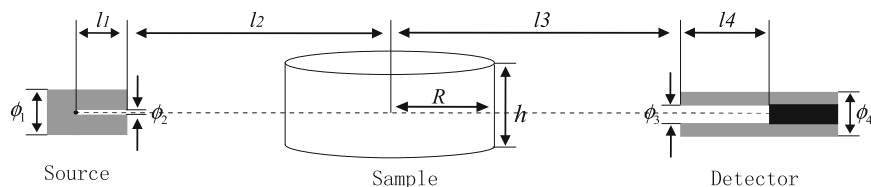
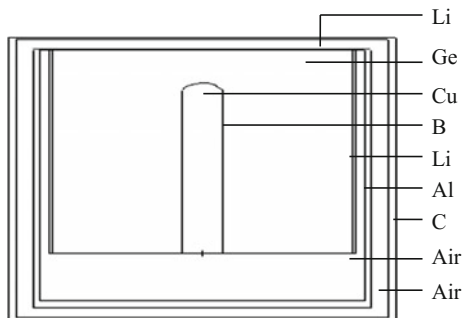


Fig. 1 Model of system

Fig. 2 Structure of HPGe detector



measurement and the self-absorption correction calculation. The model of SGS system is presented in Fig. 1.

The SGS system consists of the transmission source, sample and the detecting section as shown in Fig. 1. The length of transmission source collimator l_1 is 15 cm. Distance from the transmission source collimator's surface to the center of sample l_2 is 68.5 cm. Distance from the detector collimator's surface to the center of sample l_3 is 97 cm. The length of detector collimator l_4 is 18.5 cm. The height of sample h is 20 cm. The radius of sample R is 28 cm. The external diameter of transmission source collimator ϕ_1 is 19 cm. The internal diameter of transmission source collimator ϕ_2 is 1 cm. The internal diameter of detector collimator ϕ_3 is 8.7 cm. The external diameter of detector collimator ϕ_4 is 19 cm.

The electrical refrigeration P-type coaxial HPGe detector is used, and its structure is shown in Fig. 2. The diameter of the HPGe crystal is 7 cm, and its length is 8.26 cm. The diameter of cold finger copper is 0.9 cm and its length is 6.9 cm, the high voltage is positive 2600 V, operating temperature is 100 K, and the range of measured energy is from 4 keV to 10 MeV.

3.2 Samples

To explore the effect of different density heterogeneity for the nuclear waste drum samples in SGS analysis, several materials of different density are selected to correspond with actual contents of nuclear waste in the drum. Parameters of materials are presented in Table 1.

Table 1 Parameters of materials

Materials	Density (g.cm ⁻³)	Size (mm)
Hollow polyethylene	0.281	50 × 50 × 50
Solid polyethylene	1.037	50 × 50 × 50
Concrete	2.017	185 × 90 × 45
Glass fragments	1.438	Φ110 × 150
Fiber	0.206	Φ100 × 200
Plastics	1.411	160 × 160 × 85
Aluminum	2.762	150 × 100 × 60
Water	1.000	57 × 57 × 170

Table 2 Contents of eight samples

Number of sample	Contents
1#	Hollow polyethylene
2#	Solid polyethylene
3#	Solid polyethylene, glass fragments, plastics, water
4#	Hollow polyethylene, solid polyethylene, water
5#	Hollow polyethylene, solid polyethylene, water, glass fragments, plastics
6#	Hollow polyethylene, solid polyethylene, water, glass fragments, plastics, Concrete
7#	Hollow polyethylene, solid polyethylene, water, glass fragments, plastics, Concrete, Aluminum
8#	Hollow polyethylene, solid polyethylene, water, glass fragments, plastics, Concrete, Aluminum, Fiber

Using the several materials in Table 1 and grouping them with different methods, the eight samples of different density heterogeneity are built in SGS experimental measurement. The number and the actual contents of samples are presented in Table 2. The sources consist of ¹⁵²Eu(2.857 × 10⁸ Bq), ¹³⁷Cs(3.258 × 10⁵ Bq) and ⁶⁰Co(1.789 × 10⁵ Bq).

4 Results and Discussion

4.1 The Linear Attenuation Coefficients

Through rotating transmission scanning of the eight samples, the linear attenuation coefficients of different energy gamma ray are calculated with Eq. 3. The characteristic curves between the energy and the linear attenuation coefficient are fitted by the exponential function as shown in Fig. 3.

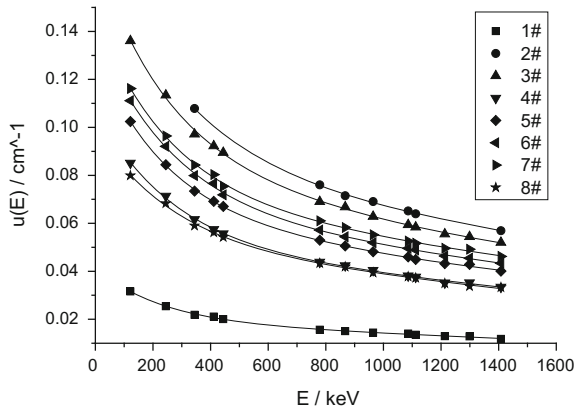


Fig. 3 Linear attenuation coefficient of gamma ray

Table 3 Linear attenuation coefficients of emission gamma ray

Energy (keV)	Linear attenuation coefficients (cm ⁻¹)							
	1#	2#	3#	4#	5#	6#	7#	8#
661.661	0.016898	0.081607	0.074695	0.047108	0.056604	0.061245	0.064947	0.046362
1173.238	0.013251	0.062565	0.057073	0.036684	0.044180	0.04758	0.050795	0.036133
1332.513	0.012402	0.058652	0.053414	0.034404	0.041540	0.044667	0.047768	0.033809

Because the sample 2# is constituted by the solid polyethylene and its thickness is large, it makes the corresponded gamma-photon can not be detected by HPGc detector. The linear attenuation coefficients of low-energy gamma ray of 121.7824 keV and 244.692 keV are lacked from characteristic curve of sample 2# shown in Fig. 3. For intermediate-energy gamma ray of 411.115, 443.976, 1212.95 and 1299.124 keV, because their respective emission branching ratios are 2.2, 3.04, 1.38 and 1.6%, they are so low that the counts of gamma-photon into detector are too little in the same transmission measurement time and a characteristic peak can not be presented. So the linear attenuation coefficients of those four energies gamma ray are lacked. Because the sample 1# is constituted by hollow polyethylene and its density is too low, it makes the lower linear attenuation coefficients than others.

For the emission gamma ray of 661.661, 1173.238 and 1332.513 keV, the linear attenuation coefficients could be determined by those fitted characteristic curves shown in Table 3.

4.2 Effect of Density

Radioactivity of samples could be determined through self-absorption correction calculation with Eq. 7. The correction radioactivity of the eight samples for

Table 4 Results of self- absorption correction of the eight radioactive samples

Number of samples	Self-absorption correction factors			Correction radioactivity (Bq)		
	661.661 keV	1173.238 keV	1332.513 keV	661.661 keV	1173.238 keV	1332.513 keV
1#	0.623040	0.690025	0.706624	3.176×10^5	1.799×10^5	1.804×10^5
2#	0.101774	0.173458	0.193543	3.163×10^5	1.802×10^5	1.802×10^5
3#	0.123507	0.202292	0.224116	3.194×10^5	1.812×10^5	1.810×10^5
4#	0.267396	0.358025	0.381627	3.289×10^5	1.827×10^5	1.837×10^5
5#	0.204966	0.290242	0.312510	3.392×10^5	1.844×10^5	1.849×10^5
6#	0.179989	0.263885	0.286311	3.372×10^5	1.851×10^5	1.862×10^5
7#	0.162266	0.241168	0.262500	3.387×10^5	1.852×10^5	1.869×10^5
8#	0.273040	0.363592	0.388038	3.392×10^5	1.841×10^5	1.868×10^5

661.661, 1773.238 and 1332.513 keV is presented in Table 4, and the relative deviations between corrected and actual radioactivity are shown in Fig. 4.

The relative deviations between corrected and actual radioactivity are less than 5% in eight samples of different density heterogeneity. With increasing of filling material density heterogeneity, the corrected radioactivity of samples and the relative deviations trend to increase gradually. It indicates that density heterogeneity determines the relative deviations directly in SGS analysis. Therefore, it is very important for reducing analysis deviation that known materials composition and distribution in the samples.

4.3 Effect of Position Migration

Figure 5 shows that the emission source is placed with equidistant migration ($d = 3.25$ cm) from the center to the border in the four samples 4# (0.541 g.cm^{-1}), 5# (0.636 g.cm^{-1}), 6# (0.684 g.cm^{-1}) and 7# (0.724 g.cm^{-1}). Eight distances from the center of sample to source, respectively, are 0, 3.25, 6.5, 9.75, 13, 16.25, 19.5, 22.75 cm. (a): Side view, (b): Vertical view.

The corrected activity of four samples for different emission source migration position is shown in Fig. 6. The density of sample 4# is low so that its corrected radioactivity is changed less in different migration position. For 661.661 keV, with average density and distance increasing gradually, the corrected radioactivity of samples 5#, 6# and 7# is obviously rising. The average density of samples is greater; the relative deviations between corrected and actual radioactivity seriously increase more. For 1173.238 and 1332.513 keV, because of their high energy and strong transmission ability, corrected activity has a rising trend but not obvious. Therefore, the density of samples, the energy and transmission ability of gamma ray are main effect factors of deviation in SGS analysis. It provides an effective idea to reduce the analysis deviation by reducing sample's size or radius suitably and measuring low-density sample.

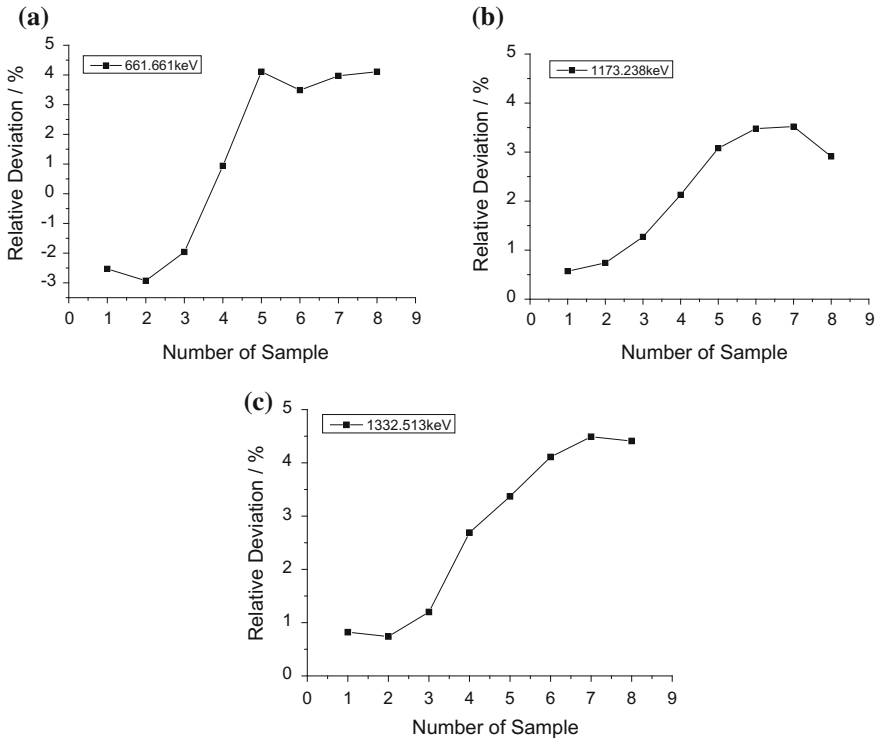
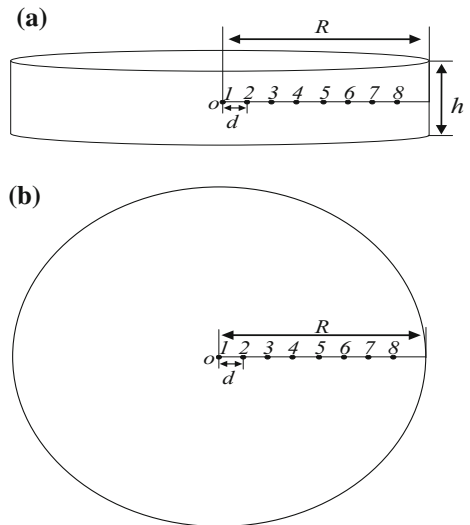


Fig. 4 Relative deviations between corrected and actual radioactivity of 661.661 keV (a) 1173.238 keV (b) and 1332.513 keV (c)

Fig. 5 Position migration of source



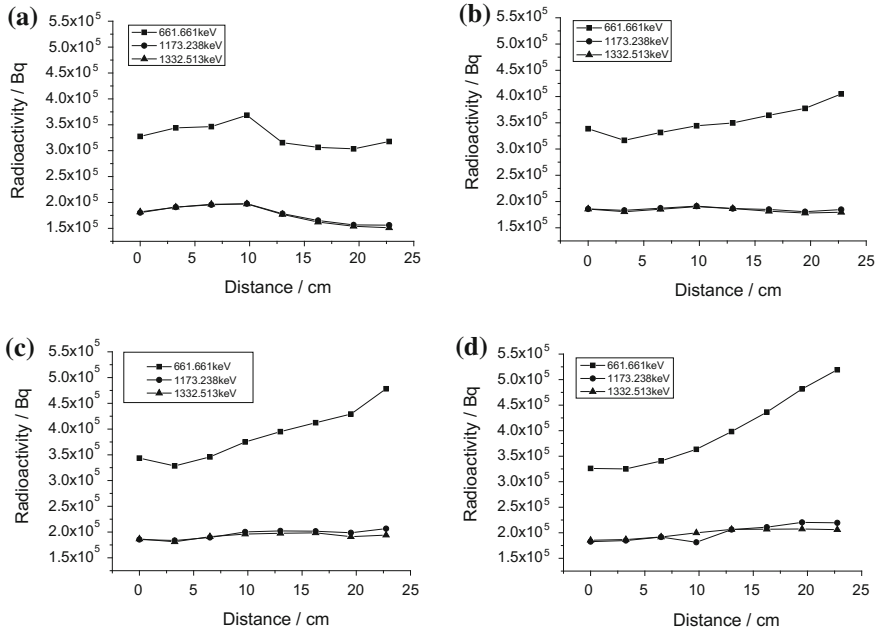


Fig. 6 Self-absorption correction results of samples 4# (a), 5# (b), 6# (c) and 7#(d)

5 Conclusions

The effect of deviation is studied in SGS analysis for different density heterogeneity nuclear waste sample segment. With filling material density heterogeneity and average density of samples increasing, the relative deviations between corrected and actual radioactivity trend to increase gradually. This method is suitable for low-density samples, and self-absorption correction analysis accuracy can be improved by reducing density of sample appropriately.

With source migrated from the center to the border in the samples, the relative deviations between corrected and actual radioactivity trend to increase gradually. The density of samples, the energy and transmission ability of gamma ray are main factors of deviation in SGS analysis. It provides an effective idea to reduce the analysis deviation by reducing sample's size or radius suitably and measuring low-density sample.

In order to improve the accuracy of the drum analysis, the tomographic gamma scanning (TGS) technique based on SGS has been put forward to analyze the nuclear waste drum [10, 11]. But considering with complexity of the TGS scanning measurement and the analysis method, we may need to explore another simple and effective method.

Acknowledgments Supported by the National Science Fund for Distinguished Young Scholars of China (No.41025015).

References

1. Parker J L. The use of calibration standards and the correction for sample self attenuation in gamma-ray nondestructive assay. New Mexico(USA): Los Alamos National Laboratory, 1984.
2. Espartero A G, Pina G, Suarez J A. Development and application of a radioactivity characterization system for low-level radioactive waste. *Nuclear Instruments and Methods in Physics Research A*, 1999, 422: 790–794.
3. Lu F, Cao B, Xin B, et al. Assay of the uranium plutonium content in process residues and wastes using the correction for sample self attenuation in segmented gamma scanning system. *Atomic Energy Science and Technology*, 1998, 32: 445–450.
4. Zhu R B, Tan Y J, Yuan X X, et al. Development of a segmented gamma-ray scanning system. *Atomic Energy Science and Technology*, 1994, 28: 16–25.
5. Lv F, Cao B, Xin B, et al. Research of small-size high resolution gamma-ray in-situ measurement instrument. Bei Jing: China Institute of Atomic Energy, 1994.
6. Xu L J, Ye H S, Zhang W D, et al. Design of reference radioactive source of waste drum used in calibration of segmented gamma scan device. *Nuclear Techniques*, 2015, 38: 050502.
7. Wang Z Q, Zong B, Hao Q, et al. Study on effect of radial-heterogeneity in segmented gamma scanning analysis. *Atomic Energy Science and Technology*, 2012, 46: 103–108.
8. Gao Q, Wang Z Q, Wang Y B, et al. Wedge-disturbing effect of segmented gamma scanner. *Atomic Energy Science and Technology*, 2011, 45: 211–216.
9. Parnis J K, Oldham K B. Beyond the beer–lambert law: the dependence of absorbance on time in photochemistry. *Journal of Photochemistry and Photobiology A*, 2013, 267: 6–10.
10. Xiao X F, Xia Y H, Lu F, et al. Tomographic gamma scanning for nondestructive assay of heterogeneous sold radioactive waste in drum. *Radiation Protection*, 2001, 21: 1–10.
11. Zhang Q H, Li F, Hui W H, et al. Research on tomographic gamma scanning technique. *Science China Phys, Mech & Astron*, 2010, 40: 983–991.

Study on In-Drum Drying Technology of Waste Concentrates

Liang Dong

Abstract The aim was to achieve the radioactive waste minimization in nuclear power plants by the treatment technology that can decrease the volume of waste concentrates, and the technological process of in-drum drying and the in-drum drying prototype device have been developed based on the investigation and survey, bench tests, and pilot experiments. Performances of in-drum drying of simulated waste concentrates are studied by the prototype device, in which boron concentrations are around 44,000 ppm and 30,000 ppm. The performances evaporated velocity of moisture, humidity and character of drying product, volume reduction ratio, and efficiency of decontaminate. The control parameters are optimized, and the prototype device is improved. The device has been improved, which is constituted with storage tank that maintains temperature by hot water, pneumatic diaphragm pump that transmits concentration, metering tank that can control the concentration volume of adding, infrared heater that controls temperature by adjusting power, jet pump that produces negative pressure, and pipe bundle condenser that condensates steam. The results show that average evaporated velocity of moisture can be attained as 5.94 kg/h, humidity of drying product is under 1.6% that meets anticipated target, character of drying product is contented demand, and the volume reduction ratio is around 5.25; treatment simulated waste concentrates whose boron concentration is around 44,000 ppm at the condition of heat temperature of 170 °C, small negative pressure in drum, adding 170 L concentration at first time, and maintaining high liquid level. It can be seen that the simulated concentrates can be disposed by the in-drum drying prototype device, and the technological targets can be met. Furthermore, the achievements of this study have been appraised in leading domestic level by China National Nuclear Corporation.

L. Dong (✉)

China Institute for Radiation Protection, Taiyuan 030006, Shanxi, China
e-mail: jianghong@cnpe.cc

Keywords Simulated waste concentrates · In-drum drying · Water evaporation rate · Volume reduction ratio · Humidity

Radioactive concentrate of nuclear power plants refers to the produces of evaporator during treatment of radioactive liquid waste. Generally, it was solidified by cement solidification technology in most of the nuclear power plants [1–3], but the volume of solidification product increased, which is not in conformity with the principle of radioactive waste minimization, also increased the subsequent expenses. The volume reduction treatment technology, such as in-drum drying technology, has been carried out in many countries [4–19].

The concentrate in-drum drying equipment had been designed and constituted by China Institute for Radiation Protection (CIRP) in 2013 depending on the literature review and a series of test and test conditions [20]. The simulation concentrate in-drum drying treatment experiments by this equipment had been done, and reasonable control parameters were researched. Then, the step for the improvement of equipment was carried on.

1 Introduction of In-Drum Drying Process

There are many workshops that research in-drum drying equipment in various countries, including Germany, USA, and France.

Though the heating mode of in-drum drying equipment that were studied is not identical, its principle is consistent. The liquid waste that was filled in drum is heated by heat energy, then the water of liquid waste becomes steam; the solid waste stayed in drum as waste sent repositories, or further development [11]. Concentrate in-drum drying process is as shown in Fig. 1.

Fig. 1 Scheme of concentrate in-drum drying process

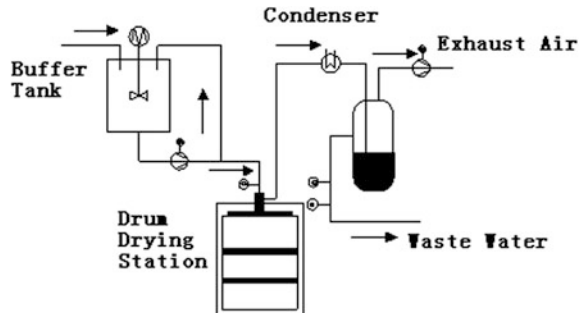


Table 1 Compositions of the simulated concentrates

Simulated concentrate (ppm)	H ₃ BO ₃ (g/L)	NaOH (g/L)	NaNO ₃ (g/L)	Na ₃ PO ₄ (g/L)	CoCl ₂ (μg/L)	SrCl ₂ (μg/L)	CsCl (μg/L)	H ₂ O (g/L)
44,000	307.2	45.7	100.0	33.3	131.0	79.0	106.0	732.1
30,000	200.0	30.0	66.0	22.0	131.0	79.0	106.0	833.0

2 Pre-study on Concentrate In-Drum Drying Treatment

2.1 Bench Test Research [21]

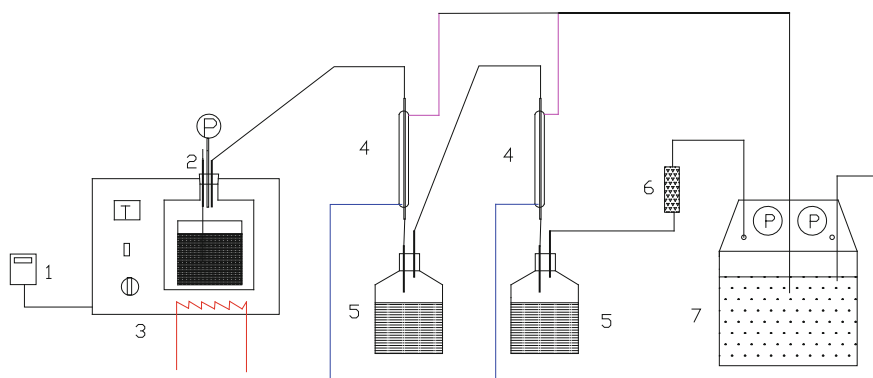
On the basis of the research, in order to understand the change of concentrate properties during the in-drum drying process, bench test that treats simulation concentrate (see Table 1) had been done as shown in Fig. 2.

Research results show that the in-drum drying technology can treat simulation concentrate, with the liquid volume reduction of the dry product as shown in Fig. 3; volume reduction ratio is about 4.25 after drying the simulated concentrate whose moisture content is 70.7%; and the drying rate can be improved by the increase of the heating temperature and vacuum degree.

2.2 Middle Test Research [22]

On the basis of bench test, the in-drum drying pilot equipment was established (Fig. 4), the middle test research for simulation concentrate (see Table 1) has been done, and the product is shown in Fig. 5.

The results showed that the in-drum drying pilot equipment treat the simulating concentrate, the process of concentrate in-drum drying is feasible, volume reduction

**Fig. 2** Sketch of bench test unit

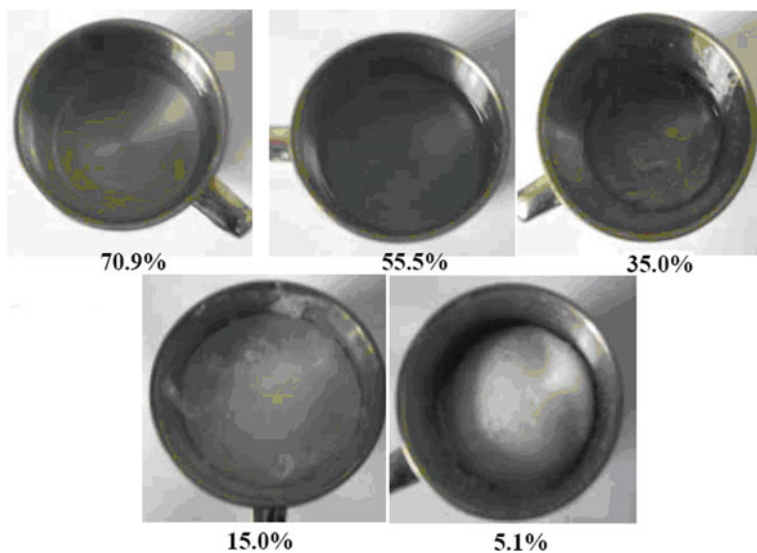


Fig. 3 Products of bench test

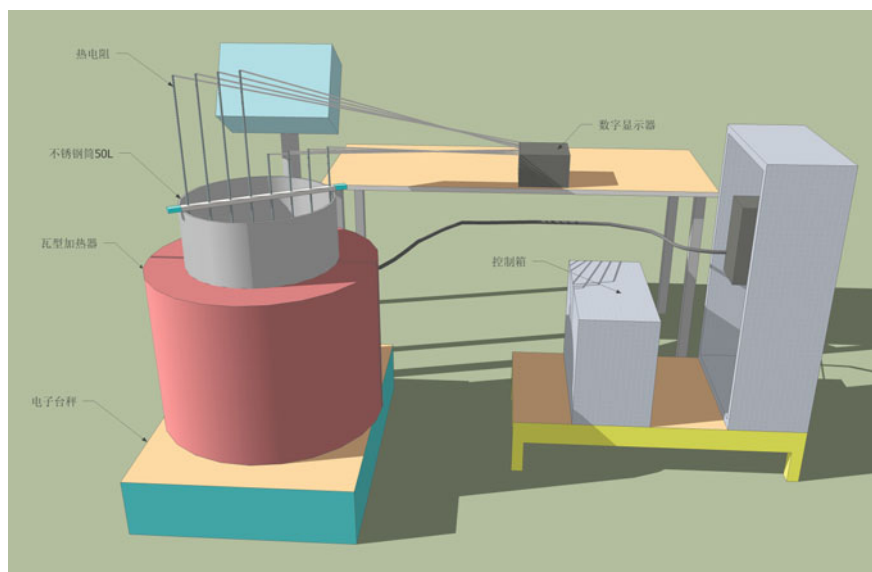


Fig. 4 Sketch of pilot equipment

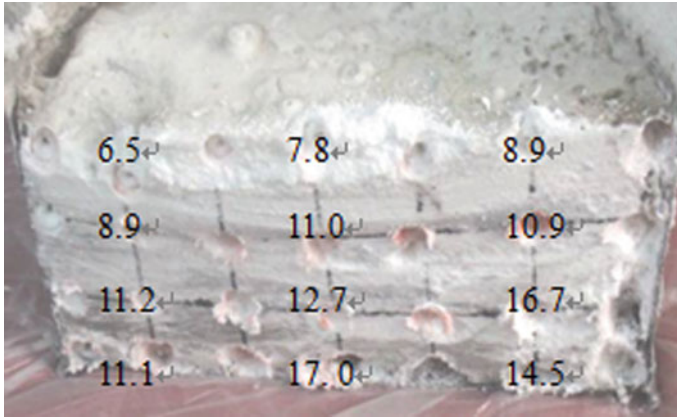


Fig. 5 Products of pilot experiment

ratio of dry product can reach 4.0, and the average moisture content of dry product is less than 15%.

3 The Establishment and Debugging of the Prototype Device [20]

The in-drum drying prototype device (200 L) of concentrate as shown in Fig. 6 was designed and constructed based on the above research. The details are described in the literature [20].

Device for the single machine debugging, the unit testing, and the whole process debugging of prototype device were completed times without number, the results show that the operation of In-drum drying prototype device (200 L) of concentrate is stable and the interrelated parameters meet the design requirements. Thereby, the experiment condition is contented.

4 Experimental Study on the Prototype Device

The object of experimental study on the prototype device is simulation concentrate that is shown in Table 1.



Fig. 6 The in-drum drying prototype device of concentrates

4.1 Procedure of Experimental

Process of simulated concentrate in-drum drying is shown in Fig. 7. A number of simulated concentrates were injected in the drum after the device is ready. The experiments were performed under the different operation parameters. During the trial, the level of concentrate in drum was kept in a high value, the quality of condensate was measured and sampled interval is 1 h; 15 L simulated concentrate was filled in drum when the volume of collected condensate has reached around 15 L, when the moisture content of production in theory or the rate for condensate collection was achieved the requirements the heating was stopped, the production was treated and analyzed after cooling.

4.2 The Determination and Calculation of Relevant Indicators

(1) Rate of evaporation

Drying stage rate of evaporation was characterized as the quality of condensed water collected per hour.

Fig. 7 Process of concentrate in-drum drying experiment

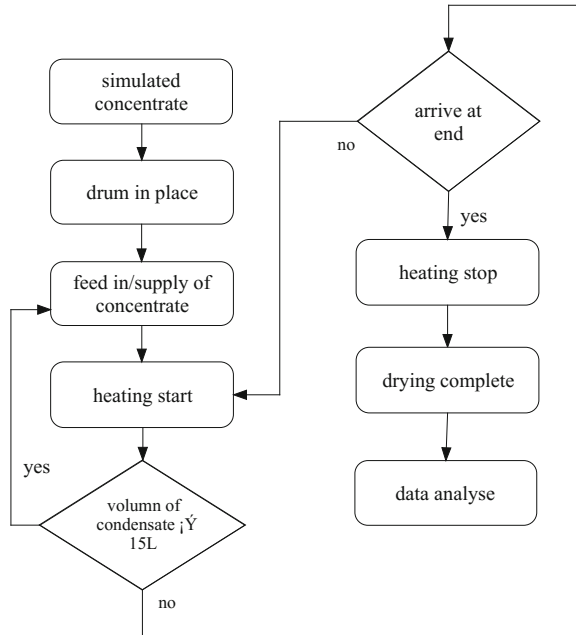
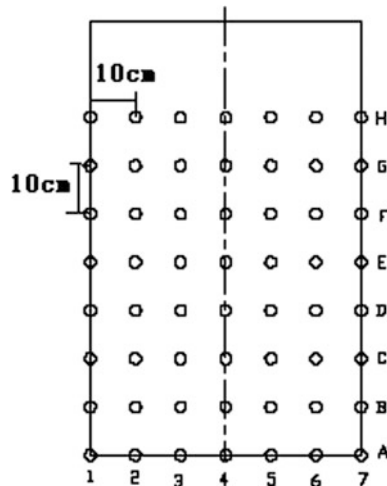


Fig. 8 The sampling point distribution for humidity analysis



- (2) Moisture content of production
The products were slit along the axial direction, then sampling and moisture content testing are shown in Fig. 8.
- (3) Volume reduction ratio
Volume reduction ratio = volume of concentrates treated (L)/volume of product (L).

4.3 The Conditions of Experiments

The experiment of simulated concentrate in-drum drying was conducted nine times, its control parameters are shown in Table 2, and the experimental results are shown in Table 3.

Table 2 The conditions of each experiment

Condition	Temperature of heater (°C)	Control mode of heating	Control mode of level	Total of drying (L)
No. 1	175/175/175	On-off	Initially 170 L, then 15 L supply while level falls 70 mm	680 (44,000 ppm)
No. 2	160/140/110	On-off		650 (44,000 ppm)
No. 3	150/160/160	On-off		730 (44,000 ppm)
No. 4	250/250/250	On-off		1000 (30,000 ppm)
No. 5	250/250/500	On-off		1000 (30,000 ppm)
No. 6	250/250/450	On-off	Initially 170 L, then XL supply while XL condensates have been collected ($X \geq 15$)	960 (30,000 ppm)
No. 7	250/250/250	On-off		700 (44,000 ppm)
No. 8	170/170/170	Power regulation		700 (44,000 ppm)
No. 9	170/170/170	Power regulation		700 (44,000 ppm)

Table 3 The results of each experiment

Serial number	Rate of evaporation (mix/min/average) (kg/h)	Average humidity of product (%)	Volume reduction ratio
No. 1	3.00/0.50/1.40	17.6	~ 4.0
No. 2	1.85/0.01/0.80	13.9	~ 4.0
No. 3	2.59/0.10/1.15	7.5	~ 4.0
No. 4	5.85/0.03/3.10	2.6	~ 7.0
No. 5	10.85/0.50/6.08	2.5	~ 7.0
No. 6	9.42/0.81/4.92	1.7	~ 7.0
No. 7	5.35/0.78/3.23	3.0	~ 4.0
No. 8	11.30/0.75/4.62	1.1	~ 5.0
No. 9	10.10/0.80/5.94	1.6	~ 5.0

Table 4 The relationship between water evaporation rate and conditions

Temperature of heater (°C)	Control mode of heating	Concentrate (B ppm)	Rate of evaporation (mix/min/average) (kg/h)
150/160/160	On-off	44,000	2.59/0.10/1.15
160/140/110	On-off	44,000	1.85/0.01/0.80
175/175/175	On-off	44,000	3.00/0.50/1.40
250/250/250	On-off	44,000	5.35/0.78/3.23
250/250/250	On-off	30,000	5.85/0.03/3.10
250/250/450	On-off	30,000	9.42/0.81/4.92
250/250/500	On-off	30,000	10.85/0.50/6.08
170/170/170	Power regulation	44,000	11.30/0.75/4.62
170/170/170	Power regulation	44,000	10.10/0.80/5.94

4.4 Results and Discussion

4.4.1 Rate of Evaporation

The following can be seen from the review of control parameters and rate of evaporation of all experiments (see Table 4):

1. The maximum and average rate of evaporation increases with the increase of heating temperature. This is because the improvement of heating temperature increased the difference in temperature between inside and outside of drum, and the energy that passed to the material per unit time is increased, thereby increasing the rate of evaporation;
2. Under the same conditions, the rate of evaporation that deals with simulated concentrate with 30,000 ppm boron is higher than the one that deals with simulated concentrate with 44,000 ppm boron, and this is because there is more water in the simulated concentrate with 30,000 ppm boron; and
3. The rate of evaporation through power regulation control heating temperature is higher than on-off control, and the main reason is power regulation control heating temperature fluctuations are small and energy transfer per unit time is relatively more.

4.4.2 Moisture Content of Production

In addition to the first trial, the humidity of other product is below 15%, that meets the requirements of indicators; distribution of product humidity is that the humidity around the center is higher than in other position. All in all, while the humidity of product is not uniform, the humidity of product on the whole is in accord with the technical indicators.

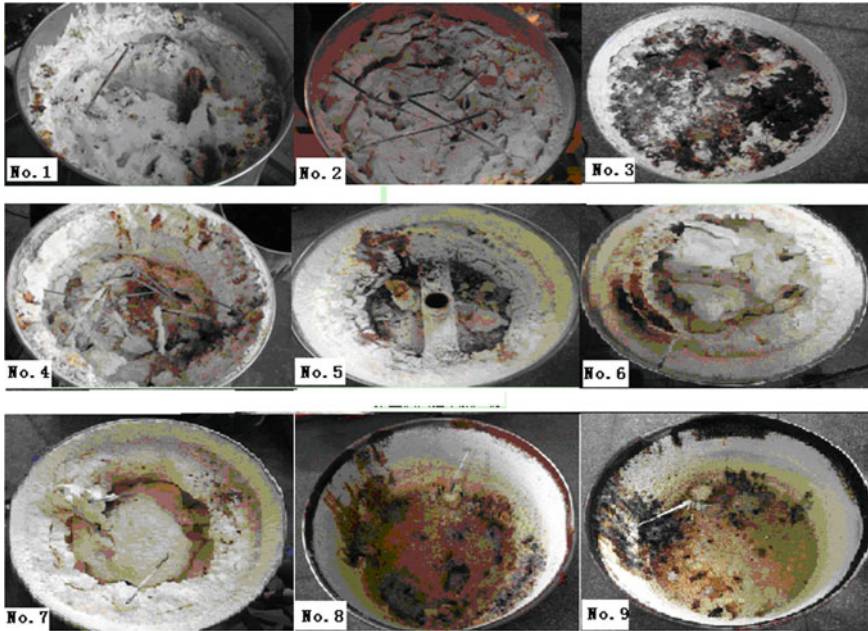


Fig. 9 Products of experiments

4.4.3 Properties of Product

The products of experiments are shown in Fig. 9. They are solid products, the humidity of which meets the requirements. But the product of first-time experiment includes three holes; the product of second experiment is cracked. There is a cavity and a through hole on the third trial product. The eighth and ninth products are solid with no holes and crack. In view of the eighth and ninth test and other seven times, the biggest different is the power regulation of the temperature control method; it can be continuous heating and maintain water evaporation drying process relatively stable so as to avoid the holes and cracks.

4.4.4 Volume Reduction Ratio

In view of the experiments of two kinds of simulated concentrate, its volume reduction ratio is from 4.0 to 7.0 (see Table 5). The volume reduction ratio of simulated concentrate with 30,000 ppm boron is 7.0, and the volume reduction ratio of simulated concentrate with 30,000 ppm boron is 4.0–5.0, mainly because of the different initial humidity of two kinds of simulated concentrate.

Table 5 The relationship between volume reduction ratio and conditions

Temperature of heater (°C)	Control mode of heating	Concentrate (B ppm)	Volume reduction ratio
150/160/160	On-off	44,000	~4.0
160/140/110	On-off	44,000	~4.0
175/175/175	On-off	44,000	~4.0
250/250/250	On-off	44,000	~4.0
170/170/170	Power regulation	44,000	~5.0
170/170/170	Power regulation	44,000	~5.0
250/250/250	On-off	30,000	~7.0
250/250/450	On-off	30,000	~7.0
250/250/500	On-off	30,000	~7.0

5 Conclusion

The radioactive concentrate in-drum drying process and the prototype device have been researched and developed, then the feasible debugging and the simulated concentrate experiment study were done. The results have shown that the simulated concentrate can be treated by in-drum drying prototype device; the average rate of evaporation can be up to 5.94 kg/h, the average humidity of product is 1.6%, and the volume reduction ratio is 5.25 when treating simulated concentrate with 44,000 ppm boron under the condition of heater temperature of 170 °C and adjusting temperature control power. It can satisfy the target whose rate of evaporation is 5–6 kg/h, the average humidity of product is less than 15%, and the volume reduction ratio is 2–6.

It is concluded from the investigative work that it is safety and feasible that treatment simulated concentrate by concentrate in-drum drying prototype device. It is necessary that study of treatment of radioactivity concentrates from nuclear power plant uses concentrate in-drum drying device.

References

1. IAEA. Processing of Nuclear Power Plant Waste Streams Containing Boric Acid. IAEA-TECDOC-911. Vienna, 1996.
2. Li Jing. Radioactive Waste Management of Daya Bay Nuclear Power Plant [J]. Electric Power, 1999,32(4):39–43.
3. Chen Liang, Chen Li, Li Jun-hua. Aanalysis of Cementation Technology for Liquid Radioactive-Waste in PWR NPPs [J]. Nuclear Power Engineering, 2009,30(2):113–116.
4. Jia Mei-lan, Iiang Dong, Cheng Wei, etc. ResearchProgressofRadioactiveWasteIn-drumDrying [J]. Equipment Environmental Engineering, 2012,9(5).
5. V.Kroselj, M.Jankovic. Characterization of In-Drum Drying Products [R]. WM06 Conference, Feb. 26-Mar. 2, 2006, Tucson, AZ.

6. Process and filling adapter for the in drum drying of liquid radioactive waste [R]. US Patent 5566727, October 22, 1996.
7. Olaf oldiges, Hans-Jürgen Blenski. A New Small Drying Facility for Wet Radioactive Waste and Liquids [R]. WM'03 Conference, February 23–27, 2003, Tucson, Arizona.
8. Dejan Škanata, Vladislav Krošelj, Milan Janković. Krko NPP. Radioactive Waste Characteristics [R]. Proceedings of the International Conference Nuclear Energy for New Europe, Portorož, Slovenia, Sept. 10–13, 2007.
9. T. L. White. Heat Transfer Enhanced Microwave Process for Stabilization of Liquid Radioactive Waste Slurry [R]. Final Report for Crada ORNL-93-0190, March, 1995.
10. Apparatus for Concentrating Salt-Containing Solutions With Microwave Energy [P]. US Patent 6080977, Jun. 27, 2000.
11. Richard Frank. Radioactive Waste Management for U.S. EPR [R]. WM Conference, Feb 24–28 2008, Phoenix, AZ.
12. Hansa Projekt. Conditioning System for Concentrates [EB/OL].: <http://www.h-p-a.de/English/uploads/file/HPA1OE-Tandem.Pdf>.
13. Hansa Projekt. Multi-Drum Dryer [EB/OL].: <http://www.in-en.com/power/html/power-1036103662527383.html>.
14. T. L. White and J. B. Berry. MICROWAVE PROCESSING OF RADIOACTIVE MATERIALS-1 [R]. Dallas, Texas: American Chemical Society, April 9–14, 1989.
15. Microwave Apparatus for In-Drum Processing of Radioactive Waste Slurry [P]. United States Patent 5324485, June 28, 1994.
16. Microwave Heating Apparatus and Method [P]. United States Patent 4940865, July 10, 1990.
17. Christian Giessmann. Microwave In-Drum Drying. Radwaste Solutions [J], Jan/Feb., 2007:21–24.
18. H. Genthner, A. Best, W. Iins. Solidification of Low Level Salt Solutions With Microwaves [EB/OL].: <http://www.wmsym.org/archives/1988/V1/45.pdf>.
19. T.L. White, E.L. Youngblood, J.B. Berry, A.J. Mattus. First Results of In-Can Microwave Processing Experiments for Radioactive Liquid Wastes [EB/OL].: http://www.osti.gov/energycitations/product.biblio.jsp?osti_id=6957438.
20. Liang Dong, Liu Zhaofeng, Yan Xiaojun, *etc.* Basic design and construction of an in-drum drying equipment for waste concentrates from NPPs [J]. Radiation Protection, 2015.35(1):31–35.
21. Liang Dong, An Hongxiang, Gao Chao, *etc.* Preliminary Study on Treatment of Waste Concentrates in NPP by Drying Technique [J]. Drying Technology and Equipment, 2013.11(4):38–45.
22. Yan Xiaojun, Liu Zhaofeng, Li Honghui, *etc.* Primary Experimental on Concentrate Drying in Electrically Heated Drum [J]. RADIATION PROTECTION BULLETIN, 2014.34(3):36–38.

Study on Radioactive Contaminated Soil Remediation Technologies and Selection Principles

Wang Shaowei, Shang Zhaorong, Wang Ping, Wei Guoliang
and Dany Yuqin

Abstract A large number of radioactive materials entered the soil environment by Fukushima nuclear accident, and large area of contaminated soil with radioactive materials became the thorniest problem of Japanese government after the accident. On the basis of the mechanism of radionuclide migration in the soil, such as physical migration, chemical migration, biological migration, and the composite of different migration processes, the series of radionuclide-contaminated soil repair methods is discussed. There are move and replace with out-soil methods aiming at physical migration, there are ion exchange method and oxidation-reduction method aiming at chemical migration, there are microbial remediation and phytoremediation aiming at biological migration. The advantages and disadvantages of different methods and applicable range are illustrated. The final remediation target is the first priority when selecting remediation methods. Then, the influence factors on remediation effect should be considered, including the principles of radiation protection, radioactive pollution levels, soil characteristics, hydrological and meteorological conditions, the radionuclide migration way influence. Finally, there will be a comprehensive comparison from method feasibility, economic affordability, and environmental and legal compatibility. The feasibility of remediation methods includes appropriate repair methods, acceptable repair time, good repair effect, etc. Economic affordability means repair costs can be bearable and as less as better. Environmental and legal compatibility refers that after the restoration the residual risk of nuclides in environment is acceptable and the long-term effect is negligible and meets the requirements of relevant laws and regulations standard.

Keywords Radioactive contamination · Soil remediation · Selection principles · Remediation technology · Factor

W. Shaowei · S. Zhaorong · W. Ping · W. Guoliang (✉) · D. Yuqin
Nuclear and Radiation Safety Center, MEP, Beijing, China
e-mail: Weiguoliang@chinansc.cn

© Springer Science+Business Media Singapore 2017
H. Jiang (ed.), *Proceedings of The 20th Pacific Basin Nuclear Conference*,
DOI 10.1007/978-981-10-2314-9_49

547

1 Introduction

The potential leakage of radioactive material pollution in nuclear facilities is one of the major environmental problems. The Fukushima nuclear accident resulted in a large number of radioactive substances into the soil environment through the airborne route, especially ^{137}Cs [1]. It would cause sustained long-term harm to the ecological environment and human health when long half-life nuclides enter into the soil. How to deal with the large area soil by radioactive pollution became the thorniest problem of Japanese government after the accident.

As the number of operational nuclear power plants in China increases continually, it is necessary to precede the scientific evaluation in radioactive contamination of the soil in order to determine the pollution scope and carry out pollution regulation after the nuclear accident. For a long time, a lot of research has been carried on refractory organics, heavy metals, and other aspects of non-radioactive soil bioremediation, while little has been done on soil polluted by radiation systematically. Meanwhile, with the decommissioning of nuclear facilities, the soil will be affected inevitably in a certain extent around those nuclear facilities. As we can see, each environmental remediation technology has its own scope. There will be a huge difference in the renovation cost when using various environmental remediation technologies under the same contaminated sites.

In this paper, based on doing a series of research on soil remediation techniques, having analyzed the advantages and disadvantages of different technologies as well as their scope, we present selective principles for radioactive contaminated site remediation techniques in order to provide technical supports for remediation on the specific contaminated site.

2 Radioactive Contaminated Soil Remediation Technology

There are amounts of radioactive soil remediation technologies, such as shoveling soil of decontamination method, which removed topsoil; deep plowing which means covering with new uncontaminated soil above those polluted soil, thereby rebuilding ecological system; agricultural chemical method, with potassium salt to prevent absorption of ^{137}Cs . Besides, there are suspended soil removal method, phytoremediation method, membrane stripping method, electrochemical method, magnetic method, precipitation, soil washing, ion exchange method, chelating extraction method, flocculation technology, and reverse osmosis ultrafiltration and so on. However, all these methods have its shortcomings. For instance, some of the technology is not mature; some usually requires a huge cost; some is not suitable for the radionuclide contamination process of large areas with low dose, which may easily destroy the structure and texture of contaminated soil causing secondary pollution; on the contrary, some is much lower cost, non-polluting, but inefficient

decontamination. The selection process must be based on the analysis of the specific conditions of the soil and the use of selective, or adopt several methods to coexist so as to strive to achieve the lowest cost and expense for maximum removal efficiency. Some decontamination methods are introduced after several radioactive soil contaminations.

Shovel contaminated soil. The soil contaminated by nuclear material (typically topsoil) should be shoveled away, transported to the specialized nuclear disposal sites for processing and disposal, which could prevent the further spread of radioactive elements fundamentally. However, the method is labor-intensive, operators will be easily exposure to radiation, and a lot of shoveling will increase processing and disposal costs. In addition, the topsoil also contains large amounts of organic matters for crop production. Shoveling all soil would further exacerbate the land crisis.

Deep plowing new soil or covered with new soil. New soil is relative to the case of the contaminated local terms. For a relatively high level of radioactive contamination of the region, the replace with out-soil is the use of deep plow method that contaminated topsoil turned to deep soil, while the lower layer were not nuclear-contaminated soil turned to the surface, so as to dilute and reduce surface contamination levels. Covering out-soil is shipped uncontaminated soil directly from the outside to contaminated soil, which, to some extent, can prevent nuclear contaminants from entering the food chain so as to form the internal radiation to human body. The advantage of this approach is to avoid pollution of soil contaminants into the food chain through contaminated soil over a layer of clean soil cover. But we must ensure that the amount of clean soil has a certain thickness, so that plant roots would not extend to the contaminated soil. Disadvantage of this method is that the soil contamination could not be removed, nor can completely rule out the potential hazards of soil contaminants.

Suspended soil removed method. This is mainly for situations, for example, paddy soil has a large amount of water-flooded soil. A thin layer of soil at the top of the water is about to stir into a paste, pumping suspension soil, sediment and then separated from the water, only to precipitate after processing. The advantage of this method is that the amount of secondary waste generated is small; the inadequacies of this approach are also drawn plenty of organic matter in the soil.

Peelable membrane. The cleaning liquid polymer compound with a variety of functional groups would quickly be sprayed by land spraying machinery the film-forming decontamination materials are coated on the contaminants, and quickly fixed nuclear contamination, control transferring and diffusion of pollution in the shortest time. After solidification of the film-forming material, surface contaminants rapid build-molding in the role of nuclear peel adhesive, and then recovered clear to the use of mechanical or manual for forming the membrane, so as to achieve on-site restoration of the natural environment and battlefield environmental purification. The surface decontamination coefficient of this method could reach 100% and have relatively low economic costs. However, there has no effect on the removal of soil penetrate inside the nuclear pollutants.

Agricultural chemical method. Agricultural chemical method refers to the use of general operational measures, so as to minimize the content of radioactive substances in soil and to inhibit the migration of radioactive materials to crops. Due to the similar chemical properties of cesium and potassium, we choose to add potassium and nitrogen into the soil under normal circumstances in general, with a high concentration of potassium and ammonium salts to prevent cesium from transferring to crops, namely food chain. The advantage of this method is that operation is simple, drawing easily, and low cost. To a certain extent, it could reduce the content of radioactive substances in plants. But the disadvantage is that radioactive substances could not be removed from the soil fundamentally, which may leave future troubles.

Phytoremediation. Phytoremediation is a method aiming at accelerating degradation of pollutants in soil through those properties, such as the use of plant accumulation of certain pollutants, plant metabolic processes of certain pollutants' transformation and mineralization, increased microbial activity of plant rhizosphere. Phytoremediation is a kind of environmental control technology, using process of plant roots absorbing water and nutrients to assimilate, transforming the contaminated carrier pollutants in order to achieve clear, repair or governance purposes. Usually we harvest plants grown in contaminated soil, and treat those plants by incineration, landfill, or any other suitable methods. Compared with other repaired techniques, phytoremediation is low cost and has small impact on the environment. It is beneficial for improving the ecological environment. Compared with other traditional chemical remediation, physics and engineering technology, phytoremediation technology is easy to operate with low investment and maintenance costs. What is more, it takes the use of solar energy, so that will not result in secondary pollution. But the disadvantage is that radioactive substances could not be removed from the soil fundamentally, which leaves future troubles.

3 Restoration Technology Selection Principles

For specific contaminated sites, we should not only consider their advantages, respectively, other factors should also be considered such as remediation goal, the final residue levels, and radioactive contamination levels, principles of radiation protection, soil type, hydrological and meteorological conditions. Finally, we take consideration of repair technology from comprehensive standards, including repair technologies feasibility, repair costs affordability, remediation goal acceptability.

3.1 Remediation Goal

Target of soil remediation is an important part of the implementation of environmental management, which is also a key indicator for technical restoration. The

remaining level of radioactivity in soil is the most immediate goal of soil remediation. In order to develop the remaining level of radioactivity, we must first clear the source of the radioactive contaminated sites and radionuclide type. Next, we consider the radiation protection principles when repairing radioactive contaminated soil and gain the goal of soil remediation via dose assessment.

The source of radionuclide could be divided into the following aspects: (a) settlement of radioactive substances caused by atmospheric nuclear tests. According to statistics, from July 16, 1945, when the USA conducted its first nuclear test till to the end of 1989, all countries conducted totally 1800 nuclear tests worldwide. Radioactive dusts would gradually settle after the atmospheric nuclear tests, causing pollution of soil, rivers, and oceans. (b) Nuclear accidents. "Ural incident," occurred in September 1957, led to polluted area up to 5000–23,000 km²; in the "Chernobyl accident," the soil within a radius range of 30 km was polluted by ⁹⁰Sr, ¹³⁷Cs, ²³⁹⁺²⁴⁰Pu, ²⁴¹Am, and other radionuclides [2]. In Ukraine, 260,000 km² area had been contaminated by ¹³⁷Cs [3]. Fukushima nuclear power plant accident resulted in surrounding soil was contaminated by ¹³⁷Cs, and the cumulative concentration reached 100,000 and 10,000 Bq/m³ [4, 5]. (c) Wide use of fertilizer containing radionuclides. The use of phosphate fertilizer containing radionuclides ²³²Th, ²³⁸U, ²²⁶Ra, and potash containing ⁴⁰K is very extensive. The use of these fertilizers containing radionuclides contamination can cause soil pollution. (d) Mineral exploitation. Development and utilization of nuclear energy requires a lot of uranium, and uranium mining and processing would pollute the surrounding soil. According to global estimates, slag volume that caused by uranium mining and uranium tailing reached 9.38×10^8 t [6].

The most immediate goal for soil remediation is remaining level of radioactivity in soil. For soil in the intervention system after accident, the screening scene and selection process should be established according to the environmental conditions surrounded by pollution, social development. Then remaining level of radioactivity in soil will be determined according to the scene. Nuclides screening method is important key to establish a dose contribution, which determines the radionuclide exposure pathways according to the established scene. Finally, according to the evaluation model to determine the relevant calculation parameters, the remaining level of radioactivity is deduced. Only when the overall interests of the radioactive contaminated site remediation more than the cost that paid for, we believe the restoration is justified.

3.2 Factors of Restoration Effect

There are various differences in radioactive contaminated soil on radionuclide types and proportions from different sources. At the same time, degree of soil pollution is also differently affected by weather conditions under such accident. Radionuclide distribution of contaminated sites, soil types, hydrological and meteorological

conditions, radionuclide morphology and nature, and the exposure pathways in polluted sites would affect repair effect.

- (a) The distribution of radionuclides. Since the source of radionuclides, the difference of nuclides released meteorological conditions, resulting in different types of radioactive nuclides in contaminated sites, scope and concentration of radionuclide distribution in the same contaminated sites. This difference reflected in the distribution of the horizontal and vertical directions of radionuclide: ① in the horizontal direction, location and extent of the high value area of soil surface contaminants; ② location and extent of different pollution concentrations in different soil depths; ③ with longitudinal migration of contaminants from the sources of change; ④ risk analysis, the probability of exceeding a specified threshold concentration. Different repairing technique has a significant difference in terms of the type and concentration of radionuclides applicability.
- (b) Soil type. Different soil types have a different impact on the adsorption and migration of radionuclides. Colloid composition is different from ordinary farmland, paddy fields, woodland, grass land soil types, resulting in large differences in physical and chemical properties of soil, pH, moisture content, redox potential, and root microorganisms. Studies have shown that the composition of different soil types in repair contaminated soil is one of the main theoretical bases for phytoremediation, because being as the center part, the plant roots gathered a lot of living matters and secretions, such as bacteria, microbes, earthworms, nematodes, which consist of a very unique “ecological restoration unit.” Therefore, remediation effect of different soil types may have significant differences.
- (c) Hydrological and meteorological conditions. Hydrological and meteorological condition determines the dominant species and its habitat ecosystems, which is of great significance to the local phytoremediation and microbial remediation. Ebbs and others studied [7] on uranium accumulation capacity to absorb the 12 species, finding that there is a huge difference between different plants on ability to accumulate uranium. Bennett [8] evaluated the potential capability of the plant concentrate radionuclides in radioactive contaminated soil. It showed that vascular plants had higher ^{99}Tc (Tc) uptake, and ^{99}Tc also had strong shoots transfer and accumulation trends nuclides form.
- (d) The morphology and properties of radionuclides. The migration ability of dissolved cation is low in clay soil. Radionuclides of different oxidation valence state have different plant absorption capacity. Generally, smaller the particle size of radionuclides, more likely to be absorbed by plants.
- (e) Exposure pathways. We need to consider the external exposure from radionuclides deposition to the ground and internal exposure from ingestion of crops. We should take into account the internal exposure inhalation of dust also. The following factors would ultimately affect the selection of repair target, environmental media parameters, dose conversion factors, crop consumption and living habits, and so on, thereby affecting the taken remediation.

3.3 Repair Technology Selection Principle

After the accident, the selection method of radioactive contaminated soil remediation program is based on the determination of soil remediation objectives, in terms of technical, economic, environmental, and social indicators. What is more, comparison studies of repairing technology also need to determine the appropriate remediation program method for restoration.

Select the repair strategy. We should confirm the overall goal of soil repair according to the soil pollution survey and the radioactivity level of soil residual. The appropriate repair strategy is determined through preliminary analysis of the repair mode, remediation technology type and application conditions, contaminated soil characteristics, hydrological and geological conditions, the level of technical and economic development.

Optimal scheme comparison of radioactive contaminated soil remediation technology. A reasonable combination of all kinds of feasible technology to achieve the overall objective as well as a potentially feasible selection of remediation programs will be provided through considering the overall objectives of the soil remediation, restoration strategy, pollution status, soil characteristics, hydrogeological conditions, repair results in screening and evaluation.

- (a) Technical indicators of operability: reliability of remediation technology, time requirement of repair scheme, availability of necessary equipment and resources, removal efficiency of contaminant, etc.
- (b) Economic indicators: start-up costs, operating costs, late stage fees, etc.
- (c) Environmental indicators: residual risk, long-term effects, healthy effects, etc.
- (d) Social indicators: compliance with current laws and regulations, relevant standards and norms; level of public acceptance.

Using the established 'comparison and selection' index system, detailed analysis of each potentially feasible remediation technology schemes can be done. For the final choice of remediation technology schemes, it can be got through various indicators comparison and comprehensive judgment, also through the expert score mode.

4 Conclusions

Radioactive contamination remediation is a long and arduous task, requiring a lot of manpower and material resources. Many contaminated technologies and measures on soil restoration practiced in Japanese Fukushima are worth for us to carry out further research. For instance, for small-scale soil contamination with a high concentration, we can take shovel soil of decontamination method; for low concentration of water in soil, deep plowing method with out-soil and suspended soil decontaminated method can be used. From the perspective of long-term

management, we should pay attention to methods of low cost as well as non-pollution, such as phytoremediation method. In addition, after the accident the first should be done is to investigate and confirm the range and extent of contaminated soil, in order to take appropriate repair techniques. Furthermore, if shovel soil of decontamination method is taken, how to save radioactive soil and how to reduce capacity are both very urgent problems. Finally, soil contamination caused by weather and other factors should also be of concern during the operation.

References

1. International Atomic Energy Agency. International Fact Finding Expert Mission Of The Fukushima Dai-Ichi NPP Accident Following The Great East Japan Earthquake And Tsunami [R].The Great East Japan Earthquake Expert Mission, Japan, 2011.
2. Kashparov V A, Lundin S M, Zvarych S I, et al. Territory contamination with the radionuclides representing the fuel component of Chernobyl fallout [J]. *Sci total environ*, 2003,317(1):105–119.
3. Francis AT, Huang JW. Proceedings of International Conference of Soil Remediation [M]. Zhejiang: Zhejiang Publisher, 2000, 150–157.
4. Endo S, Kimura S, Takatsuji T, et al. Measurement of Soil contamination by radionuclides due to the Fukushima Daiichi Nuclear Power Plant accident and associated estimated cumulative external dose estimation [J]. *J environ radio-act*, 2012, 111:18–27.
5. Yasunari T J, Stohl A, Hayano R S, et al. Cesium-137 deposition and contamination of Japanese soils due to the Fukushima nuclear accident [J]. *Proceed Natio Acade Sci*, 2011, 108 (40):19530–19534.
6. Abdelouas A. Uranium mill tailings: geochemistry mineralogy, and environmental impact [J]. *Element*, 2006,2(6):335–341.
7. EBBS S D, BRAD Y D J, KOCHIAN L V. Role of uranium speciation in the uptake and translocation of uranium by plants [J]. *Journal of Experimental Botany*, 1999, 49:1183–1190.
8. ROY BENNETT. Soil availability, plant up stake and soil to plant transfer of 99Tc 2a review [J]. *Environ Radioactivity*, 2003, 65(2):215–231.

Author Biography

Wang Shaowei Nuclear and Radiation Safety Center of MEP in China, research in environmental impact assessment on nuclear facilities.

The Importance of Influence Factors of the Fly Ash Cement Solidification

Xue-yang Liu, Zheng-hua Qian, Yan-bo Qiao, Shuai Wang,
Hong-jun Ma and Ya-ping Sun

Abstract Fly ash as an admixture of cement has been widely used in cementation. It could affect the compressive strength of cement waste form, reduce the heat of hydration, and improve fluidity of cement paste. This paper studied the effect of fly ash in the cement solidification through orthogonal test. The orthogonal test chose three factors as water-cement ratio, fineness, and content of fly ash, and each factor has three levels. This experiment added fly ash with different finenesses and contents into cement formulation with different water-cement ratios. The temperature raise curve and fluidity of the cement paste and the compressive strength of 7 days and 28 days of the cement waste form were carried out. The results show that: the influence order of factors to 7-day compressive strength in this experiment is: fineness > content > water-cement ratio, the order of the 28-day compressive strength influence is: content > fineness > water-cement ratio. This report also discussed the effect of fly ash on the heat of hydration during the cementation through the temperature raise curve of cemented waste form. Fly ash as an admixture could reduce the heat of hydration during the cementation.

Keywords Fly ash · Influence factors · Cementation

1 Introduction

Fly ash is consisted of tiny particle, which looks similar to the glass bead, and has low carbon content. When the particle size decreases and the fineness increases, the specific surface of fly ash becomes larger, and it is not easy to absorb water because of compacting structure. On the contrary, the fly ash with the large particles has more porosity can easily absorbs water, and the strength is lower than other fly ash

X. Liu · Z. Qian · Y. Qiao · S. Wang · H. Ma (✉) · Y. Sun
Center for Thorium Molten-Salt Reactor Research (TMSR),
Shanghai Institute of Applied Physics (SINAP),
Chinese Academy of Sciences (CAS), Shanghai China
e-mail: mahongjun@sinap.ac.cn

with fineness particles. At the same time, the fly ash contains SiO_2 and other active components can react with the $\text{Ca}(\text{OH})_2$ that is produced by the hydration reaction of cement to produce hydration calcium silicate [1], which can enhance the strength of cement solidified waste form. Choosing proper fly ash to be used as an admixture of cement solidification formulation can improve the fluidity of cement paste, reduce the early hydration reaction activity, and increase the late strength of cement solidified waste form. Although there have been many comprehensive and detailed experimental studies on the effect of fly ash on performances of cement paste, the research on the importance of influence factors is not enough. This study aims to make an order of the importance of influence factors of cement solidification by adding fly ash. This experiment has tested cement slurry fluidity, temperature raise, and compressive strength of form and XRD characterization to help to analyze the influence of water-cement ratio, fly ash fineness, and content on the performance of cement solidification.

2 Experimental Materials

The 42.5R ordinary Portland cement was used in the research. The secondary fly ash was from a coal-fired power plant and was screened for 80 mesh, 100 mesh, and 200 mesh.

The main composition of the secondary fly ash is shown in Table 1.

Figure 1 shows the XRD patterns of secondary fly ash; its main composition is mullite ($3\text{Al}_2\text{O}_3 \cdot 2\text{SiO}_2$), and the characteristic diffraction peak is more lenient in 2θ between $22\text{--}35^\circ$ region, which showed that amorphous vitreous silicate exists. Mullite is chemically stable and has low activity at room temperature, and it is difficult to leach in sulfuric acid solution [2].

3 Experiment Results and Discussion

Using orthogonal test method, the experiment studied the effect of water-cement ratio, fly ash fineness, and content on the compressive strength of cement solidification and tested the temperature rise curve and fluidity of representative combination. The results are as follows.

Table 1 Main composition of fly ash

Components	SiO_2	Al_2O_3	Fe_2O_3	CaO	MgO	Na_2O
Mass percent (%)	58	30	4.3	1.5	2.8	3.2

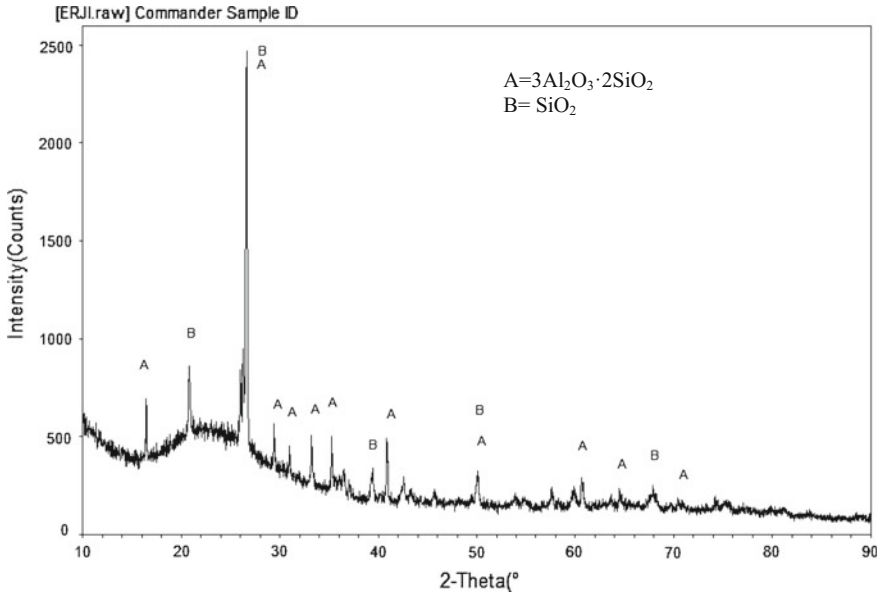


Fig. 1 XRD patterns of secondary fly ash

3.1 Results and Analysis of Orthogonal Test

The orthogonal table L9 (3³) was used in the experiment and selected the water-cement ratio, fly ash fineness and content as the experimental factors. Each factor has 3 levels, and 9 groups of tests were carried out. Both height and diameter of samples were 50 mm. The compressive strength was tested according to GB/T 17671-1999 «Method of testing cements-Determination of strength». The test results of compressive strength and the calculation results of R were shown in the table.

The R as an assessment indicator in the above table is used to measure the magnitude of the relative factors in the test. If the R of the factor is greater that means the factor is more important. And if the R is smaller, the factor is less important. Therefore, by analyzing the results of R, we could see that the order of importance of influence factors on 7-day compressive strength test in this experiment is as follows: fineness > content > water-cement ratio, the order of the 28-day test is as follows: content > fineness > water-cement ratio.

The content of fly ash has the largest influence on the early strength, and the effect on the later strength is less than fly ash particle size. With the increasing of the content of fly ash in the cement, the early strength of cement solidification waste form will decrease, and the influence will decrease with time increasing. That is similar to the results in the study by Zhang [3].

The influence of fly ash on cement paste in different periods is dominated by different factors. The reasons are as follows:

- (1) The hydration reaction of fly ash is depended on $C_a(OH)_2$ generated in cement hydration reaction. The speed of hydration reaction of fly ash is far lower than that of cement's, so the morphological effect of fly ash on cement solidification will last a long time. The part of cement is equivalently replaced by fly ash, which means the proportion of cement in the cementitious materials is reducing, which slows down the speed of the system reaction and reduces the amount of hydration reaction during the early stage [4]. Therefore, the content of fly ash in the cement is in the leading role which could affect the amount of production of cement hydration in the early period.
- (2) Some researchers have found that the specific surface area and fineness are the main factors which affect the activity of fly ash. The high-quality fly ash has low ignition loss, high content of spherical vitreous body, and high activity [1], which will improve compressive strength of cement solidification. Because the high-quality fly ash with smooth surface will be uniformly filled between the cement particles to play the role of dense packing and micro-aggregate, and the effect will reduce the cement solidification porosity and refine the pore structure. On the contrary, low-quality fly ash has coarse particles with spongy porous body, bead conjoined, and not burn the carbon, and its low strength and activity [5]. Under the same conditions, the cement combined with high-quality fly ash can get a compact microstructure and great compressive strength. Therefore, in the later stage of cement solidification, the influence of the particle size of fly ash plays a leading role.

The Table 2 also shows that the maximum compressive strength of cement solidified body is 20.7 MPa, but it cannot meet the requirements of GB 14569.1-2011 《Performance requirements for low and intermediate level radioactive waste form-Cemented waste form》 for compressive strength of cement solidified body. This is because of fly ash replacing part of cement, and this part cannot carry on hydration action at room temperature, even though there are plenty of CH hydration products of cement hydration action. At the same time, the pozzolanic reaction of fly ash in the cement is still very slow in the early stage. So the experiment will incorporate other admixture and additive into the concrete to improve the early strength of the cemented waste form in the next step research.

3.2 Temperature Rise Test Results and Analysis

The experiment selected No. 5, No. 7, No. 2 samples from Table 2 to test with temperature changes of cement paste combined with fly ash during the setting stage. Each interval 10 min recorded a set of data, and the three temperature raise curves were shown in Fig. 2.

Table 2 Test scheme and calculation results of R of L9 (3³)

Number		Water-cement ratio (%)	Content (%)	Fineness (mesh)	7-Day compressive strength (MPa)	28-Day compressive strength (MPa)
1		0.4	10	80	9.2	3.6
2		0.4	20	200	10.5	5.8
3		0.4	30	100	10.1	17.7
4		0.45	10	200	10.3	14.5
5		0.45	20	100	9.2	15.2
6		0.45	30	80	9.2	3.6
7		0.5	10	100	11.3	20.7
8		0.5	20	80	9.2	3.6
9		0.5	30	200	8.1	13.8
7 Days	K1	29.8	30.8	27.6		
	K2	28.7	28.9	30.6	Total	Total
	K3	28.6	27.4	28.9	87.1	98.5
	k1	9.93	10.27	9.20		
	k2	9.57	9.63	10.20		
	k3	9.53	9.13	9.63		
	R1	0.40	1.13	1.00		
28 Days	K1	27.1	38.8	10.8		
	K2	33.3	24.6	53.6		
	K3	38.1	35.1	34.1		
	k1	9.03	12.93	3.60		
	k2	11.10	8.20	17.87		
	k3	12.70	11.70	11.37		
	R2	3.67	4.73	14.27		

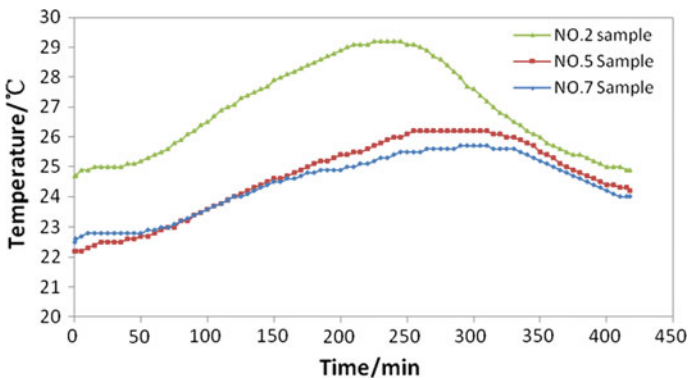


Fig. 2 Temperature rise curves of cement paste combined with different fly ashes

Table 3 Test results of fluidity of cement paste combined with fly ash

Samples	Water-cement ratio	Content wet (%)	Fineness (mesh)	Fluidity (mm)
No. 2 sample	0.4	20	200	25.9
Contrast sample	0.4	30	200	>30

Figure 1 showed that, No. 2 sample's temperature rise curve peak appeared earlier than the other two curves. The temperature rise curves of No. 5 and No. 7 sample are basically in the same trend, and the curve peak of No. 5 is higher than No. 7. That means: (1) The hydration reaction of 200 mesh's fly ash completed faster than 100 mesh's; (2) With the same fineness, the influence of water-cement ratio and content of fly ash to reaction velocity is small, and the more content of fly ash, the more heat from obvious secondary hydration reaction.

This is because the fly ash with the greater fineness, larger specific surface area, smoother surface, and compact structure is not easy to absorb water. But the fly ash with small fineness that has bigger particles and irregular surface is easier to absorb water [6, 7]. Therefore, the cement in No.2 sample could be more exposed to the water and fully hydrated.

3.3 Fluidity Test Results and Analysis

The fluidity of cement paste with fly ash was tested, and the test method is according to GB/T 2419-2005 «Test method for fluidity of cement mortar». The results are showed in Table 3.

The results showed that: under the same water–cement ratio, with the amount of fly ash increasing, the fluidity of cement paste was obviously improved, and the water requirement was decreased.

This is because the fly ash with small particles is mainly composed of vitreous spherical particles, and its surface is smooth and compact, which has dense physical filling effect. Therefore, fly ash can effectively disperse cement particles and replace more particles filled with water to lubricate paste. And at the same water-cement ratio, with more amount of fly ash, the replacement of the filling water is more, and the fluidity is better.

4 Conclusions

- (1) The effect of fly ash content on the compressive strength of 7 days is the largest, the fineness of the influence is the second, and the water-cement ratio has least effect. The effect of fly ash fineness on the compressive strength of

28 days has the greatest influence, and the content of fly ash and the water-cement ratio have little effect [8].

- (2) The effect of fly ash fineness on the cement hydration reaction velocity is more obvious, and the water-cement ratio and fly ash content have little effect. The higher fineness of fly ash, the faster of the hydration reaction of cement paste. With the same particle size and adding more fly ash, the cement paste will generate more hydration reaction heat, which indicates obvious secondary hydration reaction;
- (3) The content of fly ash is increased, and the fluidity of cement paste is obviously improved.

References

1. Qian Jueshi. Characteristics of fly ash and fly ash concrete [M]. Beijing: Science Press, 2002, (in Chinese)
2. LIANG Jin-kui, LIU Xiao-rong, LUO Lin-gen etc. Research on Strengthening Leaching of the Valuable Elements in Fly Ash [J]. MINING AND METALLURGICAL ENGINEERING, 2008, 28(6):76–79, 83Reference2
3. ZHANG Hua-ying, GUO Ming-chun, Li Yuan. The experimental research of concrete with large percentage fly ash [J].Journal of Foshan University (Natural Science Edition), 2008, 26 (2):54–56
4. Zhou Xiao-chen, Wang Xin-you. The Influence of Fly-ash on the Workability of the High Performance Concrete [J]. FLY ASH COMPREHENSIVE UTILIZATION, 2003, (2):27–30
5. Jia Xiao, Shiqiong Zhou. Experimental Study of Effect of Fly Ash on Bond Performance of Sand in cement [J]. COAL ASH CHINA, 2005(6):22–25
6. Yongjie Xue, Dongxing Xuan, Yan Zeng. Effect of Fly Ash Fineness on Performanc of Cementitious Matter/Sand in Cement [J]. COAL ASH CHINA, 2006(2):10–11, 14
7. LIU Bao-ju, XIE You-jun, ZHANG Yan-qing. Influnce of Fly Ash on Properties of Cement-based Materials [J]. JOURNAL OF BUILDING MATERIALS, 2003,6(4):426–430
8. Qian Zhenghua, Liu Xueryang, Qiao Yanbo. The Reaserch Development of Cementation of Simulated Radioactive Fluoride Liquid Wastes [R].TMSR-DNE-WM-TR-2015-11, (in Chinese)

Author Biography

Liu Xue-yang received his master degree form East China University of Technology. Then he worked at Shanghai Institute of Applied Physics, Chinese Academy of Sciences. His current research interest is the management of radioactive wastes, molten-salt reactor radwaste disposal and vitrification of high level wastes.

The Influence of Thermal Irradiation Synchronously Aging on the Structure of Modified Sodium Bentonite

Wei Liu, Shuaiwei Zhao, Liang Dong, Zhontian Yang, Honghui Li, Jianqin Liu and Lei Wan

Abstract In order to study the influence of thermal irradiation (γ) synchronously aging on the properties of bentonite, the Gaomiaozhi(GMZ)-modified sodium bentonite was investigated by heating (90 °C) and irradiating(dose rates 85, 170, 610 Gy/h; cumulative doses 0.28, 0.37, 0.74 MGy). The results of thermal analysis and XRD showed that the influence of heating and irradiating on the thermal properties, phase components, and structures of the GMZ-modified sodium bentonite is no obvious, the γ -ray cumulative dose effects and dose rate effects are generally weak.

Keywords Modified sodium bentonite · Thermal irradiation synchronously aging · Gamma cumulative dose effect · Dose rate effect

1 Introduction

Clay minerals are of crucial importance in the safety and long-term performance of underground high-level radioactive waste disposal concepts. The major component of engineered barriers is bentonite. The bentonite is affected by the heat and irradiation that produced from the waste, so it is crucial to investigate the influence of heat and irradiation on the properties of bentonite.

The changes of physico-chemical properties are caused by the effect of heat and irradiation. The stability of Al-O and Si-O band is destroyed by irradiation, so defects are formed in the crystal structure [1, 2]. Gournis et al. [3] found that the radiation induces paramagnetic defect centers. The results of [4, 5] indicated the concentration of the defect depends on the granulometrical fraction (clay fraction or coarse fraction), the coarse fraction has a higher concentration in defects than the clay fraction, and the concentration of radiation-induced defects increased with

W. Liu (✉) · S. Zhao · L. Dong · Z. Yang · H. Li · J. Liu · L. Wan
CNNC Key Laboratory on Geological Disposal of High-Level Radioactive Waste,
China Institute for Radiation Protection, Taiyuan 030006, China
e-mail: fflglw@126.com

increasing dose. The concentration of the defects is even more sensitive in the presence of mobile water molecules [6]. Moreover, after the effects of heat and irradiation, the crystal particle size decreases [7, 8]; this creates an increased specific surface area [8], and in addition, the property swelling is alterative [9, 10] found the GMZ-modified sodium bentonite maintains its ability of water absorption after γ irradiation for 5 MGy, then thermal aging for 1 year at 230 °C. Due to radiolysis of the interlayer and pore water, it generates the redox species that can result the change of valence state for iron (form Fe^{3+} to Fe^{2+}); this may alter the swelling property, CEC, specific surface area, and layer charge [9, 11, 12]. The transformation of the dissolution and adsorption about nuclides is caused by irradiation, Al^{3+} ions decreases, Si^{4+} ions increases [6], and the adsorption capacity for $^{137}\text{Cs}^+$ decreases [9, 13] found that the GMZ-modified Na bentonite was more stable than natural Ca bentonite during both thermal aging and electron irradiation aging, and it was appropriate to chose natural Na bentonite or modified Na bentonite as buffer material.

In the former study, the great dose rates (form several hundred Gy/h to several tens kGy/h) and large cumulative doses (form several MGy to 30 MGy) were used to study the cumulative dose effects on clay minerals, but there are few studies on the effect of dose rate. This is because that the initial surface dose rates of the waste containers are about 2 Gy/h and drop off by an order of magnitude within 200 years [11, 14]; it is unrealistic that the samples received large cumulative doses are obtained by using such small dose rates in laboratory experiment. So, in the present work, in order to be close to the true conditions, the GMZ-modified sodium bentonite was irradiated by small dose rates (from several tens Gy/h to several hundred Gy/h), and the influence of heat and irradiation (includes the effects of cumulative doses and dose rates) on the structure is investigated.

2 Methods and Materials

In the present work, the GMZ-modified sodium bentonite [7] was investigated, and the average water content is 8.62%.

The samples were packed in closed buckets that were made of iron and wrapped by self-temperature limiting heating belt, and the thickness of the container is 1 mm. They were irradiated at 90 °C in ^{60}Co gamma sources of 37,000 Ci, and the irradiated conditions were listed in Table 1.

After aging, the samples were analyzed by thermal analysis (NETZSCH STA449F3, parameters: platinum crucible with cover, nitrogen-30 ml/min, heating rate 10 °C/min, mass 16 ± 0.5 mg) and X-ray diffraction(XRD) (Dandong haoyuan DX2700; $\text{CuK}\alpha$, range 4–70°2 θ , step size 0.02°, counting time 1 s or 3 s).

Table 1 Experimental conditions

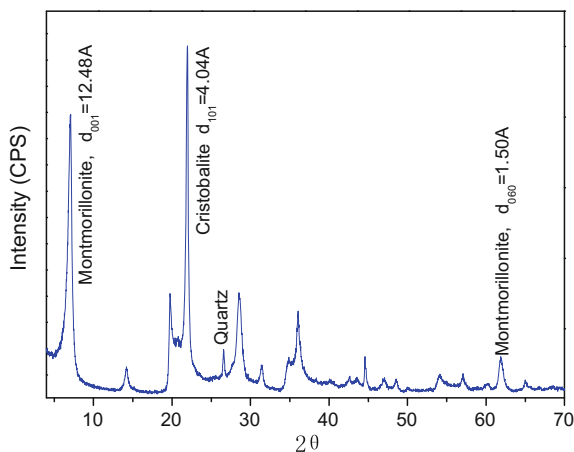
Sample ID	Experimental conditions		Exposed time (h)
	γ -exposed rate (Gy/h)	γ -irradiated dose (MGy)	
1#	85	0.28	3294
2#	85	0.37	4353
3#	170	0.37	2176
4#	170	0.74	4353
5#	610	0.37	607
6#	Reference		

3 Results and Discussion

3.1 The Analyses of Reference (6#) Sample

The GMZ-modified sodium bentonite mostly contains montmorillonite and cristobalite, and trace quartz (Fig. 1). The d_{001} of montmorillonite is 12.48 Å, constancy with one layer of water molecule in the interlayer, and the d_{060} is 1.50 Å, so this sample is indeed dioctahedral mineral. This sample has the similar curve of differential scanning calorimetry(DSC) for Smectite minerals [15]; in the range of 25–950 °C, there are three endothermic valleys (Fig. 2); and in the range of 50–150 °C, the shape and bulk of the valley reflect function for water absorption/dehydration to some extent [15]. In the DSC curve, the first endothermic valley is big, so the sample contains some water; this corresponds with water content 8.62% in the sample. In the range of 530–750 °C, it has the second endothermic valley and also corresponds with another mass loss step in TG curve, and it primarily loses crystal water in this stage. The peak temperature of the second endothermic valley reflects the thermal stability of bentonite [15]. In the range of

Fig. 1 XRD spectra of reference sample



830–910 °C, it has the third endothermic valley, and there is no obvious mass loss step; the structure of bentonite breaks up in the stage.

3.2 The Thermal Analyses of Aged Samples

The samples have the similar TG curves, so there is a representative line in following thermal curve pictures.

3.2.1 The Analyses of Aged Samples with Different Accumulative Doses

The DSC curves between 6# sample and aged samples (1#, 2#, 3#, 4#) are basic agreement (Figs. 3 and 4), there are three endothermic valleys, and they have similar TG curves with two mass loss steps (Figs. 3 and 4). But, they have some discrepancies of the peak shape and peak area for the first endothermic valleys, which indicate that the surface and interlayer water content of the samples before and after aging has some difference, and this is due to gamma ray induced part of water radiolysis [16] and water evaporation caused by long-term effect at high temperature (90 °C).

According to the data (Table 2), it is obvious that the peak temperatures of the first endothermic valley for aged samples are lower than 6# sample; this is because the surface and interlayer water content decreases after aging, and the peak temperatures of the second and third endothermic valley are almost constant, all close to 690 °C for the second peak temperature and 880 °C for the third peak temperature; they indicate that the thermal stability and skeleton construction of all samples are basically unchanged. But, the endothermic values of the second endothermic valley for aged samples are lower (reduced 11–19% compared to 6#

Fig. 2 Thermal curve of reference sample

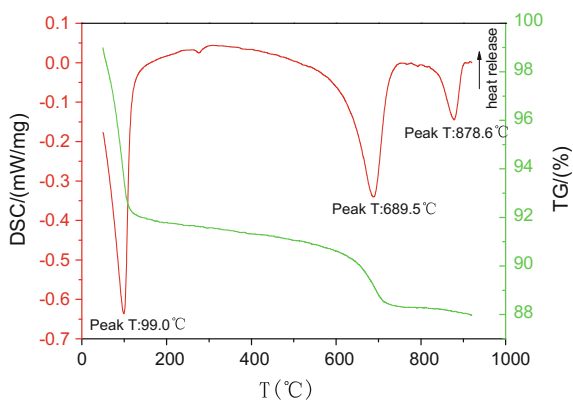


Fig. 3 Thermal curve of Na bentonite with different cumulative dose at 85 Gy/h

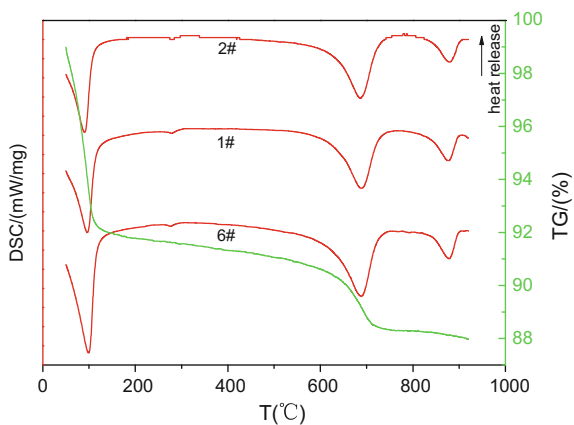


Fig. 4 Thermal curve of Na bentonite with different cumulative dose at 170 Gy/h

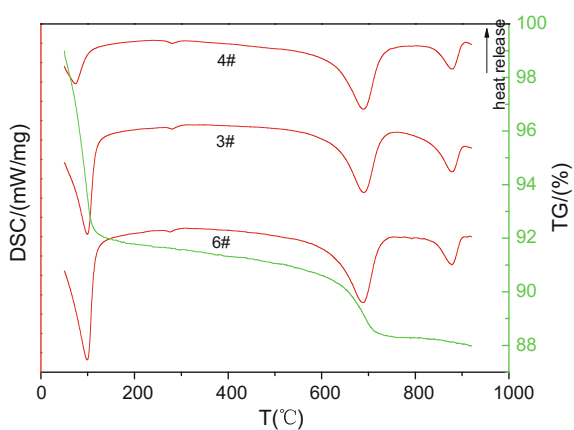
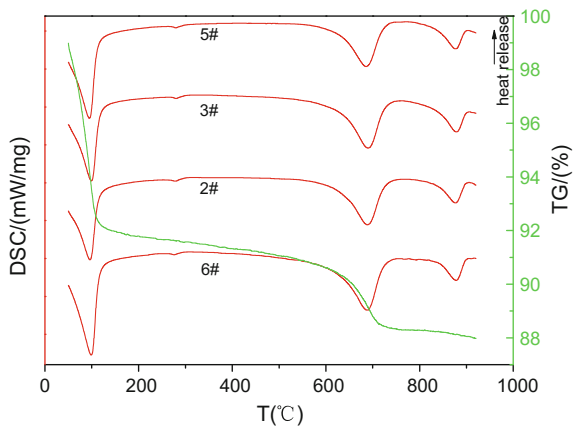


Table 2 Thermal results of Na bentonite after aging

Samples ID	The 1st endothermic valley	The 2nd endothermic valley		The 3rd endothermic valley	
	Peak T (°C)	Peak T (°C)	Endothermic value (J/g)	Peak T (°C)	Endothermic value (J/g)
6#	99.0	689.5	168.20	878.6	36.02
1#	95.4	687.7	136.40	878.2	36.62
2#	88.7	687.0	149.70	879.8	33.87
3#	96.9	690.1	149.30	878.8	40.23
4#	71.9	687.9	144.60	879.3	33.38
5#	93.4	686.7	125.70	877.6	35.24

Fig. 5 Thermal curve of Na bentonite with different dose rate at 0.37 MGy



sample) than 6# sample, so it seemingly indicates that effect of aging influences the crystal water of modified sodium bentonite.

3.2.2 The Analyses of Aged Samples with the Same Accumulative Doses but Different Dose Rates

There are also similar thermal curve between the aged samples and 6# sample (Fig. 5), and the peak temperatures of the first endothermic valley for aged samples are also smaller than 6# sample; the variety is resulted by the surface and absorption water loss after aging. Similarly, the peak temperatures of the second and third endothermic valley are 690 and 880 °C, which indicate that under high temperature (90 °C) and cumulative dose 0.37 MGy with different dose rate, the influence on the thermal stability and skeleton construction of modified sodium bentonite are almost small. But, the endothermic values of the second endothermic valley for aged samples are also lower (reduced 11–25% compared to 6# sample) than 6# sample.

3.3 The X-Ray Diffraction Analyses of Aged Samples

3.3.1 The Analyses of Aged Samples

1. The analyses of samples with different accumulative doses

Except the first diffraction peak of low angle, other diffraction peak positions and shapes of the aged samples are basically the same with 6# sample, but the intensities for aged samples are lower than 6# sample, and decrease with the increase of accumulative doses (Figs. 6 and 7). When the accumulative dose is 0.74 MGy, the

Fig. 6 XRD spectra of Na bentonite with different cumulative dose at 85 Gy/h

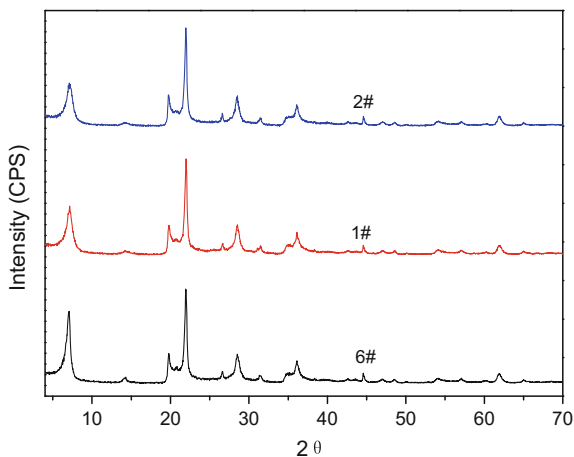
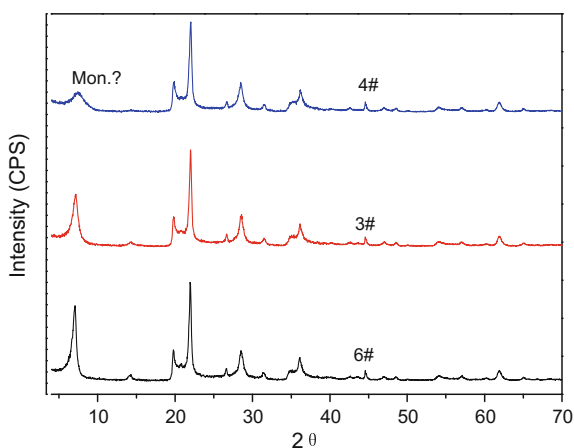


Fig. 7 XRD spectra of Na bentonite with different cumulative dose at 170 Gy/h



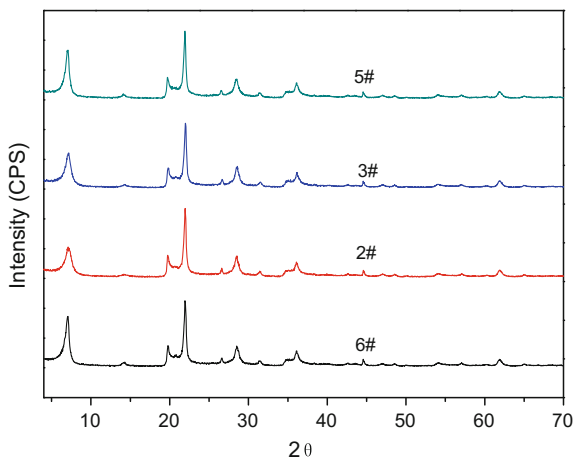
first diffraction peak of low angle is obviously widen, the peak position moves to high angle, and the intensity is lower than 6# sample.

2. The analyses of aged samples with the same cumulative dose but different dose rates

It can be seen from Fig. 8, the diffraction peak positions, shapes, and intensities of the aged samples are basically the same with the ones of 6# sample except the (001) diffraction peak of the montmorillonite; after aging, the intensities are lower than that of 6# sample, and decrease with the decrease of the dose rates.

According to the data (Table 3), the first diffraction peak position of 4# sample obviously removes to high angle, the d space is 11.78 Å, the full width at half maximum (FWHM) is 3.14 times of that for 6# sample, the height reduces 80%,

Fig. 8 XRD spectra of Na bentonite with different dose rate at 0.37 MGy



and the peak area also reduces 40%; it needs further confirmation whether the peak belongs to new phase caused by the effect of aging. Except that the position and FWHM of (001) diffraction peak of the montmorillonite for 5# sample decrease and d space increase, for other sample, the FWHM increases with increase of cumulative doses under the same dose rate; the d space, peak height and area decrease with increase of cumulative doses under the same dose rate; and the peak height and

Table 3 Results of quantitative analysis after aging

Samples ID	Phase	(hkl)	2θ (°)	d (Å)	FWHM	Height	Area
6#	Mon.	(001)	7.08	12.47	0.639	1010	31,726
1#	Mon.	(001)	7.17	12.33	0.900	623	25,978
2#	Mon.	(001)	7.19	12.28	0.970	578	25,938
3#	Mon.	(001)	7.10	12.45	0.710	821	28,685
4#	Mon.?	(001)?	7.50	11.78	2.006	226	18,669
5#	Mon.	(001)	7.07	12.49	0.611	975	28,378
6#	Mon.	(060)	61.81	1.50	0.600	148	6178
1#	Mon.	(060)	61.84	1.50	0.597	149	6001
2#	Mon.	(060)	61.84	1.50	0.625	142	5702
3#	Mon.	(060)	61.83	1.50	0.578	152	6002
4#	Mon.?	(060)?	61.82	1.50	0.588	147	5274
5#	Mon.	(060)	61.81	1.50	0.591	147	5875
6#	Cri.	(101)	21.96	4.04	0.308	1386	20,257
1#	Cri.	(101)	21.98	4.04	0.309	1399	21,004
2#	Cri.	(101)	21.96	4.04	0.301	1445	21,828
3#	Cri.	(101)	21.95	4.05	0.303	1415	20,555
4#	Cri.	(101)	21.99	4.04	0.351	1264	20,784
5#	Cri.	(101)	21.93	4.05	0.294	1415	20,530

Table 4 Water content of Na bentonite after aging

	6#	1#	2#	3#	4#	5#
Water content (%)	8.62	5.37	5.36	5.86	1.64	7.51

area decrease with decrease of dose rate under the same cumulative doses. The d_{060} space is 1.50 Å for all samples, and there is no formation of trioctahedral minerals [17]. After aging, the position, d space, peak area, and FWHM of the (101) diffraction peak for the cristobalite in all modified sodium bentonite are basically unchanged except 4# sample. For the 4# sample, the FWHM of the (101) diffraction peak becomes widen and peak height decrease.

As previously stated [10], the vary of d_{001} space for montmorillonite has relation to the water content. One observes in Table 4 that the water content of aged samples is lower than 6# sample especially the 4# sample, and it is in accord with the results of thermal analysis. To validate that the varieties of aged samples under the effect of heating (90 °C) and simultaneously irradiating with different dose rates and cumulative doses are caused by the vary of water content after the affect of aging or transforming new phase, the experiments of the oven-drying (105 °C and 24 h), water uptake in constant temperature and humidity box (25 °C and relative humidity 100%), and natural water absorption were investigated, and then, the samples were studied by XRD.

3.3.2 The Results of the Samples for Oven-Drying and Water Uptake

For all samples, after oven drying, the shapes positions and intensities of all diffraction peaks are basically the same, the intensities are low and width and the d-spaces are $(9.72 \pm 0.10)\text{Å}$ (Fig. 9) to the first diffraction peak of low angle. The diffraction spectrum is a basic agreement for all samples after water absorption for 10 min in the constant temperature and humidity box (Fig. 10). As the data (Table 5) shows, the water contents are close and the d-spacings are almost the same ($12.44 \pm 0.8 \text{ Å}$) as that of the first diffraction peak of low angle for all samples. The position and d space of the first diffraction peak of low angle for 4# and 6# sample are close after oven-drying and water uptake in constant temperature and humidity box, but the intensities of 1#, 2#, and 4# sample are lower than that of 6# sample, and the shapes are widen.

3.3.3 The Results of the Samples for Natural Water Uptake

After natural water absorption for 114 days, the intensity for the first diffraction peak of low angle for 4# sample is still lower than that of 6# sample, and the XRD spectrums for other samples are the same with the spectrum of 6# sample (Fig. 11). The data in Table 6 show that the FWHM for the first diffraction peak of low angle is still bigger than that of 6# sample, but smaller than that sample which does not

Fig. 9 XRD spectra of drying aged Na bentonite

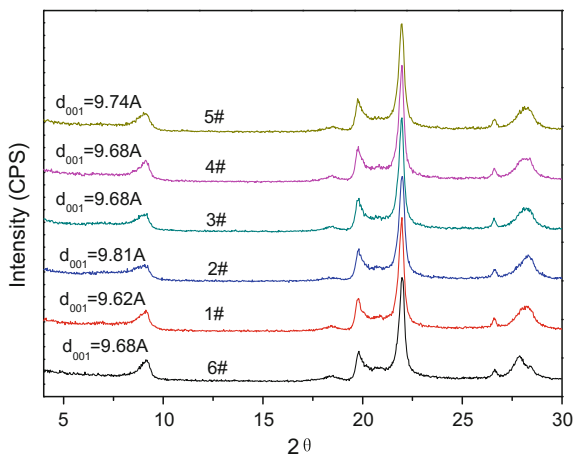


Fig. 10 XRD spectra of Na bentonite after absorbed water in constant temperature and humidity box

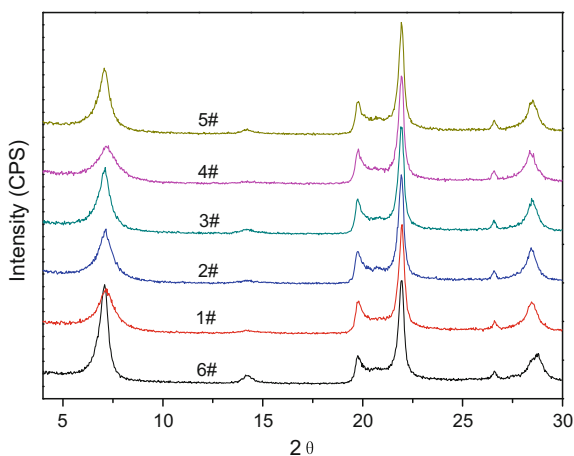
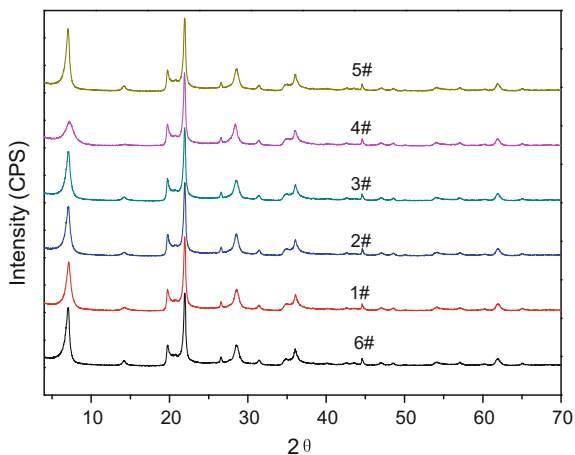


Table 5 Results of quantitative analysis of aged samples after absorbed water in constant temperature and humidity box

Samples ID	2θ(°)	d ₀₀₁ (Å)	Water content (%)
6#	7.09	12.46	8.62
1#	7.12	12.40	8.09
2#	7.15	12.36	8.07
3#	7.06	12.51	8.16
4#	7.09	12.46	8.12
5#	7.09	12.46	8.12

absorb water, and the height is up to 36% of 6# sample; it is higher than the sample of nonabsorbent water (22% of 6# sample); the FWHM, heights, and areas of the first diffraction peak of low angle for other aged sample are slightly lower, and this

Fig. 11 XRD spectra of aged samples after natural absorbed water**Table 6** Results of quantitative analysis of aged samples after natural absorbed water

Samples ID	Phase	(hkl)	2θ (°)	d (Å)	FWHM	Height	Area
6#	Mon.	(001)	7.07	12.49	0.644	3271	13,3947
1#	Mon.	(001)	7.08	12.47	0.644	2723	12,7311
2#	Mon.	(001)	7.14	12.37	0.695	2630	13,0154
3#	Mon.	(001)	7.10	12.44	0.651	2701	123,560
4#	Mon.	(001)	7.21	12.25	1.209	1189	92,648
5#	Mon.	(001)	7.07	12.50	0.632	3363	131,426
6#	Cri.	(101)	21.94	4.05	0.292	4163	90,503
1#	Cri.	(101)	21.94	4.05	0.293	4203	92,648
2#	Cri.	(101)	21.94	4.05	0.297	4160	90,694
3#	Cri.	(101)	21.93	4.05	0.290	4193	90,926
4#	Cri.	(101)	21.91	4.05	0.294	4185	91,489
5#	Cri.	(101)	21.93	4.05	0.289	4233	93,177

Table 7 Water content of aged samples after natural absorbed water

	6#	1#	2#	3#	4#	5#
Water content (%)	8.62	7.93	7.63	5.78	7.66	8.68

is mostly because that the water content still has some diversity (Table 7). The positions, d-spacing, FWHM, heights, and areas of (101) diffraction peak for cristobalite phase are the same after natural water absorption for 114 days (Table 7).

According to the results of the aged samples, aged samples for oven-drying and water absorption in the constant temperature and humidity box and nature state, the formation of diffraction peak for d space 11.78Å is caused by the decrease in water

content after aging, and it belongs to the (001) diffraction peak of montmorillonite. The varieties of the position, shape and intensity, and FWHM of the first diffraction peak of low angle is caused by the loss of water in the samples under the effect of heating (90 °C) and synchronously irradiating with different dose rates and cumulative doses; the vary is reversible under the aging condition, and there is no visible change of the mineral compositions.

4 Conclusions

Thermal analysis, in conjunction with XRD spectrum, was used to study the influence of structure under the effect of heating (90 °C) and synchronously irradiating using different dose rates and cumulative doses in GMZ-modified sodium bentonite. The changes of the first endothermic valley and the first diffraction peak for the low angle were found, but the varieties are reversible after absorbing water again.

In the present study, the influence of heating and irradiating on the thermal properties, phase components, and structures of the GMZ-modified sodium bentonite is no obvious, and the cumulative dose effects and dose rate effects of γ ray are generally weak.

References

1. Th. Allard and G. Calas. Radiation effects on clay mineral propertise [J]. *Applied clay science*, 2009, 43:143–149.
2. Th. Allard, E. Balan, G. Calas, et al. Radiation-induced defects in clay minerals: A review [J]. *Nuclear instruments and methods in physics research B*, 2012, 277:112–120.
3. D. Gournis, A.E. Mantaka-Marketon, M.A. Karakassides, et al. Ionizing radiation-induced defects in smectite clays [J]. *Phys Chem Minerals*, 2001, 28: 285–290.
4. J. Dies, C. de las Cuevas and F. Tarrasa. The influence of irradiation temperature on the thermoluminescence response of rock salt irradiated in the MGy range [J]. *Radiation Protection Dosimetry*, 1999, 85:487–492.
5. J. Dies, L. Miralles, F. Tarrasa, J.J. Pueyo, et al. Thermoluminescence response of calcic bentonite subjected to conditions of high nuclear waste underground storage [J]. *Radiation Protection Dosimetry*, 2002, 100:389–394.
6. R. Pushkareva, E. Kalinichenko, A. Lytovchenko, et al. Irradiation effect on physico-chemical properties of clay minerals [J]. *Applied Clay Science*, 2002, 21: 117–123.
7. Liang Dong, Liu Wei, Yang Zhontian, et al. A preliminary study on the influences of thermal and γ -rays irradiation aging on modified sodified sodium bentonite [J]. *Journal of Radiation Research and Radiation processing*. 2012, 30:187–192.
8. R Pusch, O Karnland, A Lajudie et al. MX 80 clay exposed to high temperatures and gamma radiation [R]. SKB Technical Report 93–03, 1992.
9. A.S. Pente, Prema Giresan, R.K. Bajpai, et al. Heat and radiation induced alterations in sorption and swelling characteristics of bentonite clays from north-west India [C]. Nantes, France: 2010. 493–494.

10. Zhao Shuaiwei, Yang Zhontian, Liu Wei, et al. Influences of γ -rays irradiation-thermal sequential aging on the microstructure of modified sodium bentonite [J]. *Journal of Radiation Research and Radiation processing*, 2013, 31: 040403-1-040403-5.
11. M. Plötze and G. Kahr. Alteration of clay minerals—gamma-irradiation effects on physicochemical properties [J]. *Applied Clay Science*, 2003, 23: 195–202.
12. Michael Holmboe, Mats Jonsson. Influence of γ -radiation on there activity of montmorillonite towards H_2O_2 [J]. *Radiation Physics and Chemistry*, 2011.
13. Yang Zhontian, Liang Dong and Liu Wei. Stability of GMZ natural Ca-bentonite and modified Na-bentonite under thermal and electron irradiation aging [J]. *New Chemical Materials*, 2013, 41:112–114.
14. D.T. Reed and D.D. Scott. Gamma and alpha radiation levels in a basalt high-level waste repository: potential impact on container corrosion and packing properties [M]. *Academic Press*, 1987. 325–338.
15. Luo Taian and Liu Xiaodong. Analysis on mineral composition and character of bentonite from the Guangfeng deposit in Jiangxi [J]. *IM & P Industrial Minerals and Processing*. 2004, 10:16–18.
16. D. Gournis, A.E. Mantaka-Marketou, M.A. Karakassides, et al. Effect of γ -irradiation on clays and organoclays: a Mössbauer and XRD study [J]. *Phys Chem Minerals*, 2000, 27:514–521.
17. S. Kaufhold, R. Dohrmann, T. Sanden, et al. Mineralogical investigations of the first package of the alternative buffer material test-I. Alteration of bentonites [J]. *Clay Minerals*, 2013, 8: 199–213.

The Introduction of the Safety Assessment of HLW Disposal in 2014–2017 in China

Hong-hui Li

Abstract In China, “The Law on Prevention and Control for Radioactive Pollution” issued in 2003 determined that the high-level waste will be disposed in a deep central geological repository. The main work of China Institute for Radiation Protection (CNNC-mandated comprehensive research) about HLW disposal is safety assessment. In 2006–2010, the CIRP have done some of the works about safety criteria and safety requirements: public radiation protection for post-closure of repository: 0.3 mSv/a; timescale: 10,000a. The CIRP also have established SA methodology and routine. Some software about safety assessment such as AMBER, Ecology, GoldSim, ProFlow can be familiarly used. The main works in 2014–2017 about the safety assessment that will be done are the research of safety requirements of the EBS and host rock, the research of safety function of the EBS and host rock, establishing the safety indicators’ system of the EBS and host rock, establishing the FEPs list and the scenario analysis in the conceptual and planning stage, the near-field temperature simulation based on the conceptual design of the repository, and the safety assessment of Beishan Preliminary Repository. Some of the above-mentioned work details will be introduced in this paper. The scenario development is the key step in HLW geological disposal. The features, events, and processes (FEPs) should be first considered. The FEPs can be sorted and grouped to form the scenario. It is very useful and has reference value for developing the FEPs of HLW geological disposal in a conceptual and planning stage in China by introducing the FEPs’ established and sorted methods. The FEPs list will be built in 2014–2017. Some of the works will be researched in 2014–2017. The details of these works will be introduced in this paper.

Keywords High-level waste (HLW) · Safety assessment · Safety criteria · Safety requirements

H. Li (✉)

China Institute for Radiation Protection, Taiyuan, Shanxi, China
e-mail: jianghong@cnpe.cc

1 Introduction

High-level radioactive waste is the inevitable product of the nuclear power development. The whole world has paid more attention to the safety disposal of the waste so as to maintain the sustainable development of nuclear power. Safe disposal of high-level radioactive waste is a challenging task facing the scientific and technological world.

Safety assessment is a procedure for evaluating the performance of a disposal system and, as a major objective, its potential radiological impact on human health and the environment. Potential radiological impacts after closure of a disposal facility may arise from gradual processes, such as degradation of barriers, and from discrete events that may affect the containment and isolation of the waste. Safety assessments serve different purposes at different stages in the development of a disposal facility. At an early stage, safety assessments should be used to determine the feasibility of major disposal concepts, to direct site investigations, and to assist in initial decision making. Their use is of greater importance in the stages following early concept development and site selection. Such assessments should then be developed to assist in system optimization and facility design by carrying out comparative assessments for various items such as alternative waste package designs and closure measures. Safety assessments should be carried out periodically throughout disposal facility planning, construction, and operation and prior to closure and are used to develop and progressively update the safety case. The post-closure safety case is the synthesis of evidence, analyses, and arguments that quantify and substantiate a claim that the disposal facility will be safe after closure and beyond the time when active control of the facility can be relied on.

“The Law on Prevention and Control for Radioactive Pollution” issued in 2003 determined that HLW will be disposed in a deep central geological repository. “Regulations on Safety of Radioactive Waste Management” issued in 2012 determined that the engineering, safety technology research, underground experiment, siting, and construction activity in relation to deep geological disposal facility of HLW should be performed under CAEA. HLW will be isolated at least 10,000 y after the repository closure.

“The Guides for R&D Program for Disposal of HLW” issued by CAEA, MST, and MEP in 2006 outlines the major R&D goals.

- Objectives: URL, 2020; Repository, middle of this century,
- R&D and siting phase (–2020),
- URL experiments (–2040), and
- Prototype verification and repository construction (after 2040).

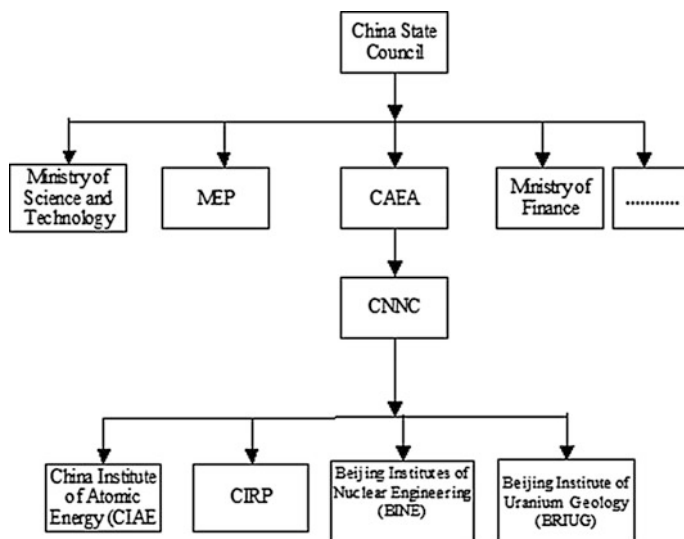


Fig. 1 The organization related to HLW disposal in China

2 Organization Related to HLW Disposal

The organization is related to HLW disposal (see Fig. 1). On the top of the figure is the China state council. Under the China state council are Ministry of science and technology, Ministry of environment protection (MEP), China Atomic Energy Authority (CAEA), Ministry of Finance, and so on. The China National Nuclear Cooperation (CNCC) belongs to CAEA. The divisions of the work of the four research aspects are as follows: disposal engineering, siting and characterization, disposal chemistry, and safety assessment. Figure 2 shows the divisions of the work of CNCC: Beijing Institute of Nuclear Engineering's major work is disposal engineering; Beijing Institute of Uranium Geology's major work is siting and characterization; China Institute of Atomic Energy's major work is disposal chemistry; China Institute for Radiation Protection's major work is safety assessment.

3 Current Progress in CIRP

Based on the HLW geological disposal primary conceptual design, the nuclide transport pathways in HLW geological disposal system were analyzed.

The conceptual model and the mathematical model of the nuclide migration were developed using the compartment model.

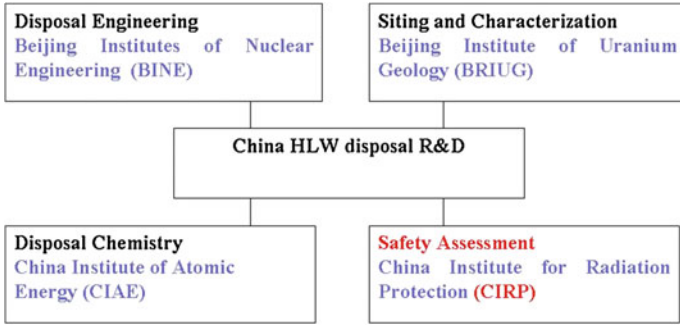


Fig. 2 The divide of the work of CNNC

The nuclide release calculation under the reference scenario was implemented in current GoldSim software. Figure 3 shows the near-field model implemented in GoldSim.

Figure 4 shows the release rates from near field; from Fig. 4, we can see that ¹³⁵Cs is the key release radionuclide in the period 1000–500000a after the repository closure. The peak release rate is 1.69×10^4 Bq/a;

Figure 5 shows the release rates from host rock; from Fig. 5, we can see after the year of 7×10^5 , because of the glass is dissolved ⁹³mNb is the key release radionuclide. The peak release rate is 1.24×10^4 Bq/a;

Figure 6 shows the dose produced by the HLW disposal; from Fig. 4, we can see the maximum dose/a is 0.00 μ Sv. The key radionuclides are ¹³⁵Cs, ⁷⁹Se, and ²²⁹Th.

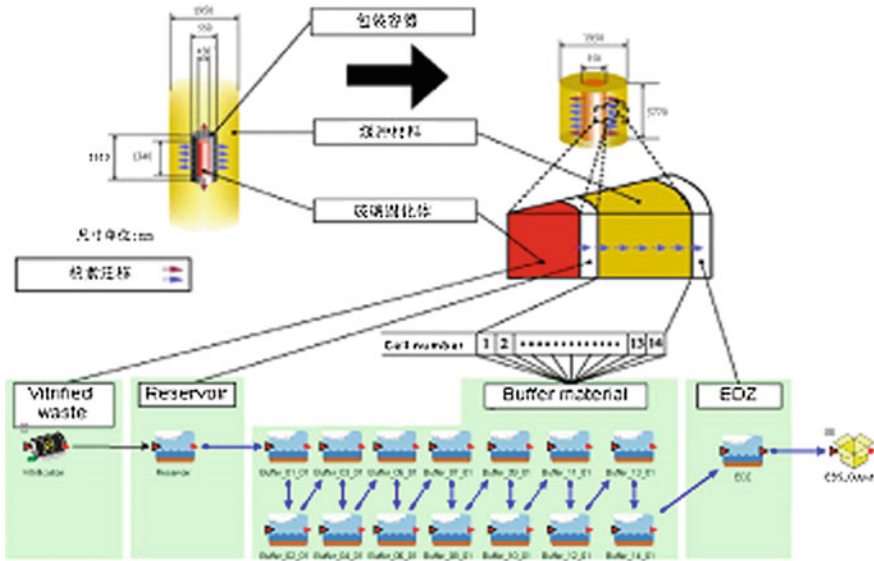


Fig. 3 Near-field model implemented in GoldSim

Fig. 4 Release rates from near field

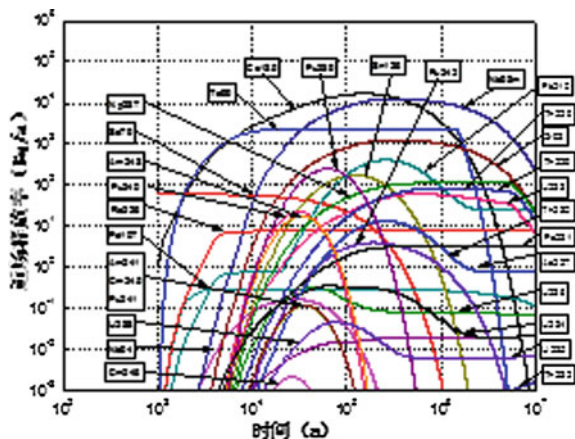


Fig. 5 Release rates from host rock

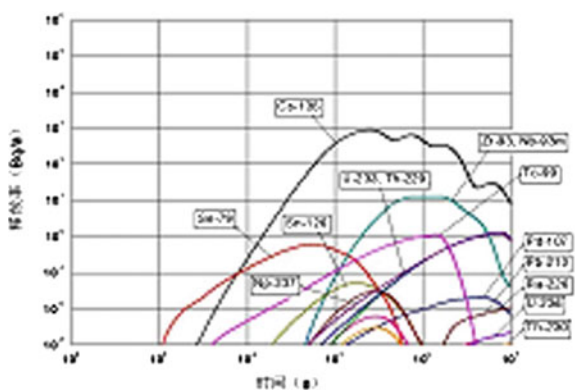
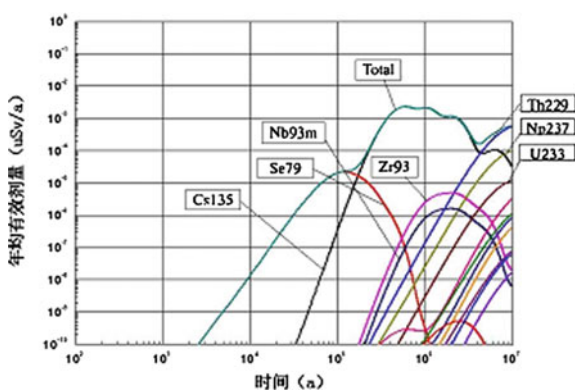


Fig. 6 The dose produced by the HLW disposal



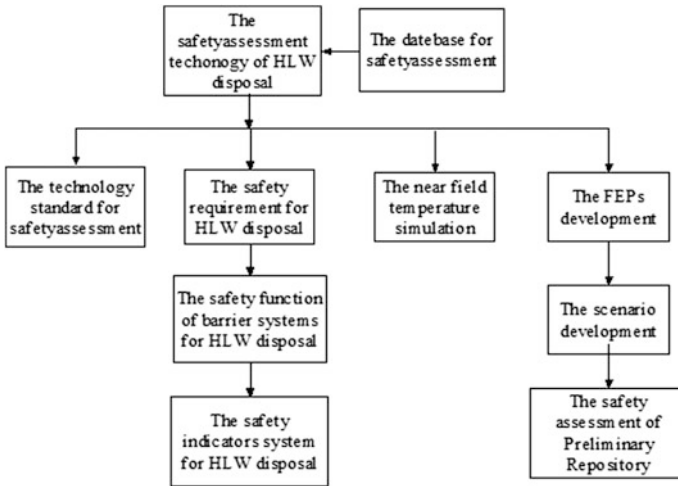


Fig. 7 The works of the safety of HLW disposal in 2014–2017

4 The Outline of the Main Work about Safety Research of HLW Disposal in 2014–2017

Figure 7 shows the main work about safety research of HLW disposal of CIRP. The main works in 2014–2017 about safety assessment that will be done are the research of safety requirements of the EBS and host rock, the research of safety function of the EBS and host rock, establishing the safety indicators system of the EBS and host rock, establishing the FEPs list and the scenario analysis in the conceptual and planning stage, the near-field temperature simulation based on conceptual design of the Repository, and the safety assessment of Beishan Preliminary Repository.

5 Safety Assessment

5.1 Iterative Approach to Safety Assessment

This approach involves the following activities, which usually iterate and/or overlap:

- (a) Definition of the objectives of the assessment, safety requirements, and performance criteria;
- (b) Acquisition of information and description of the disposal system, including waste form, site characteristics, and engineered structures;

- (c) Identification of features, events, and processes that might influence long-term performance;
- (d) Development and testing of conceptual and mathematical models of the behavior of the system and its components;
- (e) Identification and description of relevant scenarios;
- (f) Identification of the pathways potentially leading to the transfer of radionuclides from the disposal facility to humans and to the environment;
- (g) Conduct of the assessment by conceptual and mathematical modeling;
- (h) Evaluation of the robustness of the assessment;
- (i) Comparison of the assessment results with the assigned safety requirements; and
- (j) Additional considerations.

5.2 The Scenario Development

The scenario development is the key step in HLW geological disposal. The features, events, and processes (FEPs) should be first considered. The FEPs can be sorted and grouped to form the scenario. It is very useful and has reference value for developing the FEPs of HLW geological disposal in a conceptual and planning stage in China by introducing the FEPs' established and sorted methods. Figure 8

Fig. 8 The flow of the America FEPs ridding

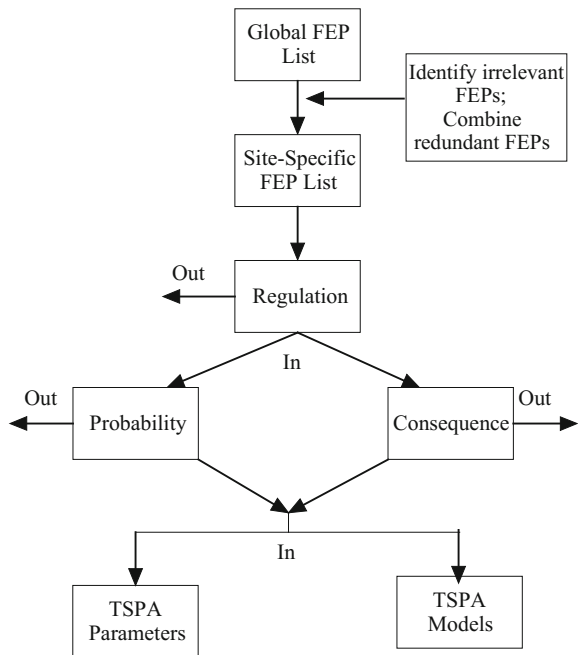


Table 1 The interaction matrix showing of Sweden

Rock-type quality	2	3	2	1	0	0	0	0	2	10
0	Discontinuities	4	3	0	0	0	0	0	4	11
2	3	Rock Stress	3	0	0	0	0	0	4	12
2	3	4	Construction	0	0	0	0	1	2	12
1	2	2	0	Backfill	1	0	1	3	10	
0	0	0	0	1	Carister	1	1	4	7	
0	0	0	0	1	1	Waste	4	4	10	
2	2	3	0	3	3	2	Heat	4	19	
2	4	3	3	3	3	1	3	Water flow/migration/gas	22	
9	16	19	11	9	8	4	10	27	Tot 113	

1: Heat to systems is 19, system to heat is 10

4: 'Critical' interaction

3: Strong interaction

2: Medium interaction

1: Weak interaction

0: No interaction

shows the flow of the America FEPs ridding. Table 1 illustrates the interaction matrix showing of Sweden.

5.3 The Safety Requirement for HLW Disposal

5.3.1 Safety Objectives

We have investigated the research on safety principle and the safety objectives of all other countries in the world. Dose and risk for future generations and

Table 2 Safety objectives of the other countries

Countries	Safety objectives	Another limit
IAEA	Dose: 0.3 mS v/year; Risk: $10^{-5}/a$	–
Canada	Basic scenario: 0.3 mS v/a; for destroy events: 1 ms v/a	–
USA	No human intrude: 0.15 mS v/year; human intrude (not beyond 10000 year): 0.15 mS v/year	Not consider the risk (scenario $<10^{-8}/$ year); human intrude beyond 10000 year): 3.5 mS v/year
Sweden	Risk: $10^{-6}/$ year (the dose change coefficient $0.073 Sv^{-1}$)	–
Finland	Basic Scenario: 0.1 mS v/year	–
France	Basic scenario: 0.25 mS v/year	Dose is suit for 10000y. Beyond of this time is only for reference.
Korea	Basic scenario: 0.1 mS v/year; for destroy events: $10^{-6}/$ year	Human intrude: 1mS v/year
Switzerland	Dose: 0.3 mS v/year; risk: $10^{-6}/$ year	Dose corresponding to high probability scenario; risk corresponding to low probability scenario
UK	Dose: 0.3 mS v/year; risk: 10^{-6}	Dose corresponding to high probability scenario; risk corresponding to low probability scenario
Belgium	Dose: 0.1-0.3 mS v/year; risk: $10^{-5}/$ year	Dose corresponding to high probability scenario; risk corresponding to low probability scenario
Spain	Dose: 0.1 mS v/year; risk: $10^{-6}/$ year	Dose corresponding to high probability scenario; risk corresponding to low probability scenario
Germany	Dose: 0.3 mS v/a	Timescale ($\sim 10,00,000y$)
Netherlands	Basic scenario: 0.1 mS v/year	Optimization objectives: 0.04 mS v/year
Czech	Dose: 0.25 mS v/year	Not consider the scenario (the risk $<10^{-6}/$ year)
Hungary	Dose: 0.1 mS v/year; for absolute destroy events; risk: $10^{-5}/$ year	Not consider the risk (scenario $<10^{-7}/$ year)

supplementary safety indicators (fluxes, concentrations, and time) were considered. The IAEA and ICRP think the public radiation protection for post-closure of HLW repository: 0.3 mSv/a, and the corresponding risk is 10^{-5} . The safety objectives of the other countries in the world are illustrated in Table 2.

Based on the safety objectives of IAEA, ICRP, and other countries, the safety objectives of China are as follows: public radiation protection for post-closure of repository: 0.3 mSv/a; risk: 10^{-5} /a; and timescale: ($\sim 10,000$ y).

5.3.2 Safety Requirement, Safety Function, and Safety Indicators

We have investigated the research on safety requirements of all other countries in the world. The safety requirement of EBS system was put forward.

The research of safety function of the EBS, host rock, and site, establishing the safety indicators' system of EBS, host rock, and site will be done in 2014–2017.

5.3.3 Other Works About Safety Assessment

The other works include the temperature evolution based on the conceptual design of the Repository, the near-field temperature simulation based on the conceptual design of the Repository, the safety assessment of Beishan Preliminary Site. The Web site of PBNC2016 is <http://www.pbnc2016.org/>. For more information, please visit the Web site.

6 Conclusions

The organization related to HLW disposal and the current progress in CIRP were introduced in this paper. Based on the HLW geological disposal primary conceptual design, the nuclide transport pathways in HLW geological disposal system were analyzed. Based on the normal scenario, the safety assessment was done: the maximum dose/a of public people.

The scenario development is the key step in HLW geological disposal. The features, events, and processes (FEPs) should be first considered. The FEPs can be sorted and grouped to form the scenario. It is very useful and has reference value for developing the FEPs of HLW geological disposal in a conceptual and planning stage in China by introducing the FEPs' established and sorted methods.

The works about the research of safety requirements of the EBS and host rock, the research of safety function of the EBS and host rock, establishing the safety indicators system of the EBS and host rock, establishing the FEPs list and the scenario analysis in the conceptual and planning stage, the near-field temperature simulation based on conceptual design of the Repository, and the safety assessment

of Beishan Preliminary Repository will be done in 2014–2017. This sample is illustrated to help your understanding on the paper format. We are looking forward to seeing you at the PBNC-2016.

References

1. Scenario development methods and practice. an evaluation based on the NEA workshop on scenario development Madrid, Spain, May 1999. OECD Radioactive waste management.
2. Scenario development methodologies. SKB technical report, 94-28, Sweden.
3. FEP report for the safety assessment SR-SITE.2010, SKB technical report, TR-10-45, Sweden.
4. FEP Management for Safety Assessment. Project Opalinus Clay, TECHNICAL REPORT 02-23, 2002年12月, Switzerland.
5. Project SAFE Scenario and system analysis. Svensk Kärnbränslehantering AB September 2001. R-01-13. SFR- Sweden.
6. Sumio Masuda, Hiroyuki Umeki, Morimasa Naito and so on. Key aspects of the second progress report in the Japanese R&D programme for HLW disposal. WM'99 CONFERENCE, FEBRUARY 28 - MARCH 4, 1999.

The Melting Treatment of Radioactive Steel Scrap from Decommissioning Nuclear Facility

Junxian Deng, Xin Li and Feng Deng

Abstract Large amount of radioactive scrap will come out from reactor decommissioning. The melting treatment can be used for the volume reduction, the recycle and reuse of the radioactive scrap to reduce the mass of the radioactive waste disposal and to reuse most of the metal. The melting treatment has the advantages in the volume reduction, the conditioning, the radionuclide confinement, the reduction of radioactivity concentration, the easy monitoring of radioactivity, and the good decontamination effect for several radionuclides. To use the melting technology, other decontamination technology should be performed ahead, the decontamination effect of the melting should be predicted, the utility of recycle and reuse should be defined, and the secondary waste should be controlled effectively.

Keywords Reactor decommissioning • Radioactive scrap • Melting treatment

1 Introduction

Substantial quantity of steel scrap would be generated from dismantling equipment and piping of decommissioning nuclear reactor. The major part of the scrap is of low level contaminated. To reuse and recycle the scrap would recover the valuable material and conserve the available space of the final repository.

J. Deng (✉)

China Nuclear Power Engineering Cooperation Ltd,
Nuclear Reactor Engineering, Beijing, China
e-mail: djx0628@sina.com

X. Li

China Nuclear Power Engineering Cooperation Ltd,
Nuclear Facility Decommissioning, Beijing, China
e-mail: lx_mantoya@126.com

F. Deng

China Nuclear Power Engineering Cooperation Ltd,
Nuclear Power Engineering, Beijing, China
e-mail: dengfeng@cnpe.cc

2 The Generation of Radioactive Waste Metal

After reactor's final shutdown and discharge of irradiated fuel, the inventory of residual radionuclide is divided in two categories.

2.1 *The Neutron-Activated Material*

These materials are located in or near by reactor core and are exposed by neutron. The reactor core is the most activated part of reactor structure. The parts exposed to lower neutron fluence are the biological shielding.

2.2 *The Contaminated Material*

The contamination is generated from two parts of diffusion: The corrosion and erosion products which are carried by reactor coolant going through the reactor core induced by exposure becoming the activated products; the fission products which leak out through the clad of the defective fuel.

The contamination is caused by the leakage from the reactor primary loop, the treatment, and storage system of radioactive effluent and waste; the accident in maintenance action and refueling operation. The gas contamination may cause the deposition of radioactive substance on the wall, ceiling, and ventilation system.

After reactor's final shutdown and before decommissioning work beginning the nuclear fuel and the fluid have been removed from reactor; however in certain case, especially the reactor is experienced abnormal event such as fuel element defect, these residual products are stored and they should be included in radioactive inventory.

Notice that in general activated parts are contaminated, the contaminated area that may not be activated for the contaminated substance is transferred to certain area beyond the extent effected by neutron fluence.

The material of reactor coolant system is stainless steel, even its corrosion rate is very low. In the coolant loop, the soak area of coolant is very large, so total amount of corrosion product is quite large. The corrosion generated on material surface and corrosion products are not standstill. The surface-oxidized layer and deposit layer are formed by the main part of corrosion products from the basic metal. By the influence of coolant temperature and PH value, the corrosion products will be dissolved, suspended, deposited, and peeled off. The corrosion products from reactor core and coolant loop are transmitted each other by these dissolution and deposition process continuously. After certain period, the constitutions of the corrosion products deposited everywhere are almost the same. Most of the corrosion products in the coolant are suspended in water; they are very easy to deposit on

the surface of the equipment and piping especially the dead angle, crevice, and where the velocity of fluid flowing is lower; only a few corrosion products are dissolved.

3 The Effect of Melting Treatment

3.1 The Volume Reduction

The major positive advantage of the melting technology is volume reduction (two to ten times for metals). Early-year melting plant for radioactive material is the waste experimental volume reduction facility (WERF) in USA, and the melting plant used for volume reduction of radioactive waste metal is UK steel technique. Their purpose is volume reduction.

3.2 The Conditioning

By melting technology, the waste metals become the compact form. In melting process, the radioactive nuclides remained in the melting material are distributed homogeneously and after solidified they are fixed efficiently, the further conditioning is unnecessary.

3.3 The Reduction of Waste Metal Radioactivity

As a decontamination technique, the melting is effective only in the case that the contamination is volatile or it is accumulated in slag, dross (such as Pu) is not in molten. There are big differences of the decontamination effectiveness among these existing radioactive nuclides. In melting process, ^{137}Cs is concentrated in the ash collected by filter of ventilation system. As ^{137}Cs , removing the occupational exposure of the casting worker during further melting will be obviously reduced. It is expected that the radioactive nuclides are distributed in molten, slag, and filter ash. The nuclides of iron group such as ^{60}Co , ^{63}Ni 90% are in molten, about 10% is in slag. The nuclides of ^{90}Sr , ^{154}Eu , and actinides are concentrated in slag (about 95%). The nuclide of ^{137}Cs is in slag and ash separately each half and half. Most the tritium can be volatilized at 250 °C (85–90%) and at 660 °C almost all of the tritium is released; in a special case, the tritium can be removed in off gas by molecular sieve. The substance in different composition can be separated by melting technology. The separation extent is dominated by existing physical and chemical properties of radioactive nuclides. The effect of melting decontamination is related

to certain factor as the additive, the melting temperature, and the melting duration. As the melting of 15,000 t waste metal in Siempelkamp, Germany, after melting in the ingot, there are most of ^{55}Fe , ^{60}Co , ^{63}Ni , ^{125}Sb , ^{95}Nb , ^{96}Nb , nearly half of ^{144}Ce , ^{54}Mn , ^{103}Ru , ^{106}Ru , less of ^{95}Zr , ^{65}Zn , a bit of ^{152}Eu , ^{154}Eu , ^{134}Cs , ^{137}Cs , ^{90}Sr , ^{235}U , ^{238}U , ^{241}Am , ^{231}Th , ^{234}Th , $^{234\text{m}}\text{Pa}$, and $^{110\text{m}}\text{Ag}$ [1]. The prevailing nuclide is ^{60}Co , its half-life is 5.3 years, and the other nuclides remained have even shorter half-life. Therefore, the ingots which have proper lower radioactivity concentration can be recycled after storage for certain duration. In Studsvik, Sweden, the ingots with the radioactivity concentration lower than 14 and 7 Bq/g will be stored for 20 years. After the radioactivity concentration is lower than 1 and 0.5 Bq/g the ingots can be released, remolded, or unrestrictive released as the regulation (the new license is no longer necessary). The ^{60}Co is remained in ingot, so the steel contaminated by ^{60}Co should be decontaminated before melting, and the testing result in Japan indicates that the steel contaminated by ^{60}Co and ^{63}Ni can be decontaminated by oxidation and reduction.

Another positive effect of melting treatment is that the radioactive nuclides in the contaminated waste metal are diffused in whole ingot. Radioactivity concentration in bulk metal can be reduced by homogeneous and may reach the criterion for recycle.

After melting treatment part of radioactive nuclides are concentrated in the dross and are solidified on the top of ingot, they can be cut off for treatment as radioactive waste. The ingots have lower radioactivity than that of pervious one, so there are the effect of decontamination.

3.4 The Waste Recycle and Reuse

For the most of the decommissioning projects, melting is a proper approach for metal recycle. The ingots can be restrictive or unrestrictive released and be reused after storage and decay for certain duration. An advance requirement for widely use of melting treatment technology is to establish the regulation of precise limitation for specific radioactivity in unrestrictive release and reuse. There is the provision for this in China National Standard GB13367 and GB17567. In Germany, the provision for this is that the ingots with specific radioactivity higher than 74 Bq/g should be decontaminated, for that cannot be decontaminated should be conditioned and deposited, for the ingots with specific radioactivity lower than 74 Bq/g should be melted; after the treatment, the ingots with specific radioactivity higher than 3.7 Bq/g can be reused in nuclear field; the ingots with specific radioactivity between 3.7 Bq/g and 0.37 Bq/g can be released but can not be used in daily life; the ingots with specific radioactivity lower than 0.37 Bq/g can be unrestrictive released. In Sweden, the provision for this is that the ingots with specific radioactivity lower than 1.1 Bq/g can be released and melted and the ingots with specific radioactivity lower than 0.5 Bq/g can be freely released.

As an option, some ingots with specific radioactivity higher than the level for free release can be melted and be manufactured for shielding bulk or be rolled for the container used for radioactive waste recycled in nuclear industry.

As IAEA Safety Serious No. III-P-1.1, the individuals' dose limitation in key group is very low and the collective dose should be lower than 1 men.Sv. If personal dose is lower than 10 mSv/year, both criterions should be met. An expert group from CEC give a recommendation of 1 Bq/g for β and γ emission clearance (CEC Radiation Protection No. 43 Luxembourg), this recommendation value will be modified. SSK, Germany, recommended a more serious value of 0.1 Bq/g total radioactive level for unrestricted released and 1 Bq/g for directly be sent to cast plant.

The values in other countries are in between these two values, such as in Japan (0.5 Bq/g) or in UK (0.4 Bq/g).

3.5 Easy Radioactivity Monitoring for Waste Metal

The radioactive waste metals often come from the equipments which have complex geometries, making it extremely difficult, time-consuming, and expensive to determine the exact location and level of radioactivity on internal surfaces. The melting treatment eliminate nonachievable area, the radioactivity remaining in the ingot is distributed homogeneously. The radioactivity can be determined by sampling of each ingot, the monitoring processes of radioactive metal characterization are simplified.

3.6 The Generation of Secondary Waste

The secondary waste is from the slag solidified on the top of ingot and from the dust in filter of ventilation system. The secondary waste is only between 1 and 4% of the weight of melted metal. With the addition of the liner and waste tool, the total is 5–10% of the weight of melted metal.

The total of the particle generated typically is about 1% of the weight of melted metal. Some research indicates that aerosol with diameter about 1 μm and less is generated in melting operation. The aerosol can be successfully recovered with prefilter followed by HEPA. Several types of filter are tested. The data from the test indicate that the electrical filter is more efficient than others.

The slug is generated by the nonmetal taken from the surface of the ingot and the melting additive and oxidizes from the crucible. The weight of the slug generated during the melting operation is 5% of total weight of the metal treated. If the metal will be reused, the slug and the ingot should be separated. The slug separated will be immobilized in solid matrix as radioactivity level. If the melted metal is the disposed waste, the slug separation is not important.

4 The Melting Technology Development in the World

4.1 Early-Year Melting Facility

- Were experimental volume reduction facility in USA.

A melting plant for radioactive materials, the purpose is volume reduction, for the low cost of waste disposed at that time; the plant was stopped in 1975.

- The melting plant for radioactive steel scrap volume reduction of steel technique UK.

The plant was operated during 1981 to 1985. It was stopped for economical reason.

4.2 Recent Melting Facility

- Carla plant in Siempelkamp, Germany

3.2-t middle-frequency induction furnace. The steel, brass, copper, aluminum, and lead have been melted. The special radioactivity concentration of the waste is up to 200 Bq/g. The operation started from 1989.

- Studsvik, Sweden

A 2-t induction furnace for steel and a smaller electrical arc furnace for aluminum were operated first; and then, two set of 3.5-t induction furnaces were operated, the output is 1.5 t/h, 6 ingots each lot, 600 kg each ingot. The operation was started from 1992.

- Infante plant in Marcoule CEA-UDIN, France

1.4-t electrical arc furnace, the special radioactive concentration is up to 250 Bq/g, and it was started from 1992.

- SEG in USA

20-t induction furnace, the melted coupon has the waste with heavy contamination up to 20 kBq/g and the doze rate up to 0.12 Sv/h, and it was started from 1992.

- Testing plant in Japan

- Testing plant in

4.3 *The Melting Treatment Technology*

- Conventional metal melting

The induction furnaces are used for most of the melting, such as the special furnace of Siempelkamp cast plant in Kredfeld, Germany; the melting furnace in Saclay, France., 700 kg each lot, the maximum of radioactivity concentration of the waste is 10^4 Bq/kg(Co, Sr, Cs) it was started at 1986.

- Electroslag melting

Such as the electroslag melting facility in Japan, its capacity is 100 kg each lot.

- Plasma melting

It is heated by plasma gun.

5 Conclusions

- The decontamination effect of the melting for radioactive scrap

For the actinides, the isotopes of europium, strontium, silver, zirconium, and zinc, the effect of decontamination by melting is obvious; for the isotopes of cerium, manganese, ruthenium, there is certain effect; but for the isotopes of iron, cobalt, nickel, antimony, niobium, there is no any obvious effect. For reaching the identical goal, the other decontamination technology such as high-pressure water jet, ultrasonic, mechanical, chemical decontamination technology should be performed ahead.

- The recycle and reuse of the radioactive scrap

The radioactive scrap should be measured precisely to determine the radioactive nuclides and their radioactivity concentration and then the performance of the decontamination and further measurement. It is better to reach the clearance level and then to be reused. The regulation of precise limitation for special radioactivity in recycle and reuse and the method of measurement should be defined. To avoid overstock, the usage and direction of the cast ingot should be practicable.

- The effective control of the secondary waste

The secondary waste consists of liter dust in off gas, sludge, waste tools, and furnace liner.

- We set up melting unit the operation is successfully the improvement should be done.

References

1. M.Sappok, Recycling of metallic materials from the dismantling of nuclear plants, *Kerntechnik* Vol. 56 No. 6, 1991, 376–378.
2. IAEA, Methods for the Minimization of Radioactive Waste from Decontamination and Decommissioning of Nuclear Facilities, Technical Reports Series No 401, IAEA, Vienna, 2001, 89–91.
3. IAEA, State of Art Technology for Decontamination and Dismantling of Nuclear Facilities, Technical Repots Series No. 395, IAEA, Vienna, 1999, 95–98.
4. IAEA, Radiological Characterization of Shut Down Nuclear Reactors for Decommissioning Purposes, Technical Reports Series No. 389, IAEA, Vienna, 1998,14–16.
5. IAEA, Status of Technology for Volume Reduction and Treatment of Low and Intermediate Level Solid Radioactive Waste, Technical Reports Series No. 360, IAEA, Vienna, 1994, 45–50,73–83.
6. Manfred LASER, Melting makes the most of scrap metals, *Nuclear Engineering International* Vol. 39 No. 476, March 1994, 51–52.
7. K.Pelugrod et al, Decommissioning of Nuclear Installation, EUR12690, Elsevier applied science,1990, 473–503.
8. IAEA, Managing Low Radioactivity Material from the Decommissioning of Nuclear Facilities, Technical Report Series No. 462, IAEA, Vienna, 2008, 33–36.

The Radioactive Waste Minimization of Tianwan NPP Units 3&4

Tiejun Liu, Zhiyin Zhang and Xiaorui Qu

Abstract TianWan NPP units 3&4 adopt WWER, the wet waste generation rate is higher than the other PWR nuclear power plants in China, and the waste volume to be disposed is relatively high because of the plan of preliminary cementation solution for the wet waste. To satisfy the waste minimization requirement of authority department, the design measurements to reduce radioactive waste from the source are taken for Tianwan NPP units 3&4 and the radioactive waste treatment center shared by Tianwan units 1 ~ 6 is under construction. Drying, super-compaction, and grouting process are used in the waste treatment center to treat radioactive waste, packaging with concrete high integrity container, and the waste volume to be disposed for one unit per year will be less than 50 m³ under the precondition that the waste packages are able to meet the requirements of near-surface disposal facilities.

Keywords Tianwan nuclear power plant · Waste minimization · Solid radioactive waste · Waste treatment center · Waste volume reduction

1 General

Tianwan NPP units 3&4 which adopt Russian WWER are under construction. The radioactive wet waste generation rate of WWER is higher than the improved M310 and AP1000 reactors constructed at the same period, and the comparison of raw solid waste generation rate with the different reactors is listed in Table 1.

T. Liu (✉) · Z. Zhang · X. Qu
Radioactive Waste Treatment, China Nuclear Power Engineering Co., Ltd, Beijing, China
e-mail: Liutj@cnpe.cc

Z. Zhang
e-mail: Zhangzy@cnpe.cc

X. Qu
e-mail: Quxr@cnpe.cc

Table 1 WWER, Improved M310, and AP1000 solid waste generation rate for one unit

Waste type		WWER raw waste reality generation rate ^a	Improved M310 raw waste reality generation rate ^b	AP1000 raw waste expected generation rate ^c
Wet waste	Spent resin	13.9 m ³	2.7 m ³	11.33 m ³
	Still residue	13 m ³	2 m ³	No still residue
				Chemical liquid waste 17.4 m ³
	Sludge	1 m ³	Non	Non
	Spent filter cartridge	Non	17 set	4 sets, total 0.15 m ³
Dry waste	Compactable waste	95.4 m ³	100 m ³	134.5 m ³
	Non-compactable waste	2.9 m ³	4 m ³	6.62 m ³

Note ^aThe raw waste generation rate of WWER refer to the reality waste generation data of Tianwan NPP unit 1&2 from 2007 to 2012 [1]

^bThe raw waste generation rate of Improved M310 reactor refer to the reality waste generation data of Daya Bay NPP from 2002 to 2012 [1, 2]

^cThe raw waste generation rate of AP1000 reactor refer to the design document of Sanmen NPP [1]

At early stage, Tianwan NPP units 3&4 planned to use cementation process to treat radioactive wet waste and the steel drum was adopted as waste package container. Because the volume increase factor of cementation process is relatively high, only the annual waste package from wet waste treatment per unit has reached 71 m³ after calculation. Then the waste minimization requirement of national authority department in “Safety requirements to new nuclear power plant to be constructed during the twelve-five-years period” can’t be reached, the requirement is the waste volume of one unit to be disposed can’t exceed 50 m³/year.

To meet the waste minimization requirement of national authority department, reduce the waste disposal cost, and provide better waste treatment solution to the environment, Tianwan Nuclear Power Base decided to construct the Radioactive Waste Treatment Center (T4UKT) shared by 6 units and took measurements to reduce the radioactive waste from the source; T4UKT adopts volume reduction process to treat radioactive waste; the waste minimization requirement of authority department can be satisfied; and the near-surface disposal requirement to waste package can be satisfied.

2 Waste Minimization Solution

The Tianwan NPP units 3&4 use source control, rational sorted collection, and treatment process improvement measurements to realize waste minimization. Together with reference to successful waste minimization experience in

Tianwan NPP units 1&2, the design solution optimization and management measurement enhancement are actualized to reduce the radioactive waste package generation rate and improve the waste minimization level. It can be ensured that the annual radioactive waste package volume generated will not be exceeded 50 m³ per unit and the near-surface disposal requirement to waste package can be satisfied at the same time.

2.1 Source Control

According to the operation experience of Chinese nuclear plant, the major factors which affect waste generation rate include the following: operation management level, good condition of related equipment, generation of radioactive waste, and usage of consumable material. Under the strict management regulations, adopting the high reliable equipment and ensuring safe and stable operation can decrease the equipment leakage and maintain the equipment effectively.

2.1.1 The Source Control Measurement from Design Aspect

Reduce the Generation Rate of Still Residue and Spent Resin

For the Drain Water Processing System (KPF) of Tianwan NPP units 1&2, all the collected wastewater was evaporated. A bypass pipe is added in KPF system of Tianwan NPP unit 3&4, the liquid waste whose radioactivity is lower than 2000 Bq/L will be demineralized in KPF60 subsystem instead of evaporation, and the volume of still residue is reduced (Fig. 1).

A mobile tank for slightly contaminated spent resin is added in Liquid Radioactive Waste Storage System (KPK) of Tianwan NPP units 3&4; the spent resins from secondary loop such as steam generator blowdown system (LCQ) are collected separately and stored for decay and further clearance release, and these spent resin cannot be processed as radioactive spent resin.



Fig. 1 Degradable protection articles and its treatment equipment

Adopt Degradable Protection Articles to Reduce the Generation of Dry Active Waste

According to the operation experience of Qinshan NPP, Daya Bay NPP, and Tianwan NPP, the dry active waste consists of more than 80% plastic, paper, and cotton material. When the traditional protection articles are seriously contaminated, they need to be collected and treated as dry active waste, and for the soft waste, springback occurs seriously after super-compaction, so the volume reduction effect of super-compaction is not perfect. The degradable protection articles are made of PVA, and they will dissolve in hot water; the contaminated degradable protection articles can be sent to the degradable waste treatment equipment; it becomes carbon dioxide, liquid waste and small amount of secondary waste after dissolution, filtration, and hot oxidization; the liquid waste and gaseous waste can meet discharge requirement; and the small amount of solid secondary waste will be super-compacted and grouted.

Tianwan NPP units 3&4 will also adopt degradable work clothes and one-time protection articles instead of traditional cotton protection articles. The compactable dry active waste will be reduced to 40% of the original volume [3, 4].

2.1.2 The Source Control Measurement from Operation Aspect

After Tianwan NPP units 3&4 start operation, the beneficial waste minimization practice of Tianwan NPP base and other Chinese nuclear power plant will be referred [3]. The publicity, training, and management will be enhanced to shape the waste minimization and environment protection concept of staff. The train of work skill will be enhanced to form the good work habit and avoid the unnecessary generation of radioactive waste.

2.2 Rational Sorting

The waste generation during nuclear power plant operation and maintenance is strictly sorted before the collection and treatment process. The reusable fluid from the primary loop is sent back to the primary loop for reuse.

The spent resin is collected by radioactivity level, whereas the low- and intermediate-level spent resins are stored in spent resin tank to decay for a period of time before transported to T4UKT for treatment. The spent resin from important plant use water middle cooling circuit (KAA) and steam generator blowdown system (LCQ) filters is normally slightly contaminated, and they will be transported to special area of waste temporary storage depository for storage and decayed until the clearance release.

The dry active wastes are sorted into compactable dry waste, moisture compactable dry waste, and non-compactable dry waste before treatment according to their characteristics.

The dose rate of spent filter cartridge from ventilation system is very low; most of the radionuclides are short-lived, and they will be transported to special area of waste temporary storage depository for storage and decay until clearance release.

The big size waste whose dose rate is very low will not be treated as radioactive waste, and they will be transported to special area of waste temporary storage depository for storage and decay until clearance release.

2.3 Adoption of Advanced Waste Treatment Process

Firstly ensure that the waste package can meet near-surface disposal requirements, and then comprehensively compare the maturity, economy, and waste minimization effect [5, 6], and Tianwan NPP units 3&4 select to adopt the waste treatment process in Fig. 2 to treat and reduce the volume of solid radioactive waste after analysis and argumentation.

The waste volume reduction equipment is installed in T4UKT building, T4UKT is a separated building which is constructing together with Tianwan NPP units 3&4 and will be shared by Tianwan NPP units 1–6, the centralized treatment mode is adopted, and various kinds of solid radioactive waste collected in nuclear island will be transported to T4UKT for treatment by special transport vehicle.

2.3.1 Spent Resin Treatment System

To improve the volume reduction factor of spent resin hot-compaction process, the grinding step is added in the spent resin hot-compaction process in Tianwan NPP waste treatment center; the non-radioactive b do not need to be added anymore, and the volume reduction factor can reach 1.65 (the over-pack container is not considered).

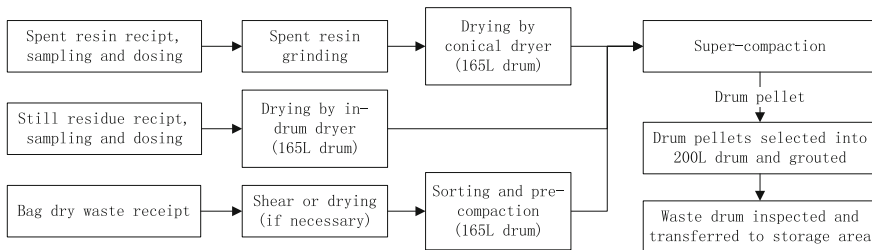


Fig. 2 Waste treatment process flow diagram of waste treatment center

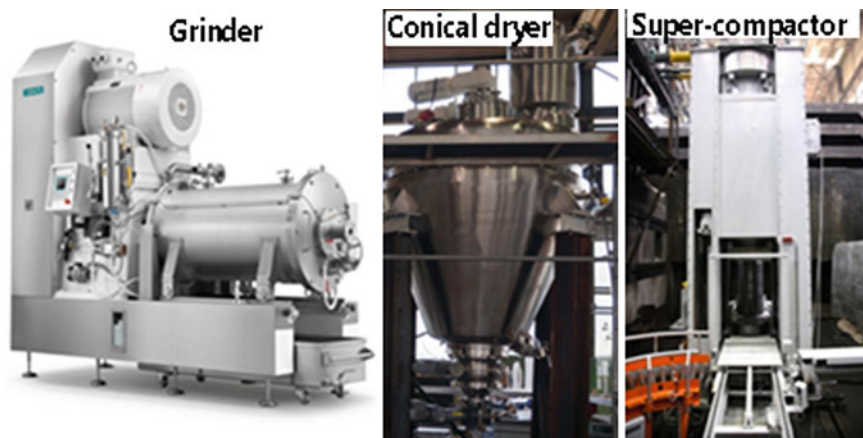


Fig. 3 Equipment photograph of spent resin treatment system

To satisfy the near-surface disposal requirement, the 200 L waste drum with spent resin is loaded into concrete high integrity container (HIC), and the volume increase factor of HIC is 3.5 times to a 200 L drum (Fig. 3).

2.3.2 Still Residue Treatment System

The still residue in-drum dryer is heated by electrical heating jacket; the sealed filling head, drip pan, and demister are on the top; and the necessary condenser and steam–water separator are provided. The volume reduction factor of drying and compaction processes to still residue and hydrocyclone sludge can reach 7 (the over-pack container is not considered).

The 200 L waste drum with salt of still residue is loaded into concrete high integrity container (HIC), and the volume increase factor of HIC is 3.5 times to a 200 L drum (Fig. 4).

2.3.3 Dry Waste Treatment System

The dry active waste is sorted into non-compactable waste, directly super-compactable waste, compactable waste, and moisture waste and is treated separately. The sorting glove box consists of hydraulic unit, necessary operator platform, steel drum lifting device, gates, etc.

The shear glove box contains a fixed hydraulic shear which is to shear thin-wall metal parts and pipe, and the sheared waste is loaded into 165 L steel drum for super-compaction and grouting.



Fig. 4 Equipment photograph of still residue in-drum dryer



Fig. 5 Equipment photograph of dry waste sorting box, precompactor, and shearing box

The volume reduction factor can reach 4.1, and the waste drum containing super-compacted and grouted waste drum can meet near-surface disposal requirement (Fig. 5).

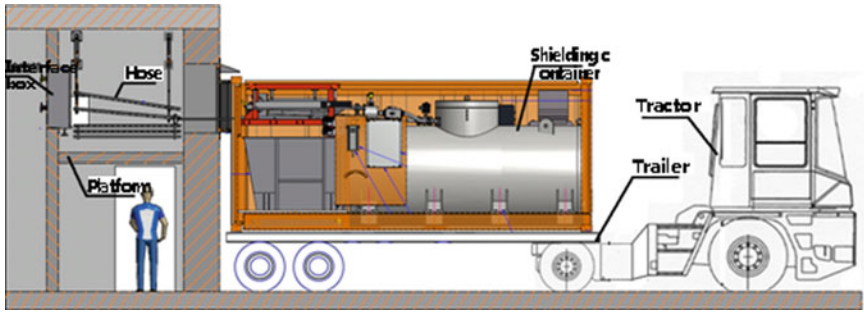


Fig. 6 Diagram of tank wagon receiving still residue in nuclear auxiliary building

2.3.4 Wet Waste In-Site Transportation Solution

The spent resin and still residue collected in nuclear islands are transported to the waste treatment center for treatment, and the interface equipment for liquid waste transportation is installed separately in auxiliary building of units 3&4.

Firstly, the spent resin tank wagon and the still residue tank wagon are parked outside of auxiliary building; the quick couplings are connected; the spent resin or still residue is loaded into tank wagon; and finally, the spent resin or still residue is transported to waste treatment center and unloaded. The anti-leakage quick couplings are installed in interface box of auxiliary building and waste treatment center, and the quick couplings need flush before disconnection (Fig. 6).

3 Effect of Waste Minimization Solution

After the application of waste minimization solution in this article, the waste package volume of Tianwan NPP units 3&4 which adopt WWER type is 83.5 m³/year per unit (design value after conditioning) and 48.8 m³ (expected value after conditioning) (see Table 2 for details).

Combining with source control and rational sorting measurements, Tianwan NPP units 3&4 adopt drying, super-compaction, and grouting process in T4UKT together with concrete high integrity container; the waste treatment process is relatively mature; and these waste minimization measurements can ensure that the waste package can meet near-surface disposal requirement and the expected volume of waste package to be disposed from Tianwan NPP unit 3&4 per year per unit will not exceed the 50 m³ target.

If Tianwan NPP units 3&4 adopt the cementation process selected at early stage to treat wet waste and adopt super-compaction process to treat dry active waste (without degradable protection articles), the expected volume of waste package to be disposed from Tianwan NPP units 3&4 per year per unit will be 97.4 m³, and this waste package volume is nearly twice of the current solution.

Table 2 Waste package volume of Tianwan NPP units 3&4 for one unit per year

Waste type	Raw waste volume		Treatment process	Waste package volume		Container of waste package	
	Expected value ^a (m ³)	Design value (m ³)		Expected value ^a	Design value		
Wet waste	Spent resin	13.9	20.4	Hot compaction	42.1 drum	61.8 drum	Concrete HIC (700 L)
	Still residue	13	20	Drying and compaction	9.3 drum	25 drum	Concrete HIC (700 L)
	Hydrocyclone sludge	1	1.5	Drying and compaction	0.2 drum	1.1 drum	Concrete HIC (700 L)
Dry active waste	Compactable dry waste	38.16	66	Super-compaction and grouting	46.5 drum	80.5 drum	200 L steel drum
	Degradable waste	57.24	99	Degradation, compaction and grouting	2.4 drum	4.1 drum	200 L steel drum
	Non-compactable dry waste	2.9	5	Grouting	14.5 drum	25 drum	200 L steel drum
Total waste package volume					48.8 m ³	83.5 m ³	

Note ^aThe expected value of raw waste refers to the practical raw waste generation of Tianwan NPP units 1&2 from 2007 to 2012

4 Conclusion

The waste minimization solution of Tianwan NPP units 3&4 is improved based on the cementation solution selected at early stage. Raw waste generation rate is reduced by source control and rational sorting, waste treatment center is constructed and shared by the whole NPP site, the radioactive waste is treated, and the volume is reduced by the adoption of drying, super-compaction, and grouting process. The waste package generation volume can be effectively reduced, and the pressure of in-site storage and final disposal can be released. The waste package after treatment can meet storage, transportation, and disposal requirement.

By adoption of improved waste minimization solution, the volume of waste package to be disposed from Tianwan NPP units 3&4 is significantly reduced, the waste package can meet near-surface disposal requirement, the expected waste package volume is 48.8 m³/a unit, and the volume is only 50% of the cementation process; the waste minimization requirement in “Safety requirements to new nuclear power plant to be constructed during the twelve-five-years period” can be satisfied. The waste disposal cost is cut down, and the good economy benefit and society benefit can be foreseen.

References

1. Zhang Zhiyin, Yan Cangsheng, Huang Laixi. The radioactive waste minimization in nuclear power plant [M]. Beijing: China Atomic Energy Publishing Company, 2013: 98–99
2. Daya Bay nuclear power operation and management Co. Ltd, The 2012 yearbook of Daya Bay nuclear power operation and management Co. Ltd [M], 2012
3. Zhang Yuan, Li Guanghua, Mu Jinde, The radioactive solid waste management and minimization practice in Tianwan NPP [J]. Radiation protection communication, 2010, 30 (1):35–39
4. Jia Xiaohong. The application of degradation technology in Tianwan NPP [J]. Application technology, 2014, 9(second): 181–182
5. IAEA, TECDOC-1504, Innovative Waste Treatment and Conditioning Technologies at Nuclear Power Plants[M]. Vienna: IAEA, 2006
6. Zhou Yan, Zhang Haifeng. The discuss about the application of hot-super-compaction technology for treatment of low and intermediate level radioactive spent resin in NPP [J]. China Atomic Energy Publishing Company, 2012, 46 supplement, 142–146

The Management Status and Advices of Radioactive Solid Waste from Development and Utilization of Mineral Resources

Caixia Lv, Shujun Xie, Keyan Teng, Qing Sheng and Ailing Zhang

Abstract This paper analyzed the determination Then, we gave some advices.and characteristics of radioactive solid waste for company on the mineral resources development and utilization, also pointed out the current situation on temporary storage, minimization, and disposal of radioactive solid waste.

Keywords Development and utilization of mineral resource · Radioactive solid waste management

1 Introduction

Some typical mineral resources associated with radionuclide, such as uranium and thorium, rare earths, niobium, tantalum, coal, vanadium, zirconium, and other mineral resources, are included in the development and utilization of mineral resource of management directory (the first batch of directory) [1]. Like nonferrous mineral (molybdenum ore, copper ore), boron and iron ore mineral, phosphate mineral, and so on are not included in the directory. With the development and utilization of mineral resources, the radionuclides were separated and enriched in the treatment process. Partially, radionuclides enter into the various types of products or by-products, some of them enter into the environment in the form of gaseous and liquid emissions, and the rest of them enter into processing waste or sludge from liquid waste treatment and then become radioactive solid waste. Then, they will produce damage to the environment. Here, we summarized the current management status of radioactive solid waste during the development and utilization process of the mineral resources and meanwhile make some suggestions in radioactive solid waste temporary storage, treatment and disposal, and management.

C. Lv (✉) · S. Xie · K. Teng · Q. Sheng · A. Zhang
Nuclear and Radiation Safety Center, MEP, Beijing, China
e-mail: jianghong@cnpe.cc

2 Determination of the Solid Radioactive Waste in the Process of Development and Utilization of the Mineral Resources

At present, it is not very clear whether the radioactive waste generated is in the process of the development and utilization of mineral resources. According to the *Safety of Radioactive Waste Management Regulations*, “article 2: the Radioactive waste in this Regulations contained radionuclides, or polluted by radionuclides, or radionuclide concentration or activity is greater than the defined clearance levels by National standard, and they will not used in the future” [2]. There are several standards in China, defined clearance levels, such as GB18871-2002 (*Basic standards for protection against ionizing radiation and for the safety of radiation sources*), GB17567-1998 (*Clearance levels for recycle and reuse of steel and aluminum from nuclear facilities*), and GB27742-2011 (*Activity concentration for material not requiring radiological regulation*). The level be specified as “the levels are only appropriate apply to the workplace where or the small amount of radioactive material in the where there are well-organized, well-trained staffs and industrial applications and laboratory or medical applications Sources “ in the Appendix A of GB18871-2002 [3] should not apply to solid waste generated in the process of development and utilization of the mineral resources. The clearance levels in the GB17567 (*Clearance levels for recycle and reuse of steel and aluminum from nuclear facilities*) apply to the steel and aluminum materials from the decommissioning of nuclear facilities or the application of nuclear technology. The exempt activity concentration of natural radionuclide is 1 Bq/g, clearly defined in the GB27742-2011 (*Activity concentration for material not requiring radiological regulation*). Therefore, this standard is valid for the radionuclide that they are in the natural decay chain of long-term equilibrium conditions [4]; in other words, the values in this standard are applicable for the decaying chain beginning with U-238, U-235, and Th-232. These values in this standard can also be, respectively, used for each decay products from these decay chains or are applicable to the decay chain beginning with decay products, such as the decay product Ra-226 as decay parent; in addition, they include the natural radionuclide in this region; namely, total values contain the so-called background values [4]. Therefore, solid waste generated in the process of development and utilization of the mineral resources is considered as radioactive solid waste when the activity concentration exceeds 1 Bq/g. Classification and management of the above radioactive solid waste should be in accordance with GB9133 (*Classification of radioactive waste*) and GB14500 (*Regulations for radioactive waste management*).

3 The Characteristics of Radioactive Solid Waste Are Generated in the Process of Development and Utilization of the Mineral Resources

Development and utilization of mineral resources are involved in many industries. Radioactive solid waste is produced from mining, smelting and separation, waste water treatment, and other processes. Generally, the radioactive solid waste from the development and utilization of the mineral resources had common characteristic as follows:

- (1) Radionuclides are all natural radionuclides and are represented by uranium and thorium series decay chains, mainly U-238, Th-232, Ra-226, etc. They are all longlife radionuclide, and the nature of the radioactive solid waste from the uranium mining metallurgy is basically similar.
- (2) The quantity and activity concentration scope of radioactive solid waste are large. The scope is between 1 and 1000 Bq/g, the dates show there were 400 companies in seven provinces from the “the state and advices research of development and utilization of radioactive pollution” be completed in 2000. Radioactive solid waste is generated; there were 3Mt that the activity concentrations were under 2×10^4 Bq/kg, and there were 8 Mt that the activity concentrations were beyond 2×10^4 Bq/kg [5]. The environmental pollution prevention and control of rare earth industry are investigated in Jiangxi and Jiangsu provinces in 2015. The survey data showed that the activity concentration of radioactive solid wastes of the two provinces was in the range of 1–100 Bq/kg. Tables 1, 2, and 3 show the measurement results of radioactive solid waste of the rare earth [6].
- (3) Some waste can be recycled and reused. Such as the slag, the content of rare earth reached 1–10%, and the acid slag also contains high levels. The residue of uranium content in partial waste reached the uranium mining level, but some waste residue may affect the dissolution performance of uranium in slag after high-temperature calcination process, and the recovery of uranium needs further research.
- (4) After separation and enrichment of metal thorium, a large number of materials could be produced containing high thorium; because the development and utilization of thorium-based molten salt reactor are still in infancy, this kind of material is not expected to use in the short term. Although this resource can

Table 1 Activity concentrations of radioactive solid waste from the rare earth smelting in Sichuan Province (Bq/g)

Sample	Gross α	Gross β	^{238}U	^{232}Th	^{226}Ra
Cerium richment	176	64	–	21.5	2.2
Lead slag	2480	932	8.9	314	10.6
Iron thorium slag	224	81.7	0.43	23.5	3.6

Table 2 The activity concentrations of the slag from the rare earth separation in Jiangxi Province (Bq/g)

Sample	Gross α	Gross β	^{238}U	^{232}Th	^{226}Ra
The acid slag	30–75	24–35	9.7	2.2	4.4
The other slag	7–8	3–5	0.8	0.26	0.15

Table 3 The activity concentrations of the slag from the rare earth separation in Guangdong Province (Bq/g)

Sample	Gross α	Gross β	^{238}U	^{232}Th	^{226}Ra
The acid slag	185	34.2	0.913	3640	3850
Inorganic sludge	3.27	1.22	0.15	0.21	0.012

not reflect value in a short period of time, the storage cost is too high for the enterprise, if as waste to dispose, it will cause the waste of resources. It maybe reuse value, whether this kind of material is waste are being discussed.

4 Temporary Status of Associated Mine Radioactive Solid Waste

According to the requirements of *the People's Republic of China Radioactive Pollution Protection*, “Radioactive solid wastes produced during the process of development and utilization of uranium (thorium) mines and associated radioactive mines, shall be stored and disposed by building the tailings; and the tailings should conform to the requirements of radioactive pollution protection” [1]. A lot of tailings were produced from the development and utilization of mineral resources; the tailings were built for the storage of radioactive solid wastes, and most of small- and medium-sized enterprises produced dozens to thousands of tons per year. It was not necessary to build tailings storage. In recent years, related national departments strengthen the regulatory of radioactive solid wastes from the development and utilization of the mineral resources. Figures 1, 2, and 3 show three different ways of staging [6]; Fig. 4 show the warning labels for an enterprise.

From the study of the radioactive solid wastes, we can see all of the ground of the warehouse hardened treatment; most of the doors have logo on ionizing radiation, and part of the warehouse lack ventilation, merely by natural ventilation. It brings difficult to retrieve for adopting the pit for the treatment of radioactive solid waste.



Fig. 1 Slag warehouse in Sichuan

5 Disposal of the Radioactive Solid Waste from the Development and Utilization of Mineral Resources

According to the regulation of *the People's Republic of China Radioactive Pollution Protection* and the disposal way of uranium mining radioactive solid waste, radioactive solid waste during the development and utilization of mineral resources should be disposed by building tailings, or be filled into the underground stope. Now, like Baogang Group and Ningxia Orient Ta Ind Co, all build tailings storage, and plan to close, and use clay to cover the surface until radon exhalation rate is lower than $0.74 \text{ Bq/m}^2 \text{ S}$. Yunnan Lincangxinyuan Germanium Industrial Co. Ltd., backfills tailings into the underground stope [4]. But most of small- and medium-sized enterprises did not dispose the radioactive solid waste, because there was no conditions and necessity of building the tailings.

At present, radioactive solid waste disposal during the development and utilization of mineral resources is a major problem to the enterprise development and radiation environmental safety. The nature of the waste was same with uranium mining and metallurgy slag (except some zircon sands). Therefore, the disposal way



Fig. 2 Acid slag warehouse in Jiangsu

of uranium tailings during storage and treatment is possible, but it is impossible for each company build tailings. A large number of small- and medium-sized enterprises do not know the disposal way of radioactive waste disposal, and there are no policies on disposal way. Some companies try to pay for the disposal of radioactive solid wastes by uranium mining and metallurgy tailings disposal, but it is inconformity with domestic policies.

6 Minimization of Radioactive Solid Waste

Radioactive waste minimization is a necessary principle of radioactive solid waste management, and the nuclear fuel cycle and nuclear technology application industry in China do a lot of work in minimizing [8], but the minimization work of radioactive solid waste management during the development and utilization of mineral resources is not enough in the following aspects:



Fig. 3 Slag warehouse in Jiangsu



Fig. 4 Warning labels of slag warehouse

- (1) Monitoring system for radioactive solid waste was not established, and radioactive solid waste without classification was stored. Founded in the survey, almost all companies had no monitoring ability on radioactive solid waste, and they did not entrust other companies to monitor.

- (2) The company has lack of the consciousness of waste minimization and lack of minimization power. According to *the People's Republic of China Radioactive Pollution Protection*, the radioactive solid waste disposal expenses were undertaken by the operators; because radioactive solid waste disposal work did not develop, the radioactive solid waste disposal expenses had no legal basis, so just consider to disposal costs from minimize waste.
- (3) The clearance work of radioactive solid waste is not good enough. Because the process of exploitation and utilization of mineral resources is greater, the content of radionuclide in material was different, and some parts were below clearance level, so they could be cleared for reducing the radioactive solid waste. But we know that most companies do not know the clearance procedures in the research.

7 Recommendation of Radioactive Solid Waste Management

Due to the characteristics of radioactive solid waste from the exploitation and utilization of mineral resources, and they did not build perfect systems of radiation protection and radiation environmental protection, the personnel have lack of understanding on radiation protection and radiation environmental protection, led to the annual collective effective dose equivalent was greater than the nuclear industry during the development and utilization of mineral resources [9]. Therefore, it is necessary to strengthen the radioactive solid waste management of exploitation and utilization of mineral resources and reduce the radiation environment risk.

- (1) The development and utilization of mineral resources in industry should strengthen the study and training of radiation environmental safety laws and regulation standards, improve the recognition to the importance of radioactive waste management, and enhance the management ability of radiation environmental safety. In the process of the survey, we find that most of the enterprise management personnel have lack of radiation safety knowledge, and they do not know how to manage the radioactive solid waste. For example, many companies did not know the condition of radioactive temporary library. Relevant departments also do not organize studying and training of professional knowledge and management knowledge.
- (2) Environmental protection department should organize personnel to study on radiation environmental safety regulation standards and perfect the standard system of exploitation and utilization of mineral resources, and all the environmental protection supervision departments and enterprises have clear standards; at present, it is needed to develop the disposal means of research on the radioactive waste residues, whose radioactive level is higher than exempt level. Develop radioactive solid waste policy study from the national level,

- including utilization of uranium tailings, radioactive waste of interprovincial transport policy, and regulatory policy. Local environmental protection department should develop local rules and regulations of radiation environmental safety management standards according to the actual situation of the region, actively develop concentration dispose, and establish regional depot.
- (3) Encourage the relevant units to carry out the acid slag comprehensive utilization research, for minimizing the waste. Radioactive solid wastes during the development and utilization of mineral resources contain radioactive elements of uranium and thorium and other valuable metals; therefore, it is necessary to carry out acid slag comprehensive recycling and centralized treatment, to change the waste into resources, at the same time, to reduce the amount of radioactive solid wastes and radioactive level, and to achieve the target of minimizing the radioactive waste.
 - (4) Make the radioactive solid waste monitoring, packaging, and staging specification. Monitoring of radioactive solid waste is the basis of the radioactive solid waste management. Company should identify radioactive solid waste at the environmental impact assessment phase, build radioactive solid waste monitoring capacity, consummate monitoring plan, and strengthen monitoring on waste rock, tailings slag, and other slags from production process at trial production stage, and monitoring frequency can be reduced properly after stability production. Packing should meet the requirements of retrieving, and the temporary repository should be designed by qualified unit to meet the store requirement.
 - (5) Develop radioactive solid waste disposal technic and political study and promote radioactive solid waste during the development and utilization of mineral resources of disposal work. Reduce the risk of radiation through the disposal of radioactive solid waste, and at present, disposal policy is mainly to limit the conditions at the development and utilization of mineral resources. The disposal work is considered as a whole, breaking the barrier of the industry, region limit, realize resources sharing by country. At the same time, we should study the safety and environment impact, including contained thorium high residual and various properties of the waste residue entering into uranium tailings, the influence of underground water when tailings entering into mined-out area, long-term regulatory policy after disposal, etc.

References

1. *The People's Republic of China Radioactive Pollution Protection*, 2003.
2. *The mineral resources development and utilization management directory (the first batch of directory)*, 2013.
3. *Basic standards for protection against ionizing radiation and for the safety of radiation sources (GB18871-2002)*.
4. Activity concentration for material not requiring radiological regulation(GB27742-2011).

5. *Current Situation and Policies of radioactive contamination associated radioactive mineral resources development and utilization*, Shuai Zhenqing, 2001.
6. *Investment report of Radioactive slag storage from rare earth mining, smelting and separation of Jiangxi and Jiangsu provinces*, Xie ShuJun, 2015.
7. *Investment report on radiation environmental Safety regulation of development and utilization mineral resources for Yunnan provinces*, Xie ShuJun, 2015.
8. *Research and Application in the clearance of radioactive waste minimization*, Xiong Zhonghua, 2007.
9. *China's three decades of nuclear industry radiation environment quality assessment*, Panziqiang, 1990.

The Study of Microwave Ashing for Spent Radioactive Resin

Chao Gao, Meilan Jia and Yadong Wang

Abstract In order to improve radioactive spent radioactive resin management, spent resin just like other organic waste needs to be treated to be inorganic. The microwave ashing can meet the processing requirements of radioactive waste resin and can solve the problems for the waste resin processing on nuclear power plants. The radioactive waste resin microwave ashing process changes the waste resin into ash by microwave. Microwave ashing technics can treat spent resin as inorganic by microwave penetration and volumetric heating. Microwave ashing process can remove almost all organic components in spent resin. For the ashes, the product of microwave ashing process, the risk level will be near zero and the volume and weight will be minimized. For the spent resin, moisture content is about 50%, with microwave power density 10 w/g; the weight reduce rate is more than 90%. The study of microwave ashing for spent resin show that the processing of microwave ashing can achieve spent resin ashing, and the treatment effect suffices the requirements of the radioactive waste treatment. The ashes will be safety for storage and disposal.

Keyword Microwave ashing spent resin

1 Introduction

Spent radioactive ion exchange resin (hereinafter referred to as spent resin) belongs to the wet solid waste in nuclear power plants, accounting for the total amount of solid waste 1/4. General PWR nuclear power plant produces spent resin for about several cubic meters to ten cubic meters a year in one unit. The Daya Bay Nuclear Power station produced only 62.6 m³ in nine years (1994–2002) of two units. But due to the different on the design concepts, the AP1000 reactors may be estimated at 20.8 m³/a.

C. Gao (✉) · M. Jia · Y. Wang
China Institute for Radiation Protection, Taiyuan, Shanxi, China
e-mail: cau-227@163.com

Spent resin is an organic waste, radiation, or pyrolysis, and biodegradation will produce H_2 , CH_4 , NH_3 , and other flammable gases; spent resin contains more sulfur and nitrogen, the products from incineration may rust equipment and storage containers; spent resin is a disseminated substance; the spent resin must be effectively stabilized and packaged to meet the radioactive waste transport and final disposal requirements.

At present, Chinese running nuclear plants for spent resin have are two approaches: One is cement solidification, like in Daya Bay Nuclear Power Plant and Qinshan Phase II nuclear power plant, and the other is temporary, such as in Qinshan Phase I and in Qinshan Phase III nuclear power plant.

The cement solidification capacities seriously. At present, the main use of nuclear power plants is the barrel mixing cement curing process. The process is simple, but capacities seriously (about 5 times) may make the costs on transportation, temporary storage, and final disposal improving greatly, and the spent resin is still organic phase and is still radiolysis phenomena during storage, and the radiolysis gases, such as H_2 , CH_4 , C_2H_4 , and NH_3 , will give the disposal great impact.

The spent resin in temporary is in the potential risk. Though the small capacity, the spent resin is also itself, and there are still radiolysis gases. In addition, in long-term storage, the spent resin may be chalking and, in the absence of stirring circumstances, would cause compaction and clogging pipes, and make retrieval difficult. For example, The Jose Cabrera Nuclear Power Station, in Spain, had a 4 m^3 spent resin tank, and in the late 1960s to the early 1980s, the spent resin had filled tank and now completely blocked pipes; the spent resin cannot transfer out, Spanish released international to seek back to take low-dose technology, this lesson is not a minority, and you need to get our attention.

The AP1000 nuclear power plants, Zhejiang Sanmen nuclear power plant, and Shandong Haiyang nuclear power plant will use some new approaches to treat the spent resin, such as super hot compress treatment and the HIC process. Although there is more volume reduction, the nature of the resin does not change; there are still the radiolysis gases.

Now, the other processes, including the radionuclide separation and oxidative decomposition, are in the laboratory or pilot phase. Therefore, we need an effective new way to deal with the spent resin. The new technology should not only achieve the ultimate safe disposal of spent resin, but also achieve the minimization of the amount of disposal; by achieving high-volume production process, the product can meet the conditioning requirements.

Microwave treatment on the radioactive waste and hazardous waste has been used widely, with its apparent volume reduction, selective heating, thermal inertia, the process quickly, adaptability, mobility, etc. The use of microwave frequency electromagnetic wave technology is heated instantaneously through the material of the energy propagation inside the object to be heated, the heating characteristics from the inside. Then, to compare the microwave, steam, electric, and oil, the microwave is the best for fast heating, uniformity heating, the short processing time, and so on.

Spent radioactive resin microwave ashing process is that uses microwave to rapid drying of spent resin, carbonization spent resin, and ashing process spent resin, to achieve inorganic resin, so that f, C, H, and O to H₂O and CO₂ are discharged.

In order to make the process of the spent resin effective, we have carried out the spent resin microwave ashing preliminary study.

2 Study

The microwave ashing process for spent resin can be divided into many parts, mainly including the selection of microwave power density and the atmosphere control parameter verification.

2.1 *Microwave Power Density*

The factors for microwave treatment are power, time, and material, according to preliminary study. The process time only has influence on treatment efficiency; the process power and the amount of material have influence on treatment effect. Therefore, it is necessary to carry out the choice of power density test.

In the consideration of the experimental operation, choose different weight of resin and same microwave power for the experiment on power density range. The specific data are shown in Table 1. The test product appearance is shown in Fig. 2. The following conclusions can be drawn:

- (1) In the same conditions, the greater the power density, the greater the weight loss ratio, and the better the treatment effect, but higher economic cost;
- (2) The power density is more than or equal to 10 w/g, the weight loss ratio tends to be consistent, considering to get larger product weight loss ratio is the power density of 10 w/g in the lower microwave power.

2.2 *Atmosphere Control Level Selection*

In the microwave ashing process, the atmospheres have great influence on the product. The microwave ashing process can be divided into two parts, reducing atmosphere and oxidizing atmosphere. Reducing atmosphere is mainly used for the carbonization stage; oxidizing atmosphere is mainly used for ashing stage. Considering safety and cost, the nitrogen was chosen as a reducing atmosphere and oxygen was chosen as oxidizing atmosphere.

Study on atmosphere control parameters follows the use of 50-g resin.

First open the nitrogen to fix flow blowing inside the furnace, to ensure that the oxygen in the furnace is fully discharged, and to prevent in the carbide phase because the oxygen in the furnace too much affects the outcome of the trial. Then, continue to pass through the nitrogen and turn on the microwave, and then, carbonization stage began. After the end of the carbide phase, stop adding nitrogen and continue to add oxygen, and then, ashing stage began, until the gas is no longer generated after ashing stage end.

The following conclusions can be drawn:

- (1) The ashing product almost has no relationship with air pipe position, but if the pipe is close with the top vent, part of the gas will directly discharge from the port;
- (2) N_2 flow of 5 L/min is appropriate, if the flow is too small to meet the test requirements, and if the flow is too large, it will take away the heat of the resin, affecting the treatment effect;
- (3) If the oxygen is directed to the jet, product weight loss ratio is about 95%. Therefore, it can be used as 8 L/min for the O_2 flow rate to carry out experimental study.

2.3 Parameter Validation Test

According to preliminary experiments, the control parameters are 50-g resin (50% water), microwave power density is 10 w/g; the nitrogen flow is 5 L/min, and the oxygen flow is 8 L/min.

For the experimental study, the initial addition of resin 50.12 g, after the test to get the gray white test product 3.17 g, weight loss ratio of 95.78%.

By the test data, the control parameters can meet the microwave ashing process control requirements for spent resin.

3 Conclusions

The microwave ashing process is feasible and determines some key parameters. It is recommended to improve the equipment and methods for further experimental research.

References

1. Dominic a. Davies, Christina Schnik, Jack Silver, Josel.Sosa-Sanchez, Philip G. Riby. A high-yield microwave heating method for the preparation of (phthalocyaninato) bis (chloro) silicon (IV) [J]. Porphyrins Phthalocyanines, 2001(5).
2. Christian Giessmann. Microwave in-drum drying [J]. Radwaste Solutions. 2007, 21–24.
3. Ching-Hong Hsieh, Shang-Lien Loa, Pei-Te Chiuieh, Wen-Hui Kuan, Ching-Lung Chen. Microwave enhanced stabilization of heavy metal sludge [J]. Journal of Hazardous Materials. 2007, 160–166.
4. R.L. Schulz, G.G. Wicks, D.C. Folz, D.E. Clark. Overview of hybrid microwave technology [J]. Journal of the South Carolina Academy of Science. 2011, 9(1) 25–29.
5. Mário H. Gonzaleza, b, Gilberto B. Souzaa, Regina V. Oliveirac, Lucimara A. Foratod, Joaquim A. Nóbregac, Ana Rita A. Nogueiraa. Microwave-assisted digestion procedures for biological samples with diluted nitric acid: Identification of reaction products [J]. Talanta. 2009(79):396–401.
6. Supitcha RUNGRODNIMITCHAI, Wachira PHOKKHANUSAI, Natthapong SUNGKHAHO. Preparation of silica gel from rice husk ash using microwave heating [J]. Materials and Minerals. 2009(11):45–50.
7. Cheng Juan, Li Quan-wei. New research on the oxidative decomposition technology for spent radioactive ion exchange resin [J]. Journal of Isotopes, 2012, 5(25):124–128.
8. Rao Shan-shan, Li Yu-jin, Duan De-hong. The application of microwave digestion on pretreatment of environmental samples [J]. Journal of Gansu Lianhe University (Natural Science Edition). 2005, 19(1).
9. Cheng Qiong, Jiang Shu-bin, Ma Jun-ge. Development and preliminary validation of a large-capacity rapid ashing apparatus for biologic sample [J]. Modern Scientific Instruments.2011, 6:71–73.
10. Lu Jun. Discussion on design scheme of Ap1000's radioactive waste treatment [J]. Nuclear Power Engineering.2010, 6:121–126.

Author Biography

Chao Gao China Institute for Radiation Protection, title: associate researcher, master of engineering, research area: radioactive waste treatment and disposal.

Preliminary Study on the Vitrification of Molten Salt Reactor Radwastes Containing Fluorides by Phosphate Glass

Yan-bo Qiao, Ya-ping Sun, Xue-yang Liu, Zheng-hua Qian, Shuai Wang and Hong-jun Ma

Abstract The fluoride-containing waste from molten salt reactor should be embedded in a stable, chemically resistant matrix for final disposal, and the matrix should be easily stored or disposed. However, the solubility of halides in borosilicate-based glasses is so low that the traditional glasses are inappropriate for the immobilization of radioactive waste containing fluorides because of the poor load capacity. In this paper, the vitrification of MSR fluoride-containing waste by phosphate glass was performed. The research investigated the source item of MSR fluoride-containing waste, and simulated nonradioactive waste was prepared. Sodium aluminophosphate and iron phosphate glasses were chosen as host matrixes in our preliminary experiment. The material structure and properties of the wasteforms were analyzed by XRD, Raman, and SEM. Chemical durability was carried out by the product consistency test method. The results showed that the metal fluorides could be well solidified in the phosphate-based glasses. The wasteforms exhibited good performance with high-effective waste loading, lower cost, and fine stability. Our work is of great significance for the scientific management and safety disposal of radwastes from molten salt reactor and contributes to the long-term sustainable development of molten salt reactor.

Keywords Vitrification · Radioactive waste treatment · Molten salt reactor · Fluorides

1 Introduction

Molten salt reactors (MSRs) use the liquid molten salt as the fuel solvent and coolant. Different from light water reactors (LWRs), molten salt reactor does not have fuel pellets; instead, its nuclear fuel is dissolved in molten fluoride salts such as lithium fluorides or sodium fluorides [1–4]. The fuel and molten salt reprocessing

Y. Qiao (✉) · Y. Sun · X. Liu · Z. Qian · S. Wang · H. Ma
Shanghai Institute of Applied Physics, Chinese Academy of Sciences, Shanghai, China
e-mail: qiaoyanbo@sinap.ac.cn

© Springer Science+Business Media Singapore 2017
H. Jiang (ed.), *Proceedings of The 20th Pacific Basin Nuclear Conference*,
DOI 10.1007/978-981-10-2314-9_57

could reduce the volume of the high-level wastes; however, significant quantities of radwastes containing fluorides are still left. These wastes will bring particular problems because of their high-level radioactivity and complex chemical properties. Storage of the waste in metal containers is only a short-term solution because of the eventual corrosion of metal containers and resulting release of radioactive. Some fluorides in MSR waste are soluble in water and require no exposure to water. This made it necessary to embed the fluoride-containing radioactive wastes in a stable, chemically resistant matrix for final disposal, and the matrix should be more easily stored or disposed.

Glass solidification is the most widely used technology for the treatment of high-level liquid waste. Borosilicate glass is the generally accepted wasteform for the oxide radwastes from the LWRs [5]. However, the immobilization of the fluoride-containing wastes in borosilicate glass directly is not feasible due to the very low solubility of fluorides [6, 7]. The low solubility usually results in phase distribution during the vitrification and lowers the quality of the wasteform. Some wastes containing significant amounts of heavy metal oxides (e.g., UO_2 , La_2O_3) also have lower solubilities in borosilicate glasses. This decrease in the waste loading will make the volume of the wasteform undesirably large. Based on these considerations, alternative type of wasteform should be developed; in particular, a feasible approach is to seek other glass matrix.

Phosphate-based glasses possess apparent advantages of lower melt temperatures and lower viscosity relative to borosilicate glasses, so they were originally investigated as potential hosts for spent nuclear fuel waste, but these early glasses had poor durability and the melts were generally highly corrosive. However, some researches based on the adjusting of the glass composition (e.g., addition of Al_2O_3 and Fe_2O_3) have improve the durability of the phosphate glasses and the refractory corrosion [8]. Iron phosphate glasses have been proposed for immobilizing CsCl and SrF_2 extracted from HLW tank sludges because of their high radioactivity and short half-lives [9]. Aluminofluorophosphate glass matrix was recommended for immobilizing spent melt containing alkali-metal chlorides which as the diluents in reprocessing of spent fuel for fast reactors by the pyroelectrochemical method [10]. Certain calcium aluminosilicate glasses have been suggested for treating chloride-containing incinerator wastes [11]. Sodium aluminophosphate glass was chosen as the glass matrix for HLW in the former Soviet Union [12]. Even the recent studies proposed that glass compositions based on iron phosphate could be as an alternative host for the vitrification of HLW which contains relatively high concentrations of actinide elements, because the actinides solubilities in these glasses being higher than that of silicate-based glasses [13].

In this study, we have investigated the feasibility of employing sodium aluminophosphate as immobilization hosts for simulated MSR radwastes containing both actinide and fluorides. The structure and properties of the wasteforms were characterized by X-ray diffraction (XRD), scanning electron microscopy (SEM), and Raman spectroscopy. Leaching tests were performed in deionized water using the product consistency test A (PCT-A method), which simulate extreme conditions of underground repositories (moist air and high temperature). Our results indicated

that sodium aluminophosphate glass exhibited high solubility and desirable chemical stability.

2 Experimental

2.1 Waste Stream Compositions

The commonly simulated non-radioactive waste was employed to represent a number of specific radioactive wastes generated during the reprocessing of used TMSR fuel. The designated non-radioactive-simulated fluoride-containing wastes consist of Cs, Sr, Zr, Ce, and Sm, with the compositions shown in Table 1. Sm was used as a surrogate for tetravalent radionuclides; Cs for Ru, Cs; ^{88}Sr for ^{90}Sr , Ba; Ce and Zr for itself actinide elements (U, Pu, Th); and Sm for surrogated trivalent actinide elements (Am, Cm). MF_n was used to represent the various fluorides as shown in Table 1.

2.2 Sample Preparation

The glasses with compositions listed in Table 2 were prepared from mixtures of reagent grade constituents. Well-mixed powders were first preheated to 300 °C (heating rate is 10 °C/min) in alumina crucibles and kept for 3 h to evaporate ammonia and water in the batches. Then, the batches were melted in air at 1000–1250 °C for 30 min. The fused glass mass was poured into a preheated steel mold, held at 450 °C for 1 h to relieve internal stresses, and then cooled to room temperature. The experiments aimed at establishing the maximum amount of fluorides that could be incorporated into the glasses. Melting schedules were adjusted according to the viscosity of the melt and the observed volatility.

2.3 Characterization

X-ray diffraction (XRD) was employed to performed identification the limits of glass formation and crystalline phases present in the glass samples (D8 advance, Bruker, Geman) using a Ultima IV diffractometer with $\text{CuK}\alpha$ radiation. Raman spectra on glass powders are recorded by using a laser of wavelength 532 nm

Table 1 Compositions of the MSR-simulated waste

Fluoride	CsF	SrF ₂	ZrF ₄	CeF ₄	SmF ₃
mol%	8.4	8.3	29.7	15.8	37.8

Table 2 Compositions of sodium aluminum and iron phosphate glasses (mol%)

Sample	Na ₂ O	Al ₂ O ₃	P ₂ O ₅	Fe ₂ O ₃	Simulated wastes (mol%)
NAP1	40.2	19.6	40.2	0	3.8
NAP2	40.2	19.6	40.2	0	19.6
NAP3	40.2	19.6	40.2	0	27.5
NAFP1	35.6	11.5	42.1	10.8	4.4
NAFP2	34.9	16.6	41.3	7.2	6.4
NAFP3	35.6	11.5	42.1	10.8	8.5

radiation and a Renishaw in Via spectrometer coupled with an optical microscope (HR800, Renishaw, England). Chemical durability measurements have been conducted according to Product Consistency Test A (PCT-A) [14]. The glass samples were crushed manually in an agate mortar and sieved to 75–150 μm . Powders were washed abiding by PCT operating procedure, then mixed with distilled water at a ratio of 10 ml/g, and held at 90 °C for 7 days in a stainless steel vessel. Upon the completion of each test period, the normalized elemental mass was determined by chemical analysis of the leachate using the ICP-AES (Na, Al, P, Fe) and ICP-MS (Cs, Sr, Zr, Ce, Sm) methods.

3 Results

3.1 X-Ray Diffraction (XRD)

Figure 1a shows the XRD patterns of the sodium aluminum phosphate glasses with different waste loadings. No crystalline phases were detected by XRD when the simulated waste content is low. For those samples with simulated wastes ratio more than 19.6 mol%, the crystalline phase was detected and the major crystalline phase is monazite (Sm, Ce, Zr)PO₄(46-1392). Figure 1b shows the XRD patterns of the iron phosphate glasses with different waste loadings. For those samples with high waste loading, peak regime revealed the presence of a number of additional crystalline phases, including monazite FePO₄ (29-0715), AlPO₄ (31-0029,11-0500), and Na₃PO₄ (33-1272).

3.2 Raman

Raman spectra of fluoride-containing glasses of NAP and NAFP are shown in Fig. 2. The peaks in the spectra from the glasses occur at similar frequencies as those from the phosphates glasses of iron, calcium, sodium, and sodium aluminum phosphate, and similar assignments can be made for the peaks in the spectra from

Fig. 1 XRD patterns of sodium aluminum and iron phosphate glasses

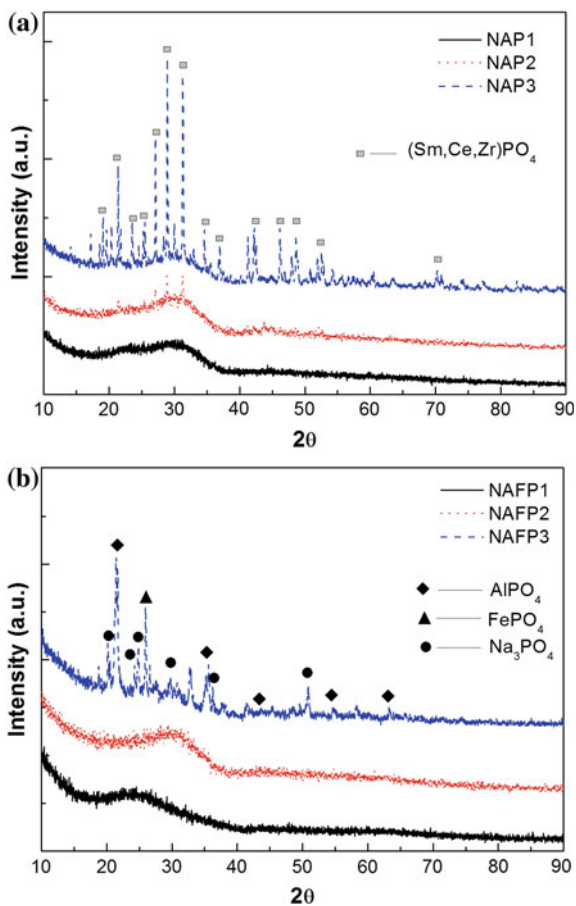
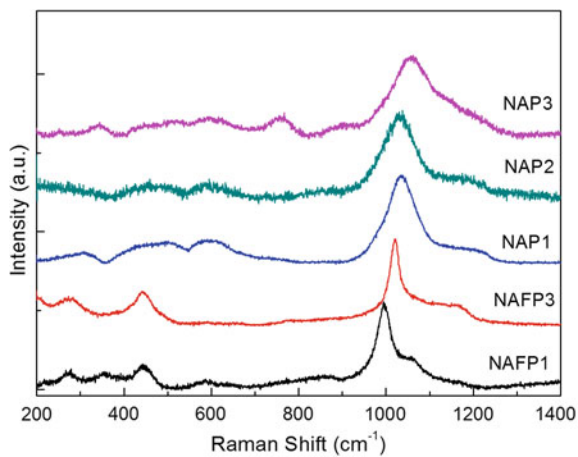


Fig. 2 Raman spectra of sodium aluminum and iron phosphate glasses



the glasses [16–19]. The most intense peak in each spectrum, at frequencies from ~ 1060 to ~ 1100 cm^{-1} , can be assigned to the symmetric stretch of a non-bridging oxygen on a Q^1 -tetrahedron, the $(\text{PO}_3)_{\text{sym}}$ mode. The higher frequency shoulders evident in each spectrum could be due to asymmetric PO_3 modes associated with the Q^1 -tetrahedra, but also could be due to symmetric PO_2 -stretching modes associated with Q^2 -tetrahedra. Likewise, the shoulders near ~ 1000 cm^{-1} could be assigned to other PO_3 modes associated with the Q^1 -tetrahedra, or to PO_4 modes associated with the Q^0 -tetrahedra units in the glasses. The bands of NAFPs between 700 and 800 cm^{-1} are related to the symmetric P–O–P-stretching modes associated with linkages to Q^1 -tetrahedra. Raman modes observed at 200–600 cm^{-1} are typical of rocking motion of PO_4 tetrahedra and/or the motion of cationic polyhedra. With increasing waste loading, the $(\text{PO}_1)_{\text{sym}}$ band increases in relative amplitude without significant frequency shift, whereas the high-frequency (P = O) $_{\text{sym}}$ band decreases in relative intensity and decreases in frequency.

3.3 Chemical Durability

On the completion of each test period, the normalized elemental mass was determined by chemical analysis of the leachate using the method by ICP-AES or ICP-MS. Data were corrected by subtracting the normalized analysis for accompanying blank solutions. Fluorine ion electrode was used to analyze F ion concentration, and the pH values of the leachate were also measured during the tests. The lower the ion concentration in the leachate, the better chemical stability will be. PH of leachate can also characterize the chemical stability of the sample, variate as small as possible (PH for all the sample initial leachate is 7).

Table 3 Chemical stability performance of NAP and NAFP compared with the other glasses (g/m^2)

Normalized mass release	NAP1	NAFP1	FZ-1 ^a	ARM-1 ^b	CVS-IS
r_{Al}	0.175	0.000	0.795	0.09	
r_{Na}	0.026	0.009	0.723	0.27	1.1–1.5
r_{P}	0.187	0.010	0.246		
r_{F}	0.055	0.005			
r_{Fe}		0.000	<10		
r_{Cs}	0.204	0.013			0.06–0.13
PH_i/PH_f	8.4/7	8.92/7	5.4/9.4	10.47/–	5.9/~ 10.3

^aFZ-1 is an iron phosphate glass waste form made at UMR (18Na2O-26Fe2O3-46P2O5-10other, wt%) and tested (PCT) at PNNL

^bARM-1 is a standard reference borosilicate glass used at Savannah River Laboratory

^cCVS-IS is a standard glass made by Pacific Northwest National Labs (PNNL) and has a nominal composition of 53.3SiO₂, 10.5B₂O₃, 11.3Na₂O, 3.7Li₂O, 2.4Al₂O₃, 7.0Fe₂O₃, 3.9ZrO₂, 1.3Nd₂O₃, and 6.6 others, wt%

The leaching rate (g/m^2) was calculated on the basis of the normalized elemental mass loss. The leaching of samples demonstrates that the normalized all ions release $\leq 0.2 \text{ g}/\text{L}$ within the $2 \text{ g}/\text{m}^2$ Hanford specification [15]. The releases of Sr^{2+} , $\text{Ce}^{3+/4+}$, Zr^{4+} , and Sm^{3+} are lower than Na^+ , P^{5+} , Fe^{3+} , Al^{3+} , F^- , and Cs^+ , which indicates that the former are likely bonded differently or in different phases. The deionized water pH used in the PCT test is from 8 to 9.5 for the NAP and from 4.5 to 9 for the NAFP wasteforms. PH increase is potentially detrimental to the glass durability since the corrosion of glass is more readily. Furthermore, it is noted that the quantity releasing from the wasteforms did not change clearly if the wasteform is crystallized.

The chemical stability performance of the NAP and NAFP glass is shown in Table 3. The data from FZ-1, ARM-1, and CVS-IS are used to compare with the results in this study. Sodium, phosphorus, aluminum, strontium, and iron released are quite low, typically less than released from the two borosilicate glasses as

Fig. 3 SEM photographs of before PCTs of the **a** NAP1 and **b** NAFP1 glasses

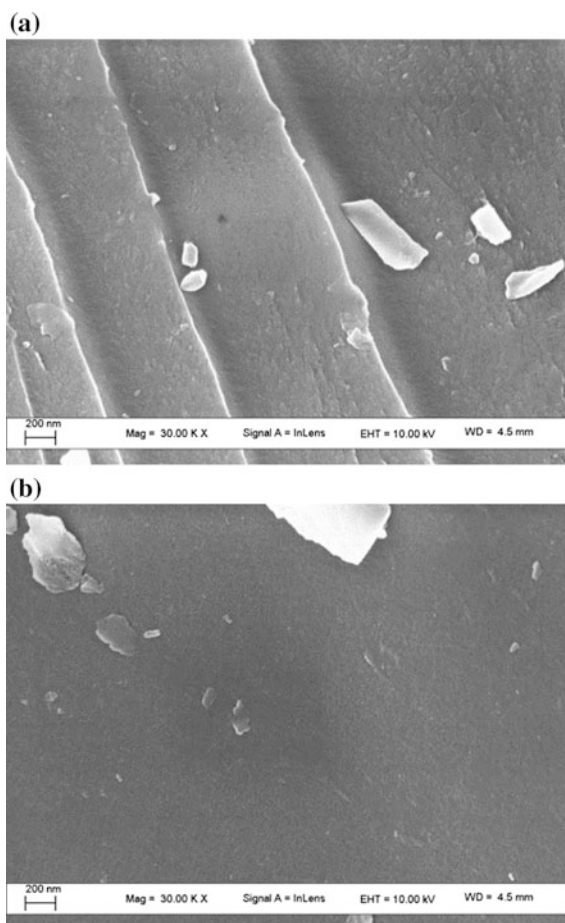
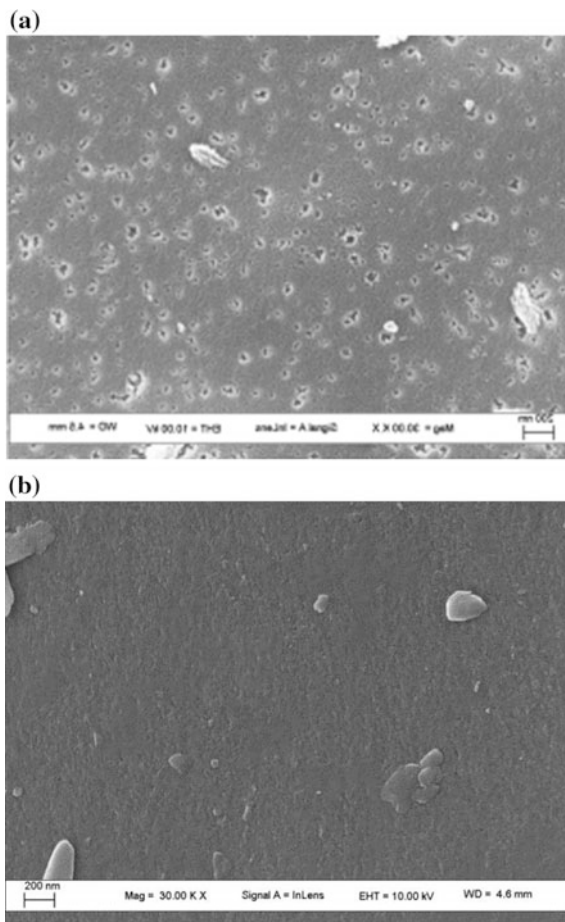


Fig. 4 SEM photographs of after 7 days PCTs of the **a** NAP1 and **b** NAFP1 glasses



shown in Table 3. The dissolution rate of these phosphate glasses was better than that of the borosilicate ARM-1, CVS-IS glasses, and as good as even better iron phosphate glass FZ-1 in distilled water.

The visually noticeable corrosion of the NAP and NAFP glasses particles was confirmed by their appearance after PCT testing. The SEM photographs of before PCT tests of the NAP and NAFP glasses are shown in Fig. 3a and b. The SEM photographs of after 7 days PCT tests of the NAP and NAFP glasses are shown in Fig. 4a and b. The SEM images of the glasses show sharp corners and edges as shown in Fig. 3. And the glasses after PCT tests are also absent of any detectable corrosion layer on the surface, which is a clear evidence of the excellent chemical durability of NAP and NAFP wasteforms which also can conclude from Table 3.

4 Discussion

The low melting temperatures and poor chemical resistance of phosphate-based glasses are related to PO_4 groups in ring structures. For strengthening structural of the glass network and hence increasing chemical resistance, network modifiers (e.g., Na_2O) and network intermediates (e.g., Al_2O_3) were added. The ratio of Na_2O to P_2O_5 in the present samples is 1.00, and the Al_2O_3 -to- P_2O_5 ratio is 0.49. Hudgens et al. [18] have reported that the structure of glasses around this composition consists predominantly of AlPO_4 groups together with some tetraphosphate and/or triphosphate groups. The expected presence of a larger proportion of AlPO_4 groups explains the structural stability (and durability) of this glass compared to binary alkali phosphate glasses. The generally good chemical durability is primarily due to the presence of strong, hydration-resistant Al-O-P bonds in these glasses [9]. This consistent with Raman spectra that the NAP glasses consist of the Q^1 and Q^0 units with a little/without the Q^2 units, and the latter own poor chemical durability of the waste glasses was attributed to dominance of easily hydrolysable P-O-P bonds, which upon hydration get depolymerized through formation of terminal $-\text{OH}$ groups.

XRD shows that devitrification tendency increases with increasing fluorides content. This tendency can be explained by a broadly linear relation between the modifier cation field strength, Z/r^2 (Z , r represent ionic charge and ionic radius, respectively), and the atomic percentage of modifier cation [19]. In the study, ionic field strength is lowering with the M^{n+} (Sm^{3+} , Ce^{4+} , Zr^{4+}) addition. This is related to higher crystallization tendency of phosphate glasses with partial replacement of Al^{3+} by M^{n+} up to 20 mol%. The previous studies show that aluminum atoms appear in a environment of four-, five-, and sixfold coordinations [19], while the (Sm, Ce, Zr) atom coordination numbers are six or greater than six [20]. The higher crystallization tendency with the content of incorporation (Sm, Ce, Zr) may be related to the higher coordination number, which can lead to a strong polymerization effect easier.

Fe_2O_3 can act as both an intermediate and a glass-modifying oxide in phosphate glass, which presents in the glass network in both the Fe^{2+} and Fe^{3+} states and provides the greatest durability by replacing P-O-P bonds with more durable P-O-Fe^{2+} or P-O-Fe^{3+} bonds. But the addition of Fe_2O_3 to NAP glasses decreases waste loading markedly, and the crystallization tendency increasing with the addition of Fe_2O_3 may demonstrate that iron ions break the phosphate network into smaller parts and make them less constrained by the neighboring units [21]. Therefore, it might be prudent to limit the addition of Fe_2O_3 into the NAP glass.

5 Conclusions

The immobilization of fluoride-containing waste in glass has studied in the paper. Phosphate glasses were mixed with simulated wastes and reacted in air in the temperature range of 1000–1250 °C. Crystallization tendency increased with the simulated non-radioactive waste content, and monazite (Sm, Ce, Zr)PO₄ crystalline phases were found in the NAP glasses with high waste loading. The addition (~10 mol%) of Fe₂O₃ constituent decreases the waste loading, but improved the chemical durability significantly. The length of phosphate chain will be shortened, and the asymmetric BO increases with increasing incorporated simulated wastes. The PCT in distilled water conducted on these samples indicated the dissolution rate of phosphate glasses in this work was better than that of the borosilicate ARM-1, CVS-IS glasses, and as good as even better iron phosphate glass FZ-1.

The waste forms exhibit good performance with high-effective waste loading, low cost, and fine stability. Our work is of great significance for the scientific management and safety disposal of radwastes from molten salt reactor and contributes to the long-term sustainable development of molten salt reactor.

References

1. JIANG M, XU H, DAI Z. Advanced fission energy program-TMSR nuclear energy system. *Bulletin of Chinese Academy of Sciences*, 2012, 27(3):366–374.
2. D. F. Williams, F. J. Peretz. Characterization of the Molten Salt Reactor Experiment Fuel and Flush Salts, ORNL-CF-9606116, 1996.
3. R. B. Lindauer. Processing of the MSRE Flush and Fuel Salts. ORNL-TM-2578, 1969.
4. P. N. Haubenreich, R. B. Lindauer. Consideration of Possible Methods of Disposal of MSRE Salts, ORNL/CF-7211, 1972.
5. I. W. Donald, B. L. Metcalfe, R. N. J. Taylor. The Immobilization of High Level Radioactive wastes using ceramics and glasses, *J. Mater. Sci.*, 1997, 32:5851–5887.
6. C. W. Forsberg, E. C. Beahm, J. C. Rudolph. Direct Conversion of Halogen-Containing Wastes to Borosilicate Glass, *Mater. Res. Soc. Symp. Proc.*, 1997, 465:131–137.
7. S. Donze, L. Montagne, G. Palavit, G. Antonini. Structure and Properties of Phosphate Glasses Prepared from Lead and Cadmium Chlorides, *Phys. Chem. Glasses*, 2001, 42: 133–138.
8. W. Donald, B. L. Metcalfe, S. K. Fong, L. A. Gerrard, D. M. Strachan, R. D. Scheele, A Glass-Encapsulated Calcium Phosphate Wasteform for the Immobilization of Actinide-, Fluoride-, and Chloride-Containing Radioactive Wastes from the Pyrochemical Reprocessing of Plutonium Metal, *J. Nucl. Mater.*, 2007, 361:78–93.
9. Mesko, M., Day, D., Bunker, B., Immobilization of CsCl and SrF in iron phosphate glass. *Waste Management* **2000**, 20 (4), 271–278.
10. Lavrinovich, Y. G., Kormilitsyn, M., Konovalov, V., Tselishchev, I., Tomilin, S., Chistyakov, V., Vitrification of chloride wastes in the pyroelectrochemical method of reprocessing irradiated nuclear fuel. *Atomic Energy* **2003**, 95 (5), 781–785.
11. Siwadamrongpong, S., Koide, M., Matusita, K., Prediction of chloride solubility in CaO–Al₂O₃–SiO₂ glass systems. *Journal of non-crystalline solids* **2004**, 347 (1), 114–120.
12. Brezhneva, N., Kuznetsov, D., Minaev, A., Oziraner, S. In Prospects for using phosphate glasses for strong fixation of radioactive wastes, Scientific and Technical Conference on

- Investigations Concerning Neutralizing Liquid, Solid, and Gaseous Wastes and Decontamination of Contaminated Surfaces, 1973; pp 2–7.
13. G. K. Marasinghe, M. Karabulut, C. S. Ray, D. E. Day, D. K. Shuh, P. G. Allen, M. L. Saboungi, M. Grimsditch, D. Haeffner. Properties and Structure of Vitrified Iron Phosphate Nuclear Wasteforms, *J. Non-Cryst. Solids*, 2000, 253&264:146–154.
 14. Standard Test methods for Determining Chemical Durability of Nuclear, Hazardous, and Mixed Waste Glasses: the Product Consistency Test (PCT). ASTM, Conshohocken, USA, 2002.
 15. Jantzen, C. M., Engineering Study of the Hanford Low Activity Waste (LAW) Steam Reforming Process (U). WSRC, TR **2002**, 317.
 16. Zhang, L.; Brow, R. K., A Raman Study of Iron–Phosphate Crystalline Compounds and Glasses. *Journal of the American Ceramic Society* **2011**, 94 (9), 3123–3130.
 17. Xiao-Feng, L.; Yuan-Ming, L.; Guang-Fu, Y.; Shi-Yuan, Y., Effect of CeO₂ Doped On the Structure of Phosphate Calcium Glass. *Chinese Journal Of Inorganic Chemistry* **2011**, 27 (1), 35–39.
 18. Hudgens, J. J.; Brow, R. K.; Tallant, D. R.; Martin, S. W., Raman spectroscopy study of the structure of lithium and sodium ultraphosphate glasses. *Journal of non-crystalline solids* **1998**, 223 (1), 21–31.
 19. Tiwari, B., Pandey, M., Sudarsan, V., Deb, S., Kothiyal, G., Study of structural modification of sodium aluminophosphate glasses with TiO₂ addition through Raman and NMR spectroscopy. *Physica B: Condensed Matter* **2009**, 404 (1), 47–51.
 20. Bingham, P., Hand, R., Forster, S., Lavaysierre, A., Deloffre, F., Kilcoyne, S., Yasin, I., Structure and properties of iron borophosphate glasses. *Physics and Chemistry of Glasses-European Journal of Glass Science and Technology Part B* **2006**, 47 (4), 313–317.
 21. Donald, I.; Metcalfe, B., Thermal properties and crystallization kinetics of a sodium aluminophosphate based glass. *Journal of non-crystalline solids* **2004**, 348, 118–122.

Author Biography

Yanbo Qiao received his PhD degree from Shanghai Institute of Optics and Fine Mechanics, Chinese Academy of Sciences in 2009. Then, he worked as a postdoctoral fellow in National Institute of Advanced Industrial Science and Technology (AIST), Japan. He joined Shanghai Institute of Applied Physics, Chinese Academy of Sciences in 2012. His current research interests are the management of radioactive wastes, molten salt reactor radwastes disposal and vitrification of high-level wastes.

Part III
Acquiring Medical and Biological
Benefits

An Organic Adsorbent Resin for Ga-68 Generator

Ming-Hsin Li

Abstract A gallium-68 generator is a device used to extract the positron-emitting isotope Ga-68 of gallium from a source of decaying germanium-68. We meet the needs created by the rapid development of positron emission tomography (PET); a new Ge-68/Ga-68 generator has been developed.

Keywords Ge-68/Ga-68 · Generator

A gallium-68 (Ga-68) radioisotope generator consists of a citrate eluent and a generating column. The citrate eluent is conducted to the generating column to desorb the Ga-68 radioisotope. Thus, the form of citrate gallium is generated by an eluent containing the Ga-68 radioisotope [1, 2]. The generating column is partially brimming over with ion-exchange resin with glucamine groups to adsorb the radioisotopes Ge-68 and Ga-68. A Ga-68 radioisotope-generating method is also revealed.

By elution under reduced pressure, this organic resin (N-methylglucamine group) generator provides a Ga-68 solution in citrate form, ready for use in the preparation of many radiopharmaceuticals [3]. Since the Ga-68 recovery yield is high (75–80%) and the elution time very short (less than 2 mm), these products possess maximum activity. Owing to its very slight Ge-68 leakage (<0.0002% per elution), the organic resin generator is long-lasting and, more importantly, the radiotoxicity of the labeled derivatives is kept to a minimum. The citrate Ga-68 obtained in this way has been used to label several radiopharmaceuticals [4].

Methods: A gallium-68 (Ga-68) radioisotope generator consists of a citrate eluent and a generating column. The citrate eluent is conducted to the generating column to desorb the Ga-68 radioisotope. Thus, the form of citrate gallium is generated by an eluent containing the Ga-68 radioisotope. The generating column is partially brimming over with ion-exchange resin with glucamine groups to adsorb

M.-H. Li (✉)
Institute of Nuclear Energy Research, Longtan, Taiwan
e-mail: mhli@iner.gov.tw

the radioisotopes Ge-68 and Ga-68. A Ga-68 radioisotope-generating method is also revealed.

Conclusions: In summary, a Ga-68 radioisotope generator and a method applied in the same in accordance with the current invention are characterized by the use of an organic resin (i.e., ion-exchange resin with glucamine groups) and its selective adsorption for Ga-68 in contrast with Ge-68 to generate Ga-68 nuclide. The equipment in line with the present invention is easily to operate, more simply design, and suitable for various hospitals and research institutes to offer the public better clinic diagnosis in the area of nuclear medicine and promotion.

Results: As shown in Fig. 1, when the amount of the added citrate eluent is enough, such as 10 ml, the 0.1 or 0.2 M citrate eluent (as the curves labeled with rhombuses and triangles, respectively) or the 0.1 or 0.2 M citrate eluent at pH = 9

Fig. 1 Elutriation rate of Ga-68

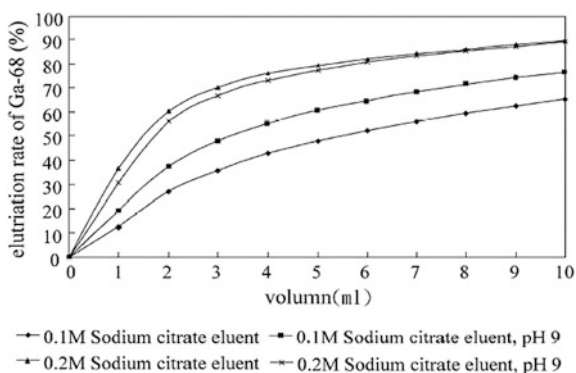


Fig. 2 Ga-68 generator



(as the curves labeled with squares and crosses, respectively) can show a high performance of the Ga-68 elutriation rate (nearly 50%). Taking the 0.2 M citrate eluent 10 ml as an example, its elutriation rate is 45 ppm. On the other hand, the elutriation rate of the Ga-68 radioisotope is up to 75.5% (Fig. 2).

References

1. H. Arino, "A new $^{68}\text{Ge}/^{68}\text{Ga}$ radioisotope generator system," *Int. J. Appl. Radiat. Isot.*, 29, 117(1978).
2. C. Loch and B. Maziere, "A new generator for ionic gallium-68," *J. Nucl. Med.*, 21, 171(1980).
3. M. Nakayama, "A new $^{68}\text{Ge}/^{68}\text{Ga}$ generator system using an organic polymer containing N-methylglucamine groups as adsorbent for ^{68}Ge ," *Appl. Radiat. and Isot.*, 58, 9 (2003).
4. P. Antunes and M. Ginj, "Are radiogallium-labelled DOTA-conjugated somatostatin analogues superior to those labelled with other radiometals?" *Eur. J. Nucl. Med. Mol. Imaging.*, 34, 982 (2007).

Assessment of Production Channels of Isotopes for Combined PET/SPECT Imaging

Chary Rangacharyulu, Ramy Tannous and Christine K. Roh

Abstract We propose to integrate the positron emission tomography (PET) and the single-photon emission computed tomography (SPECT) into one single isotope-based medical imaging technique [1]. This technique overcomes several imaging artifacts due to photon scattering and absorption. More importantly, a three-fold coincidence eliminates the need for back-projection algorithms while providing the data for multiple image reconstructions with judicious software cuts. To be useful for practical applications, the candidate isotopes must meet several criteria such as cost and ease of production, biological compatibility, relative intensities of the positron emissions, and the gamma rays. From an analysis of nuclear data, we identified six candidate isotopes which are amenable to production at proton cyclotrons of 20–60 MeV energies via (p,xn) reactions. They are 43-Sc, 73-Se, 75-Br, 77-Kr, 85-Y, and 123-Xe with half-lives of $1 < T_{1/2}(\text{hr}) < 5$ and SPECT gamma rays less than 400 keV energies. The 43-Sc can also be produced by low-energy alpha beam facilities ($E_\alpha \sim 12$ MeV).

Keywords Nuclear · medical imaging · PET/SPECT combined · Single isotopes · Production channels

1 Introduction

Nuclear imaging is being increasingly employed for medical diagnostics. While the computed tomography (CT) is the modernized X-ray imaging, single-photon emission computed tomography (SPECT) and positron emission tomography (PET) are the more recent imaging technologies where short-lived isotopes are administered to the patient. In case of SPECT, intensity distributions of single photons emitted by a radio isotope are measured to reconstruct the source distributions in the patient's body through back-projection techniques. The workhorse

C. Rangacharyulu (✉) · R. Tannous · C.K. Roh
University of Saskatchewan, Saskatoon, SK, Canada
e-mail: chary.r@usask.ca

for this technique is the 140 keV gamma emissions of the ^{99m}Tc decay of 6 h half-life. The positron emission tomography is a bit more involved measurement of the two annihilation photons (511 keV) in coincidence, which allows for a better determination of flight paths of the photons. Again, back-projection technique is employed for the source distribution reconstruction, which constitutes the imaging.

2 Combined PET/SPECT Imaging

In a previous publication [1], we have addressed the well-known artifacts of these imaging techniques and proposed to marry the PET and SPECT into one single isotope-based combined imaging. A judicious choice of an isotope with single photon of energy is quite distinct from the annihilation photons (511 keV) to satisfy dual energy criterion. As articulated in Ref. [1], this imaging technique minimizes the scattering and absorption artifacts. More importantly, a radiologist can be presented with multiple images from the data obtained with one single isotope in one setting. For example, seven distinct images can be presented as below:

- (a) 3-photon coincidence events analyzed with software cuts as 3-photon events, 2-photon events, and 1-photon events (3 images)
- (b) 2-photon coincidence events analyzed as 2-photon events and 1-photon events (2 images)
- (c) single-photon events (2 images one for each energy)

In selecting the candidate isotopes for medical imaging, we required that they meet several criteria to be useful and economical.

We arrived at six candidate isotopes. They are as follows:

- (i) ^{43}Sc of 3.9 h half-life, emitting photons of 373 keV;
- (ii) ^{73}Se of 7.15 h half-life, emitting photons of 67 and 361 keV energies;
- (iii) ^{123}Xe of 2.1 h half-life with a photon of 149 keV;
- (iv) ^{85}Y and ^{85m}Y of 2.7 and 4.9 h half-lives with a photon of 232 keV;
- (v) ^{77}Kr of 75 min half-life of 130 and 147 keV energies;
- (vi) ^{75}Br of 97 minutes half-life emitting a photon of 286 keV energy.

3 Isotope Production

An important criterion for the choice of a medical isotope is the economics of production channel. It depends on the reaction process, the energies of beam species, and more importantly the cost of production channel. One of the reasons PET imaging by FDG is expensive is due to the low natural abundance of ^{18}O (0.2%). In our choice of isotopes, an important consideration is that the nuclear reaction

Table 1 Candidate isotopes of combined PET/SPECT imaging

Isotope of interest ($T_{1/2}$)	Target abundance (%)	Production reaction	Threshold (MeV)
^{43}Sc (3.9 h)	^{40}Ca (97)	α, p	3.9
^{73}Se (7.15 h)	^{75}As (100)	$p, 3n$	22
^{123}Xe (2.08 h)	^{127}I (100)	$p, 5n$	37.1
^{85}Y (2.68 h) $^{85\text{m}}\text{Y}$ (4.86 h)	^{88}Sr (83)	$p, 4n$	35.5
	^{87}Sr (7)	$p, 3n$	24.2
	^{86}Sr (10)	$p, 2n$	15.7
^{77}Kr (74.4 m)	^{81}Br (49)	$p, 5n$	41.4
	^{79}Br (51)	$p, 3n$	23.1
75Br (97 m), 74Br (25 m)	^{80}Se (50)	$p, 6n$	50.5
		$p, 7n$	62.5
	^{78}Se (24)	$p, 4n$	33.3
		$p, 5n$	45.4
^{75}As (100)	$^3\text{He}, 3n$	13.8	

Listed are the half-lives, the target material for production of the isotopes, the target's natural abundance, the nuclear reaction for production, and the threshold energy for the process [2]

proceeds through non-exotic processes and that they are of high cross-sections on targets of high natural abundances with particle beams of moderate energies. The Table 1 lists the isotope of interest, the candidate target material(s), natural abundances, and the production channel, i.e., the nuclear reaction of interest. The last column lists the threshold energies, which only specify the minimum energy for desired process to occur, but not the optimum energies.

3.1 Production Criteria

As the end goal is to produce the isotopes in the chemical form amenable to further processing for medical applications, careful attention must be paid to interfering activities. It is preferred that we create clean isotope at the production stage. If this is not possible, we should be able to separate out the non-desirable isotopes from the isotope of interest by chemical means. An example is the moly cow, where the isotope $^{99\text{m}}\text{Tc}$ is chemically separated from the parent ^{99}Mo isotope. The interfering activities occur in many ways, and we have to examine each one case by case to get a ballpark figure of the energies of projectiles for the reactions. While this serves as a guide, only detailed experimental investigations can help determine the optimum production channels and the energies. Below, we provide a brief description of the prospective production channels of individual isotopes and the concerns.

4 Production of Individual Isotopes

Below, we provide a detailed discussion of the production channels of two isotopes with commonly available projectiles, to illustrate some of the considerations.

4.1 ^{43}Sc Isotope

This isotope is already considered a candidate for blood flow studies and PET imaging. The positron emission is accompanied by a 373 keV gamma ray, a good candidate for SPECT imaging.

Two modes of production suggest themselves. The first as indicated in the Table 1 is the $^{40}\text{Ca}(\alpha,p)$ reaction. The nuclear data Web site provides the cross-section for this channel as shown in Fig. 1.

The Fig. 1 shows (α,p) and (α,n) cross-sections on ^{40}Ca target, resulting in the production of ^{43}Sc and ^{43}Ti . Incidentally, the ^{43}Ti decays to ^{43}Sc with a half-life of 0.5 s, thus augmenting the production of isotope of our interest, if we use alpha beams of about 12 MeV energies or higher. One would limit to projectile energies $E_\alpha < 20$ MeV to avoid the possibility of contaminants due to other channels such as (α,pn) and (α,d) . Another channel of interest to produce this isotope is by $^{44}\text{Ca}(p,2n)^{43}\text{Sc}$ reaction which has a threshold of 14.5 MeV proton kinetic energies. The cross-section for this process exhibits a broad maximum at about 23 MeV proton energies. While the proton beam energies can be easily achieved at small cyclotrons, one has to be concerned about the competing (p,n) and $(p,3n)$ reactions resulting in other Scandium isotopes. Also, the natural abundance of the ^{44}Ca is just about 2% of calcium, which makes the production expensive and involves chemical separation process for the product.

Fig. 1 $^{40}\text{Ca}(\alpha,p)$ and $^{40}\text{Ca}(\alpha,n)$ reaction data. See text for details. Data from Ref. [3]

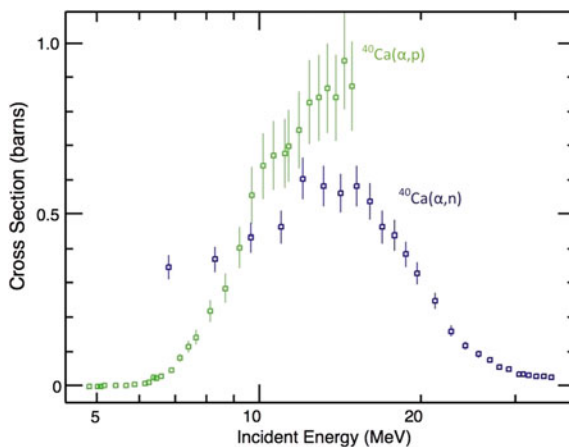
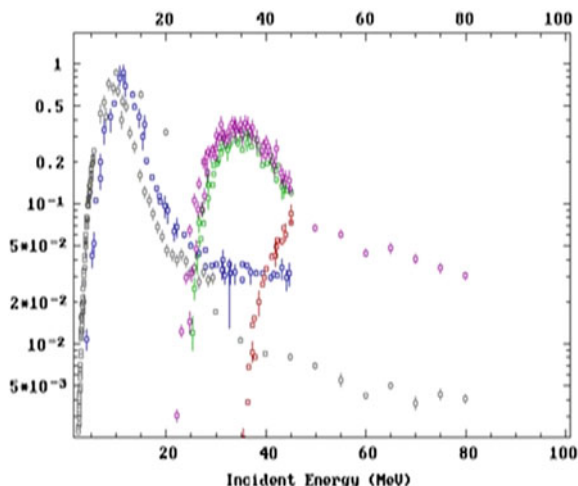


Fig. 2 $^{75}\text{As}(p,xn)$ $x = 2, 3, 4$ reaction cross-sections from Ref. [3]



4.2 ^{73}Se Isotope

A complicated situation occurs for production ^{73}Se by $^{75}\text{As}(p,3n)$ reaction. The target isotope ^{75}As is of 100% natural abundance, a desirable feature. The $^{75}\text{As}(p,3n)$ reaction has a threshold of $E_p = 22$ MeV with a maximum cross-section at about 35 MeV.

However, the (p,xn) cross-sectional data at the National Nuclear Data Web site shown in Fig. 2 exhibits a complex structure.

The $(p,2n)$ and $(p,4n)$ processes produce interfering activities of ^{74}Se and ^{72}Se , respectively. Thus, an optimization of beam energies and assessment of interfering radioactivities is of crucial importance.

Similar evaluations of production channels for each of the other isotopes are essential.

5 Conclusions

We identified the prospective isotopes for combined PET and SPECT medical imaging. We presented the possible production channels, which are achieved at moderate-energy proton cyclotrons and alpha beams of energies of about $E_\alpha \sim 12$ MeV. We are in the process of carrying out prototype measurements.

Acknowledgments This project was funded by the Natural Sciences and Engineering Research Council of Canada.

References

1. C. Rangacharyulu and Christine K. Roh, 2015 *Isotopes for combined PET/SPECT imaging*, Journal Radioanalytical and Nuclear Chemistry, DOI [10.1007/s10967-015-3945-4](https://doi.org/10.1007/s10967-015-3945-4) and references therein.
2. This data is derived from public domain data bases such as <http://education.jlab.org/itselemental/iso024.html> and <http://nndc.bnl.gov>.
3. Data from the National Nuclear Data Centre Website: <http://nndc.bnl.gov>.

Author Biographies

Chary Rangacharyulu is a professor of Physics and Engineering Physics at the University of Saskatchewan. His research interests are medical isotopes, nuclear physics, and particle physics.

Ramy Tannous is a student at the University of Saskatchewan.

Christine Roh is a student at the University of Saskatchewan.

Part IV
Student Program

2D Multi-group Transport Calculation on Hexagonal Geometry with the Method of Characteristics

Haodong Shan, Hong Yu and Li Xu

Abstract The method of characteristics (MOCs), which is a critical solution of neutron transport equation, has the ability to deal with complex geometry and could be easily coded in parallel computer. MOC has been used more and more widely in reactor physics calculation, as the computers developed. The MOC code ACMOC (assembly calculation on method of characteristics) is aimed to describe and calculate the fine hexagonal geometry by 2D multi-group transport calculation and to provide the effective multiplication factor and neutron flux distribution. ACMOC is going to be applied to sorts of FR assemblies such as fuel assembly and other assemblies with some structure change of geometry definition or the whole core neutronics calculations. Square geometry in PWRs has been handled before, while hexagonal geometry in FRs is more complex and generates more symmetry, which makes it hard to be calculated since the definition of the boundary condition is hard. At the same time, comparing with ordinary PWRs, FRs need more elaborate cross-sectional data of nucleus, which leads to more energy groups and more Legendre orders, because the reaction of fast neutron is various and complex in broad scale of energy. To achieve the proper accuracy, the numbers of energy groups and reaction types are increased in the multi-group database. This paper shows multi-group transport calculation code ACMOC, including the solution of geometry preprocessing and the transport equation. Through preliminary verification using macroscopic cross section and microscopic cross section, difference between ACMOC and recognized codes is less than 1%.

Keywords Transport equation · Method of characteristics · Hexagon · Modular ray tracing · ACMOC

H. Shan (✉) · H. Yu · L. Xu
China Institute of Atomic Energy, P.O. Box 275-95, Beijing 102413, China
e-mail: shanhaodong@126.com

© Springer Science+Business Media Singapore 2017
H. Jiang (ed.), *Proceedings of The 20th Pacific Basin Nuclear Conference*,
DOI 10.1007/978-981-10-2314-9_60

1 Introduction

MOC has been developed for decades, basis of which is to calculate the transport equation in discrete angular. Though the accuracy of MOC is perfect, it was not used widely until the computer’s speed increased highly at the end of twentieth century.

MOC begins with the time-independent transport equation:

$$\begin{aligned} \vec{\Omega} \cdot \nabla \Psi(\vec{r}, E, \vec{\Omega}) + \Sigma \Psi(\vec{r}, E, \vec{\Omega}) \\ = Q_s(\vec{r}, E, \vec{\Omega}) + Q_f(\vec{r}, E, \vec{\Omega}). \end{aligned} \tag{1}$$

The symbols in the Eq. (1) are the same as the usual meaning. For g energy group, given a set of discrete directions $\vec{\Omega}_n, n = 1, 2, \dots, N$ (including polar and azimuthal angles, shown in Fig. 1), and corresponding quadrature weights, the transport equation is described as Eq. (2) [1].

$$\begin{aligned} \vec{\Omega}_n \cdot \nabla \Psi_g(\vec{r}, \vec{\Omega}_n) + \Sigma_g \Psi_g(\vec{r}, \vec{\Omega}_n) \\ = Q_{s,g}(\vec{r}, \vec{\Omega}_n) + Q_{f,g}(\vec{r}, \vec{\Omega}_n). \end{aligned} \tag{2}$$

where $\vec{\Omega}_n$ is one of the discrete directions and g is the number of energy groups. Take Fig. 2 as the target, which is a 2D problem, and integrate the right of Eq. (2) into $Q(s)$. For a specific angle, Eq. (2) can be transferred into Eq. (3).

$$\sin \theta \frac{d}{ds} \psi_g(s) + \Sigma_g(s) \psi_g(s) = Q(s). \tag{3}$$

Fig. 1 Discrete direction set in MOC

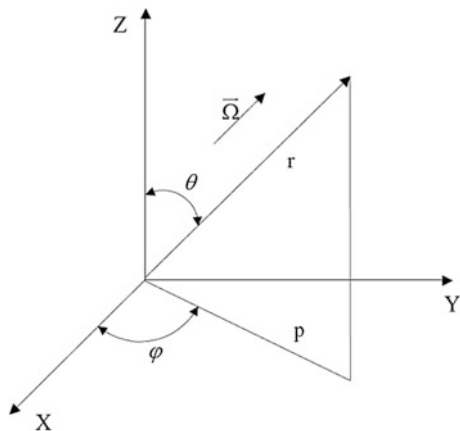
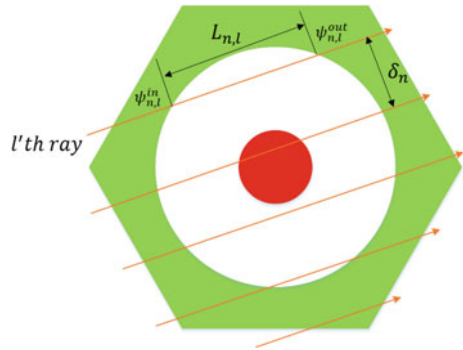


Fig. 2 Geometric tracking module in MOC



$\sin \theta_n$ is the sine of polar angle; s and $L_{n,l}$ are the position and track length of the ray projected to the x - y plane in the x - y - z coordinate system with the model being uniform and infinite in z -direction. In the area of a same material (e.g., the white area in Fig. 2), it is assumed that $Q(s)$ and $\Sigma_g(s)$ of Eq. (3) are constant. Then, Eq. (4) is obtained by integration.

$$\psi_{g,n,l}(L_{n,l}) = \psi_{g,n,l}^{in} * e^{-\frac{\Sigma}{\sin \theta_n} * L_{n,l}} + \frac{Q}{\Sigma} \left(1 - e^{-\frac{\Sigma}{\sin \theta_n} * L_{n,l}} \right). \quad (4)$$

Both $\psi_{g,n,l}^{in}$ and mesh-averaged angular flux $\overline{\psi_{g,n,l}}$ are calculated through Eq. (4). $\overline{\psi_{g,n}}$ is described as follows:

$$\overline{\psi_{g,n}} = \frac{Q_{g,n}}{\Sigma_g} + \frac{\sin \theta_n}{\Sigma_g * A_{i,j}} \sum_{l \in ij \text{ mesh}} \delta_n \left(\psi_{g,n,l}^{in} - \psi_{g,n,l}^{out} \right). \quad (5)$$

where δ_n is the interval between adjacent rays for direction $\vec{\Omega}_n$ and $A_{i,j}$ is the area of mesh (i, j). Note that $L_{n,l}$ need to be modified to get the actual mesh area.

Given the weights of every angular, the average neutron flux in a cell is shown as Eq. (6).

$$\psi_g = \sum_{n=1}^N \omega_n \cdot \overline{\psi_{g,n}}. \quad (6)$$

By repeating the process in all cells, average angular fluxes and average flux are calculated.

2 Geometry Preprocessing MRT

Geometry preprocessing is indispensable for the MOC calculation. In this stage, the macroscopic cross section of each material and the track length of each ray across the meshes in every angle are calculated. The work can be very difficult and cost

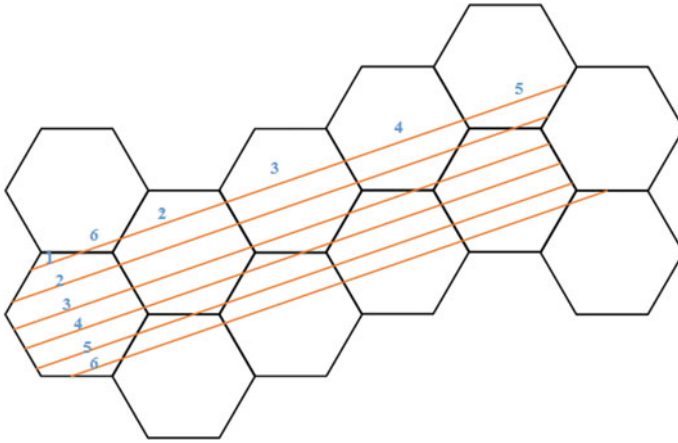


Fig. 3 MRT for hexagonal geometry

amounts of CPU time if we take the whole target as a unit. To simplify the schedule of the geometry preprocessing, the modular ray tracing (MRT) of iterative geometry is developed [2]. Figure 3 shows the MRT in hexagonal geometry. It can fall into two types due to the different units, CMRT for cells, and AMRT for assemblies. Rectangle preprocessing has been normal [3], and hexagon processing can be achieved in a similar way.

By analyzing hexagons with MRT (Fig. 3), MOC line-generating method of hexagonal geometry is listed as follows:

- (1) Given an integer N , then the number of azimuths in the scale of $0\text{--}60^\circ$ is $N - 1$, the azimuth φ can be decided by:

$$\tan \varphi_m = \sqrt{3} \frac{m}{2N - m}, \quad m = 1, 2, \dots, N - 1. \tag{7}$$

in which chosen N_φ ($N_\varphi < N - 1$) azimuths; weights of them have the relationship as in Eq. (8) [4].

$$\sum_m^{N_\varphi} \omega_m \cos(3s\varphi_m) = \begin{cases} \frac{\pi}{3}, & \text{if } s = 0 \\ 0, & \text{if } s = 1, 2, \dots, N_\varphi - 1 \end{cases} \tag{8}$$

- (2) For φ_m , the density of MOC (distance of every two adjacent MOC lines) is follows:

$$\delta A_m = \frac{a \times \sin \varphi_m}{m}. \tag{9}$$

There are $2N$ MOC lines for one same azimuth in a single hexagon with this method.

- (3) Based on the $0\text{--}60^\circ$ MOC lines, MOC lines of $0\text{--}360^\circ$ azimuths can be obtained by a reflection in 60° for five times.

The code ACMOC (assembly calculation in the method of characteristics) has applied the CMRT to hexagonal geometry. It can generate series of MOC lines and calculate all the useful information of MOC lines on sorts of cells, with the definition of the amount and arrangement of discrete angles as input. The distribution of materials in the cell should be given as well.

3 Schedule of Transport Algorithm

Two-dimensional multi-group transport code ACMOC is based on the MOC and the MRT. It is divided into 4 types of calculations according to the boundary condition. Both the microscopic and macroscopic cross-sectional data can be used as input database.

3.1 *Cross-sectional Database*

There are two kinds of cross-sectional data used in ACMOC:

- (1) Macroscopic cross-sectional data, which are imported as parameters in an input card. Number of energy groups and cross-sectional details can be defined as you wish.
- (2) Microscopic cross-sectional database, which is AMPX-formatted NVITAMIN-C multi-group database (171 groups) based on ENDF/B-VI and CENDL-2. The NVITAMIN-C database is given as a separate input file, in which the cross-sectional data have been modified the Bondarenko factor by using the BONAMI module in PASC-1 system [5].

3.2 *Definition of Boundary Condition*

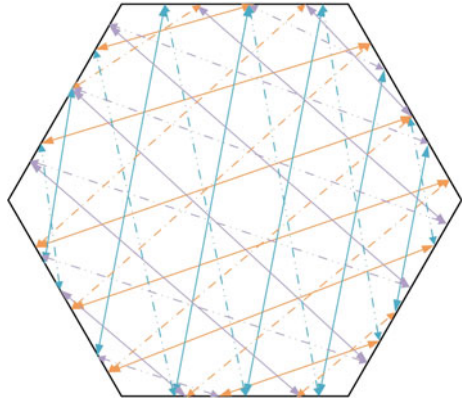
The code ACMOC can deal with 4 types of boundary conditions, that is,

- (1) Vacuum boundary condition:

Make the incoming neutron flux as zero before every cycle.

- (2) White boundary condition:

Fig. 4 Reflected boundary condition of hexagonal assembly



Sum all the outgoing neutron angular fluxes in the last cycle, and make all the incoming neutron angular flux average of the sum in the current cycle.

(3) Reflected boundary condition:

The definition of reflected boundary condition for hexagonal geometry is more complex than that of the rectangle case. ACMOC code defines suitable reflected boundary condition for hexagonal geometry, and more memory is used to store the outgoing neutron fluxes in this schedule. Figure 4 shows the definition of reflected boundary condition of hexagonal assembly.

(4) Given boundary condition:

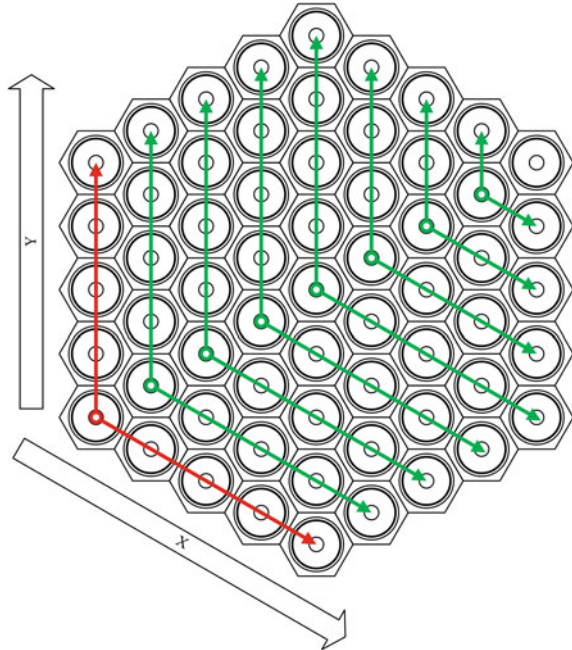
Make incoming neutron angular flux of every side the certain value, which is given by input.

3.3 *Process of Calculation*

It is the method of geometry preprocessing that decides the process of calculation. The calculation should follow the MOC line of cells by using MRT.

Figure 5 shows the 60° calculation in ACMOC, and the red line is the first calculation line, in which the corner cell is the beginning cell of whole calculation. Given the boundary condition as input, for example the zero-boundary condition, the incoming neutron angular fluxes from the boundary of red line are zero. Firstly, calculate the beginning cell of red line, and then calculate the red line in two separate directions (x and y coordinates as shown in Fig. 5). Secondly, with all the calculation of red line ended, incoming neutron angular flux from boundary of the next line (the first green line) is obtained, and then, the calculation process of green

Fig. 5 Process of calculation of ACMOC



line could be calculated as well as the red line. The rest can be done in the same manner. The 60° calculation is finished after all lines are calculated. Whole calculation is done as soon as all the other five 60° calculation is finished.

4 Preliminary Verification for ACMOC

Main structure of ACMOC has been finished, and preliminary verification has been done. There are two typical examples listed as follows.

4.1 Macroscopic Cross-Sectional Problem

DRAGON [6] is a multi-functional MOC code, which can be used for hexagonal geometry calculation. The results of DRAGON and ACMOC can be compared in a macroscopic test, while macroscopic cross-sectional data can be given in input card in DRAGON as well as ACMOC.

The example 01 of macroscopic cross section is shown in Fig. 6.

The number of rings extents from 6 to 8 (the number is 1 when there is only 1 cell). For a single cell, the length of side is 0.231 cm. The number of energy groups is 2, and macroscopic cross-sectional data are listed as in Table 1.

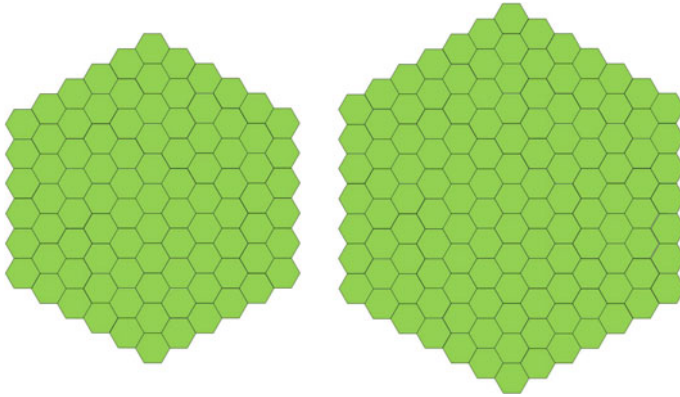


Fig. 6 Schematic diagram of example 01

Table 1 Macroscopic cross section in example 01

Type of cross section	1st group	2nd group
Total (1/cm)	1.0	2.0
Scattering (1=>) (1/cm)	0.2	0.2
Scattering (2=>) (1/cm)	0.0	0.1
Fissional (1/cm)	0.5	1.0
Average number of fissional neutrons	2.0	2.0
Fissional spectrum	0.1	0.9

Effective multiplication factors of ACMOC and DRAGON in vacuum and reflected boundary condition are listed in Table 2.

Results in reflected condition are perfect, and those in vacuum condition fit well with DRAGON. Meanwhile, results in vacuum condition of ACMOC will be more close to that of DRAGON, considering the description of geometry is different between them. In DRAGON, every hexagonal cell is divided into 6 triangles which could be divided as well. Later works will be taken on to elaborate the geometry description and to decrease this difference between ACMOC and DRAGON. The efficiency of ACMOC is similar to or even higher than DRAGON, as Table 2 shows.

4.2 Microscopic Cross-Sectional Problem

ACMOC is developed to be used in assembly calculation of CEFR (Chinese Experimental Fast Reactor, the first sodium-cooled fast reactor in China), using the NVITAMIN-C as the input cross-sectional data. The number of energy groups is 171, and the maximum Legendre order in scattering cross section is 3.

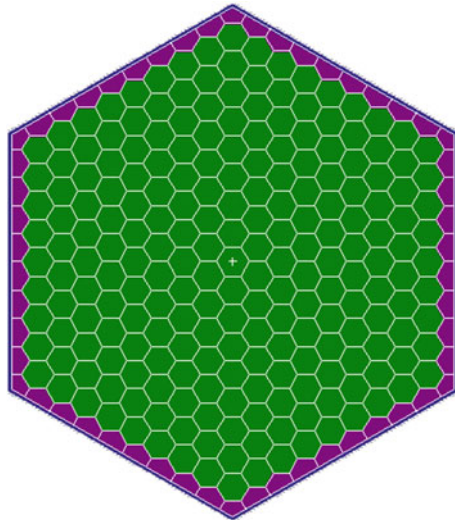
Table 2 Keff in different conditions

Cir	Code	Vacuum		Reflected ^a	
		Keff	Time/s	Keff	Time/s
6	DRAGON	0.980181	2.037	1.098684	2.212
	ACMOC	0.977489	2.044	1.098684	0.218
	Difference ^b	-2.69‰	3.4%	0‰	-90.1%
7	DRAGON	1.009771	6.032	1.098684	5.708
	ACMOC	1.002969	3.541	1.098684	0.234
	Difference	-6.80‰	-41.3%	0‰	-95.9%
8	DRAGON	1.026953	12.504	1.098684	13.111
	ACMOC	1.021259	6.599	1.098684	0.390
	Difference	-5.69‰	-47.2%	0‰	-97.0%

^aThis result is based on the *k*-infinite (given a very big value to length of cell)

^bThe difference of keff is absolute difference

Fig. 7 Schematic diagram of example 02



Choose the geometry module in Fig. 7 (the number of cycles extents from 9 to 11, length of side for the cell is 0.404 cm, and width of tube is 0.2 cm), and use the fuel material of CEFR-MOX (MOX fuel will be used in the future); results of multi-group calculation in ACMOC and MCNP [7] are listed in Table 3.

Considering the difference between NVITAMIN-C lib cross section by ACMOC and pointwise cross-sectional database by MCNP, result of vacuum condition fits well with MCNP. One of this difference comes from the different description of calculation model and difference between MOC and Monte Carlo method, which will be modified in future.

Table 3 Results for a whole FR assembly (vacuum boundary)

Cir	L (cm) ^a	ACMOC	MCNP	Difference
9	6.466	0.190064	0.19320	-0.00314
10	7.044	0.213635	0.21741	-0.00378
11	7.621	0.237629	0.24192	-0.00429

^a L is the length of side for this assembly

5 Conclusion

Two-dimensional multi-group transport code ACMOC is developed and applied to calculation of hexagonal geometry. Process of MRT for hexagons and structure of MOC transport calculation has been designed. There are four types of boundary condition and two type of cross section that ACMOC can deal with. Results of typical examples are in good agreement with other recognized codes, the efficiency of ACMOC is good as well.

This paper provides support for later works on ACMOC. The aim of ACMOC is to be used in neutron calculations of FRs (single assembly or even the whole core), which is much more complex than the prior examples. To get a better accuracy and efficiency, description of geometry ought to be elaborated [8] and parallel module might be led to ACMOC.

ACMOC has potential to be a high-accuracy 2D MOC multi-group transport code, which can be applied to the critical calculation and homogenization calculation of single FR assembly.

Acknowledgement Thanks to my teacher YU Hong and colleague XU Li who provide guidance and advises through the research. It is the Natural Science Foundation of China (91326107) which provides support for this scheme.

References

1. N. Cho, "Fundamentals and Recent Developments of Reactor Physics Methods," *Nuclear Engineering and Technology*, 2 2005.
2. J.-Y. CHO, K.-S. KIM, H.-J. SHIM, J.-S. SONG, C.-C. LEE and H.-G. JOO, "Whole Core Transport Calculation Employing Hexagonal Modular Ray Tracing and CMFD Formulation," *Journal of NUCLEAR SCIENCE and TECHNOLOGY*, vol. 45, no. 8, pp. 740-751, 2008.
3. G. S. Lee and N. Z. Cho, "Two-dimensional whole-core transport calculations of the OECD benchmark problem C5G7 MOX by the CRX code," *Prog. Nucl. Energy*, 2004.
4. W. Filippone, S. Woolf and R. Lavigne, "Particle Transport Calculations with the Method of Streaming Rays," *Nucl. Sci. Eng.*, pp. 77-119, 1981.
5. W. Yaoqing, J. oeppe, J. B. M. d. Haas, H. Gruppelaar and J. Slobben, "The Petten AMPX/SCALE Code System PASC-1 for Reactor Neutronics Calculations," Netherlands Energy Research Foundation, 1988.

6. G. MARLEAU, A. H. EBERT and R. ROY, "A USER GUIDE FOR DRAGON VERSION5," Institut de g'enie nucl'aire D'epartement de g'enie physique Ecole Polytechnique de Montr' eal, 2015.
7. X.-M. Team, MCNP-A General Monte Carlo N-Particle Transport Code, Los Alamos National Laboratory, 2003.
8. G. Lee and N. Cho, "2D/1D fusion method solutions of the three-dimensional transport OECD benchmark problem C5G7 MOX," *Progress in Nuclear Energy*, pp. 410–423, 2006.

A Detection of ^{226}Ra Concentration in Water Around a Decommissioned Uranium Mine in Hunan Province

Hui Jin and Tianyuan Xin

Abstract In this paper, a certain decommissioned uranium mine in Hunan province, which was regarded as the object of the research, was, respectively, sampled from its surrounding drinking water, irrigation water, and natural lake water and analyzed by co-precipitated barium sulfate emanation scintigraphic detection of eight samples of ^{226}Ra concentration, which the values of the order of 0.0614 Bq/L, 0.0330 Bq/L, 0.0489 Bq/L, 0.0489 Bq/L, 0.0751 Bq/L, 0.0694 Bq/L and 0.0532 Bq/L. By comparing the relevant national standards (^{226}Ra concentration in drinking water is not over 0.1 Bq/L, etc.), it is concluded that the ^{226}Ra concentrations of water nearby the decommissioned uranium mine comply with the national standards, but they were much higher than the consistencies of ^{226}Ra in comparable water. This paper illustrates the importance and necessity of environmental radioactivity monitoring about the decommissioned uranium mine and makes the higher request to relevant environmental managements.

Keywords Decommissioned uranium mine · Environmental water samples · ^{226}Ra

H. Jin (✉)

Radiation Protection and Environment Engineering, School of Nuclear Science and Technology, University of South China, ChangShengWest Road no. 28, ZhengXiang District, Hengyang 421001, China
e-mail: mijue2012@msn.cn

T. Xin

Nuclear Engineering and Nuclear Technology, School of Nuclear Science and Technology, University of South China, ChangShengWest Road no. 28, ZhengXiang District, Hengyang 421001, China

1 Introduction

Nuclear energy is playing an increasingly indispensable role in the economic development of modern society. Compared with the traditional energy which is highly polluting enterprises with high energy consumption, the nuclear energy seems to be “the cleanest and most cost-effective power resources” and have wide development prospects. The uranium mineral resources regarded as primary raw material of nuclear power production attract much attention in the current global economy development strategy. Since 1950s, a great number of large military industry uranium mines, which made an indelible contribution to the development of national nuclear industry, gradually appeared nationwide. Until 1990s, some of these were closed down for the shrinking reserves, the exhaustion of uranium mine and the adjustment of national strategic. The government and supervision of the environmental radioactivity level about the retired uranium mine is an essential part of the nuclear industry system, and its related technical research is still a sector hot spot. Nevertheless, in reality, there still are a large number of problems to be solved in practice about environment monitoring and treatment around decommissioned uranium mines.

This paper is mainly talking about the concentrations of radium-226 of sample water near a retired uranium mine in Hunan province. Target uranium mine (hereinafter, it is referred as D uranium for convenience) is one of the earliest uranium mines in China, which is located in the southeastern Hunan province and is adjacent to Xiangjiang River. The mine built in 1958 by the aids of Soviet Union shut down in 1985 and went bankrupt in 2003. It acts a significant role in the development of nuclear industry in China, especially for a series of early major national strategy such as the first atomic bomb of China. The area has abundant rainfall and is affected by the monsoon, so more than 50% of annual precipitation concentrates in April to June. The annual average temperature is 18 °C, while annual average sunshine is 1812 h.

2 Basic Condition of the Retire Mine

The uranium mine is located in concave structure's shaft part of central south region, surrounded by the intermittent band of the formation of ancient down the mountain ridge, which is a typical basin with large area in the cretaceous and paleogene red layer of red hilly tableland. The mine of D uranium belongs to the sedimentary ore, which located in the geological zone in south China. Its structure is complex, both east-west and north-south minerals. D mine has five work area, most of all are underground mine while a few are open. The average grade of the uranium is 2‰, and the highest could be up to 3‰ [1]. Mine tailings dams are built in valley, which have covered with the topsoil and vegetation. It surrounded by a cement wall, of which the height is 1.4 m, and the thickness is about 0.4 m. The

cover of the tailings reservoirs are consists of rock layer and yellow soil covering with herbs, shrubs, and trees (such as pine, locust tree, Chinese catalpa tree, and orange tree). There are also some waste dump covered by soil, rocks, and kind of plant. The concrete retaining wall and trenching are built in case of the surface water and groundwater inflows in pile.

3 Experimental Procedure

3.1 Sampling

According to water sample collection standards [2, 3], we made a detailed sampling plan including sampling points, sampling method, sampling tools, sampling route, and transportation of sample. The sampling stuff were all being trained to taking samples precisely and skillfully before working, and we tried to avoid the error in sampling and experimental results as much as possible.

First, we took the water strictly according to the plan. Because this paper is aimed to measure the concentrations of radium-226 of sample water near D uranium mine, we sampled the water at 8 points including drinking water, the irrigation water, and the lake water, which can ensure the samples' representative and typicality as far as possible. Then, we recorded the data according to the experimental methods and steps above-mentioned. Eight points are located in the three work area of D uranium, and we named three work areas by #1, #2, and #3 (as the Fig. 1 shows). The points include pool of #1, residents' home well of #1, lake water

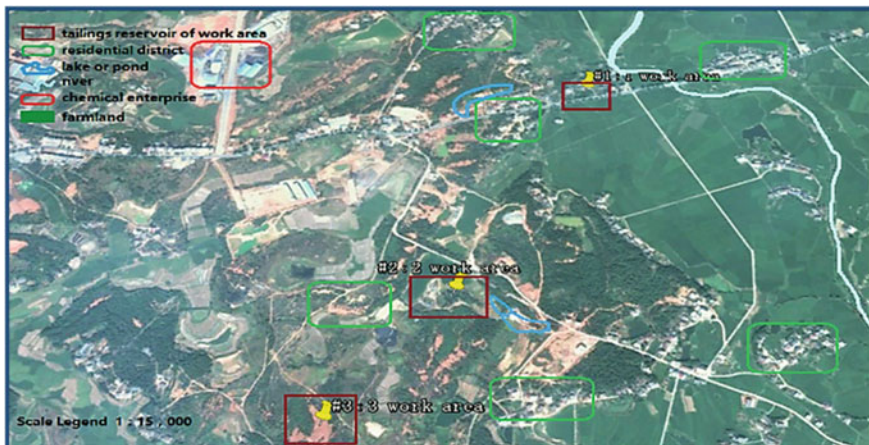


Fig. 1 Location of the target uranium mine. Here are some *key marks* showed in the Fig. 1: tailings reservoirs of work areas, main residential districts, extensive lake or pond, river, and major chemical enterprise in region interior of the decommissioned uranium mine. The preliminary perceptual cognition about the mine's situation could be obtain.

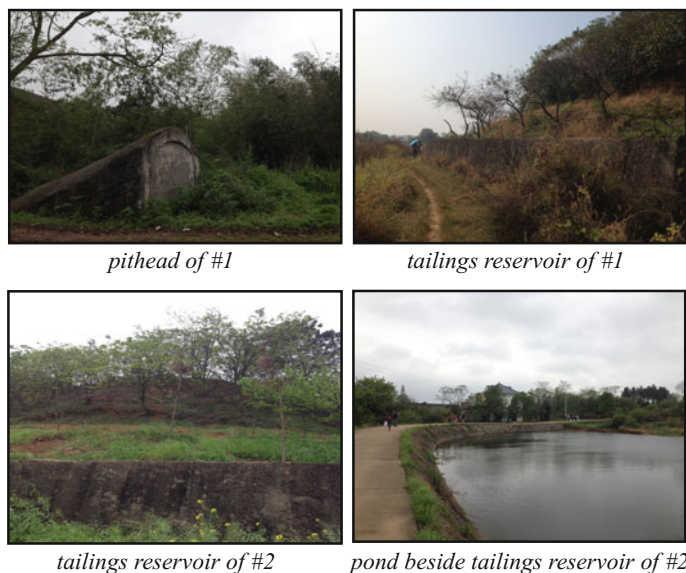


Fig. 2 Environment around tailings reservoirs of the decommissioned uranium mine

besides #2, irrigation water around #3, lake water besides #3, farmhouse around #3, shop nearby #3, and water of Health Drinking Water Engineering (Fig. 2).

3.2 Pretreatment for the Sample

After sampling, add 10 mL of nitric acid immediately to the water in order to restrain or prevent microbial activity and to prevent the nuclide (radium-226) adsorbing on the container wall. Next, the water samples need to be lay aside. After rest for 6 days in the lab, we let radium-226 reach the decay balance in order to facilitate the late experimental tests.

3.3 Laboratory Operations

According to the national standards of measurement for Radium-226 in water, we have 2 methods: iron hydroxide—calcium carbonate emanation scintillation method and barium sulfate precipitation emanation and scintillation method [4]. We combined the condition of laboratory and chose barium sulfate coprecipitation and emanating scintillation method. In other words, it took barium sulfate as the carrier and precipitate radium in water. Then it is dissolved in alkaline EDTA solution and

sealed in diffuser for accumulation of radon. Next transferred to the scintillation chamber and calculate the concentrations of radium-226.

4 Analysis of Data

4.1 Integration of Data

The following experimental data were obtained (Table 1).

And we can calculate the concentration of ²²⁶Ra in determined water sample by the formula (1):

$$C_{Ra} = \frac{Kn_0}{R(1 - e^{-\lambda t})V} \tag{1}$$

Table 1 Original record of samples measurement

Sample	Location	Closure time/d	Average/cpm	Background/cpm
1	#1Pool	5	165.7	7.7
2	#1Well water	5	110.0	8.3
3	#2Lake water	5	150.0	9.7
4	#3Irrigation water	4	129.3	8.3
5	#3Lake water	4	183.3	9.7
6	#3Form	4	163.0	7.7
7	#3Grocery	4	137.0	8.3
8	Drinking water system	4	140.3	7.7

Remark: the data counted once every 300 s, K of scintillation chamber is 13.65 Bq/(m³/cpm)

Fig. 3 Radon accumulated in diffuser is transferring into scintillation cell

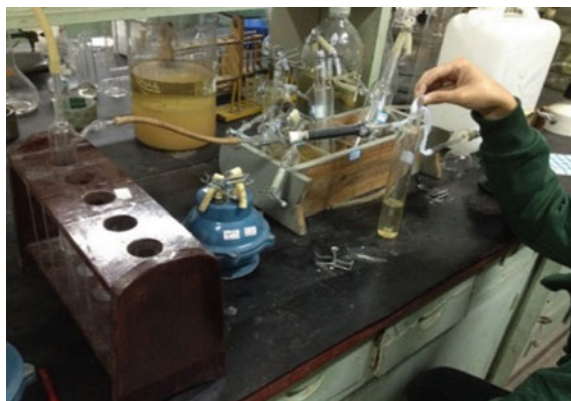
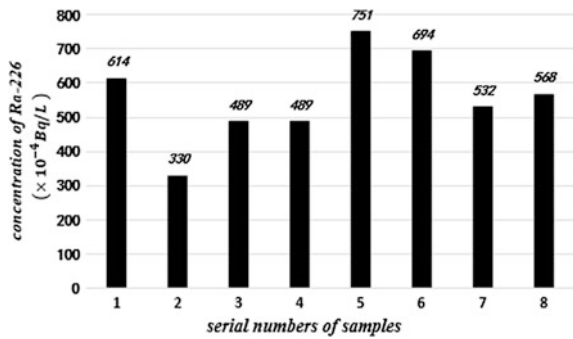


Fig. 4 GW1016 intelligent scaler is counting



Fig. 5 Results on concentration of ^{226}Ra about the determined samples



In the above formula (1):

C_{Ra} : concentration of ^{226}Ra in determined water sample, Bq/L;

K : scale factor of scintillation chamber, $13.65 \text{ Bq}/(\text{m}^3\text{cpm})$;

R : recovery rate of the whole experience, 95%;

$1 - e^{-\lambda t}$: build-up factor, and the t was defined as the blocking time transferring sample into diffuser;

V : initial volume of determined water sample, 5L.

The normative calculation, in accordance with the above formula, is shown in (Figs. 3, 4 and 5).

4.2 Conclusions

Lake water of #3 was sampled from tailings pile from work area 3, which the linear distance to a large lake is less than 200 meters. Due to the closeness to the tailings pile, groundwater is more likely to seepage into the lake, and the rain may wash the

ore heap and will also take the material with radionuclide into the lake. So lake water of #3 has the highest of radium-226.

The concentrations of #1 residents' home well is relatively low because the residents live a little far from the tailings pile point and the well water was taken from deep groundwater (50 m). Obviously, the concentration should be the lowest. In other words, the underwater near D uranium is not being polluted by the tailings surrounding on the whole.

Actually, the distance between the mine tailings pile and 8 sample points is no more than 1 km, so D uranium has affected the concentrations of radium-226 in water. From the result, we can get the conclusion that the environmental radioactive level of the neighborhood of retired uranium mine is relatively higher than usual. According to standard [5], the concentrations of radium-226 in drinking water should be no more than 0.1 Bq/L [5]; otherwise, it cannot be used as drinking water for people. Through the literature [6], the domestic typical value of radioactive concentration of natural radionuclide in rivers and lakes is 4.38×10^{-3} Bq/L while the world's ten largest river is 2.59×10^{-3} Bq/L, the Yellow River water system is 11.80×10^{-3} Bq/L, Hot springs of Chicheng in Hebei is 55.00×10^{-3} Bq/L, artesian well of Songshan is 34.00×10^{-3} Bq/L, White temple of Beijing hot springs is 102.00×10^{-3} Bq/L, and HongShang temple is 117.00×10^{-3} Bq/L. We can compare and make conclusions that:

1. The radium-226 concentration of water samples from the target mine are lower than the drinking water standards, so its radioactive level is within an acceptable range. But it is an indisputable fact that the average is very close to the limit value of standard, such as the highest concentration of radium-226 is 0.0751 Bq/L. As for #3 lake water, what make the concentration very high is that it comes from the ore reservoir and natural rainwater and might also comes from the lake next to the tailings and waste dump which contains high levels of radionuclide effluent.
2. The average concentration of water samples from D uranium mine is 0.05585 Bq/L, which is nearly 8 times more than the domestic typical value of radioactive concentration of natural radionuclide in rivers.
3. The average concentration value of water samples from D uranium mine is almost as much as the concentration in hot spring. Hot springs, in fact, come from the natural groundwater, so the concentration of radium-226 was higher than usual. What is more, today there are an increasing number of people paying more attention to hot spring because it would contact with human body directly.

To sum up, though the radium-226 concentration of water samples from the target mine are lower than the drinking water standards, they are still at a higher level. So we can draw a conclusion that although many measures were taken, the environmental radioactive level of the neighborhood of retired uranium mine is relatively higher than usual and had cause serious influence.

At the same time, some significant information was obtained when we had interviews with the local residents. The diseases incidences of respiratory system

and skin have been held up so well, such as lung cancer, as a resident said, plenty of local youth always were fail to enlist and were refused, for they did not pass physical examination. And cattle fed in peasant household also suffer from lung illness frequently. To be frank, local residents are practically clear about that they live around the decommissioned uranium and the water and air contained radioactive substance are primary villains, which coincide with the information that we consulted [7].

What is more, they also realize the problem and think of economic capacity, For the majority local residents, only drinking water is distilled water or mineral water transported from other places while other domestic water are taken from local reservoirs constructed by administrative department of decommissioned uranium mine—that is, namely tap water and well water, which all directly come from surface water in the locality. In addition, there are also little residents who take domestic water including drinking water from wells. Therefore, even though the radioactive level of target area that we detected through experiment—here we regard the ^{226}Ra concentration in water around a decommissioned uranium mine as an illustrative quota—do not exceed the range of national standard, and the mine has been decommissioned for nearly 30 years, the radioactivity has been making some negative influences on production-living of residents and nation environment, even threatening residents' life and health.

5 Suggestions

- (1) Put more attention to the relevant research about how to deal with the retired uranium mine. Get more access to decrease the pollution to the water of the neighborhood of retired uranium mine, especially for the underwater.
- (2) Classify the management for dealing with the water near the tailings pile. Cover clay, tree, or grass after compaction and set the retaining wall and drainage. Slope stability to avoid natural tumble gravel or the rains washed out the radionuclide into the surrounding water. At the same time, do regular inspection and maintenance.
- (3) The environmental protection department should increase their effort in monitoring the water quality near the retired uranium mine. As for local health department, they should pay more attention to residents' health and do examination for them regularly. Discover disease earliest and ensure people's life and health.
- (4) At last, the residents should keep away from the management area of retired uranium mine in order to reduce additional radiation dose. After management, long-term monitoring mechanism should be established to ensure the dose turn back to an acceptable level to the public.

References

1. PAN Ziqiang, WANG Zhibo, CHEN Zhuzhou et al., Radiological Environmental Quality Assessment of the Nuclear Industry in China over the past 30 Years, [M]. Beijing: Atomic Energy Press, 1990.
2. Water quality-Guidance on sampling techniques from lakes, natural and man-made (GB/T14581-93) Nuclear Industry in China over the past 30 Years, [M]. Beijing: Atomic Energy Press, 1990.
3. HJ/T52-1999, Water quality-Guidance on sampling techniques of rivers, 1999.
4. GB11214—89, National Standard of the People's Republic of China, analysis and determination of in water [S] State Bureau of Environmental Protection (1989).
5. Ministry of Public Health, GB 5749-85 Standards for Drinking Water Quality[M].Beijing: Standards Press of China, 1985.
6. Li Ting, Measurement and analysis of natural radioactive elements Ra-226 and Rn-222 in thermal groundwater, [D], China University of Geosciences, 2013.
7. CHEN Diyun, WANG Xiangyun, CHEN Yongheng, Implications of Radionuclide Removing to Environment in Cattle Raised Near U Mine Area, China Environmental Science, 2000,20 (5) 465–468.

A Study of Spray Application by a Fire Truck for the Mitigation of Severe Accident Outside the Nuclear Power Plant

JongWook Go, Irfan Younus and ManSung Yim

Abstract When a severe accident occurs, large amounts of radioactive materials may be released. This possibility also increases the public's fear of nuclear power plants (NPPs). Also, the economic impact of a severe accident can be huge as shown in the Fukushima accidents. Given these considerations, technologies to prevent the dispersal of these materials are desirable. Technologies to capture the radioactive materials have been studied. One example of such technology is to use spray. Use of spray inside nuclear power plant has been developed with the use of alkaline water. In this study, we propose to use spray technology to collect the materials released outside the plant. Although there are various types of liquids that can be used with spray technology, this study investigated water spray as the baseline technology because seawater and freshwater are readily available near NPPs. To deploy the spray technology, use of a fire engine specially equipped with a "boom" that can be extended to reach higher locations was envisioned in this study. The capability of the spray technology was analyzed through computational fluid dynamics (CFD) analysis. By using a CFD modeling-based simulation, this study investigated the effectiveness of fire engine-mounted sprays in reducing dispersion of radioactive materials in a severe accident. In particular, this study examined the role of the distance of the spray nozzle from the containment and nozzle angle, to improve the effectiveness of the spray.

Keywords Spray · Fire truck · Severe accident · CFD · Nuclear power plant · Source term reduction

J. Go (✉) · I. Younus · M. Yim
Korea Advanced Institute of Science and Technology (KAIST),
Daejeon, Republic of Korea
e-mail: gowe1234@kaist.ac.kr

I. Younus
e-mail: irfan.pnra@kaist.ac.kr

M. Yim
e-mail: msyim@kaist.ac.kr

1 Introduction

The Fukushima Daiichi nuclear disaster has eroded the public's confidence in the use of nuclear power as a safe source of energy. This is especially true for residents who live near nuclear power plants (NPPs), because they are afraid of being exposed to radiation released during a severe accident. As a result, public acceptance has decreased, and the regulation of nuclear power has become more restrictive. To improve the safety of NPPs, technologies that filter radioactive aerosols, such as Filtered Vented Containment System (FVCS), have been developed and are currently being installed at NPPs. Use of spray technology outside NPPs to prevent dispersion of radioactive substances in a severe accident situation is also proposed [1].

Spray equipment can be suitable for capturing radioactive aerosols because it has been successfully applied in a variety of industrial applications. An important requirement for the successful use of spray technology is the ability to implement the technology at a NPP site in a short time frame. An added benefit of the quick application of this technology is the positive effect it can have on the public by providing a method to reduce the impact of airborne releases from a NPP. This study is to develop a numerical methodology to investigate the use of fire truck mounted and its performance in capturing the released radioactive materials. The investigation in this study is limited to a lab-scale environment. The role of the distance of the spray nozzle from the containment and nozzle angle was examined in this study to improve the effectiveness of the spray. To support this study, the ANSYS CFX code was used and the particle source term was modeled to analyze the effectiveness of spray technology in capturing solid particles. This modeled source term was based on the numerical modeling work for the analysis of venturi scrubber performance [2, 3].

2 Mathematical modeling

Generally, the Eulerian method is used to solve behavior of fluid. However, if particles, such as droplets or solid particles in fluid flow, are considered, it is better to model the behavior of these particles using the Lagrangian method. If the Eulerian and Lagrangian methods are coupled, particles and fluid flow can both be analyzed at the same time. As analyzing the behavior of sprayed water droplets in fluid flow is important in this study, coupling the Lagrangian and Euler method was undertaken.

2.1 Conservation Equations

To calculate flow behavior of fluids, the Eulerian method is commonly used. In this case, conservation Eqs. (1) and (2) have to be solved. However, solving these

equations is difficult because of the turbulence effect. Therefore, the Reynolds-averaged Navier-Stokes (RANS) equations are proposed to simplify the turbulence problem.

Equation (1) is the continuity equation relative to mass conservation in incompressible flow and at steady state.

$$\nabla \cdot \mathbf{U} = 0 \quad (1)$$

To solve the momentum conservation equation in turbulence flow, the following Eq. (2), which is called RANS equation, is used.

$$\frac{\partial \mathbf{U}}{\partial t} + \nabla \cdot (\rho \mathbf{U} \mathbf{U}) = -\nabla P + \rho \mathbf{g} + \nabla \cdot \left[\mu \left(\frac{\partial U_i}{\partial x_j} + \frac{\partial U_j}{\partial x_i} \right) - \rho U'_i U'_j \right] \quad (2)$$

This research also requires the analysis of the behavior of air and dust particles. In this study, the particles were assumed to be titanium dioxide (TiO₂) dust in connection with future experiments. It was further assumed that the dust behaves as if it were part of the air. Therefore, the behaviors of air and TiO₂ dust can be solved by using the above equations.

2.2 Turbulence Modeling

Turbulent viscosity can be derived using the k - ε model. The model calculates turbulence kinetic energy (k) and dissipation (ε). These calculations are based on turbulence kinetic energy and dissipation differential Eqs. (3) and (4), respectively. In essence, these two equations make up the k - ε model [4].

$$\frac{\partial(\rho k)}{\partial t} + \frac{\partial}{\partial x_j} (\rho U_j k) = \frac{\partial}{\partial x_j} \left[\left(\mu + \frac{\mu_t}{\sigma_k} \right) \frac{\partial k}{\partial x_j} \right] + P_k - \rho \varepsilon + P_{kb} \quad (3)$$

$$\frac{\partial(\rho \varepsilon)}{\partial t} + \frac{\partial}{\partial x_j} (\rho U_j \varepsilon) = \frac{\partial}{\partial x_j} \left[\left(\mu + \frac{\mu_t}{\sigma_\varepsilon} \right) \frac{\partial \varepsilon}{\partial x_j} \right] + \frac{\varepsilon}{k} (C_{\varepsilon 1} P_k - C_{\varepsilon 2} \rho \varepsilon + C_{\varepsilon 1} P_{\varepsilon b}) \quad (5)$$

2.3 Particle Transport Equation

In the CFD, behavior of sprayed droplets can be calculated by the following Eq. (5) using the Lagrangian method. The forces influencing the behavior of a particle are drag and buoyancy. The following equation represents these forces on a single droplet [5].

$$m_p \frac{dU_p}{dt} = \frac{1}{2} C_D \rho_F A_F |\mathbf{U}_F - \mathbf{U}_P| (\mathbf{U}_F - \mathbf{U}_P) + \frac{\pi}{6} d_p^3 (\rho_P - \rho_F) \mathbf{g} \quad (5)$$

where m_p is mass of a water particle, \mathbf{U}_P is velocity of a water particle, C_D is drag coefficient, ρ_F is density of fluid around a particle, A_F is projection area of a water particle, \mathbf{U}_F is velocity of fluid around a particle, d_p is diameter of a water particle, ρ_P is density of water, and \mathbf{g} is gravity acceleration.

2.4 Droplet Breakup Model

Droplets can be deformed and broken easily because droplets are a kind of fluid. To treat deformation and breakup, mathematical models are needed. The Taylor analogy breakup (TAB) model was proposed by O'Rourke and Amsden to treat deformation of a sprayed droplet mathematically. The TAB model uses a one-dimensional Eq. (6) to derive this fluid particle distortion [6].

$$\ddot{y} = \frac{2\rho_F |\mathbf{U}_F - \mathbf{U}_P|^2}{3\rho_p r^2} - \frac{5\mu_p}{\rho_p r^2} \dot{y} - \frac{8\sigma}{\rho_p r^3} y \quad (6)$$

where μ_p is the viscosity of a droplet, r is the radius of a droplet, and σ is surface tension of a droplet.

Because one particle (a parent particle) can break up into much smaller particles (child droplets), the cascade atomization and breakup (CAB) model was developed from the TAB model and used to determine the size of child droplets. The following CAB equation is used to calculate the size of child droplets after breakup [7].

$$\frac{r_{P, \text{Child}}}{r_{P, \text{Parent}}} = e^{-K_{br} t} \quad (7)$$

where

$$K_{br} = \begin{cases} k_1 \omega \\ k_2 \omega \sqrt{We} \\ k_3 \omega We^{3/4} \end{cases} \quad (8)$$

$$k_3 = k_2 / We_{t2}^{1/4} \quad (9)$$

$$k_2 = k_1 \frac{\sqrt{1 - C_k C_b / 2 C_f We_t}}{a \cos(1 - C_k C_b / C_f We_t)} \quad (10)$$

2.5 Collection Efficiency

In this study, a key consideration is the collection of solid particles. Therefore, it is required to model the capture of particles. There are three mechanisms to capture solid particles when using droplets: diffusion, interception, and impaction. If the size of a solid particle is larger than 5.0 μm , the effect of diffusion and interception can be neglected because the dominant mechanism for particle capture is impaction. [8] In this study, it is assumed that dust particles are 10 μm . Therefore, the solid particle collection efficiency of a single droplet can be calculated using the following Eq. (11) for the process of impaction proposed by Calvert [9].

$$\eta_s = \left(\frac{\psi}{\psi + 0.7} \right)^2 \quad (11)$$

where ψ is an inertial impaction parameter defined by Eq. (12).

$$\psi = \frac{\rho_p d_s^2 |\mathbf{U}_F - \mathbf{U}_P|}{9\mu d_p} \quad (12)$$

where d_s is the diameter of a solid particle and μ is the viscosity of the fluid around that particle.

A single droplet can capture multiple solid particles. This relationship can be calculated by the following Eq. (13).

$$N_c = \eta_s \frac{\pi d_p^2}{4} |\mathbf{U}_S - \mathbf{U}_P| \frac{N_s}{dV} \quad (13)$$

where U_s is the velocity of a solid particle, N_s is the number of solid particles, and dV is the element volume.

Particle source term was modeled using the above Eqs. (11), (12), and (13) to simulate the quantity of solid particles captured. And the total collection efficiency was calculated using the following Eq. (14).

$$\eta_{\text{total}} = 1 - \frac{\dot{m}_{\text{out,solid}}}{\dot{m}_{\text{in,solid}}} \quad (14)$$

where $\dot{m}_{\text{out,solid}}$ is mass flow rate to leave the domain and $\dot{m}_{\text{in,solid}}$ is mass flow rate of inflow into the domain.

3 Numerical Simulation

3.1 Flow State

To consider the effect of turbulence, the widely used k- ϵ model was selected. This analysis was performed on an incompressible flow at steady state. Air and water properties were assumed to be constant at 25 °C. By coupling the Eulerian and Lagrangian approaches, we can analyze three-phase flow. Water particles were analyzed using the Lagrangian approach, while the Eulerian approach was applied to TiO₂ dust and air. While TiO₂ dust was assumed as part of the air-like fluid, the TiO₂ particle diameter was assumed to be 10 μm to solve Eq. (12) and (13).

3.2 Mesh

Figure 1 shows a mesh for this CFD analysis. To construct an unstructured mesh, ICEM CFD, a software program specifically designed to construct meshes, was used. This domain has 2.19 million hexahedron elements and 2.11 million nodes. To efficiently conduct our analysis, a smaller mesh size was used around containment, while a slightly larger mesh size was used in other areas.

3.3 Boundary Conditions

Figure 2 shows the boundary conditions in this simulation. For the inlet boundary, the velocity of air was assumed to be 0.5 m/s. On the outlet boundary, the gauge pressure was set at 0 Pa. On the ground, a no-slip condition was applied and a free-slip wall condition was applied to the side walls because the viscous effect is

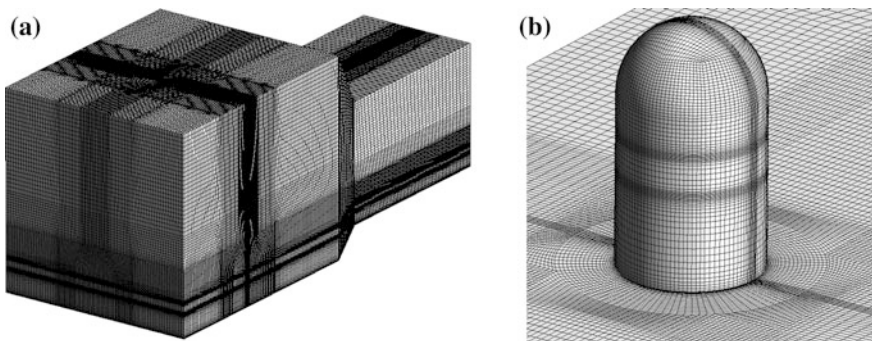


Fig. 1 Mesh for numerical analysis

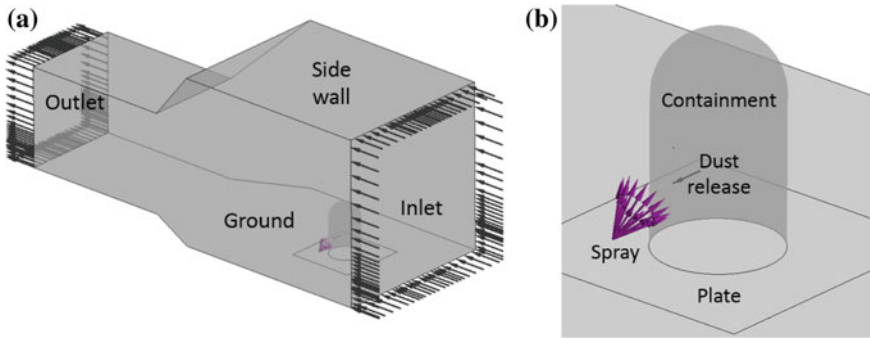


Fig. 2 Boundary conditions

not important on side walls. For the dust release region, it was assumed that dust is released at 0.001 kg/s and release velocity is 10 m/s. To simulate water spray, a particle injection model was used. Nozzle angles from the ground were assumed at 30, 45, and 60°, and spray distances were assumed at 60 and 90 cm from the containment. The water flow rate was set at 6 L/min, and the sprayed angle from the nozzle was assumed at 55° at the spray point. Figure 2b identifies the spray plate. On the plate, all of the water particles can be absorbed. On the containment wall, it is assumed that water particles can lose all of their momentum due to inelastic collisions.

3.4 Convergence Criteria

To decide convergence finish, the RMS residuals and imbalances were considered. If the RMS residuals are lower than 10^{-4} , and if imbalances are lower than 5%, it was assumed that converge was achieved.

4 Results and Discussion

4.1 Dust Removal Efficiency

In a severe accident situation, to minimize damage from radioactive substances, the aerosols have to be captured. Therefore, dust removal efficiency has to be evaluated in this study.

Figure 3 shows the efficiency of TiO_2 removal by water particles in this analysis. At 60 cm from the containment and 30° of nozzle angle, removal efficiency is about

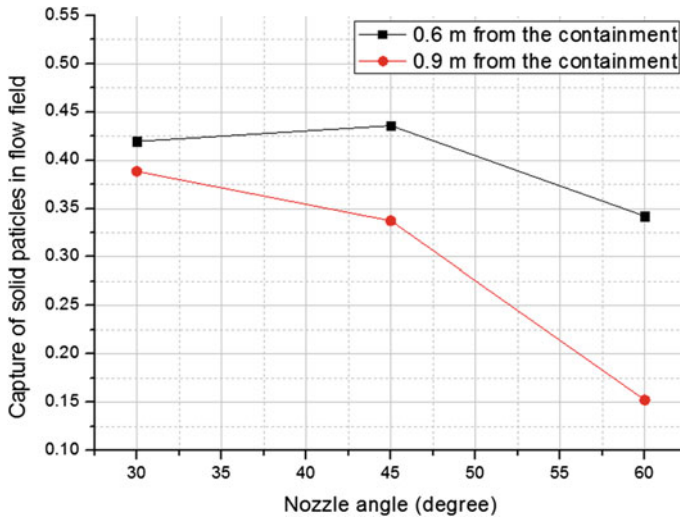


Fig. 3 Capture efficiency of TiO_2 in flow field

40%. And, at 45° of nozzle angle, the efficiency improved to $\sim 44\%$. At 60° of nozzle angle, the efficiency dropped to $\sim 35\%$.

At 90 cm from the containment and 30° of nozzle angle, the result was a little better than the one estimated at 60 cm and 30° . However, the efficiency rapidly decreased with the increase of angle giving much efficiency than at 60 cm. And, at 90 cm and 30° , the efficiency dropped to a value around 15%.

Results indicate that if spray is close to the containment, the removal efficiency is larger in general.

4.2 Collection of Water Particles

If water particles can successfully capture the radioactive materials released, the spray technology can be considered effective. However, if some portion of the particles is dispersed by the wind, it could be said that the technology has failed to perform the mission. Thus, how well water particles are collected by the spray should be analyzed.

Figure 4 shows the collection efficiency of water particles on plate. At 60 cm from the containment, collection efficiencies are little higher than at 90 cm. And collections efficiencies decreased with the increase of angle. This is because many of the water particles go over the top of the containment and are blown by free stream with increase of nozzle angle.

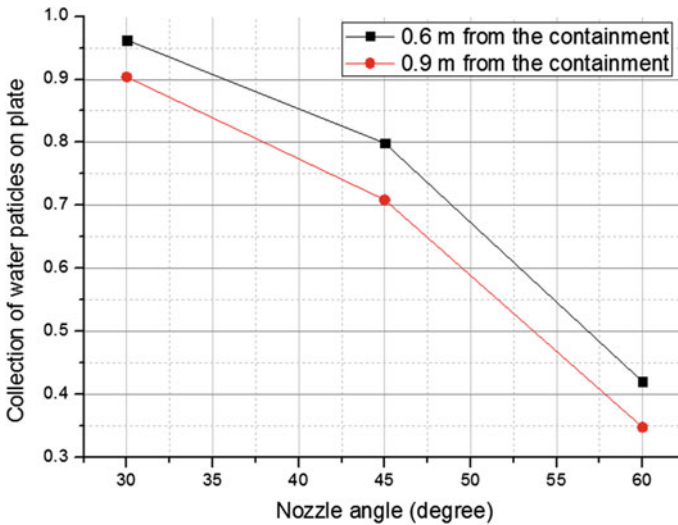


Fig. 4 Collection efficiency of sprayed water particles on plate

5 Summary

In this study, the numerical analysis methodology used in evaluating a venturi scrubber was implemented to evaluate the use of spray technology for capturing contaminants released external to the reactor containment. To support the numerical simulation, ANSYS CFX was selected and the mesh was constructed by ICEM CFD. By using the proposed numerical methodology, the efficiency of dust removal and capturing water particles were calculated and evaluated. Summary of the findings is listed below:

- (1) Capture efficiency of TiO_2 dust by water particles is the highest at 60 cm from the containment and 45° of nozzle angle because many of the points have water particles and TiO_2 dust. Also, the velocity of water particles is higher than other cases.
- (2) Collection efficiency of water particles on plate is the highest at 60 cm from the containment and 30° of nozzle angle. This is because most of the water particles collide the containment surface.
- (3) If the capture efficiency of TiO_2 dust and the collection efficiency of water particles are considered together, the best case is at 60 cm from the containment and 30° of nozzle angle.
- (4) In this study, the numerical modeling, used in analyzing venturi scrubber, was applied for calculating dust removal efficiency in an external flow. The approach seems appropriate to analyze the performance of a spray system installed on a fire engine.

Future work is needed to validate the results based on experimental investigations. Additional evaluations need to be performed to analyze the effect of water film when modeling the behavior of water particles on the wall. Once the validation work is successful, further analysis is needed to optimize the use of spray technology mounted on a specialized fire truck in a severe accident situation.

Acknowledgments This work was supported by the Nuclear Power Core Technology Development of the Korea Institute of Energy Technology Evaluation and Planning (KETEP) under the Ministry of Trade, Industry & Energy, Republic of Korea (No. 20131510400050).

References

1. Ali, M., Yan, C., Sun, Z., Wang, J., & Gu, H. (2013). CFD simulation of dust particle removal efficiency of a venturi scrubber in CFX. *Nuclear Engineering and Design*, 256, 169–177.
2. Pak, S. I., & Chang, K. S. (2006). Performance estimation of a Venturi scrubber using a computational model for capturing dust particles with liquid spray. *Journal of hazardous materials*, 138(3), 560–573.
3. Younus, I., & Yim, M. S. (2015). Out-containment mitigation of gaseous iodine by alkaline spray in severe accident situation. *Progress in Nuclear Energy*, 83, 167–176.
4. Launder, B. E., & Spalding, D. B. (1972). *Lectures in mathematical models of turbulence*.
5. Haider, A., & Levenspiel, O. (1989). Drag coefficient and terminal velocity of spherical and nonspherical particles. *Powder technology*, 58(1), 63–70.
6. O'Rourke, P. J., & Amsden, A. A. (1987). The TAB method for numerical calculation of spray droplet breakup (No. LA-UR-87-2105-Rev.; CONF-871142-1-Rev.). Los Alamos National Lab., NM (USA).
7. Tanner, F. X. (2004). Development and validation of a cascade atomization and drop breakup model for high-velocity dense sprays. *Atomization and sprays*, 14(3).
8. Kim, H. T., Jung, C. H., Oh, S. N., & Lee, K. W. (2001). Particle removal efficiency of gravitational wet scrubber considering diffusion, interception, and impaction. *Environmental Engineering Science*, 18(2), 125–136.
9. Calvert, S. (1970). Venturi and other atomizing scrubbers efficiency and pressure drop. *AICHE journal*, 16(3), 392–396.

Application of Planar Laser-Induced Fluorescence to Measurement of Concentration Field in the Downcomer

Tingjie Zhao, Sichao Tan, Xiaoyu Wang, Yunjia Yang
and Ruiqi Wang

Abstract In recent years, inhomogeneous boron dilution has recently become one of the most important issues in PWR safety. In this paper, planar laser-induced fluorescence (PLIF) was applied to the visualization measurement of concentration distribution of boron in a downcomer channel. An aqueous solution of a fluorescent dye simulated the boron solution. The visual mixing phenomena were recorded by the high-speed camera with high-resolution information. The laser dye used here was rhodamine B(RhB), and the 532-nm laser has eliminated the Gaussian distribution. Intensity distribution was measured by one CCD, and then according to the distribution of intensity, the concentration fields in the downcomer channel can be obtained. The concentration fields under different volume flow rates were discussed. The results show the diffusion process of boron and the concentration distribution of boron, which are important for the study of inhomogeneous boron dilution in the design and research of reactor system. Besides this technique has been specially developed to improve whole-field concentration measurements, which will have the extensive application of nuclear industry.

Keywords Planar laser-induced fluorescence · Downcomer channel · Concentration field · Visualization measurement

T. Zhao (✉) · S. Tan · X. Wang · Y. Yang · R. Wang
Fundamental Science on Nuclear Safety and Simulation Technology Laboratory,
Harbin Engineering University Harbin, Harbin 150001, People's Republic of China
e-mail: zhaotingjie2010@163.com

S. Tan
e-mail: tansichao@hrbeu.edu.cn

X. Wang
e-mail: xiaoyurainer@163.com

1 Introduction

In recent years, mixing phenomenon and mixing degree of coolant inside the reactor coolant system are one of the focuses of experimental study during normal operation or accidents. Adopting passive safety in the nuclear power plant, emergency core cooling system (ECCS), core makeup tank (CMT), and in-containment refueling water storage tank (IRWST) are filled with high boron acid concentration. Boron acid is used to control the reactivity in pressurized water reactors (PWR). In some accidents, the slug water with higher boron concentration would be injected into the downcomer and then mixed with ambient water with lower boron concentration. The mixing of different boron concentrations would change core reactivity and even lead to local boron dilution transients. And therefore, nuclear safety-related issues of mixing are one of the most important focuses.

The current methods of the mixing experimental study mainly include particle tracer technique, electrical conductivity probe technology, and laser-induced fluorescence technique. The particle tracer technique is that the solid particles are added in the fluid and along with the fluid motion [1] and then flow characteristic is studied by analysis of flow track. Although the technique can measure flow field information of fluid mixing, it can only analyze relative magnitudes of concentration and cannot realize the real-time visual observation. The electrical conductivity probe technology is that sodium chloride is used as tracer in the experiment and the concentration distribution is determined by measuring the conductivity with sensors [2]. However, the typical measurement methods are implemented with intrusive devices, which are point measurements, and maybe significantly perturb local velocity and concentration fields. Besides, these methods are limited by time response. So non-intrusive diagnostics is attractive because the inherent ability provides local measurements with minimal perturbation of the flow. LIF technique is attractive for a variety of reasons as described earlier.

LIF technique is used as the non-intrusive experimental techniques to study visual mixing and local concentration distribution [3], temperature fields [4], and liquid film thickness [5] with good spatial and temporal resolution. In this paper, the technique is used in the experiment.

The transport of concentration is determined by the turbulent dispersion and molecular diffusion. Besides, in the experiment as well as in the reactor, the flow is turbulent. At turbulent flow regimes, the turbulent dispersion plays a primary role and the portion of molecular diffusion can be negligible [2]. So it is possible to use a tracer to replace the boron. In the experiment, rhodamine B (RhB) is used to simulate the boron as tracer. The concentration is determined by measuring the fluorescent intensity.

In our study, the target was the experimental investigation of the mixing and the concentration distribution on the way where high concentration of boron injected the vertical downcomer channel from the horizontal inlet lines in a systematic way.

2 Principles of LIF Technique

LIF is a technique of measurements and has the advantage properties such as whole field, indirect, and non-intrusive. The method has been successfully applied to the full fields of concentration distribution. Many scholars at home and abroad have also gradually carried out research.

The fluid was measured by adding RhB under the 532-nm laser with appropriate wavelength, and then the fluorescence with special intensity was emitted. The main principle of LIF is shown as Eq. 1, and detail was described by Lemoine [6].

$$I = K_{\text{opt}} V_c I_0 \Phi \varepsilon_1 C e^{-C(\varepsilon_1 b + \varepsilon_2 e)} \quad (1)$$

As is shown from Eq. 1, K_{opt} is an optical calibration constant, V_c is the collection volume, and I_0 is the incident intensity of the laser beam. ε_2 is the molar extinction coefficient of the fluorescence signal, which is much lower than the coefficient ε_1 [6]. C is the dye concentration, and Φ is quantum yield of dye which changes with pH and temperature [6, 7].

The expression for the fluorescence intensity has considered the attenuation of the incident laser beam intensity. When the laser passes through the distance b , laser intensity has been absorbed. Besides, fluorescence emission is attenuated while passing along the distance e in the aqueous solution (see Fig. 1).

However, if the term $C(\varepsilon_1 b + \varepsilon_2 e)$ is weak enough, the influence of Beer's absorption on the laser beam path can be ignored. In other words, the concentration is low enough and the path is very short; therefore, the fluorescence intensity is directly proportional to the concentration as other parameters keeping constant or known [7]. Equation 1 can be simplified as:

$$I = K_{\text{opt}} V_c I_0 \varepsilon_1 C \Phi(T, pH) \quad (2)$$

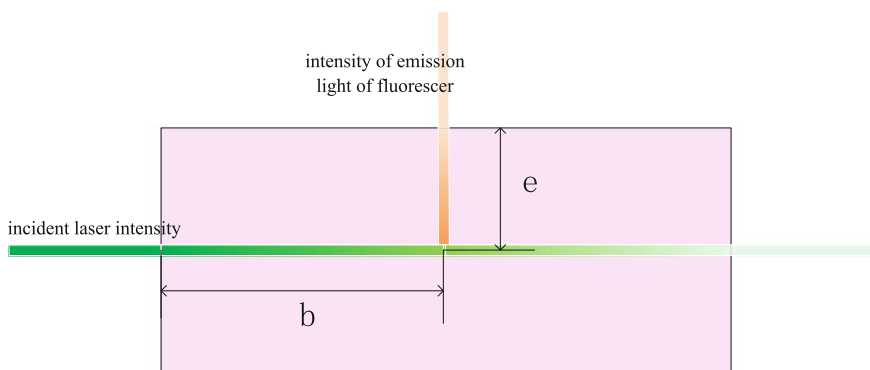


Fig. 1 The process of emitting fluorescence

Besides, the molecular transition time and the lifetime of the excited state are very short, generally less than 10^{-9} s [8]. Therefore, the fluorescence technique is able to trace the change of concentration, temperature, and pH. So the technique can be used to measure the concentration in the downcomer.

3 Experimental Container and System

The experimental system includes a circulating water tank, a circulating pump, a flowmeter, a pressure gauge, a thermometer, a dye tank, a peristaltic pump, annular channel of experimental section, and the corresponding connection pipe and some valves, and so on at normal atmospheric pressure. The experimental system is shown in Fig. 2. The open loop was used in the experiment, and fluid mixed with dyes flowed into the liquid waste receiver tank. The top of experiment container set up two exhaust valve in order to exclude non-condensable gas. The water in the tank was driven by a circulating pump and flowed through the return valve, bypass valve, and flowmeter into the experimental section of the annular channel. Circulation flow rate was controlled by bypass valve opening. Flow condition of the system was monitored through the flowmeter, thermometer, and pressure gauge. The dyes in the liquid tank, driven by the peristaltic pump, flowed through an internal injection syringe in the shape of L into the experimental section. And vertical view of experiment container is shown in Fig. 3, which is processed by organic glass. Diameter of outer ring is 14 cm, while diameter of inner ring is 12 cm. The downcomer gap is 1 cm. Besides, the outside hexagonal prism is to reduce and even eliminate the influence of the refractive index changes in optical path.

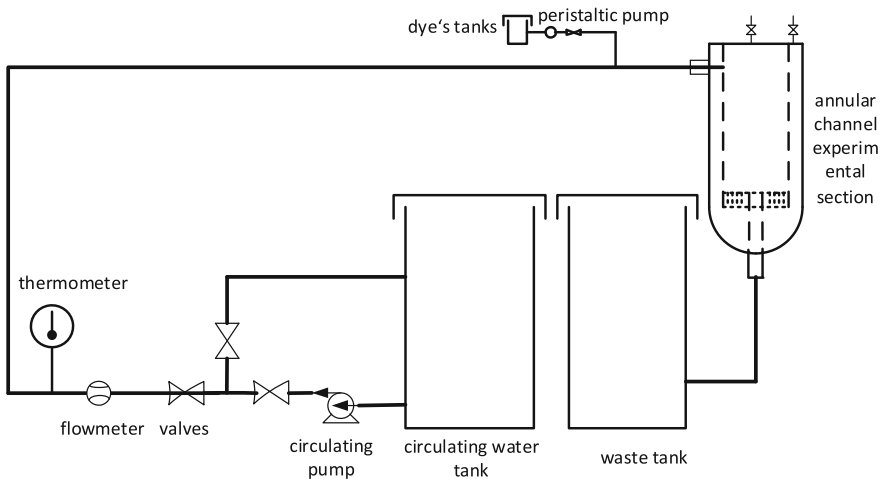


Fig. 2 The experimental system

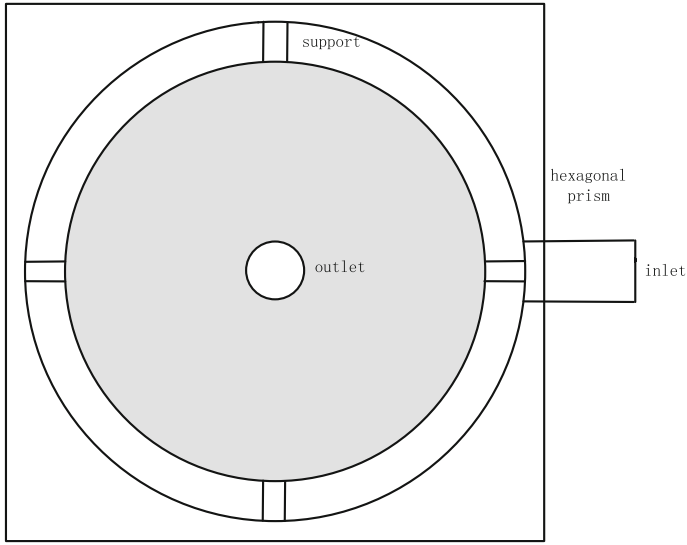


Fig. 3 The vertical view of test container

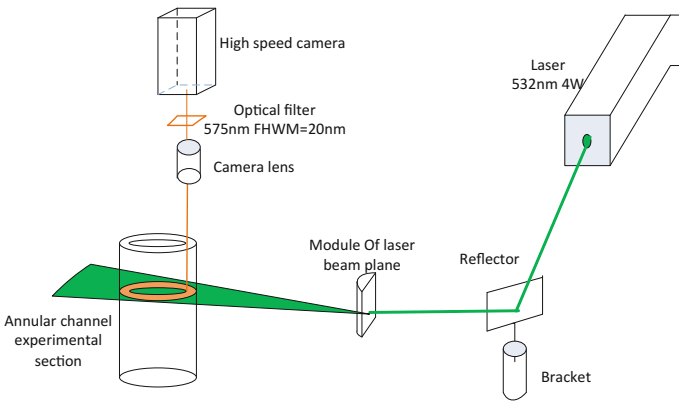


Fig. 4 Schematic diagram of optical system

Schematic diagram of optical system is shown in Fig. 4. As the experimental section, 532-nm laser beam travels through the optical module into a laser beam plane in the interface studied. RhB in the liquid was excited, and the fluorescence with emission spectra peak of 580 nm was emitted [9]. And then high-speed camera was utilized to shoot the intensity distribution of dye after entering into the annular channel, in order to conduct visualization research of dye concentration fields. The picture was processed in accordance with the corresponding relation between fluorescence intensity and dye concentration, dye concentration distribution of

different velocities was acquired, and characteristics of mixing were conducted consequently. The mixed fluid of outlet flows into liquid waste receiver tank, without recycle.

4 Results and Discussion

4.1 *Experimental Phenomenon*

In analysis of experimental data, the factors influencing dye's concentration distribution are mainly the position of dye's injection, inlet velocity, and density contrast between injecting flow and the liquid of annular channel. In this paper, concentration distribution was studied under different inlet velocities over time. The downcomer was filled with deionized water at the initial condition of the experiment.

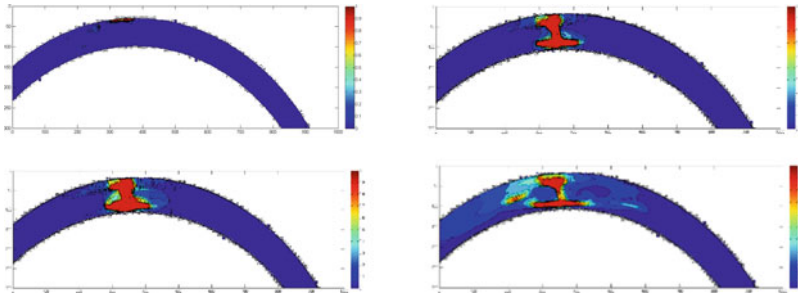
Because of the random characteristics of turbulent flow, the contour map of the instantaneous concentration can only reflect the particular distribution characteristics. In order to obtain more complete concentration distribution information and reflect the changes of concentration field over time, images of continuous shooting 100 frames were superimposed and then the concentration distribution of homogenization processing for the time was obtained. At last, concentration distribution was normalized processing. The results showed that dye's distribution contours are smooth and can reflect dye's distribution rule from statistical characterization in Fig. 5.

The results were described below as the time evolution after fluid mixed with the dye injected into circular downcomer. At the beginning, the slug passed through the downcomer gap and then impinged on the in wall and started spreading around the cylindrical torus. As we can see from the pictures above, the flow tilted to the right injected into the annular downcomer, and the direction of jet momentum tilted to the right direction mainly. So dyes spread more quickly in the right direction, while dyes spread more slowly on the left side. However, the dyes concentration gradually spread and tend to be more uniform over time.

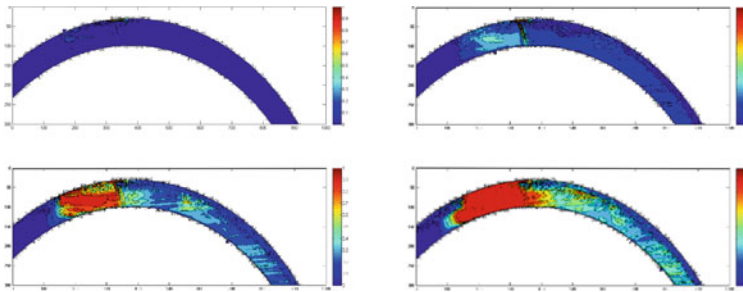
The experimental results under different velocities are compared in Fig. 5. The results showed that the higher the velocity is, the more quickly the dye's concentration mixes to an intermediate concentration level at the same time. Several radial streaks are also visible in the mixing region. When velocity is very small, mixing action of liquid is weak, and dye's diffusion phenomenon is not obvious. With the increase in velocity, diffusion phenomenon is more obvious.

4.2 *Coefficient of Variation*

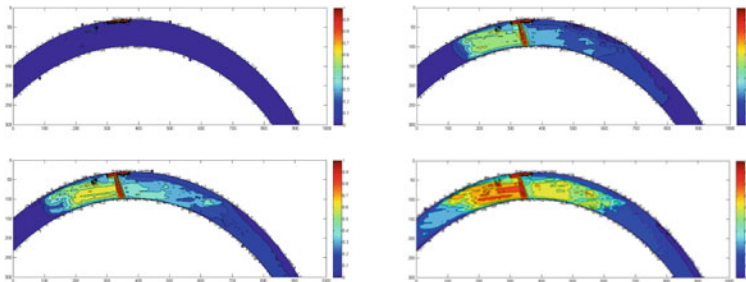
The coefficient of variation was used in the process of images' analysis. Coefficient of vibration was used to analyze PLIF picture in this paper. If measurement scale



(a) low velocity (the four pictures are respectively the temporal average concentration of 1~100f, 1000~1100f, 2000~2100f, 3000~3100f)



(b) medium velocity (the four pictures are respectively the temporal average concentration of 1~100f, 1000~1100f, 2000~2100f, 3000~3100f)



(c) high velocity (the four pictures are respectively the temporal average concentration of 1~100f, 1000~1100f, 2000~2100f, 3000~3100f)

Fig. 5 Evolution of concentration distribution with time under different velocities

between two sets of data is big or data dimension between two sets of data is different, it is not appropriate to use standard deviation to compare directly. Coefficient of vibration was adopted to compare the discrete degree of experimental data, in order to eliminate the influence of measurement scale and dimension. In this experiment, concentration distribution caused by diffusion varies greatly at different time, so coefficient of vibration was applied to compare the degree of concentration mixing. The definition is

$$COV = \frac{\sqrt{\frac{1}{n-1} \sum_{i,j} [C(x_i, y_j) - \frac{1}{n} \sum_{i,j} C(x_i, y_j)]^2}}{\frac{1}{n} \sum_{i,j} C(x_i, y_j)}$$

In the formula, x_i, y_j represents the information of pixel dot in the positioning system. $C(x_i, y_j)$ represents the concentration of the position (x_i, y_j) . According to the definition of coefficient of vibration, a lower COV value represents a more uniform distribution of dye concentration, that is to say the flow is mixed at a higher extent [10].

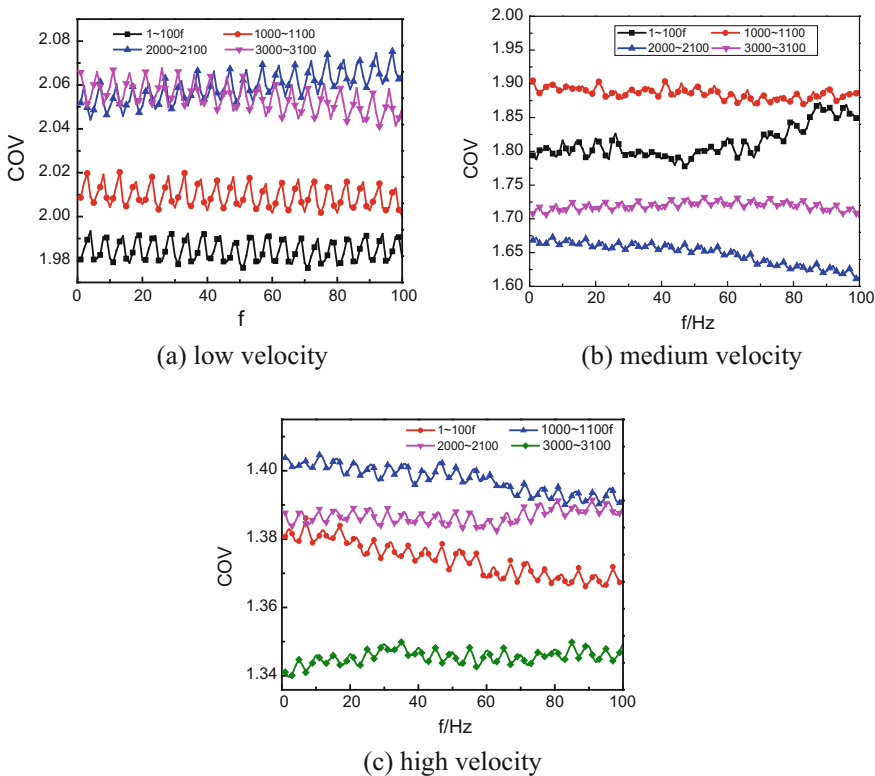


Fig. 6 The changes of coefficient of variation under different velocities

In data processing, in order to compare concentration distribution under different velocities, every 1000 frames of image segmentation are divided and then the last 100 frames of each segment are analyzed by coefficient of variation analysis. The results of concentration distribution are shown in Fig. 5 at different time.

The results are shown in Fig. 6. Coefficient of variation is in the range of 1.97–2.09 and the average of 1.99 under low velocity, while it is in the range of 1.60–1.95 and the average of 1.69 under medium velocity. Under high velocity, coefficient of variation is in the range of 1.33–1.45 and the average of 1.36. The results above show that the higher the velocity is, the larger the coefficient of variation and the more uniform the concentration distribution. This presents the higher the velocity, the more uniform the fluid mixes [11], which indicates that application of PLIF technique to measurement of concentration fields in the downcomer channel is feasible and effective.

5 Conclusions

In the study, rhodamine B is used to simulate boron in the experiment. The concentration is determined by measuring the fluorescent intensity. Planar laser-induced fluorescence was applied to the visualization measurement of concentration distribution of boron in the downcomer channel. In the experiment, fluorescence images were normalized and homogenized for the time. With the help of the method above, concentration distribution can be measured quantitatively. The paper also discussed the concentration fields under different velocities. The results showed that the greater the velocity is, the more quickly the dye's concentration mixed to an intermediate concentration level at the same time. Besides, the coefficient of variation was introduced to the quantitative description of concentration, and the distribution was simply analyzed. This technique has been specially developed to improve whole-field concentration measurements, which will have the extensive application to nuclear industry.

References

1. Zhang W, Wang Y, Xu Z, et al. Application of Particle Image Velocimetry to Measurement of Poiseuille Flow and Flow around a Circular Cylinder [J]. *Journal of Xian Jiaotong University*, 2002, 36(3):246–251.
2. U. Rohde, S. Kliem, T. Höhne, R. Karlsson, B. Hemström, J. Lillington, et al., "Fluid mixing and flow distribution in the reactor circuit, measurement data base," *Nuclear Engineering & Design*, vol. 235, pp. 421–443, 2005.
3. KOCHESFAHANI, M.M., and DIMOTAKIS, P.E.: Laser-induced fluorescence measurements of mixed fluid concentration in a liquid plane shear layer. *AIAA Journal*, 1985. 23(11): p. 1700–1707.

4. ROBINSON, G.A., LUCHT, R.P., and LAURENDEAU, N.M.: Two-color planar laser-induced fluorescence thermometry in aqueous solutions. Vol. 47. 2008: Optical Society of America. 2852.
5. CHERDANTSEV, A.V., HANN, D.B., and AZZOPARDI, B.J.: Study of gas-sheared liquid film in horizontal rectangular duct using high-speed LIF technique: Three-dimensional wavy structure and its relation to liquid entrainment. *International Journal of Multiphase Flow*, 2014. 67(0): p. 52–64.
6. Lemoine, F. M. Wolff and M. Lebouche, Simultaneous concentration and velocity measurements using combined laser-induced fluorescence and laser Doppler velocimetry: Application to turbulent transport. *Experiments in Fluids*, 1996. 20(5): p. 319–327.
7. Lavieille P, L.F.L.G., Temperature measurements on droplets in monodisperse stream using laser-induced fluorescence. *Experiments in Fluids*, 2000. 29: p. 429–437.
8. Lemoine, F. M. Wolff and M. Lebouche, Simultaneous concentration and velocity measurements using combined laser-induced fluorescence and laser Doppler velocimetry: Application to turbulent transport. *Experiments in Fluids*, 1996. 20(5): p. 319–327.
9. Tan, Sichao, et al. “Experimental Study of Temperature Sensitive Dyes for Planar Laser Induced Fluorescence Thermometer.” 18th International Conference on Nuclear Engineering American Society of Mechanical Engineers, 2010:343–347.
10. Gandhi V, Roberts P J, Stoesser T, et al. UV reactor flow visualization and mixing quantification using three-dimensional laser-induced fluorescence [J]. *Water research*, 2011, 45(13):3855–3862.
11. Lin K L, Rong shan B I, Tan X S, et al. Using PLIF Technology to Study the Turbulent Mixing Characteristic in a Liquid-Liquid Ejector [J]. *Journal of Chemical Engineering of Chinese Universities*, 2009, 23(1):28–33.

Assessing the Conservatism in EPZ Determined on Plume Centerline Dose: A CALPUFF-Based Method Used in Level 3 PSA

Weipeng Shu, Yawei Mao and Wei Liu

Abstract Emergency preparedness is the final level of the defense in depth in nuclear safety. Emergency planning zone (EPZ), the basis for emergency preparedness, is usually determined based on centerline doses, with the hypothetical individual located directly under plume path throughout the exposure. This conservative assumption with no credit taken for wind shifts could overestimate projected doses and accordingly provide a margin in EPZ. However, over-conservatism does no good to emergency preparedness, but brings in unnecessary fear among the public. To assess the conservatism in plume EPZ determined on centerline doses, we propose here a best estimate approach based on CALPUFF dispersion model to account for wind shifts in Level 3 probability safety assessment (PSA). Doses from CALPUFF-based method in real atmospheric conditions are then compared in detail with centerline doses from PAVAN and MACCS, on a case-by-case basis. Results of this study demonstrate that neglect of wind shifts in dose assessment could result in unrealistic Level 3 PSA results and significant conservatism in plume EPZ, especially when wind direction changes frequently. These results highlight the importance of characterizing real atmospheric conditions and treating wind shift in dose assessment for dividing plume EPZ. Despite its preliminary nature, this study makes an interesting attempt to integrate a realistic assessment of offsite consequences in nuclear emergency planning and preparedness, which could benefit to develop a reasonable conservative emergency plan to better protect the public from radiological releases, and contribute to building public trust in nuclear safety.

W. Shu

Department of Engineering Physics, Tsinghua University, Beijing, China

W. Shu (✉) · Y. Mao · W. Liu

China Nuclear Power Engineering Co., Ltd., Beijing, China

e-mail: shuwp14@mails.tsinghua.edu.cn

© Springer Science+Business Media Singapore 2017

H. Jiang (ed.), *Proceedings of The 20th Pacific Basin Nuclear Conference*,

DOI 10.1007/978-981-10-2314-9_64

Keywords CALPUFF · Level 3 PSA · Emergency planning zone · Dose · Centerline

1 Introduction

Following the lessons learned from the Fukushima accident, there has been increasing concern about Level 3 probability safety assessment (PSA). Based on upstream Level 1 and Level 2 PSAs, Level 3 PSA quantifies the offsite consequences arising from nuclear accidents, in terms of radiological doses, health effects, and economic costs, which could be applied in site selection, dividing the emergency planning zone (EPZ) of a nuclear power plant (NPP), etc. The concept of EPZ was introduced by NUREG-0396 report [1] as a vital basis for emergency preparedness and response (EPR), which is the final level of defense in depth for nuclear safety. Thus, to better protect public health and safety from radiological releases in nuclear accidents, EPZ size should be properly determined.

EPZ is usually determined by comparing the projected doses arising from postulated radiological releases to generic intervention levels (GILs) and dose thresholds, by deterministic safety analysis (DSA) and (or) PSA. In reality, wind direction may change over time during the exposure (e.g., 2 days, 7 days). Therefore, an individual would be exposed to radiation (considering the dominant dose pathways during emergency phase–inhalation) only when located downwind the radiological release site following accidental releases. However, projected doses used to determine EPZ are centerline doses, which are evaluated using straight-line Gaussian plume model (with no credit taken for real atmospheric conditions such as wind shifts). This unrealistic assumption, indicating that the hypothetical individual is always located under the path of the plume and exposed to the Gaussian peak of the air concentrations throughout the exposure, overestimates the dose levels and consequently results in conservative EPZ.

However, as was pointed out in a report by The American Society of Mechanical Engineers (ASME), unduly conservative Level 3 PSA and EPZ “could result in unwarranted actions that poorly serve radiological protection of people” and “unfounded fear” [2]. US Nuclear Regulatory Commission (NRC) Regulatory Guide 1.145 also stated briefly the rationale for considering the dynamic change in wind direction in offsite radiological consequence assessment [3]. Nevertheless, it still remains unclear how significant the aforementioned conservatism in Level 3 PSA and EPZ would be, and whether they are reasonable in state-of-the-art of EPR. Thus we propose here a CALPUFF-based method to account for real atmospheric conditions (e.g., wind shifts) in Level 3 PSA and conduct comparisons between the doses from CALPUFF-based method and PAVAN or MACCS. In short, the aim of

this preliminary study is to assess the conservatism incorporated in the use of plume centerline doses to determine plume EPZ.

2 Methods

2.1 General Approach

To assess the margin and conservatism in Level 3 PSA results and corresponding EPZ resulted from failing to consider wind shifts in dose assessment, comparisons were conducted between centerline doses from MACCS or PAVAN, and more realistic gridded doses from CALPUFF-based method, on a case-by-case basis (see Fig. 1).

H site where wind direction changes frequently as shown in Fig. 2 was chosen to perform a complete case study. In addition, a complementary case study was performed for F site, where wind direction is relatively constant during the exposure. Wind rose diagrams for H and F sites are shown in Fig. 3.

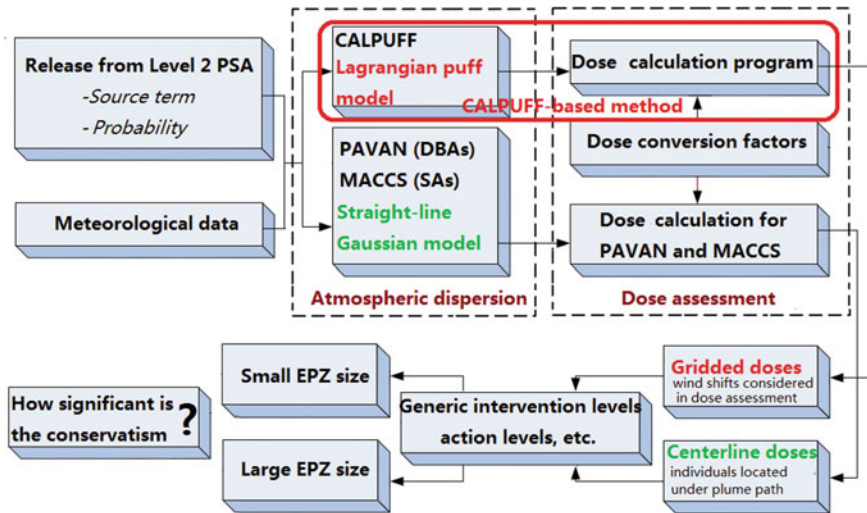


Fig. 1 Flowchart depicting the general approach of the present study

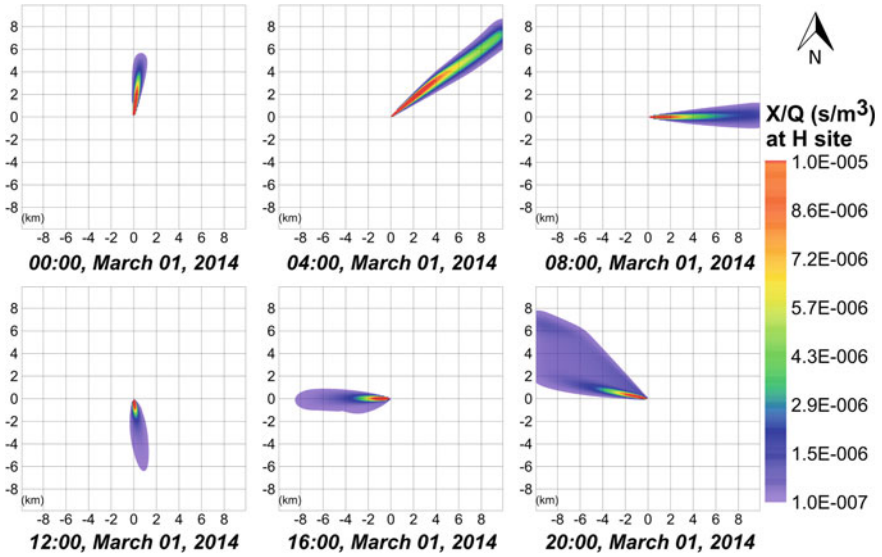


Fig. 2 Hourly averaged ground-level relative concentration at H site

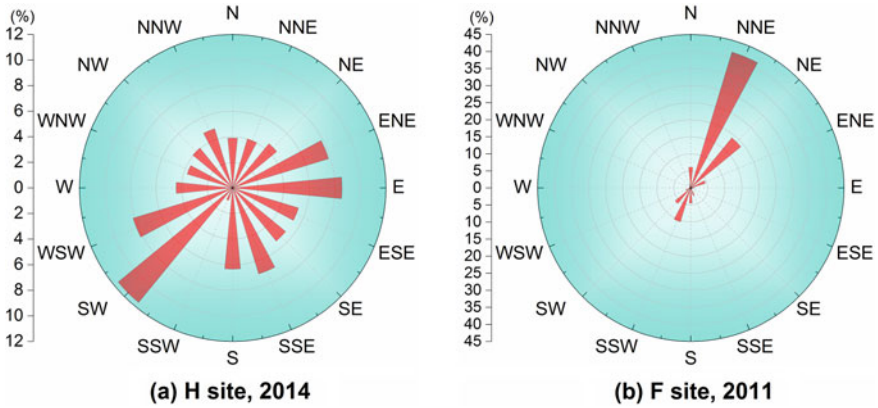


Fig. 3 Wind rose diagrams for H site and F site

2.2 Model Description

2.2.1 PAVAN and MACCS

PAVAN was developed by Pacific Northwest Laboratory (PNL) and is used by NRC to estimate the air and ground-level concentrations for evaluating the consequences of design basis accidents (DBAs) for NPPs. MACCS was developed by

Sandia National Laboratories (SNL) to evaluate the consequences (e.g., radiological doses, health effects, economic consequences) following severe accidents (SAs) at NPPs. These two codes were used in this study to estimate centerline doses arising from DBAs and SAs respectively, based on straight-line Gaussian plume model.

2.2.2 CALPUFF-Based Method

A realistic method based on CALPUFF dispersion model and a dose assessment program was developed in this study to provide the best estimate of projected doses arising from accidental radiological releases in the vicinity of a NPP.

CALPUFF is a Lagrangian puff model which is approved by the US Environmental Protection Agency as a guideline model. Many features (e.g., dry/wet deposition and plume rise) are integrated in CALPUFF. It is worth underlining that CALPUFF provides more realistic dispersion results in rapidly time- and space-varying atmospheric conditions, than do PAVAN and MACCS. To the best of our knowledge, although no attempts have been made to use CALPUFF in offsite dose assessment, some studies have proved CALPUFF to be feasible in nuclear field [4–6].

For each site, a quadrilateral mesh with a 0.1-km cell size was constructed in the $20 \times 20 \text{ km}^2$ region around the release site. Based on the site-specific information and meteorological data, hourly average X/Q values and deposition fluxes for each selected node in the mesh were calculated by CALPUFF and inputted into a gridded dose assessment program. Based on data obtained from CALPUFF, source terms and dose conversion factors (DCFs), this program then calculated the gridded fields of projected doses for the various exposure ways, assumed no protective actions taken. General ideas for dose calculations of the three pathways—cloudshine, groundshine, and inhalation—are similar with those in other researches [7]. Yet a major simplification was employed in decay and ingrowth simulation, where the parent radionuclides' contribution to their daughter nuclides was not included in dose calculations. This may lead to underestimation of dose levels.

2.2.3 Dose Sorting

Centerline doses from PAVAN or MACCS and realistic gridded doses from CALPUFF-based method are sorted in different ways.

For PAVAN and MACCS, centerline X/Q values were calculated based on the yearly meteorological data and then ordered from greatest to smallest to obtain the X/Q values at a certain percentile level (for example the 95th percentile X/Q is defined as the X/Q value exceeded 5% of the total number of sequences in the dataset). Centerline doses assuming certain percentile meteorology were then calculated using the same percentile X/Q values. It should be noted there is only one dose sample for each weather sequence at a certain distance, due to the use of straight-line Gaussian plume model (depicted in Fig. 4a).

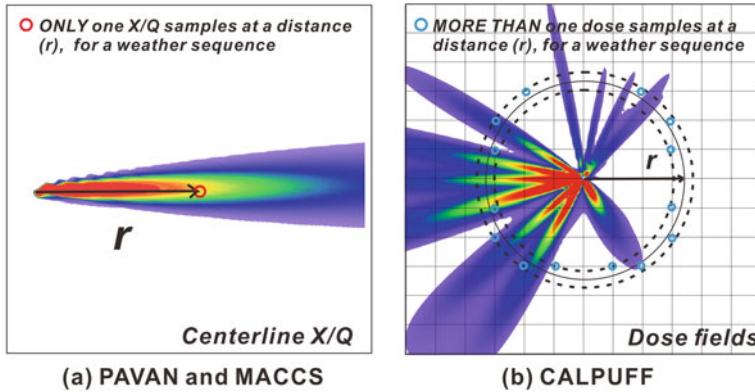


Fig. 4 X/Q (PAVAN and MACCS) and dose (CALPUFF-based method) at a certain distance for a weather sequence

While for CALPUFF-based method, the object to be sorted was a dose but not a X/Q value. Firstly, doses based on real meteorological conditions were calculated for each node in the mesh constructed around the NPP, at 6-h intervals (corresponding to 1460 weather sequences conducted in a year). Then, for each type of dose and each distance (r), the dose values for all the nodes inside a specified distance ring (depicted in Fig. 4b) from 1460 trials were combined together and ordered from greatest to smallest to obtain the dose at a certain percentile level. This sorting method accounts for the impacts of wind shift in dose assessment, by including doses at different angular locations.

2.2.4 Generic Intervention Levels and Action Levels

As for GILs and dose thresholds used for determining plume EPZ, this paper adopted general optimization intervention levels for emergency protective action (hereinafter GILs) and dose action levels for expected interventions in any situation in GB 18871—2002 [8].

3 Results

3.1 Design Basis Accidents

For H site, large break loss-of-coolant accident (LB-LOCA)—the severest DBA of AP1000—was analyzed. Figure 5 plots 95th percentile effective and thyroid doses in 7 days versus distance, obtained from CALPUFF-based method and PAVAN respectively. For both of the effective dose and thyroid dose case, PAVAN results

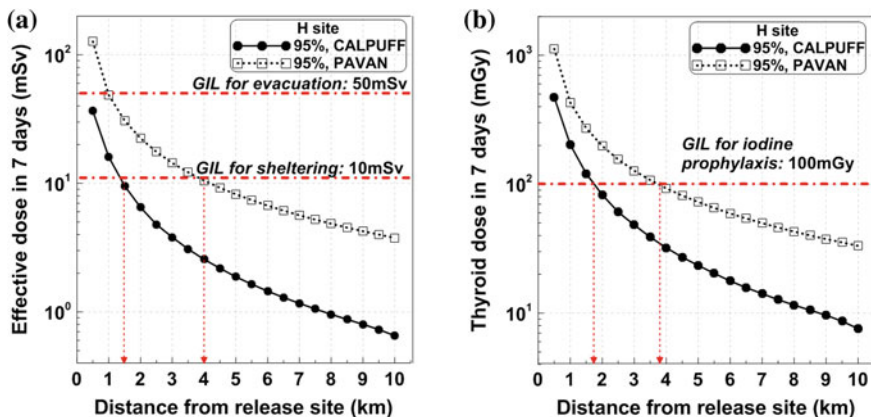


Fig. 5 95th percentile effective dose and thyroid dose in 7 days from LB-LOCA of AP1000 versus distance, at H site

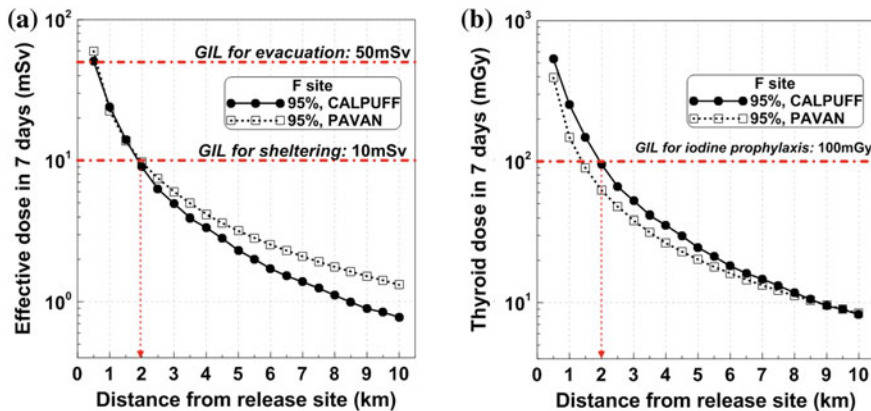


Fig. 6 95th percentile effective dose and thyroid dose in 7 days from DBALOCA of M310 versus distance, at F site

are approximately 3 to 5 times as great as CALPUFF results, at different distances. For PAVAN, as is seen in the figure, 7-day effective dose above 10 mSv and 7-day thyroid dose above 100 mGy are unlikely to occur beyond 4-km distance. For CALPUFF-based method, the critical distance of 7-day effective dose exceeding 10 mSv and 7-day thyroid dose exceeding 100 mGy is 2 km. Therefore, an outer zone of 2 km (CALPUFF) or 4 km (PAVAN) could meet the technical criteria on plume EPZ for NPPs.

Regarding F site, Fig. 6 plots the datasets of the same pattern as for H site, except that DBALOCA of M310 is chosen as the representative DBA. Different from H site, CALPUFF and PAVAN results for F site stay almost the same at various distances, resulting in a same outer plume EPZ size of 2 km.

The discrepancy between H and F sites could be interpreted by the difference in wind direction. Rapidly change in wind direction is common at H site (see Fig. 2), thus individual doses at locations other than directly under the plumes would be significantly smaller than centerline doses (referring to PAVAN). As for F site, wind direction is usually constant during the exposure period (2 days or 7 days). Therefore, the radiation doses received by a hypothetical individual located downwind (e.g., northeast to the NPP at F site) from CALPUFF-based method would be close to centerline doses from PAVAN. Besides, high-percentile doses are received by the individuals, which are located downwind the release site, according to the dose-sorting method for CALPUFF. These abovementioned facts are the reasons why 95th percentile doses from CALPUFF-based method are close to those from PAVAN, for F site.

3.2 *Severe Accidents*

With respect to severe accidents, we took H site as an example to analyze the discrepancies in dose and EPZ results between CALPUFF-based method and MACCS. In dividing plume EPZ, projected doses from the most severe accidents are to be compared to the action levels for serious deterministic effects, while most of the severe accidents (i.e., less-severe accidents) are compared to correlative GILs. Six release categories are identified for evaluation of potential offsite doses from AP1000 severe accidental releases, with BP, CFE, CFI, CFL, and CI chosen as worst SAs, while IC the less-severe SA.

3.2.1 *Deterministic Safety Analysis*

Figure 7 are prepared to show the comparisons of 50th percentile acute red bone marrow doses in 2 days from the five worst release categories between CALPUFF and MACCS results. It is seen that the discrepancies between CALPUFF and MACCS results vary with different release categories, stemming from different release fractions and release timings. MACCS doses are approximately 10 to 50 times as great as CALPUFF results. Based on BP release category which led to the highest acute red bone marrow doses, the 1 Gy dose threshold would not be exceeded beyond 4.5 km (from MACCS) or 0.5 km (from CALPUFF-based method).

With regard to acute thyroid doses in 2 days, calculation results show that 50th percentile doses outputted from MACCS are generally hundreds times greater than those from CALPUFF-based method. To show two datasets in a comparable way, 80th percentile doses is in lieu of 50th percentile doses for CALPUFF-based method, to provide plots for acute thyroid dose in Fig. 8. As is seen in the figure, despite at a lower percentile level, MACCS results are still 5 to 50 times greater than CALPUFF results, for the five release categories. On the basis of 80th

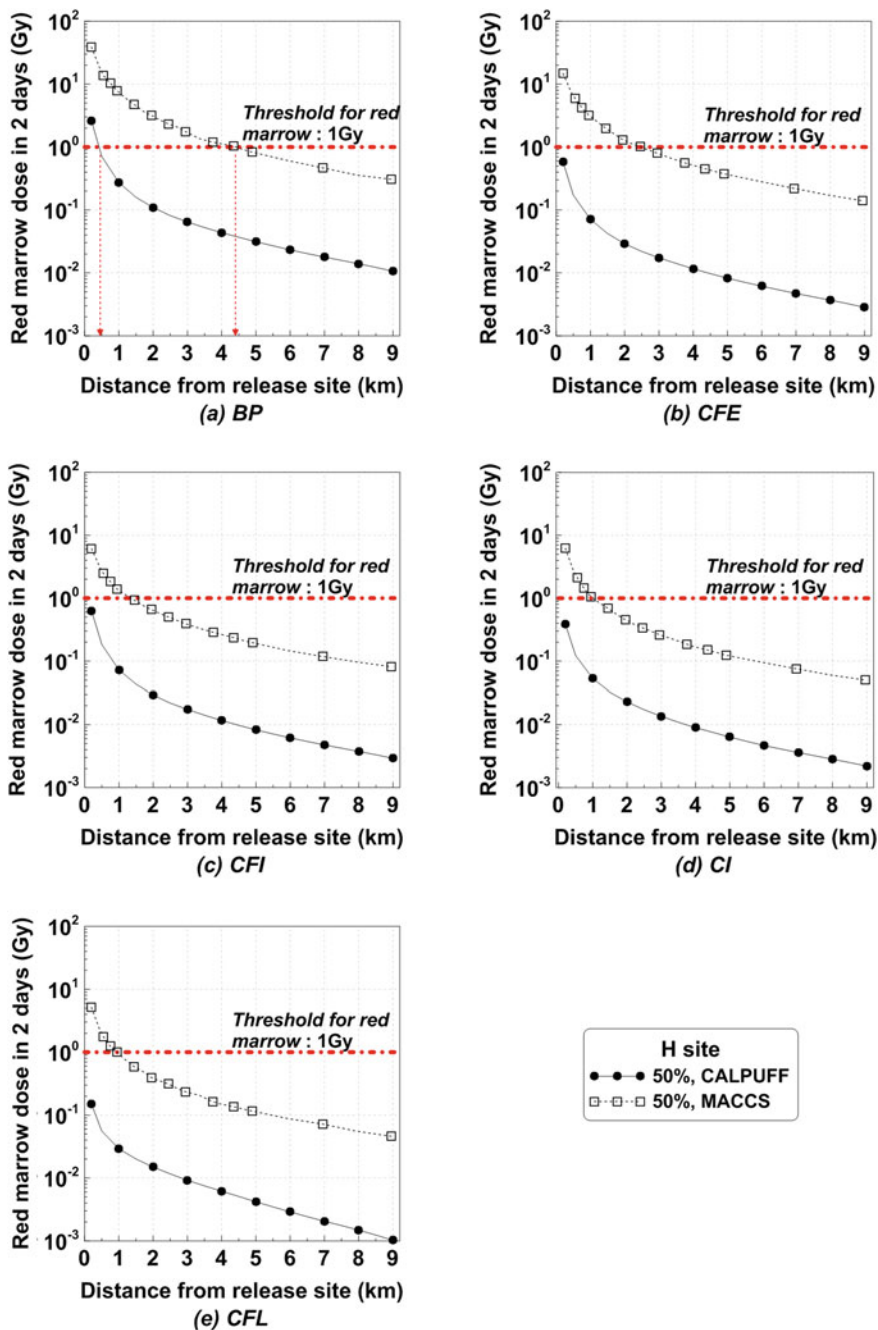


Fig. 7 50th percentile red marrow dose in 2 days from five most severe accidents versus distance, at H site

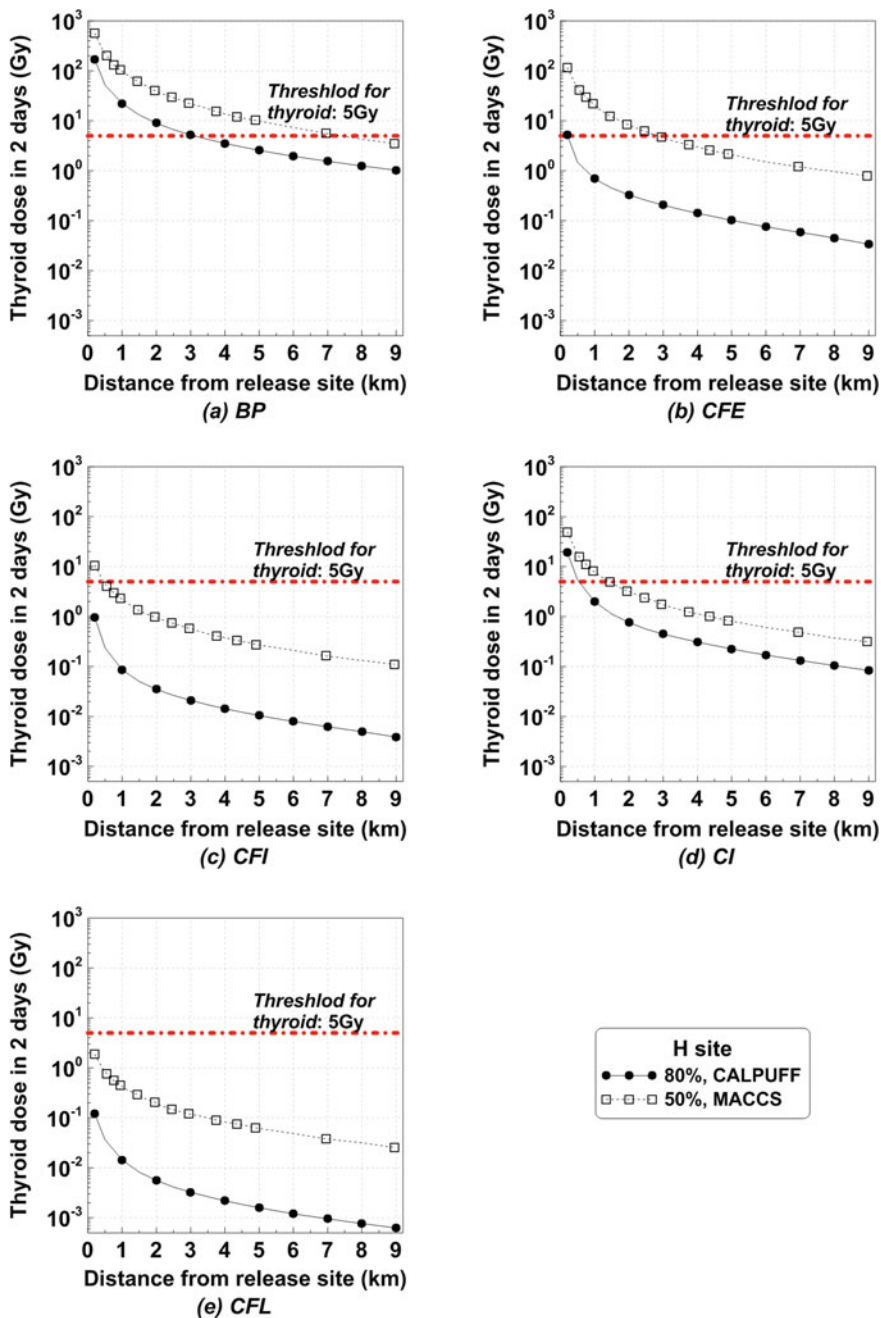
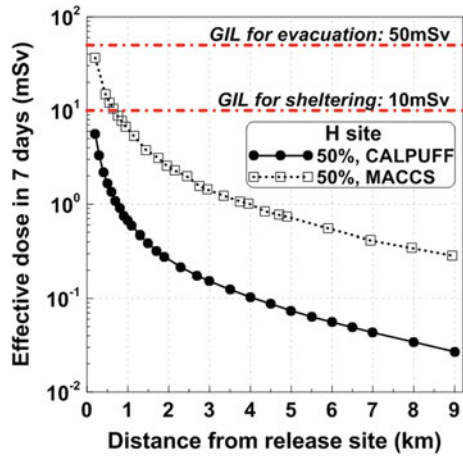


Fig. 8 50th (MACCS) and 80th (CALPUFF) percentile thyroid dose in 2 days from five most severe accidents versus distance, at H site

Fig. 9 50th percentile effective dose in 7 days from the less-severe accident versus distance, at H site



percentile doses from CALPUFF method, the critical distance for 5 Gy threshold would be around 3 km, which is smaller than the distance of 7 km, determined by 50th percentile doses from MACCS calculation.

As for the less-severe accident–IC release category, Fig. 9 provides similar plots as does Fig. 5a. The 50th percentile effective doses in 7 days from MACCS are 6 to 10 times as great as those from CALPUFF-based method. In addition, 50th percentile 7-day effective doses from CALPUFF-based method above 10 mSv are unlikely to occur outside the site boundary.

3.2.2 Probabilistic Safety Assessment

Based on the radiological doses resulting from the six severe accidental release categories, the complementary cumulative distribution function (CCDF) was utilized to analyze the conditional probability of exceeding some critical doses thresholds and GILs.

For the most severe accidents, each dose exceedance probability was calculated by summing up the conditional probabilities of the five release categories by the corresponding probability weighting factors (frequencies). Figure 10 plots the probabilities of the acute red bone marrow dose in 2 days exceeding 1 Gy, and the acute thyroid dose in 2 days exceeding 5 Gy versus distance, obtained from CALPUFF-based method and MACCS. It can be seen in the figure that the probabilities from CALPUFF are about one order of magnitude smaller than those from MACCS code, beyond 2 km.

For the less-severe accident–IC release category, the probabilities of 2-day effective dose exceeding 10 mSv and 7-day thyroid dose exceeding 100 mGy versus distance are plotted in Fig. 11. Exceedance probabilities of both dose types from CALPUFF-based method are seen to drop sharply with distance, and are smaller than those from MACCS.

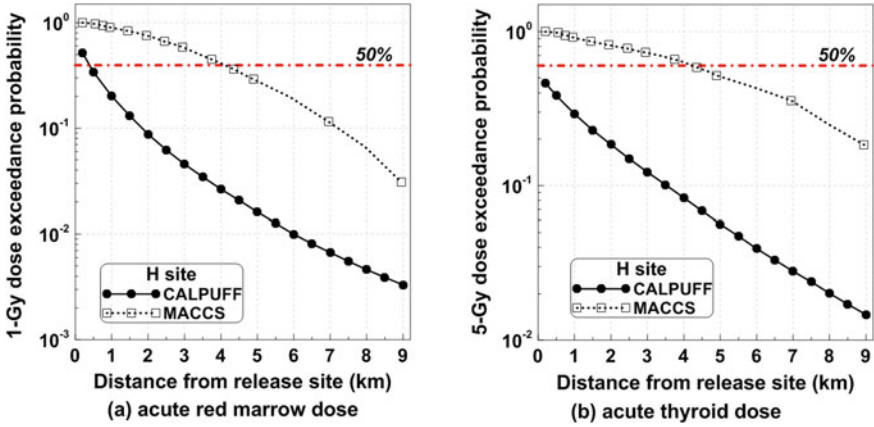


Fig. 10 (a) conditional probability of acute red marrow dose exceeding 1 Gy; (b) conditional probability of acute thyroid dose exceeding 5 Gy versus distance, at H site

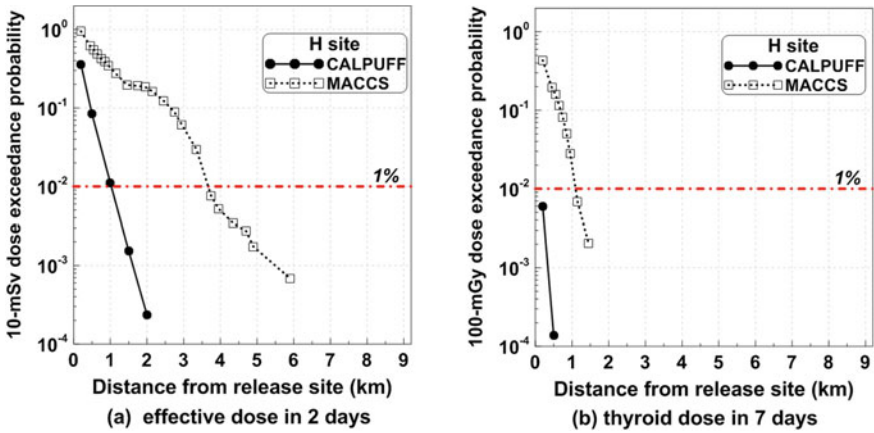


Fig. 11 (a) conditional probability of 2-day effective dose exceeding 10 mSv; (b) conditional probability of 7-day thyroid dose exceeding 100 mGy versus distance, at H site

4 Discussion

Our findings demonstrate that the use of centerline dose could result in overestimated Level 3 PSA results and accordingly provide significant margin and conservatism in plume EPZ, if wind direction changes rapidly during the exposure. In contrast, if wind direction is relatively constant, the use of centerline doses in dividing EPZ would be more acceptable and lead to realistic results. These results highlight the importance of characterizing real atmospheric conditions and treating wind shift in dose assessment for dividing plume EPZ.

It is worth underlining that the present study is not necessarily directed at reducing EPZ size, for there are still many non-technical factors to be considered, which is beyond our scope. We would also like to point out that, sensitivity analysis has not been performed on the simplifications and assumptions (e.g., in dose calculation) employed in this study. Besides, we have not taken a further step to study the case for ingestion–exposure–pathway EPZ yet.

Despite its preliminary nature, this study has made an interesting attempt to conduct a realistic other than conservative assessment of offsite consequences arising from postulated accidents of NPPs, and apply the best estimate of assessment results in emergency planning and preparedness. This realistic evaluation of offsite risks provides a comprehensive perspective in developing a reasonable conservative emergency plan, which is benefit to a better protection of the public from radiological releases, and contributes to build public trust in nuclear safety.

5 Conclusions

This study proposed a best estimate approach to account for wind shifts in Level 3 PSA (dose assessment), by combining CALPUFF dispersion model with a gridded dose assessment program. In summary, this study has proved that the use of centerline doses could result in overestimated Level 3 PSA results, and accordingly provide significant margin and conservatism in plume EPZ, especially for NPPs where wind direction changes frequently. Besides, the importance in characterizing real atmospheric conditions and treating wind shift in dose assessment for dividing plume EPZ is highlighted.

References

1. Collins H E, Grimes B K, Galpin F. Planning basis for the development of state and local government radiological emergency response plans in support of light water nuclear power plants[R]. Nuclear Regulatory Commission, Washington, DC (USA). Office of Nuclear Reactor Regulation; Environmental Protection Agency, Washington, DC (USA). Office of Radiation Programs, 1978.
2. The American Society of Mechanical Engineers. Forging a New Nuclear Safety Construct [EB/OL]. <https://www.asme.org/about-asme/who-we-are/standards/forging-a-new-nuclear-safety-construct>, 27 Jan. 2016.
3. US Nuclear Regulatory Commission. Atmospheric dispersion models for potential accident consequence assessment at nuclear power plants[J]. Regulatory Guide 1.145, 1983.
4. Alfred M K, William G, Mahesh P, Joseph S S. A real-time meteorological analysis and dispersion prediction system for emergency preparedness[R]. Chattanooga, 2003.
5. Chen XQ, Yang DJ. Reverse estimation of accidental release amounts from Fukushima Daiichi Nuclear Power Plant by environmental monitoring data[J]. Journal of Nuclear & Radiochemistry, 2012, 34(2):83–87.

6. Lin HT, Ji YZ, Liu XJ. Impact analysis of nuclear power plant accidents on reservoir using CALPUFF model[J]. Southern Energy Construction, 2015, 2(4):57–61.
7. Huang T, Qu JY, Li H, Cao JZ. Preliminary study on plume emergency planning zone for AP1000[J]. Atomic Energy Science and Technology, 2011, 45(12):1472–1477.
8. GB 18871—2002. Basic standards for protection against ionizing radiation and for the safety of radiation sources[S][D], 2003.

Preparation and Properties of Multifunctional Pt/Ce_{0.7}Zr_{0.3}O₂ Honeycomb Catalyst for Detritiation

Quanwen Wu, Wenhua Luo, Jingwen Ba, Xiayan Yan
and Daqiao Meng

Abstract Detritiation devices are required in tritium system because of its radioactivity. The method of catalytic oxidation and adsorption is widely used for atmosphere detritiation, but cannot be used in glove box detritiation because of the oxygen-lean atmosphere. A Ce-based oxide-loaded honeycomb catalyst is prepared as a multifunctional detritiation catalyst. The properties of Ce-based support and catalyst are characterized by X-ray diffraction (XRD), N₂ adsorption/desorption (Brunauer–Emmet–Teller BET method), and H₂ temperature-programmed reduction (H₂-TPR), and the catalytic performance is tested under both oxygen-rich and oxygen-lean atmospheres. The Pt/Ce_{0.7}Zr_{0.3}O₂ honeycomb catalyst will oxidize hydrogen isotope at room temperature with high space velocity when oxygen is sufficient. When oxygen is deficient, H₂ is also fully oxidized by the catalyst at 250 °C, with the oxygen supply from the support reducing.

Keywords Detritiation · Catalyst · Ce-based oxide · Honeycomb catalyst

1 Introduction

Because of its permeability and radioactivity, tritium must be rigorously fenced in tritium systems [1]. Detritiation devices are required in tritium system; for example, in the inner deuterium/tritium fuel cycle of International Thermonuclear Experimental Reactor (ITER), glove box detritiation system (GDS), vent detritiation system (VDS), and atmosphere detritiation system (ADS) are equipped [2, 3]. The method of catalytic oxidation and adsorption is widely used for atmosphere detritiation, in which tritium is first oxidized by catalysis and then tritiated water vapor is adsorbed by absorbent. But traditional granular catalyst has large gas resistance, which limited the space velocity for detritiation. Honeycomb catalyst can enormously increase the gas handling capacity due to its low pressure drop and

Q. Wu · W. Luo · J. Ba · X. Yan · D. Meng (✉)
China Academy of Engineering Physics, Mianyang, Sichuan, China
e-mail: lwuo123@163.com

high dispersity of active ingredients, but has not been practically used in detritiation so far [3–9]. In GDS, metal getter (Zr_2Fe alloy et al.) and oxidizer (copper oxide and manganese dioxide et al.) are usually used, but it is easily envenomed by gaseous impurity (e.g., oxygen) [10–13]. The method of catalytic oxidation and adsorption is not used in GDS because the glove box is sometimes filled with inert atmosphere. $Ce_{0.7}Zr_{0.3}O_2$ is used as the support of catalyst here because of its function for oxygen storage. So catalyst $Pt/Ce_{0.7}Zr_{0.3}O_2$ can be used in GDS; and when coated on honeycomb substrate, the honeycomb catalyst $Pt/Ce_{0.7}Zr_{0.3}O_2$ -HC is available both in ADS and in GDS. Catalysts $Pt/Ce_{0.7}Zr_{0.3}O_2$ and $Pt/Ce_{0.7}Zr_{0.3}O_2$ -HC are prepared. The properties of carrier and catalytic performance of catalysis are tested, and finally, the cyclical detritiation for tritium container is carried out to verify the feasibility.

2 Materials and Methods

CeO_2 and $Ce_{0.7}Zr_{0.3}O_2$ (signed as CZ here and in the following) are prepared by sol–gel from the precursor of $Ce(NO_3)_3 \cdot 6H_2O$ and $ZrO(NO_3)_2 \cdot H_2O$. And the oxides are tested by BET, XRD, and H_2 -TPR. Pt/CZ is prepared by impregnating using the precursor of $H_2PtCl_6 \cdot 6H_2O$, and the catalytic activities are evaluated by H_2 conversion rate in gas mixture. The catalyst is deposited on the honeycomb substrate of cordierite using ultrasonic technology to prepare honeycomb catalyst Pt/CZ -HC. Catalytic activities of honeycomb catalysts are evaluated by H_2 conversion rate in gas mixture with different H_2 concentrations and various flow rates.

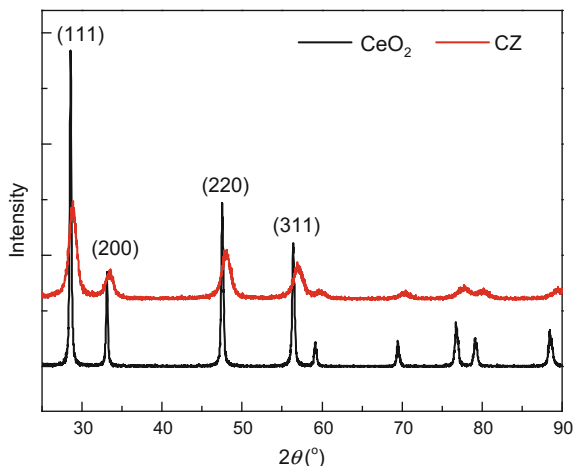
3 Results

The specific surface area of catalyst supports CeO_2 and CZ sintered at 500 °C is 56 m^2/g and 84 m^2/g , respectively, which indicate that Zr conduces to the increase in specific surface area. When sintered at 700 °C, the surface area of CeO_2 declines to about 10 m^2/g , while CZ is still 60 m^2/g , indicating the thermal stability of support is increased by Zr doping. Briefly, the addition of Zr in CeO_2 improves the thermal stability of CeO_2 , and increases the specific surface area, which is beneficial to the dispersal of active element.

Figure 1 is the XRD profile of CeO_2 and CZ. The patterns show the fluorite-type structure of ceria (PDF 00-034-0394). No additional peaks were detected in CZ pattern, which indicates the formation of solid solution CeO_2 - ZrO_2 . The peaks in CZ pattern shifted to higher angles because of Zr^{4+} (with lower ionic radius than Ce^{4+}) inserting into the CeO_2 cell.

The H_2 -TPR result of CeO_2 and CZ is shown in Fig. 2. Pure CeO_2 has two reduction peaks, about 520 °C and 820 °C, corresponding to the reduction of surface O and bulk O reducing, respectively. For CZ, the reduction peak for bulk O disappears, and the intensity of surface O reduction increases, indicating that Zr

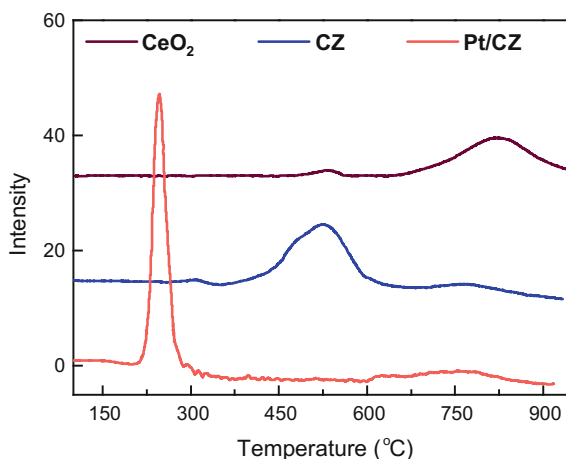
Fig. 1 XRD patterns of catalyst carriers CeO_2 and CZ



promotes the moving of O from bulk to surface. The reduction temperature for surface O is not changed by doping of Zr. But the loading of Pt changes the reduction temperature from about 520 °C to about 230 °C, indicating that loading of Pt significantly promotes the surface O reducing. The reason may be concluded to two reasons. On one hand, H_2 is dissociated to H atom on Pt and the spillover of H atom to the support accelerates the reduction of CZ [14]. On the other hand, the strong interaction between Pt and CZ improves the redox properties of CZ [15]. Just because of the collective function of Pt and Zr, the reduction temperature of Pt/CZ is low and the oxygen storage capacity of Pt/CZ is large, which makes it practicable in GDS.

Figure 3 shows the results of catalytic properties for Pt/CZ powder, evaluated by the conversion rate of H_2 . The ratio of H_2/O_2 is 3:1 in the inlet gas flow, which

Fig. 2 H_2 -TPR profiles for carrier CeO_2 , CZ, and catalyst Pt/CZ



means O_2 is not enough for H_2 oxidizing. Pt/Al_2O_3 is tested for comparison. The H_2 conversion rate catalyzed by Pt/Al_2O_3 is always about 70%, even if the temperature is higher than 250 °C. The conversion rate of hydrogen is higher than 70% when the temperature reaches 180 °C, the temperature at which the CZ begins to reduce in the assistance of Pt (shown in Fig. 2). And the conversion rate reaches 100% at about 210 °C, which indicates that the support is substantially reduced and releases enough oxygen for hydrogen oxidation. When oxygen in CZ exhausts, the conversion rate decreases to 70% again, and the rate lasts until the temperature goes back to the room temperature. In order to reuse the catalyst, Pt/CZ is re-oxidized under different temperatures. The result indicates that after re-oxidized under 400 °C, the catalyst recovers as the fresh samples. From the results, the advantages of Pt/CZ compared with oxidizers used in GDS can be summarized as follows. First, the running temperature is 250 °C, about 100 °C lower than that of oxidizers. Second, the normal catalysis works when the oxygen is exhausted, while no oxidation works when oxidizers are exhausted. Third, Pt/CZ is easily recovered by re-oxidation.

While the catalyst Pt/CZ was tested to be useful for detritiation in oxygen-deficient atmosphere, it should also be tested in oxygen-sufficient atmosphere at high space velocity when coated on honeycomb substrate, in order to verify the feasibility in ADS. Honeycomb catalyst $Pt/CZ-HC$ (Φ 8 mm \times 20 mm) was prepared and tested, and the result is shown in Table 1. The conversion rate of H_2 was 100% at room temperature, when the H_2 concentration ranged from 3000 to 5000 ppm. The corresponding space velocity ranged from 1.6×10^4 to 3.2×10^4 h^{-1} , which was much higher than that of traditional particle catalyst. The space velocity for particle catalyst was usually lower than 2000 h^{-1} [16], so catalyst $Pt/CZ-HC$ could increase the detritiation performance by elevating the gas space velocity without decreasing the conversion rate.

Because of the hydrogen isotopic effect [7, 17], the test with tritium was necessary. So cyclical detritiation with $Pt/CZ-HC$ catalyst for tritium containers was

Fig. 3 Conversion rate of H_2 catalyzed by Pt/CZ powder under oxygen lack atmosphere

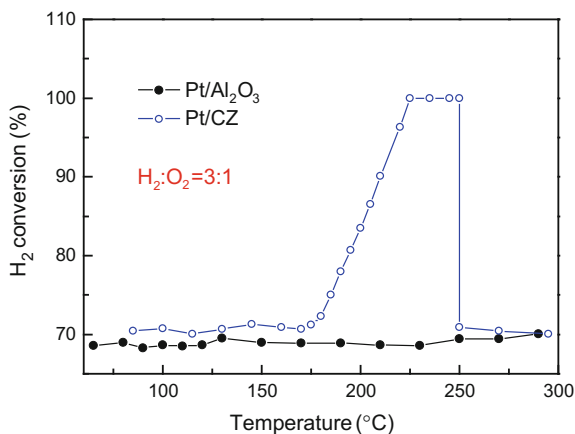


Table 1 Results of catalytic test for Pt/CZ-HC under oxygen-sufficient atmosphere

Space velocity (h^{-1})	Temperature ($^{\circ}\text{C}$)	H_2 concentration (ppm)	Conversion rate (%)
1.6×10^4	21	2980	100
3.2×10^4	20	5040	100

Table 2 Results of cyclical detritiation

Tritium $C_0(\text{Ci}\cdot\text{L}^{-1})$	Detritiation time (min)	Tritium $C_t(\text{Ci}\cdot\text{L}^{-1})$	Volume (m^3)
2.0×10^{-1}	190	1.82×10^{-2}	2.2
$8.0 \times 10^{-1\text{a}}$	240	2.4×10^{-1}	2.2

^aReactor is filled with traditional particle catalyst

carried out. The result is shown in Table 2, and the data in second row were for the contrastive test filled with particle catalyst. The space velocity for Pt/CZ-HC was about $1 \times 10^4 \text{ h}^{-1}$, and the contrastive test filled with particle catalyst was 1440 h^{-1} . The results show that the concentration of tritium decreases faster when using Pt/CZ-HC catalyst, and the final equilibrium concentration was lower.

4 Conclusions

The results suggest that Pt catalyst supported on Ce-based oxide could oxidize tritium at room temperature when under oxygen-sufficient atmosphere, while under oxygen-deficient (or inert) atmosphere, it also worked at about $250 \text{ }^{\circ}\text{C}$ by reducing the support. When loaded on honeycomb substrate, the detritiation performance would be significantly elevated due to its regular structure. In a word, the catalyst Pt/CZ-HC was a multifunctional detritiation catalyst, which can be used both in GDS and in ADS with high space velocity.

References

1. G.Q. Jiang, D.L. Luo, G.D. Lu, L.X. Sun, Tritium and industry techniques of tritium, National Defense Industry Press, Beijing, China (2007).
2. M. Glugla, D.K. Murdoch, H. Geibler, P. Herrmann, R. Kraemer, T.L. Le, Design of a catalytic exhaust clean-up unit for ITER, Fusion Eng. Des. 39–40 (1998) 893–899.
3. H. Yoshida, O. Kveton, J. Koonce, D. Holland, R. Haange, Status of the ITER Tritium Plant design, Fusion Eng. Des. 39–40 (1998) 875–882.
4. T. Uda, T. Sugiyama, Y. Asakura, K. Munakata, M. Tanaka, Development of high performance catalyst for oxidation of tritiated hydrogen and methane gases, Fusion Sci. Technol. 48 (2005) 480–483.
5. T. Uda, M. Tanaka, K. Munakata, Characteristics of honeycomb catalysts for oxidation of tritiated hydrogen and methane gases, Fusion Eng. Des. 83 (2008) 1715–1720.

6. M. Tanaka, T. Uda, Y. Shinozaki, K. Munakata, Hydrogen and methane oxidation performances of hybrid honeycomb catalyst for tritium removal system, *Fusion Eng. Des.* 84 (2009) 1818–1822.
7. K. Munakata, T. Wajima, K. Hara, K. Wada, Y. Shinozaki, K. Katekari, K. Mochizuki, M. Tanaka, T. Uda, Oxidation of hydrogen isotopes over honeycomb catalyst, *J. Nucl. Mater.* 417 (2011) 1170–1174.
8. T. Uda, M. Tanaka, K. Munakata, Scaling up experiments of honeycomb catalyst for oxidation of hydrogen and methane gases, *Fusion Eng. Des.* 87 (2012) 900–904.
9. Q.W. Wu, et al 2015 Preparation and catalytic properties of honeycomb catalyst for hydrogen isotope oxidation *Fusion Engineering and Design* 92 46.
10. Arthur N. et al 1995 Design optimization of metal getter reactors for removing tritium from flowing gas streams *Fusion Technology* 28 1558.
11. Heics A.G. et al 1994 Development of a Secondary Enclosure Clean up System for Tritium Systems 15th IEEE/NPSS Symposium.
12. Erica J.L. et al 2000 Operation of a Tritium Glovebox Clean up System Using Zr-Mn-Fe and Zr₂Fe Metal Getters *International Symposium on Metal Hydrogen Systems*.
13. Huang Z.Y. et al 2010 Hydrogenation and detritiation of Zr₂Fe alloy in inert atmosphere *Chemical Engineering (China)* 38 205.
14. Ranga G.R. 1999 Influence of metal particles on the reduction properties of ceria-based materials studied by TPR *Bull. Mater. Sci.* 22 89.
15. Giiulio Deganello, Francesco Giannici, Antonino Martorana, Giuseppe Pantaleo, Antonio Prestianni, Metal-Support Interaction and Redox Behavior of Pt (1 wt%)/Ce_{0.6}Zr_{0.4}O₂, *Journal of Physic and Chemistry B*, 2006, 110: 8731–8739.
16. Arthur Nobile, Heidi Reichert, Roger T. Janezic, David R. Harding, Lance D. Lund, Walter T. Shmayda, Design of the OMEGA laser target chamber tritium removal system, *Fusion science and technology* 2003 43: 522–539.
17. Nishikawa M, Isayama T, Shinnai K. Oxidation of tritium gas in glovebox atmosphere using CuO column. *J Nucl Sci Technol*, 1983, 20(2): 145–153.

Classification Methodologies for Nuclear Spent Fuel Forensic

Sanghwa Lee, Seungmin Lee and Gyunyoung Heo

Abstract The purpose of this study is to estimate the burning history of spent nuclear fuel using statistical data mining. The fuel history is characterized by burn-up, enrichment and cooling time, which are termed as nuclear forensic. While there are representative nuclear forensic methods such as a burn-up indicator, this study aims to develop a more flexible and robust method which is available under noisy and/or missing observations. In order to perform nuclear forensic, the classification of reactor types where the nuclear fuel is burned in is prerequisite. This study is focused on the development of such classification methods. For accurate classification LDA (linear discriminant analysis), QDA (quadratic discriminant analysis) and SVC (support vector classification) were used for classifiers. Additionally, the results from multiple classifiers were merged and voted for better classification performance, which is called ensemble process. For the development of methods, the data, which were used in this study, were created by ORIGEN-ARP code and include the information on burn-up, enrichment, cooling time and the type of reactor in terms of more than 70 nuclides. ECMiner (specialized data mining toolbox) was used for the model development and evaluation.

Keywords Spent fuel · Nuclear forensic · Classification · Data mining · Ensemble model

S. Lee (✉) · G. Heo
Kyung Hee University Deogyong-Daero Giheung-Gu, Yongin-Si,
Gyeonggi-Do 17104, Korea
e-mail: gheo@khu.ac.kr

S. Lee
Korea Institute of Nuclear Nonproliferation and Control Yuseong-Daero,
Yuseong-Gu, Daejeon-Si 34054, Korea

1 Introduction

There are some studies, which discover the origin of nuclear material using measured weight of nuclides, and several classification methods were used. Robel [1] used PLS-DA (partial least square–discrimination analysis), CART (classification and regression tree) and K-NN (K-nearest neighbor) methods for classification. They classified the origin of UOC (uranium ore concentrate), country and source, using these classifiers. Jones [2] suggested a methodology for determining the reactor type using nuclide analysis of nuclear spent fuel. In this study, they used FISPIN (FISsion Product Inventory), similar to ORIGEN-ARP, code to make nuclide data. PCA (principal component analysis) and LE (Laplacian eigenmaps) were used to reduce dimensionality, and four classifiers, LDA (linear discriminant analysis), QDA (quadratic discriminant analysis), random forest and Parzen window, were used.

This paper focused on the classification of five types of nuclear fuel in order to check availability considering Korean situation. This study inherited existing classifiers and used SVC (support vector classification) which received attention as classifier. In order to confirm the work of classifiers in actual situation, OECD/NEA data were used.

The descriptions of nuclear forensic algorithm using several classifiers are explained in Sect. 2, and the verifications of algorithm using ORIGEN data are explained in Sect. 3.

2 Development of Nuclear Forensic Algorithm

The nuclear forensic algorithm is classification problem, which uses weight of nuclide to independent variable and uses fuel types to dependent variable. In this paper, five types of nuclear fuel, CE16 (Combustion Engineering 16*16), WH14 (Westinghouse 14*14), WH17 (Westinghouse 17*17), VVER (Vodo-Vodyanoi Energetichesky Reactor) and GE7 (General Electric 7*7), were used. Except a GE7, which was BWR-type reactor, four types of nuclear fuel were PWR-type reactor. The BWR-type reactor was added for confirm that PWR- and BWR-type reactors can be classified. The VVER fuel type was added for confirming that PWR-type reactors, which were located in foreign country, can be classified. Three classifiers, LDA, QDA and SVC, were used. LDA and QDA were used in preceding research, and SVC was added.

2.1 Generation of ORIGEN-ARP Data

Sample data consist of 74 independent variables, nuclides, and 4 dependent variables, such as reactor type, burn-up, enrichment and cooling time. Sample data were generated by ORIGEN-ARP. Seventy-four nuclides, which were used as independent variable, were selected from references [3–6] and isotope information in OECD/NEA database [7]. ORIGEN-ARP code generated sample data using the combination of reactor types, burn-up, enrichment and cooling time as independent variables and using weight of nuclides as dependent variable. However, this study was the problem of inverse estimation using weight of nuclides. In this study, the weights of nuclides were used for independent variable and fuel types were used for dependent variable.

The number of sample data was 27,900 per each fuel type. The total number of sample data was 139,500. Ranges of burn-up, enrichment and cooling time were based on PWR-type reactor operational history in Korea. Each set produced weight of nuclides after 1 MTU burn-up. Table 1 shows burn-up history of ORIGEN-ARP sample data. Burn-up was divided per 500 MWD, 30 sections. Enrichment was divided per 0.15 w/o, 30 sections. Cooling time was divided per 1 year, 31 sections.

2.2 Classification Methodologies

Data classification is composed of two steps. In the first step, a classifier which describes a predetermined set of data is built. This is the learning step (or training phase), which builds a classifier using training set data. Each datum which consists of training set is called tuple. Tuple X is n-dimensional attribute vector $X = \{x_1, x_2, \dots, x_n\}$. In this study, each ORIGEN data was used as attribute vector and weight of nuclide was used as x_i .

In the second step, the model is used for classification. In this step, test set data are used. If training set data are used, a classifier tends to overfit the data. For preventing these problems, test set data are used, which were not used to construct the classifier and were independent of the training set data. Accuracy of a classifier is the ratio of test set data that are correctly classified by classification model.

In this paper, LDA, QDA and SVC were used for classifying the five nuclear fuel types. Since different classifiers can result in different results upon training and testing conditions, this study attempted to accumulate the results from many sources

Table 1 Burn-up history of ORIGEN-ARP sample data

Dependent variable (operational history)				Independent variable
Fuel type	Burn-up	Enrichment	Cooling time	No. nuclides
CE16, WH14, Wh17, GE7, VVER	38,000–52,500 (30 section)	15.0–5.85 (30 section)	0–30 (31 section)	74

of classifiers and tried to merge and finally decide the conclusion. Descriptions of classifier were excerpted from reference [8].

(1) **LDA**

LDA (linear discriminant analysis) focuses on the best discrimination between classes of data for dimensionality reduction. It is the method of maximizing ratio of between-class scatter to within-class scatter.

Consider each unit consists of p variables and belongs to class1 or class2. Equation 1 shows the mean vector and variance–covariance matrix of unit X .

$$\begin{aligned} E[x] &= \begin{cases} \mu_1 & x \text{ belong to Class1} \\ \mu_2 & x \text{ belong to Class2} \end{cases} \\ \text{Var}[x] &= \Sigma \end{aligned} \tag{1}$$

Consider n_1 units belong to class1 and n_2 units belong to class2.

$$\begin{aligned} \text{class1} &: x_i^1, i = 1, \dots, n_1 \\ \text{class2} &: x_i^2, i = 1, \dots, n_2 \end{aligned} \tag{2}$$

Fisher’s linear discriminant makes a classification rule based on new variable, which was made by the linear combination of original variables. The classification rule is called discriminant function. Equation 3 shows the discriminant function.

$$Z = w_1X_1 + w_2X_2 + \dots + w_pX_p = w'x \tag{3}$$

where X is the independent variable and w is the coefficient of the discriminant function. LDA determines w and classifies unit X with each class following a classification rule. Equation 4 shows example of the classification rule.

$$\begin{aligned} |\widehat{w}'(x - \bar{x}^{(1)})| \leq |\widehat{w}'(x - \bar{x}^{(2)})| & \text{classify } x \text{ with class1} \\ |\widehat{w}'(x - \bar{x}^{(1)})| > |\widehat{w}'(x - \bar{x}^{(2)})| & \text{classify } x \text{ with class2} \end{aligned} \tag{4}$$

LDA is unsuitable for the data which have same mean value such as nonlinear, because LDA starts with assumption that the middle (mean value) of class has most of class data.

(2) **QDA**

LDA starts with the assumption that variance–covariance matrixes are same irrespective of class. If variance–covariance matrixes are different from each class, quadratic discriminant function is derived. It is, therefore, called QDA (quadratic discriminant analysis).

Suppose each unit belong to class1 or class2. Equation 5 shows mean vector of each class.

$$\hat{\mu}_j \leftarrow \bar{x}^{(j)} \leftarrow \frac{1}{n} \sum_{i=1}^{n_j} x_i^{(j)}, \quad j = 1, 2 \tag{5}$$

where n_j is the number of units which belong to class j .

Equation 6 shows a sample variance–covariance matrix of class.

$$\hat{\Sigma}_j \leftarrow S_j \leftarrow \frac{1}{n_j - 1} \sum_{i=1}^{n_j} (x_i - \bar{x}^{(j)}) (x_i - \bar{x}^{(j)})' \quad j = 1, 2 \tag{6}$$

Equation 7 shows a discriminant function of class k .

$$U_k = \ln \pi_k - \frac{1}{2} \ln |\Sigma_k| - \frac{1}{2} (x - \mu_k)' \Sigma_k^{-1} (x - \mu_k) \tag{7}$$

Equation 8 shows a classification rule.

$$U_k = \max_j U_j \tag{8}$$

Were classify X with class k .

(3) SVC

SVC (support vector classification) is an algorithm that uses a nonlinear mapping to transform the original training data into a higher dimension. Within this new dimension, it searches for the linear optimal separation hyperplane. The training time of SVC takes long time, but it has strengths, high accuracy.

Suppose that data are classified with two classes. Equation 9 shows the data set.

$$D = (X_1, y_1), (X_2, y_2), \dots, (X_D, y_D) \tag{9}$$

where X_i is the set of training tuples that belong to class y_i . There are an infinite number of separating lines that classify data. The line, which has minimum classification error on previously unseen tuple, is required. SVC approaches this problem by searching for the MMH (maximum marginal hyperplane). One expects the hyperplane with the large margin to be more accurate in classifying future data tuples than the hyperplane with smaller margin. This is why SVC searches for the MMH.

The case when data are linearly inseparable applies kernel function to training data. The kernel function, which was used in SVC, is polynomial kernel, RBF (Gaussian radial basis function) kernel and sigmoid kernel. Equation 10 shows each kernel function.

Polynomial kernel of degree h : $K(X_i, X_j) = (X_i \cdot X_j + 1)^h$

RBF (Gaussian radial basis function)kernel: $K(X_i, X_j) = e^{-\frac{\|X_i - X_j\|^2}{2\sigma^2}}$ (10)

Sigmoid kernel: $K(X_i, X_j) = \tanh(kX_i \cdot X_j - \delta)$

The kernel chosen does not generally make large difference in resulting accuracy. In this study, RBF kernel was used.

2.3 Implementation

In this paper, the classifiers were built by ECMiner [9] software, which was commonly used for data mining. Figures 1 and 2 show run screen of ECMiner program. Figure 1 shows the build classification models using training set data.

The model evaluation node shows the misclassification ratios of classification models, which were built using training set data. The accuracy of a classifier on a

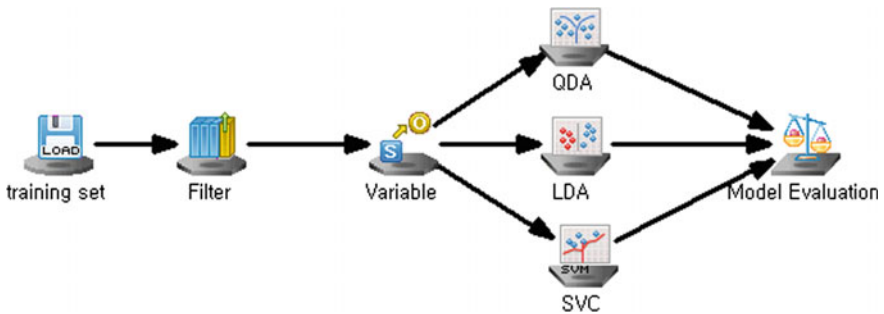


Fig. 1 Build classification model using training set

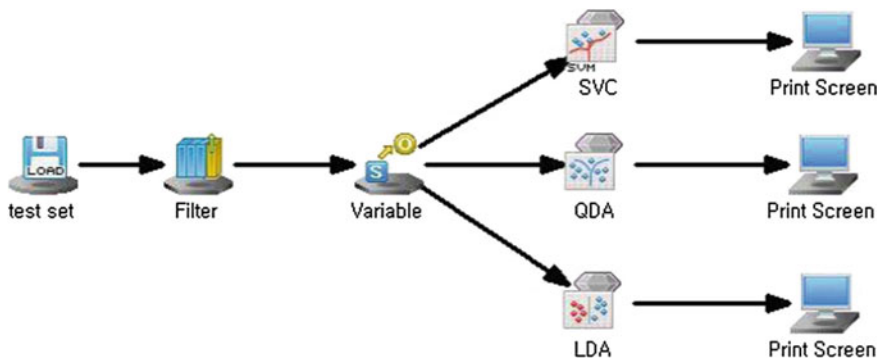


Fig. 2 Output screen of model evaluation node

Table 2 Classification model (SVC) verification using test set

[est.]	CE16 (%)	GE7 (%)	VVER (%)	WH14 (%)	WH17 (%)
CE16	99.94	0.00	0.06	0.00	0.00
GE7	0.00	100	0.00	0.00	0.00
VVER	0.03	0.00	93.47	0.00	6.50
WH14	0.00	0.00	0.00	100	0.00
WH17	0.01	0.00	3.87	0.00	96.12

Total misclassification rate: 2.09%

given test set is the percentage of test set data that are correctly classified by the classifier. Figure 2 shows the verification of classification models using test set data.

Table 2 shows a classification result of the test set data using the classification model, which was built using training set data. Screen-printing node shows the estimated class of the test set data, which were calculated using a discriminant function of the classifier.

3 Algorithm Verification

ORIGEN data were used to verify the algorithm. Two types of verification were performed. First one focused on the relation between classifier and misclassification rate. Second one focused on the relation between the number of nuclides and misclassification rate.

In order to verify the algorithms, 75% of the ORIGEN data were used for training set and the other 25% were used for test set. Figure 3 shows the schematic diagram of the algorithm verification.

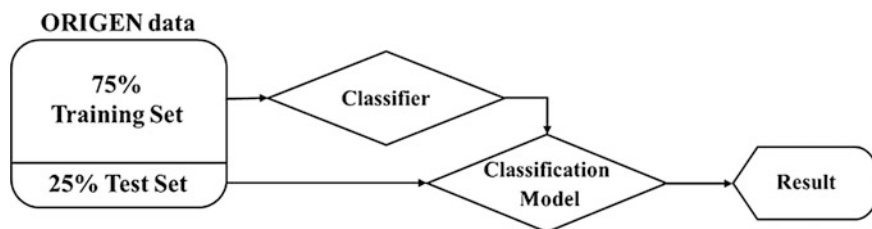
**Fig. 3** Schematic diagram of algorithm verification

Table 3 Classification result of LDA

[est.]	CE16 (%)	GE7 (%)	VVER (%)	WH14 (%)	WH17 (%)
CE16	85.05	0.00	10.09	2.98	1.88
GE7	0.00	100	0.00	0.00	0.00
VVER	6.18	0.00	88.28	0.51	5.03
WH14	6.33	0.00	1.16	92.51	0.00
WH17	1.00	0.00	14.43	0.01	84.55

Total misclassification rate: 9.92%

3.1 Misclassification Rate Using Simulation Data

Misclassification rate is defined as the number of misclassified data to the number of total data.

$$\text{Misclassification rate} = \frac{\text{The number of misclassified data}}{\text{The number of total data}} \quad (11)$$

In this paper, LDA, QDA and SVC were used for classifier. Each classifier has different character. It is described in Sect. 2. For these reasons, the misclassification rates had difference though equal data set was used. Tables 3, 4 and 5 show the misclassification rate of LDA, QDA and SVC, respectively.

The first row heading of Tables 3, 4 and 5 indicates the estimated assembly, and the first column is the real assembly of the test set. The percentage at each cross shows the correct classification fraction of the test set. Misclassification rate of GE7, which was BWR-type reactor, was the lowest. Verification results show that the misclassification rate was low in order of SVC, QDA and LDA. These misclassification rates are similar to result of Robel [5]. Even though the characteristics between PWR and BWR are not clear, this model proved that it is able to distinguish two of them quite nicely. Meanwhile, the misclassification rate of LDA was the highest because linear classification was difficult due to nature of the data.

Table 4 Classification result of QDA

[est.]	CE16 (%)	GE7 (%)	VVER (%)	WH14 (%)	WH17 (%)
CE16	94.36	0.00	2.37	2.95	0.32
GE7	0.00	100	0.00	0.00	0.60
VVER	2.75	0.00	88.70	1.18	7.37
WH14	1.72	0.00	0.31	97.98	0.00
WH17	1.31	0.00	8.48	0.15	90.07

Total misclassification rate: 5.78%

Table 5 Classification result of SVC

[est.]	CE16 (%)	GE7 (%)	VVER (%)	WH14 (%)	WH17 (%)
CE16	99.94	0.00	0.06	0.00	0.00
GE7	0.00	100	0.00	0.00	0.00
VVER	0.03	0.00	93.47	0.00	6.50
WH14	0.00	0.00	0.00	100	0.00
WH17	0.01	0.00	3.87	0.00	96.12

Total misclassification rate: 2.09%

Table 6 The number of nuclides of OECD/NEA data

Sample name	H. B. Robinson-2	Genkai-1	Calvert Cliffs-1	Fukushima Daini-2	Takahama-3
No. nuclides	11	14	16	36	38

3.2 Misclassification Rate Using OECD/NEA Data

The number of detected nuclides may be limited due to shortage of time and/or available detectors in real situation. For these reasons, the number of nuclides, which are available to build a classification model, can change, and appropriate classification methods should be adoptable at any number of nuclides.

In order to consider a certain real situation, we used OECD/NEA database. The number of nuclides revealed in OECD/NEA data was different case by case. In this paper, five OECD/NEA data, H. B. Robinson-2, Genkai-1, Calvert Cliffs-1, Fukushima Daini-2 and Takahama-3, were used to check the performance of the proposed model in that situation of different number of nuclides. Table 6 shows the number of nuclides of each OECA/NEA data.

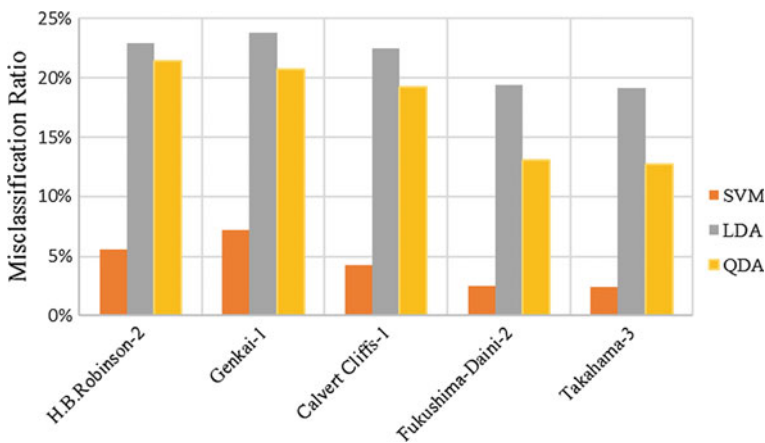


Fig. 4 Misclassification rate from the model using different number of nuclides

The classification models were redeveloped using the only available nuclides for each power plant and produced results. Figure 4 shows the misclassification rate upon the different number of nuclides.

One observation is that less number of nuclides may result in larger misclassification rate than that from the full set nuclides model. Additionally, the error is decreasing with increasing number of available nuclides. This means the measurement of nuclides is of great importance. Among the classifiers, the misclassification rate of SVC was the lowest at any number of nuclides.

4 Conclusions

This study compared the performance of three classifiers, LDA, QDA and SVC, when they used simulation data and OECD/NEA data. Verification results showed that SVC has disadvantage, which takes a long time to build classification model, but it has higher classification accuracy.

Even though we used the information of OECD/NEA data in terms of the available nuclides, we did not attempt to verify the performance of the classifiers using the measured value of OECD/NEA database.

Therefore, further study plans are as follows:

- To design classifier which has robustness to measurement error of real data such as OECD/NEA database
- To suggest a complementary methodology for the case of OECD/NEA data which consist of few nuclides

Acknowledgments This work was supported by the Nuclear Safety Research Program through the Korea Nuclear Safety Foundation (KORSAFe), granted financial resource from the Nuclear Safety and Security Commission(NSSC), Republic of Korea (No. 1305016).

References

1. M. Robel, "Nuclear Forensic Inferences Using Iterative Multidimensional Statistics", Institute of Nuclear Materials Management 50th Annual Meeting, July 12–16(2009)
2. A. E. Jones, "Classification of Spent Fuel for Nuclear Forensics," *Analytical Chemistry*, 86, 5399–5405(2014)
3. G. Nicolaou, "Determination of the origin of unknown irradiated nuclear fuel", *Journal of Environmental Radioactivity*, 86, 313–318(2006)
4. G. Nicolaou, "Identification of unknown irradiated nuclear fuel through its fission product content", *Journal of Radioanalytical and Chemistry*, vol. 279, No. 2, 503–508(2009)
5. M. Wallenius, "Origin Determination of Reactor Produced Plutonium by Mass Spectrometric Techniques: Application to Nuclear Forensic Science and Safeguards", Faculty of Science of the University of Helsinki, 2001

6. M. R. Scott, “Nuclear Forensics: Attributing The Source of Spent Fuel Used in An Rdd Event”, Texas A&M University, 2005
7. www.oecd-nea.org/sfcompo/Ver.2/Eng/
8. J. Han, “Data Mining: Concepts and Techniques”, Morgan Kaufmann, 2011
9. Internet homepage, <http://ecminer.com/en/>

Author Biographies



Sanghwa Lee He was born in Republic of Korea, in 1992. He is currently a college undergraduate in Kyung Hee University, South Korea.

His research interest is nuclear forensic using machine learning and data mining methods.



Seungmin Lee He is a researcher in KINAC (Korea Institute of Nuclear Nonproliferation and Control), South Korea.

His research interest is nuclear security, including nuclear forensics.



Gyunyoung Heo He is an Associate Professor and the director of Mainformatics Laboratory in Kyung Hee University, South Korea.

His research interest is the analysis of performance and reliability for industrial plants on the basis of statistical and intelligent data processing. His major activities are the development of plant simulation codes, operator aid systems and probabilistic safety assessments for nuclear facilities. He is interested in their synergetic outcomes to improve nuclear safety.

Developing a Conceptual Design of Suction-Based Ex-containment Radioactive Release Barrier System and Defining its Design Limits

Seong-Woo Kang and Man-Sung Yim

Abstract In a typical nuclear power plant, physical barriers and engineered safety systems are designed to protect the workers and the public in case of a severe accident from the in-containment radiological inventory, called the source term. If the barriers fail and the radioactivity leaks out to the environment, however, there is no engineered system to prevent the dispersion of the radioactive releases. Such radioactive release occurred in Fukushima, and as a result, the public's fear of the nuclear energy increased. Now, the public may not accept the assurance that the likelihood of another such accident is very low. Therefore, it may be essential for the nuclear industry to gain the public trust by developing comprehensively engineered safety systems that can prevent or reduce the consequences of such accident. One such safety system currently being researched is called the Integrated Portable Suction-Centrifugal Filtration System (IPS-CFS), a suction-based ex-containment radioactive release barrier system. To design such safety system, the radioactive source term at the release to the environment must be well characterized. The purpose of this paper was to present a conceptual design of the IPS-CFS and to develop its design requirements. An extended station blackout accident sequence with no recovery of auxiliary feedwater to the steam generators was chosen to simulate one of the worst-case scenarios that can cause significant radioactive releases to the environment. Based on the MAAP4-simulated source term data and with conservative assumptions, physical properties of interest such as the temperature of the radioactive release and the release speed of the radioactive materials were estimated. In addition, possible radiation doses to the exposed workers in the vicinity of the IPS-CFS were estimated conservatively to define the required decontamination factor of the system to keep the workers' doses below the regulatory limit set by the Nuclear Regulatory Commission (NRC). However, due to the number of conservative assumptions taken in this primary analysis, more detailed

S.-W. Kang · M.-S. Yim (✉)

Nuclear and Quantum Engineering, Korea Advanced Institute of Science and Technology (KAIST), Daejeon, South Korea
e-mail: msyim@kaist.ac.kr

S.-W. Kang

e-mail: seongwookang@kaist.ac.kr

and realistic source term analysis for the required worst-case scenario must be performed in the future to refine the design requirements.

Keywords Source term · Severe accident · Radioactive release barrier system · Radiation dispersion prevention system · MAAP4

1 Introduction

After the Fukushima Daiichi Nuclear Power Plant accident, the nuclear industry, regulators, and governments began to review the existing weaknesses of the nuclear power plants and have taken steps to avoid another such accident [1, 2]. As one of the ways to prevent another massive radioactive release into the environment, many countries now require installation of safety systems to avoid over-pressurization of the containment through either internal decay heat removal, external cooling of the containment surface, or controlled containment venting [3]. Implementation of such safety systems would improve the plant safety by maintaining the containment integrity in case of another severe accident. One such system widely implemented around the world is called the Filtered Containment Venting System (FCVS), also known as the Containment Filtered Venting System (CFVS) [4].

The FCVS may prevent or delay the over-pressurization of the containment through controlled release of radioactive materials. By opening a controlled flow path for the steam and the non-condensable gas generated by molten core-concrete interaction (MCCI), pressure buildup inside the containment can be prevented or delayed, likely avoiding the structural failure of the containment, thereby reducing the probability of uncontrolled radioactive releases into the environment. The decontamination efficiency of such system is typically about 99.9% for long-lived radionuclides and 99% for iodine gases [5]. Disadvantage of such system is that it must be installed inside the containment, and the cost of a FCVS is more than 20 million US dollars; its use is limited to the containment and is very expensive [6]. However, for many countries, advantages of having such system trump disadvantages. In Korea, one pressurized heavy water reactor (PHWR) has installed in the FCVS, and other units are planned to be equipped by 2018 [7].

In addition to the implementation of the above-mentioned safety systems, the nuclear industry, regulators, and governments took actions to resolve public anxiety because the Fukushima accident has increased the public's fear of using the nuclear energy. In Korea, the Korean Institute of Nuclear Safety (KINS) began an operation of 24-hour emergency response task force [8]. The Korean Government re-evaluated the radiation effect to the public and toughened the inspection of the radiation contamination in imports through airports and harbors. The nuclear industry and the regulators gave efforts to reinforce public communication by providing information through briefings, inquiries, Internet bulletin boards, and news [9].

However, general public's view on the concept of risk differs from that of professional engineers and scientists. Although professional engineers define a risk of an event by weighing both the consequence and the likelihood, the public weighs the consequence far more than the likelihood when assessing the risk, even if the likelihood of such event is near zero [10]. Therefore, the public may not accept the notion that another uncontrolled severe accident will not occur with the implementations of better regulations, improved human operator actions, and installations of safety systems such as the FCVS. To improve the public acceptance, it may be essential to develop new comprehensively engineered safety systems designed to avoid or lessen the effects of uncontrolled release accidents even when the containment fails, however unlikely such failure may be. Designs of such systems including the one investigated in this paper are being developed at KAIST [11]. To design such systems, detailed information about the source term at the release point to the environment must be known.

The source term information may only be simulated using the integrated severe accident computer codes because of the difficulty in performing physical experiments for such extreme conditions. The integrated severe accident computer codes are used to assess the source term data for the severe accident sequences identified in a typical Level 2 Probabilistic Safety Assessment. One such integrated code is MAAP4, a fast-running computer code that can simulate the severe accident sequences in nuclear power plants of various types, including the pressurized water reactors (PWRs). With input-specified various system faults, initiating events, and subsequent accident sequences including operator actions and activation of safety systems, MAAP4 is able to quantitatively analyze the source terms corresponding to such inputs [12].

In this paper, the conceptual design of a portable suction-based ex-containment barrier system called the Integrated Portable Suction-Centrifugal Filtration System (IPS-CFS) is introduced, and the design limits of the IPS-CFS are presented. The design limits are drawn based on the MAAP4 code simulation for an extended station blackout (SBO) accident with conservative assumptions about the radionuclide release. MAAP4.0.6 is used for the simulation of the accident sequence for a typical 1000 MWe Korean reactor.

2 Proposed Design

2.1 Design Configuration of the Integrated System

The IPS-CFS is a comprehensive suction-based ex-containment barrier and treatment system. In order to prevent (or at least reduce) the dispersion of the radionuclides into the environment, proposed design must collect the released radionuclides and treat the collected radioactive materials simultaneously. The IPS-CFS is designed as a portable system so that it may be used at any location

inside the power plant, including the containment and the auxiliary building. A schematic of the IPS-CFS is shown in Fig. 1.

The IPS-CFS is comprised of six major parts: a suction arm, an initial container with scrubber to cool the incoming materials and remove some radionuclides, a centrifugal filtration device, a compartment for absorbed particles in liquid and solid phase (larger particles), a compartment for absorbed particles in gas phase (smaller particles), and transportation devices (trucks and trailers). All must be resistant to high temperature and high radioactivity. They also must stay stable during the initial high-momentum conditions during the containment depressurization stage. Each part for the IPS-CFS is explained below:

- (1) **The suction arm** is designed with a suction nozzle to collect the radioactive materials without letting them escape to the environment and with a vent line to guide the collected radioactive materials into the treatment compartments of the IPS-CFS.
- (2) **The initial container for the incoming radioactive materials** is designed to cool the radioactive materials to reduce volumetric flow rate and to reduce radioactivity. The compartment would be filled with water with caustic soda and other additives for optimum iodine retention in the water pool. The radioactive materials would then flow into the centrifugal filtration device to be separated based on particle sizes. The container must be small enough to fit inside the truck.
- (3) **The centrifugal filtration device** is chosen to separate the radioactive particles based on the particle sizes to further increase the treatment capability of the system by designing different filtration compartments for particles with different sizes. A conceptual design is shown in Fig. 2. The size of this compartment should be compact enough to fit inside the truck or the trailer.

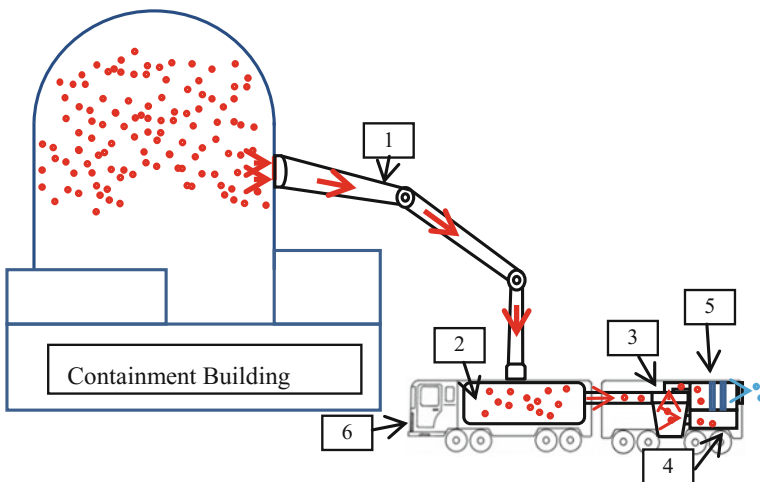


Fig. 1 Concept of the integrated portable suction-centrifugal filtration system

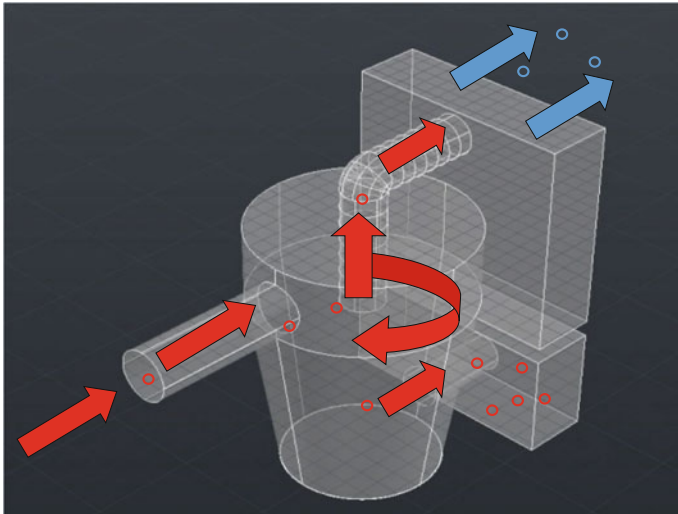


Fig. 2 Conceptual design of the centrifugal filtration device

- (4) **The compartment for absorbed particles in liquid and solid phases** is designed to contain the separated large particles with $\text{NaOH} + \text{Na}_2\text{S}_2\text{O}_3$ as an absorber. Most of the radioactive releases are assumed to be in gas forms, and some large-sized particles would have been removed in the initial container. Therefore, the size of this compartment may be small enough to fit inside the trailer.
- (5) **The compartment for absorbed gas particles** is designed with granular active carbon as an absorber, with series of different filters to effectively remove most of the radioactivity before releasing the treated gas into the environment to accommodate the high incoming volumetric rate of the radioactive gases into the IPS-CFS. This compartment is extremely important, as the workers operating the IPS-CFS must receive less than the effective dose limit for the workers while at the vicinity of the IPS-CFS.
- (6) **The transportation device** most likely in a form of a truck and a trailer, is required for the portability of the IPS-CFS. Figure 3 shows a type of Aircraft Rescue and Firefighting (ARFF) truck used for fire suppression technology. Figure 3 shows an ARFF vehicle from Rosenbauer with length, width, and height of 13, 3, and 3.65 m, respectively [13]. It is likely that the truck size criteria must meet the width and height of this ARFF vehicle for transportability on the road. The trailer should also have similar width and height.



Fig. 3 An ARFF vehicle from rosenbauer

2.2 General System Requirements

Portability and flexibility are two of the main requirements in designing the IPS-CFS. Huge uncertainty exists in analyzing containment behaviors and predicting containment failure locations in case of severe accidents. Radiation levels around the plant may differ significantly based on geography and wind direction [14]. Therefore, the IPS-CFS should have the capability to travel inside the plant after the exact location of damaged section is detected (using unmanned aerial vehicles or other mobile monitoring technologies) and must be resistant to various weather conditions. The suction arm of the IPS-CFS must be able to attach and seal the rupture opening of the containment (or auxiliary building) while resisting the momentum of the released radioactive materials and outside wind conditions. Because the size of the rupture area is unknown before the accident, the suction arm must be able to cover wide range of the damaged area. Then, a controlled flow path that can withstand the initial high volumetric flow rate is required, so that the collected radioactive materials can be guided to the treatment system in a stable manner.

When the radiation source term is released uncontrollably, the radioactive gas has high temperature and is released with high speed. Therefore, the compartments of the IPS-CFS that directly touch the radioactive gas must withstand the high temperature and high momentum while maintaining both its suction and filtration efficiency during the operation. It is essential that the IPS-CFS is designed to be resistant to the corrosion because the leakage of the radionuclides from the containment (or the auxiliary building) will happen for weeks and even months. Since radioactivity will leak for a long time even after the initial depressurization stage, the IPS-CFS should be able to be used with external power source once it is set stationary.

If uncontrolled radioactive materials are released into the environment, the area would become dangerous for the workers with high levels of radiation. Thus, the workers using the IPS-CFS should be able to stay inside the transportation device

with capability to protect the workers from the radioactivity during the emergency operation. A remote control capability of the IPS-CFS should strongly be considered to reduce the dose intake to the workers.

In this report, temperature of the radioactive release, mass release rate, volumetric release rate, and release speed are conservatively defined using the data from the severe accident code simulation for extended SBO with no recovery of auxiliary feedwater to the steam generators for the period of 72 h. Furthermore, dose rates due to the radioactive release are estimated to find recommended values for the decontamination factor so that the dose intake of the workers in operation would not exceed the dose limit set by the US Nuclear Regulatory Commission (NRC).

3 Methods

3.1 Source Term Simulation Using MAAP4.0.6

The source term analysis of the containment rupture scenario from over-pressurization from extended SBO with loss of auxiliary feedwater system is simulated for 72 h. The power plant parameter file has been provided for a 1000 MWe PWR reactor from Korea Atomic Energy Research Institute for research purposes. Default parameter values from MAAP4 for the severe accident models were used in the simulations. A benchmark test for the default model parameter values was performed. Zion plant parameter file provided with code installation was simulated for an extended SBO accident, and the results were compared with the source term data from NUREG-1465 for mass fraction release of the cesium and iodine into the containment. This is shown in Fig. 4 [15].

For the 1000 MWe Korean power plant, the ultimate containment failure pressure with 5% probability/95% confidence level is 1.01 MPa, from severe accident management guidelines [16]. This value was used as criteria for the containment failure criteria during the MAAP4 simulation. Containment failure mode was assumed to be a containment rupture with circular shape. Containment integrity research at Sandia National Laboratories defined a rupture as a containment breach that would rapidly depressurize the containment, with representative hole size of approximately 1.0 ft², so this value was used for the accident analysis [17]. Location of the failure is assumed to be at the cylindrical wall of the upper containment. For the simulation, it was assumed that the radioactive release to the environment would occur only through the containment failure. The initial and boundary conditions are shown in Table 1.

The containment nodalization scheme and the junction scheme used in the accident simulation are shown in Table 2.

As a benchmark test for the simulation results used in this report, the mass fraction releases of each fission product (FP) group was compared with the data from a research article written by a member of Korean Hydro and Nuclear Power

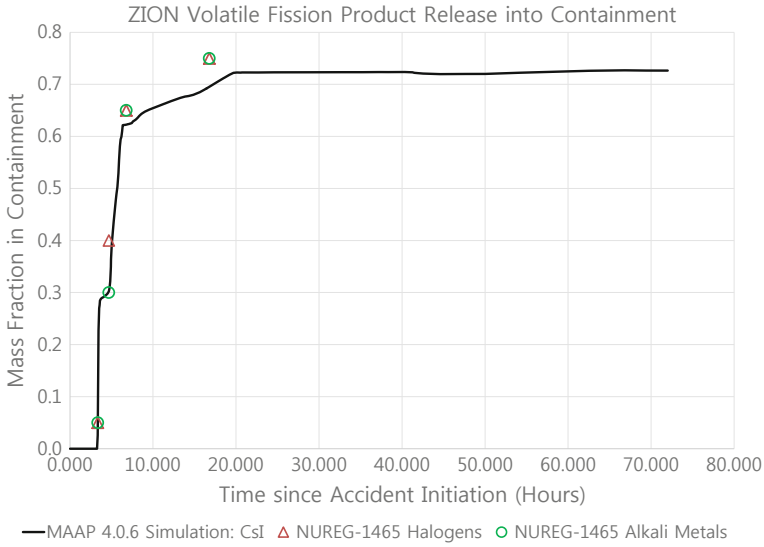


Fig. 4 Benchmark testing for default MAAP4 model parameter values

Table 1 Initial and boundary conditions for the containment

Reactor power	2815 MWt
Containment total free volume	$7.78 \times 10^4 \text{ m}^3$
Containment rupture failure pressure	1.01 MPa
Containment rupture size	$9.29 \times 10^{-2} \text{ m}^2$ (1 ft ²)
Containment rupture location	Cylindrical wall

Table 2 Containment scheme

#	Containment nodalization	Containment junction
1	Cavity compartment	Cavity through bypass → Lower compt
2	Lower compartment	Cavity through tunnel → Lower compt
3	Upper compartment	Lower compt → Annular compt
4	Annular compartment	Lower compt → Upper compt
5	Containment dome	Annular compt → Upper compt
6	Containment sump	Upper compt → Dome
7	Auxiliary building	Annular compt → Sump compt
8	Environment	Upper compt → Environment

(KHNP). The data from KHNP used different containment nodalization and junction scheme. In the MAAP4 simulation for this report, the containment failed at 49.0 h after the accident, compared with the 58.4 h from the KHNP simulation. The simulated data generally match well with the KHNP simulation data, and they are

shown in Figs. 5 and 6, both in a logarithmic scale. The timescales are different because the KHNP simulation was for 168 h, whereas the simulation for this report was for 72 h.

For the MAAP4 simulation, following outputs were collected for 72-hours extended SBO simulation: mass releases and mass fraction releases of each FP group; temperature, pressure, and the density of the gas inside the containment; and the containment gas mass flow rate into the environment (i.e., through Junction 8). From the output data and the previously defined containment rupture size, the radioactive gas volumetric flow rate and the gas release speed were calculated. For the density

Fig. 5 Mass fraction release for extended SBO accident (simulated by KHNP)

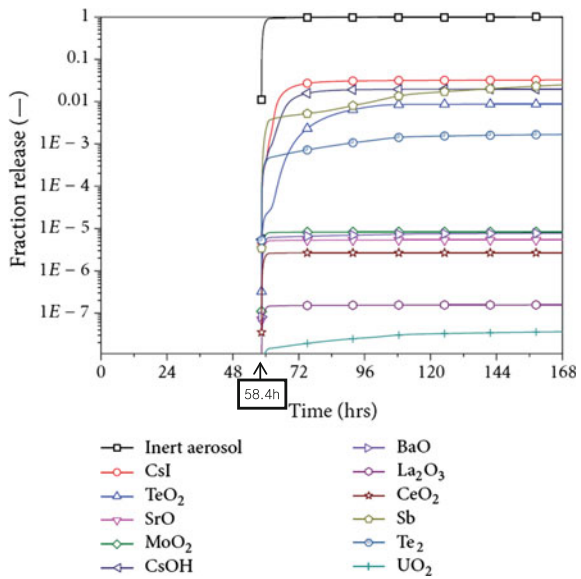
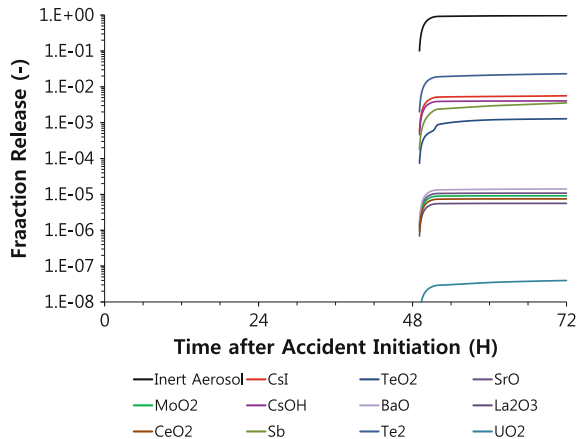


Fig. 6 Mass fraction release for extended SBO accident



calculation, the sum of the mass of fission products, steam, and gases inside the containment was divided by the containment volume. The volumetric flow rate was calculated for the gas released into the environment (i.e., at the atmospheric pressure) by using the density of the radioactive gases at atmospheric pressure. The gas release rate at the release point of the containment was calculated by using the density of the gas inside the containment (i.e., at the containment pressure).

3.2 Dose Estimation

In the source term analysis, MAAP4 code divides fission products into 12 different FP groups by default [18]. The FP groups with the representative radionuclide(s) for each group are listed in Table 3. If several different isotopes of the radionuclides in a FP group exist, the radionuclide with a half-life longer than few days and shorter than 100 years was selected to represent the corresponding FP group for the dose estimation. From MAAP4 simulation, which gives cumulative mass released into the environment for each FP group, the mass of each fission product released in each hour was calculated for up to 72 h.

The mass of each fission product released during each hour was used to estimate the radiation dose by calculating activity of each representative radionuclide and converting the activity to doses. It was assumed that each FP group in Table 3 was comprised entirely of the representative fission product (in column 1). Each fission product was assumed be entirely made of the representative radionuclides (in column 2), O-16, and H-1. The equation to estimate the dose rates from the mass of the FP releases is as follows:

$$D = \lambda \times (m_i/M_i) \times 1000 \times n_{ij} \times N_A \times C_{ij}$$

Table 3 MAAP4 fission products and representative radionuclides

FP group	Representative fission product	Representative radionuclides
1	Noble gases	Not analyzed
2	CsI	Cs-137, I-131
3	TeO ₂	Te-123 m
4	SrO	Sr-90
5	MoO ₂	Mo-99
6	CsOH	Cs-137
7	BaO	Ba-133
8	La ₂ O ₃	La-140
9	CeO ₂	Ce-144
10	Sb	Sb-125
11	Te ₂	Te-123 m
12	UO ₂	U-232

where

- D Estimated dose (mSv/h)
- λ Decay constant (s^{-1})
- m_i Mass released of the fission product i (kg/h)
- M_i Molar mass of the fission product i (g/mol)
- n_{ij} Number of moles of radionuclide ij in a mole of fission product i
- N_A Avogadro's number = 0.6022×10^{24} (molecules/mole)
- C_{ij} Conversion ratio from activity to dose for defined distance (mSv/h-Bq)

To calculate dose rate or dose for a given activity of an isotope, one must take into account the distance from the radioactive source as well as the energy of the emitted radioactivity. One cannot simply convert from an activity to a dose rate but rather must do a complicated calculation on an isotope-by-isotope and a distance-by-distance basis [19]. However, a program called Rad Pro Calculator uses the formulas and can calculate the dose rate from chosen radionuclide's activity, assuming a point source. This program was used to find dose rates at 10 m away with 1 Bq activity of each representative radionuclide to estimate the conversion factors. The estimated factors were then used to calculate the effective dose from the calculated radionuclide activity. The information about the representative radionuclides is shown in Table 4. For the distance away from the radioactive source, 10 m was chosen as a reference value because the ARFF vehicle shown in Fig. 3 has length of 13 m, making it highly unlikely that a worker would go within 10 m of the treated materials that are being released into the environment after going through the filtration system.

The results were then compared with the recommended emergency dose limits for the workers shown in Table 5 to estimate the required decontamination factor of the overall filtration system. During a catastrophic nuclear power plant severe accident, emergency personnel may be unavoidably exposed to the annual dose limits set by the NRC. To account for such unavoidability, the US Environmental Protection Agency (EPA) has recommended the response worker guidelines in

Table 4 Information about the representative radionuclides

Radionuclide	Half-life (y)	Decay constant (s^{-1})	Conversion ratio with a point source assumption (Bq \rightarrow mSv/hr)
Cs-137	30.07	7.30946E-10	7.34837E-13
Te-123 m	0.3280	6.70220E-08	4.66319E-13
Sr-90	28.78	7.63709E-10	2.60864E-13
Mo-99	0.007527	2.91994E-06	1.05573E-11
Ba-133	10.51	2.09130E-09	3.15959E-13
I-131	0.02198	1.00023E-06	4.56882E-13
La-140	0.004598	4.78073E-06	2.64043E-12
Ce-144	0.7805	2.81598E-08	2.83117E-14
Sb-125	2.758	7.96880E-09	5.27838E-13
U-232	68.90	3.19007E-10	1.50443E-14

Protection Action Guides and Planning Guidance for Radiological Incidents. For the emergency personnel, the 25-rem worker guideline provides assurance to the workers whose exposures will not result in detrimental deterministic health effects, although it could still increase the risk of stochastic effects such as cancer risk. That limit is recommended for lifesaving or protection of large populations, including during the worst-case severe accidents with radiation releases [20].

4 Results and Discussions

The simulation in this report was for the extended SBO accident without auxiliary feedwater system for 72 h without any safety system to relieve the containment over-pressurization. As shown in Fig. 7, the pressure rapidly builds up until the containment rupture occurs at 49 h after the accident initiation, which results in rapid depressurization until becoming in stable at near atmospheric pressure. For the purpose of this research, which is interested in characteristic of the radioactive source term when it is released into the environment, two different time periods during the accident sequence were examined: during depressurization of the containment (1) and during the stable stage (2). The beginning of the pressure equilibrium period was defined as when the change of rate in pressure per hour is less than 1% after the start of the depressurization process.

Figures 8, 9, and 10, respectively, show the mass flow rate, volumetric flow rate, and the release speed of the radioactive source term into the environment.

At the rapid depressurization stage, the amount of gas flowing outside the containment is enormous (mostly gas and steam), with maximum mass flow rate of 100–120 kg/s, maximum volumetric flow rate of 300–300 m³/s, and the maximum release speed of 200–250 m/s, respectively. However, even after the initial depressurization stage, radioactive gases were being released continuously at noticeable speed. The results from the simulation for the maximum temperature as well as ranges for the mass flow rate, volumetric flow rate, and release speed are shown in Table 6.

If the IPS-CFS is to be designed to prevent even the initial uncontrollable radioactive releases, it is recommended to withstand the temperature of over 200 °C without degradation, mass flow rate of over 100 kg/s, volumetric flow rate of over 330 m³/s, and release speed of over 230 m/s. However, this is assuming that the radioactive release happens at extremely high pressure, and such extreme condition

Table 5 Annual occupational dose limits and calculated emergency personnel hourly dose limits

Target	Rem	mSv	Duration
Occupational workers	5	50	per year
	0.0005708	0.005708	per hour
Emergency workers, for protection of large populations	25	250	per year
	0.002853	0.02853	per hour

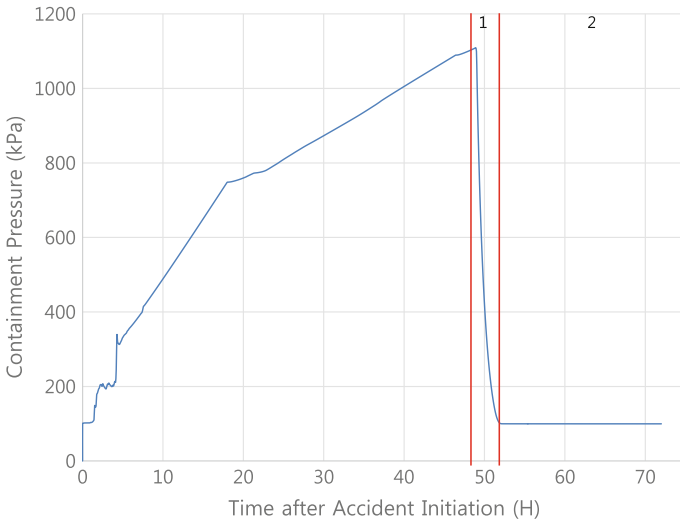


Fig. 7 Containment pressure versus time

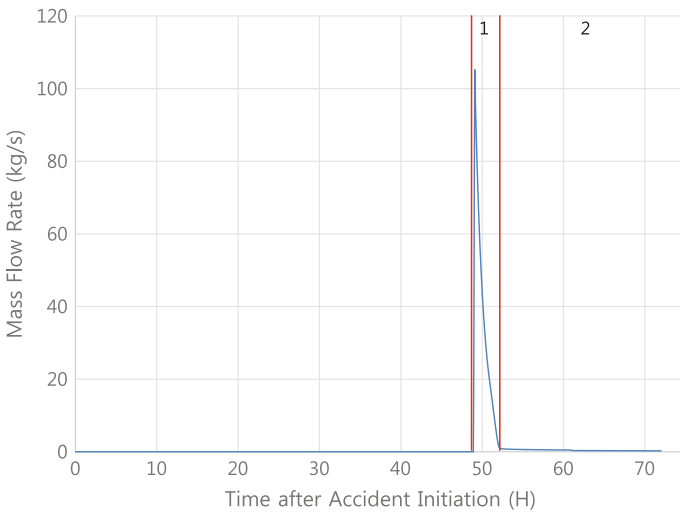


Fig. 8 Mass flow rate of the release versus time

lasts only for first few hours after the initial release, as shown in Table 7. Just in an hour, the mass flow rate and the volumetric flow rate drop by more than half. The release speed at the release point of the containment does not drop as rapidly, because the density of the radioactive release drops rapidly during depressurization, which counteracts the effect of decreasing mass flow rate in calculating the release speed.

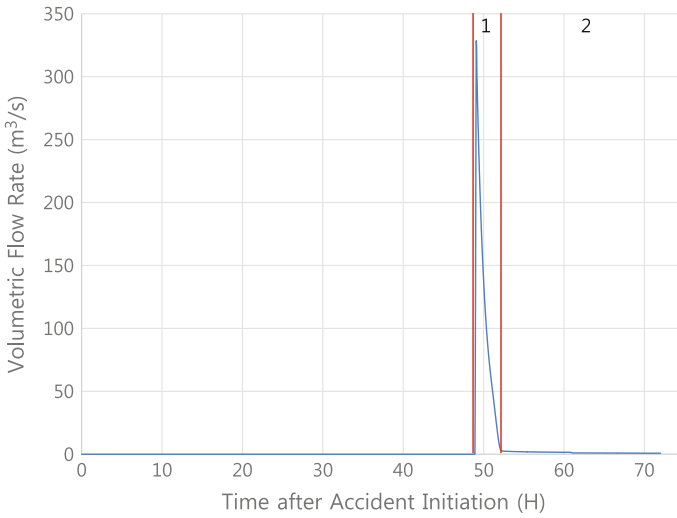


Fig. 9 Volumetric flow rate to the environment versus time

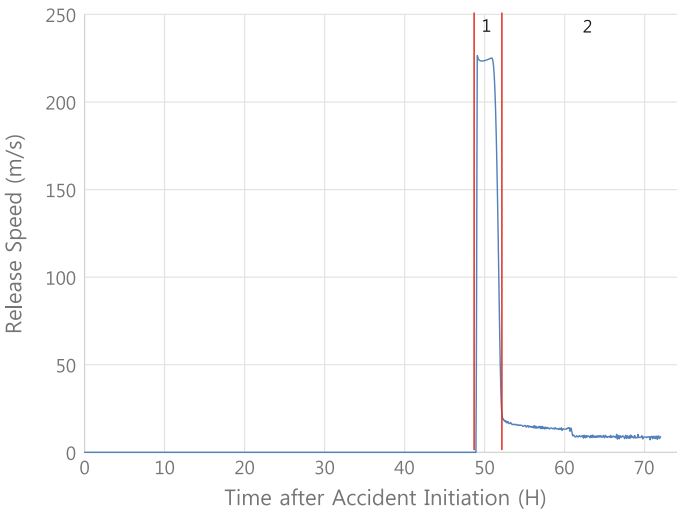


Fig. 10 Source term speed at the release point versus time

Because such a rapid change in conditions occurs during the depressurization stage and also during first few hours of the stable stage, the following design limits for the IPS-CFS were drawn for different durations. Table 8 shows the durations in which the IPS-CFS must withstand the specified temperature and flow rates. The limiting values are rounded-up maximum values during the specified time period.

Table 6 Physical characteristics of the radioactive release for the MAAP4 simulation

	Depressurization stage		Stable stage	
	Max	Min	Max	Min
Temperature (°C)	201.6	169.5	179.4	173.4
Mass flow rate (kg/s)	105.2	1.169	0.9732	0.2182
Volumetric flow rate (m ³ /s)	328.5	3.651	3.039	0.6813
Release speed (m/s)	226.5	26.17	21.87	7.170

The extreme conditions in the initial depressurization stage cause real difficulty in designing the IPS-CFS. A diffuser can decrease the release speed but would cause even further increase in volume of the radioactive releases. A nozzle may decrease the volumetric flow rate but may cause increase in release speed. To account for this problem, the suction arm must be robust enough to last such condition for first few hours, and the initial container of the IPS-CFS should have a cooling mechanism (possibly a cryogenic system) to rapidly cool the incoming hot radioactive materials to decrease the volume. If water is used for the cooling mechanism, formation of hydrogen must be accounted for in design consideration of the system as well.

Physical characteristics of the source term release are important in the design of the IPS-CFS, but the treatment requirement must be set to limit the dose rates from the treated and released gas. The regulators and the public are more interested in possible health effects and doses than the physical characteristics of the radioactive releases. Because it may physically be challenging to stop the radioactive gas from leaking outside the containment during the depressurization stage, the source term analysis should at least estimate how much radioactivity is released to the environment uncontrollably before the radiation leakage can be controlled through operation of the radiation dispersion system. Dose estimates from the simulation data are shown in Table 9.

As shown in Table 9, about 90% of the total dose is released during the depressurization stage. So the IPS-CFS should have short preparation time, with the whole system preferably be ready before the actual release, so that once the radioactive release is detected, it can travel to the exact location within minutes.

Hourly doses of the released radionuclides after containment failure are shown in Fig. 11. Iodine accounts for most of the doses, so the hourly doses are plotted with and without I-131 for comparison purpose. If the IPS-CFS can treat and prevent the radioactive iodine releases, it can significantly reduce the radiation dose.

For the regulating purposes, decontamination factor may also be of the interest. Decontamination factor (DF) is related to the % of activity removed through the technology [21]. Assuming all radioactive materials are successfully collected by the IPS-CFS (i.e., suction efficiency of 100%) and assuming that the activity is directly proportional to the dose rate for the simplification of the calculation,

Table 7 Physical characteristics during the depressurization stage

Time after release (H)	Mass flow rate (kg/s)	Volumetric flow rate (m ³ /s)	Release speed (m/s)
0.000	105.194	328.484	91.206
0.083	96.672	301.875	226.513
0.167	89.085	278.182	225.136
0.250	82.215	256.729	224.361
0.333	75.942	237.141	223.919
0.417	70.190	219.180	223.661
0.500	64.905	202.675	223.514
0.583	60.042	187.491	223.438
0.667	55.564	173.507	223.413
0.750	51.436	160.618	223.426
0.833	47.630	148.732	223.470
0.917	44.118	137.765	223.539
1.000	40.876	127.643	223.627
1.083	37.886	118.305	223.733
1.167	35.125	109.685	223.853
1.250	32.576	101.725	223.985
1.333	30.223	94.376	224.126
1.417	28.049	87.588	224.274
1.500	26.041	81.319	224.429
1.583	24.187	75.528	224.589
1.667	22.473	70.176	224.754
1.750	20.889	65.228	224.917
1.833	19.409	60.607	225.074
1.917	17.971	56.118	225.065
2.000	16.595	51.821	224.237
2.084	15.161	47.344	217.571
2.167	13.716	42.830	210.682
2.251	12.247	38.242	200.838
2.335	10.770	33.631	187.802
2.419	9.293	29.020	171.422
2.502	7.859	24.540	152.313
2.587	6.457	20.163	130.625
2.670	5.089	15.891	106.656
2.754	3.816	11.916	82.167
2.838	2.692	8.405	59.074
2.926	1.775	5.543	39.450
3.013	1.169	3.651	26.171
3.096	0.973	3.039	21.870

Table 8 Design limits of the IPS-CFS based on the physical conditions of the radioactive release

Time after release (H)	Depressurization stage		Stable stage	
	0-1	1-3	3-5	5~
Duration (H)	1	2	2	Long term
Temperature (°C)	210	180	180	180
Mass flow rate (kg/s)	110	41	1	1
Volumetric flow rate (m ³ /s)	330	130	5	2
Release speed (m/s)	230	230	30	15

Table 9 Total estimated dose released for each radionuclide

Radionuclide	Total dose released (mSv)	Dose released in depressurization period (mSv)	Doses released in depressurization period (%)
Cs	1906.585	1727.189	90.59073
I	177253	152634.6	86.11112
Te	3596.904	1757.325	48.85660
Sr	35.77389	33.35865	93.24859
Mo	20397.95	19058.43	93.43306
Ba	5.480482	4.877834	89.00374
La	223769.7	209105.9	93.44691
Ce	19.42319	18.15141	93.45227
Sb	146.5083	83.27252	56.83810
U	0.037215	0.025147	67.57315
Total	427131.4	384423.1	90.00113

required DF of the overall filtration system to maintain the dose limit to the workers set by the NRC is found using the following equation,

$$DF_{req} = [1 - (D - 0.02853)/(D)]^{-1}$$

where

DF_{req} Overall decontamination factor required to reduce the dose rate down to the emergency personnel dose limit

D Estimated total dose rate (mSv/h)

The results are shown in Fig. 12 for each hour.

Many countries require DFs greater than 100 for iodine and greater than 1000 for other aerosols. High removal efficiencies have DF greater than 10,000 [3]. However, primarily due to I-131 releases, the DF of greater than 1,000,000 is recommended for the design of the IPS-CFS for the depressurization stage and greater than 100,000 for the stable stage. It may require that the filtration systems to

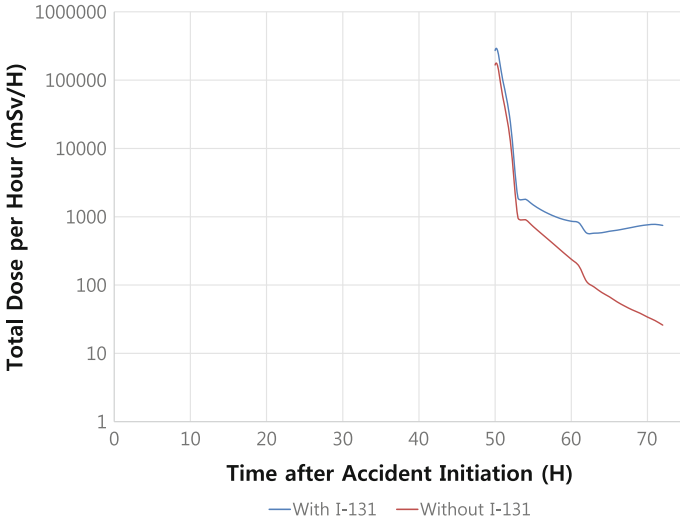


Fig. 11 Hourly dose versus time



Fig. 12 Required decontamination factor versus time

be lined in series to reduce the radioactive releases to fit the criteria of meeting the dose limits for the workers.

The results, both the physical characteristics and the dose estimations, come from a worst-case scenario with conservative assumptions and simplifications. More detailed and less conservative scenario, more realistic assumptions, and detailed calculations may be required to further define the design limits of the IPS-CFS.

5 Conclusions

The results have assumed conservative accident scenarios, conservative accident conditions, and conservative radioactivity assumptions in defining the limits of the IPS-CFS. The task of designing a radioactive dispersion system that can successfully prevent such releases, especially the releases from high pressure, seems to be challenging. However, as more technologies develop and more realistic source term analyses are performed, better design limits of the IPS-CFS may be defined. With the invention of a technology that can effectively prevent the dispersion of the uncontrolled radioactive releases in case of another Fukushima-like accident, it will result in increased safety of the nuclear power plants for both the public and the workers and the increase in the public acceptance of nuclear energy.

Acknowledgments This work was supported by the Nuclear Power Core Technology Development of the Korea Institute of Energy Technology Evaluation and Planning (KETEP) under the Ministry of Trade, Industry and Energy, Republic of Korea (No. 20131510400050).

REFERENCES

1. Lessons Learned from the Fukushima Nuclear Accident for Improving Safety of U.S. Nuclear Plants. The Nuclear Regulatory Commission. 2014 July 31.
2. Safety Issues and Recommendations. Fukushima Daiichi: ANS Committee Report. 2012 March.
3. OECD/NEA/CSNI Status Report on Filtered Containment Venting. 2014 July.
4. C. Hillrichs et al. Review of European Filtered Containment Venting Systems. 2012.
5. H. Rust et. al. Pressure release of containments during severe accidents in Switzerland. Nuclear Engineering and Design. Volume 157, Issue 3. Pages 337–352. 1995 August.
6. The Debate over Nuclear Reactor Venting. Forum on Energy. 2013 March 14.
7. Y. J. Choi, et al. Status of Filtered Containment Venting in Korea. IAEA. 2015.
8. Report of the Korean Government Response to the Fukushima Daiichi Nuclear Accident. OECE/NEA Policy Issue 0. 2011 August.
9. National Report for the Second Convention on Nuclear Safety Extraordinary Meeting. Korea Institute of Nuclear Safety. 2012 May.
10. P. Slovic. Perception of Risk. Science 236: 280–285. 1987.
11. S. Lee. An Unmanned Aerial Vehicle-based Radiation Surveillance System. Korea Electronics Technology Institute. IAEA EPR 2015.
12. MAAP4 – Modular Accident Analysis Program for LWR Power Plants. EPRI. 1994.
13. Panther, ARFF Vehicles. Rosenbauer.
14. Fukushima on the Globe. <<http://fukushimaontheglobe.com/the-earthquake-and-the-nuclear-accident/whats-happened>>. Accessed 2016 Jan.
15. Accident Source Terms for Light Water Reactors. NUREG-1465.
16. S.W. Lee et. al. Containment Depressurization Capabilities of Filtered Venting System in 1000 MWe PWR with Large Dry Containment. Korea Hydro and Nuclear Power. Hindawi Publishing Corporation. 2014.
17. Containment Integrity Research at Sandia National Laboratories. U.S. NRC. NUREG/CR-6906. 2006.

18. J.W. Park et. al. Severe Accident Source Term Analysis for a 4000 MWt Evolutionary Pressurized Light Water Reactor. Proceedings of the Korean Nuclear Society Autumn Meeting, 2000 October.
19. George Chabot. Relationship Between Radionuclide Gamma Emission and Exposure Rate. Health Physics Society.
20. Protective Action Guides and Planning Guidance for Radiological Incidents. EPA. 2013.
21. Decontamination Technologies. Argonne National Laboratory. IAEA.

Author Biographies

Seong-Woo Kang is a master's student in Nuclear and Quantum Engineering at Korea Advanced Institute of Science and Technology (KAIST). He has a bachelor's degree in Nuclear Engineering from Texas A&M University. Under the corresponding author Professor Yim in Nuclear Energy Environment and Nuclear Security Laboratory, Mr. Kang is currently researching ways to reduce uncertainties in source term analysis.

Yim Man-Sung's research activities cover technical and policy issues in back-end nuclear fuel cycle, nuclear safety, severe accidents, security, and non-proliferation.

Development and Validation of Subchannel Code SUBSC

Jun Chen, Liangzhi Cao, Chuanqi Zhao, Hongchun Wu and Zhouyu Liu

Abstract SUBSC was developed to simulate thermal–hydraulic phenomena in the core of pressurized water reactors, as well as innovative reactors operated with supercritical water as coolant. Both precise IAPWS-IF97 formulations and approximating polynomial correlations were implemented to calculate properties of water. A typical PWR fuel assembly problem, a supercritical water heat transfer experiment, and the steady state bundle benchmark of the pressurized water reactor subchannel and bundle tests (PSBT) were applied to validate this code. The SUBSC predicted results showed good agreement with experimental data and results obtained from COBRA, demonstrating feasibility and accuracy of this code. In order to improve efficiency, a restarted GMRES algorithm with preconditioning was implemented for solving the pressure correction equation. The numerical results showed the efficiency could be enhanced dramatically as the size of the problem being solved became large.

Keywords Subchannel · SUBSC · Validation · GMRES

1 Introduction

Historically, system codes, subchannel codes, and computational fluid dynamics (CFD) codes are used for the analysis of thermal–hydraulic (T/H) performance of nuclear power plants (NPPs). Generally, the system code cannot simulate the local behavior of the rod bundle [1], and the requirements for CFD are still large, although it is state-of-art T/H approach. So subchannel codes are typically used to simulate T/H behavior within a fuel bundle in nuclear reactors [2].

J. Chen · L. Cao · H. Wu · Z. Liu (✉)

School of Nuclear Science and Technology, Xi'an Jiaotong University, Xi'an, Shaanxi, China
e-mail: zhouyuliu@mail.xjtu.edu.cn

C. Zhao

China Nuclear and Radiation Safety Center, Beijing, China

© Springer Science+Business Media Singapore 2017

H. Jiang (ed.), *Proceedings of The 20th Pacific Basin Nuclear Conference*,

DOI 10.1007/978-981-10-2314-9_68

Therefore, an in-house accurate and efficient subchannel code SUBSC was developed and validated in this paper. It starts with an overview about the basic equations and numerical approach. Subsequently, the sufficient validation against other codes and high-quality experimental data is described. The following sections focus on a preconditioned GMRES method used for solving the time-consuming pressure correction equation in order to improve efficiency.

2 Conservation Equations and Numerical Approach

For an axial control volume j in channel i surrounded by volumes of neighboring channels n through a gap k (see Figs. 1 and 2), the SUBSC code employs homogeneous equilibrium method for the two-phase calculation assuming the homogeneous mixture of fluid and vapor at thermal equilibrium.

2.1 Conservation Equations

SUBSC solves the following four finite difference conservation equations for mixture mass, energy, axial momentum, and lateral momentum:

Mass conservation equation:

$$A_i \frac{\Delta X_j}{\Delta t} (\rho_{ij} - \rho_{ij}^n) + m_{ij} - m_{ij-1} + \Delta X_j \sum_{k \in i} e_{ik} w_{kj} = 0 \tag{1}$$

Fig. 1 Control volume for mass, energy, and axial momentum balance equations (lateral view)

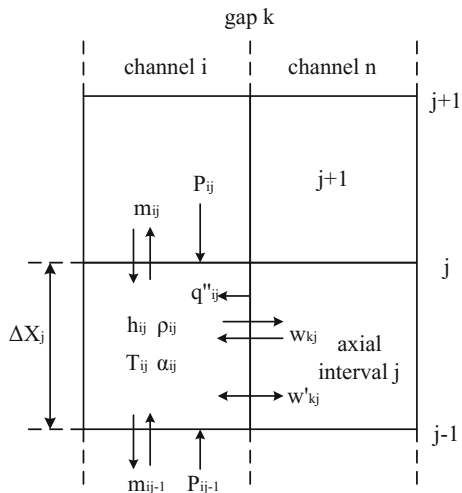
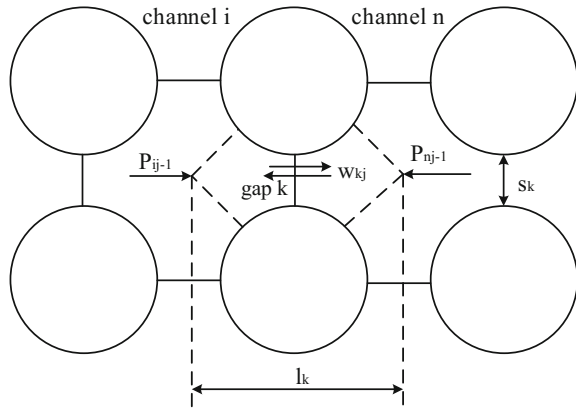


Fig. 2 Control volume for lateral momentum balance finite difference equation (*top view*)



Energy conservation equation:

$$\begin{aligned} & \frac{A_i}{\Delta t} \left[\rho''_{ij} (h_{ij} - h^n_{ij}) + h_{ij} (\rho_{ij} - \rho^n_{ij}) \right] + \frac{1}{\Delta X_j} (m_{ij} h^*_{ij} - m_{ij-1} h^*_{ij-1}) \\ & = \sum_{k \in i} e_{ik} w_{kj} h^*_{kj} + \sum_{r \in i} P_{ir} q''_{rj} - \sum_{k \in i} w'_{kj} (h_{ij} - h_{nj}) - \sum_{k \in i} C_k s_k (T_{ij} - T_{nj}) \end{aligned} \quad (2)$$

Axial momentum equation:

$$\begin{aligned} & \frac{\Delta X_j}{\Delta t} (m_{ij} - m^n_{ij}) + m_{ij} U'_{ij} - m_{ij-1} U'_{ij-1} + \Delta X_j \sum_{k \in i} e_{ik} w_{kj} U^*_{kj} = -A_i (P_{ij} - P_{ij-1}) \\ & - g A_i \Delta X_j \rho_{ij} \cos \theta - \frac{1}{2} \left(\frac{\Delta X_j f_{ij} \phi^2}{D_h \rho_{ij}} + K_{ij} v'^* + \left(\frac{1}{\rho_{ij}} - \frac{1}{\rho_{ij-1}} \right) \right) |m_{ij}| \frac{m_{ij}}{A_i} \\ & = -f_T \Delta X_j \sum_{k \in i} w'_{kj} (U'_{nj} - U'_{nj}) \end{aligned} \quad (3)$$

Lateral momentum equation:

$$\begin{aligned} & \frac{\Delta X_j}{\Delta t} (w_{kj} - w^n_{kj}) + \overline{U'_{kj}} w^*_{kj} - \overline{U'_{kj-1}} w^*_{kj-1} = \frac{s_k}{l_k} \Delta X_j P_{kj-1} \\ & - \frac{1}{2} \left(K_G \frac{\Delta X_j v'^*}{s_k l_k} \right)_{kj} |w_{kj}| w_{kj} \end{aligned} \quad (4)$$

where i and j are the subchannel indices; k denotes the gap between subchannel i and j ; the superscripts $*$ stands for donor cell; s_k and l_k are the gap thickness and the effective distance between two adjacent channels. The main unknowns in the above conservation equations are the enthalpies h_{ij} , the axial and lateral flow rates m_{ij} and w_{kj} , the pressure p_{ij} , and the void fractions α_{ij} .

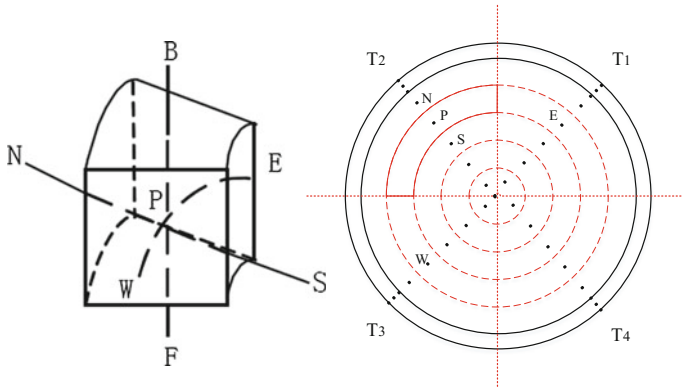


Fig. 3 Control volume for 3-D heat transfer equation

The heat flux q'' in the energy equation is calculated from heat transfer in the fuel rod by solving the following 3-D (radial-axial-azimuthal) conduction equation.

$$\rho c_p \frac{\partial T}{\partial t} = \frac{1}{r} \frac{\partial}{\partial r} \left(\lambda \cdot r \frac{\partial T}{\partial r} \right) + \frac{1}{r^2} \frac{\partial}{\partial \varphi} \left(\lambda \frac{\partial T}{\partial \varphi} \right) + \frac{\partial}{\partial z} \left(\lambda \frac{\partial T}{\partial z} \right) + S \quad (5)$$

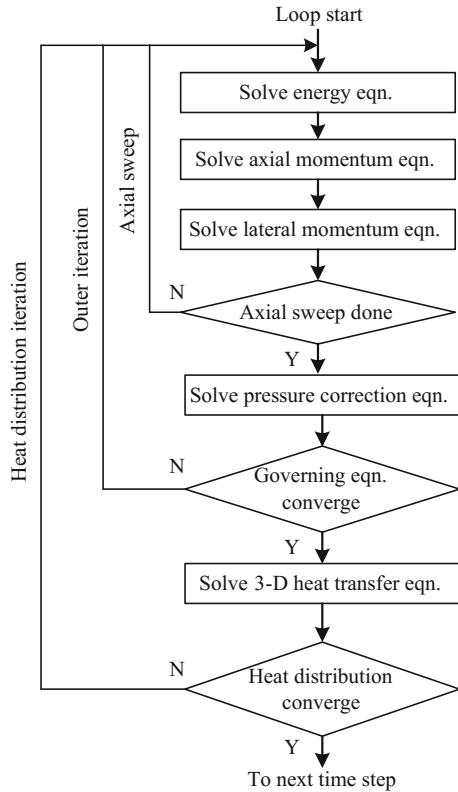
where ρ , c_p , and λ represent density, heat capacity, and thermal conductivity of control volume (see Fig. 3); S is the generalized source term.

2.2 Numerical Solution Methodology

The four coupled Eqs. (1)–(4) form a nonlinear system of algebraic equation and are solved iteratively with Newton–Raphson method. At each iteration, an axial sweep is performed from the inlet to the outlet. For each axial layer, the mixture enthalpies are calculated first from the energy conservation equation; then the volume temperatures and the mixture density can be updated. After that axial and lateral flow rates can be solved with a tentative pressure. Finally, the pressure correction equation (mass equation) is solved to get the pressure correction δP and update the tentative pressure and flow rates as follows:

$$\begin{aligned} P_{ij} &= \tilde{P}_{ij} + \delta P_{ij} \\ m_{ij} &= \tilde{m}_{ij} + \frac{\partial m_{ij}}{\partial P_{ij}} (\delta P_{ij} - \delta P_{ij-1}) \\ w_{kj} &= \tilde{w}_{kj} + \frac{\partial w_{kj}}{\partial P_{kj-1}} (\delta P_{ij-1} - \delta P_{lj-1}) \end{aligned} \quad (6)$$

Fig. 4 SUBSC calculation flow



where the top mark means the value at the end of previous iteration.

A flow diagram of the numerical process is shown in Fig. 4.

3 Validation of SUBSC

3.1 PWR Fuel Assembly Problem

SUBSC was first applied to calculate a quarter assembly whose geometry was shown in Fig. 5, and the geometry parameters were given in Table 1. The heat transfer model used was Dittus–Boelter correlation; $f = 0.184 \cdot Re^{-0.2}$ was chosen as single phase friction model. The coolant inlet mass flow rate was 11.124 kg/s, and the system pressure was 14.91 MPa.

Figure 6 shows coolant temperature along four typical channels. The results of SUBSC agree well with COBRA solution [3]. The similar trend is also observed for coolant mass flow and cross-flow rates given in Figs. 7 and 8. The code-to-code comparison indicated that SUBSC was developed correctly.

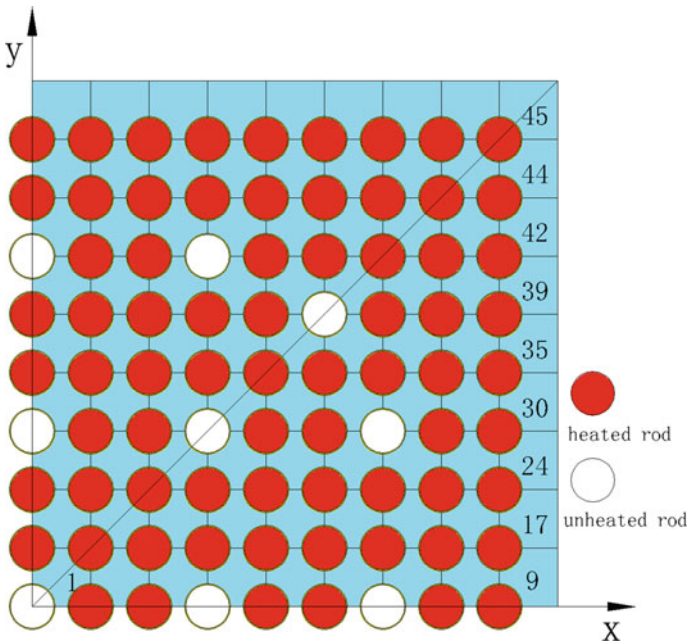


Fig. 5 PWR quarter fuel assembly

Table 1 Geometry parameters of PWR fuel assembly

Parameters	Value
Radial size	0.215 m
Vertical length	4.267 m
Number of fuel rods	265
Rod diameter	9.5×10^{-3} m
Rod pitch	1.194×10^{-2} m

3.2 *Supercritical Pressure Water Heat Transfer Experiment*

In order to verify SUBSC with more realistic measured data, an experimental test on heat transfer to supercritical water flowing upward in a seven-rod test bundle carried out by the Japanese Atomic Energy Agency (JAEA) was simulated in this part. Figure 9 shows the cross-sectional configuration of the seven-rod test bundle [4].

The simulated fuel rods were 8 mm in diameter with 1500 mm heated length and were loaded in a hexagonal array. The rods were heated uniformly in the axial direction by indirect-type electrical heat. Six sheathed thermocouples which were embedded into U-groove at the surface of the rod were used to measure the rod surface temperatures. The thermocouples were installed on surfaces which faced to

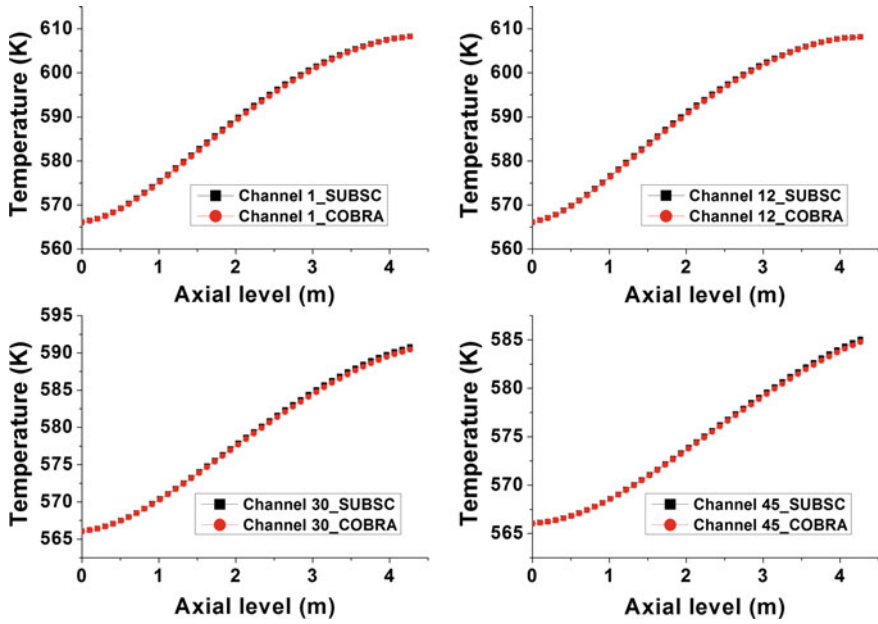


Fig. 6 Comparison of coolant temperature along typical channels

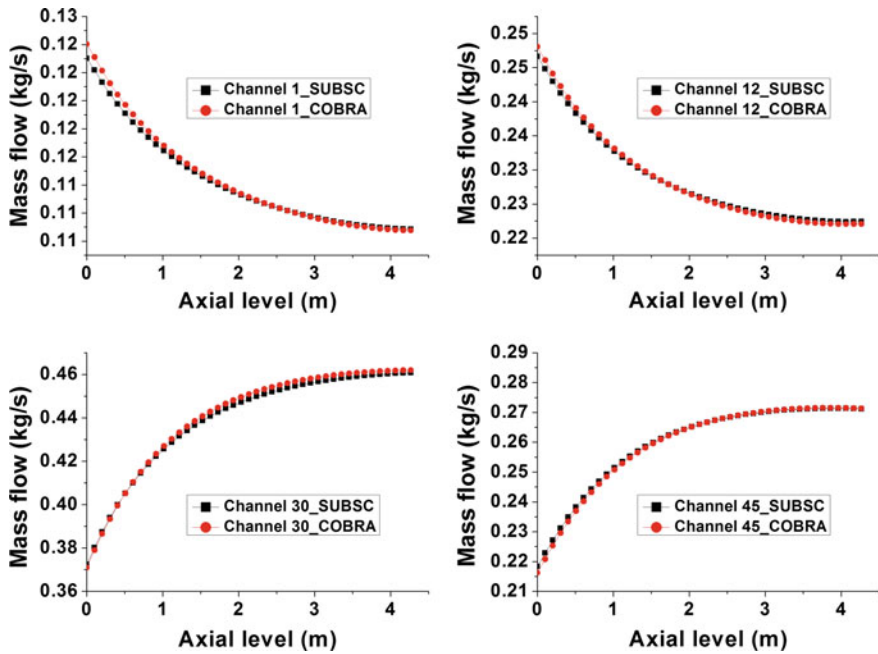


Fig. 7 Comparison of coolant mass flow rate along typical channels

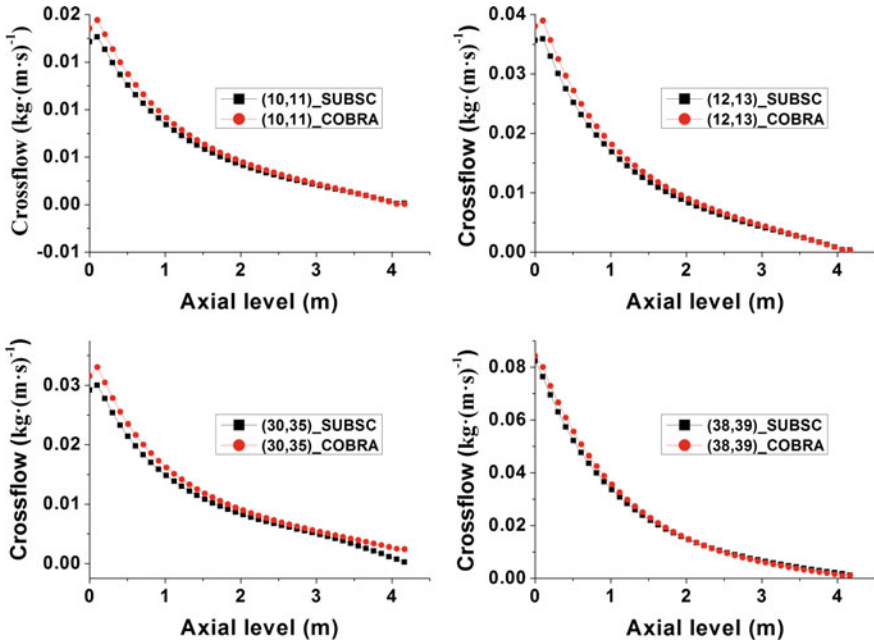
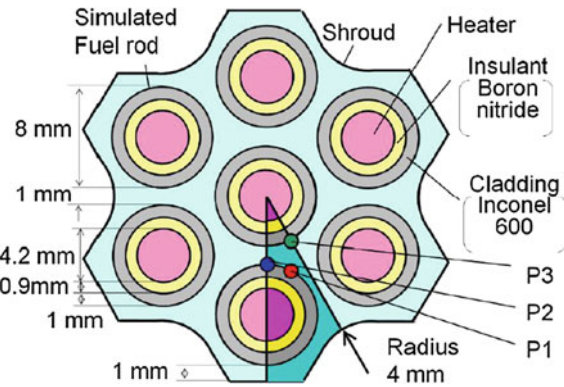


Fig. 8 Comparison of coolant mass cross-flow flow rate at typical gaps

Fig. 9 Cross-sectional configuration of the test section



the center of subchannels (P2 and P3) and on surfaces which faced to the narrowest area between the rods (P1). Figure 10 shows the locations of thermocouples.

Two different analyses including low inlet enthalpy and high inlet enthalpy conditions were performed. The major experiment conditions were summarized in Table 2. Dittus–Boelter heat transfer correlation was used.

Figure 11 shows the wall temperatures calculated using SUBSC together with experimental data and COBRA-TF-SC result for the low inlet enthalpy condition

Fig. 10 Locations of thermocouples

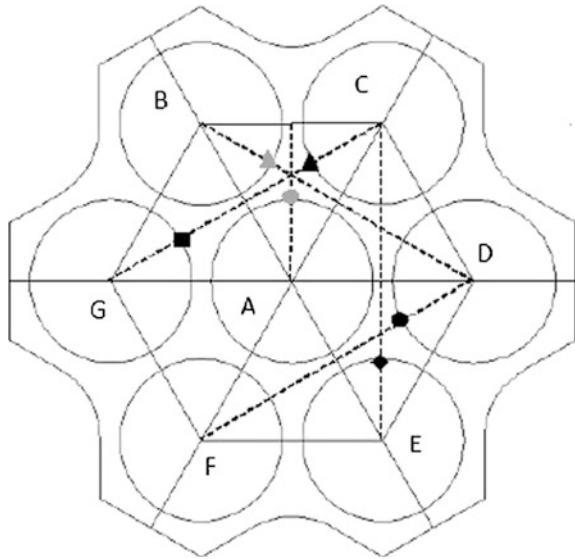


Table 2 Experiment conditions for the two cases

Analysis cases	Pressure/MPa	Mass velocity/kg/m ² s	Inlet enthalpy kJ/kg	Heat power per rod/kW
Low inlet	25	1448	357	20 (center rod) 23 (other rods)
High inlet	25	1412	1033	34

Fig. 11 Comparison of the rod surface temperature of low inlet enthalpy case

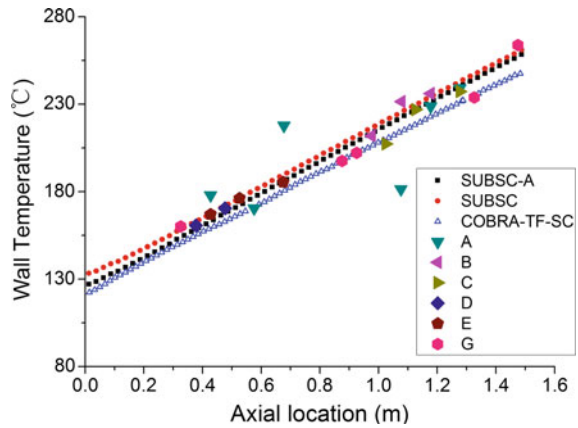
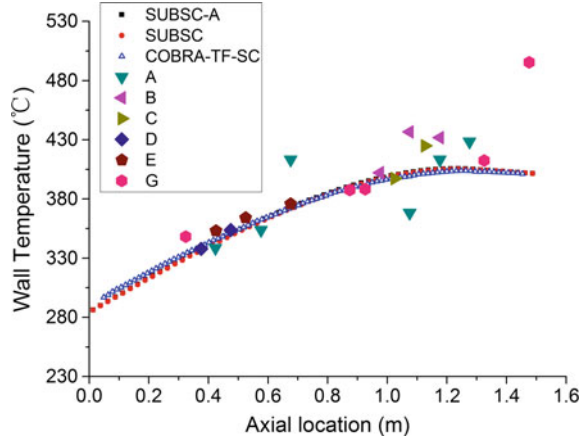


Fig. 12 Comparison of the rod surface temperature of high inlet enthalpy case



case. SUBSC-A represents the wall temperature of the rod A; SUBSC means the average wall temperature of all the rods except A. The points A–G are the measured values provided by JAEA.

Results predicted by SUBSC agree well with measurements. Also the results of SUBSC and COBRA-TF-SC are identical to each other. Because the heat power on the rod A is less than others, the wall temperature of the rod A is less than values of other rods.

Experimental data and numerical results for the high inlet enthalpy case were given in Fig. 12. Also the similar trend of the wall temperature was obtained for SUBSC and COBRA-TF-SC; both agree well with the experimental data in low fluid enthalpy region. However, the codes underestimated the experimental data as bulk enthalpy approached the pseudocritical enthalpy. This should due to the fact that Dittus–Boelter correlation is not adequate near the critical and pseudocritical points.

3.3 PSBT Steady State Bundle Benchmark

SUBSC is further verified with high-quality experimental data provided by PSBT benchmark. Table 3 gives an overview about the chosen three test bundle geometries (referenced as cases B5, B6, and B7) used in the present paper for thermal equilibrium quality simulations. B5 had a uniform axial power profile while B6 and B7 had a cosine profile. The central rod was replaced by a thimble rod with a diameter of 12.24 mm for the case B7. The radial power profile was described by 9 central rods having a relative power of 1.0 together with the boundary rods heated with a relative power of 0.85. Table 4 gives the range of boundary conditions for the above tests [5]. Important models of SUBSC code used for this benchmark were summarized in Table 5.

Table 3 Geometry of test bundles for quality measurements

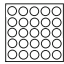
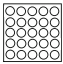

Case name	B5	B6	B7
Configuration			
Number of heated rods	25	25	24
Number of thimble rods	0	0	1
Rod pitch (mm)	12.6	12.6	12.6
Rod diameter (mm)	9.5	9.5	9.5
Guide tube diameter (mm)	–	–	12.4
Heated length (mm)	3658	3658	3658
Assembly inner width (mm)	64.9	64.9	64.9
Radial power shape	A	A	B
Axial power shape	Uniform	Cosine	Cosine
Mixing vane spacers	7	7	7
No mixing vane spacers	2	2	2
Simple spacers	8	8	8

Table 4 Boundary conditions for steady state bundle quality tests

Pressure range (bar)	48.13–165.78
Mass flux (kg/(m ² s))	555.56–4211.22
Power (kW)	972–3541
Inlet temperature (°C)	144–306.8

Table 5 SUBSC models for PSBT benchmark calculation

Parameters	Value
Rod conduction model	3-D conduction
Heat transfer correlation	Dittus-Bolter
Two-phase models	Homogeneous equilibrium
Hydraulic Resistance models	
Bundle friction factor	0.184 $Re^{-0.2}$
Cross-flow resistance factor	0.5
Spacer loss coefficient(MV/NMV/SS)	1.0/0.7/0.4

MV Mixing vane, *NMV* No mixing vane *SS* Simple spacer

The bundle-averaged thermal equilibrium quality based on the experimentally determined densities at three axial elevations: 2.216 m (lower), 2.669 m (middle), and 3.177 m (upper) was provided and used to validate SUBSC [6]. Figures 13, 14, and 15 show the comparison of the calculations with the measured quality at the

Fig. 13 Comparison of the calculated and measured thermal equilibrium quality at lower elevation

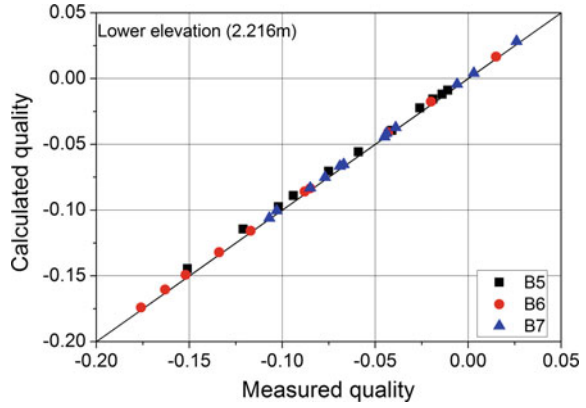


Fig. 14 Comparison of the calculated and measured thermal equilibrium quality at middle elevation

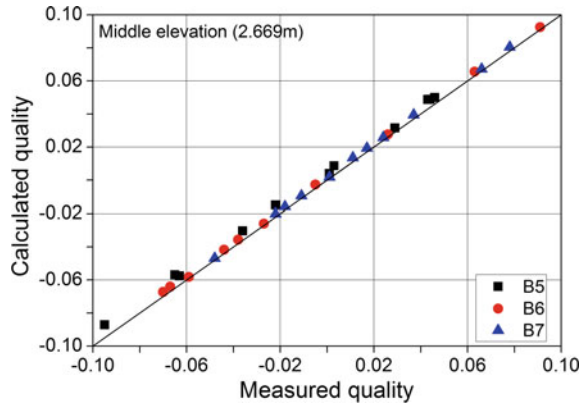


Fig. 15 Comparison of the calculated and measured thermal equilibrium quality at upper elevation

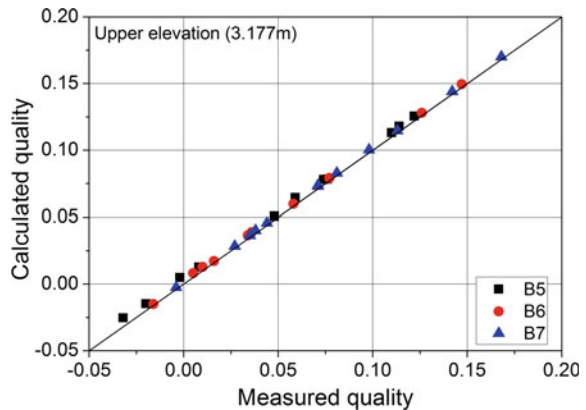


Table 6 Comparison of wall time between Gaussian elimination and GMRES method

Cases	Number of mesh cells	Original wall time (second)	Post-improvement wall time (second)
1/4 assembly	3402	13	13
Full assembly	13,608	122	66

three levels. SUBSC agree well with the measured data for all three cases at all elevations with the maximum error 0.007 at the middle elevation of case B5.

From the comparisons with COBRA and the high-quality experimental data for the PWR fuel assembly problem, the supercritical water heat transfer experiment and the PSBT steady state bundle benchmark, the feasibility, and accuracy of SUBSC were proven. The following part focused on the efficiency of the code.

4 Implementation of GMRES Iteration Solver

The pressure correction equation solved in SUBSC is a large matrix of size N by N , with N being the total number of control volumes. The equation was originally solved with Gaussian elimination method. This solver requires storage of full N by N matrix even though most of the coefficients are zero and is efficient only for small problems. For large, three-dimensional flow problems iterative solution methods are usually more efficient. Among the iterative methods, stationary ones such as Gauss-Seidel, successive over-relaxation is not efficient for solution of the linearized hydrodynamic equations, primarily because the coefficient matrix is weakly diagonally dominant [7]. In the last few decades, considerable research has been done on a more efficient non-stationary class of iteration method based on Krylov subspace including conjugate gradient method, Bi-CGSTAB, and GMRES. Because the rate of convergence of the Krylov method can be considerably increased by the use of a good preconditioner [8], a restarted GMRES algorithm with incomplete LU factorization preconditioner is implemented in SUBSC for solving the pressure correction equation. Table 6 presents the comparison of wall time observed between Gaussian elimination and GMRES method for two models. Both Gaussian elimination and GMRES method are efficient for small flow problems while the latter has much better performance dealing with large problems.

5 Conclusions

The object of the research here is to develop an in-house accurate and efficient subchannel code for thermal-hydraulic simulation application. The sufficient numerical results compared with COBRA and experiment data show the code was

successfully developed. The preconditioned GMRES algorithm was carried out to solve the pressure correction equation to reduce computational and memory burden. In order to further improve the performance of SUBSC and apply it to a full realistic PWR analysis, parallelization based on domain decomposition is on the way.

Acknowledgments This work is supported by National Natural Science Foundation of China (11522544).

References

1. X.J. Liu and X. Cheng, "Sub-channel/system coupled code development and its application to SCWR-FQT loop," *Nuclear Engineering and Design*, 285 (2015) 39–47.
2. U. Imke and V.H. Sanchez. "Validation of the subchannel code SUBCHANFLOW using the NUPEC PWR tests (PSBT)", *Science and Technology of Nuclear Installations*, 2012.
3. Stewart CW, Wheeler C, et al. COBRA-IV: The Model and Method, Pacific Northwest Labs, Richland, WA, USA, 1977.
4. Lokuliyana WD. Simulating SCWR thermal-hydraulics with the modified COBRA-TF subchannel code. MCMASTER UNIVERSITY, 2014.
5. A. Rubin, A. Schoedel, et al. OECD/NRC benchmark based on NUPEC PWR subchannel and bundle tests (PSBT), Volume I: Experimental database and final problem specifications. US NRC OECD Nuclear Energy Agency, 2010.
6. A. Rubin OECD/NRC benchmark based on NUPEC PWR subchannel and bundle tests (PSBT) – analysis using subchannel code CTF and system code TRACE. The Pennsylvania State University, 2011.
7. T.J. Downar and H.G. Joo, "A preconditioned Krylov method for solution of the multi-dimensional, two fluid hydrodynamics equations," *Annals of Nuclear Energy*, 28, 12, 2001.
8. Y. Saad. Iterative Method for Sparse Linear Systems, 2nd ed., Society for Industrial and Applied Mathematics, Philadelphia, 2003.

Wall Temperature Fluctuation Under Flow Pulsation in a Vertical Tube

Xin Liu, Sichao Tan, Hongsheng Yuan and Li Feng

Abstract Flow boiling has been receiving lots of attention and researches because it is commonly encountered in nuclear reactors and steam generators. Experimental studies on heat transfer in a circular tube with constant wall heat flux were carried out in laminar flow regime. The experiments were under steady and pulsating conditions and performed over a range of $<500 Re <2000$ and under atmospheric pressure. The wall temperature near inlet (T_{wl}) was investigated. The experiment results show that in a pulsation period, the wall temperature fluctuates periodically and has a sharp drop when the inlet pressure fluctuates intensely. The rise time of T_{wl} accounts for 80–85% of one pulsation period. The experiment results demonstrate that the pulsating period and amplitude have a strong influence on this phenomenon. The pulsating period and amplitude influence the shape of the wall temperature curve. Only when the fluid in the wave trough starts boiling, the phenomenon of sharp drop of wall temperature occurs, and a small wave trough appears in the rising of the wall temperature if the boiling time is long. Furthermore, the flow regime transition induced by buoyancy or the intense fluctuation of inlet pressure could be the reasons for a sharp drop of wall temperature.

Keywords Wall temperature · Pulsating flow · Heat transfer · Flow regime transition

1 Introduction

Pulsating flow occurs frequently in engineering flow, such as there working under ocean conditions, with periodic open–close of valves and where flow instabilities occur. In recent years, there has been a growing interest in the floating nuclear

X. Liu · S. Tan (✉) · H. Yuan · L. Feng
Fundamental Science on Nuclear Safety and Simulation
Technology Laboratory, College of Nuclear Science and Technology,
Harbin Engineering University, Harbin, Heilongjiang, China
e-mail: 15045693580@163.com

© Springer Science+Business Media Singapore 2017
H. Jiang (ed.), *Proceedings of The 20th Pacific Basin Nuclear Conference*,
DOI 10.1007/978-981-10-2314-9_69

757

power plant. However, such plants will suffer from periodic motions such as heaving, rolling and pitching, and periodic fluctuation of flow may arise. The periodic fluctuation of flow can induce the fluctuation of other thermal parameters such as wall temperature, and the fluctuation of wall temperature can imperil the safety operation of power appliance. So there have been lots of researches on the heat transfer characteristic of pulsating flow. Bergles [1, 2] conducted experiments on heat transfer characteristic on pulsating flow and showed that pulsation has an enhancement on heat transfer. Martinelli [3] performed experimental study on pulsating flow under Re between 1400–77,000 and the frequency of 0.22–4.4 Hz. The result shows that heat transfer coefficient under pulsation condition is nearly one time bigger than steady condition. Lemlich [4] studied the heat transfer characteristic of a 0.5 inch horizontal circular tube under Re between 2000–20,000 and the frequency of 1.5 Hz. They concluded that with the increasing of Re , the effect of pulsation on enhancing the heat transfer minished. Darling [5] used water and 50% glycerinum to study the heat transfer on pulsating flow. The experiment results indicate that when the flow is under turbulent condition, the effect of pulsating flow to heat transfer is different according to the location of the control value. When the flow is under laminar condition, the pulsating flow has no effect on heat transfer. Although many researches on pulsating heat transfer characteristics have been studied, an agreement cannot be reached at all.

As mentioned above, the wall temperature fluctuation in pulsating flow appears frequently in floating nuclear power plant, but the research on it is not enough. In this paper, the variation characteristic of temperature on heating wall is investigated, and the influencing factors of pulsation on it are also checked.

2 Experimental Apparatus and System Verification

The experimental apparatus consisted of major three parts: a main flow loop, a cooling system and a data acquisition system. Figure 1 shows a schematic of the whole experimental apparatus. By installing reservoir to keep the inlet working fluid at a constant temperature, the reservoir is composed of heating instrument and cooling tube, which are used to regulate the fluid temperature. The reservoir could also serve as a deaeration chamber to remove the dissolved gas. Distilled water is delivered to the test section by a gear pump, and with an actuating motor control, the pump can generate a continuously sinusoidal flow. Before going to the test section, distilled water pass through a line filter to remove solid particles that might cause damage to the turbine flowmeter. The test section is set vertically, and the water will go upward through the test section. After going through the test section, the water returns to the inlet reservoir.

The test section is a stainless steel pipe with the size of $\varnothing 8 \times 1$ mm and the heated length of 500 mm. The test section is directly heated by applying a DC current through two copper electrodes that were welded at the inlet and outlet. The locations

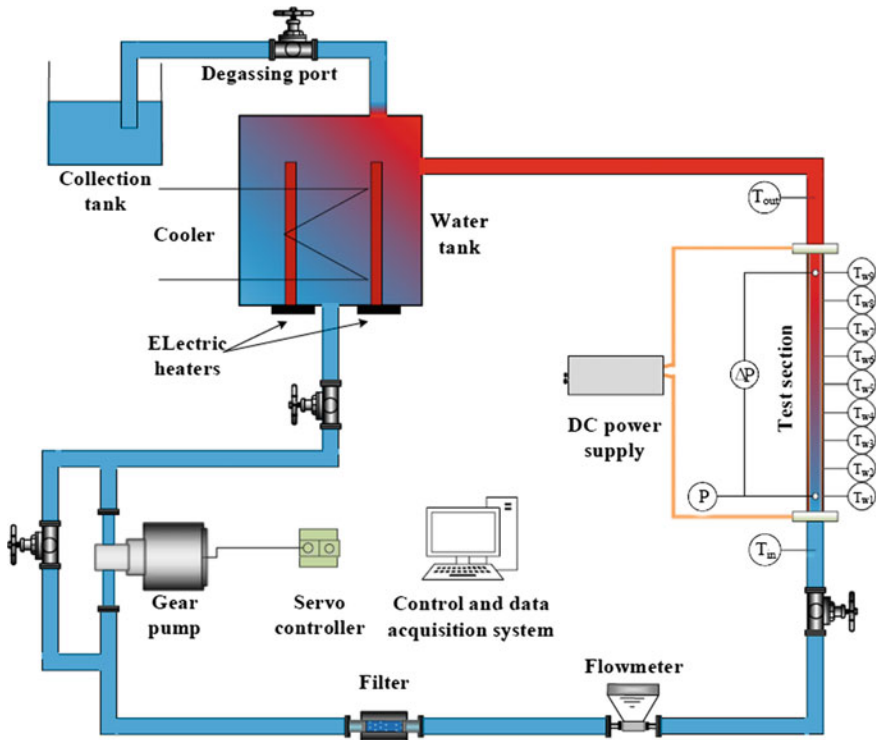


Fig. 1 Schematic of the test apparatus

of thermocouples to the inlet of the heating channel are as follows: 50, 100, 150, 200, 250, 300, 350, 400 and 450 mm. The location of the pressure tubes to the beginning of the heating channel are as follows: 50 and 450 mm.

The flow rate of the experimental loop is measured by a turbine flow meter installed in the downstream of the pump, and the turbine flow meter is made by Panasonic with an accuracy of $\pm 1\%$. The pressure drop is measured by the transducer which has the test span of -1.5 to 1 kPa and the accuracy up to 0.075% . The inlet pressure is measured by the pressure transducer with the test span of 5 – 1000 psia, and the accuracy is $\pm 0.08\%$. The inlet fluid temperature and the outer pipe surface temperatures are measured by T-type thermocouples with an accuracy of ± 0.3 °C.

There are three main parameters characterize a pulsating flow, namely pulsating period, pulsating amplitude and mean flow rate. In the present study, the system pressure is atmospheric pressure, and the mean flow rate keep constant, changing the pulsating period and amplitude to research the influence to the wall temperature. The range of the pulsating amplitude is 0.1 – 0.3 and the period of the pulsation is 5 – 30 s.

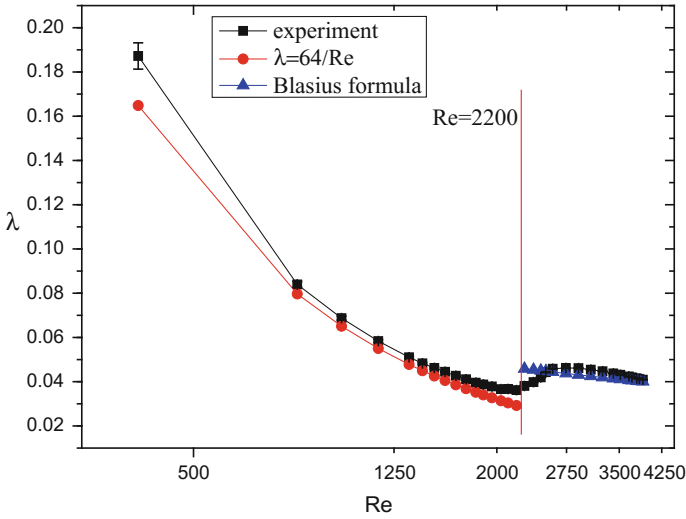


Fig. 2 Effect of Re on λ

To check the reliability of the experimental apparatus and the accuracy of the data acquisition systems, the adiabatic experiment and single phase heating experiment were carried, the results of the experiments are shown in Figs. 2 and 3, and the λ and the Nu in experiment are well correspond to the classical formula. So the experimental apparatus and the data acquisition systems are in good condition, and the data acquired in boiling experiment on the pulsating condition are credible.

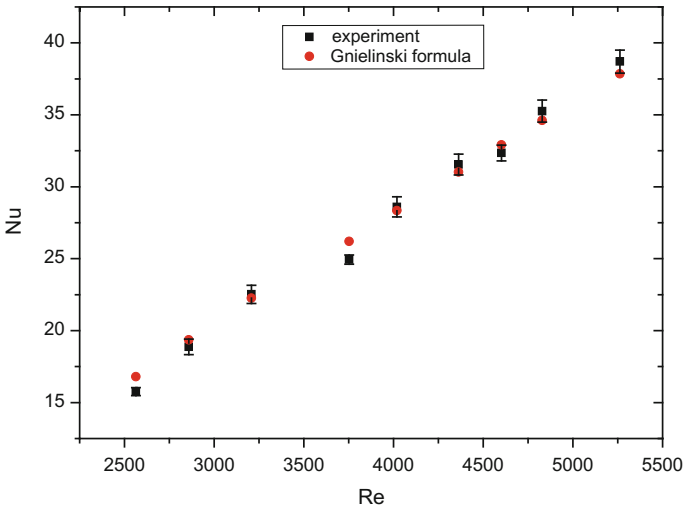


Fig. 3 Comparison on Nu between the experimental results of single phase heat transfer and the calculation results of Gnielinski

3 Results and Discussion

3.1 Experimental Phenomenon of Wall Temperature Under Pulsating Condition

In this experimental study, the system pressure is 0.1 MPa, the effect of pulsation on the variation of wall temperature is illustrated in Fig. 4. The average volume flow is 0.008 m³/h. The pulsating period (T) is 10 s, and the pulsating amplitude (A) is 0.24 ($A = D/M$, D means the D value between max value and mean value, M means the mean value). The average temperature of inlet water is 23.8 °C, and the heating power is 700.6 W. As shown in Fig. 4, the T_{w1} means the first temperature measuring point along the flow direction. During the rising time, the slope of T_{w1} firstly increased and then decreased, and T_{w1} has a sharp drop after the T_{w1} increased to a maximum. This phenomenon under the pulsating condition is called the sharp drop of wall temperature (SDW), and the ratio of sharp drop time to the period called α and under this pulsating condition α is 16%.

The fluctuation of T_{w1} with flow rate is shown in Fig. 5a, b. In one period, when time is in region1 ($27 \leq t \leq 27.5$ s), the flow rate is in a minimum range and T_{w1} rises gradually; when time is in region2 ($27.5 \leq t \leq 29$ s), T_{w1} has a large drop till to the lowest point of the wall temperature with the increasing of flow rate; when time is in region3 ($29 \leq t \leq 31.8$ s), the rising slope of T_{w1} decreases slowly with the increasing of flow rate; and when time is in region4 ($31.7 \leq t \leq 37$ s), the rising slope of T_{w1} increases with the decreasing of flow rate.

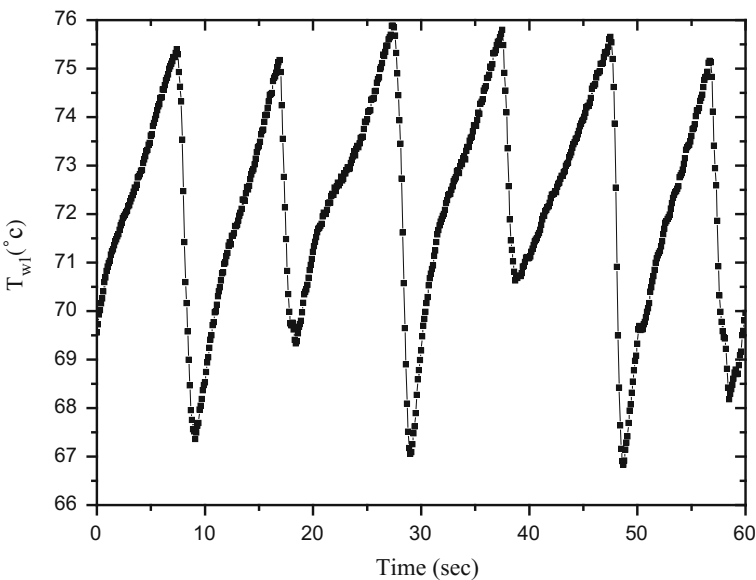


Fig. 4 Time variation of T_{w1}

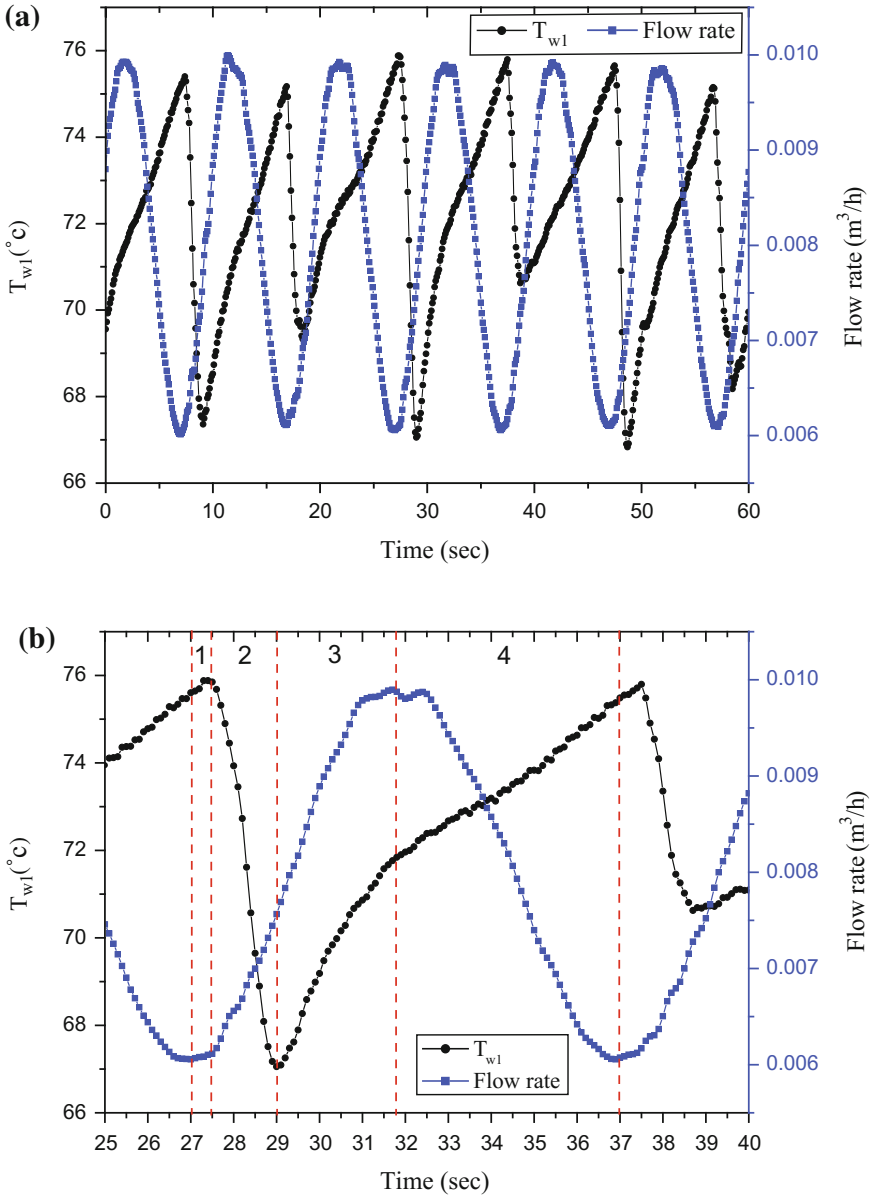


Fig. 5 Variation of the T_{wl} with the flow rate

The fluctuation of T_{wl} with the pressure drop in the test section is shown in Fig. 6. In the bottom of the flow rate, the pressure drop fluctuation becomes bigger suddenly, and T_{wl} has a suddenly drop when the pressure drop begin to fluctuate intensely.

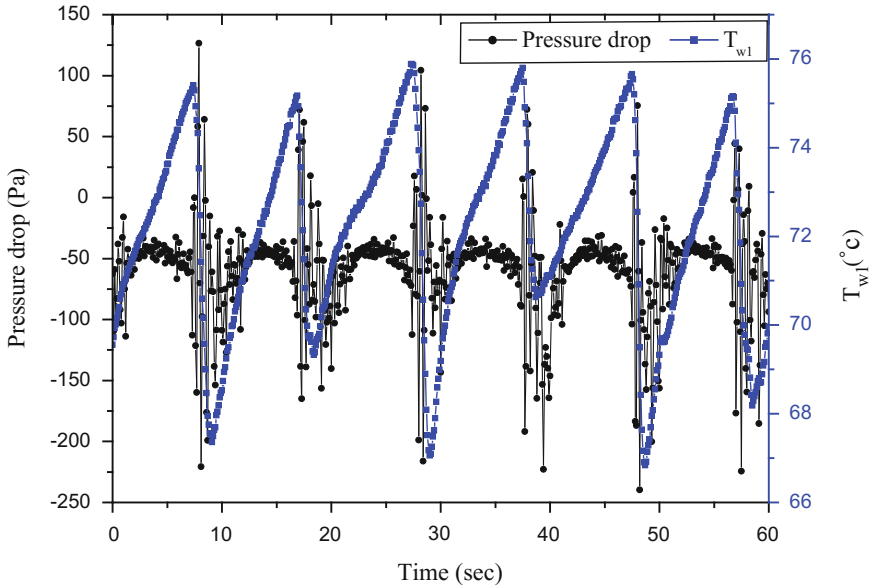


Fig. 6 Time variations of T_{wl} and pressure drop

3.2 Effect of the Pulsating Period

Figure. 7 shows the influence of pulsating period on the phenomenon of SDW, the range of the average flow rate is 0.00977–0.00987 m³/h, and the range of pulsating amplitude is 0.287–0.293. When the pulsating period is 10 s, the phenomenon of SDW happens. In one period, T_{wl} keeps on rising and then suddenly drops when the pressure drop fluctuates intensely, and α is 18.7%. When the pulsating period is 20 s, T_{wl} rises with the increasing of the flow rate and begins to decrease before flow rate reaches the maximum value, and after the flow rate decreases for a while, T_{wl} rises again till the flow rate drop to the lowest, and on the lowest of the flow rate, the pressure drop fluctuates intensely and T_{wl} drops suddenly. In one pulsating period, the ratio of the fluctuation magnitude of T_{wl} in its first declining to a whole period is β . In this pulsating condition, β is 13% and α is 4.62%. When the pulsating period is 30 s, the fluctuation of the T_{wl} is similar to the period of 20 s, but the magnitude of T_{wl} in its first declining is bigger than the magnitude on period of 30 s. β is 26.11% and α is 4.057%. Hence, the pulsating period mainly influences the fluctuation of wall temperature to the flow rate through the effect of wall thermal inertia. When the period is small, the variation of the surface wall temperature cannot response the flow rate timely, so in the top of the flow rate, the wall temperature keeps increasing all the time. When the period is longer, the time of the flow rate in the range of the top changes longer, and the wall temperature can response the change in the flow rate in a certain extent. When the period is small

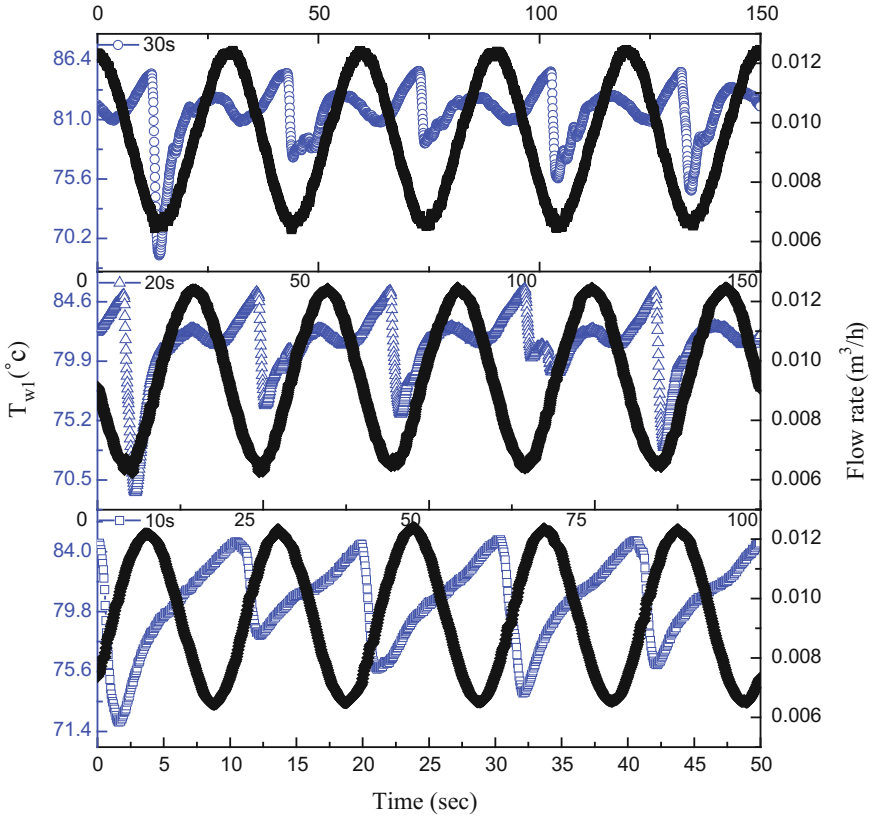


Fig. 7 Influence of pulsating period to SDW ($A = 0.3$)

enough, the wall temperature cannot response to the change in flow rate not at all, and the phenomenon of SDW cannot happen. As shown in Fig. 8, the influence of the pulsating period on the phenomenon of SDW, and when the period is 5 s, the wall temperature changes erratically and SDW cannot happen.

3.3 Effect of Pulsating Amplitude

Figure 9 shows the influence of pulsating amplitude on the phenomenon of SDW, the range of the average flow rate is from 0.00941–0.00987 m^3/h , and the pulsating period is 20 s. When the amplitude is 0.1, the phenomenon of SDW cannot happen. When the amplitude is 0.2, T_{wl} has a sudden drop as the fluctuation of pressure drop becomes fierce. But there is no fovea in the rising process of T_{wl} . When the amplitude is 0.3, both SDW and fovea in the rising process happen. From above experimental phenomenon, we can conclude that the influence of amplitude is

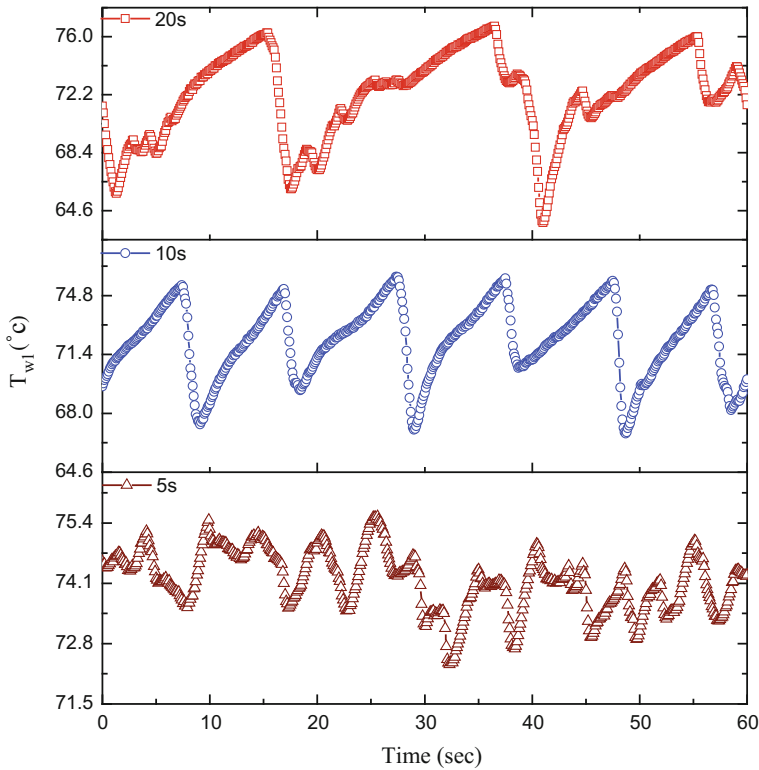


Fig. 8 The influence of the pulsating period on the phenomenon of SDW

similar to the period. The effect of the wall temperature response to flow rate is obvious at the large pulsating amplitude. And the amplitude is the key point that decides whether the phenomenon of SDW happens, as the amplitude decides the minimum of the flow rate. Boiling is a necessary factor to induce the phenomenon of SDW.

3.4 Analysis on the Experimental Phenomenon

As shown in Fig. 10, T_{wI} has a sharp drop just as the inlet pressure fluctuates intensely, and the amplitude of the pressure is between 65–85%. From the variation of the T_{wI} in Figs. 6 and 9, we can see that the sharp drop of the T_{wI} and the intense fluctuation of the pressure drop happen almost at the same time, so it can be concluded that subcooled boiling occurs in the outlet of the test section when the flow rate reaches the minimum, and the bubbles emerge and vanish that induce the pressure drop and inlet pressure fluctuate intensely. And then the intense fluctuation

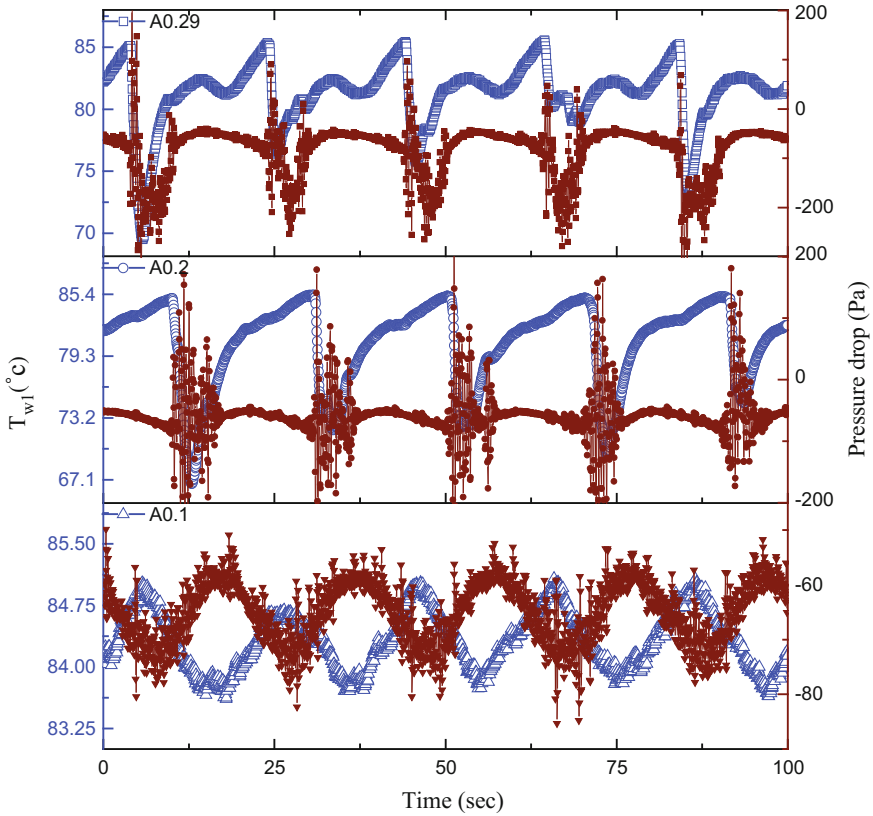


Fig. 9 Influence of pulsating amplitude to SDW ($T = 20$ s)

of the inlet pressure may induce the sharp drop of the wall temperature. According to the energy gradient theory of Dou [6–8], the theory stated that the total energy gradient in the transverse direction and in the streamwise direction of the main flow dominates the disturbance amplification or decay. It is stated that the energy gradient in transverse direction tries to amplify the small disturbance, while viscous friction in streamwise direction could resist or absorb this small disturbance. The initiation of instability depends upon the two roles for given initial disturbance. According to the research of Yuan [9], the intense fluctuation of the inlet pressure may reduce the laminar-turbulent transition Re . The intense fluctuation of the inlet pressure reduces the threshold of the energy gradient on the transition, so the flow state in the inlet turns to turbulence and the convective heat transfer coefficient has a sudden rise, and then inducing a sharp drop of the wall temperature. When the flow rate rises and the fluid in the outlet could not boil, the inlet pressure fluctuates gently, and the fluid in the inlet could be relaminarization. Ohmi [10] investigates the flow regime transition in pulsating condition. The analysis shows that transition from laminar to turbulence occurs in the decelerating phase of lower velocity and

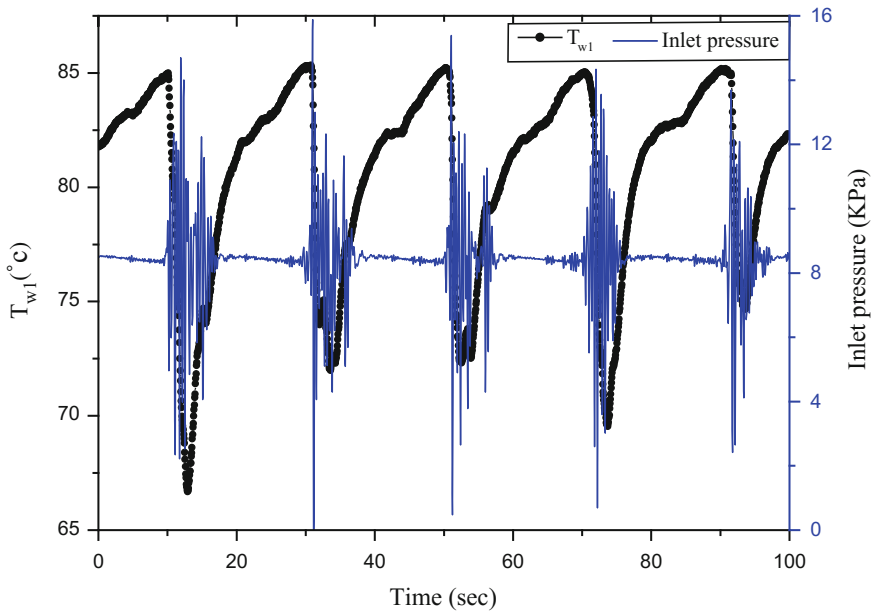


Fig. 10 Time variations of $T_{w,l}$ and inlet pressure

relaminarization occurs in the accelerating phase. The phenomenon of SDW may be induced both by the pressure disturbance and decelerating phase, as to other wall temperatures not occurs SDW the reason may be that the flow pattern is turbulence in the whole pulsating period downstream. Rouai [11] investigated the influence of buoyancy and flow transition in a vertical heated tube and found the large fluctuation in wall temperature. The explanation is that the effect of buoyancy cannot be neglected when the Re is lower. The fluctuation is believed to result from the creation and breaking up of a flow structure consisting of large scale buoyancy-induced turbulent eddies near the heated wall.

In order to investigate the reason for fluctuation of the wall temperature, the steady condition experiments have been investigated. The range of the flow rate in the steady condition is within a pulsating condition which occurs the phenomenon of SDW. As shown in Fig. 11, $T_{w,l}$ has a sharp decline when the flow rate is 0.01151 and 0.01129 m^3/h , and the Re is 1448 and 1454, respectively. According to Fewster's research [12], a transition will happen, caused by buoyancy, when Re arrives 1500 in the vertical circular tube flow with heat addition. When the flow changed from laminar into turbulence, local heat transfer coefficient will rise and then the wall temperature will decrease due to turbulence perturbation and combined mixing effects. When mass flow rate keeps increasing, the effects of buoyancy decreased, compared to fluid inertial effects, so that the transition phenomenon cannot happen, which caused the local heat transfer coefficient to decrease and wall temperature to increase.

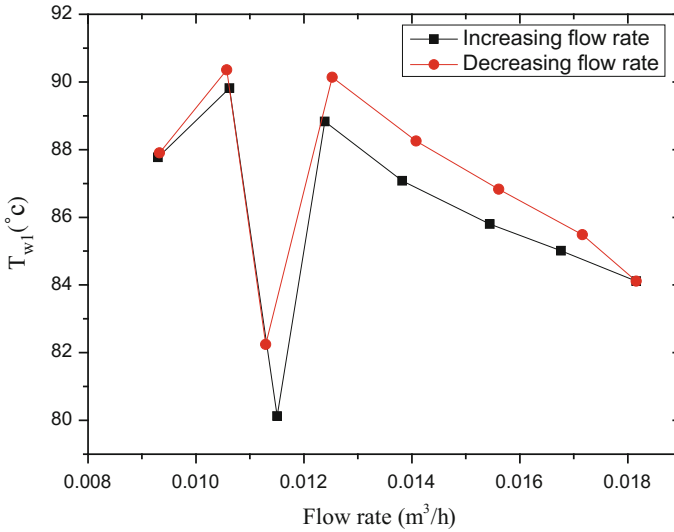


Fig. 11 Variation of the T_{wl} with the flow rate under steady condition

4 Conclusions

By researching the fluctuation of the wall temperature in the vertical pipe under pulsating condition, the following concluding remarks can be drawn:

- (1) In a pulsating period, when the pressure drop of the test section or the inlet pressure fluctuates intensely, the wall temperature near the inlet has a sharp drop and this phenomenon is called the sharp drop of wall temperature, and the sharp falling range of the wall temperature is between 5 and 18 °C under different pulsating conditions.
- (2) The pulsating amplitude and period mainly affect the fluctuation of wall temperature to the flow rate through the effect of the wall inertia, the bigger of the pulsating amplitude or period, the fovea in the rising phase of the wall temperature is more obvious. In addition, the pulsating amplitude decides whether the phenomenon of the SDW occurs.
- (3) It can be inferred that it is the transition from laminar to turbulent of the flow that induce the sharp drop of the wall temperature, and on the basis of the other researchers theory [6, 10, 11], the transition could be induced by the intense pressure disturbance, the effect of decelerating phase and buoyancy.

References

1. Bergles, A.E. Heat transfer enhancement—The encouragement and accommodation of high heat fluxes. *Journal of Heat Transfer*, 1997. **119**(1): p. 8–19.
2. Bergles, A.E. *Heat transfer enhancement—The maturing of second-generation heat transfer technology*. Heat Transfer Engineering, 1997. **18**(1): p. 47–55.
3. R.C.M.Martineli, L.M.B. S.Takahi, *Heat transfer to a Fluid Flowing Periodically at low Frequencies in a Vertical Tube*. SAME, 1943. **Vol.65**: p. P789–798.
4. R. Lemlich, *Vibration and Pulsation Boost Heat Transfer*. Scheming. May 15,1961: p. 171–176.
5. B. Darling, G. *Heat Transfer to liquids in intermittent flow*. Petroleum, May 1959: p. 177–180.
6. Dou, H.S. *Energy Gradient Theory of Hydrodynamic Instability*. Of National University Of Singapore, 2005.
7. Dou, H.S. *Mechanism of flow instability and transition to turbulence*. International Journal of Non-Linear Mechanics, 2006. **41**(4): p. 512–517.
8. Dou, H.-S, B.C. Khoo, and H.M. Tsai, *Determining the critical condition for turbulent transition in a full-developed annulus flow*. Journal of Petroleum Science and Engineering, 2010. **73**(1): p. 41–47.
9. 袁红胜, et al. 矩形通道内加减速条件下流态转换特性研究. 核动力工程, 2014(06): p. 162–166.
10. Ohmi, M, M. Iguchi, and I. Urahata, *Transition to Turbulence in a Pulsatile Pipe Flow Part I, Wave Forms and Distribution of Pulsatile Velocities near Transition Region*. Bulletin of Jsme, 1982. **25**(200): p. 182–189.
11. Rouai, N.M. *Influences of buoyancy and imposed flow transients on turbulent convective heat transfer in a tube*. University of Manchester, 1987.
12. Fewster, J. *Mixed forced and free convective heat transfer to supercritical pressure fluids flowing in vertical pipes*. 1976, The University of Manchester.

Author Biography

Liu Xin Fundamental Science on Nuclear Safety and Simulation Technology Laboratory, College of Nuclear Science and Technology, Harbin Engineering University, nuclear thermal-hydraulic under ocean condition.

Experimental Study on Natural Circulation Flow in Rectangular Channel Under Rolling

Jiangwen Wang, Puzhen Gao and Chong Chen

Abstract The characteristics of natural circulation flow under rolling motion in a narrow rectangular channel were studied experimentally. The test section in the experiment is a rectangular channel with 1100 mm long made of stainless steel, and the cross-sectional dimension is 2 mm \times 40 mm. And a direct current power supply is used to heat the rectangular channel. Distilled water is chosen to be the working fluid. The experimental facility is driven by a crank and rocker mechanism, and the mechanism is controlled by an electric motor. The rolling angles are 10°, 15°, 20°, and the rolling periods are 10, 15 and 20 s. Rolling influenced the flow in two ways. First, the changing of the position changed the driving force. Second, the additional force due to rolling caused additional pressure drop. From the results, it is found that the flow rate will fluctuate due to rolling motion. The frequency of the fluctuation is the same as the rolling frequency. The fluctuation of the flow is aggrandized with the enhanced rolling motion. But with the increase in the temperature at the inlet, the amplitude of the flow decreases. The experiment also shows that there is a reverse flow if the subcooling at the inlet and the amplitude of the fluctuation are large and the heat flux is low.

Keywords Natural circulation flow · Rectangular channel · Rolling motion

1 Introduction

After the accidents of Three Mile Island, Chernobyl and Fukushima, nuclear experts paid much attention on nuclear safety. Natural circulation is an important way to remove decay heat under accident. And it is an important way to keep a reactor in safe. However, natural circulation is excessively sensitivity to the operating conditions. The ocean condition, such as rolling, can change the effective

J. Wang · P. Gao (✉) · C. Chen

Fundamental Science on Nuclear Safety and Simulation Technology
Laboratory, Harbin Engineering University, Harbin, Heilongjiang, China
e-mail: gaopuzhen@hrbeu.edu.cn

height of the loop and introduce three acceleration, called tangential acceleration, centripetal acceleration and coriolis acceleration. The additional acceleration can be viewed as an additional driving force, and they can lead to some complex phenomena. In recent years, some investigations were conducted to analyze the characteristic of natural circulation under rolling motion condition.

Pang [1] established the fundamental theoretical model of nuclear power system under ocean condition. And then Gao [2] carried out some researches to find out the influence of rolling and pitching on natural circulation flow. Murata et al. [3] carried out many researches on a model reactor fixed on rolling facility. They found flow rate changed periodically with the change of rolling angle. And many researchers [4–6] also found the periodic changes of flow rate under rolling. Thereafter, Murata [7] conducted a series of studies about the characteristic of heat transfer. And the results show that the heat transfer is enhanced due to the internal flow and the heat transfer coefficient is the function of the Richardson number.

Yan [8] established a model of laminar flow under rolling motion and studied the pulsatile flow theoretically. They pointed out that the tangential force has a main impact on laminar flow and the centrifugal force has no affection. In the following study [9], they found the effect of coriolis force is too small to be ignored.

It can be seen from the above discussions that the research on natural circulation flow is limited due to the sensibility of the flow to the environment. And these studies mainly concentrate on round pipe. However, rectangular channel has compact structure and excellent ability of heat exchange, major application in nuclear industry. So more researches should be conducted to learn more about the characteristics of natural circulation flow in rectangular channel under rolling.

2 Experimental Apparatus

2.1 Test Loop

Figure 1 shows the experimental loop. The working liquid is distilled water. The test loop consists of a rectangular channel, a condenser, a pressurizer to maintain the pressure of the system, a flowmeter to measure the flow rate and a preheater to maintain the inlet water temperature.

The water is first heated in the preheater until the inlet water temperature reaches the desired value. And then it flows into the test section and heated continually. And next the heated working fluid will be cooled in the condenser. So finally the cool water returns to the preheater. Thus, a closed natural circulation is formed. The test section is a rectangular channel which is made of stainless steel with the cross-sectional dimension $2\text{ mm} \times 4\text{ mm}$ and 1100 mm long. A direct current power supply is used to heat the test section. For the rectangular channel, the thermocouples are placed at 125, 275, 475, 685, 825, 965, 1045 mm from the inlet. And the pressure drops from 175 to 875 mm and 875 to 1075 mm are measured, as shown in Fig. 2.

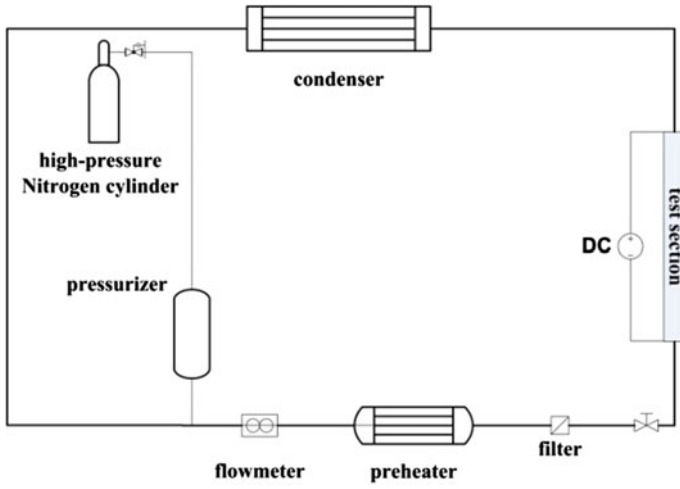
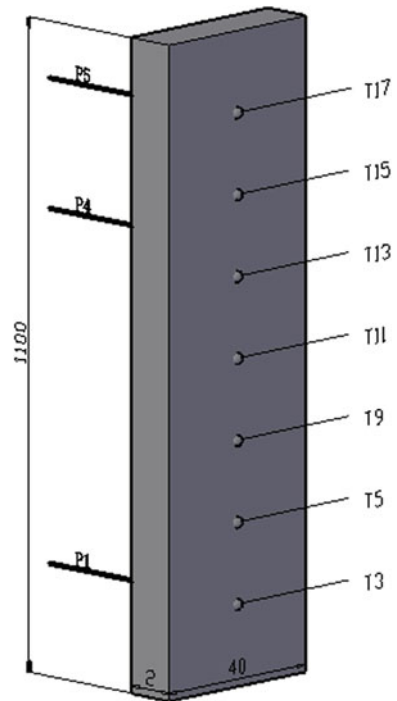


Fig. 1 Experimental loop

Fig. 2 Test section



2.2 Rolling Platform

The experimental facility is fixed on a platform which is driven by a crank and rocker mechanism, and it can roll periodically around an axis. The rolling can be controlled by an electric motor with a frequency converter through a gearbox, as shown in Fig. 3.

The range of the rolling angle can be changed by adjusting the length of the rocker and linkage. The rolling period can be changed by controlling the speed of the electric motor through the frequency converter. In this experiment, the rolling is in sine rule,

$$\theta = \theta_m \sin\left(\frac{2\pi t}{T}\right)$$

So the angular velocity and angular acceleration can be presented as

$$\omega = \frac{d\theta}{dt} = \theta_m \frac{2\pi}{T} \cos\left(\frac{2\pi t}{T}\right)$$

$$\beta = \frac{d\omega}{dt} = -\theta_m \left(\frac{2\pi}{T}\right)^2 \sin\left(\frac{2\pi t}{T}\right)$$

where θ is the momentary angle, rad. θ_m is the maximum angle, rad. ω is the angular velocity, rad/s. And β is the angular acceleration, rad/s². T is the period, s.

The range of the experimental parameters is: the system pressure from 0.1 to 0.3 MPa, the rolling angle 10°, 15°, 20°, the rolling periods 10, 15 and 20 s, the inlet subcooling 20–70 °C.

Prior to the study, a forced circulation was conducted to check the reliability of experimental data acquired from the experimental system. Figure 4 shows the results of the verification experiment.

Spiga [10] and Shah [11] presented the simplified theoretical equations to calculate the friction factor of laminar flow. And Leon [12] modified the Blasius equation to calculate the friction factor of turbulence flow taking the aspect ratio

Fig. 3 Rolling platform

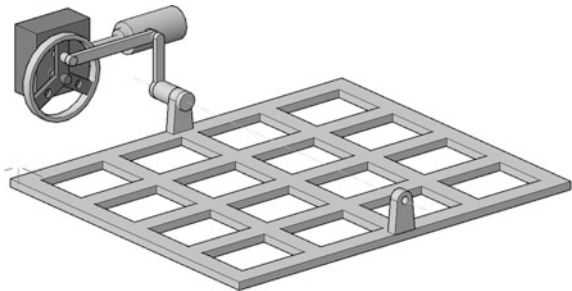
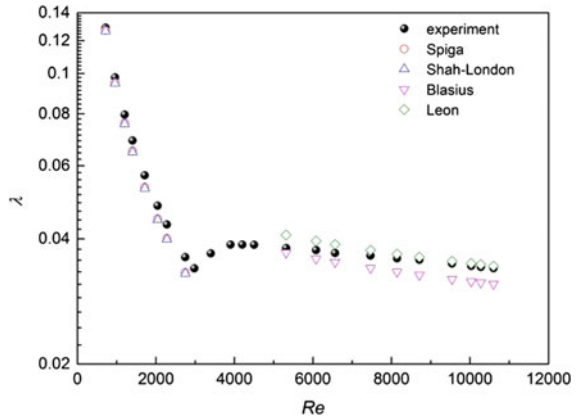
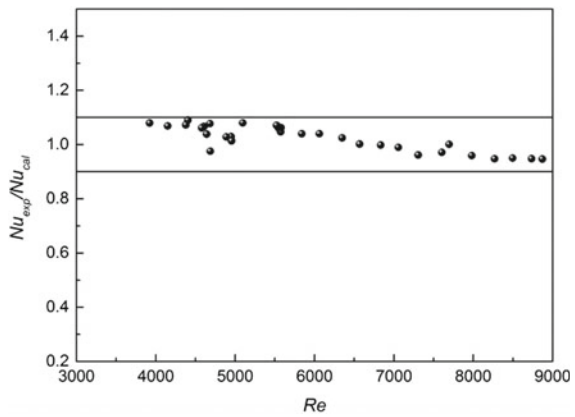


Fig. 4 Results of verification experiment



a. results of friction coefficient



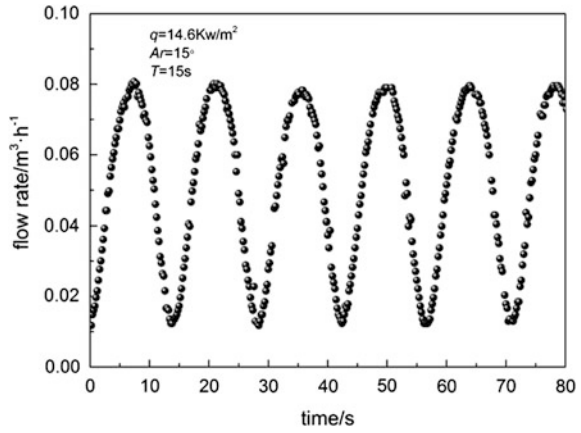
b. results of heat transfer

into account. In laminar flow, the experimental values closed to Spiga and Shah-London equations. In turbulence flow, the experimental values are bigger than Blasius predicted values but almost the same as the Leon values. The result agrees with Wang chang [13]. For the Nu number, the error between experimental value and calculated value by using Gnielinski equation was 10%. So the data acquisition system is reliable.

3 Phenomena Discussion

Figure 5 shows that when the apparatus is rolling, the flow is also changing as the same frequency of rolling.

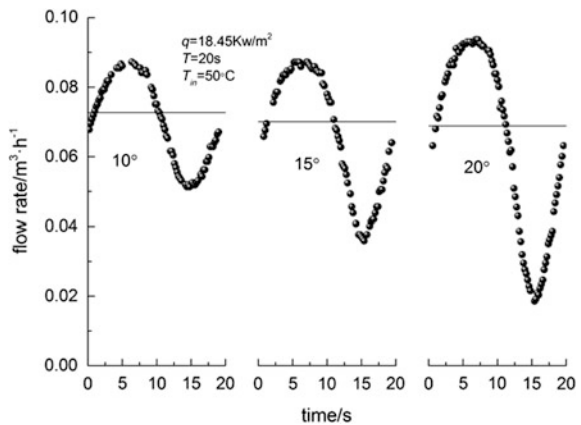
Fig. 5 Fluctuation of flow rate



3.1 Effect of Rolling Amplitude

Figure 6 shows the effect of rolling amplitude during a period. The horizontal line is the mean value. The fluctuation of volume flow rate enhanced and average value decreased with larger rolling angle under the same condition. First, the increase in the amplitude changes the tilt angle and driving head. It has a certain influence on the horizontal section. Second, the additional acceleration increased for increased rolling amplitude and caused more additional pressure drop. Rolling has a greater impact on the trough for small flow rate.

Fig. 6 Flow rate under different rolling amplitude



3.2 Effect of Rolling Period

As shown in Fig. 7, the rolling period influences the flow fluctuant amplitude and period. The horizontal line is the mean value during a period. The fluctuation of volume flow rate enhanced and the mean value decreased with the decrease of rolling period. Decreased period means larger additional acceleration, which can cause more additional pressure drop.

3.3 Effect of Inlet Temperature

Figures 8 and 9 show the effect of test section inlet temperature on flow rate and on the relative amplitude (the ratio of instantaneous rate and average rate). Higher inlet temperature means larger density difference in the loop and larger driving head. The integral density in the loop reduced causes the fluctuant amplitude of the additional pressure drop decreased. So, the effect of driving head is enhanced and the additional force is subdued. As a result, the average rate increased and the amplitude decreased.

3.4 Reverse Flow

It is found that there is a reverse flow, as shown in Fig. 10, if the amplitude of velocity is greater than the mean velocity, which destroys the steady temperature field and harmful to the safety of the reactor. The effective method to suppress it is enhancing the driving force to subdue the influence of additional force, such as increased the reactor power or increased rolling period, as shown in Figs. 11 and 12.

Fig. 7 Effect of rolling period on flow rate

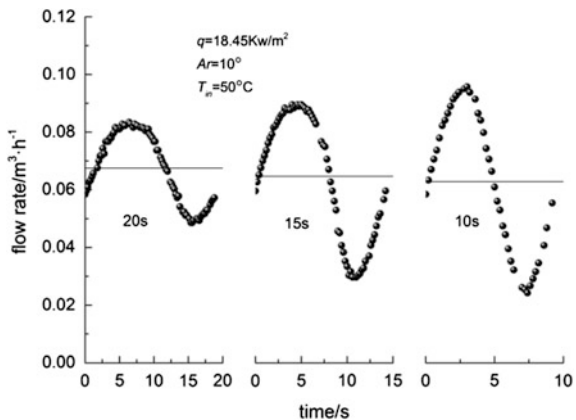


Fig. 8 Effect of inlet temperature on flow rate

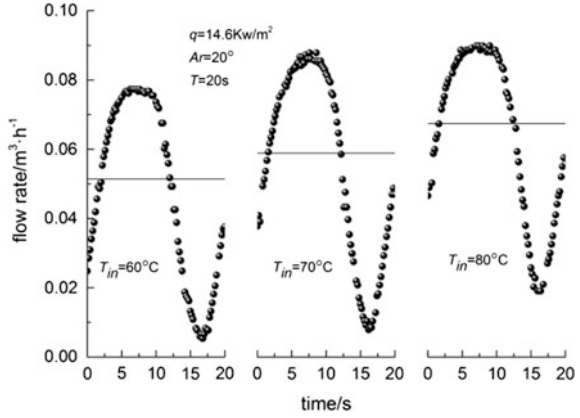


Fig. 9 Effect of inlet temperature on amplitude

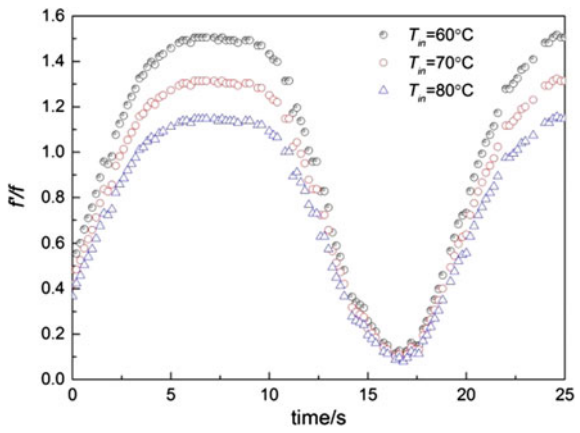


Fig. 10 Reverse flow and inlet temperature fluctuation

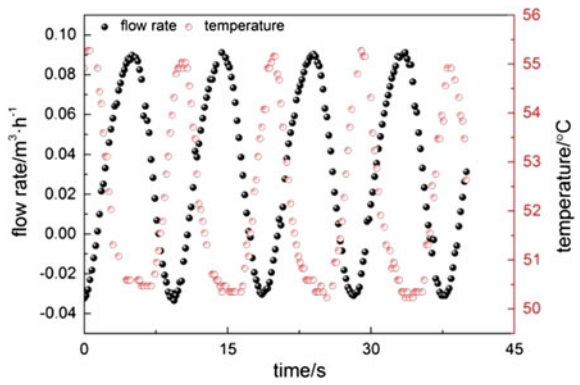


Fig. 11 Effect of power on reverse flow

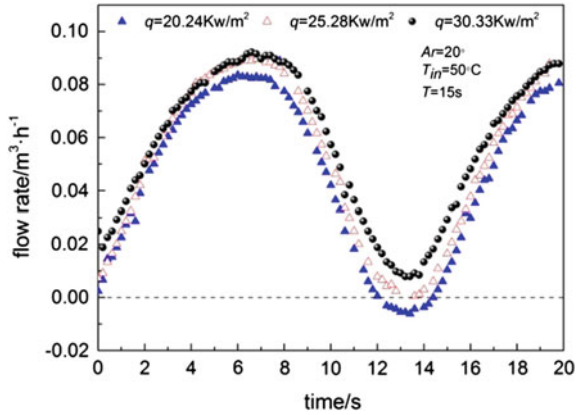
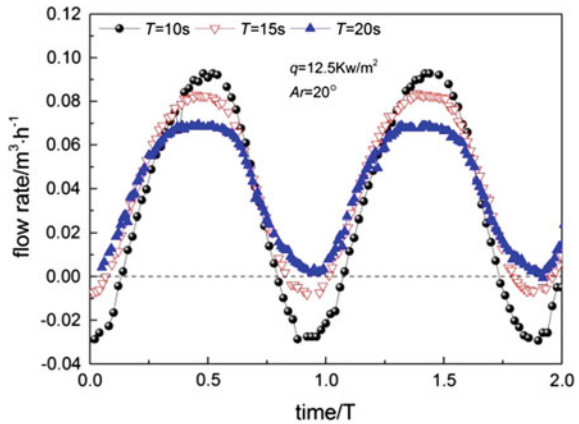


Fig. 12 Effect of rolling period on reverse flow



4 Conclusions

In this paper, the characteristics of natural circulation flow under rolling motion in a narrow rectangular channel were studied experimentally. The conclusions can be listed as those following:

1. Rolling motion can fluctuate the flow, and the changing period of the flow is the same as the rolling period.
2. The fluctuation of the flow is aggrandized with the enhanced rolling motion.
3. With the higher inlet water temperature, the amplitude of the flow is little.
4. A reverse flow will be formed for great additional force.

Acknowledgment This paper is funded by the International Exchange Program of Harbin Engineering University for Innovation-oriented Talents Cultivation.

References

1. Pang F.G., Gao P.Z., Wang Z.X. Theoretical research for effect of ocean conditions on natural circulation[J]. *Nuclear Power Engineering*, 1995, 16:330–335.
2. Gao P.Z., Liu S.L., Wang Z.X. Effects of pitching and rolling upon natural circulation[J]. *Nuclear Power Engineering*, 1999, 20:228–231.
3. Murata H., Iyori I., Kobayashi M. Natural circulation characteristics of a marine reactor in rolling motion[J]. *Nuclear Engineering and Design*, 1990, 118:141–154.
4. Tan S.C., Pang, F.G., Gao P.Z. Experimental study on the effect of rolling motion upon single-phase natural circulation[C]. 13th Int. Conf. Nuclear Engineering (ICONE-13), Beijing, China, Paper No. ICONE13-50094. 2005.
5. Tan S.C., Gao P.Z., 2007. Experimental and theoretical study on natural circulation capacity under rolling condition[C]. 15th Int. Conf. Nuclear Engineering(ICONE-15), Nagoya, Japan, Paper No. ICONE15-10120. 2007.
6. Tan S.C., Su G.H., Gao P.Z. Heat transfer model of single-phase natural circulation flow under a rolling motion condition[J]. *Nuclear Engineering and Design*, 2009, 239: 2212–2216.
7. Murata H., Sawada K., Kobayashi M. Natural circulation characteristics of a marine reactor in rolling motion and heat transfer in the core[J]. *Nuclear Engineering and Design*, 2002, 215: 69–85.
8. Yan B.H., Yu L., Yang Y.H. The model of laminar pulsatile flow in tubes in rolling motion[J]. *Nuclear Engineering and Design*, 2010, 240: 2805–2811.
9. Yan B.H., Yu L., Yang Y.H. Theoretical model of laminar flow in a channel or tube under ocean conditions[J]. *Energy Conversion Management*, 2011, 52: 2587–2597.
10. M. Spiga, G.L. Morini. A symmetric solution for velocity profile in laminar flow through rectangular ducts[C]. *International Communications in Heat and Mass Transfer*, 1994, Vol. 24 (4): 469–475.
11. Shah R.K., London A.L. *Laminar flow forced convection in ducts: a source book for compact heat exchanger analytical data*[M]. Academic press New York, 1978.
12. Troniewski L, Ulbrich R. Two-phase gas-liquid flow in rectangular channels[J]. *Chemical Engineering Science*, 1984, 39 (4): 751–765.
13. Wang chang. *Study of Flow and Heat Transfer in Rectangular Channel in Periodic Force Field*[D]. Harbin: Harbin Engineering University, 2013.

High-Heat-Flux Heat Removal Using a Porous-Micro-Channel

Junki Ohashi, Akihiro Tsukamoto, Koji Enoki and Tomio Okawa

Abstract To enable high-heat-flux heat removal from the heated surface, the performance of the method using a porous-micro-channel (a small channel containing a porous metal plate) as the flow channel of coolant was investigated experimentally. The main experimental parameters were the channel size, mass flux and liquid subcooling. It was shown that the nucleate boiling heat transfer is enhanced if the porous plate is placed in the flow channel. It was also found that the micro-bubble emission boiling (MEB) takes place even in the porous-micro-channel if the mass flux and liquid subcooling are high enough. In addition, the flow oscillation that was frequently encountered in the normal channel containing no porous plate did not occur in the porous-micro-channel within the experimental conditions tested in this work. It was considered that the porous-micro-channel is useful to ensure high-heat-flux heat removal without significant flow oscillation.

Keywords Heat transfer enhancement · Boiling heat transfer · Porous-micro-channel · Critical heat flux · Micro-bubble emission boiling · Frictional pressure loss · Flow oscillation

J. Ohashi (✉) · A. Tsukamoto · K. Enoki · T. Okawa
Department of Mechanical Engineering and Intelligent Systems,
The University of Electro-Communications, Chofu-shi, Tokyo, Japan
e-mail: ohashi@eel.mi.uec.ac.jp

A. Tsukamoto
e-mail: tsukamoto@eel.mi.uec.ac.jp

K. Enoki
e-mail: enoki.koji@uec.ac.jp

T. Okawa
e-mail: okawa.tomio@uec.ac.jp

1 Introduction

High-heat-flux heat removal is one of the key technologies in the development of the nuclear fusion reactors, since the diverter and the first wall in the fusion reactor experience significantly high heat flux over 10 MW/m^2 during normal operation. In addition, the development of the method to ensure high-heat-flux heat removal is requested also for the cooling of high-power-density electronic devices such as the high-performance CPU and the inverter for the electric vehicle and fuel cell vehicle.

One of the most promising heat removal methods would be the one using the micro-bubble emission boiling (MEB). In MEB, numerous tiny bubbles are produced on the heated surface to achieve very high value of critical heat flux (CHF) greater than 14 MW/m^2 [1]. Several sophisticated ideas have been reported to apply MEB to large heated surfaces [2]. However, the detailed mechanisms to cause MEB and the thermal-hydraulic conditions under which MEB takes place have not sufficiently been elucidated.

Hanzawa and Okawa [3] conducted the experiments of flow boiling using the porous-micro-channel (the small rectangular channel containing a porous metal plate) as the test section. They reported that the MEB took place even in the porous-micro-channel and the CHF was enhanced in several experimental conditions. It is hence considered that the use of the porous-micro-channel is a promising method to achieve high-heat-flux heat removal. In view of this, using the channel size, mass flux and liquid subcooling as the main experimental parameters, the boiling heat transfer in the porous-micro-channel is explored in the present work.

2 Experimental Descriptions

2.1 Test Section

The test section is schematically shown in Fig. 1. The end face of a copper block containing cartridge heaters was used as the heated surface. The heated surface was circular in shape and 9 mm in diameter. It was bonded smoothly with the stainless steel plate by means of electron beam welding to construct the bottom face of the flow channel. The two type-K thermocouples were embedded in the copper block to calculate the wall heat flux q and the wall superheat ΔT_{sat} . A transparent polycarbonate jig was placed on the stainless steel plate to construct the rectangular flow channel. The flow channel was 11 or 16 mm in width, 2 mm in height and 70 mm in length. To investigate the effect of the porous-micro-channel on the heat transfer characteristics, the porous plate made of nickel called MF-20 was placed in the flow channel. The photograph of MF-20 is depicted in Fig. 2. The size of the porous plate was the same as that of the flow channel.

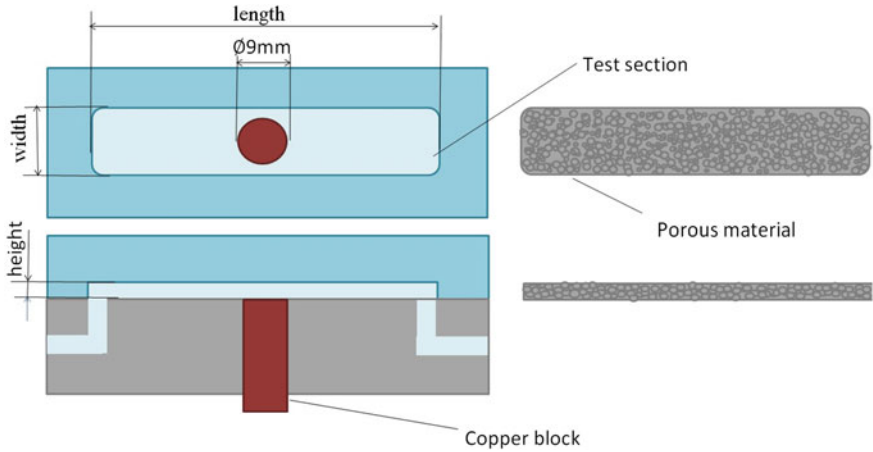


Fig. 1 Schematic diagram of the test section

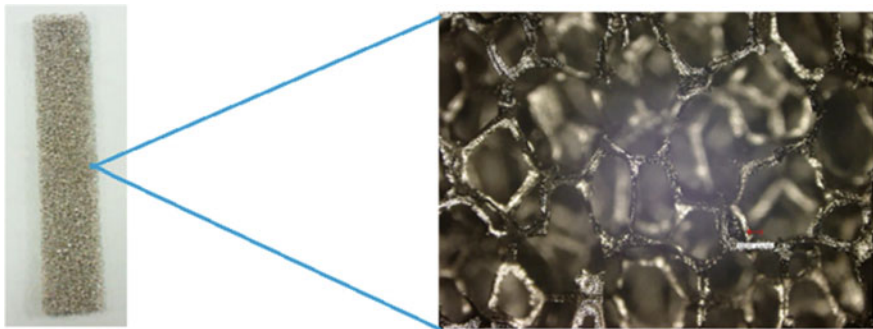


Fig. 2 Photograph of the porous plate (MF-20)

2.2 Experimental Procedure

Filtrated tap water was used as the test fluid.

After adjusting the inlet subcooling ΔT_{sub} and the mass flux G at desired values, the power applied to the cartridge heaters in the copper block was increased step by step. The values of q and ΔT_{sat} to draw the boiling curves were calculated when the equilibrium state was reached after the stepwise increase in the heater power. When q was too high and ΔT_{sat} continued to rise, it was judged that the CHF condition was reached and the experiment was completed immediately. It is noted that the experiment was completed also when the copper block temperature exceeded 700°C or ΔT_{sat} exceeded 100 K to avoid the damage of the experimental apparatus.

Table 1 Main experimental conditions

Parameter	Range
Flow channel	Normal, porous-micro
L_{wide} (mm)	11 (narrow), 16 (wide)
G (kg/m ² s)	100, 200, 400
ΔT_{sub} (K)	20, 30, 40

2.3 Experimental Conditions

Main experimental conditions are summarized in Table 1. Here, the normal and porous-micro channels denote the flow channels containing no porous material and MF-20, respectively. We also focused on the channel width relative to the size of the heated surface. Since the heated surface was 9 mm in diameter, the channel width L_{wide} was comparable for the narrow channel (11 mm) while greater to some extent for the wide channel (16 mm). The values of G and ΔT_{sub} were set within 100–400 kg/m² s and 20–40 K, respectively.

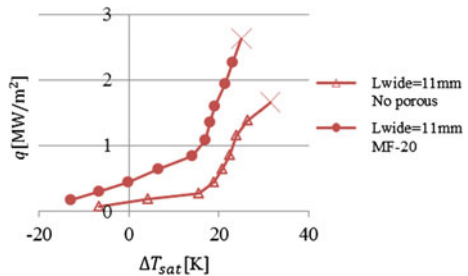
3 Experimental Results

3.1 Boiling Curves (Effects of the Experimental Parameters on the Heat Transfer Characteristics)

In the boiling curves shown below, the data corresponding to CHF are indicated with the cross symbols (×) and the symbols filled with the black color are used when the CHF was not reached.

First, Fig. 3 compares the boiling curves for the normal and porous-micro-channels under the condition of $L_{wide} = 11$ mm, $G = 400$ kg/m² s and $\Delta T_{sub} = 30$ K. In these cases, the slope of the boiling curve became steeper when the nucleate boiling was incepted and then the CHF condition was reached. The heat transfer coefficient is always higher, and the CHF is also higher for the porous-micro-channel. In the porous-micro-channel, the flow field should be much

Fig. 3 Comparisons of the boiling curves measured for the normal channel and the porous-micro-channel ($L_{wide} = 11$ mm, $G = 400$ kg/m² s and $\Delta T_{sub} = 30$ K); the cross symbols correspond to the data of CHF



more complicated than that in the normal channel. The heat transfer enhancement found in Fig. 3 may hence be attributed to the complicated flow field formed in the porous-micro-channel.

The effect of ΔT_{sub} in the porous-micro-channel was explored under the condition of $L_{wide} = 16$ mm and $G = 400$ kg/m² s. The measured boiling curves are delineated in Fig. 4. For $\Delta T_{sub} = 20$ K, the boiling state moved directly from nucleate boiling to CHF. For $\Delta T_{sub} = 30$ and 40 K, however, a noticeable increase in the wall superheat ΔT_{sat} is found. In particular, the increase in ΔT_{sat} leads to significant increase in CHF when $\Delta T_{sub} = 40$ K. From the shape of boiling curves, it is considered that MEB occurred to increase CHF when ΔT_{sat} was high enough.

The effect of the mass flux G under the condition of $L_{wide} = 16$ mm and $\Delta T_{sub} = 30$ K is explored in Fig. 5. At the low mass flux of $G = 100$ kg/m² s, the boiling state moved directly to the CHF, while at the higher mass fluxes of $G = 200$ and 400 kg/m² s, it can be seen that the value of ΔT_{sat} increased noticeably before the CHF condition was reached. This is also considered as the sign of the occurrence of MEB. It can hence be said that the MEB is more likely to occur when the mass flux is high even in the porous-micro-channel.

Fig. 4 Effect of the inlet subcooling ΔT_{sub} on the boiling curves measured for the porous-micro-channel ($L_{wide} = 16$ mm and $G = 400$ kg/m² s)

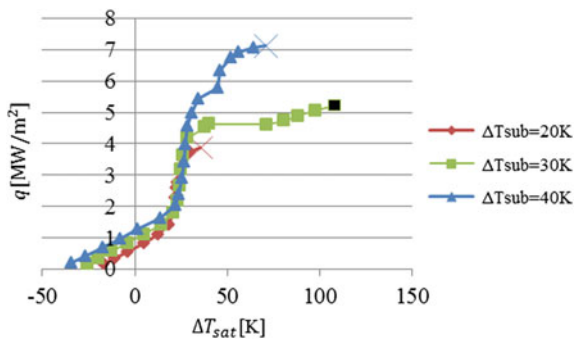


Fig. 5 Effect of the mass flux G on the boiling curves measured for the porous-micro-channel ($L_{wide} = 16$ mm and $\Delta T_{sub} = 30$ K)

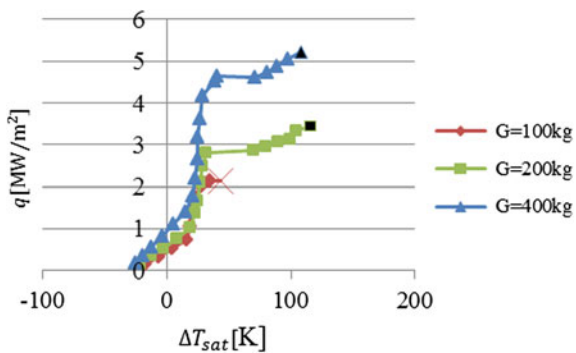
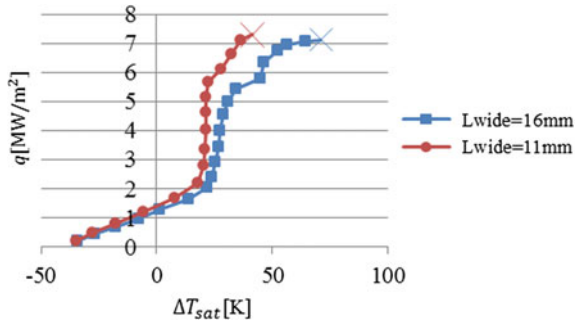


Fig. 6 Effect of the channel width L_{wide} on the boiling curves measured for the porous-micro-channel ($G = 400 \text{ kg/m}^2 \text{ s}$ and $\Delta T_{\text{sub}} = 40 \text{ K}$)



Finally, the effect of the channel width L_{wide} under the condition of $G = 400 \text{ kg/m}^2 \text{ s}$ and $\Delta T_{\text{sub}} = 40 \text{ K}$ is presented in Fig. 6. It can be seen that the values of CHF are in the similar range, but the heat transfer coefficient is higher in the narrow channel. In the wide channel, the subcooled liquid may flow in the regions between the heated surface and the channel side walls. On the other hand, in the narrow channel, the subcooled liquid is more forced to be conveyed to the heated surface since the gap distance between the heated surface and the side walls is small. It is considered that the heat transfer was enhanced since the subcooled liquid was supplied to the heated surface more efficiently in the narrow channel.

As shown in the boiling curves presented above, MEB usually occurred when ΔT_{sub} was equal to or higher than 30 K and G was equal to or higher than $200 \text{ kg/m}^2 \text{ s}$. Further studies are considered necessary, but the condition for MEB to occur was not noticeably different between the normal channels and the porous-micro-channels in the experimental setup tested in this work. It was also found that the boiling heat transfer after the onset of MEB was higher in the narrow channel than in the wide channel.

3.2 Flow Patterns

In both the normal and the porous-micro-channels, if the value of q was sufficiently low, the flow pattern in the test section was the single-phase liquid flow or the small-bubble flow and the flow was stable. However, as schematically shown in Fig. 7, the flow pattern transition when the heat flux was further increased was considerably different between the two flow channels.

First, in the normal channel, the flow pattern always varied from the small-bubble flow to the large-bubble flow when the heat flux was high enough. The time-elapsd images of the large-bubble flow are depicted in Fig. 8. In this flow pattern, large bubbles occupying the whole channel cross section were produced at the heated surface periodically. As shown in Fig. 8, the bubbles were extended not only in the direction downstream of the heated surface but also upstream. As can be expected from the figure, the flow was intermittent and unstable in the large-bubble

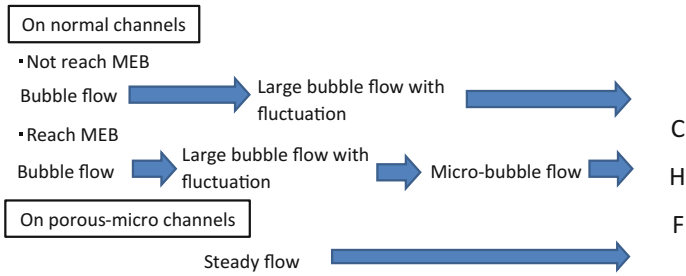


Fig. 7 Flow pattern transition with an increase in the heat flux before reaching the CHF condition

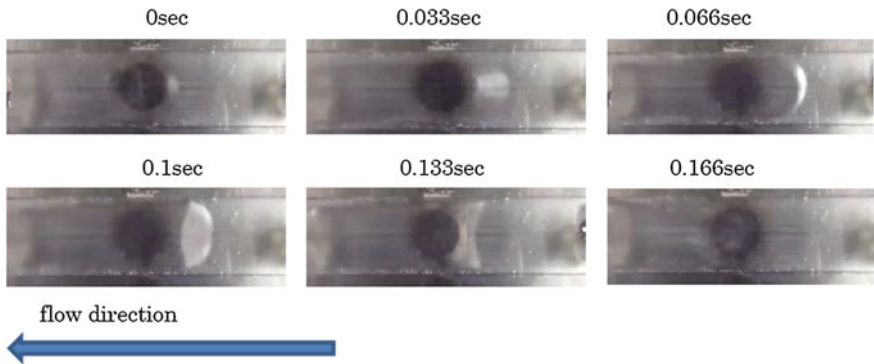


Fig. 8 Time-elased images of the large-bubble flow in the normal channel ($G = 100 \text{ kg/m}^2 \text{ s}$, $\Delta T_{\text{sub}} = 20 \text{ K}$, $q = 1.55 \text{ W/m}^2$)

flow and the oscillation of the pressure loss was intensified significantly. When the liquid subcooling ΔT_{sub} and/or the mass flux G was not high enough, further increase in q led to the flow pattern transition from the large-bubble flow to the film boiling flow and the CHF condition was reached, while when ΔT_{sub} and G were sufficiently high, the flow pattern varied from the large-bubble flow to MEB flow before reaching the CHF condition. The time-elased images of MEB flow are presented in Fig. 9. The bubbles are not clearly seen in the figure, and numerous tiny bubbles were produced at the heated surface in this condition. If q was further increased, ΔT_{sat} continued to increase and the CHF condition was eventually reached. Another notable observation in the normal channel was the generation of significant noise during the large-bubble flow and the MEB flow. It is considered that this noise was associated with the pressure wave produced when the bubbles were condensed in the subcooled liquid. It is concerned that the pressure wave produced in the large-bubble flow and the MEB flow may induce the damage of the channel wall as in the case of cavitation [4].

Next, in the porous-micro-channel, the large-bubble flow was not observed and the flow was fairly stable under all the experimental conditions tested in this work.

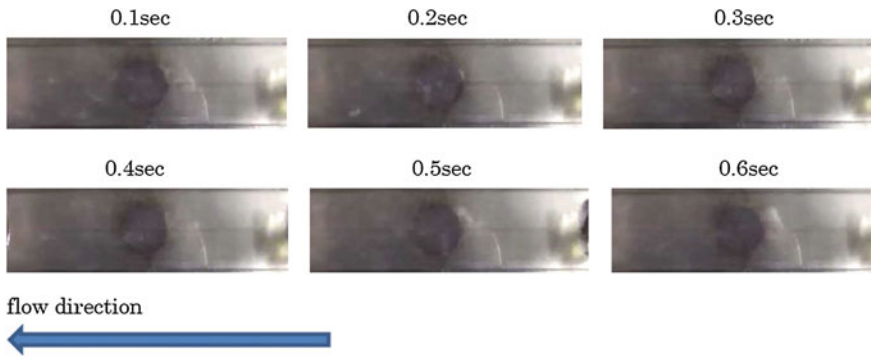


Fig. 9 Time-elased images of MEB in the normal channel ($G = 400 \text{ kg/m}^2 \text{ s}$, $\Delta T_{\text{sub}} = 30 \text{ K}$, $q = 5.77 \text{ W/m}^2$)

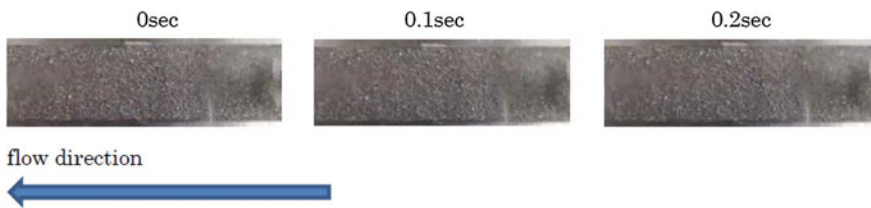


Fig. 10 Time-elased images of MEB in the porous-micro-channel ($G = 400 \text{ kg/m}^2 \text{ s}$, $\Delta T_{\text{sub}} = 30 \text{ K}$, $q = 5.77 \text{ W/m}^2$)

It is considered that the mixing enhancement by the porous plate contributed to mitigating the large-bubble formation. Figure 10 presents the time-elased images of the test section under the condition that the measured boiling curve suggested the occurrence of MEB. It can be confirmed that no large bubbles were produced in this condition. An important finding in this case is that no significant noise was generated even in the MEB flow. It is hence considered that the porous-micro-channel is useful to mitigate the noise or the pressure wave that is frequently encountered in the MEB in ordinary flow channels. Although the mixing enhancement in the porous-micro-channel is considered to contribute to the dramatic noise reduction, further study is obviously needed to clarify the detailed noise reduction mechanism during MEB.

4 Conclusions

The heat removal performance and the flow pattern of the flow boiling in the small rectangular channel containing a porous plate (porous-micro-channel) were explored experimentally in this work. Main conclusions are summarized as follows.

- (1) The porous-micro-channel is effective to enhance the nucleate boiling heat transfer. This can be attributed to the complex flow field produced in the porous-micro-channel.
- (2) As in the ordinary channel, MEB (micro-bubble emission boiling) in the porous-micro-channel occurs when the liquid subcooling and the mass flux are high enough.
- (3) The nucleate boiling heat transfer was enhanced in the narrow channel in which the channel width was comparable to the heated surface diameter. It was considered that in the wide channel, significant amount of subcooled liquid flowed in the regions between the heated surface and the channel side walls to bypass the heated surface.
- (4) With an increase in the heat flux, the oscillatory large-bubble flow was always observed before the occurrence of MEB in the normal channel, while in the porous-micro-channel, no such flow pattern was observed. It is considered that the mixing effect by the porous structure prohibited the formation of large bubble and the onset of flow instability.
- (5) In the MEB in the porous-micro-channel, significant noise frequently encountered in ordinary flow channels was dramatically reduced. This result is believed to be promising for applying the MEB to high-heat-flux heat removal from the practical industrial devices.

References

1. G. Wang, P. Cheng, Subcooled flow boiling and microbubble emission boiling phenomena in a partially heated microchannel, *International Journal of Heat and Mass Transfer*, Vol. 53, pp. 79–91 (2009).
2. K. Suzuki, et al., Application of boiling heat transfer to high-heat-flux cooling technology in power electronics, *Transactions of the Japan Institute of Electronics Packaging*, Vol. 4, No. 1, pp. 127–133 (2011).
3. D. Hanzawa, T. Okawa, A study on phase change heat removal technique using a porous-microchannel, *Transactions of the JSME*, Vol. 81, No. 827, pp. 1–12 (2015).
4. Y. Kato, *Cavitation (fundamentals and recent advances)*, Maki Shoten (1999) [in Japanese].

Neutronics Characteristics Study of Conceptual Space Heat-Pipe-Cooled Fast Reactor Core

Hui Zhao, Hongli Chen, Chong Chen, Qin Zeng and Haoran Zhang

Abstract With the continuous development of space exploration activity, the demand for space energy is increasing. Energy supply has become a very important guarantee for the normal operation of all kinds of space equipment. Therefore, the high-power and long-life space nuclear reactor, which can be operated automatically and not be affected by environment, becomes a very important choice for space energy system. In this paper, a space fast reactor core design scheme based on an integrated structure which combines the nuclear fuel rods and the central cooling heat-pipes was proposed initially. The fuel rod is a regular hexagonal prism, and the evaporator section of the heat-pipe is placed in the central hole of the fuel rod. The control of the reactor depends on six control drums in the side of the reflector. The neutronics characteristics of the reactor core were studied. The reactor core design scheme was calculated and analyzed through the establishment of the core calculation models by means of MCNP. The main dimensions and physical parameters of the reactor core were given, and the critical reactivity, power distribution and burnup of the reactor core were obtained. The fuel filling rate was improved because of the compact layout of the design scheme, which led to a reduction in the critical mass and the core volume of the reactor. At the same time, the use of structural material also decreased. As a result, the total mass of the core reduced. An increasing relative density of heat-pipe arrangement could avoid the problem generated by the failure of single heat-pipe effectively. Consequently, it has high safety and good reliability.

Keywords Space nuclear reactor · Heat-pipe · Reactivity · Power distribution · Burnup

H. Zhao (✉) · H. Chen · C. Chen · Q. Zeng · H. Zhang
School of Nuclear of Science and Technology, University of
Science and Technology of China, Hefei, Anhui, China
e-mail: huizhao9@mail.ustc.edu.cn

© Springer Science+Business Media Singapore 2017
H. Jiang (ed.), *Proceedings of The 20th Pacific Basin Nuclear Conference*,
DOI 10.1007/978-981-10-2314-9_72

791

1 Introduction

With the development and implementation of deep space exploration programs in the world, the space base construction on the moon or other planets will be of great scientific, military and political value in the future. These space bases will experience the exchange of extreme high- and low-temperature conditions every day and night, so energy supply and management has become an important guarantee for the normal and stable operation of the bases. Traditional “solar array + battery pack power configuration” has been unable to meet the demand. Not affected by the environment, long-life, safe and reliable space nuclear reactor has become the inevitable choice of space energy [1]. The space nuclear reactor is comprised of the reactor core, thermoelectric conversion device, heat-pipe radiator. Due to the complexity of the space base environment, the space nuclear reactor core should take passive cooling technology, the heat-pipe cooling has the best transient thermal feedback, the optimal reliability and the lowest maintenance requirements. Therefore, the space nuclear reactor core design should adopt the heat-pipe cooling, the heat generated by the fuel rods is taken out by the heat-pipe, and then to provide energy supply through the energy conversion system.

At present, the high-power and long-life space nuclear reactor, which can be operated stably and reliably, has become a very important and advanced research topic in the design and research of space base energy system. The USA, Russia, Japan and other countries have had a strong interest in space nuclear reactor. They have researched and proposed dozens of space nuclear reactor system programs. Cooling methods include heat-pipe cooling, liquid-metal cooling and gas cooling. The research, design, construction, debugging and flight test of space nuclear reactor will be a long-term process. In this paper, we put forward a kind of core design of space nuclear reactor and carry out the basic technology research on energy problem of space base, in order to provide reference for energy system research of the future space exploration mission [2].

2 Design Concept

2.1 Core Type

It has become an international development trend that fast reactor has been chosen in space nuclear reactor [1].

The arrangement of fast reactor core could be more compact as there is no requirement for moderator, which could be more convenient in the emission task. The fissionable nuclide can be effectively used in fast reactor and thus to reduce the negative influence caused by the reduction of fissile nuclide concentration. Moreover, the control drums can be arranged outside of the reactor to simplify the core structure and improve the reliability as the neutron leakage in fast reactor core is large.

2.2 *Cooling Method*

At present, cooling methods of space nuclear reactor include heat-pipe cooling, liquid-metal cooling and gas cooling. Gas cooling using inert gas as a coolant does not interact with structural materials, which can be used at high temperature without boiling problems. But the transient thermal feedback performance of gas cooling method is poor, and there is a problem of single point failure. The liquid-metal cooling has the advantages of small volume and light weight, but there is also a problem of single point failure. Heat-pipe cooling with a passive circulation and minimum maintenance requirements has the best transient thermal feedback performance and can avoid the problem generated by the failure of single heat-pipe. Therefore, the scheme adopts heat-pipe cooling method.

2.3 *Thermoelectric Conversion Method*

The thermoelectric conversion method is related to the design of the core power and the heat discharge system. The main methods are static thermocouple conversion, dynamic Sterling cycle and closed Brayton cycle. Although the conversion efficiency of dynamic conversion is high (23–35%), but the reliability and maintenance is poor. Static thermocouple conversion technology is mature and reliable, so it is selected in the design scheme [3].

In summary, the electrical power required by the space base is generally between 10–100 kW, and the lifetime needs to be more than 5 years [4]. Referring to the domestic and external development trend of space nuclear reactor and considering the level of technology development in China, this paper puts forward a design scheme of space nuclear reactor core with the thermal power of 1000 kW, the electric power of 60 kW, the static thermoelectric conversion efficiency of 6%, the lifetime more than 10 years.

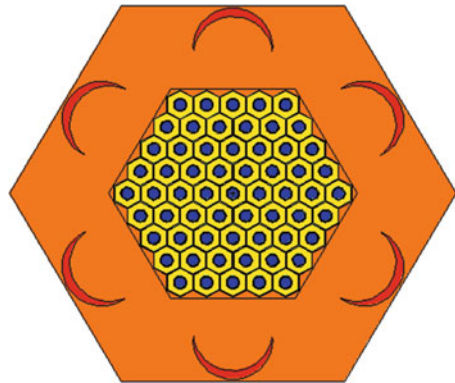
3 *Design Scheme and Model Establishment*

The space nuclear reactor adopts UN with a 43% initial enrichment as fuel, and the density of the fuel is 13.6 g/cm^3 . The reflector includes the whole active area of the core, and its material is BeO. There are six sets of control drum surrounding the core by evenly arranged. The main structure material of control drum is BeO, and the absorber material is B_4C . The absorber is inlaid in the control of the control drum to control the reactivity of space nuclear reactor. Some key design parameters of space nuclear reactor core are shown in Table 1.

Table 1 Main design parameters of space nuclear reactor core

Design parameters	Design value
Core thermal power	1000 kWth
Thermoelectric conversion efficiency	6%
Electric power	60 kWe
Core lifetime	10 years
Number of fuel rods (including heat-pipe)	61
Number of control drums	6
Total height of the core	740 mm
Margin of the core (regular hexagon)	440 mm
Active area height	600 mm
Margin of the active area (regular hexagon)	244 mm
The thickness of the reflector	Side face: 98 mm Upper/Lower face: 70 mm
The diameter of control drums	90 mm
The height of control drums	600 mm
Absorber size	Crescent, most thickness is 10 mm

Space nuclear reactor based on an integrated structure which combines the nuclear fuel rods and the central cooling heat-pipes could be designed with close arrangement. This arrangement is better than other schemes that heat-pipe and the fuel rod are arranged adjacently [5]. The critical mass and volume reduce significantly. Meanwhile, the mass of the structural material also reduces significantly. The cross section of the core and the active area is regular hexagon. The structure model of the core is shown in Fig. 1.

Fig. 1 Core structure model

4 Neutronics Analyses

Neutronics analyses had been performed by means of MCNP. The calculation process ignored other structures and components out of the reflector.

4.1 Reactivity Analysis

The critical parameters of the core reactor core in various states through the MCNP calculation are shown in Table 2. The result illustrated that the preliminary design of the core could meet the requirements of the space nuclear reactor, while the total reactivity was negative. In case of an accident, even if half of the control drums got stuck outside, the rest of the drums could also achieve a safe shutdown of the core.

For the space nuclear reactor, the large risk comes from the crash of the launch process. Because of the high concentration fuel and the large fuel loading, there is a critical safety risk if the launch fails and the reactor falls into the sea. The core was divided into two modules in the design, and each module could be launched individually [6]. The k_{eff} which was 0.87303, illustrated that the design could avoid the critical risk effectively.

4.2 Power Distribution

Space nuclear reactor has been designed as a fast reactor, with a BeO reflector. Due to the moderation and reflection of the reflector, the fission reaction rate of the fuel element was higher in the edge of the core [7]. Therefore, the power in the center and the core edge of the core was more than that of other position. The average power of each fuel rod was 16.39 kW. The relative power distribution is shown in Fig. 2.

The maximum power peaking factor reduced greatly because of the compact layout of the design scheme. The maximum power peaking factor of the core was 1.09, which appeared in the central fuel rod of the reactor core with 17.8 kW for its

Table 2 Critical parameters of space nuclear reactor

Calculation state	k_{eff}	$\Delta k/k\%$
Initial state (cold state)	1.02503	2.44
Initial state (Hot state)	1.02444	2.39
Put into all control drums	0.91447	-9.36
Put into five control drums	0.93302	-7.18
Put into three control drums	0.96660	-3.46
1/2 core fall into the water	0.87303	-14.5
Full power operation for ten years	1.00773	0.76

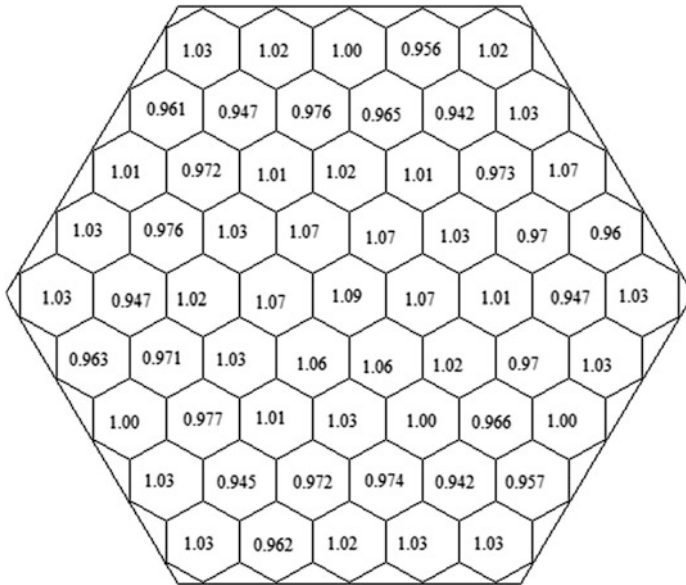


Fig. 2 Relative power distribution of the core

power. Taking into account the heat-pipe cooling of the core, the maximum heat transfer limit of the heat-pipe is more than 25 kW [8]. It is big enough for the heat-pipe to cool the core safely.

In addition, there may be some factors that cause the failure of the heat-pipe during the operation of the space nuclear reactor core. With a failure of one heat-pipe, the power needs to transfer of the six heat-pipes around it will increase a factor of 1/6 to be 20.6 kW, which is still under the heat-pipe heat transfer limit [8]. So the heat generated from the core could be brought out effectively, and the security of the whole system could be guaranteed.

4.3 Burnup Analysis

The change in the effective multiplication factor and the burnup is showed in Figs. 3 and 4, while the space nuclear reactor had operated for ten years with full power. The absolute burnup of the fuel was 14.48 GWd/MTU. The k_{eff} was gradually reduced to 1.0073, which indicated that the reactivity of the reactor could basically meet the lifetime of the design requirements.

Fig. 3 k_{eff} of the core during operation

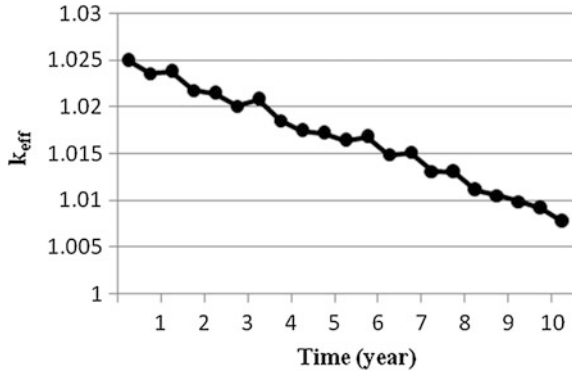
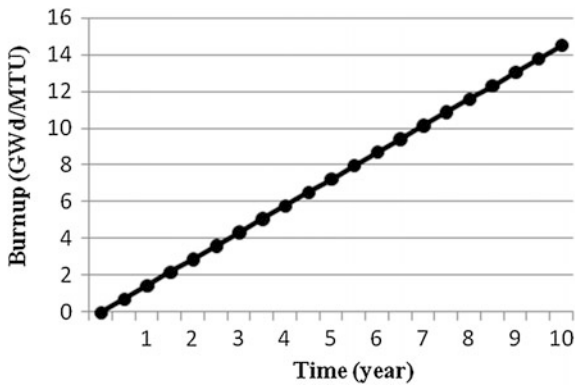


Fig. 4 Burnup of the core during operation



5 Conclusions

The design of space nuclear reactor based on an integrated structure which combines the nuclear fuel rods and the central cooling heat-pipes could be arranged closely. This new arrangement improves the fuel filling ratio. As a result, the critical mass and volume reduce significantly, which is conducive to flatten power distribution. The next step will take into account the effects of temperature distribution and transient safety based on the work of this paper with a more sophisticated model. Then more accurate analysis and calculation of physical parameters should be implemented for a further optimization design scheme.

References

1. ZHANG Ming, Cai Xiaodong, Du Qing, et al. Research on nuclear reactor in space application. *Spacecraft engineering*[J], 2013, 22(6): 249–255.
2. Rosen R, Schnyer A D. Civilian uses of nuclear reactors in space. *Science & Global Security* [J]. Gordon and Breach Science Publishers, 1989, 147–164.

3. WANG Sanbing, HE Chaohui. Weight control in design of space nuclear reactor system[J]. *Technological Sciences*, October 2013 Vol. 56 No. 10: 2594–2598.
4. Lee Mason, David Poston, Louis Qualls. System concepts for affordable fission surface power [R]. Brook Park, Cleveland, and Fairview Park, Ohio: Glenn Research Center, 2008.
5. Fission Surface Power Team. Fission Surface Power System Initial Concept Definition. NASA/TM, 2010-216772.
6. Jeffrey C. King and Mohamed S, El-Genk. S⁴ Reactor: Operating Lifetime and Estimates of Temperature and Burnup Reactivity Coefficients[C]. *Space Technology and Applications International Forum-STAIF 2006*.
7. Aaron E. Craft, Jeffrey C. King. Reactivity control schemes for fast spectrum space nuclear reactors[J], *Nuclear Engineering and Design*, 2011(241) 1516–1528.
8. Li Hua-qi, Jiang Xin-biao, CHEN Li-xin, et al. Heat Transfer Capability Analysis of Heat-pipe for Space Reactor[J], *Atomic Energy Science and Technology*, 2015, 49(1): 89–95.
9. Jeffrey C. King. A Methodology for the Neutronics Design of Space Nuclear Reactors [J]. *AIP Conf. Proc.* 699, 319 (2004); doi:[10.1063/1.1649589](https://doi.org/10.1063/1.1649589).
10. King J C, El-Genk M S. Submersion-Subcritical Safe Space(S4) reactor [J]. *Nuclear Engineering and Design*, 2006, 236(17): 1759–1777.
11. El-Genk M S. Space nuclear reactor power system concepts with static and dynamic energy conversion[J]. *Energy Conversion and Management*, 2008, 49(3): 420–411.

Numerical Simulation on Thermal Stratification in the Containment after LOCA

Ke Zhao, Tianmin Xin, Yong Yu and Hui Wang

Abstract The accident of Fukushima nuclear power plant suggests in case beyond design basis external events together with all power lose, safety injection pump of the containment spray system will be disabled. In order to prevent the above-mentioned accident, designers add PCS in the design of ACP1000. In the system property experiment which had finished certified that heat extraction ability can absolutely meet the request in the accident condition. In order to describe thermal stratification after LOCA, We used SOLIDWORKS to build the geometry model, ICEM to mesh, and CFX to carry out numerical system. Till now, consequently, we can tentatively draw the conclusion about thermal stratification in the containment which is built in this simulation after LOCA: In the 0–400 s after LOCA, no matter the height of the heat exchanger in the containment, air is stratified distribution, and the higher the air height, the higher the temperature of air. And the higher the heat exchanger, the highest temperature in the containment appeared the later, and the temperature of the highest temperature area is relatively low.

Keywords LOCA · Geometry model · Meshing · CFX · Numerical simulation

1 Introduction

In March 2011, a severe accident happened in Fukushima nuclear power plant. Earthquake and tsunami caused the power plant to lose full power, the reactor cannot be cooled down, the pressure of the containment exceeded the design pressure, and containment inside accumulated lots of hydrogen, and lots of radiation released to the environment.

External events such as earthquake and tsunami may lead to an beyond design basis accident in the nuclear power plant, and blackout will lead to failure of the

K. Zhao · T. Xin · Y. Yu · H. Wang (✉)
China Nuclear Power Engineering Co. Ltd. Beijing, Beijing, China
e-mail: leon1216@qq.com

pump of the containment spray system. After the main steam line break or LOCA, because of the failed containment spray system pump, the temperature and the pressure in the containment will rise gradually and finally, it may go beyond the maximum design pressure. According to the reasons mentioned above, third-generation plants such as AP1000 of Westinghouse and its safety system use passive safety system so that severe nuclear accident will hardly happen again.

ACP1000 is a third-generation advanced technology 1000-meV class pressurized water reactor developed by CNNC and possessed itself of all-round prevention and mitigation measures against severe accidents. Its conception of combination of both active and passive design enables the HPR1000 to respond in a better way to the uncertainty by the lack of application of passive technology. Passive containment heat removal system can remove the heat in a long term in the case of BDBA, which includes blackout and spray system failure so that the pressure and temperature can be reduced to a range of safety level and the containment can maintain its integrity.

Passive containment heat removal is composed by three series, using internal containment heaters. And the containment is cooled down through condensation on the heat exchanger, convection and radiation heat transfer between the mixed gas and the heat exchanger.

By the water flow in the heat exchanger tube, it will continuously remove the heat in the containment to the water tank outside the containment depending on the density difference.

Passive containment heat removal time can continue for at least 72 h, and 72 h later operator can consider other ways of water supplement.

Although PCS heat removal capacity had been fully verified, but when there was a serious accident, the containment temperature distribution still need to get more attention and severe temperature distribution might affect heat transfer capacity of the PCS system. In this paper, we used the numerical simulation method to do the research about the temperature stratification after LOCA accident in the geometric model we had established on the base of design document.

2 Numerical Simulation Program Development and Implementation

During the LOCA accident, when reactor coolant with high temperature and high pressure released from primary coolant pipe, containment pressure will increase and the integrity of the containment structure may be destroyed. PCS performance verification experiments had proved: Mixture of steam, air, helium and heat capacity can meet the requirements of the PCS.

Currently non-condensable gases steam condensation mainly includes theoretical analysis and experimental research. Existing commercial computational fluid dynamics software rarely contains non-condensable gases steam condensation

model, so the inclusive, accepted classical theory and analysis methods are still in the exploration and research stage by far. This article focuses on the simulation calculation about temperature stratification after LOCA in the containment, and we use hot air instead of steam to study the initial temperature stratification after the accident.

We use ANSYS CFX to do the numerical simulation. The common flow of CFD is as below:

1. Define goals	2. Identify domain
3. Geometry	4. Mesh
5. Physics	6. Solver settings
7. Compute solution	8. Examine results

(1) Geometric model

Geometric model is built based on “containment comprehensive performance test experimental equipment design” by 3D modeling software SOLIDWORKS and had simplified to some extent. First, we built every part and then assembled them.

The simulation model we need to establish mainly composed: containment (bottom, cylinder, hemisphere shell), heat exchanger (simplified as regular rectangular shape, and the heat transfer area is equivalent to the design plan) and break pipes (source term tube, simplified as square tube).

In the “containment comprehensive performance test experimental device design” (HEU), the internal space of the containment simplified to three layers; the main part is the large space above the platform, the break tube is above the platform, and it is sprayed upward. And walls in the model are set to the insulating wall except heat exchanger plates of PCS, and therefore we had not considered the influence of other two platforms for temperature stratification. In the actual geometric modeling, we eventually delete the internal platforms.

Dimensions of the components of the model are in the table (Table 1).

(2) Mesh

After the establishment of geometric model, we saved the files of SOLIDWORKS as “.x_t” and import it into ICFM-CFD taking the three-dimensional mesh.

Table 1 Geometric model and dimension of each part

Geometric model	Dimension/mm
Bottom	R4250
Cylinder	R4250 × H12250
Hemisphere shell	R4250 × H4250
Heat exchanger plate	200 × 800 × 1600
Source term tube	300 × 300 × 300

We used structured grids to improve grid quality, in order to improve the final computational accuracy. Since the geometry of the three-dimensional structure has a circular arc, we need to use O-GRID BLOCK to fix the mesh distortions, and at the same time it can generate intensive boundary layer area in the near vicinity of the wall.

The final number of grid is 150,438, and mesh quality was equal or greater than 0.4 (a indicator to describe the meshing quality, the general requirements of numerical simulation software for mesh quality must be greater than 0.2) (Fig. 1).

(3) Numerical Simulation

(a) Model selection

Material selection: Air ideal gas

Fluid model:

Heat transfer model: Total energy model. On the base of consideration of convective heat transfer and heat exchange, we also take into account the heat changes by the kinetic energy. This model is suitable for high speed flow and heat transfer modeling of compressible flows.

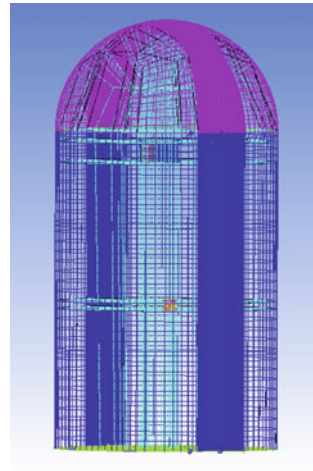
Turbulence model: Turbulent flow conditions. We need supplement turbulent kinetic energy equation and turbulent dissipation rate equation to reflect the turbulence characteristics. The standard k - ε model equation form as follows:

Turbulent kinetic energy equation (k equation):

$$\frac{\partial(\rho k)}{\partial t} + \frac{\partial(\rho u_i k)}{\partial x_i} = \frac{\partial}{\partial x_j} \left[\alpha_k \mu_{eff} \frac{\partial k}{\partial x_j} \right] + G_k - \rho \varepsilon$$

Kinetic energy dissipation equation (ε equation):

Fig. 1 Containment internal three-dimensional structure and mesh



$$\frac{\partial(\rho\varepsilon)}{\partial t} + \frac{\partial(\rho u_i \varepsilon)}{\partial x_i} = \frac{\partial}{\partial x_j} \left[\alpha_\varepsilon \mu_{eff} \frac{\partial k}{\partial x_j} \right] + \frac{C_{1\varepsilon}^*}{k} G_k - C_{2\varepsilon} \rho \frac{\varepsilon^2}{k}$$

Combustion model and the thermal radiation model: do not consider

(b) Boundary conditions setting

Inlet boundary conditions: using the mass flow inlet, the inlet gas temperature was set to a constant 300 °C;

Heat exchanger wall was set to no-slip wall conditions; the temperature is set at 30 °C;

In addition to the steam inlet, the other wall was set to free-slip boundary condition, adiabatic wall.

(c) The initial conditions

Setting as unsteady flow, the total simulation time was 400 s.

(d) The basic assumptions

λ Steam–air mixture was replaced by single phase air ideal gas, for which density is set to 1.125 kg /m³;

λ Heat exchange occurs only at the designated wall (which area was equivalent to the actual heat transfer area), and the other wall was all set to adiabatic wall.

3 Preliminary Results of the Numerical Simulation

Simulation scheme: At certain inlet temperature (300 °C), with the same inlet mass flow, put heat exchanger plates at different heights: YH = 7.5 m above the bottom and YH = 9.0 m above the bottom.

After the simulation, we analyzed the results and reached a preliminary conclusion. Besides, we can change the inlet temperature and the inlet flow rate to do further analysis in the subsequent simulations (Table 2).

The results:

Select a XZ plane in the model, the principle of selection was that the plane can simultaneously pass through the source term tube and the heat exchanger plate. We choose different point in time after the accident happened (the initial time was the moment that the LOCA accident happened), and then we draw the contour of temperature of two operating conditions at different time point.

Table 2 Main physical parameters of selected conditions

	Height of heat exchanger (YH)/m	Mass flow rate of the inlet/(kg/s)
Operating condition 1	7.5	0.4
Operating condition 2	9	0.4

When the heat exchanger height is 7.5 meters and the time of continuous discharging was 250 s, 350 s and 400 s, the contours of temperature are shown below (Fig. 2).

When the YH was 9 meters and the time of continuous discharging was 250 s, 350 s and 400 s, the contours of temperature are shown below (Fig. 3).

From the images, we can draw a preliminary conclusion: In the geometric model of this simulation, from the accident to 400 s later, the temperature distribution in the containment was stratification. And if we change the height of the heat exchanger, the temperature stratification of the basic law has not changed: The temperature of each layer was rose with the increase in height; as time goes on, the average temperature was rose.

From the images above, we know that in the geometric model of this simulation, from the accident to 400 s later, at a particular point in time.

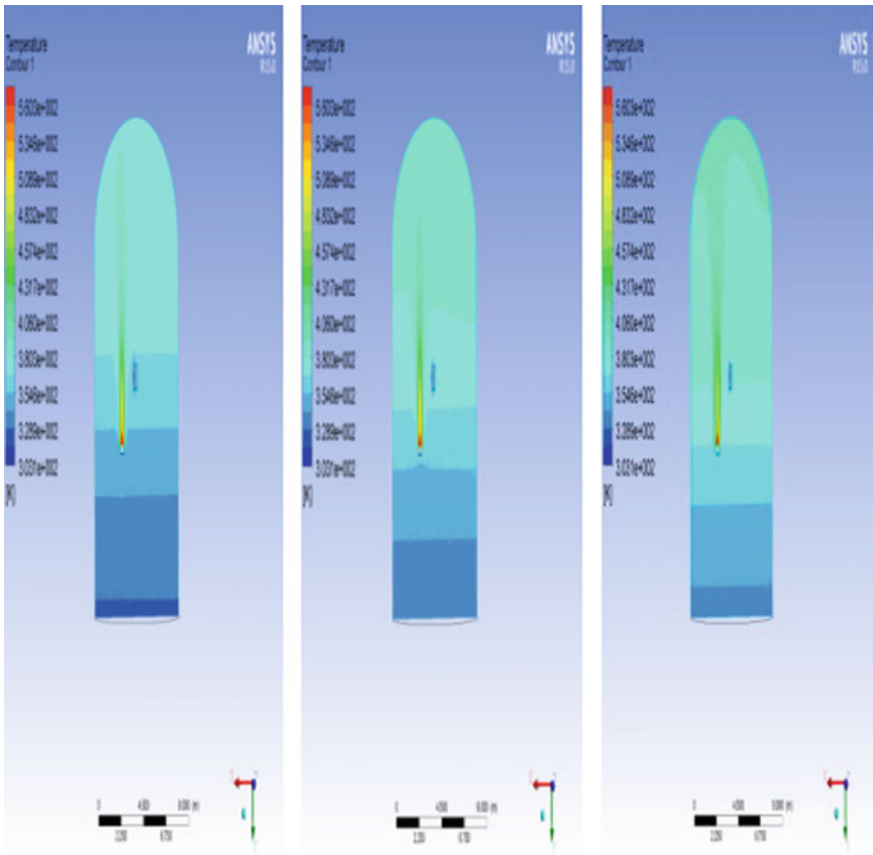


Fig. 2 YH was 7.5 meters during the discharge temperature contours (from left to right: 250 s, 350 s, 400 s)

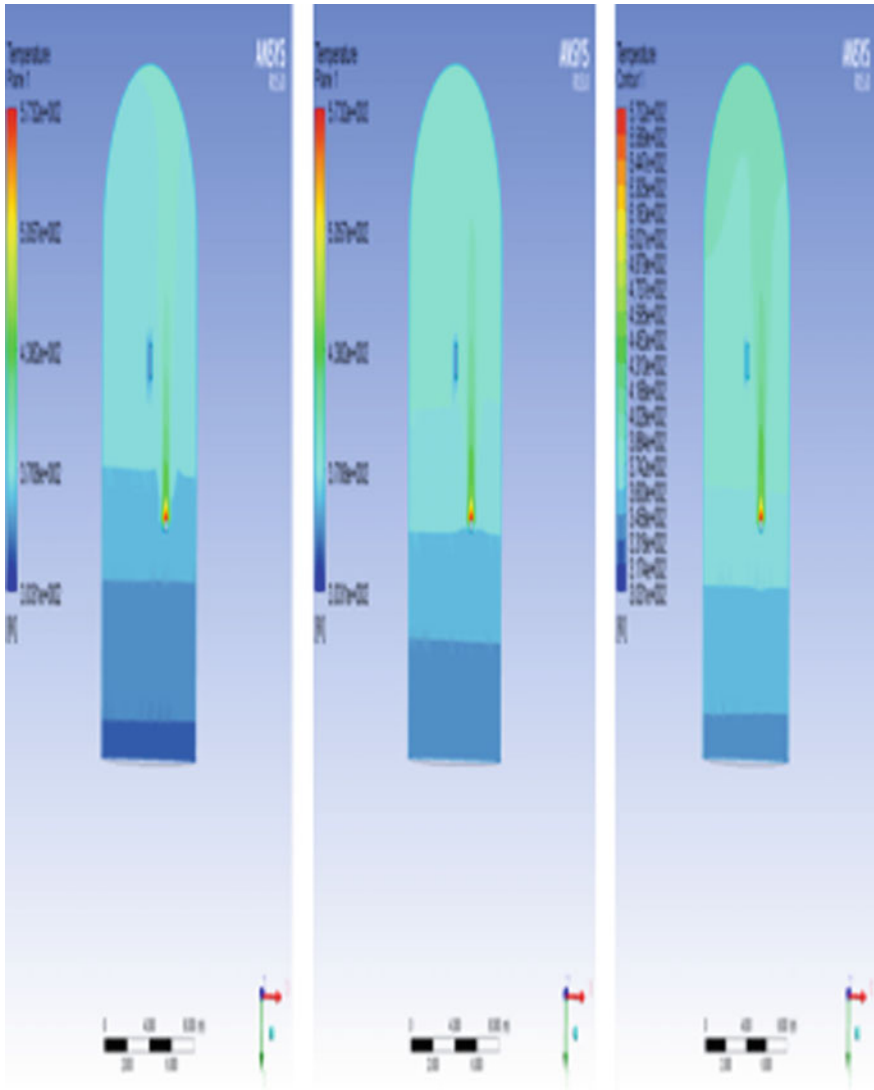


Fig. 3 YH was 9 meters during the discharge temperature contours (from left to right: 250 s, 350 s, 400 s)

In the upper region, YH = 7.5 meters (condition 1), the temperature was greater than the temperature of the same position in YH = temperature 9.0 m (condition 2). And at the same time, the lower temperature portion in the condition 2 was larger than the condition 1.

In order to do further analysis about the thermal stratification and the influence of the height of the heat exchanger to the heat transfer, we choose five points of

different Y values on this XZ plane and measured the change of the temperature as time goes on. These points, respectively, were Y = 2.5 m, Y = 5.5 m, Y = 8.5 m, Y = 10.5 m and Y = 12.5 m. And in the two different conditions mentioned above, the data we obtained were shown below (Fig. 4).

We can get the time that the temperature of each point rising to 340 K; the results were shown below (Table 3).

At the time 350 s, the temperature of five different points is shown below (Table 4).

According to the data mentioned above, for the upper space of the geometric model, during the 0-400 s after LOCA, the higher the heat transfer position, the lower the temperature of the upper space (comparing the two different conditions at

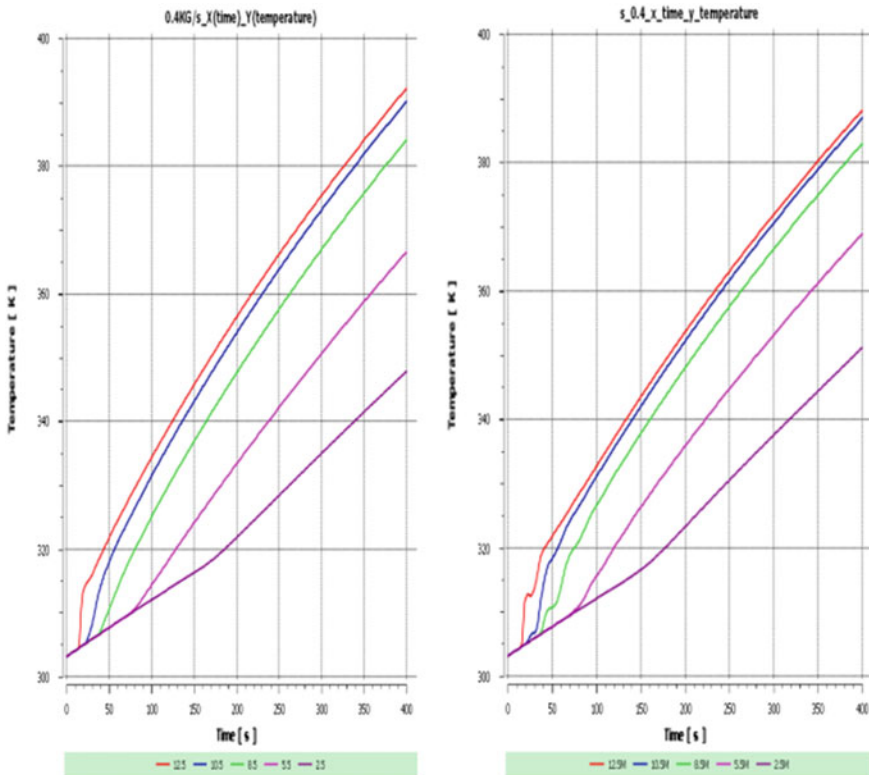


Fig. 4 Variation of temperature of five different points with time (left is 7.5 m)

Table 3 Time that the temperature of each point rising to 340 K in different conditions

	12.5 m	10.5 m	8.5 m	5.5 m	3.5 m
Condition 1	134	142	161	223	320
Condition 2	125	137	165	240	341

Table 4 Temperature of five different points at 350 s

	12.5	10.5	8.5	5.5	3.5
Condition 1	380	379	375	361	344
Condition 2	384	382	376	359	341

a same time), and the longer the time to get a specific temperature; for the lower space of the geometric model, the lower the heat transfer position, the lower the temperature of the lower space, and the longer the time to get a specific temperature. And this is easy to understand, because the closer to the heat transfer, the quicker that temperature fell down. But to the whole containment, the highest temperature appeared at the upper space of the containment, so the higher the heat transfer position, the later that it comes to the highest temperature, and this is conducive to the integrity of the containment and avoids the overpressure accident.

4 Summary

According to the results, we can draw a preliminary conclusion: In the geometric model we built, during the 0–400 s after the LOCA happened, no matter the height of the heat exchanger, at a certain time, the temperature of the lower space of the containment is lower, and the temperature was higher in the upper space. The temperature gradually increased from the low section to high section, and the temperature distribution in the containment was stratification. And the height of the heat exchanger had influence on the thermal distribution. Simulation results showed that, in the geometric model we built, during the 0–400 s after the LOCA happened, the higher the heat transfer position, the later that it comes to the highest temperature; at a same time, the highest temperature in the containment was lower than the heat exchanger which had a lower height.

References

1. CNPE.HEU. Containment comprehensive experimental performance test equipment overall layout design (version A) [R] .2014
2. Wang Fujun. Computational fluid dynamics analysis software -CFD Principles and Applications [M]. Beijing: Tsinghua University Press, 2004
3. Ji Bingbing, Chen Jinmei. ANSYS ICEM CFD Meshing technology and example explanation [M] Beijing: China Water Power Press, 2012
4. Zhang Dongyang. The characteristics of steam condensate of vertical light tube which contain air outside the tube [D]. Harbin HEU

Optimal Control Rod for Boron-Free Small Modular PWR

Jiwon Choe, Ho Cheol Shin and Deokjung Lee

Abstract This paper proposes a new control rod material for a boron-free small modular pressurized water reactor (SMPWR) to compensate the loss of the soluble boron. To design control rod for SMPWR is difficult due to the large amount of reactivity control necessity and the multiple roles of control rod, i.e., the excess reactivity control, the coarse/fine power control, and the axial shape control and shutdown. This paper presents a study of various control rod materials: B_4C , Ag-In-Cd, and HfB_2 . The rod worth and the excess reactivity control capability will be assessed for the SMPWR using Studsvik's reactor core design code system, CASMO-4E/SIMULATE-3.

Keywords Control rod · Small modular reactor · Pressurized water reactor · Reactor design

1 Introduction

One of the design requirements of small modular pressurized water reactor (SMPWR) is the compact size for transportation from a factory to the site. The soluble boron-free operation can decrease the core size and the liquid radioactive waste and further remove the corrosion problem caused by boric acid. The SMPWR needs a large amount of burnable absorber (BA) material and a reactivity control mechanism to compensate the loss of the soluble boron. The design of the control rod for SMPWR becomes difficult due to the large amount of reactivity control

J. Choe · D. Lee (✉)
Ulsan National Institute of Science and Technology,
Ulsan, Republic of Korea
e-mail: deokjung@unist.ac.kr

H.C. Shin
Korea Hydro and Nuclear Power Central Research Institute (KHNP-CRI),
Daejeon, Republic of Korea

necessity and the multiple roles of control rod, i.e., the excess reactivity control, the coarse/fine power control, and the axial shape control and shutdown.

This paper presents a study of various control rod materials: B_4C , Ag-In-Cd, and HfB_2 . The rod worth and the excess reactivity control operation will be assessed for the SMPWR using Studsvik's reactor core design code system, CASMO-4E/SIMULATE-3 [1–3]. The optimal control rod pattern, group and material are decided through the assessment.

2 Control Rod for SMPWR

2.1 Core Design of SMPWR

The design parameters of SMPWR are summarized in Table 1. The thermal power is 200 MWt, and the power density is 58.4 KW/L. The geometry of fuel assembly (FA) is based on the Westinghouse 17x17 FA [4]. A total of 37 FAs are loaded into the core. The fuel material is UO_2 with enrichment of 4.90 w/o ^{235}U . The R-BA, a thin layer of Zr- ^{167}Er , has been used as a BA material [5]. The active core height is 2.0 m. There is no soluble boron in the moderator. The fuel cycle length is 26.5 months. The 4.45 of 3D pin peaking factor (Fq) and ± 0.4 of axial offset (AO) are suitable limitations for 200 MWt of PWR core [6]. The shutdown margin is to make subcritical state with all rods in (ARI) at CZP.

The two-batch loading pattern is shown in Fig. 1. The BA in TY01 is 1 mm of ^{167}Er 5% for 88 pins, and the BA in TY02 is 2 mm of ^{167}Er 15% for 216 pins. There is 10 cm of cutback at the top and bottom, and the BA material is R-BA with natural Gd 10% in Gd-Zr. The excess reactivity variations over core burn-up are shown in Fig. 2.

Table 1 Design parameters of SMPWR [7]

Parameters	Value	Unit
Thermal power	200	MW
Power density	58.4	KW/L
Fuel cycle length	884	EFPD
FA type	17 × 17	Westinghouse
Fuel material	UO_2	
BA material	R-BA	
Fuel enrichment	4.90	w/o ^{235}U
Number of FAs	37	
Active core height	2.0	m
Fq limit	4.4	
AO limit	± 0.4	
Shutdown margin	<0	% at CZP
Boron concentration	0	ppm

Fig. 1 Loading pattern of SMPWR

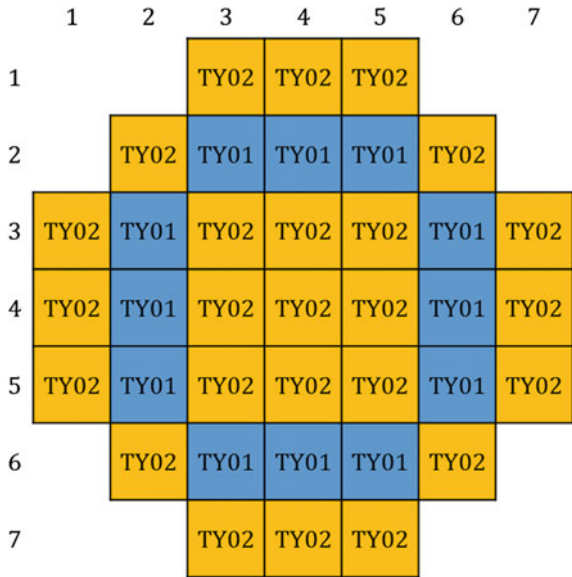
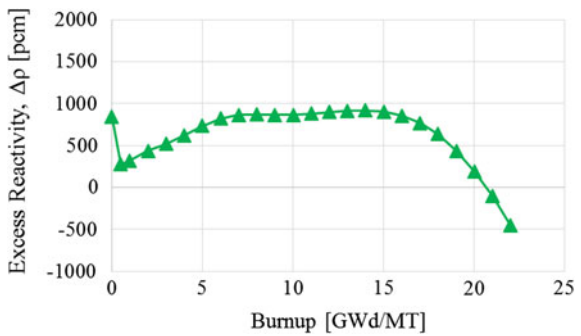


Fig. 2 Excess reactivity variation over core burn-up



2.2 Control Rod Material

Three types of control rod materials have been analyzed in this paper. Boron carbide (B_4C) and Ag-In-Cd (AIC) are existing materials which have long been used in commercial PWRs. Hafnium diboride (HfB_2) is a new absorber material proposed for SMPWR.

B_4C has 81.0 cm^{-1} of high macroscopic absorption cross section in thermal energy because of ^{10}B . It is a useful ceramic material for commercial applications. Melting temperature is high due to chemically stable refractory compound. Its behavior acts like a fuel pellet: It generates heat due to reactions with neutrons, expands thermally, cracks and relocates, produces transmutation products of Li and gaseous He, swells as a result and releases gas. The quantitative effects are

significantly less than in fuel, but the impact occurs caused by partial control rods residing in the core for excess reactivity control of SMPWR. It is the most widely used absorber in reactors, including its application in all boiling water reactors (BWR), some of the PWRs and all of the fast breeder reactors (FBR), but the integrity is low for Westinghouse-type FA [8].

The macroscopic absorption cross section of AIC is 9.9 cm^{-1} in thermal energy due to ^{113}Cd . This alloy has a long history of excellent performance in contemporary commercial PWRs because of the following advantages: low swelling rate and good structural integrity for 12 reactor years or more, absence of gaseous or large quantities of low-density transmutation products that would cause significant swelling, lower propensity for mechanical interaction with the cladding than B4C because of its compatibility with stainless steel and nickel base alloy cladding, good fabrication technology, and slower corrosion rate than B4C if in contact with coolant; However, there are some disadvantages too: the material cost shows big variations, both the melting point and the weight are relatively high compared to B4C, the neutron worth is lower than that of B4C, and the storage and disposal cost is higher than B4C owing to post-irradiation high energy, long-lived gamma emitters [8].

The absorption cross section of HfB₂ is 55.0 cm^{-1} in thermal energy. Metallic Hf was actively considered as an absorber material for early US Naval reactors and commercial PWRs before the development of AIC alloy. The cost of AIC was cheaper than that of Hf at that time, but it is comparable these days because of the price rise of AIC. Hf has 4.81 cm^{-1} of high absorption cross section due to the presence of 4 isotopes with high neutron absorption cross section over the range of thermal and epithermal neutron energies that can provide a longer nuclear life than B₄C. It has excellent coolant corrosion resistance, which is better than Zircaloy, potentially eliminating the need for cladding. The swelling rate is low because of the absence of gaseous transmutation products. It has good mechanical properties and their resistance to radiation. Also, the melting point is high. However, its structure is anisotropic and hexagonal close packed (HCP) structure that can result in irradiation-induced dimensional changes. There is potential for hydriding and related dimensional changes, if not protected by a tenacious oxide film. The cost is higher than that of B₄C. This paper uses HfB₂, because its macroscopic absorption cross section is four times higher than pure Hf [8].

2.3 Control Rod for SMPWR

Only control rods can be used for excess reactivity control due to the absence of soluble boron. Figure 3 shows four groups of control element assemblies (CEAs) loaded in a checkerboard pattern. The rod worth of each CEA group, the reactivity control operation, and the shutdown margin from hot full power (HFP) to hot zero power (HZIP) are analyzed for the performance comparison.

Fig. 3 CEA group pattern of SMPWR

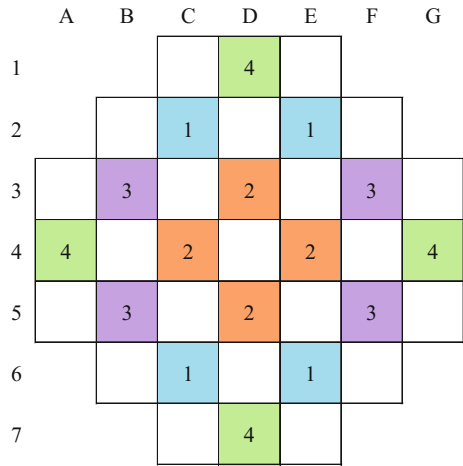


Figure 4 shows the rod worth for each material and each CEA group at the beginning of cycle (BOC, 0 GWd/MT), middle of cycle (MOC, 10 GWd/MT), and end of cycle (EOC, 20 GWd/MT). The rod worth of B₄C is the lowest among all materials, because the radius is smaller than the others due to fission gas generation. The rod worth of HfB₂ is around 500 pcm higher than that of Ag-In-Cd. The rod worths of CEA group 1 (G1) and G3 are higher than those of CEA G2 and G4, because there is a low amount of BA in FAs at CEA G1 and G3 positions. The rod worths of CEA G2 and G4 increase as BAs burn out, but the rod worth of CEA G4 is much lower than that of CEA G2 due to its position.

The results of excess reactivity control with each material are shown in Figs. 5 and 6. B₄C CEA uses G1 and G3 for this control due to the low rod worth. On the other hand, AIC or HfB₂ CEAs are capable of controlling the excess reactivity with only G1. The AO is shifted to a lower region due to control rod insertion, but all the

Fig. 4 Control rod worth of each CEA group

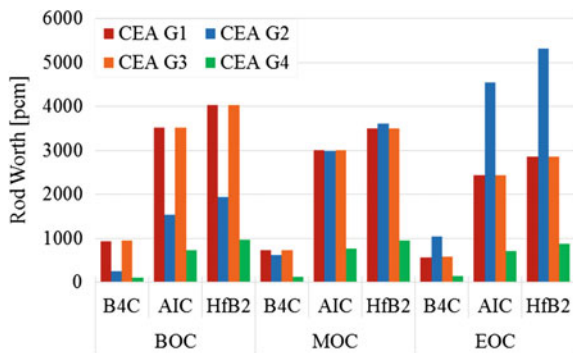


Fig. 5 Axial offset behavior

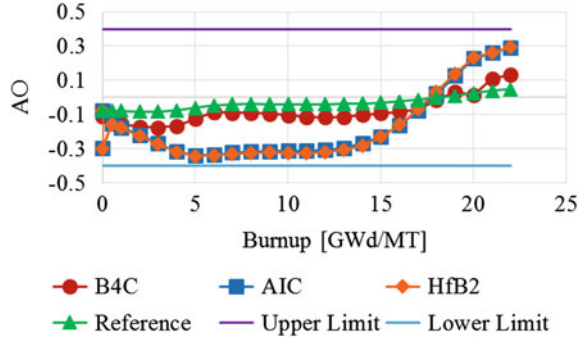
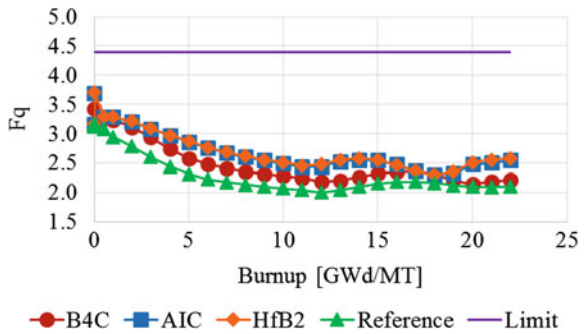


Fig. 6 3D pin peaking factor behavior



cases satisfy the design limit as shown in Fig. 5. The Fq behaviors of all the cases also satisfy the design limits in Fig. 6.

The shutdown margins at CZP in all rods in (ARI) state are summarized in Table 2. The excess reactivity at BOC is similar to the excess reactivity at MOC, but the spectrum at BOC is harder due to the large amount of BA. Therefore, the neutron absorptions by control rods at BOC are smaller. The AIC CEA cannot maintain a subcritical state at BOC even in an ARI condition; in contrast, HfB₂ CEA can make the core subcritical at CZP over all burn-ups.

Table 2 Shutdown margin at CZP

Margin [pcm]	AIC	HfB ₂
BOC (0.0 GWd/MT)	-2193	672
BOC (0.5 GWd/MT)	-1186	1570
MOC (10.0 GWd/MT)	251	3334
EOC (20.0 GWd/MT)	1481	4481

3 Conclusions

This paper presents the performance analysis of three control rod materials for a boron-free SMPWR to compensate the loss of the soluble boron. The rod worth, excess reactivity control operation, and shutdown margin are analyzed for B_4C , AIC, and HfB_2 . Both B_4C and AIC are used as control rod materials in commercial PWRs, but these materials have insufficient rod worths for the boron-free SMPWR. The HfB_2 is the only control rod material which can satisfy the design limits of AO, Fq, and shutdown margin during the excess reactivity control without boron.

References

1. *CASMO-4E: Extended capability CASMO-4 user's manual*, Studsvik Scandpower Inc. (2009)
2. *CMS-LINK user's manual*, Studsvik Scandpower Inc. (2009)
3. *SIMULATE-3: advanced three-dimensional two-group reactor analysis code user's manual*, Studsvik Scandpower (2009)
4. J. A. Barsic, *17x17 next generation fuel (17x17 NGF) reference core report*, Westinghouse Electric Company LLC, (2008)
5. Jiwon Choe, "New burnable absorber for long-cycle low boron operation of PWRs", *Annals of Nuclear Energy*, **88**, pp. 272–279. (2016)
6. Justin R. M., *Feasibility study on a soluble boron-free small modular reactor*, Oregon State University, Oregon, US, (2013)
7. Jiwon Choe, "Preliminary design of boron-free small modular pressurized water reactor", *PHYSOR 2016*, Sun Vally, Idaho, US & May 1 – 5 (2016)
8. A. Strasser, *Control assembly technology report*, FMTR Volume III, A.N.T International (2014)

Author Biography

Jiwon Choe is a graduate student in doctoral course at Ulsan National Institute of Science and Technology (UNIST) in Ulsan, Republic of Korea. Her research topic is reactor core design. Prof. Deokjung Lee, who is the corresponding author of this paper, is an assistant professor in UNIST. His research area is computational nuclear reactor physics.

Power Optimization of Steam Generators Under Fault Conditions

Huasong Cao, Peiwei Sun and Jianmin Zhang

Abstract Under fault conditions, it is important maintain the safety of nuclear power plant. Meanwhile, it is also necessary to generate its maximum power output, especially for small modular reactors, to improve the economy. The helical-coiled once-through steam generator of IRIS is chosen as a research object. The moving boundary method is applied to derive its thermal-hydraulic model. It is divided into subcooled region, boiling region, and superheated region. Through comparisons between calculated results and design data, the model is proved to be accurate enough for the optimization study. Sensitivity analysis is performed to investigate the influences on the thermal power from the steam generator key operation parameters. Feedwater flow rate and average coolant temperature are selected as optimized variables, and the thermal power is chosen as the objective function. The constraints on the tube temperature, reactor outlet temperature, circulation ratio, and reactor inlet temperature are chosen as limits. Polynomial fit algorithm is applied to derive their relationship. Optimization is obtained to find its maximal value. The results of optimization under the fault conditions are reasonable for practical application. Finally, hybrid algorithm is proposed as an alternate method for further study.

Keywords IRIS · Thermal-hydraulic model · Optimization · Polynomial fit algorithm · Hybrid algorithm

Nomenclature

ρ	Fluid density/kg·m ⁻³
H	Enthalpy/J·kg ⁻¹
P	Fluid pressure/Pa
A	Area/m ²

H. Cao · P. Sun (✉) · J. Zhang
School of Nuclear Science and Technology, Xi'an Jiaotong University, Xi'an, Shaanxi, China
e-mail: sunpeiwei@mail.xjtu.edu.cn

H. Cao
e-mail: caohuasong@stu.xjtu.edu.cn

q	Thermal flux/ $\text{J}\cdot(\text{m}^2\cdot\text{s})^{-1}$
g	Gravitational acceleration/ $\text{m}\cdot\text{s}^{-2}$
d_i	Tube inside diameter/m
D	Spiral coil diameter/m
h_{mac}	The macrocomponent of convection heat transfer
h_{mic}	The microcomponent of convection heat transfer
W	Mass flow rate/ $\text{kg}\cdot\text{s}^{-1}$
Z	Height/m
V	Flow velocity/ $\text{kg}\cdot\text{s}^{-1}$
f_{cc}	Spiral pipe friction factor
f_{ss}	Straight pipe friction factor

1 Introduction

International Reactor Innovative and Secure (IRIS) is an integral pressurized water reactor with 335MWe, which is being designed by an international team—led by Westinghouse. IRIS features an integral vessel that contains all the major reactor coolant system components, including the reactor core, the steam generators, and the pressurizer [1]. The design yields enhanced safety, security, and reliability, along with competitive economy. As a result of the integration, design makes the IRIS containment smaller than that of traditional pressurized water reactor, and the overall size of the plant is also reduced significantly.

The steam generator (SG) of IRIS as shown in Fig. 1 is a helical-coil tube bundle SG with the primary fluid outside the tubes. The design parameters of SG are given in Table 1. There are eight SG modules located in the annular space between the core barrel and the reactor vessel [2]. Each SG module mainly consists of a central inner column. The tube coils are 1.64 m in diameter. Each SG has 656 tubes. The tubes are connected to the vertical sides of the lower feedwater header and the upper steam header [2].

Steam generator is a critical equipment between the primary and secondary sides. If the heat in the reactor cannot be carried away by the steam generator timely, it will do harm to the safety of the reactor. Under fault conditions, the operation of the steam generator should be carefully treated. The safety should be guaranteed, and at the same time the economy also needs to be considered, especially for the small modular reactors. This paper aimed to optimize the load level of steam generator under the fault conditions. A steady-state thermal-hydraulic model was established. To improve the thermal power between primary side and secondary side, a optimization method was proposed with the faulty assumption that a certain number of helical tubes were blocked.

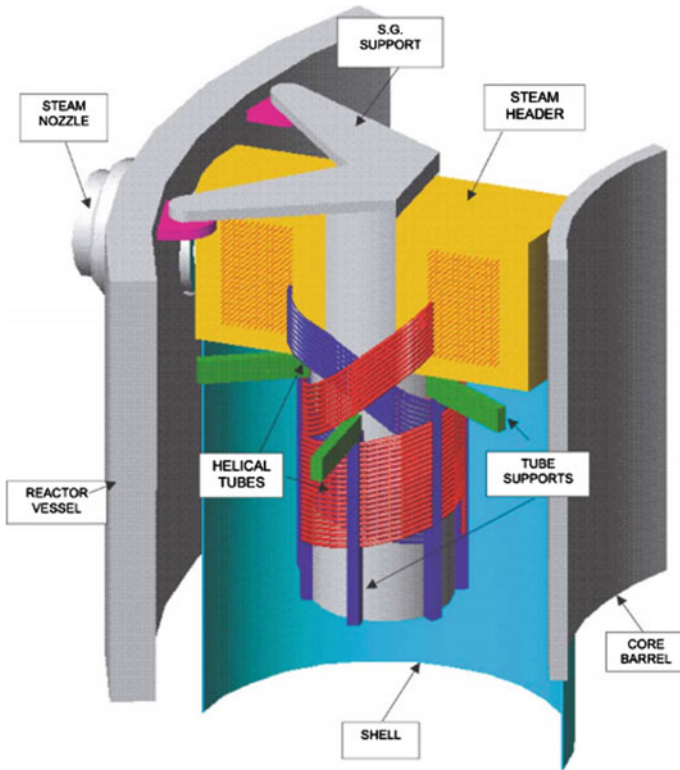


Fig. 1 IRIS steam generator module [3]

2 Thermal-Hydraulic Model of the Iris Steam Generator

2.1 The Basic Assumptions

Several assumptions are made to derive the thermal-hydraulic model.

- (1) The helical tubes are averaged, and the SG can be represented by a single tube;
- (2) The thermal properties at the cross-section of the tube are uniform;
- (3) The heat transfer in the axial direction is neglected; and
- (4) The fluid is considered to be in the thermal equilibrium state.

Table 1 SG design parameters of IRIS [3]

Rated power	125 MW
Tube outside diameter	17.46 mm
Tube thickness	2.11 mm
Tube inside diameter	13.24 mm
Number of helical rows	21
Tubes number	656
Tube bundle average length	32 m
SG height (headers centerline)	7.9 m
SG overall height	8.5 m
Primary-side inlet temperature	328.4 °C
Primary-side outlet temperature	292 °C
Feedwater temperature	223.9 °C
Steam temperature	317 °C
Primary-side pressure	15.5 MPa
Steam outlet pressure	5.8 MPa
Primary flow rate	589 kg/s
Secondary flow rate	62.5 kg/s
Primary-side pressure loss	72 kPa
Secondary-side pressure loss	296 kPa

2.2 Fundamental Equations

Fundamental conservation equations of mass, energy, and momentum are applied to develop the thermal-hydraulic model. Since only steady state is considered, the terms with time derivatives are zero. Then, the following equations are obtained.

(1) Mass equation:

$$W_{\text{in}} = W_{\text{out}} \quad (1)$$

(2) Energy equation:

$$W_{\text{out}}H_{\text{out}} - W_{\text{in}}H_{\text{in}} = Q \quad (2)$$

(3) Momentum equation:

$$\Delta P = \bar{\rho}g(z_2 - z_1) + G^2(v_2 - v_1) + f \frac{L}{D} \frac{\bar{\rho}V^2}{2} \quad (3)$$

2.3 Heat Transfer Correlations

At the secondary side of the steam generator, it goes through subcooled water, two-phase water/steam, and superheated steam. Therefore, three regions are divided based on the thermal properties: subcooled region, the boiling region, and the superheated region. Different heat transfer correlations are used to obtain the heat transfer coefficients. Most correlations are applicable for straight tubes, and correction is needed to extend to the helical-coil tubes.

- (1) In the subcooled region, the Mori and Nakayama heat transfer correlation [4] is adopted:

$$Nu = 1/41Re^{5/6}Pr^{0.4}(di/D)^{1/12} \left[1 + \frac{0.061}{[Re(di/D)^{2.5}]^{0.16}} \right] \quad (4)$$

This correlation is for helical tubes and the structure characteristics have been considered. Therefore, there is no need for correction.

- (2) In the boiling region, the famous Chen's correlation [5] is used

$$h = h_{\text{mac}} + h_{\text{mic}} \quad (5)$$

$$h_{\text{mac}} = 0.023 F \frac{\lambda_f^{0.6} G^{0.8} (1-x)^{0.8} C p_f^{0.4}}{\mu_f^{0.4} D e^{0.2}} \quad (6)$$

where F is Reynolds number factor and described by

$$F = \begin{cases} 1.0, & X_u^{-1} \leq 0.1 \\ 2.35(X_u^{-1} + 0.213)^{0.736}, & X_u^{-1} > 0.1 \end{cases} \quad (7)$$

where

$$X_u^{-1} = \left(\frac{x}{1-x} \right)^{0.9} \left(\frac{\rho_f}{\rho_g} \right)^{0.5} \left(\frac{\mu_g}{\mu_f} \right)^{0.1} \quad (8)$$

$$h_{\text{mic}} = 0.00122S \frac{\lambda_f^{0.79} C p_f^{0.45} \rho_f^{0.49}}{\sigma^{0.5} \mu_f^{0.29} H_{fg}^{0.24} \rho_g^{0.24}} (T_w - T_{\text{sat}})^{0.24} (P_w - P)^{0.75} \quad (9)$$

$$S = \begin{cases} \left[1 + 0.12(Re'_{TP})^{0.14}\right]^{-1}, & Re'_{TP} < 32.5 \\ \left[1 + 0.42(Re'_{TP})^{0.78}\right]^{-1}, & 32.5 \leq Re'_{TP} < 70 \\ 0.1, & Re'_{TP} \geq 70 \end{cases} \quad (10)$$

$$Re'_{TP} = \frac{G(1-x)De}{\mu_f} F^{1.25} \times 10^{-4} \quad (11)$$

- (3) In the superheated region, the heat transfer coefficient can be calculated by Dittus-Boelter correlation for cooling the primary side:

$$Nu = 0.023 Re^{0.8} Pr^{0.4} \quad (12)$$

At the primary side, the heat transfer correlation is also described by Dittus-Boelter correlation for heating secondary side:

$$Nu = 0.023 Re^{0.8} Pr^{0.3} \quad (13)$$

The correction coefficient helical tube is defined by

$$\frac{f_{cc}}{f_{ss}} = \left[Re \left(\frac{R_O}{R_C} \right)^2 \right]^{1/20} \quad (14)$$

2.4 The Pressure Drop Calculation

The pressure drop along the tube is

$$\Delta P = \bar{\rho}g(z_2 - z_1) + G^2(v_2 - v_1) + f \frac{L \bar{\rho} V^2}{D} \quad (15)$$

where, f is

$$f = \max(f_L, f_T) \quad (16)$$

f_L is for the laminar flow,

$$f_L = \frac{64}{Re}, Re < 2320 \quad (17)$$

f_T is for the turbulent flow,

$$f_T = 0.117 \left(\frac{\varepsilon}{D} + \frac{68}{Re} \right)^{0.25} \quad (18)$$

When it is two-phase flow, the friction factor should be corrected by the two-phase friction pressure drop multiplication factor:

$$\phi_{f0}^2 = 1 + x \left(\frac{\rho_f}{\rho_g} - 1 \right) \quad (19)$$

3 The Steady-State Results and Analysis

A Fortran program is developed to carry out the steady-state calculation. Reactor outlet temperature, feedwater temperature, coolant pressure, steam pressure, coolant flow rate, and feedwater flow rate are selected as input parameters. The outputs are reactor inlet temperature, steam temperature, and thermal power.

The temperature distribution of coolant, secondary water, and the tube is shown in Fig. 2. Figure 2a is the calculated results, and Fig. 2b is from the Relap5 results.

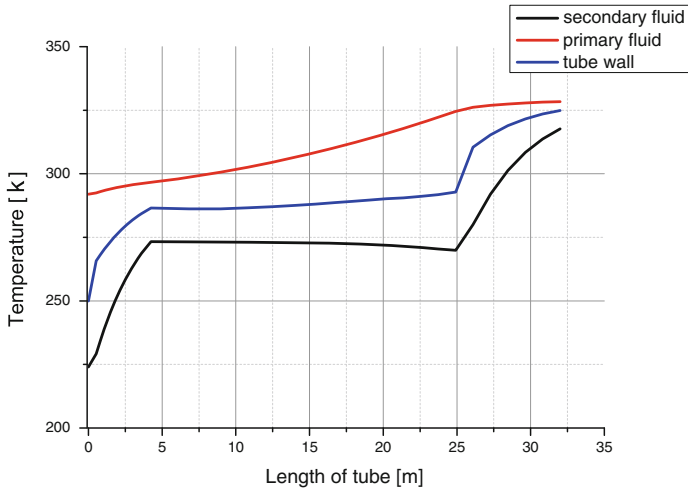
As shown in Fig. 2, the calculated temperature distribution of primary side, secondary side, and tube is consistent with that from Relap5. The primary-side fluid is cooled by the secondary-side fluid. Thus, the temperature of the primary side reduces along the tube. The temperature of the secondary-side fluid in the sub-cooled region increases. When the fluid enters the boiling region, it is saturated and the temperature is constant. The fluid in the superheated region becomes single-phase steam. The temperature of the steam increases for the heat released from the primary-side fluid.

The calculated reactor outlet temperature and steam temperature are shown in Table 2, and design values [1] are also given as comparisons. The calculated results are close to the design data, and the error is in the allowable range.

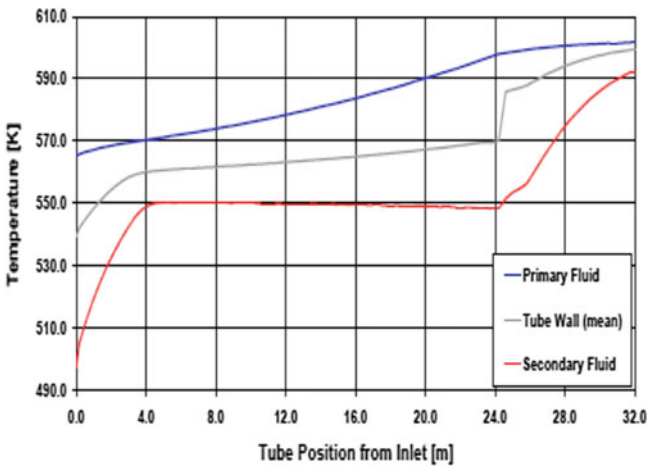
The distribution of the heat flux along the tube is shown in Fig. 3. It is obvious that the curve can be divided into three regions for different heat transfer mechanisms in different regions. The calculated results agree well with those from Relap5.

The pressure drop distribution is shown in Fig. 4. The calculated total pressure drop at the secondary side is 0.34 MPa, which is close to 0.35 MPa calculated by Relap5 [1].

The results of steady-state model agree well with those of the design values and the literature data. Therefore, the model developed can predict the steady-state behavior of the steam generator. The accuracy of the model is high enough for the further study of steam generator power optimization.



(a) Calculated

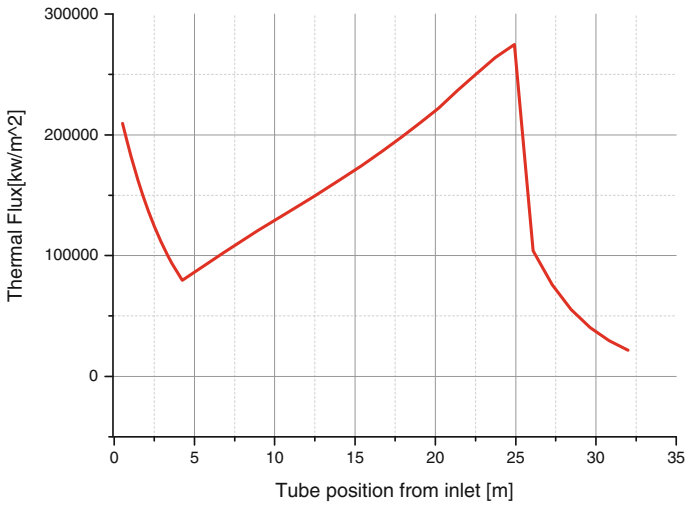


(b) Relap5

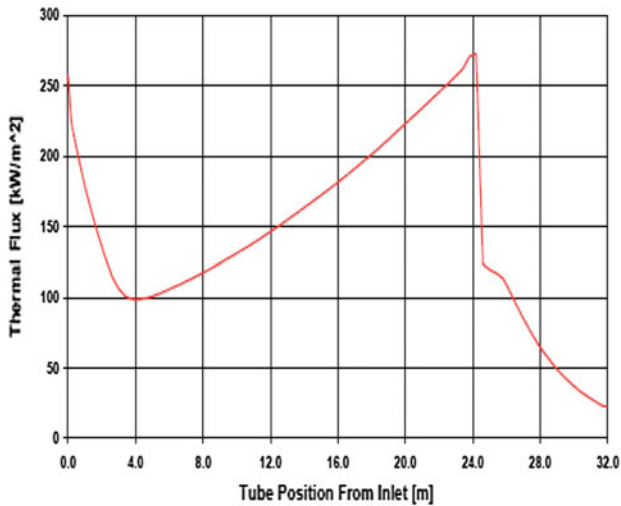
Fig. 2 Temperature distribution along the tube

Table 2 Steady-state calculated results

	Reactor inlet temperature/°C	Steam temperature/°C
Calculated results	292.27	317.75
Design data	291.95	317.0
Error	0.11%	0.24%



(a) Calculated



(b) Relap5

Fig. 3 Heat flux distribution along the tube

4 Power Optimization

4.1 Sensitivity Analysis

The power optimization of once-through steam generator is based on the steady-state model. Before the optimization process, sensitivity analysis is performed to investigate the influences on the thermal power from the steam generator

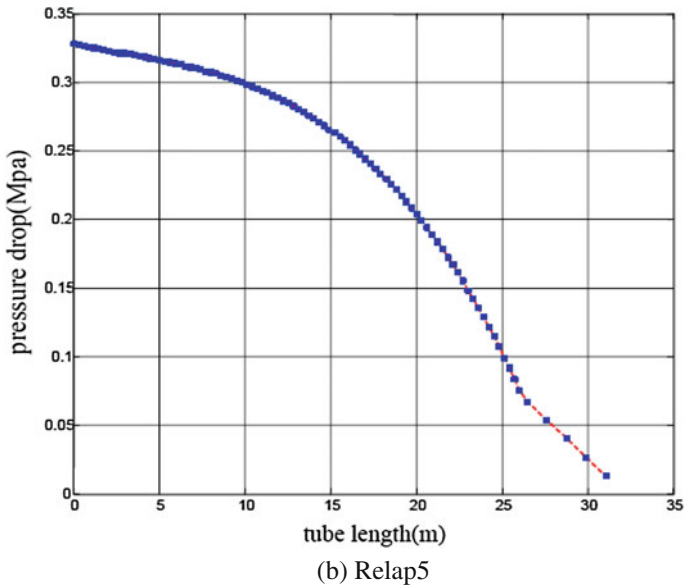
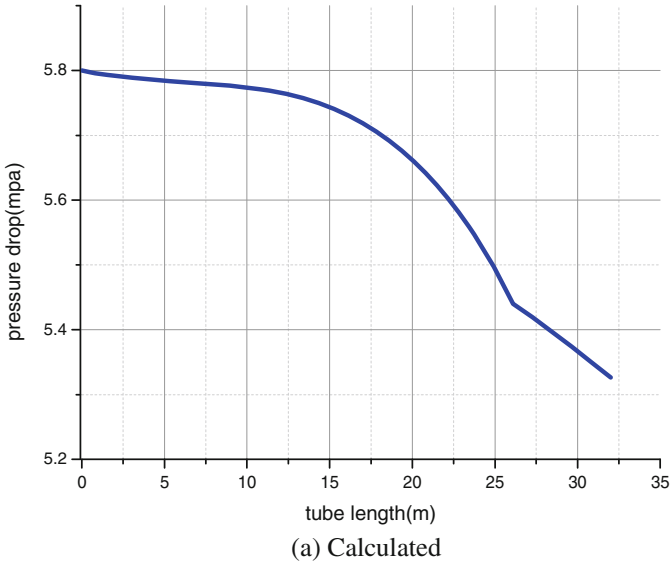


Fig. 4 Pressure drop distribution along the tube at the secondary side

key operation parameters. Four parameters are considered: feedwater flow rate, feedwater temperature, coolant flow rate, and average coolant temperature. To perform the sensitivity analysis, one parameter is disturbed at a time while the others are kept constant. The disturbances are introduced at 100% full power. The results are shown in Figs. 5, 6, 7, and 8.

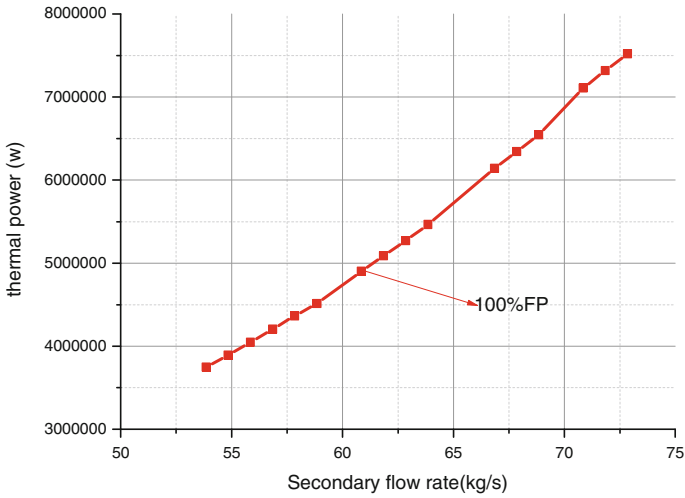


Fig. 5 The thermal power at different feedwater flow rates

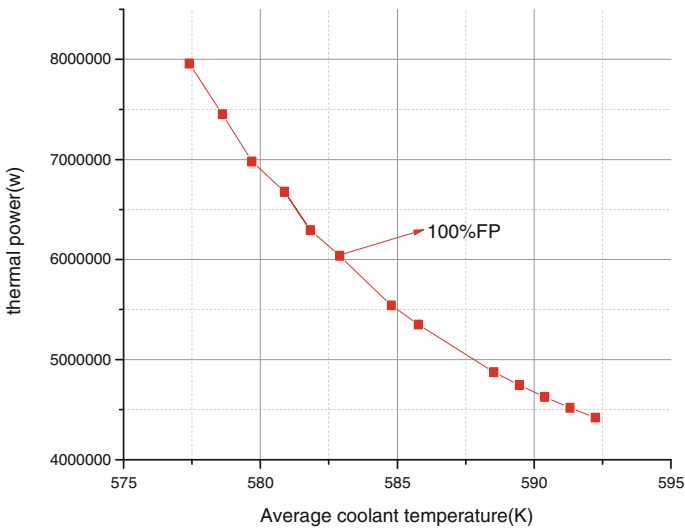


Fig. 6 Thermal power at different average coolant temperatures

The relationship between the thermal power and feedwater flow rate is shown in Fig. 5. It can be seen that the relationship is almost linear. The reason can be explained by the following equation:

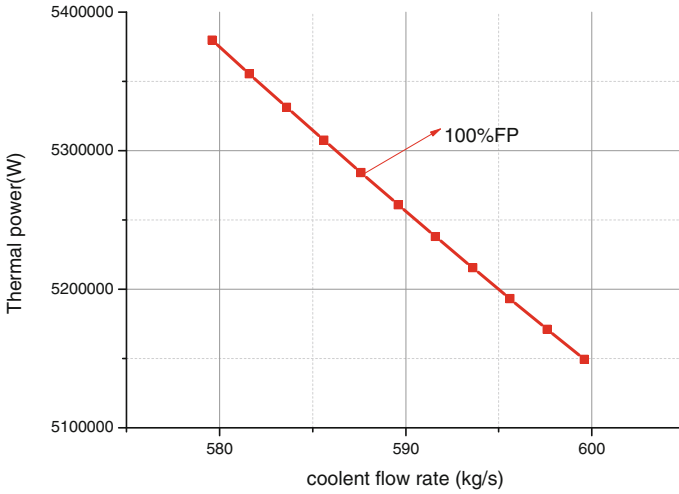


Fig. 7 The thermal power at different coolant flow rates

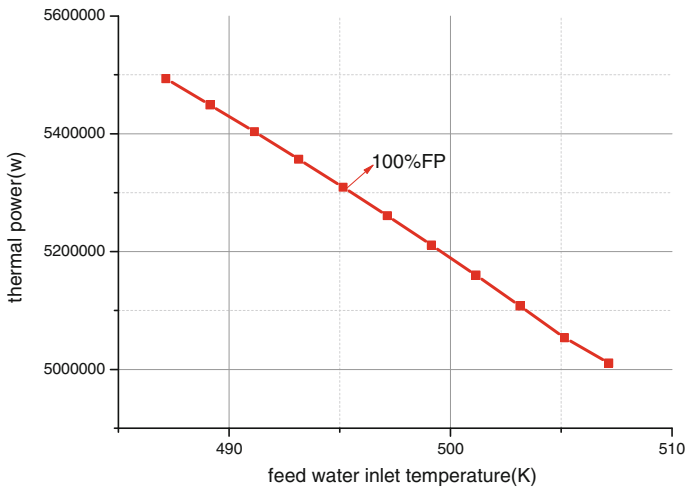


Fig. 8 Thermal power at different feedwater temperatures

$$Q = (H_{out} - H_{in}) * W \tag{20}$$

where, Q is the thermal power; Hout is the steam enthalpy; Hin is the feedwater enthalpy; and W is the feedwater flow rate. Feedwater temperature is unchanged. The steam temperature changes little, which can be proved by Table 3 from the results of Fortran. The steam temperature changes 1.59%, which is very little

Table 3 Steam temperature at different feedwater rates

Feedwater rate/kg/s	73.85	71.85	65.85	63.85	61.85
Steam temperature/°C	314.45	316.75	317.05	318.38	319.54

compared to 16.25% of feedwater rate. Therefore, the thermal power is in a linear relationship with the feedwater flow rate.

Figure 6 shows the relationship between average coolant temperature and the thermal power. The thermal power is almost in an inverse proportion to the average coolant temperature. The reason is that difference in temperature of coolant between inlet and outlet reduces as the increase of the average coolant temperature. According to Eq. (20), the coolant flow rate W is constant, and the difference in enthalpy reduced. Therefore, thermal power is reduced.

The relationship between the thermal power and the coolant flow rate is shown in Fig. 7. The thermal power reduces as the increase of the coolant flow rate. The reason is that the steam temperature is reduced as the increase of coolant flow rate. The feedwater temperature is constant. According to Eq. (20), $H_{out}-H_{in}$ decreases, and the feedwater flow rate W is constant, thus making the thermal power decreased.

The relationship between the reactor outlet temperature and the thermal power is shown in Fig. 8. Increasing the inlet temperature of secondary will make the $(H_{out}-H_{in})$ decreased with the constant outlet temperature. The secondary flow rate is constant. Thus, the thermal power will be reduced.

4.2 Steam Generator Power Optimization

During operation of IRIS, the feedwater temperature and coolant flow rate are kept constant. Therefore, in this paper, the average coolant temperature and feedwater flow rate are chosen as optimized variables and the thermal power as the objective function. Meanwhile, the constraints on the reactor outlet temperature, tube temperature, the reactor inlet temperature, and the circulation ratio are chosen as limitation conditions:

- (1) The tube temperature is T_W , $T_W < 400$ °C;
- (2) Reactor outlet temperature is T_{OUT} , 300 °C $< T_{OUT} < 330$ °C;
- (3) The circulation ratio is s , $1.25 < s < 1.45$;
- (4) Reactor inlet temperature is T_{in} , 270 °C $< T_{in} < 300$ °C.

The optimized variables can be expressed: $X = [T_{AV}, W_C]$. The objective of optimization can be expressed: $F_{heat} = F(X)$.

4.2.1 Polynomial Fit Algorithm

The fault conditions studied are the blockage of tubes. The number of tubes is changed to simulate different power conditions. Control variable method is used in the steady-state model to get the thermal power under the different feedwater flow rate and average coolant temperature. The obtained data are used for polynomial fitting. The results of the fitting are then used to find the optimal results. In this study, 10% of the tubes are blocked. The fitted polynomial from experimental data is as follows:

$$\begin{aligned}
 f(x,y) = & -1.524e+012 - 7.143e+009 * x + 1.107e \\
 & + 010 * y + 8.287e+005 * x^2 + 3.614e+007 * x * y \\
 & - 2.997e+007 * y^2 + 1.157e+004 * x^3 - 6934 * x^2 * y \\
 & - 6.045e+004 * x * y^2 + 3.589e+004 * y^3 - 16.18 * x^4 \\
 & - 13.05 * x^3 * y + 8.39 * x^2 * y^2 + 33.47 * x * y^3 - 16.04 * y^4
 \end{aligned}$$

where, x is the feedwater flow rate; y is the average coolant temperature; and f(x,y) is the thermal power. Three-dimensional diagram of the results is shown in Fig. 9.

The extreme value can be calculated with the method of taking partial derivative to f(x, y). A program has been developed to perform the optimizing calculation. Meanwhile, the limitations should be considered. The results with optimization and the results without optimization are compared in Table 4. The feedwater flow rate is increased, the coolant flow rate is reduced, and the thermal power is increased significantly compared to that without optimization.

Values without optimization are obtained under the normal condition. The results of limits are listed in Table 5. The limits are satisfied.

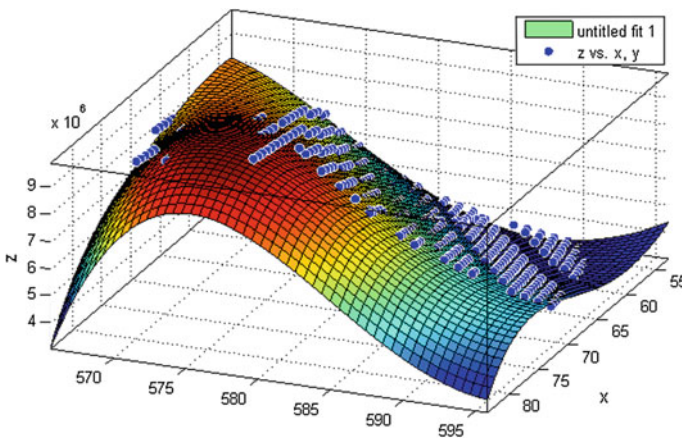


Fig. 9 Three-dimensional simulation diagram

Table 4 The results of optimization

	Feedwater flow rate	Reactor outlet temperature	Reactor inlet temperature	Coolant average temperature	Thermal power
Optimal values	70.85 (kg/s)	323.49 (°C)	284.73 (°C)	304.15 (°C)	7874.85 (KW)
Values without optimization	62.85 (kg/s)	328.35 (°C)	291.16 (°C)	309.75 (°C)	5504.72 (KW)

Table 5 The results of limits

	Calculated result	Range
Reactor outlet temperature/°C	323.49	300–330
Reactor inlet temperature/°C	284.78	270–300
Circulation ratio	1.27	1.25–1.45
Tube temperature/°C	291.23	<400

The obtained results are applicable under the tube blockage conditions. The optimal thermal power is found by seeking extreme values. But, it cannot be proved whether the optimized value is the most suitable. Therefore, an alternate hybrid algorithm is investigated.

4.2.2 Hybrid Algorithm

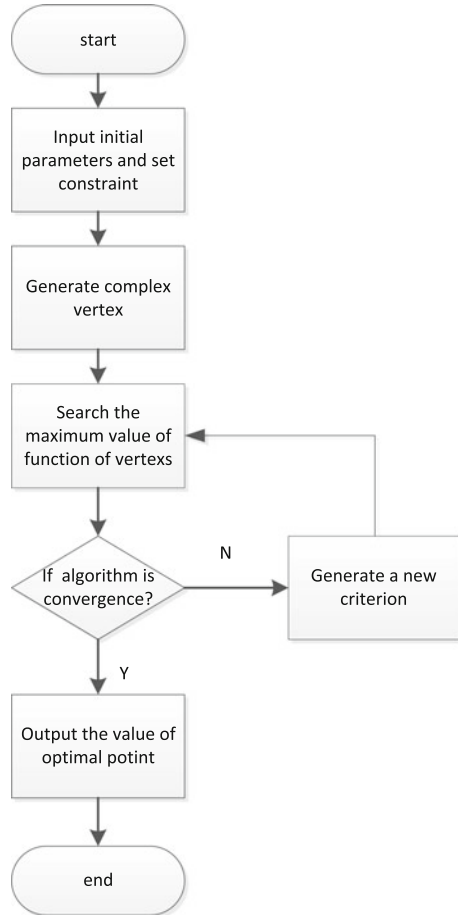
It selects k design points ($n + 1 \leq k \leq 2n$) in the feasible region of N -dimensional as peaks of initial hybrid algorithm. Comparing the object function value of each peak, the point of maximum object function value is selected as a bad point. The center of other points besides the bad point is selected as mapping centralizing to find the mapping of bad points. If the bad point is inferior to these points, the bad point will be replaced. Iteration continues until optimal point is found or convergence accuracy is achieved.

The hybrid algorithm can be applied in optimizing by calling constraint functions and objective function. The diagram of the hybrid algorithm is shown in Fig. 10. Composite parameters and convergence accuracy are set as follows:

- (1) The optimization variables $N = 2$;
- (2) The number of composite vertex $k = 2 N$;
- (3) Convergence accuracy: $\left\{ \frac{1}{K} \sum_{j=1}^K [f(X^j) - f(X^L)]^2 \right\}^{1/2} \leq \varepsilon$

Therefore, the optimization contains restrain function and objection function module. The optimal solution under the fault conditions can be found by calling each other of the two modules. This method can be used to find the maximum thermal power under the condition of different numbers of the tubes blocked by

Fig. 10 The diagram of hybrid algorithm [6]



changing the average temperature of primary side and secondary flow rate. The results are not obtained at this stage of study.

5 Conclusions

Based on the fundamental conversation equations of mass, energy, and momentum, a steady-state thermal-hydraulic model of the steam generator of IRIS is developed. Moving boundary method is adopted. Three regions are divided based on the thermal properties: subcooled region, the boiling region, and the superheated region. The results are compared with those obtained from Relap5, and it is proved the model is accurate enough for further study of the power optimization. Sensitivity analysis is performed to investigate the influences on the thermal power from the steam generator key operation parameters. The relationships between the

thermal power and feedwater flow rate, feedwater temperature, coolant flow rate, and average coolant temperature are analyzed.

The average coolant temperature and feedwater flow rate are chosen as optimized variables. The thermal power is to be optimized. The constraints on the tube temperature, reactor outlet temperature, circulation ratio, and reactor inlet temperature are chosen as limits. Polynomial fit algorithm is used to perform the optimization. The fault condition is that the 10% of tubes is blocked. A fitted polynomial is derived from the data with different feedwater flow rate and the average coolant temperature. The maximum thermal power is found by solving the fitted polynomial under the fault conditions. The thermal power is 30.1% larger than that without optimization. The results of optimization are reasonable for practical application. For further study, hybrid algorithm is proposed to extend the optimization for more general cases.

Acknowledgments This project was supported by the National Natural Science Foundation of China (Grant No. 11405126), the China Postdoctoral Science Foundation (Grant No. 2014M552455), and the Fundamental Research Funds for the Central Universities (xjj2014040).

References

1. Cinotti L, Bruzzone M, Meda N, et al. Steam Generator of the International Reactor Innovative and Secure. 10th International Conference on Nuclear Engineering, American Society of Mechanical Engineers, 2002:983–990.
2. Carelli M D, Conway L E, Oriani L, et al. The Design and Safety Features of the IRIS Reactor. Proceedings of International Conference on Nuclear Engineering ICONE11, Tokyo, 2004, 230:151–167.
3. Petrović B, Carelli M D, Čavlina, Nikola. International Reactor Innovative and Secure. 6th International Conference on Nuclear Option in Countries with Small and Medium Electricity Grids, Hrvatska znanstvena bibliografija i MZOS-Svibor, 2006:313–318.
4. Vaidyanathan G. Development of one-dimensional computer code DESOPT for thermal hydraulic design of sodium-heated once through steam generators. International Journal of Nuclear Energy Science & Technology, 2010, 5(2):143–161.
5. Vaidyanathan G, Kothandaraman A L, Kumar L S S, et al. Development of one-dimensional computer code DESOPT for thermal hydraulic design of sodium-heated once through steam generators. International Journal of Nuclear Energy Science & Technology, 2010, 5(2):143–161.
6. Qin H M, Yan C Q, Wang J J. Optimal design of nuclear reactor primary circuit weight. Yuan zi neng Ke xue Ji shu/Atomic Energy Science & Technology, 2011, 45(5):572–577.

Author Biography

Huasong Cao is the graduate of School of Nuclear Science and Technology at Xi'an Jiaotong University. His research area is at nuclear reactor control.

Propagation of Nuclear Data Uncertainties for PWR Burnup Calculation

Chenghui Wan, Liangzhi Cao, Hongchun Wu, Tiejun Zu
and Wei Shen

Abstract As the nuclear data are from either the experiment measurements or the estimation models, uncertainties would arise from the insufficient measurements and/or modeling uncertainties. The uncertainties in nuclear data would have effects on the best-estimated prediction results of the reactor system. In this paper, our home-developed code UNICORN, which has the capability of uncertainties analysis for the neutron physics calculations, has been applied to quantify the response uncertainties of the PWR burnup calculation introduced by the uncertainties of multigroup microscopic cross-section libraries. The burnup benchmark proposed by UAM (“Uncertainty Analysis in Modeling”) is selected for the demonstration purpose. Relative uncertainties of k_{∞} , two-group constants and isotope concentrations with the fuel burnup introduced by the nuclear data uncertainties are quantified. It is observed that the relative uncertainty of the eigenvalue is 0.5%; the relative uncertainties of the two-group constants vary between 0.3% (for the $\Sigma_{r,2}$) and 1.9% (for the $\nu\Sigma_{f,2}$); the relative uncertainties for the isotope concentrations can reach 30%. These relative uncertainties introduced by the nuclear data are significant for the neutron physics calculations and cannot be ignored.

Keywords Uncertainty analysis · Statistical sampling method · Burnup calculation

1 Introduction

In order to provide the confidence bounds for the best-estimated predictions for the nuclear research, industry, safety and regulation, uncertainty analysis has been proposed and required for predictions of the reactor system [1]. As the neutronics

C. Wan (✉) · L. Cao · H. Wu · T. Zu
Xi’an Jiaotong University, Xi’an, Shaanxi, China
e-mail: chenghuiwan@stu.xjtu.edu.cn

W. Shen
Canadian Nuclear Safety Commission, Ottawa, ON, Canada

calculations are prerequisite for the reactor system, the result uncertainties introduced by the neutronics calculations would be propagated to and impact the prediction results of the thermal hydraulics, fuel, and safety analysis. Therefore, uncertainty analysis for the neutronics calculations is the basic requirement for the reactor design. The nuclear data uncertainties have been proved to be the most significant sources of uncertainty for the neutronics calculations [2]. According to the previous researches, the uncertainties of the neutronics responses introduced by the cross-section uncertainties are significant [3]. In this context, it is necessary to quantify the prediction uncertainties of the neutronics calculations introduced by the nuclear data uncertainties, determining more confident and approximate safety margins.

Two categories of methodologies have been widely applied to perform uncertainty analysis for the neutronics calculations: One is the first-order perturbation theory method, which requires little extract computation time, e.g., the TSUNAMI code [4]; the other is the statistical sampling method, which samples the cross-section library and then execute neutron physics calculations for the sample. By comparing these two kinds of methodologies, the first-order perturbation theory method ignores the nonlinear effects. Moreover, different perturbation models are required to be established for different responses according to specific calculation models, while large amount of responses existed for burnup calculations. However, for the statistical sampling method, there is no approximation to the uncertainty results and for different responses, and no more extract efforts are required. In this context, the statistical sampling method has been widely applied to the uncertainty analysis for the neutron physics calculations.

According to the UAM, the purpose of burnup benchmark, the Exercise I-1b, is to quantify the eigenvalues, few-group constants and the isotope concentrations as well as their uncertainties with depletions [1]. Using the sampling method to perform uncertainty analysis for the burnup calculation, the NRG proposed a TMC (Total Monte Carlo) approach, [5]. This approach samples the evaluation data in ENDF6 format and then uses the NJOY code to generate the samples of the cross-section library with the ACE format, which is used to the executions of neutron transport and depletion calculations using coupling of the MCNP code and TRITON code. This kind of approach requires very large amount of computation time, because large samples of the ACE-format cross-section libraries would be generated and corresponding large amount of execution for the neutron transport calculations with the MCNP code is also required. In this paper, our home-developed UNICORN code has been applied to perform the uncertainty analysis for the burnup calculations, also applying the statistical sampling method. Different with the TMC approach, in UNICORN, the nuclear data samples are generated from the standard WIMSD-4 formatted [6] multigroup microscopic cross-section library, then the deterministic method utilizes the cross-section sample to execute the neutron transport and depletion calculations. Compared with the TMC approach, the UNICORN code can save large amount of computation time. As different methods and approaches have been applied for TMC and UNICORN to

perform uncertainty analysis for PWR burnup calculations, thus the uncertainty result difference is given in this paper.

The paper is organized as follow. Firstly, the burnup benchmark of UAM is introduced. Then the strategy to perform uncertainty analysis for the burnup calculation has been explained, and following which brief introduction of UNICORN is given. Finally, the uncertainty results obtained by UNICORN have been compared with those by the TMC approach.

2 TMI-1 Pin-Cell Burnup Benchmark

The UAM expert group establishes a frame to propagate the cross-section uncertainties in LWR design and safety estimations. For Phase I (Neutronics Phase), Exercise I-1b (Cell Burnup Physics) is to quantify the uncertainties in the depletion calculation due to the basic nuclear data. The typical fuel rod of TMI-1 PWR, proposed by UAM has been selected as the pin-cell model to perform the uncertainty analysis [1]. The requested output parameters of uncertainty analysis include the uncertainties of criticality value k_{∞} , the homogenized two-group cross sections with thermal energy cutoff to be 0.625 eV, and the isotope concentrations.

3 Strategy of Uncertainty Analysis

For simulating the burnup of nuclear fuel, the typical scheme generally includes the evaluation of flux by solving the neutron transport equation and determination of the change of isotope concentrations through the depletion calculations. This scheme can be characterized as shown in Fig. 1.

According to the simulation scheme for the burnup calculation, at one specific burnup step (not the first one), the uncertainty sources consist of two parts: the nuclear data uncertainties and the isotope concentration uncertainties of the previous-one burnup step. These two uncertainty sources would result in the

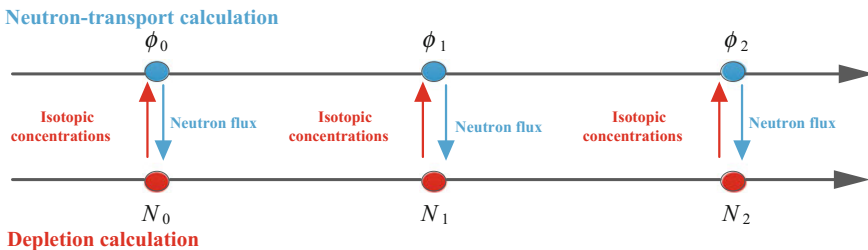


Fig. 1 Simulation scheme for burnup calculation

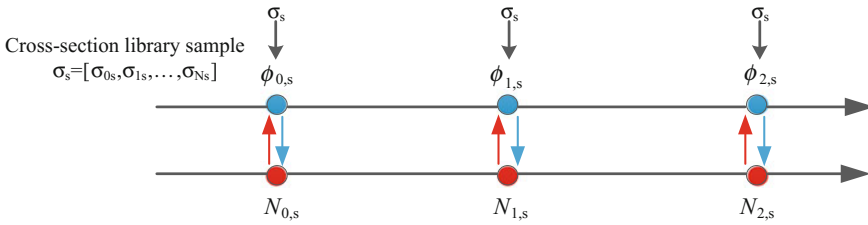


Fig. 2 Uncertainty analysis strategy for burnup calculation

uncertainties of neutron flux and isotope concentrations at this current burnup step, which would become the uncertainty sources of the next burnup step. In this context, in order to perform uncertainty analysis for the burnup calculation, these two kinds of uncertainty sources at each burnup step should be taken into account to obtain the complete uncertainty results. Therefore, the strategy of uncertainty analysis for the burnup calculation using the statistical sampling method can be characterized as shown in Fig. 2. The samples of multigroup microscopic cross-section library are generated at the beginning of coupled neutron transport and depletion calculations. With each cross-section library sample, the burnup calculations are executed and corresponding response samples can be obtained, including the k_{∞} , few-group constants and isotope concentrations at different burnup depth. With all the response samples, the uncertainties of responses can be quantified utilizing the statistical calculations.

4 Introductions of the UNICORN Code

In this paper, our home-developed uncertainty analysis code, UNICORN was used to perform uncertainty analysis for the burnup calculations, quantifying the effects of nuclear data uncertainties to the neutronics responses. The flowchart of the UNICORN code is shown in Fig. 3. Dragon5 [7] was used to perform the neutron transport calculations and depletion calculations in UNICORN.

As generating the samples of cross-section library is actually the process of perturbing the cross-section library around the expectation values, according to the cross-section covariance matrices. Therefore, a newly multigroup cross-section perturbation model has been established and applied in the UNICORN code. This perturbation model has been verified and introduced in detail in our previous work [8]. A brief introduction of the multigroup cross-section perturbation model implemented in UNICORN is made in this section.

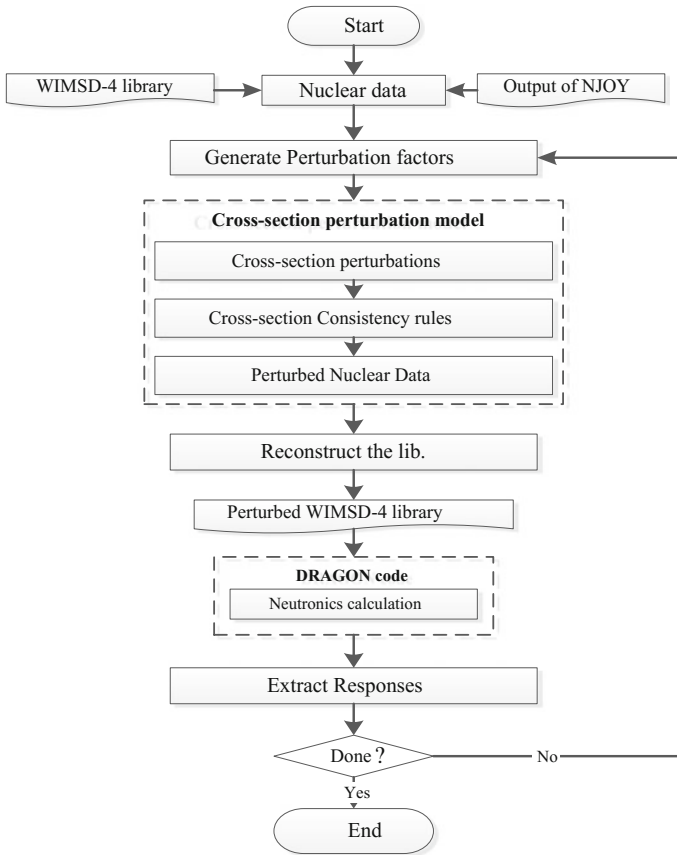


Fig. 3 Flowchart of the UNICORN code

4.1 Generation of Multigroup Cross Sections

The multigroup cross-section library is required and essential for the deterministic code to execute the neutron physics calculations. The point-wise cross sections dependent with energies and temperatures can be converted into specific multigroup format by using the weighting flux $\phi(E, \sigma_0)$.

$$\sigma_{x,g}(T, \sigma_0) = \frac{\int_{\Delta E_g} \sigma_x(E, T) \phi(E, \sigma_0) dE}{\int_{\Delta E_g} \phi(E, \sigma_0) dE} \tag{1}$$

where T, E and σ_0 stand for the temperature, energy and background cross section; $\sigma_x(E, T)$ represents the point-wise cross section of type x . For the cross-section types without resonance, the weighting flux is only dependent on the energy (can be

formulated as $\phi(E)$, and for the cross-section types with resonances, the weighting flux is relative to both the energy and background cross sections. For convenience, the weighting flux is characterized as $\phi(E, \sigma_0)$ following.

Applying the narrow resonance (NR) approximation, the weighting flux $\phi(E, \sigma_0)$ within resonance energy regions can be characterized.

$$\phi(E, \sigma_0) = \frac{\sigma_p^r + \sigma_0}{\sigma_t(E) + \sigma_0} \psi(E) \quad (2)$$

where σ^r and $\sigma_t(E)$ stand for the potential scattering cross section and total cross section for the resonant isotopes, and $\psi(E)$ represents the $1/E$ shape. The multigroup resonance cross sections can be obtained by substituting Eqs. (2) into (1).

4.2 Perturbation Propagations

As the multigroup cross sections are generated using corresponding point-wise cross sections, the multigroup cross-section perturbations would be consistent with the perturbations propagated from the point-wise cross sections. In this paper, it is assumed that the perturbation of the g th group of type x is achieved by adding the uniform relative perturbation to the point-wise cross section within the energy range of the g th group.

$$\sigma'_x(E, T) = (1 + \delta_{x,g})\sigma_x(E, T) \quad E_{g-1} \leq E \leq E_g \quad (3)$$

where E_{g-1} and E_g stand for the lower and upper energy boundaries of the g th group; $\sigma'_x(E, T)$ represents the perturbed point-wise cross section of type x .

For the cross sections without resonance, the weighting flux is independent of the point-wise cross sections and would remain un-perturbed when cross sections perturbed. Therefore, the perturbations of the point-wise cross sections propagated to the multigroup ones are linear.

$$\sigma'_{x,g}(T) = \frac{\int_{\Delta E_g} \sigma'_x(E, T) \phi(E) dE}{\int_{\Delta E_g} \phi(E) dE} = (1 + \delta_{x,g})\sigma_{x,g}(T) \quad (4)$$

However, for the cross sections with resonances, the perturbation propagations from the point-wise cross sections to the multigroup ones are nonlinear. The weighting flux within the resonance energy regions would be perturbed simultaneously due to the perturbations to the point-wise cross sections, as shown in Eq. (2). Therefore, the perturbations existed in the weighting flux introduced by the perturbed point-wise cross sections should be determined. Submitting the perturbed point-wise cross section and the perturbed weighting flux into Eq. (1), the perturbed multigroup cross sections with resonances can be written as:

$$\sigma'_{x,g}(T, \sigma_0) = \frac{\int_{\Delta E_g} \sigma'_x(E, T) \phi'(E, \sigma_0) dE}{\int_{\Delta E_g} \phi'(E, \sigma_0) dE} = (1 + \delta_{x,g}) \sigma_{x,g}(T, \sigma'_0) \quad (5)$$

where σ'_0 represents the perturbed background cross sections due to perturbations of the point-wise cross sections.

$$\sigma'_0 = \frac{\sigma_0}{1 + \delta_{t,g}} \quad (6)$$

where $\delta_{t,g}$ is the relative perturbation of the total cross section due to perturbations of cross-section type x .

With applications of Eqs. (4) and (5), the sampled or perturbed multigroup cross sections can be determined and converted to multigroup microscopic cross-section library with specific format to execute the neutron physics calculations.

5 Uncertainty Analysis Results

In order to perform the uncertainty analysis for burnup calculation of the TMI-1 pin-cell, 69-group microscopic cross-section library with the WIMSD-4 format was generated based on ENDF/B-VII.0 in this paper. The isotopes with cross-section uncertainties analyzed include ^1H , ^{16}O , ^{59}Co , ^{99}Tc , ^{103}Rh , ^{101}Ru , ^{103}Ru , ^{106}Ru , ^{105}Pd , ^{107}Pd , ^{108}Pd , ^{109}Ag , ^{127}I , ^{133}Cs , ^{131}Xe , ^{134}Xe , ^{135}Xe , ^{143}Nd , ^{145}Nd , ^{147}Pm , ^{149}Sm , ^{151}Sm , ^{154}Gd , ^{155}Gd , ^{156}Gd , ^{157}Gd , ^{158}Gd , ^{160}Gd , ^{153}Eu , ^{155}Eu , ^{167}Er , ^{232}Th , ^{233}U , ^{234}U , ^{235}U , ^{238}U , ^{238}Pu , ^{239}Pu , ^{240}Pu , ^{241}Pu , ^{242}Pu , ^{237}Np , ^{239}Np , ^{241}Am , ^{243}Am , ^{242}Cm , ^{243}Cm and ^{244}Cm . The covariance matrices of these analyzed isotopes were generated from ENDF/B-VII.1. The uncertainties of eigenvalue, isotope concentrations and two-group constants have been quantified for the burnup of 0.0, 10.0, 30.0, 50.0 and 60.0 GWd/tU.

In order to compare the relative uncertainties obtained by UNICORN and the TMC approach [9], the relative uncertainties of isotope concentrations introduced by the same isotope cross sections as the TMC approach are compared in Table 1.

As shown in Table 1, the relative uncertainties of isotope concentrations obtained by the UNICORN code are numerically comparable with those by the TMC approach. Moreover, the trends of isotope concentration uncertainties with respect to the depletions are consistent between UNICORN and TMC. The numerical differences of these two approaches could be caused by the method differences used for the neutron transport and depletion calculations applied by the TMC approach and the UNICORN code. Compared with the uncertainties analysis approach utilized by the TMC, the UNICORN code can compute comparable uncertainty results more efficiently.

Table 1 Comparisons of the relative uncertainties (%) for isotope concentrations

ISO	10.0 Gwd/tU		30.0 Gwd/tU		50.0 Gwd/tU		60.0 Gwd/tU	
	1	2	1	2	1	2	1	2
¹³⁴ Cs	4.71	5.23	4.38	4.94	4.06	4.56	3.89	4.35
¹⁴³ Nd	0.29	0.31	0.91	0.96	1.60	1.73	1.97	2.16
¹⁴⁹ Sm	5.07	5.06	5.24	5.23	5.46	5.55	5.58	5.75
¹⁵¹ Sm	5.50	4.87	6.64	5.99	6.90	6.35	6.98	6.50
¹⁵¹ Eu	4.85	4.33	6.63	6.18	7.06	6.98	7.26	7.43
¹⁵⁵ Eu	27.9	26.3	33.2	31.1	35.4	32.9	35.6	33.1
¹⁵⁵ Gd	27.3	25.3	29.9	27.9	28.3	26.4	26.7	25.0
²³⁴ U	0.31	0.32	0.98	1.05	1.74	1.92	2.15	2.40
²³⁵ U	0.11	0.11	0.48	0.54	1.22	1.49	1.78	2.24
²³⁶ U	1.50	1.41	1.44	1.39	1.40	1.42	1.39	1.48
²³⁷ Np	4.10	4.00	3.34	3.82	3.11	3.59	3.03	3.46
²³⁸ Pu	4.60	4.10	3.41	3.73	3.01	3.40	2.89	3.26
²³⁹ Pu	1.15	1.54	1.43	1.93	1.81	2.44	2.00	2.69
²⁴⁰ Pu	1.57	1.84	1.78	2.13	2.01	2.46	2.12	2.63
²⁴¹ Pu	1.49	1.88	1.43	1.77	1.72	2.11	1.91	2.35
²⁴² Pu	2.72	2.95	2.46	2.64	2.41	2.54	2.43	2.51
²⁴³ Am	2.95	3.21	2.59	2.89	2.36	2.74	2.26	2.68
²⁴⁴ Cm	3.21	3.49	2.92	3.21	2.73	3.11	2.67	3.10

1 represents the relative uncertainties obtained and published by the TMC approach; 2 stands for the relative uncertainties obtained by UNICORN

Based on the comparisons, the complete relative uncertainties of isotope concentrations, whose relative uncertainty exceeds 1%, introduced by all the analyzed isotopes in this paper are shown in Table 2.

It can be observed that the relative uncertainties of the isotope concentrations introduced by the cross-section uncertainties can reach up to be 33% for ¹⁵⁵Eu and 28% for ¹⁵⁵Gd. For the other isotopes, the relative uncertainties at the end of cycle are all no more than 10%.

The relative uncertainties for k_{∞} and two-group constants are as shown in Table 3.

It can be observed that the relative uncertainties of k_{∞} and the two-group constants vary with the fuel burnup. Relative uncertainties for most of the responses vary lightly with the fuel burnup, while for $\Sigma_{a,2}$, $\nu\Sigma_{f,1}$, $\nu\Sigma_{f,2}$ and $\Sigma_{s,2,1}$, the relative uncertainties become larger with higher burnup. The largest relative uncertainty of the two-group constants can be up to 1.9% for the $\nu\Sigma_{f,2}$, the smallest relative uncertainty of the two-group constants is 3.0‰ for the $\Sigma_{t,2}$.

The uncertainties analysis for the TMI-1 pin-cell burnup calculation demonstrate that, the relative uncertainties of k_{∞} , the two-group constants and the isotope concentrations introduced by the nuclear data uncertainties are significant for the neutron physics calculations and cannot be ignored.

Table 2 Relative uncertainties (%) for isotope concentrations

Iso	10.0 Gwd/tU	30.0 Gwd/tU	50.0 Gwd/tU	60.0 Gwd/tU
²³⁵ U	0.11	0.52	1.41	2.11
²³⁴ U	0.32	1.05	1.91	2.39
²³⁶ U	1.35	1.35	1.38	1.44
¹⁵¹ Sm	4.86	5.98	6.31	6.46
¹⁴⁹ Sm	5.06	5.21	5.50	5.68
¹⁴³ Nd	0.31	0.96	1.72	2.15
¹⁵⁵ Gd	25.32	28.01	26.48	25.11
¹⁵⁵ Eu	26.28	31.18	32.95	33.16
¹⁵¹ Eu	4.33	6.14	6.86	7.26
¹³⁴ Cs	5.22	4.93	4.55	4.33
²⁴⁰ Pu	1.71	1.82	2.03	2.16
²³⁹ Pu	1.44	1.81	2.28	2.52
²³⁷ Np	4.02	3.92	3.91	3.93
²⁴¹ Pu	1.69	1.58	1.93	2.18
²³⁸ Pu	5.90	5.24	4.94	4.98
²⁴⁴ Cm	12.15	11.15	9.98	9.38
²⁴³ Am	1.88	2.52	3.89	4.65
²⁴² Pu	2.87	3.07	4.04	4.64

Table 3 Relative uncertainties (%) of k_{∞} and two-group constants

Res	0.0 Gwd/tU	10.0 Gwd/tU	30.0 Gwd/tU	50.0 Gwd/tU	60.0 Gwd/tU
k_{∞}	5.17E-01	4.97E-01	4.86E-01	4.96E-01	5.21E-01
$\Sigma_{t,1}$	1.04E+00	1.04E+00	1.04E+00	1.03E+00	1.02E+00
$\Sigma_{t,2}$	3.04E-01	2.98E-01	2.98E-01	3.03E-01	3.07E-01
$\Sigma_{a,1}$	9.09E-01	9.40E-01	9.87E-01	1.04E+00	1.06E+00
$\Sigma_{a,2}$	2.99E-01	4.29E-01	8.35E-01	1.31E+00	1.55E+00
$\nu\Sigma_{f,1}$	5.58E-01	5.48E-01	7.65E-01	1.20E+00	1.42E+00
$\nu\Sigma_{f,2}$	3.79E-01	4.27E-01	8.85E-01	1.52E+00	1.86E+00
$\Sigma_{s,11}$	1.05E+00	1.05E+00	1.04E+00	1.03E+00	1.03E+00
$\Sigma_{s,12}$	1.25E+00	1.26E+00	1.28E+00	1.31E+00	1.32E+00
$\Sigma_{s,21}$	5.86E-01	6.54E-01	9.28E-01	1.33E+00	1.56E+00
$\Sigma_{s,22}$	3.30E-01	3.29E-01	3.28E-01	3.29E-01	3.29E-01

6 Conclusions

In this paper, our home-developed code, UNICORN has been applied to perform uncertainties analysis for the PWR pin-cell burnup calculation. The numerical results of the uncertainty analysis demonstrate that for the isotope concentrations, the relative uncertainties can be up to 33%. For k_{∞} and the two-group constants, the relative uncertainties vary with the fuel burnup, and the relative uncertainty of k_{∞} is

about 0.5%; the relative uncertainties of the two-group constants vary from 0.3% (for the $\Sigma_{f,2}$) to 1.9% (for the $\nu\Sigma_{f,2}$). These relative uncertainties introduced by the nuclear data uncertainties are significant for the neutron physics calculations and cannot be ignored.

Acknowledgments This work is supported by the National Natural Science Foundation of China (Grant No. 11522544).

References

1. K. Ivanov, M. Avramova, S. Kamerow, et al. 2013. Benchmarks for Uncertainty Analysis in Modelling (UAM) for the Design, Operation and Safety Analysis of LWRs. OECD Nuclear Energy Agency. NEA/NSC/DOC(2013)7.
2. M. Pusa, 2012. Incorporating Sensitivity and Uncertainty Analysis to a Lattice Physics Code with Application to CASMO-4. *Annals of Nuclear Energy* 40, 153–162.
3. W. Wieselquist, A. Vasiliev, H. Ferroukhi, 2012. Nuclear Data Uncertainty Propagation in a Lattice Physics Code Using Stochastic Sampling. PHYSOR 2012, Tennessee, USA.
4. B. T. Rearden, L. M. Petrie, M. A. Jessee, 2009. SAMS: Sensitivity Analysis Nodule for SCALE. Nuclear Science and Technology Division, Vol. II, Sect. F22.
5. A. J. Koning, D. Rochman, 2008. Towards sustainable nuclear energy: putting nuclear physics to work. *Ann. Nucl. Energy* 35 (11), 2024–2030.
6. F. Leszczynski, D. L. Aldama, A. Trkov, 2007. WIMS-D Library Update: Final Report of a Coordinated Research Project. International Atomic Energy Agency.
7. G. Marleau, A. Hébert, R. Roy, 2014. A User Guide for DRAGON Version 4. Technical Report, IGE-294.
8. C. Wan, L. Cao, H. Wu, et al. 2015. Code development for eigenvalue total sensitivity analysis and total uncertainty analysis. *Ann. Nucl. Energy* 85, 788–797.
9. C. J. Díez, O. Buss, A. Hofer, et al. 2015. Comparison of nuclear data uncertainty propagation methodologies for PWR burnup simulations.

Research on Multi-objective Optimization Method for Maintenance Decision of Nuclear Power Plant

Lv Yan, Liu Jingquan and Zeng Yuyun

Abstract How to balance multiple conflicting optimization objectives to make nuclear power plant maintenance safe and economic is the key to make decision for nuclear power plant maintenance. This paper proposes a new kind of maintenance model in which the system level, incompletely maintenance, and sequential maintenance characteristics are included. The model introduces age reduction factor measuring the maintenance effect, obtains the system reliability by the adjacency matrix method and the structural function matrix method. At the same time, the influence of the replacement of each component on the system reliability and total cost is taken into account, and the formula for calculating the reliability and the total cost is derived. Then, using the NSGA-II algorithm [the non-dominated sorting genetic algorithm (two generation)] to make the multi-objective optimization of the model, obtaining the multi-objective maintenance plan about a system for the whole life of a nuclear power plant and making suggestions for maintenance decision making. Finally, an example is presented to verify the calculation steps, make the economic analysis and multi-objective optimization of the maintenance program.

Keywords Multi-objective optimization · Incomplete maintenance · System level · Incompletely maintenance · Sequential maintenance

1 Introduction

After the Fukushima nuclear accident, public opinion has more requirements to the safety of nuclear power plants and the requirements about maintenance are also paid more attention. At the same time, on the one hand, maintenance costs have been accounted for life cycle management about 30% and economic efficiency

L. Yan (✉) · L. Jingquan · Z. Yuyun
Tsinghua University, Beijing, China
e-mail: lvyan90@126.com

L. Jingquan
e-mail: jingquan@tsinghua.edu.cn

affects nuclear powers' competitiveness compared to other energy sources. On the other hand, a power plant exists, and a large number of excessive maintenance result in unnecessary waste of maintenance costs. Therefore, how to make the safety higher and the cost lower is of great significance to the development of nuclear powers' maintenance.

At present, the aim of nuclear power plant maintenance modeling is to optimize the maintenance at the component level, namely to make the individual component reliability as optimization objective so that ignores the change in system caused by the interaction between component reliability, and the latter for a system is more important. Meanwhile, traditional maintenance models mostly do not consider preventive replacement, but only assume periodic maintenance to simplify the model. These can be improved so that the maintenance model will be closer to the actual situation. In the optimization of maintenance goals, mostly is to simplify the multi-objective problem into single-objective problem by making other objective functions to constrain for simplifying process except the most important one.

The first section of this study is based on the maintenance in system level, considering the interaction among the components, and specifies how the adjacency matrix and structure function matrix method works that simplifies the complex network among various components to the disjoint minimal path set so that we can get the system reliability from component reliability. The second section explains, in the modeling process, how the age reduction factor is introduced to describe imperfect maintenance in the whole life cycle on system reliability, and the preventive maintenance is also included. At the same time, periodic maintenance will be changed to successive maintenance which is more suitable to the actual satiation. Maintenance model's precision is greatly improved by these changes. The third section is using NSGA-II multi-objective optimization algorithm to directly solve the multi-objective problem which about the system reliability and maintenance cost to find out the global optimal solution and provide support for the nuclear power plant maintenance decision. The last section provides a calculating example to illustrate the calculation steps, make multi-objective optimization and economic analysis of the maintenance program.

2 Complex Network System Reliability Calculation Method

A complex system which contains series, parallel, standby, bridging, and other multiple connections is called net system. For a network system, if we want to get system reliability, the connection of the system needs to be dealt with, so that we can get the relationship between system and each component.

This section uses the adjacency matrix method obtaining the minimal path set and make it disjoint by structure function matrix method. System reliability can be calculated by this way.

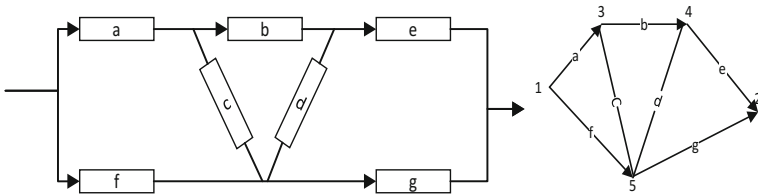


Fig. 1 System equivalent network diagram

2.1 Adjacency Matrix Method

The adjacency matrix method is to firstly convert the complex network system into an equivalent network graph, then draw the graph information from the network graph to generate the adjacency matrix, and through the matrix operation we can get the system path set [1].

Figure 1 represents the logical relationship among devices are transformed into an equivalent network diagram.

The adjacency matrix is defined as:

$$C_{ij} = \begin{cases} 0, & i \text{ and } j \text{ is not directly connected to a arc} \\ x, & i \text{ and } j \text{ directly connected through arc } x \end{cases}$$

For the network diagram in Fig. 1, the adjacency matrix is as follows:

The matrix contains the information of component location, for this matrix, and defines its multiplication (Fig. 2):

$$c_{ij}^{(r)} = \begin{cases} \sum_{k=1}^n c_{ik} c_{kj}^{(r)}, & i \neq j \\ 0, & i = j \end{cases}, \quad r = 2, 3, \dots \tag{1}$$

Extracting the element of each matrix's first row and second column, we can get the minimal path set: *fg, abc, adg, cef, abeg, acde, bcdf*.

Fig. 2 Adjacency matrix

$$C = \begin{bmatrix} 0 & 0 & a & 0 & f \\ 0 & 0 & 0 & 0 & 0 \\ 0 & 0 & 0 & b & c \\ 0 & e & 0 & 0 & d \\ 0 & g & c & d & 0 \end{bmatrix}$$

2.2 Structure Function Matrix Method

After finding out the minimal path set, it is necessary to carry out the disjoint processing so that the reliability of the components can be brought directly into the system to obtain the exact solution of the system reliability.

Structure function matrix method converts the minimal path set to matrix S with only 0 and 1. The numbers of rows are the numbers of the path set, and the numbers of columns are the numbers of components. Each row represents a minimal path, and if component j is in line i , $S(i,j) = 1$, or else, $S(i,j) = 0$.

The benefits of the method is able to put complicated process completely transformed the sum of rows in matrix so that greatly simplifying the calculation.

Figure 3 represents the structure function matrix.

Based on the recursive method of set theory:

$$T = K_1 \cup K_2 \cup \dots \cup K_n = K_1 + \overline{K_1}K_2 + \overline{K_1}\overline{K_2}K_3 + \dots + \overline{K_1}\overline{K_2}\overline{K_3}\dots\overline{K_{n-1}}K_n \tag{2}$$

In Fig. 3, $S_1 = fg$, so

$$\begin{aligned} \overline{S_1}S_2 &= \overline{fg}abc = (\overline{f} + f\overline{g})abc \\ \overline{S_1}\overline{S_2}S_3 &= \overline{fg}abcadg = (\overline{f} + f\overline{g})(\overline{a} + a\overline{b} + ab\overline{c})adg \end{aligned} \tag{3}$$

It means that:

$$\begin{aligned} S_1 &= [0 \ 0 \ 0 \ 0 \ 0 \ 1 \ 1] \\ S_2 &= [1 \ 1 \ 1 \ 0 \ 0 \ 0 \ 0] \\ &\dots \\ S_n &= [0 \ 1 \ 1 \ 1 \ 0 \ 1 \ 0] \end{aligned} \tag{4}$$

$$\begin{aligned} \overline{S_1} &= \begin{bmatrix} 0 & 0 & 0 & 0 & 0 & -1 & 0 \\ 0 & 0 & 0 & 0 & 0 & 1 & -1 \end{bmatrix} \\ \overline{S_2} &= \begin{bmatrix} -1 & 0 & 0 & 0 & 0 & 0 & 0 \\ 1 & -1 & 0 & 0 & 0 & 0 & 0 \\ 1 & 1 & -1 & 0 & 0 & 0 & 0 \end{bmatrix} \\ &\dots \\ \overline{S_n} &= \begin{bmatrix} 0 & -1 & 0 & 0 & 0 & 0 & 0 \\ 0 & 1 & -1 & 0 & 0 & 0 & 0 \\ 0 & 1 & 1 & -1 & 0 & 0 & 0 \\ 0 & 1 & 1 & 1 & 0 & -1 & 0 \end{bmatrix} \end{aligned} \tag{5}$$

Fig. 3 Minimal path set structure matrix

$$S = \begin{bmatrix} 0 & 0 & 0 & 0 & 0 & 1 & 1 \\ 1 & 1 & 1 & 0 & 0 & 0 & 0 \\ 1 & 0 & 0 & 1 & 0 & 0 & 1 \\ 0 & 0 & 1 & 0 & 1 & 1 & 0 \\ 1 & 1 & 0 & 0 & 1 & 0 & 1 \\ 1 & 0 & 1 & 1 & 0 & 1 & 0 \\ 0 & 1 & 1 & 1 & 0 & 1 & 0 \end{bmatrix}$$

The following rules are defined:

1. The path of exchange between two components means the sum of each row of matrix.
2. If any element of the matrix operation results in 2, -2, then change it to 1, -1.
3. If the column of the original matrix is 1, -1 or -1, 1, and the result of the addition is 0, the row will be deleted.

By calculating from the rules, the final disjoint minimal path set is as follows:

$$\begin{aligned} \text{DMPS} = & fg + abc\bar{f} + cef\bar{g} + abc\bar{e}\bar{f}\bar{g} + \bar{a}bcd\bar{f}g \\ & + ab\bar{c}\bar{d}\bar{e}\bar{f}g + \bar{a}bcde\bar{f}\bar{g} + \bar{a}bcd\bar{e}\bar{f}\bar{g} \end{aligned} \tag{6}$$

By the methods above, we can get the system reliability about complex net system.

3 Developing the Model of Nuclear Power Plant Maintenance

3.1 The Theory of Maintenance and Age Reduction Factor

There are three types of maintenance based on the maintenance effect: minimal maintenance, complete maintenance, and incomplete maintenance. The facility will function well after minimal maintenance, while its failure rate cannot be decreased; complete maintenance provides a reboot of the used facility, making its reliability, failure rate return to the level of new facility; incomplete maintenance, which is applied in most scenarios, is a kind of maintaining process lying between those two mentioned above, able to improve the reliability of the facility to some extent [2].

In this model, incomplete maintenance is mainly discussed, and the extent of each incomplete maintenance is described by age reduction factor. Age reduction factor denotes the service age reduced by incomplete maintenance; it can be set as a constant or variable depending on the situation. And it is usually derived by specialists' opinions or calculation [3].

$R(t)$ denotes the reliability of the facility after service time t . Age reduction factor being α , after incomplete maintenance, the reliability becomes $R(t - \alpha T)$.

$$\begin{aligned}
 \lambda_1 &= \lambda(t), & 0 \leq t < T \\
 \lambda_2 &= \lambda(t - \alpha_1 T), & T \leq t < 2T \\
 &\dots \\
 \lambda_i &= \lambda\left(t - \sum_{j=1}^i \alpha_j T\right), & (i - 1)T \leq t < iT \\
 &\dots \\
 \lambda_{N-1} &= \lambda\left(t - \sum_{j=1}^{N-1} \alpha_j T\right), & (N - 2)T \leq t < (N - 1)T \\
 \lambda_N &= \lambda\left(t - \sum_{j=1}^{N-1} \alpha_j T\right), & (N - 1)T \leq t \leq NT
 \end{aligned} \tag{7}$$

The reliability of facility at each period is derived above. Note the expression of the last period is a little different, for there will not be maintenance at the end of this period.

3.2 Assumptions of the Model of Maintenance

Such assumptions are made below for the model based on what really happens during maintenance:

1. The nuclear power system has the same service life as the plant, which is 40 years. A major overhaul is due every 18 months, lasting 1 month. These figures are set as constants for convenience.
2. Each preventive maintenance is undertaken during the major overhaul. And the interval between two maintenance is multiples of the periods of overhaul (18 months).
3. The reliability of the facility can be exponential distribution, Weibull distribution, or normal distribution. The exponential distribution means the failure rate is constant; therefore, the facility cannot be repaired. The facility with the two other distributions is aging, and its failure rate increasing with time.
4. If a component fails during overhaul, it will be minimally maintained rather than replaced.
5. The times of minimal maintenance during the interval of overhaul conforms to non-homogeneous Poisson distribution, and the duration of each maintenance conforms to log-normal distribution.
6. Each component has a designed service life. Incomplete maintenance is undertaken if the component is within its designed life when maintained. And if the component is beyond its designed life before next maintenance, it will be replaced this time.

Table 1 Model parameter description

Parameter	Symbol
Overhaul cycle	T
The N time for preventive replacement	N
The i time for preventive maintenance	C_{pm_i}
Fixed cost of preventive maintenance	C_f
Variable cost of preventive maintenance	C_v
Minimal maintenance cost	C_{mr}
Unit shutdown loss	C_s
Preventive replacement cost	C_{pr}
Age reduction factor	α_i
Preventive maintenance time	t_{pm_i}
Minimal maintenance time	t_{mr}
Maintenance cost adjustment factor	a
Maintenance time adjustment coefficient	b

7. None of the facility is maintained if the last time of maintenance coincides with the expiry date of the plant.
8. The cost of minimal maintenance and preventive replacement is fixed.
9. Age reduction factor changes with the cost of maintenance, and it varies each time.

3.3 Maintenance Model Parameters

Table 1 lists the main parameters of the model (Figs. 4 and 5)

3.4 The Derivation of System Reliability and Total Cost Function

Figure 6 represents the flowchart for obtaining system reliability and total cost function [4].

The preventive maintenance cost at each node is as follows:

$$C_{pm_i} = C_f + i \cdot C_v, \quad i = 1, 2, \dots, N \tag{8}$$

Then, the age reduction factor in each node is as follows:

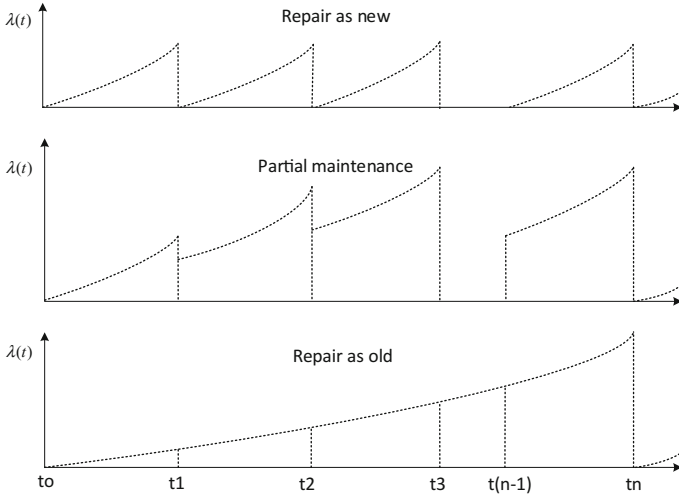


Fig. 4 Water supply system net diagram

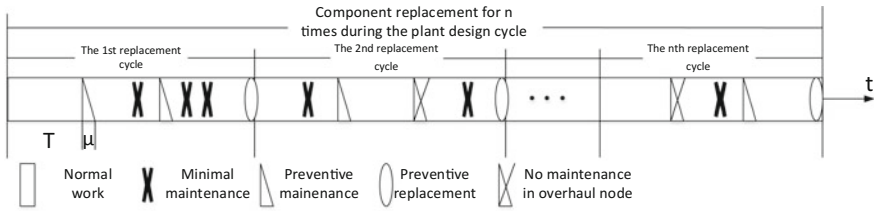
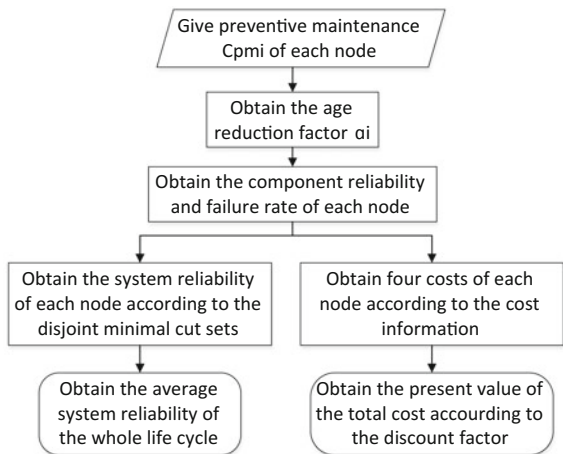


Fig. 5 Preventive maintenance successively schedule chart including preventive replacement, breakdown

Fig. 6 Obtained flowchart of the objective function



$$\alpha_i = \begin{cases} \left(a \frac{C_{pm_i}}{C_{pr}}\right)^{b \cdot i}, & i = 1, 2, \dots, N - 1 \\ 1, & i = N \end{cases} \tag{9}$$

The reliability and failure rate formula can be obtained from formula (7):

$$\lambda_i = \begin{cases} \lambda \left[\left(i - \sum_{j=1}^i \alpha_j \right) T \right], & i = 1, 2, \dots, N - 1 \\ \lambda \left[\left(N - \sum_{j=1}^{N-1} \alpha_j \right) T \right], & i = N \end{cases} \tag{10}$$

$$R_i = \begin{cases} R \left[\left(i - \sum_{j=1}^i \alpha_j \right) T \right], & i = 1, 2, \dots, N - 1 \\ R \left[\left(N - \sum_{j=1}^{N-1} \alpha_j \right) T \right], & i = N \end{cases} \tag{11}$$

The component reliability at each maintenance node can be derived from formula (6) so that we can get system reliability:

$$R_{sys} = DMPS(R_a, R_b, \dots, R_g) \tag{12}$$

Total cost is composed of four parts: preventive maintenance cost, preventive replacement cost, minimal maintenance cost, and unit shutdown loss.

The preventive maintenance cost at node is presented in formula (8).

The preventive replacement cost has been assumed to be constant: C_{pr} . But it is necessary to pay attention that the complex of introducing preventive replacement is that the replacement cycle will impact age reduction factor. Thus, it will affect the whole reliability and failure rate distribution.

It has been assumed that the number of failures in the maintenance intervals is subject to a non-homogeneous Poisson process, and the minimal maintenance cost per time is constant. Then, the minimal maintenance cost is as follows:

$$C_{mr_i} = \sum_{j=1}^n c_{mr} n_i = c_{mr} \sum_{j=1}^n \int_{T_{j-1}}^{T_j} \lambda_i(t) dt \tag{13}$$

Among them, the times of system faults are [5]

$$n_i = \int_{T_{j-1}}^{T_j} \lambda_i(t) dt \tag{14}$$

The shutdown loss contains three items, which are preventive maintenance, preventive replacement, and minimal maintenance. The first two of them can be consolidated for they all happened during the overhaul period.

The minimal maintenance time is as follows:

$$T_{mr} = \sum_{i=1}^N t_{mr}n_i = t_{mr} \int_{T_{j-1}}^{T_j} \lambda_i(t)dt \tag{15}$$

Among them, t_{mr} is the average time of minimal maintenance, which is obtained by the assumed log-normal distribution.

Preventive maintenance time T_{pm} is overhaul period, which is regarded as constant. As a result, the shutdown loss for each overhaul cycle is as follows:

$$C_s = c_sT_{pm} + c_sT_{mr} = c_sT_{pm} + c_s t_m \sum_{j=1}^n \int_{T_{j-1}}^{T_j} \lambda_i(t)dt \tag{16}$$

By formulas (8), (13), (16), and the constant for prevention replacement, we can obtain the total cost of all components for each preventive maintenance cycle:

$$TC_i(a, b, \dots, g) = T_{pr_i} + T_{pm_i} + T_{mr_i} + C_s \tag{17}$$

For the decision made today, the future cost should be discounted to the present reasonably, namely calculating the present value of the cost of different periods. Therefore, the total cost function for the entire life cycle is given as:

$$TC = \sum_{i=1}^{i=Life} npv_i = \sum_{i=1}^{i=Life} \frac{TC_i}{1+r} \tag{18}$$

Finally, the two system’s objective function to be optimized is obtained:

$$\begin{cases} \max & R_{sys} = DMPS(R_a, R_b, \dots, R_g) \\ \min & TC = \sum_{i=1}^{i=Life} npv_i = \sum_{i=1}^{i=Life} \frac{TC_i}{1+r} \end{cases} \tag{19}$$

4 Multi-objective Maintenance Optimization

4.1 Multi-objective Optimization Description

The paradigm of multi-objective optimization is as follows:

$$\begin{aligned} \text{Min } & y = f(x) = (f_1(x), f_2(x), \dots, f_k(x)) \\ \text{s.t. } & e(x) = (e_1(x), e_2(x), \dots, e_m(x)) \leq 0 \\ & x = (x_1, x_2, \dots, x_n) \in X \\ & y = (y_1, y_2, \dots, y_n) \in Y \end{aligned}$$

In this problem, there are k objective functions, m constraints, and n variables. A collection of Pareto optimal solutions is derived after solving this problem. Here are several important concepts below about this paradigm: [6].

1. Pareto dominance: x^0 dominates x^1 if and only if:

$$\begin{aligned} f_i(x^0) &\geq f_i(x^1), \quad \forall i \in \{1, 2, \dots, M\} \\ f_i(x^0) &> f_i(x^1), \quad \exists i \in \{1, 2, \dots, M\} \end{aligned}$$

2. Pareto optimal solution: A solution that is not dominated by any other solutions is Pareto optimal solution.
3. Pareto optimal front: The collection formed by the objective function values corresponding with Pareto optimal solutions is called Pareto optimal front.

$$P_F = \{f(x) = (f_1(x), f_2(x), \dots, f_M(x)) | x \in P_s\}$$

In the final optimal collection, a solution cannot be dominated by any other within the collection.

4.2 NSGA-II for Solving Multi-objective Pareto Optimal Solution Set

Multi-objective optimization problem is traditionally solved by transforming it into a single-objective problem, that is, by choosing the most important objective function and turning the others into constraints. This method is flawed because it tends to ignore many good options [7].

Fig. 7 NSGA-II schematic diagram

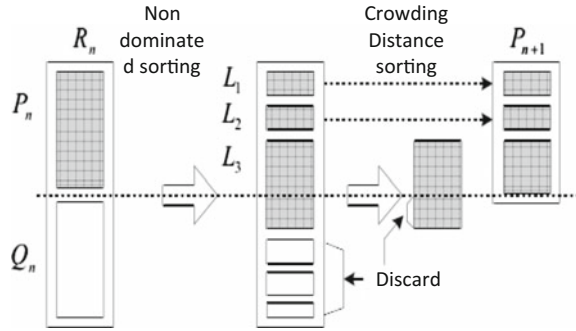
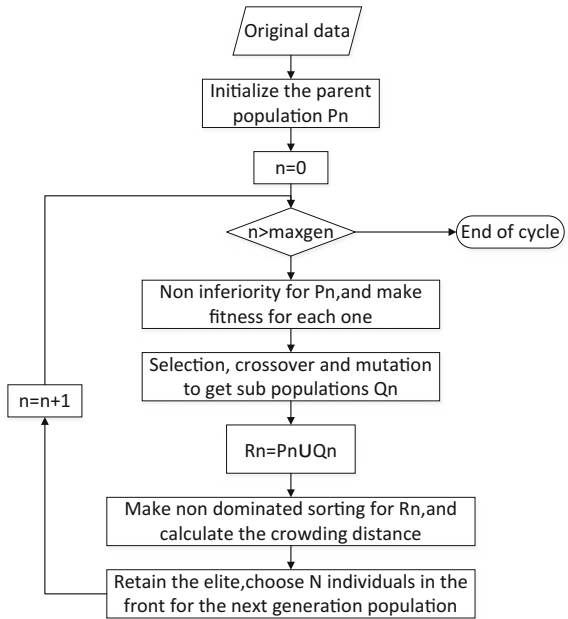


Fig. 8 NSGA-II logic block diagram



NSGA-II is an improved genetic algorithm. Genetic algorithm has an inherent advantage when it comes to multi-objective optimization.

Figure 7 is the schematic diagram of the algorithm in which the main difference to the traditional genetic algorithm is non-dominated sorting and crowding distance sorting. Non-dominated sorting is used to screen the former ones in ranking in each generation and leave their genes to the next generation. Crowding distance sorting is used to estimate the intensive degree between the Pareto solution and the surrounding ones. Figure 8 represents the specific logic block diagram.

Through coding the maintenance information of each components of nuclear power plant maintenance model, we can get the primary population P_0 which

includes each maintenance plan with the system reliability and the total cost information. Then, order non-dominated sorting of each individual, and through binary tournament selection, crossover, mutation, we can obtain Q_0 . Then, a new species group called $R_0 = P_0 \cup Q_0$ is obtained. And carry it on the non-dominated sorting and crowding distance sorting to get the next generation of population.

5 Example Verification

5.1 Seeking System's Disjoint Minimal Path Set

Figure 9 represents the network diagram about the water supply system.

The adjacency matrix C can be obtained from Fig. 9.

$$C = \begin{bmatrix} 0 & 0 & a & 0 & 0 & 0 & 0 & 0 \\ 0 & 0 & 0 & 0 & 0 & 0 & 0 & 0 \\ 0 & 0 & 0 & b & d & 0 & 0 & 0 \\ 0 & 0 & 0 & 0 & 0 & c & 0 & 0 \\ 0 & 0 & 0 & 0 & 0 & 0 & e & 0 \\ 0 & 0 & 0 & 0 & 0 & 0 & 0 & f \\ 0 & 0 & 0 & 0 & 0 & 0 & 0 & g \\ 0 & h & 0 & 0 & 0 & 0 & 0 & 0 \end{bmatrix}$$

By calculating, the minimal path set is as follows: $abcfgh, adefgh$.

The structure function matrix is obtained according to the minimal path set:

$$S = \begin{bmatrix} 1 & 1 & 1 & 0 & 0 & 1 & 1 & 1 \\ 1 & 0 & 0 & 1 & 1 & 1 & 1 & 1 \end{bmatrix}$$

According to the structure function matrix, the final disjoint minimal path set matrix is as follows:

$$DMPS = \begin{bmatrix} 1 & 1 & 1 & 0 & 0 & 1 & 1 & 1 \\ 1 & -1 & 0 & 1 & 1 & 1 & 1 & 1 \\ 1 & 1 & -1 & 1 & 1 & 1 & 1 & 1 \end{bmatrix}$$

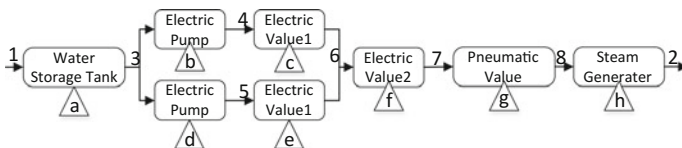


Fig. 9 Water supply system net diagram

So, the disjoint minimal path set is:

$$abcfgh + \bar{a}bdefgh + ab\bar{c}defgh \tag{20}$$

5.2 The Process of Maintenance Optimization

System parameters are assigned as shown in Table 2.

Then, the parameters of each component are assigned, as shown in Table 3.

After parameters initialization, it is necessary to code the maintenance plan variables, and the coding information should include the maintenance situation of each component on each maintenance node. In this regard, we use binary code: 1 represents maintenance and 0 represents no maintenance.

In this example, the life of plant is 40 years, overhaul cycle is 18 months, and overhaul time is about 1 month, so there are 25 maintenance nodes. The total component number is 8, so the length of code is $25 * 8 = 200$. Each maintenance scheme can be used from the length of the 200 binary strings for representation.

Initial population can be artificially set; bringing it into the system reliability function and the total cost function, we may get a set of system reliability and total cost results for the individual. Figure 10 represents the change in component reliability considering the age reduction factor and preventive replacement. For each preventive replacement making component reliability with a certain degree of recovery, the reliability will be set to 1 at the node of preventive replacement.

Put the population which contains maintenance message into NSGA-II algorithm to optimize, so as to obtain the Pareto optimal solution set, as shown in Fig. 11.

Each solution in the set cannot be dominated by others, which is mean to each point on the Pareto frontier corresponding to a set of system average reliability, and total cost should be taken into account by decision maker in nuclear power plant.

Figure 11 presents the following:

Table 2 Example system parameters

Input	Data
System name	Water supply system
System node number	8
System component number	8
System age: year	40
Overhaul cycle: year	1.5
Overhaul time: year	0.1
Discount rate	0.03
Unit shutdown loss: 10Ths	1000
Minimal maintenance cost: 10Ths	2
Age reduction factor <i>a</i>	1
Age reduction factor <i>b</i>	0.005

Table 3 Example component parameters

Parameters	Water storage tank	Pneumatic value	Electric value 2	Electric pump	Electric value 1	Steam generator
Component number	<i>a</i>	<i>g</i>	<i>f</i>	<i>b, d</i>	<i>c, e</i>	<i>h</i>
Design life	40	10	10	20	15	40
Fixed cost of preventive maintenance: 10Ths	2	1	1	2	1	10
Variable cost of preventive maintenance: 10Ths	0.2	0.1	0.1	0.2	0.1	1
Preventive replacement cost: 10Ths	50	90	20	200	30	1000
Reliability model	Exponential	Exponential	Weibull	Weibull	Weibull	Weibull
Exponential distribution: λ	0.015	0.02	–	–	–	–
The Weibull distribution: λ	–	–	0.02	0.03	0.02	0.03
The Weibull distribution: α	–	–	2	3	2	3

1. With the increase of genetic algebras, Pareto optimal front moves to the left, namely better maintenance plan was screened out.
2. With the increase of genetic algebras, the shape of Pareto optimal front is gradually converging to smooth curve from the initial scattered point front.
3. For the initial population is generated randomly, individual selection rate is high at the original generation, the number of individuals in each generation of the

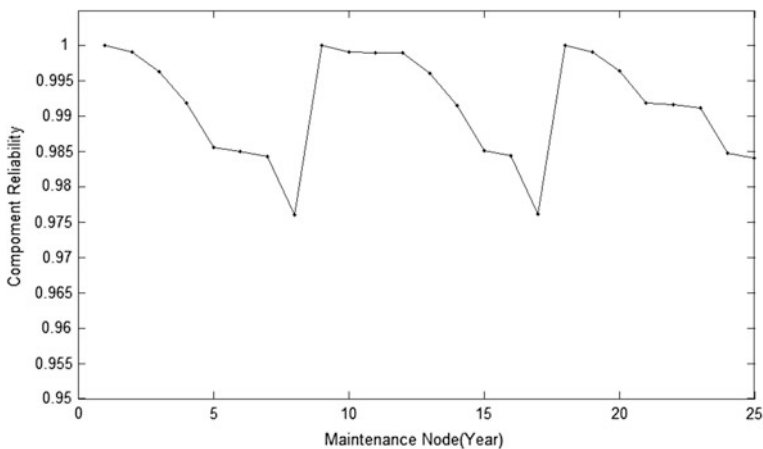


Fig. 10 Component reliability changes

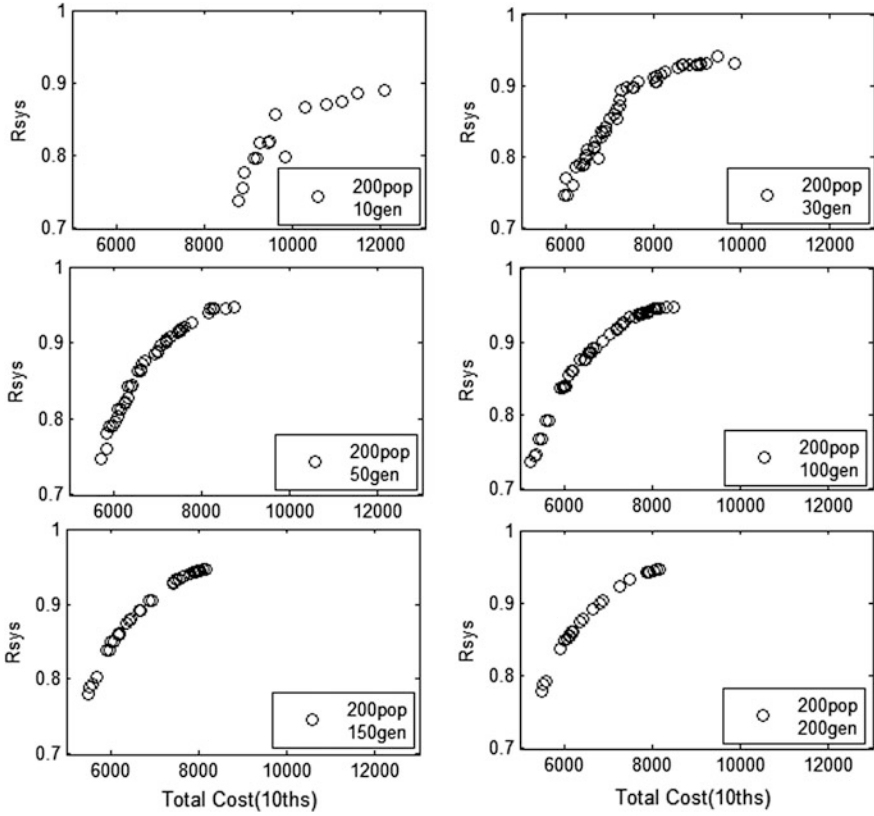


Fig. 11 Pareto optimal solution sets of different algebras

Table 4 Example system parameters

Order	R_{sys}	TC	Order	R_{sys}	TC
1	0.7794	5486	13	0.8792	6423.3
2	0.7894	5532.7	14	0.8912	6643.4
3	0.7932	5598.3	15	0.8993	6822.7
4	0.8382	5924.3	16	0.9044	6880.1
5	0.8498	6025	17	0.9236	7254.1
6	0.8500	6076.3	18	0.9327	7487.5
7	0.8556	6094.3	19	0.9337	7490.5
8	0.8558	6145.6	20	0.9431	7888.1
9	0.8600	6159.9	21	0.9433	7955.4
10	0.8602	6211.2	22	0.9452	8035.2
11	0.8609	6215.9	23	0.9456	8102.6
12	0.8751	6378.1	24	0.9458	8153.9

Table 5 Final maintenance plan to solution 16

Maintenance node	Running time (y)	Water storage tank <i>a</i>	Electric pump <i>b</i>	Electric value <i>c</i>	Electric pump <i>d</i>	Electric value <i>e</i>	Electric value <i>f</i>	Pneumatic value <i>g</i>	Steam generator <i>h</i>
1	1.6	M	-	-	-	-	-	-	M
2	3.2	M	-	-	-	-	-	M	-
3	4.8	M	-	-	-	-	-	-	M
4	6.4	M	-	-	-	M	-	-	M
5	8	M	-	-	-	-	-	-	M
6	9.6	-	-	-	-	-	R	R	M
7	11.2	M	M	-	-	-	-	M	M
8	12.8	M	-	-	-	-	-	-	M
9	14.4	M	-	R	-	R	-	-	-
10	16	M	-	-	-	M	-	M	M
11	17.6	M	-	-	-	-	-	-	M
12	19.2	M-	R	-	R	-	R	R	M
13	20.8	M	-	-	-	-	-	-	M
14	22.4	-	-	-	-	-	-	-	-
15	24	M	-	-	M	-	-	-	M
16	25.6	M	-	-	-	-	M	-	-
17	27.2	M	-	-	-	-	-	-	M
18	28.8	M	-	M	-	-	R	R	M
19	30.4	M	-	M	-	-	-	M	M
20	32	-	-	-	-	-	-	M	M
21	33.6	-	-	-	-	-	-	M	-
22	35.2	-	-	-	-	-	-	M	-
23	36.8	-	-	-	-	-	-	M	-

(continued)

Table 5 (continued)

Maintenance node	Running time (y)	Water storage tank <i>a</i>	Electric pump <i>b</i>	Electric value <i>c</i>	Electric pump <i>d</i>	Electric value <i>e</i>	Electric value <i>f</i>	Pneumatic value <i>g</i>	Steam generator <i>h</i>
24	38.4	–	–	M	–	–	–	–	M
25	40	–	–	–	–	–	–	–	–

M Maintenance*R* Replacement

population gradually increased and individual corresponding solution is gradually increased. When arriving to certain algebra, population number will be up to the maximum, but different individuals may correspond to the same solution, Therefore, the Pareto optimal front point is becoming less and less instead.

Taking 200 generations on Fig. 11 as an example, through iteration, we get 24 solutions of the non-dominated solution set, and the details are shown in Table 4.

5.3 Screening of Pareto Solution Sets

The Pareto optimal solution set obtained by using the multi-objective optimization should be combined with practical constraints for selection in practical application. Therefore, here are the criteria for the selection [8].

Regulators of nuclear power plant have mandatory requirement for the safety of operation. Therefore, we can take the criterion which is the combination of the lower limit of the reliability, the upper limit of the cost, and the lower limit of the reliability benefit from unit cost $I = \Delta \overline{R}_{\text{sis}} / \Delta TC$, so that we can reduce the number of the solutions. After the screening of the program, the decision makers can select from them and whatever the final choice is, it is Pareto optimal.

According to the screening criteria, 16, 17, 18, 19 in Table 4 are the solutions which should be recommended to decision makers. They will finally select one as the final plan according to the actual situation in the four solutions.

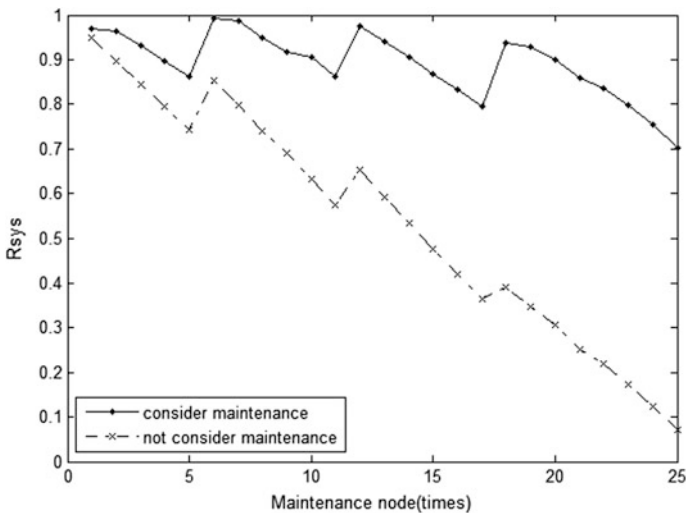


Fig. 12 Change in system reliability with time

If solution 16 is selected, the corresponding final solution P is as shown in Table 5. Through the solution P , we can also see from Fig. 12 that the improvement of system reliability with maintenance compared to no maintenance.

6 Conclusions

In this paper, through analyzing the nuclear power plant system maintenance, the maintenance model based on imperfect maintenance is established in which the characteristics include system-level, preventive replacement, and successive maintenance. The process of obtaining disjoint minimal path set through deriving the structure function matrix method greatly simplifies the calculation. In the process of maintenance modeling, the formula for system average reliability and total cost is derived. At the same time, using improved genetic algorithm NSGA-II to make multi-objective optimization toward the model and obtaining the Pareto optimal solution set. Meanwhile, give the selection criteria of the solution set for further processing. Finally, the decision maker will obtain a certain amount of free discretion of a series of maintenance program.

At present, the further research includes embedding the optimal module into the database of life cycle management of the nuclear power plant and providing support for the prevention of nuclear power plant.

References

1. Cao Jinhua, Cheng Kan (2006). An introduction to mathematics of reliability [M]. Beijing, HEP.
2. Lapa, Celso Marcelo F., Claudio Marcio NA Pereira, and Marcio Paes de Barros. "A model for preventive maintenance planning by genetic algorithms based in cost and reliability." *Reliability Engineering & System Safety* 91.2 (2006): 233–240.
3. Wang Dalin (2010). *Maintenance and Life Cycle Management for Nuclear Plant Components Based on Reliability*. Tsinghua University.
4. Vu, H. C., Do, P., Barros, A., & Berenguer, C. (2014). Maintenance grouping strategy for multi-component systems with dynamic contexts. *Reliability Engineering & System Safety*, 132, 233–249.
5. Zuo Hongfu, Cai Jing, Wang Huawei(2008). *The theory and method of maintenance decision*. Beijing, Aviation Industry Press.
6. Busacca, P. Giuggioli, Marzio Marseguerra, and Enrico Zio. "Multiobjective optimization by genetic algorithms: application to safety systems." *Reliability Engineering & System Safety* 72.1 (2001): 59–74.
7. Lei Deming, Yan Xiping (2009). *Multi-objective intelligent optimization algorithm and its application*. Beijing, Science Press.
8. Zio, E., & Bazzo, R. (2011). A clustering procedure for reducing the number of representative solutions in the Pareto Front of multiobjective optimization problems. *European Journal of Operational Research*, 210(3), 624–634.

Simulation Analysis of Condensation Heat Transfer Inside C-type Tubes Based on RELAP5/MOD3.2

Wangsheng Tian, Xiixin Cao, Zhongning Sun, Yongyong Yang and Wenjing Lei

Abstract The RELAP5/MOD3.2 code was validated experimentally for simulating the condensation heat transfer characteristics inside C-type tubes of the passive residual heat removal heat exchanger. In order to eliminate the effects of the boiling model out of tubes when simulating condensation, the C-type tube condensation simulation, in which the wall temperature was given, was performed using RELAP5/MOD3.2 code. Comparing the simulation results with the experimental data, it is found that the maximum relative deviation between the experimental and calculated condensation heat transfer coefficients exceeds 80% in the range of experimental data, and the change tendency of the average condensation heat transfer coefficient is obviously different with the increase in the outlet condensate Reynolds. RELAP5/MOD3.2 code uses Chato model to calculate the condensation of the horizontal part and uses the Nusselt model to calculate the condensation of the vertical part when simulating the C-type condensation experiment in the range of experimental parameters. The results show that the standard code in RELAP5/MOD3.2 cannot give completely reliable predictions when simulating the condensation heat transfer characteristics inside the C-type tubes.

Keywords Passive · RELAP5 · Condensation heat transfer · C-type tubes · Condensation model assessment

1 Introduction

The RELAP5/MOD3.2 code has been developed to best estimate safety analysis of the nuclear power plant transients and loss-of-coolant accidents (LOCA) [1]. The CAP1400 nuclear power plant designed independently by China employs the third-generation nuclear power technology [2], and its passive residual heat removal

W. Tian · X. Cao (✉) · Z. Sun · Y. Yang · W. Lei
Fundamental Science on Nuclear Safety and Simulation Technology Laboratory,
Harbin Engineering University, Harbin, Heilongjiang, China
e-mail: caoxiixin@hrbeu.edu.cn

system (PRHRS) is designed to remove the primary loop stored heat and reactor decay heat in order to improve the inherent safety under the emergency conditions. The main component of the PRHRS is the passive residual heat removal heat exchanger (PRHR HX) which consists of the in-containment refueling water storage tank (IRWST) and the C-type tubes submerged in the IRWST. When the code in RELAP5/MOD3.2, which was developed for evaluating the second-generation nuclear power technology, is used to analysis the PRHRS of the CAP1400 nuclear power plant, its suitability must be verified.

Although some researches, which assessed the PRHRS cooling ability using the RELAP5 code, have been done [3, 4], uncertainties are known to exist in many RELAP5/MOD3.2 correlations, especially for condensation models. The standard condensation models in RELAP5/MOD3.2 have been assessed and improved separately in a vertical condensing tube with laminar and turbulent condensation films and on the horizontally stratified condensation using previous data from various condensation experiments [5]. The horizontally stratified condensation model with or without noncondensable gases was investigated compared with the direct contact condensation experimental data and some previous experimental data. The results show that the horizontally stratified condensation model overpredicts the experimental data in both cocurrent and countercurrent conditions [6]. In addition, the modified codes were used to simulate a horizontally stratified tube experiment and two kinds of vertical tube experiment in the presence of noncondensable gases at a low pressure, and simulation result showed that the modified RELAP5/MOD3.2 codes give a better prediction for the experimental data than that of the standard codes [7]. Yu Lei et al. used the principle experiment platform and the PRHR that is one-tenth of its actual size to evaluate the RELAP5/MOD3.2 code. They found that the condensation coefficient in vertical tube calculated from RELAP5/MOD3.2 code is under estimate [8]. Yuxian Rao et al. give six vertical in-tube condensation models and implement them into the RELAP5/MOD3.2 code. And the prediction accuracy of these models is given [9].

Although the RELAP5/MOD3.2 condensation models have been assessed separately in the vertical and horizontally tubes, it is significantly different in many conditions in the C-type tube. So the applicability of the condensation models in simulating the C-type tube condensation needs further confirmation when the code is used to simulating the PRHR of the CAP1400 advanced reactor. In this paper, an experiment simulating the PRHR HX and the assessment of the condensation model in standard RELAP5/MOD3.2 code simulating the C-type tube condensation will be shown.

2 Standard RELAP5/MOD3.2 Condensation Models

There are two kinds of standard condensation models in RELAP5/MOD3.2 code. One is interfacial heat transfer, occurring through an assumed interface between the liquid and vapor phases, and the other is wall heat transfer, occurring when the wall has contact with the two-phase mixture fluid [1].

The interfacial condensation heat transfer can be divided into vertically and horizontally stratified flow, and in this paper, this group will not be treated.

For the wall heat transfer, there are two kinds of condensation models used in RELAP5/MOD3.2—the default and the alternative [1]. In the inclined case, the Nusselt–Shah–Colburn–Hougen correlations are active in the default model, and Nusselt University of California–Berkeley (UCB) correlations which are active in the alternative model are revised for the interfacial shear and noncondensable gases' effect in vertical tubes. In the horizontal case, the Chato [10] correlation is active in both the default and the alternative models replacing Nusselt [11] correlation which applies to laminar condensation inside tubes. The default model uses the maximum value of the Nusselt and Shah [12] correlation. When the Shah model is activated in RELAP5, it is not used until the condensation heat transfer coefficient calculated by the Shah correlation becomes larger than that of Nusselt correlation, and the Shah correlation is used in both horizontal and vertical conditions. The Colburn–Hougen [13] correlation is used for condensation with non-condensing gas, and it is not treated in this paper.

3 Experimental Facility

An experiment system simulating the PRHR HX has been established, and the pure steam condensation experiment inside the C-type tubes has been performed. The experimental system is shown in Fig. 1. It consists of the condensation loop, the boiling loop, the cooling water loop, and related measurement facilities.

The test section consists of three C-type tubes placed side by side, respectively, with the 129, 141, and 153 mm length. The distance between each two C-type tubes is 38 mm, and all of the test tubes are made of stainless steel with 22 mm diameter and 3 mm thickness. At 13 different axial locations, two K-type thermocouples are welded onto the different places of the outer surface of the C-type tubes to measure the outer wall temperatures. There are 13 group K-type thermocouples located 100 mm away from the C-type tubes, which measure the water temperatures in the different place of the experimental water tank. The mass flow of the condensate water is measured by the condensate measuring tank. The temperature and pressure of the inlet-saturated vapor and the outlet condensate water are obtained from the experiment-related measurement facilities.

In the experiment, the pressure of the boiling water in experimental water tank is the local atmospheric pressure. The pressure of the saturated vapor flowing into the

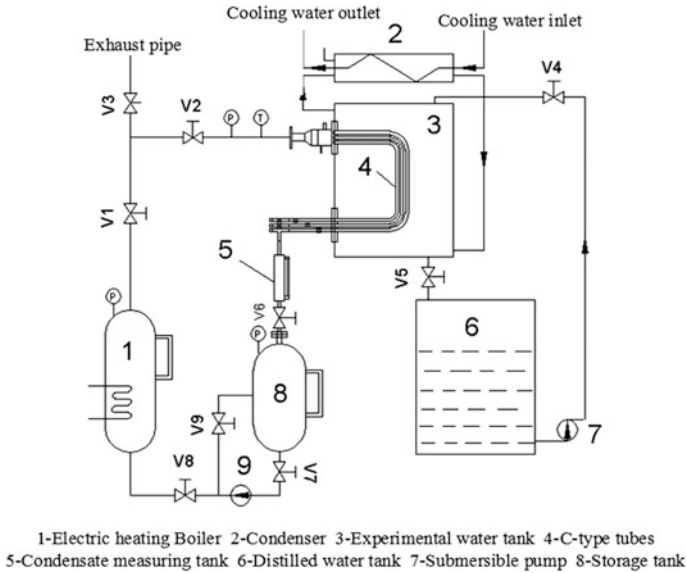


Fig. 1 PRHR HX condensation experimental device

C-type tubes submerged in the water of the experimental water tank ranges from 0.18 to 0.54 Mpa.

4 The RELAP5/MOD3.2 Nodalization Scheme

The PRHR HX experiments consist of the condensation inside the C-type tubes and the pool boiling out of the C-type tubes, and the wall temperatures of the outer surface of the C-type tubes are obtained in the experiment. In order to avoid the effect of pool boiling out of the C-type tubes, the RELAP5/MOD3.2 code model which gives the outer surface wall temperatures of the C-type tubes is established. Figure 2 gives the RELAP5/MOD3.2 nodalization scheme of the experiment.

RELAP5/MOD3.2 nodalization of this simulation which represents the condensation heat transfer circuit contains time-dependent volume, single-junctions, branches, pipes, and the heat structures.

The time-dependent volume 310 acting as the electric heating boiler is used to simulate to produce saturated pure steam which flow into the C-type tubes. Branches, 320, 321, and 322, are used to simulate the average steam orifice of the inlet tubes. For the simulation of the C-type tubes, three time-dependent pipes, 330, 331, and 332, which model the condensation heat transfer part of the C-type tubes, are, respectively, connected to the pipes, 323, 324, and 325, of the inlet part, and the pipes, 338, 337, and 336, of the outlet part, which represent the no-heat-exchange

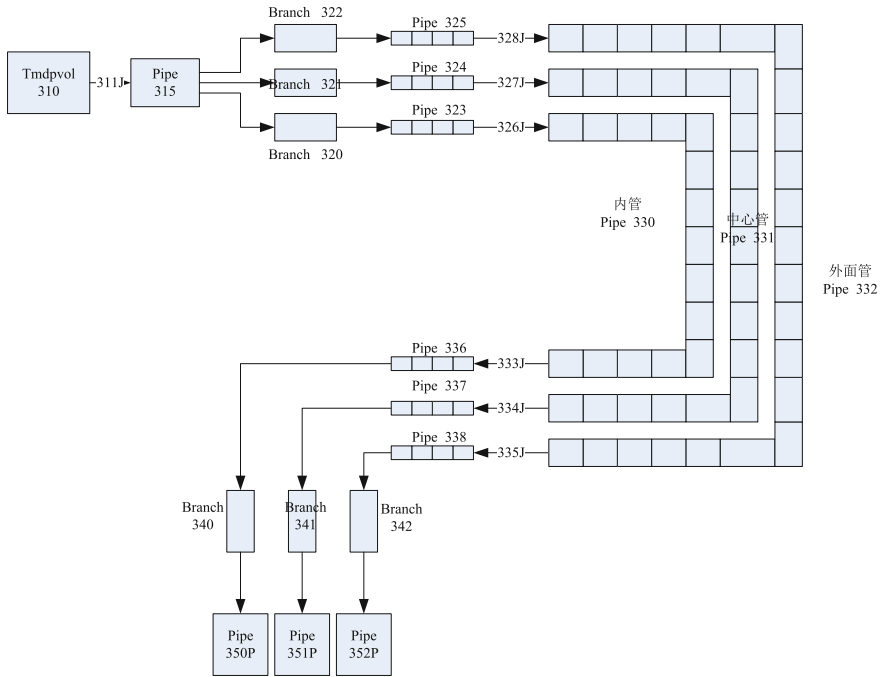


Fig. 2 RELAP5/MOD3.2 nodalization scheme of the experiment

part in order to eliminate the effect of the entrance effect. The three branches, 340, 341, and 342, simulating the condensate measuring tanks, are, respectively, connected to pipes, 350, 351, and 352, which represent the storage tank. Three heat structures, connected to condensation heat transfer part of the three C-type tubes, are used to represent the outer surface wall temperature boundary conditions, and the temperatures at 13 different axial locations are different because of the coupling effect of the condensation inside tubes and the boiling outside the tubes.

5 Simulation Results and Discussions

Nine inlet-saturated steam pressure condensation experiments are simulated using RELAP5/MOD3.2 code. The simulation result contains the average condensation heat transfer coefficient, average inter surface heat flux, condensate mass flow rate, outlet condensate temperature, out condensate Reynolds Number, and the flow regimes in the C-type tubes.

5.1 Comparison of the Average Condensation Heat Transfer Coefficient

Figures 3, 4, and 5 show the comparison of the average condensation coefficient of the C-type tubes with the change of the inlet-saturated steam pressure. The standard condensation models in RELAP5/MOD3.2 cannot give the completely reliable

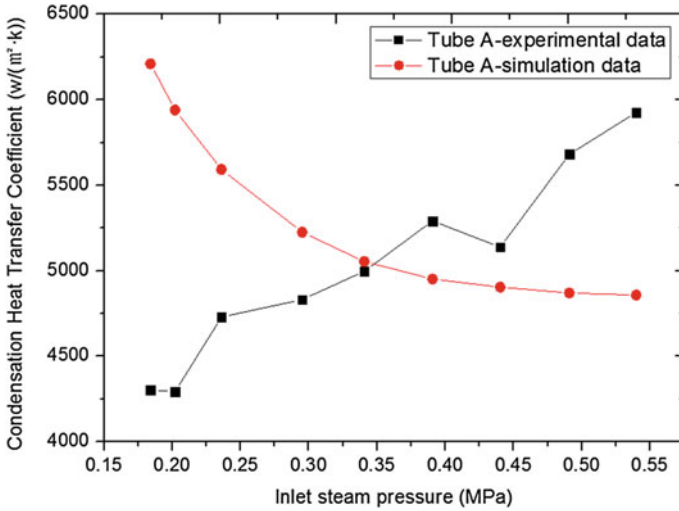


Fig. 3 Comparison of the average condensation coefficient of tube A

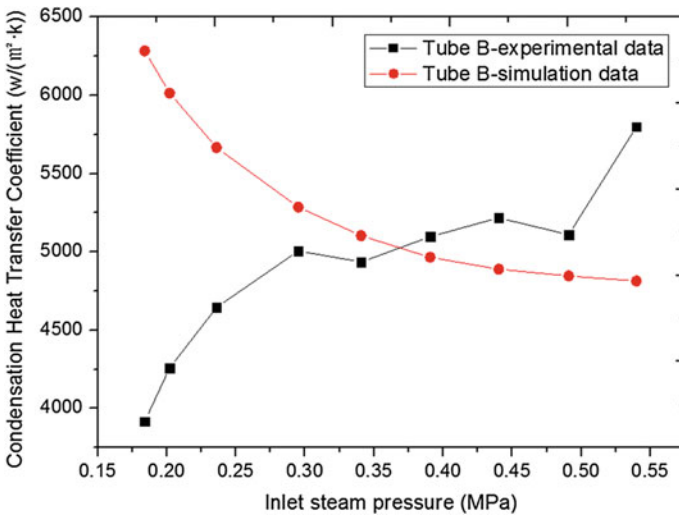


Fig. 4 Comparison of the average condensation coefficient of tube B

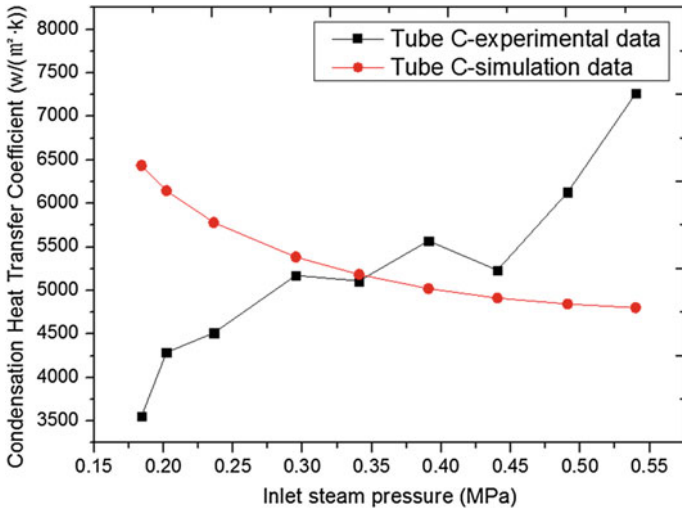


Fig. 5 Comparison of the average condensation coefficient of tube C

condensation coefficient predictions, and the changing trend of the simulating result is completely opposite compared with the experimental result. In the range of the inlet steam pressure from 0.3 to 0.5 Mpa, the maximum relative deviation between the experimental and simulating average condensation coefficients is 21%, and the average relative deviation is 6.67%. However, the maximum relative deviation

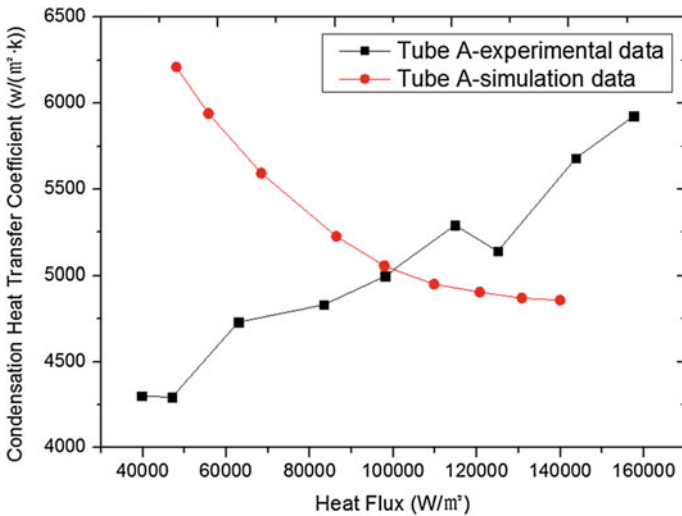


Fig. 6 Comparison of the average condensation coefficient of tube A

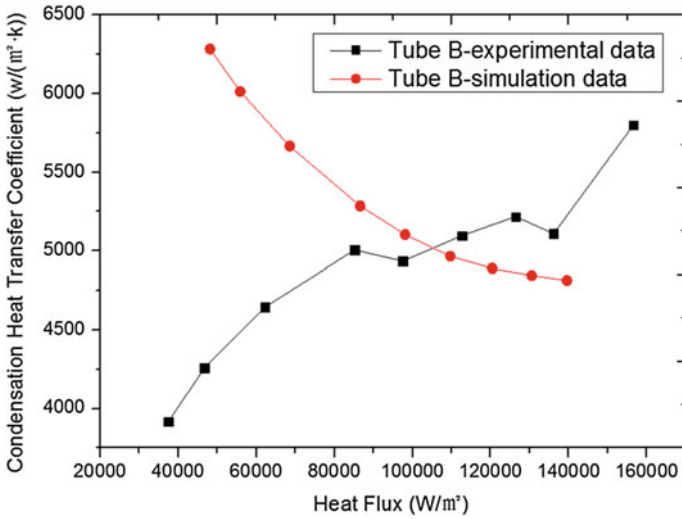


Fig. 7 Comparison of the average condensation coefficient of tube B

between the experimental and simulating average condensation coefficients exceeds 80% in other experimental conditions.

Similarly, with the change in the average intersurface heat flux of the C-type tubes, comparison of the average condensation coefficient between the experimental data and the simulation data has the same result and the comparison is shown in

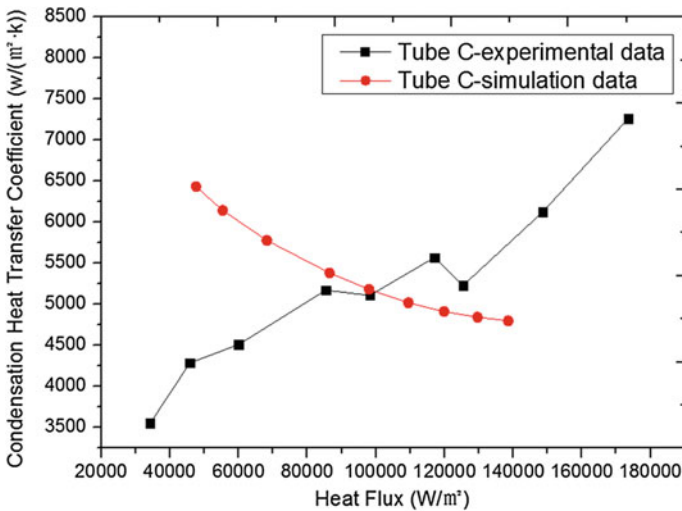


Fig. 8 Comparison of the average condensation coefficient of tube C

Figs. 6, 7, and 8. Only in the range of the heat flux from 100,000 to 130,000 W/m², the simulation result can give reasonable predictions.

5.2 Comparison of the Condensate Mass Flow Rate

Figures 9, 10, and 11 show the comparison of the outlet condensate mass flow rate with the increase in the inlet steam pressure of the three tubes, respectively. When the inlet steam pressure is lower than 0.35 Mpa, the outlet condensate mass flow rate predictions using the standard condensation models are higher, and it is lower when the inlet steam pressure is higher than 0.35 Mpa. Furthermore, in the range of the inlet steam pressure from 0.3 to 0.5 Mpa, the maximum relative deviation between the experimental and simulating outlet condensate mass flow rate is 12.5%, and the average relative deviation is 3.8%. In other experimental conditions, RELAP5/MOD3.2 code cannot give any reliable predictions.

5.3 Comparison of the Outlet Condensate Temperature

Comparison of the outlet condensate temperature of the three C-type tubes, which have the same conditions of the inlet-saturated steam pressure and outer surface wall temperatures, is shown, respectively, in Figs. 12, 13, and 14. The simulation

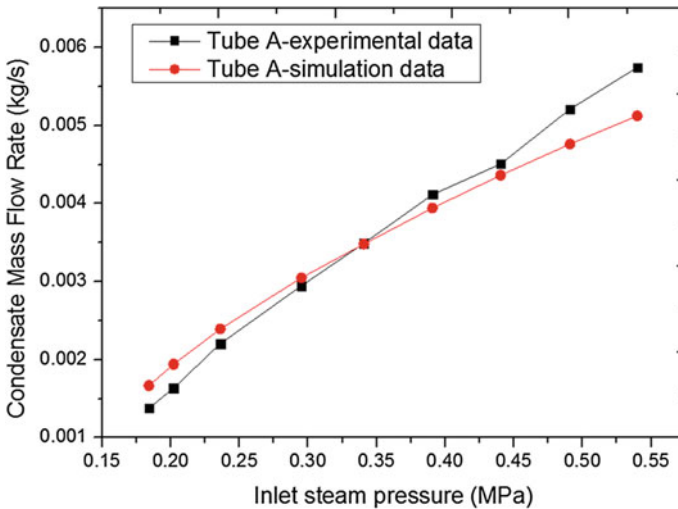


Fig. 9 Comparison of the outlet condensate mass flow rate of tube A

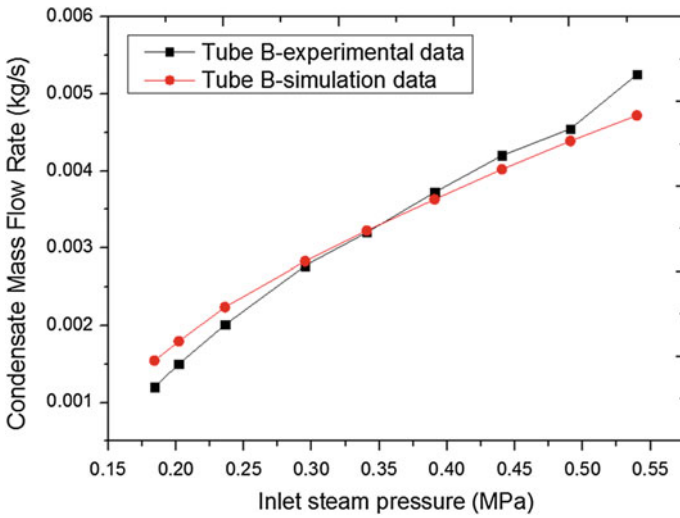


Fig. 10 Comparison of the outlet condensate mass flow rate of tube B

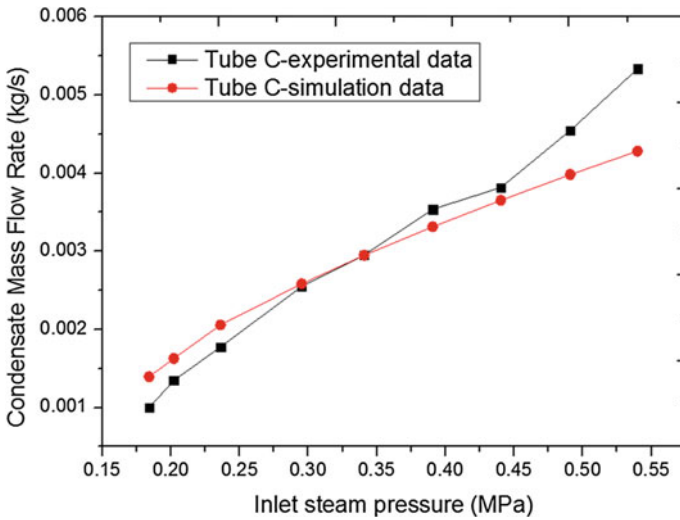


Fig. 11 Comparison of the outlet condensate mass flow rate of tube C

results are lower than the experimental data, and the difference is increasing with the increase in the inlet steam pressure.

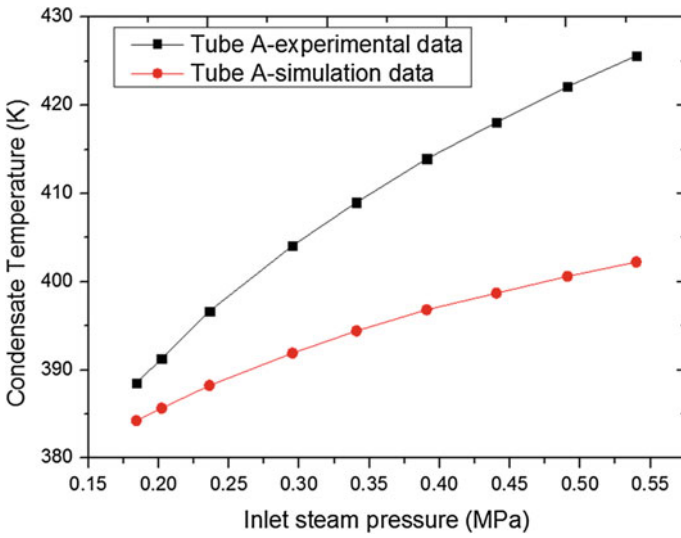


Fig. 12 Comparison of the outlet condensate temperature of tube A

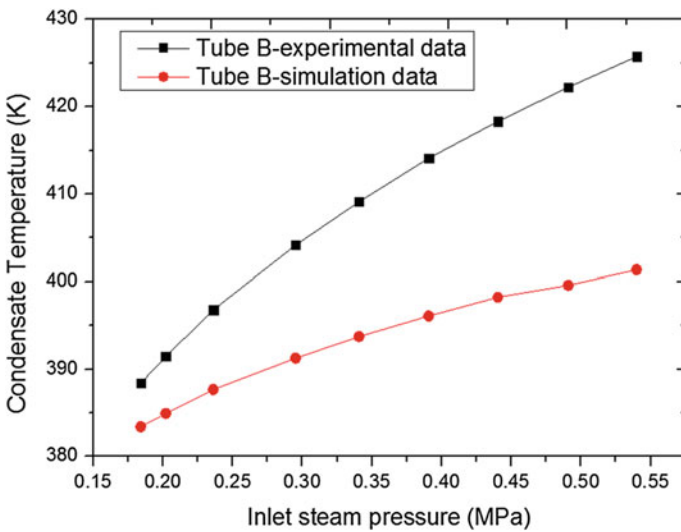


Fig. 13 Comparison of the outlet condensate temperature of tube B

5.4 Condensation Model Comparison and Analysis

From the RELAP5/MOD3.2 simulation results, the flow regime of the horizontal part of the three C-type tubes is horizontal stratified, and in the vertical part the flow

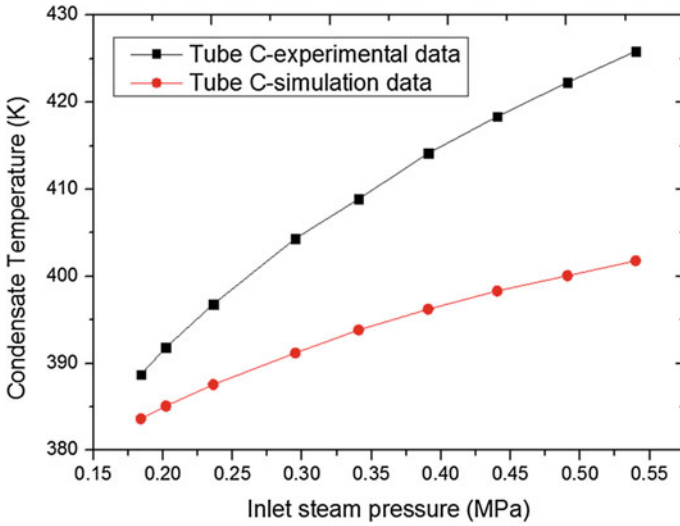


Fig. 14 Comparison of the outlet condensate temperature of tube C

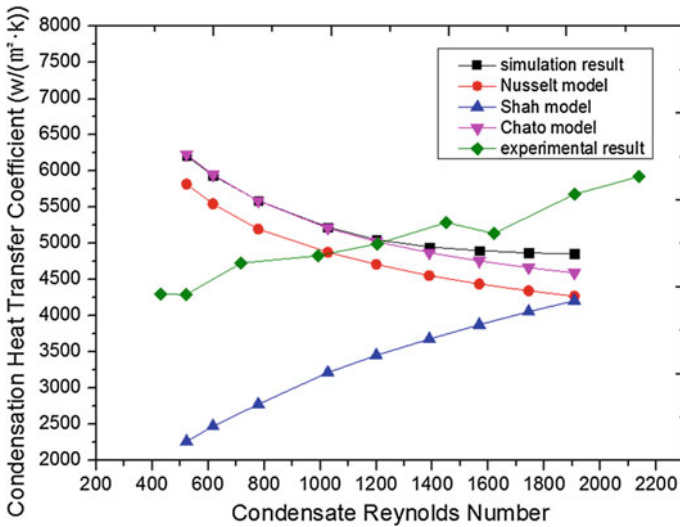


Fig. 15 Comparison of the average condensation coefficient of tube A

regime is annular mist. Figures 15, 16, and 17 show the comparison of the average condensation coefficient of the three C-type tubes calculated using different condensation models which may be used in the simulation of RELAP5/MOD3.2 code. In the condensation experiment, the outlet condensate Reynolds Number is varied

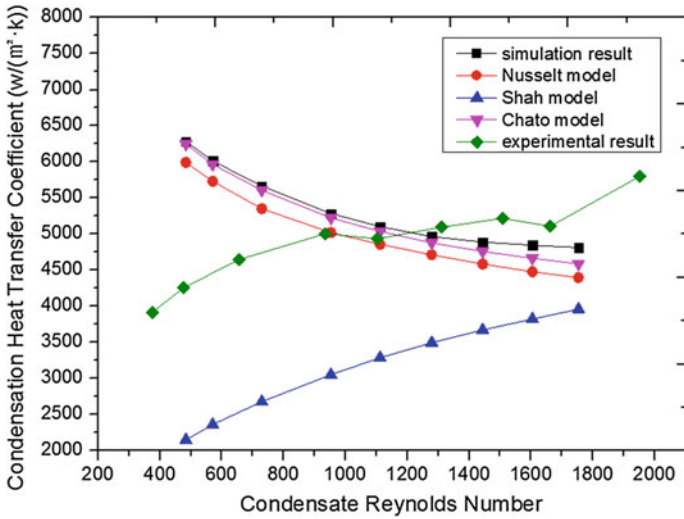


Fig. 16 Comparison of the average condensation coefficient of tube B

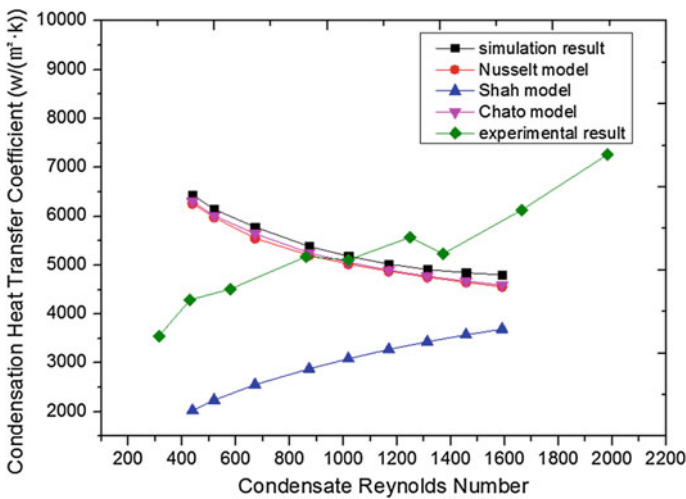


Fig. 17 Comparison of the average condensation coefficient of tube C

in the laminar flow region. The average condensation coefficient calculated using the Nusselt model and the Chato model is almost the same as the simulation result; that is to say, RELAP5/MOD3.2 code uses Chato model to calculate the condensation of the horizontal part and uses the Nusselt model to calculate the condensation of the vertical part when simulating the C-type condensation experiment. And the simulation result shows that Chato condensation model and Nusselt

condensation model cannot completely predict the condensation inside the C-type tubes. RELAP5/MOD3.2 needs to modify the standard condensation models or use new condensation models when simulating the condensation experiment inside C-type tubes.

6 Conclusions

The standard condensation models of the RELAP5/MOD3.2 code for saturated steam condensation inside the C-type tubes are assessed using condensation experiment inside the C-type tubes. The following are the conclusions:

- (1) The standard RELAP5/MOD3.2 condensation models cannot give completely the reliable predictions for the condensation coefficient, and the changing trend of the simulating result is completely opposite compared with the experimental result. In this study, only in the range of the heat flux from 100,000 to 130,000 W/m², the simulation result can give reasonable predictions.
- (2) In the same conditions of the inlet-saturated steam pressure and outer surface wall temperatures, the simulation of the standard RELAP5/MOD3.2 code gives lower predictions of the outlet condensate temperature, and the difference is increasing with the increase in the inlet steam pressure. Furthermore, in the range of the inlet-saturated steam pressure from 0.3 to 0.5 Mpa, the maximum relative deviation between the experimental and simulating outlet condensate mass flow rate is 12.5%. In other experimental conditions, RELAP5/MOD3.2 code cannot give any reliable predictions.
- (3) RELAP5/MOD3.2 code uses Chato model to calculate the condensation of the horizontal part and uses the Nusselt model to calculate the condensation of the vertical part when simulating the C-type tube condensation in the range of experimental parameters. And these models cannot completely predict the condensation heat transfer inside the C-type tubes. New condensation models need to be used when simulating condensation experiment inside C-type tubes.

Acknowledgments The paper is funded by the International Exchange Program of Harbin Engineering University for Innovation-oriented Talents Cultivation.

References

1. V. H. RANSOM, J. A. TRAPP, and R. J. WAGNER. RELAP5/MOD3 Code Manual, Volume IV: Models and Correlations [M]. IV, Idaho National Engineering Laboratory. 1995 (6).
2. Liu, H., Liang, D. A review of clean energy innovation and technology transfer in China [J]. Renewable and Sustainable Energy Reviews, Volume 18, February 2013, Pages 486–498.

3. D. Lioce, M. Asztalos, A. Alemberti, L. Barucca, M. Frogheri, G. Saiu. AP1000 passive core cooling system pre-operational tests procedure definition and simulation by means of Relap5 Mod. 3.3 computer code [J]. *Nuclear Engineering and Design*, Volume 250, September 2012, Pages 538–547.
4. J. Zou, Q. Li, L.L. Tong, X.W. Cao. Assessment of passive residual heat removal system cooling capacity [J]. *Progress in Nuclear Energy*, Volume 70, January 2014, Pages 159–166.
5. Ki Yong Choi,* Hyun Sik Park, Sang Jae Kim, Hee Cheon No, Yong Seok Bang. Assessment and Improvement of Condensation Models in RELAP5/MOD3.2 [J]. Korea Advanced Institute of Science and Technology, Department of Nuclear Engineering 373-1 Kusong Dong, Yusong Gu, Taejon 305–701, Korea.
6. Ki Yong Choi*, Heung June Chung, Hee Cheon No. Direct-contact condensation heat transfer model in RELAP5/MOD3.2 with/without noncondensable gases for horizontally stratified flow [J]. *Nuclear Engineering and Design*, Volume 211, Issues 2–3, February 2002, Pages 139–151.
7. Hyun Sik Park, Hee Cheon NO, Young Seok Bang. Analysis of experiments for in-tube steam condensation in the presence of noncondensable gases at a low pressure using the RELAP5/MOD3.2 code modified with a non-iterative condensation model [J]. *Nuclear Engineering and Design*, Volume 225, Issues 2–3, November 2003, Pages 173–190.
8. YU Lei, XIE Hai-yan, GUI Xue-wen, CAI Zhang-sheng. Assessment of RELAP5 Code by Experiments of Passive Residual Heat Removal System [J]. *Atomic Energy Science and Technology*, 2008, 42(8):678–684.
9. Yuxian Rao*, Lei Yu, Weitong Li, Fan Zhang. A choice of pure steam vertical in-tube condensation model for simulating a passive residual heat removal system [J]. *Nuclear Engineering and Design*, *Nuclear Engineering and Design*, Volume 293, November 2015, Pages 112–118.
10. Chato, J.C., et al. Laminar condensation inside horizontal and inclined tubes [J]. *Am. Soc. Heating Refrigeration Air Conditioning Eng.* 1962, J. 4, 52.
11. Nusselt, W.A. The surface condensation of water vapor [J]. *Z. Ver. Deutsch. Ing.* 1916, (60) 541–546.
12. Shah, M.M. A general correlation for heat transfer during film condensation inside pipes [J]. *Heat Mass Transfer*, Volume 22, 1979, Pages 547–556.
13. Colburn, A.P., et al. Design of cooler condensers for mixtures of vapors with noncondensing gases [J]. *Ind. Eng. Chem.* 1933, 26 (11), 1178.

Sodium-Cooled Fast Breed Reactor Fuel Failure Detection Based on Cover Gas Monitoring

Han Rui and Chen Shu-ming

Abstract The fission gas activity monitors are used to detect the fission gas migrated to the cover gas plenum. The cladding of fuel element is one of the most important protective barriers. If the failure occurs on fuel pin, the fission gas released from the failed pin into coolant will lead to the increase of radioactivity level of the primary coolant. And in sodium-cooled fast reactor, the fission gas will transport from coolant into reactor cover gas plenum. In this work, according to the fission gas monitoring data from the cover gas, the models of fission gas release and migration as well as program are established based on MATLAB code. The number of failed fuel pins can be calculated by this program in different power, which can discover the fuel failure in time and evaluate the failure; it is very significant to the safety of reactor operation.

Keywords Gas leakage · Fission gas · Migrate · Models and codes · CEFR

1 Introduction

If the fuel element fails, the fission gas firstly releases from fuel pellets into fuel pin gap, and then it could escape from the failure pin into the coolant which will lead to the increasing of radioactivity level in the primary coolant system; the radioactive fission gas migrates from the coolant to the reactor cover gas plenum finally. According to the data from the fission gas monitoring, the model of fission gas release and migration was established adopting a calculation method. This model can calculate the number of failed fuels, discover the fuel failure, and evaluate the failure which is very significant to the safety of reactor operation.

H. Rui (✉) · C. Shu-ming
China Institute of Atomic Energy, Beijing, China
e-mail: hanrui401@sina.com

C. Shu-ming
e-mail: csm@ciae.ac.cn

The sodium-cooled fast reactor develops so fast that gets more attentions [1]. The nuclear safety of reactor is of high concern. It should be ensured that the radioactive products can be contained completely. With regard to the sodium-cooled fast reactor, the fuel rod cladding is the first shield against radioactive material, which can accept more than 90% of fission product. There are two kinds of fuel failures—one is gas leakage and the other is caused by the contact between cladding and coolant with the release of delayed neutron. In general, the fuel failure always occurs with gas leakage, if it turned deteriorate, the delayed neutron precursor will release. So the difference between the two phases is that the delayed neutron is detected. The cover gas monitoring system detects the change in fission gas radioactivity to judge the fuel element cladding failed or not. Generally, the reactor monitoring system is used to detect fuel failure but not the number of failed rods.

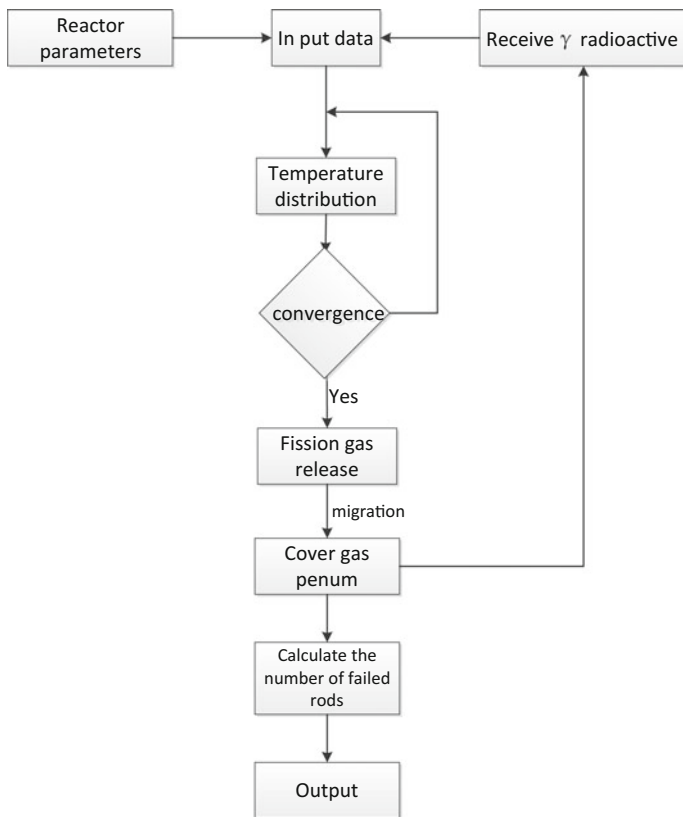


Fig. 1 Calculation flow diagram

In this paper, a model to calculate the number of the failures through monitoring the radioactivity in the cover gas is proposed. The program flow is shown in Fig. 1.

2 Temperature Distribution of the Fuel Rod

The temperature distribution of the fuel rod affects the release of fission gas directly. That the calculation of temperature is an important part of the design and safety analysis of fuel assembly. Accurate calculation of the temperature distribution of the fuel rods will affect other parameters' calculation. The temperature distribution of the fuel rod reflects the change of the power level and the fission rate of the fuel rods.

The fuel assembly of China Experimental Fast Reactor (CEFR) is under equilateral triangle arrangement and consists of 61 fuel rods. By the long, thin cylinder construction of fuel rod, the distribution of which using one dimension heat conduction equation as calculation model. In this model, the axial heat conduction is neglected.

The temperature distribution of the fuel rod includes the coolant temperature, the temperature of the surface of the cladding, the fuel surface temperature, and the central temperature of the fuel. The temperature distribution of the fuel rod is calculated starting from the inlet coolant temperature of the core. The total release of fission gas is calculated when the temperature of the fuel rod converges.

2.1 Coolant Temperature Distribution

The surface temperature of the fuel rods is closely related to the coolant temperature. Heat exchange between subflow channels is neglected with a purpose to simplify calculations.

$$T_{\text{cool}}(z) = T_{\text{coolant}} + \frac{2L'\alpha q_1}{\pi G_m C_p} \sin(\pi L/2L') \left(1 + \frac{\sin(\pi Z/L')}{\pi Z/2L'} \right) \quad (1)$$

where

- $T_{\text{cool}}(z)$ Coolant temperature at position z ;
- T_{coolant} Core inlet coolant temperature, using CEFR-rated operating value;
- q_1 Linear power of fuel rod;
- C_p Specific heat of sodium as coolant;
- L' Neutron flux extrapolation distance, typically assumed to be 135% of the height of the fuel rod in terms of experience.

2.2 Outer Surface Temperature of the Fuel Rod Cladding

$$\begin{aligned}
 T_{ec}(z) &= T_{cool}(z) + \frac{q_l(z)}{\pi D h_1} \\
 &= T_{coolant} + \frac{\alpha}{G_m C_p} \times \int_{-L/2}^z q_l(z) dz + \frac{q_l(z)}{\pi D h_1}
 \end{aligned} \tag{2}$$

where

- $T_{ec}(z)$ Outer surface temperature of fuel rod cladding at position z ;
 L Height of the fuel rod;
 h_1 Heat transfer coefficient;
 D The outer radius of the fuel rod cladding.

2.3 Radial Temperature Distribution of the Fuel Rod Cladding

$$T(R_{ic}) = T_{ec}(z) + \frac{q_l}{2\pi \lambda_k} \ln(R_{ec}/R_{ic}) \tag{3}$$

where

- R_{ec} Outer radius of the cladding;
 R_{ic} The inner radius of the cladding;
 λ_k Heat conductivity of cladding material.

2.4 The Outer Surface Temperature of Fuel Pellets

$$T_S(z) = T(r_{ic}) + \frac{q_l}{2\pi R_f h_g} \tag{4}$$

where

- $T_S(z)$ The outer surface temperature of fuel pellets;
 R_f The outer radius of fuel pellets;
 h_g Gas gap conductivity

2.5 Radial Temperature Distribution of Fuel

$$T_r(r, z) = T_S(z) + \frac{q_l}{4\pi} \frac{R_0^2}{R_0^2 - R_f^2} \times \left(1 - \frac{R_f^2}{R_0^2} \ln \left(\frac{R_0^2}{R_f^2} \right) \right) / \lambda_p \quad (5)$$

where

- $T_r(r, z)$ The temperature of fuel pallet at position z ;
- R Radial coordinates of cylindrical coordinate system;
- Z Axial coordinates of cylindrical coordinate system;
- R_o The inner radius of fuel pallets;
- λ_p Heat conductivity of the fuel rod.

3 Models of Fission Gas Release from UO_2

Some of the gaseous fission products are produced during the fission process, and some by the fission process directly; the others are produced by the decay of radionuclides to the steady state. For example, iodine decays into xenon. Most of the fission gas is xenon and followed by krypton. Krypton and xenon produced by fission are single atoms in the fuel; these solute atoms precipitate and gather to form bubble when saturation is obtained.

Only stable and long-life isotopes are significant to fission gas release. Most of the fission gas is composed of xenon and krypton. The release rate of fission gas depends on the temperature and burn-up of fuels [2]. The size and the growth rate of the bubble are depending on the rate of obtaining or losing gas atoms. With the growth of grain boundary bubbles, they are connected to each other, and finally the channel is formed due to the escape of the gas bubbles. The release rate of gas depends on the burn-up and temperature of the fuel.

The fuels of CEFBR are at high temperature. The main factors affecting the release of fission gas from UO_2 crystal are the dynamic process of grain growth. The gas release rate is mainly due to the temperature gradient driving force of fission caused by bubble migration.

Surface bubble growth mainly affects the release of fission gas in two aspects. On the one hand, fission causes a large amount of fission gas atoms to gather together in the grain boundary, which accelerates the fission gas atoms through the grain boundary, so increases the rate of grain growth. On the other hand, the defects in the grain boundary are swept out to inhibit grain growth by limiting the grain size. To a certain extent, it also affects the release of fission gases.

According to the modified differential equation of Ainscough of grain growth which describes the grain growth kinetics, the process can be written as:

$$\frac{dI}{dt} = k_m \left(\frac{1}{I} - \frac{1}{I_m} \right) \quad (6)$$

$$k_m = 5.27 \times 10^7 \exp \left(- \frac{2.67 \times 10^5}{R(T + 371(1 - \exp(-\frac{B}{2700}) + 0.04 \times B))} \right) \quad (7)$$

$$I_m = 2.23 \times 10^3 \exp \left(- \frac{7620}{T - 520(1 - \exp(-\frac{B}{8400}))} \right) + 5 \left(1 - \exp \left(- \frac{B}{8400} \right) \right) \quad (8)$$

where

dI/dt The grain growth kinetics;

T Fuel temperature;

B Burn-up.

Marcin Szuta demonstrated and analyzed the defect trap model at high temperature, through which the release rate R_i of gaseous fission product from UO_2 crystal was obtained [3].

$$\frac{dM}{dt} = \beta_{if} + \alpha_1 f M_r + g_3 f M_{tr} - \alpha_2 M - g N_{tr} M \quad (9)$$

$$\frac{dM_{tr}}{dt} = g N_{tr} M - g_2 f M_{tr} - g_3 f M_{tr} - \lambda_i M_{tr} - \frac{1}{2} M_{tr} I^2 \frac{dI}{dt} N \quad (10)$$

$$\frac{dM_r}{dt} = \alpha_2 M - \alpha_1 f M_r - \lambda_i M_r - \frac{1}{2} M_r I^2 \frac{dI}{dt} N \quad (11)$$

$$R^i = g_2 f M_{tr} (S \times r_0) + \frac{1}{2} \pi (M_{tr} + M_r) I^2 \frac{dI}{dt} N \quad (12)$$

where

M Concentration of intermediate gas atoms;
 M_{tr} Concentration of gas atoms in the bubbles;
 M_r Concentration of gas atoms in the matrix;
 S Total surface area;
 $g_1, g_2, g_3, \alpha_1, \alpha_2, S_0, S_1, B_0, \tau$ Constants.

4 Models of Fission Gas Migration

The fuels are treated as the UO_2 single crystal in order to apply this release model of fission gas behavior in the fuel. Moreover, it is assumed that the fission gas release rate from the fuel pin into the gap is affected by the volume.

$$R^{is} = R^i \cdot (S \times \bar{r}) \quad (13)$$

Due to the temperature and the fission rate are spatially varying under operation. The fuel rod is divided into axial and radial sections and is divided into a plurality of coaxial cylinders. As a result of that, the fission gas release rate of the chosen isotope from a whole fuel rod can be obtained.

$$R_k^i = \int_{-H/2}^{H/2} \int_{r_1}^{r_2} R^{is}(T, f) 2\pi r dr dz \quad (14)$$

where

R_k^i The fission gas release rate from the whole fuel rod

The fission gas release from fuel pellets will transfer to the coolant if the fuel cladding fails. After a certain period of time, the fission gas in the primary coolant transfers to the reactor cover gas plenum. Then the fission gas reaches the sampling circuit of the cover gas monitoring system and it can be detected eventually.

4.1 Migrate to Coolant

The rate of fission gas release from the failed cladding into the primary coolant is proportional to the number of the fission gas atoms. The escape rate constant is introduced to describe the speed of fission gas entering the coolant through the failed cladding.

According to the mass conservation of fission gas in the gap between the pellet and the cladding [4], the number of fission gas atoms can be written as:

$$\frac{dN_i^g(t)}{dt} = R_k^i - (v_i(t) + \lambda_i)N_i^g(t) \quad (15)$$

where

- $N_i^g(t)$ The number of fission gas atoms for chosen isotope in the gap at time t ;
- $v_i(t)$ The escape rate constant of fission gas migrating from the failed cladding into the coolant;
- λ_i The decay constant of isotope i .

The fission gas diffuses following sodium in the process of coolant cycling around the reactor core after transported into the primary coolant. At certain period of time, the fission gas in the primary coolant will transfer to the reactor cover gas plenum.

4.2 Migration to the Cover Gas

The speed of fission gas migration from the primary loop to the cover gas plenum is mainly determined by the amount of fission gas atoms at the boundary between primary loop and cover gas plenum. The conservation equation for the number of fission gas atoms in the coolant can be written as:

$$\frac{dN_i^c}{dt} = v_i(t)N_i^g(t) - (\lambda_i + \lambda_e(t))N_i^c \quad (16)$$

where

N_i^c The number of fission gas atoms in the primary coolant;

$\lambda_e(t)$ The migration coefficient of fission gas transporting from the coolant into cover gas plenum, use experimental parameters.

4.3 Fission Gas Detected in the Sampling Circuit

After fission gas migrated to the cover gas plenum, it diffuses and decays, and eventually reaches the steady state.

$$\frac{dN_i^a}{dt} = \lambda_e(t)N_i^c(t) - (\lambda_i + \lambda_j(t))N_i^a \quad (17)$$

N_i^a The number of fission gas atoms in the cover gas plenum;

$\lambda_j(t)$ The coefficient of disappearance due to purification.

4.4 Calculating the Number of Fuel Failures

There are five isotopes (^{133}Xe , ^{135}Xe , $^{85\text{m}}\text{Kr}$, ^{87}Kr , ^{88}Kr) which should be monitored in the cover gas monitoring system. According to the model established above, the calculation of fission gas radioactivity in the cover gas plenum with

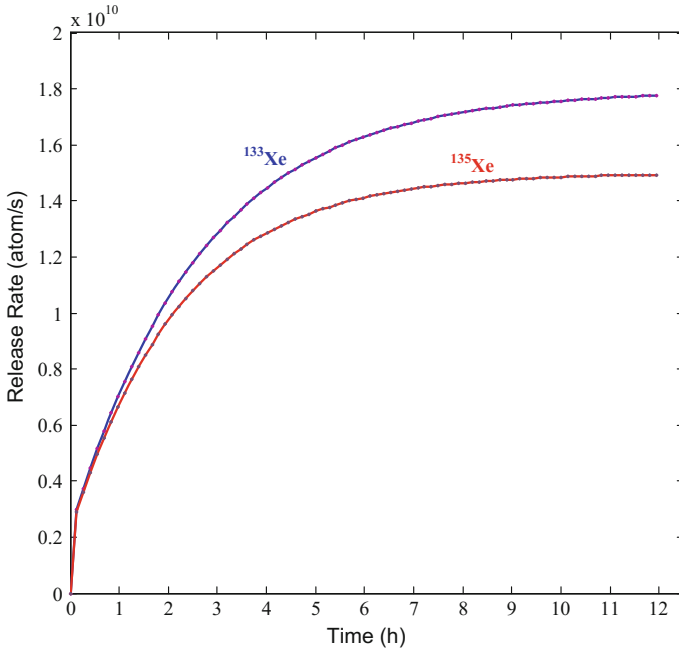


Fig. 2 Release rate of xenon in CEFR when burn-up is 40 MWd/kgU

single fuel rod failure happened will be obtained. Finally, the number of failures should be obtained according to the monitoring data.

$$AC_i = \lambda_i N_i^a \tag{18}$$

$$n = \frac{A_i^m}{AC_i/V_g} \tag{19}$$

where

AC_i The theoretical radioactivity of the considered isotope for one gas-leaking fuel rod;

A_i^m Measured radioactivity in the cover gas plenum;

N The number of fuel element gas-leaking;

V_g The volume of cover gas plenum.

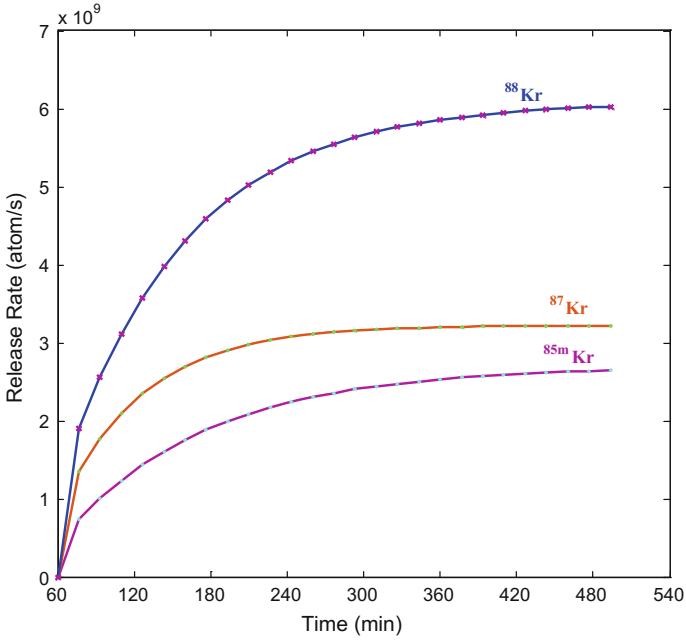


Fig. 3 Release rate of krypton in CEFR when burn-up is 40 MWd/kgU

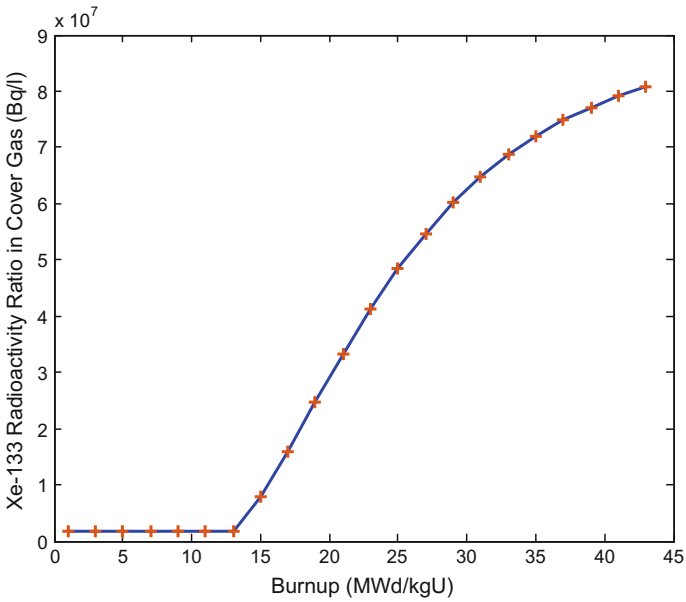


Fig. 4 Radioactivity ratio of ¹³³Xe in cover gas when one fuel element gas-leaking

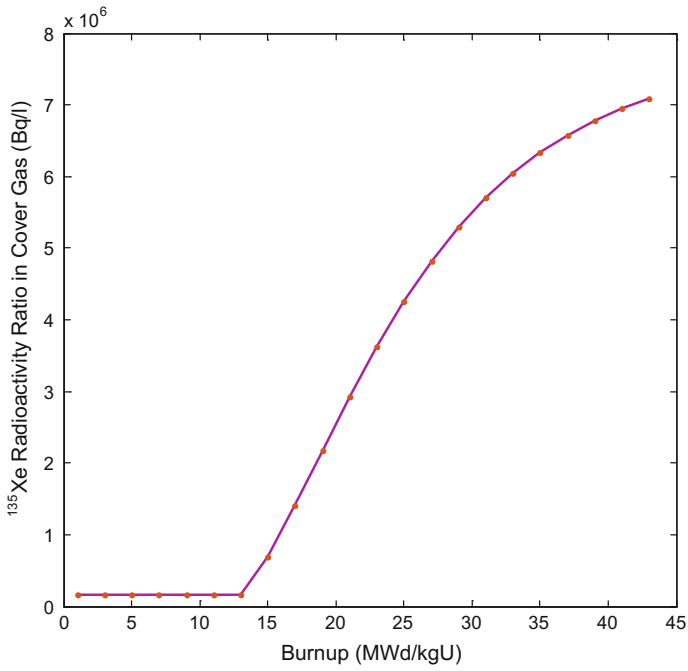


Fig. 5 Radioactivity ratio of ^{135}Xe in cover gas when one fuel element gas-leaking

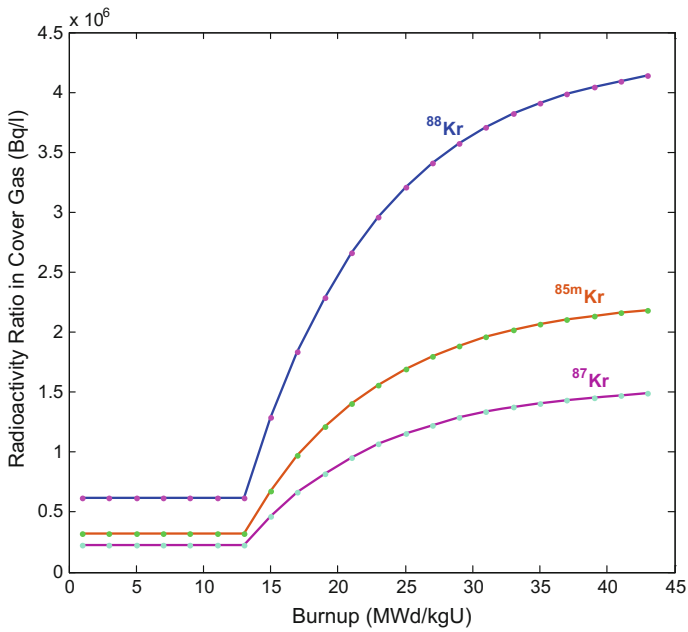


Fig. 6 Radioactivity ratio of krypton in cover gas when one fuel element gas-leaking

5 Conclusions

Taking CEFR as a benchmark of the program and using related parameters, the radioactivity ratio of five isotopes in the cover gas plenum when one fuel element failed is shown in the following pictures (Figs. 2, 3, 4, 5 and 6).

Through calculating the radioactivity of these five isotopes separately, we can get the number of failures.

In summary, in this work a model for identifying the number of failed fuel pins has been proposed. This model is based on the transfer process of fission gas from the fuel to the reactor cover gas plenum. Based on this model, the activity of these isotopes can be obtained. Comparing theoretical calculation and actual monitoring value, each of the five isotopes can evaluate the number of failures.

References

1. Douglas K. Warinner: The LMFBR Fuel-design environment for endurance testing, Primarily of Oxide fuel elements with local faults, Nuclear Engineering August 18, 1980.
2. Donald R. Olander Fundamental Aspects of Nuclear Reactor Fuel Elements. U.S. Energy Research And Development Administration, 1976
3. Marcin Szuta, Modification of Re-Crystallization Temperature of Uranium Dioxide in Function of Burn-Up and Its Impact On Fission Gas Release-High Temperature Release, IAE MONOGRAPHS volume 7.
4. QIU Chun-hua, Xiong Wen-bin, DUAN Tian-ying, Modeling, Calculating and Analyzing of Failed Fuel Detection System of China Experiment Fast Reactor, Atomic Energy Science and Technology, Vol. 44, No.2.

Study on Two-Phase Flow Instabilities in Straight and Helical Tubes

Ruiting Dong, Fenglei Niu and Yuan Zhou

Abstract In this paper, test section consisted of two heated straight channels which have a cross section of $25 \text{ mm} \times 2 \text{ mm}$ or two helical channels which have a cross section of $\text{Ø}25 \text{ mm}$, and effects of system pressure, mass flux, inlet subcooling in two-phase flow instability are discovered by means of RELAP5/MOD3.3 and multivariable frequency domain control theory. Then experimental data in two straight channels are adopted to demonstrate the RELAP5 and multivariable frequency domain control theory results. The thermal hydraulic behavior and parametric effect study are simulated and compared with the experimental data. The RELAP5 results show that increases in the system pressure, mass velocity, and inlet subcooling tend to stabilize the system, and the frequency domain theory presents the same result as frequency domain theory shows. The effects of system pressure, mass velocity, and inlet subcooling are simulated to find the differences between straight and helical pipes and contrast the RELAP5 with multivariable frequency domain control theory in simulating density wave oscillation to investigating their advantages and disadvantages in straight and helical tubes.

Keywords Two-phase flow instability · Straight tube · Helical tube · RELAP5 · Frequency domain theory

1 Introduction

The flow instabilities in parallel channels could be classified into two types: static instabilities and dynamic instability. The latter type, particularly density wave oscillation (DWO), is one of the most common two-phase flow instabilities in

R. Dong (✉) · F. Niu
Beijing Key Laboratory of Passive Nuclear Power Safety and Technology,
North China Electric Power University, Beijing, China
e-mail: 1142212039@ncepu.edu.cn

Y. Zhou
School of Nuclear Science and Engineering, Shanghai Jiaotong University, Shanghai, China

nuclear reactor. Extreme circumstances, such as mechanical vibrations and thermal fatigue, can be caused by flow rate, system pressure, and power oscillations. Straight and helical pipes fit well in different reactors. Some studies show that helical tubes have the advantages of efficient heat transfer performance and small space distribution, but higher cost of manufacture is required. Researches on both of the straight and helical pipes play a significant role in the security of nuclear reactor circulation.

In this paper, DWOs in straight and helical pipes are studied by time domain method and frequency domain method. It aims at finding the advantages and disadvantages on time domain method and frequency domain method for researching two-phase flow instability and the differences between straight and helical pipes for increasing flow rate, system pressure, and inlet subcooling.

2 Numerical Simulation

2.1 Time Domain Method

RELAP5/MOD3.3 code is chosen as simulation tool for time domain method to apply to the straight and helical parallel channel system. Water is used as the test fluid. The system and channel parameters are presented in Tables 1, 2, 3 and Fig. 1. Straight tubes are 1000 mm long and have 25 mm \times 2 mm cross section, and helical tubes are 6000 mm long and have \varnothing 25 mm cross section, which refer to the experimental data by Zhou [1] and Davide [2]. A direct current heating element is applied, along the wall of constant thickness, to provide an essentially uniform heat flux for pipe 250 and 350 (Fig. 2).

Table 1 Range of system parameters in straight channel

Items	Values
System pressure, p	1.00–10.00 Mpa
Inlet rate of flow, w	0.01–0.04 kg/s
Inlet subcooling, ΔT_{sub}	20.0–50.0 °C
Heat input, q	0–837 kw/m ²

Table 2 Range of system parameters in helical channel

Items	Values
System pressure, p	5.00–8.00 Mpa
Inlet rate of flow, w	0.01–0.06 kg/s
Inlet subcooling, ΔT_{sub}	20.0–60.0 °C
Heat input, Q	10–95 kw

Table 3 A main geometrical data of the helical channel

Items	Values
Inner diameter, d	25 mm
Outer diameter	30 mm
Coil diameter, D	1000 mm
Coil pitch	500 mm
Tube length	6 m
Heated section length	4.5 m
Riser length	2.05 m

Fig. 1 Cross section of rectangular channel

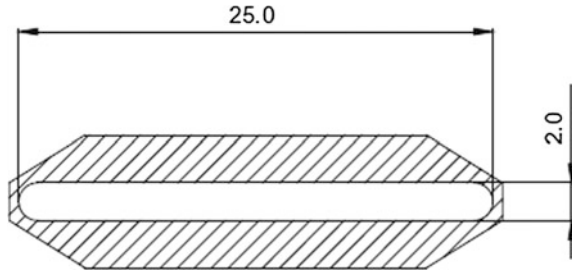
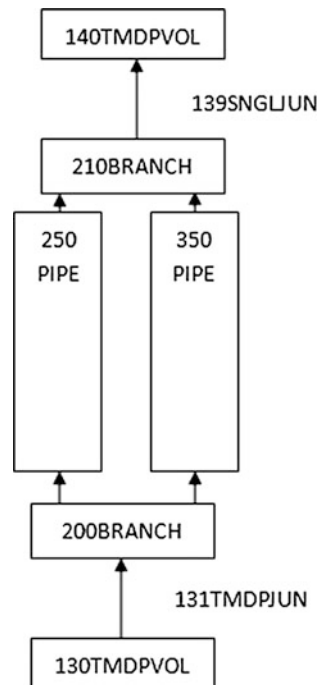


Fig. 2 RELAP5 nodalization of two parallel straight or helical channels



2.2 Frequency Domain Method

2.2.1 Assumptions

The following assumptions are made in the model derivation process [3–5]:

- (1) In the secondary loop, the heat transfer and flow parameters of every sub-segment control unit are uniform, which are represented by the mean values.
- (2) The single-phase flow is incompressible and the two-phase flow is under thermodynamic equilibrium.
- (3) The semiempirical formulae of flow and heat transfer under steady-state condition are applicable for this case.
- (4) The fluid is assumed to be ideal fluid.
- (5) The potential energy and the kinetic energy in the energy conservation equation are neglectable.
- (6) The heat conduction in the axial is neglected.

2.2.2 Transfer Matrix

Nomenclature

θ	Transfer function
δ	Disturbance quantity
Ω	Frequency of phase change
Φ_{f_0}	Two-phase friction multiplier
$\Phi(x)$	Two-phase local resistance multiplier
w	Rate of flow
p	System pressure
Δp	Pressure drop

The channels are divided into a number of control units. In the control units, the relationship between pressure drop disturbance $\delta\Delta p$ and flow rate perturbation δw can be expressed as:

$$\begin{aligned}\delta\Delta p_{l,j}(s) &= \theta_{l,j}(s)\delta w_{in,j}(s) \\ \delta\Delta p_{ip,j}(s) &= \theta_{ip,j}(s)\delta w_{in,j}(s) \\ \delta\Delta p_{v,j}(s) &= \theta_{v,j}(s)\delta w_{in,j}(s)\end{aligned}\quad (1)$$

The relationship between the disturbance of external loop pressure drop $\delta\Delta p_t(s)$ and the flow rate perturbation $\delta w_t(s)$ can be expressed as:

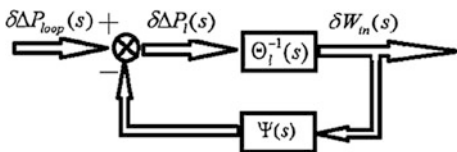
$$\begin{aligned}\delta\Delta p_t(s) &= \theta_t(s)\delta w_t(s) \\ \delta w_t(s) &= \sum_j^n \delta w_{in,j}(s)\end{aligned}\quad (2)$$

Using the linearized perturbation theory and the Laplace transformation, the system transfer matrix can be expressed as:

$$\begin{aligned}
 \delta w_{in}(s) &= \Theta_l^{-1}(s) \cdot \delta \Delta p_l(s) \\
 \delta \Delta p_l(s) &= \delta \Delta p_{loop}(s) - \Psi(s) \cdot \delta w_{in}(s) \\
 \Psi(s) &= \Theta_{tp}(s) + \Theta_v(s) + \Theta_t(s) \\
 \delta w_{in}(s) &= [\delta w_{in,1}(s) \quad \delta w_{in,2}(s) \cdots \delta w_{in,n}(s)]^T \\
 \delta \Delta p_l(s) &= [\delta \Delta p_{l,1}(s) \quad \delta \Delta p_{l,2}(s) \cdots \delta \Delta p_{l,n}(s)]^T \\
 \delta \Delta p_{loop}(s) &= [\delta \Delta p_{loop,1}(s) \quad \delta \Delta p_{loop,2}(s) \cdots \delta \Delta p_{loop,n}(s)]^T \\
 \Theta_l^{-1}(s) &= \begin{bmatrix} \theta_{l,1}^{-1}(s) & \cdots & 0 \\ \vdots & \ddots & \vdots \\ 0 & \cdots & \theta_{l,n}^{-1}(s) \end{bmatrix} \\
 \Theta_{tp}(s) &= \begin{bmatrix} \theta_{tp,1}(s) & \cdots & 0 \\ \vdots & \ddots & \vdots \\ 0 & \cdots & \theta_{tp,n}(s) \end{bmatrix} \\
 \Theta_v(s) &= \begin{bmatrix} \theta_{v,1}(s) & \cdots & 0 \\ \vdots & \ddots & \vdots \\ 0 & \cdots & \theta_{v,n}(s) \end{bmatrix} \\
 \Theta_t(s) &= \begin{bmatrix} \theta_t(s) & \cdots & \theta_t(s) \\ \vdots & \ddots & \vdots \\ \theta_t(s) & \cdots & \theta_t(s) \end{bmatrix}_{n \times n}
 \end{aligned} \tag{3}$$

When perturbation of the inlet flow occurs, flow disturbance causes enthalpy disturbance, leading to the changes in the boiling boundary, superheating boundary, and density distribution inside the channel. The changes in flow, density, and boundary positions cause the changes in pressure drop in the liquid area, two-phase area, and superheated steam area. The flow change in each channel results in the

Fig. 3 Schematic of a multichannel feedback system



change in the flow and pressure drop in the external loop. On the other hand, the change in the pressure drop of the external loop will lead to the change in the inlet flow of each channel. These effects make a multichannel feedback system, which is shown in terms of the block diagram as given in Fig. 3.

3 Straight Tubes

3.1 Effects of System Pressure

System pressure is one of the most significant parameters in two-phase flow instability. The relation among exit quality, period, system pressure, and the Nyquist curves with 2 different system pressure conditions (3.0, 7.0 MPa) is shown in Fig. 4. As the pressure increases, the heat flux and exit quality both increase. For this, it can be seen that higher quality is required to retain the same void fraction when the pressure increases. The frequency method shows that with increasing the system pressure, Nyquist curves get away from the origin, for the density difference

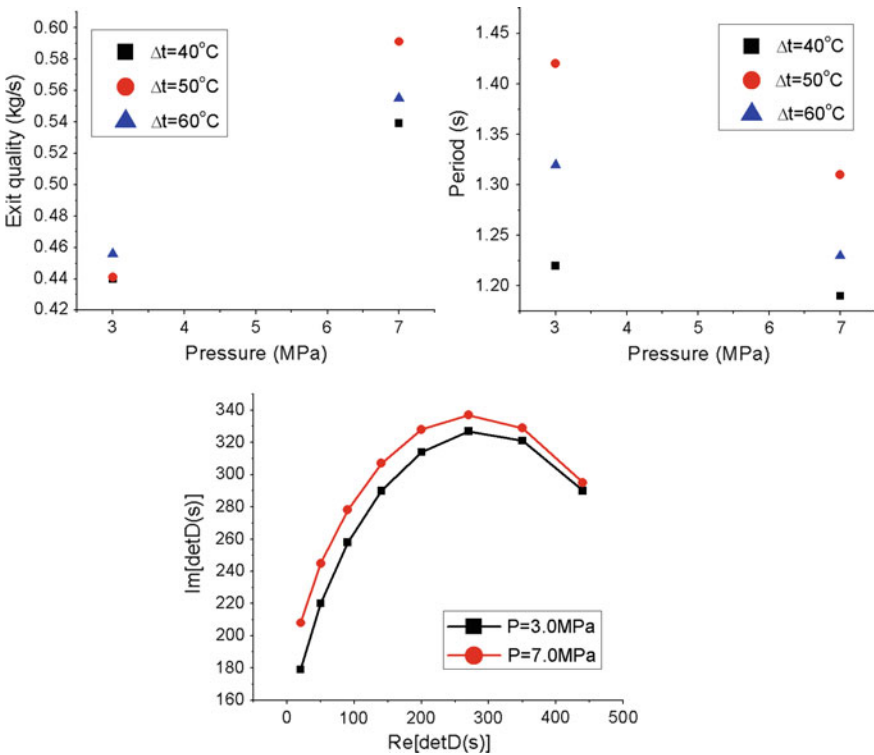


Fig. 4 Results of experiment and frequency domain method for system pressure

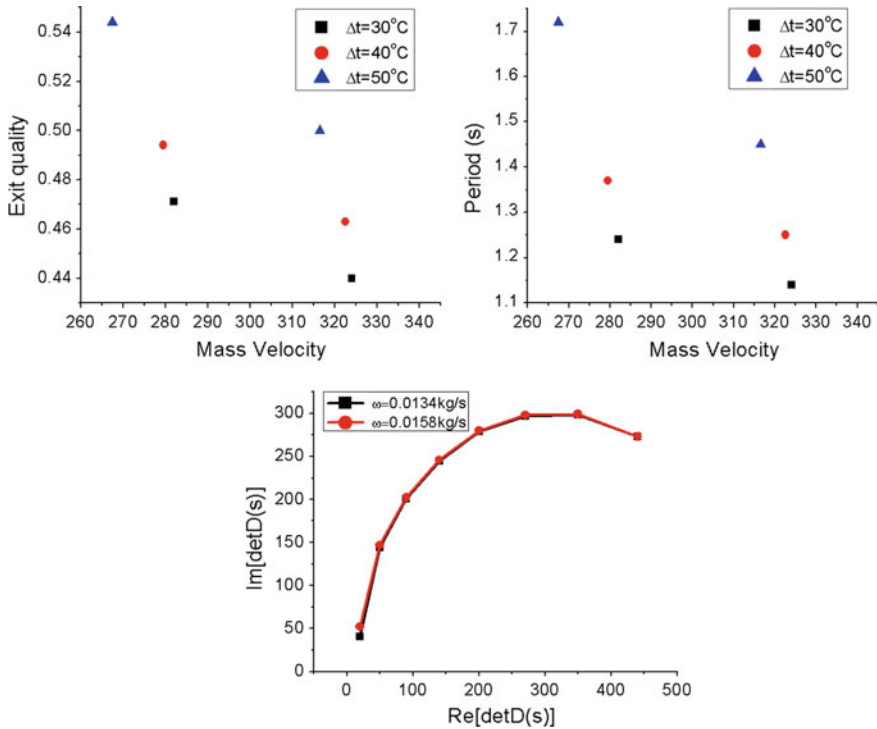


Fig. 5 Results of experiment and frequency domain method for mass velocity

between the vapor and the water decreases, and the saturation temperature rises, so the void fraction and pressure drop in two-phase area will decrease, which reinforce the system stability. Therefore, increase in the system pressure tends to stabilize the system.

3.2 Effects of Mass Velocity

DWOs are affected to a large extent by mass velocity. The relation among exit quality, period, mass velocity, and the Nyquist curves with 2 different mass velocity conditions (0.0134, 0.0158 kg/s) is shown in Fig. 5. As the mass velocity increases, the heat flux and exit quality both decrease linearly. The frequency method shows that with increasing the mass velocity, Nyquist curves get away from the origin. There are two main reasons for this: One is that the period decreases with increasing the mass flux. This is because the oscillation periods correspond to 1–2 times the amount of time required for a fluid particle to travel through the test section. Another is that higher mass flux corresponds to longer single-phase region or higher

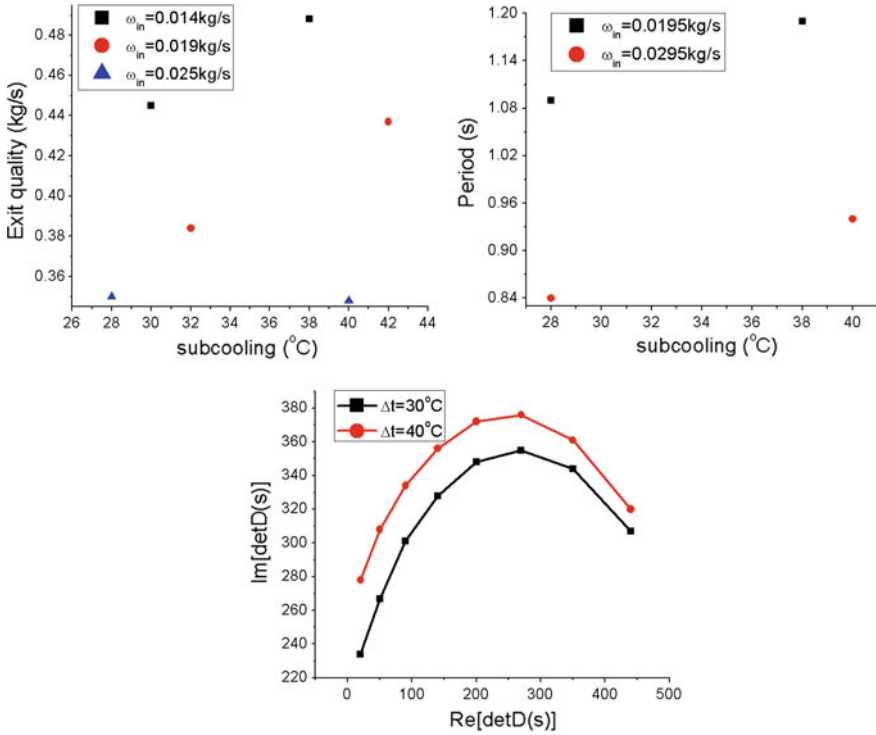


Fig. 6 Results of experiment and frequency domain method for inlet subcooling

inlet resistance. The Nyquist curves show that the later occupies a major role in effects of mass velocity. Therefore, increase in the mass velocity tends to stabilize the system.

3.3 Effects of Inlet Subcooling

Inlet subcooling is another important parameter in two-phase flow instability. The relation among heat flux, exit quality, period, inlet subcooling, and the Nyquist curves with 2 different inlet subcooling conditions (30, 40 °C) is shown in Fig. 6. As the inlet subcooling increases, the heat flux and exit quality both increase. The frequency method shows that with increasing the inlet subcooling, Nyquist curves get away from the origin. When the inlet subcooling increases, the fluid required more heat flux to boiling, and it corresponds to higher inlet subcooling resulted in longer single-phase section and shorter two-phase section. Then the mass velocity becomes lower in both single- and two-phase sections. Therefore, increase in the inlet subcooling tends to stabilize the system.

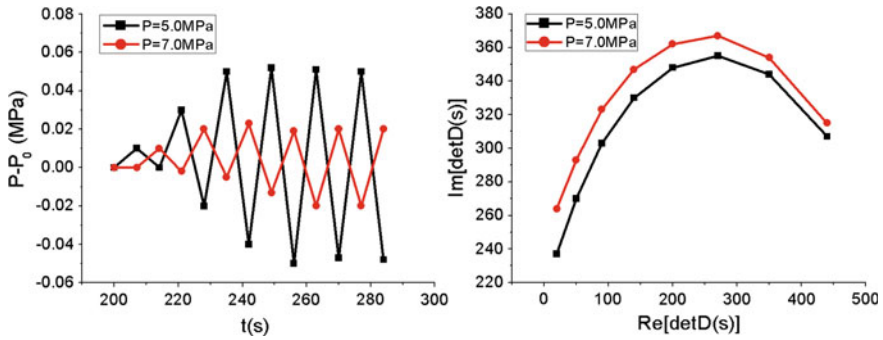


Fig. 7 Results of RELAP5 and frequency domain method for system pressure

4 Helical Tubes

4.1 Effects of System Pressure

The system pressure oscillation and the Nyquist curves with 2 different system pressure conditions (5.0, 7.0 Mpa) are shown in Fig. 7. The amplitude decreases with increasing the system pressure. The frequency method shows that with increasing the system pressure, Nyquist curves get away from the origin, which is similar to the result in straight channels. Therefore, increase in the system pressure tends to stabilize the system.

4.2 Effects of Mass Rate

The mass rate oscillation and the Nyquist curves with 2 different mass rate conditions (0.014, 0.028 kg/s) are shown in Fig. 8. The amplitude decreases with

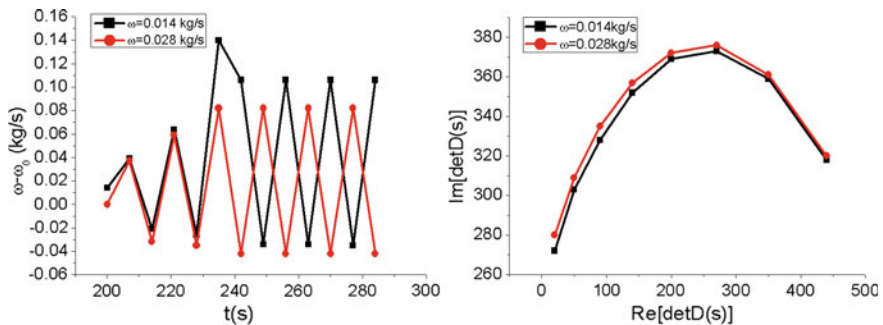


Fig. 8 Results of RELAP5 and frequency domain method for mass velocity

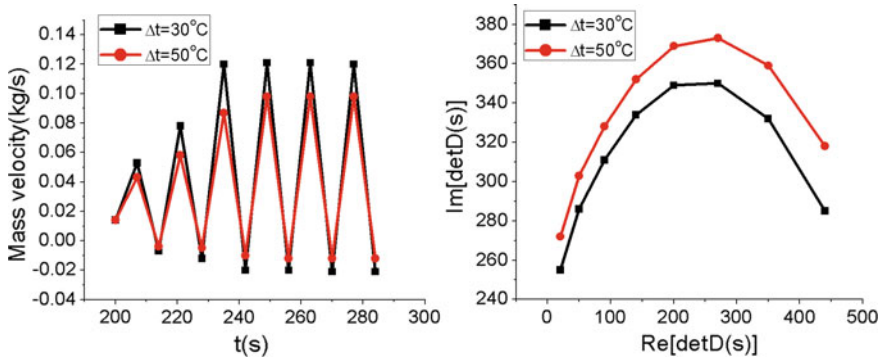


Fig. 9 Results of RELAP5 and frequency domain method for inlet subcooling

increasing the mass rate, and the frequency method shows that with increasing the mass velocity, Nyquist curves get away from the origin. The results and discussion of RELAP5 and frequency method are close to those in straight pipes. Therefore, increase in the mass velocity tends to stabilize the system.

4.3 Effects of Inlet Subcooling

The inlet subcooling oscillation and the Nyquist curves with 2 different system pressure conditions (30, 50 °C) are shown in Fig. 9. The mass velocity amplitude decreases with increasing the inlet subcooling, and the frequency method shows that with increasing the inlet subcooling, Nyquist curves get away from the origin, which is similar to the result in straight tubes. Therefore, increase in the inlet subcooling tends to stabilize the system.

5 Conclusions

The thermal–hydraulic behaviors of DWO in straight and helical pipes are investigated by RELAP5 and multivariable frequency domain control theory in this paper. The phenomena of flow instability in straight and helical parallel channels and effects of thermal hydraulic parameters on the flow instability are presented. The simulated results show the following:

- (1) Effects of thermal hydraulic parameters on the flow instability in straight tubes are similar to those in helical tubes. There are the same tendencies of oscillation amplitudes and exit quality with increasing system pressure, mass velocity, and inlet subcooling, as well as the results of both. Therefore, considering the

advantages of efficient heat transfer performance and small space distribution, helical tubes may be a better choice for steam generators.

- (2) With the comparison of time domain method (RELAP5) and frequency domain method results, it is obvious to investigate that RELAP5 can provide specific relationship among the system parameters, when frequency domain method presents the overall trends with changing system parameters. If a parameter is influenced by just one factor, the RELAP5 will perform well than frequency domain method. But if a parameter is influenced by several factors, frequency domain method can be a better choice to simulate the phenomena of flow instability in straight and helical channels.

Acknowledgments This research activity has been performed with the financial support from Beijing Key of Passive Technology for Nuclear Energy, North China Electric Power University, Beijing 102206, China.

References

1. Yuan Zhou, et al., 2012. Experimental study of two phase flow instability in parallel narrow rectangular channels. *Ann. Nucl. Energy* 50, 103–110.
2. Davide Papini, et al., 2014. Experimental and theoretical studies on density wave instabilities in helically coiled tubes. *International Journal of Heat and Mass Transfer* 68, 343–356.
3. Yuan Zhou, et al., 2013. Capability of RELAP5 MOD3.3 code to simulate density wave instability in parallel narrow rectangular channels. *Ann. Nucl. Energy* 50, 103–110.
4. Yunlong Zhou, et al., 1992. A design procedure of steam generator with multistart helical tubes. *Nuclear Power Engineering* 6, 1–8.
5. Fenglei, N.I.U., 1997. Flow Instability Analysis of 10 MW High Temperature Gascooled Test Reactor Steam Generator. INET, Tsinghua University, Beijing (Master degree dissertation).

Validation of the Cross-Calibration Multispectral Infrared Thermography in Surface Temperature Measurements

Auve Benjamin, Huber Alexander, Sergienko Gennady, Joffrin Emmanuel, Sun Jun, Huber Valentina, Price Marcus and Silburn Scott

Abstract The tokamak is nowadays one of the most promising methods to meet today's energy needs without CO₂ emissions and radioactive wastes. Moreover, the undertaking aiming to connect the tokamak to the electric grids is on its way [the Join European Torus (JET), then the International Thermonuclear Experimental Reactor (ITER) and finally the Demonstration Power Plant (DEMO)]. Surface temperatures in in-vessel are important parameters to know whether the JET ITER-like walls can withstand the high temperatures. To get these surface temperatures, many means exist to measure the surface temperature without any contact, in one of which the pyrometry method uses pre-calibrated multispectral infrared (IR) cameras. In this paper, a new method, called the cross-calibration method, was described to calculate surface temperatures by multispectral infrared cameras without any pre-calibration. By calculating the neutral density (ND) filters transmissivities and normalized digital levels for various configurations, the calibration coefficients in the cross-calibration method were validated and the error on

JET Contributors (See Appendix of F. Romanelli et al., 25th IAEA Fusion Energy Conference, 2014, Russia).

A. Benjamin (✉) · S. Jun
Institute of Nuclear and New Energy Technology, Tsinghua University,
100084 Beijing, China
e-mail: Ben.auve@gmail.com

H. Alexander · S. Gennady
Forschungszentrum Jülich GmbH, Institut für Energie- und
Klimaforschung—Plasmaphysik, Partner of the Trilateral
Euregio Cluster (TEC), 52425 Jülich, Germany

J. Emmanuel
CEA, IRFM, F-13108 St. Paul-lez-Durance, France

H. Valentina
Forschungszentrum Jülich GmbH, Supercomputing Centre,
52425 Jülich, Germany

P. Marcus · S. Scott
CCFE, Culham Science Centre, Abingdon OX14 3DB, UK

the surface temperatures could be evaluated within 10%. Given that the environment in the vessel is highly contaminated during the operations, many contaminants due to partial oxidation and others deposits can distort the measuring results on the cameras. Thus, it is essential to be able to re-calibrate the infrared cameras; we will be able to remotely cross-calibrate cameras without sending people inside the tokamak.

Keywords Tokamak · Multispectral infrared thermography · Pyrometry · Cross-calibration

1 Introduction

Infrared thermography is an essential tool to measure the surface temperatures and the heat loads on the JET divertor target tiles. In operation since 1983, the JET facility machine is a large experimental device, which forms part of the European Fusion Program. Its aim is to confine and study the behavior of plasma in conditions and dimensions approaching those required for a fusion reactor. The plasma is created in the toroidal-shaped vacuum vessel of the machine (shown below) in which it is confined by magnetic fields. The power is exhausted mainly in the divertor. JET was explicitly designed to study plasma behavior in conditions and dimensions approaching those required in a fusion reactor. Today, its primary task is to prepare the construction and operation of ITER, acting as a test bed for ITER technologies and plasma-operating scenarios. Recently, JET has been upgraded to become more ITER-like to conduct dedicated studies for ITER. The upgrade aimed to equip the vessel with an inner wall made of the same materials planned for ITER—beryllium and tungsten.

The calibration of the infrared camera systems is a critical issue because of the transmission degradation of the experimental campaign (owing to deposition on the front optical components, to neutrons, to gamma rays, etc.) and because of restricted possibilities for the calibration. Therefore, a new self-calibrated method which is based on the operation of two or more cameras at different wavelengths in the near infrared (NIR) and medium wavelength infrared (MWIR) spectral range is introduced; it does not require the absolute calibration of individual camera systems.

The aim of the project was to develop the models for temperature and power load measurements by self-calibrated multispectral imaging thermography based on the uncalibrated camera system. This paper includes the feasibility study of multispectral infrared thermography methods as well as the temperature and power load validation of experimental data of previous campaigns. The advantages and limits of the new method were both discussed in theoretical analyses, especially on the sensitivity of surface temperatures induced by measurement errors.

This paper includes the feasibility study of the self-calibrated multispectral infrared thermography method with the development of the mathematical model

and the analysis of the minimization of the error of surface temperatures. Many factors leading to this final error have been considered, such as the error due to the analysis of the region of interest (ROI) on one shot of the camera and the error due to emissivity. The entire process of optimization involves the wavelength range, camera sensitivity and dynamical range, and analysis of ND filters. The experimental section firstly deals with the cross-calibration of NIR and MWIR cameras with the blackbody. Then, this work validates the cross-calibration model thanks to a multispectral imaging system based on one NIR and one MWIR cameras with the same field of view (FoV). Experimental data from previous campaigns are used for this final validation part.

2 Theory

2.1 Planck's Law

To cope with the high temperature surface reached the in-vessel, the temperature has been evaluated thanks to the two CCD camera systems. The principle is mainly found thanks to the Planck's law [1]:

$$L = \frac{c_1}{\lambda^4} \frac{\varepsilon}{\exp\left(\frac{c_2}{\lambda T}\right) - 1} \quad (1)$$

with

$c_1 = 2c$ First radiation constant
 $c_2 = h \cdot c / k$ Second radiation constant
 L Spectral radiance photons $s^{-1} m^{-2} m^{-1} sr^{-1}$.

Many systems and methods based on two wavelengths have existed for a long time, but each method relies on specific constraints. Herein, the purpose of this paper goes one-step further and aims to calculate the temperature of a wall without any calibration. Indeed, this will enable not to enter in-vessel to calibrate each camera.

In the following parts, the cross-calibration worked out to avoid any calibration, and the pyrometry method, which is similar but provides alternative results, is presented. This entire feasibility study is accompanied with a sensitivity study for the cross-calibration method.

2.1.1 The Pyrometry Method

This method differs from the previous one in the sense that it only takes one shot with the infrared and the protection cameras. Hence, one can calculate the signal ratio between these two shots [2]:

$$SR(\lambda_1, \lambda_2) = \frac{DL(\lambda_2, \varepsilon, T)}{DL(\lambda_1, \varepsilon, T)} = \frac{k_2}{k_1} * \frac{\lambda_1^4}{\lambda_2^4} * \frac{\exp\left(\frac{c_2}{\lambda_1 T}\right) - 1}{\exp\left(\frac{c_2}{\lambda_2 T}\right) - 1} \tag{2}$$

In the above equation, we consider that the object reacts as a gray body and that we detect only the emitted object radiance. Then, if we make the approximation like in the cross-calibration method ($c_2 \gg \lambda_1 T_2$), the following equation is obtained:

$$SR(\lambda_1, \lambda_2) = \frac{DL(\lambda_2, \varepsilon, T)}{DL(\lambda_1, \varepsilon, T)} = \frac{k_2}{k_1} * \frac{\lambda_1^4}{\lambda_2^4} * \frac{\exp\left(\frac{c_2}{\lambda_1 T}\right)}{\exp\left(\frac{c_2}{\lambda_2 T}\right)} \tag{3}$$

This relevant equation enables to infer the temperature of the object:

$$\frac{1}{T} = \frac{1}{c_2} * \frac{\lambda_1 * \lambda_2}{\lambda_2 - \lambda_1} * \left(\ln(SR(\lambda_1, \lambda_2)) + 4 \ln\left(\frac{\lambda_2}{\lambda_1}\right) + \ln\left(\frac{k_1}{k_2}\right) \right) \tag{4}$$

To sum-up, this method will be experienced in the next part “4.1.1 Cross-calibration” but it involves that one already knows the calibration coefficients (k_1 and k_2) to use the Eq. (4).

2.2 The Cross-Calibration Method

2.2.1 Getting the Temperature and the Calibration Coefficients

The principle of this method is based on one protection camera (λ_1) and one infrared camera (λ_2). Emissivities of each camera, called ε_1 and ε_2 , are well considered independently. To pursue in the cross-calibration, two shots should be taken at two different temperatures T_1 and T_2 with both cameras.

In our case, DL_{ij} corresponds to the digital level we measure straightly with each camera. Given that the cameras grab the photon flux, the DL_{ij} terms are proportional to the spectral radiance L (photons $s^{-1} m^{-2} m^{-1} sr^{-1}$):

$$DL_{11} = k_1 \frac{c_1}{\lambda_1^4} \frac{\varepsilon_1}{\exp\left(\frac{c_2}{\lambda_1 T_1}\right) - 1} \tag{5}$$

$$DL_{12} = k_1 \frac{c_1}{\lambda_1^4} \frac{\varepsilon_1}{\exp\left(\frac{c_2}{\lambda_1 T_2}\right) - 1} \tag{6}$$

$$DL_{21} = k_2 \frac{c_1}{\lambda_2^4} \frac{\varepsilon_2}{\exp\left(\frac{c_2}{\lambda_2 T_1}\right) - 1} \tag{7}$$

$$DL_{22} = k_2 \frac{c_1}{\lambda_2^4} \frac{\varepsilon_2}{\exp\left(\frac{c_2}{\lambda_2 T_2}\right) - 1} \quad (8)$$

In more details, k_1 and k_2 represent the product of the transmittance and the S . For the next parts, they are called “calibration coefficients” and depend only on the camera:

$$A_1 = k_1 \frac{c_1}{\lambda_1^4} \varepsilon_1 \quad (9)$$

$$A_2 = k_2 \frac{c_1}{\lambda_2^4} \varepsilon_2 \quad (10)$$

The first step of our calculations is to show that we do not need to know T_1 to get T_2 :

$$1 = \frac{\left(1 + \frac{DL_{22}}{DL_{21}} \left(\exp\left(\frac{c_2}{\lambda_2 T_2}\right) - 1\right)\right)^{\lambda_2/\lambda_1}}{1 + \frac{DL_{12}}{DL_{11}} \left(\exp\left(\frac{c_2}{\lambda_1 T_2}\right) - 1\right)} \quad (11)$$

By assuming that $c_2 \gg \lambda_1 T_2$, which is possible given that $c_2 = 14387.77 \mu\text{m K}^{-1}$, that our temperature range is within 800–1400 K and that the wavelength is around 1 μm , the temperature is obtained:

$$T_2 = \frac{c_2}{\lambda_2 \ln\left(\frac{1 - \frac{DL_{22}}{DL_{21}}}{\left(\frac{DL_{12}}{DL_{11}}\right)^{\lambda_1/\lambda_2} - \frac{DL_{22}}{DL_{21}}}\right)} \quad (12)$$

Once the temperature T_2 is finally known, one can calculate the remaining unknown terms:

$$T_1 = \frac{c_2}{\lambda_1 \ln\left(1 + \frac{DL_{12}}{DL_{11}} \left(\exp\left(\frac{c_2}{\lambda_1 T_2}\right) - 1\right)\right)} \quad (13)$$

$$A_1 = DL_{12} \left(\exp\left(\frac{c_2}{\lambda_1 T_2}\right) - 1\right) \quad (14)$$

$$A_2 = DL_{22} \left(\exp\left(\frac{c_2}{\lambda_2 T_2}\right) - 1\right). \quad (15)$$

2.2.2 An Alternative Method to Get the Calibration Coefficients

This method consists in calculating the calibration coefficients firstly without any calibration of the cameras. Using the same notation as in Eqs. (14) and (15), we have the following:

$$DL_1(t) = \frac{A_1}{\exp\left(\frac{c_2}{\lambda_1 T(t)}\right) - 1} \tag{16}$$

$$DL_2(t) = \frac{A_2}{\exp\left(\frac{c_2}{\lambda_2 T(t)}\right) - 1} \tag{17}$$

Hence, one can assume that:

$$T(t) = \frac{c_2}{\lambda_1 \ln\left(1 + \frac{A_1}{DL_1(t)}\right)} \tag{18}$$

$$T(t) = \frac{c_2}{\lambda_2 \ln\left(1 + \frac{A_2}{DL_2(t)}\right)} \tag{19}$$

By combining these two equations, we finally get:

$$\left(1 + \frac{A_1}{DL_1(t)}\right)^{\lambda_1} - \left(1 + \frac{A_2}{DL_2(t)}\right)^{\lambda_2} = 0 \tag{20}$$

By taking several shots at different temperatures with each camera, we can immediately call a new term:

$$S = \sum_i \left[\left(1 + \frac{A_1}{DL_{1i}}\right)^{\lambda_1} - \left(1 + \frac{A_2}{DL_{2i}}\right)^{\lambda_2} \right]^2 \tag{21}$$

S should converge to zero when we set the calibration coefficients A_1 and A_2 . In practice, we will measure several digital levels DL_{1i} and DL_{2i} at different temperatures, and we will evaluate with an optimization algorithm the right constants A_1 and A_2 to minimize S . We will present you this method in the next chapter “3.1 Experimental.”

2.3 Sensitivity of the Cross-Calibration

The cross-calibration presented in the previous part has one major issue: the sensitivity of the calculations. As seen in Eq. (12), we measure the ratios DL_{22}/DL_{21} and DL_{12}/DL_{11} to directly calculate the temperature T_2 . In this context, we decided to pay attention on the impact of these ratio measurements on the calculated temperature T_2 .

In these above figures, the 0.98 and 3.9 μm wavelengths and a temperature T_1 (700 °C) are used. These results are theoretical. Figure 1 allows us to find out the ratio ranges for many temperatures.

In Fig. 2, different wavelengths and temperatures (T_1 and T_2) were set and ratios of DL were made varying. We chose several ranges of temperature for T_2 to also compare in which range of temperature the deviation is the highest (Fig. 3).

Fig. 1 Internal view of the vessel (ITER-like wall)

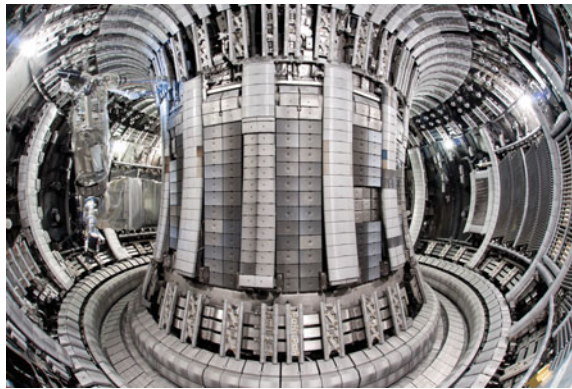
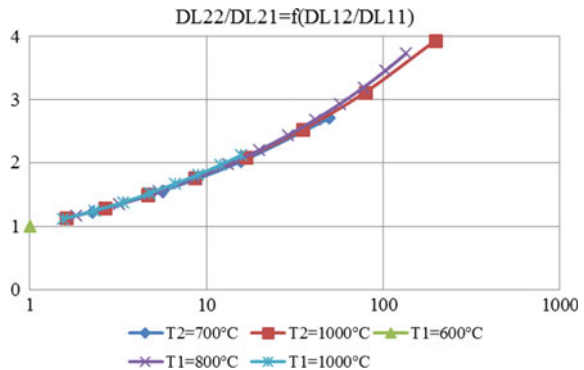


Fig. 2 Range of the ratios



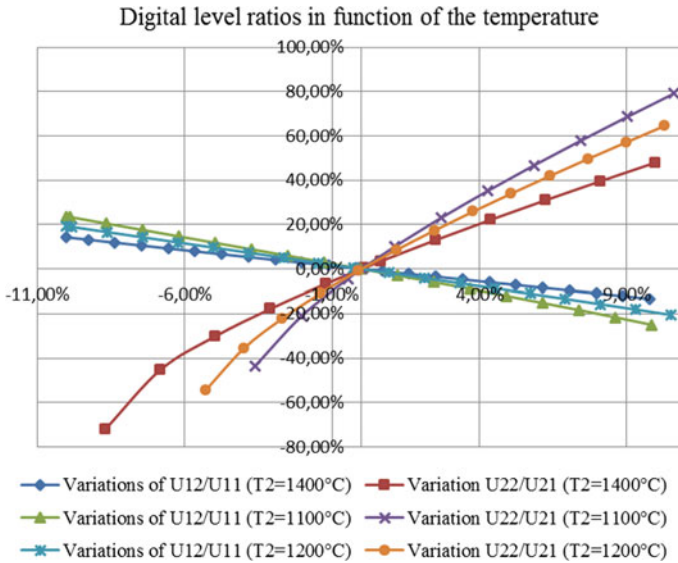


Fig. 3 Error on the temperature in function of the error on the ratio measurements

The first observation to make is that a very little variation of both ratios can lead to a big impact on the accuracy of the temperature (1% of error on the DL_{22}/DL_{21} ratio can involve 10% of error on the temperature).

The second one reveals that the DL_{22}/DL_{21} ratio is much more sensitive than the other one; we have to get a quite better resolution with the infrared camera.

The advantage that the error is reversed for both ratios can be used to compensate the final error on temperature T_2 . The higher the temperature is, the lesser the impact of the ratios error on the temperature will be.

3 Experiments

3.1 Cross-Calibration with the Blackbody

Our first goal in the experimental part was to cross-calibrate the protection (NIR) camera with the blackbody. To do so, we used one reference camera, usually taken for every calibration, with two IR filters: 0.98 and 1.016 μm . Then, we set up the blackbody to reach certain temperatures between 600 and 1200 °C. The idea was to evaluate the digital level received by the camera with each NIR filter for the range of temperature one can encounter in-vessel.

Given that the phenomenon of saturation is strongly present for temperatures above 800 °C, we had to use ND filters to diminish the intensity of light. In our experience, we worked with 5 ND filters:

Table 1 Normalized digital levels

HS Temp	ND filter	Mean DL (background subtracted)	DL _{normalized} (background subtracted)
604.58	0	35.46	35.46
604.59	0.2	19.53	35.17
604.57	0.5	11.54	34.36
604.56	1	3.83	–
604.57	1.3	1.31	–
1009.71	1	209.25	–
1009.66	1.3	208.99	–
1009.63	2	73.18	6903.77
1009.58	2.2 (2.0 + 0.2)	40.36	6857.97
1009.55	2.5 (2.0 + 0.5)	24.09	6767.84
1009.53	3 (2.0 + 1.0)	8	6602.95

- 0.2 OD
- 0.5 OD
- 1.0 OD
- 1.3 OD
- 2.0 OD

It led us to find out a way to calculate precisely the transmissivity of each ND filter. Provided the transmissivity of two ND filters is the product of both transmissivities, we have been able to measure every transmissivity with several combinations of filters. To better understand, let us see an extract of the array of the measurements from the cross-calibration (Table 1).

The background was subtracted for each shot with the camera thanks to a shot at the atmosphere temperature. The background was around 33 digital levels (DL) in our case.

The mean value of each shot can be obtained with the JUVIL [3] software. It was created by our team in the JET.

3.1.1 Calculation of the ND Filters Transmissivities

Once we got enough measurements with the camera for different temperatures and many combinations of ND filters each time, the first step is to calculate the transmissivities. In the above example, we can know the transmissivity of the 0.2 ND filter by two ways:

$$T_{0.2} = \frac{DL(604\text{ }^{\circ}\text{C}, 0.2\text{ OD})}{DL(604\text{ }^{\circ}\text{C}, 0\text{ OD})} \quad (22)$$

Table 2 Transmissivities

Transmissivities	Wavelength 0.98 μm	Wavelength 1.016 μm
0.2 OD	0.5640	0.5550
0.5 OD	0.3564	0.3358
1.0 OD	0.1343	0.1115
1.3 OD	0.0618	0.0493
2.0 OD	0.0160	0.0118

$$T_{0.2} = \frac{\text{DL}(1009\text{ }^\circ\text{C}, 2.2\text{ OD})}{\text{DL}(1009\text{ }^\circ\text{C}, 0.2\text{ OD})} \tag{23}$$

By making the average of these two results, we can directly obtain the transmissivity of the 0.2 ND filter. With this method, we managed to obtain the following transmissivities (Table 2).

These results are quite relevant compared to the documentation provided by THORLABS on their Web site (<https://www.thorlabs.com>).

3.1.2 Calculation of the Normalized Digital Level

Thanks to the known transmissivities, we will evaluate the real digital levels due to the blackbody. We just had to divide each digital value measured via the camera by the transmissivity of the ND filters used during the measurement.

You can see that certain values have been removed from the array, and there are two reasons:

- The digital level (DL) is too low, so that the value is too sensitive and not reliable;
- The digital level (DL) is saturated, so that the value is not relevant.

We worked with 8 bits for the camera, so the saturation level was around 255 DL. Given that we subtracted the background, the digital level should be inferior to 222 DL (255-33) to be relevant. In practice, we did not consider any value above 200 DL, it turned out that our saturation level was lower than expected.

3.1.3 Calculation of the Calibration Coefficients

We finally come to the calibration part. Our goal is to find out the calibration coefficients as mentioned in Eqs. (14) and (15). By simplifying Eq. (16), if we suppose that $c_2 \gg \lambda T$, we can easily express the digital level in function of the temperature:

$$\text{DL}(\lambda, T) = a + b * \exp\left(-\frac{c_2}{\lambda T}\right) \tag{23}$$

with

- a constant which should be null
- b constant which corresponds to the calibration coefficient
- $c_2 = 14387.77 \mu\text{m K}^{-1}$ Second radiation constant
- T Temperature in Kelvin
- λ Wavelength in μm

“a” and “b” are the two constants we have to infer thanks to the array of measurements we made previously. Now, we can insert this equation in our array, as follows (Table 3).

To find out the “a” and “b” values that match to our measurements, we used an optimization algorithm which aims to diminish the total error by making vary “a” and “b”. The error corresponds to the difference between the theoretical and experimental digital to the square. At the end of the optimization, we finally got the following calibration coefficients (Table 4).

The calibration coefficients are expressed for wavelength in microns and temperatures in kelvin. We notice that both constants “a” are equal to zero which proves the reliability of our experience. Moreover, the graphics inferred from these results are quite good as we can see as follows (Figs. 4 and 5).

The fit curves well overlay the different points of the curves which represent the points we measured with the blackbody. We can easily distinguish the differences compared to the fit curves thanks to the 5% error bars present in each graphic. For high temperature (>900 °C), every point is within the 5% range, whereas for low

Table 3 Calculation of the interpolation coefficients

HS Temp	ND Filter	DL normalized (background subtracted)	$a + b * \exp(-\frac{c_2}{\lambda T})$	Error
604.58	0	35.46	43.260	60.85
604.59	0.2	35.17	43.269	65.49
604.57	0.5	34.36	43.253	78.98
1009.63	2	6903.77	7056.288	23260.8
1009.58	2.2	6857.97	7053.252	38133.7
1009.55	2.5	6767.84	7051.431	80,422.8
1009.53	3	6602.95	7050.217	200050.2
			Total error:	342072.8

Table 4 Interpolation coefficients

	Wavelength 0.98 μm	Wavelength 1.016 μm
a	0	0
b	97896127.190	439491341.788

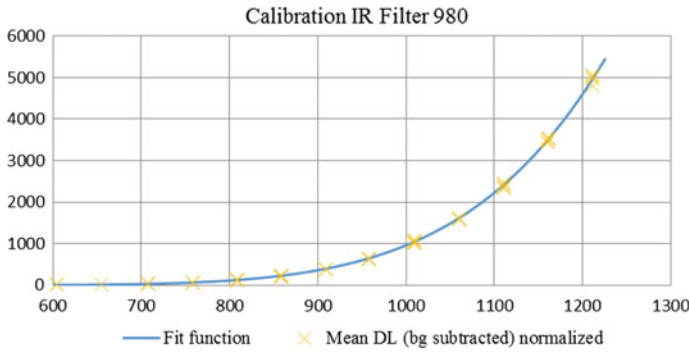


Fig. 4 Fit function (IR filter 980 μm)

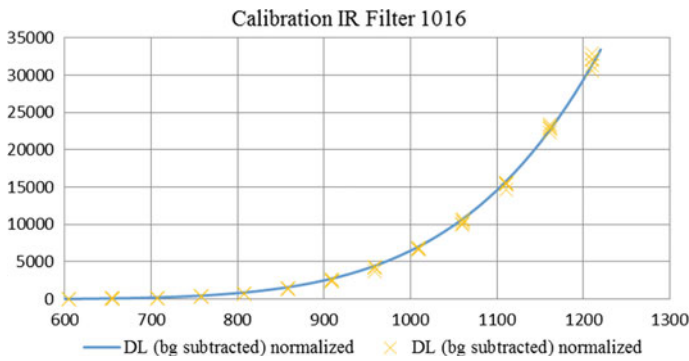


Fig. 5 Fit function (IR filter 1016 μm)

temperatures (<850 °C), our measurements start being questionable for the 1016 IR filter as we can see in the following graphics (Figs. 6 and 7).

Although the calibration for the 1016 IR filter is less relevant for low temperatures, the curve still fits well for 980 IR filter. All these gaps will be considered for our further analysis.

3.2 Accuracy of the Measurements

In the theoretical part “2.4 Sensitivity of the cross-calibration,” we concluded with the fact that the calculation of the temperature is very sensitive and strongly depends on accurate ratio measurements. To avoid any mistake and to know in which part of the process we can be more accurate, we evaluated the overall accuracy of our measurements. We split the final error into 5 different errors:

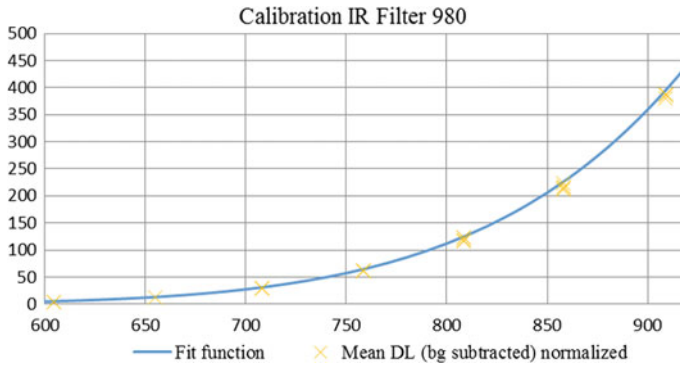


Fig. 6 Low temperatures (IR filter 980 μm)

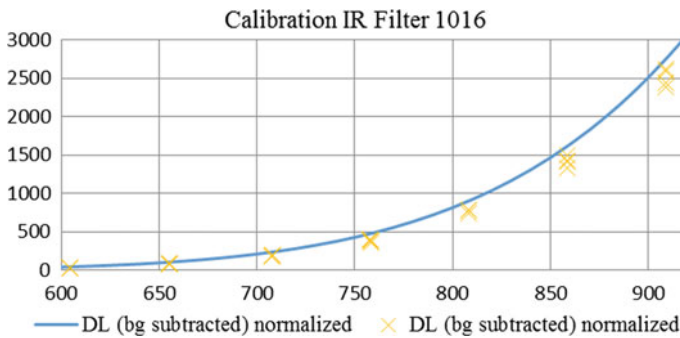


Fig. 7 Low temperature (IR filter 1016 μm)

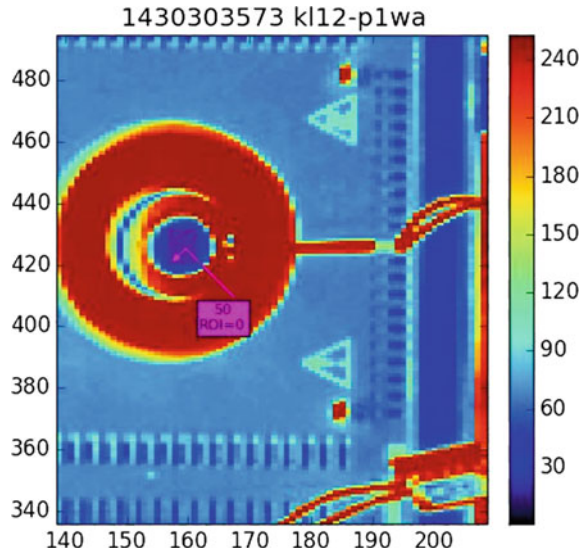
- Error due to analysis
- Error due to the oven
- Error due to the filters
- Error due to ICLS
- Error due to emissivity.

3.2.1 Error Due to Analysis

To better understand this error, we must consider a picture taken with the reference camera we used during the calibration. Once we took the picture with a defined IR filter and ND filter and the oven heated up, we should extract the digital level by choosing a region of interest (ROI) in this even picture (Fig. 8).

After one chooses a region of interest that must correspond to the higher part of the picture, the JUVIL software gives the user the mean digital level in the ROI and the standard normalized deviation. This last information indicates how the

Fig. 8 Example of region of interest



measurements oscillate around the mean value. Then, we can immediately collect the possible error on our analysis of each picture.

During our experiences, we tried to avoid all the standard normalized deviation over 1%. In practice, we took the normalized standard deviation for each combination of ND filter and for every temperature of the oven we used for the calibration. Thus, we found out a mean standard normalized deviation (error) of 0.569% for the 980 μm filter and 0.717% for the 1016 μm filter.

3.2.2 Error Due to Oven

Given that the thermometer in the oven is not reliable one hundred percent, our team had to consider these uncertainties in the calculation of the temperature. Indeed, all our calibration measurements were based on the temperature given by this thermometer.

After having conducted measurements with a pyrometer, we have been able to know the differences of temperature between the value given by the oven thermometer and the real temperature: ± 2 $^{\circ}\text{C}$. Then, thanks to the fit curves found in the “3.1.3 Equations to get the calibration coefficients” section, we can evaluate the digital level difference for this 2 $^{\circ}\text{C}$ error (Table 5).

We should be careful because these relative errors correspond only to the optical density (OD) errors, not the digital level errors. Let us analyze the impact of these errors on the digital levels.

According to what we discovered above for the 1016 IR filter, if we consider that:

Table 5 Optical density error

OD _{relative} error	IR filter 980 μm (%)	IR filter 1016 μm (%)
ND filter 0.2	1.47	1.40
ND filter 0.5	2.08	2.16
ND filter 1	2.01	5.35
ND filter 1.3	2.46	2.63
ND filter 2	2.33	3.82

Table 6 Errors due to analysis

DL _{relative} error	IR filter 980 μm (%)	IR filter 1016 μm (%)
ND filter 0.2	1.45	1.38
ND filter 0.5	2.04	2.12
ND filter 1	1.97	5.08
ND filter 1.3	2.41	2.57
ND filter 2	2.28	3.68

$$OD_{\text{error}}(0.2) = OD(0.2) * (1 + 0.014) \quad (24)$$

Then, the digital level calculated with the error would be:

$$DL_{\text{error}} = \frac{DL_{\text{measured}}}{OD_{\text{error}}(0.2)} \quad (25)$$

whereas the right digital level would be:

$$DL = \frac{DL_{\text{measured}}}{OD(0.2)} \quad (26)$$

If we compare both Eqs. (25) and (26), we can easily say for the combination of the 0.2 ND filter and the 1016 IR filter that:

$$DL_{\text{relativeerror}} = \left| \frac{DL_{\text{error}} - DL}{DL} \right| = \left| \frac{1}{(1 + 0.014)} - 1 \right| \quad (27)$$

Therefore, we directly find out the digital level relative error for every ND filter (Table 6).

3.2.3 Error Due to the Integrating Sphere

Once the fit curves of each IR filter were displayed, we used an in-vessel calibration light source (ICLS) to get a uniform scattering without any spatial dependency [4].

Table 7 Error due to ICLS

Relative error	IR filter 980 μm (%)	IR filter 1016 μm (%)
Lamp 1	1.681	1.669
Lamp 3	1.630	1.547

The ICLS contains an integrating sphere with four lamps (of known radiance), so our goal was to match each lamp with the temperature it corresponds. We analyzed only 2 lamps: Lamp 1 and Lamp 3. Thanks to the documentation, we have been able to get the relative error of the integrating sphere (Table 7).

3.2.4 Error Due to Emissivity

One more time, with the pyrometer, we have both seen the impact of the emissivity on the temperature measurement and inferred that the accuracy of the emissivity in the blackbody is very good: <1% error.

Let us analyze the consequences of the emissivity on the temperature measurements with the pyrometer (Table 8).

We can observe the strong impact of the emissivity; this is exactly why we always need to take into consideration this element in our calculations due to many variations in-vessel of emissivity.

3.2.5 Overall Error

Now that the problem has been split into different errors coming from many sources, one can gather all these information to calculate the overall error in our measurements (Table 9).

We can see that the error on the digital level can reach around 9 percent maximum. This accuracy would have been acceptable if it had been for the temperature

Table 8 Error due to emissivity

Temperature (pyrometer) ($^{\circ}\text{C}$)	Indicated temperature (oven) ($^{\circ}\text{C}$)	Emissivity
660	656.7	1
666	656.5	0.9
672	656.5	0.8
681	656.3	0.7
692	656.2	0.6
703	656.2	0.5
718	656.1	0.4
737	656	0.3
765	655.9	0.2
817	655.9	0.1

Table 9 Overall error

Error	IR filter 980 μm Lamp 1 (%)	IR filter 980 μm Lamp 3 (%)	IR filter 1016 μm Lamp 1 (%)	IR filter 1016 μm Lamp 3 (%)
$T = 600\text{ }^{\circ}\text{C}$	6.37	6.36	8.73	8.71
$T = 700\text{ }^{\circ}\text{C}$	5.96	7.78	8.42	8.39
$T = 800\text{ }^{\circ}\text{C}$	5.70	7.78	8.22	8.20
$T = 900\text{ }^{\circ}\text{C}$	5.54	7.78	8.10	8.07
$T = 1000\text{ }^{\circ}\text{C}$	5.43	7.78	8.02	7.99
$T = 1100\text{ }^{\circ}\text{C}$	5.35	7.78	7.96	7.94
$T = 1200\text{ }^{\circ}\text{C}$	5.30	7.78	7.92	7.90

but as we saw in the part “2.4 Sensitivity of the cross-calibration,” few percent difference in the calculation of the digital level ratio can lead to huge impacts on the temperature measurements.

4 Results with Two Cameras: KL9B [5]–KL2D

At this stage, we correctly understand the cross-calibration with its sensitivity and the possible errors we can encounter; we are going to try this method on a sample. This is a picture of the wall in-vessel taken with the KL9B camera. We took the same picture with the same frames with another camera: the KL2D. Here are the features of each camera:

- KL9B: infrared camera, central wavelength 3900 nm, FWHM (full width at half maximum) 1600 nm
- KL2D: protection camera, central wavelength 980 nm, FWHM 20 nm

Our team used the opportunity that the tokamak was not in operation to also calibrate the KL9B with the same process we used in the “Equation to get the calibration coefficients.” This allowed us to calculate the calibration coefficients for this infrared camera and to compare with the results of the cross-calibration we will see after. The constant values for these cameras are as follows:

- a (intercept) = 75.27 SI Unit
- $b = 78\ 932.54$ SI Unit.

4.1 Theoretical/Experimental Comparisons

4.1.1 Comparisons for the Cross-Calibration

Once we have taken measurements and calibrated both cameras (KL9B and KL2D), we are going to see how far our calibrations are compared to the theoretical equations. To do so, we created three different arrays: the first one which is linked to the experimental values and the second one which relates to the theoretical values and the last one which follows the process to calculate the calibration coefficients as described in the “2.3 The cross-calibration method” section (Table 10).

The first observation one can note here concerns the temperature T_2 that experimentally cannot be calculated. This error is due to the logarithm which is negative considering the Eq. (12). Let us analyze where this error comes from by comparing the theoretical values (Table 11).

As expected, whereas the ratio for the KL2D camera (980 nm IR Filter) is excellent, the ratio for the KL9B camera (3900 nm IR Filter) is less accurate. Indeed, we can remember that the calibration curve we found for this camera had intercept which was due to errors during the measurements. We can now consider the last array to see the calibration coefficients we can obtain with the cross-calibration process.

We considered the mean value for the A_1 and A_2 calibration coefficients given in Table 12. As expected, the values for the KL2D camera (980 nm IR filter) are quite reliable and relevant. Whereas the calibration coefficient for the KL9B camera are completely different, it proves that the calibration measurements were not enough accurate.

Table 10 Experimental values (cross-calibration)

Experimental values				
T_1 (°C)	T_2 (°C)	DL ₂₂ /DL ₂₁ (3900 nm)	DL ₁₂ /DL ₁₁ (980 nm)	T_2 evaluated (°C)
600.85	801.15	2.009	22.918	–
600.85	701.05	1.516	5.628	–
499.55	701.05	2.579	50.903	–
499.55	600.85	1.701	9.045	–

Table 11 Theoretical values (cross-calibration)

Theoretical values				
T_1 (°C)	T_2 (°C)	DL ₂₂ /DL ₂₁ (3900 nm)	DL ₁₂ /DL ₁₁ (980 nm)	T_2 calculated (°C)
600.85	801.15	2.237	22.918	801.145
600.85	701.05	1.556	5.628	701.048
499.55	701.05	2.724	50.903	701.049
499.55	600.85	1.750	9.045	600.850

Table 12 Calibration coefficients

KL2D camera		KL9B camera	
$A1$	b	$A2$	b
236,677,589.11	236,670,819.47	43,900.14	78,932.54

4.1.2 Comparisons for the Pyrometry Method

In the previous part “2.2 The pyrometry method,” we saw that with the knowledge of the calibration coefficients, we could directly calculate the temperature of a hot surface with its intensity of light. We can see in reference [6] that we can evaluate the intensity of light with more accuracy thanks to the integral of the spectral transmission. As for the cross-calibration method, let us see the comparison between experiences and theory (Table 13).

In theory, this method works well. Now, for the experimental values, we are going to display two different arrays: one for each combination of calibration coefficients. Indeed, we saw in the previous part that the calibration coefficient we found was not the same if we calculate with the cross-calibration and if we take the ones from the experimental fit curve (Tables 14 and 15).

Table 13 Theoretical values (pyrometry)

Theoretical values (integral)				
Hot source temperature (°C)	Integral(λ_1)—numerical	Integral(λ_2)—numerical	DL ₂₂ /DL ₁₂	T_2 (°C)
600	7.0030E-09	9.9596E-05	38.93191987	603.37
700	3.6752E-08	1.5583E-04	11.60716973	702.17

Table 14 Experimental values (pyrometry)

Experimental values			
Hot source temperature (°C)	KL2D(980 nm)—DL background subtracted	KL9B (3900 nm)—DL background subtracted	T (°C)
600	11.80	1273.08	554.27
700	66.40	1930.41	644.90

Note These values are obtained with the calibration coefficients calculated from the cross-calibration method

Table 15 Experimental values (pyrometry)

Experimental values			
Hot source temperature (°C)	KL2d (980 nm)—DL background subtracted	KL9b (3900 nm)—DL background subtracted	T (°C)
600	11.80	1273.08	593.26
700	66.40	1930.41	693.15

Note These values are obtained with the calibration coefficients measured with the fit curves

We can see that for the first range of experimental values, the gap is important: around 8%. Concerning the second range of experimental values, these ones are relatively good: around 1%. This gives us an important piece of information which explains that the calibration coefficients measured with the fit curves are probably much more reliable than the other ones.

It is unavoidable to consider that in these calculations of the temperature, we supposed emissivities did not depend on the wavelengths.

4.2 Analysis of One Pulse

The pulse No. 86531 is the picture we took with both KL9B and KL2D cameras. During our period of analysis, it was the only picture available due to database issues. In this pulse, the heat shows up to 1050° on the ITER-like wall and reaches a peak at around 48 s: We decided to analyze the decreasing slope due to its sharpness.

To picture where the area we observe is, we are going to represent the entire JET's vessel (Fig. 9).

The interaction of the plasma with the wall materials is a source of many questions as “how this material migrates through the plasma and redeposits on a different location of the wall” and “what is the impact of these emissivities on our

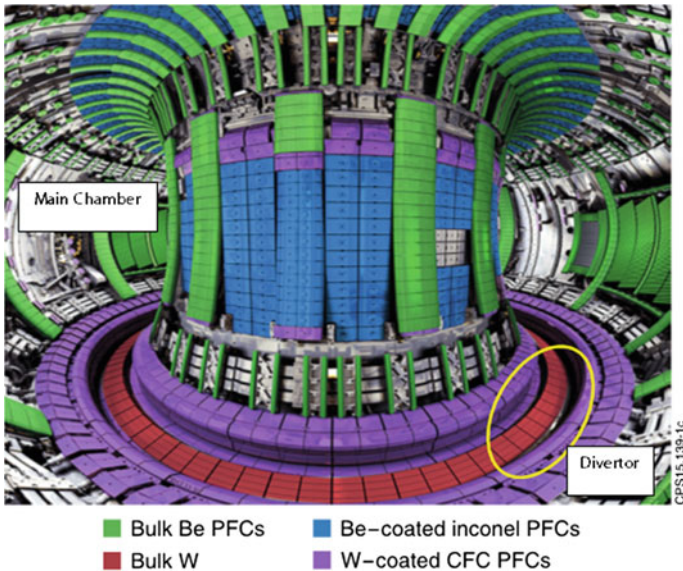


Fig. 9 Region of analysis

measurements.” For this reason, we should well consider in which part of the vessel we work.

We selected these two shots for both cameras, taken in the divertor in-vessel. To avoid any mistake, we should focus on the same area for both cameras. However, nothing allows us to be sure that we analyze the very same area. So, we decided to analyze the results with many different ROI (Region of Interest) for each camera. Below are the two shots for both cameras KL2D and KL9B with different ROIs (Figs. 10 and 11).

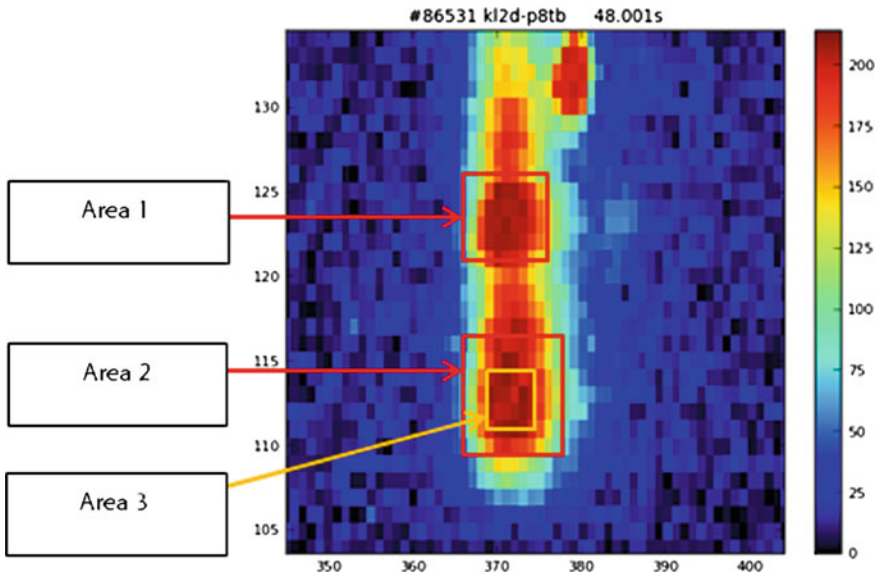


Fig. 10 Regions of interest (KL2D)

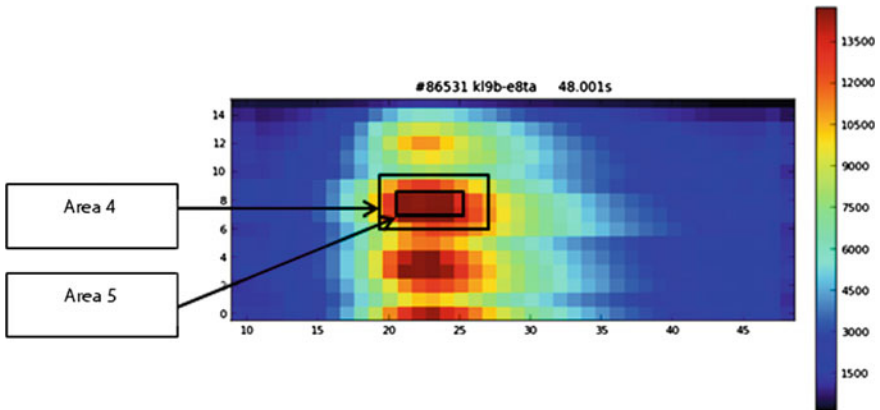


Fig. 11 Regions of interest (KL9B)

Thanks to the best range of measurements for each camera, we can now attend to get relevant results for temperature calculations. By following the cross-calibration process, we obtain (Table 16).

To have a better understanding of these results, we are going to explain each part row by row:

- “N°”: It represents different combinations of 2 times we chose to analyze after 48.081 s (which represent the sharpest part of the data curve, see figure below) (Fig. 12 and Table 17):
- “Measurements”: This row corresponds to the temperature at both times of the combination;
- “Theoretical”: it represents the temperature T_1 and T_2 calculated with the cross-calibration process and the theoretical ratios;
- “Ratio KL2D”: As seen in the previous part, it is the ratio for the protection system of the JET ITER-like wall (PIW) camera with the best accuracy;

Table 16 Theoretical and experimental results

No	Measurements		Theoretical		Area 1	Area 5	Experimental		
	T_1 (°C) with KL11a	T_2 (°C) with KL11a	T_1 (°C)	T_2 (°C)	Ratio KL2D	Ratio KL9B	T_1 (°C)	T_2 (°C)	$\epsilon_2(T_1)/\epsilon_2(T_2)$
1	873.70	939.00	873.67	938.97	2.1413	1.2172	733.87	769.89	1.036
2	834.00	939.00	833.98	938.97	3.1637	1.3516	835.31	919.50	1.059
3	811.75	939.00	811.73	938.97	4.0897	1.4404	739.13	833.91	1.073
4	772.40	939.00	772.38	938.98	6.8699	1.6501	755.66	888.85	1.097
5	749.00	939.00	748.98	938.98	9.5008	1.7987	772.16	938.15	1.113
6	750.70	939.00	750.68	938.98	9.2771	1.7878	776.81	938.94	1.111
7	721.60	939.00	721.59	938.98	14.112	1.9920	752.76	938.85	1.131
8	824.00	876.00	823.98	875.98	1.9099	1.1834	1037.4	847.08	1.029
9	781.00	876.00	780.99	875.98	3.2082	1.3557	787.34	901.05	1.055

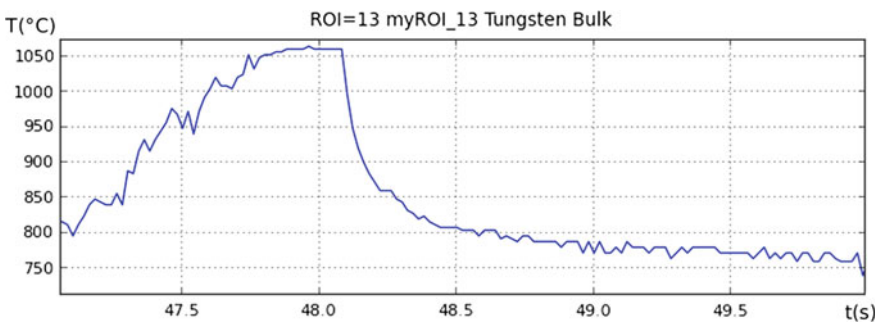


Fig. 12 Temperature on the 86531 pulse

Table 17 Combinations of pictures at different times

No	Combinations
1	48.081–48.101 s
2	48.081–48.121 s
3	48.081–48.141 s
4	48.081–48.181 s
5	48.081–48.221 s
6	48.081–48.261 s
7	48.081–48.301 s
8	48.101–48.141 s
9	48.101–48.181 s

- “Ratio KL9B”: As seen in the previous part, it is the ratio for the IR camera with the best accuracy;
- “Experimental”: It finally calculates the temperature T_1 and T_2 thanks to the cross-calibration process and the “Ratio KL2D” and “Ratio KL9B” rows.

Now, several results can be underlined from this array:

- The theoretical calculations of the temperatures are totally relevant, which proves that the cross-calibration is well feasible in theory.
- When we calculate the mean error of the temperature T_2 between experimental and theoretical, we finally obtain an average of 4% difference.

5 Conclusions

This report aimed both to summarize the information on the tools we used for the calibration of the cameras and to introduce a new way to calibrate the camera directly in the vessel. This is what we called the cross-calibration. Implementing this method would make one-step further in the multispectral infrared thermography, except that some barriers exist to use it. Our work was based on a feasibility study to show how this new method could be used and what the limits are.

With an approach half experimental and half theoretical, the work we did allows to evaluate the optical density of the ND filters in the laboratory. Thus, we have been able to plot the fit curves for two different infrared filters: 980 and 1016 nm. In parallel, a study about the sensitivity of the method started and proved that the accuracy of our measurements should not exceed 2% in certain conditions to get a final temperature error below 10%. This discovery led us to start an analysis of the overall error on our measurements and the results brought us to a potential error up to 8%.

Once we knew where the possible errors could come from, our team decided to experimentally try both methods we detailed in theory: the pyrometry method and the cross-calibration. With the good calibration coefficients, it reassured that the pyrometry method well worked. At the contrary, for the cross-calibration, it did not

work at first. With the understanding that it was due to our measurements, we tried to work on the accuracy of our measurements and tried several ways to extract the data from the pictures we got. At the end, the cross-calibration managed to provide us results with a variation of 4%.

Our team underlined two different ways to calculate the high surface temperature: one well-known method with the pyrometry and the other one completely new. The issues concerning the accuracy are real but our last task showed up that it is possible to find a way to deal with it. We tried to implement a process to decrease the sources of error, but this work can be carried further.

Acknowledgements The entire work has been possible thanks to Gennady Sergienko who developed this idea. He sets up all the theoretical formulas that enabled to make experiments, optimizations, and analyses.

References

1. F. Meriaudeau, "Real Time Multispectral High Temperature Measurement: Application to control in the industry", Le2i, 2007.
2. D. Melyukov, C. Sortais, D. Farcage, A. Semerok, P.-Y. Thro and E. Gauthier, "Temperature measurement at large distance of plasma-facing surfaces in fusion reactor by active pyrometry", 10th International Conference on Quantitative InfraRed Thermography, 2010.
3. V. Huber, A. Huber, D. Kinna, I. Balboa, S. Collins, N. Conway, P. Drewelow, C. F. Maggi, G. F. Matthews, A. G. Meigs, Ph. Mertens, M. Price, G. Sergienko, S. Silburn, A. Wynn and K.-D. Zastrow, "In-vessel calibration of the imaging diagnostics for the real-time protection of the JET ITER-like wall", 21st Topical Conference on High-Temperature Plasma Diagnostics, 2016.
4. T. M. Biewer, D. L. Hillis, M. F. Stamp, K.-D. Zastrow, and JET-EFDA Contributors, "A proposed in-vessel calibration light source for the Joint European Torus", 17th Topical Conference on High Temperature Plasma Diagnostics, 2008.
5. I. Balboa, S. Silburn, P. Drewelow, V. Huber, A. Huber, D. Kinna, M. Price, G. F. Matthews, S. Collins, J. Fessey, M. Rack, P. Trimble and K.-D. Zastrow, "Recent developments of in-vessel calibration of mid-IR cameras at JET", 21st Topical Conference on High-Temperature Plasma Diagnostics, 2016.
6. C. Pereira, T. Roesgen, S. Walz, S. Airaghi, "The Use of Multispectral Infrared Thermography in Re-entry Vehicles", 11th International Conference on Quantitative InfraRed Thermography, 2012.

Author Biography

Auve Benjamin is a master student from the Ecole Centrale de Lille, a French multidisciplinary engineering school. During his internship at the JET (Oxford, England), he worked in the Viewing Systems and Thermal Measurements team. He is currently studying for a double-degree at the Institute of Nuclear and New Energy Technology at Tsinghua University (Beijing, China).

Validation of Wall Friction Model in Multidimensional Component of Mars with Two-Phase Flow Experiments Describing ECC Behavior in Downcomer

Chi-Jin Choi, Jin-Hwa Yang, Hyoung-Kyu Cho, Dong-Jin Euh and Goon-Cherl Park

Abstract Nowadays, high-precision analysis of multidimensional phenomena is one of the issues in nuclear engineering to predict thermal–hydraulic phenomena in a nuclear reactor more precisely under accident conditions. For this reason, the nuclear reactor safety analysis codes have adopted 3D component which is for better prediction of the multidimensional phenomena. However, current 3D components have a fundamental flaw in their applicability since most of the constitutive models in the components were ones developed for the one-dimensional pipe flow. Nevertheless, the constitutive models have been validated rarely based on local measurement database that is from multidimensional phenomena. This insufficient validation of constitutive models led to the present study to simulate multidimensional experiments and validate associated physical models. This study focused on the two-phase flow occurred in the upper downcomer region of a PWR (Pressurized Water Reactor) which adopts the direct vessel injection system during the reflood phase of LBLOCA (Large Break Loss of Coolant Accident). In this study, two sets of experiment describing ECC (Emergency Core Coolant) behavior in the upper downcomer were selected for providing benchmark data to assess the wall friction model in 3D component of MARS-KS (MARS-MultiD). One is the 2D film flow experiment and the other is the MIDAS (Multidimensional Investigation in Downcomer Annulus Simulation) test. Both experiments were conducted at KAERI (Korea Atomic Energy Research Institute). In the former experiment, liquid film velocity and liquid film thickness were measured and these measured data were compared with the simulation results of MARS-MultiD in order to assess the wall friction model in the code. The comparison result was that wall friction model in MARS-MultiD, H.T.F.S. (Heat Transfer and Fluid Flow Service) correlation underestimates the magnitude of the wall friction force. Then the code was modified by introducing Wallis model instead of H.T.F.S. correlation as a wall friction model in MARS-MultiD and the improved results could be obtained with this modified

C.-J. Choi · J.-H. Yang · H.-K. Cho (✉) · G.-C. Park
Seoul National University, Gwanak-Gu, Seoul, Korea
e-mail: chohk@snu.ac.kr

D.-J. Euh
Korea Atomic Energy Research Institute, Yuseong-Gu, Daejeon, Korea

code. After that, the second experiment, MIDAS test, was simulated with the modified code. In this simulation, ECC bypass fraction was calculated and compared with the experimental data. The result showed that the modified MARS-MultiD predicts the trend of bypass fraction more accurately than the default MARS-MultiD. From these assessment results with two experiments, the necessity of modifying the default wall friction model in MARS-MultiD was confirmed to predict the ECC behavior in downcomer precisely.

Keywords Wall friction model · Two-phase multiplier · Multidimensional module · Direct ECC bypass · MIDAS

1 Introduction

Recently, nuclear reactor safety analysis codes such as RELAP5-3D, TRACE, SPACE, CATHARE, and MARS-KS adopted multidimensional module to simulate multidimensional hydraulic phenomena more precisely in under accident conditions. However, current three-dimensional module uses the same correlations in the existing one-dimensional modules that were developed for one-dimensional pipe flow. Therefore, the constitutive correlations and models may not predict the real phenomena exactly. Furthermore, even the existing one-dimensional correlation cannot predict the one-dimensional pipe flow well. The previous study from Yao and Ghiaasiaan [1] showed that wall friction model in MARS that is targeted constitutive model of this study underestimates the wall shear stress in one-dimensional pipe flow condition (1). Nevertheless, the constitutive models have been validated rarely based on local measurement database that is from the multidimensional phenomena. This insufficient validation of constitutive models led to the present study to simulate multidimensional experiments and validate associated physical models.

In this study, two set of experiments conducted by KAERI were simulated by MARS-MultiD code to validate the wall friction model. Both experiments describe ECC behavior in the upper downcomer region of a PWR which adopt DVI system. First of all, two-dimensional film flow experiment was simulated to assess the H.T. F.S. correlation in default MARS-MultiD. Then the wall friction model was replaced by Wallis model following the reference of Yao and Ghiaasiaan [1]. The modified MARS-MultiD simulated both experiments: two-dimensional film flow and MIDAS test. As a result, the Wallis model is found to be more proper wall friction model than H.T.F.S. correlation for describing ECC behavior in downcomer.

2 Two-Dimensional Film Flow Experiment

2.1 Experimental Facility and Test Conditions

Two-dimensional film flow experiment is a kind of air–water conceptual problem describing direct ECC bypass in upper downcomer (2). The schematics of experimental facility are shown in Fig. 1. The test section was made as an unfolded-shaped acrylic plates describing upper downcomer with a 1/10 reduced scale of APR1400 (Advanced Power Reactor 1400 MWe). The water is injected into the test section through a nozzle and made a two-dimensional liquid film falling down the wall. The air is injected into the test section laterally by air blower. At the end of the test section, the air and water were separated by a separator and the water returned to the storage tank through the drain line at the bottom of the test section and separator. The air exited through the top of the separator.

Yun et al. [3] developed the modified linear scaling method which preserves Wallis parameter between model and prototype, and it was used to define the test conditions. Based on the system code analysis, 0.63 m/s of inlet liquid velocity and 5~15 m/s of lateral air velocity were selected as experimental conditions.

2.2 Local Measurement Methods

2.2.1 Ultrasonic Thickness Gauge for Local Liquid Film Thickness Measurement

The pulse–echo-type ultrasonic thickness gauge defines thickness from the round-trip time of an ultrasonic wave. It is following as Eq. (1)

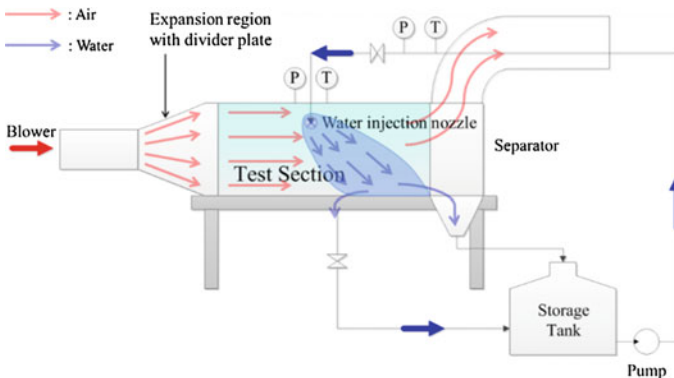


Fig. 1 Schematics of experimental facility

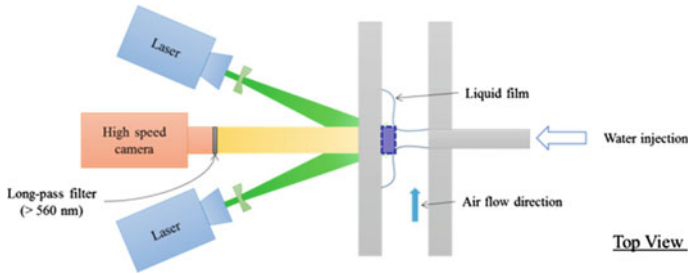


Fig. 2 Depth-averaged PIV method for measurement of liquid film velocity

$$\delta_f = \frac{c_f(T)\Delta t}{2} \tag{1}$$

2.2.2 Depth-Averaged PIV Method for Local Liquid Film Velocity Measurement

In the experiment, depth-averaged PIV concept was developed to measure the local film velocity. The incident laser illuminated the liquid film in the front of the test section in diagonal directions and the averaged velocity data along the depth direction were obtained (Fig. 2).

2.3 Experimental Results

The interaction between the falling liquid film and the lateral air induces momentum transfer through the interface. Figure 3 shows the local liquid film velocity and thickness with different air velocity (0 m/s, 15 m/s).

3 Assessment of Wall Friction Model in MARS-MultiD

3.1 Wall Friction Model in MARS-MultiD

MARS-MultiD code determines wall shear stress from overall two-phase pressure gradient, which is based on a two-phase multiplier approach. One of the two-phase multiplier approaches, H.T.F.S. (Heat Transfer and Fluid Flow Service) correlation (Eq. (3)), is used in MARS-MultiD and it is correlated with empirical data over very broad ranges of phasic volume fractions, phasic flow rates, and flow regimes (5).

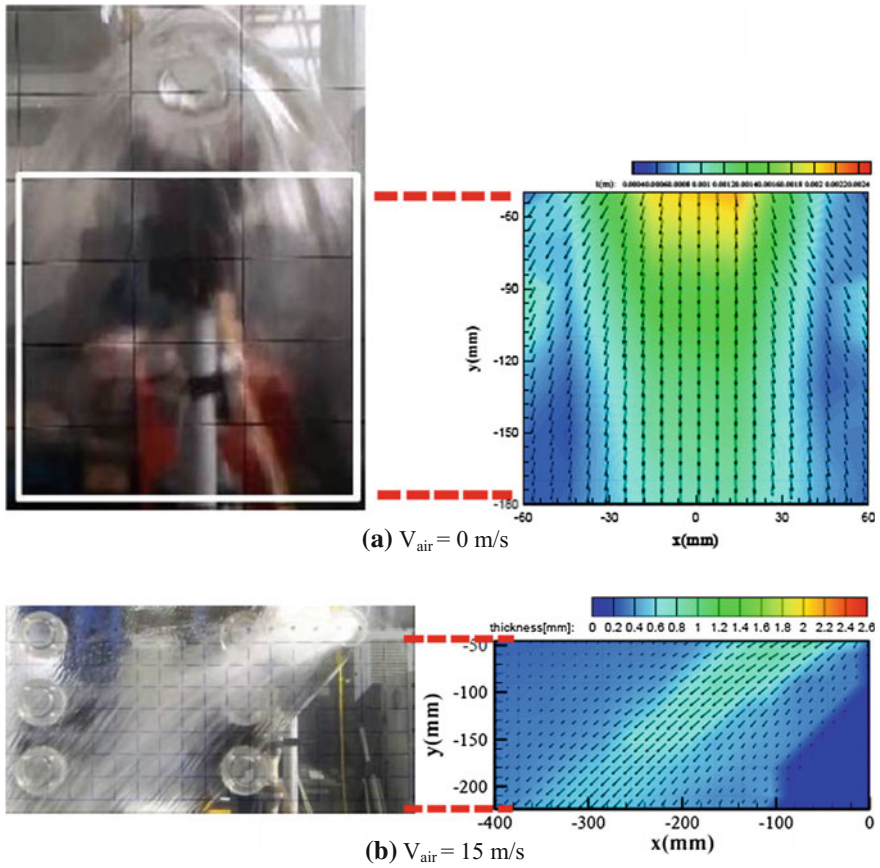


Fig. 3 Local liquid film velocity and thickness

$$\left(\frac{dp}{dx}\right)_{2\phi} = \Phi_f^2 \left(\frac{dp}{dx}\right)_f = \Phi_g^2 \left(\frac{dp}{dx}\right)_g \tag{2}$$

$$\Phi_f^2 = 1 + \frac{C}{\chi} + \frac{1}{\chi^2} \quad \text{for the liquid---lone condition} \tag{3}$$

$$\Phi_g^2 = \chi^2 + C\chi + 1 \quad \text{for the vapor---lone condition} \tag{4}$$

$$\chi^2 = \frac{\Phi_g^2}{\Phi_f^2} = \frac{\left(\frac{\partial P}{\partial x}\right)_f}{\left(\frac{\partial P}{\partial x}\right)_g}$$

where C is the coefficient which is defined with mass flux, G, and Baroczy dimensionless property index, Λ , as follows:

$$2 \leq C = -2 + (28 - 0.3\sqrt{G}) \left(\exp \left[-\frac{(\log_{10} A + 2.5)^2}{2.4 - G \cdot 10^{-4}} \right] \right) \tag{5}$$

where, $\Lambda = \frac{\rho_f}{\rho_g} \left(\frac{\mu_f}{\mu_g} \right)^{0.2}$

3.2 Assessment Results

3.2.1 Modeling of Test Section

The test section used in the two-dimensional film flow experiment was nodalized for calculation with MARS-MultiD code and specific geometrical data were shown in Fig. 4. Numbers of total volumes that consist of the test section are 189 and 21 volumes along the x-direction and 9 volumes along the y-direction. The water is injected into a volume (x, y = 10th, 8th) in the test section, and the air is injected into the right side of the test section.

3.2.2 Calculation Results

First of all, to assess the wall shear stress independently, no air injection case was simulated. The calculation results with MARS-MultiD are presented in Fig. 5. The contour graph of void fraction (Fig. 5a) shows that injected water directly falls down to the bottom of the test section. The marked red box in Fig. 5a corresponds to a region which is between the cold leg and the downcomer in APR1400, and the liquid film velocity and thickness in the region were compared with the experimental results (Fig. 5b c). Overall calculated liquid film velocities were faster than the experimental results, and these discrepancies were maximized at both sides of the control area ($x = \pm 50$ mm). The calculated liquid film thicknesses were thinner

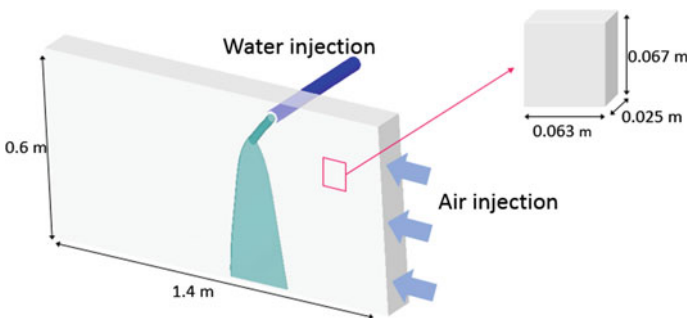


Fig. 4 Nodalization of test section

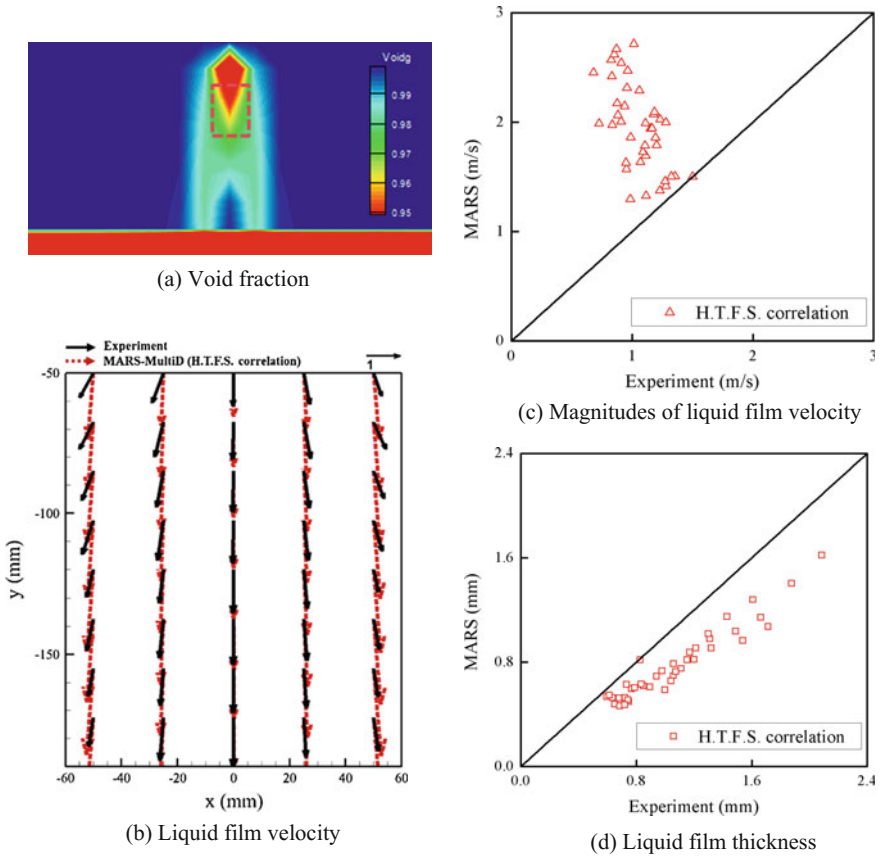


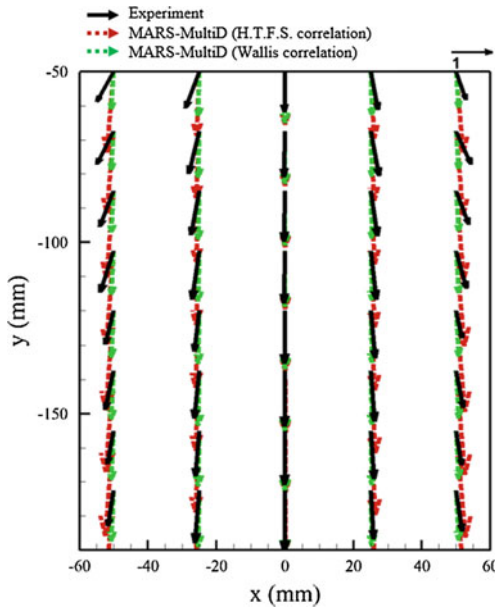
Fig. 5 Calculation results without air injection

than experimental results. This relation between liquid film velocity and thickness is acceptable considering conservation of mass flow. The calculation results show that wall friction model in MARS-MultiD, H.T.F.S. correlation, underestimates the wall shear stress in the two-dimensional film flow condition.

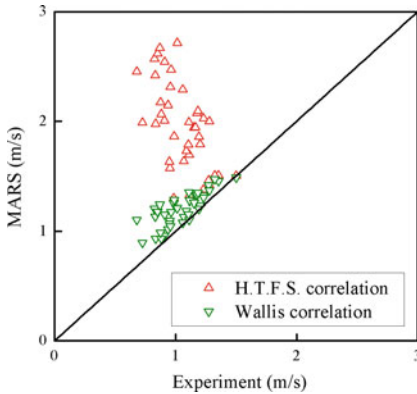
3.3 Modification of Wall Friction Model

3.3.1 Application of Wallis Model

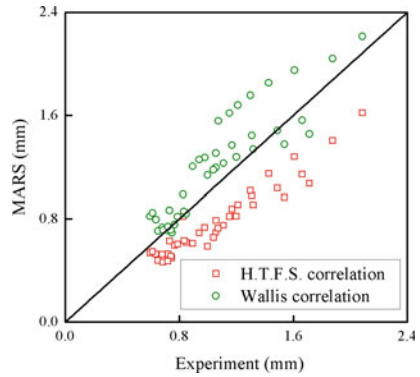
From the assessment results, the necessity of increasing wall shear stress in the MARS-MultiD was confirmed. And there was a study about assessment of two-phase multiplier model from Yao and Giaiaasiaan which proposed to use the



(a) Liquid film velocity



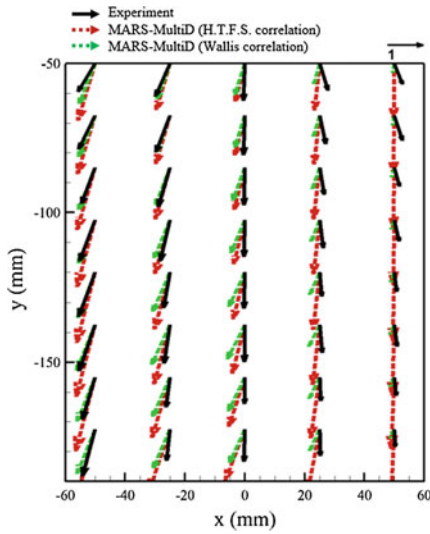
(b) Magnitudes of liquid film velocity



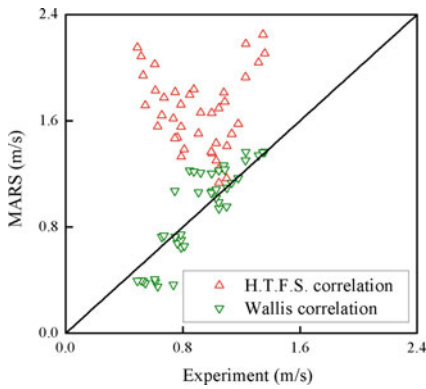
(c) Liquid film thickness

Fig. 6 Calculation results with Wallis correlation ($v_g = 0\text{ m/s}$)

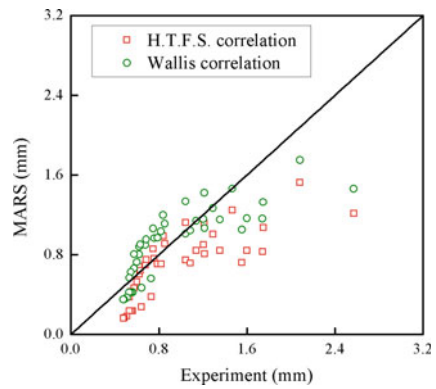
Wallis model rather than Lockhart–Martinelli’s correlation (1). Considering H.T.F.S. correlation is no different from Lockhart–Martinelli’s correlation except for some coefficients, the results from Yao and Ghiaasiaan give the validity to using Wallis model in MARS-MultiD. Besides, SPACE code already adopted Wallis model as a wall friction model in annular flow regime following the reference of Yao and Ghiaasiaan. The Wallis two-phase multiplier is shown in Eq. (6). It is expressed as



(a) Liquid film velocity



(b) Magnitudes of liquid film velocity

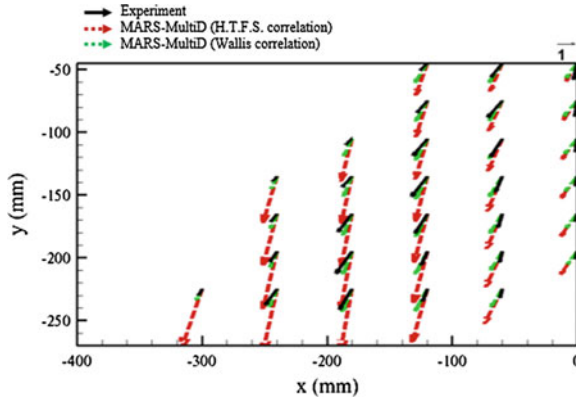


(c) Liquid film thickness

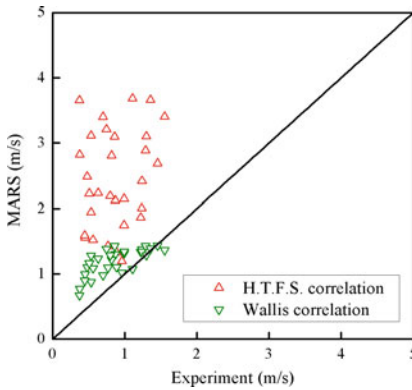
Fig. 7 Calculation results with Wallis correlation ($v_g = 7 \text{ m/s}$)

a function of void fraction. Then the two-phase pressure gradient becomes single-phase pressure gradient due to the elimination of $(1 - \alpha)^2$ term (Eq. (7)). The modified MARS-MultiD was created by adopting this Wallis two-phase pressure gradient.

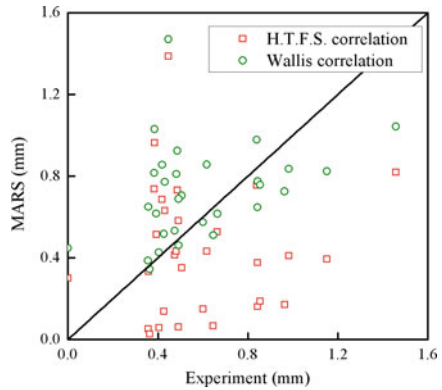
$$\Phi_{f,Wallis}^2 = \frac{1}{(1 - \alpha)^2} \tag{6}$$



(a) Liquid film velocity



(b) Magnitudes of liquid film velocity



(c) Liquid film thickness

Fig. 8 Calculation results with Wallis correlation ($v_g = 11$ m/s)

$$\begin{aligned}
 \left(\frac{dp}{dx}\right)_{2\phi} &= \Phi_{f,Wallis}^2 \left(\frac{dp}{dx}\right)_f \\
 &= \frac{1}{(1-\alpha)^2} \left[\frac{2f_{1\phi,f}(1-\alpha)^2 \rho_f V_f^2}{D} \right] = \frac{2f_{1\phi,f} \rho_f V_f^2}{D}
 \end{aligned}
 \tag{7}$$

3.3.2 Two-Dimensional Film Flow Analysis

Aforementioned two-dimensional film flow calculation was conducted again with modified MARS-MultiD. The comparison results with default MARS-MultiD that uses H.T.F.S. correlation and modified MARS-MultiD that uses Wallis model are

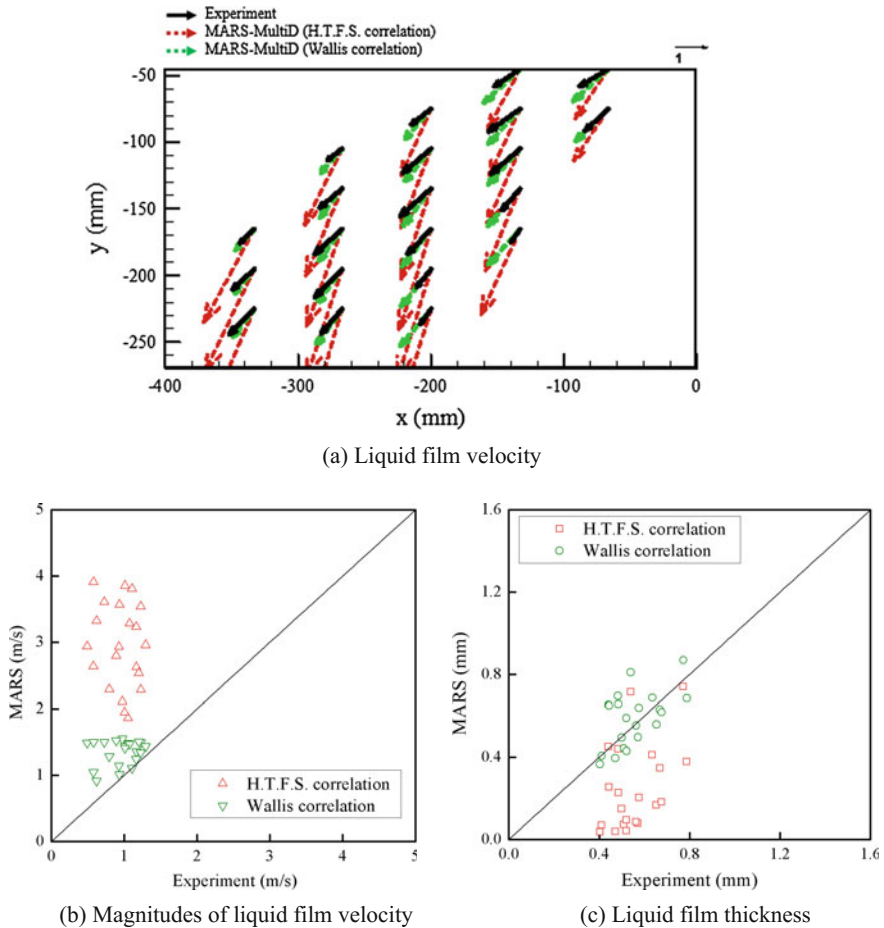


Fig. 9 Calculation results with Wallis correlation ($v_g = 15$ m/s)

presented in Figs. 6, 7, 8 and 9. Table shows the error and error reduction ratio of each of the calculation cases and those are defined as follows (Table 1):

$$(\text{Error}) = \frac{1}{n} \sum_i^n \frac{|\text{Exp.} - \text{Cal.}|}{\text{Exp.}} \tag{8}$$

$$(\text{Error reduction ratio}) = \frac{\text{Previous} - \text{Modified}}{\text{Previous}} \Big|_{\text{error}} \tag{9}$$

In case of no air injection, modified MARS-MultiD predicted the liquid film velocity and thickness better than default MARS-MultiD. In particular, the

significant discrepancies at both sides of the control area were improved. It is because Wallis model calculates the wall shear stress larger than H.T.F.S. correlation. The overall error reduction ratios are 84% for liquid film velocity and 38% for liquid film thickness. In cases of air injection, the results were also improved in modified MARS-MultiD. One thing to be noticed is the direction of the liquid film velocity in the case of 7 m/s air injection. The direction of the liquid film velocity on the right side of the control area was different from the experimental results. In real situation, the injected water is impinged at the wall of the test section and it causes the water to be spread out in all directions. However, current system code such as MARS has a limitation of simulating the impinging phenomenon.

3.3.3 MIDAS Analysis

MIDAS test was simulated with modified MARS-MultiD to confirm the applicability of Wallis model under different conditions from two-dimensional film flow experiment. The experiment is steam–water separate effect test focusing on the multidimensional thermal–hydraulic phenomena in downcomer during the reflood phase of LBLOCA. From the simulation of MIDAS test, ECC bypass fraction (Eq. (10)) was obtained and compared with experimental results and default MARS-MultiD's results. The nodalization of the MIDAS calculation is shown in Fig. 10. There are three test cases, which are DVI-4 injection, DVI-2 injection, and DVI-2&4 injection. DVI-4 nozzle is the nearest to the broken cold leg and DVI-2 nozzle is the farthest from the broken cold leg.

Figure 11 shows the calculated liquid void fraction in DVI-2&4 case at the same time. The liquid void fraction was larger in modified MARS-MultiD than default MARS-MultiD. This result has consistent meaning with the result from

Table 1 Code calculation error

Air velocity	Wall friction model	Film velocity error (%)	Film thickness error (%)
0 m/s	H.T.F.S.	95.89	26.38
	Wallis	15.64	16.26
	Error reduction ratio	84	38
7 m/s	H.T.F.S.	100.78	28.89
	Wallis	16.63	23.38
	Error reduction ratio	83	19
11 m/s	H.T.F.S.	231.92	63.14
	Wallis	54.13	46.66
	Error reduction ratio	77	26
15 m/s	H.T.F.S.	238.42	59.94
	Wallis	51.19	18.25
	Error reduction ratio	79	70

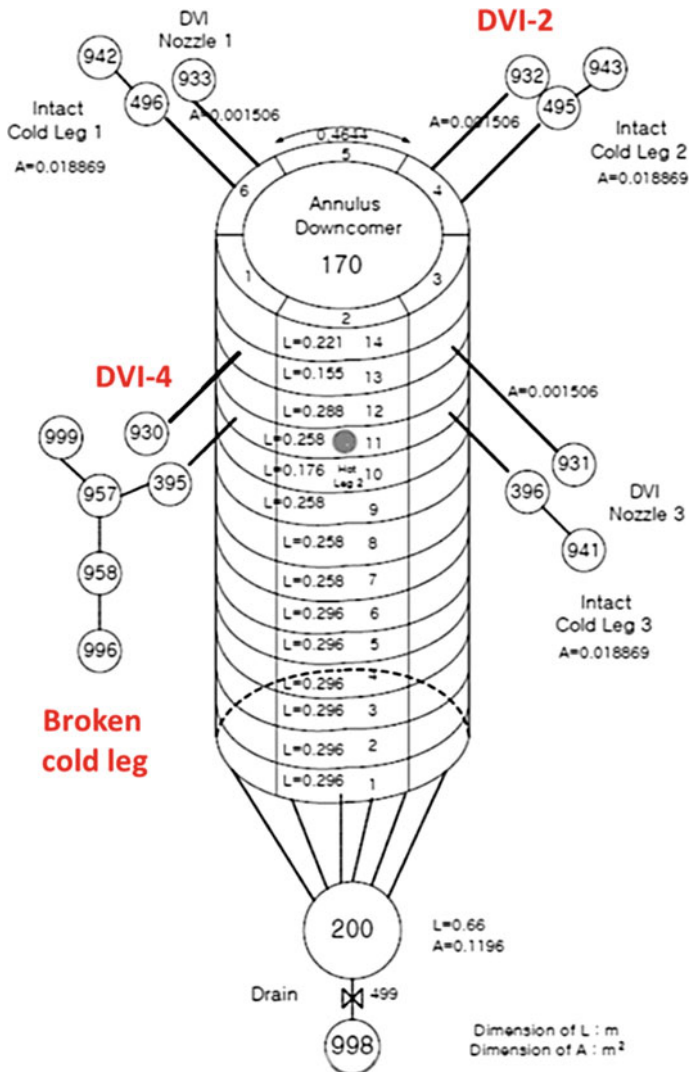


Fig. 10 Nodalization for MIDAS test (4)

two-dimensional film flow analysis that Wallis model predicts the wall shear stress larger than H.T.F.S. correlation.

$$(\text{Bypass fraction}) = 1 - \frac{m_{f,penetration}}{m_{Total,ECC,in} + m_{Total,stm,in} - m_{stm,break}} \quad (10)$$

The comparison of bypass fraction is shown in Fig. 12. At first, in DVI-4 injection case, the bypass fraction from modified MARS-MultiD was relatively

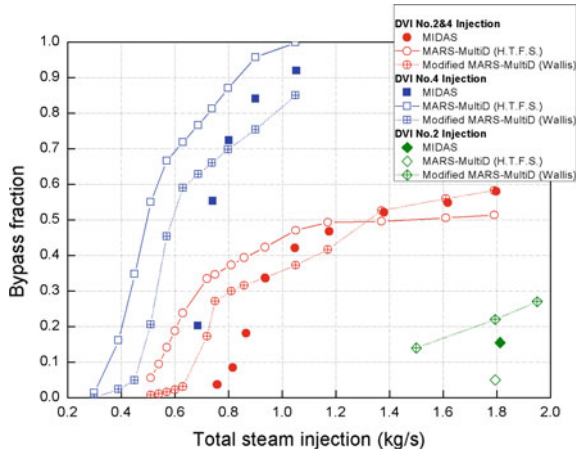


Fig. 11 Liquid void fraction in the case of DVI-2&4 injection

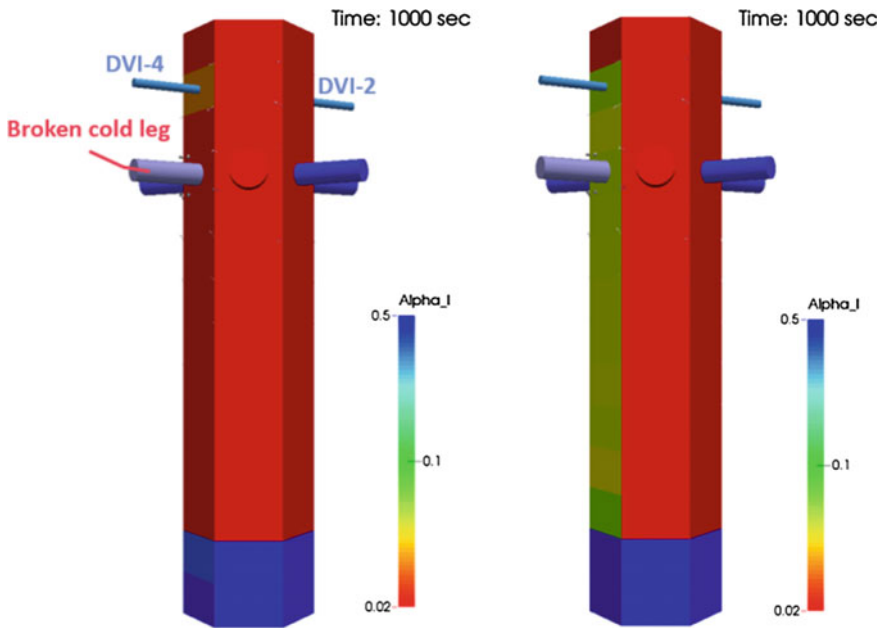


Fig. 12 Comparison of ECC bypass fraction

lower than that from default MARS-MultiD. It is because larger wall shear stress in modified MARS-MultiD holds the liquid film against interfacial shear stress. In DVI-2 injection case, the bypass fraction from modified MARS-MultiD was higher than that from default MARS-MultiD. It can be also understood by the effect of

larger shear stress in modified MARS-MultiD. The curve of DVI-2&4 injection is sum of the curves of DVI-2 and DVI-4 injection. At the high steam flow rate, the trend of increasing bypass fraction agreed well with the experimental results due to the bypass in DVI-2 injection. As a result, Wallis model predicted overall bypass fraction better than H.T.F.S. correlation.

4 Conclusion

To assess the feasibility of the wall friction model in MARS-MultiD, two-dimensional film flow experiment was simulated using MARS-MultiD. The results showed that H.T.F.S. correlation which is the two-phase multiplier model in MARS-MultiD underestimates the wall shear stress. Then the wall friction model was replaced by Wallis model according to the reference of Yao and Ghiaasiaan. After that, the two-dimensional film flow experiment was simulated again with modified MARS-MultiD and improved results were obtained. Additionally, MIDAS test was simulated by modified MARS-MultiD and obtained bypass fraction. Compared with default MARS-MultiD, modified MARS-MultiD got improved results as well. In conclusion, the Wallis model is more proper than H.T.F.S. correlation as a wall friction model to describe ECC behavior in the upper downcomer region.

Acknowledgment This work was supported by the Nation Research Foundation of Korea (NRF) grant funded by the Korea government (MSIP) (No. 2012M2A8A4004176), and the Nuclear Safety Research Program through the Korea Foundation Of Nuclear Safety(KOFONS) grant funded by the Nuclear Safety and Security Commission(NSSC), Republic of Korea (No. 1305011).

References

1. Yao, G.F. and Ghiaasiaan, S.M. "Wall friction in annular-dispersed two-phase flow", Nuclear Engineering and Design, Volume 163, pp. 149–161 (1996)
2. Yang et al. "Experimental study on two-dimensional film flow with local measurement methods", Nuclear Engineering and Design, Volume 294, pp. 137–151 (2015)
3. Yun, B.J. Cho, H.K. Song, C.H. Park, G.C. "Scaling for the ECC bypass phenomena during the LBLOCA reflood phase", Nuclear Engineering and Design, Volume 231, pp. 315–325 (2004)
4. Wallis, G.B. One-Dimensional Two-Phase Flow, pp. 315–329, McGraw-Hill (1969)
5. Korea Atomic Energy Research Institute, MARS Code Manual Volume 1: Code Structure, System Models, and Solution Methods, KAERI/TR-2812/2004 (2007)
6. Korea Atomic Energy Research Institute, MARS Code Manual Volume 4: Developmental Assessment Report, KAERI/TR-3042/2005 (2009).